MMT Symposium

60th Anniversary of Mechanism and Machine Theory

June 21-23, 2026 **Porto, Portugal**

Book of Abstracts

Editors

Paulo Flores | University of Minho

Carlos Fernandes | University of Porto

Filipe Marques | University of Minho

Pedro Marques | University of Porto

João Marafona | University of Porto

Stéphane Portron | University of Porto

MMT Symposium

60th Anniversary of Mechanism and Machine Theory

Book of Abstracts

PROGRAM INCLUDED

Edited by

Paulo Flores ▪ Carlos Fernandes ▪ Filipe Marques

Pedro Marques ▪ João Marafona ▪ Stéphane Portron

June 21-23, 2026 | Porto, Portugal

Title:

BOOK OF ABSTRACTS
Mechanism and Machine Theory Symposium 2026

Edited by:

Paulo Flores, CMEMS, Universidade do Minho, Portugal
Carlos Fernandes, FEUP, Universidade do Porto, Portugal
Filipe Marques, CMEMS, Universidade do Minho, Portugal
Pedro Marques, FEUP, Universidade do Porto, Portugal
João Marafona, INEGI, Universidade do Porto, Portugal
Stéphane Portron, INEGI, Universidade do Porto, Portugal

ISBN:
978-989-49155-0-8

First Edition, June 2026

Copyright © 2026
Departamento de Engenharia Mecânica, Faculdade de Engenharia da Universidade do Porto
Rua Dr. Roberto Frias s/n, 4200-465 Porto, Portugal

Welcome Message

On behalf of the Organizing Committee of the Mechanism and Machine Theory Symposium 2026, we are delighted to welcome all participants.

The inaugural issue of the Mechanism and Machine Theory journal was published in the Spring of 1966, under the editorship of Professor Crossley, the father and the first Editor-in-Chief. In 2026, we celebrate the 60th anniversary of our journal. During this long journey, hundreds of volumes have been published uninterruptedly, featuring innumerable articles by thousands of authors associated with leading research groups in the vast field of mechanism and machine science worldwide. This is the motto behind the organization of the MMT Symposium 2026, which has two primary aims: first, to bring together researchers in the field of mechanism and machine science to exchange ideas and research results; and second, to celebrate the 60 years of the Mechanism and Machine Theory journal, the official IFToMM voice since 1972.

This symposium serves as a meeting point for the mechanisms and machines community and provides an opportunity to exchange high-level, up-to-date information on theory and applications within this scientific domain. The MMT Symposium gathers around 200 submissions from 35 countries and territories, representing most of the active research groups worldwide:

Austria (3)	Germany (9)	Lithuania (2)	Slovakia (1)
Belgium (3)	Greece (3)	Mexico (12)	Slovenia (1)
Brazil (2)	Hong Kong (1)	Netherlands (2)	South Korea (1)
Canada (7)	Hungary (4)	Norway (1)	Spain (15)
China (49)	India (2)	Peru (1)	Switzerland (1)
Colombia (1)	Israel (3)	Poland (6)	Taiwan (1)
Czechia (2)	Italy (23)	Portugal (9)	Turkey (1)
Finland (2)	Japan (6)	Romania (3)	United Kingdom (4)
France (7)	Kazakhstan (5)	Russia (2)	USA (7)

The topics of the meeting include, but are not limited to, biomechanical engineering, cable-driven mechanisms, computational kinematics, dynamics of rotating machinery, gears and transmissions, mechanics of robots and manipulators, mechanism design, mechatronics, micro-mechanisms, multibody dynamics, reconfigurable mechanisms, and theoretical kinematics. Thematic sessions have been organized around these topics to better promote discussion and foster cooperation among participants.

We would like to express our appreciation to all members of the Scientific Committees, who have been instrumental in promoting the symposium and ensuring that all relevant topics in mechanism and machine science are properly addressed. We are also grateful to all staff members, colleagues, and students whose dedicated work has been fundamental to the organization of the MMT Symposium; without whom this event would not have been possible. We also want to thank all authors and presenters for sharing their ideas and results, as well as all participants for making this event a reality. We invite all of you to take an active part in the symposium throughout this three-day journey. Finally, we extend our gratitude to all attendees of the MMT Symposium. We wish each of you not only a pleasant stay in Porto but also, above all, a schedule of unquestionable scientific quality and practical relevance.

Porto, June 2026
Carlos Fernandes
Paulo Flores
Symposium Chairs

Contents

Symposium Organization **6**

Honorary Chair

Symposium Chair

Executive Committee

Honorary Scientific Committee

Scientific Committee

Symposium Information **8**

Symposium Venue

Instructions for Presenters

Wireless Internet Access

Secretariat Open Hours

Name Badges

Coffee-Breaks

Lunches

Working Room

Reuleaux Models Collection Exhibition **12**

Collection Description

Exhibition Location

Social Program **14**

Welcome Reception

Symposium Tour

Symposium Banquet

Scientific Program **17**

Program at a Glance

Daily Sessions

Book of Abstracts **49**

Symposium Organization

Honorary Chair

Andrés Kecskeméthy Germany

Symposium Chairs

Paulo Flores Portugal

Carlos Fernandes Portugal

Executive Committee

Filipe Marques Portugal

Pedro Marques Portugal

João Marafona Portugal

Stéphane Portron Portugal

Timo Bazuin Elsevier

Honorary Scientific Committee

Alfonso Fuentes USA

Andrés Kecskeméthy Germany

Bernard Roth USA

Burkhard Corves Germany

Clément Gosselin Canada

Daniel Condurache Romania

Daniel Martins Brazil

Feng Gao China

Hamid M. Lankarani USA

I-Ming Chen Singapore

J. Michael McCarthy USA

Jian Dai United Kingdom

Jorge Ambrósio Portugal

Jorge Seabra Portugal

Larry Howell USA

Marco Ceccarelli Italy

Ousama Khatib USA

Philippe Velex France

Pier Paolo Valentini Italy

Qiaode Jeffrey Ge USA

Teresa Zielinska Poland

Tian Huang China

Terry Shoup USA

Venkat Krovi USA

Scientific Committee

Alessio Artoni Italy
Ashitava Ghosal India
Carl Nelson USA
Carlos Fernandes Portugal
Chin-Hsing Kuo Australia
Damien Chablat France
Diogo Neto Portugal
Domenico Mundo Italy
Dongming Gan USA
Evangelos Papadopoulos Greece
Filipe Marques Portugal
Gordon R. Pennock USA
Guangbo Hao Ireland
Huafeng Ding China
Huijuan Feng China
Javier Cuadrado Spain
Jia Ma China
José I. Pedrero Spain
Juan A. Carretero Canada
Katia Cavalca Brazil
Ketao Zhang United Kingdom
Leila Notash Canada
Marco Carricato Italy
Marco Cirelli Italy
Mariana R. Silva Portugal
Martin Pfurner Austria
Matteo Verotti Italy
Miguel T. Silva Portugal
Olivier Bruls Belgium
Paulo Flores Portugal
Philippe Wenger France
Qiang Tian China
Raffaele Di Gregorio Italy
Sheng Li USA
Weizhong Guo China
Xianwen Kong United Kingdom
Xin-Jun Liu China
Xinxin Yu Finland
Yukio Takeda Japan
Zhang-Hua Fong Taiwan
Zhihua Zhao China

Symposium Information

Symposium Venue

The MMT Symposium takes place at the Faculty of Engineering of the University of Porto (FEUP), in Porto. For suggestions on what to visit in the city, check out the Porto City Break (3 days | official guide) or Accessible Porto.

The origins of FEUP date back to 1762, with the creation of the Nautical Classroom, which later became the Royal Academy of Marine and Commerce of the City of Porto in 1803. In 1837, it was renamed the *Academia Polytechnica do Porto* (Polytechnic Academy of Porto), considered the first engineering school in the country.

Aerial view of FEUP campus

The MMT Symposium takes place at Building B (Aulas) of the Faculty of Engineering of the University of Porto, Campus da FEUP, Porto, Portugal. See campus map below.

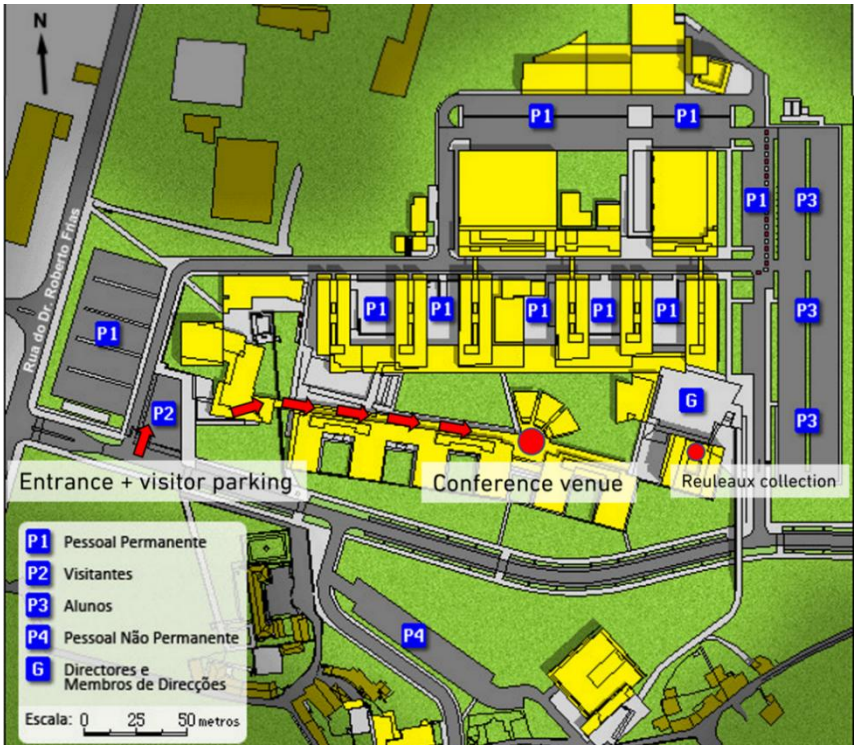

Conference registration location at FEUP

A detailed map of the conference venue is provided below, indicating the session rooms, secretariat, and coffee and lunch breaks areas, all located on the ground floor. Attendees participating in sessions in Room Terry Shoup and Room John Uicker are advised to access these rooms from the first floor.

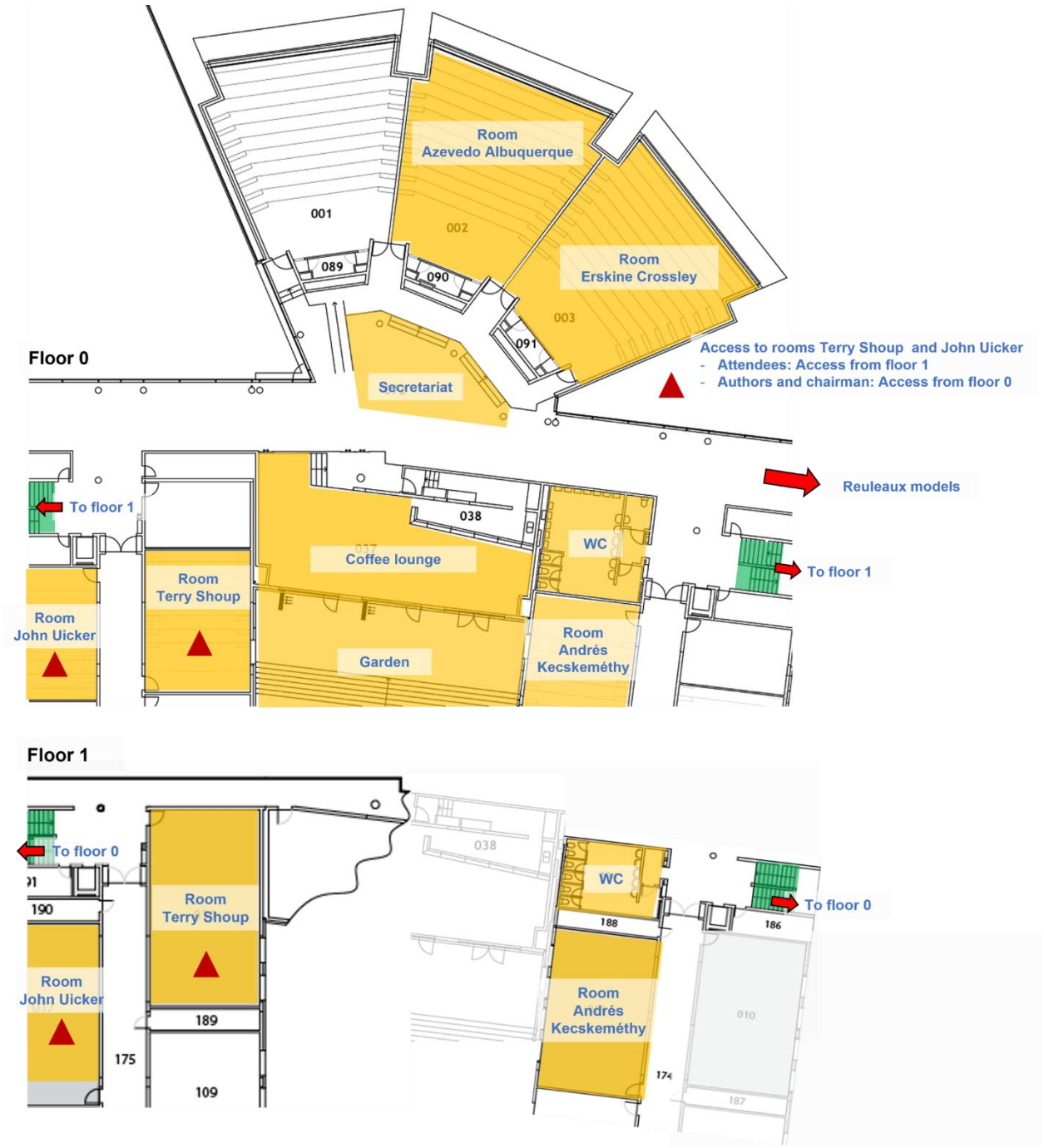

Instructions for Presenters

- Each oral presentation will take 15 minutes, including a 3-minute discussion. The chairperson of each session will manage the time for presentation and discussion.
- Presenters will be informed as the presentation time limit approaches (i.e. 2-minute warning).
- The files required for presentation (PowerPoint, PDF or other) should preferably be sent to mmtpresentations@gmail.com **at least 2 hours before the session starts**. Alternatively, they may be uploaded and tested during the coffee or lunch breaks.
- The symposium rooms are equipped with a Windows PC, with Microsoft Office and Acrobat PDF Reader, connected to a data projector. The use of personal computers is not recommended.
- Technical support will be provided on-site by the MMT Symposium staff (yellow badges).
- Posters should be placed in the assigned location by the symposium organization.

Wireless Internet Access

In order to have wireless connectivity to the Internet you must follow the steps below.

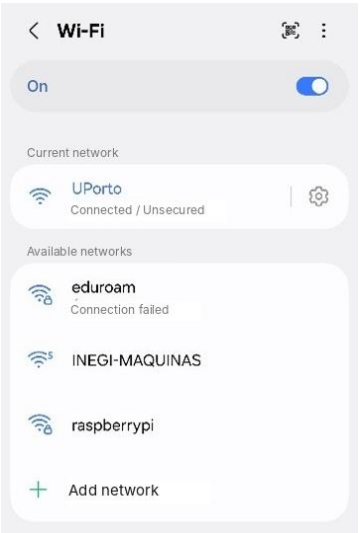

Step 1: Browse available wireless networks and select **UPorto**.

Step 2: Your device will connect directly but notify it needs authentication. Upon clicking on the notification, it brings up a new page. On this page, enter the following credentials:

Username: **FEUPguest_events**

Password: **UPorto.062026**

Step 3: The wireless network connection will be successful.

Secretariat Open Hours

During the Welcome Reception (see Social Program), the secretariat will be located at the entrance of the venue:

- Sunday, June 21, 15h – 18h

During the conference, the secretariat will be located, next to the symposium rooms (see map of the venue):

- Monday, June 22, 7:30 – 16:15
- Tuesday, June 23, 8:00 – 12:30

Name Badges

Please use your name badge at all times, including technical sessions, coffee-breaks, lunches and social events.

Coffee-Breaks

The coffee-breaks will take place in the Coffee Lounge (see map of the venue) next to the symposium rooms and will be open to all participants. Kindly wear your name badge.

Lunches

Lunches will take place at the Coffee Lounge and the adjoining Garden (see map of the venue) and will be open to all participants. Kindly wear your name badge.

Working Room

Room Andrés Kecskeméthy will be available throughout the symposium for participants who need to work or hold meetings. Please see the venue map for its location.

Reuleaux Models Collection Exhibition

Collection Description

The University of Porto houses one of the world's largest and most significant surviving collections of historical Reuleaux kinematic models, comprising 113 pieces.

Still during the XIX century, Azevedo Albuquerque, the late responsible for the course of Rational Mechanics and Kinematics at *Academia Polytechnica do Porto,* introduced the method of Franz Reuleaux. In 1880 The academic board of the *Academia Polytechnica do Porto* acquired the Gustav Voigt kinematics models, which are still owned by FEUP.

Exhibition Location

A free-access exhibition of the collection's models is available throughout the two-day symposium, on the ground floor of FEUP's library (see map of the venue). The exhibition will be open to visitors from 8:30 till 19:30.

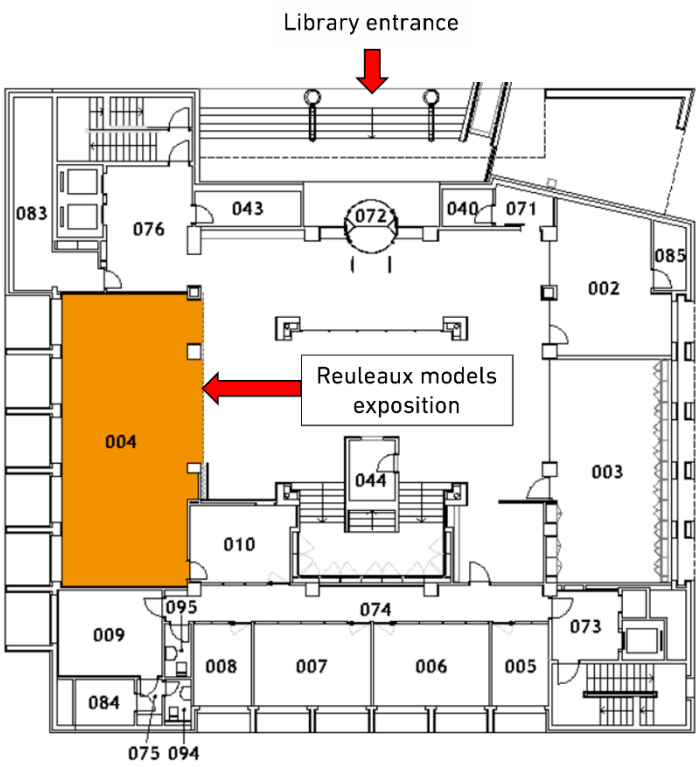

Location:
FEUP Library

Social Program

Welcome Reception – Sunday, June 21 ■ 15:00-18:00

The Welcome Reception and pre-registration will take place at *Círculo Universitário do Porto*. This is one of the noble spaces of the University of Porto. *Círculo Universitário do Porto* is installed in one of the nineteenth-century palaces located in this area of *Campo Alegre*. This XIX century palace is framed within a romantic garden composed of camellias and centenary trees and serves as the official "house" of all of University of Porto *Alumni*. Please make sure to join us to celebrate the start of MMT Symposium while enjoying this noble space with refreshments and a musical performance.

Círculo Universitário do Porto

Location:
Círculo Universitário do Porto
Rua do Campo Alegre, nº 877
4150-180 Porto

How to get there:

By Metro: The nearest metro station is "Casa da Música" and is about a 30-minute walk away. Once on the surface, you can take bus 204 towards "Foz" and get off at "Gólgota" or "Planetário" in Campo Alegre. The Metro pass ("Andante") must be acquired before travelling at any metro station. For more information: https://en.metrodoporto.pt/

By Bus: The University Circle is served by the following bus lines: 200, 204, 207, 902, 903. Regardless of the starting point, the nearest bus stop is "Gólgota" or "Planetário". If you do not have a bus ticket ("Andante"), you can buy one on board. For more information: https://www.itinerarium.pt/en

Port Wine Reception "*Porto de Honra*" - Monday, June 22 ■ 17:45

Historically associated with special occasions, *Porto* wine has naturally found its place in moments of celebration and recognition. Closing the first day of MMT Symposium, this *Porto de Honra* symbolically celebrates 60th anniversary of the inaugural issue of the Journal of Mechanisms, published under the editorship of Professor Francis Rendel Erskine Crossley in the spring of 1966.

University Garden

Location:
FEUP Outer Garden

Curiosity:

The Faculty of Engineering of the University of Porto (FEUP) is the largest of the 14 Faculties that make up the University of Porto, currently one of the most prestigious Higher Education Institutions in Europe. With almost 10,000 students and more than 600 professors and researchers spread over six departments, FEUP is located in a true innovation district, where the strong presence of engineering, health sciences and entrepreneurship is highly conducive to the innovation process.

São João do Porto MMT Symposium Banquet – Tuesday, June 23 ■ 19:00

The *São João* (St. John) MMT Symposium Banquet will take place at *Hilton Porto Gaia*. The venue is very close to the heart of St. John's festival. This Festival has been celebrated for hundreds of years, at least since the XIV century. On St. John's day the city is boiling with activity from dusk to dawn. Hundreds of thousands of people flood the historic streets of Porto to celebrate and share.

If you go by Metro, get off at the "Jardim do Morro" metro station and enjoy one of the best views of Porto. Afterwards, walk down the hill for a small walk along the Douro River before finally reaching the venue.

Hilton Porto Gaia

Location:
Hilton Porto Gaia
Rua de Serpa Pinto 124,
4400-307 Vila Nova de Gaia

How to get there:

By Metro: The nearest metro station is "Jardim do Morro" **Please buy the Metro pass ("Andante") at least one day in advance**. Available at any metro station. http://www.metrodoporto.pt

Curiosity:

The Hilton Porto Gaia is the result of an extensive and meticulous refurbishment of former Port wine warehouses in the historic district of Vila Nova de Gaia and opened its doors to the public in September 2021.

After the *São João* MMT Symposium Banquet is closed It is suggested that MMT Symposium participants enjoy the St. John's Festival fireworks.

Hot air ballons

São João Fireworks

MMT Symposium

60th Anniversary of Mechanism and Machine Theory

SCIENTIFIC PROGRAM

June 21-23, 2026 | Porto, Portugal

Program at a Glance

Time	Sunday, June 21
15:00-18:00	**WELCOME RECEPTION AND PRE-REGISTRATION** – Círculo Universitário do Porto

Time	Monday, June 22			
07:30	REGISTRATION			
08:30	**OPENING CEREMONY** – Room Azevedo Albuquerque			
08:50	**KEYNOTE LECTURE I** – PEDRO CAMANHO – Room Azevedo Albuquerque			
09:30	**TECHNICAL SESSIONS I**			
	Robots and Manipulators Room Azevedo Albuquerque	**Multibody Dynamics** Room Erskine Crossley	**Mechanism and Machine Design** Room Terry Shoup	**Computational Kinematics** Room John Uicker
11:00	Coffee-Break and Poster Session			
11:30	**TECHNICAL SESSIONS II**			
	Robots and Manipulators Room Azevedo Albuquerque	**Multibody Dynamics** Room Erskine Crossley	**Control and Mechatronics** Room Terry Shoup	**Gears and Transmissions** Room John Uicker
13:00	Lunch			
14:00	**TECHNICAL SESSIONS III**			
	Robots and Manipulators Room Azevedo Albuquerque	**Miscellaneous Online Session** Room Erskine Crossley	**Nonlinear Systems and Vibration** Room Terry Shoup	**Biomechanics** Room John Uicker
15:45	Coffee-Break and Poster Session			
16:15	**TECHNICAL SESSIONS IV**			
	Robots and Manipulators Room Azevedo Albuquerque	**Mechanism and Machine Design** Room Erskine Crossley	**Control and Mechatronics** Room Terry Shoup	**Gears and Transmissions** Room John Uicker
17:45	**PORT WINE RECEPTION** – University Garden			

Time	Tuesday, June 23			
08:00	Registration			
09:00	**Technical Sessions V**			
	Computational Kinematics Room Azevedo Albuquerque	**Multibody Dynamics** Room Erskine Crossley	**Gears and Transmissions** Room Terry Shoup	**Compliant Mechanisms** Room John Uicker
10:45	Coffee-Break and Poster Session			
11:15	**Technical Sessions VI**			
	Computational Kinematics Room Azevedo Albuquerque	**Multibody Dynamics** Room Erskine Crossley	**Gears and Transmissions** Room Terry Shoup	**Compliant Mechanisms** Room John Uicker
13:00	Lunch			
14:00	**Technical Sessions VII**			
	Rotating Machinery Room Azevedo Albuquerque	**Biomechanics** Room Erskine Crossley	**Mechanism and Machine Design** Room Terry Shoup	**Robots and Manipulators** Room John Uicker
15:30	**KEYNOTE LECTURE II** – Paulo Flores – Room Azevedo Albuquerque			
16:00	**AWARDS AND CLOSING CEREMONY** – Room Azevedo Albuquerque			
19:00	**BANQUET** – Hilton Porto Gaia			

Monday, June 22

07:30	REGISTRATION

08:30–08:50	**OPENING CEREMONY** – Room Azevedo Albuquerque

KEYNOTE LECTURE I	**Monday, June 22 • 08:50 – 09:30**
Room Azevedo Albuquerque	CHAIR **Paulo Flores**

Time	Presenting Author	Title
08:50	Pedro Camanho	**Design and analysis of composite systems across the scales based on physical and data-driven models**

TECHNICAL SESSIONS I – A	**Monday, June 22 • 09:30 – 11:00**

ROBOTS AND MANIPULATORS

Room Azevedo Albuquerque	CHAIR **Tan Sy Nguyen**

Time	ID	Presenting Author	Title
09:30	38	Joshua Flight	**Feasible wrench sets of redundant parallel manipulators** Joshua Flight; Clément Gosselin
09:45	60	Yi Han	**Design of a cable-driven hybrid serial-parallel skeletal morphing wing for hypersonic aircraft** Yan Wang; Hui Yang; Siqiang Xing; Yi Han
10:00	70	Xiaofei Liu	**Type synthesis and performance optimization of 2R1T parallel mechanisms with third-order actuation redundancy** Xiaofei Liu; Yu Wang; Zongqiang Feng; Jiantao Yao; Yongsheng Zhao
10:15	158	Donglai Xu	**A bipedal robot based on multi-loop coupled parallel leg mechanism** Donglai Xu; Sheng Guo; Fuqun Zhao; Xiaodong Jin; Marco Carricato
10:30	195	Dmitry Malyshev	**Method for optimization of planar parallel robots taking into account singularities based on automatic derivation of kinematic dependencies** Larisa Rybak; Dmitry Malyshev; Dmitry Dyakonov
10:45	201	Kevin Gaitan	**Actuation redundancy management of the 3-DOF PercuCob-RCM parallel manipulator** Kevin Gaitan; Juan Sandoval; Stéphane Caro

TECHNICAL SESSIONS I - B	Monday, June 22 • 09:30 – 11:00	
MULTIBODY DYNAMICS		
Room Erskine Crossley	CHAIR **Hamid Lankarani**	
Time	ID	Presenting Author	Title
09:30	1	Basilio Lenzo	**How to obtain analytical solutions for vehicle phase plane equilibrium and stability analysis** Basilio Lenzo; Mariagrazia Tristano
09:45	20	Angelo Domenico Vella	**Lumped–mass tyre modelling for road–envelope analysis** Angelo Domenico Vella; Alessandro Vigliani
10:00	131	Kun Wang	**DEM-multibody coupling simulations of spring tires interacting with granular terrain** Kun Wang; Qiang Tian; Haiyan Hu
10:15	88	Kaiming Zhang	**A coupled multibody–granular dynamics framework for high-fidelity simulation of lunar robot locomotion** Kaiming Zhang; Yang Yu; Zhijun Song; Jingchang Xie; Kunen Peng
10:30	114	Máté Antali	**Analysis and improvements of the classical model of railway wheelset dynamics** Máté Antali
10:45	189	Xinxin Yu	**Comparison of different wheel-rail constraint-based contact approaches** Erik Snellman; Xinxin Yu

TECHNICAL SESSIONS I - C			Monday, June 22 • 09:30 – 11:00
MECHANISM AND MACHINE DESIGN			
Room Terry Shoup			CHAIR **Shane Johnson**
Time	ID	Presenting Author	Title
09:30	56	María Ramírez Berasategui	**Bridging theory and reality: Integrating VVUQ standards and low-cost experimental analysis in mechanism synthesis education** Ramon Gutiérrez Moizant; Fernando Viadero-Monasterio; Miguel Meléndez-Useros; María Ramírez-Berasategui; Daniel García-Pozuelo Ramos
09:45	26	Benedict Röder	**Neural density estimation for the synthesis of crank-driven four-bar mechanisms** Benedict Röder; Henrik Ebel; Peter Eberhard
10:00	188	Ibai Ulacia	**DMLab: Design and modelling of machine elements** Ibai Ulacia; Aurea Iñurritegui; Aitor Arana; Jon Larrañaga
10:15	83	André Pedroso	**Mechanical development of an automatic equipment for bioplastic film testing** David Pinto; Raul Campilho; José Barbosa; Filipe Lopes; Francisco da Silva; David Almeida; André Pedroso
10:30	91	Shiwei Liu	**Cuboid-shaped Bricard-Sarrus metastructures with constant-zero stiffness** Shiwei Liu, Long Li; Shengnan Lyu; Xilun Ding
10:45	140	Sajjad Keshtkar	**Spherical four-bar control moment gyroscope: Concept and rotating-torque generation** Sajjad Keshtkar; Hirohisa Kojima; Francisco Geu Flores; Wojciech Kowalczyk

TECHNICAL SESSIONS I - D	Monday, June 22 • 09:30 – 11:00

COMPUTATIONAL KINEMATICS

Room John Uicker	CHAIR **Manfred Husty**

Time	ID	Presenting Author	Title
09:30	115	Robin Chhabra	**Geometry of multibody motion: An intrinsic lie groupoid approach** Robin Chhabra; Yael Karshon; M. Reza Emami
09:45	124	Daniel Condurache	**Higher-order Cayley transforms and shadow Rodrigues dual vectors: A unified framework for rigid-body kinematic** Daniel Condurache; Mihail Cojocari
10:00	68	Ilie Talpasanu	**The matroid method in computational mechanics of mechanisms** Ilie Talpasanu; Alexandru Talpasanu
10:15	16	Huiping Shen	**Topology design and performance analysis of parallel mechanisms with fewer joints** Ju Li; Yue Guo; Huiping Shen
10:30	87	Wanting Wang	**Tolerance analysis of mechanisms with unilateral constraints** Wanting Wang; Zhihua Zhao
10:45	192	Giorgio Figliolini	**Kinematic geometry and envelope curves of vehicles when moving along linear tractrices** Giorgio Figliolini; Chiara Lanni; Jorge Angeles

11:00 - 11:30	Coffee-Break and Poster Session

TECHNICAL SESSIONS II – A	Monday, June 22 • 11:30 – 13:00

ROBOTS AND MANIPULATORS

Room Azevedo Albuquerque	CHAIR **Olivier Bruls**

Time	ID	Presenting Author	Title
11:30	109	Haoju Wen	**Systematic design of reconfigurable hybrid origami robots** Haoju Wen; Wenjun Chris Zhang
11:45	146	Karol Muñoz	**Comparison of prism-based tensegrity joint architectures** Karol Muñoz; Mathieu Porez; Philippe Wenger
12:00	105	Aislinn Mcaleenan	**Tolerance design and metrology-assisted fabrication and assembly of parallel robots for high precision surgical operations** Aislinn Mcaleenan; Yan Jin; Dan Sun; Johnny Moore
12:15	74	Yukio Takeda	**Planar parallel mechanism driven along a curved guide** Yukio Takeda; Shota Fujisaka; Masashi Yoshii; Ryota Shioya; Ming Jiang; Koichi Kato; Mathias Huesing; Burkhard Corves; Tomoya Tanaka; Shogo Miura
12:30	186	Anatol Pashkevich	**Equivalent transformations of MSA- and VJM-based stiffness models** Alexandr Klimchik; Anatol Pashkevich
12:45	175	Qizhi Meng	**Enhancing distal motion-force interaction performance of articulated-platform parallel mechanisms via internal parameter design of closed-loop passive limbs** Qizhi Meng; Burkhard Corves; Andrés Kecskeméthy

TECHNICAL SESSIONS II – B	Monday, June 22 • 11:30 – 13:00	
MULTIBODY DYNAMICS		
Room Erskine Crossley	CHAIR **Alessandro Cammarata**	
Time	ID	Presenting Author	Title
11:30	85	Roberto Guida	**Introduction to discrete flexible multibody modelling approach for ball bearings with deformable rings** Roberto Guida; Andrea De Martin
11:45	203	Jorge Ambrósio	**Impact of new joining processes of new materials of the structure of an automobile on its vehicle handling dynamics** Jorge Ambrósio; Pedro Millan; Lucas da Silva
12:00	174	Jozef Bucha	**Virtual model of a bus using the FMI standard for co-simulation with Matlab/Simulink** Jozef Bucha; Ján Danko; Tomáš Milesich
12:15	159	Pavel Polach	**Approaches to modeling leaf springs in railway vehicles and their validation** Pavel Polach; Michal Hajžman; Ondřej Skála; Kamil Šimeček
12:30	3	Yongjun Pan	**Optimizing ride comfort in four-wheel hub-motor electric vehicles via multibody dynamics and multi-objective algorithms** Ling Ma; Yongjun Pan; Wei Liu; Aki Mikkola
12:45	199	Paulo Flores	**A geometric characterization for performance evaluation of lubricated clearance joints in multibody systems** Bassam Alshaer; Paulo Flores; Hamid Lankarani

TECHNICAL SESSIONS II – C	Monday, June 22 • 11:30 – 13:00	
CONTROL AND MECHATRONICS		
Room Terry Shoup	CHAIR **Evangelos Papadopoulos**	
Time	ID	Presenting Author	Title
11:30	112	Jason Bettega	**Collocated control of an underactuated cable-driven parallel robot through disturbance observer and inverse dynamics** Jason Bettega; Salvatore Marrazzo; Dario Richiedei; Alberto Trevisani
11:45	178	Xinrong Li	**Multibody dynamics-based feedforward control strategies for wellbore trajectory tracking in directional drilling systems** Xinrong Li; Kejie Wang; Jiaqi Chen; Ningyu Wang; Gexue Ren
12:00	33	Nathanaël Jarrassé	**Controller design for velocity transmission of Bowden-cable actuators** Yaodong Lu; Pablo Nocito; Yannick Aoustin; Sébastien Mick; Qiaoling Meng; Hongliu Yu; Nathanaël Jarrassé
12:15	187	Bálint Bodor	**Stability investigation of the model predictive controller: A semi-analytical approach** Bálint Bodor; Szabolcs Berezvai
12:30	200	Karol Zielonka	**Modeling, simulation and sensitivity testing of automotive automatic control systems due to backlash and friction** Dariusz Żardecki; Mirosław Gidlewski; Marek Jaśkiewicz; Leszek Jemioł; Karol Zielonka
12:45	106	Ricardo de Castro	**Safe and robust autonomous drifting of vehicles** Ricardo de Castro; Basilio Lenzo; Marco Adami; Marco Cortese; Marco Cazzola; Giovanni Righetti, Tommaso Belluco; Matteo Massaro; Berrydal Moshe; Justin Arroyo

TECHNICAL SESSIONS II – D	Monday, June 22 • 11:30 – 13:00

GEARS AND TRANSMISSIONS

Room John Uicker	CHAIR **Domenico Mundo**

Time	ID	Presenting Author	Title
11:30	40	José I. Pedrero	**Analysis of the contact stress of beveloid helical gears with parallel axes** Miryam B. Sánchez; Giovanni Mottola; Miguel Pleguezuelos; Alfonso Fuentes-Aznar; Jose I. Pedrero; Marco Carricato
11:45	45	Hui Guo	**A calculation method for the asymmetric helical gear meshing stiffness considering the slice coupling effect** Zhihui Hou; Hui Guo; Shengwen Hou; Xiaoping Ran; Yuhang Ruan
12:00	82	Alfonso Fuentes	**Simulation and validation of the transmission error and meshing stiffness of internal helical gears with profile modification** Miguel Pleguezuelos; Miryam B. Sánchez; Andrés F. Hidalgo; Jose I. Pedrero; Alfonso Fuentes
12:15	79	Francisco Ricardo	**Artificial neural network for modelling gear mesh stiffness** Francisco Ricardo; João Marafona; Stéphane Portron; Carlos Fernandes; Pedro Marques; João Tavares
12:30	183	Mattin Maiztegui	**Accurate real contact area computation of anisotropic rough surfaces** Mattin Maiztegui; Jon Larrañaga; Ibai Ulacia
12:45	154	Siyuan Liu	**A universal design and gear surface quality control methodology of face-milled hypoid gear with large range of offset and shaft angle** Siyuan Liu; Chaosheng Song; Caichao Zhu

13:00 - 14:00	Lunch

TECHNICAL SESSIONS III - A	Monday, June 22 • 14:00 – 15:45		
ROBOTS AND MANIPULATORS			
Room Azevedo Albuquerque		CHAIR **Marco Carricato**	
Time	ID	Presenting Author	Title
14:00	101	Pietro Davide Maddio	**Enhancing snake robot stiffness in confined spaces: Pose optimization with obstacle avoidance** Yinjun Zhao; Pietro Davide Maddio; Alessandro Cammarata; Rosario Sinatra; Yingzhong Tian; Fengfeng Xi
14:15	147	Hung Hon Cheng	**Cable anchor sensitivity analysis for reconfigurable cable robots** Hung Hon Cheng; Josie Hughes
14:30	100	Olivier Bruls	**An ALE-SE(3) beam formulation for the simulation of cable-driven soft robots** Olivier Devigne; Olivier Bruls
14:45	165	Erwei Li	**Configuration design and continuous workspace feasibility analysis of an over-redundant cable-driven refueling mechanism based on a shipborne gantry crane** Zhiwei Jia; Erwei Li; Hansen Ma
15:00	152	Jorge Francisco Aznar Ortega	**Kinematics and workspace of a cuspidal modular parallel robot** Adrián Peidró; Paula Mollá-Santamaría; Jorge Francisco Aznar Ortega; Luis Miguel Jiménez; Oscar Reinoso
15:15	141	Bogdan Gherman	**Thermal-based stiffness modulation of flexible surgical instruments for robot-assisted minimally invasive surgery** Doina Pisla; Bogdan Gherman; Ionut Zima; Alexandru Pusca; Adrian Pisla; Marius Miclaus; Calin Vaida; Damien Chablat
15:30	102	Aikaterini Smyrli	**Morphological intelligence in passive dynamics: A design investigation of biomechanically-inspired bipedal robots** Aikaterini Smyrli; Evangelos Papadopoulos

TECHNICAL SESSIONS III - B	Monday, June 22 • 14:00 – 15:15

MISCELLANEOUS - ONLINE SESSION

Room Erskine Crossley	CHAIR **João Marafona**

Time	ID	Presenting Author	Title
14:00	27	Dongming Gan	**Dynamic energy-optimal anchor configuration on general convex surfaces, enabled by geodesic-based force-consistent modeling** Lei Jin; Dongming Gan; Maitha Alqaydi; Mohamed Abduljawad; Yahya Mohammed; Tarek Taha; Ahmad Alattar
14:15	130	Akshay Menon	**Kinematic and static analysis of a cable driven continuum robot** Akshay Menon; Ashitava Ghosal
14:30	144	Madhu Raghavan	**Zero stiffness mechanism for constant compression pressure on prismatic and pouch cells in battery modules** Madhu Raghavan; Chinmaya Patil; Shashank Ramesh
14:45	148	Konstantin Ivanov	**Creation of a class of self-regulating mechanisms** Konstantin Ivanov
15:00	120	Yogesh Pratap Singh	**A Gough-Stewart platform based external fixation system for deformity correction in orthopedics** Yogesh Pratap Singh; Kiran Saldanha; Ashitava Ghosal
15:15	133	Raul Alberto Bernal-Orozco	**Modeling and control-oriented simulation of DBD plasma actuators for aerodynamic performance enhancement** Raul Alberto Bernal-Orozco; Oliver Marcel Huerta-Chavez; Genaro Carreon-Carrera

TECHNICAL SESSIONS III - C			Monday, June 22 • 14:00 – 15:45
NONLINEAR SYSTEMS AND VIBRATION			
Room Terry Shoup			CHAIR **Mattia Battarra**
Time	ID	Presenting Author	Title
14:00	128	Witold Luty	**Unsteady-state tire cornering under dynamic normal load variations** Witold Luty; Karol Zielonka
14:15	135	Tigran Parikyan	**Modal analysis of engines and powertrains with AVL EXCITE™: An overview** Tigran Parikyan
14:30	142	Edgar Eliseo Franco Ortiz	**Ring-down analysis using a three-axis accelerometer for a trajectory with a trapezoidal velocity profile** Edgar Eliseo Franco Ortiz; Carlos Rodriguez Donate; Jacob Gonzalez Villagomez; Luis Manuel Ledezma Carrillo
14:45	155	Zbyněk Šika	**Optimization of nonlinear active absorbing for compliant planar mechanisms** Zbyněk Šika; Jan Krivošej; Jakub Švadlena
15:00	167	Leonel Maximiliano Gomez Villarejo	**Inverse acoustic fingerprinting for non-invasive identification of precessing vortex core in combustion chambers** Leonel M. Gomez Villarejo; Oliver M. Huerta Chavez; Raul A. Bernal Orozco; Luis A. Rodriguez Salinas; Gibran J. Garnica Castro
15:15	25	Yizhar Or	**Experiments and analysis of twistcar-type robots** Yizhar Or; Rom Levy; Anna Zigelman; Ari Dantus; Zitao Yu
15:30	123	Hanna Zsofia Horvath	**The effect of contact force models on the stability of two-wheeled trailers with a simplified model** Hanna Zsofia Horvath; Mate Antali

TECHNICAL SESSIONS III - D	Monday, June 22 • 14:00 – 15:45	
BIOMECHANICS		
Room John Uicker	CHAIR **Nicola Sancisi**	
Time	ID	Presenting Author	Title
14:00	18	Nursultan Zhetenbayev	**Torque-angle modeling of a two-degree-of-freedom ankle prosthesis** Zhanar Bigaliyeva; Sayat Akhmejanov; Nursultan Zhetenbayev; Aidos Sultan; Arman Uzbekbayev; Ozhikenov Kassymbek; Yerkebulan Nurgizat; Abu Alim Ayazbay; Gani Sergazin
14:15	47	Aidos Sultan	**Design and prototype development of a research-oriented passive foot prosthesis with a dual-spring elastic mechanism and shock-absorbing sole** Nursultan Zhetenbayev; Aidos Sultan; Ussama Abujazar; Ozhikenov Kassymbek; Yerkebulan Nurgizat; Gani Sergazin
14:30	97	Lorenzo Maggi	**Design and validation of an impedance-controlled robotic system for biomechanical joint characterization** Lorenzo Maggi; Matilde Tomasi; Nicola Secciani; Benedetto Allotta; Alessio Artoni
14:45	122	Christian Mele	**Design of a rigid and compliant inverted 4-bar mechanism to emulate polycentric misalignment for lower-limb exoskeleton mannequins** Christian Mele; Jhilik Bose; James Tung; Katja Mombaur
15:00	126	Linan Yin	**Influence of human body variability on seat-to-head transmissibility** Linan Yin; Jianqiao Guo; Yanfei Jin; Jingwei Meng; Qiang Tian; Haiyan Hu
15:15	161	Sérgio Gonçalves	**Gravity compensation mechanisms for passive and quasi-passive exoskeletons** Marla Weltken; Sérgio Gonçalves; Miguel Tavares da Silva
15:30	80	Marko Ackermann	**Assessing the tipping over risk of rollators during standing up in younger and older adults** Marko Ackermann; Katja Mombaur

15:45 - 16:15	Coffee-Break and Poster Session

TECHNICAL SESSIONS IV - A			Monday, June 22 • 16:15 – 17:45
ROBOTS AND MANIPULATORS			
Room Azevedo Albuquerque			CHAIR **Doina Pisla**
Time	ID	Presenting Author	Title
16:15	22	Shaoheng Hu	**ODE-based dynamic modeling of multi-loop robots and its application to MPC** Shaoheng Hu; Xianwen Kong; Guodong Yin
16:30	52	Zvi Chapnik	**Sample-efficient learning of body-environment interaction of an underactuated system** Zvi Chapnik; Yizhar Or; Shai Revzen
16:45	64	Yi Han	**Design and kinematics of modular variable-stiffness skeleton mechanism for Z-folded morphing wing based on waterbomb-origami** Yi Han; Hui Yang; Yan Wang
17:00	116	Xiaofei Liu	**Design and kinematic characteristic analysis of a novel redundantly actuated parallel mechanism for high-precision grinding** Yanhua Tang; Yaning Li; Yu Wang; Xiaofei Liu; Jinyang He; Yuantao Bu
17:15	69	Jian Zheng	**A novel series elastic actuator with mechanical stoppers for Assist-As-Needed in sit-to-stand assistance** Ming Jiang; Jian Zheng; Seunghyun Kim; Hiroto Miyatake; Kotaro Muramatsu; Jun Nango; Yukio Takeda
17:30	164	Esdras S. da Silva	**Experimental validation of a mechanically synchronized modular legged robot for in-pipe locomotion** Esdras S. da Silva; Rafael W. Duarte; Gustavo Queiroz; Duber F. Vergara; Gustavo V. Souza; Henrique Simas; Tiago C. Pinto; Daniel Martins

TECHNICAL SESSIONS IV - B	Monday, June 22 • 16:15 – 17:45

MECHANISM AND MACHINE DESIGN

Room Erskine Crossley	CHAIR **Marco Cirelli**

Time	ID	Presenting Author	Title
16:15	8	Guanglei Wu	**FEA-based structural design of a serial variable stiffness joint** Guanglei Wu; Bin Niu
16:30	32	Yangyang Xiao	**Multi-lattice topology optimization with competitive weighting and penalty-driven lattice selection under dynamic loading** Yangyang Xiao; Shu Li; Nikos D. Lagaros; Jie Geng
16:45	76	Shane Johnson	**Modeling and robustness characterization of large-stroke QZS mechanisms under ultra-low frequency excitation** Shun Bi; Shane Johnson
17:00	121	Maria Cristina Valigi	**A novel gripper for space debris collection** Silvia Logozzo; Sebastiano Angelella; Maria Cristina Valigi
17:15	153	Fengfeng Xi	**Kinematic modeling of a metamaterial system for morphing structure applications** Aaron Benatar; Fengfeng Xi; Amitabha Ghosh
17:30	23	Rico Zöllner	**Tribology in material handling: Winches, nonlinear rope friction, fiber ropes, fused filament fabrication components** Rico Zöllner; Raimond Hofmann; Martin Anders; Thorsten Schmidt

TECHNICAL SESSIONS IV - C	Monday, June 22 • 16:15 – 17:45

CONTROL AND MECHATRONICS

Room Terry Shoup	CHAIR **Sajjad Keshtkar**

Time	ID	Presenting Author	Title
16:15	34	Paweł Olejnik	**A multi-axis gimbal mechanism as an experimental platform for controlled rotational excitation** Paweł Olejnik; Łukasz Kuźnicki; Maciej Rożniata
16:30	63	Lei Chen	**HQP-based adaptive compliant control for constrained operations of space manipulators** Lei Chen; Jun He; Feng Gao
16:45	19	Nursultan Zhetenbayev	**Experimental validation of a bluetooth-based remote-controlled ankle exoskeleton for rehabilitation** Aknur Duisebayeva; Gulzhamal Tursunbayeva; Nursultan Zhetenbayev; Aidos Sultan; Ozhikenov Kassymbek; Gani Sergazin
17:00	86	Tan Sy Nguyen	**Design and prototyping of a new collaborative hand cart for moving heavy payloads in factories** Tan Sy Nguyen; Olivier Couillard
17:15	169	Luis Alfonso Rodríguez Salinas	**Synthesis and structural characterization of nanostructured tin dioxide via sol-gel for acetone sensing application** Luis A. Rodriguez Salinas; Georgina García Pacheco; Jacobo E. Munguia Cervantes; Alfredo López Monroy; Leonel M. Gómez Villarejo
17:30	185	Jorge Luis Cervantes Fraustro	**Synthesis and structural characterization of nanostructured titanium dioxide via sol-gel for memristive CO sensing in aerospace applications** Jorge L. Cervantes Fraustro; Georgina García Pacheco; Jacobo E. Munguía Cervantes; Gerardo Villa Martínez

TECHNICAL SESSIONS IV - D	Monday, June 22 • 16:15 – 17:45

GEARS AND TRANSMISSIONS

Room John Uicker	CHAIR **Alfonso Fuentes**

Time	ID	Presenting Author	Title
16:15	166	Shibo Mu	**Meshing theory of point-contact Archimedean face worm gear drive** Shibo Mu; Xingwei Sun; Zhixu Dong; Jianlong Zhao; Liya Jin; Weifeng Zhang; Yin Liu; Heran Yang; Haosheng Hao; Yaping Zhao
16:30	118	Yuansheng Zhou	**A computer-aided optimization method for complex transmission systems of face gears via mechanism-data fusion** Bingquan Lu; Yuansheng Zhou; Zhongwei Tang; Jinyuan Tang
16:45	151	Aurea Iñurritegui	**Full-scale validation of fretting-map predictions for aerospace-grade crowned involute splines AISI 9310** Aurea Iñurritegui-Marroquin; Andrea Mura; Aitor Arana; Ander Elkoro; Francesca Cura
17:00	103	Jing Chong Low	**Non-dimensionalized spectral analysis of gear shape deviation networks: Identification of kinematic errors via node-normalized Laplacian and scale-invariant discrete Fourier transform** Jing Chong Low; Daisuke Iba; Yuichiro Seo; Shu Takata; Naoki Yamashita; Kunitoshi Kawano
17:15	55	Zhen Chen	**Computerized design, tooth contact analysis and stress analysis of pure rolling spiral bevel gears for orthogonal shafts transmission** Zhen Chen; Wenwei Luo; Chao He; Kai Zhu; Xiaoping Xiao; Yangzhi Chen; Alfonso Fuentes
17:30	127	Xiaoping Xiao	**Methods of TCA and LTCA for pure-rolling bevel line gear with the actively designed contact trace** Xiaoping Xiao; Hualin Xie; Chao He; Kai Zhu; Zhen Chen; Yangzhi Chen

17:45 – 19:00	**PORT WINE RECEPTION** – University Garden

Tuesday, June 23

08:00	REGISTRATION

TECHNICAL SESSIONS V – A	Tuesday, June 23 • 09:00 – 10:45

COMPUTATIONAL KINEMATICS

Room Azevedo Albuquerque			CHAIR **Giorgio Figliolini**
Time	ID	Presenting Author	Title
09:00	6	Huiping Shen	**New insights into three fundamental issues of parallel mechanisms and its research progresses** Huiping Shen; Xingyu She; Ju Li; Pengda Ye
09:15	14	Vincenzo Di Paola	**Families of screw systems** Vincenzo Di Paola; Jonathan Selig
09:30	125	Daniel Condurache	**Closed-form Baker–Campbell–Hausdorff–Dynkin formula for rigid body displacements and its significance for Mechanism and Machine Theory** Daniel Condurache; Mihai Cojocari
09:45	66	Manfred Husty	**Complete singularity analysis of KINOVA Link 6 type robots** Manfred Husty; Calin Vaida; Bogdan Gherman; Damien Chablat; Doina Pisla
10:00	156	Yucai Hu	**Developable triangle-based Kokotsakis polyhedra** Yucai Hu; Guoqiang Zhu; Ke Chen
10:15	196	Qiaode Jeffrey Ge	**Towards a methodology for interpretable embodied kinematic intelligence via null-space analysis of G-pose matrix** Qiaode Jeffrey Ge; Huan Liu
10:30	113	Enrique Carrillo Li	**Kinematic synthesis of a vertex-coupled single-DOF open-sheet, finite-thickness Yoshimura pattern using sliding multi-hinge fold modules** Enrique Roberto Carrillo Li; Lena Zentner; Enrique Pujada Gamarra; Daniel Lavayen Farfan; Jorge Antonio Rodríguez Hernández

TECHNICAL SESSIONS V – B	Tuesday, June 23 • 09:00 – 10:45

MULTIBODY DYNAMICS

Room Erskine Crossley			CHAIR **Jorge Ambrósio**
Time	ID	Presenting Author	Title
09:00	36	Francisco Novais	**Estimation of friction parameters utilizing experimental data** Francisco Novais; Filipe Marques; Paulo Flores; Hamid M. Lankarani
09:15	65	Alessandro Cammarata	**A frictional contact formulation for planar mechanisms** Alessandro Cammarata; Rosario Sinatra; Pietro Davide Maddio
09:30	94	Victor Smeets	**Frame friction model identification for a weaving loom system** Victor Smeets; Frank Naets; Konstantinos Gryllias
09:45	119	Balazs Janos Bekesi	**Three-parameter bifurcation analysis of a minimal mechanical model with LuGre friction** Balazs Janos Bekesi; Gabor Csernak
10:00	180	Zhiwen Xiao	**Reduced-order modeling of bearings and gears for accurate stress computation** Zhiwen Xiao; Zhilu Qi; Xinrong Li; Gexue Ren
10:15	96	Jialiang Sun	**Topology optimization and assembly dynamics of a large space structure via heterogeneous modules** Jialiang Sun; Quanchen Duan; Dingfeng Ding
10:30	129	Evangelos Papadopoulos	**Exploiting passive dynamics for steady-state walking on level and inclined terrain** Anargyros-Nektarios Skafidas; Aikaterini Smyrli; Evangelos Papadopoulos

TECHNICAL SESSIONS V – C	Tuesday, June 23 ▪ 09:00 – 10:15	
GEARS AND TRANSMISSIONS		
Room Terry Shoup		CHAIR **Alessio Artoni**
Time	ID	Presenting Author	Title
09:00	54	Antonella Castellano	**Beyond exploratory synthesis: How to design a multimode power-split transmission for maximum performance of hybrid electric vehicles** Antonella Castellano; Marco Cammalleri
09:15	150	Elias Rechreche	**Multi-objective optimization of the flexibility and life-span of grid couplings** Elias Rechreche; Jerôme Bruyere; Quentin Le Guennec; Philippe Velex
09:30	5	Mattia Battarra	**State of the art review and comparison on rattle index formulations for gear train applications** Fabio Bortoluzzi; Mattia Battarra; Emiliano Mucchi; Giorgio Dalpiaz
09:45	184	José Ángel Moncalián Cruz	**Study of planet phasing influence on the efficiency of a planetary gear** José Ángel Moncalián Cruz; Miguel Iglesias Santanmaría; Alberto Díez Ibarbia; Javier Sánchez Espiga; Alfonso Fernández del Rincón; Fernando Viadero Rueda
10:00	170	Ibai Ulacia	**On the feasibility of predicting rolling contact fatigue from uniaxial S-N curves** Ibai Ulacia; Iñigo Llavori; Mattin Maiztegui; Aitor Arana; Jon Larrañaga

TECHNICAL SESSIONS V - D	Tuesday, June 23 • 09:00 – 10:45

COMPLIANT MECHANISMS

Room John Uicker			CHAIR **Just Herder**
Time	ID	Presenting Author	Title
09:00	143	Domas Syaifoel	**Pseudo-rigid-body modeling can simulate complex compliant mechanisms without solving kinematics** Domas Syaifoel; Just Herder; Michaël Wiertlewski
09:15	44	Hannes Jahn	**Comparing different beam axis for asymmetric compliant hinges** Hannes Jahn; Lena Zentner
09:30	59	Nadine Wahl-Warnken	**Influence of angular errors on the constant-force behavior of a straight beam** Nadine Wahl-Warnken; Lena Zentner
09:45	31	Haoqian Wang	**Soft joint–contact coupled theoretical model for large-deformation thick-panel square-twist origami** Haoqian Wang; Haibo Qu; Nikos D. Lagaros; Sheng Guo
10:00	72	Pierre Mougenot	**Novel minimally invasive retractor for pancreatectomy** Pierre Mougenot; Bogdan Gherman; Calin Vaida; Paul Tucan; Doina Pisla; Damien Chablat
10:15	117	Sogo Koma	**Development of a microfluidic device that converts channel deformation into fluid displacement: experimental evaluation of the influence of channel constriction width on fluid moving distance** Sogo Koma; Daisuke Iba; Mitsuki Nabeta; Rintaro Mita; Naoki Yamashita; Hitoshi Shimasaki; Junichi Hongu
10:30	28	Jiaqiang Yao	**Chained beam constraint model for contact modeling (CBCM-CT): Using contact-position as undetermined coefficient** Chengcheng Sun; Jiaqiang Yao; Ruiyu Bai; Haoyu Zhang; Guimin Chen

10:45 - 11:15	Coffee-Break and Poster Session

TECHNICAL SESSIONS VI - A	Tuesday, June 23 • 11:15 – 13:00

COMPUTATIONAL KINEMATICS

Room Azevedo Albuquerque			CHAIR **Martin Pfurner**
Time	ID	Presenting Author	Title
11:15	30	Enrique Pujada	**Displacements analysis of the Miura-ori pattern with double-hinge thickness accommodation** Enrique Pujada Gamarra; Lena Zentner; Daniel Lavayen Farfán; Jorge Antonio Rodriguez-Hernandez
11:30	139	Giorgio Figliolini	**Kinematic properties of the instantaneous centers of zero velocity and acceleration according to their trajectories and centrodes** Giorgio Figliolini; Chiara Lanni; Luciano Tomassi
11:45	145	Andreas Mair	**Snapping four bar mechanisms: Discrete assembly configurations in closed-loop linkages** Andreas Mair; Daren A. Thimm; Martin Pfurner
12:00	58	Hui Yang	**Type synthesis of lower-mobility parallel mechanisms for morphing nose based on an atlas method** Zhonghao Huang; Hui Yang; Yan Wang
12:15	53	Álvaro Noriega	**Solving the problem of dimensional kinematic synthesis using an evolution strategy that utilizes knowledge of derivatives** Álvaro Noriega; Igor Fernández de Bustos; María del Rocio Fernández
12:30	197	Gustavo V. Souza	**Automated extraction and graph-based representation of mechanism diagrams: Bridging computer vision, structural synthesis, and engineering education** Gustavo Valdatti Souza; Angel Esley Garcia Caceres; Andrea Piga Carboni; Daniel Martins
12:45	104	Yu Wang	**Degree of freedom analysis of multi-loop coupled mechanisms based on mechanism-truss transformation method** Yu Wang; Xiaofei Liu; Yuantao Bu; Yuan Jiang; Jiantao Yao; Yongsheng Zhao

TECHNICAL SESSIONS VI - B			Tuesday, June 23 ▪ 11:15 – 12:45
MULTIBODY DYNAMICS			
Room Erskine Crossley			CHAIR **Xinxin Yu**
Time	ID	Presenting Author	Title
11:15	61	Xinyan Li	**Variable-step Lie-group generalized-α integration: Simplified parameter updates and accuracy estimates** Xinyan Li; Zhihua Zhao
11:30	177	Jiayi Zhou	**On the numerical errors of multibody dynamics Jacobians induced by the Rodrigues formula** Jiayi Zhou; Zhiwen Xiao; Gexue Ren
11:45	194	Márton Kuslits	**Modeling of screw mechanisms for control - a multibody approach** Márton Kuslits
12:00	134	Antonio Carlo Bertolino	**Modeling ball recirculation in multibody ball screw drives** Antonio Carlo Bertolino; Roberto Guida; Andrea De Martin; Massimo Sorli
12:15	21	Andrzej Urbaś	**Comparative research of some dynamics models of crank-slider mechanism with counterweight** Andrzej Urbaś; Jacek Stadnicki
12:30	29	Duo Zhang	**Optimizing the cruising speed for trains in a metro-based underground logistics system using multibody dynamics and multi-objective algorithms** Duo Zhang; Gisella Tomasini; Yuan-Peng He; Fang-Ru Zhou; Zi-Yu Tao

TECHNICAL SESSIONS VI – C	Tuesday, June 23 ▪ 11:15 – 12:45	
GEARS AND TRANSMISSIONS		
Room Terry Shoup		CHAIR **José I. Pedrero**
Time	ID	Presenting Author	Title
11:15	46	Aurea Iñurritegui	**Carburized induced tooth distortions in geared transmissions: Thermo-metallurgical FE prediction and experimental validation** Aurea Iñurritegui; Xuban Telleria; Gurutz Cortabitarte; Aitor Arana
11:30	99	Rui Mouzinho	**Thermo-mechanical modelling of hybrid polymer gears** Rui Mouzinho; Stéphane Portron; Carlos Fernandes
11:45	81	Yuichiro Seo	**Shape evaluation of tooth profile sections bounded by the left and right tooth profile deviations of injection-molded plastic gears** Yuichiro Seo; Daisuke Iba; Jing Chong Low; Shu Takata; Naoki Yamashita
12:00	13	Khadija Boujallabia	**Injection vs. oil bath lubrication impact on power loss and thermal behaviour in an FZG test rig** Khadija Boujallabia; Büşra Duran; Jérôme Cavoret; Thibaut Torres; Christophe Changenet; Fabrice Ville
12:15	93	Luca D'Angelo	**Analytical approach for compliance identification in lightweight spur gears** Luca D'Angelo; Marco Cirelli; Oliviero Giannini; Pier Paolo Valentini
12:30	149	Ramon Ruiz-Orzaez	**Computerized generation, tooth contact analysis and stress analysis of pericyclic gear drives** Ignacio Gonzalez-Perez; Ramon Ruiz-Orzaez; Alfonso Fuentes-Aznar

TECHNICAL SESSIONS VI - D	Tuesday, June 23 ▪ 11:15 – 13:00

COMPLIANT MECHANISMS

Room John Uicker			CHAIR **Pier Paolo Valentini**
Time	ID	Presenting Author	Title
11:15	35	Hussein Naddaf	**High-precision multi-axis flexure-based compliant mechanism: predictive modelling and experimental validation** Hussein Naddaf; Michael Gomez; Nicola Bailey
11:30	39	Zhuoran Li	**Design, analysis, and experimental investigation of a novel wedge-type self-locking connection mechanism for aircraft opening covers** Zhuoran Li; Shujun Chen; Jie Chen; Jing Zhao
11:45	89	Marco Cirelli	**Higher-order kinematic analysis of compliant four-bar linkage: Theory and application to a flexible Roberts mechanism** Marco Cirelli; Luca D'Angelo; Gabriele Alcamo; Pier Paolo Valentini
12:00	107	Matteo Verotti	**Morphing of planar flexures** Orazio Sorgonà; Luca Bruzzone; Oliviero Giannini; Matteo Verotti
12:15	136	Just Herder	**Initially-curved variable-thickness flexures improve performance in compliant mechanisms, a straight-line generator example** Flip Colin; Abdullah Yasir; Erwin Mulder; Just Herder
12:30	43	Vivien Platl	**Dynamic analysis of curved compliant mechanisms** Vivien Platl; Lena Zentner
12:45	9	Dung-An Wang	**Kinetostatic modeling of a compliant honeycomb lattice** Hoang Lam Pham; Quoc Huy Pham; Dung-An Wang

13:00 - 14:00	Lunch

TECHNICAL SESSIONS VII - A			Tuesday, June 23 ▪ 14:00 – 15:30
ROTATING MACHINERY			
Room Azevedo Albuquerque			CHAIR **Ibai Ulacia**
Time	ID	Presenting Author	Title
14:00	10	Martin Eizmendi	**Dynamic testing of four-point contact slewing bearings: A way to a method** Martin Eizmendi; Iker Heras; Mikel Portilla; Josu Aguirrebeitia
14:15	110	Dennis Janssens	**Non-intrusive quasi-static torque measurement in gearboxes using a housing-mounted fiber Bragg grating sensor** Dennis Janssens; Sidney Goossens; Frank Naets
14:30	12	Rushen Deng	**A coupled lubrication model for the valve plate pair in high-pressure aviation piston pumps considering spindle deformation** Runlim Chen; Wenhui Li; Wenhao Chen; Rushen Deng; Jianning Gu; Tianzhao Wang; Jun Zha
14:45	37	Tobias Baumann	**A novel finite element-based slice model for line contacts in rolling bearings** Tobias Baumann; Daniel Singer; Till Budde; Stephan Tremmel
15:00	77	Mikel Portilla	**On the friction torque in slewing bearings: Towards a new approach** Mikel Portilla Gutierrez; Martin Eizmendi Saiz; Iker Heras Miguel; Josu Aguirrebeitia Celaya
15:15	172	Pello Alberdi	**Optimizing ball bearing contact angle for minimum power loss under combined loads** Pello Alberdi; Aitor Arana; Aitor Oyanguren; Jon Larrañaga; Ibai Ulacia

TECHNICAL SESSIONS VII - B	Tuesday, June 23 • 14:00 – 15:30

BIOMECHANICS

Room Erskine Crossley			CHAIR **Sérgio Gonçalves**
Time	ID	Presenting Author	Title
14:00	2	Airi Hatsushiro	**Comparative evaluation of machine learning methods for motion-related pain prediction in lumbar disc herniation patients** Airi Hatsushiro; Yuta Tawaki; Toshiyuki Murakami; Teresa Zielinska
14:15	57	Manuel Romeo	**Kinematics evaluation of a lower limb musculoskeletal model based on parallel mechanisms with in vivo measured data** Manuel Romeo; Nicola Sancisi; Michele Conconi; Raphael Dumas
14:30	15	Domenico Mundo	**On the use of a novel driving simulator for the assessment of upper limb impairment in post-stroke patients** Francesca Alvaro; Mathjis Vivet; Michele Perrelli; Rocco Adduci; Domenico Mundo
14:45	48	Yerkebulan Nurgizat	**Structural design and numerical simulation of a semi-active transfemoral knee prosthesis adapter** Nursultan Zhetenbayev; Yerkebulan Nurgizat; Aidos Sultan; Didar Serik; Ussama Abujazar; Kassymbek Ozhikenov; Gani Sergazin
15:00	62	Nicola Sancisi	**Evaluation of a two-dof mechanism to model the ankle complex** Nicola Sancisi; Manuel Romeo; Raphael Dumas; Michele Conconi
15:15	182	Nuno Carmo	**Biomechanical assessment of reclined occupant postures in automated vehicles using LS-DYNA simulations** Nuno Carmo; Ana Martins; Marta Carvalho

TECHNICAL SESSIONS VII – C	Tuesday, June 23 ▪ 14:00 – 15:30	
MECHANISM AND MACHINE DESIGN		
Room Terry Shoup	CHAIR **Maria Cristina Valigi**	
Time	ID	Presenting Author	Title
14:00	92	Victor Zhidchenko	**Data-driven structural strain estimation for a forestry crane using LSTM and transformer networks** Sohaib Mustafa Saeed; Victor Zhidchenko; Heikki Handroos
14:15	111	Pavel Zevzikov	**Development of a prototype compressed-air generator using water hammer energy** Pavel Zevzikov; Marijonas Bogdevicius
14:30	157	Jorge Francisco Aznar Ortega	**Optimal design of a suspended parallel robot for wall plastering** Jorge Francisco Aznar Ortega; Adrián Peidró Vidal; Paula Mollá Santamaría; Óscar Reinoso García
14:45	198	Larisa Rybak	**Development and research of a multimodal robot with ground and aerial modes** Larisa Rybak; Dmitry Malyshev; Vladislav Cherkasov
15:00	173	Hongfang Chen	**Optimal measurement area identification and accuracy enhancement of a CMM based on IPSO-SAA** Zishuai Wang; Zeru Lyu; Zhaoyao Shi; Hongfang Chen

TECHNICAL SESSIONS VII - D	Tuesday, June 23 • 14:00 – 15:30

ROBOTS AND MANIPULATORS

Room John Uicker			CHAIR **Yukio Takeda**
Time	ID	Presenting Author	Title
14:00	160	Tan Sy Nguyen	**A planar parallel robot with a remote-controlled orientable two-finger gripper** Tan Sy Nguyen; Simon Foucault
14:15	108	Seniz Ertugrul	**Design and experimental validation of an underactuated four-finger variable stiffness gripper with sensorless force estimation** Ozan Kaya; Ertugrul Bayraktar; Seniz Ertugrul
14:30	24	Pier Paolo Valentini	**Real-time prompt-based 3D object detection and pose kinematics for interactive cobot grasping** Marco Cirelli; Luca D'Angelo; Pier Paolo Valentini
14:45	193	Angelos Iliakis	**A compact SPS-based parallel mechanism for worm-like robot locomotion in confined environments** Angelos Iliakis; George Nikolakopoulos; Panagiotis Koustoumpardis
15:00	132	Ziyue Li	**Reconfiguration-enabled workspace reshaping and motion planning for a legged lander** Ziyue Li; W.Z. Guo Guo
15:15	51	Jie Wang	**Follow-the-leader performance of a dual-ended spring-based self-extending continuum robot** Jie Wang; Calvin S. H. Ng; Zheng Li

KEYNOTE LECTURE II	Tuesday, June 23 • 15:30 – 16:00
Room Azevedo Albuquerque	CHAIR **Andrés Kecskeméthy**

Time	Presenting Author	Title
15:30	Paulo Flores	**60th Anniversary of Mechanism and Machine Theory**

16:00 – 16:15	**AWARDS AND CLOSING CEREMONY** - Room Azevedo Albuquerque
19:00 – 23:00	**BANQUET** - Hilton Porto Gaia

Poster Session		Permanent Exhibition
ID	Presenting Author	Title
4	Carlos Fernandes	**Summit-counting method for statistical mixed-lubrication gear friction modeling** Miguel Dias; Carlos Fernandes
11	Jernej Mlinarič	**Transferable time-frequency representations for data-efficient end-of-line quality inspection of electric motors** Jernej Mlinarič; Boštjan Pregelj; Gregor Dolanc
41	Yonghong Chen	**Relative position error identification and compensation for dual-cone enveloping hourglass worm via SAO-BP neural network** Zhenglin Yang; Yonghong Chen; Jin Gao; Chenyang Dou; Fei Liu; Wenjun Luo; Bingkui Chen
42	Yonghong Chen	**Research on meshing performance investigations of the curve-constructed hourglass worm drive** Jin Gao; Yonghong Chen; Zhengling Yang; Chenyang Dou; Fei Liu; Wenjun Luo; Bingkui Chen
78	Chenyang Dou	**Error adaptability analysis on a novel point contact face worm gear drive based on geometric element** Chenyang Dou; Yonghong Chen; Jin Gao; Zhenglin Yang; Fei Liu; Wenjun Luo; Bingkui Chen
90	Miroslaw Rucki	**Application of digital twin in the control system for the zirconia-based ceramics electroconsolidation device** Waldemar Samociuk; Edvin Hevorkian; Dmitrij Morozow; Leszek Chałko; Paweł Stączek; Miroslaw Rucki
95	Miroslaw Rucki	**Additively manufactured cycloidal gears: Comparative analysis of three materials** Krzysztof Olejarczyk; Marcin Wikło; Miroslaw Rucki; Artūras Kilikevičius
179	Yunge Zou	**NVH-aware co-optimization of topology, parameter and control for distributed range-extended electric powertrains** Yuxin Zhang; Yunge Zou; Xin Ye
181	Yunge Zou	**Research on the design and optimization methodology of multi-mode multi-gear transmission architecture for electric vehicles based on graph theory** Yunge Zou; Yuxin Zhang; Yantao Si
202	Leonor Guimarães	**Design and optimisation of tilt-in-space wheelchair mechanism** Leonor Guimarães; Mariana Rodrigues da Silva; Filipe Marques

MMT Symposium

60th Anniversary of Mechanism and Machine Theory

Book of Abstracts

June 21-23, 2026 | Porto, Portugal

Index

ID 1	**How to obtain analytical solutions for vehicle phase plane equilibrium and stability analysis** Basilio Lenzo; Mariagrazia Tristano	62
ID 2	**Comparative evaluation of machine learning methods for motion-related pain prediction in lumbar disc herniation patients** Airi Hatsushiro; Yuta Tawaki; Toshiyuki Murakami; Teresa Zielinska	64
ID 3	**Optimizing ride comfort in four-wheel hub-motor electric vehicles via multibody dynamics and multi-objective algorithms** Ling Ma; Yongjun Pan; Wei Liu; Aki Mikkola	66
ID 4	**Summit-counting method for statistical mixed-lubrication gear friction modeling** Miguel Dias; Carlos Fernandes	68
ID 5	**State of the art review and comparison on rattle index formulations for gear train applications** Fabio Bortoluzzi; Mattia Battarra; Emiliano Mucchi; Giorgio Dalpiaz	70
ID 6	**New insights into three fundamental issues of parallel mechanisms and its research progresses** Huiping Shen; Xingyu She; Ju Li; Pengda Ye	72
ID 8	**FEA-based structural design of a serial variable stiffness joint** Guanglei Wu; Bin Niu	74
ID 9	**Kinetostatic modeling of a compliant honeycomb lattice** Hoang Lam Pham; Quoc Huy Pham; Dung-An Wang	76
ID 10	**Dynamic testing of four-point contact slewing bearings: A way to a method** Martin Eizmendi; Iker Heras; Mikel Portilla; Josu Aguirrebeitia	78
ID 11	**Transferable time-frequency representations for data-efficient end-of-line quality inspection of electric motors** Jernej Mlinarič; Boštjan Pregelj; Gregor Dolanc	80
ID 12	**A coupled lubrication model for the valve plate pair in high-pressure aviation piston pumps considering spindle deformation** Runlim Chen; Wenhui Li; Wenhao Chen; Rushen Deng; Jianning Gu; Tianzhao Wang; Jun Zha	82
ID 13	**Injection vs. oil bath lubrication impact on power loss and thermal behaviour in an FZG test rig** Khadija Boujallabia; Büşra Duran; Jérôme Cavoret; Thibaut Torres; Christophe Changenet; Fabrice Ville	84
ID 14	**Families of screw systems** Vincenzo Di Paola; Jonathan Selig	86
ID 15	**On the use of a novel driving simulator for the assessment of upper limb impairment in post-stroke patients** Francesca Alvaro; Mathjis Vivet; Michele Perrelli; Rocco Adduci; Domenico Mundo	88
ID 16	**Topology design and performance analysis of parallel mechanisms with fewer joints** Ju Li; Yue Guo; Huiping Shen	90
ID 18	**Torque-angle modeling of a two-degree-of-freedom ankle prosthesis** Zhanar Bigaliyeva; Sayat Akhmejanov; Nursultan Zhetenbayev; Aidos Sultan; Arman Uzbekbayev; Ozhikenov Kassymbek; Yerkebulan Nurgizat; Abu Alim Ayazbay; Gani Sergazin	92

ID 19 **Experimental validation of a bluetooth-based remote-controlled ankle exoskeleton for rehabilitation** 94
Aknur Duisebayeva; Gulzhamal Tursunbayeva; Nursultan Zhetenbayev; Aidos Sultan; Ozhikenov Kassymbek; Gani Sergazin

ID 20 **Lumped–mass tyre modelling for road–envelope analysis** 96
Angelo Domenico Vella; Alessandro Vigliani

ID 21 **Comparative research of some dynamics models of crank-slider mechanism with counterweight** 98
Andrzej Urbaś; Jacek Stadnicki

ID 22 **ODE-based dynamic modeling of multi-loop robots and its application to MPC** 100
Shaoheng Hu; Xianwen Kong; Guodong Yin

ID 23 **Tribology in material handling: Winches, nonlinear rope friction, fiber ropes, fused filament fabrication components** 102
Rico Zöllner; Raimond Hofmann; Martin Anders; Thorsten Schmidt

ID 24 **Real-time prompt-based 3D object detection and pose kinematics for interactive cobot grasping** 104
Marco Cirelli; Luca D'Angelo; Pier Paolo Valentini

ID 25 **Experiments and analysis of twistcar-type robots** 106
Yizhar Or; Rom Levy; Anna Zigelman; Ari Dantus; Zitao Yu

ID 26 **Neural density estimation for the synthesis of crank-driven four-bar mechanisms** 108
Benedict Röder; Henrik Ebel; Peter Eberhard

ID 27 **Dynamic energy-optimal anchor configuration on general convex surfaces, enabled by geodesic-based force-consistent modeling** 110
Lei Jin; Dongming Gan; Maitha Alqaydi; Mohamed Abduljawad; Yahya Mohammed; Tarek Taha; Ahmad Alattar

ID 28 **Chained beam constraint model for contact modeling (CBCM-CT): Using contact-position as undetermined coefficient** 112
Chengcheng Sun; Jiaqiang Yao; Ruiyu Bai; Haoyu Zhang; Guimin Chen

ID 29 **Optimizing the cruising speed for trains in a metro-based underground logistics system using multibody dynamics and multi-objective algorithms** 114
Duo Zhang; Gisella Tomasini; Yuan-Peng He; Fang-Ru Zhou; Zi-Yu Tao

ID 30 **Displacements analysis of the Miura-ori pattern with double-hinge thickness accommodation** 116
Enrique Pujada Gamarra; Lena Zentner; Daniel Lavayen Farfán; Jorge Antonio Rodriguez-Hernandez

ID 31 **Soft joint–contact coupled theoretical model for large-deformation thick-panel square-twist origami** 118
Haoqian Wang; Haibo Qu; Nikos D. Lagaros; Sheng Guo

ID 32 **Multi-lattice topology optimization with competitive weighting and penalty-driven lattice selection under dynamic loading** 120
Yangyang Xiao; Shu Li; Nikos D. Lagaros; Jie Geng

ID 33 **Controller design for velocity transmission of Bowden-cable actuators** 122
Yaodong Lu; Pablo Nocito; Yannick Aoustin; Sébastien Mick; Qiaoling Meng; Hongliu Yu; Nathanaël Jarrassé

ID 34 **A multi-axis gimbal mechanism as an experimental platform for controlled rotational excitation** 124
Paweł Olejnik; Łukasz Kuźnicki; Maciej Rożniata

ID 35 **High-precision multi-axis flexure-based compliant mechanism: predictive modelling and experimental validation** 126
Hussein Naddaf; Michael Gomez; Nicola Bailey

ID 36 **Estimation of friction parameters utilizing experimental data** 128
Francisco Novais; Filipe Marques; Paulo Flores; Hamid M. Lankarani

ID 37 **A novel finite element-based slice model for line contacts in rolling bearings** 130
Tobias Baumann; Daniel Singer; Till Budde; Stephan Tremmel

ID 38 **Feasible wrench sets of redundant parallel manipulators** 132
Joshua Flight; Clément Gosselin

ID 39 **Design, analysis, and experimental investigation of a novel wedge-type self-locking connection mechanism for aircraft opening covers** 134
Zhuoran Li; Shujun Chen; Jie Chen; Jing Zhao

ID 40 **Analysis of the contact stress of beveloid helical gears with parallel axes** 136
Miryam B. Sánchez; Giovanni Mottola; Miguel Pleguezuelos; Alfonso Fuentes-Aznar; Jose I. Pedrero; Marco Carricato

ID 41 **Relative position error identification and compensation for dual-cone enveloping hourglass worm via SAO-BP neural network** 138
Zhenglin Yang; Yonghong Chen; Jin Gao; Chenyang Dou; Fei Liu; Wenjun Luo; Bingkui Chen

ID 42 **Research on meshing performance investigations of the curve-constructed hourglass worm drive** 140
Jin Gao; Yonghong Chen; Zhengling Yang; Chenyang Dou; Fei Liu; Wenjun Luo; Bingkui Chen

ID 43 **Dynamic analysis of curved compliant mechanisms** 142
Vivien Platl; Lena Zentner

ID 44 **Comparing different beam axis for asymmetric compliant hinges** 144
Hannes Jahn; Lena Zentner

ID 45 **A calculation method for the asymmetric helical gear meshing stiffness considering the slice coupling effect** 146
Zhihui Hou; Hui Guo; Shengwen Hou; Xiaoping Ran; Yuhang Ruan

ID 46 **Carburized induced tooth distortions in geared transmissions: Thermo-metallurgical FE prediction and experimental validation** 148
Aurea Iñurritegui; Xuban Telleria; Gurutz Cortabitarte; Aitor Arana

ID 47 **Design and prototype development of a research-oriented passive foot prosthesis with a dual-spring elastic mechanism and shock-absorbing sole** 150
Nursultan Zhetenbayev; Aidos Sultan; Ussama Abujazar; Ozhikenov Kassymbek; Yerkebulan Nurgizat; Gani Sergazin

ID 48 **Structural design and numerical simulation of a semi-active transfemoral knee prosthesis adapter** 152
Nursultan Zhetenbayev; Yerkebulan Nurgizat; Aidos Sultan; Didar Serik; Ussama Abujazar; Kassymbek Ozhikenov; Gani Sergazin

ID 51 **Follow-the-leader performance of a dual-ended spring-based self-extending continuum robot** 154
Jie Wang; Calvin S. H. Ng; Zheng Li

ID 52 **Sample-efficient learning of body-environment interaction of an underactuated system** 156
Zvi Chapnik; Yizhar Or; Shai Revzen

ID 53 **Solving the problem of dimensional kinematic synthesis using an evolution strategy that utilizes knowledge of derivatives** 158
Álvaro Noriega; Igor Fernández de Bustos; María del Rocio Fernández

ID 54 **Beyond exploratory synthesis: How to design a multimode power-split transmission for maximum performance of hybrid electric vehicles** 160
Antonella Castellano; Marco Cammalleri

ID 55 **Computerized design, tooth contact analysis and stress analysis of pure rolling spiral bevel gears for orthogonal shafts transmission** 162
Zhen Chen; Wenwei Luo; Chao He; Kai Zhu; Xiaoping Xiao; Yangzhi Chen; Alfonso Fuentes

ID 56 **Bridging theory and reality: Integrating VVUQ standards and low-cost experimental analysis in mechanism synthesis education** 164
Ramon Gutiérrez Moizant; Fernando Viadero-Monasterio; Miguel Meléndez-Useros; María Ramírez-Berasategui; Daniel García-Pozuelo Ramos

ID 57 **Kinematics evaluation of a lower limb musculoskeletal model based on parallel mechanisms with in vivo measured data** 166
Manuel Romeo; Nicola Sancisi; Michele Conconi; Raphael Dumas

ID 58 **Type synthesis of lower-mobility parallel mechanisms for morphing nose based on an atlas method** 168
Zhonghao Huang; Hui Yang; Yan Wang

ID 59 **Influence of angular errors on the constant-force behavior of a straight beam** 170
Nadine Wahl-Warnken; Lena Zentner

ID 60 **Design of a cable-driven hybrid serial-parallel skeletal morphing wing for hypersonic aircraft** 172
Yan Wang; Hui Yang; Siqiang Xing; Yi Han

ID 61 **Variable-step Lie-group generalized-α integration: Simplified parameter updates and accuracy estimates** 174
Xinyan Li; Zhihua Zhao

ID 62 **Evaluation of a two-dof mechanism to model the ankle complex** 176
Nicola Sancisi; Manuel Romeo; Raphael Dumas; Michele Conconi

ID 63 **HQP-based adaptive compliant control for constrained operations of space manipulators** 178
Lei Chen; Jun He; Feng Gao

ID 64 **Design and kinematics of modular variable-stiffness skeleton mechanism for Z-folded morphing wing based on waterbomb-origami** 180
Yi Han; Hui Yang; Yan Wang

ID 65 **A frictional contact formulation for planar mechanisms** 182
Alessandro Cammarata; Rosario Sinatra; Pietro Davide Maddio

ID 66 **Complete singularity analysis of KINOVA Link 6 type robots** 184
Manfred Husty; Calin Vaida; Bogdan Gherman; Damien Chablat; Doina Pisla

ID 68 **The matroid method in computational mechanics of mechanisms** 186
Ilie Talpasanu; Alexandru Talpasanu

ID 69 **A novel series elastic actuator with mechanical stoppers for Assist-As-Needed in sit-to-stand assistance** 188
Ming Jiang; Jian Zheng; Seunghyun Kim; Hiroto Miyatake; Kotaro Muramatsu; Jun Nango; Yukio Takeda

ID 70 **Type synthesis and performance optimization of 2R1T parallel mechanisms with third-order actuation redundancy** 190
Xiaofei Liu; Yu Wang; Zongqiang Feng; Jiantao Yao; Yongsheng Zhao

ID 72 **Novel minimally invasive retractor for pancreatectomy** 192
Pierre Mougenot; Bogdan Gherman; Calin Vaida; Paul Tucan; Doina Pisla; Damien Chablat

ID 74 **Planar parallel mechanism driven along a curved guide** 194
Yukio Takeda; Shota Fujisaka; Masashi Yoshii; Ryota Shioya; Ming Jiang; Koichi Kato; Mathias Huesing; Burkhard Corves; Tomoya Tanaka; Shogo Miura

ID 76 **Modeling and robustness characterization of large-stroke QZS mechanisms under ultra-low frequency excitation** 196
Shun Bi; Shane Johnson

ID 77 **On the friction torque in slewing bearings: Towards a new approach** 198
Mikel Portilla Gutierrez; Martin Eizmendi Saiz; Iker Heras Miguel; Josu Aguirrebeitia Celaya

ID 78 **Error adaptability analysis on a novel point contact face worm gear drive based on geometric element** 200
Chenyang Dou; Yonghong Chen; Jin Gao; Zhenglin Yang; Fei Liu; Wenjun Luo; Bingkui Chen

ID 79 **Artificial neural network for modelling gear mesh stiffness** 202
Francisco Ricardo; João Marafona; Stéphane Portron; Carlos Fernandes; Pedro Marques; João Tavares

ID 80 **Assessing the tipping over risk of rollators during standing up in younger and older adults** 204
Marko Ackermann; Katja Mombaur

ID 81 **Shape evaluation of tooth profile sections bounded by the left and right tooth profile deviations of injection-molded plastic gears** 206
Yuichiro Seo; Daisuke Iba; Jing Chong Low; Shu Takata; Naoki Yamashita

ID 82 **Simulation and validation of the transmission error and meshing stiffness of internal helical gears with profile modification** 208
Miguel Pleguezuelos; Miryam B. Sánchez; Andrés F. Hidalgo; Jose I. Pedrero; Alfonso Fuentes

ID 83 **Mechanical development of an automatic equipment for bioplastic film testing** 210
David Pinto; Raul Campilho; José Barbosa; Filipe Lopes; Francisco da Silva; David Almeida; André Pedroso

ID 85 **Introduction to discrete flexible multibody modelling approach for ball bearings with deformable rings** 212
Roberto Guida; Andrea De Martin

ID 86 **Design and prototyping of a new collaborative hand cart for moving heavy payloads in factories** 214
Tan Sy Nguyen; Olivier Couillard

ID 87 **Tolerance analysis of mechanisms with unilateral constraints** 216
Wanting Wang; Zhihua Zhao

ID 88 **A coupled multibody–granular dynamics framework for high-fidelity simulation of lunar robot locomotion** 218
Kaiming Zhang; Yang Yu; Zhijun Song; Jingchang Xie; Kunen Peng

ID 89 **Higher-order kinematic analysis of compliant four-bar linkage: Theory and application to a flexible Roberts mechanism** 220
Marco Cirelli; Luca D'Angelo; Gabriele Alcamo; Pier Paolo Valentini

ID 90 **Application of digital twin in the control system for the zirconia-based ceramics electroconsolidation device** 222
Waldemar Samociuk; Edvin Hevorkian; Dmitrij Morozow; Leszek Chałko; Paweł Stączek; Miroslaw Rucki

ID 91 **Cuboid-shaped Bricard-Sarrus metastructures with constant-zero stiffness** 224
Shiwei Liu, Long Li; Shengnan Lyu; Xilun Ding

ID 92 **Data-driven structural strain estimation for a forestry crane using LSTM and transformer networks** 226
Sohaib Mustafa Saeed; Victor Zhidchenko; Heikki Handroos

ID 93 **Analytical approach for compliance identification in lightweight spur gears** 228
Luca D'Angelo; Marco Cirelli; Oliviero Giannini; Pier Paolo Valentini

ID 94 **Frame friction model identification for a weaving loom system** 230
Victor Smeets; Frank Naets; Konstantinos Gryllias

ID 95 **Additively manufactured cycloidal gears: Comparative analysis of three materials** 232
Krzysztof Olejarczyk; Marcin Wikło; Miroslaw Rucki; Artūras Kilikevičius

ID 96 **Topology optimization and assembly dynamics of a large space structure via heterogeneous modules** 234
Jialiang Sun; Quanchen Duan; Dingfeng Ding

ID 97 **Design and validation of an impedance-controlled robotic system for biomechanical joint characterization** 236
Lorenzo Maggi; Matilde Tomasi; Nicola Secciani; Benedetto Allotta; Alessio Artoni

ID 99 **Thermo-mechanical modelling of hybrid polymer gears** 238
Rui Mouzinho; Stephane Portron; Carlos Fernandes

ID 100 **An ALE-SE(3) beam formulation for the simulation of cable-driven soft robots** 240
Olivier Devigne; Olivier Bruls

ID 101 **Enhancing snake robot stiffness in confined spaces: Pose optimization with obstacle avoidance** 242
Yinjun Zhao; Pietro Davide Maddio; Alessandro Cammarata; Rosario Sinatra; Yingzhong Tian; Fengfeng Xi

ID 102 **Morphological intelligence in passive dynamics: A design investigation of biomechanically-inspired bipedal robots** 244
Aikaterini Smyrli; Evangelos Papadopoulos

ID 103 **Non-dimensionalized spectral analysis of gear shape deviation networks: Identification of kinematic errors via node-normalized Laplacian and scale-invariant discrete Fourier transform** 246
Jing Chong Low; Daisuke Iba; Yuichiro Seo; Shu Takata; Naoki Yamashita; Kunitoshi Kawano

ID 104 **Degree of freedom analysis of multi-loop coupled mechanisms based on mechanism-truss transformation method** 248
Yu Wang; Xiaofei Liu; Yuantao Bu; Yuan Jiang; Jiantao Yao; Yongsheng Zhao

ID 105 **Tolerance design and metrology-assisted fabrication and assembly of parallel robots for high precision surgical operations** 250
Aislinn Mcaleenan; Yan Jin; Dan Sun; Johnny Moore

ID 106 **Safe and robust autonomous drifting of vehicles** 252
Ricardo de Castro; Basilio Lenzo; Marco Adami; Marco Cortese; Marco Cazzola; Giovanni Righetti, Tommaso Belluco; Matteo Massaro; Berrydal Moshe; Justin Arroyo

ID 107 **Morphing of planar flexures** 254
Orazio Sorgonà; Luca Bruzzone; Oliviero Giannini; Matteo Verotti

ID 108 **Design and experimental validation of an underactuated four-finger variable stiffness gripper with sensorless force estimation** 256
Ozan Kaya; Ertugrul Bayraktar; Seniz Ertugrul

ID 109 **Systematic design of reconfigurable hybrid origami robots** 258
Haoju Wen; Wenjun Chris Zhang

ID 110 **Non-intrusive quasi-static torque measurement in gearboxes using a housing-mounted fiber Bragg grating sensor** 260
Dennis Janssens; Sidney Goossens; Frank Naets

ID 111 **Development of a prototype compressed-air generator using water hammer energy** 262
Pavel Zevzikov; Marijonas Bogdevicius

ID 112 **Collocated control of an underactuated cable-driven parallel robot through disturbance observer and inverse dynamics** 264
Jason Bettega; Salvatore Marrazzo; Dario Richiedei; Alberto Trevisani

ID 113 **Kinematic synthesis of a vertex-coupled single-DOF open-sheet, finite-thickness Yoshimura pattern using sliding multi-hinge fold modules** 266
Enrique Roberto Carrillo Li; Lena Zentner; Enrique Pujada Gamarra; Daniel Lavayen Farfan; Jorge Antonio Rodríguez Hernández

ID 114 **Analysis and improvements of the classical model of railway wheelset dynamics** 268
Mate Antali

ID 115 **Geometry of multibody motion: An intrinsic lie groupoid approach** 270
Robin Chhabra; Yael Karshon; M. Reza Emami

ID 116 **Design and kinematic characteristic analysis of a novel redundantly actuated parallel mechanism for high-precision grinding** 272
Yanhua Tang; Yaning Li; Yu Wang; Xiaofei Liu; Jinyang He; Yuantao Bu

ID 117 **Development of a microfluidic device that converts channel deformation into fluid displacement: experimental evaluation of the influence of channel constriction width on fluid moving distance** 274
Sogo Koma; Daisuke Iba; Mitsuki Nabeta; Rintaro Mita; Naoki Yamashita; Hitoshi Shimasaki; Junichi Hongu

ID 118 **A computer-aided optimization method for complex transmission systems of face gears via mechanism-data fusion** 276
Bingquan Lu; Yuansheng Zhou; Zhongwei Tang; Jinyuan Tang

ID 119 **Three-parameter bifurcation analysis of a minimal mechanical model with LuGre friction** 278
Balazs Janos Bekesi; Gabor Csernak

ID 120 **A Gough-Stewart platform based external fixation system for deformity correction in orthopedics** 280
Yogesh Pratap Singh; Kiran Saldanha; Ashitava Ghosal

ID 121 **A novel gripper for space debris collection** 282
Silvia Logozzo; Sebastiano Angelella; Maria Cristina Valigi

ID 122 **Design of a rigid and compliant inverted 4-bar mechanism to emulate polycentric misalignment for lower-limb exoskeleton mannequins** 284
Christian Mele; Jhilik Bose; James Tung; Katja Mombaur

ID 123 **The effect of contact force models on the stability of two-wheeled trailers with a simplified model** 286
Hanna Zsofia Horvath; Mate Antali

ID 124 **Higher-order Cayley transforms and shadow Rodrigues dual vectors: A unified framework for rigid-body kinematic** 288
Daniel Condurache; Mihail Cojocari

ID 125 **Closed-form Baker–Campbell–Hausdorff–Dynkin formula for rigid body displacements and its significance for Mechanism and Machine Theory** 290
Daniel Condurache; Mihai Cojocari

ID 126 **Influence of human body variability on seat-to-head transmissibility** 292
Linan Yin; Jianqiao Guo; Yanfei Jin; Jingwei Meng; Qiang Tian; Haiyan Hu

ID 127 **Methods of TCA and LTCA for pure-rolling bevel line gear with the actively designed contact trace** 294
Xiaoping Xiao; Hualin Xie; Chao He; Kai Zhu; Zhen Chen; Yangzhi Chen

ID 128 **Unsteady-state tire cornering under dynamic normal load variations** 296
Witold Luty; Karol Zielonka

ID 129 **Exploiting passive dynamics for steady-state walking on level and inclined terrain** 298
Anargyros-Nektarios Skafidas; Aikaterini Smyrli; Evangelos Papadopoulos

ID 130 **Kinematic and static analysis of a cable driven continuum robot** 300
Akshay Menon; Ashitava Ghosal

ID 131 **DEM-multibody coupling simulations of spring tires interacting with granular terrain** 302
Kun Wang; Qiang Tian; Haiyan Hu

ID 132 **Reconfiguration-enabled workspace reshaping and motion planning for a legged lander** 304
Ziyue Li; W.Z. Guo Guo

ID 133 **Modeling and control-oriented simulation of DBD plasma actuators for aerodynamic performance enhancement** 306
Raul Alberto Bernal-Orozco; Oliver Marcel Huerta-Chavez; Genaro Carreon-Carrera

ID 134 **Modeling ball recirculation in multibody ball screw drives** 308
Antonio Carlo Bertolino; Roberto Guida; Andrea De Martin; Massimo Sorli

ID 135 **Modal analysis of engines and powertrains with AVL EXCITE™: An overview** 310
Tigran Parikyan

ID 136 **Initially-curved variable-thickness flexures improve performance in compliant mechanisms, a straight-line generator example** 312
Flip Colin; Abdullah Yasir; Erwin Mulder; Just Herder

ID 139 **Kinematic properties of the instantaneous centers of zero velocity and acceleration according to their trajectories and centrodes** 314
Giorgio Figliolini; Chiara Lanni; Luciano Tomassi

ID 140 **Spherical four-bar control moment gyroscope: Concept and rotating-torque generation** 316
Sajjad Keshtkar; Hirohisa Kojima; Francisco Geu Flores; Wojciech Kowalczyk

ID 141 **Thermal-based stiffness modulation of flexible surgical instruments for robot-assisted minimally invasive surgery** 318
Doina Pisla; Bogdan Gherman; Ionut Zima; Alexandru Pusca; Adrian Pisla; Marius Miclaus; Calin Vaida; Damien Chablat

ID 142 **Ring-down analysis using a three-axis accelerometer for a trajectory with a trapezoidal velocity profile** 320
Edgar Eliseo Franco Ortiz; Carlos Rodriguez Donate; Jacob Gonzalez Villagomez; Luis Manuel Ledezma Carrillo

ID 143 **Pseudo-rigid-body modeling can simulate complex compliant mechanisms without solving kinematics** 322
Domas Syaifoel; Just Herder; Michaël Wiertlewski

ID 144 **Zero stiffness mechanism for constant compression pressure on prismatic and pouch cells in battery modules** 324
Madhu Raghavan; Chinmaya Patil; Shashank Ramesh

ID 145 **Snapping four bar mechanisms: Discrete assembly configurations in closed-loop linkages** 326
Andreas Mair; Daren A. Thimm; Martin Pfurner

ID 146 **Comparison of prism-based tensegrity joint architectures** 328
Karol Muñoz; Mathieu Porez; Philippe Wenger

ID 147 **Cable anchor sensitivity analysis for reconfigurable cable robots** 330
Hung Hon Cheng; Josie Hughes

ID 148 **Creation of a class of self-regulating mechanisms** 332
Konstantin Ivanov

ID 149 **Computerized generation, tooth contact analysis and stress analysis of pericyclic gear drives** 334
Ignacio Gonzalez-Perez; Ramon Ruiz-Orzaez; Alfonso Fuentes-Aznar

ID 150 **Multi-objective optimization of the flexibility and life-span of grid couplings** 336
Elias Rechreche; Jerôme Bruyere; Quentin Le Guennec; Philippe Velex

ID 151 **Full-scale validation of fretting-map predictions for aerospace-grade crowned involute splines AISI 9310** 338
Aurea Iñurritegui-Marroquin; Andrea Mura; Aitor Arana; Ander Elkoro; Francesca Cura

ID 152 **Kinematics and workspace of a cuspidal modular parallel robot** 340
Adrián Peidró; Paula Mollá-Santamaría; Jorge Francisco Aznar Ortega; Luis Miguel Jiménez; Oscar Reinoso

ID 153 **Kinematic modeling of a metamaterial system for morphing structure applications** 342
Aaron Benatar; Fengfeng Xi; Amitabha Ghosh

ID 154 **A universal design and gear surface quality control methodology of face-milled hypoid gear with large range of offset and shaft angle** 344
Siyuan Liu; Chaosheng Song; Caichao Zhu

ID 155 **Optimization of nonlinear active absorbing for compliant planar mechanisms** 346
Zbyněk Šika; Jan Krivošej; Jakub Švadlena

ID 156 **Developable triangle-based Kokotsakis polyhedra** 348
Yucai Hu; Guoqiang Zhu; Ke Chen

ID 157 **Optimal design of a suspended parallel robot for wall plastering** 350
Jorge Francisco Aznar Ortega; Adrián Peidró Vidal; Paula Mollá Santamaría; Óscar Reinoso García

ID 158 **A bipedal robot based on multi-loop coupled parallel leg mechanism** 352
Donglai Xu; Sheng Guo; Fuqun Zhao; Xiaodong Jin; Marco Carricato

ID 159 **Approaches to modeling leaf springs in railway vehicles and their validation** 354
Pavel Polach; Michal Hajžman; Ondřej Skála; Kamil Šimeček

ID 160 **A planar parallel robot with a remote-controlled orientable two-finger gripper** 356
Tan Sy Nguyen; Simon Foucault

ID 161 **Gravity compensation mechanisms for passive and quasi-passive exoskeletons** 358
Marla Weltken; Sérgio Gonçalves; Miguel Tavares da Silva

ID 164 **Experimental validation of a mechanically synchronized modular legged robot for in-pipe locomotion** 360
Esdras S. da Silva; Rafael W. Duarte; Gustavo Queiroz; Duber F. Vergara; Gustavo V. Souza; Henrique Simas; Tiago C. Pinto; Daniel Martins

ID 165 **Configuration design and continuous workspace feasibility analysis of an over-redundant cable-driven refueling mechanism based on a shipborne gantry crane** 362
Zhiwei Jia; Erwei Li; Hansen Ma

ID 166 **Meshing theory of point-contact Archimedean face worm gear drive** 364
Shibo Mu; Xingwei Sun; Zhixu Dong; Jianlong Zhao; Liya Jin; Weifeng Zhang; Yin Liu; Heran Yang; Haosheng Hao; Yaping Zhao

ID 167 **Inverse acoustic fingerprinting for non-invasive identification of precessing vortex core in combustion chambers** 366
Leonel Maximiliano Gomez Villarejo; Oliver Marcel Huerta Chavez; Raul Alberto Bernal Orozco; Luis Alfonso Rodriguez Salinas; Gibran Jalil Garnica Castro

ID 169 **Synthesis and structural characterization of nanostructured tin dioxide via sol-gel for acetone sensing application** 368
Luis Alfonso Rodriguez Salinas; Georgina García Pacheco; Jacobo Esteban Munguia Cervantes; Alfredo López Monroy; Leonel Maximiliano Gómez Villarejo

ID 170 **On the feasibility of predicting rolling contact fatigue from uniaxial S-N curves** 370
Ibai Ulacia; Iñigo Llavori; Mattin Maiztegui; Aitor Arana; Jon Larrañaga

ID 172 **Optimizing ball bearing contact angle for minimum power loss under combined loads** 372
Pello Alberdi; Aitor Arana; Aitor Oyanguren; Jon Larrañaga; Ibai Ulacia

ID 173 **Optimal measurement area identification and accuracy enhancement of a CMM based on IPSO-SAA** 374
Zishuai Wang; Zeru Lyu; Zhaoyao Shi; Hongfang Chen

ID 174 **Virtual model of a bus using the FMI standard for co-simulation with Matlab/Simulink** 376
Jozef Bucha; Ján Danko; Tomáš Milesich

ID 175 **Enhancing distal motion-force interaction performance of articulated-platform parallel mechanisms via internal parameter design of closed-loop passive limbs** 378
Qizhi Meng; Burkhard Corves; Andrés Kecskeméthy

ID 177 **On the numerical errors of multibody dynamics Jacobians induced by the Rodrigues formula** 380
Jiayi Zhou; Zhiwen Xiao; Gexue Ren

ID 178 **Multibody dynamics-based feedforward control strategies for wellbore trajectory tracking in directional drilling systems** 382
Xinrong Li; Kejie Wang; Jiaqi Chen; Ningyu Wang; Gexue Ren

ID 179 **NVH-aware co-optimization of topology, parameter and control for distributed range-extended electric powertrains** 384
Yuxin Zhang; Yunge Zou; Xin Ye

ID 180 **Reduced-order modeling of bearings and gears for accurate stress computation** 386
Zhiwen Xiao; Zhilu Qi; Xinrong Li; Gexue Ren

ID 181 **Research on the design and optimization methodology of multi-mode multi-gear transmission architecture for electric vehicles based on graph theory** 388
Yunge Zou; Yuxin Zhang; Yantao Si

ID 182 **Biomechanical assessment of reclined occupant postures in automated vehicles using LS-DYNA simulations** 390
Nuno Carmo; Ana Martins; Marta Carvalho

ID 183 **Accurate real contact area computation of anisotropic rough surfaces** 392
Mattin Maiztegui; Jon Larrañaga; Ibai Ulacia

ID 184 **Study of planet phasing influence on the efficiency of a planetary gear** 394
José Ángel Moncalián Cruz; Miguel Iglesias Santanmaría; Alberto Díez Ibarbia; Javier Sánchez Espiga; Alfonso Fernández del Rincón; Fernando Viadero Rueda

ID 185 **Synthesis and structural characterization of nanostructured titanium dioxide via sol-gel for memristive CO sensing in aerospace applications** 396
Jorge Luis Cervantes Fraustro; Georgina García Pacheco; Jacobo Esteban Munguía Cervantes; Gerardo Villa Martínez

ID 186 **Equivalent transformations of MSA- and VJM-based stiffness models** 398
Alexandr Klimchik; Anatol Pashkevich

ID 187 **Stability investigation of the model predictive controller: A semi-analytical approach** 400
Bálint Bodor; Szabolcs Berezvai

ID 188 **DMLab: Design and modelling of machine elements** 402
Ibai Ulacia; Aurea Iñurritegui; Aitor Arana; Jon Larrañaga

ID 189 **Comparison of different wheel-rail constraint-based contact approaches** 404
Erik Snellman; Xinxin Yu

ID 192 **Kinematic geometry and envelope curves of vehicles when moving along linear tractrices** 406
Giorgio Figliolini; Chiara Lanni; Jorge Angeles

ID 193 **A compact SPS-based parallel mechanism for worm-like robot locomotion in confined environments** 408
Angelos Iliakis; George Nikolakopoulos; Panagiotis Koustoumpardis

ID 194 **Modeling of screw mechanisms for control - a multibody approach** 410
Márton Kuslits

ID 195 **Method for optimization of planar parallel robots taking into account singularities based on automatic derivation of kinematic dependencies** 412
Larisa Rybak; Dmitry Malyshev; Dmitry Dyakonov

ID 196 **Towards a methodology for interpretable embodied kinematic intelligence via null-space analysis of G-pose matrix** 414
Qiaode Jeffrey Ge; Huan Liu

ID 197 **Automated extraction and graph-based representation of mechanism diagrams: Bridging computer vision, structural synthesis, and engineering education** 416
Gustavo Valdatti Souza; Angel Esley Garcia Caceres; Andrea Piga Carboni; Daniel Martins

ID 198 **Development and research of a multimodal robot with ground and aerial modes** 418
Larisa Rybak; Dmitry Malyshev; Vladislav Cherkasov

ID 199 **A geometric characterization for performance evaluation of lubricated clearance joints in multibody systems** 420
Bassam Alshaer; Paulo Flores; Hamid Lankarani

ID 200 **Modeling, simulation and sensitivity testing of automotive automatic control systems due to backlash and friction** 422
Dariusz Żardecki; Mirosław Gidlewski; Marek Jaśkiewicz; Leszek Jemioł; Karol Zielonka

ID 201 **Actuation redundancy management of the 3-DOF PercuCob-RCM parallel manipulator** 424
Kevin Gaitan; Juan Sandoval; Stéphane Caro

ID 202 **Design and optimisation of a tilt-in-space wheelchair mechanism** 426
Leonor Guimarães; Mariana Rodrigues da Silva; Filipe Marques

ID 203 **Impact of new joining processes of new materials of the structure of an automobile on its vehicle handling dynamics** 428
Jorge Ambrósio; Pedro Millan; Lucas da Silva

HOW TO OBTAIN ANALYTICAL SOLUTIONS FOR VEHICLE PHASE PLANE EQUILIBRIUM AND STABILITY ANALYSIS

Basilio Lenzo[1], Mariagrazia Tristano[1]

[1] Università di Padova, Dept. of Industrial Engineering, Via Venezia 1, 35131 Padua, Italy {basilio.lenzo@unipd.it}

1 INTRODUCTION

Vehicle phase planes have long been studies in the literature [1]. Stability control algorithms are often based on heuristic techniques based on the comparison between vehicle equilibria calculated at some given inputs (typically including steering angle and longitudinal speed) and the vehicle states, to discern whether the vehicle is or not in a safe operating condition [2] and to intervene, or not, accordingly (e.g. through Electronic Stability Control [3]).
However, vehicle equilibria may only be found numerically [4]. This work shows how to find equilibria in analytical form.

2 THE PROPOSED METHODOLOGY

The methodology herein proposed is based on the use of the single-track vehicle model and a non-typical tire model [5]. The latter is the key to obtain an analytical solution.
The model (Fig. 1) equilibrium equations are the classical [6]:

$$\beta = F_{yf} + F_{yr} m v_x - r \tag{1}$$

$$r = F_{yf} a_1 - F_{yr} a_2 J_z \tag{2}$$

with congruence equations:

$$\alpha_f = \delta - \beta - r a_1 v_x \tag{3}$$

$$\alpha_r = -\beta + r a_2 v_x \tag{4}$$

where β is the sideslip angle and r the yaw rate, v_x the longitudinal velocity, δ the steering angle at the wheel, F_{yf} and α_f and F_{yr} and α_r are respectively the lateral tire force and slip angle at the front (f) and rear (r) axle, a_1 and a_2 the front and rear semi-wheelbases, m the vehicle mass and J_z the vehicle moment of inertia around a vertical axis through the center of mass.
The tire model here used is:

$$F_{yi} = \frac{k\alpha_i}{c_{1i}\sqrt{(k\alpha_i)^2} + c_{2i}} \quad i \in f, r \tag{5}$$

where k is a constant factor. The model has similar behavior as other well-known models such as Pacejka [7] or Dugoff [8].
To obtain equilibria, Eq. (1)-(2) are set to zero, leading to:

$$F_{yf} + F_{yr} = m v_x r \tag{6}$$

$$F_{yf} a_1 - F_{yr} a_2 J_z = 0 \tag{7}$$

Isolating F_{yr} from Eq. (6) and substituting the result in Eq. (7):

$$F_{yf} a_1 + F_{yf} a_2 - m v_x r a_2 = 0 \tag{8}$$

where the wheelbase is $l = a_1 + a_2$, and then

$$F_{yf} l = m v_x r a_2 \tag{9}$$

Now, the tire model in Eq. (5) is introduced to provide F_{yf} as a function of α_f, solve for α_f, do the same for α_r and replace the result in Eq. (3)-(4), then solve them for β and r (note that this cannot be done earlier because slip angles are functions of r).

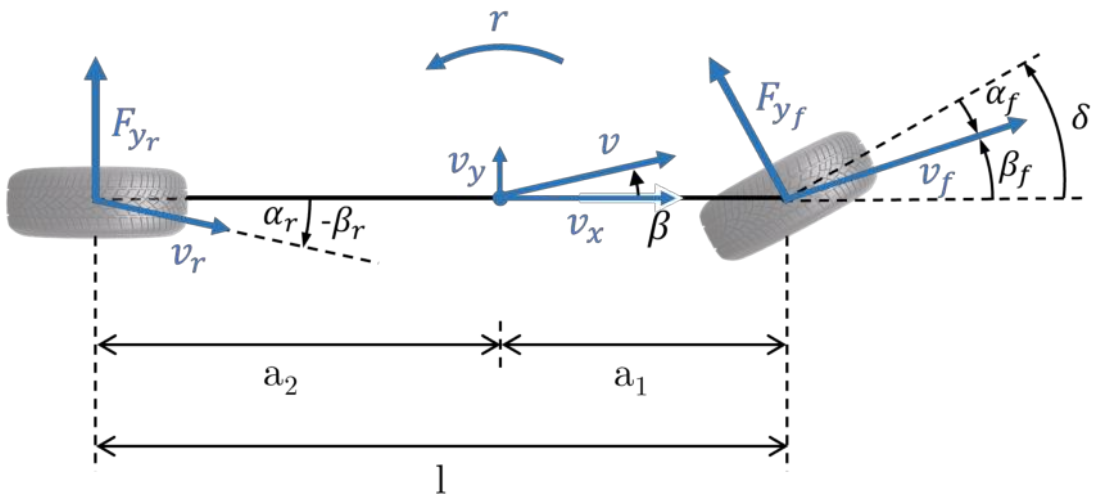

Figure 1: Single-track model.

The presentation will show how this leads to equations impossible to solve when using any of the existing tire models (Pacejka, Dugoff, etc.). Instead, the tire model herein used leads, ultimately, to finding the analytical solution of a vehicle-parameter-dependent third order polynomial, which is indeed possible. The presentation will also show examples comparing the analytical solution with classical numerical solutions for some case studies.

REFERENCES

[1] Bobier-Tiu, C. G., Beal, C. E., Kegelman, J. C., Hindiyeh, R. Y., & Gerdes, J. C. (2019). Vehicle control synthesis using phase portraits of planar dynamics. Vehicle System Dynamics, 57(9), 1318–1337.

[2] Guo, N., Zhang, X., Zou, Y., Lenzo, B., Du, G., & Zhang, T. (2021). A supervisory control strategy of distributed drive electric vehicles for coordinating handling, lateral stability, and energy efficiency. IEEE Transactions on Transportation Electrification, 7(4), 2488–2504.

[3] Van Zanten, A. T., Erhardt, R., Landesfeind, K., & Pfaff, G. (2000). Vehicle stabilization by the vehicle dynamics control system ESP. IFAC Proceedings Volumes, 33(26), 95-102.

[4] Zubov, I., Afanasyev, I., Gabdullin, A., Mustafin, R., & Shimchik, I. (2018). Autonomous drifting control in 3D car racing simulator. In 2018 International Conference on Intelligent Systems (IS) (pp. 235-241). IEEE.

[5] Tristano, M., Lenzo, B. (2025). Analytical solution of vehicle phase-plane equilibria through the Root-Rational tyre model. Vehicle System Dynamics, 1-19.

[6] Lenzo, B. (2025). Vehicle Dynamics—Fundamentals. In Vehicle Dynamics, Control and Design (pp. 1-60). Cham: Springer Nature Switzerland.

[7] Pacejka, H. (2005). Tire and vehicle dynamics. Elsevier.

[8] Bian, M., Chen, L., Luo, Y., Li, K. (2014). A dynamic model for tire/road friction estimation under combined longitudinal/lateral slip situation (No. 2014-01-0123). SAE Technical Paper.

COMPARATIVE EVALUATION OF MACHINE LEARNING METHODS FOR MOTION-RELATED PAIN PREDICTION IN LUMBAR DISC HERNIATION PATIENTS

Airi Hatsushiro[1], Yuta Tawaki[1], Toshiyuki Murakami[1], Teresa Zielinska[2]

[1] Department of System Design Engineering of Keio University, Yokohama 223-8522, Japan
{airiyumemiku@keio.jp; y.tawaki@keio.jp; mura@sd.keio.jp}
[2] Faculty of Power and Aeronautical Engineering, Warsaw University of Technology,
Warsaw 00-665, Poland {Teresa.Zielinska@pw.edu.pl}

1 INTRODUCTORY INFORMATION AND APPLIED METHODS

Low back pain is one of the most common musculoskeletal disorders globally, and lumbar disc herniation (LDH) represents a major underlying pathology. Patients with LDH often describe motion-dependent pain that fluctuates during daily activities, yet the biomechanical mechanisms responsible for these fluctuations remain unclear. Traditional clinical assessments rely on subjective scoring or snapshot imaging, which cannot capture how mechanical loading throughout a movement influences pain perception. Advances in musculoskeletal simulation now allow detailed reconstruction of internal biomechanical states, while machine learning provides tools to analyse large, correlated feature sets [1]. However, these two methodologies have rarely been combined to model pain during realistic motion. The objective of this study is therefore twofold: (1) to identify biomechanical parameters most strongly associated with pain during different functional movements in LDH, and (2) to evaluate whether moment-to-moment pain intensity can be predicted using these parameters through time-series modelling. A 24-year-old female patient diagnosed with unilateral L4–L5 LDH performed three functional tasks—trunk flexion, trunk extension, and crouching/standing—each executed at slow, normal, and fast self-selected speeds. These movements were chosen to represent common daily activities that provoke pain in LDH. Pain was assessed using the Numerical Rating Scale (NRS, 0–10) immediately after each trial. To approximate continuous pain trajectories aligned with the motion cycles, the discrete NRS values were interpolated across the time-normalised movement. Kinematic data were recorded using a VICON system (100 Hz) with ground reaction forces collected through force platforms. Data processing was performed in OpenSim using the Rajagopal full-body musculoskeletal model. After scaling and inverse kinematics, inverse dynamics and static optimisation produced 373 biomechanical parameters, including joint kinematics, joint torques, muscle forces for 80+ muscles, and three-dimensional joint reaction forces. For each movement–speed combination, six feature-selection techniques were applied: Lasso Regression [2], Adaptive Lasso Regression [3], Elastic Net [4], Random Forest [5], XGBoost [6], and LightGBM [7]. Each method produced a ranked list of pain-related parameters, from which the top 20 were retained. This approach allowed identification of both linear and non-linear predictors while handling the high dimensionality of the dataset. The selected features served as inputs to Long Short-Term Memory (LSTM) models, trained to predict pain intensity over the course of the movement. Models were evaluated using RMSE and visual inspection of predicted versus constructed pain trajectories.

2 RESULTS AND DISCUSSION

Across the nine movement–speed conditions, Elastic Net demonstrated the highest stability and produced the largest number of overlapping features, particularly for trunk flexion and crouching tasks. Frequently selected biomechanical parameters included pelvic tilt and vertical translation, lumbar lateral flexion angle, anteroposterior and vertical lumbar joint reaction forces, and muscle forces from deep hip stabilisers (iliacus), gluteal muscles (gluteus medius), and knee flexors (short head of the biceps femoris). The consistent appearance of these parameters suggests that both lumbar segment loading and pelvic–hip compensation strategies are important contributors to pain during dynamic motion. Fig.1 shows the actual and predicted pain levels obtained using Elastic Net. The LSTM prediction results further reflected the biomechanical characteristics of each movement. In slow-speed conditions, pain predictions were smoother, with lower RMSE values, because the underlying movements were more mechanically stable and less variable. Normal-speed trials displayed moderate accuracy. Fast movements, particularly fast trunk extension, produced the highest RMSE values, indicating difficulty in predicting pain under conditions of rapid loading, increased range of motion, and greater neuromuscular demand. A visual comparison of predicted and constructed pain curves showed that the model captured general patterns of pain escalation and reduction, though peak intensities were sometimes

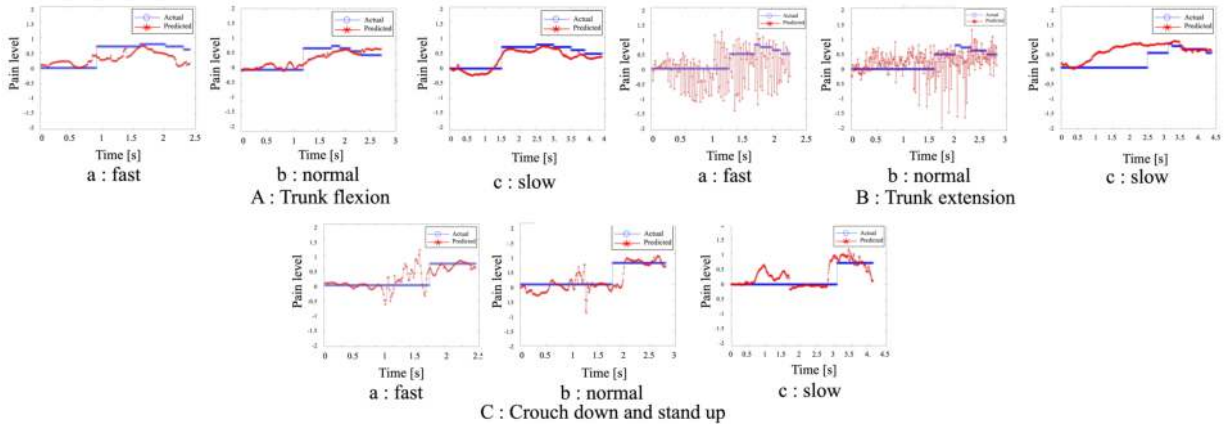

Figure 1: Results of predicted and actual pain levels obtained using Elastic Net.

underestimated during high-speed tasks. The biomechanical variables identified by multiple feature-selection methods align with known mechanisms of LDH-related pain. Increased lumbar reaction forces and exaggerated pelvic motions have been associated with instability or protective guarding, both of which can elevate pain perception. The repeated selection of hip stabilising muscles supports the notion that LDH patients adopt compensatory strategies to offload the lumbar spine. These strategies may reduce local spinal loading but increase muscular effort elsewhere, potentially contributing to secondary discomfort. The variability in movement speeds confirms that pain prediction is more reliable during controlled, slow movements, whereas dynamic, rapid tasks introduce variability that challenges both simulation and machine learning models. The strong performance of Elastic Net indicates that hybrid regularisation is well-suited to biomechanical datasets with correlated variables, whereas tree-based methods tended to overfit when sample sizes were limited.

3 CONCLUSION

This study presents a compact yet comprehensive workflow combining musculoskeletal simulation, multi-method feature selection, and LSTM modelling to analyse pain in dynamic tasks for an LDH patient. The approach successfully identified biomechanical features strongly associated with pain and demonstrated that movement-specific pain can be predicted with reasonable accuracy, especially in slow and moderate speeds. Although based on a single participant, the methodology is scalable and can be extended to multi-subject studies aimed at developing personalised, movement-based pain assessments and rehabilitation strategies. Future work will incorporate larger datasets, sensor-based data collection for real-world applicability, and optimisation of deep-learning architectures to improve prediction robustness.

REFERENCES

[1] K. Deshmukh, A. Kule, P. Bangal, S. Udar, and S. Khiani, "Pain sense: Intelligent pain mapping system for spinal cord injuries," in *3rd International Conference on Pervasive Computing and Social Networking*, 2023, pp. 1569–1572.

[2] R. Tibshirani, "Regression shrinkage and selection via the lasso," *Journal of the Royal Statistical Society B*, vol. 58, pp. 267–288, 1996.

[3] H. Zou, "The adaptive lasso and its oracle properties," *Journal of the American Statistical Association*, vol. 101, pp. 1418–1429, 2006.

[4] H. Zou and T. Hastie, "Regularization and variable selection via the elastic net," *Journal of the Royal Statistical Society Series B: Statistical Methodology*, vol. 67, no. 2, pp. 301–320, 2005.

[5] R. Genuer, J.-M. Poggi, and C. Tuleau-Malot, "Variable selection using random forests," *Pattern Recognition Letters*, vol. 31, no. 14, pp. 2225–2236, 2010. [Online]. Available: https://www.sciencedirect.com/science/article/pii/S0167865510000954

[6] T. Chen and C. Guestrin, "Xgboost: A scalable tree boosting system," in *22nd ACM SIGKDD International Conference on Knowledge Discovery and Data Mining*, 2016, pp. 785–794.

[7] G. Ke, Q. Meng, T. Finley, T. Wang, W. Chen, W. Ma, Q. Ye, and T.-Y. Liu, "Lightgbm: a highly efficient gradient boosting decision tree," in *31st International Conference on Neural Information Processing Systems*, 2017, pp. 3149–31 578.

OPTIMIZING RIDE COMFORT IN FOUR-WHEEL HUB-MOTOR ELECTRIC VEHICLES VIA MULTIBODY DYNAMICS AND MULTI-OBJECTIVE ALGORITHMS

Ling Ma[1], Yongjun Pan[1], Wei Liu[1], Aki Mikkola[2]

[1]State Key Laboratory of Mechanical Transmission for Advanced Equipment, College of Mechanical and Vehicle Engineering, Chongqing University, Chongqing, 400044, China, {yongjun.pan@cqu.edu.cn}

[2]Department of Mechanical Engineering, Lappeenranta University of Technology, 53850, Lappeenranta, Finland, {aki.mikkola@lut.fi}

1. ABSTRACT

The integration of transmission systems in four-wheel hub motor-driven (4WHMD) electric vehicles enhances efficiency and handling but introduces greater unsprung mass, which compromises ride comfort relative to centralized motor-driven (CMD) vehicles. This paper proposes an optimization framework to mitigate this issue, advancing mechanism design through multibody dynamics analysis and multi-objective optimization. First, high-fidelity multibody dynamics models for both 4WHMD and CMD vehicles are established, capturing nonlinear suspension behavior and wheel - ground interactions to quantify vibrational energy transfer and ride comfort metrics. Second, a comparative study between the two vehicle types is conducted. Third, a surrogate model is developed using design of experiment (DOE) and Gaussian process regression (GPR), enabling rapid evaluation of suspension parameters while reducing computational complexity. Finally, multi-objective simulated annealing (MOSA), non-dominated sorting genetic algorithm (NSGA-II), and a hybrid multi-objective optimization algorithm (HMOA) are applied to optimize ride comfort, balancing five performance indices through a trade-off strategy. The optimized 4WHMD vehicle achieves better vertical and roll acceleration than the CMD baseline, though it performs worse in suspension dynamic deflection and wheel dynamic load. Among the methods, HMOA demonstrates the strongest comprehensive ability for global and local search. This research contributes to the development of high-performance mechanical systems through integrated dynamic modeling and intelligent optimization techniques.

2. ELECTRIC VEHICLE DYNAMICS MODELING AND PERFORMANCE EVALUATION

The hub motor drive system integrates the motor directly within the wheel, removing traditional components such as drive shafts and differentials. This design not only simplifies the vehicle's mechanical architecture but also creates new opportunities for vehicle dynamics control. However, it also introduces distinct challenges, making the establishment of an accurate vehicle dynamics model essential. In this section, a multibody dynamics modeling method is employed to develop such a model. This approach accounts for the varied structures and dynamic characteristics of different suspension types, resulting in a model that is both accurate and suitable for comprehensive performance evaluation[1-3].

The most apparent distinction between centralized motor-driven (CMD) and four-wheel hub motor-driven (4WHMD) electric vehicles lies in the placement of the drive motors. In a CMD configuration, the motors are mounted on the vehicle body, forming part of the sprung mass, and deliver power to the wheels through a series of transmission components. Conversely, in a 4WHMD vehicle, the motors are integrated directly into the wheel hubs, contributing to the unsprung mass, and apply torque to the wheels without intermediate drivetrain elements. The CMD vehicle studied here utilizes four motors, two front and two rear, while maintaining the same centroid position and overall dimensions as the 4WHMD variant for a consistent comparison. Consequently, the two models differ primarily in the mass and inertia distribution of both the vehicle body and the wheels. We select several typical working conditions and conduct simulation analysis. We systematically measure five distinct riding comfort indices and subsequently calculate the root mean square (RMS) for each index. On this basis, we further quantified and calculated the relative range for each indicator, and selected the indicators with the largest relative range through comparative sorting, using this as a starting point for subsequent targeted research.

3. MULTI-OBJECTIVE OPTIMIZATION OF RIDING COMFORT

This section concentrates on formulating the multi-objective optimization problem for riding comfort. Notably, a surrogate model is utilized to replace the vehicle dynamics model, enabling faster optimization. This process includes creating a design of experiment (DOE) and using Gaussian process regression (GPR) to build mathematical relationships, as well as implementing the MOSA, NSGA-II, and HMOA algorithms to solve the optimization problem. The optimization results are shown in the following figure. There are significant differences in search strategies for Pareto optimal solutions among

different optimization algorithms, and each algorithm has its own characteristics. Among them, MOSA algorithm has strong local search ability, NSGA-II algorithm has more outstanding global search ability, and HMOA algorithm can balance global exploration and local mining, while also having high optimization efficiency.

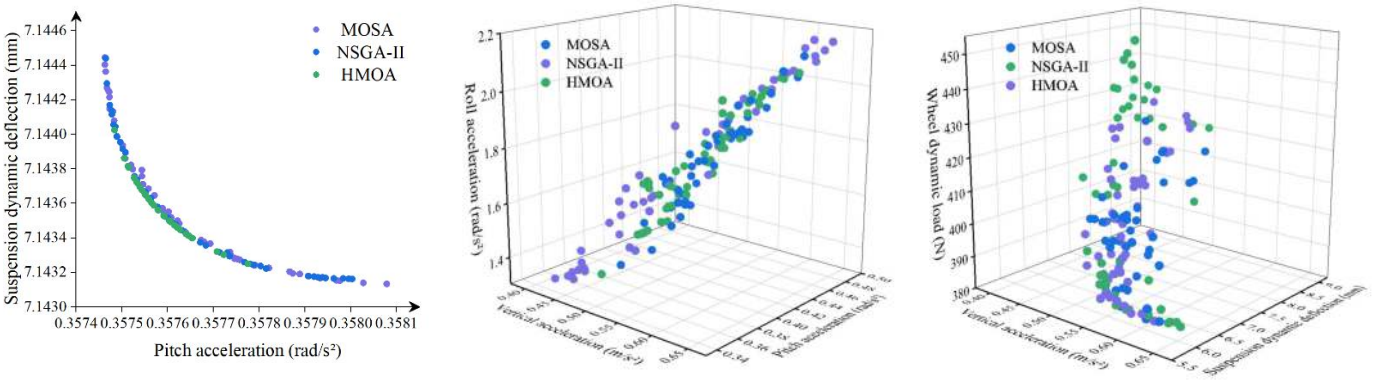

(a) Optimization of CMD (b) Optimization of FWD (c) Optimization of FWD

Figure 1. Optimization results and Pareto set

4. DISCUSSIONS

In such a large number of Pareto solution sets, we use distance index to select the optimal solution, which is the final optimization result of the corresponding optimization problem. Considering that this optimization work was completed under random road excitation conditions, the optimized values have good results under the original operating conditions. However, to verify that the optimization results can remain effective and universal under various operating conditions, we specifically selected pulse excitation as a supplementary verification case and compared the vertical acceleration response time-domain curves of two vehicles (before and after optimization). The results indicate that the pulse excitation response corresponding to the optimized vehicle parameters has significantly decreased compared to before optimization.

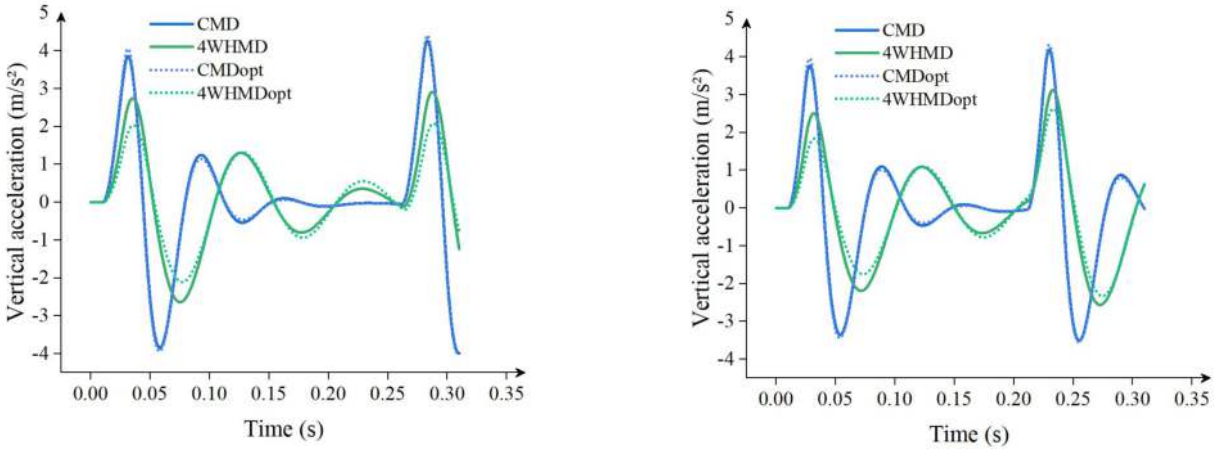

(a) Vehicle speed 40 km/h (b) Vehicle speed 50 km/h

Figure 2. Optimized vehicle indicator evaluation

ACKNOWLEDGMENTS

This study was funded in part by the National Natural Science Foundation of China (Project No. 12572046).

REFERENCES

[1] García de Jalón, J., Álvarez, E., de Ribera, F.A., Rodríguez, I., Funes, F.J.: A fast and simple semi-recursive formulation for multi-rigid-body systems. In: Advances in Computational Multibody Systems. Computational Methods in Applied Sciences, vol. 2, pp. 1–23 (2005).

[2] García de Jalón, J., Callejo, A., Hidalgo, A.F., Efficient solution of Maggi's equations. J. Comput. Nonlinear Dyn. 7(2), 021,003 (2012).

[3] Pan Y., Callejo A., Bueno J.L., Wehage R.A., García de Jalón J., Efficient and accurate modeling of rigid rods. Multibody System Dynamics, 40 (1), pp. 23 - 42 (2017).

SUMMIT-COUNTING METHOD FOR STATISTICAL MIXED-LUBRICATION GEAR FRICTION MODELING

Miguel A.S. Dias[1], Carlos M.C.G. Fernandes[1,2]

[1] Faculdade de Engenharia, Universidade do Porto, Rua Dr. Roberto Frias s/n, Porto, 4200-465, Portugal, {cfernandes@fe.up.pt}
[2] INEGI, Universidade do Porto, Rua Dr. Roberto Frias 400, Porto, 4200-465, Portugal

1 INTRODUCTION

A statistical model is proposed to predict the coefficient of friction of cylindrical gears along the path of contact. The model combines the Greenwood–Williamson asperity contact formulation [2] with Moes' film thickness equations [3]. A key challenge of such models is the estimation of surface roughness summit parameters. This work compares commonly used summit selection methods from the literature and proposes a new approach that is simple to implement and provides consistent predictions of the gear coefficient of friction.

2 STATISTICAL FRICTION MODEL FOR GEARS

The proposed model follows Johnson's load-sharing concept, in which the normal load F_n is jointly supported by asperity contact (F_c) and hydrodynamic lubrication (F_H). This leads to Eq. (1), where γ_1 and γ_2 are the lubricant and asperity scaling factors, respectively [1]:

$$F_n = F_c + F_H = \frac{F_n}{\gamma_2} + \frac{F_n}{\gamma_1} \quad \Leftrightarrow \quad 1 = \frac{1}{\gamma_2} + \frac{1}{\gamma_1}. \tag{1}$$

The asperity force F_c obtained from Eq. (1) is equated to the Greenwood–Williamson asperity contact force F_c^{GW}, yielding the system of equations in Eq. (2). The solution is obtained iteratively by adjusting γ_1 until the difference between F_c and F_c^{GW} is minimized, as illustrated in Figure 1.

$$\begin{cases} F_c = \dfrac{2}{3} n A_c E' \beta^{\frac{1}{2}} \sigma_s^{\frac{3}{2}} \, \mathrm{F}_{\frac{3}{2}} \left(\dfrac{h - d_d}{\sigma_s} \right) \\ \dfrac{1}{\gamma_1} + \dfrac{1}{\gamma_2} = 1 \end{cases} \tag{2}$$

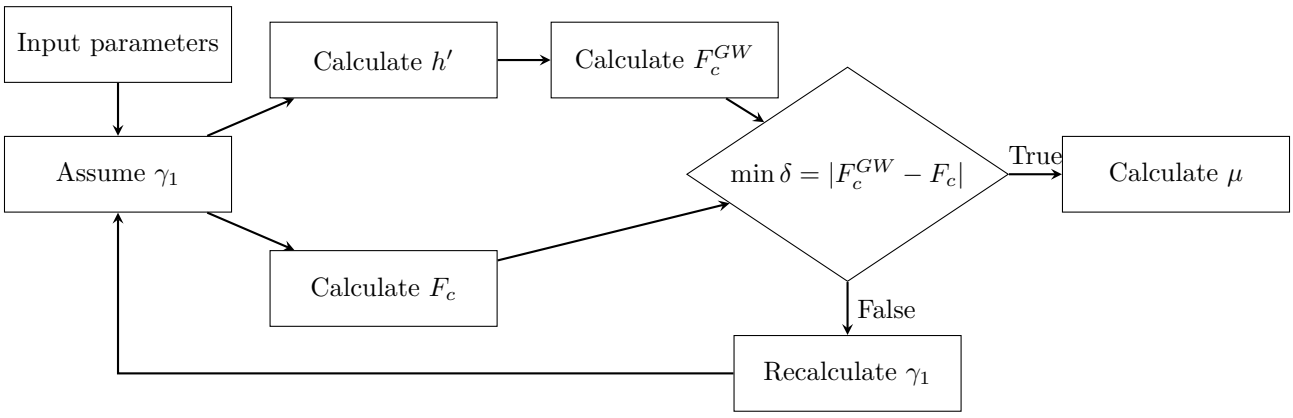

Figure 1: Flowchart of the numerical method with force convergence.

After convergence, the coefficient of friction μ is computed using Eq. (3). The hydrodynamic friction force is evaluated using the Bair–Winer rheological model, with the limiting shear stress determined experimentally from ball-on-disc tests for the lubricant under study.

$$\mu = \frac{\mu_c F_c + F_{f,H}}{F_n}. \tag{3}$$

3 SUMMIT COUNTING METHODS

Several summit selection methods have been reported in the literature. In this work, the most common approaches are compared, namely the local maximum, threshold, watershed segmentation, and Nayak methods. Based on their limitations, a new summit counting method is proposed and experimentally validated.

3.1 Proposed summit counting method

The proposed approach is a matrix-based selection method, conceptually similar to the local maximum method. The matrix size $N_x \times N_y$ is defined based on both the sampling interval and the summit radius (β), according to Eq. (4):

$$N_i = \left\lceil \frac{2\beta_i}{\Delta_i} \right\rceil. \tag{4}$$

This criterion reduces summit over-selection and provides a clear physical interpretation, in contrast to threshold-based methods where limits are arbitrarily defined.

A limitation of the method is the possible need for rectangular matrices ($N_x \neq N_y$), which may introduce inaccuracies for ellipsoidal summits. To address this, a weighting mask is introduced. The mask assigns unit weight within an ellipse defined by semi-axes β_x and β_y, with weights gradually decreasing to zero outside this region. The selection matrix is multiplied by this mask, reducing the influence of distant points during summit identification. An example of summit selection provided by the proposed alghoritm is given in Figure 2.

4 VERIFICATION WITH EXPERIMENTS

Figure 3 presents the predicted coefficient of friction along the path of contact, described by the dimensionless coordinate ξ. The locally predicted values are averaged and compared with experimentally measured mean friction coefficients obtained at a wheel speed of 200 rpm for three identical gear sets operating under different pinion torques (G1: 215.6 N m, G2: 319.2 N m, and G3: 98.8 N m). The model accurately reproduces both the magnitude and the evolution of the coefficient of friction, including its variation associated with surface modifications occurring during the running-in phase.

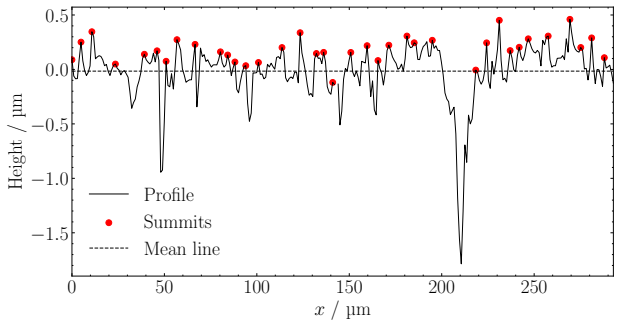

Figure 2: Proposed matrix-based summit selection method.

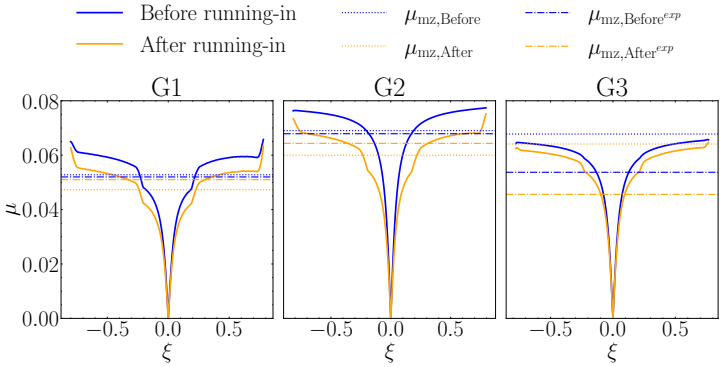

Figure 3: Comparison between model results and experimentally derived coefficient of friction of gears.

ACKNOWLEDGMENTS

The authors gratefully acknowledge the funding through LAETA under the project UID/50022/2025.

REFERENCES

[1] K. L. Johnson, J. A. Greenwood, S. Y. Poon, A simple theory of asperity contact in elastohydro-dynamic lubrication, in *Wear*, 19 (1972) 91–108. doi:10.1016/0043-1648(72)90445-0.

[2] A. Greenwood, J. B. P. Williamson, Contact of nominally flat surfaces, in *Proceedings of the Royal Society of London. Series A. Mathematical and Physical Sciences*, 295 (1966) 300–319. doi:10.1098/rspa.1966.0242.

[3] H. Moes, Lubrication and Beyond, University of Twente, Netherlands, 2000.

STATE OF THE ART REVIEW AND COMPARISON ON RATTLE INDEX FORMULATIONS FOR GEAR TRAIN APPLICATIONS

Fabio Bortoluzzi[1], Mattia Battarra[1], Emiliano Mucchi[1], Giorgio Dalpiaz[1]

[1] University of Ferrara, Dept. of Engineering, Via G. Saragat 1, 44123, Ferrara, Italy, {fabio.bortoluzzi@unife.it; mattia.battarra@unife.it; emiliano.mucchi@unife.it; giorgio.dalpiaz@unife.it}

1 INTRODUCTION

The widespread replacement of internal combustion engines by electric powertrains is progresively shifting the focus of noise and vibration analysis. As electric motors are inherently quieter, gear transmissions have emerged as a comparatively more prominent source of noise. In gear transmissions, the dominant noise component is typically associated with the meshing frequency. However, when gears operate in idle or lightly loaded conditions, driving torque fluctuations may promote tooth detachment thanks to the presence of backlash. These repeated impacts excite structural resonances and generate the characteristic impulsive noise known as rattle. Research on this phenomena, particularly the neutral or idling rattle observed in vehicles equipped with diesel engines, has advanced significantly since the early 1980s. Initial investigations primarily aimed to model the nonlinear dynamics of the meshing process and to identify key parameters influencing rattle onset. All these works start from the definition of a proper indicator, namely the rattle index, specifically designed to detect the presence of rattle and its characteristics. Within this context, the most direct indicator is certainly represented by the Transmission Error (TE), which was used as a reference since the very first works on tooth detachment phenomena [1]. With the aim of having more general and quantitative indicators, several authors have proposed over time alternative indices capable of both detecting the presence of the phenomenon and estimating its severity.

Over the past four decades, a wide variety of Rattle Indices (RIs) have been proposed in the literature, each relying on different physical quantities, modeling assumptions, and signal-processing strategies. However, the lack of a unified framework for comparing these indices has hindered their systematic evaluation and practical selection. This work presents a comprehensive state-of-the-art review and comparative assessment of RI formulations for gear train applications, involving more than 80 journal articles regarding RI definition and 11 indicators compared [2, 3, 4, 5, 6, 7, 8, 9, 10, 11]. The primary objective is to collect, classify, and critically analyze the most relevant RIs proposed in the literature, evaluating their capability to (*i*) reliably detect the onset of rattle, (*ii*) quantify its severity in a continuous manner, and (*iii*) remain robust when applied to transmission layouts of increasing complexity. The ultimate goal is to provide a unified reference for researchers and practitioners, offering a clearer understanding of the relationships between the various indices and supporting a more informed selection of suitable metrics for future studies on gear rattle.

2 ANALYSIS AND RESULTS

Beyond the theoretical review, the present work provides a systematic numerical comparison of the selected RIs using a unified modeling framework. Three representative transmission configurations are considered: (i) a single spur gear pair operating under idle conditions, (ii) a single-branch three-gear train with a central idler, and (iii) a multi-speed transmission. For all configurations, a lumped-parameter model with backlash nonlinearity, time-varying mesh stiffness, and Rayleigh damping is employed to investigate the indices' ability to discriminate between no-rattle, single-sided rattle, and double-sided rattle regimes. The analysis includes both time-averaged metrics (Root Mean Square, i.e. RMS, or decibel levels) and instantaneous, time-resolved evaluations to assess how accurately each index captures individual impact events and contact transitions. Figure 1 reports an example of the achieved comparison for the single gear pair layout when affected by single-side and double-side impact behavior. Parameter A describes the amplitude of the sinusoidal input rotational velocity that acts as the external excitation.

Results show that most indices are effective in distinguishing between rattle-free and rattling conditions, although significant differences emerge in their sensitivity to excitation amplitude and impact topology. Indices designed primarily as global severity measures exhibit monotonic trends with increasing excitation but generally fail to discriminate between single- and double-sided impacts. Conversely, force- and torque-based indices provide clearer insight into the instantaneous dynamics of impacts and are better suited for analyzing complex interactions in multi-mesh systems.

3 CONCLUDING REMARKS

This study highlights that no single RI can be regarded as universally optimal. Instead, the choice of an appropriate RI must be guided by the transmission layout, the available measurements, and the specific objective of the analysis. By providing a unified comparative framework and highlighting the strengths and limitations of the main formulations, this work aims to support researchers and practitioners in the informed selection of RIs for future numerical and experimental investigations.

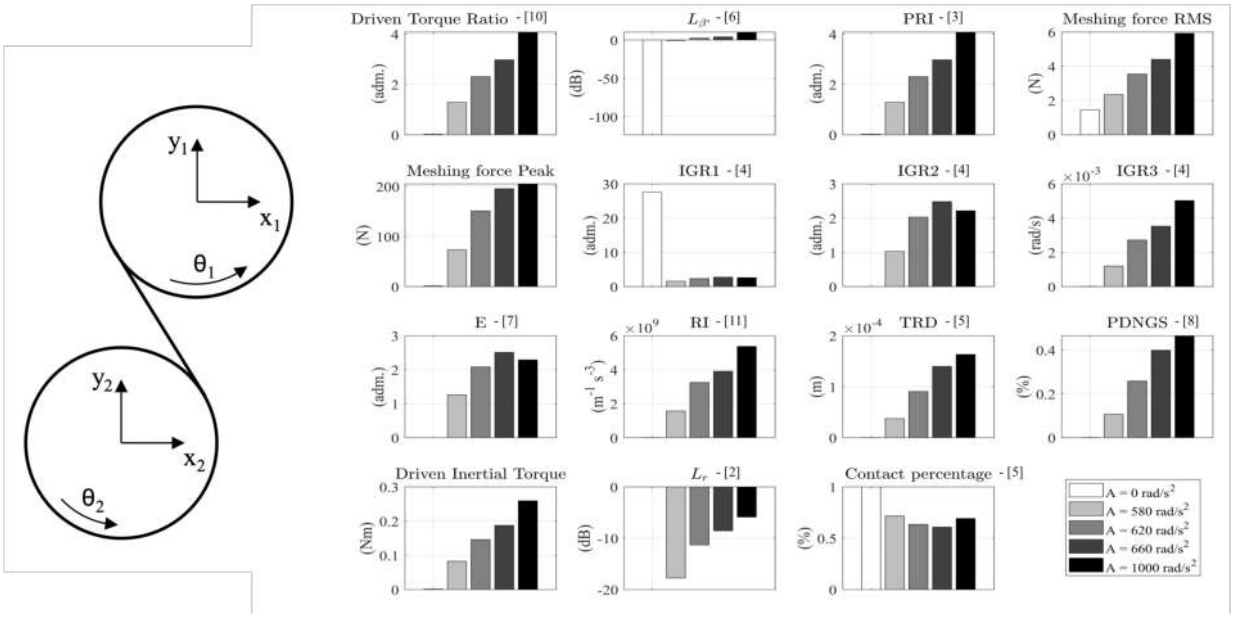

Figure 1: Schematic of the single gear pair model and RI level comparison in single-side and double-side impact behaviour.

REFERENCES

[1] A. Kahraman and R. Singh, "Non-linear dynamics of a spur gear pair," *Journal of sound and vibration*, vol. 142, no. 1, pp. 49–75, 1990.

[2] A. Donmez and A. Kahraman, "Experimental and theoretical investigation of vibro-impact motions of a gear pair subjected to torque fluctuations to define a rattle noise severity index," *Journal of Vibration and Acoustics*, vol. 144, no. 4, p. 041001, 2022.

[3] F. Pizzolante, M. Battarra, G. D'Elia, and E. Mucchi, "A rattle index formulation for single and multiple branch geartrains," *Mechanism and Machine Theory*, vol. 158, p. 104246, 2021.

[4] R. Brancati, E. Rocca, and S. Savino, "A gear rattle metric based on the wavelet multi-resolution analysis: experimental investigation," *Mechanical Systems and Signal Processing*, vol. 50, pp. 161–173, 2015.

[5] A. Rivola and M. Troncossi, "Dynamic analysis of a motorbike engine timing system: Experimental and numerical investigation of the geartrain," *Mechanical systems and signal processing*, vol. 48, no. 1-2, pp. 325–338, 2014.

[6] R. Singh, H. Xie, and R. Comparin, "Analysis of automotive neutral grear rattle," *Journal of sound and vibration*, vol. 131, no. 2, pp. 177–196, 1989.

[7] W.-B. Shangguan, X.-L. Liu, Y. Yin, and S. Rakheja, "Modeling of automotive driveline system for reducing gear rattles," *Journal of Sound and Vibration*, vol. 416, pp. 136–153, 2018.

[8] D. Robinette, R. S. Beikmann, P. Piorkowski, and M. Powell, "Characterizing the onset of manual transmission gear rattle part i: Experimental results," *SAE International*, vol. 2, pp. 1352–1364, 2009, sAE Technical Paper 2009-01-2063.

[9] E. Rigaud and J. Perret-Liaudet, "Investigation of gear rattle noise including visualization of vibro-impact regimes," *Journal of Sound and Vibration*, vol. 467, 2020.

[10] M. De la Cruz, S. Theodossiades, H. Rahnejat, and P. Kelly, "Numerical and experimental analysis of manual transmissions-gear rattle," SAE Technical Paper, Tech. Rep., 2009.

[11] D. Guo, Y. Zhou, Y. Wang, F. Chen, and X. Shi, "Numerical and experimental study of gear rattle based on a refined dynamic model," *Applied Acoustics*, vol. 185, p. 108407, 2022.

NEW INSIGHTS INTO THREE FUNDAMENTAL ISSUES OF PARALLEL MECHANISMS AND ITS RESEARCH PROGRESSES

Huiping SHEN[1] Xingyu SHE[2] Ju LI[3] Pengda YE[4]

Research Center for Advanced Mechanism Theory, Changzhou University, Jiangsu 213164, P.R.China

{1.shp65@126.com; 2.sxy86541365@163.com; 3.wangju0209@163.com; 4.yepengda@126.com}

1.INTRODUCTION

Research on parallel mechanisms（PM）has spanned over four decades to date. The diversity of PMs and intrinsic coupling of their topological loops have long constrained progress in mechanism analysis and design. With increasing complexity, traditional methods face bottlenecks such as redundant representation and solving difficulties when describing multi-loop, multi-degree-of-freedom（DOF）systems, particularly in areas such as forward kinematics, DOF calculation and motion decoupling *et.al,* which lead to gaps between theoretical and practical challenges[1]. To overcome these limitations, it is essential to return to the fundamental nature of topology, re-examine core scientific issues such as the principles of forward kinematics, efficient calculation method of DOF, and motion decoupling identification criterion. By establishing deep connections between topological characteristics and these issues, the following three new insights on mechanism theory and methods are already developed in the work, *i.e.*, 1) a topological characteristic-based method for forward position solutions, 2) an efficient and convenient DOF calculation method considering optimal paths, and 3) a topology analysis-based motion decoupling identification criterion that eliminates the need of Jacobian matrix computation.

2.TOPOLOGICAL CHARACTERISTICS-BASED KINEMATICS－A NEW PARADIGM

The development of the kinematics for PMs has evolved from theoretical kinematics (TK) in the 18th/19th centuries, through computational kinematics (CK) in the 20th century, to topological characteristics-based kinematics (TCK) proposed by author in the 21st century, representing three distinct stages of progressive advancement[1].

The differences in the fundamental ideas between TCK and TK in establishing position equations are given in the following four aspects: (1) For core idea: TCK emphasizes establishing position equations based on the intrinsic topological features of mechanisms. While TK primarily relies on explicit geometric constraints (such as link lengths and angles) to establish position equations and solves the positional problems, typically without in-depth consideration of their topological characteristics. (2) For constraint conditions: TCK considers both explicit geometric constraints and implicit topological constraints, enabling the revelation of deeper level kinematics of the mechanism. While TK depends solely on explicit geometric constraints, potentially overlooking auxiliary constraints introduced by topological characteristics. (3) For modeling and solution methods: TCK simplifies modeling via topological analysis, enabling efficient solutions (e.g., symbolic/closed-form). While TK uses algebraic/numerical methods aiming for numerical solutions, often without deep topological exploration.(4) Application goals: TCK aims to establish mapping laws between the topological characteristics and kinematics/dynamics modeling and solution methods. While TK focuses on solving specific kinematics through computational tools, emphasizing calculation efficiency. The effectiveness and convenience of the topological characteristic-based method for forward solutions have been checked by a large number of PMs.

3.DOF CALCULATION FORMULA CONSIDERING OPTIMAL PATHS – A NEW FORMULA

For over 190 years, researchers worldwide have proposed more than 30 distinct formulas for calculating DOF. These include the three earliest classical DOF formulas, like:① Moroskine Formula,② Grübler-Kutzbach Formula,③ Zhang Formula and Freudenstein-Alizade Formula. Each formula has limitations and drawbacks. Subsequently, seven major DOF formulas were developed, *i.e.*,④Zhao-Zhou-Feng Formula, ⑤Dai-Huang-Lipkin Formula, ⑥Huang-Zhao-Zhao Formula,⑦ Kong-Gosselin Formula,⑧ Gogu Formula,⑨ Rico et al. Formula, and ⑩ Yang-Sun Formula. These existing non-instantaneous DOF formulas do not consider optimal path loops when calculating DOF[2].

For complex PMs with multiple loops, although the correctness of the DOF calculation result is independent of the selection of the optimal path, inappropriate path selection can lead to complexity, redundancy, high computational load.

Therefore, the author propose a convenient DOF calculation method based on optimal paths. For this, two concepts are introduced, *i.e.*, shortest loop and optimal path. Shortest loop (S-loop) means a loop with the minimum DOF in the PM or mechanism. While optimal path means a collection of the shortest loops. Thus, at the S-loop level, the formula for calculating the non-instantaneous DOF of general over-constrained mechanisms and non-over-constrained PMs is proposed as[3].

$$F = \sum_{i=1}^{v} F_j = F_1 + F_2 + ... + F_j + ... + F_v \tag{1}$$

$$F_j = \sum f_j - \xi_j \tag{2}$$

$$\xi_{Lj} = \dim.\left\{\left(\bigcap_{i=1}^{j} M_{bi}\right) \bigcup M_{b(i+1)}\right\} \tag{3}$$

Where, F_j —added DOFs introduced by the new chains that compose the new j^{th} loop.

v — number of loops ($v = m - n + 1$, n —number of links, m —number of joints).

ξ_i — number of independent displacement equations for the j^{th} loop.

$\bigcap_{i}^{j} M_{bi}$ − POC sets generated by the sub-PM composed of the first jth branch chain.

$M_{b(i+1)}$ — POC set generated by the end link of (j+1)th branch chain.

The effectiveness and convenience of this DOF calculation formula also have been tested by a great number of PMs.

4.EFFICIENT IDENTIFICATION CRITERION FOR MOTION DECOUPLING BASED ON TOPOLOGICAL ANALYSIS – A NEW CRITERION

Currently, the Jacobian matrix-based method is generally employed to determine whether a given PM possesses motion decoupling characteristics. However, the process of analyzing and computing the Jacobian matrix is relatively complex. Based on an analysis of the relationships among the topological characteristics of mechanism limbs, limb position self-determinism, and the pose parameters of the moving platform, the authors propose a concise and practical criterion for judging motion decoupling, *i.e.*, if part of the pose information of the base point on the moving platform can be derived from a motion-decoupling limb with (partial) position self-determinism, then the PM must be motion-decoupled (including full or partial decoupling)[4]. This criterion can effectively identify the motion decoupling properties of any multi-loop planar or spatial parallel mechanisms, thus providing a new perspective and an effective method. In addition, an analytical method and formula for quantifying the motion decoupling performance of PMs is also presented recently[5], the effectiveness and convenience of which have been validated by a great number of PMs.

5.CONCLUSIONS

Parallel mechanisms have spanned more than 40 years to date. The complexity of their topological structures has led to challenges and confusion in their analysis and design. The three new insights on mechanism theory and methods presented in the paper will open new windows for PM community.

REFERENCES

[1] Shen Huiping, “Topological Characteristics-Based Kinematics for Robotic Mechanism”, *Beijing:Higher Education Press*, 2021.

[2] Yang Tingli, Liu Anxing, Shen Huiping, et al, “Topology Design of Robot Mechanisms”, *Springer*, 2018.

[3] Shen Huiping, “Topological analysis for parallel robotic mechanisms—Methods, Techniques and Applications”, *Nanjing: Jiangsu Phoenix Education Publishing House Co., Ltd*, 2025.

[4] Shen Huiping, Li Ju, Li Tao, et al, “A New Method for Motion-Decoupling Identification of Parallel Mechanisms”, *Journal of Mechanisms and Robotics*, 2025, 17(8): 081004.

[5] Shen Huiping, She Xingyu , Li Ju ,et al, “An analytical method and formula for quantifying the motion decoupling performance of parallel mechanisms”, *Mechanism and Machine Theory*, 2025, 217(000).

FEA-BASED STRUCTURAL DESIGN OF A SERIAL VARIABLE STIFFNESS JOINT

Guanglei Wu, Bin Niu

State Key Laboratory of High-performance Precision Manufacturing, School of Mechanical Engineering, Dalian University of Technology, Dalian 116024, China, {gwu@dlut.edu.cn; niubin@dlut.edu.cn}

1. INTRODUCTION

In the process of fine surface assembly tasks, traditional rigid robots cannot adapt to the requirements of flexibly/compliance, which may cause surface scratches and losses. In this light, the robot design equipped with compliant joint has attracted more and more researchers' attentions [1][2]. In this work, a joint with serial variable stiffness is presented and fabricated, in order to make the joint stiffness adaptive to the interaction environment and external payload.

2. DESIGN CONCEPT OF THE FLEXIBLE JOINT

The working principle of the variable stiffness joint presented in this paper is depicted in Fig. 1. Analog to the friction clutch, the joint is composed of driving input shaft, friction parts, control mechanism and output shaft. Stiffness adjustment of the joint is realized by changing the pressure or the relative position among the friction elements in serial between the input and output elements, where the motion and torque are transmitted by means of friction between them. The working modes of the joint includes three different phases, namely, zero-stiffness mode, adjustable stiffness mode and maximum stiffness mode.

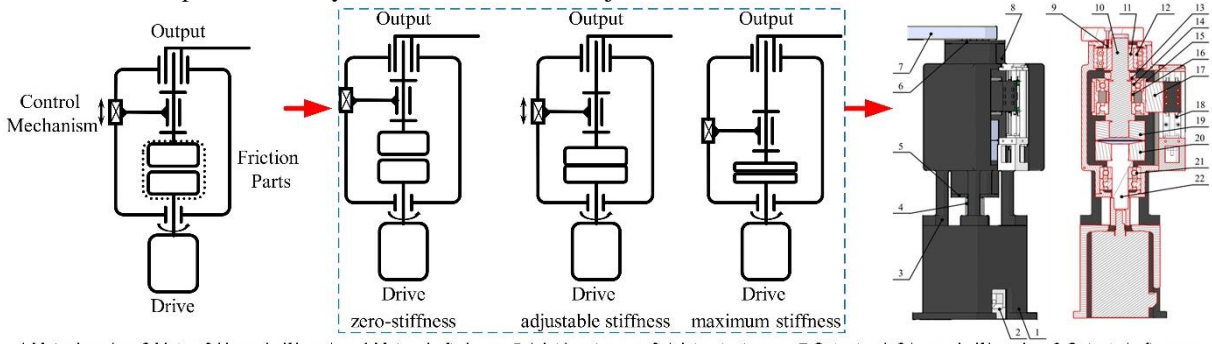

1.Motor housing 2.Motor 3.Upper half housing 4.Motor shaft sleeve 5.Joint input cover 6.Joint output cover 7.Output rod 8.Lower half housing 9.Output shaft cover 10.Output shaft 11.Output shaft sleeve 12.Double row angular contact ball bearing 13.Round nut and stop gasket 14.Adjusting angular contact ball bearing 15.Fork sleeve 16.Shaft sleeve 17.Adjusting fork 18.Linear module 19.Output friction disc 20.Input friction disc 21.Input angular contact ball bearing 22.Input shaft

Figure 1. Schematic diagram of joint structure and the different working modes.

3. DESIGN OF STIFFNESS GENERATION MECHANISM

Considering the complex nonlinear static characteristics of contact state between the two elements in friction pairs, FEA approach is adopted to model the varying stiffness of the joint, and curve fitting can be applied to deduce the analytical stiffness model based on the FE results for the joint design and evaluation. The corresponding FE modeling with is shown in Fig. 2, together with the simulation results in context of rubber-aluminum alloy as friction pair.

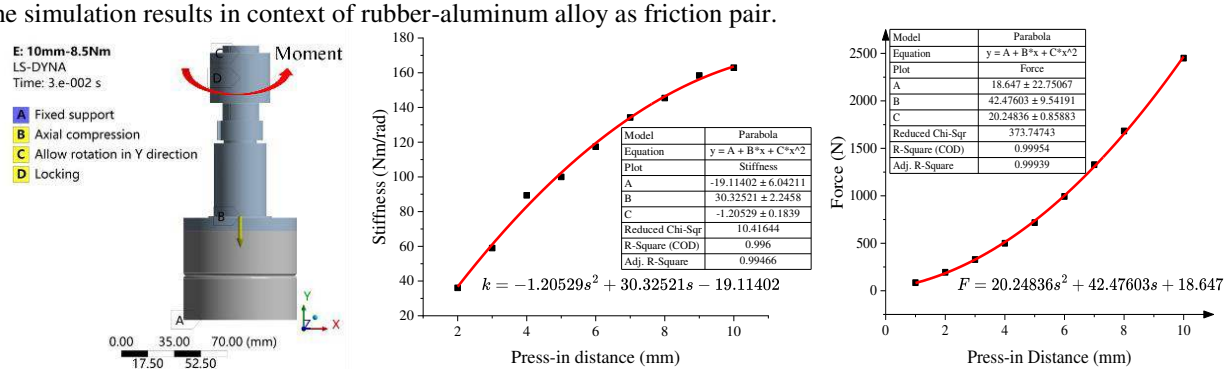

Figure 2. FEA model with LS-DYNA module, stiffness curve by rubber-aluminum compression, force curve by rubber compression

The simulation results show that the stiffness varying range of rubber-aluminum alloy is about 0.6299-2.843 Nm/°from which it can be seen that the rigidity of rubber-aluminum alloy has a larger bandwidth of stiffness change [3], which can meet the design requirements. Moreover, the torsional stiffness shows a quadratic relationship varying with the rubber compression.

4. PROTOTYPE OF THE JOINT AND EXPERIMENTAL TEST

In order to verify the nonlinear stiffness characteristics of the serial joint, a physical prototype is built to carry out experiments, as shown in Fig. 3, of which the most components are fabricated by 3D printing technology for lightweight design, except the input shaft made up of 7075 aluminum alloy. The ball screw to control the position of the output friction disk is selected with repeatability accuracy ±0.005mm.

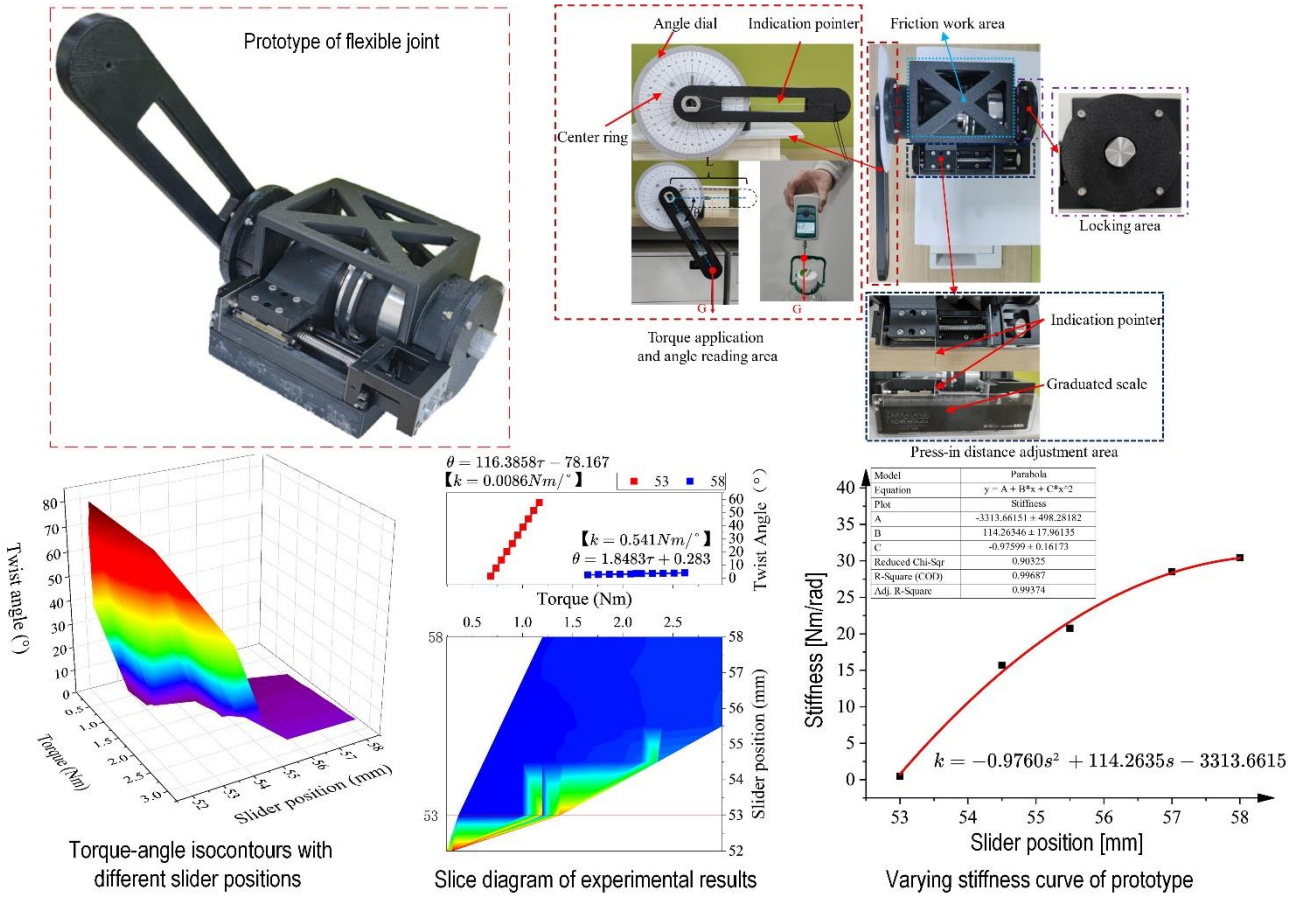

Figure 3. Prototype of the flexible joint and experimental test results.

From the test results, it can be seen that when the two friction discs are pressed more tightly, that is, the position data of the slider becomes larger, the smaller the torsion angle is, the higher the stiffness is. The experimental data are processed by means of the least square method to obtain the joint stiffness-slider position curve. The goodness of fit index, Adj. $R^2 = 0.99374$, is close to 1, indicating that the fitting effect is good. Moreover, the stiffness and the position of slider are expressed in the form of the quadratic relationship $k = As^2 + Bs + C$, which agrees with the FEA simulation results. The experimental results validate the design principle of the joint.

5. CONCLUSIONS

A flexible joint is designed, analyzed and fabricated, and the joint stiffness model is established by means of the combination of finite element simulation method and the curve fitting method. The nonlinear relationship is verified experimentally that is implemented to a physical prototype. Moreover, in adjustable stiffness mode, the joint has a large stiffness range, where the maximum stiffness is about 4.5 times larger than the minimum. The compact and simple structure shows the potential of applications in robotic manipulators for the designed joint.

REFERENCES

[1] S. Wolf, G. Grioli, et al., "Variable stiffness actuators: Review on design and components", *IEEE/ASME Transactions on Mechatronics*, 21(5), 2418-2430, 2015.

[2] R. V. Ham, T. G. Sugar, B. Vanderborght, K. W. Hollander and D. Lefeber, "Compliant actuator designs", *IEEE Robotics & Automation Magazine*, 16(3), 81-94, 2009.

[3] L. R. Treloar, "Stress-strain data for vulcanized rubber under various types of deformation", *Rubber Chemistry and Technology*, 17(4), 813-825, 1944.

KINETOSTATIC MODELING OF A COMPLIANT HONEYCOMB LATTICE

Hoang Lam Pham, Quoc Huy Pham, Dung-An Wang

Graduate Institute of Precision Engineering, National Chung Hsing University, 250 Kuo Kuang Rd, Taichung, Taiwan, { iuh.hoanglam@gmail.com; quochuy110902@gmail.com; daw@dragon.nchu.edu.tw}

1. INTRODUCTION

Compliant cellular structures, particularly honeycomb lattice topologies, have emerged as a paradigm-shifting class of metamaterials in precision engineering, soft robotics, and morphing aerostructures. Fig. 1(a) illustrates several applications of a honeycomb lattice in robotic probing and force sensing. Fig. 1(b) shows a honeycomb-based shear force sensor integrated into a robotic gripper end effector. Unlike traditional rigid-body mechanisms, these compliant architectures achieve mobility and force transmission through the elastic deformation of flexible members, offering distinct advantages such as zero backlash, reduced part count, and intrinsic energy absorption capability. However, the effective utilization of compliant honeycombs in high-performance applications is frequently bottlenecked by the lack of computationally efficient modeling tools capable of capturing their complex, coupled kinetostatic behavior.

The primary challenge in analyzing these mechanisms lies in their distributed compliance. Under operational loads, the constituent flexure beams often undergo large, nonlinear deflections that invalidate standard linear beam theories. While finite element analysis (FEA) provides high fidelity, it is computationally expensive and ill-suited for the iterative phases of conceptual design and topology optimization. To bridge this gap, this work presents a closed-form kinetostatic modeling framework for compliant honeycomb lattices utilizing the beam constraint model (BCM). The BCM, which analytically captures geometric nonlinearities and elastokinematic constraints of beam flexures without the extensive discretization required by FEA, offers a superior balance between accuracy and computational cost. We derive an energy-based BCM that accurately predicts stiffness, and mobility in this work. Validation of its performance against nonlinear FEA results and experiments, demonstrates the efficacy of the developed model as a rapid design tool for next-generation compliant metamaterials.

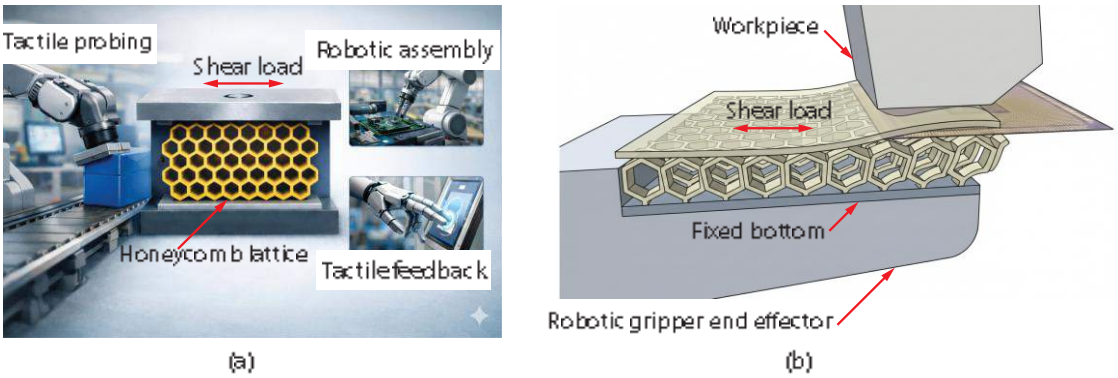

Figure 1. (a) Applications of a honeycomb lattice in probing and sensing. (b) A honeycomb-based shear force sensor integrated into a robotic gripper end effector.

2. MODEL AND EXPERIMENT

Fig. 2(a) shows a regular hexagonal honeycomb lattice with $l = h = 5$ mm, $w = 1$ mm, and $\theta = 30^{o}$. The out-of-plane dimension of the lattice is 3 mm. The material of the lattice has a Young's modulus and Poisson's ratio of 2.15 MPa and 0.35, respectively. The bottom of the lattice is fixed. A shear displacement $\delta(= 5$ mm$)$ is applied at the top of the lattice. Structurally, the lattice comprises multiple independent kinematic chains and a network of nodes that form the basis for the equilibrium equations. An equilibrium-based BCM is defined by the load-displacement relationships of individual beams and the equilibrium and compatibility conditions between beams. An energy-based BCM may provide better numerical stability and convergence when solving for large and complex deflections of lattice structures. A BCM based on total strain energy

minimization for the honeycomb lattice is developed in this investigation. Fig. 2(b) shows the deflections Δ_x^i and Δ_y^i and end slope α_i of the ith segment of the lattice. L_i and θ_i are the length and the inclination angle of the ith segment, respectively. X-Y and x_i-y_i represent the global and local Cartesian coordinate system, respectively. The strain energy V_i of the ith segment can be written as [1]

$$V_i = \frac{E_i I_i}{L_i}\left\{\frac{b_i^2 p_i^2}{24L_i^2} + \frac{1}{2}\begin{bmatrix}\frac{\Delta_y^i}{L_i} & \alpha_i\end{bmatrix}\begin{bmatrix}12 & -6\\ -6 & 4\end{bmatrix}\begin{bmatrix}\frac{\Delta_y^i}{L_i}\\ \alpha_i\end{bmatrix} - \frac{p_i^2}{2}\begin{bmatrix}\frac{\Delta_y^i}{L_i} & \alpha_i\end{bmatrix}\begin{bmatrix}-\frac{1}{700} & \frac{1}{1400}\\ \frac{1}{1400} & -\frac{11}{6300}\end{bmatrix}\begin{bmatrix}\frac{\Delta_y^i}{L_i}\\ \alpha_i\end{bmatrix}\right\} \quad (1)$$

where E_i, I_i, L_i and b_i are the Young's modulus, second moment of the cross-sectional area, length and in-plane thickness, respectively, of the ith segment. The axial force p_i of the ith segment normalized by $\frac{E_i I_i}{L_i^2}$, can be expressed as

$$p_i = \left[210(2\alpha_i^2 - 3\alpha_i\frac{\Delta_y^i}{L_i} + 18(\frac{\Delta_y^i}{L_i})^2 + 30\frac{\Delta_x^i}{L_i})\right] \Big/ \left[11\alpha_i^2 - 9\alpha_i\frac{\Delta_y^i}{L_i} + 9(\frac{\Delta_y^i}{L_i})^2 + 525(\frac{b_i}{L_i})^2\right] \quad (2)$$

Fig. 3(a) shows the reaction force, f, in the X direction as a function of the input displacement, δ, based on the energy-based BCM. The results predicted by the BCM agree with those of the finite element analyses and experiments. The experimental f-δ curve was measured by an experimental setup as shown in Fig. 3(b).

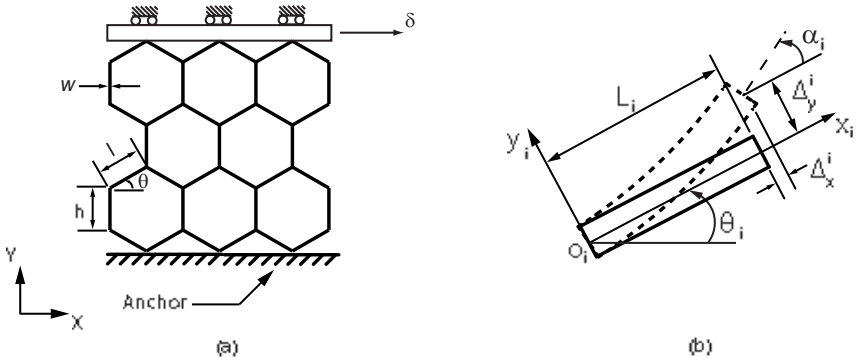

Figure 2. Schematic of (a) a honeycomb lattice and (b) the deflections and end slopes of the ith segment in the BCM.

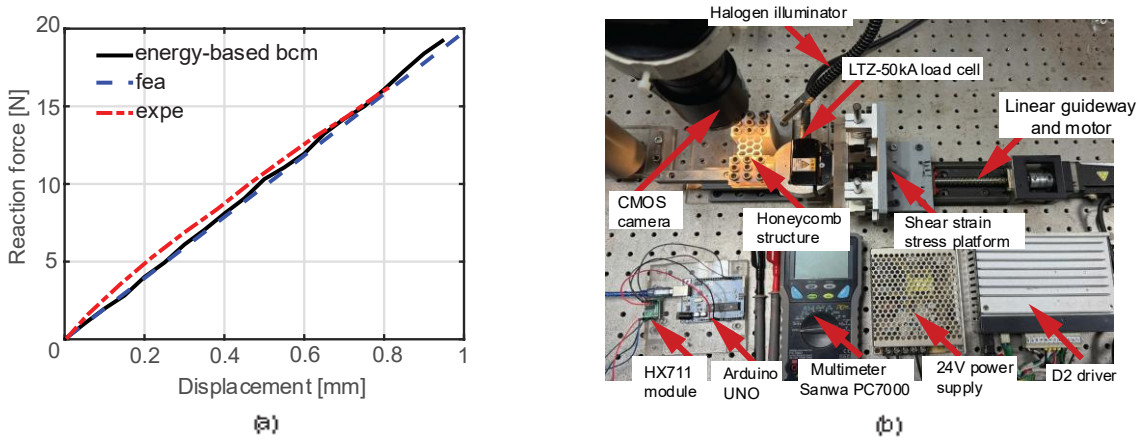

Figure 3. (a) f-δ curves based on the BCM model, the finite element analyses and experiments. (b) Experimental setup.

3. CONCLUSIONS

An energy-based BCM implementation that overcomes convergence difficulties in lattice-type compliant mechanisms is developed and verified by experiments. A strategy that facilitates systematic equation formulation within the BCM framework can be extended to other compliant mechanisms with complex geometry and kinematic behaviors. This study advances the kinetostatic modeling and design of planar, lattice-type compliant mechanisms, offering a robust computational tool for both academic and industrial applications.

ACKNOWLEDGMENTS

The computing facilities provided by the National Center for High-Performance Computing (NCHC) are greatly appreciated.

REFERENCES

[1] S. Awtar, K. Shimotsu and S. Sen, "Elastic averaging in flexure mechanisms: A three-beam parallelogram flexure case study". *J. Mechanisms and Robotics*, 132, 081009, 2010.

DYNAMIC TESTING OF FOUR-POINT CONTACT SLEWING BEARINGS: A WAY TO A METHOD

Martin Eizmendi[1], Iker Heras[1], Mikel Portilla[1], Josu Aguirrebeitia[1]

[1] University of the Basque Country (UPV/EHU), Plaza Ingeniero Torres Quevedo 1, Bilbao, Spain, {martin.eizmendi@ehu.eus; iker.heras@ehu.eus; mikel.portilla@ehu.eus; josu.aguirrebeitia@ehu.eus}

1. INTRODUCTION

Literature concerning structural analysis of four-point contact slewing bearings (4PCSB) focuses mainly on static and friction problems. Static modelling provides the basis for calculating bearing stiffness, static load-carrying capacity [1] and for solving the friction problem itself. The resolution of the friction problem is necessary to calculate the resistant torque that must be overcome to rotate the bearing [2], or to predict the wear damage [3]. Besides, experimental work carried out on these bearings is oriented for the validation of static models [1], for determining friction torque [4] under varying loads and speeds, and for testing damage modes that the bearing may suffer during its service life as fatigue or wear [5]. Nonetheless, no models nor experiments assess their response against variable external forces, which can excite the bearing dynamically in some applications. In this scenario, the authors previously addressed this topic from a theoretical standpoint. This included finite element (FE) and mechanistic modelling [6] and damping modelling to quantify the minimum damping capability of these components [7]. Now, in this work, the results of the first experimental tests are reported. A procedure for the dynamic testing of these bearings is proposed along with the observed phenomena.

2. MATERIALS AND METHOD

The method used to dynamically excite the bearing consists on the next. The outer ring of the bearing is coupled to the armature of a shaker by means of an expander, while a seismic mass of 31 kg is mounted on the inner ring. The inertia of this mass is the responsible of loading axially the bearing due to the motion of the vibration table (see Fig. 1(a).). A preloaded 4PCSB with a mean diameter of 232 mm, half-inch ball size, and a ball–raceway conformity of 0.95 is tested. In particular, this specimen is 100% filled with balls and is tested without lubrication. This enables the identification of the minimum damping capability of the bearing, provided solely by the ball–raceway contacts. The preload level is measured in terms of friction torque in idling conditions. In order to estimate it at ball-raceway contact deformation level, the friction model developed in [2] is used, yielding a preload of 9 μm at each contact diagonal.

The experimental procedure consists on the next. First, a low-level sine sweep test from 20 to 2000 Hz at 3 Hz/s is conducted to identify the dynamic behaviour of the whole assembly. This test allows the flexibility of the setup to be evaluated. To this end, all the components are monitored at different locations in multiple test rounds. This type of test is essential for efficiently and safely identifying the frequency band in which the bearing is dynamically excited, from the standpoint of both the assembly and the shaker integrity. Once the frequency band of interest is identified, the sweep test is replaced by sine-spot excitation tests, allowing sufficient dwell time at each excitation frequency for the resonance to fully develop. Tests are conducted at different vibration levels, reaching bearing loads of up to 18 kN. From measured signals at the rings via accelerometers, the transmissibility of the bearing is computed. The mechanistic model developed in [6,7] is used to interpret the experimental observations.

3. RESULTS

The sweep test results indicate that the vibration mode of the entire assembly occurs at a frequency around 900 Hz. In this mode, the seismic mass, the bearing, and the expander are observed to vibrate in phase with each other, and 90° out of phase with respect to the armature motion, which constitutes the excitation. However, when focusing on the relative motion between the bearing rings, it is observed that they vibrate in phase up to approximately 1300 Hz, beyond which their relative motion becomes progressively out-of-phase, first approaching 90° and ultimately 180°. This behaviour indicates that, beyond the 1300 Hz, one ring approaches to resonate relative to the other.

Fig. 1(b). shows the transmissibility curves between the rings when the assembly is subjected to sine-spot excitation beyond the 1300 Hz at different excitation levels. These are tracked as a function of the commanded acceleration at the seismic mass and consequent inertial load. Each curve is fitted through least squares to the transmissibility expression of a single-degree-of-freedom linear model, yielding loss-factor values ranging between 0.011 and 0.009.

Sine spot simulations are launched using the mechanistic model [6] to construct the transmissibility curves (Fig. 1(c)). The model is fed with the geometrical and preload data previously described. The experimentally identified loss factor of 0.01 is adopted for feeding the implemented damping model [7]. Measured acceleration levels on the outer ring are used as base excitation input

for each test. For the loading levels reached in the bearing, the mechanistic model reproduces the gradual frequency shift observed in the transmissibility curves as the excitation level increases. Based on the nonlinearities considered in the model, the one activated in the simulations corresponds to the Hertz softening effect [8]. However, according to the mechanistic model, this resonance occurs within a higher frequency range than that observed experimentally.

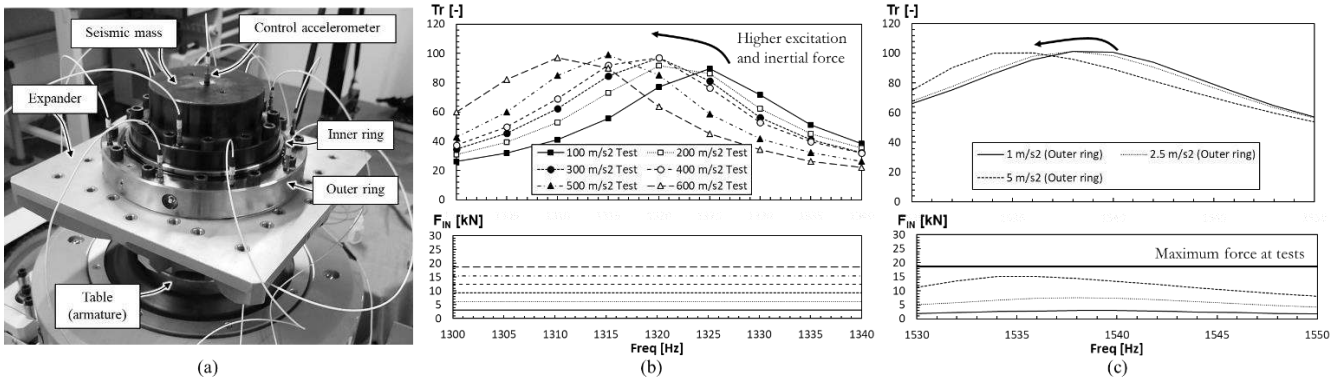

(a) (b) (c)

Figure 1. Dynamic testing of 4PCSBs: (a) Experimental set-up; (b) Experimental results; (c) Simulations.

4. CONCLUSIONS

A testing procedure is presented to dynamically excite a 4PCSB. This comprises of a sweep test to identify the bearing resonance in the assembly, followed by sine-spot tests to refine and excite dynamically the bearing at different load levels. Based on performed tests and simulations, the following main conclusions are drawn:

- Due to the flexibility of the assembly components, the bearing is not dynamically solicited at the main vibration mode of the system. Instead, the bearing rings resonate against each other as a result of modal superposition at a higher frequency. A combination of modal and harmonic analyses via FE modelling can help to clarify this behaviour.
- The flexibility of the assembly components causes the resonant frequency of the bearing to differ from that estimated according to the mechanistic model. This indicates that the rigid-ring assumption is overly restrictive. In line with the previous conclusion, a FE modelling approach can be useful for overcoming this limitation.
- Despite the limitations associated with the rigid-ring assumption, the mechanistic model reproduces both the transmissibility levels and the frequency shifting tendency observed experimentally. In particular, a loss factor equal to 0.01 to represent damping in steel-to-steel contact seems to be reasonable for capturing the minimum damping capability of the bearing under the tested conditions. Pending additional tests, this value is highly consistent with dry ball-raceway contact damping results reported in the literature [8].

ACKNOWLEDGMENTS

This publication is part of grants PID2021-122746OB-I00 and PID2024-158830OA-I00 funded by MCIU/AEI /10.13039/501100011033/ and FEDER/UE. Thanks also to the Basque Government for the financial support through project number IT1542-22 and to Iraundi S.A. slewing bearing manufacturer.

REFERENCES

[1] S. Zupan and I. Prebil, “Carrying angle and carrying capacity of a large single row ball bearing as a function of geometry parameters of the rolling contact and the supporting structure stiffness”, *Mechanism and Machine Theory*, 36, 1087–1103, 2001.

[2] I. Heras, M. Aguirrebeitia, I. Abasolo, I. Coria and I. Escanciano, “Load distribution and friction torque in four-point contact slewing bearings considering manufacturing errors and ring flexibility”, *Mechanism and Machine Theory*, 137, 23–36, 2019.

[3] D. Cubillas, M. Olave, I. Llavori, I. Ulacia, J. Larrañaga, A. Zurutuza and A. Lopez, “Semi-analytical methodology for fretting wear evaluation of unlubricated pitch bearing raceways under operative and non-operative periods”, *Wind Energy Science*, 10(2), 401–415, 2025.

[4] O. Menck, K. Behnke, M. Stammler, A. Bartschat, F. Schleich and M. Graßmann, “Measurements and modeling of friction torque of wind turbine blade bearings”, *Journal of Physics: Conference Series*, 2265(2), 022087, 2022.

[5] K. Behnke and F. Schleich, “Exploring limiting factors of wear in pitch bearings of wind turbines with real scale tests”, *Wind Energy Science*, 8(2), 289–301, 2023.

[6] M. Eizmendi, I. Heras, M. Abasolo and J. Aguirrebeitia, “Four-point contact slewing bearing dynamics: Guidelines for FE modelling and mechanistic model correlation”, *Finite Elements in Analysis and Design*, 247, 104347, 2025.

[7] M. Eizmendi, I. Heras, J. Aguirrebeitia and M. Abasolo, “Hysteretic damping model for the dynamic response in four-point contact slewing bearings”, *Mechanism and Machine Theory*, 214, 106150, 2025.

[8] J. Sabot, P. Krempf and C. Janolin, “Non-linear vibrations of a sphere-plane contact excited by a normal load”, Journal of Sound and Vibration, 214(2), 359–375, 1998.

TRANSFERABLE TIME-FREQUENCY REPRESENTATIONS FOR DATA-EFFICIENT END-OF-LINE QUALITY INSPECTION OF ELECTRIC MOTORS

Jernej Mlinarič[1], Boštjan Pregelj[2], Gregor Dolanc[3]

[1] Jožef Stefan International Postgraduate School, Jamova cesta 39, 1000 Ljubljana, Slovenia, {jernej.mlinaric@ijs.si}
[2] Jožef Stefan Institute, Jamova cesta 39, 1000 Ljubljana, Slovenia, {bostjan.pregelj@ijs.si}
[3] Jožef Stefan Institute, Jamova cesta 39, 1000 Ljubljana, Slovenia, {gregor.dolanc@ijs.si}

1. INTRODUCTION AND MOTIVATION

End-of-Line (EoL) quality inspection is a critical stage in the manufacturing of electric motors, where every produced unit must be inspected within strict cycle-time constraints before release for further integration or end users. Modern EoL inspection systems rely on non-invasive vibration and acoustic measurements acquired during short, controlled tests that enable the detection of mechanical, electromagnetic, and assembly-related faults without disassembly [1, 2]. However, increasing product variability and tighter manufacturing tolerances place growing demands on the robustness, scalability, and adaptability of diagnostic algorithms.

Traditional EoL inspection approaches are typically based on signal processing and manually engineered features combined with expert-defined thresholds or classical machine learning classifiers [1]. Although these methods are effective in stable production environments, they require extensive expert involvement during commissioning and are difficult to adapt to multiple motor variants. This limitation is particularly noticeable during the ramp-up phase of new motor variants, where only a small number of labeled fault samples are available, significantly limiting the applicability of learning methods based on large amounts of data.

Recent advances in deep learning (DL) using time–frequency representations of vibration and acoustic signals have shown strong potential for automated fault detection [2, 3]. In particular, Mel-frequency spectrograms (MFSs) provide a compact and noise-robust representation of signal energy over time and frequency, emphasizing low- and mid-frequency regions that are highly relevant for rotating machinery diagnostics [2]. Nevertheless, most existing DL approaches are trained independently for each motor type, resulting in long commissioning times and limited reuse of prior diagnostic knowledge.

This study addresses the challenge of developing data-efficient EoL diagnostic models that generalize to various motor variants produced on the same or similar manufacturing lines. Although such variants may differ in geometric or electrical parameters, they share common physical fault mechanisms, including imbalance, bearing defects, rotor eccentricity, and assembly inaccuracies. The diagnostic task is formulated as a motor quality classification problem based on vibration and acoustic signals acquired during standardized EoL test cycles. The focus is on evaluating the transferability of learned time–frequency representations from a source motor variant with abundant data to target variants with limited labeled samples [1, 4].

2. SIGNAL REPRESENTATION AND TRANSFER LEARNING FRAMEWORK

The proposed approach is based on vibration and acoustic signals acquired by industrial-grade sensors integrated into an EoL inspection system [1, 2]. Measurements are performed during short, controlled test runs under predefined operating conditions. These signals capture the combined effects of mechanical dynamics, electromagnetic excitation, and structural resonances relevant to motor condition assessment.

Instead of relying on extensive manual signal processing and feature engineering, the raw signals are directly transformed into MFSs [2]. The Mel transformation maps linear frequency to a perceptually motivated scale, providing enhanced resolution in low- and mid-frequency ranges where many mechanical fault signatures are concentrated. The resulting time–frequency representations preserve both spectral and temporal information and form a standardized input suitable for convolutional neural networks, while reducing sensitivity to minor speed variations and measurement noise [3].

A transfer learning framework is used to reuse diagnostic knowledge across motor variants [1, 4, 5]. A deep neural network is first trained on MFSs obtained from a large dataset of a mass-produced motor variant, learning hierarchical representations of discriminative time–frequency patterns associated with healthy and faulty conditions. For new motor types with limited labeled data, the learned representation is transferred by reusing the convolutional feature extractor and adapting only the classification layers. This approach assumes that low- and mid-level time–frequency features remain largely unchanged in similar motor designs, while higher-level decision boundaries require limited adjustment [4]. The proposed framework significantly reduces training effort and commissioning time compared to training models from scratch, enabling efficient deployment of EoL diagnostics under industrial constraints [1, 5]. Figure 1 illustrates the suggested transferable time-frequency representation learning framework for EoL quality inspection.

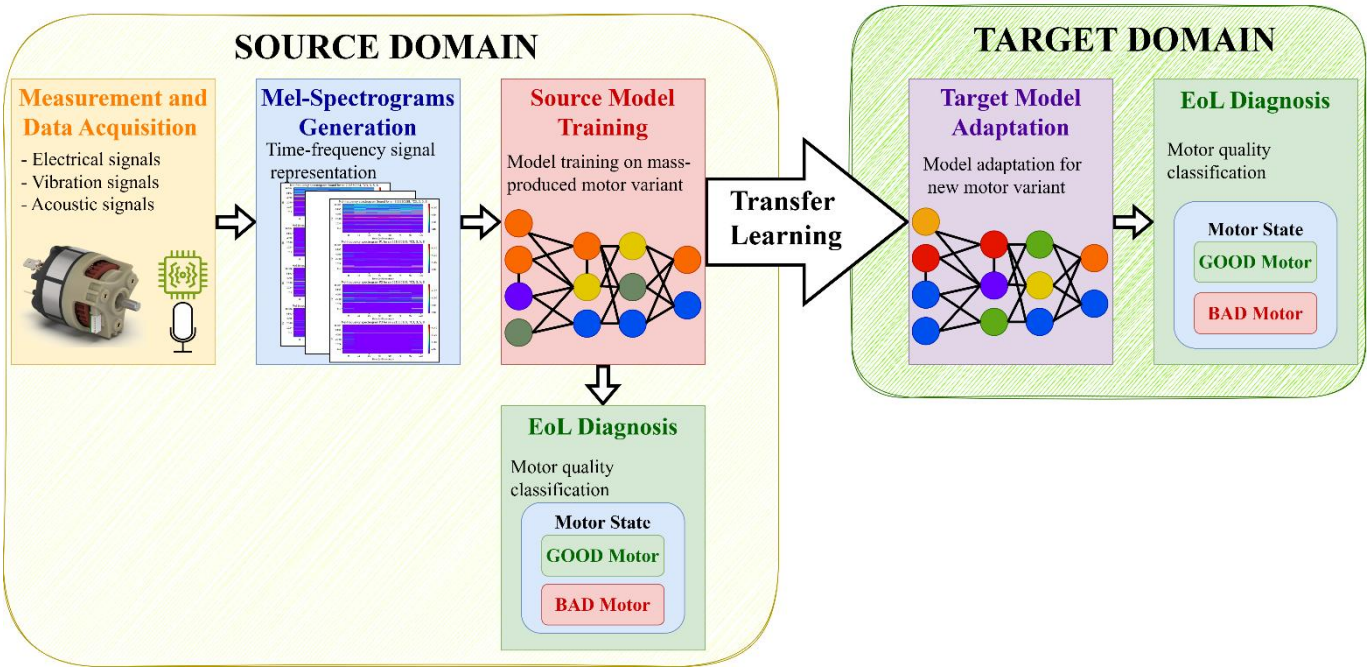

Figure 1. Transferable time-frequency representation learning framework for EoL quality inspection.

3. CONCLUSION

The proposed approach was evaluated on industrial datasets collected from an operational EoL inspection system [1, 2]. A source dataset comprising several thousand motors was used to train the base model, while target datasets representing new motor variants contained only a limited number of labeled samples. The results demonstrate that transfer learning enables reliable motor quality classification in low-data regimes. Compared to models trained from scratch, transferred models achieve higher accuracy and improved robustness despite the scarcity of target-domain data, indicating that MFS-based time–frequency representations capture diagnostic features that generalize across related motor variants [1, 3].

In addition to quantitative performance, the findings highlight the practical benefits of representation reuse for industrial deployment. By transferring learned diagnostic knowledge, commissioning time can be significantly reduced and dependence on expert-defined features minimized, while remaining compatible with industrial constraints such as short cycle times, data imbalance, and product variability [1, 5]. Furthermore, the results suggest strong potential for extending the framework toward self-supervised or semi-supervised pretraining on large collections of healthy motor data [5]. Future work will focus on multi-sensor data fusion, anomaly detection, broader classes of rotating machinery, and tighter integration with real-time end-of-line inspection systems.

ACKNOWLEDGMENTS

Authors are grateful for the financial support of Slovenian Research and Innovation Agency in the scope of grant P2-0001 and L2-4454.

REFERENCES

[1] J. Mlinarič, B. Pregelj, P. Boškoski, G. Dolanc and J. Petrovčič, "A transfer learning approach to machine learning-based end-of-line quality inspection," *Advances in Production Engineering and Management,* vol. 20, no. 2, pp. 277-290, 2025.

[2] J. Mlinarič, B. Pregelj and G. Dolanc, "End-of-Line Quality Control Based on Mel-Frequency Spectrogram Analysis and Deep Learning," *Machines,* vol. 13, no. 7, 2025.

[3] M. Bhuiyan and J. Uddin, "Deep Transfer Learning Models for Industrial Fault Diagnosis Using Vibration and Acoustic Sensors Data: A Review," *Vibration,* vol. 6, pp. 218-238, 2023.

[4] K. Weiss, T. M. Khoshgoftaar and D. Wang, "A survey of transfer learning," *Big Data,* vol. 3, no. 1, 2016.

[5] P. Yan, A. Abdulkadir, P. Luley, M. Rosenthal, G. Schatte, B. Grewe and T. Stadelmann, "A Comprehensive Survey of Deep Transfer Learning for Anomaly Detection in Industrial Time Series: Methods, Applications, and Directions," *IEEE Access,* vol. 12, pp. 3768-3789, 2023.

A COUPLED LUBRICATION MODEL FOR THE VALVE PLATE PAIR IN HIGH-PRESSURE AVIATION PISTON PUMPS CONSIDERING SPINDLE DEFORMATION

Runlin Chen[1], Wenhui Li[1], Wenhao Chen[1], Rushen Deng[1], Jianning Gu[3,4], Tianzhao Wang[3,4], Jun Zha[2,*]

[1] School of Mechanical Engineering, Xi'an University of Technology, Xi'an 710048, China, {chenrunlin@xaut.edu.cn; 2240221192@stu.xaut.edu.cn; 2240221259@stu.xaut.edu.cn; 2230220042@stu.xaut.edu.cn}

[2] School of Mechanical Engineering, Xi'an Jiaotong University, Xi'an 710049, China, {jun_zha@xjtu.edu.cn}

[3] Aviation Key Laboratory of Science and Technology on Aero Electromechanical System Integration, Nanjing 211102, China, {www.1198@foxmail.com; 11825001@zju.edu.cn}

[4] AVIC Nanjing Engineering Institute of Aircraft Systems, Nanjing 211102, China, {www.1198@foxmail.com; 11825001@zju.edu.cn}

1. ABSTRACT

The escalating operational pressure and speed in aviation piston pumps impose increasingly stringent demands on the lubrication performance of the critical valve plate pair. During operation, radial forces and torques acting on the cylinder block are channeled through the main spindle, subjecting it to elastic deformation. The resulting spindle deformation induces a tilt in the cylinder block, thereby compromising the integrity of the lubrication film and posing a direct threat to the operational reliability of the valve plate pair. To address this challenge, this paper proposes a novel lubrication model for the valve plate pair that fully considers the effects of spindle deformation. The analysis couples the mechanical equilibrium of the cylinder block with the forces and moments generated by spindle deformation. This coupling directly integrates the structural mechanics of the spindle into the hydrodynamic model of the lubrication film. The proposed model is solved numerically to analyze the influence of various operating conditions on lubrication performance. Analysis of the results identifies outlet pressure as the most critical factor affecting cylinder block tilt, where higher pressure directly amplify the overturning effect. Notably, the model reveals that in regions of reduced oil film thickness, a strong hydrodynamic pressure effect is generated at the auxiliary support structures. This localized pressure generates a restoring moment, which counteracts the overturning moment and effectively suppresses cylinder block tilt. This self-balancing mechanism is crucial for mitigating eccentric wear and preventing excessive leakage. Experimental tests were conducted to validate the model's predictions of cylinder attitude and oil film thickness under various operating conditions. The measured data closely align with the theoretical predictions, effectively validating the accuracy and reliability of the proposed coupled model. This study establishes a robust theoretical foundation and an effective analytical method for the anti-overturning design of valve plate pairs in high-pressure piston pumps, thereby providing a critical tool for failure prevention and reliability enhancement.

2. INTRODUCTION

In the actual operation of an axial piston pump, the cylinder block undergoes tilting deformation due to the overturning moment generated under alternating pressure. This deformation directly affects the oil film distribution in the valve plate pair and may even lead to severe wear, thereby reducing the pump's operational performance and service life [1]. To address this issue, Wang Z et al. [2] compared the lubrication characteristics of the valve plate pair under both non-tilting and tilting conditions of the cylinder block, finding that the hydrodynamic effect can significantly enhance the cylinder block's load carrying capacity. However, most existing studies have primarily focused on the lubrication performance of the valve plate pair itself, without fully considering the coupling effect between spindle deformation and the cylinder block. In this study, the influence of spindle deformation on the lubrication performance of the valve plate pair is systematically analyzed by incorporating spindle deformation into the lubrication model of the valve plate pair. Additionally, oil film thickness tests are conducted to verify the accuracy of the numerical simulation results.

3. METHODOLOGY

Firstly, the load on the plunger is determined through kinematic and mechanical analysis, after which the combined force exerted by all plungers on the cylinder block is obtained. The spindle is discretized to construct a static analysis model, which is used to solve for the rotation angles of the midpoint of the spindle spline in the x- and y-directions. By combining these rotation angles with the initial film thickness of the valve plate pair, the film thickness distribution equation is established. The Reynolds equation is then solved using the finite difference method to obtain the pressure distribution of the valve plate pair and to calculate its axial load-carrying capacity. Based on the load equilibrium condition, the film thickness is iteratively corrected, and the initial spindle torque is iteratively solved to finally determine the oil film and pressure distribution of the valve plate pair. The detailed calculation procedure is illustrated in Figure 1.

To validate the oil film thickness distribution of the valve plate pair, the end-face overturning angle test method proposed in Reference [3] is employed. Combined with oil film thickness data measured at axial locations, this approach enables accurate characterization of the oil film thickness distribution on the cylinder block.

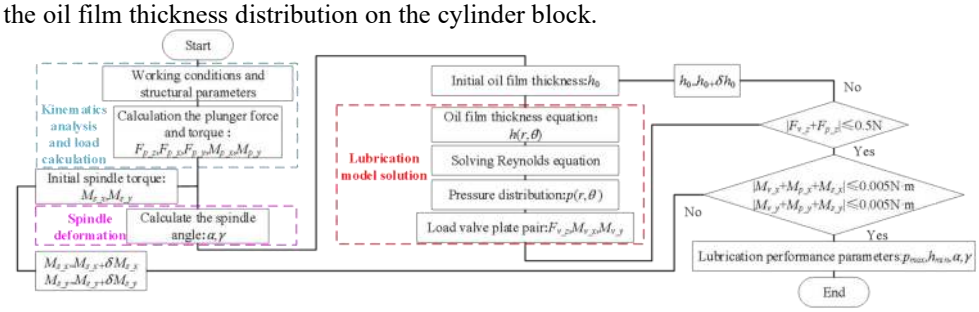

Figure 1. Calculation flowchart

4. RESULTS

At an outlet pressure of 35 MPa and a rotational speed of 4000 rpm, the numerical and experimental results of the oil film thickness distribution are presented in Fig. 2(a) and (b), respectively, while the corresponding numerical results of the pressure distribution on the valve plate pair are shown in Fig. 2(c). The oil film thickness and pressure distribution results at 35 MPa and 1000 rpm are provided in Fig. 3(a) and (b), and those at 25 MPa and 4000 rpm are given in Fig. 3(c) and (d).

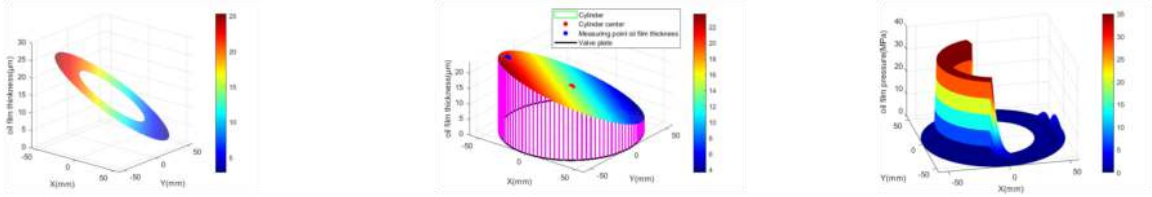

(a)Numerical calculation (b)Experimental results (c)Oil film pressure

Figure 2. Comparison of film thickness distribution and pressure distribution.

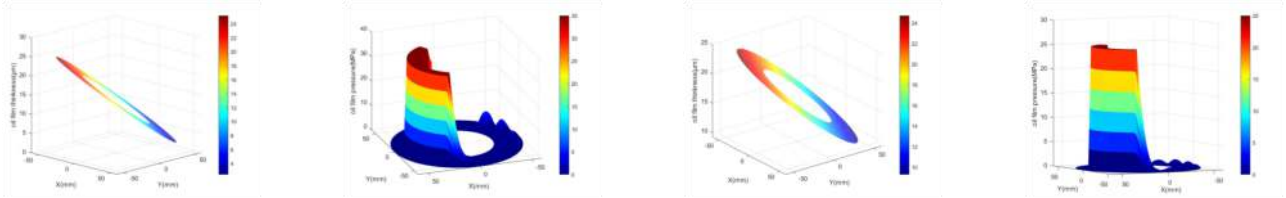

(a)Oil film thickness(35-1000) (b)Oil film pressure(35-1000) (c)Oil film thickness(25-4000) (d)Oil film pressure(25-4000)

Figure 3. The distribution of oil film thickness and pressure under different working conditions.

As illustrated in Fig. 3, a notable hydrodynamic effect is generated within the auxiliary support zone of the port plate pair, which helps to counteract the overturning moment. Moreover, the distribution of the oil film exhibits clear variations under different operating conditions.

5. CONCLUSIONS

In this study, a lubrication analysis model for the valve plate pair coupled with spindle deformation is established. The lubrication characteristics of the valve plate pair under various operating conditions are investigated, and oil film thickness tests are conducted for validation. The main conclusions are as follows:

(1) In the region of thinner oil film, the auxiliary support generates a significant hydrodynamic effect, which effectively counteracts cylinder tilting.

(2) As rotational speed increases, the minimum oil film thickness of the port plate pair gradually increases. Conversely, higher outlet pressure reduces the minimum oil film thickness and exacerbates cylinder tilting.

ACKNOWLEDGMENTS

The work is supported by Aviation Science Foundation (No. 20182876003).

REFERENCES

[1] ZHANG J, CHEN Y, XU B, et al, “Effects of splined shaft bending rigidity on cylinder tilt behaviour for high-speed electro-hydrostatic actuator pumps”. *Chinese Journal of Aeronautics*, 32(2): 499-512, 2018.

[2] Wang Z, Hu S, Ji H, et al, “Analysis of lubricating characteristics of valve plate pair of a piston pump”. *Tribology International*, 126, 49-64, 2018.

[3] Xu H, Zhang J, Sun G, et al. “The direct measurement of the cylinder block dynamic characteristics based on a non-contact method in an axial piston pump”. *Measurement*, 167, 2021.

INJECTION VS. OIL BATH LUBRICATION IMPACT ON POWER LOSS AND THERMAL BEHAVIOUR IN AN FZG TEST RIG

Khadija Boujallabia[1], Büşra Duran[1], Jérôme Cavoret[1], Thibaut Torres[2], Christophe Changenet[2], Fabrice Ville[1,*]

[1] INSA Lyon, CNRS, LaMCoS, UMR5259, 69621 Villeurbanne, France,
{khadija.boujallabia@insa-lyon.fr ; busra.duran@insa-lyon.fr ; fabrice.ville@insa-lyon.fr ; jerome.cavoret@insa-lyon.fr}
[2] LabECAM, ECAM LaSalle, 69005 Lyon, France, {thibaut.torres@ecam.fr; christophe.changenet@ecam.fr}

1. INTRODUCTION

The method of lubrication can significantly influence power losses and the thermal behaviour of mechanical systems. In mechanical transmission systems, lubrication deterioration results in gear failure which includes tooth surface pitting and wear [1]. But lubrication also has a major influence on gear thermal rating. This study aims to compare the impact of injection lubrication and oil sump lubrication on total power loss and temperature distribution within the oil, and gears of an FZG test rig.

2. EXPERIMENTAL PROCEDURE

An FZG test rig was used to perform comparison tests between injection and oil bath lubrication methods. It consists of a test box (1) and a driven box (3), both assembled with spur gears, as shown in Figure 1. A clutch (2) applies torque to the pinion shaft, through a lever arm and multiple weights, introducing a load into the closed-loop system [2]. Both gearboxes contain gears, rolling element bearings (REBs), lubricants, and seals. This machine is commonly used to assess efficiency of gear oils [3][4], and torque loss measurements [4][5].

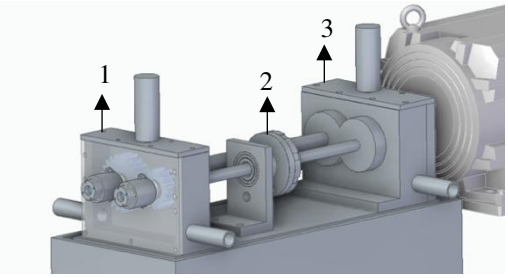

Figure 1. 3D model of the FZG test rig

The FZG is a closed-loop mechanical system. Therefore, the torque measured is directly indicative of the system's power losses. The temperature of the oil bath in the driven box, test box, and of the wheel and pinion teeth over the duration of all tests was also of interest when comparing the lubrication methods. Monitoring the thermal behaviour is a crucial step to evaluate the efficiency of injection and oil bath lubrication methods. To adequately compare injection lubrication and oil bath lubrication methods, multiple tests have been performed by varying the input speed, level of oil in the test box, injection temperature and oil flow rate. The tests have been performed at two rotational speeds of the wheel shaft: 1500 rpm and 3000 rpm. The oil flow rate controlled by the injection pressure varies between 1.2 L/min and 3.4 L/min, and oil levels H1 (64 mm) and H2 (72 mm) were tested in the case of dip-lubrication. Load 3 (35.3N.m on the pinion), was used for all tests.

3. RESULTS

For all tests, the power losses under both injection and oil bath lubrication were plotted as a function of the temperature of the oil bath in the driven box. According to the test results, injection lubrication is accompanied by less power loss in the system, while considering the power supply for the pump.

The results indicate that a substantial amount of energy can be saved by using injection lubrication, which allows the operating cost of an industrial machine to be reduced. Increasing the oil flow rate is accompanied by an increase in total power loss in the system. Regarding the thermal behaviour of the gear teeth, increased injection pressure (and so oil flow rate) leads to an increase in tooth temperatures. This is explained by the fact that higher injection pressure increases gear load-independent power losses associated with oil splashing.

4. USE OF A HIGH-SPEED CAMERA

A high-speed camera of the brand PHANTOM VEO 610L was used to capture the behaviour of the lubricant under both injection and oil bath lubrication methods, an example is shown in Figure 2. Investigating the flow in a gearbox with dip-lubrication and injection lubrication is challenging both numerically and experimentally, as multiple phenomena are encountered in this flow (lubricant liquid, air, bubbles, thin films, turbulence, heat and mass transport, drastic changes in lubricant properties due to heat flash and pressure rise in the contact region and around [6]). The high-speed camera was used to capture detailed images and videos of both oil bath and injection lubrication methods. Multiple phenomena such as fling-off cooling [7], and churning were observed. In the case of injection lubrication, fling-off cooling results in a sequence of intermittent process of transient and forced heat convection, which helps cool the gear teeth [7]. Previous work by Torres *et al.* [8] on oil-jet lubrication of a rotating spur gear confirmed that the turbulence induced by the oil jet increases heat transfer.

Figure 2. High-speed camera images captured under oil bath lubrication

5. DISCUSSION AND CONCLUSION

This study investigated the impact of injection and oil bath lubrication methods on the total power losses in an FZG machine, and their influence on the gear bulk temperatures. The experiments performed reveal that the power dissipated in the case of the injection lubrication is lower than the case of oil bath lubrication, under the same testing conditions. This study reveals that increased injection oil flow rate leads to an increase in teeth temperatures. To go further, future investigations could explore the effect of varying the positioning of the oil-jet nozzle, as well as the effect of different oil types.

ACKNOWLEDGMENTS

This study is sponsored by the Laboratory of Mechanical Contacts and Structures, LaMCoS.

REFERENCES

[1] A. R. Lansdown, Liquid Lubricants - Functions and Requirements, Swansea, Great Britain: Swason tribology Center, 1972.

[2] K. Michaelis, « Testing procedure for gear lubricants with the FZG test rig» Ind Lub Tribol, vol. 21, pp. 91-94, 1974.

[3] D. Hargreaves et A. Planitz, « Assessing the energy efficiency of gear oils via the FZG test machine Tribology International» vol. 42, p. 918–925, 2009.

[4] B. Duran, J. Cavoret, Y. Diab, D. Philippon, F. Ville, A. Ruellan et F. Berens, « Influence of Oil Degradation on Power Losses and Thermal Behaviour of a Gear Transmission Test Rig» HAL open science, 2025.

[5] M. Hammami, C. M. Fernandes, M. S. A. Ramiro Martins, M. Haddar et J. Seabra, « Torque loss in FZG-A10 gears lubricated with axle oils» Tribology International, vol. 131, pp. 112-127, 2019.

[6] Z. Várhegyi, G. Kristóf, « Mass Flux Distribution Measurements and Visualizations of a Fluid Sheet Generated by a Partially Immersed Dip-Lubricated Gear », *Periodica Polytechnica Mechanical Engineering*, p. 66–81, 2016.

[7] G. van Heijiningen, « Fling-off cooling of gear teeth» vol. 17, 1984.

[8] T. Torres, C. Changenet T. Touret et B. Guilbert, « A New Experimental Methodology to Study Convective Heat Transfer in Oil JetLubricated Gear Units» Lubricants MDPI, p. 408, 2023.

FAMILIES OF SCREW SYSTEMS

V. Di Paola[1], J.M. Selig[2]

[1] Università degli Studi di Genova, Dipartimento di Ingegneria Meccanica, Energetica, Gestionale e dei Trasporti, Genova, 16145, Italy {vincenzo.dipaola@edu.unige.it}
[2] London South Bank University, School of Engineering, 103 Borough Rd., London, SE1 0AA, U.K. {seligjm@lsbu.ac.uk}

1 INTRODUCTION

The study of screw systems has a long history with many applications in robot kinematics, dynamics gripping, motion planning and, of course, mechanism theory. Apart from Ball's original work [1] which considers two-systems of screws, Felix Klein also considered the general problem in [8]. In [7], Hunt classified screw systems by inspection, that is he listed all the possibilities he could imagine. Then in [5] and [6] a mathematically sound classification was given, although it turned out to be substantially the same as Hunt's original classification. A cleaner mathematical proof was then given by Donelan and Gibson in [3] together with the invariant theory of the adjoint representation of $SE(3)$. An alternative view of the classification was given by Rico Martínez and Duffy in [9] and [10]. This alternative emphasised some special cases that were implicit in the original Gibson-Hunt classification. In response, Donelan and Gibson produced a coarser classification by altering the notion of equivalence of screw systems, see [4]. This has led to some confusion as to the status of the classification and, in our opinion, a reluctance among many in the mechanisms community to take advantage of these ideas.

In our view, part of the difficulty is a misunderstanding of the mathematical concept of a "classification". In mathematics this term has a precise meaning, given a set and equivalence relation on the set, we can partition the set into equivalence classes. Every element of the set in an equivalence class is related to every other element in the class by the relation and to no elements in any other class. The old-fashioned jargon is to say that the equivalence classes are mutually exclusive and totally exhaustive, see [2]. Often the equivalence relation is given by the action of a group on the set, and in the case of screw systems this is the case.

A screw system is a linear system of twists, the space of all twists is the Lie algebra $se(3)$. So, a screw system is a vector subspace $se(3)$. Alternatively, we can also think of a screw systems a projective plane in the space of screws $\mathbb{P}^5$. These are not quite the same things but the only difference is a projectivisation. That is, there is a one-to-one correspondence between the vector subspaces of $se(3)$ and the projective planes in $\mathbb{P}se(3)$. If the vector subspace has dimension $n < 6$, its projectvisation has dimension $n - 1$. Such a screw system is usually referred to as an n-system. Often a screw system will be specified in terms of a set of basis vectors, for example a 2-system can be written as,

$$\mathcal{S} = \{\mathbf{s} : \mathbf{s} = a\mathbf{s}_1 + b\mathbf{s}_2\} = \text{Span}(\mathbf{s}_1, \mathbf{s}_2). \tag{1}$$

The twists $\mathbf{s}_1$ and $\mathbf{s}_2$ are called the basis elements of the screw system. The coefficients a and b are real numbers. Three, four and five systems can be defined similarly using three, four and five basis twists respectively. Now the group acting on the set of n-systems is a combination of the group of rigid-body displacements and the group of possible changes of basis in the system. So, two n-systems of screws are considered equivalent if and only if, there is a change of basis and a rigid displacement that transforms one system to the other. The Gibson-Hunt classification does this and there is no real dispute that the classification given in [5, 6] gives all possible systems with no duplications. The confusion seems to occur over how the screw systems are grouped into families. To clarify, consider 1-systems, that is single screws. It is common to say that there are three types of screws: pitch zero, non- zero pitch screws and infinite pitch screws. But this is really a "shorthand". Screws are classified by their pitch, screws with the same pitch can be rigidly transformed into each another but screws with different pitches cannot. So there are an infinite number of one systems, one for each possible value of the pitch plus the infinite pitch case. The grouping into 3 families is convenient but seemingly arbitrary. Why single out the pitch zero case? Isn't it just part of a continuum with non-zero pitch cases. Alternatively, why not make a distinction between the systems with positive pitch, right-handed screws and negative pitch left-handed screws to give 4 families?

In this work we will explore some possible ways to group screw systems into families using various objective techniques. For example, in [4], Donelan and Gibson classify the screw systems up to equivalence under the group of similarity transformation. These transformations do not preserve pitch but cannot map a right-handed screw to a left-handed one. For 1-systems this results in a classification into the 4 classes described above. What would happen if different

group actions were considered, for example the general affine group or the group of conformal transformations? Another approach will also be considered. Each screw system has an isotropy group or stabiliser group. This is the group of isomorphisms that map the system to itself. In [11], there is evidence that the families preferred by Gibson and Hunt correspond to systems with conjugate isotropy groups.

2 CONCLUSION

The contribution of this work is not in the novelty of the material, almost all of which has already been published. Perhaps the concept of a "family" of screw systems is new, although it is implicit in the literature. Rather, the main aim of this work is to clarify terms and concepts with the hope that these powerful methods will be more accessible to the mechanisms and machine theory community.

REFERENCES

[1] R. S. Ball, *The Theory of Screws*, Cambridge University Press, Cambridge, 1900.

[2] N. Bourbaki, *Theory of Sets*, *Éléments de mathématiques*, Vol. 1, reprint ed., Springer, 2004.

[3] P. S. Donelan and C. G. Gibson, "First-Order Invariants of Euclidean Motions," *Acta Applicandae Mathematicae*, 24:233–251, 1991.

[4] P. S. Donelan and C. G. Gibson, "On the Hierarchy of Screw Systems," *Acta Applicandae Mathematicae*, 32:267–296, 1993.

[5] C. G. Gibson and K. H. Hunt, "Geometry of screw systems—1: Screws: Genesis and geometry," *Mechanism and Machine Theory*, 25(1):1–10, 1990.

[6] C. G. Gibson and K. H. Hunt, "Geometry of screw systems—2: Classification of screw systems," *Mechanism and Machine Theory*, 25(1):11–27, 1990.

[7] K. H. Hunt, *Kinematic Geometry of Mechanisms*, Oxford Engineering Science Series, Clarendon Press, Oxford, 1990.

[8] F. Klein, "Notiz betreffend dem Zusammenhang der Liniengeometrie mit der Mechanik starrer Körper," *Mathematische Annalen*, 4:403–415, 1871.

[9] J. M. Rico Martínez and J. Duffy, "Classification of screw systems–I. One- and two-systems," *Mechanism and Machine Theory*, 27(4):459–470, 1992.

[10] J. M. Rico Martínez and J. Duffy, "Classification of screw systems–II. Three-systems," *Mechanism and Machine Theory*, 27(4):471–490.

[11] J. M. Selig, *Geometrical Fundamentals of Robotics*, 2nd ed., Springer-Verlag, New York, 2005.

ON THE USE OF A NOVEL DRIVING SIMULATOR FOR THE ASSESSMENT OF UPPER LIMB IMPAIRMENT IN POSTSTROKE PATIENTS

Francesca Alvaro[1], Mathijs Vivet[2], Michele Perrelli[1], Rocco Adduci[1], Domenico Mundo[1]

[1] University of Calabria - DIMEG, via Bucci Cubo 45C Rende (Cs), Italy, {domenico.mundo@unical.it}
[2] Siemens Industry Software NV, Interleuvenlaan 68, B-3001 Leuven, Belgium {mathijs.vivet@siemens.com}

1. INTRODUCTION

Globally, neurological conditions like stroke are a major cause of disability, significantly impairing sensorimotor functions and depriving individuals of their independence in Activities of Daily Living (ADLs). These impairments, which manifest as muscle weakness, atrophy, and lack of coordination, often trigger "learned nonuse". In this scenario, patients instinctively rely on their healthy limb, eventually neglecting the paretic arm even if it regains functionality. A traditional approach to promote patient's recovery from stroke-related impairment relies on manual physical therapy. To overcome limitations deriving from the reduced availability of therapists, while guaranteeing a high level of therapy customization, robotic rehabilitation is proposed by scientists as a viable alternative. It allows for high-intensity, repetitive training that incorporates the patient's own motor intentions [1]. Recently, Alvaro et al. have developed a novel driving simulator that allows to administer robotic rehabilitation for the upper limb [2]. The proposed system enables bilateral rehabilitation to boost motor cortex activation and specifically targets complications like learned nonuse. Furthermore, it offers multiple training modalities to match the patient's changing neurophysiological status, from the high neuroplasticity of the acute phase to the functional recovery of the chronic stage.
In this work, the driving simulator is exploited as a device that enables the implementation of a Machine Learning (ML) clustering algorithm for the quantification of upper-limb impairment in post-stroke patients.

2. ARCHITECTURE OF THE DRIVING SIMULATOR FOR UPPER LIMB REHABILITATION

The prototype of the novel driving simulator is shown in Fig. 1(a). It allows the administration of bilateral therapy through driving exercises provided in a user-friendly game-like software with captivating tasks and tunable difficulty. Multiple driving scenarios are created in a virtual environment. The main innovative characteristic is the structure, presented in Fig. 1(b). The steering wheel comprises two kinematically uncoupled handles, to allow independent motion of impaired and of healthy arms.

a b

Figure 1. Physical prototype of the proposed driving simulator (a) and schematic of the semi-active steering wheel (b)

The working principle consists in making the impaired limb track the steering trajectory traced by the healthy one. While the latter moves actively, the former's side is automatized through different training modalities: passive, assistive, active – assistive, active and resistive. During the execution of rehabilitation tasks, (bio)mechanical quantities are acquired and processed by the robot which, in turn, provides sensorial feedback and switches among training modalities.

3. ML CLUSTERING ALGORITHM FOR IMPAIRMENT ASSESSMENT

The proposed approach aims to quantify levels of upper limb impairments in poststroke patients starting from kinematic and dynamic data extracted during a steering exercise. No experimental data derived from patients is available yet; consequently, the dataset has been created in a simulation environment, through the software *Opensim [3]*, redesigning the same ecosystem of the physical driving simulator, for a subsequent transfer to it. The *MoBL-ARMS Upper Extremity Model* has been selected, presenting 7 DoFs and 50 Hill-type muscles. A steering wheel has been added to simulate the scenario of interest as shown in Fig. 2(a).
The procedure begins with the simulation of a healthy steering maneuver, in which the maximum reachable value of muscular activation is equal to 1 (100%). The healthy condition is achieved by providing a prescribed motion, and markers data extracted from it are then used as reference for inverse kinematics and Computed Muscle Control. For the latter, some constraints have

been introduced to obtain various realistic poststroke behaviors; firstly, manipulating (reducing) the maximum achievable levels of activation per set of muscles grouped by arm segment (shoulder, upper arm, forearm and hand) and then constraining the rotation of the steering wheel to exactly follow the reference, leaving the other DoFs free to slightly detach from healthy positions, simulating possible compensatory behaviors, deriving from the reduced levels of activation of the Design Of Experiment (DOE), accomplished integrating Opensim in *Simcenter HEEDS* [4]. The steering wheel comprises an actuator compensating for the missing torque of the arm, for impaired conditions. Kinematic (angular positions) and dynamic data (torque generated by the wheel) obtained from simulations are preprocessed and joined, obtaining multivariate timeseries defining the dataset, which is fed to a K-means approach for feature-based timeseries clustering. The analysis indicated a quantity of ten clusters as the optimal one. Data processing and clustering have been implemented comparing Python libraries and AI Studio [5].

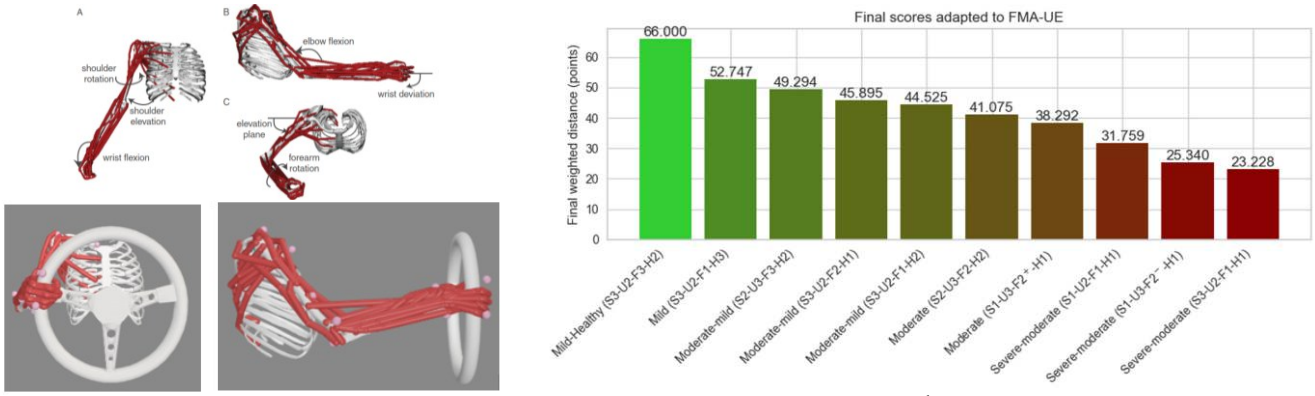

a b

Figure 2. (a) Complete upper limb model with the steering wheel and (b) Clusters parameters mapped to FMA-UE scores

4. RESULTS AND DISCUSSION

For a more objective evaluation and discussion, cluster distances have been mapped to Fugl-Meyer Assessment for Upper Extremity (FMA-UE) scores. Mapping has been possible since the model used in the simulations comprises all the DoFs and metrics used in the evaluation. Based on the overall scores and assigning the mild/healthy cluster as reference, remaining clusters have been divided into severe-moderate [FMA-UE score of 22-32], moderate [FMA-UE score of 33-42], moderate-mild [FMA-UE score of 43-52] and mild [FMA-UE score of 53-66], considering the influence of the arm segments, hence shoulder (S), upper arm (U), forearm (F) and hand (H), as reported in Fig. 2(b). No severe [FMA-UE score of 0-22] cluster emerged. In a severe cluster one would expect both highly diverging kinematics and high steering torque from the actuator.

The index flanking the subgroup letter refers to the group related to the activation value. The DOE has been accomplished allowing the maximum level of activation value to vary according to five limits: (1) 15%, (2) ~36%, (3) ~58%, (4) ~79% and (5) 100% ($\Delta = 0.2125$). Consequently, the index refers to the combination of maximum activations defining the cluster. However, not all muscles in a group give the same contribution and not all muscles groups require maximum activation for this specific exercise; consequently, muscular groups have been defined involving the muscles of that specific segment that reach higher activations and are affected by the upper limits. Subsequently, the set of indices defining the code is obtained, firstly, by computing the mean of maximum activations for each group and, secondly, a weighted mean of the occurrences of each index combination, since multiple similar combinations could belong to the same cluster. To note is also the fact that, in some impaired cases, activations may result higher than reference ones, emulating possible compensatory behaviors. In this way, the ten clusters emerging from the ML approach are able to represent different levels of impairment.

Proved the suitability of the methodology, it may be easily transferred to a real-life scenario, employing the driving simulator and possible patients, collecting biomechanical data through sensors and achieving more realistic scenarios, being activation data recovered from EMG sensors and not artificially imposed or limited. This approach may be of support for clinicians in the decision-making process of therapy administration.

ACKNOWLEDGMENTS

We acknowledge co-funding from Next Generation EU, through the Decree of the Italian Ministry of University n° 118/2023.

REFERENCES

[1] P. Maciejasz, J. Eschweiler, K. Gerlach-Hahn, A. Jansen-Troy, and S. Leonhardt, “A survey on robotic devices for upper limb rehabilitation”, *Journal of NeuroEngineering and Rehabilitation,* 11:3, 2014

[2] F. Alvaro, R. Adduci, M. Perrelli, F. Cosco, F. Tedesco, D. Mundo, “A novel driving simulator for poststroke robotic rehabilitation of the upper limb”, *IEEE Transactions on Neural Systems and Rehabilitation Engineering*, under review

[3] Seth, A., Hicks J.L., Uchida, T.K., Habib, A., Dembia, C.L., Dunne, J.J., Ong, C.F., DeMers, M.S., Rajagopal, A., Millard, M., Hamner, S.R., Arnold, E.M., Yong, J.R., Lakshmikanth, S.K., Sherman, M.A., Ku, J.P., Delp, S.L. OpenSim: Simulating musculoskeletal dynamics and neuromuscular control to study human and animal movement. PLoS Comp. Biology,14(7). (2018)

[4] Simcenter HEEDS, Siemens Software. https://plm.sw.siemens.com/en-US/simcenter/integration-solutions/heeds/

[5] Data Analytics and AI Platform, Altair RapidMiner. https://altair.com/altair-rapidminer

TOPOLOGY DESIGN, PERFORMANCE ANALYSIS OF PARALLEL MECHANISMS WITH FEWER JOINTS

Ju LI[1] Yue GUO[2] Huiping SHEN[3]

Research Center for Advanced Mechanism Theory, Changzhou University, Jiangsu 213164, P.R.China

{1.wangju0209@163.com； 2.18811975100@163.com；3.shp65@126.com}

1. INTRODUCTION

Continuous innovation in topology design of parallel mechanisms(PMs) has led researchers to progressively shift from focusing on basic functional indicators such as degrees of freedom (DOF) and position and orientation characteristics (POC) to integrating performance metrics like workspace and motion decoupling for the systematic optimization or design of specific mechanisms[1,2]. Additionally, traditional PMs often suffer from structural complexity, significant error accumulation at the moving platform, and challenges in motion control due to and the abundance of kinematic pairs within each limb. It is noteworthy that for limbs composed of single-DOF kinematic pairs, a lower POC dimension at the limb's end generally corresponds to a reduced number of required kinematic pairs.

In response, this paper proposes a topology design method for PMs based on limbs with fewer kinematic pairs, and the PMs constructed accordingly are termed "PMs with fewer kinematic pairs". Owing to their reduced number of kinematic pairs and simplified structure, such PMs theoretically offer advantages such as high motion accuracy, improved reliability, and lower manufacturing costs. They hold significant academic value and promising application prospects for advancing manufacturing equipment. Building upon this concept, this paper presents three recent advancements by our team in the study of such PMs, including the proposal of 1) type of PM composed of limbs with fewer kinematic pairs, 2) an improved-optimized-limb-based design method for PMs with fewer kinematic pairs, and 3) a minimal-kinematic-pair-limb-based design method for PMs with fewer kinematic pairs.

2. DEFINITIONS AND DESIGN APPROACHES

Both the number and the type of limbs influence the total number of kinematic pairs in a PM[2,3]. This paper focuses on the effect of limb type, specifically studying PMs composed of limbs with the minimum or a relatively small number of kinematic pairs—referred to as limbs with fewer kinematic pairs—thus forming PMs with fewer kinematic pairs.

For limbs consisting only of single-DOF kinematic pairs, a lower POC dimension of the limb generally implies a smaller number of required kinematic pairs. Here, the number of kinematic pairs refers either to the count of single-DOF pairs or to the equivalent number after converting multi-DOF pairs into single-DOF pairs.

Based on the POC dimension, limbs with fewer kinematic pairs are classified into two categories below.

- If the POC dimension of a limb equals that of the moving platform of the PM, it is classified as a limb with the minimum number of kinematic pairs.
- If the POC dimension of a limb is slightly larger than that of the moving platform (with a difference of at most 2), it is regarded as a limb with a relatively small number of kinematic pairs.

A PM with fewer kinematic pairs is accordingly defined as one in which all limbs belong to the above categories of limbs with fewer kinematic pairs.

Furthermore, based on the specific types of limbs, PMs with (2~6) DOF and fewer kinematic pairs can be categorized into three major classes. The first class consists of PMs with fewer kinematic pairs constructed entirely from simple limbs. The second class comprises those formed by a combination of simple limbs and hybrid limbs. The third class includes PMs with fewer kinematic pairs that are composed of two or more hybrid limbs.

In practical design, the following important principles and considerations must be adhered to.

(1) Lower pairs, specifically prismatic pairs (P) and revolute pairs (R), should be prioritized to simplify the structure, enhance reliability, and reduce costs.

(2) In terms of the selection and arrangement of actuated pairs, a simple limb typically incorporates only one actuated pair, while a hybrid limb may be equipped with two actuated pairs. To facilitate precise measurement and control of motion parameters, prismatic pairs are generally preferred as the actuated pairs.

(3) When the PM incorporates special topological structures such as parallelograms, an equivalent principle should be applied. For example, treating the four revolute joints forming a parallelogram as a single prismatic pair, before uniformly evaluating and comparing the number of kinematic pairs to ensure consistency in the analytical basis.

3. DESIGN BASED ON IMPROVED-OPTIMIZED LIMBS

Based on the improved-optimized limb design method, a number of the existing PMs are refined and optimized. In each PM, the limbs identified for improvement are equivalently replaced with limbs featuring fewer kinematic pairs. Subsequently, a comprehensive topological analysis was conducted for both the original and improved PMs, covering the position and orientation characteristic set (POC), DOF, coupling degree(k), and motion decoupling degree (D_d).The results demonstrate that four novel PMs are obtained while their fundamental functionality remained unchanged[3~4], thereby verifying the effectiveness of the improved-optimized design approach.

4. EXAMPLES

Following the design method based on limbs with fewer kinematic pairs, four PMs with reduced kinematic pairs are first developed[4]. These comprise three single-mode PMs of 3T, 2T1R, and 3T1R types, along with one dual-mode PM with 3-DOF, capable of switching between 3T and 2T1R motion patterns, as shown in Figure 1. Furthermore, all limbs in these PMs are designed with fewer kinematic pairs.

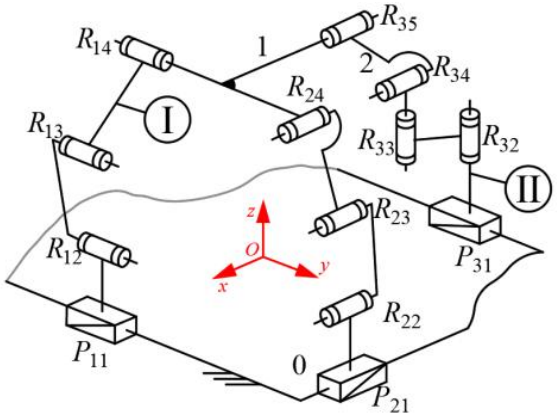

Fig .1 A 3-DOF dual-mode PM with fewer pairs

5.CONCLUSIONS

This study systematically proposes the innovative concept of PMs with fewer kinematic pairs, establishes their classification system and design principles, and develops a comprehensive topological design methods. Furthermore, research on PMs with fewer kinematic pairs not only enriches the theoretical framework of PM design but also promotes the trend toward structural simplification.

REFERENCES

[1] Yang Tingli, Liu Anxing, Shen Huiping, et al, “Topology Design of Robot Mechanisms”, *Springer*, 2018.
[2] Shen Huiping, Li Ju, Li Tao, et al, “A New Method for Motion-Decoupling Identification of Parallel Mechanisms”, *Journal of Mechanisms and Robotics*, 2025, 17(8): 081004.
[3] Shen Huiping, “Topological analysis for parallel robotic mechanisms—Methods, Techniques and Applications”, *Nanjing: Jiangsu Phoenix Education Publishing House Co., Ltd*, 2025.
[4] Guo Yue, “Topology Design and Performance Analysis of Parallel Mechanisms with Fewer Pairs”, *Changzhou University*, 2026

TORQUE-ANGLE MODELING OF A TWO-DEGREE-OF-FREEDOM ANKLE PROSTHESIS

Bigaliyeva Zhanar[1], Akhmejanov Sayat[1], Zhetenbayev Nursultan[2,3], Sultan Aidos[2], Uzbekbayev Arman[3], Kassymbek Ozhikenov[1], Nurgizat Yerkebulan[2,3], Ayazbay Abu Alim[1], Sergazin Gani[3]

[1] Satbayev University, 22 Satbaev str., 050013, Almaty, Kazakhstan, {zh.bigaliyeva@satbayev.university; akhmejanov.s@stud.satbayev.university; ozhikenov@satbayev.university}

[2] Almaty University of Power Engineering and Telecommunications, 126/1 Baitursynuly str., 050013, Almaty, Kazakhstan, {n.zhetenbaev@aues.kz; a.sultan@aues.kz; a.uzbekbayev@aues.kz; y.nurgizat@aues.kz; a.ayazbay@aues.kz}

[3] ALT University named after Mukhamedzhan Tynyshpaev, 97 Shevchenko str., 050013, Almaty, Kazakhstan, {g.balbayev@alt.edu.kz}

1. INTRODUCTION

The ankle joint plays a key role in human gait, contributing to energy storage, release, and impact absorption [1–2]. Most conventional prostheses provide only one degree of freedom, typically limited to dorsiflexion–plantarflexion motion, which may reduce stability and adaptability [2]. Recent studies have shown that torque–angle behavior is a critical factor influencing control stability and energy efficiency in ankle prostheses [3–5]. Hybrid solutions combining active and passive mechanisms are therefore of particular interest.

In this work, a two-degree-of-freedom (2-DoF) ankle prosthesis is proposed, where dorsiflexion–plantarflexion motion is actively driven, while inversion–eversion is achieved through passive compliance. The study focuses on modeling and analysis of the torque–angle relationship.

2. PROSTHESIS CONCEPT AND MODELING

2.1 Kinematic Model

The prosthesis includes two independent motion planes. A simplified geometric model is used to describe foot–ground interaction. Figure 1 shows the coordinate system and key points. Point B corresponds to ground contact, while point A represents the actuator force application.

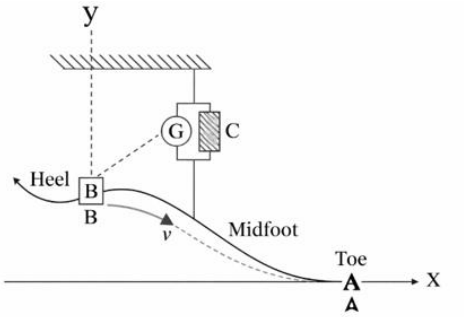

Figure 1. Kinematic model and coordinate system of the 2-DoF ankle prosthesis.

The foot geometry is approximated with a total length $L_f \approx 0.25\ m$. The motion ranges are defined as:

$$\theta_{dp} \in [-15°, +20°]$$
$$\theta_{ie} \in [-8°, +8°]$$

2.2 Torque–Angle Relationship

The ankle torque is initially modeled using a linear stiffness approximation:

$$\tau = k\theta$$

The actuator-generated torque is defined as:

$$\tau = F_h \cdot d_h$$

where F_h is the actuator force and d_h is the effective lever arm. To account for dynamic effects, the model is extended as:

$$\tau = I\ddot{\theta} + b\dot{\theta} + k\theta$$

where I is the inertia and $b$is the damping coefficient. Figure 2 illustrates the force and torque distribution used in the model.

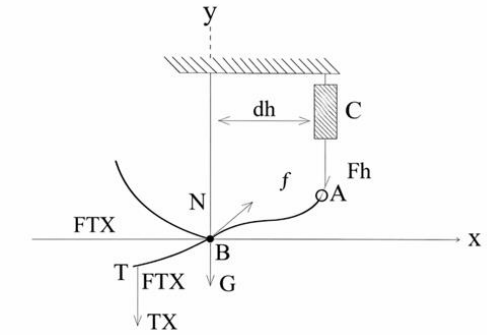

Figure 2. Force and torque distribution in the ankle mechanism.

3. RESULTS AND PROTOTYPE

Numerical simulations indicate that the torque–angle relationship remains approximately linear under typical walking conditions, validating the simplified model. The proposed hybrid configuration improves stability by combining active control in the sagittal plane with passive lateral compliance. A CAD model and laboratory prototype were developed to validate the concept. Figure 3 shows the CAD model and prototype.

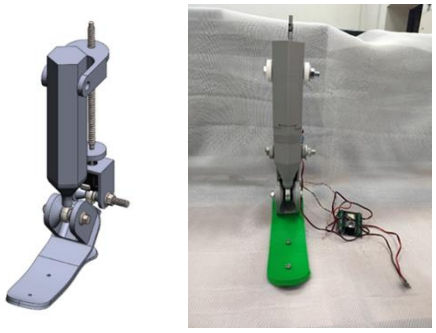

a) b)

Figure 3. CAD model and experimental prototype of the 2-DoF ankle prosthesis.

Preliminary tests confirm consistency between modeling results and prototype behavior.

4. CONCLUSION

A torque–angle model of a 2-DoF ankle prosthesis was developed and evaluated. The proposed hybrid configuration demonstrates stable behavior and efficient force transmission. The results confirm the feasibility of combining active dorsiflexion–plantarflexion control with passive inversion–eversion compliance. Future work will focus on experimental validation and adaptive control strategies.

ACKNOWLEDGMENTS

This research was funded by the Science Committee of the Ministry of Science and Higher Education of the Republic of Kazakhstan within the framework of the program BR24992820.

REFERENCES

[1] S.H. Collins, M.B. Wiggin and G.S. Sawicki, “Reducing the energy cost of human walking using an unpowered exoskeleton”. *Nature*, 522(7555), 212–215, 2015. https://doi.org/10.1038/nature14288.

[2] N.P. Fey, G.K. Klute and R.R. Neptune, “The influence of energy storage and return foot stiffness on walking mechanics and muscle activity in below-knee amputees”. *Clinical Biomechanics*, 26, 1025–1032, 2011. https://doi.org/10.1016/j.clinbiomech.2011.06.007.

[3] H. Herr, “Exoskeletons and orthoses: classification, design challenges and future directions”. *Journal of NeuroEngineering and Rehabilitation*, 6, 21, 2009. https://doi.org/10.1186/1743-0003-6-21.

[4] B. Vanderborght, A. Albu-Schäffer, A. Bicchi *et al.*, “Variable impedance actuators: A review”. *Robotics and Autonomous Systems*, 61(12), 1601–1614, 2013. https://doi.org/10.1016/j.robot.2013.06.009.

[5] A. Sultan, N. Zhetenbayev, Y. Nurgizat, A. Ayazbay, K. Ozhikenov and G. Sergazin, “Analysis of the lower limb prosthesis market and research of advanced prosthetic methods”. In: *New Trends in Medical and Service Robotics*, MESROB 2025, Mechanisms and Machine Science, vol. 186. Springer, Cham, 2025. https://doi.org/10.1007/978-3-031-96081-9_19.

EXPERIMENTAL VALIDATION OF A BLUETOOTH-BASED REMOTE-CONTROLLED ANKLE EXOSKELETON FOR REHABILITATION

Duisebayeva Aknur[1], Tursunbayeva Gulzhamal[1,4], Zhetenbayev Nursultan[1,2,3], Sultan Aidos[2], Kassymbek Ozhikenov[1], Sergazin Gani[3]

[1] Satbayev University, 22 Satbaev str., 050013, Almaty, Kazakhstan, {aknurt2014@gmail.com; ozhikenov@satbayev.university}

[2] Almaty University of Power Engineering and Telecommunications, 126/1 Baitursynuly str., 050013, Almaty, Kazakhstan, {n.zhetenbaev@aues.kz; a.sultan@aues.kz}

[3] ALT University named after Mukhamedzhan Tynyshpaev, 97 Shevchenko str., 050013, Almaty, Kazakhstan, {g.balbayev@alt.edu.kz}

[4] Eurasian National University, 2 Satbaev str., 10000 Astana, Kazakhstan {t.gulzhamal@outlook.com}

1. INTRODUCTION

Telemedicine-based rehabilitation technologies have significantly improved access to remote monitoring and therapy, particularly for patients in remote areas [1–3]. The integration of wearable sensors and robotic exoskeletons enables continuous motion tracking and adaptive rehabilitation control [4–5]. Recent developments in ankle exoskeletons incorporate wireless communication for real-time monitoring and remote adjustment of therapy parameters. However, many systems remain complex and focused on laboratory environments.

This work presents the experimental validation of a Bluetooth-based ankle exoskeleton with remote control and predefined physiological motion limits, aiming at a compact and practical rehabilitation solution.

2. EXPERIMENTAL PROTOTYPE AND TEST BENCH DESCRIPTION

The proposed system consists of a remote-control unit and an executive unit connected via Bluetooth communication. The remote device measures ankle inclination using an MPU-6050 sensor and transmits data to the control unit, which actuates the motors to generate ankle motion in both sagittal and transverse planes. Figure 1 shows the integrated prototype and wireless control architecture.

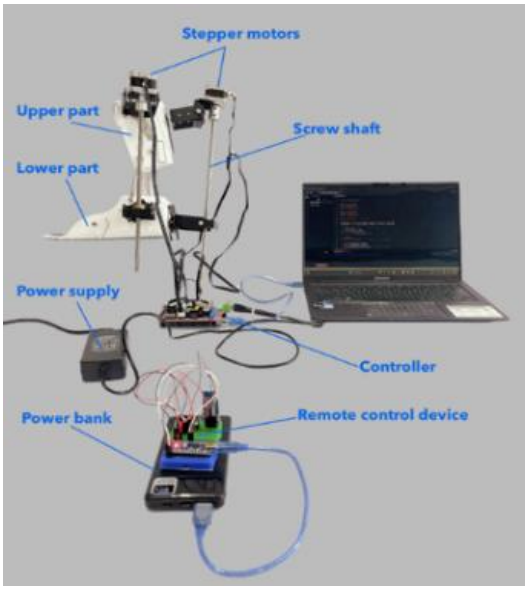

Figure 1. Experimental ankle exoskeleton prototype integrated with wireless platform components.

To ensure safe operation, predefined physiological limits are applied to dorsiflexion, plantarflexion, inversion, and eversion angles. Control signals are constrained when these limits are exceeded.

3. EXPERIMENTAL RESULTS

Experimental validation focused on eversion–inversion motion in the frontal plane. Figure 2 illustrates the system behavior: (a) eversion up to 15°, (b) neutral position, and (c) inversion up to −20°, controlled via the remote device.

a) b) c)

Figure 2. Exoskeleton motion in the frontal plane: (a) eversion; (b) neutral; (c) inversion.

A complete motion cycle lasted approximately 12 s, with smooth transitions between motion phases. Figure 3 shows the time variation of the ankle joint angle.

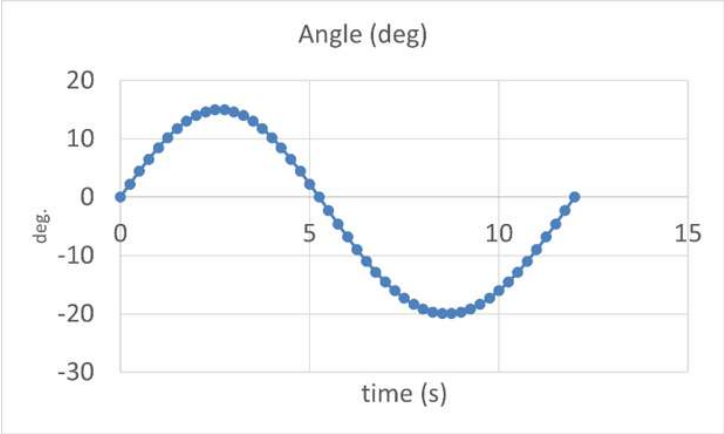

Figure 3. Ankle joint angle during eversion–inversion cycle.

The results demonstrate stable, cyclic, and physiologically compliant motion. The wireless control system provided reliable real-time synchronization between the remote device and the exoskeleton.

4. CONCLUSION

This study experimentally validated a Bluetooth-based remote-controlled ankle exoskeleton for rehabilitation. The system ensures smooth ankle motion within physiological limits and demonstrates stable wireless communication and control performance. The proposed solution is suitable for both clinical and home-based rehabilitation. Future work will focus on expanding control strategies and conducting user-based validation.

ACKNOWLEDGMENTS

This research was funded by the Science Committee of the Ministry of Science and Higher Education of the Republic of Kazakhstan within the framework of the program BR24992820.

REFERENCES

[1] A. Haleem, M. Javaid, R.P. Singh, R. Suman, *Telemedicine for healthcare: Capabilities, features, barriers, and applications*, Sensors International, Vol. 2, 100117, 2021.

[2] R.S. Weinstein, A.M. Lopez, B.A. Joseph, K.A. Erps, M. Holcomb, G.P. Barker, E.A. Krupinski, *Telemedicine, telehealth, and mobile health applications that work: Opportunities and barriers*, American Journal of Medicine, Vol. 127(3), pp. 183–187, 2014.

[3] E. Parimbelli, B. Bottalico, E. Losiouk, M. Tomasi, A. Santosuosso, G. Lanzola, S. Quaglini, R. Bellazzi, *Trusting telemedicine: Risks, safety, legal implications and liability of involved stakeholders*, International Journal of Medical Informatics, Vol. 112, pp. 90–98, 2018.

[4] S. Hussain, P.K. Jamwal, P. van Vliet, N.A. Brown, *Robot assisted ankle neuro-rehabilitation: State of the art and future challenges*, Expert Review of Neurotherapeutics, Vol. 21, pp. 111–121, 2021.

[5] L.N. Awad, A. Esquenazi, G.E. Francisco, et al., *The ReWalk ReStore soft robotic exosuit: Safety, reliability, and feasibility of exosuit-augmented post-stroke gait rehabilitation*, Journal of NeuroEngineering and Rehabilitation, Vol. 17, 80, 2020.

LUMPED–MASS TYRE MODELLING FOR ROAD–ENVELOPE ANALYSIS

Angelo Domenico Vella[1], Alessandro Vigliani[1]

[1] Politecnico di Torino, Corso Duca degli Abruzzi 24 10129, Torino, Italy
{angelo.vella@polito.it; alessandro.vigliani@polito.it}

1. INTRODUCTION

Modelling tyre–terrain interaction represents one of the most challenging aspects in the automotive field, as it enables the simulation-based analysis of traction, handling, and noise–vibration–harshness (NVH) vehicle performance. Widely adopted approaches rely on empirical tyre models, which are computationally efficient but require many parameters and extensive, often proprietary, calibration procedures [1]. These aspects limit both physical interpretability and scalability to different tyre configurations. On the other hand, numerical approaches such as finite element methods provide a highly accurate description of tyre and wheel structural behaviour, but they require detailed material data and are computationally demanding, making them unsuitable for large-scale or parametric simulations. Within a broader research activity aimed at investigating the ride comfort and safety of electric scooters [2,3], this study presents a novel parametric lumped-mass tyre–wheel model. The model is conceived for both two–wheeled and four–wheeled vehicles, with a specific focus on road-envelope behaviour and tyre dynamics over uneven surfaces. The formulation is implemented in the time domain, is fully transparent, and explicitly represents the structural contributions of the belt, sidewalls, and tyre–road contact interaction with a rigid surface. Model parameters are customised on a commercial electric kick-scooter tyre through affordable quasi-static experimental tests combined with an optimisation-based tuning procedure. The calibrated model is finally employed to simulate tyre traversal over cleat-type obstacles under different vertical loading conditions.

2. MODEL DEVELOPMENT

The lumped-mass tyre–wheel (LMTW) model, illustrated in Figure 1, consists of a rigid wheel represented by a single lumped inertia with six degrees of freedom and a tyre belt discretised through a set of lumped masses, each endowed with three translational degrees of freedom. Adjacent belt nodes are interconnected in both the circumferential (^{c}) and transversal (^{t}) directions by stiffness and damping elements, accounting for: (i) normal (along $\boldsymbol{n}^{c\pm}$ and $\boldsymbol{n}^{t\pm}$), (ii) bending (along $\boldsymbol{\psi}^{c}$ and $\boldsymbol{\psi}^{t}$) and (iii) shear (along $\boldsymbol{\lambda}$ and $\boldsymbol{\mu}$) interactions. The coupling between the belt and the wheel is modelled through additional stiffness and damping elements representing (i) the radial (along $\boldsymbol{\rho}$), (ii) bending (along $\boldsymbol{\gamma}$), and (iii) torsional (along $\boldsymbol{\xi}$) compliance of the sidewall. The contribution of the internal air inflation pressure is explicitly included as a distributed force acting on the belt structure and is directed along $\boldsymbol{\nu}$. Tyre–road interaction is modelled through a hard-contact geometric constraint in the normal direction ($\boldsymbol{\sigma}$) combined with a regularised Coulomb friction law in the tangential direction ($\boldsymbol{\tau}$), ensuring numerical robustness during obstacle traversal.

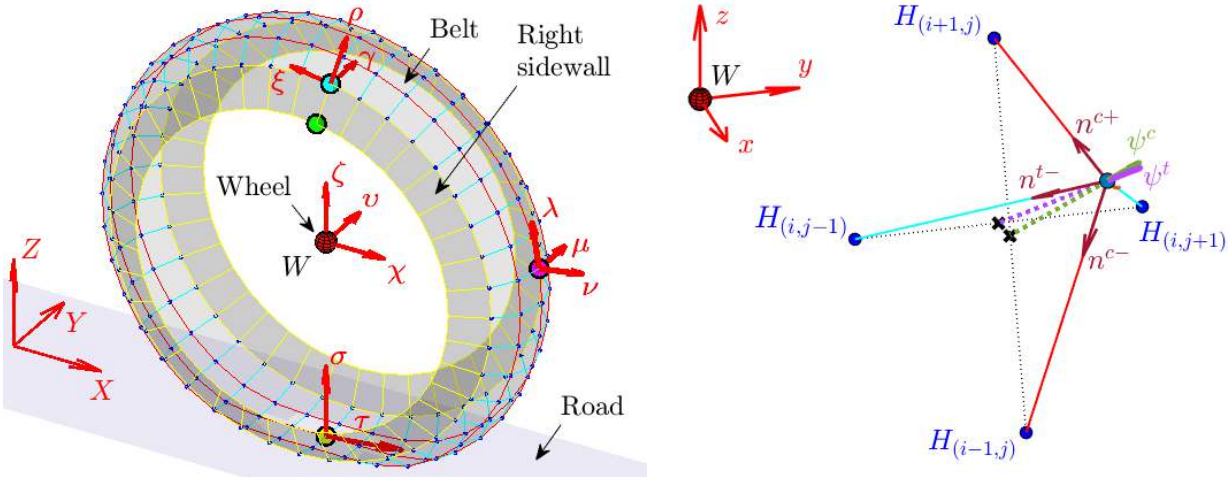

Figure 1. LMTW structure, reference frames and unit vectors used for the computation of node interactions in the circumferential/transversal direction within the belt and with the wheel through the right and left sidewalls.

3. MODEL CALIBRATION

The LMTW model is calibrated on the tyre–wheel system of a commercial electric scooter. The calibration of the belt and sidewall stiffness is designed to reproduce the evolution of the radial deflection and of the contact footprint dimensions as functions of the applied vertical load. Quasi-static experimental tests are performed using a tensile–compression testing machine operated under displacement control (left panel of Figure 2). The crosshead is moved at a low constant rate while the applied load is continuously recorded. In parallel, pressure-sensitive films are used to measure the tyre–ground contact footprint, which is approximated by an equivalent elliptical shape and characterised through its semi-axes. The model parameters are identified through an optimisation procedure that minimises the discrepancy between experimental measurements and LMTW predictions. A comparison between experimental results and numerical trends is reported in the right panel of Figure 2.

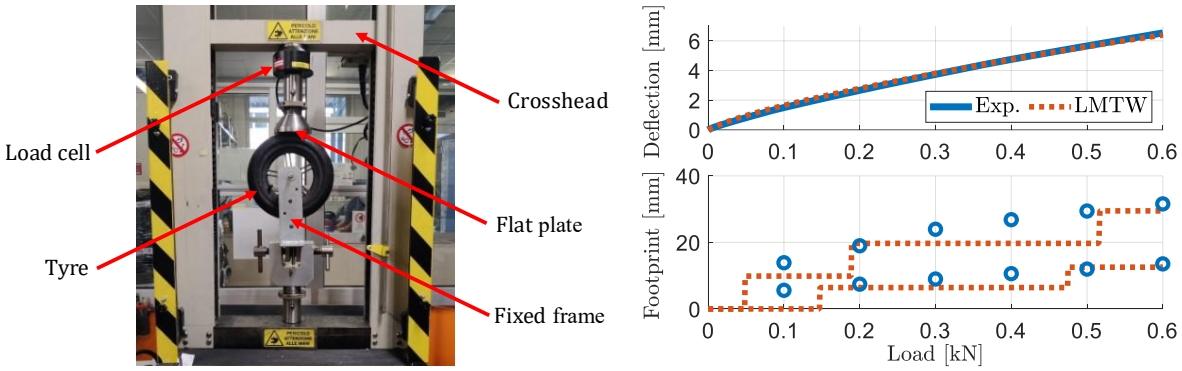

Figure 2. Experimental setup for tyre loading tests (left). Experimental–numerical comparison after the model calibration in terms of radial deflection and equivalent footprint semi-axes as functions of the applied vertical load (right).

4. SIMULATIONS AND RESULTS

The LMTW model is tested to demonstrate its applicability to road-envelope analysis through the simulation of tyre traversal over a cleat with a height of 20 mm and a length of 100 mm. The simulation consists of different phases as shown in the left panel of Figure 3. The tyre is first inflated up to the nominal pressure of 3.5 bar while an upward vertical force is applied to counteract gravity and prevent ground contact. Subsequently, a constant vertical load is applied to the wheel, considering two loading conditions (100 N and 500 N), representative of typical vertical loads for e-scooter applications. Finally, the wheel angular speed about its spin axis ($\boldsymbol{v}$) is gradually increased up to approximately 1.0 rad/s. The right panel of Figure 3 shows the vertical trajectory of the wheel centre, offset by the initial static deflection, compared with the geometric trajectory of an equivalent rigid wheel. The rigid-wheel case exhibits sharp transitions at the cleat edges, reflecting a purely geometric interaction with the road profile. In contrast, the LMTW predictions show a smoother and more progressive envelope, highlighting the filtering effect introduced by tyre compliance, especially at higher vertical loads. A single simulation, performed on a standard desktop workstation (Intel® Core™ i7-14700F, 32 GB RAM), with the adopted discretisation ($N_c = 72$, $N_t = 9$) and time step of 0.02 ms, requires approximately 790 s of CPU time to reproduce 10 s of physical time.

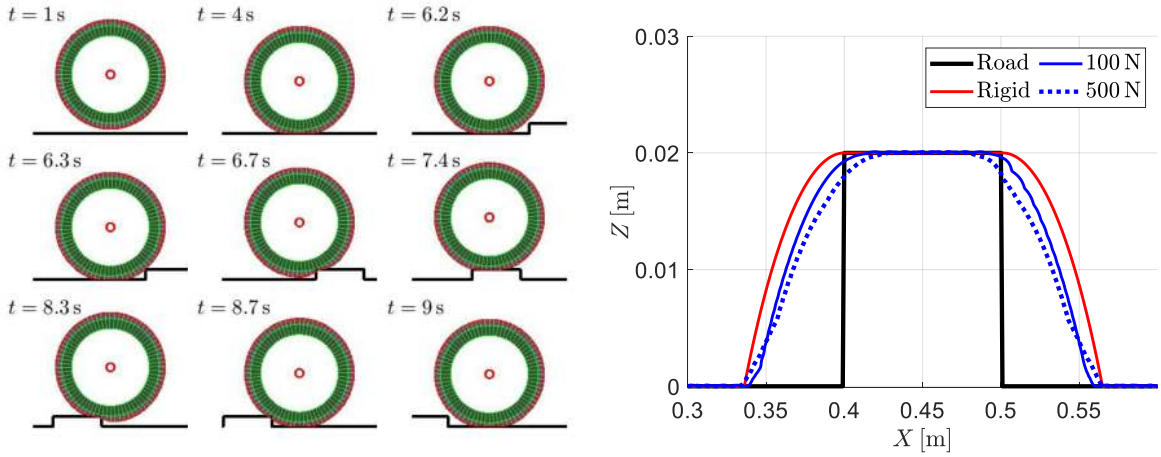

Figure 3. Nine snapshots extracted from the cleat traversal simulation under a vertical load of 500 N (left). Road profile and wheel–centre vertical trajectory during cleat traversal: equivalent rigid wheel and LMTW predictions for two different vertical loads (right).

REFERENCES

[1] H.B. Pacejka, E. Bakker, The magic formula tyre model, Vehicle System Dynamics 21 (1992) 1–18.

[2] A.D. Vella, A. Vigliani, Research on the Longitudinal Dynamics of an Electric Scooter, SAE Int. J. Veh. Dyn. Stab. NVH 7 (2022) 35–51. https://doi.org/10.4271/10-07-01-0003.

[3] A.D. Vella, E. Digo, L. Gastaldi, S. Pastorelli, A. Vigliani, Statistical Analysis of the Vibrations Transmitted From an Electric Kick Scooter to Riders, Exp. Tech. (2024). https://doi.org/10.1007/s40799-023-00693-7.

COMPARATIVE RESEARCH OF SOME DYNAMICS MODELS OF CRANK-SLIDER MECHANISM WITH COUNTERWEIGHT

Andrzej Urbaś[1], Jacek Stadnicki[1]

[1] University of Bielsko-Biala, Willowa 2, 43-309 Bielsko-Biala, Poland, {aurbas@ubb.edu.pl; jstadnicki@ubb.edu.pl}

1. INTRODUCTION

Modern methods for simulating the dynamics of linkage mechanisms that take into account the flexibility of the links require their discrediting into either rigidly connected flexible elements or flexible connected rigid elements. The models created in this way lead to various systems of differential equations of motion, which, in order to simulate the movement of the mechanism under operating conditions, require the development of appropriate algorithms with the help of which they are integrated, often with a very small time step. In practical engineering applications, efficiency is an important criterion when selecting a model, and consequently a method for modelling the dynamics of a linkage mechanism. Naturally, the more efficient a model is, the more useful it will be. The efficiency measure can be the use of computer resources during simulation, e.g. processor operation time (CPU time). The paper presents a comparative research of the effectiveness and quality of the results of two models of the dynamics on the example of the crank-slider mechanism with counterweight and a flexible link.

2. DYNAMICS MODEL OF THE CRANK-SLIDER MECHANISM

The analysed mechanism is presented in Fig.1. Its model consists of a rigid crank with a counterweight in variants [1], a rigid or flexible connecting rod and a slider that slides between two symmetrical bumpers. The crank is subjected to driving torque $\mathbf{t}_{dr}$ and resisting torque $\mathbf{t}_{res}$. To compare the effectiveness of the models with flexible connecting rod the rigid finite element method, in both classical ($RFEM_c$) and modified approaches ($REFM_m$), is applied [2,3].

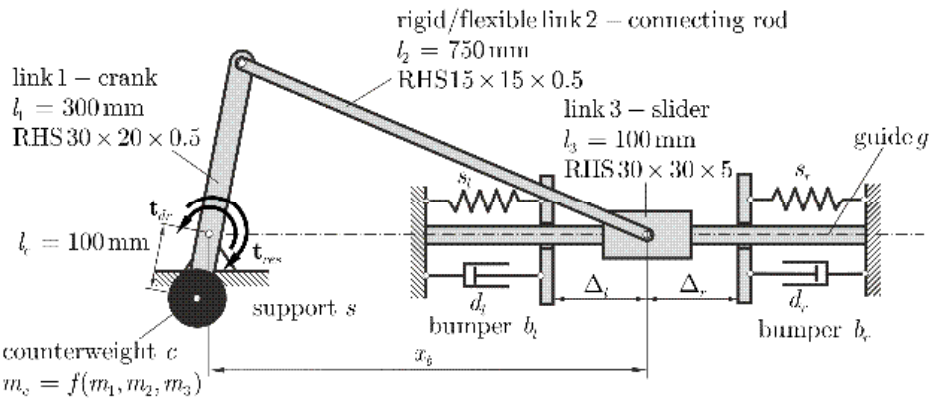

Figure 1 Crank-slider mechanism with counterweight.

In the rigid finite element method, the flexible link is replaced by a set of n_{rfe} rigid finite elements connected by n_{sde} massless and dimensionless spring-damping elements. In the classical approach, both tension, shearing and bending of the flexible link are considered, whereas in the modified approach only bending is taken into account.

The formalism of joint coordinates and homogeneous transformation matrices is applied to describe the kinematics of the mechanism. The vector of generalised coordinates consists of the following components:

$$\mathbf{q} = \begin{bmatrix} \hat{\psi}_1 & \tilde{\mathbf{q}}_2^{\mathrm{T}} & \hat{\psi}_3 \end{bmatrix}^{\mathrm{T}}, \tag{1}$$

where: $\tilde{\mathbf{q}}_2 = \begin{cases} \left[\hat{\psi}_{2,1} \;\vdots\; \widehat{\mathbf{q}}_2^{\mathrm{T}}\right]^{\mathrm{T}} & \text{if} \quad RFEM_c, \\ \left[\hat{\psi}_{2,1} \;\vdots\; \hat{\mathbf{q}}_2^{\mathrm{T}}\right]^{\mathrm{T}} & \text{if} \quad RFEM_m, \end{cases}$ $\widehat{\mathbf{q}}_2 = \left[\hat{x}_{2,2} \quad \hat{y}_{2,2} \quad \hat{\psi}_{2,2} \;\vdots\; \cdots \;\vdots\; \hat{x}_{2,n_{rfe}} \quad \hat{y}_{2,n_{rfe}} \quad \hat{\psi}_{2,n_{rfe}}\right]^{\mathrm{T}}$, $\hat{\mathbf{q}}_2 = \left[\hat{\psi}_{2,2} \;\vdots\; \cdots \;\vdots\; \hat{\psi}_{2,n_{rfe}}\right]^{\mathrm{T}}$.

Dynamics' equations of the mechanism are derived using the Lagrange equations of the second kind:

$$\begin{bmatrix} \mathbf{M} & \mathbf{C}^T \\ \mathbf{C} & \mathbf{0} \end{bmatrix} \begin{bmatrix} \ddot{\mathbf{q}} \\ \mathbf{f} \end{bmatrix} = \begin{bmatrix} \mathbf{t}_{dr} - \mathbf{t}_{res} + \mathbf{h} \\ \mathbf{d} \end{bmatrix}, \tag{2}$$

where: $\mathbf{M}$ is the mass matrix of the mechanism, $\mathbf{C}$ is the constraint matrix related to the cut-joint (prismatic joint),

$\mathbf{f}$ is the vector of unknown reactions in the cut-joint, $\mathbf{h}$ is the vector of the right side of the dynamics equations,

$$\mathbf{h}^{(m)} = \begin{cases} -\mathbf{e}-\mathbf{g} & \text{if rigid connecting rod,} \\ -\mathbf{e}-\mathbf{g}-\mathbf{s} & \text{if flexible connecting rod,} \end{cases}$$

$\mathbf{e}$ is the vector of the Coriolis, gyroscopic and centrifugal forces, $\mathbf{g}$ is the vector of the gravity forces, $\mathbf{s}$ is the vector defining the spring and damping properties of the connecting rod, $\mathbf{d}$ is the vectors of the right side of the constraints.

3. NUMERICAL RESULTS

Figs 2a and 2b present some exemplary results of the simulations, i.e. the influence of the flexibility of the connecting rod and the types of counterweights on the time courses of the crank's angular velocity and the slider's acceleration. The slider acceleration time courses are transformed into their frequency spectra using the FFT, as shown in Fig. 2c.

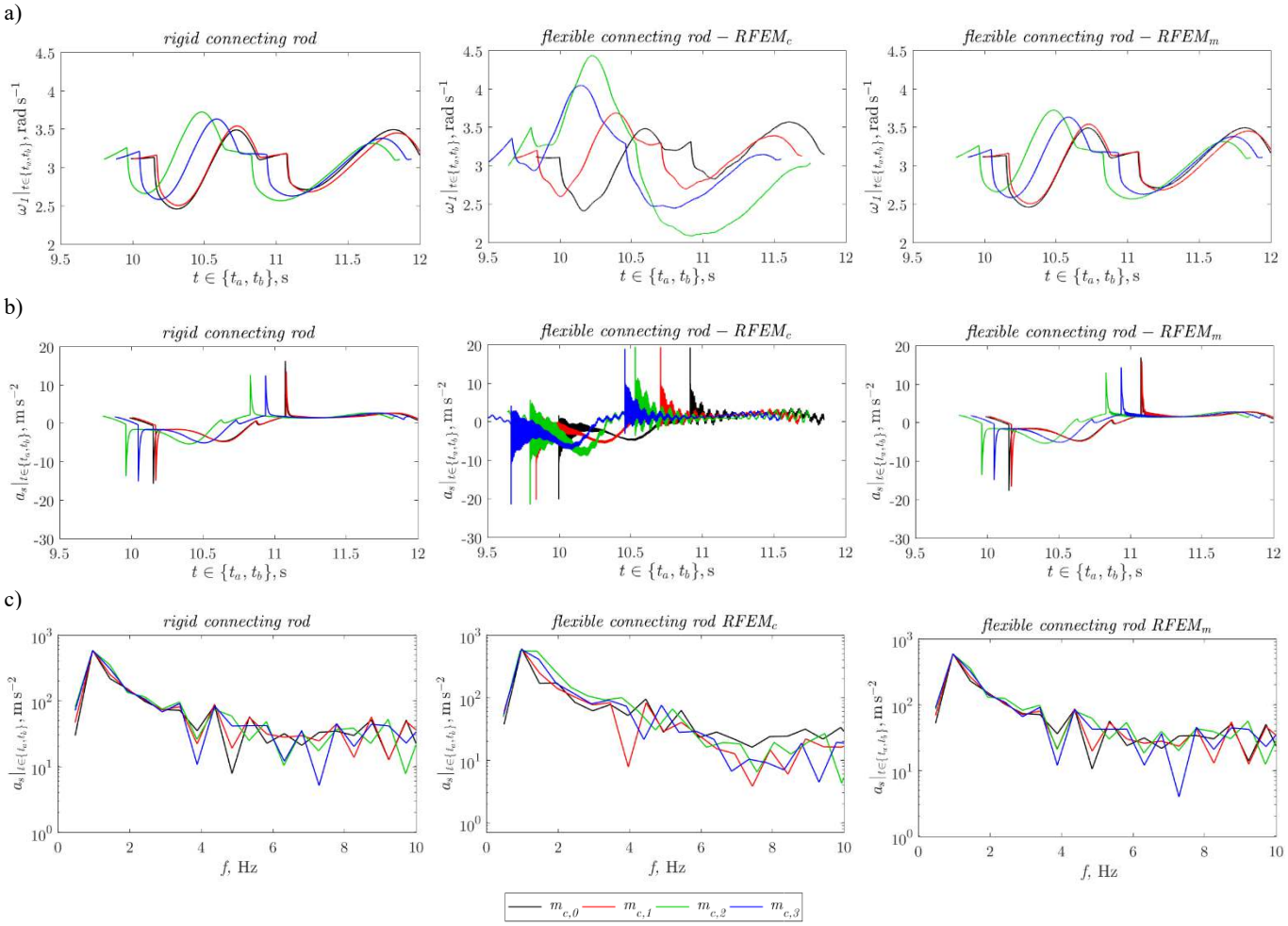

Figure 2. a) Time courses of the angular velocity of the crank, b) Time courses of the acceleration of the slider, c) Frequency spectra of the acceleration of the slider.

As expected, the dynamics of the rigid connecting rod mechanism model are influenced only by the bumpers acting on the slider. However, the connecting rod flexibility is manifested in the form of higher-frequency vibrations (Fig.2b), and the model using *RFEM$_c$* method, in particular, is more adequate to reality and allows for taking into account these vibrations. The computational time required to simulate the mechanism motion, using a personal computer equipped with an Intel(R) Core(TM) i7-14700F processor (2.10 GHz) and 32.0 GB of RAM, was 31 s for the mechanism with a rigid connecting rod. For the mechanism incorporating a flexible connecting rod, the simulation times were 1590 s and 970 s when the *RFEM$_c$* and *RFEM$_m$* modeling approaches were applied, respectively. The quality assessment of the simulation results of the applied mechanism dynamics models will be discussed during the conference.

REFERENCES

[1] J.J. Dicker, G.R. Pennock, J.E. Shigley, Theory of machines and mechanisms, Oxford University Press, New York, 2023.
[2] J. Kruszewski, S. Sawiak, E. Wittbrodt, The Rigid Finite Element Method, Science and Technical Publishers, Warsaw, 1999 (in Polish).
[3] A. Urbaś, Modelling of the dynamics of boom cranes with a complex kinematic structure, University of Bielsko-Biala Press, Bielsko-Biala, 2023.

ODE-BASED DYNAMIC MODELING OF MULTI-LOOP ROBOTS AND ITS APPLICATION TO MODEL PREDICTIVE CONTROL

Shaoheng Hu[1], Xianwen Kong[2], Guodong Yin[1]

[1]School of Mechanical Engineering, Southeast University, Nanjing, 211189, China, {101300669@seu.edu.cn; ygd@seu.edu.cn}
[2]School of Engineering and Physical Sciences, Heriot-Watt University, Edinburgh EH14 4AS, UK, {X.Kong@hw.ac.uk}

1. INTRODUCTION

Multi-loop robots (parallel and hybrid mechanisms) achieve high stiffness, compactness and reconfigurability, but their closed kinematic loops make dynamic modeling and control significantly more challenging than in serial chains [1-3]. A common remedy is to introduce loop-closure constraints using Lagrange multipliers, yielding differential-algebraic equation (DAE) models [4-6]. While DAEs are rigorous, they complicate simulation and, more importantly, create algebraic equality constraints when used inside model predictive control (MPC) which has been shown to be effective for handling multivariable coupling and constraints in robotic systems [7,8], increasing problem size and numerical sensitivity [9,10]. The target of this work is MPC-oriented modeling. This work builds an explicit ordinary differential equation (ODE) model for general multi-loop mechanisms by replacing constraints equation with physically interpretable penalty forces, and then apply online linearization to obtain an MPC prediction model.

2. METHOD

2.1. Balanced spanning tree and tree kinematics

The mechanism is represented as an undirected graph whose nodes are links and edges are joints. A rooted spanning tree (Fig. 1) is constructed using breadth-first search (BFS) [11] from the ground. The BFS expansion tends to produce a minimum-height tree, which reduces kinematic propagation depth and symbolic complexity. Joints not included in the tree are recorded as closure pairs, for which the two-incident links and joint frames are stored. With direction-consistent transforms along the unique tree paths, the pose of each link and its center-of-mass frame is obtained by sequential multiplication.

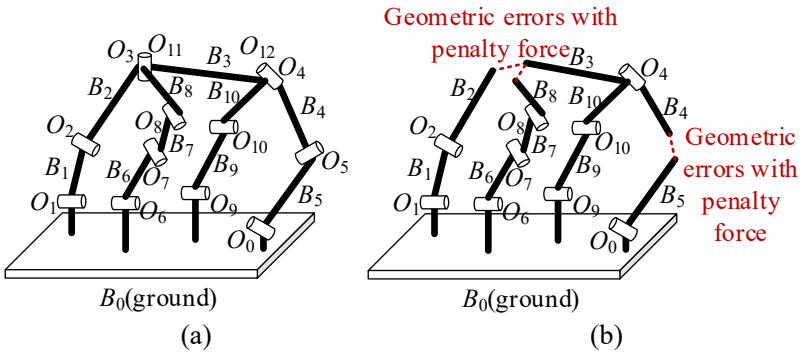

Fig. 1. Transforming a non-tree system into a tree system (a) A multi-loop mechanism (b) The tree system transformed from the multi-loop mechanism

2.2. Penalty forces and ODE dynamics

For each closure pair, loop closure is enforced by penalty-based closure forces rather than algebraic constraint equations. Joint compatibility is described using position- and axis-level geometric errors reconstructed from the joint frames on both sides. Spring-damper forces, acting on both the errors and their velocities, are applied to restore closure, as shown in Fig.2, and are mapped to generalized forces via virtual work, yielding a purely ODE-form dynamic model. To ensure physical fidelity and closed-loop controllability, the spring and damping coefficients must be properly selected so that loop-closure errors are suppressed without introducing excessive stiffness. Unlike multiplier-based DAE formulations [4-6] and stiffness-only mobility models used for mobility or modal analysis [12], this work enforces loop closure using spring–damper forces embedded directly in the dynamics, yielding an explicit ODE model suitable for MPC.

2.3. Online linearization and applying ODE formed dynamics to MPC

For MPC, this paper uses the first-order state and evaluates the explicit state function by solving the mass-matrix form at each call. Around the current operating point, a local linear model is computed using Taylor's Formula. After discretization with sampling time, the prediction model is used within a quadratic MPC formulation with input bounds. Because the prediction model originates from an ODE, there are no algebraic equality constraints from loop closure, and the MPC problem retains a compact, well-conditioned QP structure (only inequality constraints for actuator limits and optional state bounds).

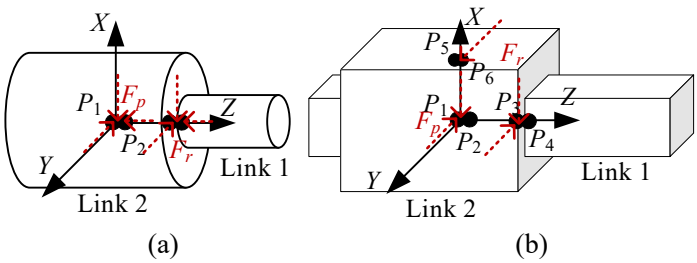

Fig. 2. Penalty forces for different type joints (a) The penalty force for rotation joint (b) The penalty force for parallel joint

3. RESULTS

3.1. Algorithm and Example

This work provides a unified pseudo-code summarizing: (1) BFS tree spanning, (2) ODE dynamic model computation, (3) linearization and ODE-to-MPC conversion, and (4) real-time MPC loop. The method is applied to a planar RRRR mechanism as an example. The modeling process is thoroughly demonstrated and the MPC controller in designed and used, providing a clear and practical understanding of how the theoretical framework is applied in practice.

3.2. Validation and Discussion

This work validates the approach on a 3-RPS parallel mechanism with multiple legs and platform constraints. The BFS tree spanning and cut-joint force recovery are fully automatic from the mechanism graph and joint transforms. Under trajectory tracking tasks, the proposed ODE-MPC formulation is compared with DAE-MPC in terms of QP problem dimension, CPU time, stabilization performance near singular configurations, and numerical stability during high-speed motion. The advantage and limitation of the method will be discussed.

4. CONCLUSION

This paper provides a complete framework for efficient dynamic modeling and MPC control of multi-loop robotic mechanisms. By combining BFS-based tree spanning, ODE dynamic modeling with constraint-force closure, and linear MPC design, the method overcomes the stiffness and computational challenges of DAE-based approaches.

ACKNOWLEDGMENTS

This work was supported in part by the National Natural Science Foundation of China under Grant 52394263 and Grant U25A20379.

REFERENCES

[1] M. Leveziel, et al., MiGriBot: A miniature parallel robot with integrated gripping for high-throughput micromanipulation, Science Robotics 7(69) (2022) eabn4292.
[2] X. Kong, C. Gosselin, Type Synthesis of Parallel Mechanisms, Springer Berlin Heidelberg (2007).
[3] Y. Tian, D. Zhang, Y.-A. Yao, et al., A reconfigurable multi-mode mobile parallel robot, Mech. Mach. Theory 111 (2017) 39–65.
[4] J. Wittenburg, General Multibody Systems, Springer Berlin Heidelberg (2008).
[5] R. Featherstone, Rigid Body Dynamics Algorithms, Springer US, Boston, MA (2008).
[6] A. Jain, Robot and Multibody Dynamics: Analysis and Algorithms, Springer Science & Business Media (2010).
[7] Y. Ding, A. Pandala, H.-W. Park, Real-time model predictive control for versatile dynamic motions in quadrupedal robots, in: Proc. IEEE Int. Conf. on Robotics and Automation (ICRA), 2019, pp. 8484–8490.
[8] Y. Ding, C. Li, Y.-H. Shin, H.-W. Park, Representation-free model predictive control for dynamic motions in quadrupeds, IEEE Trans. Robotics 37(4) (2021) 1154–1171.
[9] M. Diehl, R. Findeisen, F. Allgöwer, H.G. Bock, J.P. Schlöder, Real-time optimization and nonlinear model predictive control of processes governed by differential-algebraic equations, J. Process Control 12(4) (2002) 577–585.
[10] M. Diehl, H.G. Bock, J.P. Schlöder, A real-time iteration scheme for nonlinear optimization in optimal feedback control, SIAM J. Control Optim. 43(5) (2005) 1714–1736.
[11] V. Rozhoň, B. Haeupler, A. Martinsson, et al., Parallel breadth-first search and exact shortest paths and stronger notions for approximate distances, in: Proc. 55th Annual ACM Symposium on Theory of Computing, 2023, pp. 321–334.
[12] S. Hu, R. Li, X. Kong, Y. Li, X. Zhang, B. Corves, Y.-A. Yao, A dynamics-based method for determining the local finite mobility of single-loop spatial mechanisms, Mech. Mach. Theory 214 (2025) 106097.

TRIBOLOGY IN MATERIAL HANDLING: WINCHES, NONLINEAR ROPE FRICTION, FIBER ROPES, FUSED FILAMENT FABRICATION COMPONENTS

Rico Zöllner[1], Raimond Hofmann[1], Martin Anders[1], Thorsten Schmidt[1]

[1] Institute of Material Handling and Industrial Engineering, 01062 Dresden, Germany,
{rico.zoellner@tu-dresden.de; raimond.hofmann@tu-dresden.de; martin.anders@tu-dresden.de;
thorsten.schmidt@tu-dresden.de}

1 INTRODUCTION AND OVERVIEW

In fields traditionally dominated by steel components, such as material handling, innovative materials like plastics and fiber ropes as well as additively manufactured (AM) components (e.g., 3D-printed traction sheaves) are gaining increasing popularity. The use of plastics offers numerous advantages compared to conventional metal solutions, significant at both the system and the manufacturing levels. A key aspect is the substantial reduction of mass. Hereby, the reduction of rotating mass is particularly beneficial for rotating components. Furthermore, the high corrosion resistance of plastics extends the service life of components in demanding environments. While conventional manufacturing processes for plastic components are suitable for high-volume productions, they are economically unsuitable for small batches or customized solutions. For these cases, AM processes, such as fused filament fabrication (FFF), open up new application potentials for plastic-based machine elements.

Nevertheless, the industrialization of AM remains a challenge, partly because the properties and the behavior of these systems have not yet been sufficiently investigated. This paper deals with the tribological behavior of rope winches, i.e., the friction that occurs when a rope runs over a traction sheave. While Coulomb friction and the resulting Euler-Eytelwein equation are well established for classic wrapping traction applications, plastics and fiber ropes exhibit a more complex behavior, partly because elasticity and geometric effects cannot be neglected.

This contribution focuses on three main areas: First, a triboelastic model for rope friction is developed, which – in addition to a general friction law – also considers elasticity (Section 2). Since friction is a surface phenomenon, the approach of point forces is avoided. Instead, contact pressures and stresses are used. Second, Section 3 deals with AM traction sheaves. Their infill structure is based on triply-periodic minimal surfaces (TPMS). Third, Section 4 presents the experiments conducted on the frictional behavior and thus also serves as a validation. The contents of these sections are sketched below.

2 MODEL SETUP

Previous models of nonlinear rope friction and elasticity have mainly focused on power law friction of point forces (e.g., [1, 2]). The model in principle is shown in Figure 1. From this, using the mechanical equilibria

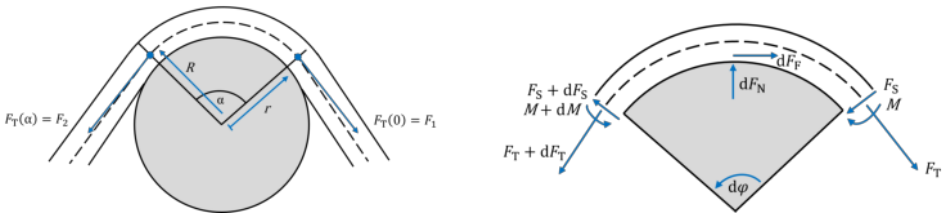

Figure 1: A rope wound around a sheave (left) and an infinitesimal free body diagram (right).

$$0 = F_N' + F_S' - F_T \quad (1)$$
$$0 = F_F' - F_S' - F_T' \quad (2)$$
$$0 = rF_F' - RF_S + M' \quad (3)$$

supplemented by material laws

$$\sigma_F = \mathcal{P}(\sigma_N) \quad \text{(stresses)} \quad \text{or} \quad F_F = \mathcal{Q}(F_N) \quad \text{(forces)} \quad (4)$$

equations of motion are derived, into which geometric aspects are explicitly incorporated through the contact area A (e.g., $F'_{\mathrm{N}} = \sigma_{\mathrm{N}} \cdot A$, cf. [3]) and the bending moment M (e.g., $M = EI/R$). To keep the model manageable, a homogeneous, linearly elastic material is assumed. The phenomenon that deformations occur due to acting forces which in turn influence the acting forces, is taken into account in the model.

3 FUSED FILAMENT FABRICATED COMPONENTS

All considered traction sheaves were printed from PLA (polylactide) and posses load-bearing TPMS infill structures. TPMS represent an effective method for reinforcing structural components, thus enabling a reduction in component mass. TPMS are widely used in AM to optimize structures w.r.t. weight and strength. TPMS are isosurfaces [4], e.g., Primitive, Diamond and Gyroid are types used in AM (see Figure 2). The complex structure of such surfaces offers various advantages but prevents the use of conventional manufacturing structures [5]. The geometry and further properties are determined by the selected TPMS type and its modulation (see [6, 7] for details).

Figure 2: Model of a traction sheave with a Gyroid infill structure (left), an AM sheave with a fiber rope in the experimental setup (middle), and comparison of experimental data with the predictions of Euler-Eytelwein and the model (right).

4 EXPERIMENTAL RESULTS AND VALIDATION

The experimental setup for measuring frictional coefficients is shown in Figure 2. The two rope forces F_1 and F_2 were measured for several material combinations and varying wrap angles. In summary, the simple Euler-Eytelwein equation approach fails, particularly for larger forces and larger wrap angles; whereas pure power law friction is unsuitable for smaller forces and angles. Therefore, a hybrid friction law (linear-power) should be used. While the effects of elasticity do play a role, friction is clearly dominant.

5 SUMMARY AND DISCUSSION

This paper aims to demonstrate how existing models for rope friction can be extended to novel material combinations. Aspects related to theory, design, and experiments will be presented. A systematic contribution is made to the study of the frictional behavior of fiber ropes, plastic ropes, and AM components.

REFERENCES

[1] J. H. Jung, N. Pan, and T. J. Kang, "Generalized capstan problem: Bending rigidity, nonlinear friction, and extensibility effect," *Tribology International*, vol. 41, no. 6, pp. 524–534, 2008.

[2] S. Yoo, T. Kim, M. Seo, J. Oh, J. Kim, H. S. Kim, and T. Seo, "Modeling and verification of multi-winding rope winch for facade operation," *Mechanism and Machine Theory*, vol. 155, p. 104105, 2021.

[3] X. Gao, L. Wang, and X. Hao, "An improved capstan equation including power-law friction and bending rigidity for high performance yarn," *Mechanism and Machine Theory*, vol. 90, pp. 84–94, 2015.

[4] H. von Schnering and R. Nesper, "Nodal surfaces of fourier series: fundamental invariants of structured matter," *Zeitschrift für Physik B Condensed Matter*, vol. 83, no. 3, pp. 407–412, 1991.

[5] R. Hofmann, C. Matthes, and T. Schmidt, "Capabilities of additively manufactured rope drums," *innoTRAC Journal*, vol. 1, pp. 26–36, 2020.

[6] X. Shi, W. Liao, T. Liu, C. Zhang, D. Li, W. Jiang, C. Wang, and F. Ren, "Design optimization of multimorphology surface-based lattice structures with density gradients," *The International Journal of Advanced Manufacturing Technology*, vol. 117, no. 7, pp. 2013–2028, 2021.

[7] Y. Jin, H. Kong, X. Zhou, G. Li, and J. Du, "Design and characterization of sheet-based gyroid porous structures with bioinspired functional gradients," *Materials*, vol. 13, no. 17, p. 3844, 2020.

REAL-TIME PROMPT-BASED 3D OBJECT DETECTION AND POSE KINEMATICS FOR INTERACTIVE COBOT GRASPING

Marco Cirelli, Luca D'Angelo, Pier Paolo Valentini

University of Rome Tor Vergata, via del Politecnico 1, 00133 Rome, Italy {marco.cirelli@uniroma2.it; luca.d.angelo@uniroma2.it; valentini@ing.uniroma2.it}

1. INTRODUCTION

Collaborative robots (cobots) are increasingly deployed in industrial and service environments to operate safely alongside humans, enabling flexible automation in tasks that require adaptability, perception, and physical interaction [1]. Unlike traditional industrial robots, cobots must operate in unstructured or semi-structured environments, handle frequent changes in object types and positions, and meet strict constraints on safety, latency, and reliability. These requirements pose significant challenges to perception, decision-making, and control, particularly when robots are expected to perform manipulation tasks with human-like robustness and responsiveness. Among these tasks, object grasping and pick-and-place operations remain some of the most critical and technically demanding [2]. Successful grasping requires reliable 3D object detection, accurate estimation of object position and orientation (6D pose), and tight integration with motion planning and control [3]. Errors in perception directly propagate to the kinematic chain, often resulting in failed grasps, collisions, or inefficient trajectories [4]. Consequently, efficient control strategies must be tightly coupled with real-time perception pipelines to ensure low-latency feedback and stable execution, especially in interactive scenarios where the environment may change dynamically, or human operators may intervene. Recent advances in artificial intelligence have significantly expanded the capabilities of robotic perception systems [5]. Deep learning based computer vision methods have demonstrated remarkable performance in object detection, segmentation, and 6D pose estimation, even in cluttered scenes and under varying lighting conditions. More recently, prompt-based and multimodal models have introduced a new paradigm in which high-level semantic information can guide low-level visual perception, enabling robots to reason about objects using natural language descriptions or task-specific prompts. This form of "reasoned vision" allows cobots to generalize to previously unseen objects, adapt to new tasks with minimal reconfiguration, and bridge the gap between symbolic task descriptions, geometric perception and motion planning.

2. METHODOLOGY

The proposed methodology is based on the use of an industrial cobot equipped with a gripper to which a depth camera is rigidly mounted. A Universal Robots UR10e cobot was used for this study, with a Robotiq 2F-85 flex-finger gripper and an Intel RealSense depth camera mounted using a rigid metal plate (Figure 1, on the right).

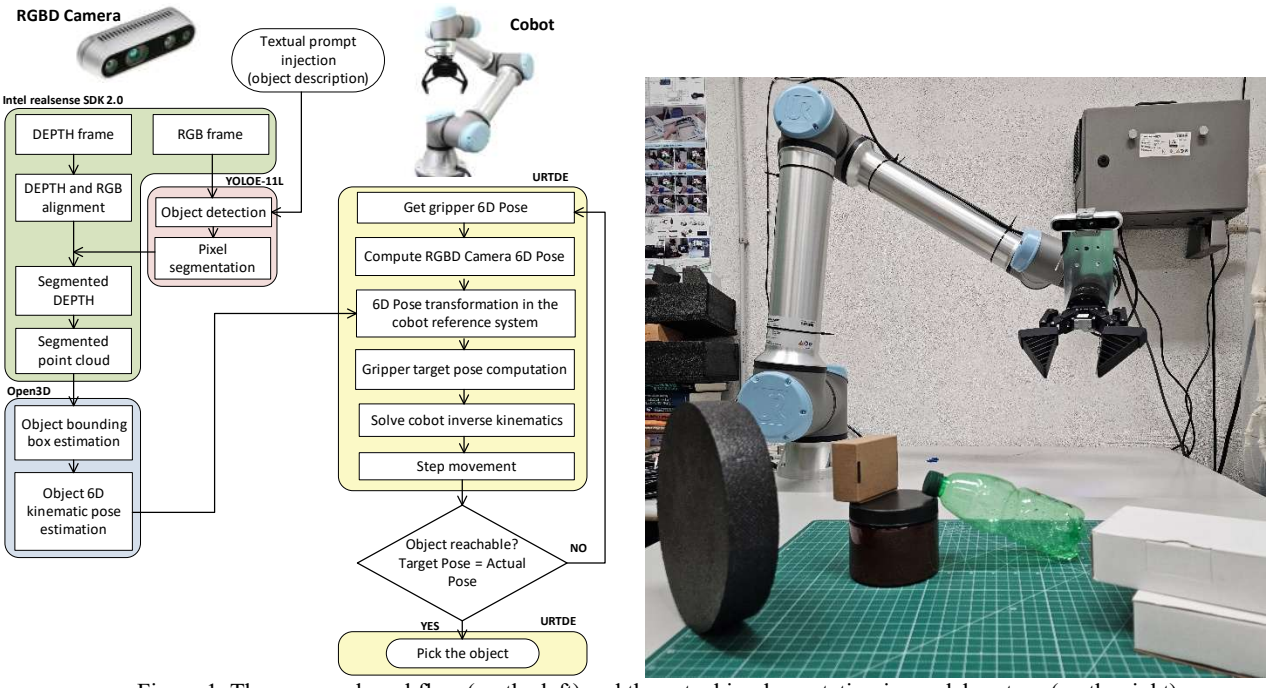

Figure 1. The proposed workflow (on the left) and the actual implementation in our laboratory (on the right).

The goal is to provide the cobot with the correct instructions (motion planning) to grasp a generic object in the work area, using a simple text prompt. From an operational point of view, these instructions specify the body's position and orientation relative to a reference system fixed to the cobot's base link (i.e., the 6D pose described by a 4x4 transformation matrix). The instructions should specify the position of the object's geometric center, which represents the optimal balanced gripping point, and the preferred direction to align the gripper's ends to achieve a stable grip. For this goal, the methodology combines and integrates four libraries in Python: the Intel RealSense SDK 2.0 for the management of input from the depth camera, the YOLOE computer vision library for real-time recognition of objects on a simple prompt, the Open3D library for the management of the point cloud and geometric operations and the URTDE library to manage the input and output with the cobot from code.
With reference to Figure 1, on the left, the methodology can be summarized following a logical workflow. The depth camera captures RGB images and depth maps simultaneously by using a global shutter. The RGB image (Figure 2, on the left) is passed to the YOLOE library along with the textual description of the object to be grabbed (the prompt). The library performs real-time object recognition and returns the image segmentation relative to the pixels it occupies. This segmentation is shared with the depth map to isolate the object's descriptive 3D points. From the segmented depth map information (Figure 2, in the middle), a point cloud is then created (Figure 2, on the right) and then passed to the Open3D library capable of estimating the bounding box of the object, its dimensions, its spatial orientation and the position of its geometric center of gravity in the camera's reference system. Finally, this information is passed to the URTDE library, which transforms it into the cobot's reference system to interpret the kinematic pose of the object to be grasped and define the corresponding 6D pose of the gripper to reach and pick the object with the correct position and orientation. The cobot's motion is then set as an interpolation in joint space using well-known inverse kinematics, which maps the end effector's absolute 6D pose to joint coordinates. During the movement to reach the object, at regular intervals, the acquisition, recognition and segmentation procedure is repeated in order to correct any errors or simply to improve the estimation of the kinematic pose of the object to be grasped, thanks to the variation of the point of view of the scene. The procedure ends when the gripper's position and orientation are close enough to the target position of the object to be gripped.

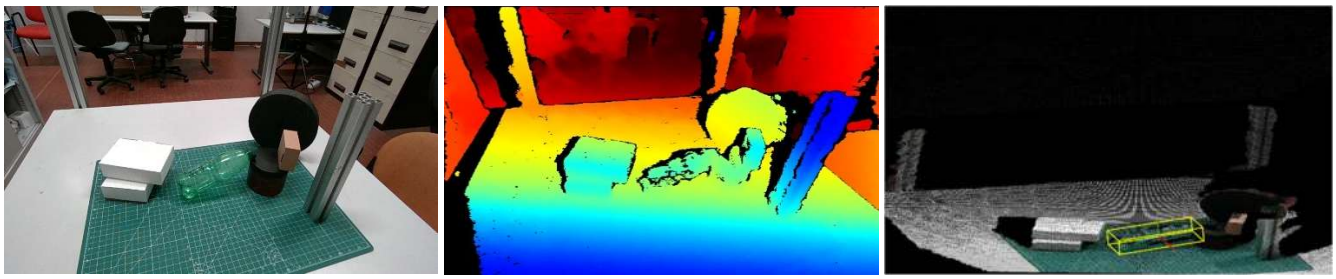

Figure 2. Data processing from depth camera: RGB image (on the left), Depth map (in the middle) and 3D point cloud with the object's oriented 3D bounding box (on the right)

3. RESULTS AND CONCLUSIONS

The proposed methodology has been tested in a laboratory environment with 40 objects of varying dimensions (5-40 cm) in known poses for benchmarking. The performance of three Intel RealSense depth cameras has been compared (D455, D435i and D405). Accuracy in bounding box location was very high (errors lower than 5 mm) while slightly greater errors were experienced for the bounding box attitude (errors lower than 10 degrees). Both inaccuracies are within tolerances for safe grasping, and therefore, the methodology seems efficient and promising. The D435i camera showed the best performance as a trade-off among accuracy, robustness, and field-of-view width. Three pose corrections during the gripper motion are the most suitable compromise to improve 6D pose estimation without an excessive computational burden. On the other hand, the proposed workflow always guarantees real-time operations. Integrating such AI-driven perception with real-time kinematic modelling and control opens new possibilities for accurate and interactive robotic manipulation. By combining prompt-based 3D object detection with real-time pose estimation and kinematic reasoning, cobots can achieve more reliable grasp synthesis and motion execution, while maintaining the responsiveness required for safe human–robot collaboration. Future work will include trajectory planning and obstacle avoidance using the same 3D information from the depth cameras, segmented using machine learning computer vision algorithms.

ACKNOWLEDGEMENT

This research was funded by Italian Ministry for Education and Research MIUR, PRIN 2022 program "Augmented Reality and Natural Interface for Computer-Aided Simulations", CUP E53D23003850006.

REFERENCES

[1] R. di Leva et al., "Force and time-optimal trajectory planning for dual-arm unilateral cooperative grasping". *Mech. Mach. Theory*, 201:105729, 2024.
[2] Y. Luo et al., "Instant Grasping Framework of Textured Objects Via Precise Point Matches and Normalized Target Poses", *J. Mech. Robot.*, 17(8):081013, 2025.
[3] J.B. Torres et al., "Supersurfaces for grasping, scene generation and contact modelling". *Mech. Mach. Theory*, 214:106075, 2025.
[4] G.Q. Fernandes et al., "Grasping capability analyses for optimal grasp synthesis", *Mech. Mach. Theory*, 214:106094, 2025.
[5] A. Saxena et al., "Robotic grasping of novel objects using vision", *Int. J. of Robot. Res.*, 27(2):157-173, 2008.

EXPERIMENTS AND ANALYSIS OF TWISTCAR-TYPE ROBOTS

Rom Levy[1], Anna Zigelman[1], Ari Dantus[1], Zitao Yu[1,2], Yizhar Or[1]

[1]Faculty of Mechanical Engineering Technion-Israel Institute of Technology Haifa, Israel * {izi@technion.ac.il}

[2] Deptartment of Aerospace and Mechanical Engineering, University of Southern California, USA.

1. SUMMARY

Twistcar is a children's riding toy car with passive wheels which is propelled by imposing oscillatory actuation of the steering handlebar. In contrast, the Snakeboard skating platform is propelled by twisting of the rider's waist. In this work, we present recent experimental results in a Twistcar robot and the Snakeboard-inspired RAPS-Twistcar robot (Rotor-Actuated Passive Steering Twistcar), and show analysis of theoretical models that explain their non-trivial dynamic behavior. For the Twistcar robot, we demonstrate direction reversal upon changing the actuation frequency, which can be only explained by incorporating wheels' skid and Coulomb-like lateral friction forces. For the RAPS-Twistcar robot with an actuated oscillating rotor and passive steering joint, we demonstrate bifurcation of transition between two different motions, one is symmetric oscillations of the passive steering angle while propelling in straight line, and the other is asymmetric oscillations of the steering angle and propelling along a circular arc. This motion was predicted theoretically in our recent theoretical work and is demonstrated here experimentally for the first time.

2. BRIEF LITERATURE REVIEW

The Twistcar, which appears in Fig. 1a, is a commercial toy car with passive wheels which is propelled by the rider imposing oscillatory actuation of the steering handlebar. Theoretical analysis of an earlier version of the same toy, named roller-racer, has been analyzed in the early work [1] as a planar under-actuated two-link system with nonholonomic constraints, representing prevention of wheels' skid in lateral direction. Our later work [2] conducted asymptotic analysis for a point-mass model of the Twistcar's dynamic equations, see Fig. 1b. Assuming small oscillations of the steering angle $\phi(t)=\varepsilon \sin(\omega t)$ with $\varepsilon \ll 1$, the analysis in [2] predicted reversal in the direction of net motion by shifting the center-of-mass (COM) position of the rider's link. Our recent work [3] extended the model to account for the two links' masses and inertias, and also incorporated energy dissipation due to wheels' rolling resistance forces. The analysis in [3] also predicted direction reversal due to COM shifting, which was also verified in experiments with a Twistcar two-link robot, shown in Fig. 1c. The experimental motion measurements in [3] indicated a significant amount of lateral skid, which was not accounted in the analysis.

The Snakeboard is a wheeled skating platform which is propelled by twisting of the rider's waist, see Fig. 1d. The early work [4] analyzed the Snakeboard's nonholonmic dynamics, where the rider's twist is represented by reciprocating rotation of an inertial rotor attached to the platform. While the model in [4] considered also actuation of the hinge angles of the Snakeboard's wheeled links, a modern variant called Waveboard, shown in Fig. 1e, has passive wheels connected to passive hinges. Inspired by these two platforms, our recent work [5] analyzed a three-link model called RAPS-Twistcar, shown in Fig. 1f. Under simplifying assumption that the links' masses are negligible relative to the rotor's mass, the analysis in [5] predicts transitions between different types of solutions. The first solution type is symmetric oscillations of the passive steering angle $\phi(t)$ about zero mean while the net propulsion is along a straight line, and the second solution type is asymmetric oscillations of $\phi(t)$ about nonzero mean value while propelling along a circular arc. The analysis shows bifurcations and stability transitions for these two solution types, upon varying the actuation frequency of the rotor's angle $\psi(t)=A \sin(\omega t)$, as shown in Fig. 2a, or varying the scaled position of the rotor $\delta = d_1/l_1$.

Recent experimental results with the Twistcar robot (Fig. 1c) under varying input frequencies ω show direction reversal as a function of ω, as shown in Fig. 2b. Due to the observed wheel skid, we relax the nonholonomic no-skid constraints in the dynamic model. When the lateral forces are considered using viscous resistance law, i.e. proportional to skid velocities, the model's numerical simulations can explain direction reversal with COM shift, but not with input frequency. When the forces in skid and roll directions are considered using static Coulomb-like law with smoothened sign functions, our model successfully captures the direction reversal due to changing input frequency, as shown in Fig. 2c.

Finally, we constructed a prototype of the RAPS-Twistcar robot, as shown in Fig. 2d. We demonstrated the transition between symmetric straight-line motion and asymmetric arc motion, upon changing the input amplitude, frequency, or links' mass ratio. The experimental observations align with our theoretical model, after generalization to incorporate all links' masses and inertias.

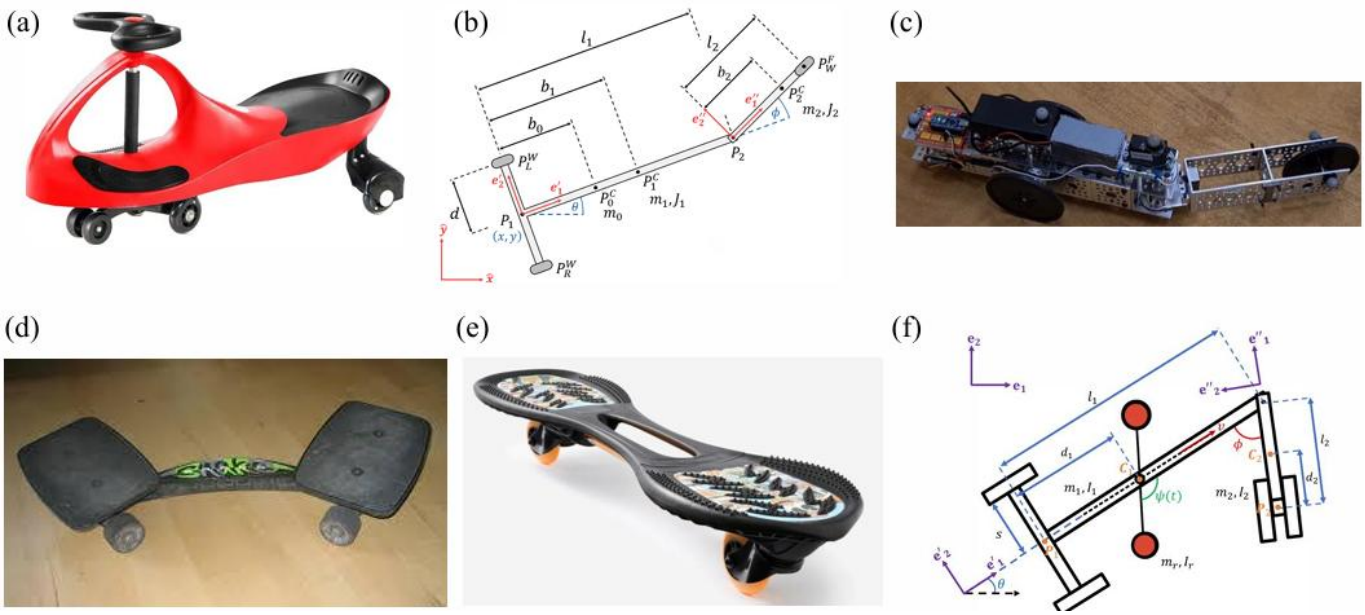

Figure 1: (a) The Twistcar toy. (b) Planar two-link Twistcar model [2,3]. (c) The Twistcar robot [3]. (d) The Snakeboard skating board. (e) The Waveboard skating board. (f) Our RAPS-Twistcar model [5].

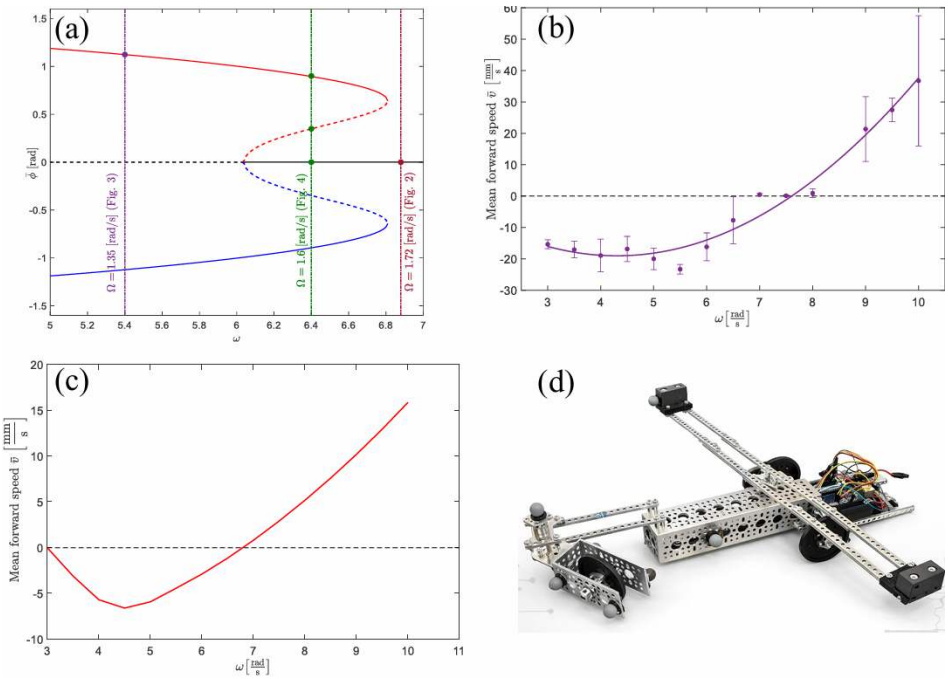

Figure 2: (a) Bifurcations and stability transitions of multiple periodic solutions for the RAPS-Twistcar model [5] - mean value of the steering angle $\bar{\phi}$ as a function of actuation frequency ω. (b) Experimental results of the Twistcar robot's mean forward speed $\bar{v}$ as a function of actuation frequency ω, demonstrating direction reversal of zero-crossing. (c) Simulation results of the skidding Twistcar model using Coulomb-like friction forces, $\bar{v}$ vs. ω, capturing the direction reversal. (d) Our RAPS-Twistcar robot prototype.

REFERENCES

[1] P. S. Krishnaprasad and D. P. Tsakiris, Oscillations, SE(2)-snakes and motion control: A study of the Roller Racer, Dynamical Systems, vol. 16, no. 4, pp. 347–397, 2001.

[2] O. Chakon and Y. Or, Analysis of underactuated dynamic locomotion systems using perturbation expansion: The Twistcar toy example, Journal of Nonlinear Science, vol. 27, no. 4, pp. 1215–1234, 2017.

[3] R. Levy, A. Dantus, Z. Yu, and Y. Or. Analysis and experiments of the dissipative Twistcar-direction reversal and asymptotic approximations. arXiv preprint at https://arxiv.org/abs/2506.19112.

[4] J. Ostrowski, A. Lewis, R. Murray, and J. Burdick. Nonholonomic mechanics and locomotion: the snakeboard example. In Proceedings of the 1994 IEEE International Conference on Robotics and Automation, pages 2391–2397 vol.3, 1994.

[5] A. Zigelman, Z. Yu, R. Levy, and Y. Or, Dynamics and multi-stability of a rotor-actuated Twistcar robot with passive steering joint, Nonlinear Dynamics (accepted 2026), arXiv preprint at https://arxiv.org/abs/2507.04846.

NEURAL DENSITY ESTIMATION FOR THE SYNTHESIS OF CRANK-DRIVEN FOUR-BAR MECHANISMS

Benedict Röder[1], Henrik Ebel[2], Peter Eberhard[1]

[1] Institute of Engineering and Computational Mechanics, University of Stuttgart, Pfaffenwaldring 9, 70569 Stuttgart, Germany, {benedict.roeder@itm.uni-stuttgart.de; peter.eberhard@itm.uni-stuttgart.de}
[2] Department of Mechanical Engineering, LUT University, Yliopistonkatu 34, 53850 Lappeenranta, Finland, {henrik.ebel@lut.fi}

1 INTRODUCTION

Planar parallel mechanisms find widespread application in various engineering domains due to their lightweight design and high-speed capabilities. There is a huge body of literature on the analysis and synthesis of mechanisms, including analytical approaches, optimization-based methods, and, more recently, data-driven techniques, see [1] for a recent review article. The design of four-bar linkages often serves as an early testbed for machine learning-based approaches because they are well-studied mechanisms with a rich history of analytical and optimization-based methods. Data-driven approaches applied to four-bar mechanism design often focus on the inverse problem of identifying mechanism parameters that produce a desired coupler-point path. This mapping is typically complex and multimodal with multiple distinct configurations generating similar paths. Being able to explore the full solution space can be very helpful for design engineers to compare alternative designs that realize nearly identical paths while offering different advantages in terms of performance, robustness, control, spatial requirements, or manufacturability. While previous methods offer sampling of multiple solutions, either via generative adversarial networks, transformer-based architectures, or traversing latent spaces of variational autoencoders, none of them offer direct access to the distribution of suitable mechanism parameters, which is a limitation overcome by this contribution.

In this work, we present a novel approach for synthesizing crank-driven four-bar mechanisms using simulation-based inference (SBI) [2], specifically neural posterior estimation (NPE). This method directly learns the full multimodal posterior distribution of mechanism parameters conditioned on desired coupler paths, enabling systematic exploration of possible solutions and assessment of parameter sensitivity. Finally, we perform a clustering in mechanism parameter space to identify diverse families of feasible mechanism configurations.

2 METHODS

As with most machine-learning approaches, a diverse and balanced dataset is of paramount importance. We therefore start from a publicly available dataset published in [3]. From this dataset, all crank-driven four-bar mechanisms are extracted, resulting in a total of 39274 samples. For each of those samples, the closed coupler-point path is re-evaluated at 0.5-degree increments of the input crank angle, resulting in 720 points on the coupler path. The inherent velocity profile is removed by resampling the coupler point at equidistant locations along the paths. Subsequently, the paths are subjected to a normalization routine to ensure translation-, rotation-, scale-, and reflection-invariance. Finally, the normalized paths are converted to grayscale images of size 64×64 and random Gaussian noise is added to the pixel values during training to counteract overfitting and improve generalization. Additionally, the four-bar linkage lengths are normalized to be ratios of the ground-link length. The normalized link lengths together with the grayscale images of the coupler paths form the training data for the NPE model.

We employ NPE to learn the posterior over four-bar mechanism parameters from grayscale images of coupler paths. The model employs a convolutional neural network (CNN) as an embedding network and neural spline flows (NSF) as conditional density estimators. The CNN extracts meaningful summary statistics from the grayscale images and the NSF learn to approximate the posterior distribution of four-bar mechanism parameters given a desired coupler path image. Both networks are jointly optimized during training using the simulated training pairs $\{(\boldsymbol{\theta}_i, \boldsymbol{x}_i)\}_{i=1}^{N}$, where $\boldsymbol{\theta}_i$ are the normalized four-bar mechanism parameters and $\boldsymbol{x}_i$ are the corresponding grayscale images of the coupler paths. The model is tasked to learn a conditional density to approximate the posterior distribution $q_\phi(\boldsymbol{\theta} \mid \boldsymbol{x}) \approx p(\boldsymbol{\theta} \mid \boldsymbol{x})$, where ϕ denotes the weights of the CNN and the NSF. The model is trained by maximizing the conditional log-likelihood of the simulated parameters under the learned density. After training, the learned density estimator enables efficient posterior inference over four-bar mechanism parameters for arbitrary target coupler path images.

3 RESULTS

A train-test split of 80/20 is employed, resulting in 31419 training samples and 7855 test samples. Training of the model with default hyperparameters typically takes around 10 minutes on a single NVIDIA RTX 4090 GPU. To assess the performance of the trained model, 10000 samples are drawn from the learned posterior distribution for a given test image of a desired coupler path, where each drawn sample represents a parameterization of a four-bar mechanism. For each four-bar mechanism, the coupler-point path is evaluated, normalized, and compared to the desired coupler path using the Chamfer distance as a metric. Of those 10000 four-bar configurations, only the best 25% of samples according to the Chamfer distance were kept for further analysis. The remaining samples are clustered using the *hierarchical density-based spatial clustering of applications with noise* (HDBSCAN) algorithm to identify diverse sets of possible solutions. A pair plot of the link length ratios reveals distinct clusters representing diverse four-bar configurations capable of generating satisfactory coupler paths. Finally, the first two dimensions of the posterior samples are shown in Figure 1a, and the best-performing predictions per cluster are visualized in Figure 1b.

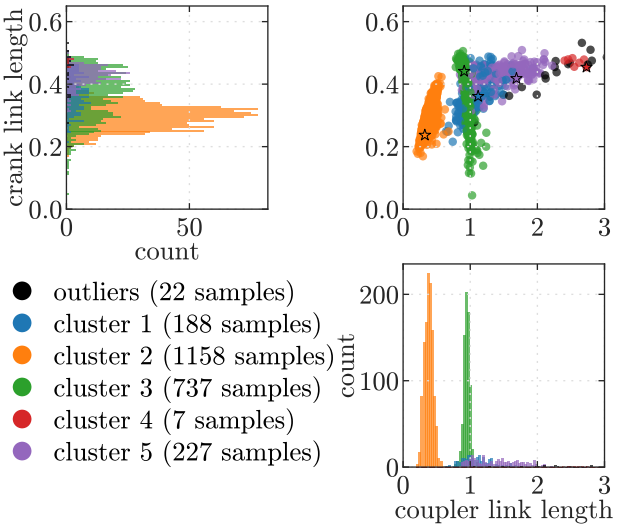

(a) Marginal distribution and pairwise scatter plot of crank- and coupler link lengths of the five-dimensional posterior samples colored by cluster.

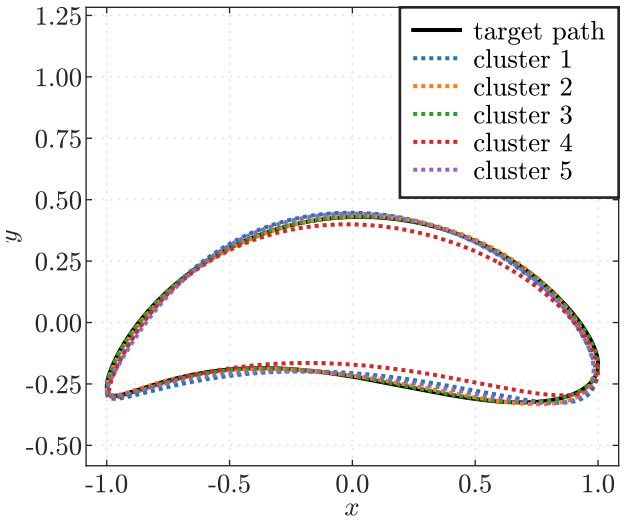

(b) Normalized path predictions of the best sample per cluster which are indicated by stars in the pair plot. The target coupler path is shown in black.

Figure 1: Distributions of the first two dimensions of the posterior samples together with the best path predictions.

4 CONCLUSION

The presented approach demonstrates the potential of neural density estimation for the dimensioning of crank-driven four-bar linkages due to its ability to expose complex multimodal posterior distributions of mechanism parameters. This allows design engineers to directly explore configurations and assess both individual sensitivities and pairwise parameter dependencies. Furthermore, unsupervised clustering of the posterior samples enables the identification of distinct solution sets, facilitating informed decision-making in mechanism design. The incorporation of an arbitrary embedding network makes the presented approach suitable for the dimensioning of more complex systems with multiple degrees of freedom as well. For the more challenging type-synthesis problem, training multiple models for each mechanism type individually could be viable, as training times were comparatively low.

ACKNOWLEDGMENTS

This work was supported by the Deutsche Forschungsgemeinschaft (DFG, German Research Foundation) under Grants 501890093 (SPP 2353, Coordination) and 501840485 (SPP 2353, Data- and Response-Surface-Driven Design Assistant for Controlled Flexible Multibody Systems). This support is highly appreciated.

REFERENCES

[1] A. Purwar and Q. J. Ge, “Advancements in kinematic synthesis: data-driven methods for mechanism design”. *Journal of Computing and Information Science in Engineering*, vol. 25, no. 12, 2025.

[2] J. Boelts, M. Deistler, M. Gloeckler, et al., “sbi reloaded: a toolkit for simulation-based inference workflows”. *Journal of Open Source Software*, vol. 10, no. 108, 2025.

[3] A. Nurizada, R. Dhaipule, Z. Lyu, and A. Purwar, “A dataset of 3M single-DOF planar 4-, 6-, and 8-bar linkage mechanisms with open and closed coupler curves for machine learning-driven path synthesis,” *Journal of Mechanical Design*, vol. 147, no. 4, 2024.

DYNAMIC ENERGY-OPTIMAL ANCHOR CONFIGURATION ON GENERAL CONVEX SURFACES, ENABLED BY GEODESIC-BASED FORCE-CONSISTENT MODELING

Lei Jin[1], Maitha AlQaydi[1], Mohamed Abduljawad[2], Yahya Mohammed[2], Ahmed AlAttar[2], Tarek Taha[2], Dongming Gan[1]

[1] Purdue University, School of Engineering Technology, West Lafayette, IN, USA
[2] Dubai Future Foundation, Dubai, United Arab Emirates
{jin209@purdue.edu; malqaydi@purdue.edu; dgan@purdue.edu}

1 INTRODUCTION

Cable-driven parallel robots (CDPRs) offer lightweight and reconfigurable solutions for large-scale surface operations[1], but their modeling becomes challenging on curved architectural surfaces where cables follow surface geodesics rather than straight lines. Cable directions vary with the end-effector position, directly affecting force equilibrium and tension feasibility and invalidating conventional planar assumptions. Although geodesic computation is well studied, existing methods mainly focus on shortest-path distances and do not provide the stable, force-consistent local cable directions required for CDPR static and dynamic analysis. In addition, the strong coupling between surface geometry, cable routing, and anchor placement makes configuration search significantly more complex, limiting the practical use of geodesic-based CDPR modeling and optimization on curved surfaces[2].

The main contributions of this work are: (1) a unified geodesic-to-force pipeline that extracts a stable and force-consistent cable direction at the end-effector by averaging the projected directions of the first k geodesic vertices; (2) a coarse-to-fine anchor refinement strategy that enables efficient large-scale configuration search.

We developed a generalized mesh-based method, and for the Dubai Metro station case we further constructed an analytical model for reference and comparison. This work is based on the cross-validation between the 3D mesh model of the Dubai Metro station, as shown in Fig. 1(a) and (b), and its corresponding analytical representation.

2 GEODESIC-TO-FORCE DIRECTION EXTRACTION AT THE END-EFFECTOR

For each EE(end-effector) location in the workspace, the geodesics of the cables connecting the EE to the anchors are calculated and used to define the local cable directions as in Fig. 1 (b). These directions are expressed in the EE tangent plane, whose unit vector $\mathbf{v}$ is determined by projecting the global upward direction onto the tangent plane, allowing subsequent force equilibrium and tension optimization.

The local force vector is defined as $\boldsymbol{\alpha} = \frac{1}{k}\sum_{i=1}^{k}(\mathbf{v}_i - \mathbf{v}_{i-1})$, where $\mathbf{v}_k$ denote the vertices of the first k geodesic segments of the geodesics returned by Potpourri3D. This local average suppresses numerical noise and small surface irregularities, yielding a robust and repeatable direction estimate consistent with the underlying surface geometry. The resulting direction $\boldsymbol{\theta}$ is then expressed in the local tangent basis $(\mathbf{u}, \mathbf{v})$ as $\boldsymbol{\theta} = \text{atan2}(\boldsymbol{\alpha}\cdot\mathbf{v}, \boldsymbol{\alpha}\cdot\mathbf{u})$.

(a) Dubai Metro station

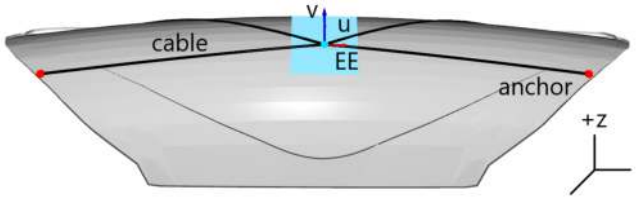

(b) 3D model of Dubai Metro Station

Figure 1: Example of curved surface structure and its 3D model.

3 STATIC FORCE DIFFERENCE ANALYSIS

On both 3D model and the analytical model, linear programming is used to calculate the local forces along 4 cables at each location in the workspace defined by $x \in [-140, 140]$ and $y \in [-25, 25]$. The difference of the highest tension

among 4 cables is calculated to illustrate how well the analytical model fits the 3D model. The results in Fig. 2 show that the force difference at more than 91.1% of the workspace points remains below 2 N. This indicates that the cross-comparison of the 3D model of the Dubai Metro station and its analytical model is valid.

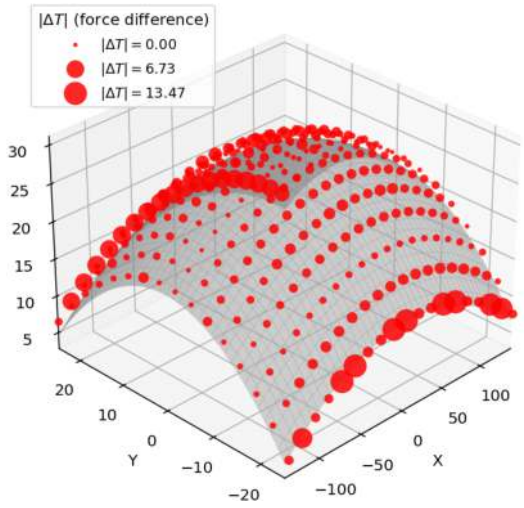

(a) Force difference on analytical model.

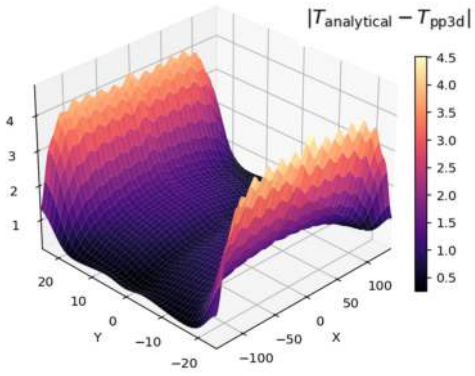

(b) Force difference shown in surf plot.

Figure 2: Diagram of local maximum force difference shown in: (a) 3D analytical model view, and (b) surf plot.

4 ENERGY OPTIMIZED CONFIGURATION THROUGH COARSE-TO-FINE SEARCHING METHOD

In the same workspace, to find the optimal set of anchors with the lowest energy consumption on a certain path, a coarse-to-fine anchor refinement method is used to reduce global exhaustive search time on a sinusoidal path. This search method starts with a coarse search with large steps in both x- and y-axis, and then follows by a refined search with small steps just around the optimal set of anchor found by coarse search. In this work, a large-step of the coarse search $x_{\text{step}} = 70$, $y_{\text{step}} = 12.5$ identifies the optimal set located in $(-140, -25)$, $(-140, 25)$, $(140, -25)$, and $(140, 25)$ in Fig. 3. Both the mesh-based surface and the analytical model fall into the same configuration right at the corners of the workspace. Then the local refinement search within a ± 2 neighborhood shows that, for the analytical model, the refinement converges to anchor locations in $(-138, -27)$, $(-138, 27)$, $(138, -27)$, and $(138, 27)$, and for the mesh-based surface, the refined solution is found in $(-140, -27)$, $(-139, 25)$, $(140, -27)$, and $(138, 25)$.

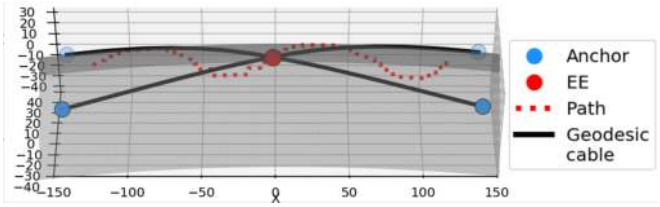

(a) 3D view.

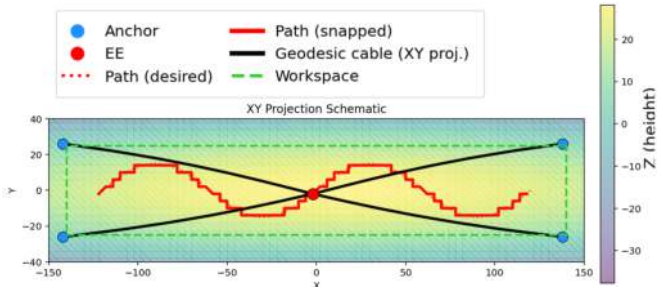

(b) Top-down 2D view.

Figure 3: Optimal anchor configuration of large step search plot from: (a) 3D view. (b) Top-down 2D view..

5 CONCLUSIONS

This work demonstrates that force-consistent geodesic modeling enables accurate static force prediction and efficient energy-optimal anchor configuration for cable-driven parallel robots operating on general convex surfaces.

REFERENCES

[1] A. Pott, *Cable-Driven Parallel Robots: Theory and Application*, Springer, Berlin, Germany, 2018.

[2] H.H. Cheng, D. Lau, and J. Hughes, "Determining Feasible Cable Attachment Locations for Cable-Driven-Parallel Robot", in *CableCon 2025*, MMS 182, pp. 261–273, Springer Nature Switzerland AG, 2025, doi:10.1007/978-3-031-94608-0_21.

CHAINED BEAM CONSTRAINT MODEL FOR CONTACT MODELING (CBCM-CT): USING CONTACT-POSITION AS UNDETERMINED COEFFICIENT

Chengcheng Sun[1], Jiaqiang Yao[2], Ruiyu Bai[2], Haoyu Zhang[2], Guimin Chen[2]

[1] Xidian University, Xi'an, Shaanxi, 710071, China, {1379342758@qq.com}

[2] Xi'an Jiaotong University, Xi'an, Shaanxi, 710049, China, {jqyao@xjtu.edu.cn; ruiyubai@xjtu.edu.cn; kiyama@stu.xjtu.edu.cn; guimin.chen@xjtu.edu.cn}

1. INTRODUCTION

Compliant mechanisms (CMs) have attracted increasing attention due to their inherent advantages over rigid mechanisms, including high repeatability, reduced wear, and backlash. They often undergo large and nonlinear deflections, which makes modeling their kinetostatic performances very challenging, especially when contact with external objects is involved. Nonlinear finite element models (FEMs) are widely used to analyze contact problems under both small and large deflections, but their accuracy strongly depends on mesh quality, and convergence issues often arise in large-deflection contact scenarios. Moreover, the high computational cost and lack of explicit analytical force-displacement relationships limit the suitability for design-oriented analysis. To bridge this gap, numerous analytical and numerical models have been developed to describe the nonlinear behavior of flexible systems, including the chained pseudo-rigid-body model (CPRBM), the Cosserat rod model, and discrete differential geometry-based approaches. Among these, CPRBM is an effective method for analyzing beam contact under large deflections by introducing boundary constraints and minimizing total system energy. Nevertheless, the inherent assumption of concentrated compliance limits its ability to fully capture geometric nonlinearity. In addition, most discretization-based approaches rely on predefined beam segmentations with fixed lengths, preventing accurate determination of the exact geometric contact location when contact occurs within an element rather than at discrete nodes. To overcome this limitation, this work proposes a general method for modeling compliant mechanisms involving contact based on the chained-beam-constraint model [1, 2] (CBCM-CT in short hereafter). CBCM-CT treats the position of the contact point on a compliant beam as an undetermined coefficient, from which the beam is split into two segments, each described using CBCM. By applying appropriate geometric constraints at the contact point S: $f'(X_S) - \tan\theta_S = 0$; $Y_S - f(X_S) = 0$; $P_{CF} + F_{CF}\tan\theta_S = 0$; the CBCM equations become solvable, providing a closed-form solution for large-deflection beams with contact interactions. The feasibility and robustness of the proposed approach are demonstrated through comprehensive comparisons with finite element simulations and experimental measurements across multiple contact scenarios, including its application to an adaptive fin-ray-inspired robotic finger. The results confirm the robustness of the proposed model and its superior accuracy-efficiency trade-off compared with conventional finite element workflows and energy-minimization methods.

2. RESULTS AND CONCLUSIONS

2.1. CBCM for contact modeling

Without loss of generality, we consider a flexible beam in contact with a rigid object whose surface is described by a convex geometry profile $f(x)$. This study focuses on the large-deflection behavior of beams in contact with the rigid object and neglects friction and contact stress distribution. As shown in Fig. 1(a), a cantilever beam of length L is fixed at the origin of the global coordinate system O-XY. A rigid object moves vertically into contact, and the actual contact point slides along the deformed centerline as deformation progresses. To describe the evolving contact consistently, a virtual contact point $S = [X_S, Y_S]^T$ is introduced, dividing the beam into two segments with unknown lengths L_a and L_b, satisfying $L_a + L_b = L$. In the deformed configuration, the initial contact point S_0 maps to the actual contact point S. The distal end is denoted as point D. Each segment is subjected to an axial force P, transverse force F, and bending moment M, producing end displacements X, Y, and rotation θ, with subscripts distinguishing the two segments. Using CBCM theory, force-deflection relationships are established for both segments. The contact force at point S, denoted as $CF_1 = [P_{CF1}, F_{CF1}]^T$, together with the unknown length L_a, requires three boundary constraints for a closed-form solution: 1) The coordinates of point S on the flexible beam and the rigid object must coincide; 2) The tangent direction of the beam segment OS at point S is constrained to have the same slope as the rigid surface at this point; 3) The resultant contact force at point S must act normal to the tangent of beam segment OS and be oriented toward the beam. Beyond the single beam-rigid object contact case, rigid components are often introduced into CMs to achieve variable stiffness characteristics, leading to prescribed positional constraints in the system. To further demonstrate the feasibility of the model under more complex contact conditions, a limit block is introduced, as shown in Fig. 1(b), and the associated constraints are formulated through geometric conditions at point C. Both contact scenarios are solved as closed-form nonlinear systems

using the *fsolve* function in MATLAB. Fig. 1(c) compares the deformed profiles predicted by the conventional FEM and the proposed model, along with the experimentally measured beam-tip positions. Good agreement is observed between the two numerical approaches, while the beam-tip coordinates predicted by the proposed model closely match the experimental results. The maximum absolute and relative errors are below 0.36 mm and 2.25%, respectively. In terms of efficiency, the proposed model requires only 0.09 and 0.28 s for the two scenarios, compared to 12 s and 13 s for the conventional FEM. These results demonstrate that the proposed model achieves a significantly improved accuracy-efficiency trade-off over conventional pre-meshed FEM approaches.

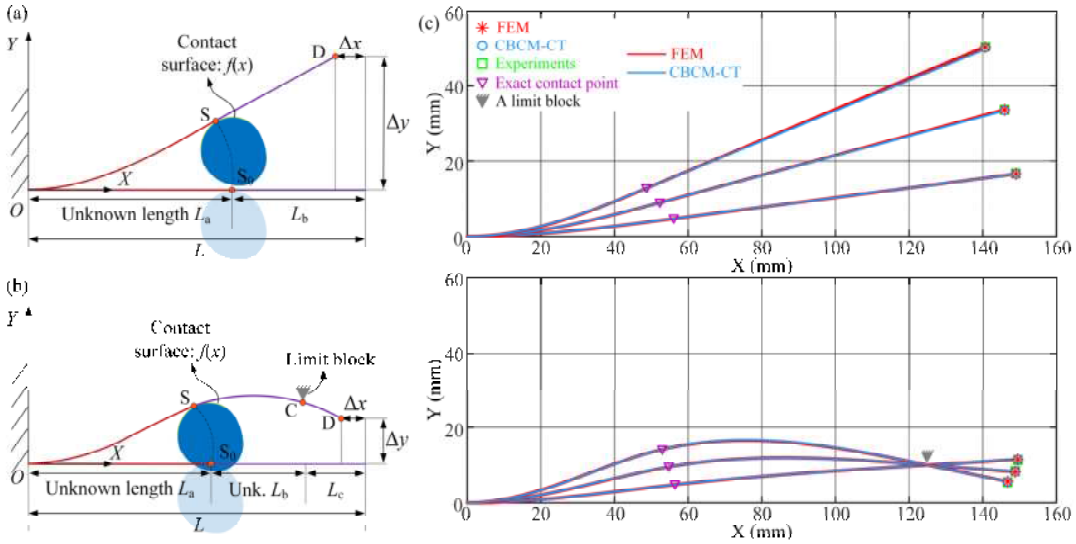

Figure 1. Large-deflection beams in two different contact scenarios.

2.2. Modeling contact of FRE finger

The proposed modeling framework is further applied to contact analysis of CMs through applicatoin to a fin-ray effect (FRE) finger, a passively actuated soft robotic finger inspired by fish-fin biomimetics. This type of finger eliminates the need for embedded actuators and achieves automatic shape adaptation through passive interaction with the grasped object. As shown in Fig. 2(a), the finger deforms passively under external load and can be modeled as a fully CM composed of multiple flexible beams. Based on the single-beam contact scenario in Section 2.1, the force-deflection relationship of the contacting beam is established, while the remaining beams are modeled using the CBCM framework. By incorporating geometric constraints and static equilibrium at the finger nodes, a closed-form kinetostatic model of the finger is derived. The predicted deformed contours and reaction forces during contact with a rigid object are validated experimentally, as shown in Fig. 2(b). In addition, the reaction forces are compared with those obtained using energy-minimization methods [3]. The results indicate that the proposed model maintains comparable accuracy while improving computational efficiency by 77.67%.

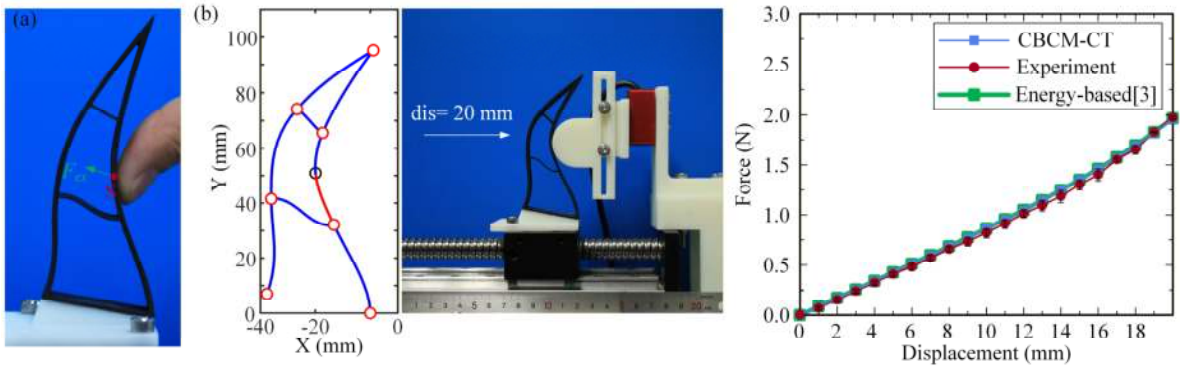

Figure 2. FRE finger and the experimental validation of the kinetostatic model.

ACKNOWLEDGMENTS

The authors gratefully acknowledge the financial support of the National Natural Science Foundation of China under grant nos. 52505037 and 52305034 and the Postdoctoral Research Project of Shaanxi Province under grant no. 31271000000092.

REFERENCES

[1] F. Ma and G. Chen, “Modeling large planar deflections of flexible beams in compliant mechanisms using chained beam-constraint model”. *Journal of Mechanisms and Robots*, 8 (2), 021018, 2016.

[2] G. Chen, F. Ma, G. Hao and W. Zhu, “Modeling large deflections of initially curved beams in compliant mechanisms using chained beam constraint model”. *Journal of Mechanisms and Robots*, 11 (1), 011002, 2019.

[3] J. Yao, Y. Fang, X. Yang, P. Wang and L. Li, “Design optimization of soft robotic fingers biologically inspired by the fin ray effect with intrinsic force sensing”. *Mechanism and Machine Theory*, 191, 105472, 2024.

OPTIMIZING THE CRUISING SPEED FOR TRAINS IN A METRO-BASED UNDERGROUND LOGISTICS SYSTEM USING MULTIBODY DYNAMICS AND MULTI-OBJECTIVE ALGORITHMS

Duo Zhang[1], Gisella Tomasini[1], Yuan-Peng He[2], Fang-Ru Zhou[1], Zi-Yu Tao[3]

[1] Department of Mechanical Engineering, Politecnico di Milano, Milan, Italy {duo.zhang@polimi.it; gisella.tomasini@polimi.it; fangru.zhou@mail.polimi.it }

[2] School of Mechanical Engineering, Southwest Jiaotong University, Chengdu, People's Republic of China { he.yuanpeng@outlook.sg}

[3] School of Mechanical and Electrical Engineering, Guangzhou University, Guangzhou, People's Republic of China { ziyu.tao@gzhu.edu.cn}

1. INTRODUCTION

Urban logistics has become a critical bottleneck for sustainable urban development, characterized by a triad of interconnected challenges: traffic congestion, environmental degradation, and energy inefficiency. In response to these challenges, attention has turned to underground space as a potential solution, leading to the concept of the underground logistics system (ULS). Metro systems, known for their efficiency and environmental benefits, often have surplus capacity during off-peak hours. Thus, the metro-based ULS, has emerged as a viable and effective approach to mitigating urban logistics issues.

Unlike passengers, cargo's characteristics, e.g. size, density, and center of gravity, are highly variable. In particular, cargo distribution changes with loading and unloading at each station, whereas passengers tend to distribute uniformly within the vehicle to maximize personal space and minimize physical contact with others. Since vehicle-cargo interaction significantly affects wheel-rail contact forces, the influence of load characteristics on metro vehicle performance under various running conditions warrants detailed investigation based on multibody dynamics. Consequently, the operation of metro-based ULS should incorporate these effects to enhance both running safety and energy efficiency.

2. METHODOLOGY

This study considers a B-type metro vehicle, commonly used in metro systems. As illustrated in Fig.1, the vehicle consists of one loaded carbody, two sideframes, and four wheelsets. The cargo shifts the carbody's center of gravity from point O (empty) to point C (loaded). An multibody dynamics (MBD) model of the metro vehicle which takes the vehicle-cargo interaction into consideration is constructed as shown in Fig. 2. The cargo is modeled as a cuboid with uneven horizontal mass distribution.

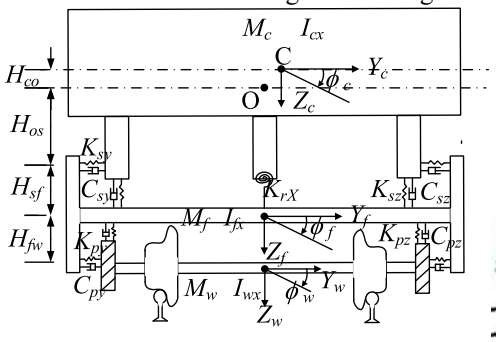

Figure 1. The model of the loaded vehicle.

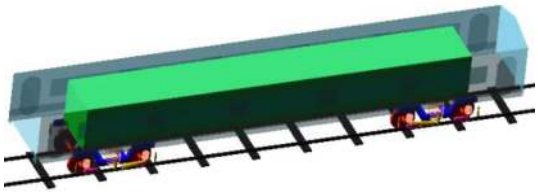

Figure 2. The MBD model of the loaded vehicle.

3. RESULTS AND ANALYSIS

The radius of curved tracks (denoted by R) and cruising speed of the metro vehicle (denoted by v) are two parameters which can represent the running conditions. Loading conditions for a metro vehicle are defined by the quantity of the cargoes (denoted by the height of the cargo model h) and the loading offset (denoted by x and y). The wheel unloading rate (UN) is adopted as the safety index [1], and the energy efficiency is evaluated through the value of energy consumed by motion resistances (ECMR) [2]. The MBD simulation results are illustrated in Fig.3.

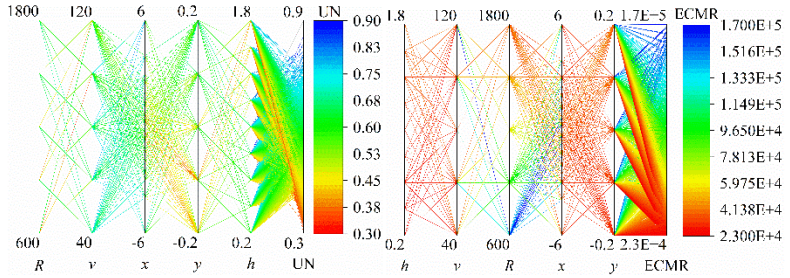

(a) (b)

Figure 3. Effects of working conditions on the running performance of vehicles: (a) running safety, and (b) energy efficiency.

Although Fig.3 provides intuitive insights into the role of each variable in vehicle performance, it remains necessary to develop precise surrogate models for predicting these indices under arbitrary conditions. The Random Forest (RF) algorithm was selected for regression due to its ability to model complex, non-linear relationships without extensive data preprocessing.

4. OPTIMIZATION OF THE CRUISING SPEED

A metro section contains multiple segments based on the consistency of loading and track characteristics, as illustrated in Fig. 4. The decision variables of the optimization model comprise the cruising speeds assigned to the predefined segments of the metro section. Two objectives are considered in this model: one is maximizing the comprehensive running safety of the section, and the other is minimizing the total energy consumption of the section. For each segment, the UN or ECMR can be predicted by the established surrogate model as a function of corresponding track and loading parameters. To ensure compliance with the safety threshold in each segment, the overall running safety of the metro section is evaluated by the maximum UN value observed across all segments.

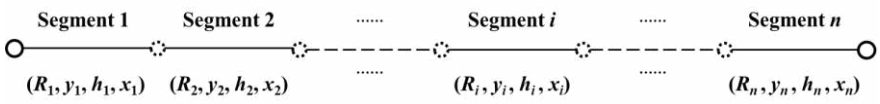

Figure 4. Schematic diagram of a metro section.

For given segments with respective track and loading conditions, the optimized cruising speeds for different segments is revealed in Fig. 5. Five benchmark scenarios with uniform cruising speeds (i.e., v=40, 60, 80, 100, 120 km/h) throughout all segments are also included for comparative analysis. The comparison shown in Fig.5 indicates that the optimization of cruising speeds in response to track and loading conditions can effectively improve the running safety and energy efficiency of metro-based ULS.

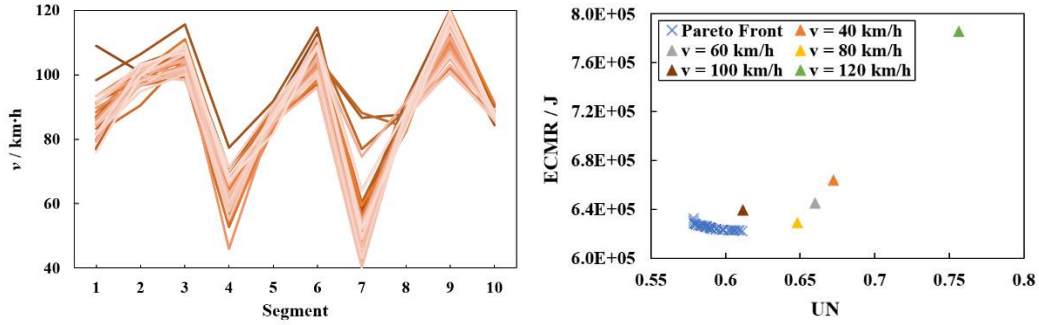

(a) (b)

Figure 5. Optimization results: (a) pareto optimal values, and (b) pareto front of the cruising speeds for different segments.

5. CONCLUSIONS

Taking into account the variation in the carbody's mass properties due to cargo loading, the dynamic equations of the loaded carbody are derived to construct the MBD model of a B-type metro vehicle. The MBD simulation results demonstrate the complex and nonlinear relationship between working conditions and metro vehicle running performance. On this base, a surrogate model is developed using the RF algorithm to predict vehicle performance under arbitrary conditions for the following bi-objective optimization of cruising speed. Compared to a uniform speed profile, the proposed optimization strategy can reduce the maximum wheel unloading ratio by up to 23.57% and ECMR by up to 20.84%.

ACKNOWLEDGMENTS

The authors would like to appreciate the funding supported by European Union's Horizon Europe Program for Marie Skłodowska-Curie Actions under Grant TEESFtrain [grant number 101198179].

REFERENCES

[1] D. Zhang, D.B. Clarke, Q. Peng, H. Gao, C. Dong, "Effect of the combined centre of gravity on the running safety of freight wagons", *Vehicle Syst Dyn*, 57(9), 1271-1286, 2019.

[2] D. Zhang, Y. Tang, Q. Peng, "A novel approach for decreasing driving energy consumption during coasting and cruise for the railway vehicle", *Energy*, 263, 125615, 2023.

DISPLACEMENTS ANALYSIS OF THE MIURA-ORI PATTERN WITH DOUBLE-HINGE THICKNESS ACCOMMODATION

Enrique Pujada Gamarra[1,2], Lena Zentner[1], Daniel Lavayen Farfan[2], Jorge A. Rodriguez Hernández[2]

[1] Technische Universität Ilmenau, Germany {enrique.pujada-gamarra@tu-ilmenau.de; lena.zentner@tu-ilmenau.de}
[2] Pontificia Universidad Católica del Perú, Perú, {epujadag@pucp.edu.pe; dlavayen@pucp.edu.pe; crodrig@pucp.edu.pe}

1 INTRODUCTION

Origami enables complex three-dimensional configurations from flat sheets and has inspired engineering applications such as deployable solar arrays [1] and foldable solar panels [2]. These applications require thick and stiff materials, which introduce geometric interferences and additional displacements that may compromise motion preservation [3, 4]. To address these issues, Lang [5] classified thickness-accommodation techniques, among which the double-hinge technique enables a fully flat folded configuration. Building on previous degree-4 vertex analyses, this work extends the investigation to the characterization of a full Miura-ori pattern.

2 THEORETICAL APPROACH

The double-hinge technique was introduced by Hoberman [6] and later discussed by Lang [5] for its flat-folding capability and moderate design complexity, though requiring additional constraints for kinematic consistency. Using Lang's nomenclature [7], Pujada [4] analyzed the technique at the level of a Miura-ori degree-4 vertex [8], accounting for material thickness and stiffness. Building on this work, a theoretical framework is proposed to characterize a full Miura-ori pattern, focusing on the three cases identified by Pujada [4].

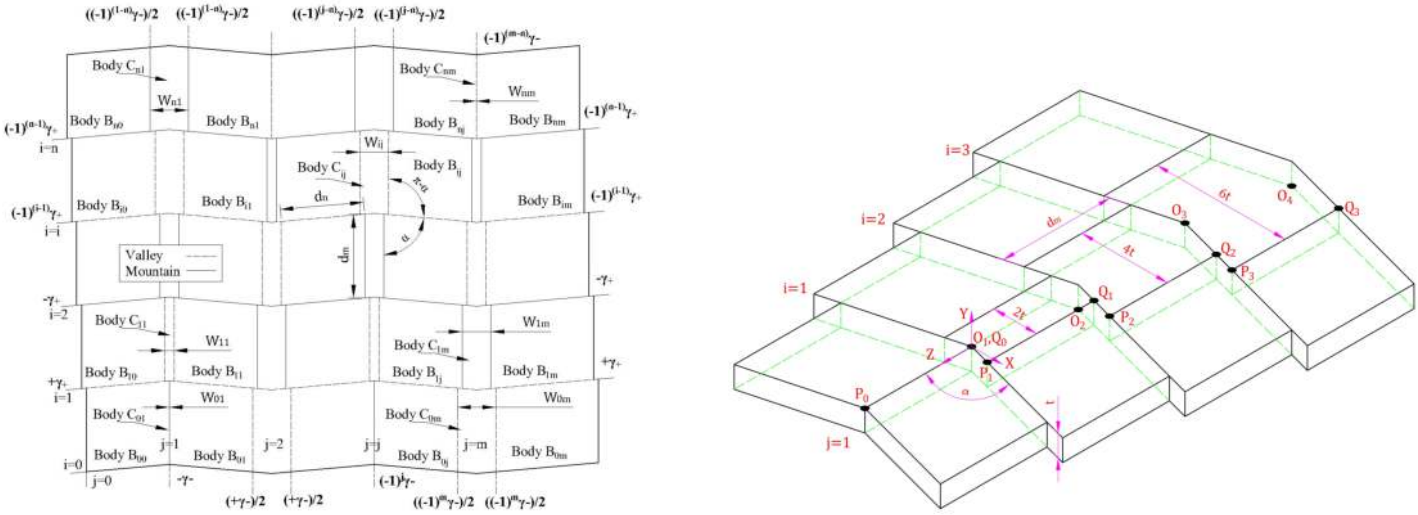

Figure 1: Left: Miura-ori double-hinge pattern in an $i \times j$ configuration. Rigth: The isometric model 3×1.

3 METHODS

Using the same theoretical nomenclature, this study extends Pujada's methodology to the full Miura-ori pattern [4], considering three cases with released joint pairs. Degrees of freedom are evaluated using Kutzbach's criterion with all joints modeled as revolute, and redundant constraints are removed due to the dependence of γ_+ and γ_- on β. Based on the feasible cases and their degrees of freedom, displacements are analyzed according to the released axes.

$$nDOF = 6(n_b-1)-n_c-n_r = 6(n_b-1)-5(Rev_{J_\beta}+Rev_{J_{\gamma_-}}+Rev_{J_{\gamma_+}}-Red_J)-(Rev_{J_\beta}-1+Rev_{J_{\gamma_-}}+Rev_{J_{\gamma_+}}-Red_J) \quad (1)$$

In the considered origami pattern, n and m denote the numbers of rows and columns, respectively, Fig. 1(a). These parameters define the configuration and the number of bodies and revolute joints: $n_b = 2nm+2m+n+1$, $Rev_{J_\beta} = nm$, $Rev_{J_{\gamma_-}} = 2m(n+1)$, and $Rev_{J_{\gamma_+}} = n(m+1)$. The resulting degrees of freedom are summarized in Table 1.

Cases	Releasing Axes	Reduction Red_J	$nDOF$	D4-Vertex	Pattern Periodicity $n \times 1$	$1 \times m$	$n \times m$	Notes
A	Lower γ_-	$2nm$	1	No	No	No	No	Early-stage folding interference
B	Upper γ_-	$2nm$	1	Yes	Yes	Yes	Yes	No restrictions
C	γ_+	$n(m+1)$	$6n(1-m)+1$	Yes	Yes	No	No	Only $i \times 1$. Over constrained $m > 1$

Table 1: Periodicity and degree-of-freedom analysis for the three cases

4 RESULTS

After developing the Miura-ori model, only cases B and C are feasible. The analysis is generalized to an $i \times j$ pattern, with folded-state displacements summarized in Table 1. In case B, aligned and parallel displacements increase with i, whereas in case C the aligned displacement is independent of i and the parallel remains limited by compensation effects.

Table 2: Displacements in Folded Status

Case	Released axes	Aligned displac. relevant to released axes γ	Parallel displac. relevant to released axes γ
B	$(+\gamma_-)/2$	$2t \sin\alpha \cos\alpha \sum_{i=1}^{n} \frac{(1-(-1)^i)}{2}$	$2t[i - \cos^2\alpha \sum_{i=1}^{n} \frac{(1-(-1)^i)}{2}] + t\frac{(1+(-1)^i)}{2}$
C	γ_+	$2t \sin\alpha$	$2t \cos\alpha \sum_{i=1}^{n} (i-1)(-1)^i$

5 CONCLUSIONS

The double-hinge technique is feasible for the Miura-ori pattern; however, only two solutions exist. In case B, displacement accumulation increases with the period, potentially leading to manufacturing challenges and interference during final folding stages. In contrast, case C is weakly influenced by the period, making it more practical, although limited to a single-column ($i \times 1$) configuration. An example is the double-hinge foldable solar panel by Pujada [2].

REFERENCES

[1] E. Landau, "Solar power, origami-style," 8 2014. [Online]. Available: https://www.jpl.nasa.gov/news/solar-power-origami-style

[2] E. Pujada-Gamarra, D. Lavayen-Farfán, D. Olivera-Oliva, and J. Rodríguez-Hernández, "Origami-inspired photovoltaic modules-development of eco-2 friendly solutions for naval and mining operations † 3," in *III International Congress: Technology and Innovation in Engineering and Computing*, 2025.

[3] M. Trautz and A. Kunstler, "Deployable folded plate structures-folding patterns based on 4-fold-mechanism using stiff plates," in *International Association for Shell and Spatial Structures (IASS). Evolution and Trends in Design, Analysis and Construction of Shell and Spatial Structures*, A. D. Cabo and C. M. L. Fernández, Eds. Editorial Universitat Politècnica de València, 2 2010, pp. 2306–2317.

[4] E. Pujada-Gamarra, L. Zentner, D. Lavayen-Farfán, and J. A. Rodriguez-Hernandez, "Analysis of the relative displacements in a thick origami with double-hinge technique for thickness accommodation," *Mechanism and Machine Theory*, vol. 210, p. 106000, 2025.

[5] R. J. Lang, K. A. Tolman, E. B. Crampton, S. P. Magleby, and L. L. Howell, "A review of thickness-accommodation techniques in origami-inspired engineering," *Applied Mechanics Reviews*, vol. 70, 1 2018.

[6] C. Hoberman, "Reversibly expandable structures," 1 1991.

[7] R. J. Lang, *Twists, Tilings and Tessellations. Mathematical Methods for Geometric Origami.* CRC Press, 2018.

[8] K. Miura, "Method of packaging and deployment of large membranes in space," in *31st Congress of the International Astronautical Federation (IAF- 80-A 31)*, vol. 618. The Institute of Space and Astronautical Science, 11 1985, p. 9.

SOFT JOINT–CONTACT COUPLED THEORETICAL MODEL FOR LARGE-DEFORMATION THICK-PANEL SQUARE-TWIST ORIGAMI

Haoqian Wang[1,2], Haibo Qu[1], Nikos D. Lagaros[2], Sheng Guo[1]

[1] Robotics Institute, School of Mechanical, Electronic and Control Engineering, Beijing Jiaotong University, Beijing 100044, China, {22110398@bjtu.edu.cn; hbqu@bjtu.edu.cn; shguo@bjtu.edu.cn}

[2] Institute of Structural Analysis and Antiseismic Research, School of Civil Engineering, Zografou Campus, National Technical University of Athens, Athens 15780, Greece, {nlagaros@central.ntua.gr}

1. INTRODUCTION

Square-twist origami units and their tessellations are widely used in deployable structures and programmable mechanical metamaterials. This is due to their strong geometric nonlinearity, multistability, self-locking capability, and high design flexibility. In our previous work, Square-twist origami metamaterials with soft joints (also termed flexible creases in origami literature) were mainly studied using finite-element analysis (FEA) [1]. These studies focused on tensile behavior, chirality effects, and parametric influences. Although accurate, FEA is computationally expensive for large parameter sweeps, contact-dominated problems, and rapid design iterations. Moreover, mechanism-level phenomena, such as folding-path selection and energy-barrier crossing, are difficult to interpret without low-order theoretical models.

In practical applications, thick-panel origami is unavoidable. Finite panel thickness introduces geometric offsets, interference, and self-contact. Consequently, rigid-origami assumptions with idealized hinges are insufficient. They cannot capture thickness-induced self-locking, rotation–extension coupling of soft joints, or stability transitions under large deformations. Our previous studies showed that a "rigid panels + soft joints" construction enables manufacturable thick-panel Square-twist origami structures [2]. However, predicting the full folding–self-locking–unfolding process at low computational cost remains challenging. This requires a unified treatment of soft-joint mechanics and global self-contact [3].

To address this issue, this paper presents a theoretical / low-order numerical model for thick-panel Square-twist origami with soft joints. A bar-and-hinge framework represents the equivalent stiffness of soft joints. Global panel contact is introduced through a potential-energy extremum formulation. An energy-consistent contact force–stiffness model is adopted. Triangle-to-triangle minimum-distance computation is employed to improve non-penetration robustness and capture self-locking behavior.

2. CONTACT-COUPLED THEORETICAL MODEL

2.1. Unified Potential-Energy Framework

The structure is discretized as "rigid panels + crease hinge lines + equivalent springs for soft joints." The total potential energy is written as:

$$\Pi(x) = \Pi_{bar}(x) + \Pi_{hinge}(x) + \Pi_{contact}(x) - W_{ext}(x) \tag{1}$$

where Π_{bar}, Π_{hinge}, and $\Pi_{contact}$ denote the bar, hinge, and contact energies, respectively; W_{ext} is the external work and x is the nodal displacement vector. Static equilibrium satisfies:

$$\Delta_x \Pi = 0 \tag{2}$$

and can be solved via Newton–Raphson iterations. lobal contact is treated using an energy-based strategy consisting of a conservative contact force field, a contact potential, and the corresponding consistent internal force and tangent stiffness. When the contact distance $d < d_0$, the internal force and stiffness tend to infinity, thereby suppressing penetration.

2.2. Soft Joints Modeling

To address the key issue in thick-panel origami that "creases are not ideal hinges," we introduce a flexible equivalent model for the crease region. The crease is treated as a locally deformable zone with finite width and material compliance (e.g., TPU soft joints), whose macroscopic effect is represented by an equivalent rotational spring or coupled springs assembled within the bar-and-hinge formulation, thereby retaining high efficiency for large deformations and multistability. This concept aligns with bar-and-hinge extensions for compliant creases: the crease is no longer characterized solely by a fold-angle degree of freedom, but

instead captures nonlinear responses and energy storage of soft joints, enabling the study of energy barriers between stable states within a unified framework.

For large-rotation folding of the square-twist origami unit, soft-joint stiffness parameters are calibrated by inverse identification using force–displacement or energy–displacement curves from prior metamaterial FEA. Using a limited set of key-path FEA data points, the equivalent crease parameters are determined to match the folding path, contact triggering point, and stiffness jumps, converting high-cost FEA-based pattern discovery into low-cost theoretical rapid prediction.

2.3. Contact Distance Computation And Self-Locking Robustness

To robustly simulate self-contact and self-locking in thick-panel Square-twist origami with soft joints, we adopt an energy-based contact formulation and assemble its consistent internal force and tangent stiffness into the Newton iterations. When the geometric gap $d < d_0$, the contact potential is activated to prevent penetration. In this work, d is taken as the triangle-to-triangle minimum distance (T2T) to improve robustness for edge-to-edge near-contact and contact detection under coarse meshes (the T2T distance is implemented using an existing analytical algorithm). Together with the folding topology of Square-twist origami, we construct candidate contact pairs, perform a coarse screening followed by accurate distance evaluation, thereby reducing contact detection cost while preserving the ability to capture self-locking. This module also helps explain the contact-triggering points and stiffness jumps observed in our previous full-process FEA.

2.4. Dynamic Extension

When barrier crossing (snap-through) or load–unload path dependence must be captured, we introduce a simplified dynamics extension within the same potential-energy framework:

$$M\ddot{x}+C\dot{x}+\nabla_x \Pi(x) = f_{ext} \tag{3}$$

where M is a lumped nodal mass matrix and C is Rayleigh damping or equivalent viscous damping. The goal is not to replace explicit-dynamics FEA, but to capture—at very low cost—the process of "crossing an energy barrier and converging to a stable folded state under contact constraints," providing mechanistic interpretation and rapid reproduction of FEA results.

As shown in Figure 1, part (a) presents the finite-element results, including the strain-energy curve and Mises stress distribution state, while part (b) shows the corresponding theoretical predictions, including the strain-energy curve and selected folding snapshots; the inset reports the reaction force of an outer-corner node during loading.

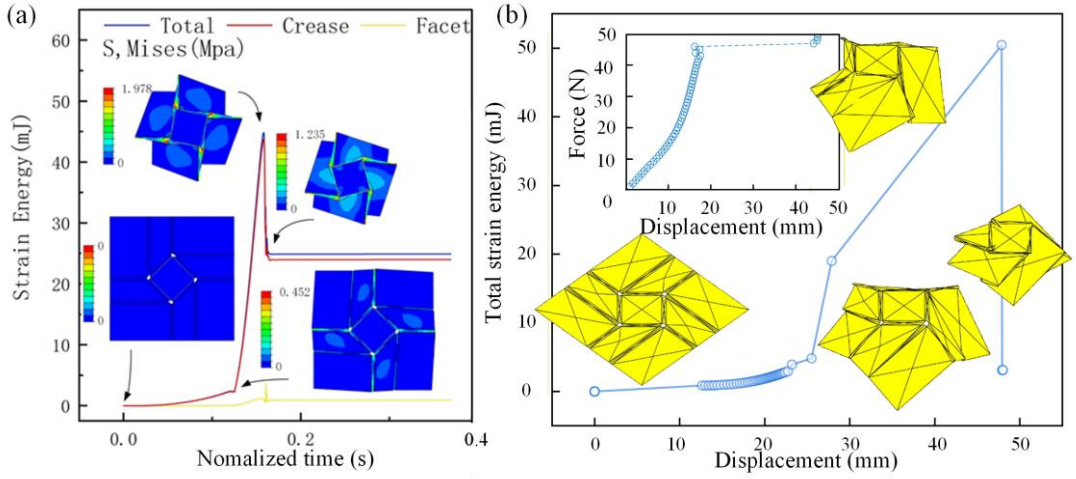

Figure 1. Theoretical modeling and finite element validation of a thick panel Square-twist origami structure with soft joints.

3. CONCLUSIONS

A unified bar-and-hinge framework with energy-consistent contact coupling is developed for thick-panel Square-Twist origami with soft joints. The model efficiently captures large-deformation folding, self-contact/self-locking, and contact-triggered stiffness changes, with robust contact handling integrated within the Square-twist formulation. In the present study, the framework is demonstrated for the transition from the initial flat configuration to a folded stable state; extension to full folding–unfolding cycles will be pursued in future work.

REFERENCES

[1] H. Wang, H. Qu, X. Wang, et al. "Tensile behavior of square-twist origami inspired mechanical metamaterials with soft joints and chirality applications". *Smart Materials and Structures*, 33, 065038 ,2024.

[2] H. Wang, X. Yang, H. Qu, et al. "Construction and analysis of a thick-panel origami gripper with soft joints based on square-twist origami tessellation". *Thin-Walled Structures*, 10, 113049, 2025.

[3] Z. Yi, "A lumped-parameter model for the mechanics of interlocked geometries: Ribbons, origami, and woven structures". *Computer Methods in Applied Mechanics and Engineering*, 446, 2025.

MULTI-LATTICE TOPOLOGY OPTIMIZATION WITH COMPETITIVE WEIGHTING AND PENALTY-DRIVEN LATTICE SELECTION UNDER DYNAMIC LOADING

Yangyang Xiao[1,3], Shu Li[2], Nikos D. Lagaros[3], Jie Geng[4]

[1] School of Aeronautic Science and Engineering, Beihang University, Beijing, China, {xiaoyangyang@buaa.edu.cn}
[2] Hangzhou International Innovation Institute, Beihang University, Hangzhou, China, {lishu@buaa.edu.cn}
[3] Institute of Structural Analysis and Antiseismic Research, School of Civil Engineering, Zografou Campus, National Technical University of Athens, Athens 15780, Greece, {nlagaros@central.ntua.gr}
[4] School of Reliability and Systems Engineering, Beihang University, Beijing, China,{gengjie@buaa.edu.cn}

1. INTRODUCTION

Lattice materials [1] provide an attractive route to adjust stiffness, shear response, and inertia for structures subjected to dynamic loading. Under impact- or vibration-governed loading conditions, design objectives often relate to time-dependent performance metrics such as absorbed energy, peak acceleration, or vibration amplitude, rather than purely static compliance [2]. However, incorporating such dynamic metrics into topology optimization (TO) remains challenging [3]. This is particularly true when (i) dynamic simulations entail substantially higher computational cost and more severe convergence issues than static analyses, (ii) multiple lattice families with distinct stiffness, shear, and weight characteristics must be considered, and (iii) the final design must be manufacturable, i.e., each element is assigned a single lattice type rather than a non-physical mixture.

This work presents a practical, automated framework for dynamic multi-lattice topology optimization driven by energy-based indicators extracted from explicit dynamics simulations. The framework couples: (1) Abaqus/Explicit for robust transient/impact analysis; (2) a Python outer loop that rewrites Abaqus input files and runs simulations in batch mode; and (3) an interpolation-based equivalent lattice-material property model that computes the relative density from the material design variables and interpolates the corresponding effective mechanical properties. A competitive weighting scheme allows different lattice types to compete within the same design domain, while penalty terms steer the solution toward discrete and manufacturable lattice assignments under global material-fraction constraints.

2. METHOD

2.1. Design Variables and Multi-Lattice Property Interpolation

Each finite element is assigned two coupled design variables: the macro relative density, denoted by $x_e \in [x_{min},\ x_{max}]$, and the competitive lattice weights, denoted by $y_{e,k}$, Here, e denotes the element index and k denotes the index of the candidate lattice family. over the candidate lattice families. A soft competition among lattice families is enforced through a simplex constraint, as given in Eq. (1). Here, $y_{e,k}$ represents the weight associated with lattice family k in element e, and the simplex constraint ensures that the competing lattice weights remain normalized.

$$\sum_{k=1}^{K} y_{e,k} = 1, y_{e,k} \geq 0 \tag{1}$$

For each lattice family, the effective properties are precomputed as functions of relative density and queried by interpolation during the optimization process. At each iteration, the effective properties of each candidate lattice family are interpolated at the current element density, and the element-wise effective properties are then obtained through weighted mixing, as defined in Eq. (2).

$$E_e = \sum_k y_{e,k} E_k(x_e), \qquad G_e = \sum_k y_{e,k} G_k(x_e), \qquad \rho_e = \sum_k y_{e,k} \rho_k(x_e) \tag{2}$$

This strategy avoids explicit unit-cell modeling while enabling stable optimization driven by explicit dynamic analysis and fair competition among lattice families with distinct stiffness, shear, and inertia characteristics.

2.2. Energy-based Objective and Lattice Selection

Abaqus/Explicit is employed for transient and impact analyses. Instead of displacement-based objectives, which may become noisy under contact and severe transient conditions, energy-based indicators directly available from the explicit solver outputs are adopted. A representative objective is the absorbed energy at the end of the loading event, as defined in Eq. (3):

$$\max J(x,y) = U_{\text{abs}}(t_{\text{end}}) \tag{3}$$

Here, U_{abs} may be taken as the internal energy (e.g., ALLIE) or the plastic dissipation energy (e.g., ALLPD), depending on the dominant energy-absorption mechanism of interest. This choice provides a robust objective signal for impact- or vibration-dominated design problems.

A global volume constraint is enforced through the macro relative density x_e. To obtain manufacturable multi-lattice layouts, two penalties are applied to the lattice weights $y_{e,k}$: a lattice-fraction penalty for controlling the global usage of each lattice family, and a competition penalty for promoting discrete element-wise lattice selection.

$$p_k = \left(\sum_e y_{e,k} V_e \right) / V_{\text{total}} \tag{4}$$

2.3. Automated Abaqus/Explicit outer loop

The optimization is implemented as a fully automated outer loop: (1) the inputs consist of an explicit FE model and a multi-lattice material database; (2) the element-wise design variables (x, y) and $y_{e,k}$ are updated; (3) the corresponding effective properties are interpolated and written into the Abaqus input deck, followed by an Abaqus/Explicit analysis and extraction of global and element-wise energy measures from the ODB; and (4) the macro relative density is updated using an OC-style scheme driven by energy-based sensitivity proxies, whereas the lattice weights are updated through penalty-driven competition to approach discrete and manufacturable lattice assignments.

3. CONCLUSION

Two beam examples subjected to identical impulsive transverse loading (clamped, Fig. 1a; cantilever, Fig. 1b) demonstrate stable convergence: the energy-based objective drops rapidly and then plateaus, while the design change approaches zero, yielding clear load paths and localized lattice-reinforced regions consistent with bending-shear demands. An automated dynamic multi-lattice topology-optimization framework is proposed by coupling Abaqus/Explicit with a Python-based outer loop and an equivalent-property model. A competitive weighting scheme with penalty scheduling enables discrete, manufacturable lattice selection subject to global volume-fraction constraints. Future work will extend the method to contact- and friction-dominated dynamics and improved sensitivities for dynamic objectives.

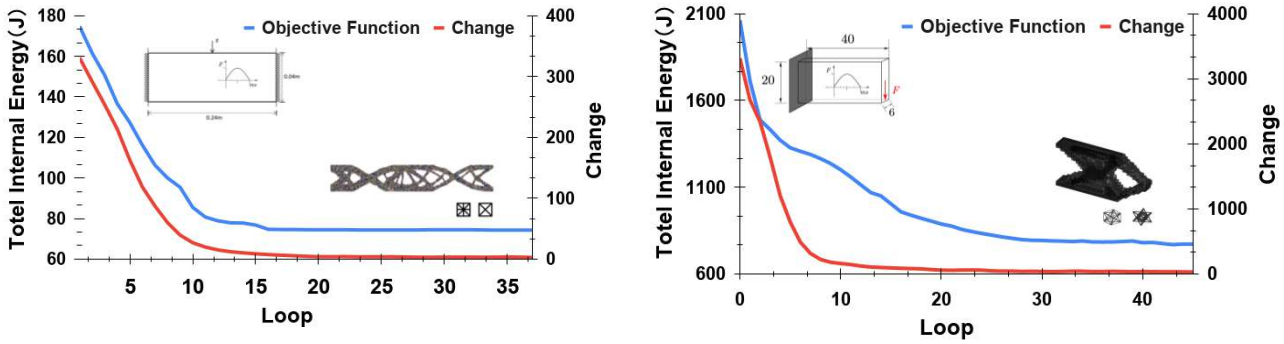

Figure 1. Convergence histories (objective and change) and final multi-lattice layouts for two beam configurations under identical impulsive transverse loading: (a) clamped beam; (b) cantilever beam.

REFERENCES

[1] T.A. Schaedler and W.B. Carter, "Architected cellular materials". *Annual Review of Materials Research*, 46, 187–210, 2016. DOI: 10.1146/annurev-matsci-070115-031624.

[2] L. Hou, J. Cai, C. Mei, G. Wang, B. Luo, and F. Lin, "Energy absorption of lattice structures under impact loading: A systematic review". *Thin-Walled Structures*, 213, 112866, 2025. DOI: 10.1016/j.tws.2025.112866.

[3] H.-M. Huang, E. Raponi, F. Duddeck, S. Menzel, and M. Bujny, "Topology optimization of periodic structures for crash and static load cases using the evolutionary level set method". Optimization and Engineering, 25, 1597–1630, 2024. DOI: 10.1007/s11081-023-09857-1.

CONTROLLER DESIGN FOR VELOCITY TRANSMISSION OF BOWDEN-CABLE ACTUATORS

Yaodong Lu[1,2], Pablo Nocito[2], Yannick Aoustin[3], Sébastien Mick[2], Qiaoling Meng[1], Hongliu Yu[1], Nathanaël Jarrassé[2]

[1] Institute of Intelligent Rehabilitation Engineering, University of Shanghai for Science and Technology, Shanghai 200093, China.{yld1996@sina.com}
[2] Sorbonne Université, CNRS UMR 7222, ISIR, F-75005, Paris, France {jarrasse@isir.upmc.fr}
[3] Nantes Université, UMR 6004, LS2N, F-44321, Nantes, France {yannick.aoustin@univ-nantes.fr}

1 PROBLEM STATEMENT

Among various transmission solutions in exosuit design, Bowden-cable transmission has emerged as an effective and widely adopted approach [1]. By allowing actuators to be placed remotely from the joints, Bowden cables substantially reduce the weight and inertia experienced by the user. In such systems, shown in Fig. 1, motion and force are transmitted through the relative displacement between a flexible inner cable and an outer sheath, enabling the transmission path to accommodate complex and continuously changing geometries. Owing to these properties, Bowden-cable transmission has been successfully employed in a variety of wearable robotic systems, including knee exosuits for children [2], elbow rehabilitation devices [3], hand exoskeletons with bidirectional finger actuation [4], and wearable cable-driven neck exosuits that preserve natural head-neck motion [5]. Despite these advantages, Bowden-cable transmission is inherently affected by complex and highly nonlinear friction between the inner cable and the outer sheath [6]. This friction includes Coulomb friction, viscous friction, stiction, and stick–slip phenomena, making accurate friction modeling extremely challenging. In some applications, such as passive rehabilitation, accurate motion tracking is a key requirement. However, owing to the complex friction phenomena inherent in the Bowden-cable transmission, noticeable delays may arise in the velocity tracking response. The velocity difference between the main and secondary joints leads to poor tracking accuracy in the control process. In this work, a new velocity-control method is proposed to resolve this problem.

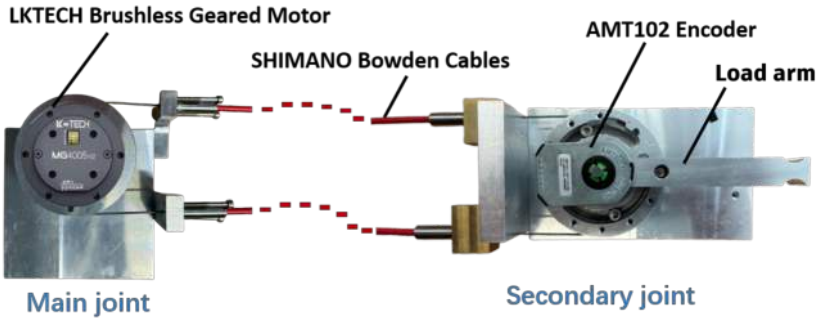

Figure 1: The experimental prototype is equipped with an LKTECH brushless geared motor for actuation of the main joint, and an AMT102 encoder is installed on the rotational axis of the secondary joint to measure its angular position and velocity.

2 METHODOLOGY AND RESULTS

To address this issue, an improved control strategy incorporating a lead compensator is adopted and formulated as follows.

$$v_m = G_c(\mathrm{s}) v_s^d \tag{1}$$

where,

$$G_c(\mathrm{s}) = K_c \frac{\alpha T \mathrm{s} + 1}{T \mathrm{s} + 1} \tag{2}$$

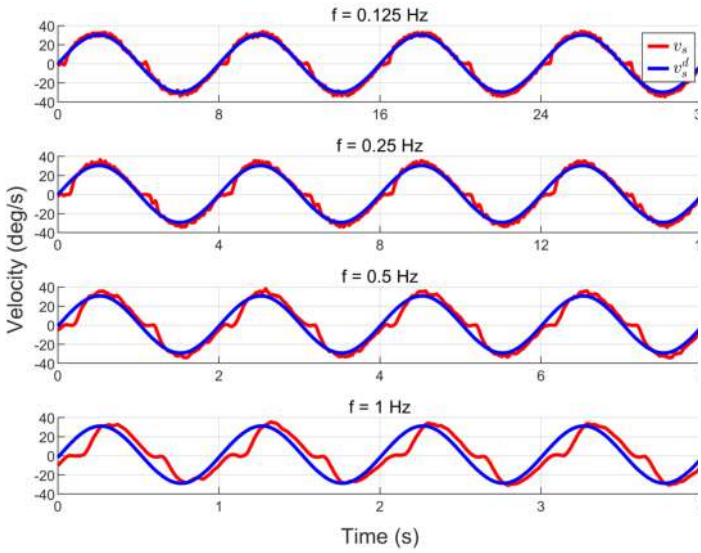

Figure 2: Velocity transmission of Bowden-cable actuator(v_s denotes the measured secondary joint velocity).

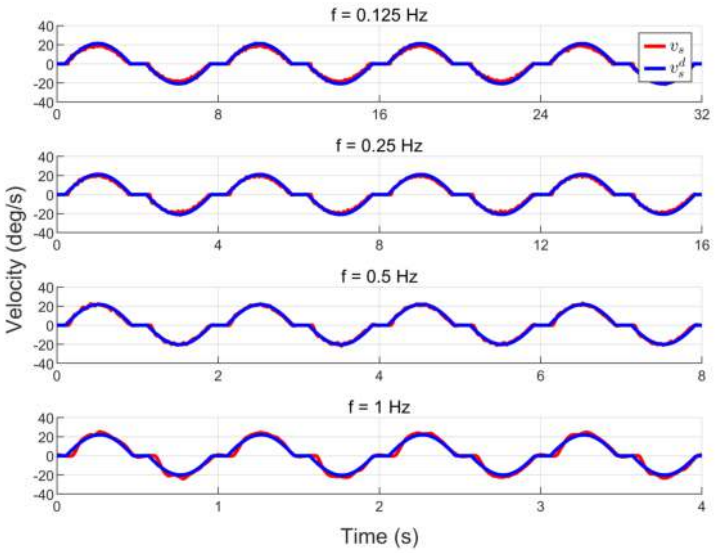

Figure 3: Velocity transmission with lead compensator

where v_m and v_s^d denote the commanded main-joint velocity and the desired secondary-joint velocity. $G_c(s)$ represents the lead compensator, in which K_c, T, and α are the parameters determined based on the desired maximum phase lead and the cut-off frequency. The experimental results, shown in Figs. 2 and 3, indicate that the average maximum absolute error and rmse have been reduced by up to 70% when a lead compensator with a 15° phase lead ($K_c = 0.84$, $\alpha = 1.7$, $T = 0.15$ s) is applied. The effectiveness of the proposed controller design has been validated through experimental results. However, residual tracking errors can still be observed. In future work, an error-based corrective term will be incorporated into the controller design to further improve tracking performance.

ACKNOWLEDGMENTS

This work was supported by the JOKER project (BPI I-démo program of the France 2030 plan) and the Reinvent project (ANR-22-EXOD-0002). The work of Yannick Aoustin was also supported by ANR project SlimDisc under Grant ANR-24-CE48-2771.

REFERENCES

[1] A. T. Asbeck, R. J. Dyer, A. F. Larusson, and C. J. Walsh, "Biologically-inspired soft exosuit," in *2013 IEEE 13th International Conference on Rehabilitation Robotics (ICORR)*. IEEE, 2013, pp. 1–8.

[2] J. J. Wiebrecht, J. A. Strick, R. J. Farris, and J. T. Sawicki, "Design and validation of a cable-driven joint actuator for pediatric knee orthoses," *Journal of Biomechanical Engineering*, vol. 147, no. 6, p. 064501, 2025.

[3] L. Zhu, C. Cui, D. Zhang, J. Tan, and C. Xu, "Modeling and control of cable-driven exoskeleton for arm rehabilitation," *Journal of Mechanisms and Robotics*, vol. 17, no. 6, p. 061010, 2025.

[4] A. Wege, K. Kondak, and G. Hommel, "Mechanical design and motion control of a hand exoskeleton for rehabilitation," in *IEEE International Conference Mechatronics and Automation, 2005*, vol. 1. IEEE, 2005, pp. 155–159.

[5] I. Bales and H. Zhang, "Kinematic benefits of a cable-driven exosuit for head-neck mobility," *IEEE Robotics and Automation Letters*, 2024.

[6] D. Chen, Y. Yun, and A. D. Deshpande, "Experimental characterization of bowden cable friction," in *2014 IEEE international conference on robotics and automation (ICRA)*. IEEE, 2014, pp. 5927–5933.

A MULTI-AXIS GIMBAL MECHANISM AS AN EXPERIMENTAL PLATFORM FOR CONTROLLED ROTATIONAL EXCITATION

Paweł Olejnik[1], Łukasz Kuźnicki[1], Maciej Rożniata[1]

[1] Department of Automation, Biomechanics, and Mechatronics, Lodz University of Technology, 1/15 Stefanowski Street, 90-537 Lodz, Poland, {pawel.olejnik@p.lodz.pl}

1 INTRODUCTION

Multi-axis gimbal mechanisms are widely used in systems requiring controlled rotational motion and precise pointing under external disturbances. Such mechanisms are commonly employed in mobile and aerospace platforms, where their dynamic behavior is strongly influenced by actuator nonlinearities, coupling between rotational axes, and time-varying disturbance conditions [1, 2, 3].

The investigated three-axis gimbal mechanism is designed as a compact, nested structure consisting of outer, intermediate, and inner rotational links. Electrical signal transmission between successive stages is realized using slip-ring assemblies, enabling continuous rotation of each axis without angular limitations imposed by cabling. This feature allows the system to generate large-angle and long-duration rotational motions, which are difficult to achieve in conventionally wired gimbal configurations.

Beyond stabilization tasks, the gimbal serves as a controlled experimental platform for dynamic excitation and evaluation of sensing and control strategies. By applying prescribed angular trajectories and disturbance profiles, the mechanism enables systematic testing of inertial measurement units (IMUs) and assessment of control performance under realistic operating conditions, including coupled axis motion and varying load distribution.

From a control perspective, the nested kinematic structure and configuration-dependent inertia of the mechanism motivate the use of control-oriented formulations rather than detailed analytical modeling. This approach aligns with experimental studies reported in the literature, where robust control strategies address modeling uncertainty and external disturbances in multi-axis gimbal systems [1, 2, 3].

The present contribution focuses on the real-time control framework implemented on the gimbal and its use as an experimental testbed for controlled rotational excitation. Emphasis is placed on the feedback structure, real-time execution, and the ability to subject both the mechanical system and embedded sensors to diverse excitation scenarios suitable for experimental validation of control strategies.

2 CONTROL-ORIENTED PROBLEM FORMULATION

The investigated experimental object is a three-axis gimbal mechanism driven by DC motors with gear reduction, intended for active stabilization and controlled excitation of angular motion with respect to an inertial frame. Due to the nested kinematic structure of the mechanism, where the inner axes are mounted on rotating outer and intermediate links, the resulting dynamics exhibit strong coupling and configuration-dependent behavior.

Rather than pursuing a full analytical multibody model, the control problem is formulated from a control-oriented perspective. Each axis is treated as a rotational subsystem influenced by inertia variation, friction, gear transmission effects, and disturbances. The primary control objective is to limit angular deviation and angular rate under prescribed excitation while ensuring smooth motion, robustness to uncertainty, and repeatable behavior.

3 SENSOR CONFIGURATION AND FEEDBACK STRUCTURE

The gimbal mechanism is equipped with an inertial measurement unit (IMU) providing angular rate and specific force data, which are processed in real time to obtain estimates of angular position and velocity. This inertial feedback reflects the global motion of the mechanical structure and constitutes the main sensing modality for closed-loop control. In addition, actuator-level digital feedback signals are available, enabling reconstruction of rotational speed at the output of each geared drive. These signals are incorporated into the control system to form a hybrid feedback structure combining inertial orientation information with local velocity measurements.

Such a configuration allows the controller to respond both to global orientation errors and to axis-specific dynamic effects, which is particularly relevant in the presence of friction, gear nonlinearities, and asymmetric mass distribution across the gimbal links. The adopted feedback structure supports a wide range of excitation scenarios and provides a consistent basis for experimental evaluation of both mechanical dynamics and inertial sensing performance.

4 IMPLEMENTED CONTROL STRATEGY

The real-time control system consists of independent axis controllers operating in discrete time with a fixed sampling period. Control laws are formulated in the angular domain, directly relating measured orientation and angular rate to the applied control input.

Angular stabilization and tracking are achieved using proportional–derivative action based on inertial feedback. To improve damping and robustness, an inner velocity feedback loop is introduced using actuator-level rotational speed measurements. This cascaded structure reduces sensitivity to friction-induced nonlinearities and variations in effective inertia, while maintaining a clear physical interpretation of the control action.

Low-order digital filtering is applied to the feedback signals to attenuate high-frequency noise without introducing excessive phase lag. The resulting control system operates deterministically in real time, enabling repeatable experiments under identical excitation conditions.

5 EXPERIMENTAL EXCITATION AND VALIDATION SCENARIOS

The implemented control framework enables the gimbal to generate controlled rotational excitations such as step inputs, harmonic motions, and broadband disturbance profiles. Excitations can be applied independently or simultaneously along multiple axes, allowing investigation of coupled dynamic effects arising from the nested structure of the mechanism.

By modifying the mass distribution of individual links, the gimbal can be configured with non-uniform and configuration-dependent moments of inertia. This enables experimental assessment of control robustness under varying dynamic conditions and provides a means to verify regulator performance in the presence of inertia asymmetry.

These capabilities make the system suitable both for experimental validation of inertial measurement units and for comparative evaluation of control structures under realistic mechanical uncertainties, consistent with experimental approaches commonly adopted in the study of controlled mechanical systems.

Figure 1 presents the experimental gimbal setup used for controller implementation and validation.

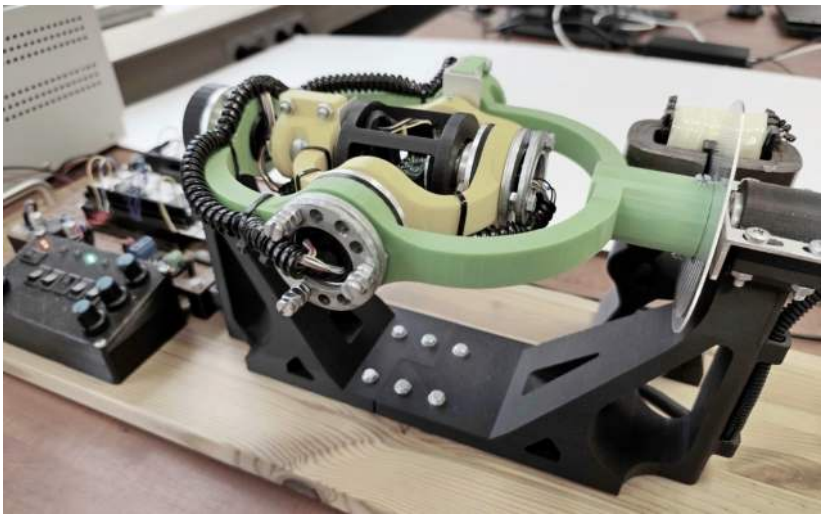

Figure 1: Experimental gimbal setup used for control development and testing.

ACKNOWLEDGEMENTS

This work has been supported by the Polish National Science Centre, Poland under the grant OPUS 26 no. 2023/51/B/ST8/00021.

REFERENCES

[1] N. Bihari, S. P. Dash, K. C. Dhankani, and J. M. Pearce, “3-D printable open source dual axis gimbal system for optoelectronic measurements,” *Mechatronics*, vol. 56, pp. 175–187, 2018. doi:10.1016/j.mechatronics.2018.07.005.

[2] A. Altan and R. Hacıoğlu, “Model predictive control of three-axis gimbal system mounted on UAV for real-time target tracking under external disturbances,” *Mechanical Systems and Signal Processing*, vol. 138, Art. no. 106548, 2020. doi:10.1016/j.ymssp.2019.106548.

[3] C. Creaser and R. Bauer, “Logic-based gimbal compensator for the double-gimbal scissored-pair control moment gyroscope using magnetic torquers,” *Advances in Space Research*, vol. 73, no. 1, pp. 254–270, 2024. doi:10.1016/j.asr.2023.10.023.

HIGH-PRECISION MULTI-AXIS FLEXURE-BASED COMPLIANT MECHANISM: PREDICTIVE MODELLING AND EXPERIMENTAL VALIDATION

H. A. Naddaf[1], M. Gomez[1], N. Y. Bailey[1]

[1] King's College London, Strand, London, WC2R 2LS, UK
{hussein.naddaf@kcl.ac.uk}, {michael.gomez@kcl.ac.uk}, {nicola.bailey@kcl.ac.uk}

1 INTRODUCTION

Current mechanical systems typically use rigid links connected via traditional joints, such as bearings. Such joints suffer from complex tribological effects such as friction, backlash, and wear that limit repeatability and necessitate lubrication and maintenance. In automation applications, these drawbacks accumulate across multiple joints and are difficult to predict, making high-precision motion challenging even with advanced control methods.

One approach to eliminate these issues is to use flexure-based compliant mechanisms (FCMs) as pseudo-joints. FCMs are mechanical designs that achieve motion through elastic deformation of flexible components [1]. FCMs exhibit high precision and durability, with demonstrated repeatability levels below 0.1 μm [2]. This high repeatability has resulted in FCMs being widely adopted in precision positioning, and micro-manipulation systems. Additionally, by enabling monolithic designs, FCMs reduce the total number of parts required, thereby making the system cheaper to manufacture and lighter. This aspect makes FCMs an attractive option for aerospace applications, while also enabling the fabrication of small-scale systems such as micro-electro-mechanical systems (MEMS) [1].

Existing efforts on FCMs have established a strong foundation in modelling and design. A large proportion of work focuses on continuum and fully compliant robots, which achieve large working volumes but are primarily intended for navigation and adaptability rather than high-precision tasks [3]. Many precision-oriented systems that incorporate FCMs are designed to operate only within small-stroke systems, where deformations remain sufficiently small for small deflection modelling assumptions to remain valid. As a result, systems that achieve both a large working volume and high precision are rare. The few reported examples of such systems are limited to single-axis revolute pseudo-joints (flexure hinges) [4]. Thus, this work expands on the research done on flexure hinges by presenting a hybrid modelling approach that combines Kirchhoff and Cosserat rod theories. The model was applied to a robotic system that features a steel rod as a multi-axis pseudo-joint capable of large-stroke, high-precision motion. The model is validated using an experimental system, yielding a maximum relative error of 0.83%.

2 ROBOTIC ARCHITECTURE AND FCM INTEGRATION

The designed and constructed system is shown in Figure 1. The FCM, which has a circular section of constant diameter, is fixed at the left-hand end and connected to a linkage mechanism at the right-hand end. The linkage mechanism consists of rigid links connected by revolute joints with ball bearings to minimise any tribological effects. The mechanism is attached to a linear-rotary actuator, which has a precision of 0.05 mm and 0.05 degrees. Figure 1(a) shows the unactuated configuration, while panels (b) and (c) show rotatory actuation through θ_1 and linear actuation of l_0, respectively. The FCM, with a diameter of 0.02 m and a length of 0.1 m, is made of spring steel (1.4310) which has a Young's modulus of 207 GPa, a Poisson's ratio of 0.3, and an elastic limit of 1556 MPa.

3 QUASI-STATIC MODELLING OF THE FCM

The system exhibits coupled behaviour, in which FCM deformation and interaction forces through the linkage mechanism are governed by a set of differential equations. FCM equations are derived using both Cosserat and Kirchhoff rod theories [3], while the boundary conditions are obtained from geometric constraints and force equilibrium of the remaining links and joints. Friction and damping at the hinges are neglected, with all components except the FCM assumed rigid; quasi-static conditions are assumed, consistent with the static experiments in this work.

The Cosserat-based model provides high accuracy but requires significant computational cost (approximately 5 s) and a highly accurate initial guess to ensure convergence. In contrast, the Kirchhoff-based model simplifies the formulation by neglecting shear and axial extension effects in the FCM, resulting in reduced accuracy but substantially lower computational effort, converging in less than 0.2 s. To make use of the advantages of both approaches, the Kirchhoff

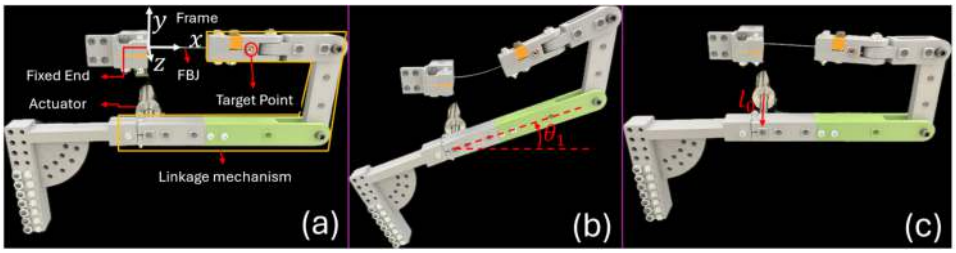

Figure 1: The rig used for experimental validation: (a) unactuated configuration, showing the linkage mechanism, FCM (spring steel rod), global reference frame, fixed end of the FCM, laser tracker target point, and linear–rotary actuator. (b) Rotary actuation by an angle θ_1. (c) Linear actuation by a displacement l_0.

model is first employed to generate an initial solution, which is then used as an initial guess for the Cosserat model. This preserves the accuracy of the Cosserat formulation while reducing the total computation time to approximately 0.35 s. All simulations were performed using the MATLAB `bvp4c` solver on a computer with an Intel i7-11800H CPU (2.3 GHz) and 16 GB of RAM, running Windows 11.

4 EXPERIMENTAL VALIDATION

To validate the mathematical models described in Section 3, a Leica AT960 laser tracker (measurement accuracy up to 5 microns) is employed to measure a target point position, with respect to the global reference frame (see Figure 1(a)). A comparison between experimental measurements and model predictions under rotary actuation for $l_0 = 0$ mm and $l_0 = 40$ mm is provided in Figure 2. In each panel, the horizontal axis is the actuation angle θ_1. Panels (a) and (c) plot the position of the target point along the y and z axis, respectively; the corresponding absolute errors ℓ_y, ℓ_z between the experimental measurement and the model are shown in panels (b) and (d). The second norm position errors remain small over the full actuation ranges, below 0.72 mm (0.83% relative error).

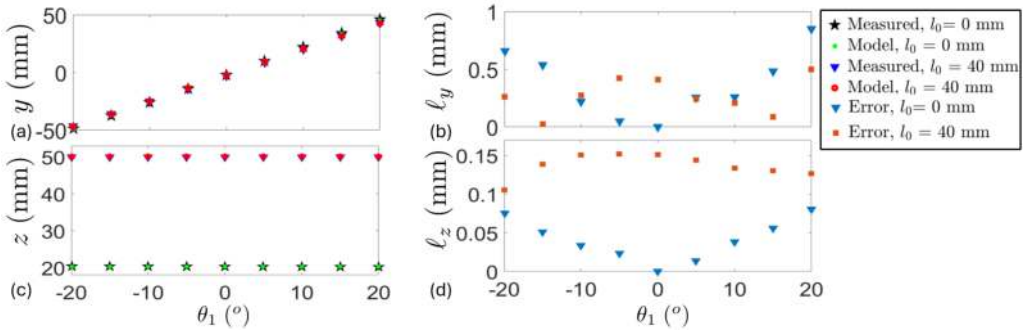

Figure 2: Comparison of measured target point positions and model predictions.

5 CONCLUSION

This abstract has presented the modelling and validation of a novel robotic system featuring a spring steel multi-axis FCM. With the help of Cosserat and Kirchhoff rod formulations, the study extends the applicability of FCMs to multi-axis and large working volumes while maintaining high precision and repeatability. The modelling accuracy is demonstrated by a relative error below 0.83%. Considering that the prototype was fabricated using 3D printing, this result indicates that the developed model reproduces the measured static behaviour within the practical manufacturing tolerances of the linkage mechanism. Such an efficient modelling approach supports the feasibility of FCMs as replacements for traditional bearings in robotic and automated machinery, offering a pathway toward high-precision, low-maintenance systems for industrial manufacturing.

References

[1] M. Ling, L. L. Howell, J. Cao, and G. Chen, "Kinetostatic and dynamic modeling of flexure-based compliant mechanisms: A survey," *Applied Mechanics Reviews*, vol. 72, no. 3, p. 030 802, 2020.

[2] M. Naves, M. Nijenhuis, B. Seinhorst, W. Hakvoort, and D. M. Brouwer, "T-flex: A fully flexure-based large range of motion precision hexapod," *Precision Engineering*, vol. 72, pp. 912–928, 2021.

[3] J. Burgner-Kahrs, D. C. Rucker, and H. Choset, "Continuum robots for medical applications: A survey," *IEEE Transactions on Robotics*, vol. 31, no. 6, pp. 1261–1280, 2015.

[4] N. Bailey, C. Lusty, and P. Keogh, "Iterative feedforward control for bearing-free multibody systems," *Journal of Mechatronics and Robotics*, vol. 5, no. 1, pp. 33–46, 2021.

ESTIMATION OF FRICTION PARAMETERS UTILIZING EXPERIMENTAL DATA

Francisco Novais[1,2], Filipe Marques[1,3], Paulo Flores[1,3], Hamid M. Lankarani[4]

[1] CMEMS-UMinho, Universidade do Minho, Campus de Azurém, Guimarães 4804-533, {fmarques@dem.uminho.pt; pflores@dem.uminho.pt}

[2] INEGI, Universidade do Porto Campus FEUP, Rua Dr. Roberto Frias 400, 4200-465 Porto, Portugal {fnovais@inegi.up.pt}

[3] LABBELS - Associate Laboratory, Braga/Guimarães, Portugal

[4] Department of Mechanical Engineering, Wichita State University, KS 67260-133, USA, {hamid.lankarani@wichita.edu}

1. INTRODUCTION

Friction has a fundamental impact on the dynamic behavior of many mechanical systems, influencing the performance of robotic manipulators, vehicle subsystems, and precision machinery, just to mention a few. Although friction has been studied for centuries, it remains a challenging problem due to its complex and nonlinear characteristics. Friction behavior involves several phenomena such as static and kinetic regimes, the Stribeck effect, stick–slip motion, presliding displacement, hysteresis, and frictional lag, which significantly affect system stability, positioning accuracy, and energy dissipation [1-3].

Historically, experimental investigation has played a crucial role in advancing the understanding of friction. Early studies by Leonardo da Vinci, Guillaume Amontons, and Charles-Augustin Coulomb relied on simple experimental devices to investigate frictional resistance and establish the well-known friction laws that remain foundational in classical mechanics. Since then, numerous experimental setups have been developed to explore different friction phenomena under controlled conditions [4-6]. These experimental rigs have enabled researchers to investigate complex behaviors such as stick-slip dynamics, hysteresis, and non-reversible friction characteristics, while also providing validation data for theoretical friction models.

Despite the large number of experimental studies on friction phenomena, the identification of parameters for advanced dynamic friction models remains a challenging task. Static friction models are relatively simple to implement, however, they are unable to capture transient and complex friction behavior [3]. In turn, dynamic friction models provide a more realistic description of friction phenomena, but they typically require the identification of several parameters that are not directly measurable and often depend strongly on the specific mechanical system under analysis.

One of the main obstacles to the practical use of these models is the difficulty of designing experimental setups capable of accurately measuring friction forces while simultaneously acquiring the kinematic quantities required to evaluate friction models. To address this challenge, this work proposes a simple and versatile experimental workbench for friction force data acquisition under controlled operating conditions. The apparatus enables the study of different contact material pairs and motion profiles while providing the data necessary to identify the parameters of dynamic friction models. In this work, experimental data are used to estimate the parameters of the LuGre friction model [7] through an optimization procedure based on a genetic algorithm, allowing a comparison between the experimentally identified parameters and commonly adopted values from literature.

2. EXPERIMENTAL APPARATUS

The developed experimental apparatus consists of a reciprocating slider mechanism as illustrated in Figure 1(a), which includes a replaceable sliding element mounted on an L-shaped slider and a pocket integrated into the base structure that enables the use of different test sheets. Both elements allow the easy replacement of the contacting materials so that several material pairs can be evaluated. For this study, anodized aluminum and brass were used as test materials.

The slider is actuated through a ball screw mechanism driven by a stepper motor, which provides controlled bidirectional motion. The driving force exerted by the screw on the slider is measured using a load cell connected to a signal amplifier, while the slider's horizontal position is recorded using a high-resolution camera. Data from these measurements were collected and synchronized using a sampling frequency of 40 Hz through a NI data acquisition system.

It must be noted that the load cell does not provide a direct measurement of the friction force acting on the slider. Thus, the equation of motion of the one-degree-of-freedom system can be established as:

$$f_{\text{ext}} - f_{\text{f}} = m\ddot{x} \tag{1}$$

where f_{ext} is the external force applied by the screw to the slider, which corresponds to the force measured by the load cell, f_{f} denotes the friction force, m represents the mass of the slider and $\ddot{x}$ is the corresponding acceleration. The recorded images provide displacement data from which velocity and acceleration are obtained.

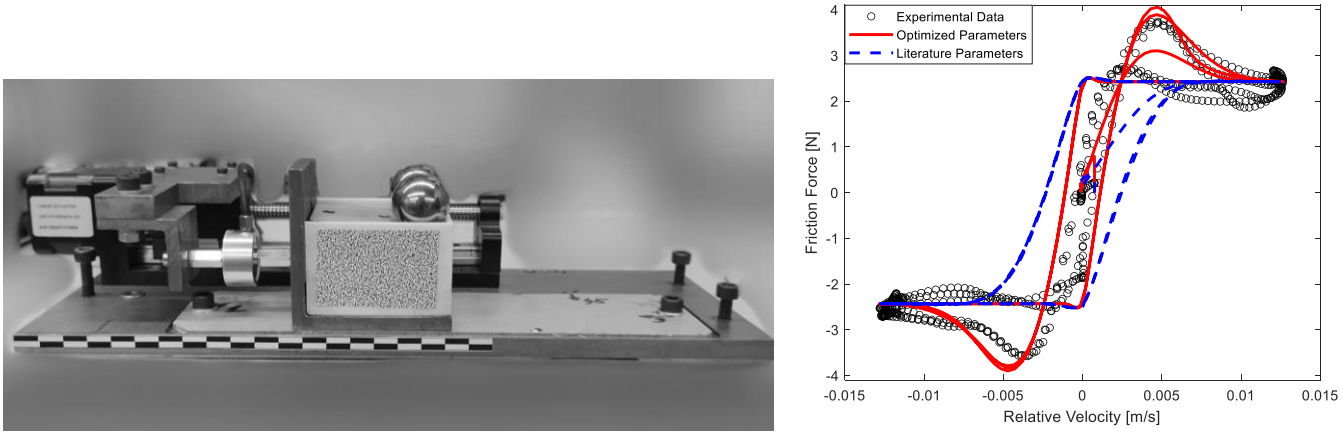

(a) (b)

Figure 1. (a) Physical model of the workbench developed for friction force data acquisition, and (b) results of the friction force vs relative velocity obtained experimentally compared with LuGre model with both literature and optimized parameters.

3. FRICTION MODEL PARAMETER IDENTIFICATION

The experimental friction force data obtained from the apparatus exhibit characteristics associated with dynamic friction behavior, including stiction peaks at motion reversal, hysteresis in the friction-displacement relationship, and non-reversible friction-velocity curves. These features cannot be accurately captured by static friction models; therefore, the LuGre dynamic friction model was selected for parameter identification. The LuGre model is characterized by six parameters, namely static friction coefficient, kinetic friction coefficient, Stribeck characteristic velocity, bristle stiffness coefficient, bristle damping coefficient and viscous friction coefficient.

Parameter identification was performed using the genetic algorithm optimization method available in MATLAB. The objective function minimizes the least-squares difference between the experimentally obtained friction force and the friction force predicted by the LuGre model. Parameter bounds were defined based on preliminary estimates obtained from the experimental data and typical values reported in literature. To improve convergence efficiency, the optimization variables were normalized before entering the genetic algorithm. Additionally, a linear inequality constraint was imposed to ensure that the static friction coefficient remains greater than the kinetic friction coefficient.

The parameter identification methodology produced consistent results across three different optimization runs, indicating a stable convergence of the genetic algorithm. The optimized static and kinetic friction coefficients were found to be close to the initial experimental estimates, while other parameters showed noticeable differences from commonly reported values in the literature.

A comparison between the LuGre model using literature parameters and the optimized parameters reveals significant differences in their ability to reproduce the experimental friction behavior. While the literature parameters can reproduce the general shape of the friction-displacement hysteresis loop, they fail to accurately capture the stiction peaks and the width of the central hysteresis region observed in the friction-velocity relationship, as demonstrated in Figure 1(b). In contrast, the optimized parameters provide a significantly better agreement with the experimental data, particularly in representing the non-reversible friction behavior and the transition between static and kinetic friction regimes.

ACKNOWLEDGMENTS

This work is funded by national funds through the FCT – Fundação para a Ciência e a Tecnologia, I.P., within the scope of the project doi.org/10.54499/UID/04436/2025.

REFERENCES

[1] B. Armstrong-Hélouvry, P. Dupont and C. Canudas de Wit, “A Survey of Models, Analysis Tools and Compensation Methods for the Control of Machines with Friction”. *Automatica*, 30(7), 1083-1138, 1984.

[2] H. Olsson, K. J. Åström, C. Canudas de Wit, M. Gäfvert and P. Lischinsky, “Friction models and friction compensation”. *European Journal of Control*, 4(3), 176–195, 1998.

[3] F. Marques, P. Flores, J. C. Pimenta Claro, and H. M. Lankarani, “A survey and comparison of several friction force models for dynamic analysis of multibody mechanical systems”. *Nonlinear Dynamics*, 86(3), 1407-1443, 2016.

[4] M. Wiercigroch, T. Sin, and F. K. Liew, “Non-reversible dry friction oscillator: design and measurements”. *Proceedings of the Institution of Mechanical Engineers, Part C: Journal of Mechanical Engineering Science*, 213(5), 1999.

[5] J. Awrejcewicz and P. Olejnik, “Occurrence of stick-slip phenomenon”. *Journal of Theoretical and Applied Mechanics*, 45(1), 33-40, 2007.

[6] J. Wojewoda, A. Stefański, M. Wiercigroch and T. Kapitaniak, “Hysteretic effects of dry friction: modelling and experimental studies”. Philosophical Transactions of the Royal Society A: Mathematical, Physical and Engineering Sciences, 366(1866), 747-765, 2008.

[7] C. Canudas de Wit, and P. Lischinsky, “A New Model for Control of Systems with Friction”. *IEEE Transactions on Automatic Control*, 40(3), 419-425, 1995.

A NOVEL FINITE ELEMENT-BASED SLICE MODEL FOR LINE CONTACTS IN ROLLING BEARINGS

Tobias Baumann[1], Daniel Singer[1], Till Budde[1], Stephan Tremmel[1]

[1] Engineering Design and CAD, University of Bayreuth, Universitätsstraße 30, 95447 Bayreuth, Germany, {tobias.baumann@uni-bayreuth.de; daniel.singer@uni-bayreuth.de; till.budde@uni-bayreuth.de; stephan.tremmel@uni-bayreuth.de}

1. INTRODUCTION

Due to external loads acting on rolling bearings, local contact deflections occur between the rolling elements and the raceway, allowing the contact partners to approach each other and form a finite contact surface. The shape of the contact surface and the resulting pressure distribution depend on the geometry of the contact partners and the applied external loads. In rolling bearings, a distinction is commonly made between point and line contacts [1]. For a roller that is in contact with the raceway without misalignment, Fig. 1 (a) illustrates the contact pressure distribution along the roller axis for two different roller profiles.
Many authors have developed different load-deflection relationships for line contacts, including Palmgren [2] and Dinnik [3]. To account for influences such as roller profile, tilting, and skewing, slice models are used in bearing simulations [4]. As shown in Fig. 1 (b), each roller is divided into n slices. When slices penetrate the raceway, as illustrated in Fig. 1 (c), the roller is in contact with the raceway. Based on the penetrations δ_i, which correspond to the local contact deflections, the normal contact forces are calculated according to the known load-deflection relationships. Interactions between the slices are often neglected as a trade-off between simulation accuracy and computational cost [4]. The latter is particularly crucial for dynamic simulations [4]. However, neglecting these interactions prevents accurate modeling of effects such as the pressure peaks at the roller ends shown in Fig. 1 (a, left). Teutsch and Sauer [5] and Yang et al. [6] therefore proposed slicing techniques in which the slices are coupled. In contrast to slice models, where the rollers are discretized in one direction, Li [7] discretized the contact surface in two directions. While the 2D discretization ensures high solution accuracy, it also incurs higher computational costs than slice models.
Teutsch and Sauer [5] reported deviations between their model and the solution of a finite element model. As we consider the solution from well-modeled finite element simulations as the benchmark, our main aim is to develop a slice model for line contacts with high accuracy and low computational cost, and to verify the solution against a 3D finite element contact simulation.

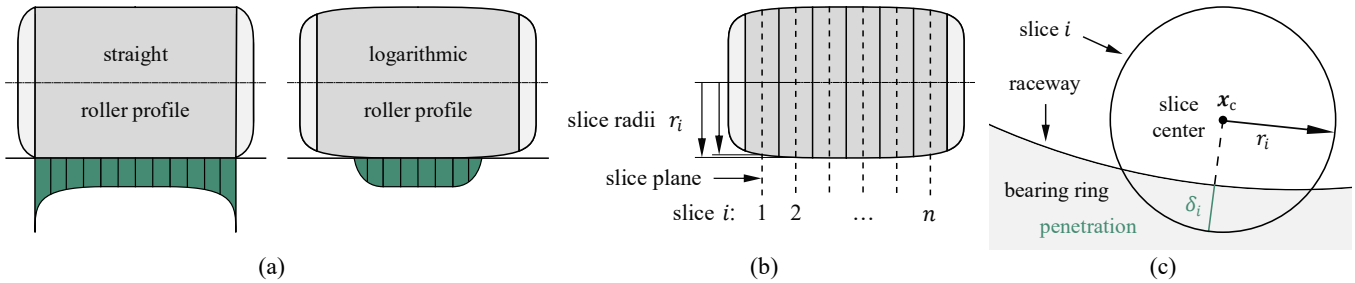

Figure 1. Roller-raceway contact: (a) contact pressure distribution [1], (b) slice model [4], and (c) slice in contact with raceway [4].

2. FINITE ELEMENT-BASED SLICE MODEL

The novel slice model uses finite element influence coefficients to express the load-deflection relationships of the slices and their interactions. The influence coefficients describe the linear-elastic displacement of slice $i = 1, \dots, n$ as a result of a unit normal force acting on slice $k = 1, \dots, n$. Therefore, the influence coefficients $c_{i,i}$ can be interpreted as the compliance of the slices and the influence coefficients $c_{i,k}$, $i \neq k$ as interactions between the slices. It is assumed that both contact partners are structured meshed in the axial direction, as shown in Fig. 2 (a). Each node row, i.e., the same axial coordinate, is considered as one slice. Mapping one or multiple element rows onto a single slice is beyond the scope of this work, but could be accomplished using the shape functions of the finite elements. Since linear-elastic behavior is assumed, the influence coefficients can be efficiently computed by performing a single LU decomposition of the stiffness matrix and solving the resulting system for multiple external unit force vectors as right-hand sides. This step is repeated for the roller and its contact partner, i.e., the raceway. The influence coefficients of the slices are then derived from the influence coefficients of the finite element nodes. Contact search is performed

as outlined in [4]. To determine the normal forces q_i from the penetrations δ_i, the following system of linear equations is solved:

$$\begin{bmatrix} c_{i,i} & \cdots & c_{i,n} \\ \vdots & \ddots & \vdots \\ c_{n,i} & \cdots & c_{n,n} \end{bmatrix} \begin{bmatrix} q_i \\ \vdots \\ q_n \end{bmatrix} = \begin{bmatrix} \delta_i \\ \vdots \\ \delta_n \end{bmatrix}. \tag{1}$$

From the normal contact force q_i, the semi-width b_i of the contact area of slice i is calculated as follows [1]:

$$b_i = \sqrt{\frac{8(1-\nu^2)}{\pi E \sum \rho_i} \frac{q_i}{l_i}} \tag{2}$$

with the Young's modulus E, the Poisson's ratio ν, the total curvature of the contacting bodies $\sum \rho_i$, and the length l_i of the slice i. According to [1], the maximum contact pressure $p_{\max_i}$ along the roller axis is

$$p_{\max_i} = \frac{2}{\pi} \frac{q_i}{b_i l_i}. \tag{3}$$

3. RESULTS AND DISCUSSION

The finite element-based slice model was verified for the roller-plate contact model shown in Fig. 2, where the lower surface of the plate is fixed and a displacement u is applied pressing the unprofiled roller into the plate [5]. As the reference solution, a finite element contact simulation is performed in Abaqus/CAE 2021 using a surface-to-surface contact discretization. The illustrated finite element contact model is the result of an extensive mesh study (meshing strategy, element type, and element size). With an increasing number of slices, the contact pressure distribution according to Teutsch and Sauer [5] converges toward the reference solution. The results from our model (FE-iCoeffs) agree better with the reference solution and require far fewer slices. The latter is relevant because the number of slices determines the matrix dimension in Eq. (1). The contact pressure of both models lies between the results of Palmgren [2] and Dinnik [3] and increases toward the edges of the roller. It should be noted that the edges of the roller represent points of singularity. Further results with roller tilting and a roller defect are shown in Fig. 3.

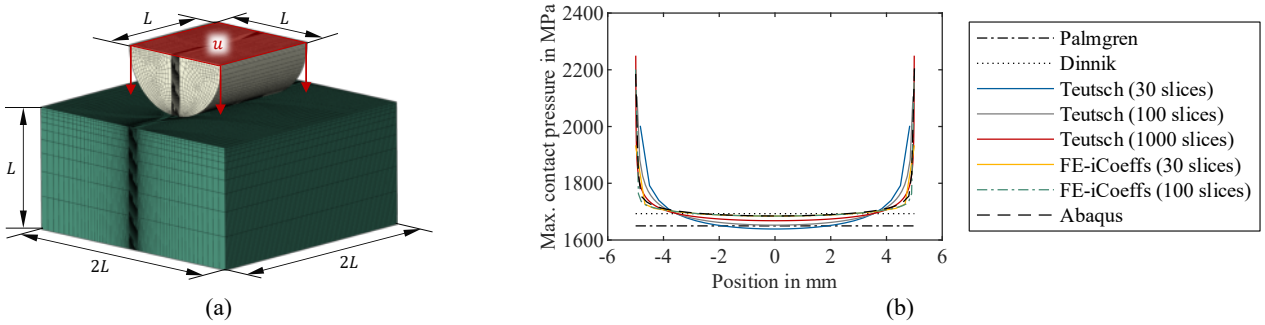

Figure 2. Roller-plate contact: (a) finite element model ($L = 10$ mm, $E = 208$ GPa, $\nu = 0.3$) and (b) contact pressure for $u = 0.01$ mm.

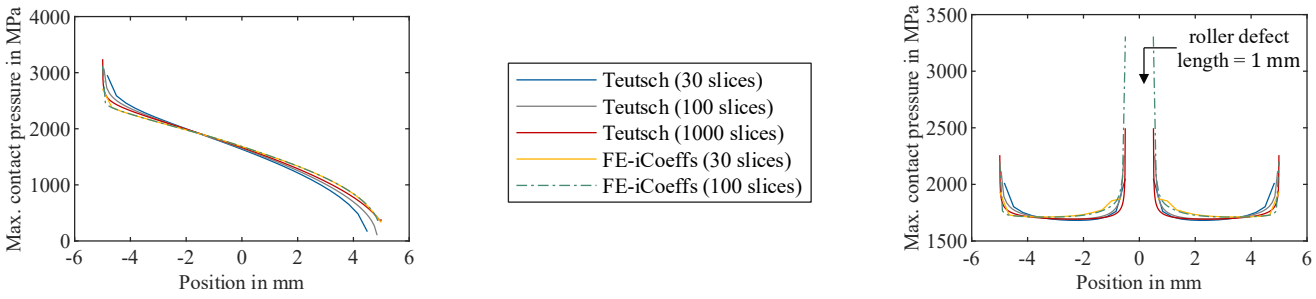

Figure 3. Roller-plate contact: contact pressure for $u = 0.01$ mm with (a) additional tilting ($6'$) of the roller and (b) roller defect.

REFERENCES

[1] T.A. Harris, M.N. Kotzalas, Essential Concepts of Bearing Technology, fifth ed., CRC Press, Boca Raton, USA, 2006.
[2] A. Palmgren, Grundlagen der Wälzlagertechnik, third ed., Franckh, 1964.
[3] H.A. Rothbart (Ed.), Mechanical design and systems handbook, 2nd ed., McGraw-Hill, New York, 1985.
[4] T. Baumann, B. Hahn, S. Tremmel, Integrating the elastic surroundings into multibody simulation of rolling bearings, Mech. Mach. Theory 220 (2026) 106365. https://doi.org/10.1016/j.mechmachtheory.2026.106365.
[5] R. Teutsch, B. Sauer, An Alternative Slicing Technique to Consider Pressure Concentrations in Non-Hertzian Line Contacts, J. Tribol. 126 (2004) 436–442. https://doi.org/10.1115/1.1739244.
[6] D. Yang, X. Wang, Y. Hou, 2023. An Improved Slicing Technique for Finite Line Contacts in the Modeling of Rolling Element Bearings. J. Tribol. 145, 084302. https://doi.org/10.1115/1.4062364.
[7] S. Li, A mathematical model and numeric method for contact analysis of rolling bearings, Mech. Mach. Theory 119 (2018) 61–73. https://doi.org/10.1016/j.mechmachtheory.2017.08.020.

FEASIBLE WRENCH SETS OF REDUNDANT PARALLEL MANIPULATORS

Joshua Flight[1], Clément Gosselin[1]

[1] Département de génie mécanique et de génie industriel, Université Laval, 1065 avenue de la Médecine, Québec (Qc), Canada, {joshua.flight.1@ulaval.ca; clement.gosselin@gmc.ulaval.ca}

1 INTRODUCTION

The maximum feasible wrench set is a fundamental characteristic of parallel manipulators (PMs). It serves to inform a designer of the maximum forces/torques that a robot architecture can transmit to its end-effector given its pose and actuator limits. Studies have shown that redundant actuation—where the manipulator has more actuators than there are dimensions in the task space—has important consequences for the kinematic and static capabilities of these types of manipulators.

Using the static-kinematic duality, we can express the linear mapping of the joint torques to the resultant wrench with the kinematic Jacobians of the manipulator. This is written as

$$\begin{aligned} \mathbf{J}^{-T}\mathbf{w} &= \mathbf{K}^{-T}\boldsymbol{\tau} \\ \mathbf{w} &= \mathbf{J}^{T}\mathbf{K}^{-T}\boldsymbol{\tau} \end{aligned} \tag{1}$$

where $\mathbf{w}$ is the n-dimensional wrench vector that the end-effector applies to its environment, $\boldsymbol{\tau}$ is the m-dimensional vector of joint torques, and $\mathbf{J}$ and $\mathbf{K}$ are the kinematic Jacobians of the PM.

2 REDUNDANCY IN PARALLEL MANIPULATORS

We consider two types of redundant actuation: kinematic redundancy and actuation redundancy [1] (see Fig. 1). A kinematically redundant PM has as many actuators as degrees of freedom (DOFs) and is therefore statically *determined*. A PM with actuation redundancy has more actuators than DOFs, and is statically *overdetermined*. These overconstraints can lead to antagonistic force components which cause internal stress at the end-effector.

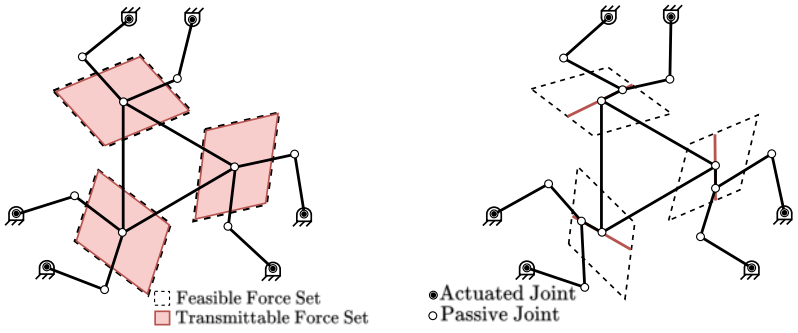

(a) Actuation Redundancy (b) Kinematic Redundancy

Figure 1: Types of redundancy in parallel manipulators. Forces are scaled by a factor of 10.

Each leg of a PM possesses its own feasible force set. A force from this set is deemed *transmittable* if it can be transmitted to the end-effector. In a PM with actuation redundancy, every force from the feasible force set of a given leg can be transmitted to the end-effector as shown in Fig. 1a. In a PM with kinematic redundancy, only forces from the feasible force set which do not induce motion of the redundant DOFs can be transmitted to the end effector [2] as shown in Fig. 1b.

3 FEASIBLE WRENCH SETS OF REDUNDANT PARALLEL MANIPULATORS

3.1 Feasible Sets in Joint-Space

The legs of a PM with actuation redundancy in a nonsingular configuration are only limited by the maximum joint torques. The feasible set in joint-space is therefore written as

$$\mathcal{B}_\infty = \{\boldsymbol{\tau} \in \mathbb{R}^m \mid ||\boldsymbol{\tau}||_\infty \leq \tau_{max}\} \tag{2}$$

which defines an m-dimensional hypercube in joint-space.
For kinematically redundant PMs, $\boldsymbol{\tau}$ must also be a minimum-norm solution to its corresponding wrench vector $\mathbf{w}$ since these are the only solutions which do not induce motion of the redundant DOFs. The feasible set is then

$$\mathcal{B}^0_\infty = \{\boldsymbol{\tau} \in \mathbb{R}^m \mid \boldsymbol{\tau} \in \text{range}((\mathbf{J}^T\mathbf{K}^{-T})^T),\ ||\boldsymbol{\tau}||_\infty \leq \tau_{max}\} \tag{3}$$

which is the intersection of the n-dimensional subspace defined by the row space of $\mathbf{J}^T\mathbf{K}^{-T}$ and the m-dimensional hypercube defined by $||\boldsymbol{\tau}||_\infty \leq \tau_{max}$.

3.2 Mapping to Wrench-Space

$\mathbf{J}^T\mathbf{K}^{-T}$ defines a linear transformation and is applied to sets $\mathcal{B}_\infty$ and $\mathcal{B}^0_\infty$ which are both convex and continuous. Bauer's maximum principle states that such functions attain their maximum at the extreme points of the sets they are applied to [3] and thus we need only consider the vertices of $\mathcal{B}_\infty$ and $\mathcal{B}^0_\infty$ when mapping to wrench-space.
This operation is trivial for PMs with actuation redundancy where the feasible set is $\mathcal{B}_\infty$. We simply map each vertex of $\mathcal{B}_\infty$ using the transformation defined in (1) and the resulting feasible wrench set is written as

$$\mathcal{W}_\infty = \{\mathbf{w} \in \mathbb{R}^n \mid \mathbf{w} = \mathbf{J}^T\mathbf{K}^{-T}\boldsymbol{\tau},\ \boldsymbol{\tau} \in \mathcal{B}_\infty\}. \tag{4}$$

For a PM with kinematic redundancy, we must determine the maximum wrenches that can be generated by minimum-norm solutions for $\boldsymbol{\tau}$ that also satisfy the actuator limits. To do so, we collect the linear inequalities as

$$\begin{bmatrix} (\mathbf{J}^T\mathbf{K}^{-T})^\dagger \\ -(\mathbf{J}^T\mathbf{K}^{-T})^\dagger \end{bmatrix} \mathbf{w} \leq \tau_{max} \begin{bmatrix} \mathbf{1}_{m\times 1} \\ \mathbf{1}_{m\times 1} \end{bmatrix}. \tag{5}$$

Then, we proceed iteratively by calculating candidate wrenches obtained by considering n active constraints at a time (i.e., n actuators at an extremum). If a candidate wrench satisfies the remaining $2m - n$ inequalities, it is added to the feasible wrench set $\mathcal{W}^0_\infty$. We repeat this procedure for each possible combination of n active constraints.

4 RESULTS

Fig. 2 shows the polyhedra representing the feasible wrench sets of the manipulators shown in Fig. 1.

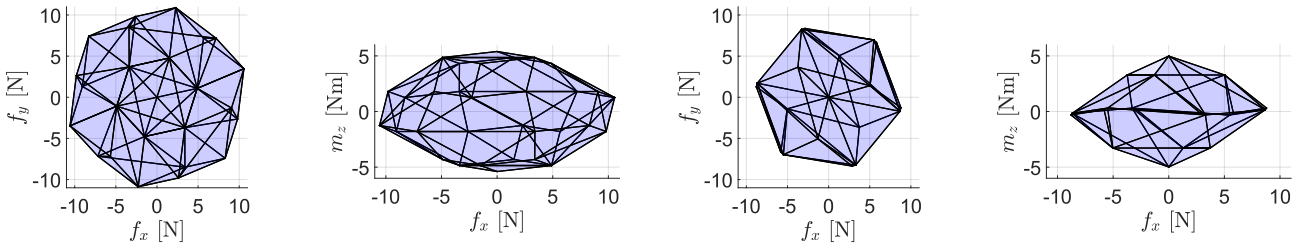

(a) Top-down view of $\mathcal{W}_\infty$ for PM in Fig. 1a
(b) Side view of $\mathcal{W}_\infty$ for PM in Fig. 1a
(c) Top-down view of $\mathcal{W}^0_\infty$ for PM in Fig. 1b
(d) Side view of $\mathcal{W}^0_\infty$ for PM in Fig. 1b

Figure 2: Polyhedra representing feasible wrench sets of the PMs in Fig. 1.

5 CONCLUSION

In this work, we present the first completely general methods for determining the maximum feasible wrench sets of PMs with kinematic or actuation redundancy. These novel methods are useful to designers for quantifying the wrenches that may be generated by a given architecture while considering the actuator limits and redundancy type.

ACKNOWLEDGMENTS

The authors would like to acknowledge the financial support of the Natural Sciences and Engineering Research Council of Canada (NSERC) through a doctoral scholarship (CGRS D) and discovery grant DG-89715 and the Institut de recherche Robert-Sauvé en santé et sécurité du travail (IRSST) through a doctoral scholarship.

REFERENCES

[1] C. Gosselin and L.-T. Schreiber, "Redundancy in parallel mechanisms: A review". *Applied Mechanics Reviews*, vol. 70, no. 1, pp. 1-15, 2018.

[2] P. Chiacchio, Y. Bouffard-Vercelli and F. Pierrot, "Force polytope and force ellipsoid for redundant manipulators". *Journal of Robotic Systems*, vol. 14, no. 8, pp. 613-620, 1997.

[3] H. Bauer, "Minimalstellen von funcktionen und extremalpunkte". *Archiv der Mathematik*, vol. 9, no. 4, pp. 389-393, 1958.

DESIGN, ANALYSIS, AND EXPERIMENTAL INVESTIGATION OF A NOVEL WEDGE-TYPE SELF-LOCKING CONNECTION MECHANISM FOR AIRCRAFT OPENING COVERS

Zhuoran Li[1], Shujun Chen[1], Jie Chen[1], Jing Zhao[1]

[1] College of Mechanical & Energy Engineering, Beijing University of Technology, Beijing 100124, China, {lzr0896@emails.bjut.edu.cn; sjchen@bjut.edu.cn; jchen@bjut.edu.cn; zhaojing@bjut.edu.cn}

1. INTRODUCTION

Traditional bolted connections for aircraft opening covers (AOCs) experience limited assembly efficiency and degraded aerodynamic performance. This has motivated the development of adaptive connection systems that can actively respond to complex service conditions. Wedge structures have been widely applied in high-load-bearing connection and locking systems due to their inherent self-locking capability and efficient force transmission. Previous studies have systematically investigated the mechanical behavior, self-locking criteria, and load-carrying characteristics of wedge-based self-locking structures. These studies have established a solid theoretical foundation for their design and application [1,2]. However, most research has focused on rigid structures or quasi-static conditions. Investigations into the self-locking stability of wedge mechanisms under vibrational environments remain limited. The introduction of flexure hinges and compliant mechanisms offers new opportunities for improving assembly adaptability, energy absorption, and impact resistance. Although existing studies indicate that properly designed flexure hinges can enhance mechanical performance while retaining sufficient load-bearing capacity, their integration with wedge self-locking mechanisms for high-reliability connection applications remains largely unexplored [3]. Under vibrational loading, tangential stiffness degradation induced by microslip at contact interfaces is recognized as a key factor in locking performance deterioration. The Iwan model has been extensively used to characterize the nonlinear behavior and energy dissipation of contact interfaces under cyclic loading. It provides an effective framework for analyzing vibration-induced self-locking failure [4]. However, its application to wedge self-locking connection mechanisms, particularly regarding structural parameters and energy evolution, remains limited. Motivated by these gaps, this study proposes a novel wedge-based self-locking connection mechanism. This mechanism integrates flexure hinge compliance with wedge surface self-locking principles, forming an over-constrained configuration to enhance anti-loosening robustness. To systematically investigate preload stability and self-locking reliability under vibrational conditions, mechanical modeling, vibration-coupled dynamic simulations, and experimental validation are conducted. The goal is to provide a technical solution for rapid connection and disconnection in aircraft opening cover structures.

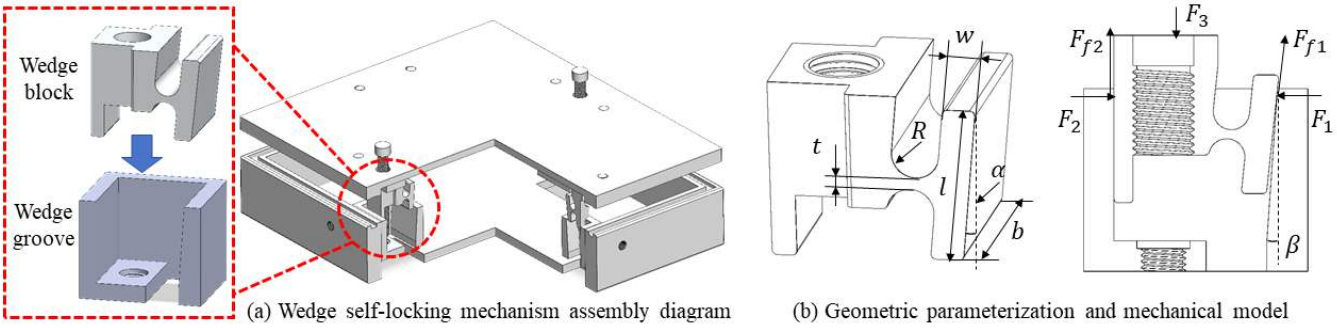

(a) Wedge self-locking mechanism assembly diagram (b) Geometric parameterization and mechanical model

Figure 1. Assembly schematic and geometric parameterization of the wedge-type self-locking mechanism

2. MODEL AND METHODOLOGY

2.1. Establishment of Mechanical Model for Flexible Wedge Self-Locking Connection Mechanism

As shown in Fig. 1a, the flexible wedge self-locking connection mechanism consists of wedge blocks and wedge grooves arranged between the aircraft fuselage and the aircraft opening covers (AOCs). During assembly, a tooling bolt rotates to drive the wedge block into the wedge groove. With the insertion of the wedge block, small elastic deformation occurs on the wedge surfaces under contact constraints, storing elastic strain energy and generating preload. Meanwhile, the rotation angle of the cantilever end varies from the initial angle α to the final angle β, leading to a stable self-locking state through the combined effects of wedge-surface friction and the elastic restoring force of the flexible hinge.

Based on this mechanism, a mechanical model is established by considering the small-deformation compliance of the flexible hinge and the self-locking behavior of the wedge contact surfaces to investigate the influence of key structural parameters. As shown in Fig. 1b, the structural parameters of a single wedge block and its force conditions during preloading are defined, where the minimum thickness t and notch radius R of the flexible hinge, together with the length l and width b of the wedge cantilever end, are identified as the parameters governing stiffness, self-locking capability, and preload performance, providing a basis for structural design and performance optimization.

2.2.Analysis of Vibration Response Characteristics of Flexible Wedge Self-Locking Mechanism

To address preload attenuation and self-locking failure under vibration, a tangential stiffness weakening model based on the Iwan model is introduced for vibration-coupled transient dynamic analysis. The results indicate that self-locking stability is strongly related to vibration input energy and wedge angle: higher vibration energy accelerates microslip at the contact interface, leading to earlier preload attenuation and eventual failure, as shown in Fig. 2a.

2.3.Surrogate Model-Driven Multi-Objective Optimization Design and Experimental Verification

A surrogate model–based multi-objective optimization framework was developed to determine the optimal parameter combination balancing preload stability and structural stress. Comparative experiments were performed on a dedicated experimental platform (Figs. 2b–c), validating the accuracy of the proposed mechanical model and vibration-coupled dynamic analysis. The results demonstrate that the preload retention capability of the optimized mechanism is significantly enhanced, as summarized in Table 1.

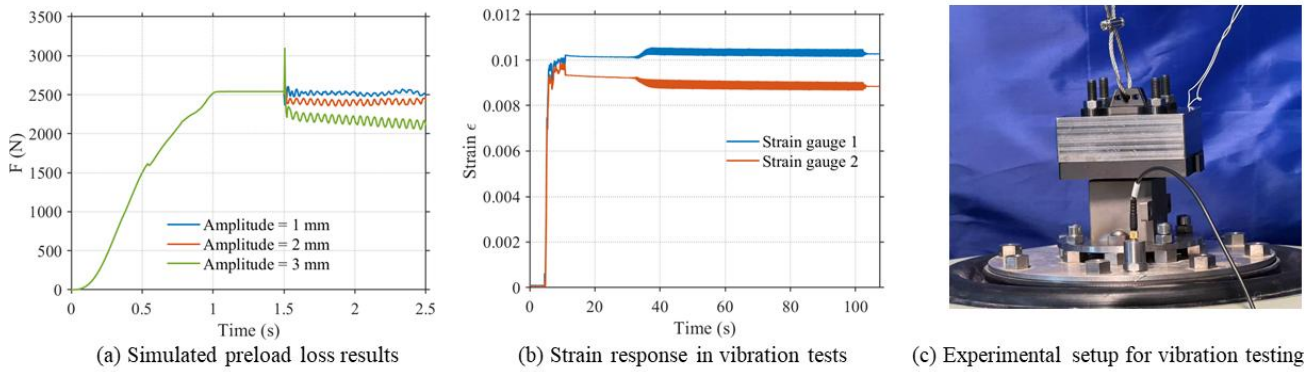

(a) Simulated preload loss results (b) Strain response in vibration tests (c) Experimental setup for vibration testing

Figure 2. Simulation responses and experimental system setup

Table 1. Comparison and analysis of results before and after optimization.

Item	Preload (N)	Preload loss ratio (%)	Applied mass(kg)	Vibration test result
Before optimization	629.159	42.094	18.87	Loosening observed at 20 Hz, 4 mm
After optimization	799.51	26.891	23.98	No loosening at 20 Hz, 4 mm

3. CONCLUSIONS

This study proposes and experimentally verifies a novel flexure hinge–wedge self-locking mechanism for aircraft opening covers under vibrational conditions. The dominant effects of geometric and contact mechanical parameters on locking stability are clarified, and the correlations among self-locking failure, wedge angle, and vibration parameters are revealed. Surrogate model–driven optimization significantly enhances the mechanism performance: the preload attenuation rate is reduced by 15.2%, the maximum load-bearing capacity reaches 23.98 kg, and the self-locking reliability achieves 100% under rated loading. Self-locking loosening is shown to be strongly correlated with vibration input energy, and the opening cover disassembly and assembly time is shortened to the minute level compared with conventional bolted joints. The proposed mechanism satisfies the application requirements of aircraft opening covers and provides an effective design basis for self-locking connection structures operating under complex vibrational environments.

REFERENCES

[1] J. Liu, H. Gong and X. Ding, “Effect of ramp angle on the anti-loosening ability of wedge self-locking nuts under vibration”. Journal of Mechanical Design, 140(7), 072301, 2018.

[2] F. Chen, J. Zhang, C. Wang, F. Yuan, W. Wang, S. Yang and Q. Di, “Three-dimensional mechanical characteristics analysis of bolted joints and loosening mechanism”. Engineering Failure Analysis, 157, 107894, 2024.

[3] K. Wu, G. Zheng, G. Chen and S. Awtar, “A body-frame beam constraint model”. Mechanism and Machine Theory, 192, 105517, 2024.

[4] H. Liu, W. Sun, D. Du, X. Liu and H. Ma, “A novel bolted joint model with stick-slip hysteresis properties considering pressure-dependent stiffness: Theoretical and experimental investigations”. Tribology International, 187, 108717, 2023.

ANALYSIS OF THE CONTACT STRESS OF BEVELOID HELICAL GEARS WITH PARALLEL AXES

Miryam B. Sánchez[1], Giovanni Mottola[2], Miguel Pleguezuelos[1], Alfonso Fuentes-Aznar[3], José I. Pedrero[1], Marco Carricato[4]

[1] UNED, Departamento de Mecánica, Juan del Rosal 12, 28040 Madrid, Spain, {msanchez@ind.uned.es, mpleguezuelos@ind.uned.es, jpedrero@ind.uned.es}

[2] University of Messina, Department of Engineering, Contrada di Dio, Sant'Agata, Messina, 98166, Italy, {giovanni.mottola@unime.it}

[3] Rochester Institute of Technology, Department of Mechanical Engineering, Kate Gleason College of Engineering, 76 Lomb Memorial Drive, 14623 Rochester, NY, USA, {afeme@rit.edu}

[4] University of Bologna, Department of Industrial Engineering, Viale del Risorgimento 2, Bologna, 40136, Italy, {marco.carricato@unibo.it}

1. INTRODUCTION

A beveloid gear is a spur or helical gear with outside radius, root radius, and shift coefficient that vary linearly along the tooth width, while the module and the base radius are constant; thus, their external profile is conical (with apex angle β_c), but they transmit torque like standard cylindrical gears. A beveloid gear can be generated quickly and cheaply by most standard hobbing machines. When mounted with parallel axes and opposite cone angles, beveloid gears allow the backlash to be controlled by small relative axial displacements (for instance, using springs): thus, they are also used for precision gearboxes [1].

Due to the variation of the shift coefficient, both undercut and pointing may arise at the extreme sections of a gear (called *heel* and *toe*, with the latter being the one closer to the cone apex). In addition, contact may occur at points on the profile with small radii of curvature: therefore, the contact stress is a critical design factor. To assess it, Hertz's equation can be used, but this requires a precise estimate of the distribution of the transmitted load along the contact line and throughout the meshing cycle.

In a previous work [2], an analytical model of the mesh stiffness and load sharing based on the minimum elastic potential energy principle was developed for beveloid *spur* gears. In this work, the same model is applied to beveloid *helical* gears. The contact geometry is investigated, considering pointing and undercut, and the contact stress is assessed. The results are validated by comparison with *Finite Element Analysis* (FEA). The proposed analytical model is computationally efficient and provides accurate results in a very short time, which greatly accelerates optimization studies.

2. ANALYTICAL MODEL

Fig. 1-left shows the plot of the parameter ξ, as defined in [2], at the inner and outer points of contact for each transverse section (defined by the axial coordinate z) of a beveloid helical pinion-wheel gear pair with parallel axes, with 18 and 120 teeth, respectively; both gears have $\beta_c = 5°$ and helix angle equal to 3°.

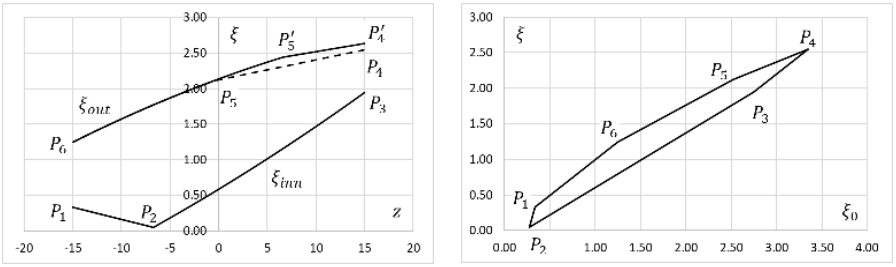

Figure 1. Limits ξ_{inn} and ξ_{out} of the contact interval at each transverse section (left) and contact map (right).

The most general case will be considered, where both undercut and vacuum gearing[1] occur (segment $P_1 - P_2$). Also, in segment $P_5' - P_4'$, the pinion would have pointed teeth, with zero tip surface. As these teeth would have very small radii of curvature (and thus large stress concentration), they would not be able to transmit power; thus, the outside radius at the pinion heel is reduced

[1] This means that the outside radius on one gear does not correspond to a contact point on the involute part of the mating tooth profile of the other gear [2].

using a conical cut with 3° apex angle, starting at the middle transverse section ($z = 0$, point P_5) and ending at the heel ($z = z_{max}$, point P_4). Figure 1-right shows the contact map of the gear pair. The parameter ξ_0, which defines the meshing position, is the value of ξ for the contact point at the profile of the pinion toe ($z = z_{min} = -15$ mm), or its extension if ξ_0 is greater than $\xi_{out}(z_{min})$. The instantaneous contact line for a tooth pair is represented by a vertical segment $\xi_0 = \xi_0'$ inside the map. The other tooth pairs simultaneously in contact correspond to $\xi_0 = \xi_0' \pm 1$, $\xi_0' \pm 2$, and so on. Note that contact begins at point P_2 (not at P_1), as the undercut is so much greater at $z = z_{min}$ than at $z = z(P_2)$ that $\xi_{inn}(z_{min}) > \xi_{inn}(z(P_2))$.
The *Single Mesh Stiffness* (SMS) $K_M(\xi_0)$ of a tooth pair is the integral over z of the infinitesimal stiffness $\mathrm{d}K_M(\xi, z)$, related to bending and contact deformations due to the force F through one tooth pair, along the instantaneous contact line (Fig. 2-left).

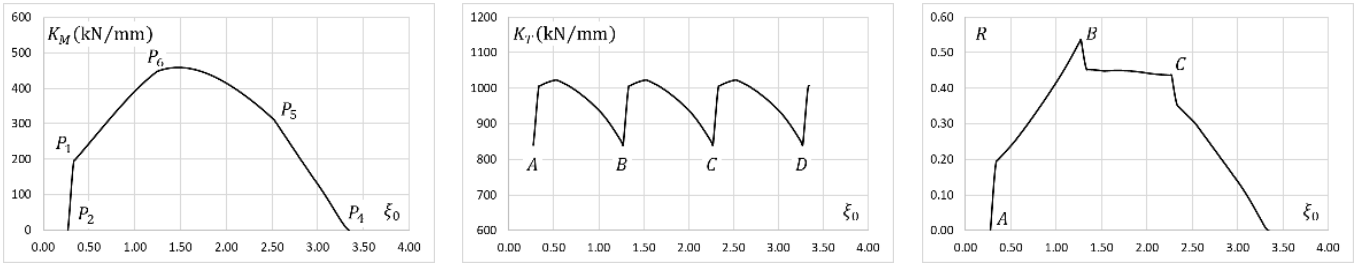

Figure 2. Plots of the SMS (left), total mesh stiffness (center), and load sharing ratio (right) as functions of the meshing position.

The *total mesh stiffness* $K_T(\xi_0)$, which varies over time, is the sum of the SMS for all the tooth pairs in contact (Fig. 2-center). As expected, $K_T(\xi_0)$ is periodic in ξ_0, with period 1. Point A corresponds to the value of ξ_0 at P_2 (start of contact). Points B, C, and D, at which $K_T(\xi_0)$ increases sharply, correspond to the start of contact of the successive tooth pairs. Finally, the *load sharing ratio* R (Fig. 2-right) is $F/F_T = K_M(\xi_0)/K_T(\xi_0)$, where F_T is the total transmitted force through all flanks; R decreases sharply when a new tooth pair starts being in contact.

3. CONTACT STRESS ANALYSIS AND FINITE ELEMENT VALIDATION

The load distribution along the instantaneous contact line is $\mathrm{d}F(\xi, \xi_0) = \big(\mathrm{d}K_M(\xi)/K_M(\xi_0)\big)F(\xi_0) = \big(\mathrm{d}K_M(\xi)/K_T(\xi_0)\big)F_T$ [2]. The contact stress $\sigma_H(\xi, \xi_0)$ is then computed using the Hertz's equation, knowing the load per unit length and the curvature radii of the involute flanks at each contact point. The maximum σ_H (along the contact line) as a function of the meshing position is in Fig. 3-left. Figures 3-center and 3-right show the FE model used for the analysis and the results obtained.

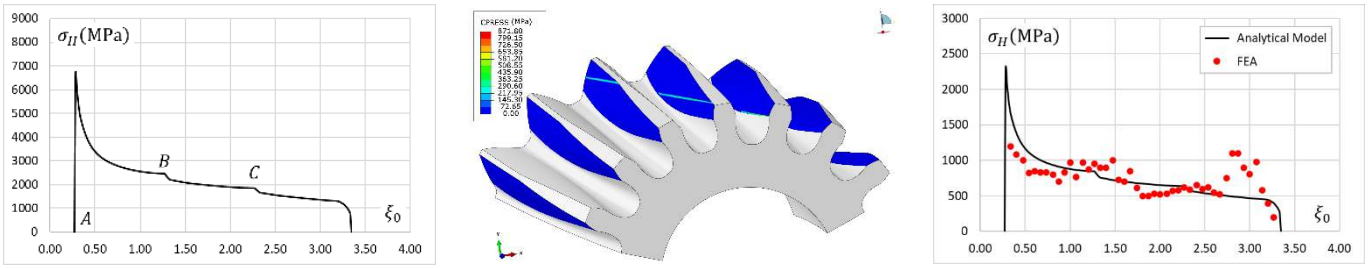

Figure 3. Maximum σ_H along the meshing cycle (left), FE model (center), and comparison of the analytical model with the FEA (right).

4. RESULTS AND DISCUSSION

The high contact stress σ_H at the beginning of contact, in point P_2, is due to the very small curvature radius of the flank profile near the undercut zone. A reduction of the cone angle β_c will result in an inner point of contact farther away from the gear axis, with higher curvature radius, thus with lower σ_H. A reduction of the face width on the toe side, removing the undercut, will result in higher load per unit length but also higher curvature radii on average, so the maximum σ_H may be lower. The proposed analytical model provides accurate results and is computationally efficient, thus enabling optimization studies. Also, it includes practically relevant design cases (pointed teeth, undercut, and vacuum gearing) which have received little attention so far.

ACKNOWLEDGEMENTS

Thanks are expressed to the Spanish Council for Scientific and Technological Research for the support of the project PID2022-142632OB-I00.

REFERENCES

[1] G. Sciarra, G. Mottola, G. Casamenti, and M. Carricato, "Omni: A low-backlash planetary Wolfrom gearbox with beveloid gears for robotic applications". *Mechanism and Machine Theory*, 214, 106098, 2025.
[2] G. Sciarra, G. Mottola, M. Pleguezuelos, M. B. Sánchez, M. Carricato, and J. I. Pedrero, "Analysis of the contact stress of beveloid gears with straight teeth and parallel axes". *Mechanism and Machine Theory*, 214, 106156, 2025.

RELATIVE POSITION ERROR IDENTIFICATION AND COMPENSATION FOR DUAL-CONE ENVELOPING HOURGLASS WORM VIA SAO-BP NEURAL NETWORK

Zhenglin Yang[1], Yonghong Chen[1], Jin Gao[1], Chenyang Dou[1], Fei Liu[1], Wenjun Luo[1], Bingkui Chen[1]

[1] State Key Laboratory of Mechanical Transmission for Advanced Equipment, Chongqing University, Chongqing 400044, PR China, {202107131131t@cqu.edu.cn; yh_chen@cqu.edu.cn; 202207131416@stu.cqu.edu.cn; 20230701015@stu.cqu.edu.cn; lfei@cqu.edu.cn; wjluo@cqu.edu.cn; bkchen@cqu.edu.cn}

1. INTRODUCTION

The dual-cone enveloping hourglass worm is widely utilized in heavy-duty transmissions due to its superior load capacity and multi-tooth meshing [1]. However, achieving high machining accuracy remains challenging, primarily due to the relative position error between the tool and workpiece during manufacturing [2]. To address this issue, neural network-based methods are often employed to identify and compensate for such errors. Yet, conventional backpropagation (BP) networks are prone to local optima, which limits prediction accuracy. Therefore, metaheuristic algorithms are frequently integrated to optimize the network's initial weights and biases [3].

This study analyzes the influence of individual relative position error on the tooth surface accuracy of the dual-cone enveloping hourglass worm. A refined SAO-BP algorithm is proposed, which incorporates a short training stage to enhance identification accuracy. The method achieves precise error identification and compensation, leading to significantly improved machining precision.

2. MAIN RESEARCH CONTENTS

Fig. 1 presents the enveloping coordinate system for the dual-cone enveloping hourglass worm with relative position errors. By introducing six relative position errors between the dual-cone grinding wheel and the worm workpiece, the influence of different relative position errors on the final machining accuracy is analyzed. Based on the coordinate system shown in Fig. 1, the tooth surface equation of the worm incorporating relative position errors is derived.

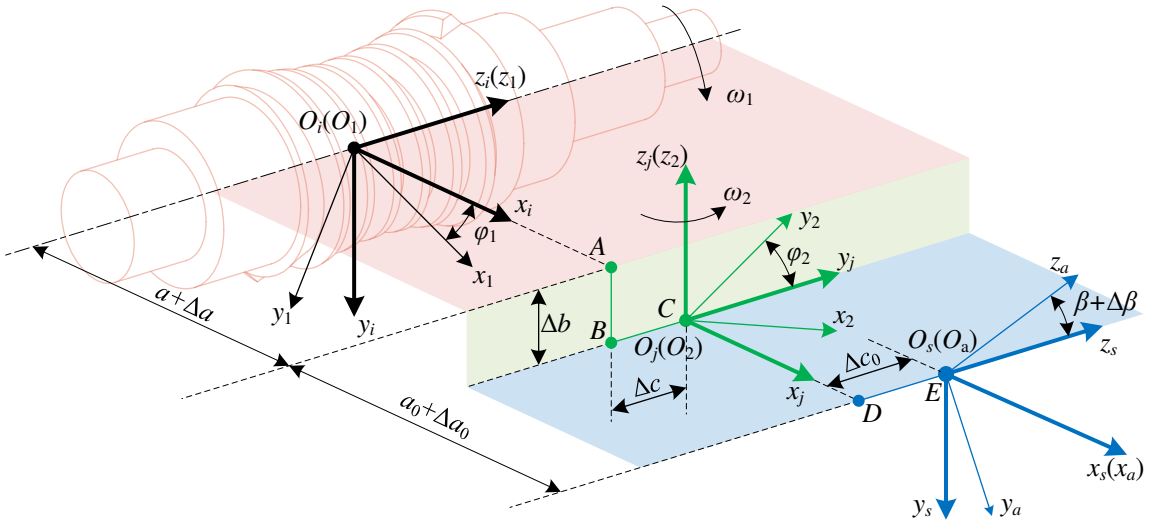

Fig. 1 Coordinate systems of dual-cone enveloping hourglass worm with relative position errors

Tooth surface accuracy is conventionally assessed through helix line deviation, which lacks suitability for comprehensive quantitative analysis. This study therefore employs the ISO 1328-1 standard to decompose helix line deviation into four key parameters: $F_{f\beta}$, $f_{H\beta}$, $f_{f\beta}$, and f_{pz}, as illustrated in Fig. 2. Each parameter quantifies distinct characteristics of machining errors, establishing a foundation for subsequent sensitivity analysis and identification of relative position errors.

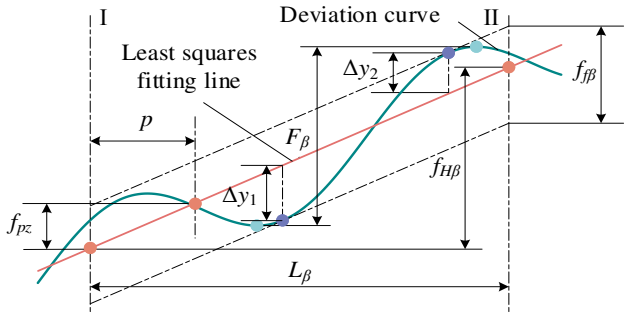

Fig. 2 Explanation of the tooth surface deviation key parameters calculation

Fig. 3 presents a sensitivity analysis of six relative position errors on tooth surface accuracy. The results indicate that center distance error and axial position error exert the most significant influence on machining precision. Consequently, subsequent analysis focuses specifically on the identification and compensation of these two dominant error sources.

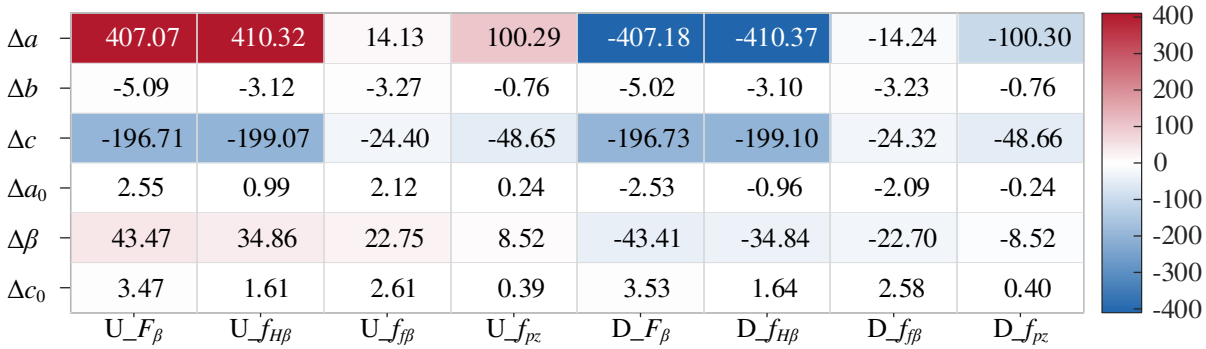

Fig. 3 Sensitivity of tooth surface characteristics to relative position errors

The proposed SAO-BP algorithm introduces a short-training phase during optimization, enabling the fitness function to assess early convergence behavior. This results in more reliable initialization and lower final error. Eight characteristic values, derived from the four helix deviation parameters extracted from both the left and right tooth surfaces, serve as input features for identifying the specific relative position error. As shown in Fig. 4, comparative experiments demonstrate that SAO-BP achieves higher identification accuracy with minimal data fluctuation among BP, PSO-BP, and SAO-BP networks, confirming its predictive advantage.

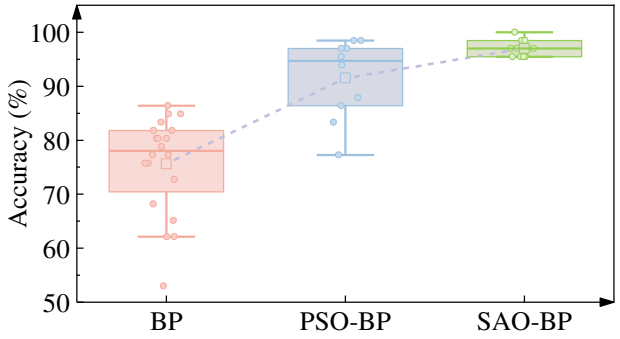

Fig. 4 Boxplots of prediction accuracy for BP, PSO-BP, and SAO-BP

ACKNOWLEDGMENTS

This work was supported by the National Natural Science Foundation of China (Grant No. 52575050) and the Natural Science Foundation of Chongqing (Grant No. CSTB2024NSCQ-LZX0028).

REFERENCES

[1] C. J. Rui, H. T. Li, J. Yang, W. J. Wei, X. Z. Dong, “A designing and generating method for grinding relief surfaces of a dual-cone double-enveloping hourglass worm gear hob”, *Journal of Mechanical Design*, 140, 123301, 2018.

[2] S. Ding, Z. Q. Song, W. W. Wu, E. K. Guo, X. D. Huang, A. P. Song, “Geometric error modeling and compensation of horizontal CNC turning center for TI worm turning”, *International Journal of Mechanical Sciences*. 167, 105266, 2020.

[3] J. L. Liu, C. Ma, S. L. Wang, “Data-driven thermal error compensation of linear x-axis of worm gear machines with error mechanism modeling”, *Mechanism and Machine Theory*. 153, 104009, 2020.

RESEARCH ON MESHING PERFORMANCE INVESTIGATIONS OF THE CURVE-CONSTRUCTED HOURGLASS WORM DRIVE

Jin Gao[1], Yonghong Chen[1], Zhengling Yang[1], Chenyang Dou[1], Fei Liu[1], Wenjun Luo[1], Bingkui Chen[1]

[1] State Key Laboratory of Mechanical Transmission for Advanced Equipment, Chongqing University, Chongqing 400044, PR China, {202207131416@stu.cqu.edu.cn; yh_chen@cqu.edu.cn; 202107131131t@cqu.edu.cn; 20230701015@stu.cqu.edu.cn; lfei@cqu.edu.cn; wjluo@cqu.edu.cn; bkchen@cqu.edu.cn}

1. INTRODUCTION

Adoption of hourglass worm drives in low-speed, heavy-duty applications such as solar rotary reducers, mining equipment, and lifting machinery has steadily increased because of their high gear ratio, high load-carrying capacity, and self-locking capability[1]. In conventional designs, the tooth flanks are formed by enveloping generation, leading to complex geometry and multi-tooth line contact. While this enhances load sharing and smoothness, it also heightens sensitivity to machining and assembly deviations, tightening tolerances and limiting manufacturing throughput.

Replacing line contact with point contact has been widely recognized as an effective way to reduce error sensitivity and facilitate manufacturing[2, 3]. However, most reported point-contact hourglass worm drives still generate the worm flank by surface enveloping, so precision grinding remains indispensable.

In this study, grounded in conjugate-curve meshing theory, a novel curve-constructed hourglass worm drive is presented, delivering high machining efficiency and overload capacity. Considering the broad availability of standard three-axis CNC lathes [4], the proposed design incorporates turning constraints to enable efficient manufacture on general-purpose equipment.

2. MAIN RESEARCH CONTENTS

The coordinate-frame system for the proposed curve-constructed hourglass worm drive is defined as shown in Fig. 1, and will be used throughout the following derivation of the conjugate curve.

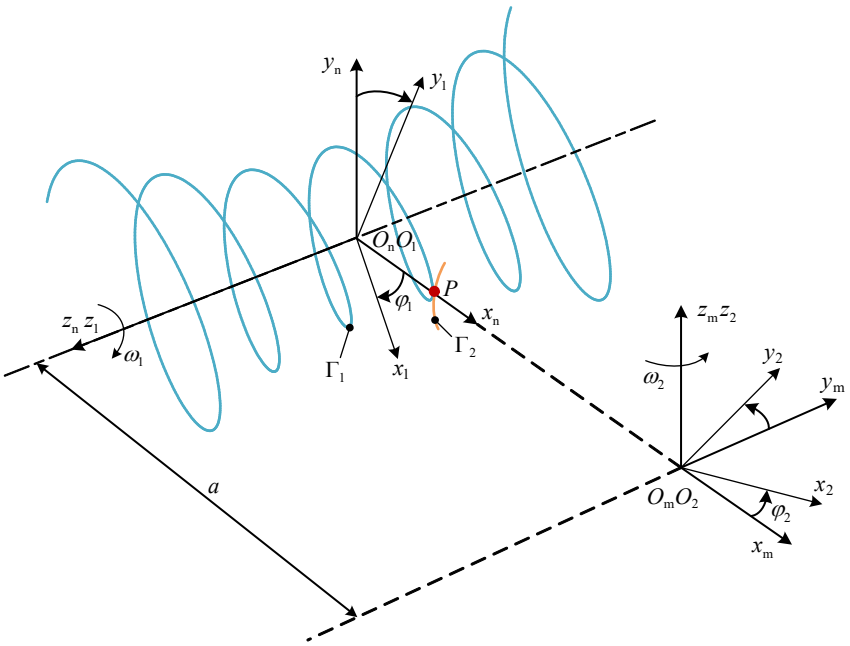

Fig. 1. Coordinate frames describing curve conjugation motion for the curve-constructed hourglass worm drive.

The meshing function of the curve-constructed hourglass worm drive is determined as

$$\Phi = \boldsymbol{n}_n \cdot \boldsymbol{v}_{12}^1 = 0. \tag{1}$$

where $\boldsymbol{n}_n$ is the unit normal vector of the toroidal worm helix along the prescribed direction, and v_{12}^{I} is the relative velocity of the hourglass worm drive.

Figure. 2 illustrates the main procedure for constructing the proposed hourglass worm pair from two main curve elements. The spatial generating curves Γ_1 and Γ_{2a} are obtained from the conjugate-curve solution, whereas the mid-plane tooth-profile curves Γ_{c1} and Γ_{c2} are a freely definable curve pair on the mid-plane. This separation endows the proposed hourglass worm drive with enhanced design flexibility.

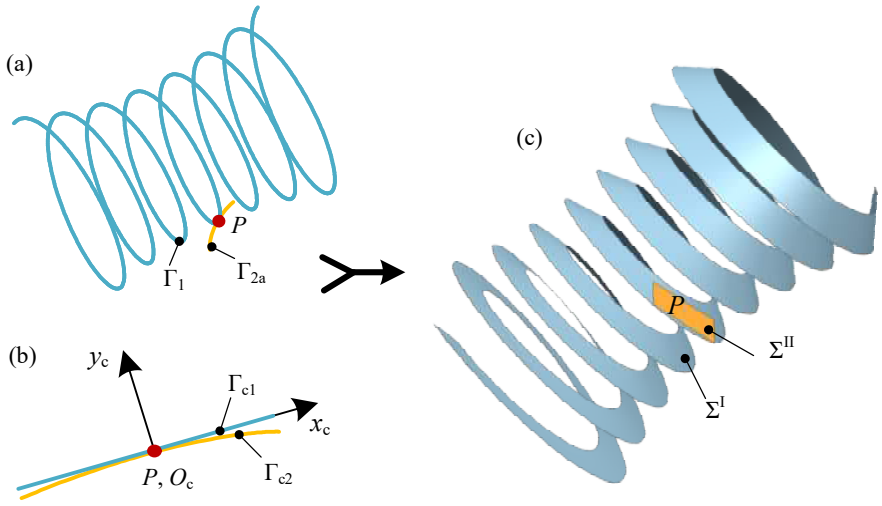

Fig. 2. Geometric construction of the tooth surfaces: (a) generating curve; (b) mid-plane tooth profiles; (c) resulting tooth surfaces.

To verify the contact characteristics and feasibility of the proposed hourglass worm drive, tooth contact analysis (TCA) is conducted, and the numerical results are shown in Fig. 3, demonstrating simultaneous multi-tooth point contact.

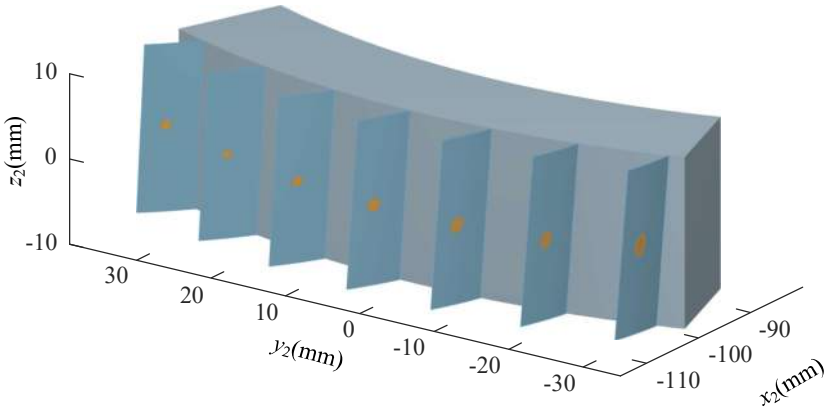

Fig. 3. Contact areas of the curve-constructed hourglass worm drive

Following the proposed design method, specific tooth surface designs with high load-carrying capacity will be developed, and prototypes will be manufactured and tested to validate their contact performance and overload capability.

ACKNOWLEDGMENTS

This work was supported by the National Natural Science Foundation of China (Grant No. 52575050) and the Natural Science Foundation of Chongqing (Grant No. CSTB2024NSCQ-LZX0028).

REFERENCES

[1]. Z.T. Li, Y.H. Chen, W.J. Luo, B.K. Chen, “Study on the meshing evolving mechanism of a novel self-evolution hourglass worm drive”, *Mechanism and Machine Theory*, 178, 105074, 2022.

[2]. Z.T. Li, Y.H. Chen, W.J. Luo, B.K. Chen, “Study on meshing performance of a novel point-contact hourglass worm drive based on modified involute”, *Mechanism and Machine Theory*, 185, 105339, 2023.

[3]. W. Ren, H.T. Li, S.L. Zhang, M.M. Li, J. Li, T.Y. Wang, M. Ma, “A method for point-contact conjugate tooth surfaces with a constant instantaneous transmission ratio generated by point-contact conjugate involute helicoids”, *Mechanism and Machine Theory*, 185, 105324, 2023.

[4]. S. Ding, H. Zhang, E. Guo, W.W. Wu, Y.F. Zhang, A.P. Song, “Integrated roughing, finishing and chamfering turning process of toroidal worm manufacture on a general CNC lathe”, *Journal of Manufacturing Processes*, 70, 341–349, 2021.

DYNAMIC ANALYSIS OF CURVED COMPLIANT MECHANISMS.

Vivien Platl[1] and Lena Zentner[1]

[1] Technische Universität Ilmenau, Max-Planck-Ring 14, 98693 Ilmenau, Germany{vivien.platl@tu-ilmenau.de}

1 INTRODUCTION

Compliant mechanisms, which achieve motion and force transmission through elastic deformation rather than rigid joints, are critical in various technical applications [1]. Key areas of those include robotics, precision engineering and microelectromechanical systems as these often require high precision, reduced weight, and minimal maintenance [2]. Their dynamic analysis is a key aspect in the design phase, with the natural frequencies being a key parameter [3] Curved compliant mechanisms introduce complex dynamic behaviors due to their geometry, making accurate analytical modeling essential for predicting natural frequencies and mode shapes. We have previously proposed an efficient analytical method as an alternative to the popular FEM analysis, which enables the fast and independent calculation of the natural frequencies of compliant mechanisms [4]. While previously only applied to straight segments, the current work demonstrates its successful extension to curved geometries using the balance spring as a representative example.

2 METHODOLOGY

The following investigations are based on our preliminary work regarding the dynamic analysis of serial compliant mechanism with the developed analytical method based on the Euler-Bernoulli beam theory and the transfer matrix method [4, 5]. In short, free vibration equations for each segment are assembled into the full mechanism using boundary and transition conditions. These can be expressed compactly in matrix-vector form, resulting in a single 6×6 system matrix $\mathbf{T}_{\text{sys}}$ whose determinant yields the natural frequencies satisfying the characteristic equation, see Eq. (1).

$$\mathbf{0} = \mathbf{T}_n \mathbf{T}_{n-1} \cdots \mathbf{T}_1 \mathbf{T}_0 \mathbf{K}_0 = \mathbf{T}_{\text{sys}} \mathbf{K}_0 \quad \rightarrow \quad 0 = |\mathbf{T}_{\text{sys}}(\omega)| \tag{1}$$

This methodology enables the rapid calculation of natural frequencies for any mechanism. Building on this foundation, the present work applies the methodology to the balance spring to demonstrate its validity for curved structures.

2.1 Balance Spring

The basic structure of a balance spring is an Archimedean spiral with a lever attached at its end, see Fig. (1 (a)). To apply the aforementioned analytical method, the spiral and its lever have to be discretized into N_{seg} straight segments of equal length L_{seg}. The Archimedean spiral is generally defined by Eq. (2).

$$r(\theta) = r_{\text{in}} + b\,\theta \quad \text{where} \quad b = \frac{r_{\text{out}} - r_{\text{in}}}{\theta_{\text{end}}} \quad \text{and} \quad \theta_{\text{end}} = 2\pi N_{\text{turn}} \tag{2}$$

The exact arc length of the spiral is derived using the polar coordinates and it can be approximated if $b \ll r(\phi)$ holds true, as given by Eq. (3).

$$s(\theta) = \int_0^{\theta} \sqrt{r(\phi)^2 + b^2}\, d\phi \;\approx\; \int_0^{\theta} r(\phi)\, d\phi, \qquad s_{\text{end}} \approx \int_0^{\theta_{\text{end}}} \left(r_{\text{in}} + \frac{r_{\text{out}} - r_{\text{in}}}{\theta_{\text{end}}} \theta \right) d\theta = r_{\text{in}} \theta_{\text{end}} + \frac{r_{\text{out}} - r_{\text{in}}}{2} \theta_{\text{end}} \tag{3}$$

Using this approximation enables the calculation of arc length for any spiral within the given limits, such as the depicted total arc length s_{end}.

2.2 Discretization

To discretize the curve into N_{seg} segments, the segment length is calculated as $L_{\text{seg}} = s_{\text{end}}/N_{\text{seg}}$. The segments endpoints are positioned along the spiral at equal arc length intervals $\sigma_k = k\, L_{\text{seg}}$ with $k = 0, 1, \ldots, N_{\text{seg}}$. To obtain the polar angle θ_k corresponding to the arc length position σ_k, the approximation from Eq. (3) is employed by setting $s(\theta_k) = \sigma_k$. This leads to the quadratic relation in Eq. (4).

$$\sigma_k = r_{\text{in}}\, \theta_k + \frac{b}{2}\, \theta_k^2 \quad \Rightarrow \quad \theta_k = \frac{-r_{\text{in}} + \sqrt{r_{\text{in}}^2 + 2b\,\sigma_k}}{b} \quad (\theta_k \geq 0), \tag{4}$$

With the obtained angles θ_k, the Cartesian coordinates (x_k, y_k) of each transition point are computed from Eq. (2) to derive the absolute orientation angle of segment m (connecting points $m-1$ and m) with $m = 1, \ldots, N_{\text{seg}}$. Finally, this enables the calculation of the relative angle between two consecutive segments, all given by Eq. (5).

$$x_k = r(\theta_k)\cos\theta_k, \quad y_k = r(\theta_k)\sin\theta_k, \quad \alpha_m^{\text{abs}} = \arctan\left(\frac{y_m - y_{m-1}}{x_m - x_{m-1}}\right), \quad \rightarrow \quad \alpha_m^{\text{rel}} = \varphi_{m+1}^{\text{abs}} - \alpha_m^{\text{abs}}. \tag{5}$$

The segment length and relative angle are used to model the balance spring with the analytical method.

3 RESULTS

For the studies, we used the balance spring from [6] as a model, see Fig. (1(b)). The FEM results were obtained through modal analysis with the element type SOLID187 in ANSYS Workbench 2023 R2 with an overall meshing of 0.1 mm to ensure convergence of the results. A parameter study regarding the optimal number of segments for discretizing the Archimedean spiral showed convergence of the first ten natural frequencies at $N_{\text{seg}} = 800$. Using the given parameters and discretizing the lever arm (constant curvature) with $N_{\text{lev}} = 20$ segments yields results with less than 1.25% relative deviation from the FEM model.

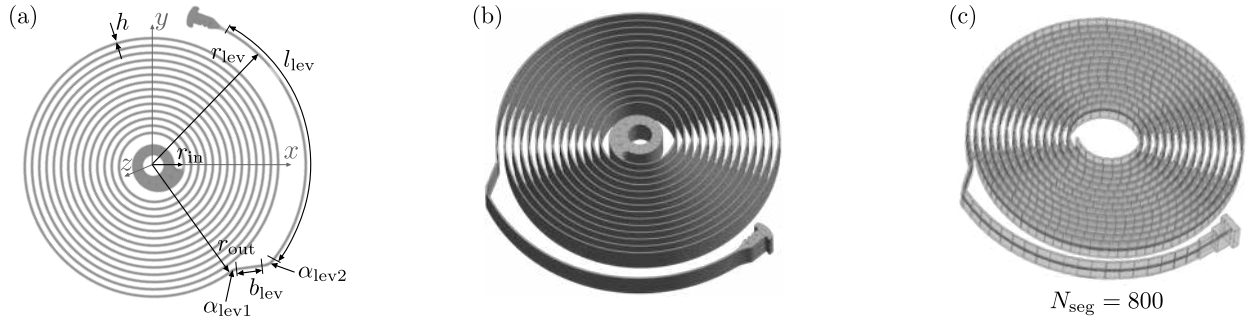

Figure 1: A curved mechanism using the example of a balance spring; (a) parameters, (b) meshed FEM model, (c) discretized structure. The following parameters were used: $N_{\text{turn}} = 14$, $r_{\text{in}} = 580.5\,\mu\text{m}$, $r_{\text{out}} = 2532.5\,\mu\text{m}$, $w = 500\,\mu\text{m}$, $r_{\text{lev}} = 2946.5\,\mu\text{m}$, $l_{\text{lev}} = 5142.5\,\mu\text{m}$, $b_{\text{lev}} = 693.25\,\mu\text{m}$, $\alpha_{\text{lev1}} = 43.97°$, $\alpha_{\text{lev2}} = -29.31°$, and material parameters for fused silica with $E = 70\,\text{GPa}$, $\nu = 0.17$ and $\rho = 2200\,\text{kg/m}^3$.

The analytical method shows excellent agreement with FEM results. Future work will entail further studies on various curved structures and validate these predictions experimentally to confirm their accuracy against real-world measurements.

ACKNOWLEDGMENTS

The authors would like to thank Christoph Weigel from the Technische Universität Ilmenau for the provision of CAD models and key parameters of the balance spring.

REFERENCES

[1] L. L. Howell, S. P. Magleby, and B. M. Olsen, *Handbook of compliant mechanisms*. Chichester West Sussex United Kingdom; Hoboken: John Wiley & Sons Inc, 2013.

[2] L. Zentner, *Nachgiebige Systeme: Klassifikation, Modellbildung und Design von Mechanismen und Aktuatoren*, 2nd ed., ser. De Gruyter STEM. Berlin and Boston: De Gruyter, 2025.

[3] M. Ling, L. L. Howell, J. Cao, and G. Chen, "Kinetostatic and dynamic modeling of flexure-based compliant mechanisms: A survey," *Applied Mechanics Reviews*, vol. 72, no. 3, 2020.

[4] V. Platl and L. Zentner, "An analytical method for calculating the natural frequencies of spatial compliant mechanisms," *Mechanism and Machine Theory*, vol. 175, p. 17, 2022.

[5] V. Platl, L. Zentner, and N. Iwatsuki, "Improving the result accuracy of the analytical method for natural frequencies of compliant mechanisms," in *Proceedings of the 2025 CCToMM Symposium on Mechanisms, Machines, and Mechatronics*, ser. Mechanisms and Machine Science, E. Lanteigne and S. Nokleby, Eds. Cham: Springer Nature Switzerland, 2025, vol. 184, pp. 40–51.

[6] C. Weigel, S. Sinzinger, and M. Hoffmann, "Deep etched and released microstructures in zerodur in a fluorine-based plasma," *Microelectronic Engineering*, vol. 198, pp. 78–84, 2018.

COMPARING DIFFERENT BEAM AXIS FOR ASYMMETRIC COMPLIANT HINGES

Hannes Jahn[1] and Lena Zentner[1]

[1] Technische Universität Ilmenau, Max-Planck-Ring 14, 98693 Ilmenau, Germany{hannes.jahn@tu-ilmenau.de}

1 INTRODUCTION

Flexure hinges are essential components of compliant mechanisms in precision engineering and weighing technology due to their friction-free motion and accurately modeling them is crucial for their development and optimization. Due to the complexity of those mechanisms, the availability of models is limited [1]. FEM is one of the most powerful models, but it has the drawbacks of complexity and the need for computational resources. Another frequently used model is the pseudo-rigid body model. It is comparably easy to apply and provides sufficient accuracy in many areas, but it has its limitations, for example, in terms of lacking information about stresses and strains. However, especially in weighing technology, these strains are important, for example, when applying strain gauges. Therefore, another well-known model, the nonlinear bending theory, can be used to analyze the deformation and stresses in compliant mechanisms [2]. This theory has proven to be well-suited for analyzing symmetrical beam structures. However, besides symmetrical flexure hinges, many mechanisms like load cells or amplifying mechanisms require asymmetric hinges to perform their tasks. We have previously developed a model based on nonlinear bending theory to analyze the deformations in load-cells, with the drawback of ignoring one of Bernoulli's assumptions—the orthogonal cross sections [3].
Recently, we introduced a new method for describing nonsymmetric hinges and fulfilling Bernoulli's assumptions [4].

2 METHODS

Regarding the midline of a asymmetric hinge, as shown in Fig. 1 (a) and regarding the stiffness $\tilde{k}$ along axis $\tilde{s}$, shown in (b), it can be observed, that the stiffness at the hinge-edges exceeds the overall stiffness of the overall beam.

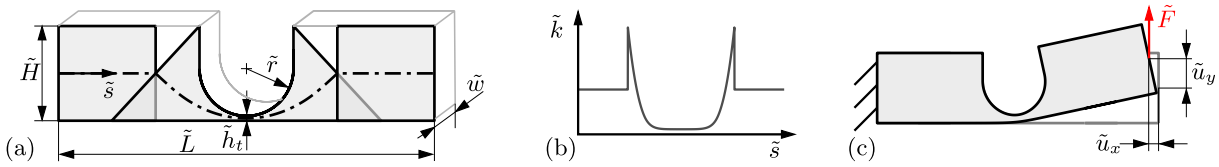

Figure 1: Asymmetric hinge: (a) beam axis $\tilde{s}$ with important parameters; (b) the respective stiffness $\tilde{k}$ along $\tilde{s}$; (c) boundary conditions (fixed on the left side and force $\tilde{F}$ at the free end) and deflections $\tilde{u}_x$, $\tilde{u}_y$

This might lead to a model that overestimates the original system's stiffness. Based on the system shown in Fig. 1, we compare three different but individually valid modeling approaches. The beam axis remains centered until:

I the cross-section captures the thin-section contour completely,

II the cross-section height of the thin-section corresponds to the surrounding beam height,

III the cross-section reaches the end of the curved part of the thin-section.

These three approaches are schematically represented in Fig. 2, the right graph shows the stiffness $\tilde{k}$ over the beam axis $\tilde{s}$ for the three approaches. Therein, the hinge of interest is shown in the background, and the foreground shows the cross-sections used for the assumptions, with the beam axis in blue. For Assumptions **II** and **III**, the vertical line (marked in green) has infinite stiffness, does not deform, and is used to connect the two elements.
Each approach is implemented in Matlab® using nonlinear calculations with no dimensions, accounting for large deflections [4]. Every dimension is eliminated by dividing by the beam's height H.
To evaluate the accuracy of each approach, the analytical results are benchmarked against Finite Element Method (FEM) simulations using 3D analysis in ANSYS® Workbench™ 2023 R2. By varying merely the height of the thin

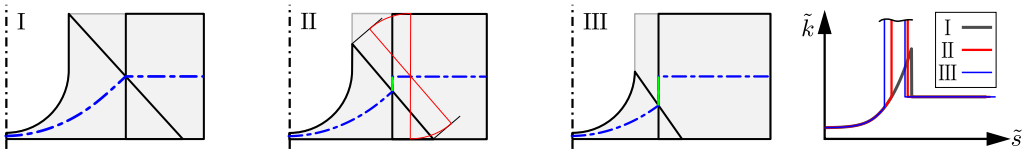

Figure 2: Schematic representation of the three modeling approaches of the beam axis and the according stiffness of the approaches

section $\tilde{h}_t$ and thus the force $\tilde{F}$ at the beam end according to Eq. 1, the deflections $\tilde{u}_x$ and $\tilde{u}_y$ as well as the maximum strains $\tilde{\varepsilon}_{\max}$ are compared.

$$\tilde{F} = \frac{0.03}{12}\tilde{h}_t^2 \tag{1}$$

3 RESULTS

Fig. 3 shows the relative deviations of the three approaches to FEM results. For the strains, there is no significant difference, since the maximum strain occurs in the middle of the hinge, where all approaches are modeled identically. The detailed view on the right shows deviations in deflection for all three approaches in the case of a relatively thick thin section. The three approaches show the greatest differences here, yet agree to the first decimal place.
These results indicate that the choice of the beam axis-approach has no significant influence on the deformation. Our comparison demonstrates that every approach provides correlation with FEM data. For the different geometries, approach **I** is most promising, because the outer contour of the thin-section is completely depicted; therefore, collision detection is feasible.

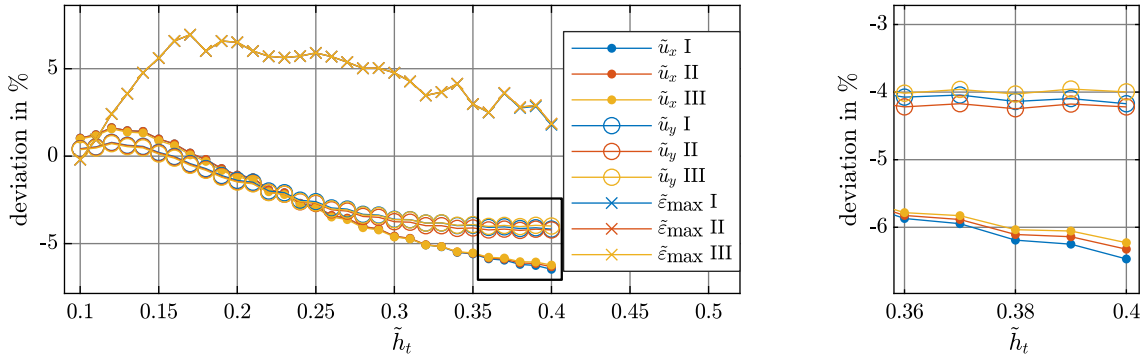

Figure 3: Relative deviations of the three approaches to FEM, with a detailed view for thick thin-sections; used parameters: $\tilde{L} = 4$, $\tilde{H} = 1$, $\tilde{w} = 1$, $\tilde{r} = 0.5$, $\tilde{E} = 1$

ACKNOWLEDGMENTS

Funding: Funded by the Deutsche Forschungsgemeinschaft (DFG, German Research Foundation) – ZE 714/22-2.

REFERENCES

[1] L. L. Howell, S. P. Magleby, and B. M. Olsen, Eds., *Handbook of compliant mechanisms*. Chichester: Wiley, 2013.

[2] L. Zentner, *Nachgiebige Systeme: Klassifikation, Modellbildung und Design von Mechanismen und Aktuatoren*, 2nd ed. De Gruyter Oldenbourg, 2025.

[3] H. Jahn, T. Fröhlich, and L. Zentner, "Development of an analytical model and method for analyzing deformation in planar load cells," *Mechanism and Machine Theory*, vol. 203, 2024.

[4] H. Jahn and L. Zentner, "Development of a midcurve for analyzing the deformation of transversely symmetric hinges," *Meccanica*, vol. 61, 2026.

A CALCULATION METHOD FOR THE ASYMMETRIC HELICAL GEAR MESHING STIFFNESS CONSIDERING THE SLICE COUPLING EFFECT

Zhihui H. [1], Hui G. [1], Shengwen H. [2], Xiaoping R. [1], Yuhang R. [1]

[1] Northwestern Polytechnical University, 127 Youyi Xi Rd. Xian 710072, China, {Guohui502@nwpu.edu.cn}
[2] Shaanxi Fast Gear Co. Ltd., 129 West Avenue, Xian 710077, China

1. INTRODUCTION

Asymmetric helical gears have achieved successful application in high-performance reducers for vehicles, helicopters, and similar systems due to their significant advantages in load capacity [1]. Accurately determining the time-varying mesh stiffness of asymmetric helical gear pairs is a prerequisite for evaluating their dynamic performance. Current numerical methods for computing mesh stiffness primarily include the finite element method and the energy-based slicing method. Although the finite element method offers high accuracy, it is computationally expensive. In contrast, the slicing method achieves a favorable balance between efficiency and accuracy, making it widely adopted in engineering practice. Although the coupling deformation effect has been investigated for symmetric gears using the slicing method, it has not been systematically extended to asymmetric helical gears. Consequently, existing models still treat the gear as a set of independent slices, overlooking the coupling deformation between adjacent slices [2], which can lead to significant deviations in predicted mesh stiffness and load distribution. To address this, this paper proposes a numerical method that simultaneously accounts for tooth modification, tooth coupling, and slice coupling effects.

2. METHODOLOGY

2.1. Improved slicing method for meshing stiffness

The traditional slicing method divides a helical gear into uniform slices along the face width. When the number of slices is insufficient, it becomes difficult to accurately capture the actual meshing behavior near the tooth entry and exit boundaries. Conversely, using an excessive number of slices reduces computational efficiency and may impair numerical convergence. To address this, an improved slicing method based on the actual contact line position is proposed, as illustrated in Fig. 1. By determining the intersection points between the contact line and the mesh zone boundaries, the gear is partitioned into several non-uniform regions along the face width, each further discretized into slices. This enables a more precise description of the actual meshing state of each helical gear slice.

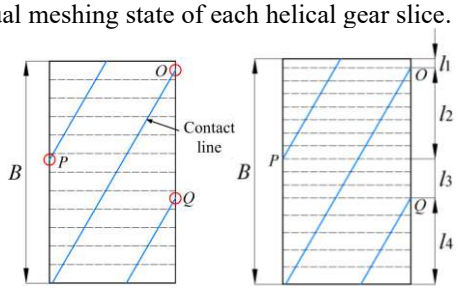

Figure 1. Traditional slicing method and improved slicing method.

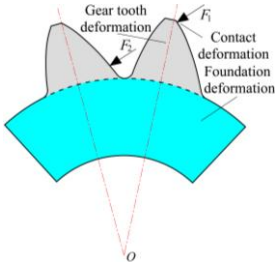

Figure 2. Schematic of gear deformation.

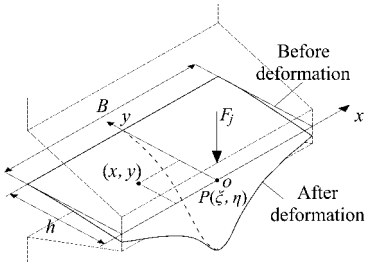

Figure 3. Schematic of a finite-width cantilever plate under load.

As shown in Fig. 2, gear meshing deformation can be categorized into tooth deformation, gear body deformation, and contact deformation. The potential energy method is adopted to calculate the bending, shear, and radial compressive deformations of asymmetric gear teeth under load [3]. A nonlinear contact deformation model based on Hertzian contact theory captures the effect of varying meshing positions on contact compliance. In addition, gear body elastic deformation and coupling deformation from tooth interactions are also considered, avoiding errors from neglecting gear body flexibility.

2.2. Quantification of slice coupling effect and mesh stiffness calculation

The slice coupling effect describes how the deformation of any loaded slice influences adjacent slices via the gear body. To quantify this, the loaded tooth is modeled as a non-uniform cantilever plate fixed at one end (Fig. 3). A deformation influence

function $K(x, y, \xi, \eta)$ between the load application point $P(\xi, \eta)$ and an arbitrary measurement point (x, y) is introduced to characterize the coupled compliance [4]. The basic idea is as follows: the helical gear is discretized into slices and equivalently treated as a spur gear model with an inclined contact line. Due to this inclination, different meshing points are located at varying tooth heights, resulting in differences in the slice coupling effect. To address this, the m-th meshing point on the helical gear is mapped to a geometrically equivalent spur gear meshing point, and a scaling factor a_m is derived based on the condition that deformations with and without coupling in the spur gear are equal [4], as formulated in Eq. (1).

$$\begin{cases} \boldsymbol{\delta}_m^u = \boldsymbol{\delta}_m^c \rightarrow \mathbf{c}_m^u \mathbf{F}_m^u = a_m \mathbf{c}_m^c \mathbf{F}_m^c \\ F = \sum_{m=1}^{n} F_m^u = \sum_{m=1}^{n} F_m^c \end{cases} \tag{1}$$

In the equation, $c_m{}^u$ and $c_m{}^u$ represent unit compliance without and with coupling, respectively; $F_m{}^u$ and $F_m{}^u$ are the corresponding load components, and F is the total load. By traversing all meshing points, deformations with coupling are obtained as $[\delta_c{}^1, \delta_c{}^2, ..., \delta_c{}^n]$. Coupled deformations are calculated using $K(x, y, \xi, \eta)$, and gear body-induced coupling follows the method in [5], enabling construction of a system compliance matrix. Finally, displacement compatibility equations are formulated in Eq. (2), from which time-varying mesh stiffness and load distribution are obtained.

$$\mathbf{cF} + \boldsymbol{\varepsilon} - x\mathbf{v} - \mathbf{w} = \mathbf{0} \tag{2}$$

where $\mathbf{c}$ is the unit compliance matrix, $\mathbf{F}$ is the load matrix, x is the tooth approach, $\boldsymbol{\varepsilon}$ is the column vector of initial separations (including geometric deviations due to tooth modifications), $\mathbf{v} = [1,1, \cdots ,1]^T$, and $\mathbf{w}$ is the column vector of residual separations.

3. RESULTS AND DISCUSSION

Using the asymmetric helical gear parameters from [2] (drive-side pressure angle 25°, coast-side 20°), the proposed method is compared with the finite element method and the coupled-tooth-only method, as shown in Fig. 4. Results show close agreement with FEM in mesh stiffness, with errors within acceptable engineering limits. More importantly, the predicted load distribution along the face width is continuous and smooth, eliminating the non-physical discontinuities in transition regions produced by traditional simplified methods—aligning more closely with the actual mechanical behavior of gear transmission.

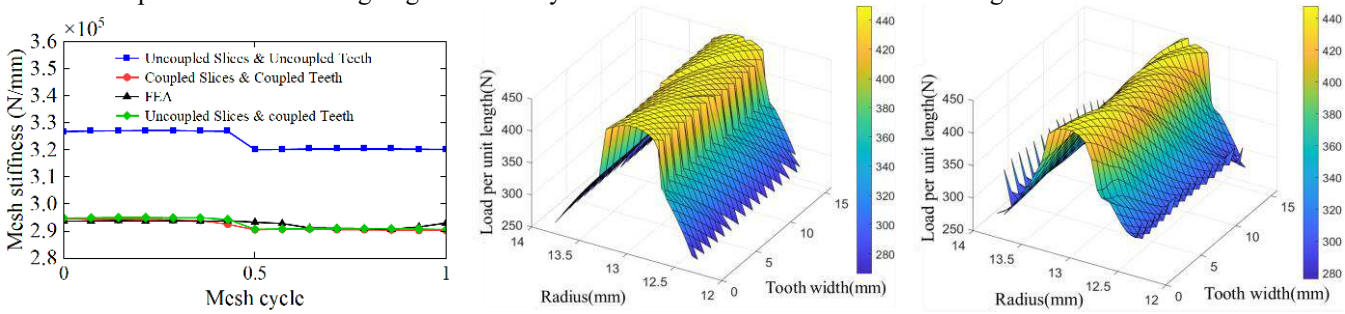

(a) Mesh stiffness of 25°/20° asymmetric helical gears

(b) Load distribution with coupled tooth only

(c) Load distribution with coupled tooth and coupled slices

Figure 4. Mesh stiffness and load distribution of asymmetric helical gears obtained using different methods

4. CONCLUSION

This study establishes a numerical method for calculating the time-varying mesh stiffness of asymmetric helical gears, incorporating tooth modification, tooth coupling, and slice coupling effects. Compared with traditional approaches, the proposed method demonstrates advantages in both mesh stiffness prediction accuracy and the fidelity of load distribution along the face width.

REFERENCES

[1] Kapelevich A L. *Asymmetric Gearing*. Boca Raton: CRC Press, 2018.

[2] Mo S, Li Y, Wang D, et al. "An analytical method for the meshing characteristics of asymmetric helical gears with tooth modifications". *Mechanism and Machine Theory*, 185(105321): 1-17, 2023.

[3] Weber C, Banaschek K. "The deformation of loaded gears and the effect on their load carrying capacity (Part I)". London: DSIR Sponsored Research, 1949.

[4] Umezawa K. "The Meshing Test On Helical Gears under Load Transmission : 1st Report, The Approximate Formula for Deflections of Gear Tooth". *Bulletin of JSME*, 15(90): 1632-1639,1972.

[5] Jordan J M, Blockmans B, Desmet W. "A linear formulation for misaligned helical gear contact analysis using analytical contact stiffnesses". *Mechanism and Machine Theory*, 187: 105373, 2023.

CARBURIZING INDUCED TOOTH DISTORTIONS IN GEARED TRANSMISIONS: THERMO-METALLURGICAL FE PREDICTION AND EXPERIMENTAL VALIDATION

Aurea Iñurritegui[1], Xuban Telleria[1], Gurutz Cortabitarte[1], Aitor Arana[1]

[1] Mondragon Unibertsitatea, Loramendi 4, Arrasate-Mondragon, Spain.
{ainurritegui@mondragon.edu; xtelleria@mondragon.edu; gcortabitarte@mondragon.edu; aarana@mondragon.edu}

1. INTRODUCTION

Carburizing is essential in gear manufacturing to achieve the surface hardness, wear resistance, and fatigue performance required for several demanding power transmission applications. Such requirements are acquired due to the carbon diffusion mechanism and the subsequent cooling, which generates a martensitic layer in the gear surface, beneficial for the high contact stresses, and cyclic loading conditions that are sustained over long service lives.
The associated non-uniform thermal field and phase-transformation generate residual stresses and tooth-level distortions (profile/lead deviations and local geometry changes) [1]. In addition, for gears or gear couplings with limited post-heat-treatment finishing (e.g., strongly modified/crowned geometries) it is particularly critical, since even small deviations can significantly affect the load distribution, and meshing behavior.

This contribution presents an experimental–numerical workflow to correlate heat-treatment-induced distortions and residual stresses in case-hardened spur gears. A coupled thermo–metallurgical–mechanical finite element (FE) model is developed, which is calibrated and validated with experimental tests: thermal histories in the quenching, hardness measurement, X-Ray Diffraction (XRD) residual stress measurements, and geometric measurement with a coordinate measuring machine (CMM). The proposed approach provides a consistent framework to link heat treatment parameters, microstructural evolution, residual stresses, and resulting gear distortions.

2. CASE STUDY AND METHODOLOGY

The case study employed in this work is a case-hardened spur gear manufactured from 16MnCr5 steel. The gear has 18 teeth, a module of 6 mm, a face width of 10 mm, and a normal pressure angle of 20°, corresponding to the reference profile D from ISO 53:1998. The gear geometry was selected to represent a typical/reference industrial carburized gear while maintaining a well-defined and geometrically simple tooth configuration.
The carburizing process of the gear was held in two diffusion stages at 925 ºC: the first, consisting of 3.5h with a carbon potential of 0.01 (weight fraction) and, the second of 1h with a carbon potential of 0.008, with an initial carbon mass fraction of 1.6×10^{-3}. Tempering was afterwards made at 850 ºC and for the following quenching process the gear was rapidly cooled in an oil bath, leading to strong and non-uniform thermal gradients.

A fully coupled thermo–metallurgical–mechanical FE model was developed in Abaqus and consists of three main stages: (i) carbon diffusion during carburizing using the DANTE plug-in, (ii) modeling of the quenching thermal field, and (iii) thermo-mechanical modelling to calculate residual stresses, hardness and distortions generated in the cooling process. Mechanical properties were defined as temperature- and phase-dependent, and phase transformation strains and volumetric changes associated with austenite decomposition were explicitly considered. The material was initially assumed to be fully austenitic at furnace temperature and the evolution toward ferrite, pearlite, bainite, and martensite was computed throughout the quenching process.
The developed model was experimentally validated, on the one hand measuring temperature evolution during quenching with thermocouples inserted at different locations of the gear. This data was used to calibrate the heat transfer coefficient and implement it in the FE model. On the other hand, residual stresses were measured in the tooth root stress with XRD and geometric distortions were measured a coordinate measuring machine (Mitutoyo CRYSTA-Apex S 7107) equipped with a 0.7 mm probe (accuracy ±0.17 μm).

3. RESULTS

The coupled thermo–metallurgical Abaqus–DANTE simulation predicts a carbon-enriched surface layer after carburizing, followed by a predominantly martensitic microstructure in the tooth region after quenching. The transient thermal response during oil quenching is obtained by fitting a temperature-dependent heat-transfer coefficient (HTC) with the thermocouple measurements at the tooth flank, tooth root, and gear body (Fig. 1(a)). This calibration allows the FE solution to capture the

experimentally observed cooling-rate differences between the tooth region (fast cooling) and the core (delayed cooling), which are the primary drivers for transformation gradients (microstructural changes), mechanical properties evolution and distortion.

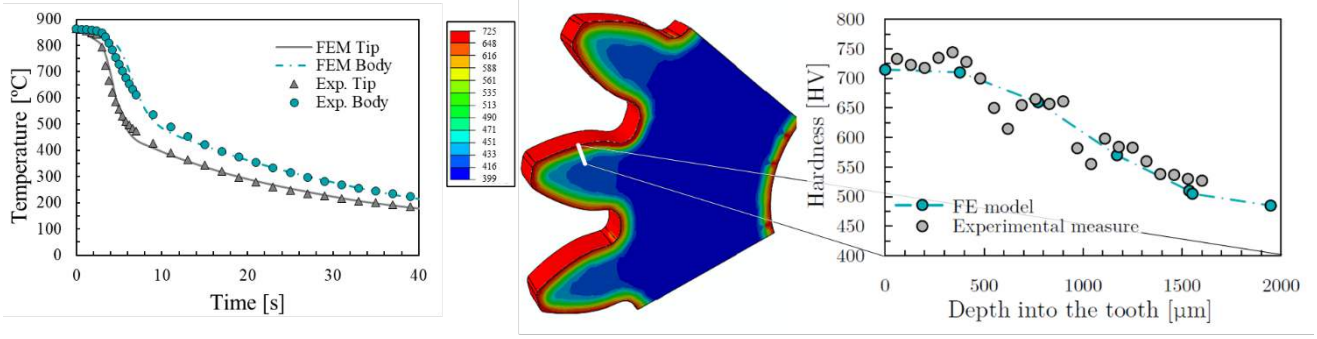

(a) (b)

Figure 1. FE vs. experimental measurement of: (a) temperature history during quenching along the tooth depth, (b) tooth Vickers-hardness along the depth of the teeth.

Based on the carburizing diffusion stages, the model predicts a carbon-enriched case. During quenching, the coupled transformation analysis predicts a predominantly martensitic case in the tooth region, with approximately 95% martensite close to the surface and a limited fraction of retained austenite beneath, transitioning to softer phases toward the middle of the gear body. Metallography confirms the presence of a martensitic case consistent with the predicted distribution, with a martensitic layer of approximately 1.5-2 mm. As observed in Fig. 1(b) the resulting hardness profile follows the expected gradient (maximum at the surface with a progressive decay toward the core), and the predicted hardness-versus-depth trend matches the experimental measurements, supporting the validity of the carbon–transformation coupling.

Moreover, the model predicts permanent deformation fields that concentrate in the toothed region, where phase-transformation strains interact with geometric constraints and generate asymmetric expansions and contractions. CMM measurements before and after heat treatment confirm systematic and repeatable tooth geometry changes, visible at the tooth root and along the active flank. The FE-predicted distortion pattern agrees with the measured deviation map, as observed in Fig. 2. As a representative scalar metric, the carburized gears exhibit, after heat treatment, an average growth at the tooth root in the normal direction of around 20 µm (average across all teeth, three measurement planes and three repetitions). These magnitudes are industrially relevant because they directly impact the required grinding for profile corrections and, more importantly, tolerance loss in gears without post-heat-treatment finishing. The validated model enables process sensitivity analyses and provides a basis for geometric pre-compensation; it can also be used to quantify the impact of heat-treatment–induced geometry variations on load distribution and fatigue-life scatter. The validated model therefore supports process sensitivity analyses and provides a basis to help predicting load distribution or fatigue-life reduction due to the geometry variations.

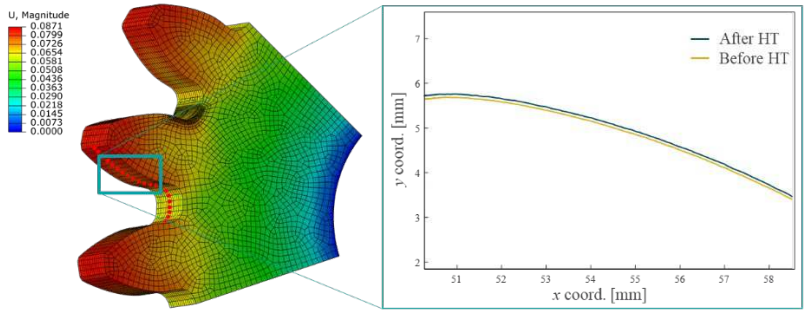

(a) (b)

Figure 2. (a) numerical and (b) experimental correlation of the geometric deviations in the spur gear flank due to carburizing heat treatment.

4. CONCLUSIONS

This study demonstrates experimentally validated prediction of heat-treatment–induced phase transformation and tooth distortions in a spur gear, providing a conservative baseline where deformations are expected to be limited. The key contribution is a validated predictive workflow that can be applied to distortion-sensitive, case-hardened mechanical transmissions, enabling distortion control and pre-compensation studies (e.g. helical gears or highly crowned spherical gear couplings).

ACKNOWLEDGMENTS

The authors acknowledge financial support from the Gipuzkoa Provincial Council under Project 2024-CIE4-000031-04-02.

REFERENCES

[1] Y. Liu, et al., “The influence of carbon content gradient and carbide precipitation on the microstructure evolution during carburizing-quenching-tempering of 20MnCr5 bevel gear”. *Surface and Coatings Technology*, 494, 131387, 2024.

DESIGN AND PROTOTYPE DEVELOPMENT OF A RESEARCH-ORIENTED PASSIVE FOOT PROSTHESIS WITH A DUAL-SPRING ELASTIC MECHANISM AND SHOCK-ABSORBING SOLE

Sultan Aidos[1,2,3], Zhetenbayev Nursultan[2,3], Ussama Abujazar [4,5], Kassymbek Ozhikenov[1], Nurgizat Yerkebulan[2,3], Sergazin Gani[3]

[1] Satbayev University, 22 Satbaev str., 050013, Almaty, Kazakhstan, {ozhikenov@satbayev.university}

[2] Almaty University of Power Engineering and Telecommunications, 126/1 Baitursynuly str., 050013, Almaty, Kazakhstan, {a.sultan@aues.kz; n.zhetenbaev@aues.kz; y.nurgizat@aues.kz}

[3] ALT University named after Mukhamedzhan Tynyshpaev, 97 Shevchenko str., 050013, Almaty, Kazakhstan, {g.balbayev@alt.edu.kz}

[4] Department of Prosthetic and Orthopedic Care, National Scientific Center for Development of Social Protection of the Ministry of Labor and Social Protection of the Republic of Kazakhstan, 112 Zhibek Zholy Avenue str., 050013, Almaty, Kazakhstan, {dr.adam.jazar@gmail.com}

[5] Kazakh National Medical University named after S.D. Asfendiyarov, 94 Tole Bi str., 050013, Almaty, Kazakhstan

1. INTRODUCTION AND RESEARCH BACKGROUND

Lower-limb prosthetic systems are generally classified as active and passive. Active devices employ actuators and control systems to improve gait performance, but their complexity and cost limit widespread use. Passive prostheses, in contrast, rely on elastic elements to store and release energy, offering higher reliability and accessibility [1–3].

In previous work, a research-oriented passive foot prosthesis based on a single elastic element was developed [4]. Although the design demonstrated feasibility, it showed limitations in load distribution, stiffness tuning, and lateral stability.

To address these issues, this study proposes a redesigned passive prosthesis (V2) based on a dual-spring mechanism combined with a shock-absorbing sole.

2. DESIGN EVOLUTION AND CONCEPTUAL REDESIGN

2.1 DUAL-SPRING ARCHITECTURE

The proposed design integrates two parallel springs symmetrically arranged along the longitudinal axis of the foot. This configuration improves load distribution and reduces stress concentration.

During the stance phase, both springs deform to store energy, which is released during push-off. Compared to a single-spring system, the dual-spring arrangement provides better adaptability and stability, particularly under asymmetric loading conditions.

2.2 MOTIVATION FOR REDESIGN

A 3D CAD model was developed to validate the geometry and structural arrangement of the system. Figure 1 illustrates the redesigned prosthesis, including:

1 – main frame
2 – support structure
3 – elastic spring elements
4 – adapter
5 – shock-absorbing sole

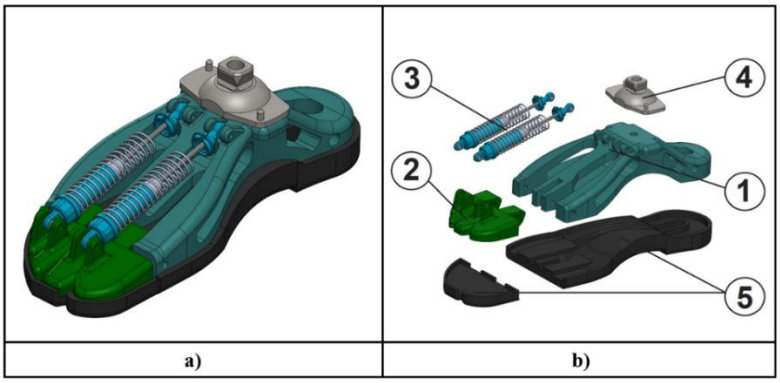

Figure 1. CAD model of the dual-spring passive foot prosthesis.

3. PROTOTYPE DEVELOPMENT

A physical prototype was fabricated based on the CAD model. The system maintains a fully passive architecture without actuators. It consists of a supporting frame, dual springs, and a shock-absorbing forefoot segment.

Compared to the previous single-spring design, the prototype demonstrates:

– improved load sharing
– enhanced energy storage
– increased lateral stability

The modular design allows easy adjustment of spring parameters for further research.

a) b)

Figure 2. Physical prototype of the V2 dual-spring passive foot prosthesis: (a) side view; (b) bottom view.

4. CONCLUSION

This work presented the design and prototype development of a passive foot prosthesis based on a dual-spring elastic mechanism. The proposed design improves mechanical performance while maintaining simplicity and reliability. The developed prototype confirms the feasibility of the concept and provides a platform for further investigation.

ACKNOWLEDGMENTS

This research was funded by the Science Committee of the Ministry of Science and Higher Education of the Republic of Kazakhstan within the framework of the program BR24992820.

REFERENCES

[1] P. Cherelle, V. Grosu, M. Cestari Soto, B. Vanderborght, and D. Lefeber, “The AMP-Foot 3, new generation propulsive prosthetic feet with explosive motion characteristics: Design and validation,” *BioMedical Engineering OnLine*, vol. 15(S3), pp. 21–36, 2016. https://doi.org/10.1186/s12938-016-0285-8

[2] K.A. Ingraham, H. Choi, E.S. Gardinier, C.D. Remy, and H.M. Herr, “Choosing appropriate prosthetic ankle work to reduce the metabolic cost of individuals with transtibial amputation,” *Scientific Reports*, vol. 8, p. 15303, 2018. https://doi.org/10.1038/s41598-018-33569-7

[3] D.E. Amiot, R.M. Schmidt, A. Law, E.P. Meinig, L. Yu, K.M. Olesnavage, V. Prost, and A.G. Winter, “Development of a passive and slope adaptable prosthetic foot,” in *Proceedings of the ASME International Design Engineering Technical Conferences and Computers and Information in Engineering Conference (IDETC/CIE 2017)*, vol. 5A, 41st Mechanisms and Robotics Conference, V05AT08A066, 2017. https://doi.org/10.1115/DETC2017-67947

[4] A. Sayat, N. Zhetenbayev, A. Sultan, A. Uzbekbayev, G. Sergazin, and K. Ozhikenov, “Development of an adaptive foot prosthesis with an elastic element and shock-absorbing sole without the use of electric actuators,” in *Artificial Intelligence in Healthcare (AIiH 2025)*, D. Cafolla, T. Rittman, and H. Ni, Eds. Lecture Notes in Computer Science, vol. 16039. Springer, Cham, 2026, pp. 217–231. https://doi.org/10.1007/978-3-032-00656-1_16

STRUCTURAL DESIGN AND NUMERICAL SIMULATION OF A SEMI-ACTIVE TRANSFEMORAL KNEE PROSTHESIS ADAPTER

Nurgizat Yerkebulan[1,2,3], Sultan Aidos[1,2,3], Zhetenbayev Nursultan[2,3], Serik Didar[1], Ussama Abujazar [4,5], Kassymbek Ozhikenov[1], Sergazin Gani[3]

[1] Satbayev University, 22 Satbaev str., 050013, Almaty, Kazakhstan, {ozhikenov@satbayev.university; d.serik@satbayev.university}

[2] Almaty University of Power Engineering and Telecommunications, 126/1 Baitursynuly str., 050013, Almaty, Kazakhstan, {a.sultan@aues.kz; n.zhetenbaev@aues.kz; y.nurgizat@aues.kz}

[3] ALT University named after Mukhamedzhan Tynyshpaev, 97 Shevchenko str., 050013, Almaty, Kazakhstan, {g.balbayev@alt.edu.kz}

[4] Department of Prosthetic and Orthopedic Care, National Scientific Center for Development of Social Protection of the Ministry of Labor and Social Protection of the Republic of Kazakhstan, 112 Zhibek Zholy Avenue str., 050013, Almaty, Kazakhstan, {dr.adam.jazar@gmail.com}

[5] Kazakh National Medical University named after S.D. Asfendiyarov, 94 Tole Bi str., 050013, Almaty, Kazakhstan

1. INTRODUCTION

The knee joint is essential for stable locomotion, and its impairment significantly affects gait performance [1]. In transfemoral prosthetics, passive and variable-damping systems are widely used due to their simplicity, while semi-active solutions provide adjustable resistance and improved adaptability [2–4]. However, the structural design of the upper mechanical module remains critical for load transfer, actuator integration, and overall system reliability [5].

This work presents the structural design and numerical evaluation of a semi-active transfemoral knee prosthesis adapter, focusing on CAD-based development and simulation of joint kinematics and actuator loading.

2. MECHANICAL DESIGN AND CAD MODELING

2.1 DESIGN CONCEPT

The proposed upper adapter module is designed as a compact load-bearing structure integrating the socket interface, hinge mechanism, and actuator housing. Key design features include compatibility with standard prosthetic interfaces, the ability to withstand axial and bending loads, compact geometry for reduced mass, and integration of actuator elements. Figure 1 shows the CAD model of the proposed design.

a) b) c)

Figure 1. Isometric CAD views of the semi-active transfemoral knee prosthesis upper module: (a) front view; (b) internal configuration; (c) rear view.

2.2 PARAMETRIC CAD MODEL

The geometry was developed as a parametric model in SolidWorks, enabling flexible modification of structural dimensions and component placement. The structure includes a load-bearing housing, a central hinge block, an actuator linkage, a socket interface, and lateral support elements. This configuration ensures stable load transfer and supports semi-active control implementation.

2.3 PROTOTYPE

A physical prototype was developed to verify the feasibility of the proposed design. The structure was manufactured using lightweight materials, while the hinge and actuator components were assembled according to the CAD model. The prototype allows qualitative evaluation of joint motion and actuator response.

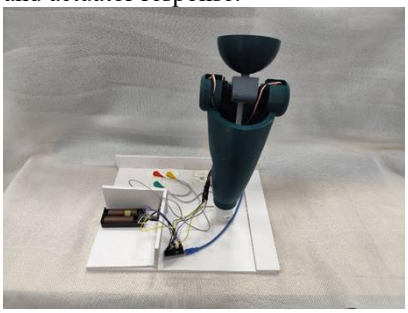

Figure 2. Experimental prototype of the semi-active transfemoral knee prosthesis upper module.

3. NUMERICAL SIMULATION

Numerical simulations were performed to evaluate the kinematic response and actuator loading of the proposed module. Figure 3 shows the results: (a) angular displacement of 40–45°, (b) smooth and symmetric angular velocity profile, and (c) motor torque within a feasible operating range. The results confirm stable joint kinematics and reliable actuator performance for semi-active operation.

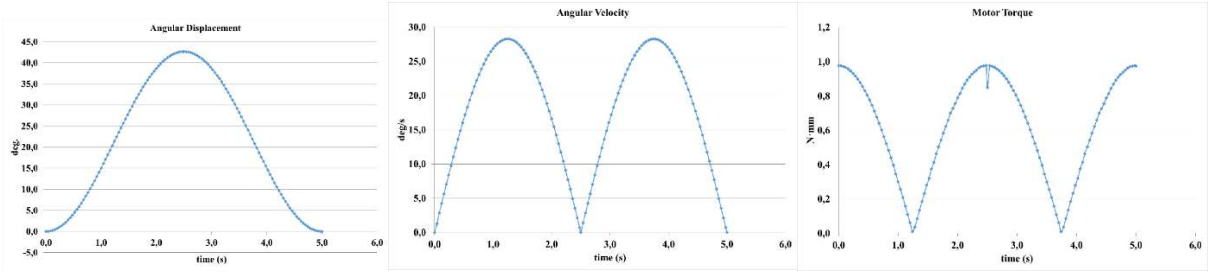

a) **b)** **c)**

Figure 3. Simulation results of the knee joint: (a) angular displacement; (b) angular velocity; (c) motor torque.

4. CONCLUSION

This study presented the structural design and numerical simulation of a semi-active transfemoral knee prosthesis adapter. The proposed design provides a compact and mechanically stable solution with feasible actuator loading characteristics. The results confirm the suitability of the architecture for semi-active prosthetic systems. Future work will focus on experimental validation and further optimization of actuator control strategies.

ACKNOWLEDGMENTS

This research was funded by the Science Committee of the Ministry of Science and Higher Education of the Republic of Kazakhstan within the framework of the program BR24992820.

REFERENCES

[1] V. Jakob, A. Küderle, F. Kluge, J. Klucken, B.M. Eskofier, J. Winkler, M. Winterholler, and H. Gassner, *Validation of a Sensor-Based Gait Analysis System with a Gold-Standard Motion Capture System in Patients with Parkinson's Disease*. Sensors, 21, 7680, 2021. https://doi.org/10.3390/s21227680

[2] J.L. Johansson, D.M. Sherrill, P.O. Riley, P. Bonato, and H. Herr, *A clinical comparison of variable-damping and mechanically passive prosthetic knee devices*. American Journal of Physical Medicine & Rehabilitation, 84(8), 563–575, 2005. https://doi.org/10.1097/01.phm.0000174665.74933.0b

[3] J. Jiang, K.M. Lee, and J. Ji, *Review of anatomy-based ankle–foot robotics for mind, motor and motion recovery following stroke: design considerations and needs*. International Journal of Intelligent Robotics Applications, 2, 267–282, 2018. https://doi.org/10.1007/s41315-018-0065-7

[4] B.A. Shafer, S.A. Philius, R.W. Nuckols, J. McCall, A.J. Young, and G.S. Sawicki, *Neuromechanics and energetics of walking with an ankle exoskeleton using neuromuscular-model-based control: A parameter study*. Frontiers in Bioengineering and Biotechnology, 9, 615358, 2021. https://doi.org/10.3389/fbioe.2021.615358

[5] S. Abdreshova, S. Akhmejanov, K. Ozhikenov, N. Zhetenbayev, Y. Nurgizat, D. Bizhanov, A. Sultan, A.-A. Ayazbay, M. Zharmagambetova, and G. Sergazin, *Development and biomechanical evaluation of a modular knee prosthesis: From conceptual V1 design to an improved V3 model*. Bioengineering, 13(2), 201, 2026. https://doi.org/10.3390/bioengineering13020201

FOLLOW-THE-LEADER PERFORMANCE OF A DUAL-ENDED SPRING-BASED SELF-EXTENDING CONTINUUM ROBOT

Jie Wang[1], Calvin S. H. Ng[1], Zheng Li[2]

[1] Department of Surgery, The Chinese University of Hong Kong, Hong Kong, China, {jiewang002@cuhk.edu.hk, calvinng@surgery.cuhk.edu.hk}
[2] Department of Surgery, Chow Yuk Ho Technology Centre for Innovative Medicine, Li Ka Shing Institute of Health Science and Multi-Scale Medical Robotics Center, The Chinese University of Hong Kong, Hong Kong, China, {Corresponding author: lizheng@cuhk.edu.hk}

1 INTRODUCTION

Precise Follow-the-Leader (FTL) deployment is desired for navigating narrow and tortuous pathways in minimally invasive interventions. Existing continuum robots (CRs) for FTL motion generally fall into two categories: extensible CRs, which vary the length of their bending sections [1, 2], and growing CRs, which advance through the translation of fixed-length bending segments [3, 4]. However, many of these designs exhibit relatively large cross-sectional dimensions, limiting their applicability in confined environments. Concentric tube robots offer a compact alternative but often suffer from restricted dexterity and motion capability [5]. Therefore, achieving FTL deployment at miniature scale while preserving a functional working channel remains challenging. To this end, we develop a miniature spring-based continuum robot featuring a compact cross-section and an integrated central working channel for tool delivery. This paper focuses on evaluating the FTL deployment performance of the proposed mechanism, demonstrating its ability to reproduce prescribed paths with high fidelity under constrained conditions.

2 ROBOT DESIGN AND FTL DEPLOYMENT PRINCIPLE

This paper presents a spring-based two-segment extensible continuum manipulator (TSEM) [6] designed for Follow-the-Leader (FTL) deployment, as shown in Fig. 1. The outer diameter (OD) of the TSEM is 4 mm, and the working channel is 1.8 mm. The TSEM consists of two compression-spring-based bending segments interconnected by three rigid spacer blocks. The drive rods of the distal segment pass through the drive tubes of the proximal segment, enabling coordinated actuation of both segments. All drive elements are routed through a flexible insertion tube to a compact actuation unit comprising three identical drive modules, where motor inputs are converted into rotational and differential translational motions via a gear train and screw-nut mechanisms.

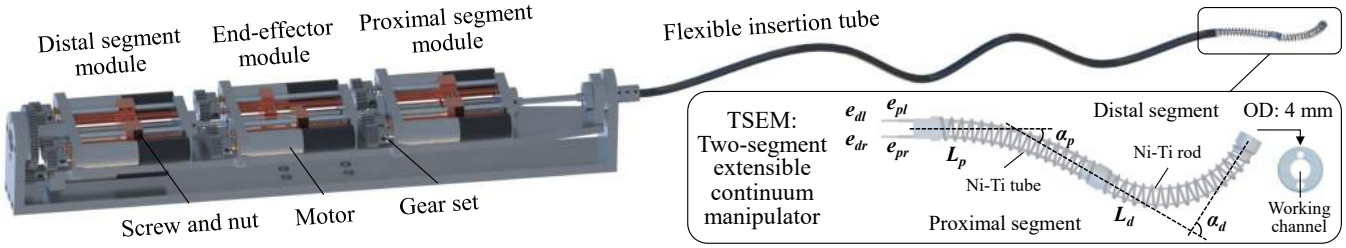

Figure 1: The miniature spring-based manipulator and its self-extension mechanism for shape-preserving deployment.

Differential actuation of the paired drive tubes/rods generates segment curvature, whereas synchronous actuation produces pure axial extension or contraction. Bending angles (α_p, α_d) and segment lengths (L_p, L_d) are expressed as:

$$\alpha_i = \frac{1}{d}(e_{ir} - e_{il}), \quad L_i = \begin{cases} L_{i0}, & |e_{il}| = |e_{ir}| \wedge e_{il}e_{ir} \leq 0 \\ L_{i0} - e_{il}, & |e_{il}| = |e_{ir}| \wedge e_{il}e_{ir} > 0 \\ L_{i0} - \min(e_{il}, e_{ir}) - \frac{1}{2}(e_{ir} - e_{il}), & |e_{il}| \neq |e_{ir}| \end{cases} \tag{1}$$

where $i \in \{p, d\}$ denotes the proximal and distal segments, d is the distance between the paired drive tubes/rods,

e_{il} and e_{ir} are the left and right drive inputs, and L_{i0} is the initial segment length. According to Eq. (1), pure segment extension is achieved by setting $e_{il} = e_{ir}$, resulting in bending-invariant extension and providing the kinematic foundation for shape-preserving FTL deployment.

3 EXPERIMENTAL RESULTS

To evaluate the FTL deployment performance, a series of planar FTL experiments were conducted, as shown in Fig. 2(**a**). Four distinct planar reference paths [insets in Fig. 2(**c**)] were used to assess the deployment capability of the TSEM. The manipulator was operated using a master–slave control scheme with a customized master interface. The TSEM shape was recorded by an industrial camera (HIKROBOT, MV-CS050-10GC) to provide visual feedback. A representative deployment sequence is presented in Fig. 2(**b**).

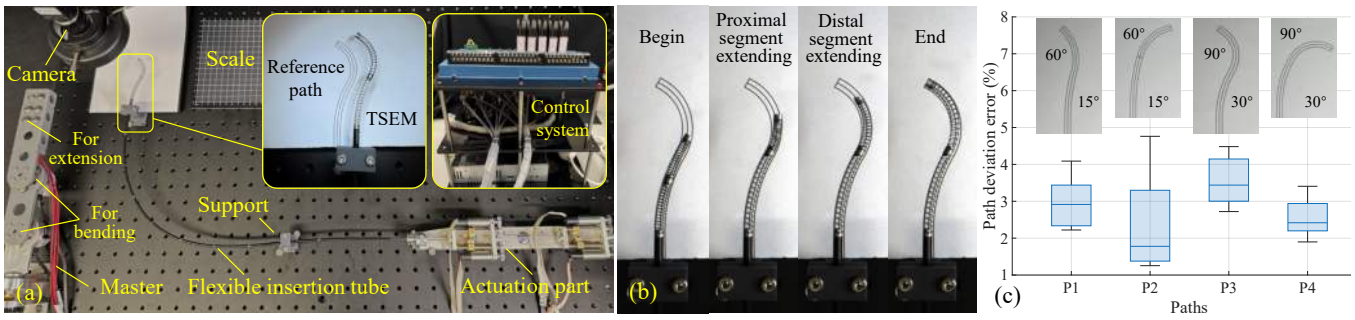

Figure 2: FTL deployment experiment: (**a**) setup, (**b**) FTL deployment sequence photographs, (**c**) path deviation error.

Each experiment was repeated five times. The path deviation error was defined as the normalized distance between the deployed TSEM backbone and the reference path, relative to the total deployed length (86 mm). The maximum deviation in each trial is summarized in Fig. 2(**c**), as it reflects the worst-case FTL fidelity. Across the four paths, the median deviation is 2.79%, with a maximum observed error of 4.76%, demonstrating consistent and repeatable shape-preserving FTL deployment.

4 CONCLUSIONS

This work presented a 4 mm-diameter spring-based two-segment extensible continuum mechanism designed for FTL deployment. The dual-ended self-extension mechanism decouples bending and extension, enabling shape-preserving FTL deployment in a miniature size. Experimental results demonstrated a median path deviation of 2.79%, confirming reliable FTL deployment performance. Future work will focus on omnidirectional bending enhancement, autonomous FTL control, and integration of the mechanism into minimally invasive surgical systems.

ACKNOWLEDGMENT

This work is supported in part by the Hong Kong Research Grant Council with project No. C4042-23GF, 14214322, 14200623, 14203424, and 14206325. The authors would also like to thank the support from AIR@INNOHK Multiscale Medical Robotics Center and Chow Yuk Ho Technology Center for Innovative Medicine.

REFERENCES

[1] E. Amanov, T.-D. Nguyen, and J. Burgner-Kahrs, "Tendon-driven continuum robots with extensible sections—a model-based evaluation of path-following motions," *The International Journal of Robotics Research*, vol. 40, no. 1, pp. 7–23, 2021.

[2] J. Wang, C. Hu, J. Kang, J. Liu, L. Ma, and H. Liao, "A novel robotic bronchoscope with a spring-based extensible segment for improving steering ability," in *2024 IEEE International Conference on Robotics and Automation (ICRA)*. IEEE, 2024, pp. 15 448–15 454.

[3] A. Degani, H. Choset, A. Wolf, and M. A. Zenati, "Highly articulated robotic probe for minimally invasive surgery," in *2006 IEEE International Conference on Robotics and Automation (ICRA)*. IEEE, 2006, pp. 4167–4172.

[4] R. Deuling, A. Akbari, S. Saini, B. Qi, M. S. Asif, and J. Sheng, "Design and development of a macroscale cable-driven follow-the-leader continuum robot," *IEEE/ASME Transactions on Mechatronics*, 2025.

[5] C. J. Nwafor, C. Girerd, G. J. Laurent, T. K. Morimoto, and K. Rabenorosoa, "Design and fabrication of concentric tube robots: A survey," *IEEE Transactions on Robotics*, vol. 39, no. 4, pp. 2510–2528, 2023.

[6] J. Wang, Y. Sun, X. Lu, J. Kang, H. G. Khor, J. Liu, B. Zhang, F. Chen, L. Ma, Y. Shen, and H. Liao, "Tsem: A two-segment spring-based self-extensible continuum manipulator for extension-based operation in curved channels," *IEEE Transactions on Mechatronics*, 2026, under review.

SAMPLE-EFFICIENT LEARNING OF BODY-ENVIRONMENT INTERACTION OF AN UNDERACTUATED SYSTEM

Zvi Chapnik[1], Yizhar Or[1], Shai Revzen[2]

[1] Faculty of Mechanical Engineering, Technion-Israel Institute of Technology Haifa, Israel

[2] Electrical Engineering and Computer Science, Ecology and Evolutionary Biology, University of Michigan, Ann Arbor, MI, USA.

1. BACKGROUND

With the exception of reaction-mass systems like rockets, virtually all locomotion propulsion is accomplished through shape-change that produces reaction forces from the environment to propel the body. In most animals, when they move quickly, and in virtually all man-made devices, these shape changes are rhythmic - they follow nearly the same sequence of body shapes, at a frequency which changes little from cycle to cycle. When the repeating shape change is pronounced, the repeating sequence is often called a periodic gait. A vast literature exists attempting to relate body shape changes to body motion: turning of wheels to motion of cars; flapping of wings to flight of birds or flies; spinning of blades to propulsion of submarines or of helicopters; cycling of legs to running or walking, etc. Many moving biological and robotic systems have passively deforming mechanical parts, most obvious among these in biology are flapping fins, bending wings, and beating flagella. In systems where momentum decays quickly, such as small bodies swimming in high-viscosity fluids [1], or walking with many legs, or more generally in cases where momentum decays quickly enough for any other reason [2], these theories of propulsion take on a particularly simple form called the motility map and arising from geometric mechanics. For many systems, the effect of momentum on body velocity is negligible, such systems are referred to as "principally kinematic" or "geometric". In these systems, body velocity v_b is related to the shape variables r and their rates $\dot{r}$ through the reconstruction equation $v_b = A(r)\dot{r}$, where $A(r)$ is the motility map encoding the effective body-environment interaction. This work [3] introduces a machine learning approach especially suited to the motility map of underactuated systems and presents an experimental study of its sample efficiency in comparison with existing methods, applied across multiple gaits of a physical robot.

2. MODELING AND LEARNING APPROACH

To learn motility maps directly from experimental data, we compare four modeling approaches that differ in expressiveness and in how they account for passive degrees of freedom. Phase-dependent total least squares (TLS) models represent body velocity as a linear function of shape velocity in the neighborhood of a nominal gait and provide a simple, interpretable baseline that has been successfully applied to gait-local system identification [4]. Gaussian mixture regression (GMR) models extend this framework by allowing nonlinear dependence on shape velocity, enabling the representation of more complex body-environment interactions while retaining a structure compatible with geometric mechanics [5]. Importantly, many locomoting systems include passive shape variables whose dynamics are not directly actuated but nonetheless influence motion. In order to account for this, we incorporate shape-underactuated dissipative-system (SUDS) variables into the model, thereby augmenting the motility-map formulation with a low-dimensional representation of passive shape dynamics driven by the actuated variables [6]. This augmentation can be applied to both linear phase-dependent total least squares models (TLS+SUDS) and Gaussian mixture regression models (GMR+SUDS), allowing a direct comparison between methods that ignore passive dynamics and those that model them explicitly.

3. EXPERIMENTAL SYSTEM

We demonstrate our analysis using a three-segment swimmer moving through a granular medium with four passive components flippers. A photograph of the robot operating in the granular bed and a schematic sketch illustrating the actuated joints and passive flippers are shown in Fig. 1A and 1B. The swimmer is actuated by two joint motors, while the flippers move passively through interaction with the surrounding grains, producing a strongly underactuated system dominated by frictional dissipation. The granular medium introduces complex body-environment interactions that are difficult to model analytically.

The swimmer's motion is recorded using marker-based motion capture, providing full body pose and measurements of both actuated and passive shape variables. High-dimensional measurements of passive deformation are reduced to a low-dimensional representation using principal component analysis, preserving the dominant modes of motion relevant to propulsion. The robot is commanded to execute 5 different periodic gaits spanning a range of joint-space geometries at 3 different frequencies. The specific periodic gaits commanded, along with a representative measured joint-space trajectory for a circular gait, are shown in Fig. 1C, demonstrating the smooth and consistent actuation used throughout all experiments.

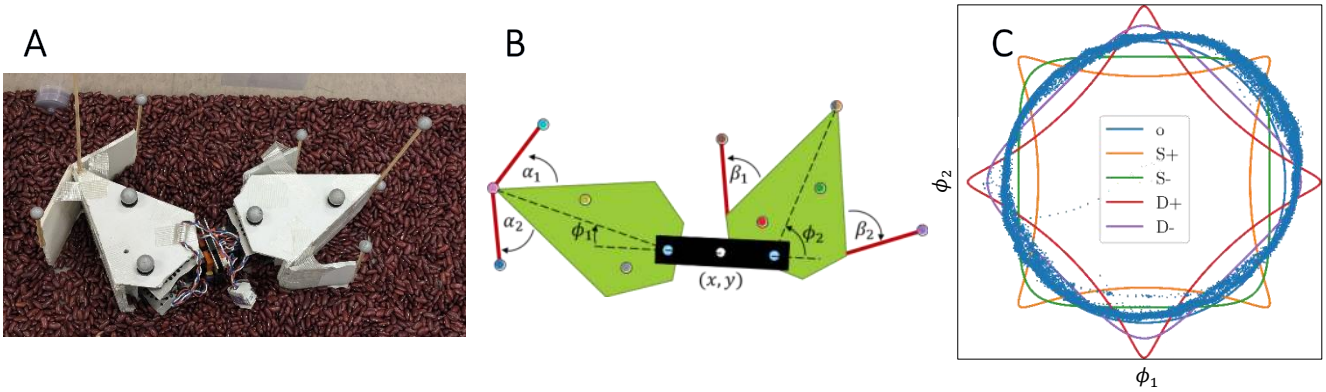

Figure 1. 4-flipper, 3-segment swimmer. A. Picture of the swimmer in the granular medium. B. Schematic sketch. C. Commanded and measured theoretical gaits, commanded values in solid lines, measured angles of the circle gaits in blue dots.

4. RESULTS

The collected data are used to train and evaluate motility-map estimated models using a bootstrap procedure that evaluates their ability to generalize across different gaits. Prediction accuracy is measured by the root-mean-square error of forward body velocity. The error distributions, grouped by how similar the training and testing gaits are geometrically, are displayed in Fig. 2A. In all gait comparisons, the GMR models show significantly lower prediction errors compared to the TLS models. Incorporating passive degrees of freedom (SUDS) further improves performance, particularly with sufficient training data.

The dependence of prediction accuracy on dataset size is illustrated in Fig. 2B for a representative actuation frequency. For small datasets, simpler models perform comparably well, while more expressive models improve gradually. As the number of training cycles increase, the combined GMR+SUDS model converges rapidly to a lower error magnitude, indicating improved sample efficiency and suggesting that it captures the dominant structure of the body-environment interaction. These results demonstrate that accurate motility-map models for strongly underactuated physical systems can be learned from limited experimental data.

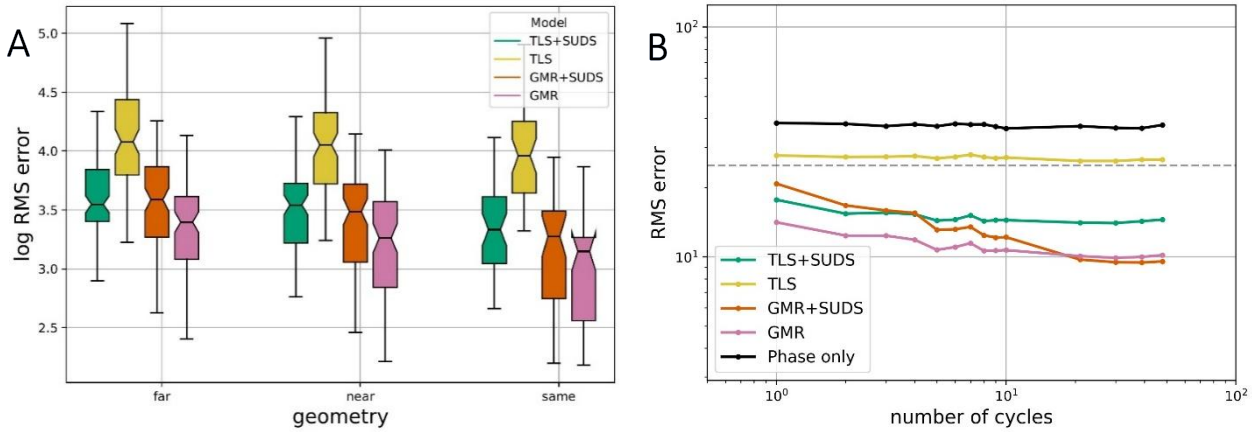

Figure 2. A. Prediction error by gait similarity and model type. The log of RMS error distributions for each category: same gait (right), near gait (middle), and far gait (left). B. The RMS error as a function of the number of cycles and model type, for ½[Hz] frequency actuation

REFERENCES

[1] Purcell, E.M., 2014. Life at low Reynolds number. *Physics and our world: reissue of the proceedings of a symposium in honor of Victor F Weisskopf* (pp. 47-67).

[2] Seipel, J., Kvalheim, M., Revzen, S., Sharbafi, M.A. and Seyfarth, A., 2017. Conceptual models of legged locomotion. *Bioinspired legged locomotion* (pp. 55-131). Butterworth-Heinemann.

[3] Chapnik, Z., Or, Y. and Revzen, S., 2026. Sample Efficient Learning of Body-Environment Interaction of an Under-Actuated System. *arXiv preprint* arXiv:2601.13777.

[4] Bittner, B., Hatton, R.L. and Revzen, S., 2018. Geometrically optimal gaits: a data-driven approach. *Nonlinear Dynamics*, 94(3), pp.1933-1948.

[5] Hu, R. and Revzen, S., 2025. Learning the Geometric Mechanics of Robot Motion Using Gaussian Mixtures. *arXiv preprint* arXiv:2502.05309.

[6] Bittner, B., Hatton, R.L. and Revzen, S., 2022. Data-driven geometric system identification for shape-underactuated dissipative systems. *Bioinspiration & biomimetics*, 17(2), p.026004.

SOLVING THE PROBLEM OF DIMENSIONAL KINEMATIC SYNTHESIS USING AN EVOLUTION STRATEGY THAT UTILIZES KNOWLEDGE OF DERIVATIVES

A. Noriega[1], I. Fernández de Bustos[2], M.d.R. Fernández[3]

[1] University of Oviedo, Campus de Viesques, C/Pedro Puig Adam, E.D.O. 5.1.12, 33203, Gijón, Spain, {noriegaalvaro@uniovi.es}

[2] University of Basque Country, Dpt. Of Mechanical Engineering, Plaza Ingeniero Torres Quevedo nº 1, 48013, Bilbao, Spain, {igor.fernandezdebustos@ehu.eus}

[3] University of Oviedo, Campus de Viesques, C/Pedro Puig Adam, E.D.O. 5.1.13, 33203, Gijón, Spain, {rocio@uniovi.es}

1. INTRODUCTION

It is well known that the problem of dimensional kinematic synthesis can be posed as a minimization problem. Some authors propose an approach based on a Newton method [1], which is very efficient for problems with many variables because it requires few iterations to converge, but it is also highly dependent on the initial approximation of the solution to the synthesis problem. This represents a problem since the function to be minimized is usually multimodal. The existence of several minima can be due to two causes. One possible cause is that the synthesis problem gives rise to an underdetermined system of equations, which can have infinite solutions (or no solution). This situation can be detected with the synthesis inequality [2].

Another possible cause is that the modeling used to define the mechanism's kinematics allows for various configurations of the mechanism to fulfill the synthesis conditions, resulting in theoretical solutions that have no practical use. This situation is a direct consequence of the nonlinearity of the geometric constraint equations used for modeling. To reduce or avoid this problem, functional constraints can be included that limit the ranges in which certain geometric parameters can vary [3]. However, this makes the synthesis problem behave similarly to a stiff problem, with very small solution attraction zones, which makes the choice of the initial approximation critical if the approach proposed in [1,3] is used.

To avoid this drawback, various authors have developed global search methods based on genetic algorithms [4] or evolution strategies [5] to successfully solve the problem of dimensional kinematic synthesis of mechanisms. The weak point of these methods is their high computational cost, as they use many evaluations of the objective function to be minimized.

The objective of this work is to develop a global search method inspired by an evolution strategy that integrates efficiency in the local convergence of Newton's method so that the approach to the dimensional kinematic synthesis problem, by not requiring an initial approximation of the solution, becomes simpler and, at the same time, the solution is achieved more efficiently because the evolution of each individual is carried out in the direction of the gradient of the objective function.

2. METHODOLOGY

The synthesis problem is posed as the minimization of the function $\Psi(\mathbf{q},\mathbf{b})$ as can be seen in Eq. 1:

$$min\ \Psi(\mathbf{q},\mathbf{b}) = min\ \frac{1}{2}\cdot\Phi(\mathbf{q},\mathbf{b})^{T}\cdot\Phi(\mathbf{q},\mathbf{b}) \qquad being \quad \nabla\Psi(\mathbf{q},\mathbf{b}) = \mathbf{J}^{\mathrm{T}}(\mathbf{q},\mathbf{b})\cdot\Phi(\mathbf{q},\mathbf{b}) \tag{1}$$

Where **q** is the vector containing the generalized coordinates of the mechanism in all synthesis positions and **b** is the vector containing the dimensional constants of the mechanism that can be modified during the synthesis solution.

The starting point was the DDM-ES, an $(\mu+\lambda)-ES$ evolution strategy presented in [5], which was modified so that the choice of an individual's mutation direction is defined by the direction and sign of the gradient, as shown in Eq. 2:

$$\begin{bmatrix}\mathbf{q}\\ \mathbf{b}\end{bmatrix}_{\text{offspring}} = \begin{bmatrix}\mathbf{q}\\ \mathbf{b}\end{bmatrix}_{\text{parent}} - |\alpha|\cdot\frac{\nabla\Psi}{\|\nabla\Psi\|} \tag{2}$$

The mutation step $|\alpha|$ is randomly generated according to a Gaussian distribution with decreasing standard deviation to ensure statistical convergence. The resulting strategy has been named Gradient Based Evolution Strategy (GB-ES), and the demonstration of its local and global convergence is the same as that developed for DDM-ES in [5].

A comparison has been carried out between the two evolution strategies described above on several well-known test functions, with between 2 and 50 variables, under identical start conditions. The results show that GB-ES performs significantly better on highly multimodal functions or difficult minima, achieving better optimums with greater accuracy and in a significantly shorter time (between 25% and 60% faster). The difference in performance increases with the number of variables.

3. RESULTS

Various well-known synthesis examples have been tested, such as the guidance of the coupling bar, shown in red in Figure 1, in an RRRR mechanism, where the actuated bar is shown in blue. The problem has been solved with and without including a functional constraint that limits the transmission angle (formed by the red and black bars). Figure 1 shows that, in both cases, a reasonable solution is obtained, but only the problem that includes the functional constraint leads to a viable solution in which all synthesis positions are achieved in the same branch of operation and with a transmission angle limited within the previously defined range (+-70º).

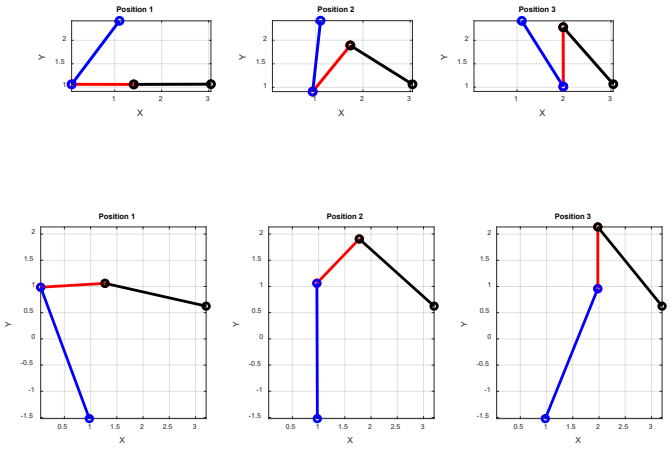

Figure 1. Solution of guidance of coupling bar' synthesis without and with functional constraints

The application to mechanisms with more links, more synthesis positions or 3D mechanisms differs from the cases analysed only in that the modelling is carried out using the same type of equations but with a greater number of variables; consequently, GB-ES will have an even greater advantage, as indicated in the previous section.

4. CONCLUSIONS

A modification of the DDM-ES method, which incorporates the use of the gradient to define the direction and sign of the mutation, has been presented. The method shown allows, by indicating only the structure of the mechanism, the volume of the space where it must be contained, and the ranges of variation allowed in the different dimensional constants, to obtain solutions to the problem of dimensional kinematic synthesis, greatly facilitating the use of this method by non-expert users.

The efficiency of this method can be significantly improved by working on the choice of the direction of mutation, in a similar way to that proposed by the standard momentum method or by Nesterov's accelerated gradient method, so as to avoid falling into local optima and that the solution oscillates around an optimum.

The efficiency can also be improved by working on the choice of the optimal mutation step, but this calculation entails an increase in computational cost that is often not cost-effective.

Finally, the time cost of this method can be greatly reduced by taking advantage of the fact that the evaluation of individuals in the population can be carried out in parallel.

ACKNOWLEDGMENTS

We are very grateful for the support of this work by the Ministry of Science and Innovation of the Government of Spain, within the framework of project PID2021-124677NB-I00.

REFERENCES

[1] J. García de Jalón and E. Bayo, *Kinematic and Dynamic Simulation of Multibody Systems: The Real-Time Challenge.* Springer-Verlag, New-York, 1994.

[2] A. Noriega, I. Fernández de Bustos, V. García-Marina, G. Urkullu, "Acerca del vínculo entre la síntesis topológica y la síntesis cinemática de mecanismos", *Libro de actas del XXV Congreso Nacional de Ingeniería Mecánica*, Santander, Spain, June 11–13, 2025.

[3] A. Noriega, I. Fernández de Bustos, V. García-Marina, "A simple and efficient way to introduce bounded ranges in parameters and functional constraints in a dimensional synthesis problem", *Proceedings of the MMT Symposium*, Guimarães, Portugal, June 26–28, 2024.

[4] I. Fernández de Bustos, *Síntesis cinemática dimensional de mecanismos mediante algoritmos genéticos*. PhD Thesis, University of Basque Country, 2004.

[5] A. Noriega, *Síntesis dimensional óptima de mecanismos mediante estrategias evolutivas*. PhD Thesis, University of Oviedo, 2008.

BEYOND EXPLORATORY SYNTHESIS: HOW TO DESIGN A MULTIMODE POWER-SPLIT TRANSMISSION FOR MAXIMUM PERFORMANCE OF HYBRID ELECTRIC VEHICLES

Antonella Castellano[1], Marco Cammalleri[1]

[1] University of Palermo, Department of Engineering, viale delle Scienze, 90128, Palermo, Italy
{antonella.castellano@unipa.it; marco.cammalleri@unipa.it}

1. INTRODUCTION

The comprehensive design of multimode power-split powertrains for hybrid electric vehicles (HEVs) remains a challenging task, primarily due to the high constructive and functional complexity of the driveline. Even specialised handbooks do not provide systematic guidelines for an integrated and guided design of power-split hybrid powertrains, including the synthesis of a transmission capable of meeting prescribed design requirements [1]. Existing approaches are largely based on exploratory numerical methods that focus on transmission topology alone, while neglecting the concurrent sizing of the internal combustion engine and the electric unit, and rarely addressing the selection of the number and type of operating modes required to satisfy given performance targets [2]. In this contribution, a dedicated procedure is introduced to determine the minimum number of operating modes needed to ensure continuous availability of the maximum onboard power, thereby maximising achievable performance for a given degree of hybridisation. The procedure is grounded in a unified parametric model and embedded within a modular and hierarchical framework for the systematic transmission design starting from vehicle-level specifications [3].

2. PARAMETRIC MODELLING OF A POWER-SPLIT UNIT

In power-split hybrid powertrains, the driveline consists of a power-split unit (PSU), composed of one or more planetary gear sets (PGs) possibly combined with ordinary gear trains, and an electric unit comprising two motor–generators (MGs) and a battery pack, which together act as an electrically controlled continuously variable unit (CVU). Within the parametric framework adopted in this work [4], any PSU can be modelled as a four-port mechanism connected with the ICE (in), the wheels (out), and the two electric MGs (i and o) (see Figure 1(a)). This formulation provides a compact and physically meaningful description of the PSU kinematics and power ratios by means of the definition of the mechanical points, defined as the overall transmission ratio τ at which a CVU shaft is stationary, according to the following definition: $\tau_{\#i} = (\omega_{out}/\omega_{in})|_{\omega_i=0}$ and $\tau_{\#o} = (\omega_{out}/\omega_{in})|_{\omega_o=0}$. For an existing PSU, the mechanical points are univocally determined by the constructive arrangement [4], whereas in the design stage a prescribed set of mechanical points can be realised through multiple constructive solutions that can be visually screened and rapidly selected by means of a PSU design chart [5], shown in Figure 1(b). In multimode transmissions, each operating mode is characterised by its own set of mechanical points, as mode shifts modify the internal kinematic connections within the PSU.

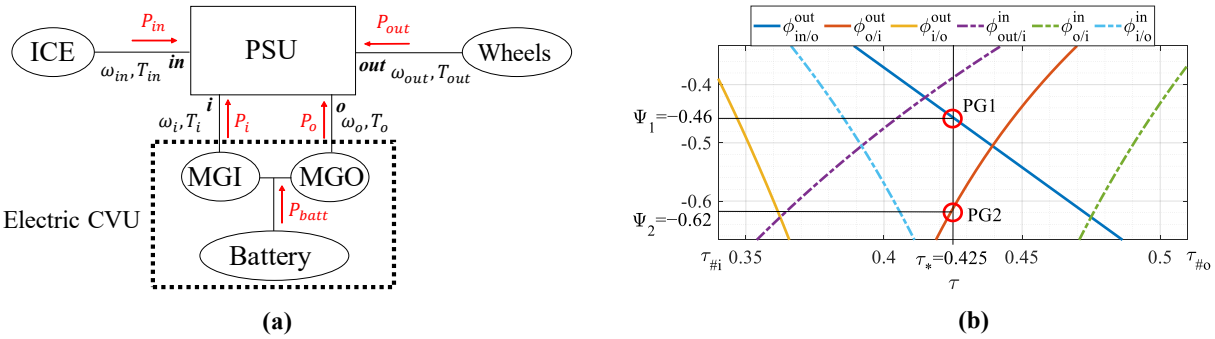

Figure 1. Generalised schematisation of a power-split hybrid powertrain (a) and PSU design chart for planetary gearing synthesis (b).

The CVU power flows are functions of the overall power ratio $\eta = -P_{out}/P_{in}$ and speed ratio $\tau = \omega_{out}/\omega_{in}$ governed only by the mechanical points. Figure 2 shows the CVU recirculation chart [3]. It graphically reports in the $\tau - \eta$ plane the sign of the MGs power P_i and P_o for a generic compound-split mode and for an input-split configuration with $\tau_{\#i} = 0$. Since the battery power satisfies $P_{batt} = P_i + P_o$, operating regions where the MGs powers have the same sign ensure that each machine handles a power flow not exceeding the battery power, whereas opposite power directions imply internal recirculation and would cause the overloading of one MG. Therefore, bearing in mind that the results shown in Figure 2 are general and apply to any corresponding constructive arrangement, during the design stage it is possible to select the mechanical points according to the desired MG power flows, even if neither the PSU constructive layout nor the CVU characteristics have been defined yet.

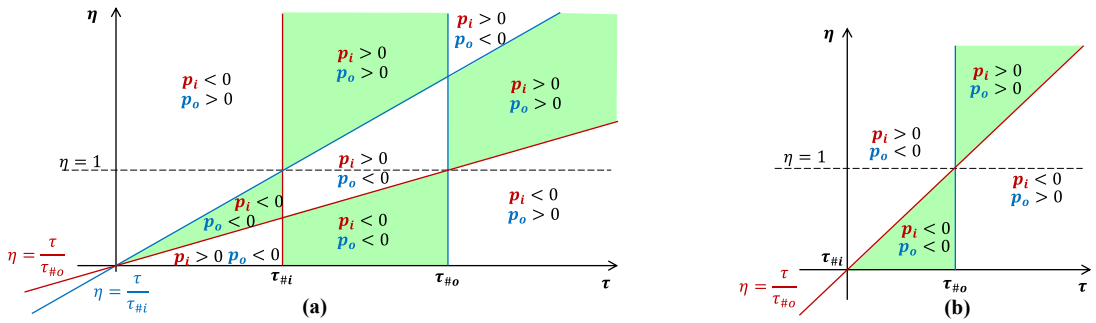

Figure 2. CVU recirculation chart for a compound-split mode (a) and an input-split mode (b): green zones indicate suggested operations.

3. IDENTIFICATION OF FUNCTIONAL MODES FOR MAXIMUM PERFORMANCE

Avoiding internal power recirculation within the electric unit is particularly critical when the powertrain is designed to ensure maximum performance. In this respect, it is desirable that the engine can operate at maximum power $P_{in,max}$ and the entire $P_{batt,max}$ can be transmitted through the MGs all over the vehicle operating range, from zero to maximum speed, while respecting adhesion limits. Therefore, in order to avoid MGs oversizing, the number and the values of the mechanical points must be selected so that the powertrain operates within the green regions of the CVU recirculation chart for all combinations of τ and η associated with maximum-performance conditions and it must be imposed $P_{o,max} = P_{i,max} = P_{batt,max}$ since the power in one MG can be zero due to null velocity or torque (see Figure 2). Moreover, it must be ensured that two adjacent modes must share the same mechanical point to guarantee synchronous mode switching. In this scenario, the following straightforward physic-based procedure has been identified to select the strictly necessary operating modes, together with their mechanical points. By way of example, the red line in Figure 3 shows the operating points corresponding to the maximum performance of a forward-wheel drive (FWD) hybrid electric car with the following design requirements: V_{max}=180 km/h, $P_{in,max}$=120 kW at 5000 rpm, and $P_{batt,max}$=70 kW. At low vehicle speeds, η is constrained by the adhesion limit, which imposes a maximum tractive force; for higher speed, $\eta = \eta_{max} = \left(P_{in,max} + P_{batt,max}\right)/P_{in,max}$, which is directly related to the desired degree of hybridisation. The first mechanical points are identified on the initial increasing linear segment of the red maximum-performance curve for $\eta = 0$, $\eta = 1$ and $\eta = \eta_{max}$. The remaining mechanical points are obtained by multiplying the previous one by η_{max}. Once the mechanical points have been defined, the constructive arrangement of the PSU can be systematically synthesised according to the procedure described in [3].

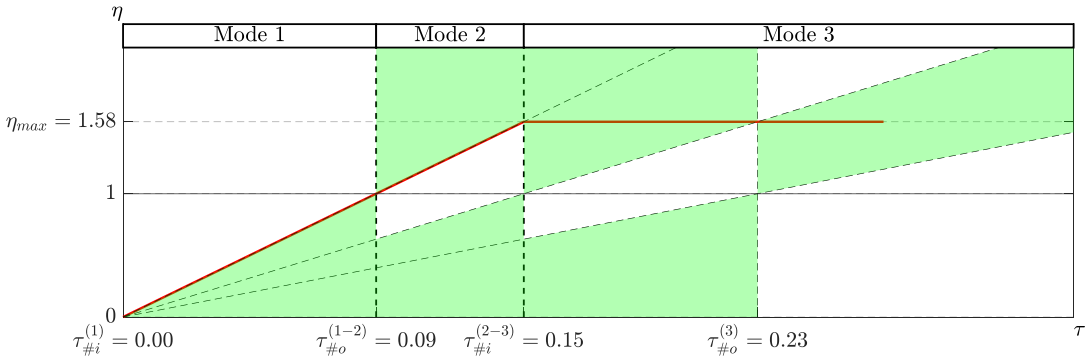

Figure 3. Identification of the number of modes and related mechanical points for the maximum performance of a FWD HEV.

4. CONCLUSIONS

This work moves beyond exploratory, topology-driven design by adopting a parametric, physics-based, performance-driven synthesis of multimode power-split HEV powertrains. As in conventional transmission design, the method targets continuous availability of the maximum onboard power under any road condition, while avoiding electric power recirculation and MGs oversizing through a minimum set of modes and mechanical points selected from the CVU recirculation chart. The resulting functional parameters then guide the systematic synthesis of the PSU constructive arrangement, directly linking vehicle requirements to transmission layout.

REFERENCES

[1] M. Ehsani, Y. Gao, S. Longo, K.M. Ebrahimi, *Modern Electric, Hybrid Electric, and Fuel Cell Vehicles*, CRC Press, 2018.
[2] Z. Zhao, P. Tang, H. Li, "Generation, Screening, and Optimization of Powertrain Configurations for Power-Split Hybrid Electric Vehicle: A Comprehensive Overview", *IEEE Trans. Transp. Electrif.* 8, 325–344, 2022.
[3] A. Castellano, M. Cammalleri, "A tailored approach for the comprehensive design of a multimode power-split e-CVT powertrain for a full-hybrid electric vehicle", *Mech. Mach. Theory* 216, 106214, 2025.
[4] M. Cammalleri, A. Castellano, "Analysis of hybrid vehicle transmissions with any number of modes and planetary gearing : kinematics, power flows, mechanical power losses", *Mech. Mach. Theory* 162, 104350, 2021.
[5] M. Cammalleri, D. Rotella, "Functional design of power-split CVTs: An uncoupled hierarchical optimized model", Mech. *Mach. Theory* 116, 294–309, 2017.

COMPUTERIZED DESIGN, TOOTH CONTACT ANALYSIS AND STRESS ANALYSIS OF PURE ROLLING SPIRAL BEVEL GEARS FOR ORTHOGONAL SHAFTS TRANSMISSION

Zhen Chen[1,2,*], Wenwei Luo[1], Chao He[1], Kai Zhu[1], Xiao Xiao[1,*], Yangzhi Chen[1], Alfonso Fuentes[3]

[1] Guangdong Ocean University, No. 1 Haida Road, Mazhang District, Zhanjiang City, Guangdong Province 524088, China, {mezhenchen@gdou.edu.cn; luoww@stu.gdou.edu.cn; 1257655470@qq.com; kaychu0523@foxmail.com; xiaoping.xiao@foxmail.com; meyzchen@scut.edu.cn}

[2] State Key Laboratory of Mechanical Transmission for Advanced Equipment, Chongqing University, No. 174 Shazheng Street, Shapingba District, Chongqing 400044, China, {mezhenchen@gdou.edu.cn}

[3] Rochester Institute of Technology, 77 Lomb Memorial Drive, Rochester, NY 14623, USA, {afeme@rit.edu}

1. INTRODUCTION

Spiral bevel gears for orthogonal shafts transmission have been widely used in various industrial fields such as aerospace, marine, automotive, and robotics due to their ability to transmit power and motion between vertical intersecting axes[1, 2]. However, the problem of transmission failure such as friction and wear, gluing, and plastic deformation caused by relative sliding of the tooth surfaces have never been completely solved. The common way to reduce the transmission failure is to use lubricants such as lubricating oils and greases. However, these lubricants can fail under extreme conditions, such as high or low temperatures, and may also pollute the environment..

Alternatives to traditional spiral bevel gear design emerged with the development of space curve meshing theory[3], new types of gears have been designed for transmission between intersecting axes. Chen et al.[4, 5] deduced a generalized space meshing equation for an arbitrary angle intersecting gear pair, and spatial helix gears were designed for transmission between arbitrary angle intersecting axes.

This paper proposed a computerized design method for pure rolling spiral bevel gears for orthogonal shafts transmission. Parameterized equations for the tooth surfaces are developed. Analysis of meshing characteristics including the maximum bending and contact stress, contact ellipses and peak-peak loaded transmission errors are discussed. The prototypes are machined by a universal 5-axis CNC machine tool to validate the contact patterns and the contact trace. The kinematic experiments further demonstrate the feasibility of the design of novel pure rolling bevel gears for orthogonal shafts.

2. MATHEMATICAL MODELS OF PURE ROLLING SPIRAL BEVEL GEARS

The meshing line, contact curves, and applied coordinate systems are shown in Fig. 1(a). The sketch of geometric dimensioning is shown in Fig. 1(b). The parameterized equations for the tooth surfaces of the pure rolling spiral bevel gears were deduced based on the active design of the pure rolling meshing line function[6]. The design parameters of the pure rolling spiral bevel gears were given in a list. Then, a 3D model of pure rolling spiral bevel gear drives for orthogonal shafts transmission with gear ratio equal to one are shown in Fig. 1(c).

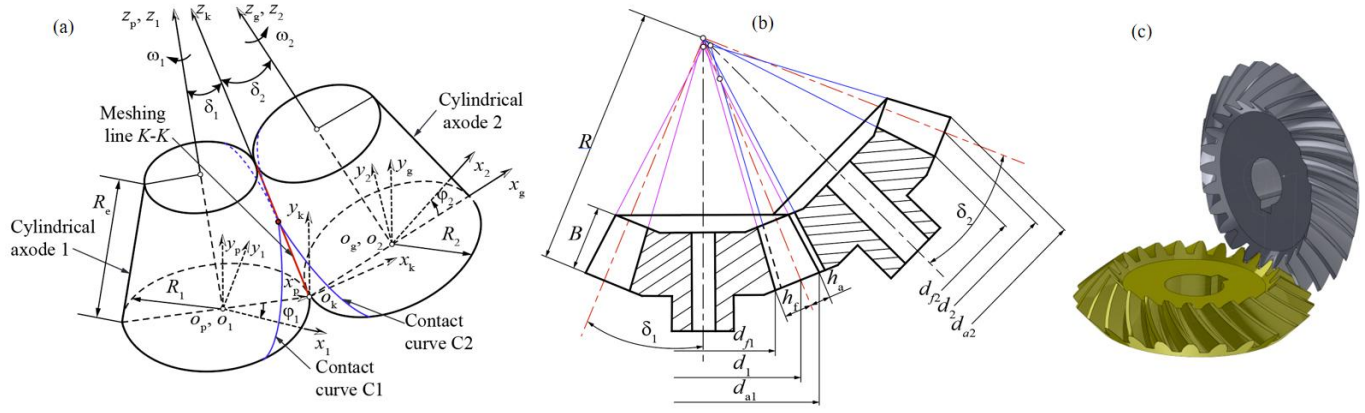

Figure 1. The mathematical model of pure rolling spiral bevel gears: (a) Applied coordinate systems; (b) sketch of geometric dimensioning; (c) 3D model

3. TOOTH CONTACT ANALYSIS AND STRESS ANALYSIS

A CAD-based tooth contact analysis (TCA) was developed to intuitively analyze transmission errors and contact patterns, as shown in Fig. 2 (a) and Fig. 2(b). Finite element models comprising five pairs of contacting teeth were applied to compare the maximum bending and contact stress for designs with different parameters, as shown in Fig. 2 (c) and Fig. 2(d).

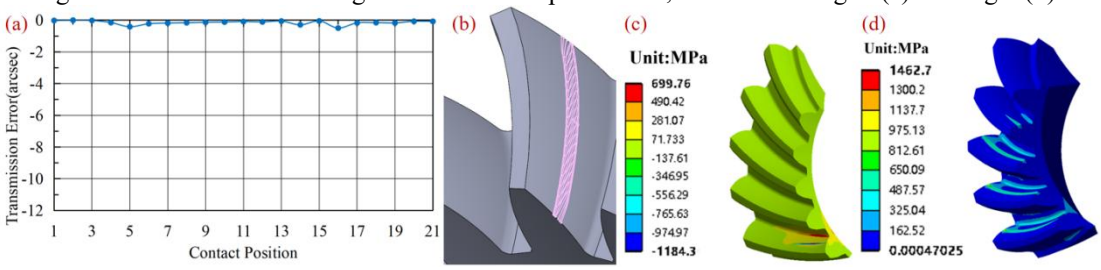

Figure 2. The tooth contact analysis and stress analysis:(a)Transmission errors;(b)Contact patterns;(c)Maximum bending stress;(d)Von Mises stresses

4. KINEMATIC EXPERIMENTS

A five-axis four-linkage machine tool was used to fabricated the prototypes of the spiral bevel gears, as shown in Fig. 3 (a) and Fig. 3(b). Then, kinematic experiments were conducted on the testing device, as shown in Fig.3(c). The contact patterns are distributed in the middle of the tooth surface in the tooth depth direction, and almost occupy the entire tooth surface in the longitudinal direction, which validated the theoretical pure rolling meshing. Besides, the instantaneous transmission ratios fluctuate around the gear ratio 1 with the standard deviations of the instantaneous transmission ratio no more than 0.05, which means that the pair of pure rolling spiral bevel gears can accurately output the designed transmission ratio, as shown in Fig.3(d).

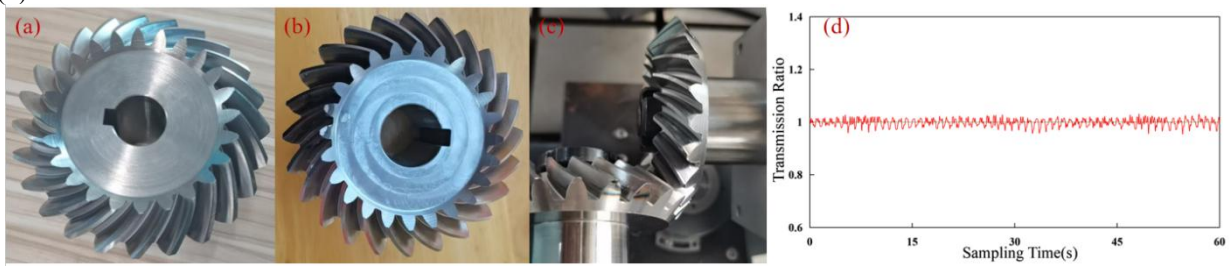

Figure 3. Pure rolling spiral bevel gear prototypes and the kinematic experiments:(a)Pinion;(b)Gear;(c)Kinematic experiments;(d)The instantaneous transmission ratios

5. CONCLUSIONS

A computerized design method for pure rolling spiral bevel gears for orthogonal shafts transmission was proposed. The main design and geometric dimension parameters were given. Parameterized equations for the tooth surfaces were developed based on the method of end face tooth profile internal rotation to achieve a predesigning unloaded function of transmission errors. A comparative analysis of meshing characteristics including the maximum bending and contact stress, contact ellipses and unloaded transmission errors were discussed. At last, the pure rolling spiral bevel gear prototypes were machined by a universal 5-axis CNC machine tool to validate the contact patterns and the contact trace. The kinematic experiments further demonstrated the feasibility of the design of novel pure rolling bevel gears for orthogonal shafts.

ACKNOWLEDGMENTS

The authors would like to acknowledge the support of the National Natural Science Foundation of China (No. 52275073 and 52405056), the State Key Laboratory of Mechanical Transmission for Advanced Equipment, Chongqing University (No. SKLMT-MSKFKT-202416), the Zhanjiang Science and Technology Planning Project (Grant No. 2025B01058).

REFERENCES

[1] F. Litvin, A. Fuentes, K. Hayasaka, “Design, manufacture, stress analysis, and experimental tests of low-noise high endurance spiral bevel gears”. *Mechanism and Machine Theory*, 41, 83-118, 2006.

[2] X. Xiao, Y. Chen, C. Ye et al., “Study on face-milling roughing method for line gears – design, manufacture, and measurement”. *Mechanism and Machine Theory*, 170, 104684, 2022.

[3] Y. Chen, Z. Chen, X. Xiao, et al., *Theory and Application Foundation of Line Gear*. Science Press, Beijing, 2025.

[4] Z. Chen and M. Zeng, “Design of pure rolling line gear mechanisms for arbitrary intersecting shafts”. *Proc. IMechE, Part C: Journal of Mechanical Engineering Science*, 233(15), 5515-5531, 2019.

[5] Z. Chen and M. Zeng, “Nonrelative sliding of spiral bevel gear mechanism based on active design of meshing line”. *Proc. IMechE, Part C: Journal of Mechanical Engineering Science*, 233(3): 1055-1067, 2019.

[6] Z. Chen, H. Zhang, X. Xiao et al., “Computerized design of asymmetric pure rolling gears with a method for predesigning the desired function of unloaded transmission errors”. *Mechanism and Machine Theory*, 213, 106072, 2025.

BRIDGING THEORY AND REALITY: INTEGRATING VVUQ STANDARDS AND LOW-COST EXPERIMENTAL ANALYSIS IN MECHANISM SYNTHESIS EDUCATION

Ramón Gutiérrez-Moizant, Fernando Viadero-Monasterio, Miguel Meléndez-Useros, María Ramírez-Berasategui, Daniel García-Pozuelo Ramos

Mechanical Engineering Department, Advanced Vehicle Dynamics and Mechatronic Systems (VEDYMEC), Universidad Carlos III de Madrid, Avda. de la Universidad 30, 28911 Leganes, Spain,{ragutier@ing.uc3m.es; fviadero@ing.uc3m.es; mmelende@ing.uc3m.es; mrami@ing.uc3m.es; dgramos@ing.uc3m.es}

1. INTRODUCTION

Traditional kinematics education often uses idealised theoretical models that neglect the inherent imperfections of physical systems. Although students typically master the mathematical derivation of mechanism motion, they often face challenges when applying these concepts to real prototypes that are subject to friction, clearances, manufacturing tolerances and measurement uncertainty.

This paper therefore presents a structured teaching methodology for a final-year Master's course in Industrial Engineering to address this gap. The proposed approach integrates mechanism synthesis, experimental measurement, optimisation and uncertainty quantification within a unified reverse engineering framework. The methodology is designed for implementation with three groups of Master's students (approximately 160 students in total) in the upcoming academic year.

The objective is to reinforce theoretical knowledge and develop critical judgement regarding the validity, robustness and reliability of models in realistic engineering conditions.

2. METHODOLOGY

The proposed workflow, illustrated in Fig. 1, is structured into four main stages: (i) experimental acquisition, (ii) data processing, (iii) optimization with uncertainty quantification, and (iv) virtual validation.

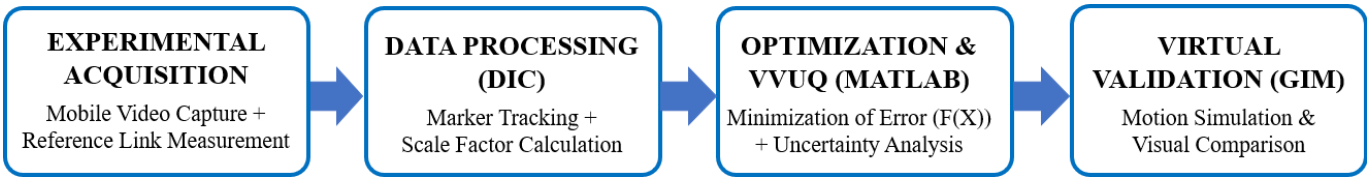

Figure 1. Proposed teaching workflow integrating experimental mobile capture, DIC processing, and computational validation.

Students begin by capturing the motion of a planar mechanism using mobile devices. A single measured reference link is used to establish a scale factor. Digital Image Correlation (DIC) techniques [1] are then applied to extract marker trajectories and infer the full mechanism geometry. This process transforms raw image data into time-dependent coordinate sets suitable for computational analysis.

The experimental coordinates are subsequently compared with a theoretical model developed in MATLAB. Parameter identification is performed by minimizing the objective function:

$$F(x) = \sum_{i=1}^{n} \left[\left(x_{th,i} - x_{exp,i} \right)^2 + \left(y_{th,i} - y_{exp,i} \right)^2 \right] \quad (1)$$

where the discrepancy between theoretical $(x_{th,i}, y_{th,i})$ and experimental trajectories $(x_{exp,i}, y_{exp,i})$ coordinates, is evaluated over *n* time steps.

To explicitly incorporate uncertainty, geometric parameters such as bar lengths are treated as random variables affected by measurement variability. A Monte Carlo simulation approach is employed [2], generating multiple realizations of the mechanism and producing a distribution of possible trajectories. This enables students to visualize variability and understand the sensitivity of kinematic performance to parameter uncertainty.

Model reliability is quantified through the probability of failure:

$$P_{fail} = \frac{Number\ of\ iterations\ with\ Error \geq \epsilon}{Total\ iterations} \quad (2)$$

where ϵ is a predefined admissible error threshold.

Finally, the optimised parameters are exported to GIM software [3,4] to simulate the physical motion of the mechanism. This step provides a qualitative visual check of the kinematic chain, ensuring the design is free from mechanical interference or singularities that purely numerical analysis might overlook.

This uncertainty-aware framework is consistent with the IFToMM Technical Committee for Reliability and aligned with the ASME VVUQ standards [5], introducing students to verification, validation, and uncertainty quantification (VVUQ) principles within a practical design context.

3. CONCLUSIONS

A comprehensive educational framework for teaching mechanism synthesis through experimental reverse engineering and uncertainty-aware optimisation has been presented. This methodology combines low-cost experimental acquisition, computational modelling, probabilistic analysis and virtual validation to create a cohesive learning cycle.

By explicitly confronting students with measurement variability and model discrepancy, the approach encourages them to critically evaluate computational results and emphasises the importance of robustness in engineering design.

The methodology will be implemented in three Master's groups in the forthcoming academic year. Future work will include a quantitative assessment of learning outcomes, compared with those of previous cohorts, to evaluate the pedagogical impact.

ACKNOWLEDGMENTS

The authors wish to acknowledge Erik Macho, Alfonso Hernández, CompMech, Department of Mechanical Engineering, UPV/EHU, for the permission to use the GIM® software. https://www.ehu.eus/compmech/software/

REFERENCES

[1] R. Harilal and M. Ramji, “Adaptation of Open Source 2D DIC Software Ncorr for Solid Mechanics Applications”. 9th International Symposium on Advanced Science and Technology in Experimental Mechanics, New Delhi, India, 2014.
[2] JCGM 101:2008, Evaluation of measurement data — Supplement 1 to the “Guide to the expression of uncertainty in measurement” — Propagation of distributions using a Monte Carlo method. BIPM, Sèvres, France, 2008.
[3] E. Macho, M. Urízar, V. Petuya, and A. Hernández, “Improving Skills in Mechanism and Machine Science Using GIM Software”. Applied Sciences, 11(17), 7850, 2021.
[4] V. Petuya, E. Macho, O. Altuzarra, C. Pinto, and A. Hernández, “Educational Software Tools for the Kinematic Analysis of Mechanisms”. Computer Applications in Engineering Education, 22(1), 72-86, 2011.
[5] ASME V&V 10-2019, *Standard for Verification and Validation in Computational Solid Mechanics*. The American Society of Mechanical Engineers, 2019.

KINEMATICS EVALUATION OF A LOWER LIMB MUSCULOSKELETAL MODEL BASED ON PARALLEL MECHANISMS WITH IN VIVO MEASURED DATA

Manuel Romeo[1], Nicola Sancisi[1], Michele Conconi[1], Raphaël Dumas[2]

[1] Department of Industrial Engineering, University of Bologna, Viale del Risorgimento 2, 40136 Bologna, Italy, {manuel.romeo2@unibo.it; nicola.sancisi@unibo.it; michele.conconi@unibo.it;}

[2] Univ Eiffel, Univ Lyon 1, LBMC UMR_T 9406, F-69622 Lyon, France, {raphael.dumas@univ-eiffel.fr}

1. INTRODUCTION

Inverse kinematics is essential for musculoskeletal modelling, but the resulting joint angles are highly influenced by the chosen kinematic model. A comprehensive musculoskeletal model (i.e., TLEM2 [1]) provided a very detailed geometry for the muscle lines of action, but at the same time, all the joints were modelled by hinges. Parallel mechanisms have been introduced into musculoskeletal models to best mimic natural joint kinematics and to define anatomical joint constraints, including articular contacts and ligaments, at the inverse kinematics step [2]. Two mechanisms for the knee (with different ligaments) and two for the ankle (with one or two degrees of freedom, DoFs) have been synthesized and implemented into the TLEM2 dataset, yielding four different versions of the model [3]. Validation of these models remains challenging due to the lack of in vivo experimental data, which would require invasive procedures for patients. The ability to predict articular joint forces was previously tested using data from instrumented prostheses, demonstrating a good match with experimental observations [3], but kinematics validation was not possible. As for the latter, one dataset in the literature provides in vivo measured kinematics with 3D trajectories of markers placed both on bone pins implanted in the femur, tibia, and calcaneus and on the skin of the thigh, shank, and foot of three participants during running [4].
In this study, we show that implementing parallel mechanisms in a scaled generic, comprehensive musculoskeletal model can replicate joint kinematics with anatomical consistency. We also evaluate the predictive capabilities of the different model versions by comparing bone-pin and model-derived kinematics during a dynamic task, such as running.

2. METHODS

2.1. Parallel mechanisms

Parallel mechanisms were synthesized based on the TLEM2 geometries [1] and a prediction of natural kinematics obtained through a congruence method [5]. Geometrical parameters were optimized to best fit this kinematics while keeping the ligaments isometric, respecting the other kinematics constraints, and avoiding mechanism singularities. The resulting one-DoF knee parallel mechanism featured two sphere-on-plane contacts and three ligaments, and included a hinge and patellar tendon for the patella. Two alternative knee mechanisms were selected: one with ACL, PCL, MCL, as in the standard definition of parallel mechanisms [2], and a second one with LCL, PCL, MCL, for comparison. The one-DoF ankle mechanism included three "talus" links and two ligaments (i.e., TiCaL and CaFiL) simulating the talocrural joint; the two-DoF ankle mechanisms presented two "talus" links and the same two ligaments. The additional DoF simulates the subtalar joint.

2.2. Musculoskeletal model and multibody computation

Parallel mechanisms were implemented in the generic TLEM2 to replace the original hinges. The model comprised 5 segments (i.e., pelvis, thigh, patella, shank, foot), 4 joints (i.e., spherical for the hip and parallel mechanisms for the knee and ankle). Four versions of the model were derived from combinations of the different knee and ankle mechanisms. The versions A1 and L1 included, respectively, the knee mechanism with ACL and with LCL, both featured the one-DoF ankle. The remaining two versions, namely A2 and L2, featured the two-DoF ankle model. After scaling based on segment lengths, the inverse kinematics step minimized *f*, namely the sum of squared distances between modelled and measured skin-marker trajectories:

$$\min_{\mathbf{Q}} f = \frac{1}{2}(\boldsymbol{\Phi}^m)^T\boldsymbol{\Phi}^m \quad \text{subject to} \begin{cases}\boldsymbol{\Phi}^k = \mathbf{0}\\ \boldsymbol{\Phi}^r = \mathbf{0}\end{cases} \tag{1}$$

with $\mathbf{Q}$ the natural coordinates for the segment poses, $\boldsymbol{\Phi}^m$ the driving (marker tracking) constraints, $\boldsymbol{\Phi}^k$ the kinematics constraints, and $\boldsymbol{\Phi}^r$ the rigid body constraints. Joint angles were derived from $\mathbf{Q}$ and described using a ZXY rotation sequence for the knee and a ZYX rotation sequence for the ankle. RMSE and the coefficient of determination (R^2) between measured and computed kinematics were determined.

3. RESULTS AND DISCUSSION

Trials (n=5) of one participant from the running dataset [4] were tested with the four versions of the model. The measured (i.e., bone pins) and model-derived (i.e., tracking the skin markers) kinematics angles of the ankle and the tibiofemoral joint were compared (see **Fig. 1**). Differences and correlations are assessed in **Tab. 1**. All models provided a good prediction of the joint angles. Ankle abduction/adduction from A2 and L2 presented a similar pattern but with a shift; A1 and L1 showed limited error but lower correlation. Ankle inversion/eversion showed low errors but still low correlation due to differences at the end of stance. Tibio-femoral flexion and abduction/adduction are well replicated. Internal/external rotation has a similar pattern but higher errors. This can be due to differences between the participant and the generic, scaled model. Moreover, this motion component is less constrained in the natural knee; this suggests that running has a more muscle-controlled internal/external kinematics, which differs from the natural kinematics from which the mechanisms were synthesized.

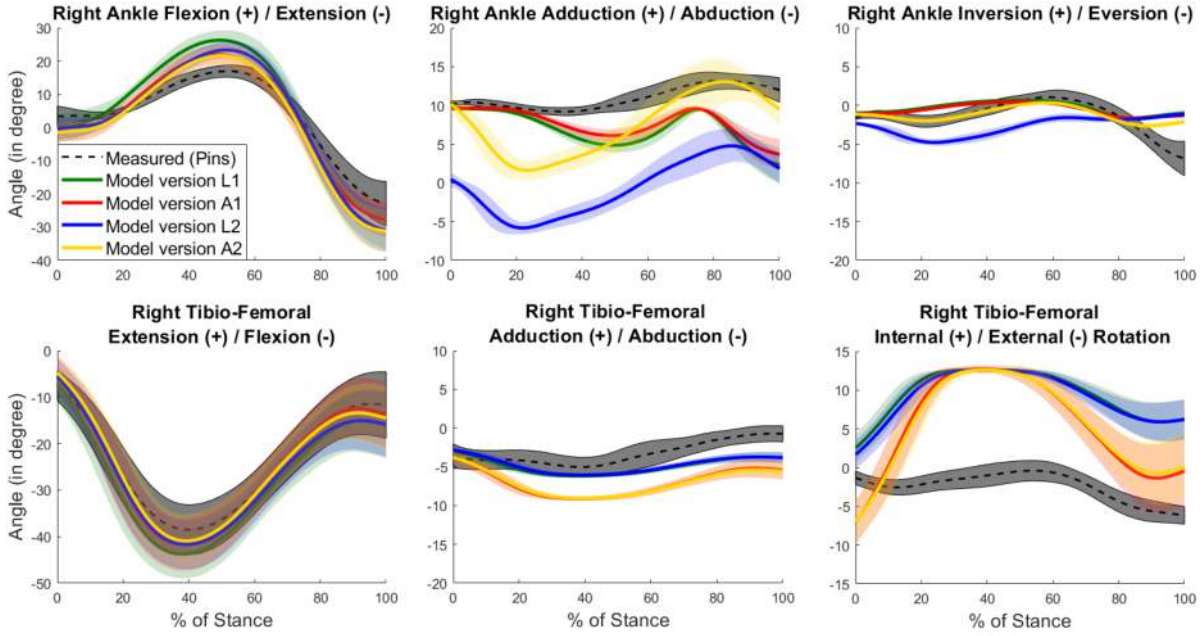

Figure 1: Measured and computed ankle and tibiofemoral kinematics.

Table 1: Root mean square error (in degree) and coefficient of determination between measured and computed ankle and tibio-femoral angles, with each version of the model.

	A1		L1		A2		L2	
	RMSE	R^2	RMSE	R^2	RMSE	R^2	RMSE	R^2
Ankle flexion/extension	4.3	0.97	6.7	0.98	5.2	0.99	5.0	0.99
Ankle adduction/abduction	4.2	<0.01	4.9	<0.01	4.7	0.83	11.9	0.86
Ankle inversion/eversion	2.0	0.38	2.1	0.34	1.6	0.57	3.0	0.01
Tibio-femoral flexion/extension	2.0	0.99	4.0	0.99	1.7	0.99	2.5	0.99
Tibio-femoral adduction/abduction	4.1	0.42	2.1	0.45	4.1	0.38	2.1	0.42
Tibio-femoral internal/external rotation	10.0	0.21	12.4	0.20	9.9	0.19	12.1	0.17

ACKNOWLEDGMENTS

This work was supported by a grant from the Franco-Italian University (Partenariat Hubert Curien) project Galileo # 48932SG.

REFERENCES

[1] V. Carbone *et al.*, "TLEM 2.0 – A comprehensive musculoskeletal geometry dataset for subject-specific modeling of lower extremity," *J. Biomech.*, vol. 48, no. 5, pp. 734–741, Mar. 2015.

[2] N. Sancisi and V. Parenti-Castelli, "A New Kinematic Model of the Passive Motion of the Knee Inclusive of the Patella," *J. Mech. Robot.*, vol. 3, no. 041003, Sep. 2011.

[3] R. Dumas, M. Conconi, and N. Sancisi, "Parallel Mechanisms for the TLEM2 Musculoskeletal Model", *Proceedings of the MMT Symposium*, Guimaraes, Portugal, June, 26-28, 2024.

[4] C. Reinschmidt, A. J. van den Bogert, B. M. Nigg, A. Lundberg, and N. Murphy, "Effect of skin movement on the analysis of skeletal knee joint motion during running," *J. Biomech.*, vol. 30, no. 7, pp. 729–732, Jul. 1997.

[5] M. Conconi, N. Sancisi, and V. Parenti-Castelli, "Prediction of Individual Knee Kinematics From an MRI Representation of the Articular Surfaces," *IEEE Trans. Biomed. Eng.*, vol. 68, no. 3, pp. 1084–1092.

TYPE SYNTHESIS OF LOWER-MOBILITY PARALLEL MECHANISMS FOR MORPHING NOSE BASED ON AN ATLAS METHOD

Zhonghao Huang[1], Hui Yang[1], Yan Wang[1]

[1] Parallel Robot and Mechatronic System Laboratory of Hebei Province, Yanshan University, Qinhuangdao 066004, China {huiyang_0431@163.com; huangzhonghao0921@163.com; wangyan_597@163.com}

1. INTRODUCTION

Future hypersonic vehicles are required to operate across a broad flight envelope, encompassing regimes from low-speed landing to high-Mach cruise, as shown in Figure. 1. To maintain optimal lift-to-drag ratios and stability throughout these phases, the aerodynamic configuration of the vehicle must possess real-time reconfigurability. However, conventional fixed-geometry designs are inevitably subject to severe performance compromises. In the frontier of hypersonic vehicle design, the morphing nose serves as a critical subsystem for optimizing aerodynamic performance across wide flight envelopes. However, this subsystem faces a severe conflict: it must possess sufficient mobility to alter the aerodynamic profile while maintaining exceptional stiffness to withstand complex, omnidirectional aerodynamic loads during high-speed flight. Existing variable-geometry mechanisms often struggle to reconcile the flexibility during reconfiguration with the rigidity during load-bearing [1]. In the absence of a tailored topological design, the morphing nose is prone to aeroelastic instability, such as flutter, under lateral winds or turbulence. Consequently, there is an urgent necessity to develop a novel class of mechanisms capable of adapting their topological properties to these hostile environments [2], satisfying the dual strict requirements of stiffness and mobility.

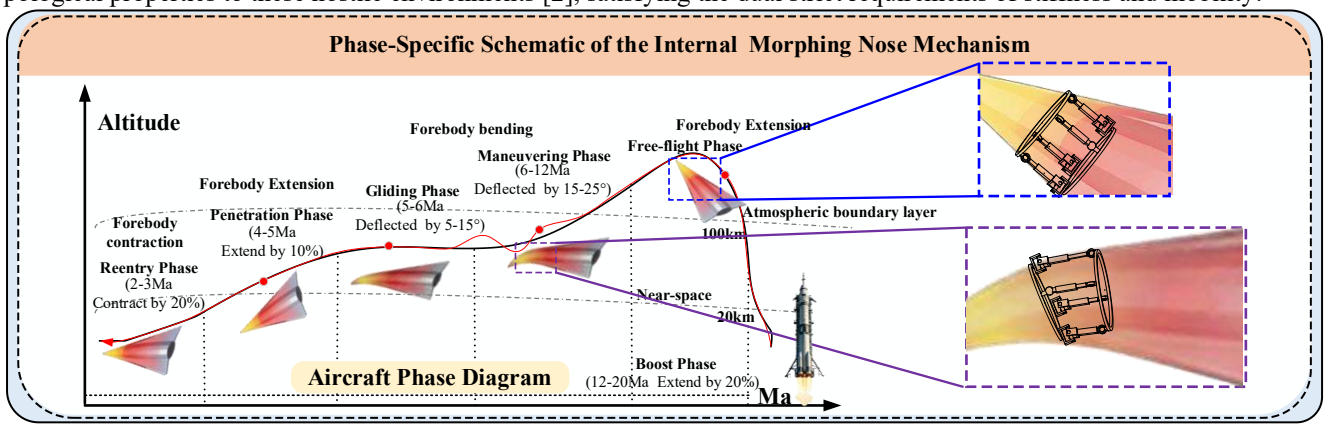

Figure. 1 Phase-Specific Schematic of the Internal Morphing Nose Mechanism

2. METHODOLOGY

To systematically generate such mechanisms, a comprehensive type synthesis framework based on constraint atlases [4][5]and screw theory is proposed. Unlike general synthesis approaches, this method explicitly embeds the bifurcation characteristic as a fundamental constraint within the design loop, as shown in Figure. 2. The synthesis process consists of three rigorous steps: First, the target bifurcation motion is mapped into a sequence of constraint screw systems, defining the required constraint evolution from the transition state to the deflected state. Second, based on the subchain constraint atlases, permissible limb structures (e.g. Class e31, e31, c11) are synthesized and classified, forming a modular library of legs that satisfy specific geometric constraints[6]. Third, a novel assembly principle is established based on the intersection logic of limb constraint spaces. By analyzing the constraint-corresponding positions, we determine the optimal geometric layout of limbs to enforce the desired rank change of the Jacobian matrix, ensuring the mechanism inherently possesses the pre-determined bifurcation behavior.

3. RESULTS

This paper investigates a specific class of lower-mobility parallel mechanisms exhibiting distinct motion bifurcation characteristics[3]. Mathematical analysis reveals a unique metamorphic behavior governed by the dependency of constraint screws: at the transition position, the mechanism possesses 3 degrees of freedom (2R1T) for versatile pose adjustment; however, once deflected about the X or Y axis into an operational state, the motion bifurcates, instantly degrading to 2 degrees of freedom (1R1T). This inherent mobility degradation serves as a mechanical lock, significantly enhancing stiffness in specific directions to resist asymmetrical aerodynamic forces without additional actuation redundancy.

Kinematic simulations verify that the proposed mechanism effectively switches between the 3-DOF reconfiguration mode and the 2-DOF high-stiffness mode, validating the theoretical design, as shown in Figure. 3. This study establishes a rigorous reverse design theory—bridging aerodynamic stability requirements to topological bifurcation synthesis—providing a theoretical foundation for the next generation of resilient morphing aerospace structures.

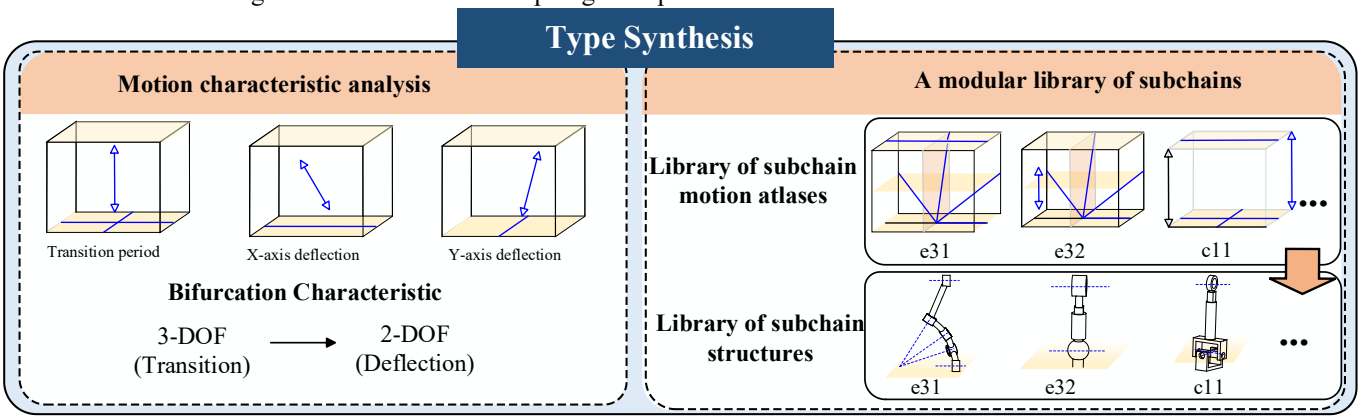

Figure. 2 Type Synthesis

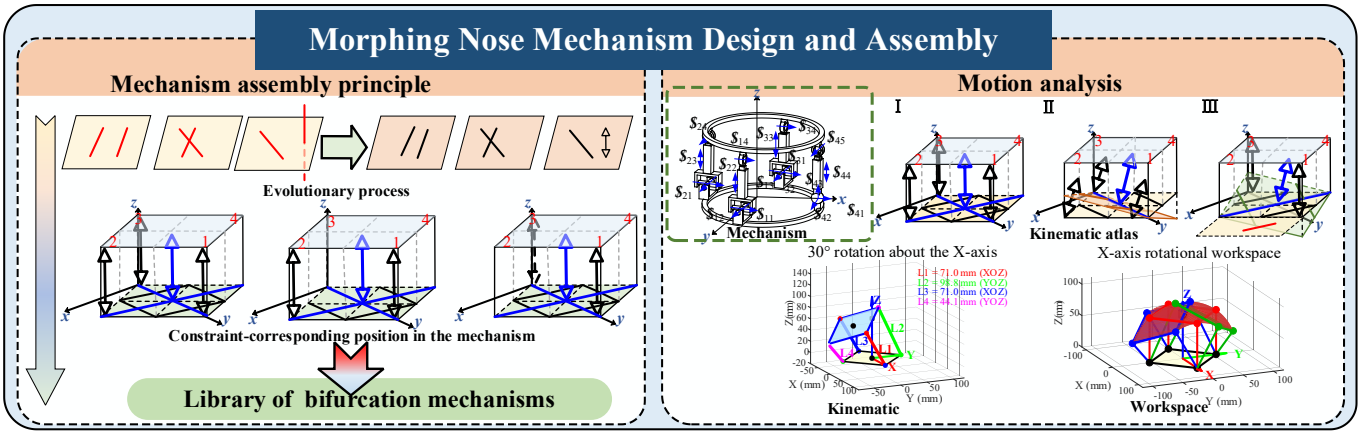

Figure. 3 Morphing Nose Mechanism Design and Assembly

ACKNOWLEDGMENTS

This work was supported by National Natural Science Foundation of China (Grant No. 52575036, 52375028), Hebei Provincial Natural Science Foundation (Grant No. E2024203052, E2024203105). The authors thank the editors and the anonymous reviewers for helping us improve the quality of this article.

REFERENCES

[1]. Schlattmann, J, Baier, H. “Variable stiffness skin for morphing wings: Design and experimental investigation”. *Mechanism and Machine Theory*, 70, 362-371, 2013.

[2]. Zhang, K, Dai, J. S. “Reconfiguration of the metamorphic parallel mechanism 3-rRPS with topological change”. *Mechanism and Machine Theory*, 74, 1-13, 2014.

[3]. Gogu, G. “Bifurcation in constraint singularities and structural parameters of parallel mechanisms”. *Meccanica* 46, 65–74 2011.

[4]. Zhang, Y., Gao, C., Xu, P, Li, B. “Type synthesis of deployable and symmetrical single-loop mechanisms for constructing aerospace platforms”. *Mechanism and Machine Theory*, 181, 105212, 2023.

[5]. Zhang, Y, Kang, X, Li, B. “A family of folding single-loop metamorphic mechanisms for aerospace manipulators: Synthesis, network, and analysis”. *Mechanism and Machine Theory*, 201, 105728, 2024.

[6]. Wang, Y, Tao, J., Wu, D. “Design and analysis of morphing forebody mechanisms with smooth shape control points for aerospace vehicles”. *Aerospace Science and Technology*, 165, 110488, 2025.

INFLUENCE OF ANGULAR ERRORS ON THE CONSTANT-FORCE BEHAVIOR OF A STRAIGHT BEAM

Nadine Wahl-Warnken[1] and Lena Zentner[1]

[1] Technische Universität Ilmenau, Fachgebiet Mechanik Nachgiebiger Systeme, 98693 Ilmenau, Deutschland, {nadine.warnken@tu-ilmenau.de; lena.zentner@tu-ilmenau.de}

1 INTRODUCTION

Constant-force mechanisms enable the generation of nearly constant output forces over a defined displacement range and are frequently realized using compliant mechanisms. Compared to active control approaches or classical joint- and transmission-based concepts, they offer a simple structure, an absence of backlash, and low maintenance requirements [1].

One realization employs a straight beam clamped at both ends. By appropriately selecting the clamping distance and clamping angles, a nearly constant force level can be achieved over a relevant displacement range [2]. While the behavior of a halved configuration employing parallel guidance has been extensively investigated [3, 4], the influence of geometric angular errors on the single-beam configuration considered here has received less attention.

The objective of this contribution is the quantitative assessment of the influence of angular errors on the constant-force behavior of a doubly clamped beam mechanism. Both a tilting of the entire mechanism and a unilateral deviation of a single clamping angle are analyzed with respect to their effect on stiffness.

2 MECHANISM AND MODELING APPROACH

The investigated mechanism consists of a straight rectangular beam of length L, area moment of inertia I and Young's modulus E, clamped at both ends (Fig. 1a). The clamping distance p denotes half of the horizontal distance between the clamping points, while the clamping angle α is defined as the angle between the beam end and the line connecting the clamping points. A displacement force F_u is applied at the midpoint of the beam and acts along the displacement u.

For suitable combinations of p and α, a nearly constant force characteristic can be obtained over a displacement range exceeding 20% of the beam length (Fig. 1b). To assess the force consistency, the quasi-linear stiffness range (QLSR) is considered. The QLSR is defined as the displacement range in which the force can be approximated by a constant stiffness $K = \frac{\Delta F_u}{\Delta u}$ with a maximum deviation of 5%. In the case of constant force, the stiffness approaches zero ($K \cdot \frac{L^3}{EI} < 2$).

The displacement force F_u is determined using geometrically nonlinear Euler–Bernoulli beam theory and computed numerically. The modeling assumptions and solution procedure follow the approaches described in [3, 5].

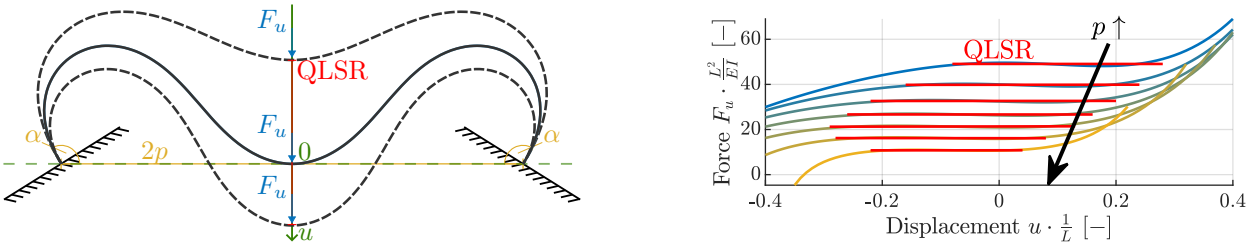

(a) Schematic model

(b) Displacement force diagram

Figure 1: Doubly Clamped Beam Mechanism

3 INFLUENCE OF ANGULAR ERRORS

First, the effect of a tilting of the entire mechanism by an angle $\Delta\gamma$ is examined (Fig. 2a). For clamping distances $p \cdot \frac{1}{L} > 0.3$, the resulting stiffness values remain small with $|K \cdot \frac{L^3}{EI}| \leq 0.5$, such that no significant deviations from the

nominal constant-force behavior are observed within the QLSR (Fig. 2b). For smaller clamping distances $p \cdot \frac{1}{L} \leq 0.3$, larger stiffness variations occur. However, due to the simultaneously increasing force level F_{op} in the QLSR, the relative deviations of the force remain limited.
Subsequently, a unilateral deviation of a single clamping angle by $\Delta\alpha$ is investigated (Fig. 2c). As shown in Fig. 2d, negative angular deviations lead to negative stiffness values, while positive deviations result in positive stiffness values. For equal magnitudes of the angular error, comparable absolute stiffness values are obtained, independent of the clamping distance p.
Compared to global tilting, the unilateral angular deviation leads to substantially larger changes in stiffness. In particular, for large clamping distances $p \cdot \frac{1}{L} > 0.8$ and low force levels in the QLSR $F_{\mathrm{op}} \cdot \frac{L^2}{EI} < 20$, the resulting stiffness increase causes pronounced deviations from the nominal force level. In this regime, even relatively small angular deviations $\Delta\alpha > 2°$ can noticeably reduce the quality of the constant-force behavior.

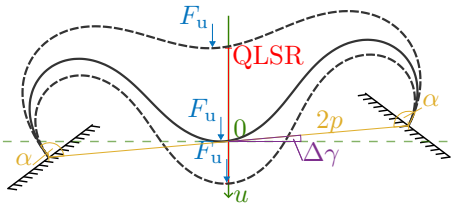

(a) Schematic model of tilting the entire mechanism

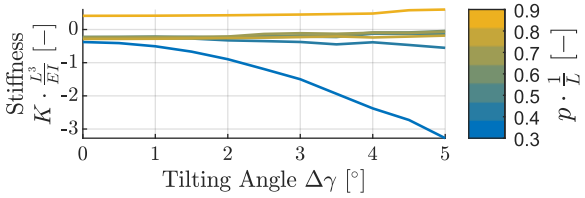

(b) Displacement force diagram of tilting the entire mechanism

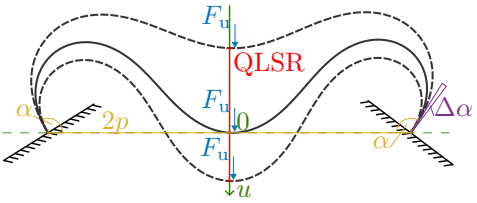

(c) Schematic model of unilateral angular deviation

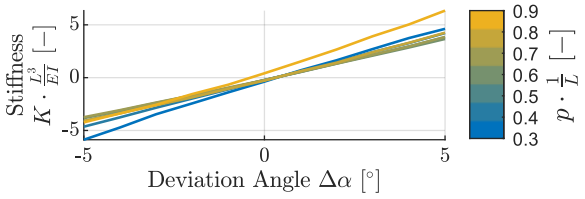

(d) Displacement force diagram of unilateral angular deviation

Figure 2: Angular Errors

4 CONCLUSIONS AND DESIGN IMPLICATIONS

The results indicate that unilateral deviations of the clamping angles have a stronger influence on stiffness and constant-force behavior than a tilting of the entire mechanism. Global tilting effects are of secondary importance and mainly affect configurations with small clamping distances. From a design perspective, these findings suggest that particular attention should be paid to the tolerance and adjustment of the clamping angles, whereas requirements on limiting global tilting may be less critical within typical design ranges.

ACKNOWLEDGMENTS

The authors thankfully acknowledge the funding of their research by the German Research Foundation (Deutsche Forschungsgemeinschaft - DFG) within the scope of the Research Training Group on Tip- and laser-based 3D-Nanofabrication in extended macroscopic working areas (GRK 2182 NanoFab), project number 274711337.
During the preparation of this work the authors used ChatGPT (GPT-5 from OpenAI) in order to improve readability and language. After using this tool/service, the authors reviewed and edited the content as needed and takes full responsibility for the content of the publication.

REFERENCES

[1] J. Ling, T. Ye, Z. Feng, Y. Zhu, Y. Li, and X. Xiao, "A survey on synthesis of compliant constant force/torque mechanisms," *Mechanism and Machine Theory*, vol. 176, p. 104970, 2022

[2] N. Warnken and L. Zentner, "Einstellbare vollständig nachgiebige Führungsvorrichtung mit konstanter Kraft, deren Entwurfsverfahren und Einstellung," *DE102024108477A1*, Deutschland, Nov 13, 2025.

[3] N. Warnken and L. Zentner, "Compliant Constant Force Guiding Mechanism," *Mechanisms and Machine Science, Microactuators, Microsensors and Micromechanisms*, Cham: Springer Nature Switzerland, 2025, pp. 12–21.

[4] N. Warnken and L. Zentner, "Untersuchungen zum Steifigkeitsverhalten von bistabilen Balken bei Einspannungsänderungen," *11. IFToMM D-A-CH Konferenz: 20./21. Februar 2025, FH Kärnten, Villach*, vol. 2025

[5] N. Warnken and L. Zentner, "A Design Algorithm for Compliant Constant-Force Mechanisms," *Mechanisms and Machine Science, New Advances in Mechanisms, Transmissions and Applications*, Cham: Springer Nature Switzerland, 2026, pp. 34–42.

DESIGN OF A CABLE-DRIVEN HYBRID SERIAL-PARALLEL SKELETAL MORPHING WING FOR HYPERSONIC AIRCRAFT

Yan Wang[1], Siqiang Xing[1], Hui Yang[1], Yi Han[1]

[1]Parallel Robot and Mechatronic System Laboratory of Hebei Province, Yanshan University, Qinhuangdao 066004, China
{ wangyan_597@163.com; huiyang_0431@163.com; xingsiqiang_0910@163.com; hy1473640730@163.com}

1. INTRODUCTION

Morphing aircraft adapt to variable flight environments by actively changing the geometric shape of their wings[1-4], offering significant research value and promising applications in enhancing aerodynamic efficiency and overall flight performance[5-6]. However, conventional morphing mechanisms are often constrained by excessive structural weight, complex actuation systems, and poor deformation continuity.

This paper proposes a cable-driven skeletal morphing wing mechanism. Leveraging cable tensioning coordinated with deformable units, this mechanism achieves multi-mode morphological transformations while offering distinct advantages in terms of weight reduction, load capacity, and remote transmission. This paper carries out three aspects of research: 1) proposing an overconstrained 2R1T parallel mechanism as the fundamental unit of the skeletal morphing wing; 2) designing a hybrid serial-parallel skeletal morphing wing mechanism and analyzing its achievable deformation modes; 3) conducting kinematic analysis of the morphing wing skeleton.

2. TYPE SYNTHESIS OF THE 2R1T-PMS

Based on screw theory, the type synthesis of constraint limbs with various DOFs is performed. Considering the distribution of the minimal number of kinematic joints within each limb of a 2R1T parallel mechanism, an overconstrained 2R1T parallel mechanism with the fewest kinematic joints is constructed by selecting four 4-DOF limbs and one 3-DOF limb. The resulting mechanism consists of five limbs, in which the axes of the constraint forces of all limbs are parallel to a common projection plane and the constraint couples are oriented in the same direction. For this optimized configuration, the kinematic screw system is established, from which the three-dimensional workspace is derived and mapped, providing a theoretical foundation for subsequent research on the deformation capabilities of the morphing wing.

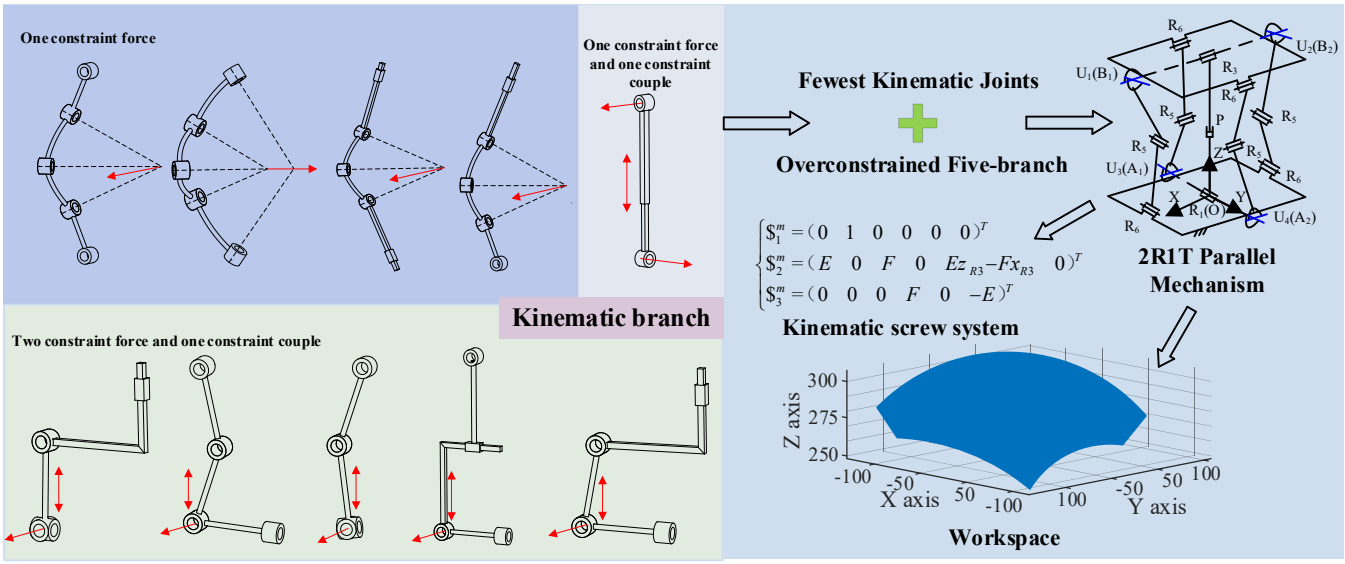

Figure 1. Graphical illustration of research on the morphing wing skeleton mechanism

3. CONSTRUCTION OF MORPHING WING SKELETON STRUCTURE

Based on the optimized 2R1T parallel mechanism unit, a hybrid serial–parallel skeletal morphing wing mechanism is developed. A kinematic model of the skeletal mechanism is established using the geometric constraints inherent in cable-driven parallel mechanisms, yielding the mapping between target deformation configurations and actuation cable length variations. Driven by cables, the mechanism enables multi-modal continuous wing deformations, including spanwise extension, bending, and

sweeping. To further analyze its kinematic behavior, a kinematic model of the serial deformation module is constructed via homogeneous transformation matrices, and the Jacobian matrix is derived to obtain the end-effector velocity.

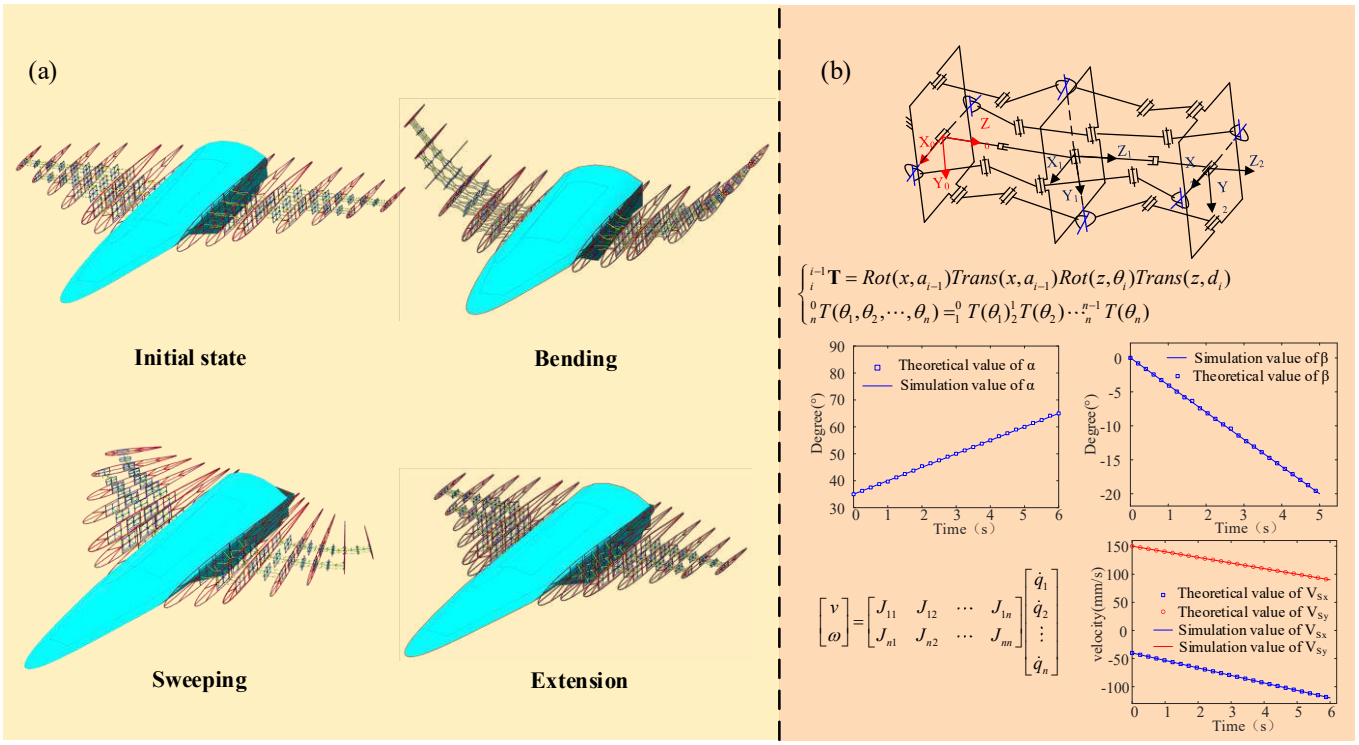

Figure 2. (a) Morphing wing skeletal structure.(b) Kinematic modeling and analysis.

4. CONCLUSION

In conclusion, this abstract demonstrates that the proposed cable-driven hybrid serial-parallel skeletal mechanism provides an optimized structural solution for hypersonic morphing wings. By effectively coordinating cable tensioning and deformable units, the design successfully overcomes traditional weight and continuity constraints while meeting the kinematic requirements for multi-mode morphing during flight.

ACKNOWLEDGMENTS

This work was supported by National Natural Science Foundation of China (Grant No. 52575036, 52375028), Science and Technology Project of Hebei Education Department (Grant No. E2024203052, E2024203105). The authors thank the editors and the anonymous reviewers for helping us improve the quality of this article.

REFERENCES

[1] Mowla M N, Durhasan T, Asadi D, et al. Aerodynamic coefficient prediction of bio-inspired camber morphing wings with flexible surfaces using an explainable transformer[J]. Aerospace Science and Technology, 2025: 111557.

[2] ZHENG K, Daochun L I, Zi K A N, et al. Design and aerodynamic characteristic analysis of flexible morphing wing based on cellular structure[J]. Chinese Journal of Aeronautics, 2025: 103572.

[3] Li D, Zhao S, Da Ronch A, et al. A review of modelling and analysis of morphing wings[J]. Progress in Aerospace Sciences, 2018, 100: 46-62.

[4] Yan B. B., Dai P., Liu R. F., et al. Adaptive super-twisting sliding mode control of variable sweep morphing aircraft[J]. Aerosp Sci Technol, 2019, 92: 198−210.

[5] Wang J, Zhao Y, Xi F, et al. Design and analysis of a configuration-based lengthwise morphing structure[J]. Mechanism and Machine Theory, 2020, 147: 103767.

[6] Tian D, Zhang J, Jin L, et al. Design and research of a new multi-loop closed-chain morphing wing mechanism[J]. Mechanism and Machine Theory, 2024, 199: 105697.

VARIABLE-STEP LIE-GROUP GENERALIZED-α INTEGRATION: SIMPLIFIED PARAMETER UPDATES AND ACCURACY ESTIMATES

Xinyan Li[1], Zhihua Zhao[1,*]

[1] School of Aerospace Engineering, Tsinghua University, Beijing, China, {zhaozh@tsinghua.edu.cn}

1 INTRODUCTION

In computational rigid-body dynamics, Lie-group generalized-α integration has been widely adopted [1, 2]. It combines Lie-algebra increments—avoiding global attitude parameterizations and reducing per-step nonlinearity—with the second-order accuracy and single-step structure of the generalized-α method [3]. The fixed-step formulation is well established, and variable-step parameter updates have been explored to some extent [4]; however, a more systematic treatment remains lacking. This work addresses variable-step integration and derives a simple parameter-update rule together with the corresponding accuracy-estimation expressions. Numerical examples demonstrate efficiency gains over the fixed-step Lie-group generalized-α integrator at the same accuracy.

2 FIXED-STEP LIE-GROUP GENERALIZED-α METHOD

This work follows the fixed-step Lie-group generalized-α formulation [1]. Compared with the classical generalized-α method, the main modification is the attitude update: the rotation is advanced by a Lie-algebra increment and mapped to $SO(3)$ via the exponential map, *i.e.*, $\mathbf{q}_{n+1} = \mathbf{q}_n \exp\widetilde{\boldsymbol{\psi}}_n$, thereby confining the nonlinearity largely to the algebraic increment $\boldsymbol{\psi}_n$. The resulting discrete system is given by Eqs. (1)–(5)

$$\mathbf{M}(\mathbf{q}_{n+1})\,\dot{\mathbf{v}}_{n+1} + \mathbf{g}(\mathbf{q}_{n+1}, \mathbf{v}_{n+1}, t_{n+1}) + \mathbf{B}^{\mathsf{T}}(\mathbf{q}_{n+1})\,\boldsymbol{\lambda}_{n+1} = \mathbf{0}, \tag{1}$$

$$\boldsymbol{\Phi}(\mathbf{q}_{n+1}) = \mathbf{0}, \tag{2}$$

$$\mathbf{q}_{n+1} = \mathbf{q}_n \exp\widetilde{\boldsymbol{\psi}}_n = \mathbf{q}_n \exp\left[h\widetilde{\boldsymbol{v}}_n + (\frac{1}{2} - \beta)h^2\widetilde{\boldsymbol{a}}_n + \beta h^2\widetilde{\boldsymbol{a}}_{n+1}\right], \tag{3}$$

$$\mathbf{v}_{n+1} = \mathbf{v}_n + (1-\gamma)h\,\mathbf{a}_n + \gamma h\,\mathbf{a}_{n+1}, \tag{4}$$

$$(1-\alpha_m)\,\mathbf{a}_{n+1} + \alpha_m\,\mathbf{a}_n = (1-\alpha_f)\,\dot{\mathbf{v}}_{n+1} + \alpha_f\,\dot{\mathbf{v}}_n. \tag{5}$$

where $\mathbf{q}$, $\mathbf{v}$, and $\mathbf{a}$ denote generalized coordinates, velocities, and accelerations; $\mathbf{M}$, the mass matrix; $\mathbf{g}$, the internal and external forces; $\boldsymbol{\Phi}$, the constraint equations; $\mathbf{B} = \partial\boldsymbol{\Phi}/\partial\mathbf{q}$, the constraint Jacobian; and $\boldsymbol{\lambda}$, the Lagrange multipliers [1]. At each step, Eqs. (1)–(2) together with the generalized-α relations (3)–(5) form an implicit nonlinear system at t_{n+1}, which is solved by Newton iteration to advance the state.

For fixed-step integration, the standard optimal parameter choice is:

$$\alpha_f = \frac{\rho_\infty}{\rho_\infty + 1}, \quad \alpha_m = \frac{2\rho_\infty - 1}{\rho_\infty + 1}, \quad \beta = \frac{1}{4}\left(1 + \alpha_f - \alpha_m\right)^2, \quad \gamma = \frac{1}{2} + \alpha_f - \alpha_m, \tag{6}$$

which ensures second-order accuracy and unconditional stability, with mild low-frequency dissipation and strong high-frequency numerical damping.

3 VARIABLE-STEP LIE-GROUP GENERALIZED-α METHOD

With variable step sizes, the Lie-group generalized-α method seeks to retain the key properties of the fixed-step scheme. Previous studies show that step-size changes primarily break second-order consistency; thus, γ must be updated step by step, whereas β, α_m, and α_f remain at their fixed-step values (Fig. 1(a,b)). A convenient way to enforce second-order accuracy is to require the local truncation errors to satisfy $\boldsymbol{I}_n^{\psi}, \boldsymbol{I}_n^{\mathbf{v}} = O(h^3)$ and $\boldsymbol{I}_n^{\mathbf{a}} = O(h^2)$ [2, 4, 5, 6].

Accordingly, the focus is placed on the acceleration-level interpolation in the generalized-α method (Eq. (5)), which underlies its tunable numerical dissipation. This interpolation implies a within-step time shift between the algorithmic

acceleration $\mathbf{a}$ and the physical acceleration $\dot{\mathbf{v}}$, i.e., $\mathbf{a}_{n+1} = \dot{\mathbf{v}}(t_{n+1} + \delta t_{n+1})$ (Fig. 1(c)). To enforce second-order consistency, the shift $\delta t_{n+1} = (\alpha_m - \alpha_f)h_{n+1}$ is constant for a fixed step, whereas it must be updated for variable step sizes. Here h_{n+1} denotes the current step size and h_n the previous one, and $s = h_{n+1}/h_n$ is the step-size ratio.

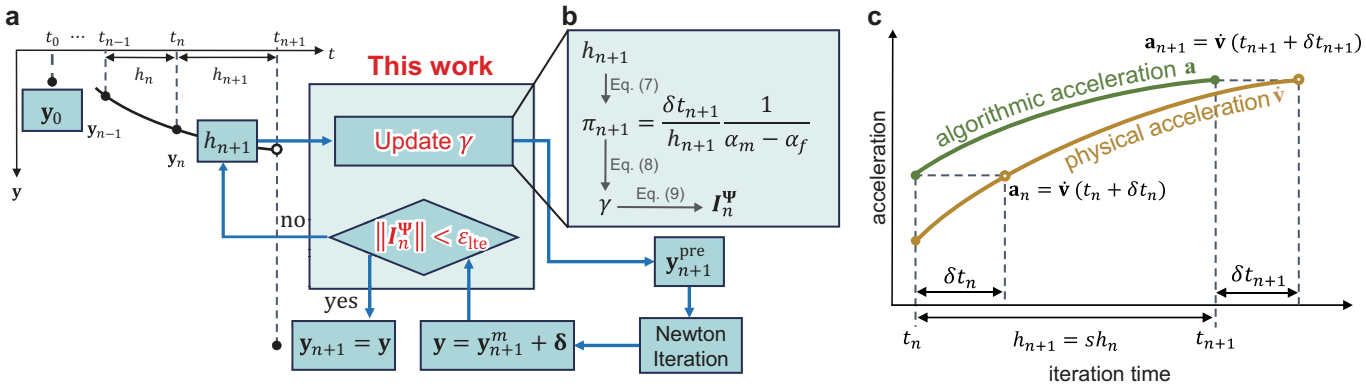

Figure 1: Variable-step Lie-group generalized-α integration. (a) Implicit update $n \to n+1$; $\mathbf{y}$ denotes the vector of unknowns. (b) Workflow for simplified parameter updates and accuracy estimates. (c) Time shift between $\mathbf{a}$ and $\dot{\mathbf{v}}$.

Enforcing the acceleration-level second-order requirement yields the recursion for the normalized time shift:

$$(1-\alpha_m)\frac{\delta t_{n+1}}{h_{n+1}} + \alpha_m \frac{\delta t_n}{h_n}\frac{1}{s} = \alpha_m - \alpha_f. \tag{7}$$

Similarly, enforcing the velocity-level second-order requirement yields a step-by-step update for γ. Here, π_n is defined as $\delta t_n/h_n/(\alpha_m - \alpha_f)$, an auxiliary variable introduced for notational convenience.

$$\gamma = \frac{0.5 - \pi_n(\alpha_m - \alpha_f)/s}{1 + (\pi_{n+1} - \pi_n/s)(\alpha_m - \alpha_f)}. \tag{8}$$

The position-level local truncation error $\boldsymbol{I}_n^{\psi}$ remains second-order under arbitrary step-size changes. Therefore, $\boldsymbol{I}_n^{\psi}$ is used to quantify the per-step accuracy and to drive the adaptive step-size controller:

$$\boldsymbol{I}_n^{\psi} = \frac{h_{n+1}^3}{6}\left\{-\left[6\beta - 1 + 3(\alpha_m - \alpha_f)\left(2\beta\pi_{n+1} + (1-2\beta)\,\pi_n\frac{1}{s}\right)\right]\ddot{\mathbf{v}}(t_n) + \frac{1}{2}[\mathbf{v}(t_n), \dot{\mathbf{v}}(t_n)]\right\}. \tag{9}$$

where

$$\ddot{\mathbf{v}}(t_n) = \frac{1}{h_{n+1}}\left[\dot{\mathbf{v}}(t_{n+1}) - \dot{\mathbf{v}}(t_n)\right] = \frac{1}{h_{n+1}}\left(\dot{\mathbf{v}}_{n+1} - \dot{\mathbf{v}}_n\right).$$

4 CONCLUSION

This work provides simplified parameter updates and a per-step accuracy estimate for variable-step Lie-group generalized-α integration, forming a theoretical basis for implementing an error-controlled variable-step solver.

REFERENCES

[1] O. Brüls and A. Cardona, "On the use of lie group time integrators in multibody dynamics," *ASME Journal of Computational and Nonlinear Dynamics*, vol. 5, no. 3, p. 031002, 2010.

[2] M. Arnold, O. Brüls, and A. Cardona, "Error analysis of generalized-α lie group time integration methods for constrained mechanical systems," *Numerische Mathematik*, vol. 129, pp. 149–179, 2015.

[3] J. Chung and G. Hulbert, "A time integration algorithm for structural dynamics with improved numerical dissipation: The generalized-α method," *ASME Journal of Applied Mechanics*, vol. 60, pp. 371–375, 1993.

[4] O. Brüls and M. Arnold, "The generalized-α scheme as a linear multistep integrator: Towards a general mechatronic simulator," in *Proc. of the IDETC/MSNDC Conference*, Las Vegas, USA, 2007.

[5] M. Arnold and O. Brüls, "Convergence of the generalized-α scheme for constrained mechanical systems," *Multibody System Dynamics*, vol. 18, no. 2, pp. 185–202, 2007.

[6] M. A. Köbis and M. Arnold, "Convergence of generalized-α time integration for nonlinear systems with stiff potential forces," *Multibody System Dynamics*, vol. 37, pp. 107–125, 2016.

EVALUATION OF A TWO-DOF MECHANISM TO MODEL THE ANKLE COMPLEX

Nicola Sancisi[1], Manuel Romeo[1], Raphaël Dumas[2], Michele Conconi[1]

[1] Department of Industrial Engineering, University of Bologna, Viale del Risorgimento 2, 40136 Bologna, Italy, {nicola.sancisi@unibo.it; manuel.romeo2@unibo.it; michele.conconi@unibo.it;}

[2] Univ Eiffel, Univ Lyon 1, LBMC UMR_T 9406, F-69622 Lyon, France, {raphael.dumas@univ-eiffel.fr}

1. INTRODUCTION

Many applications require articular models capable of replicating or predicting the behavior of human joints. Parallel mechanisms provide a direct representation of the main joint constraints (ligaments and contacts) and have been shown to be useful in this context for accurately describing joint motion in space. They allow a full definition of the joint geometry and ensure that the synthesized motion is consistent with these constraints. In musculoskeletal simulations, parallel mechanisms were also used to simultaneously minimize musculotendon, joint contact, and ligament forces during the inverse dynamics step, thereby obtaining a reliable estimate of joint forces [1]. They also proved reliable for simulating joint compliance by adding stiffness characteristics to each constraint. For the ankle joint complex, involving the tibia, talus, and calcaneus, most models used in musculoskeletal simulations feature one or two degrees of freedom (DoFs): a hinge at the tibiotalar joint and, in some cases, a second hinge at the talocalcaneal joint. A two-DoF ankle parallel mechanism for modelling the ankle complex was recently presented [2] as an extension of a previous spherical ankle mechanism [3]. It features a direct representation of the tibiocalcaneal (TiCaL) and calcaneofibular (CaFiL) ligaments, together with articular contacts, modelled by two properly oriented rigid links. There is no explicit representation of the talus: this simplifies dynamic musculoskeletal simulations by eliminating a body with a small mass whose motion cannot be easily measured experimentally. All constraints are represented as pure forces, simplifying their physical interpretation and their use for optimizing muscle and joint forces during the inverse dynamics step of musculoskeletal simulations. A generic two-DoF ankle mechanism is synthesized here from the comprehensive TLEM2 musculoskeletal dataset [4]. It is then evaluated using in vivo kinematic data collected with bone pins during running [5], with no personalization beyond scaling.

2. METHODS

2.1. Parallel mechanism topology

Experimental analyses showed that the tibiotalar motion is almost spherical, while the talocalcaneal's is almost revolute. TiCaL and CaFiL remain almost isometric during natural motion. The parallel mechanism thus features a spherical joint between the tibia and talus, a hinge joint between the talus and calcaneus, and two links between the tibia and calcaneus representing isometric ligaments. The talus will not appear in the mathematical formulation. The preliminary geometry of the mechanism is obtained from the TLEM2 geometry and the computed natural kinematics, obtained with a congruence method [6]: the spherical joint is centered at the pivot point of the tibiotalar motion; the hinge axis is the average helical axis of the talocalcaneal motion; the link for each ligament is the most isometric fiber in the corresponding insertion area during the natural plantar-dorsi flexion of the ankle. The geometrical parameters are then optimized using a validated procedure to best fit the computed natural kinematics while respecting the kinematic constraints and avoiding mechanism singularities.

2.2. Mathematical model

To remove the talus, the spherical and hinge joints are substituted by two equivalent links converging with one end at the spherical joint on the tibia and with the other end lying on the calcaneus hinge axis; the choice of their position on the hinge axis is arbitrary for the kinematics but impacts the distribution of forces at the inverse dynamics step of musculoskeletal simulations. These two links, in fact, represent the two components of the joint forces provided by the talus. An almost horizontal link, namely anterior-posterior (AP), and an almost vertical one, namely proximal-distal (PD), were used for immediate interpretation of forces. Thus, the overall two-DoF mechanism is composed of four links with constant length (Fig. 1). The closure equations are:

$$L_i = \|\mathbf{b}_i - \mathbf{R}\mathbf{a}_i - \mathbf{p}\| \quad (i = 1, \dots, 4) \tag{1}$$

where $\mathbf{b}_i$ and $\mathbf{a}_i$ are the link insertions at the tibia and calcaneus, respectively; L_i are the link lengths; $\mathbf{R}$ and $\mathbf{p}$ are the rotation matrix and position vector of the calcaneus reference system with respect to the tibia. The model can be switched to a one-DOF spherical mechanism by adding a fifth link with one end at the spherical joint and the other end arbitrarily chosen (not on the

hinge axis) in the medial-lateral direction, representing the third component of the talus constraint force. Equation (1) can be solved exactly by choosing two motion components and finding the remaining four. Here, the equations are solved using penalties to allow ligament deformations and to ensure the model can follow an imposed kinematics that may differ from its natural kinematics, while maintaining anatomical consistency. A fifth equation minimizes a measure of the root-mean-square distance (RMSD) between an isotropic distribution of virtual markers enveloping the calcaneus (a sphere with 60 mm diameter) moved using both the model and the reference experimental kinematics [7], considering a fixed tibia, hereinafter called model and reference markers. Weights are added to penalize the ligament, bone, and marker errors differently.

2.3. Evaluation

To evaluate the model, ankle kinematics measured in participants using bone pins [5] during running tasks are used. The generic ankle mechanism synthesized for TLEM2 is scaled to a single participant, and equations (1) are solved as described. Kinematic tracking differences between one-DoF and two-DoF mechanisms are quantified using the cited distance measure. Ligament elongation is also assessed.

3. RESULTS AND DISCUSSION

Both the one-DOF and the two-DOF mechanisms replicate the experimental motion. RMSD between reference and model markers is 8.52 mm and 7.39 mm for the one-DoF and two-DoF, respectively. The two-DoF mechanism shows improved motion prediction compared to one-DoF: although the tibiotalar spherical joint is close to the talocalcaneal hinge axis in the TLEM2, it still affects kinematic tracking. The differences between model and experimental kinematics can be ascribed to anatomical differences. Fig. 1 also reports the predicted ligament elongation during the stance phase of running. The two models exhibit similar elongation patterns, with low deformations in the first part of stance and higher deformations near the push-off. In this part, the two-DoF model shows a lower elongation, particularly in the lateral side. Apart from kinematic differences, the two-DoF mechanism exhibits two important characteristics that may affect joint forces. Firstly, the second DoF mobility has to be compensated by muscles, like in the natural ankle. Secondly, in the one-DoF mechanism, inversion-eversion is deputed to the tibiotalar joint, while in the two-DoF one, it is a combination of the tibiotalar and talocalcaneal joint. Though formally removed from the mathematical model, the talus motion can still be determined: the two equivalent talus links form a triangle with the talus motion. This allows the implementation of ligaments between the tibia-talus-calcaneus at a later step for more detailed deformation analyses at the ankle.

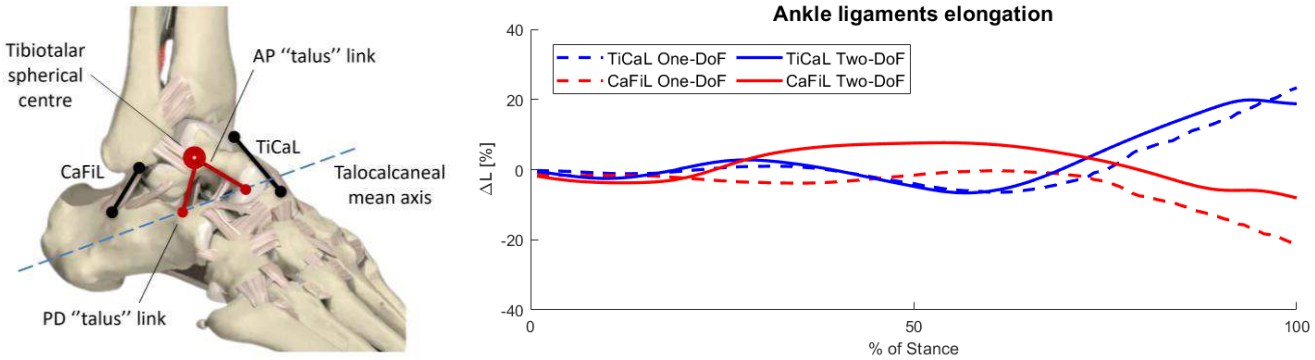

Figure 1. On the left, the two-DoF ankle parallel mechanism; on the right, TiCaL and CaFiL elongations during the stance phase of running. The dotted lines represent the elongations with the one-DoF ankle mechanism; the solid line represents those with the two-DoF one.

REFERENCES

[1] R. Dumas, M. Conconi, and N. Sancisi, "Parallel Mechanisms for the TLEM2 Musculoskeletal Model", *Proceedings of the MMT Symposium*, Guimaraes, Portugal, June, 26-28, 2024

[2] N. Sancisi, R. Dumas, V. Parenti-Castelli, and M. Conconi, "A Two-DoF Parallel Mechanism to Model the Ankle Complex," *Proceedings of the MMT Symposium*, Guimaraes, Portugal, June, 26-28, 2024.

[3] N. Sancisi, B. Baldisserri, V. Parenti-Castelli, C. Belvedere, and A. Leardini, "One-degree-of-freedom spherical model for the passive motion of the human ankle joint," *Med. Biol. Eng. Comput.*, vol. 52, no. 4, pp. 363–373, Apr. 2014.

[4] V. Carbone *et al.*, "TLEM 2.0 – A comprehensive musculoskeletal geometry dataset for subject-specific modeling of lower extremity," *J. Biomech.*, vol. 48, no. 5, pp. 734–741, Mar. 2015.

[5] C. Reinschmidt, A. J. van den Bogert, B. M. Nigg, A. Lundberg, and N. Murphy, "Effect of skin movement on the analysis of skeletal knee joint motion during running," *J. Biomech.*, vol. 30, no. 7, pp. 729–732, Jul. 1997.

[6] M. Conconi, N. Sancisi, and V. Parenti-Castelli, "Prediction of Individual Knee Kinematics From an MRI Representation of the Articular Surfaces," *IEEE Trans. Biomed. Eng.*, vol. 68, no. 3, pp. 1084–1092, Mar. 2021.

[7] C. Mazzotti, N. Sancisi, and V. Parenti-Castelli, "A Measure of the Distance Between Two Rigid-Body Poses Based on the Use of Platonic Solids," in *ROMANSY 21 - Robot Design, Dynamics and Control*, V. Parenti-Castelli and W. Schiehlen, Eds., Cham: Springer International Publishing, 2016, pp. 81–89.

HQP-BASED ADAPTIVE COMPLIANT CONTROL FOR CONSTRAINED OPERATIONS OF SPACE MANIPULATORS

Lei Chen[1], Jun He[1], Feng Gao[1]

[1] State Key Laboratory of Mechanical System and Vibration, School of Mechanical Engineering, Shanghai Jiao Tong University, Shanghai 200240, China

1 INTRODUCTION

Modern on-orbit missions, such as solar array deployment, necessitate high-precision manipulation under stringent geometric constraints [1]. Conventional motion planning and admittance control often fail due to microgravity-induced disturbances, kinematic uncertainties, and the inability to handle redundancy while avoiding singularities. These limitations frequently lead to force-trajectory mismatches and risks of structural damage [2].

To address these issues, an adaptive following control method is proposed for a 7-degree-of-freedom (7-DOF) space redundant manipulator based on Hierarchical Quadratic Programming (HQP). By employing a dexterous end-effector to apply a nominal grasping force, the contact point is allowed to translate and rotate within the contact plane during the deployment process, ensuring continuous engagement. This method leverages the HQP framework to decompose the mission into prioritized sub-objectives. This framework ensures that the solution space of each successive layer is a strict subset of the optimal solution manifold of the preceding layers, thereby maintaining the integrity of higher-priority tasks. By integrating real-time force sensor feedback, the system achieves autonomous correction of the end-effector velocity and direction, enabling high-adaptability following during the satellite solar panel deployment.

2 METHOD

Local Coordinate System Formulation. A contact frame $\{C\}$ is established at the hand-panel interface. The normal force F_{cn} (along $\mathbf{z}_c$) dictates the axial motion, while tangential components F_{ct} drive adaptive compensation to resolve kinematic conflicts. A HQP framework solves for the optimal joint acceleration $\ddot{q}$ through prioritized task optimization.

Physical Constraints. This feasible region defines the manifold that all subsequent optimization tasks must strictly satisfy. The physical limitations of joint positions, velocities, and accelerations are unified into linear inequality constraints as follows:

$$\Omega_0 = \left\{ \ddot{q} \mid \underline{\beta}(q, \dot{q}) \leq \ddot{q} \leq \overline{\beta}(q, \dot{q}), \quad A_{col}\ddot{q} \leq b_{col} \right\} \tag{1}$$

where $\underline{\beta}$ and $\overline{\beta}$ represent the dynamic upper and lower bounds of acceleration derived from motor peak torques and joint limits, while A_{col} and b_{col} denote the constraint matrix and vector for collision avoidance, respectively.

Following Motion. To ensure real-time responsiveness to the solar array's motion during the deployment task, the primary priority layer is formulated as an admittance control problem along the vertical direction:

$$\mathbf{J}_1(q)\ddot{q} = \Phi_1(q, \dot{q}, \mathbf{F}_{ext}) \tag{2}$$

where $\mathbf{J}_1$ is the task-space Jacobian matrix projected onto the vertical axis z_c, and Φ_1 maps the force tracking error and desired contact force F_d into the required acceleration space.

Soft Control. In the lateral directions, the system is designed to behave as a virtual spring-damper assembly. This secondary task ensures spatial compliance and is expressed via an abstract impedance control law:

$$\mathbf{J}_2(q)\ddot{q} = \Phi_2(q, \dot{q}, \mathbf{F}_{ext}, \Delta x) \tag{3}$$

where $\mathbf{J}_2$ is the Jacobian matrix for the lateral x_c and y_c axes, and Φ_2 utilizes the virtual stiffness and position deviation to generate corrective accelerations, thereby preventing mechanical jamming during contact.

Redundancy Optimization. The kinematic redundancy of the manipulator is exploited to enhance dexterity and avoid singular configurations. The optimization objective is to minimize the tracking error of a secondary task

acceleration $\ddot{q}_{null}$:

$$\min \frac{1}{2} \left\| \ddot{q} - (k_m \nabla w(q) - D_n \dot{q}) \right\|^2 \tag{4}$$

where $w(q)$ represents the manipulability measure, k_m is a gain coefficient, and D_n denotes the damping factor.

HQP Resolution. In each discrete control cycle, the optimal joint acceleration $\ddot{q}^*$ is determined by solving a sequence of prioritized Quadratic Programs (QPs). For the i-th priority level, the optimization problem is formulated as:

$$\begin{aligned} \ddot{q}_i^* = \arg \min_{\ddot{q} \in \Omega_{i-1}} & \frac{1}{2} \|\mathbf{A}_i \ddot{q} - \mathbf{b}_i\|^2 + \lambda \|\ddot{q}\|^2 \\ \text{s.t. } & \mathbf{A}_j \ddot{q} = \mathbf{A}_j \ddot{q}_j^*, \quad j = 1, \ldots, i-1 \end{aligned} \tag{5}$$

where $\mathbf{A}_i$ and $\mathbf{b}_i$ represent the generalized task Jacobian and the corresponding control laws at each level. The parameter λ is a regularization factor for numerical stability, and the constraint $\ddot{q} \in \Omega_{i-1}$ ensures that the current solution resides within the optimal manifold of all higher-priority tasks.

3 CONCLUSION

The control architecture of the proposed algorithm is illustrated in Fig. 1, with the corresponding numerical simulation results shown in Fig. 2. The physical validation was conducted on the experimental setup depicted in Fig. 3.
The primary contribution of this research consists in the development of an autonomous control law within a Hierarchical Quadratic Programming (HQP) framework, enabling the manipulator to adapt to the constrained arc trajectories of solar panels. Experimental results demonstrate that this approach effectively mitigates kinematic conflicts and prevents mechanical jamming, providing a robust and reliable solution for high-precision on-orbit manipulation in microgravity environments. Future research will further investigate the robustness of this hierarchical framework under complex nonlinear contact dynamics and explore its extension to a broader range of fine-manipulation tasks.

Algorithm 1 Adaptive Control Framework Based on HQP for 7-DOF Robotic Arm

Set: $\Delta t = 0.01$ s, total time T.
for $t = k\Delta t$, $k = 1, \ldots, T/\Delta t$ **do**
  Read: $q(t), \dot{q}(t), \mathbf{F}_{ext}(t)$.
  $\Omega_0 = \left\{ \ddot{q} \mid \underline{\beta} \le \ddot{q} \le \overline{\beta},\ A_{col}\ddot{q} \le b_{col} \right\}$.
  $\mathbf{J}_1 \ddot{q} = \Phi_1(q, \dot{q}, \mathbf{F}_{ext})$.
  $\mathbf{J}_2 \ddot{q} = \Phi_2(q, \dot{q}, \mathbf{F}_{ext}, \Delta x)$.
  $\min \frac{1}{2} \|\ddot{q} - (k_m \nabla w(q) - D_n \dot{q})\|^2$.
  $\Omega_{-1} \leftarrow \Omega_0$, $\ddot{q}_0^* \leftarrow 0$.
  for $i = 1, 2, 3$ **do**
    $\ddot{q}_i^* = \arg\min_{\ddot{q} \in \Omega_{i-1}} \frac{1}{2} \|\mathbf{A}_i \ddot{q} - \mathbf{b}_i\|^2 + \lambda \|\ddot{q}\|^2$, s.t. $\mathbf{A}_j \ddot{q} = \mathbf{A}_j \ddot{q}_j^*, j < i$.
    $\Omega_i \leftarrow \Omega_{i-1} \cap \{\ddot{q} \mid \mathbf{A}_i \ddot{q} = \mathbf{A}_i \ddot{q}_i^*\}$.
  end for
  $\ddot{q}^* \leftarrow \ddot{q}_3^*$.
  $\dot{q}(t + \Delta t) \leftarrow \dot{q}(t) + \ddot{q}^* \Delta t$.
  $q(t + \Delta t) \leftarrow q(t) + \dot{q}(t + \Delta t) \Delta t$.
end for

Figure 1. HQP-based adaptive control framework.

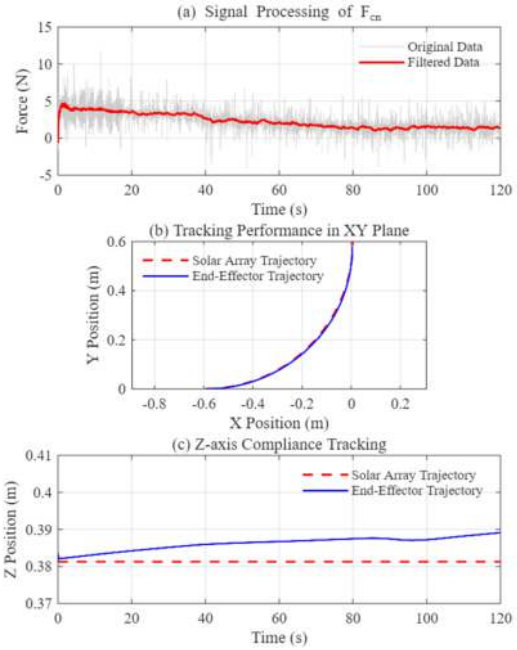

Figure 2. Simulation results.

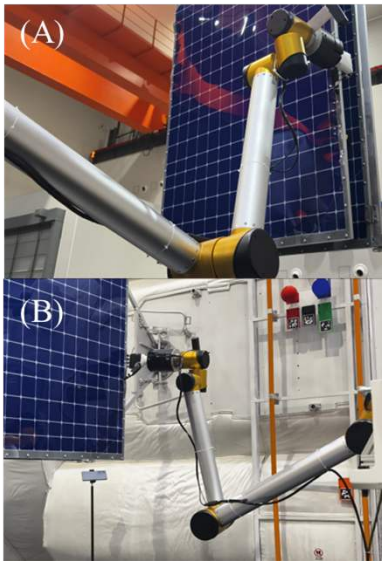

Figure 3. Experimental setup.

ACKNOWLEDGMENTS

This project was supported by the National Key Research and Development Program of China under Grant 2024YFB4006503.

REFERENCES

[1] A. Flores-Abad, O. Ma, K. Pham, and S. Ulrich, "A review of space robotics technologies for on-orbit servicing". *Progress in Aerospace Sciences*, vol. 68, pp. 1-26, 2014.

[2] N. Fallahiarezoodar and Z. H. Zhu, "Review of autonomous space robotic manipulators for on-orbit servicing and active debris removal". *Space: Science & Technology*, vol. 5, p. 0291, 2025.

DESIGN AND KINEMATICS OF MODULAR VARIABLE-STIFFNESS SKELETON MECHANISM FOR Z-FOLDED MORPHING WING BASED ON WATERBOMB-ORIGAMI

Yi Han[1], Hui Yang[1], Yan Wang[1]

[1] Parallel Robot and Mechatronic System Laboratory of Hebei Province, Yanshan University, Qinhuangdao 066004, China {hy1473640730@163.com; huiyang_0431@163.com; wangyan_597@163.com;}

1. INTRODUCTION

Next-generation aerospace equipment, such as large-span aerospace morphing aircraft, serves as a critical carrier for strategic projection and aerospace dominance capabilities. The large-span aerospace morphing vehicle imposes new requirements on morphing mechanisms. Space morphing mechanisms serve as critical enablers for morphing aircraft [1], solar sails [2-3], and space manipulators [4-6], representing an area of significant research importance. For continuous aerodynamic contour adjustment, the mechanism must be capable of multi-dimensional, continuous, and smooth morphing. Furthermore, during such morphing, it must maintain active stiffness control and stability under high external loads. However, conventional spatial mechanisms struggle to achieve continuous, smooth multi-dimensional deformation due to inherent limitations such as structural complexity and strong kinematic coupling, and their stiffness cannot be actively regulated. Consequently, there is an urgent need to investigate the creation of multi-dimensional spatial morphing mechanisms and the methods for active stiffness control and maintenance under high load-bearing conditions.

2. METHODOLOGY

To address the functional requirements of a new class of morphing wing-skeleton mechanisms, this paper conducts research in three key areas: (1) proposing a novel universal design framework for space origami mechanisms; (2) developing an active stiffness-tuning method based on cable-driven actuation; and (3) designing a novel modular morphing wing-skeleton architecture inspired by origami. Origami enables the transformation between complex three-dimensional and two-dimensional shapes, offering broad engineering applications and providing an innovative design scheme for next-generation space multi-dimensional morphing mechanisms. To fully harness the kinematic potential of origami while ensuring structural rigidity, the mountain and valley folds are replaced with rigid linkages, and the fold intersections are designed as compound hinges. Based on this principle, a Waterbomb-ori mechanism is proposed. By integrating this mechanism with an auxiliary system, a Waterbomb-ori Morphing Module (WMM) was constructed, which can perform both deployment and bending actions, and its kinematics were analyzed. An active stiffness-tuning capability is introduced into the WMM through a synthesized arrangement of multiple driving cables. This antagonistic cable routing allows for real-time stiffness adjustment during morphing, enabling adaptation to the wide-range flight conditions encountered in aerospace environments. Finally, using the stiffness-controllable WMM as a building block, a modular Waterbomb morphing wing-skeleton mechanism is developed.

3. RESULTS

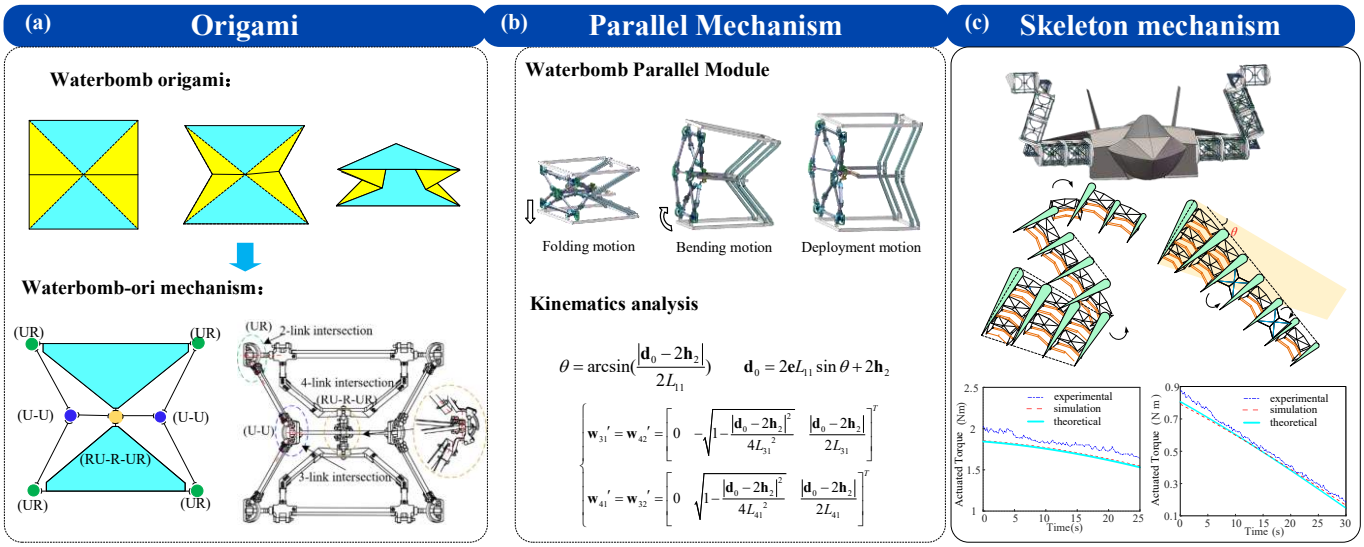

Figure 1. Graphical description of this work: a) Design concept of Waterbomb-ori mechanism; b) Design concept of Waterbomb-ori morphing module (WMM) and kinematic modeling; c) Design of Waterbomb-ori modular morphing wing skeleton mechanism.

The skeleton mechanism presented in this work features variable wingspan, adjustable sweep angle, and the ability to achieve a Z-fold configuration, all while maintaining the desired stiffness during morphing. Furthermore, this study establishes a unified framework for the innovative design of origami-inspired modular robotic systems, as well as for the active stiffness control of parallel mechanisms in the context of morphing.

ACKNOWLEDGMENTS

This research was support by National Natural Science Foundation of China (Grant No. 52375028, 52575036), Hebei Provincial Natural Science Foundation (E2024203052, E2024203105). The authors thank the editors and the anonymous reviewers for helping us improve the quality of this article.

REFERENCES

[1] Z. Fan, R. Wang, H. Huang, X. Li, Design and Analysis of an Origami-inspired Modular Thick-panel Deployable Structure, International Journal of Mechanical Sciences, Volume 282, 2024, 109579, ISSN 0020-7403.

[2] Qi, X., Huang, H., Li, B., and Deng, Z., 2016, “A Large Ring Deployable Mechanism for Space Satellite Antenna,” Aerosp. Sci. Technol.,58, pp. 498–510.

[3] Guan, Y., Zhuang, Z., Zhang, Z., and Dai, J. S. (May 18, 2023). "Design, Analysis, and Experiment of the Origami Robot Based on Spherical-Linkage Parallel Mechanism." ASME. J. Mech. Des. August 2023; 145(8): 081701.

[4] Sébastien Briot and V. Arakelian . “Complete Shaking Force and Shaking Moment Balancing of In-line Four-bar Linkages by adding a Class-two RRR or RRP Assur Group." *Mechanism and Machine Theory*, 57,13-26,2012.

[5] Z. Zhang, T. Kang, W. Yan, et al., Design and analysis of an origami-inspired redundant rigid-flexible coupling deployable manipulator, Mechanism and Machine Theory, Volume 205, 2025, 105852, ISSN 0094-114X.

[6] G. Wang, J. Wang, Y. Yao, et al., Research on programmable spatial capture mechanism and its motion characteristics based on origami principle, Mechanism and Machine Theory, Volume 181, 2023, 105179, ISSN 0094-114X.

A FRICTIONAL CONTACT FORMULATION FOR PLANAR MECHANISMS

A. Cammarata[1], R. Sinatra[1], P.D. Maddio[1]

[1] University of Catania, Via S. Sofia 64, Catania, Italy,
{alessandro.cammarata@unict.it, rosario.sinatra@unict.it, pietro.maddio@unict.it}

1 INTRODUCTION

Frictional contact plays a crucial role in the dynamic behavior of mechanical systems, influencing energy dissipation, motion stability, and force transmission [1, 2]. Accurate modeling of tangential interactions remains a significant challenge in computational contact mechanics, particularly when dealing with flexible bodies undergoing large motions. Among the various approaches for enforcing contact constraints, the penalty method offers a good balance between implementation simplicity and computational efficiency, avoiding the introduction of additional unknowns typical of Lagrangian multiplier formulations. This work extends a recently proposed area-based contact formulation [3] to include frictional effects. The frictionless method relies on the penalty approach to compute the normal contact force between two planar bodies by exploiting the geometric overlap.

2 METHODOLOGY

Contact detection is performed through a geometric inclusion test that verifies whether nodes from one body fall within the perimeter of the other. Once contact is confirmed, the algorithm identifies the intersection polygon by combining the penetrating nodes with the intersection points of the two perimeters. The force magnitude is then computed proportionally to the intersection area through a penalty coefficient, while its direction is obtained by aggregating weighted projection vectors from each penetrating node to the opposing body's surface. Each contribution is weighted by the local penetration depth, allowing deeper indentations to have a stronger influence on the overall force direction. The resulting global contact force is applied at the centroid of the overlapping region. For flexible bodies, this global force is decomposed into nodal contributions that satisfy both force and moment equilibrium, with each nodal force proportional to its local indentation and scaled by a common factor determined to minimize the residual in the equilibrium equations.

The present contribution introduces tangential forces through a regularized Coulomb friction model. The tangential force computation begins by evaluating the relative velocity between the contact points on the master and slave bodies. For each body, the velocity at the contact centroid is computed considering both translational and rotational motion components. Specifically, the velocity at the centroid accounts for the translational velocity of the body's center of mass and the contribution arising from the angular velocity and the distance between the center of mass and the contact centroid. The relative velocity between the contact surfaces is then obtained as the difference between the slave and master centroid velocities.

To determine the tangential component of this relative motion, a tangential direction vector is computed by rotating the normal force direction by 90 degrees. The tangential relative velocity is then calculated by projecting the relative velocity vector onto this tangential direction.

The friction force follows a regularized Coulomb friction model that incorporates both velocity-dependent direction and magnitude scaling, expressed as:

$$\mathbf{F}_{t,s} = -\mu \,\mathrm{sign}(v_\tau)\, \hat{\boldsymbol{\tau}}\, \sigma(|v_\tau|)\, |\mathbf{F}_s| \tag{1}$$

where μ is the friction coefficient, v_τ is the tangential component of the relative sliding velocity, $\hat{\boldsymbol{\tau}}$ is the unit tangential direction vector, $\sigma(\cdot)$ is a sigmoid function, and $|\mathbf{F}_s|$ is the magnitude of the normal contact force. The force direction is determined by the sign of the tangential velocity, ensuring that friction always opposes the relative motion. The sigmoid function $\sigma(|v_\tau|)$ modulates the force magnitude based on the sliding velocity, providing a smooth transition between sticking and sliding regimes. This regularization is essential to prevent numerical instabilities associated with the discontinuous sign function at zero velocity, which would otherwise cause convergence issues in the numerical integration.

Similar to the global normal force case, the global tangential force must be decomposed into nodal contributions for flexible body analysis. However, unlike the normal forces that naturally balance around the contact centroid, tangential forces produce a resulting moment about the contact region. Therefore, the equilibrium conditions for the

tangential force decomposition must account for both force balance and moment preservation. For the slave body, these conditions are expressed as:

$$\sum_{i=1}^{n_s} \mathbf{F}_{s,i}^{tan} = \mathbf{F}_{t,s} \tag{2}$$

$$\sum_{i=1}^{n_s} (\mathbf{p}_{s,i} - \mathbf{R}_s)^T \mathbf{F}_{s,i}^{tan} = (\mathbf{x}_c - \mathbf{R}_s)^T \mathbf{F}_{t,s} \tag{3}$$

where $\mathbf{F}_{s,i}^{tan}$ is the tangential force at the i-th contact node, n_s is the number of slave nodes in contact, $\mathbf{p}_{s,i}$ is the position of the i-th node, $\mathbf{R}_s$ is the position of the slave body centroid, and $\mathbf{x}_c$ is the centroid of the contact area. The same procedure is applied to the master body.
The first equation ensures force equilibrium, requiring that the sum of all nodal tangential forces equals the global friction force. The second equation enforces imposes equivalence, guaranteeing that the distributed nodal forces produce the same moment about the body centroid as the global friction force applied at the contact centroid.
As shown in Fig. 1, both the normal and tangential global forces are decomposed into nodal contributions acting on the contact interface.

3 CONCLUSIONS

The proposed formulation has been validated on planar mechanisms involving flexible bodies, including a planar pin-joint configuration, a cam-follower system, and a Geneva mechanism. Numerical simulations demonstrate stable dynamic behavior and accurate force transmission under frictional contact conditions, confirming the effectiveness of the proposed friction model.

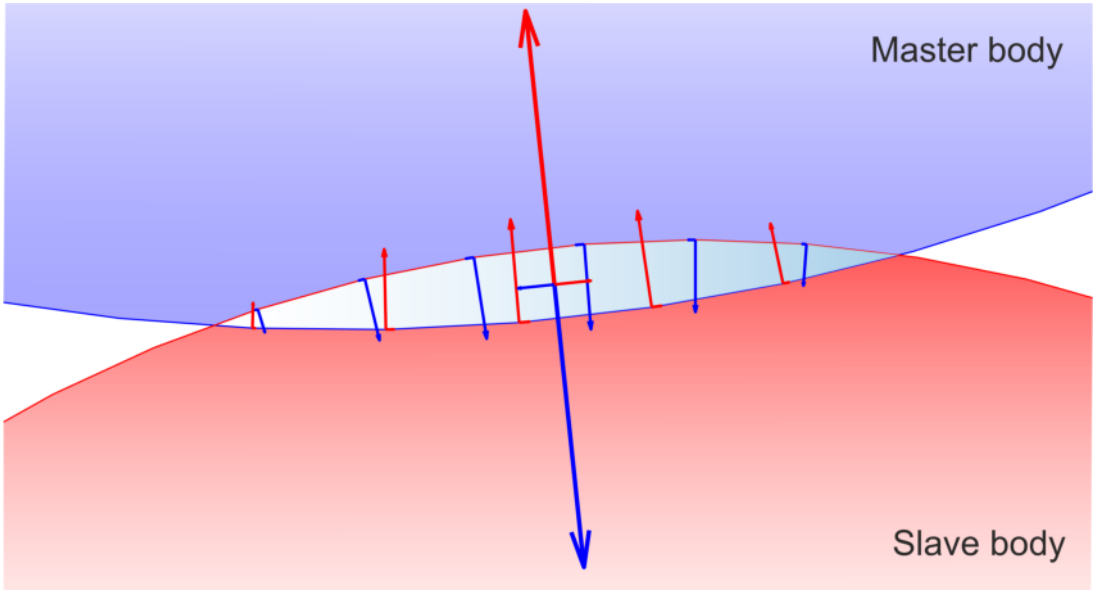

Figure 1: Normal and tangential global forces at the contact centroid with the corresponding nodal decomposition.

ACKNOWLEDGMENTS

This research was supported by the Pia.ce.ri. project, Line 1, University of Catania.

REFERENCES

[1] P. Wriggers, *Computational Contact Mechanics. 2nd ed.*, Springer, 2006.

[2] T. Laursen and J.C. Simo, "A Continuum-Based Finite Element Formulation for the Implicit Solution of Multibody, Large Deformation Frictional Contact Problems". *International Journal for numerical methods in engineering*, vol. 36, pp. 3451–3485, 1993.

[3] P.D. Maddio, R. Sinatra and A. Cammarata, "A Novel 2D Penalty Formulation for Frictionless Contact", in *Multibody System Dynamics*, pp. 1–25, 2025.

COMPLETE SINGULARITY ANALYSIS OF KINOVA LINK 6 TYPE ROBOTS USING LINE GEOMETRY

Manfred Husty[1,2], Calin Vaida[2], Bogdan Gherman[2], Damien Chablat[2,3], Doina Pisla[2]

[1] Unit of Geometry and Surveying, University Innsbruck, Austria, {manfred.husty@uibk.ac.at}
[2] Technical University of Cluj-Napoca, Cluj-Napoca, Romania, {calin.vaida,bogdan.gherman,doina.pisla@mep.utcluj.ro}
[3] École Centrale Nantes, Nantes Université, CNRS, LS2N, Nantes, France, {damien.chablat@ec-nantes.fr}

Singularity analysis of classical industrial robots, which are almost exclusively wrist partitioned, is a simple task because the determinant of the Jacobian matrix splits into several simple parts. Most of those robots have a sholder, ellbow and wrist singularity which correspond to the different factors of the singularity equation. Not long ago more general 6R robots came into the market, such as Kinova Link 6 or Fanuc CRX. These robots exhibit, from kinematic point of view, more interesting features such as 16 solutions of the inverse kinematics and much more singularities. The second fact was already analyzed in a conference paper [1] using Grassmann line geometry, but missing several cases due to lack of basic understanding of the geometry of lines. This is mainly due to the fact that the authors equate screws with straight lines. It must be mentioned that line geometry goes back to J. Plücker [2] and therefore in this paper line coordinates will be called Plücker coordinates, as it is done in the classical geometry literature.
In the following, a complete singularity analysis of the Kinova link 6 type robots [3] will be presented using two main features of any serial robot:

1. Every serial robot can be brought into a home-pose where all axes of the robot are parallel to a plane. This plane will be chosen as yz-plane of the base coordinate system [4].
2. In the columns of the Jacobian matrix of the robot are the Plücker coordinates of the instantaneous locations of the axes of the robot [4].

The Denavit-Hartenberg parameters of the Kinova type robots are $DH : \{a_3 = 0, a_4 = 0, a_6 = 0, d_1 = 0, d_2 = 0, d_6 = 0, \alpha_1 = \frac{\pi}{2}, \alpha_2 = 0, \alpha_3 = \frac{\pi}{2}, \alpha_4 = -\frac{\pi}{2}, \alpha_5 = -\frac{\pi}{2}, \alpha_6 = 0\}$. For almost all cases in the following singularity analysis all other DH parameters can have arbitrary values. The Kinova link 6 type robot in its home-pose is shown in Fig.1. When the robot is in this home pose, then only two types of matrices are necessary to compute the complete

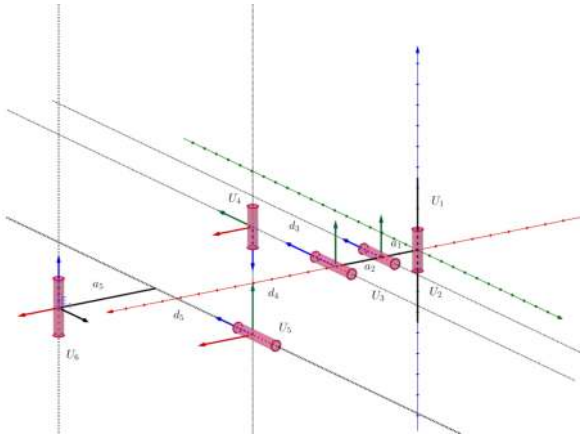

Figure 1: Kinova link 6 home-pose.

$$\mathbf{M}_i = \begin{bmatrix} 1 & 0 & 0 & 0 \\ 0 & \cos(u_i) & -\sin(u_i) & 0 \\ 0 & \sin(u_i) & \cos(u_i) & 0 \\ 0 & 0 & 0 & 1 \end{bmatrix}, \qquad (1)$$

$$\mathbf{G}_i = \begin{bmatrix} 1 & 0 & 0 & 0 \\ a_i & 1 & 0 & 0 \\ 0 & 0 & \cos(\alpha_i) & -\sin(\alpha_i) \\ d_i & 0 & \sin(\alpha_i) & \cos(\alpha_i) \end{bmatrix} \qquad (2)$$

forward kinematics. $\mathbf{M}_i$ (Eq.1) are the "motor" matrices performing the active rotations about the z-axes of the local coordinate systems and $\mathbf{G}_i$ matrices (Eq.2) do the coordinate transformations from one local coordinate system to the next (matrices written in European convention). With this setup the axes of the robot are in the z-axis of the local coordinate system and their Plücker coordinates are $y_i = [0 : 0 : 1 : 0 : 0 : 0]$. Plücker coordinates are homogeneous, therefore only the ratios are important and they transform according to Eq.3 where $\overline{\mathbf{T}}$ is a 6×6 matrix and $\mathbf{a}^{\times}$ is skew symmetric matrix belonging to the translation vector $\mathbf{a}$. For the singularity analysis only the configuration of the axes is relevant, because singularity means linear dependency between the Plücker coordinates of the axes. There is no loss

of generality to choose the fourth axis with its local coordinate system as base system for the analysis, because then the Plücker coordinates get less involved [4]. Furthermore half-tangent substitution will be applied for the rotation angles to obtain algebraic entries for the Plücker coordinates ($\cos u_i = \frac{1-U_i^2}{1+U_i^2}, \sin u_i = \frac{2U_i}{1+U_i^2}$).

$$\mathbf{T}_j = \prod_{i=1}^{j} \mathbf{M}_i \cdot \mathbf{G}_i = \begin{pmatrix} 1 & 0 \\ \mathbf{a}_j & \mathbf{A}_j \end{pmatrix}, \quad j = 1,2,3,4,5 \qquad \overline{\mathbf{T}}_j = \begin{bmatrix} \mathbf{A}_j & \mathbf{0} \\ \mathbf{a}_j^{\times}\mathbf{A}_j & \mathbf{A}_j \end{bmatrix} \tag{3}$$

Then the Plücker coordinates of the fourth axis are $\mathbf{y}_4 = [0:0:1:0:0:0]$ and the coordinates of the other axes are obtained via $\mathbf{y}_k = \overline{\mathbf{T}}_{4-k}^{-1} \cdot \mathbf{y}_4$ for $k = 3,2,1$ and $\mathbf{y}_5$ and $\mathbf{y}_6$ are obtained by a forward transformation starting from $\mathbf{y}_4$. Assembling all $\mathbf{y}_i$ in the columns of a matrix yields

$$\mathbf{J} = \begin{bmatrix} -\frac{(2U_3+2U_2)(U_2U_3-1)}{(U_2^2+1)(U_3^2+1)} & 0 & 0 & 0 & -\frac{2U_4}{U_4^2+1} & \frac{2U_4^2U_5-2U_5}{(U_4^2+1)(U_5^2+1)} \\ 0 & 1 & 1 & 0 & \frac{-U_4^2+1}{U_4^2+1} & -\frac{4U_4U_5}{(U_4^2+1)(U_5^2+1)} \\ \frac{(-U_2^2+1)U_3^2+4U_2U_3+U_2^2-1}{(U_2^2+1)(U_3^2+1)} & 0 & 0 & 1 & 0 & \frac{U_5^2-1}{U_5^2+1} \\ \frac{d_3(U_2^2U_3^2-U_2^2-4U_2U_3-U_3^2+1)}{(U_2^2+1)(U_3^2+1)} & \frac{2a_2U_3}{U_3^2+1} & 0 & 0 & \frac{d_4(U_4^2-1)}{U_4^2+1} & \frac{(-U_5^2d_5+d_5)U_4^2+(-2U_5^2a_5+4U_5d_4-2a_5)U_4+U_5^2d_5-d_5}{(U_4^2+1)(U_5^2+1)} \\ \frac{(-a_1+a_2)U_2^2-a_1-a_2}{U_2^2+1} & 0 & 0 & 0 & -\frac{2d_4U_4}{U_4^2+1} & \frac{(-U_5^2a_5+2U_5d_4-a_5)U_4^2+(2U_5^2d_5-2d_5)U_4+U_5^2a_5-2U_5d_4+a_5}{(U_4^2+1)(U_5^2+1)} \\ -\frac{2d_3(U_3+U_2)(U_2U_3-1)}{(U_2^2+1)(U_3^2+1)} & \frac{(U_3^2-1)a_2}{U_3^2+1} & 0 & 0 & 0 & \frac{2d_5U_5}{U_5^2+1} \end{bmatrix} \tag{4}$$

and one obtains for the determinant

$$\begin{aligned} S :& U_3^4U_4^3a_1d_5 + U_3^4U_4^3a_2d_5 + U_3^4U_4^3a_5d_3 - U_3^3U_4^4a_5d_4 - 2U_3^4U_4^2a_1a_5 - 2U_3^4U_4^2a_2a_5 + 2U_3^4U_4^2d_3d_5 - U_3^4U_4a_1d_5 - U_3^4U_4a_2d_5 - U_3^4U_4a_5d_3 - 2U_3^3U_4^2a_5d_4 \\ &+ 2U_3^2U_4^3a_5d_3 + U_3U_4^4a_5d_4 + 4U_3^2U_4^2d_3d_5 - 2U_3^2U_4a_5d_3 + (U_4^2+1)(U_3^2U_4^2d_4 + U_3^2d_4 - 4U_3U_4d_5 - U_4^2d_4 - d_4)(U_3^2a_1 + U_3^2a_2 + 2U_3d_4 + a_1 + a_2)U_5 \\ &+ (U_4^2+1)(U_3^2U_4^2d_4 + U_3^2d_4 - 4U_3U_4d_5 - U_4^2d_4 - d_4)(U_3^2a_1 - U_3^2a_2 - 2U_3d_4 + a_1 - a_2)U_2^2U_5 + (-U_3^4U_4^3a_1d_5 + U_3^4U_4^3a_2d_5 - U_3^4U_4^3a_5d_3 + U_3^3U_4^4a_5d_4 \\ &\cdots\cdots \\ &+ 2U_3U_4^2a_5d_4 - U_4^3a_2d_5 + U_4^3a_5d_3 - U_3^3a_5d_4 + U_3a_5d_4 + U_4a_1d_5 - U_4^3a_1d_5 + 2U_4^2a_2a_5 + U_4a_2d_5 + 2U_4^2a_1a_5 + 2U_4^2d_3d_5 - U_4a_5d_3 = 0 \end{aligned} \tag{5}$$

This equation represents a four dimensional surface in joint space (due to lack of space the equation is not fully displayed!). Relatively simple geometric considerations in either 5-dim Plücker space or in the joint space yield a lot of interesting singularity properties of the manipulator some of them are briefly summarized in the following items:

- S has degree four in U_3 and U_4 and it is quadratic in U_2 and U_5. The consequence is: fix all joints with exception of either U_3, U_4, U_2 or U_5 and let the joint fully rotate. It will hit either twice or four times a singularity.
- When $U_5 = 0, U_4 = 0, U_2 = \pm 1, U_3 = \pm 1$ the matrix $\mathbf{J}$ has rank four and the robot has infinitesimal two DoF.
- In the general singularity case the six axes are contained in a general linear complex. That is the most abundant case. And this case is missing in [1]. The reason for this is that in [1] the equation for the singularities is a functional equation where it is very difficult to find out geometric properties of the mechanism. A further reason is that there are some misleading statements in the cited literature.
- There is a big amount of subcases where the linear dependency in the matrix $\mathbf{J}$ occurs between subsets of the Plücker coordinates of the robot axes, which all can be explained easily via geometric considerations in the 5-dim Plücker space and then also in the axes configurations of the robot. But all these cases are covered by Eq.5.

ACKGNOWLEDGEMENTS

This research was funded by the project *"New smart and adaptive robotics solutions for personalized minimally invasive surgery in cancer treatment—ATHENA"*, funded by European Union-Next Generation EU and Romanian Government, under National Recovery and Resilience Plan for Romania, contract no. 760072/23.05.2023, code CF 116/15.11.2022, through the Romanian Ministry of Research, Innovation and Digitalization, within Component 9, investment I8.

REFERENCES

[1] M. Asgari, I. A. Bonev, and C. Gosselin, "Singularity analysis of Kinova's Link 6 robot arm via Grassmann line geometry," in 2024 IEEE Int. Conf. on Robotics and Automation. Yokohama, Japan: IEEE, 2024, pp. 8814–8820.

[2] Plücker, J., Neue Geometrie des Raumes, B. G. Teubner, Leipzig 1868.

[3] https://www.kinovarobotics.com/product/link-6-cobot [10.02.2026]

[4] Husty, M., Karger, A., Sachs, H., Steinhilper, W., Kinematik und Robotik, Springer 1995.

THE MATROID METHOD IN COMPUTATIONAL MECHANICS OF MECHANISMS

Ilie Talpasanu[1], Alexandru Talpasanu[2]

[1] Wentworth Institute of Technology, Douglas D. Schumann School of Engineering, Boston, MA, USA, talpasanui@wit.edu

[2] Lead Application IT Architect, Sacramento, CA, USA, alexemail04@gmail.com

1. INTRODUCTION

The Talpasanu Matroid Method is a graph-theory-based technique for the systematic kinematic analysis of complex mechanisms, developed by Ilie Talpasanu, that uses *matroid theory (specifically cycle matroids)* and directed graphs to generate minimal sets of independent linear equations for calculating link positions, velocities and accelerations without derivatives. It represents mechanisms as directed edges graphs (digraphs), uses incidence matrices, and derives kinematic equations from a cycle basis of the digraph's cycles, simplifying analysis for systems with multiple degrees of freedom and identifying singularities.

2. MATROID METHOD APPLIED TO GEARED MECHANISMS

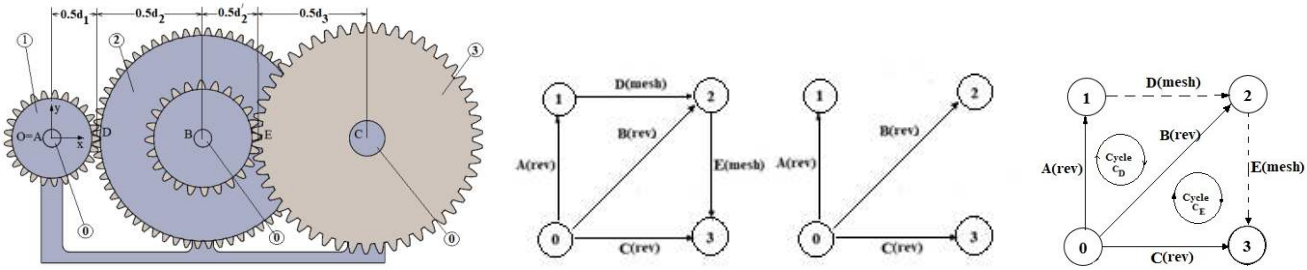

a) b) c) d)

Figure 1. a) Gear train with parallel fixed axes b) Digraph c) Spanning tree d) Cycle basis

We provide the following as an example. Given the planar parallel axes gear set (GP) illustrated in Figure 1(a), there are n = 4 links labelled with numbers 0. 1. 2. 3 4, starting with 0 which is assigned to the fixed link (casing). There are m = n -1 = 3 mobile links, labelled 1, 2, and 3. Link 2 is a compound of two gears, they rotate as a whole.There are j = j_1+ j_l = 5 joints which are labelled with capital letters: A, B, C, D, and E, where j_1=3 revolute joints at A, B, and C, and j_2 = 2 two meshing joints labelled with the last letters D and E.

2.1 Graph Representation*:* Digraph and Spanning Tree

The *digraph* attached to the mechanism is illustrated in Figure 1.b, which has n = 4 nodes (namely, the mechanism's links) and j = 5 edges (namely, the mechanism's joints). In the Matroid method, each edge is *directed* from the lower node number to the higher node number. The *spanning tree* illustrated in Figure 1(c) is obtained from a digraph as result of cutting j_2 = 2 edges for meshing joints D and E. *Note*: A graph has several spanning trees, [3]. Two more will result by cutting edges B and E, or cutting edges A and E.

2.2. Matrix Formulation: Nodes-Edges Matrix, $[\underline{G}]_{n,j}$, Cycle Basis-Edges $[C]_{c,j}$, Position Vectors Matrix $[\boldsymbol{r}]_{c,j}$

To codify the digraph's topology into matrix-form, the Matroid method uses *the incidence matrices* [G] , [C] , and [**r**].
The *incidence nodes-edges n* x *j* matrix G , left side in Eq.(1), has a row assigned to each node *n*, and a column assigned to each edge *j*. Each column *j* will have a -1-entry and a +1-entry corresponding to the two nodes n_{tail} and n_{head}.

$$[\underline{G}] = \begin{matrix} \\ 0 \\ 1 \\ 2 \\ 3 \end{matrix}\begin{matrix} \begin{matrix} A & B & C & D & E \end{matrix} \\ \begin{bmatrix} -1 & -1 & -1 & 0 & 0 \\ 1 & 0 & 0 & -1 & 0 \\ 0 & 1 & 0 & 1 & -1 \\ 0 & 0 & 1 & 0 & 1 \end{bmatrix} \end{matrix} ; \quad [C] = \begin{matrix} \\ C_D \\ C_E \end{matrix}\begin{matrix} \begin{matrix} A & B & C & D & E \end{matrix} \\ \left[\begin{array}{ccccc} 1 & -1 & 0 & 1 & 0 \\ 0 & 1 & -1 & 0 & 1 \end{array}\right] \end{matrix} \quad [\mathbf{r}] = \begin{matrix} \\ C_D \\ C_E \end{matrix}\begin{matrix} \begin{matrix} A & B & C & D & E \end{matrix} \\ \begin{bmatrix} \mathbf{r}_A & -\mathbf{r}_B & 0 & \mathbf{r}_D & 0 \\ 0 & \mathbf{r}_B & -\mathbf{r}_C & 0 & \mathbf{r}_E \end{bmatrix} \end{matrix} \tag{1}$$

The incidence cycle basis-edges incidence n x *j* matrix[C], center in Eq. (1), has c = 2 rows, one for each cycle C_D , C_E, and a column assigned to each edge *j.* Its entries are defined as*:* -1 if edge *j* is on the cycle and opposite to the cycle;+1if edge j is on the cycle and same direction as the cycle; 0 if edge j is not on the cycle. The matrix $[C] = [T_{c,j1} \ \vdots \ U_{c,c}]$ in Eq. (1), is a cycle basis matroid, as shown further, with rank c=2. The *spanning tree matrix,* $[T_{c,j1}]$ is a partition of [C] having only spanning tree's edges, and $[U_{c,c}]$ a (c x c) unit matrix *The joint position matrix*, $[\mathbf{r}]_{c,j}$, right side in Eq. (1), with joints' position vectors, Its enties are defined from matroid [C] as: $-\mathbf{r}_j$ if edge j is on the cycle and opposite to the cycle; $+\mathbf{r}_j$ if edge j is on

the cycle and same direction as the cycle; 0 if edge j is not on the cycle.

2.2.1. Latin Matrix, [L]:

The *Latin matrix*, $[\mathbf{L}]_{c,\,n}$, introduced by Talpasanu in 2001, has vector entries which are automatically generated from the multiplication of joint position matrix [**r**] and digraph's transposed incidence matrix $[\underline{G}]^T$, illustrated in Eq. (2)

$$[L] = -[r]\cdot[\underline{G}]^T \xrightarrow{yields} \begin{matrix} \\ C_D \\ C_E \end{matrix}\begin{matrix} \begin{matrix} 0 & 1 & 2 & 3 \end{matrix} \\ \begin{bmatrix} L_{BA} & L_{AD} & L_{DB} & 0 \\ L_{CB} & 0 & L_{BE} & L_{EC} \end{bmatrix} \end{matrix} = \begin{matrix} \begin{matrix} 0 & 1 & 2 & 3 \end{matrix} \\ \begin{bmatrix} \{r_A - r_B\} & \{r_D - r_A\} & \{r_B - r_D\} & 0 \\ \{r_B - r_C\} & 0 & \{r_E - r_B\} & \{r_C - r_E\} \end{bmatrix} \end{matrix} \quad (2)$$

From Eq. (2), $\sum \mathbf{r}_j = 0$ in the right-side matrix, the following statement holds for entries in the left-side matrix

Statement 1: The sum of entries on the rows in Latin matrix is zero: Cycle C_D: $\mathbf{L}_{BA} + \mathbf{L}_{AD} + \mathbf{L}_{DB} = \mathbf{0}$, and C_E: $\mathbf{L}_{CB} + \mathbf{L}_{BE} + \mathbf{L}_{EC} = \mathbf{0}$

Each vector **L** is attached to a node *n* (link): The scalar entries $\mathbf{L} = \{x_{c.j} \quad 0 \quad 0\}^T$ are expressed as function of gear diameters:

For cycle C_D: $x_{BA} = x_A - x_B = -0.5\cdot(d_1 + d_2)$; $x_{AD} = x_D - x_A = 0.5\,d_1$; $x_{DB} = x_B - x_D = 0.5\,d_2$;cycle C_E: $x_{CB} = x_B - x_C = -0.5\cdot(d'_2 + d_3)$; $x_{BE} = x_E - x_B = 0.5\,d'_2$; $x_{EC} = x_C - x_E = -0.5\,d_3$,

2.3. Cycle Matroid Fundamentals:

In 1935, Whitney introduced the math concept of *matroid* which combines the properties of graphs and matrices. As an example, given $\underline{C}$ as the cycle space (the set of *all cycles* in a digraph), and *I* the collection of independent subsets of cycles, a *cycle matroid* M is defined as the pair M= ($\underline{C}$, *I*). For the digraph in Figure (1b), the *set of all cycles* (cycle space) is $\underline{C}$ = {{C_D}, {C_E}, {C_{Per}}}, where C_D= {A, B, D}, C_E = {B, C, E}, and peripheral C_{Per} = {A, C, D, E}-this is generated from the other 2 more spanning trees from section 2.1. The set of *independent cycles* is *I* = {{C_D}, {C_E}, {C_{Per}},{C_D, C_E}, {C_D, C_{Per}},{C_E, C_{Per}}. The set $\underline{C}$ is not included in set *I*, since $\underline{C}$ is not independent (inserting a third row in the incidence matrix [C], Eq. (1), and adding the first row-entries to the second-row entries yields one result, the third row-entries). A *cycle basis* is a minimal set of cycles (a basis). A *cycle basis* in *I* is a set of simple cycles that form a basis: {C_D, C_E},{C_D, C_{Per}},{C_E, C_{Per}}. Any of these 3 sets can be selected for the kinematic equations, [3, 4].

2.4. Equations Generation for Velocities

Generates a minimal set of linear equations for absolute angular velocities by finding a cycle basis from the matroid.

$$[\dot{L}] = -[\dot{r}]\cdot[\underline{G}]^T \xrightarrow{yields} \begin{matrix} \\ C_D \\ C_E \end{matrix}\begin{matrix} \begin{matrix} 0 & 1 & 2 & 3 \end{matrix} \\ \begin{bmatrix} \dot{L}_{BA} & \dot{L}_{AD} & \dot{L}_{DB} & 0 \\ \dot{L}_{CB} & 0 & \dot{L}_{BE} & \dot{L}_{EC} \end{bmatrix} \end{matrix} = \begin{matrix} \begin{matrix} 0 & 1 & 2 & 3 \end{matrix} \\ \begin{bmatrix} \{v_A - v_B\} & \{v_D - v_A\} & \{v_B - v_D\} & 0 \\ \{v_B - v_C\} & 0 & \{v_E - v_B\} & \{v_C - v_E\} \end{bmatrix} \end{matrix} \quad (3)$$

From Eq. (3), $\sum \mathbf{v}_j = 0$ for each cycle C_D and C_E, where $\mathbf{v}_j = \dot{\mathbf{r}}$ are the linear velocities at joints *j,* therefore:

Statement 2: The sum of entries on the rows in [$\dot{\mathbf{L}}$] is zero: For cycle C_D: $\dot{\mathbf{L}}_{BA} + \dot{\mathbf{L}}_{AD} + \dot{\mathbf{L}}_{DB} = \mathbf{0}$, and cycle C_E: $\dot{\mathbf{L}}_{CB} + \dot{\mathbf{L}}_{BE} + \dot{\mathbf{L}}_{EC} = \mathbf{0}$.

Each vector $\dot{\mathbf{L}}$ is attached to a node *n* (link). The scalar entries of $\dot{\mathbf{L}}_{c,j} = \mathbf{v}_j - \mathbf{v}_{j-1} = \boldsymbol{\omega}_n \mathrm{x}\, \mathbf{L}_{cj} = \{0 \quad x_{c.j}\cdot\omega_n \quad 0\}^T$ are in the fixed frame (x_0 y_0). Then, the system of linear equations for angular velocities ω_n, Eq. (4). is

$$\begin{bmatrix} x_{BA} & x_{AD} & x_{DB} & 0 \\ x_{CB} & 0 & x_{BE} & x_{EC} \end{bmatrix} * \{\omega_0 \;\; \omega_1 \;\omega_2 \;\; \omega_2\}^T = \begin{Bmatrix} 0 \\ 0 \end{Bmatrix} \quad \Rightarrow \begin{bmatrix} -0.5\cdot(1+i_D) & 1 & i_D & 0 \\ -0.5\cdot(1+i_E) & 0 & 1 & i_E \end{bmatrix} * \{\omega_0 \;\; \omega_1 \;\omega_2 \;\; \omega_2\}^T = \begin{Bmatrix} 0 \\ 0 \end{Bmatrix}, \text{ with } \omega_0 = 0 \text{ (for the fix link 0)} \quad (4)$$

2.5. Solution.

Talpasanu, [3, 4], reported a modified form of the Gruebler criterion for mobility M of geared mechanisms, by subtracting the number of cycles $c = j_2$ in cycle basis from the number of mobile links *m*. Thus, M = m – c =3 – 2=1, therefore one gear is selected here gear 1 is actuated with ω_1. The linear system Eq. 8 of c = 2 equations is solved for c = 2 unknowns: ω_2, and ω_3.

Solution: $\omega_2 = -\omega_1/i_D$; $\omega_3 = \omega_1/i_D \cdot i_E$ and linear velocities:$\mathbf{v}_D = \{0 \;\; 0.5\; d_1\cdot\omega_1 \;\; 0 \;\}^T$; $\mathbf{v}_E = \{0 \quad -0.5\, d'_2\cdot d_1/d_2.\omega_1 \quad 0\}^T$

The gear ratios are defined as $i_D = d_2/d_1$ and $i_E = d_3/d'_2$, evidenced by (scaling), dividing by d_1 and d'_2 , the two equations in Eq.(4). One could notice that for planetary mechanisms the two equations generate the Willis equations.

Conclusions: There are several advantages by using the Matroid Method: a) *Systematic Generation*-Kinematic equations are automatically obtained from the topological structure of the mechanism; b) *Versatility*- It is applicable to spatial mechanisms with any number of links and degrees of freedom; and c) *Singularity Identification*-By calculating the rank of a Latin matrix the method can identify mechanical singularities. The Matroid method can be applied, [1, 2] to a variety of planar and spatial linkages with open and closed single and multiple cycles, as well as to geared mechanisms with parallel axes, bevel, planetary, exoskeleton, and mechanisms with cams.

REFERENCES

[1] I. Talpasanu and A. Talpasanu, *Mechanics of Machines and Mechanisms*, CRC-Taylor & Francis Press, 2019

[2] I. Talpasanu, "Kinematics and Dynamics of Mechanical Systems Based on Graph-Matroid Theory", *Ph.D. Dissertation*, University of Texas at Arlington, 2004

[3] I. Talpasanu, T.C. Yih, P.A. Simionescu, "Application of Matroid Method in Kinematic Analysis of Parallel Axes Epicyclic Gear Trains", *ASME Journal of Mechanical Design*, vol. 128, 2006.

[4] I.Talpasanu, "A General Method for Kinematic Analysis of Robotic Wrist Mechanisms", *ASME Journal of Mechanisms and Robotics*,7(3), 2015

A NOVEL SERIES ELASTIC ACTUATOR WITH MECHANICAL STOPPERS FOR ASSIST-AS-NEEDED IN SIT-TO-STAND ASSISTANCE

Ming Jiang[1], Jian Zheng[1], Seunghyun Kim[1], Hiroto Miyatake[1], Kotaro Muramatsu[1], Jun Nango[2], Yukio Takeda[1]

[1] Institute of Science Tokyo, Ookayama 2-12-1 Meguro-ku Tokyo, 152-8550 Japan, {jiang.m.889e@m.isct.ac.jp; zheng.j.a632@m.isct.ac.jp; kim.s.4fd9@m.isct.ac.jp; miyatake.h.d810@m.isct.ac.jp; muramatsu.k.499f@m.isct.ac.jp; takeda.y.2c40@m.isct.ac.jp}

[2] Yamagata University, 4-3-16 Jonan, Yonezawa-shi, 992-8510 Japan, {nango@yz.yamagata-u.ac.jp}

1. INTRODUCTION

The sit-to-stand (STS) transition is a fundamental daily movement and a key target of robotic assistance and rehabilitation. An essential challenge in STS assistance is not only providing mechanical support but also encouraging active user participation. To address this issue, Assist-As-Needed (AAN) strategies have been widely studied, in which assistance is adaptively modulated based on the user's performance, with control guided by user behavior and biomechanical models [1].

This study advances STS assistive devices by integrating a Series Elastic Actuator (SEA) with an AAN concept at the hardware level. We propose a novel SEA design with mechanical stoppers, named as an Elastic Redundant Hybrid Actuator (E-RHA), which automatically switches between two assistance modes depending on the user's motion state: a small-torque mode (STM), providing minimal elastic support via springs, and a large-torque mode (LTM) enabling trajectory-tracking assistance.

The term *Redundant* refers to a in-parallel motor configuration that allows customization of total output torque by employing multiple geared motors. *Hybrid* denotes the switch of two distinct assistance modes. In this study, elastic elements are used to implement the STM; therefore, it is referred to as the Elastic RHA (E-RHA). In the general RHA concept, the STM is not limited to elastic elements and can also be implemented through active motor actuation.

2. METHODOLOGY

2.1. Conception of E-RHA and configuration of the STS assistance device

Figure 1 illustrates the basic concept of the proposed E-RHA. The actuator consists of a fixed frame, a large-torque wheel gear (LTWG), an output arm that shares a common rotational axis, a large-torque geared motor (LTGM), torsion springs, and mechanical stoppers. The LTGM, mounted on the fixed frame, drives the LTWG. Torsion springs are installed between the LTWG and the output arm, and two mechanical stoppers are attached to the LTWG. As shown in Figure 1(b) and (c), the E-RHA operates in two modes. In LTM, the LTGM delivers sufficient torque to the output arm via the mechanical stopper to follow a predefined target trajectory. In the STM, the output arm is not in contact with the stopper, and assistance is provided solely through torsion springs.

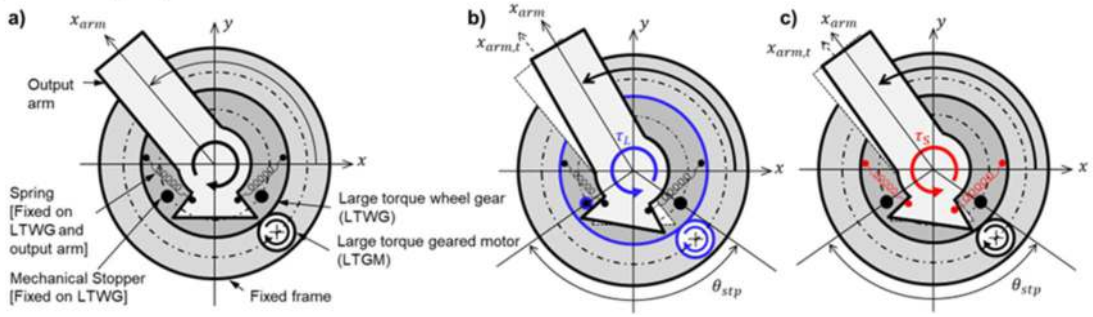

Figure 1. Concept of the proposed SEA. a) Basic configuration of the actuator. b) E-RHA working in large torque mode. c) E-RHA working in small torque mode.

The actuator is integrated into a 1-DOF chair-type STS assistive device [2] (Figure 2). The LTM section employs a DC servomotor with a harmonic drive gearbox, while the STM section integrates torsion springs and mechanical stoppers. Mode switching is governed not only by the deviation between the user's motion and the motor trajectory, but also by the stopper position, which is adjustable to accommodate different user muscle strengths.

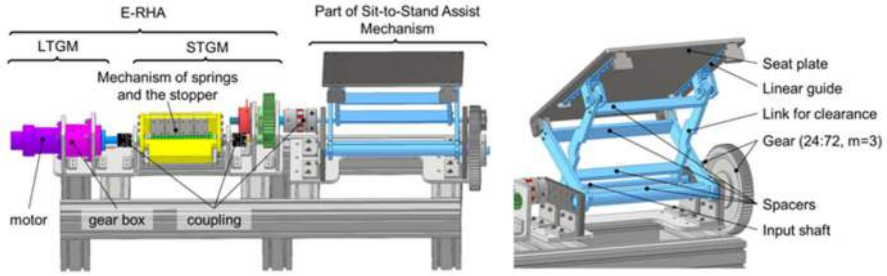

Figure 2. Integrated 1-DOF STS assistance system.

2.2. STS simulated experiments with a dummy

To evaluate the capability of the proposed E-RHA to automatically switch between the LTM and the STM during STS assistance, experiments were conducted using a dummy, as shown in Figure 3(a). The dummy has a mass of 40 kg. A lifting device actuated by two motors was used to simulate the STS motion by attaching two cables to the dummy's shoulders. Different levels of user muscle strength were simulated by adjusting the lifting force through changes in the motor input current. When the dummy was assumed to have sufficient muscle strength, the motor current of the lifting device was set to 1.8 A, referred to as the strong (S) condition. When the dummy was assumed to have weak muscle strength, the motor current was reduced to 0.9 A, referred to as the weak (W) condition. During the experiments, the STS assistive device and the lifting device were activated simultaneously, and the dummy completed the STS motion under the combined action of both systems. The seat angle and the LTM motor angle were measured, and the seat reaction force was recorded using a load cell installed beneath the seat. In addition, the torsion angle of the springs of the E-RHA was measured.

3. RESULTS

Figure 3 presents the results of the dummy experiments. Here, θ_1 denotes the motor angle of the E-RHA, and θ_2 represents the rotation angle of the seat measured from the horizontal position. In the W condition, the dummy was unable to complete the STS motion independently, resulting in an increased seat reaction force as shown in Figure 3(c). In this condition, the springs' torsion angle increased and approached its upper limit, indicating that the E-RHA switched to LTM and provided large assistive torque. In contrast, under the strong (S) condition, the seat reaction force is significantly reduced. The measured torsion angle continued to decrease, suggesting that assistance was primarily provided by elastic deformation rather than by high motor torque. These results indicate that the E-RHA adaptively adjusted its assistance characteristics in response to the dummy's simulated muscle strength.

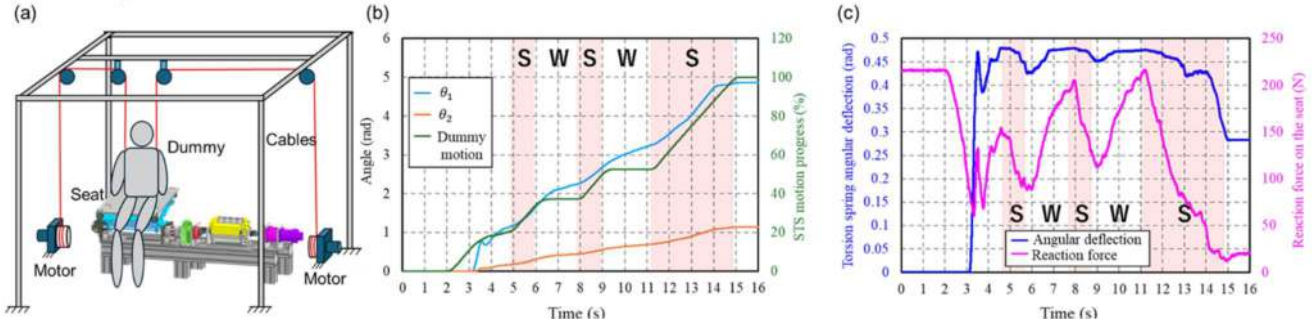

Figure 3. Results of the dummy experiment. (a) Experiment setting. (b) Variation of θ_1 and θ_2 during the STS process. (c) Seat reaction force and the deflection angle of the torsion spring under different simulated muscle strength conditions.

4. CONCLUSIONS

This paper proposes an Elastic Redundant Hybrid Actuator (E-RHA) that realizes Assist-As-Needed behavior at the hardware level. Preliminary experiments using a dummy verified the actuator's ability to automatically switch between the two assistance modes in response to simulated user capability. Future work will focus on validation through experiments with human subjects.

ACKNOWLEDGMENTS

This study is partly supported by NSK Foundation for Advancement of Mechatronics, Suzuki Foundation, JSPS KAKENHI 23K26021 and 24K21156.

REFERENCES

[1] N. Naghavi, A. Akbarzadeh, S. M. Tahamipour-Z., and I. Kardan, "Assist-As-Needed control of a hip exoskeleton based on a novel strength index," *Robotics and Autonomous Systems*, vol. 134, 103667, 2020.

[2] J. Nango, H. Yoshizawa, and J. Liu, "Design of Mechanism for Assisting Standing Movement Using Planar Linkage and Gear Train," *Journal of Advanced Mechanical Design, Systems, and Manufacturing*, vol. 4, no. 2, pp. 428–443, 2010.

TYPE SYNTHESIS AND PERFORMANCE OPTIMIZATION OF 2R1T PARALLEL MECHANISMS WITH THIRD-ORDER ACTUATION REDUNDANCY

Xiaofei Liu[1*], Yu Wang[1], Zongqiang Feng[1], Jiantao Yao[1], Yongsheng Zhao[1]

[1] School of Mechanical Engineering, YanShan University, Qinhuangdao, China, {liuxf@ysu.edu.cn; 17864277601@163.com; zqf@ysu.edu.cn; jtyaoqf@ysu.edu.cn; yszhao@ysu.edu.cn}

1. INTRODUCTION

The parallel mechanism with two rotational and one translational degrees of freedom (2R1T), owing to its compact structure, high stiffness, and superior precision, has found extensive product applications in the fields of heavy-load manipulation and high-precision machining. Redundantly actuated parallel mechanisms enhance load capacity and force distribution, but existing research is primarily focused on low-order redundancy, whereas higher-order cases remain largely unexplored despite their considerable potential for performance optimization and more complex design challenges.

This research presents a systematic methodology for the type synthesis and performance optimization of 2R1T parallel mechanisms with third-order actuation redundancy. The limb constraint arrangements for two fundamental categories of 2R1T parallel mechanisms—those with coplanar and non-coplanar rotation axes—are analyzed. Utilizing a construction-based synthesis approach, numerous novel configurations of 2R1T parallel mechanism with six limb and third-order actuation redundantly have been generated. The motion/force transmission performance is adopted as a key metric to analyze and optimize four representative mechanisms. Their performance distribution characteristics are investigated, and a dimensional optimization is conducted. A comparative analysis of the optimized results identifies the architecture with the superior transmission performance. This work provides a foundational reference for the innovative design and application of 2R1T redundantly actuated parallel mechanisms.

2. RESEARCH PROCEDURE

Feasible limb configurations that satisfy the requirements for 2R1T parallel mechanism are illustrated in figure 1.

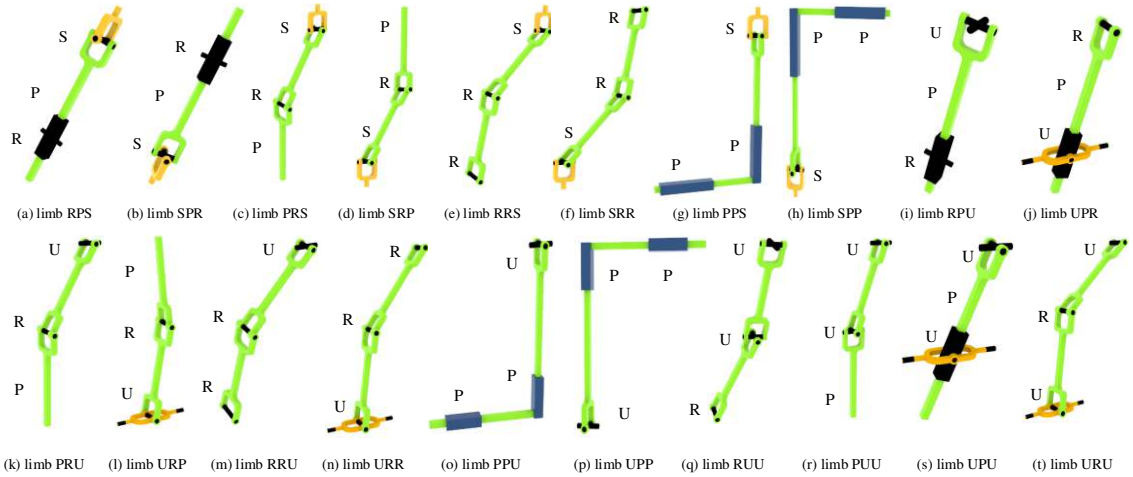

Figure1. Simplified diagram of low-degree-of-freedom limb

Novel redundantly actuated parallel mechanisms with coplanar rotation axes are illustrated in figure 2, and non-coplanar rotation axes in figure 3.

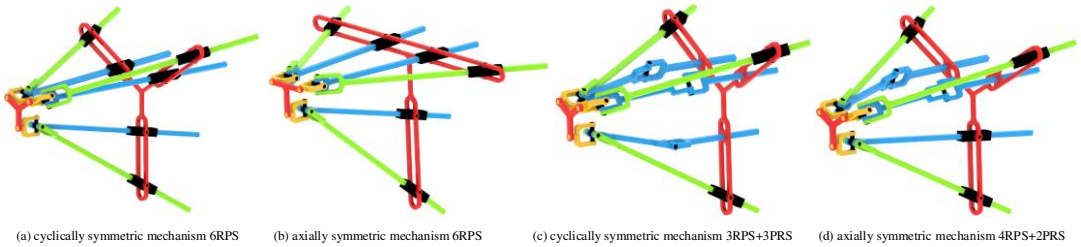

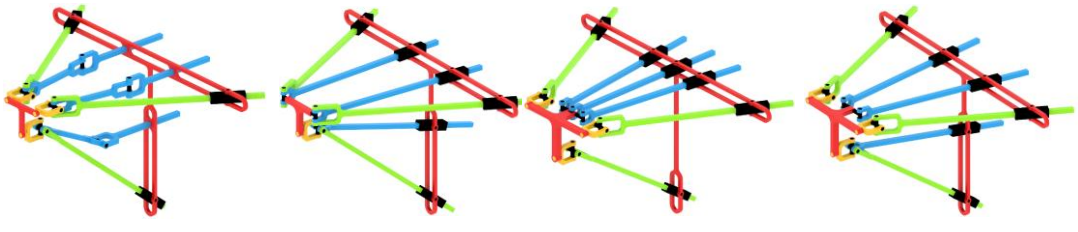

(e) axially symmetric mechanism 3RPS+3PRS (f) axially symmetric mechanism 2RPS+4RPU (g) axially symmetric mechanism 3RPS+3RPU (h) axially symmetric mechanism 4RPS+2RPU

Figure 2. Schematic diagrams of mechanisms with coplanar rotation axes

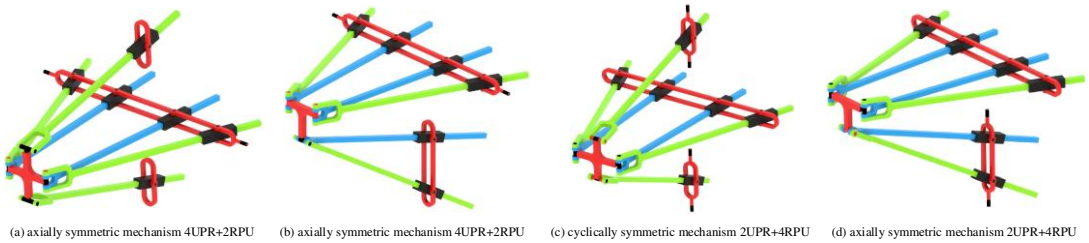

(a) axially symmetric mechanism 4UPR+2RPU (b) axially symmetric mechanism 4UPR+2RPU (c) cyclically symmetric mechanism 2UPR+4RPU (d) axially symmetric mechanism 2UPR+4RPU

Figure 3. Schematic diagrams of mechanisms with non-coplanar rotation axes

Four representative architectures—the cyclically symmetric mechanism 6RPS, the axially symmetric mechanism 6RPS, the axially symmetric mechanism 4UPR+2RPU, and the axially symmetric mechanism 2UPR+4RPU—are selected for in-depth analysis. Under identical structural parameters, the distributions of the motion/force transmission performance indices for the four mechanisms are illustrated in figure 4. The optimal performance indices obtained via dimensional optimization for each mechanism are comparatively presented in figure 5.

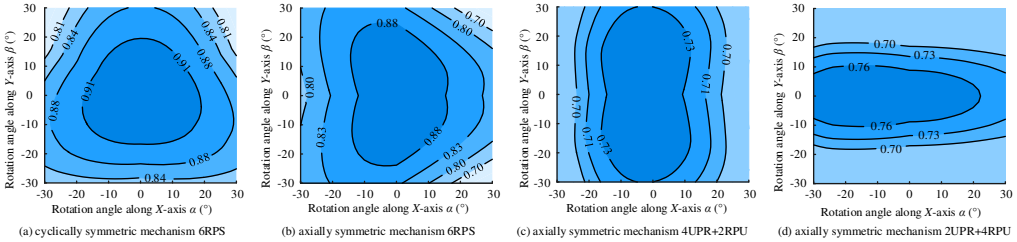

(a) cyclically symmetric mechanism 6RPS (b) axially symmetric mechanism 6RPS (c) axially symmetric mechanism 4UPR+2RPU (d) axially symmetric mechanism 2UPR+4RPU

Figure 3. Distribution of transmission performance for the four typical mechanisms before optimization

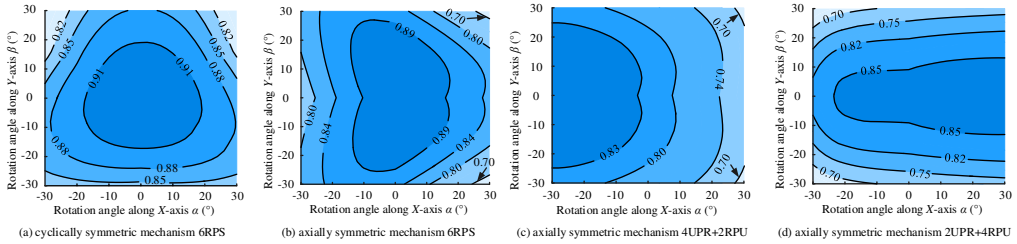

(a) cyclically symmetric mechanism 6RPS (b) axially symmetric mechanism 6RPS (c) axially symmetric mechanism 4UPR+2RPU (d) axially symmetric mechanism 2UPR+4RPU

Figure 4. Distribution of transmission performance for the four typical mechanisms after optimization

Comparison between figures 3 and 4 reveals that, both before and after optimization, the cyclically symmetric mechanism 6RPS achieves the highest motion/force transmission performance.

ACKNOWLEDGMENTS

This research is funded by the National Natural Science Foundation of China (No. 52105036) and the authors declare that they have no conflict of interest.

REFERENCES

[1] Z.M. Chen, X.W. Kong, C. Zhao, et al, "Type synthesis of 3-RSR equivalent 2R1T parallel mechanisms based on screw theory". *Mechanism and Machine Theory*, 211, 106032, 2025.

[2] R.F. Lin, W.Z. Guo, S.S. Cheng, "Type synthesis of novel 1R, 2R, 1R1T, and 2R1T hybrid RCM mechanisms based on topological arrangement and modular design method". *Mechanism and Machine Theory*, 200, 105692, 2024.

[3] K.X. Chen, R.Y. Wang, Z.L. Niu, et al, "Topology design and performance optimization of six limbs 5-dof parallel machining robots". *Mechanism and Machine Theory*, 185(4), 105333, 2023.

[4] L. Wang, Y.F. Fang, H.B. Qu, et al, "Design and analysis of novel 2R1T generalized parallel mechanisms with large rotational angles". *Mechanism and Machine Theory*, 150, 103879, 2020.

[5] L.M. Xu, W. Ye, Q.C. Li, "Design, analysis, and experiment of a new parallel manipulator with two rotational and one translational motion". *Mechanism and Machine Theory*, 177, 105064, 2022.

NOVEL MINIMALLY INVASIVE RETRACTOR FOR PANCREATECTOMY

Pierre Mougenot[1, 2], Bogdan Gherman[2], Calin Vaida[2], Paul Tucan[2], Doina Pisla[2,3], Damien Chablat[1, 2]

[1] Nantes Université, École Centrale de Nantes, CNRS, LS2N, UMR 6004, F-44000, Nantes, France, {pierre.mougenot,damien.chablat}@ls2n.fr
[2] Research Center for Industrial Robots Simulation and Testing, Technical University of Cluj-Napoca, 400114 Cluj-Napoca, Romania, {bogdan.gherman,calin.vaida,paul.tucan,doina.pisla}@mep.utcluj.ro
[3] Technical Sciences Academy of Romania, B-dul Dacia, 26, 030167 Bucharest, Romania

1 INTRODUCTION

Pancreatic cancer remains among the leading causes of cancer-related mortality, largely due to its frequent late diagnosis [1] and the high complexity of surgical resection procedures [2, 3, 4]. According to the Global Cancer Observatory, it ranked as the sixth leading cause of cancer-related deaths in 2022 [5]. Minimally invasive pancreatectomy is particularly challenging because of the organ's deep anatomical location and the extremely constrained operative workspace, which severely limits the surgeon's freedom of motion. Although surgical retractors are commonly used to improve access and visibility in confined environments, most existing designs are unsuitable for pancreatectomy due to their bulk and limited maneuverability [6].

We introduce a novel minimally invasive retractor specifically designed to address the spatial constraints of pancreatic surgery [7]. Unlike traditional devices, the proposed design eliminates the central supporting rod, thereby preserving the full working space and avoiding tool repositioning between separated compartments. The device consists of cable-actuated articulated fingers that can be deployed through a standard 10 mm trocar. Their geometry can be customized through different sequences of rigid segments and hinge types, enabling the creation of patient-adapted retraction shapes while minimizing pressure on soft tissues. Several hinge variants are considered, balancing torque, rigidity, and compatibility with either laparoscopic or robotic actuation. The retractor is also designed to operate in conjunction with a dedicated tool-holding platform [8] for enhanced stability during minimally invasive procedures.

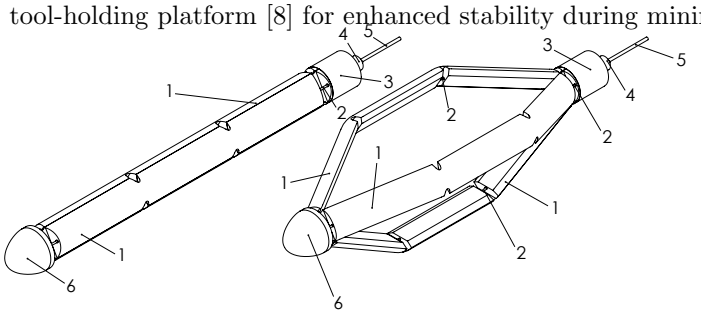

Figure 1: General view of the retractor in closed and open configurations.

Each finger consists of a sequence of rigid segments connected through hinge mechanisms. A cable routed internally through each segment—anchored at the distal end (as illustrated in Fig. 2a)—enables controlled deformation of the finger when tension is applied. By modifying the sequence of segments and hinge types, the shape of the deployed retraction space can be tailored to the surgical requirements (Fig. 2b). The cross-sectional geometry of the fingers is optimized to minimize pressure on surrounding tissues by maximizing the area of contact (length of arc in Fig. 3a). Because pancreatic surgery involves interaction with delicate and vascularized structures, maximizing this area helps reduce localized pressure and therefore lowers the risk of tissue injury. Local deformations of the fingers are governed by hinges that may be implemented in several variants (Fig. 3b). Transversely asymmetric hinges increase the torque generated during actuation, reducing the effort required from the surgeon—an advantage in laparoscopic use. Conversely, transversely symmetric hinges support dual-cable routing, increasing structural rigidity at the cost of reduced torque. These may be more suitable for robotic applications, where actuation forces are less constrained.

ACKNOWLEDGMENTS

This research was supported by the project New Smart and Adaptive Robotics Solutions for Personalized Minimally Invasive Surgery in Cancer Treatment - ATHENA, funded by the European Union – NextGenerationEU and Romanian

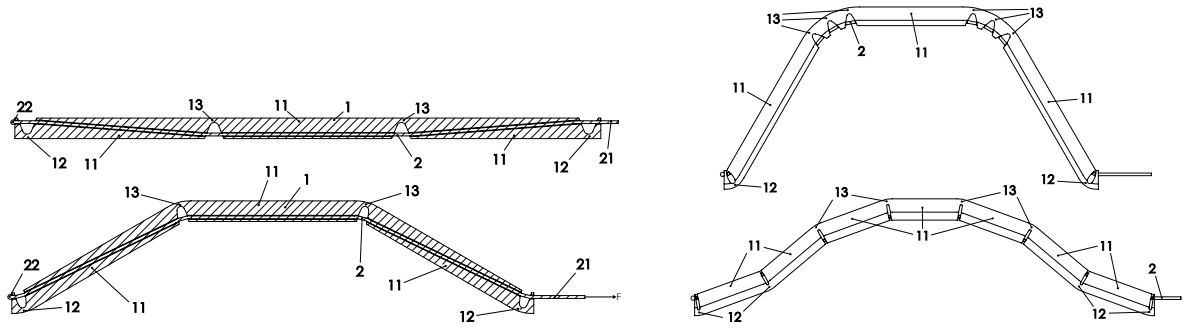

(a) (b)

Figure 2: a) Inside of a finger in one configuration and b) Different sequences for a finger.

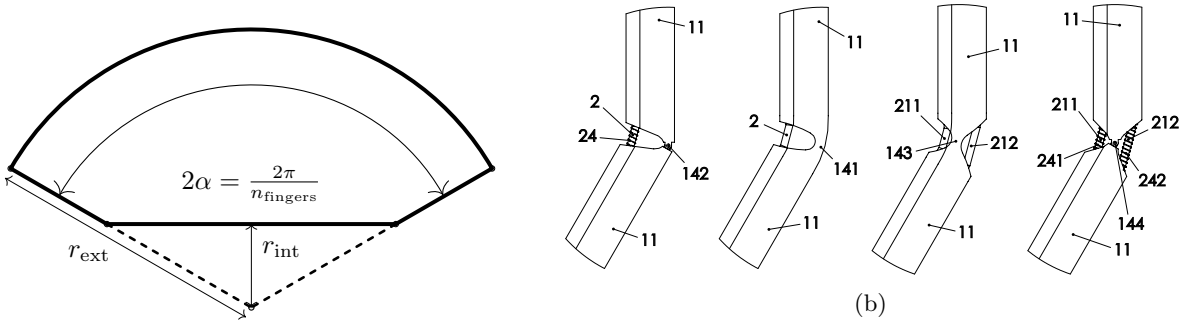

(a) (b)

Figure 3: a) Cross-section of the finger, and b) variants of the hinges with, from left to right, single pivot with a spring, transversely asymmetric flexure hinge, transversely symmetric hinge, pivot with two springs.

Government, under National Recovery and Resilience Plan for Romania, contract no. 760072 /23.05.2023, code CF 16/15.11.2022, through the Romanian Ministry of Research, Innovation and Digitalization, within Component 9, investment I8.

REFERENCES

[1] D. P. S. Sohal, F. F. Willingham, M. Falconi, K. L. Raphael, and S. Crippa, "Pancreatic adenocarcinoma: Improving prevention and survivorship," *American Society of Clinical Oncology Educational Book*, vol. 37, pp. 301–310, 2017, publisher: Wolters Kluwer.

[2] E. Cho, S. Pagkratis, H. Osman, and D. R. Jeyarajah, *Robotic Pancreaticoduodenectomy.* Cham: Springer International Publishing, 2020, p. 123–132.

[3] S. C. Kim, K. B. Song, Y. S. Jung, Y. H. Kim, D. H. Park, S. S. Lee, D. W. Seo, S. K. Lee, M. H. Kim, K. M. Park, and Y. J. Lee, "Short-term clinical outcomes for 100 consecutive cases of laparoscopic pylorus-preserving pancreatoduodenectomy: improvement with surgical experience," *Surgical Endoscopy*, vol. 27, no. 1, p. 95–103, Jan. 2013.

[4] P. W. Underwood, M. H. Gerber, and S. J. Hughes, "Pitfalls of minimally invasive pancreatoduodenectomy," *Annals of Pancreatic Cancer*, vol. 2, pp. 2–2, 2019.

[5] Global Cancer Observatory, "13 pancreas fact sheet." [Online]. Available: https://gco.iarc.who.int/media/globocan/factsheets/cancers/13-pancreas-fact-sheet.pdf

[6] P. Mougenot, B. Gherman, C. Vaida, D. Pisla, and D. Chablat, "Review on retractor design to enhance minimally invasive pancreatectomy: Addressing challenges in deep tissue access," in *New Trends in Medical and Service Robotics*, M. A. Laribi, G. Carbone, D. Pisla, and S. Zeghloul, Eds. Springer Nature Switzerland, 2025, pp. 23–32.

[7] P. Mougenot, A. Pusca, L.-C. Vaida, D. Chablat, and D. L. Pisla, "Innovative surgical retractor for minimally invasive surgery," Patent A00 439, 2025-10-03.

[8] D. Pisla, A. Pusca, B. Gherman, A. Pisla, I. Birlescu, P. Tucan, C. Vaida, and D. Chablat, "Modeling and simulation of a novel parallel robotic system for minimally invasive pancreatic surgery," *Journal of Mechanisms and Robotics*, vol. 18, no. 2, p. 024501, 2026.

PLANAR PARALLEL MECHANISM DRIVEN ALONG A CURVED GUIDE

Yukio Takeda[1], Shota Fujisaka[1], Masashi Yoshii[1], Ryota Shioya[1], Ming Jiang[1], Koichi Kato[1], Mathias Huesing[2], Burkhard Corves[2], Tomoya Tanaka[3], Shogo Miura[3]

[1] Institute of Science Tokyo, 2-12-1, Ookayama, Meguro-ku, Tokyo 152-8552, Japan, {takeda.y.2c40@m.isct.ac.jp}

[2] RWTH Aachen University, Eilfschornsteinstraße 18, Aachen, 52062, Germany, {huesing@igmr.rwth-aachen.de}

[3] Ricoh Co., Ltd., 2-7-1 Izumi, Ebina, Kanagawa, 243-0460, Japan, {tomoya.tt.tanaka@jp.ricoh.com}

1. INTRODUCTION

Research on planar parallel mechanisms has been extensively conducted from both kinematic and dynamic points of view [1–5]. Their conventional applications include positioning tables requiring precise alignment in a horizontal plane [1,3], dynamic balancers for high-speed parallel robots operating in a horizontal plane [6], manipulators in the vertical plane [5], and walking rehabilitation devices [7]. In such applications, the mechanisms are required to possess a symmetric or isotropic planar workspace and a high orientation capability. The kinematic structure of such mechanisms is constructed such that the end-effector is either symmetrically supported by multiple kinematic chains of identical structure [1,2,4,6] or its position and orientation are decoupled through an asymmetrical arrangement of the kinematic chains [3,5,7]. In contrast, for applications such as painting, welding, washing, and printing on convex and/or concave surfaces with variable geometries - where the pose of the end-effector must be controlled to adapt to the surface shape - the design requirements for the workspace differ from those in conventional applications. The required workspace is typically characterized by a thin positioning region along a curve and a small orientation range around a position-dependent central value. In addition, interference between the target surface and the mechanism must be avoided. Since the kinematic design of a planar parallel mechanism that satisfies such workspace requirements has not been explored, a novel concept for the mechanism architecture is needed. In the present abstract, we propose a planar parallel mechanism that is driven along a curved guide and discuss its kinematic characteristics. Furthermore, as a novel drive element for this mechanism, a curved-guide drive mechanism is introduced to demonstrate the feasibility of the proposed mechanism.

2. PLANAR PARALLEL MECHANISM DRIVEN ALONG A CURVED GUIDE AND ITS KINEMATICS

Figure 1(a) shows the kinematic diagram of the proposed mechanism. The output link is supported by three kinematic chains. Each chain consists of two passive revolute joints and an active joint that drives a carriage along a fixed curved guide. The shape of the curve of the guide should be designed so as to satisfy the workspace requirements of the target application.

In this abstract, the curved guide is assumed to consist of three straight segments and two quarter-arc segments that connect the straight portions, as shown in Fig. 1(a). Under this assumption, it should be noted that although position and velocity remain continuous, a discontinuity in acceleration inevitably occurs at the junctions between the straight and arc segments. In this section, the inverse displacement analysis is considered, in which the position of the carriage along the curved guide of each kinematic chain A_i $(i = 1,2,3)$ is computed for a given pose of the output link. Once the pose of the output link is specified, the position of the joint B_i connecting each chain to the output link can be easily calculated. The position of A_i corresponding to a given B_i is then determined as the intersection between a circle centered at B_i with radius l_i and either a straight line or a circular arc representing the curved guide, as illustrated in Fig. 1(b). It is essential to select the appropriate solution among the multiple solutions to ensure a continuously feasible input displacement while maintaining the same working mode. To this end, a moving coordinate frame $B_i - xy$ is introduced, where the positive direction of the x-axis is defined from the inside to the outside of the curved guide. Position of A_i is first solved in $B_i - xy$, and the correct solution is selected based on the sign of its y-coordinate. Once the unique solution in $B_i - xy$ is obtained, a coordinate transformation is performed to express the position of A_i in the base coordinate frame $O - XY$. Since the geometry of the curved guide is defined by combining multiple curves, discontinuities in the inverse solution with respect to the position of B_i - as indicated by the quarter-arc region in Fig. 1(c) - occur when $l_i > R_2$. If the point B_i of the end-effector must move between positions located on opposite sides of the boundary curve, the end-effector must move along a designed path so that the corresponding B_i does not cross this curve.

3. CURVED-GUIDE DRIVE MECHANISM

A curved-guide drive mechanism consists of a guide element and a drive element. Figure 2(a) shows its schematic structure. The guide element is composed of a main frame, two sub frames with passive rollers, and a curved guide. The main frame corresponds to the carriage of the parallel mechanism, and the joint A_i of link A_iB_i is located at the identical position of the passive revolute

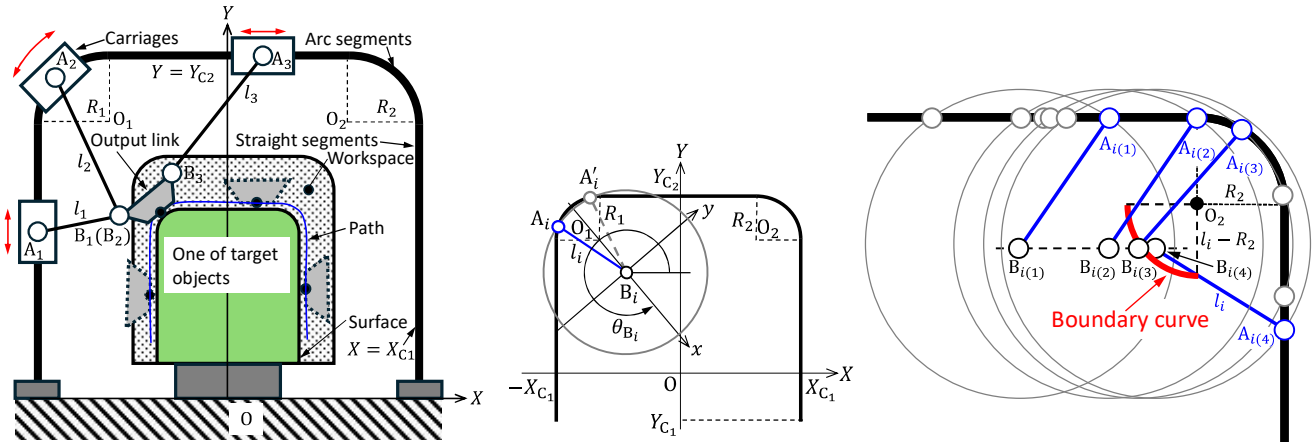

(a) Kinematic structure (b) Inverse kinematic solution (c) Boundary curve

Figure 1. Planar parallel mechanism driven along a curved guide.

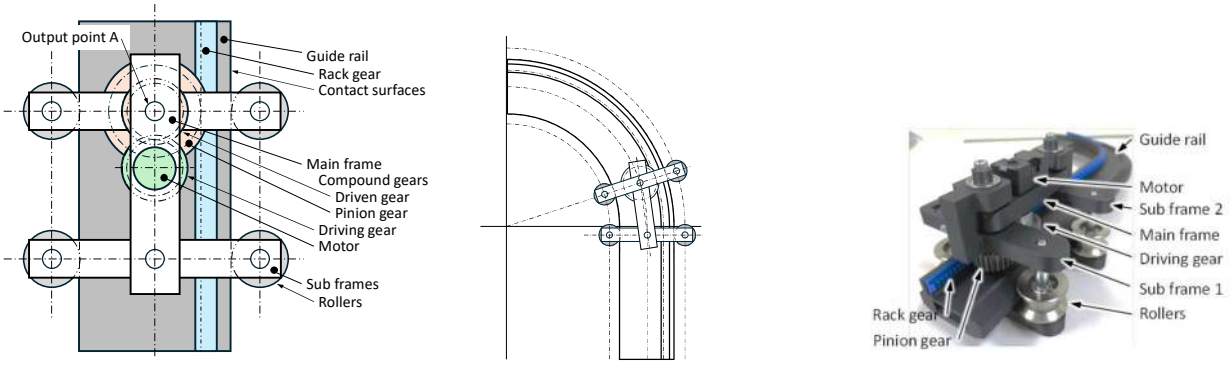

(a) Schematic diagram (b) Adaptation to line-arc continuous curve (c) 3D printed prototype

Figure 2. Curved-guide drive mechanism.

joint connecting the main and sub frames. The rollers contact the guide rail of a constant width by adjusting the distance between their contact points so that both sides of the guide rail remain engaged as shown in Fig. 2(b). Owing to this structure, each sub frame imposes a constraint force on the main frame in the normal direction of the contact curves. Consequently, the main frame is subjected to two independent constraints and is allowed to move only in the tangential direction of the guide rail.

The drive element consists of a rack-and-pinion gears and a motor mounted on the main frame. The distance between the pitch curve of the rack and the centerline of the guide rail remains constant. To realize a proper meshing between the rack and pinion gears, the pinion gear is located at the same position of the joint connecting the main frame and one of the sub frames. Using the 3D-printed prototype shown in Fig. 2(c), the feasibility of the curved-guide drive mechanism has been validated.

4. CONCLUSION AND FUTURE WORK

A novel parallel mechanism has been proposed to satisfy specific workspace requirements. Building on the results of the present study, we are currently developing a prototype of the parallel mechanism to be applied to an industrial painting robot.

REFERENCES

[1] C. Gosselin and J. Angeles, The optimum kinematic design of a planar three-degree-of-freedom parallel manipulator, *Journal of Mechanisms, Transmissions, and Automation in Design*, **110**(1), 35-41, 1988.

[2] C. M. Gosselin and J.-P. Merlet, The direct kinematics of planar parallel manipulators: Special architectures and number of solutions, *Mechanism and Machine Theory*, **29**(8), 1083-1097, 1994.

[3] Y. Takeda, H. Funabashi and N. Muramatsu, Planar in-parallel actuated mechanism with three degrees of freedom with large practically dexterous working space, *Transactions of JSME Series C*, **62**(599), 2920-2926, 1996 (in Japanese).

[4] C. Li, N. Wang, K. Chen and X. Zhang, Prescribed flexible orientation workspace and performance comparison of non-redundant 3-DOF planar parallel mechanisms, *Mechanism and Machine Theory*, **168**, 104602, 2022.

[5] T. Harada, Mode changes of redundantly actuated asymmetric parallel mechanism, *Proceedings of the Institution of Mechanical Engineers, Part C: Journal of Mechanical Engineering Science*, **230**(3), 454-462, 2015.

[6] C. Mirz, M. Hüsing, Y. Takeda and B. Corves, Design of a three-degree of freedom planar parallel mechanism for the active dynamic balancing of Delta Robots, *Robotics*, **13**(9), 129, 2024.

[7] C. Zhang, B. Lan, D. Matsuura, C. Mougenot, Y. Sugahara and Y. Takeda, Kinematic design of a footplate drive mechanism using a 3-DOF parallel mechanism for walking rehabilitation device, *J. Adv. Mech. Des., Syst., and Man.*, **12**(1), 2018.

MODELING AND ROBUSTNESS CHARACTERIZATION OF LARGE-STROKE QZS MECHANISMS UNDER ULTRA-LOW FREQUENCY EXCITATION

Shun. Bi[1], Shane. Johnson[2]

[1] Shanghai Jiao Tong University Global College, Minhang District Dongchuan Road 800, Shanghai, China, {bishun@sjtu.edu.cn}
[2] The Hong Kong University of Science and Technology (Guangzhou), Smart Manufacturing Thrust, 1 Duxue Road, Nansha District, Guangzhou, Guangdong Province, China, {shanejohnson@hkust-gz.edu.cn}

1 INTRODUCTION

Quasi-Zero Stiffness (QZS) actuators provide robust solutions for vibration isolation and force regulation. However, large-stroke applications (stroke ratios > 70%) reveal fundamental limitations in conventional modeling frameworks [1, 2, 3]. Low-order polynomial fits [4, 5] limited to $d_{QZS}/(d_{QZS} + d_{preload}) < 50\%$ fail to capture large stroke nonlinearities [6], while high-order expansions often lack physical interpretability and diverge at boundaries. This study introduces a dynamic modeling framework for an automated fiber winding system with force regulation using the QZS actuator under the severe dynamic perturbations of automated manufacturing. An adapted Ramberg-Osgood (RO) formulation is used to describe the key QZS actuator component, the constant force mechanism, with significantly fewer parameters than polynomial models. The fiber-winding system demonstrates superior tension stability under ultra-low frequency (ULF) excitation compared to traditional Series Elastic Actuators (SEA).

2 MODELING METHOD BASED ON ADAPTED RAMBERG-OSGOOD EQUATION

Recent advancements in large-stroke constant-force/torque mechanisms have made low-order polynomial fitting inadequate for characterizing nonlinear force–displacement behavior [6]. Higher-order polynomials are not analytically solvable and frequently exhibit overfitting or poor extrapolation performance beyond the calibration range. Consequently, the RO model is utilized in this study for its parametric efficiency and superior extrapolation stability. While originally developed for material stress-strain characterization, we adapt the equation to describe structural force-displacement:

$$x = \frac{F_{\mathrm{RO}}}{k} + \alpha \left(\frac{F_{\mathrm{RO}}}{k} \right)^n$$

The adapted RO equation remains implicit. However, within the operational regime of the QZS force-regulation system, the control objective maintains displacement within a high-stroke operating range where the linear term $\frac{F_{\mathrm{RO}}}{k}$ is negligible relative to the nonlinear component. This justifies an explicit asymptotic approximation: $F_{\mathrm{RO}}(x) \approx k(\frac{x}{\alpha})^{1/n}$. Substituting the PID control law $u(t)$ and this explicit relation into the governing equation of motion $m\ddot{x}(t) + c\dot{x}(t) + F_{\mathrm{RO}}(x) = u(t) + F_{\mathrm{ext}}(t)$ yields the final dynamic form:

$$m\ddot{x} + c\dot{x} + k \left(\frac{x}{\alpha} \right)^{1/n} = u(t) + F_{\mathrm{ext}}(t)$$

As illustrated in Fig.1 a), the adapted RO model accurately captures the experimental force–displacement data of the large stroke constant-force mechanism well. Within the large-stroke regime, the asymptotic approximation maintains high fidelity to the QZS behavior while significantly reducing the computational cost of solving the implicit form of the equation, requiring fewer parameters than higher order polynomial benchmarks.

3 QZS ACTUATOR FORCE REGULATION EXPERIMENTAL RESULT

Following the RO characterization, we implemented a displacement-based PID controller within a fiber-winding system. The actuator performance was benchmarked under Hookean spring conditions and the proposed QZS mechanism, targeting a 20 N tension setpoint. A stadium-shaped mandrel induced periodic speed fluctuations to simulate severe dynamic perturbations. The PID controller dynamically adjusted the inlet speed to compensate for these variations (Fig. 1c). This system, evolved from Ye's study [7], enhances adaptability for diverse constant-torque and constant-force configurations. Experimental observations confirm the PID controller effectively maintains both SEA and QZS systems within operational bounds.

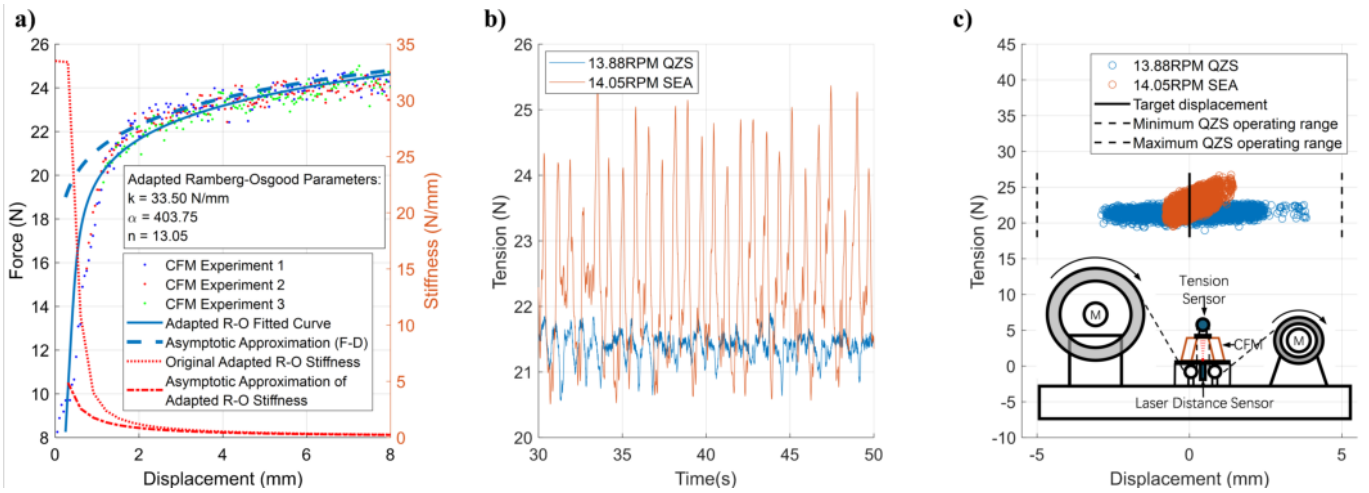

Figure 1: a) Experimentally characterized force–displacement relationship of the CFM, fitted by the adapted Ramberg–Osgood equation, and comparison with the asymptotic approximation for large-stroke deformation. b) Fiber tension fluctuation results for the displacement PID-controlled SEA and the QZS force-regulation system. c) Tension–displacement relationship under dynamic force regulation, together with the corresponding experimental setup.

As expected, the low stiffness of the QZS system in its operating range results in larger displacement fluctuations but significantly attenuated tension fluctuations. Tension fluctuation results (Fig. 1b) indicate a standard deviation of $\sigma_{SEA} = 1.123$ for the SEA system, compared to $\sigma_{QZS} = 0.207$ for the QZS system. This demonstrates an **81.55% suppression** of fiber tension fluctuations ($\frac{\sigma_{SEA}-\sigma_{QZS}}{\sigma_{SEA}}$), substantially enhancing system robustness for high-precision manufacturing.

REFERENCES

[1] B. y. Li, C. g. Shuai, W. Xu, and Z. h. Yang, "Review on Low Frequency Control of Quasi-Zero Stiffness". in *2021 13th International Conference on Computer and Automation Engineering (ICCAE)*, 20-22 March 2021 2021, pp. 59-63, doi: 10.1109/ICCAE51876.2021.9426128. [Online]. Available: https://ieeexplore.ieee.org/document/9426128/

[2] P. Wang and Q. Xu, "Design and modeling of constant-force mechanisms: A survey." *Mech. Mach. Theory*, https://doi.org/10.1016/j.mechmachtheory.2017.08.017 vol. 119, pp. 1–21-1–21, 2018.

[3] J. Cai, Q. Gao, and X. Zhang, "Proportional-retarded control of a quasi-zero-stiffness vibration isolator". *Journal of Sound and Vibration*, vol. 578, p. 118309, 2024/05/26/ 2024, doi: https://doi.org/10.1016/j.jsv.2024.118309.

[4] A. C. Thewes, P. Schmitt, P. Löhler, and M. Hoffmann, "Design and Characterization of an Electrostatic Constant-Force Actuator Based on a Non-Linear Spring System". *Actuators*, vol. 10, no. 8, 2021, doi: 10.3390/act10080192

[5] J. Xu et al., "Design of quasi-zero stiffness joint actuator and research on vibration isolation performance". *Journal of Sound and Vibration*, vol. 479, p. 115367, 2020/08/04/ 2020, doi: https://doi.org/10.1016/j.jsv.2020.115367.

[6] S. Bi, T. U. Rehman, and S. Johnson, "Iterative optimization to enhance effective compliance for design of large stroke constant torque mechanisms". *Mechanism and Machine Theory*, vol. 214, p. 106061, 2025/10/15/ 2025, doi: https://doi.org/10.1016/j.mechmachtheory.2025.106061.

[7] S. Ye, Y. Mo, H. Ou, S. Bi, and S. Johnson, "Tension Control in Filament Winding Using Constant Force Mechanisms," in ASME 2023 International Mechanical Engineering Congress and Exposition, 2023, vol. Volume 6: Dynamics, Vibration, and Control, V006T07A057, doi: 10.1115/imece2023-114308. [Online]. Available: https://doi.org/10.1115/IMECE2023-114308

ON THE FRICTION TORQUE IN SLEWING BEARINGS: TOWARDS A NEW APPROACH

Mikel Portilla[1], Martin Eizmendi[1], Iker Heras[1], Josu Aguirrebeitia[1]

[1] University of the Basque Country (EHU), Plaza Ingeniero Torres Quevedo 1, Bilbao, Spain, {mikel.portilla@ehu.eus; martin.eizmendi@ehu.eus; iker.heras@ehu.eus; josu.aguirrebeitia@ehu.eus}

1. INTRODUCTION

Four-Point Contact Slewing Bearings (4PCSBs) are large sized rolling bearings designed for orientation purposes (e.g., wind turbines, radio telescopes, or armoured vehicle turrets). In such applications, these bearings are usually subjected to large tilting moments, as well as loads in axial or radial direction, and typically operate under oscillatory motion at low rotational speeds.

Friction torque is a key parameter to consider in the design or selection of slewing bearings, as its accurate prediction is essential for the proper sizing and control of orientation systems that enable the relative rotation between the bearing rings. Moreover, the availability of a reliable calculation tool is of significant industrial interest from the perspective of condition monitoring.

In this regard, several calculation tools are available to directly estimate the friction torque based on bearing design parameters and applied external loads. For instance, the National Renewable Energy Laboratory (NREL) [1] proposed a simplified formulation in which the friction torque is expressed as a function of the applied loads, a friction coefficient, and the pitch diameter. Despite its ease of use, the main drawback of this method lies in its limited accuracy, as it does not account for parameters such as the osculation ratio or ball preload, which ultimately govern the resulting friction torque. Consequently, this approach is only suitable for obtaining a first rough approximation. To overcome these limitations, Escanciano [2] proposed the Bearing-Torque-Map concept, a data-driven black-box approach in which the friction torque is estimated from a set of normalized and design parameters. Despite the versatility of this method, key aspects such as assembly effects, manufacturing errors, and ring flexibility are not considered, which constitute critical factors underlying its limitations.

As an alternative to the aforementioned black-box approaches, a physics-based modelling strategy can be adopted. In this context, and given that 4PCSBs typically operate at low rotational speeds, the load distribution problem and the kinematics can be solved in a decoupled manner. Once both are solved, the computation of the friction torque becomes straightforward.

Each of these problems can be addressed either through Finite Element (FE) simulations or by means of mechanistic models. In industrial practice, the load distribution problem is frequently solved via FE simulations, as they allow structural flexibility effects to be accounted for —an aspect of particular relevance in slewing bearings. Additionally, FE modelling enables the inclusion of other potentially critical factors, such as assembly conditions and manufacturing tolerances. Once the load supported by each rolling element is known, the kinematic problem can be solved to determine the friction forces acting on the balls. This problem is formulated independently for each rolling element, and the analytical formulation proposed by Joshi et al. [3] showed to provide accurate results [4]. Nevertheless, this formulation is computationally complex and often exhibits convergence issues.

In this context, there is currently no calculation tool reported in the literature that enables the estimation of friction torque with both high accuracy and low computational cost, while remaining easy to implement. To address this gap, the present research investigates the feasibility of an innovative approach aimed at developing a black-box model that solves the kinematics at the ball level, giving a previously known load distribution. This approach is referred to as the Ball-Torque-Map, in contrast with the Bearing-Torque-Map developed in [2], whose reliability is intended to depend solely on the accuracy of the load distribution used as input.

2. MATERIALS AND METHODS

In order to provide an initial assessment, this work maps the behaviour of each rolling element of a specific slewing bearing as a function of the contact forces acting along the two contact diagonals (Q_i and Q_j), based on the analytical method proposed by Joshi et al. [3]. To normalize the analysis and with a view to future extensions of this work, contact forces are expressed relative to the static load-carrying capacity of the corresponding contacts ($Q_{i,n}$ and $Q_{j,n}$), as defined in ISO 76:2006.

This case study considers a slewing bearing with a pitch diameter of 1000 mm, a ball diameter of 25 mm, and an osculation ratio of 0.94. A friction coefficient of 0.1 [2,4] is assumed for the ball–raceway contact. To enhance numerical convergence, the formulation proposed by Heras [4] is adopted together with the full-sliding hypothesis, which was shown to be valid for friction torque assessment [4]. Finally, a total of 10 000 simulations were carried out for different combinations of $Q_{i,n}$ and $Q_{j,n}$.

3. RESULTS

The results obtained for the Ball-Torque-Map are presented in Fig. 1, which compares the simulations based on the model proposed by Joshi et al. with those derived from the approximate functional formulation.

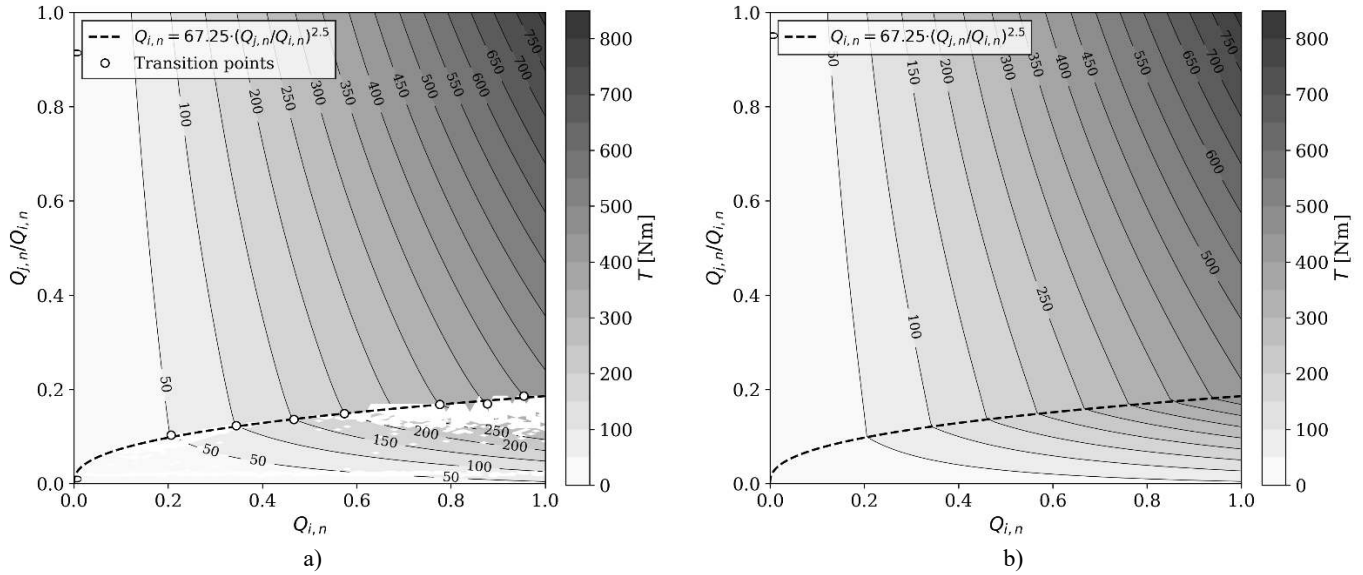

Figure 1. Ball-Torque-Maps: a) results from the simulations with the model by Joshi; b) deduced functional approximation.

Results show that the trend of the friction torque bands exhibits an abrupt change beyond a certain region of the plot, reflecting a transition in bearing kinematics. When both contact diagonals are similarly loaded, the ball rolls about its vertical axis, corresponding to the region above the threshold. Conversely, when one of the contact diagonals carries a predominant load, the axis of rotation of the ball is tilted by 45° with respect to the vertical, corresponding to the region below the threshold [2]. This kinematic transition follows the expression given below and is represented in Fig. 1 by a dashed line:

$$Q_{i,n} = 67.25 \cdot \left(\frac{Q_{j,n}}{Q_{i,n}}\right)^{2.5} \tag{1}$$

Once this threshold is defined, a piecewise function is derived (Eq. (2)) that fits the Ball-Torque-Map for this specific bearing geometry in both kinematic regimes, as shown in Fig. 1(b).

$$\begin{cases} T = Q_{i,n}^{1.1} \cdot \left(39.76 + 2069 \cdot \left(\frac{Q_{j,n}}{Q_{i,n}}\right)^{0.9}\right) & if \ \frac{Q_{i,n}{}^{3.5}}{Q_{j,n}{}^{2.5}} < 67.25 \\ T = Q_{i,n}^{1.3} \cdot \left(385.4 + 431.5 \cdot \left(\frac{Q_{j,n}}{Q_{i,n}}\right)^{1.2}\right) & if \ \frac{Q_{i,n}{}^{3.5}}{Q_{j,n}{}^{2.5}} > 67.25 \end{cases} \tag{2}$$

4. CONCLUSIONS

This work demonstrates that the proposed approach constitutes a viable solution for estimating the friction torque in 4PCSBs, thereby justifying further research along this line. Future work will focus on applying the same procedure while varying the bearing design parameters, with the aim of deriving a generic functional approximation for the Ball-Torque-Map applicable to any bearing geometry and loading condition.

ACKNOWLEDGEMENTS

Thanks to Ministry of Science, Innovation and Universities of the Government of Spain for the financial support through Project PID2024-158830OA-I00 funded by MICIU /AEI /10.13039/501100011033 and by FEDER, UE.

REFERENCES

[1] T. Harris, J. H. Rumbarger, and C. P. Butterfield, "Wind Turbine Design Guideline DG03: Yaw and Pitch Rolling Bearing Life," 2009. [Online]. Available: https://docs.nrel.gov/docs/fy24osti/89161.pdf

[2] I. Escanciano García, *PhD Thesis: Friction torque in ball slewing bearings for wind turbines*. University of the Basque Country (EHU), Bilbao, Spain, Jan. 2023. http://hdl.handle.net/10810/69186

[3] A. Joshi, B. Kachhia, H. Kikkari, M. Sridhar, D. Nelias, Running Torque of slow speed two-point and four-point contact bearings, Lubricants 3 (2015) 181–196, https://doi.org/10.3390/lubricants3020181.

[4] I. Heras Miguel *PhD Thesis: Four-point contact slewing bearings for wind turbines: advances in structural modelling and friction torque calculation*. University of the Basque Country (EHU), Bilbao, Spain, Feb. 2018. http://hdl.handle.net/10810/26651

ERROR ADAPTABILITY ANALYSIS ON A NOVEL POINT CONTACT FACE WORM GEAR DRIVE BASED ON GEOMETRIC ELEMENT

Chenyang Dou[1], Yonghong Chen[1*], Jin Gao[1], Zhenglin Yang[1], Fei Liu[1], Wenjun Luo[1], Bingkui Chen[1]

[1] State Key Laboratory of Mechanical Transmission for Advanced Equipment, Chongqing University, Chongqing 400030, China, {20230701015@stu.cqu.edu.cn ; yh_chen@cqu.edu.cn ; 202207131416@stu.cqu.edu.cn ; 202107131131t@cqu.edu.cn ; lfei@cqu.edu.cn; wenjun.luo@163.com ; bkchen@cqu.edu.cn}

1. RESEARCH BACKGROUND

Industrial robots are widely applied in various fields of national economic production. However, the mainstream transmission forms of existing robot joint reducers still fail to meet the performance requirements of high rigidity and high overload capacity in processing fields such as grinding, cutting and polishing. Based on the preliminary research findings of the project team and the technological development status abroad, face worm gear drive [1, 2] is an effective approach to address the insufficient rigidity of the middle and rear joints in processing-oriented industrial robots. Compared with bevel gear drives and hypoid gear drives, the face worm gear drive offers advantages including a larger transmission ratio, higher load-carrying capacity, and insensitivity to the axial position error of the worm. Compared with spiroid gear drives, the face worm gear drive not only features better manufacturability but also effectively eliminates the jamming phenomenon caused by the deformation of the spiroid worm toward its small end.

Nevertheless, the end-face transmission structure is relatively sensitive to machining errors and assembly errors [3]. Therefore, carrying out an error adaptability analysis of the novel point-contact face worm gear drive and mastering the law of its transmission accuracy under various error conditions are of great significance for improving the joint performance of industrial robots.

2. MATHEMATICAL MODEL

The novel face worm gear drive proposed in this paper is a multi-tooth point contact transmission based on the spatial curve meshing principle. First, the conjugate curves and meshing points are derived from the cylindrical helix based on geometric relationships, then the normal tooth profiles at the meshing points are constructed, and finally the tooth surfaces are generated by sweeping the normal tooth profiles along the conjugate curves.

On the basis of the original coordinate relationships, errors in all directions are incorporated into the relationships [4, 5]. The meshing function with machining errors can be calculated and simplified as follows.

$$\begin{cases} \Phi = P\cos(\theta+\varphi_w)+Q\sin(\theta+\varphi_w)+W=0 \\ P=\begin{pmatrix} -p\cos\alpha\sin\Delta_1\left(\left(A+\Delta_a\right)\cos\Delta_2-ZA\sin\Delta_2\right)+\cos\alpha\cos\Delta_1 r_1^2- \\ p\theta\cos\Delta_1\sin\alpha\sigma_1+\sin\alpha\left(-ZA\cos\Delta_2-\left(A+\Delta_a\right)\sin\Delta_2\right)\sigma_1 \end{pmatrix}/\sigma_1 \\ Q=\begin{pmatrix} \sin\alpha\sin\Delta_1\left(\left(A+\Delta_a\right)\cos\Delta_2-ZA\sin\Delta_2\right)-p^2\theta\cos\alpha\cos\Delta_1/\sigma_1 \\ +p\cos\alpha\left(-ZA\cos\Delta_2-\left(A+\Delta_a\right)\sin\Delta_2\right)/\sigma_1 \end{pmatrix} \\ W=\cos\alpha\left(\left(A+\Delta_a\right)\cos\Delta_1\cos\Delta_2-ZA\cos\Delta_1\sin\Delta_2-p\left(\sin\Delta_1+i_{wg}\right)\right)r_1/\sigma_1 \\ \sigma_1=\sqrt{p^2+r_1^2} \end{cases} \tag{1}$$

Where, θ is the helix angle, φ_w is the worm rotation angle,α is the tooth surface pressure angle, p is the helix parameter, A denotes the center distance, ZA denotes the axial mounting distance, Δ_1 and Δ_2 denote the shaft angle errors, Δ_l represents the axial error of the worm gear, and Δa stands for the center distance error.

3. TOOTH CONTACT ANALYSIS (TCA) AND TRANSMISSION ACCURACY MODEL

Tooth contact analysis is carried out based on the error-included mathematical model to investigate the contact state between the error-included face gear tooth surfaces and the original worm tooth surfaces. The criteria for good tooth surface contact are established, and based on the Multi-objective Optimized Walrus Algorithm, the actual rotation angle of the worm gear is calculated under the given input angle of the worm. According to the instantaneous rotation angle data of the worm and face gear, the instantaneous transmission ratio and transmission error are further calculated. Finally, the influence laws of various assembly errors on transmission accuracy under different working conditions are obtained.

4. EXPERIMENTAL VERIFICATION

To verify the influence law of different assembly errors, namely axial displacement error, radial offset error, and shaft angle error, on the transmission accuracy of the worm-face gear drive, and to further validate the correctness of the theoretical TCA results under error conditions, experimental tests were carried out. The experimental research adhered to the principles of single variable control and repeated verification, ensuring the reliability and repeatability of the experimental data, which provided experimental support for the optimization of assembly processes and the control of transmission accuracy in engineering practice. The abstract figure of this paper is specifically shown in Figure 1.

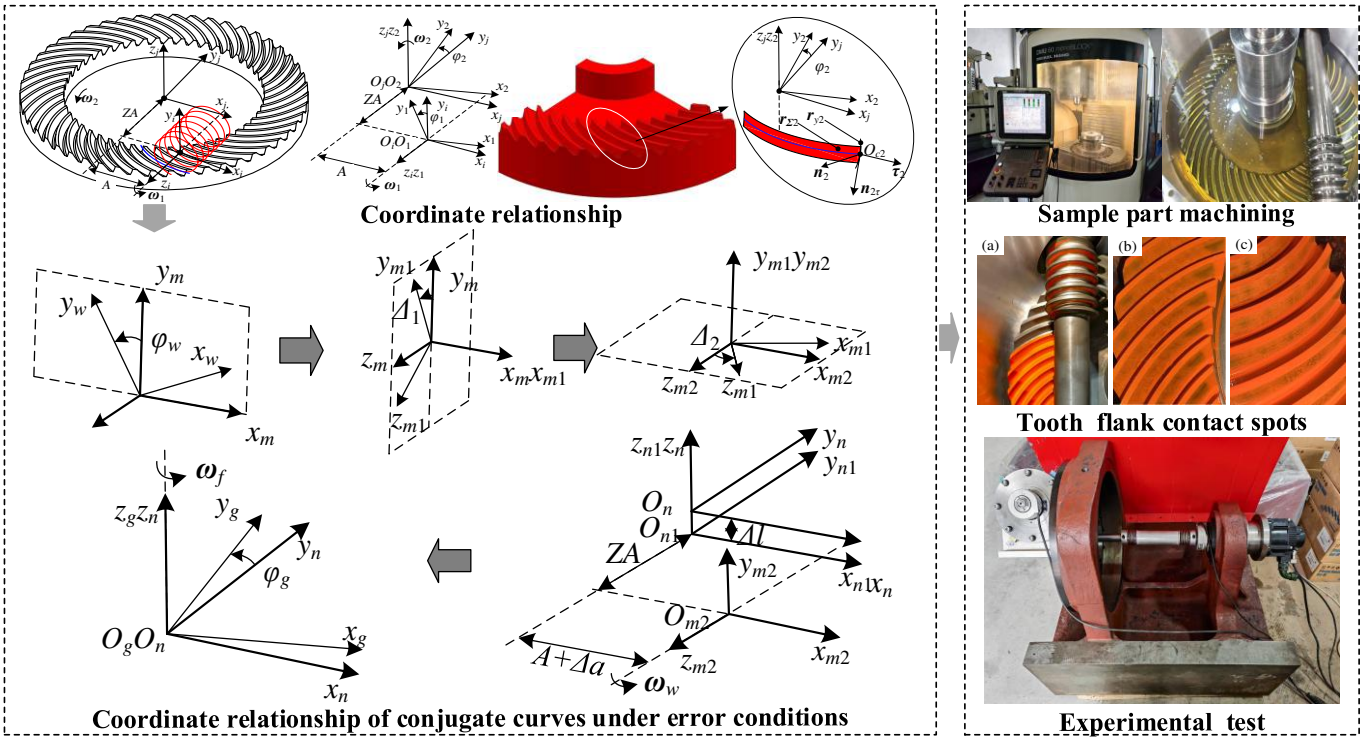

Figure 1. Summary diagram of transmission accuracy solution for novel point-contact worm-face gear drive.

ACKNOWLEDGMENTS

This work was supported by the National Natural Science Foundation of China (Grant No. 52575050) and the Natural Science Foundation of Chongqing (Grant No. CSTB2024NSCQ-LZX0028).

REFERENCES

[1] W.X. Xian, Y.H. Chen, J. Gao, et al., “Meshing performance investigations on face worm gear drive with the variable worm cone angle”. *Journal of Advanced Mechanical Design, Systems, and Manufacturing*, 17(6), 2300273, 2023.

[2] S.B. Mu, X.W. Sun, Z.X. Dong, et al., “Meshing theory of point-contact conical-envelope cylindrical worm-face worm gear drive”. *Mechanism and Machine Theory*, 205, 105870, 2025.

[3] Q.X. Meng, Y.P. Zhao, Z.Y. Yang, et al., “Meshing theory and error sensitivity of mismatched conical surface enveloping conical worm pair”. *Mechanism and Machine Theory*, 145, 103681, 2020.

[4] S. Ding, Z.Q. Song, W.W. Wu, et al., “Geometric error modeling and compensation of horizontal CNC turning center for TI worm turning”. *International Journal of Mechanical Sciences*, 167, 105266, 2020.

[5] C.Y. Dou, Y.H. Chen, F. Liu, et al., “Meshing performance investigations on a novel end-face roller enveloping cylindrical worm drive with non-backlash”. *Mechanism and Machine Theory*, 182, 105235, 2023.

ARTIFICIAL NEURAL NETWORK FOR MODELLING GEAR MESH STIFFNESS

Francisco H.J. Ricardo[1,2], João D.M. Marafona[1], Stéphane Portron[1], Carlos M.C.G. Fernandes[2], Pedro M.T. Marques[2], João Manuel R.S. Tavares[2]

[1] INEGI, Universidade do Porto, Campus FEUP, Rua Dr. Roberto Frias 400, 4200-465 Porto, Portugal {fricardo@inegi.up.pt}
[2] FEUP, Universidade do Porto, Rua Dr. Roberto Frias s/n, 4200-465 Porto, Portugal {fhricardo@up.pt}

1 INTRODUCTION

Gear mesh stiffness is a major source of noise and vibration in gear pairs. Consequently, numerous models, including analytical, finite element, hybrid and approximate analytical, have been developed over time to describe this intrinsic characteristic of gear transmissions. Among these, approximate analytical models generally require lower computational effort, whereas finite element methods provide higher accuracy. In dynamic and optimisation analyses, an accurate characterisation of gear mesh stiffness is essential; however, it should be achieved with reduced computational cost. For this reason, several authors [1, 2] have proposed analytical-approximate models to estimate gear mesh stiffness as reliably as possible maintaining a low computational cost. Previous studies [1, 2] have shown that, while these approaches capture the magnitude of gear mesh stiffness accurately, they often fail to reproduce its exact shape. This discrepancy in shape, even if small, can significantly influence the results of dynamic analyses, as demonstrated in [1, 2]. With the rise of artificial intelligence, machine learning models have been applied to gear transmission. Recently, surrogate models have been used to estimate static transmission error and gear mesh stiffness [3, 4]. The models proposed in these works capture both the shape and magnitude of the curves at low computational cost. Therefore, this work proposes a model to determine the single tooth pair gear mesh stiffness by estimating the structural single tooth pair slice gear mesh stiffness using an artificial neural network (ANN). In this way, the proposed approach improves the model developed by Marafona et al. [1] by replacing the parabolic approximation of the structural single tooth pair slice gear mesh stiffness with a curve predicted by an ANN.

2 ANALYTICAL DATASET GENERATION

During the development of an artificial neural network (ANN), the first and fundamental step is to acquire a representative dataset of the phenomenon under analysis, capturing the key variables and their relationships. Moreover, this dataset should be as reliable as possible, as it constitutes the foundation for both training and testing the proposed model. To generate such a dataset, a population of gears must be defined. In this work, the range of geometric parameters considered is listed in Table 1.

Table 1: Gear parameters range.

Parameter	$z/-$	$\alpha/^\circ$	$\beta/^\circ$	m_n/mm	b/mm	$x/-$	E/GPa	ν/-
Range	18 : 300	20	0 : 40	DIN 780[a]	$3\,m_\mathrm{n} : 14\,m_\mathrm{n}$	$-1 : 1$	180 : 220	0.3

[a] All module values from DIN 780 Series I.

It is noteworthy that the transverse structural stiffness (bending, shear and axial compressive components) of a single tooth is computed considering the maximum available area of the tooth flank. Additionally, since the aim is to estimate the transverse structural single tooth stiffness per unit width, the stiffness obtained using the potential energy method was divided by the facewidth b for each gear. At this stage, the dataset for developing the machine learning model is created. Initially, the dataset consists of 7 input features (listed in Table 1) and 20000 samples, with the target vector discretised into 100 points across the maximum usable area of the tooth flank.

3 MACHINE LEARNING MODEL

Once the dataset is generated, it is divided into two subsets: a training set (80%) and a test set (20%). The next step is to preprocess the training set. Analysis of the input features revealed that the normal module and the facewidth exhibit a high correlation; therefore, the latter was discarded. In addition, the pressure angle was also removed, as it is constant across the entire dataset and does not provide additional information to the model. Consequently, the final feature set comprises the number of teeth z, helix angle β, normal module m_n, profile shift coefficient x,

and Young's modulus E. Additionally, the input features and the target variable were transformed using Z-score standardisation and Min-Max normalisation, respectively. Finally, an artificial neural network was developed, and its hyperparameters were optimised. The tuned hyperparameters included the number of hidden layers, the number of neurons per layer, the initial learning rate, the decay rate, the dropout rate, and the batch size. Table 2 presents an overview of the adopted neural network architecture. During the optimisation process, five-fold cross-validation was employed to ensure a robust evaluation of the model's performance. This strategy helped mitigate overfitting by assessing the ANN's generalisation capability across different subsets of the training data, leading to a more reliable selection of hyperparameters.

Table 2: Architecture of the Artificial Neural Network.

Input layer	Hidden layer 1	Hidden layer 2	Output layer
Neurons: 5	Neurons: 128 Initialiser: he_normal Activation: ReLU Batch Normalisation Dropout: 0.1	Neurons: 16 Initialiser: he_normal Activation: ReLU Batch Normalisation Dropout: 0.1	Neurons:100 Activation: Tanh

After defining the ANN architecture, the model was trained using the entire training set and subsequently evaluated on the test set. Figure 1(a) represents the distribution of the R-squared values over the entire test set, while Figure 1(b) shows the case with the lowest R-squared ($R^2 = 0.9911$). Noted that the vertical axis of Figure 1(b) represents the inverse of the transverse structural stiffness per unit width. These results demonstrate that the proposed model accurately captures both the shape and magnitude of the transverse structural tooth slice mesh stiffness.
Further developments are ongoing, with different normalisation and feature engineering techniques being investigated to enhance the performance of the ANN.

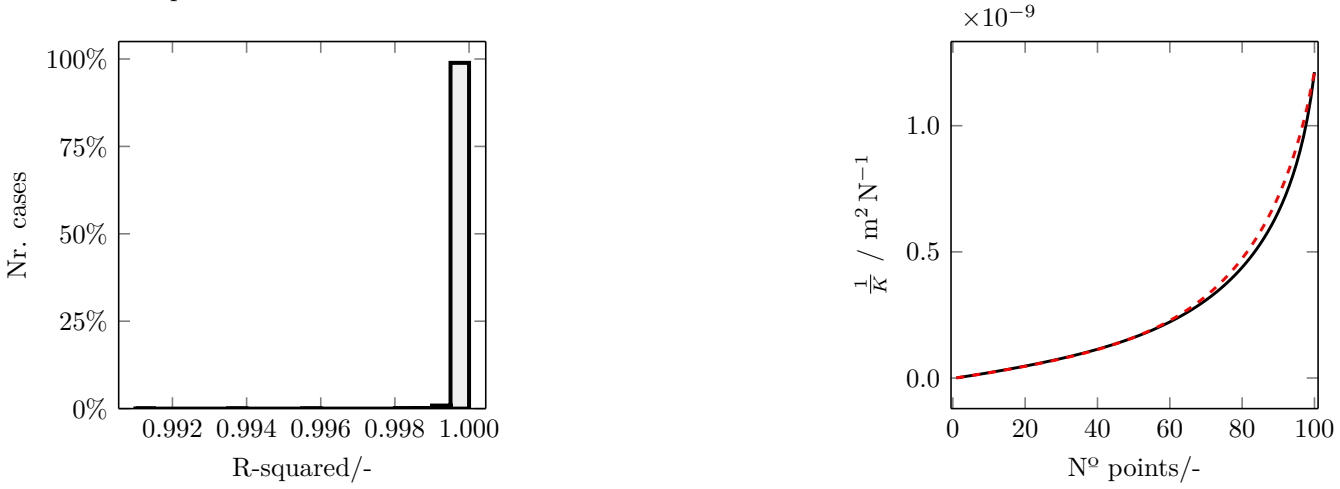

(a) R-squared.

(b) Worst case: PEM (——) and ANN (- - -).

Figure 1: Artificial neural network performance.

ACKNOWLEDGMENTS

- LAETA under project UID/50022/2025 (https://doi.org/10.54499/UID/50022/2025);
- *Fundação para a Ciência e a Tecnologia*: CEECINST/00096/2021/CP2801/CT0003 (https://doi.org/10.54499/CEECINST/00096/2021/CP2801/CT0003).

REFERENCES

[1] J. D. Marafona, P. M. Marques, S. Portron, R. C. Martins, and J. H. Seabra, "Gear mesh stiffness and dynamics: Influence of tooth pair structural stiffness asymmetry," *Mechanism and Machine Theory*, vol. 190, p. 105 447, 2023, ISSN: 0094-114X.

[2] F. H. Ricardo, J. D. Marafona, and P. M. Marques, "Modelling gear mesh stiffness including axial effects: Approximate approach," *Mechanism and Machine Theory*, vol. 217, p. 106 221, 2025, ISSN: 0094-114X.

[3] E. Sakaridis, C. Kalligeros, C. Papalexis, G. Kostopoulos, and V. Spitas, "Symmetry preserving neural network models for spur gear static transmission error curves," *Mechanism and Machine Theory*, vol. 187, p. 105 369, 2023, ISSN: 0094-114X.

[4] H. Mohamed, N. Brödling, and F. Duddeck, "Efficient analysis of time-varying mesh stiffness of helical gear pair using neural networks and autoencoders," *Forschung im Ingenieurwesen*, vol. 89, p. 82, 2025, ISSN: 0015-7899.

ASSESSING THE TIPPING OVER RISK OF ROLLATORS DURING STANDING UP IN YOUNGER AND OLDER ADULTS

Marko Ackermann[1], Katja Mombaur[1,2]

[1] Karlsruhe Institute of Technology (KIT), Adenauerring 12, Karlsruhe, Germany, {marko.ackermann@kit.edu}
[2] University of Waterloo, 200 University Avenue West, Waterloo, Canada, {katja.mombaur@kit.edu}

1 INTRODUCTION

Rollators are prescribed to provide support and improve stability during walking, but in practice they are also used to support standing up and sitting down [1]. However, because conventional rollators are light and have a reduced base of support (BoS), they are prone to tipping over, resulting in a limited capacity of transmitting horizontal support forces. This is critical as the use of walking aids is a risk factor for falling and is associated with a higher risk of severe injuries in older adults [2]. Many falls result from rollator use when users try to pull themselves up. Despite the importance of rollator stability, there are few studies on the mechanical determinants of stability and the associated risk of tipping over of these mobility assistive devices, particularly during standing up and sitting down. The objective of this study is to investigate the risk of tipping over or slipping considering the mechanical properties of rollators and the typical handle support force profiles measured under ideal conditions for younger and frail older adults.

2 METHODS

The proposed approach encompasses the measurement of typical vertical and horizontal force profiles applied on fixed handles (Fig. 1.a) of a static lab device that does not move (Fig. 1.b,c) while standing for younger (Fig. 1.b) and frail older adults (Fig. 1.c). The applied handle forces are then compared to the rollator's static equilibrium conditions as a function of its mechanical properties (Fig. 1.d).

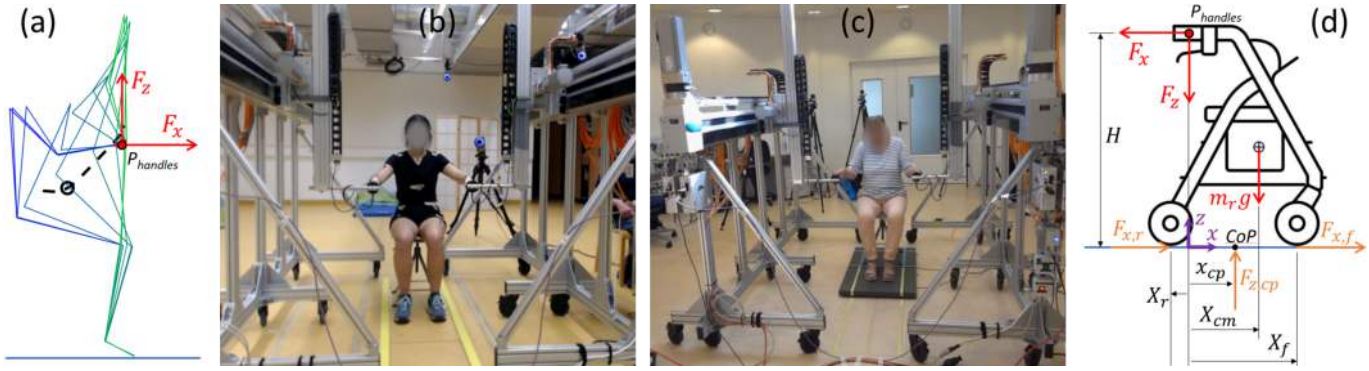

Figure 1: (a) snapshots of average participant poses while standing up with handle force components (red); experimental setup for collection of handle forces by younger (b) and frail older adults (c); (d) handle forces (red) and rollator's properties.

Horizontal and vertical forces applied by fixed instrumented handles (Robotiq FT 300) were collected for 15 younger adults (3 female, 27.5 ± 4.9 yrs) in a motion capture lab [3] (Fig. 1.b), and for 18 frail older adults with difficulties standing up unassisted (15 female, 83.7 ± 5.6 yrs) in a clinical setting (Fig. 1.c). Handles were placed in front of participants by a robotic assistance device comprising two cartesian robots, one placed on each side of the participant (Fig. 1.b,c, [3]), so as to simulate the position of handles provided by conventional rollators. Horizontal F_x and vertical F_z force components were filtered (zero-lag Butterworth, 6 Hz) and 80^{th}-percentile curves were computed for younger (Fig. 2.a) and frail older (Fig. 2.b) adults to represent ideal force profiles to support standing up in the $F_z \times F_x$ plane. The stable region for the rollators in terms of the two handle force components on the sagittal plane was computed by enforcing static equilibrium equations considering the rollator's mechanical properties and Coulomb friction, resulting in the following inequality constraints in Eq. 1 to prevent tipping over backward and forward, respectively,

$$F_z \geq m_r g \left(\frac{X_{cm} - X_r}{X_r} \right) - \frac{H}{X_r} F_x \,, \quad F_z \geq m_r g \left(\frac{X_{cm} - X_f}{X_f} \right) - \frac{H}{X_f} F_x \,, \tag{1}$$

where H is the handles' height, m_r is the rollator's mass, g is gravity acceleration, and X_r, X_{cm}, and X_f are the horizontal rear wheels, rollator's center of mass and front wheels positions with respect to the handles, respectively (Fig. 1.d, positive forward), and the inequality constraints in Eq. 2 to prevent slipping backward and forward, respectively,

$$F_z \geq -m_r g + \frac{1}{\mu} F_x \,, \quad F_z \geq -m_r g - \frac{1}{\mu} F_x \,, \tag{2}$$

where μ is the coefficient of friction. To assess stability for typical rollators, the mechanical properties of a conventional rollator (Kesser, KS-RS01, Fig. 2.a, $m_r = 8.5$ kg, $H = 0.87$ m, $X_r = -0.205$ m, $X_{cm} = 0.126$ m, $X_f = 0.270$ m) and a robotic rollator (SkyWalker, Fig. 2.b, $m_r = 23.3$ kg, $H = 0.99$ m, $X_r = -0.245$ m, $X_{cm} = 0.320$ m, $X_f = 0.395$ m) were measured and the coefficient of friction was assumed as 0.5, which is within the range reported in the literature.

3 RESULTS

The results show that conventional rollators are prone to tipping over backward during standing up (Fig. 2.a), as the 80^{th}-percentile force curves surpass the stability envelope (green area) by violating first the corresponding constraint (blue line). This is particularly critical for frail older adults (red), who tend to apply larger horizontal forces to the handles. The tested robotic rollator is more stable due to its larger BoS and mass, with the center of mass shifted to the front. This rollator type can experience backward slipping, particularly when used by frail older adults, as the force patterns are closer to violating this condition (yellow) before the backward tipping one (blue).

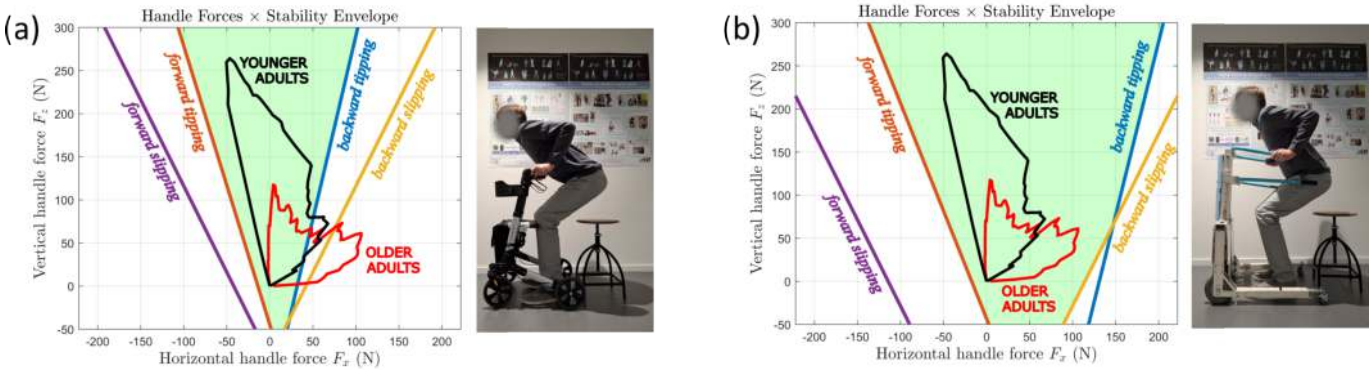

Figure 2: (a) Stability Envelope (shaded green) for a conventional rollator (a) and a robotic rollator (b) against 80^{th}-percentile curves of measured handle support forces for younger (black) and frail older (red) adults, with stability conditions in colors.

4 DISCUSSION AND CONCLUSIONS

The results evidence that the current design of conventional rollators, which focus on minimization of mass and overall dimensions, is detrimental to stability during standing up assistance. Importantly, the risk of rollators tipping over or slipping backward was shown to be greater for frail older adults in spite of the lower handle force magnitudes, as this population relies on a support strategy based on horizontally pulling the handles, rather than pushing them downward as observed in younger adults. These findings evidence that the effective and safe use of rollators and walkers to support standing up, particularly for the target population of frail older adults, requires larger BoS and would benefit from the stabilizing effect of a larger mass, whenever possible. When BoS and mass are larger, as in the tested robotic rollator, backward slipping can occur before tipping. This can be addressed, for instance, by effective braking systems, and wheels with higher grip. These conclusions extend to similar mobility assistive devices such as walkers and standing aids.

REFERENCES

[1] V. Komisar et al., "Circumstances of falls during sit-to-stand transfers in older people: a cohort study of video-captured falls in long-term care". *Archives of Physical Medicine and Rehabilitation*, vol. 104, pp. 533-540, 2023.

[2] B. A. West et al., "Assistive device use and mobility-related factors among adults aged ≥ 65 years". *Journal of Safety Research*, vol. 55, pp. 547-150, 2015.

[3] M. Ackermann et al., "Active robotic assistance for standing and sitting: experimental evaluation of handle trajectories". *Journal of NeuroEngineering and Rehabilitation*, 2026. (www.doi.org/10.1186/s12984-025-01849-9)

SHAPE EVALUATION OF TOOTH PROFILE SECTIONS BOUNDED BY THE LEFT AND RIGHT TOOTH PROFILE DEVIATIONS OF INJECTION-MOLDED PLASTIC GEARS

Yuichiro Seo[1], Daisuke Iba[1], Jing Chong Low[1], Shu Takata[1],Naoki Yamashita[1]

[1] Kyoto Institute of Technology, 1 hashigami-cho, Matsugasaki, Sakyo-ku, Kyoto 606-8585, Japan
{ seoyuu1210@gmail.com ;iba@kit.ac.jp ; jingchong1998@gmail.com ;shukun0617@gmail.com ;naoki@kit.ac.jp}

1. INTRODUCTION

In injection molding, high-temperature molten plastic is injected into a mold, and the product is formed through shrinkage during the cooling and solidification process. However, this shrinkage behavior induces characteristic molding errors on the tooth surface geometry. Conventional gear accuracy evaluation methods have difficulty assessing such shrinkage-induced tooth surface deformations, which strongly depend on the characteristics of injection molds, from a comprehensive perspective. [1] Therefore, this study proposes a novel evaluation method that synthesizes the left and right tooth profile deviations of injection-molded gears, enabling simple and global assessment of pointed tooth tips and tilted tooth tips across the entire gear.

2. EVALUATION METHOD

This study proposes an evaluation method for pointed tooth tips and tilted tooth tips of injection-molded gears using the left and right tooth profile deviation diagrams. Specifically, the left and right tooth profile deviation curves are added and subtracted, and the resulting slopes are evaluated using a first-order approximation.

2.1. DC Component Removal

Firstly, the left and right tooth profiles are measured using a gear measuring machine. As in previous studies, the DC components are removed from the right and left tooth profile deviations, $\widehat{f_{\alpha \mathrm{R}_i}}(x)$, and $\widehat{f_{\alpha \mathrm{L}_i}}(x)$ using Eqs. (1) and (2). [2][3]

$$f_{\alpha \mathrm{R}_i}(x) = \widehat{f_{\alpha \mathrm{R}_i}}(x) - f_{\alpha \mathrm{R_DC}_i}(x) \quad (1)$$

$$f_{\alpha \mathrm{L}_i}(x) = \widehat{f_{\alpha \mathrm{L}_i}}(x) - f_{\alpha \mathrm{L_DC}_i}(x) \quad (2)$$

In this study, the tooth geometry is evaluated by synthesizing the left and right tooth profile deviations. However, the presence of a DC component makes the evaluation sensitive to pitch errors. Therefore, the DC component is removed to facilitate accurate detection of tooth deformation. In addition, the outermost 10% of the tooth tip and root regions, where the profile largely deviates from the involute geometry, are excluded from the analysis.

2.2. Evaluation Profile

Figure 1 shows the representative tooth profile patterns considered in this study. The measured right and left tooth profiles are indicated by red and blue lines, respectively. Figure 1(a) shows the ideal left and right tooth profiles, Fig. 1(b) shows the profiles with a pointed tooth tip, and Fig. 1(c) shows the profiles with a tilted tooth tip (tooth tilted to the right).

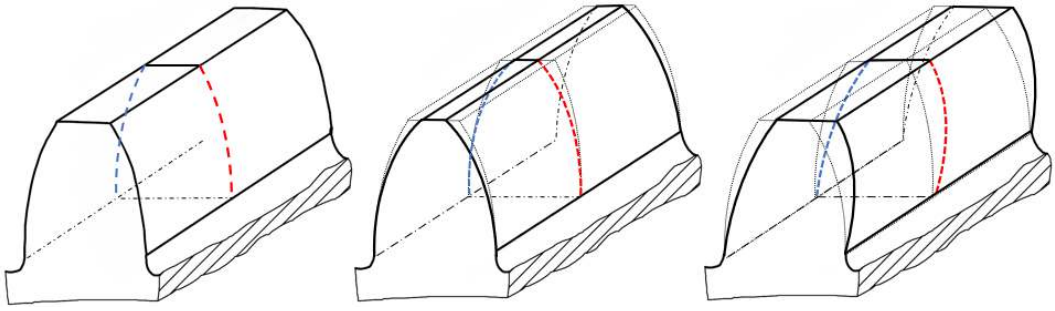

(a) Ideal tooth (b)Pointed tooth tip (c) Tilted tooth tip to the right

Fig.1 Tooth profile patterns investigated in this study

2.3. Evaluation Method for Pointed Tooth Tip

To evaluate tooth profiles with a pointed tooth tip, the information from the left and right tooth profile deviations is integrated. Specifically, the left and right tooth profile deviations after DC component removal are added. This synthesized tooth profile

deviation diagram is referred to as the pointed tooth tip evaluation diagram. Using Eq. (3), the pointed tooth tip evaluation diagram for the i-th tooth, $f_{\mathrm{Pointed}_i}(x)$, is obtained, where $f_{\alpha \mathrm{R}_i}(x)$ represents the right tooth profile deviation after DC component removal and $f_{\alpha \mathrm{L}_i}(x)$ represents the left tooth profile deviation after DC component removal. Here, x denotes the rolling distance and increases from the tooth root towards the tooth tip. When the slope of the pointed tooth tip evaluation diagram is negative, it indicates a pointed tooth tip as shown in Fig. 1(b). In contrast, a positive slope corresponds to a tooth tip that becomes thicker. The slope $\mathrm{G}_{\mathrm{Pointed}_i}(x)$ is a crucial parameter in this study. and is derived using a first-order approximation.

$$f_{\mathrm{Pointed}_i}(x) = \frac{f_{\alpha \mathrm{R}_i}(x) + f_{\alpha \mathrm{L}_i}(x)}{2} \tag{3}$$

2.4. Evaluation Method for Tilted Tooth Tip

To evaluate the degree of a tilted tooth tip, the information from the left and right tooth profile deviations is integrated. Specifically, the measured left and right tooth profile deviations after DC component removal are subtracted. This synthesized tooth profile deviation diagram is referred as the tilted tooth tip evaluation diagram. Using Eq. (4), the tilted tooth tip evaluation diagram for the i-th tooth, $f_{\mathrm{Tilted}_i}(x)$ is obtained. The notation is the same as that in the previous section. Similarly, the slope of the tilted tooth tip evaluation diagram is derived using a first-order approximation, yielding $\mathrm{G}_{\mathrm{Tilted}_i}(x)$

$$f_{\mathrm{Tilted}_i}(x) = \frac{f_{\alpha \mathrm{R}_i}(x) - f_{\alpha \mathrm{L}_i}(x)}{2} \tag{4}$$

3. GEAR SPECIFICATION

The gear evaluated in this study is a spur gear manufactured by injection molding with three gates. Table 1 shows the gear specification. Figure 2 shows the left and right tooth profile deviation curves of the measured gear, where the deviation curve of the i-th tooth is vertically offset by $i \times 10\mu\mathrm{m}$ to overlay the profiles of all teeth in a single plot. In Fig. 2, the blue and red curves represent the left and right tooth profile deviations, respectively.

Table 1 Gear Specification

Gear data	
Normal Module [mm]	0.75
Number of Teeth [-]	24
Normal Pressure Angle [deg.]	20
Helix Angle [deg.]	0
Addendum Modification Coefficient [-]	0
Face Width [mm]	2

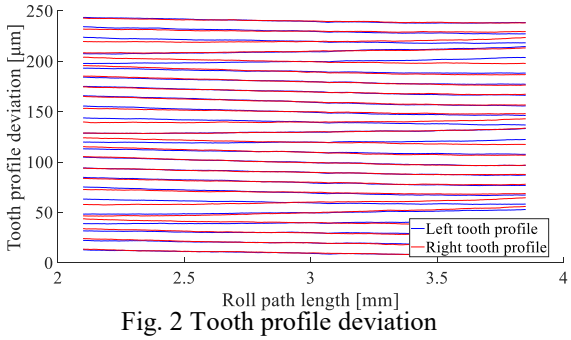

Fig. 2 Tooth profile deviation

4. RESULTS

Using the method described in the previous section, the slopes of the evaluation diagrams, $\mathrm{G}_{\mathrm{Pointed}_i}(x)$ and $\mathrm{G}_{\mathrm{Tilted}_i}(x)$, were calculated. The results are shown in Figs. 3(a) and 3(b). In Fig. 3, the vertical axis represents the slope values, and the horizontal axis represents the tooth number. These results indicate that the 5th, 13th, and 21st teeth located at the weld line, which corresponds to the region of the melt fronts meet of molten plastic flow, exhibit a thickened tooth tip profile, and the degree of tooth tilting varies from right to left across the gear. The validity of the evaluation method proposed in study was confirmed.

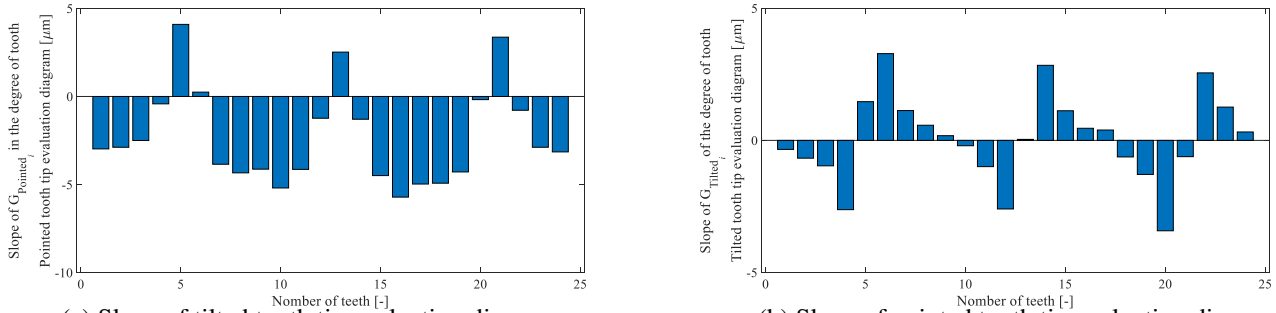

(a) Slope of tilted tooth tip evaluation diagram (b) Slope of pointed tooth tip evaluation diagram

Fig.3 Relationship between the proposed method's slope and tooth number

REFERENCES

[1] ISO 1328-1:2013, *Cylindrical gears—Flank tolerance classification—Part 1*, ISO, Geneva.

[2] SEO, Yuichiro, et al. *Shape evaluation of all transverse sections bounded by the left and right tooth helix deviations of injection-Molded plastic gears. Forschung im Ingenieurwesen*, 2025, 89.1: 133.

[3] TAKATA, Shu, et al. *Eigen analysis of graph laplacian derived from gear shape deviation networks. Forschung im Ingenieurwesen*, 2025, 89.1: 111.

SIMULATION AND VALIDATION OF THE TRANSMISSION ERROR AND MESHING STIFFNESS OF INTERNAL HELICAL GEARS WITH PROFILE MODIFICATION

Miguel Pleguezuelos[1], Miryam B. Sánchez[1], Andrés F. Hidalgo[1], José I. Pedrero[1], Alfonso Fuentes-Aznar[2]

[1] UNED, Departamento de Mecánica, Juan del Rosal 12, 28040 Madrid, Spain,
{mpleguezuelos@ind.uned.es, msanchez@ind.uned.es, af.hidalgo@ind.uned.es, jpedrero@ind.uned.es}

[2] Rochester Institute of Technology, Department of Mechanical Engineering, Kate Gleason College of Engineering, 76 Lomb Memorial Drive, 14623 Rochester, NY, USA, {afeme@rit.edu}

1. INTRODUCTION

Load sharing between tooth pairs in simultaneous contact, its distribution along the contact line over the tooth face, the mesh stiffness, and the transmission error of internal helical gears have been studied in several previous works, but the required solving techniques based on the Finite Element Method (FEM) remain computationally expensive and time-consuming. Comprehensive optimization studies and generalized conclusions require extensive sensitivity analyses that take into account a broad range of design parameters. Consequently, an approximate analytical method that provides preliminary results for validation against a small number of FEM simulations would offer a computationally efficient alternative.

In this work, an analytical model has been developed for the simulation of the time-varying mesh stiffness (TVMS), the quasi-static transmission error (QSTE), and load sharing ratio (LSR) of internal helical gear transmissions. It is based on the hypothesis of minimum elastic potential energy and is a generalization of a similar model for internal spur gears previously developed [1]. The proposed analytical model is validated against results obtained from the Finite Element Method (FEM).

2. ANALYTICAL MODEL

The curve of single mesh stiffness (SMS) $K_M(\xi)$ of an internal spur tooth-pair is shown in Fig. 1-left [1]. ξ is the contact point parameter, as described in [1]. This curve is valid for the SMS of each transverse section of a helical pair considering a differential face width $\mathrm{d}b$, thus:

$$\mathrm{d}K_M(\xi) = K_M(\xi)\,\mathrm{d}b/b = K_M(\xi)\,\mathrm{d}\xi/\varepsilon_\beta \tag{1}$$

where b is the face width and ε_β is the axial contact ratio. The SMS of the helical tooth-pair will be the integral of $\mathrm{d}K_M(\xi)$ along the instantaneous contact line over the tooth-pair:

$$K_M(\xi_0) = \int_{\xi_{inf}(\xi_0)}^{\xi_{sup}(\xi_0)} \mathrm{d}K_M(\xi) = \frac{1}{\varepsilon_\beta}\int_{\xi_{inf}(\xi_0)}^{\xi_{sup}(\xi_0)} K_M(\xi)\mathrm{d}\xi \tag{2}$$

which will be a function of the mesh position parameter ξ_0 [1]. Fig. 1(center) shows the SMS of a helical tooth-pair whereas Fig. 1(right) shows the contact map, which is defined by the limits of the contact line (ξ_{inf}, ξ_{sup}) at any mesh position[1]. By following the same procedure as described in [1], the following expressions for the QSTE $\delta(\xi_0)$, TVMS $K_T(\xi_0)$, and LSR $R(\xi_0)$ are obtained:

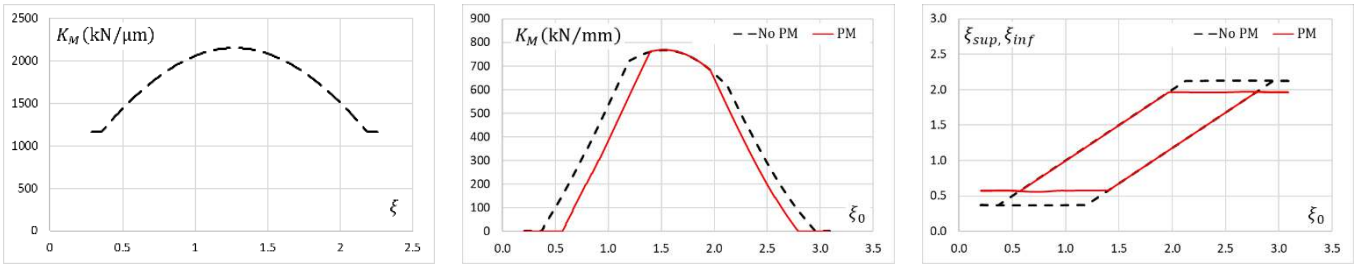

Figure 1. Plots of the SMS of the transverse section (left), SMS of the helical tooth-pair (center), and contact map (right); with (solid line) and without (dashed line) profile modification.

[1] $\xi_{inf}(\xi_0)$ and $\xi_{sup}(\xi_0)$ depend on the load $F_T R(\xi_0)$ for which an iterative calculation is required.

$$\delta(\xi_0) = \frac{F_T + \sum_j \int_{\xi_{inf}(\xi_0+j)}^{\xi_{sup}(\xi_0+j)} dK_M(\xi)\left(\delta_G(\xi) + \delta_R(\xi)\right)}{\sum_j \int_{\xi_{inf}(\xi_0+j)}^{\xi_{sup}(\xi_0+j)} dK_M(\xi)}$$

$$K_T(\xi_0) = \frac{F_T}{\delta_r(\xi_0)} \tag{2}$$

$$R(\xi_0) = \frac{1}{F_T}\int_{\xi_{inf}(\xi_0)}^{\xi_{sup}(\xi_0)} \mathrm{d}K_M(\xi)\left(\delta(\xi_0) - \delta_G(\xi) - \delta_R(\xi)\right)$$

where F_T is the transmitted load, and $\delta_G(\xi)$ and $\delta_R(\xi)$ are the approach distance and the depth of profile modification, as described in [1], respectively. Their plots are shown on Fig. 2.

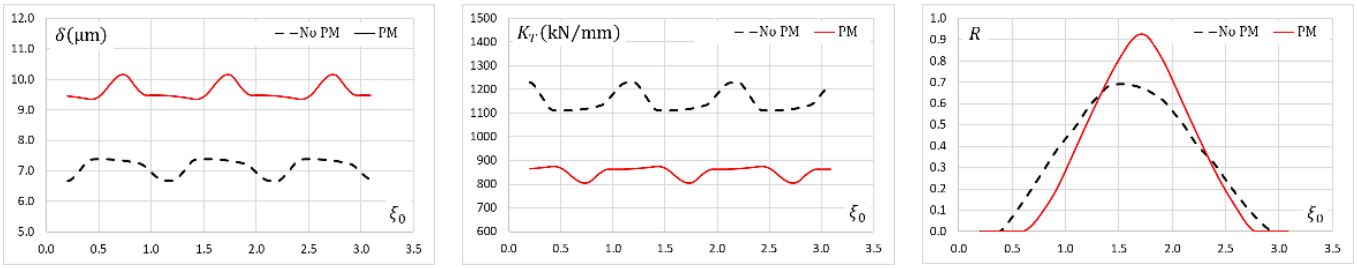

Figure 2. QSTE function (left), TVMS (center), and LSR (right) of helical gear with (solid line) and without (dashed line) profile modification.

3. FEM VALIDATION

The QSTE function has been assessed from the tooth deflections and deformations obtained from a Finite Element Analysis and compared with the QSTE function provided by the analytical method presented. A parabolic profile modification consisting of a parabolic tip relief of 15 μm depth and 1 mm length has been applied to all teeth. The obtained results are shown in Fig. 3.

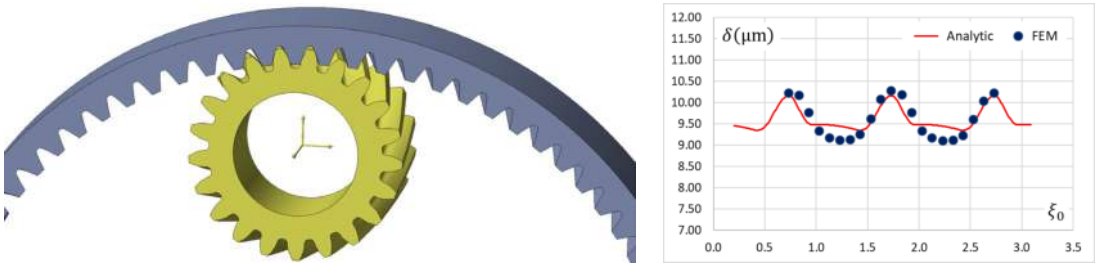

Figure 3. Results of the Finite Element Analysis of helical gear with parabolic profile modification: solid model (left) and comparison between analytic and FEM QSTE (right).

The analytical results show good agreement with the FEM data, maintaining a maximum error of 0.3 μm. This consistency in both trend and magnitude validates the analytical approach for initial engineering estimates.

4. RESULTS AND DISCUSSION

The applied profile modification is used to avoid the mesh-in impact induced by the tooth deflections due to the load, which is a source of dynamic load, noise and vibrations. However, profile modification influences the QSTE function (Fig. 2-left). Specifically, it increases the average value of the QSTE function. However, the critical parameter is its time variation, which induces accelerations and decelerations, and, consequently, dynamic loads. Dynamic loads are related to the peak-to-peak amplitude of the transmission error function (PPTE). For the helical gear considered in Fig. 2, the profile modification increases the average transmission error from 7 μm to 9.5 μm, but the PPTE remains unchanged, around 0.75 μm. It should be noted that a depth of modification of 15 μm is relatively large for this gear. A depth equal to the maximum QSTE without profile modification (7.5 μm, Fig. 2-left) is enough to avoid mesh-in impact. For a depth of 7.5 μm the PPTE decreases to 0.7 μm.

ACKNOWLEDGMENTS

The authors acknowledge the support of the Spanish Council for Scientific and Technological Research for project PID2022-142632OB-I00.

REFERENCES

[1] J.I. Pedrero, M.B. Sánchez, and M. Pleguezuelos, “Analytical model of meshing stiffness, load sharing, and transmission error for internal spur gears with profile modification”, *Mechanism and Machine Theory*, 197, 105650, 2024.

MECHANICAL DEVELOPMENT OF AN AUTOMATIC EQUIPMENT FOR BIOPLASTIC FILM TESTING

David E.C. Pinto[1,2], Raul D.S.G. Campilho[1,2], José C.I. Barbosa[2], Filipe M.F.M. Lopes[2], Francisco J.G. Silva[1,2], David J.P. Almeida[1], André F.V. Pedroso[1]

[1] CIDEM, ISEP – School of Engineering, Polytechnic of Porto, R. Dr. António Bernardino de Almeida, 431, 4200-072 Porto, Portugal, [afvpe@isep.ipp.pt]

[2] INEGI – Pólo FEUP, Rua Dr. Roberto Frias, 400, 4200-465 Porto, Portugal

1. INTRODUCTION

Plastics are an essential part of modern life and are used in a wide variety of applications and industries. In the packaging industry they have become dominant, and the trend is for their use to continue to increase [1]. However, their disposable nature means that they are abandoned in the environment, leading to a series of harmful environmental consequences [2]. To mitigate this problem, the Sustainable Plastics project, financed by European funds, has developed compounds incorporating biodegradable polymeric materials, which are intended to replace conventional plastics and be inserted into existing production chains. This work aims to design an equipment to test the hot knife cutting and welding process in these compounds, identified as the greatest technical difficulty in incorporating them into the infrastructure used to produce fruit and vegetable bags typically found in supermarkets. This equipment will be developed following the Design Science Research (DSR) methodology [3] and should be highly configurable, capable of recreating conditions in a real production environment and working with the rolls of biodegradable compound supplied for testing, having unwinding and winding functions. The entire mechanical design of the equipment was developed and the main electrical and control components that make it up were selected. All the objectives initially proposed for this work were met.

2. RESULTS AND DISCUSSION

The work carried out led to the equipment shown in Figure 1 and Figure 2. The equipment specifications are as follows:

- Dimensions – 2105×1203×1690 mm^3;
- Weight – 450 kg;
- Maximum processing speed – 100 m/min;
- Tension control zones:
  - Processing;
  - Winding.
- Film rolls compatibility:
  - $\Phi < 200$ mm;
  - Width < 430 mm.
- Maximum film pull force – 125 N;
- Maximum cutting and sealing temperature – 250 °C.

The developed proof-of-concept is divided in a cutting and welding module, winding module, and electrical and control module. The figures also show the path intended for the film. To operate the equipment, the film must be put in the presented pathway. It must be attached to cardboard cores with tape in the exit roller. Both the entry and exit rollers must be then pressurized with compressed air to lock the relative rotation of the rollers and cardboard cores. The cutting and welding module must be then put in its rest mode, using the coupling mechanism. Then, the user must turn on the equipment and use the human-machine interface (HMI) included to set the intended parameters for the process, namely target temperature of the knife, linear speed of the web, and web tension in both the processing and winding zones. When the temperature of the knife reaches the intended target temperature, the knife should be put in its operation mode, and the process should be started using the HMI. When the entry roll is empty, the process is finished, and the exit rolls can be removed of the exit roller by depressurizing it.

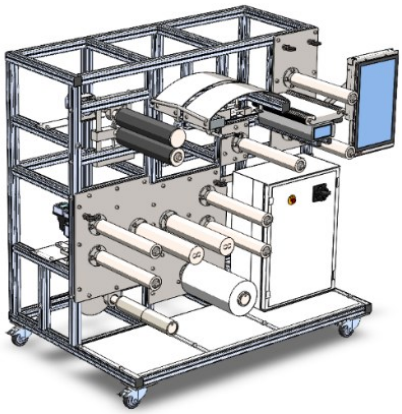

Figure 1. Equipment designed and intended path for the film.

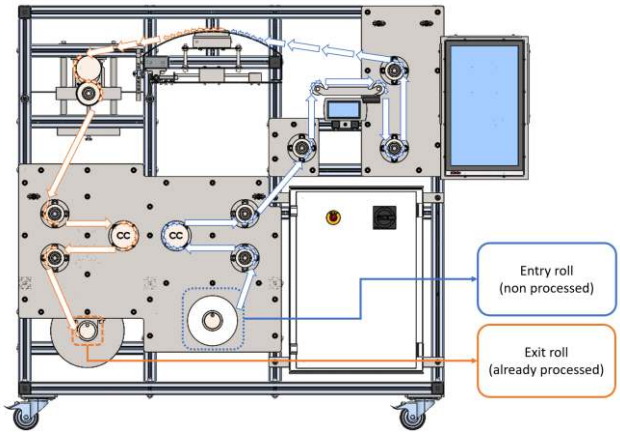

Figure 2. Frontal view of the equipment.

This study successfully developed a test and demonstration machine for cutting and welding polymer films used in the production of fruit and vegetable bags commonly found in supermarkets. The need for this equipment arose from the challenges associated with integrating new biodegradable polymeric compounds into existing production lines, particularly in the cutting and welding stages. To address these challenges, a highly configurable system was designed, allowing process parameters such as hot knife temperature, film speed, and tension to be adjusted for testing different materials. The machine met all initially defined objectives, including a roll-to-roll system, a heated cutting knife, the ability to replicate real production conditions, and high parameterization capacity. However, certain aspects, such as budget constraints, were not evaluated due to the custom nature of the components. Additionally, the control logic and user interface (HMI) were not implemented, as the focus was primarily on the mechanical design. The developed equipment is a valuable tool to promote the use of biodegradable polymer films in industrial applications.

Keywords: Biodegradable polymer films, Hot knife cutting and welding, Roll-to-roll testing equipment, Mechanical design and prototyping, Design Science Research methodology, Sustainable packaging machinery

References:

1. Mifsud, S., P. Refalo, and A. Rochman. *Biodegradable polymers for cosmetic packaging: A technical and life cycle perspective*. in *Mater. Res. Proc*. 2023.
2. Voznyakovskii, A., D. Rashidov, S.K. Tabarov, I. Shugalei, F.K. Sodikov, S.P. Ismatov, A.Y. Neverovskaya, and A. Vozniakovskii, *Modern Approaches to Disposal of Polymers for Household Use.* Russian Journal of General Chemistry, 2024. **94**(13): p. 3554-3560.
3. Ramalho, P., R. Campilho, F. Silva, A. Pedroso, and R. Sales-Contini, *Productivity improvement of control cable manufacturing machine for the automotive industry.* Mechanics Based Design of Structures and Machines, 2024: p. 1-24.

INTRODUCTION TO DISCRETE FLEXIBLE MULTIBODY MODELLING APPROACH FOR BALL BEARINGS WITH DEFORMABLE RINGS

Roberto Guida[1], Andrea De Martin[1]

[1] Politecnico di Torino, Corso Duca degli Abruzzi, 24, Italy, {roberto.guida@polito.it; andrea.demartin@polito.it}

1. INTRODUCTION

Bearings are often modeled as rigid elements, but thin-walled or thin-ring bearings, like those in harmonic drives, experience elastic deformation that affects geometry, load distribution, stress, wear, fatigue, stiffness, resonance, and positioning accuracy. Furthermore nonlinear contact and friction effects can cause hysteresis and vibration, which rigid models cannot capture. Harmonic drives [1] are particular examples which rely on controlled deformation of a flexible gear via a bearing-supported wave generator, so accurate prediction of kinematic errors, torque ripple, hysteresis, vibration, and fatigue requires modeling bearing flexibility and contact mechanics. Classical models (lumped-parameter, stiffness-matrix, Hertzian contact, elastohydrodynamic lubrication) are computationally efficient but inadequate for highly deformable configurations. Instead advanced numerical and FEM models improve predictions but are costly and often limited in dynamics or geometry. Modeling deformable bearings in harmonic drives remains challenging due to multiscale coupling of flexspline elasticity, contact, friction, and nonlinear dynamics. To address this, a Discrete Flexible Multibody bearing model is proposed, representing bearing rings as interconnected bodies to efficiently simulate elastic deformation, nonlinear stiffness, contact, and dynamic interactions within a multibody framework.

2. MODEL OVERVIEW

The bearing is modeled using a Discrete Flexible Multibody (DFM) formulation [2] in which the outer ring is discretized into flexible sectors, while the inner ring, rolling elements, and cage are represented as interacting bodies governed by linear and nonlinear contact laws. This approach captures rigid-flexible coupling, load distribution, contact compliance, and low-frequency dynamic behavior at substantially lower computational cost than full three-dimensional finite element simulations [3].

The inner ring geometry is defined as an ideal ellipse obtained by statically modifying its undeformed radius with a prescribed deformation amplitude. This elliptical profile rotates at the angular velocity of the wave generator. The combined effect of rotation and geometric eccentricity generates normal and tangential contact forces that are transmitted through the rolling elements. The balls are modeled both as dynamic bodies and as compliant force-transmitting elements. These interactions induce deformation in the outer ring, which is represented as a set of dynamically coupled sectors interconnected by restoring forces that maintain structural continuity. Contact interfaces are described using spring-damper elements (Fig. 1) to account for energy dissipation and to suppress spurious high-frequency oscillations. The contact model parameters were derived from published literature data and established theoretical descriptions of the system's dynamic behavior.

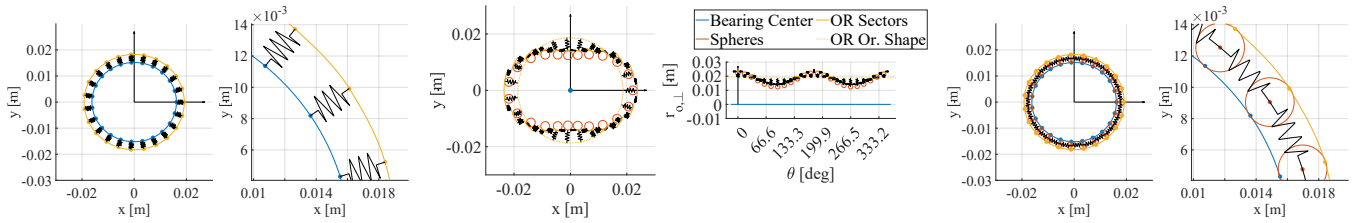

Figure 1. Bearing spring systems modeling for: a) hertzian bearing forces, b) sectors homogenization and anchoring forces, and c) cage constraint forces.

Once the governing equations of motion are solved and the trajectories of the ball centers are obtained, the corresponding contact locations on the inner and outer rings are determined through an elliptical correction procedure. This correction accounts for the instantaneous ring geometry and local contact-induced deformations. Its periodicity depends on both the eccentricity of the ellipse and the radius of the rolling elements. The force transmitted through each ball is evaluated using Hertzian contact theory, incorporating the effective radii of curvature of the contacting bodies. The angular positions and deflections of the outer-ring sectors are then determined from the balance between the discrete contact forces and the homogenizing restoring forces that drive the structure toward its undeformed configuration. The cage forces, responsible for maintaining ball spacing, are also included in the formulation.

Finally, after identifying the contact points along the outer ring, the global deformation field is obtained by modeling each segment between adjacent contacts as a supported Euler-Bernoulli beam. By enforcing appropriate boundary conditions and distributed loading, the complete deformation of the outer ring is reconstructed.

3. PRELIMINARY RESULTS

Prior to analyzing the dynamic response, the static equilibrium of the bearing-cam assembly is established, as it defines the baseline load distribution and provides the initial conditions for time-dependent simulations. The static analysis considers rolling-element compression and radial dilation of the outer-ring sectors, which together characterize the equilibrium state resulting from the imposed elliptical inner-race geometry, the applied preload, and the structural compliance of the outer ring. Under static conditions, rolling-element compression varies with angular position according to the eccentricity of the ellipse, attaining its maximum along the major axis and its minimum along the minor axis, while remaining strictly positive due to preload. The outer-ring dilation exhibits the same angular periodicity, with peak radial expansion aligned with the major semi-axis. Although both quantities share a similar spatial distribution, their force-displacement responses differ because of the distinct stiffness contributions of the ring structure and the nonlinear Hertzian contact relationship governing ball-race interactions. Static equilibrium is satisfied when the contact forces transmitted through the rolling elements are balanced locally by the elastic reactions of the discretized outer-ring sectors at every angular coordinate, yielding a mechanically consistent reference configuration for subsequent dynamic analysis.

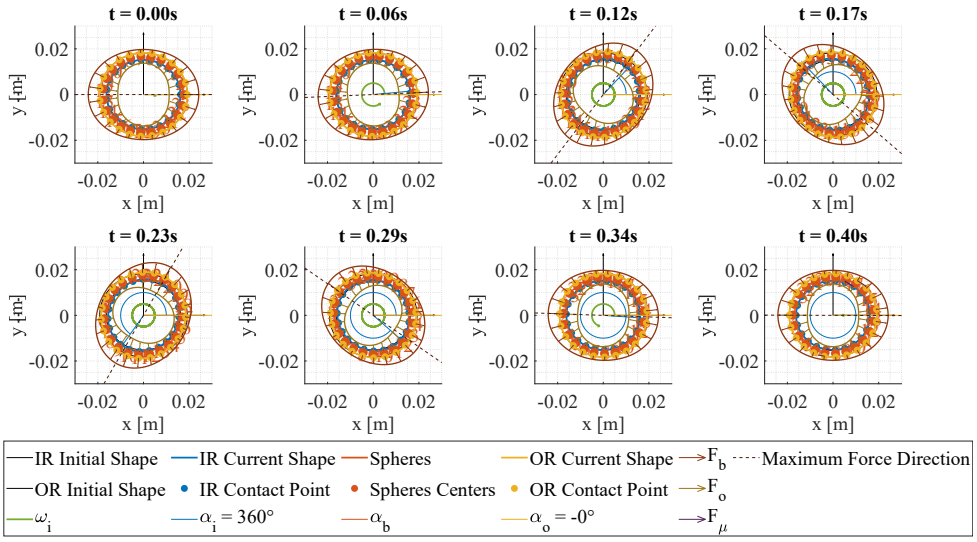

Figure 2. Representation of the dynamic configurations of the deformable bearing keyed on the rotating elliptical cam.

The dynamic deformation of the compliant bearing mounted on the rotating elliptical cam is illustrated in the time sequence shown in Fig. 2. Each frame presents the instantaneous configuration of the inner and outer rings, together with the rolling elements and associated contact points, thereby visualizing the evolution of the system under rotation. Relative to the undeformed reference state, the outer ring exhibits a nonuniform, time-dependent radial response driven by the continuous migration of the load zone. While the inner ring maintains the prescribed rotating elliptical profile, the outer ring deformation reflects the circumferential progression of the loaded region, with individual sectors alternately expanding and relaxing.

4. CONCLUSIONS

The paper presents a DFM model for bearings with flexible rings, capturing ring deformation, rolling-element dynamics, and nonlinear contact efficiently. It reproduces load redistribution, migrating contact zones, and coupled motion, bridging simple analytical models and full FEM simulations. The approach enables system-level studies, design optimization, and future extensions for nonlinear effects, wear, and digital-twin-based condition monitoring.

ACKNOWLEDGMENTS

PRIN2022 1265/2023 "Multi-phase fault tolerant MW range generation systems for hybrid-electric aircrafts" funded by the Italian Ministry of University and Research (MIUR).

REFERENCES

[1] H. Dong, K.-L. Ting and D. Wang, “Kinematic fundamentals of planar harmonic drives”. *Journal of Mechanical Design*, 133(1), 2011.

[2] A.A. Shabana, “Flexible multibody dynamics: review of past and recent developments”. *Multibody System Dynamics*, 1(2), 189-222, 1997.

[3] E. Azzuni and S. Guzey, “Behavior of thin elastic circular rings with large deformations under nonuniform loads”. *Journal of Pressure Vessel Technology*, 141(1), 011201, 2019.

DESIGN AND PROTOTYPING OF A NEW COLLABORATIVE HAND CART FOR MOVING HEAVY PAYLOADS IN FACTORIES

Tan Sy Nguyen[1], Olivier Couillard[2]

[1] Université du Québec à Rimouski, Rimouski, Québec, Canada, {tansy_nguyen@uqar.ca}
[2] Université de Sherbrooke, Sherbrooke, Québec, Canada, {olivier.couillard@USherbrooke.ca}

1 INTRODUCTION

In modern industrial factories, the material handling tasks to move heavy components across the floor remain a significant bottleneck. While automated systems like conveyors and robotic arms are common, they lack the flexibility required for dynamic, non-linear workflows. Conversely, traditional manual hand carts often subject workers to excessive physical strain, increasing the risk of injuries and reducing overall operational efficiency. This study proposes a new collaborative hand cart, which aims to bridge the gap between manual labor and full automation. By integrating ergonomic design principles with collaborative features, this system is specifically tailored to assist operators in transporting heavy payloads with greater ease and safety.

2 MECHANICAL DESIGN

The mechanical design of this cart, illustrated in Figure 1, is divided into two primary subsystems: the mobile platform and the handle mechanism. The platform is a mobile robot equipped with four omnidirectional wheels that enable seamless, holonomic movement in any direction. The handle mechanism is designed to detect user-applied forces for intuitive human interaction. It features a handle that captures push-pull actions and utilizes a spring-return system to restore its neutral position. Additionally, a spring-loaded parallelogram structure is integrated to detect rotational intent, which similarly centers itself once the interaction ends.

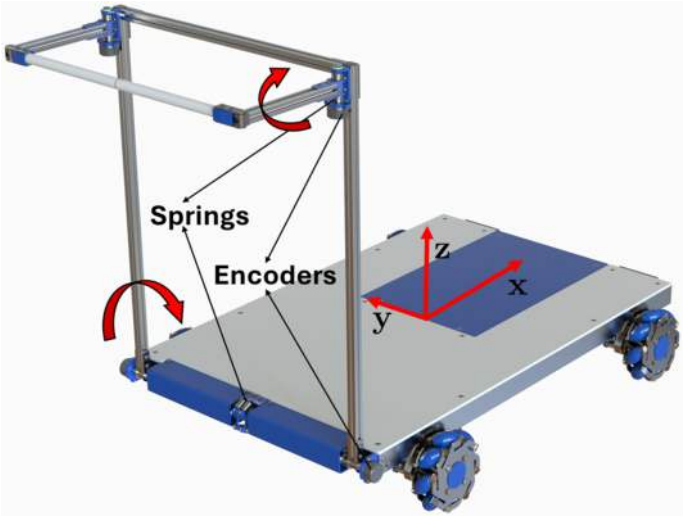

Figure 1: Mechanical design of the proposed hand cart.

3 PROPOSED CONTROL METHOD

The authors propose a hierarchical architecture to control this collaborative device, as illustrated in the block diagram in Figure 2. The high-level controller consists of three primary components. First, it measures the two deflection angles of the handle, (α, β), relative to their initial positions. Given the spring stiffness, the interaction force (along the x-axis) and torque (about the z-axis) are estimated as:

$$\boldsymbol{f}_h = \boldsymbol{K} \begin{bmatrix} \alpha \\ \beta \end{bmatrix} \tag{1}$$

in which $\boldsymbol{K} = diag([k_1, k_2])$ represents the stiffness of the springs attached to the two revolute joints. Simultaneously, an admittance model for free motion is applied, following the approach in [1] to determine the desired velocity vector in the $Oxyz$ reference frame $\boldsymbol{v}_d = [v_x, \omega_z]^T$:

$$\boldsymbol{f}_h = \boldsymbol{M}_v \dot{\boldsymbol{v}}_d + \boldsymbol{C}_v \boldsymbol{v}_d. \tag{2}$$

In this study, the authors focus on two specific degrees of freedom: translation along the x-axis v_x and rotation about the z-axis ω_z. $\boldsymbol{M}_v = diag([m_x, I_z]), \boldsymbol{C}_v = diag([c_x, c_z])$ are respectively the virtual mass and damping in the corresponding directions. In the discrete-time domain, the desired velocity for the mobile platform is calculated as:

$$\boldsymbol{v}_d(k) = \boldsymbol{M}_v^{-1} \left[\boldsymbol{f}_h(k) - \boldsymbol{C}_v \boldsymbol{v}_d(k-1)\right] T_s + \boldsymbol{v}_d(k-1) \tag{3}$$

where T_s denotes the sampling time. Finally, similar to the approach in [2], the robot's kinematic model is applied to determine the desired angular velocities for four wheels, $\boldsymbol{\Omega}_d = [\omega_{1d}, \omega_{2d}, \omega_{3d}, \omega_{4d}]^T$, based on the Jacobian matrix $\boldsymbol{J}$:

$$\boldsymbol{\Omega}_d = \boldsymbol{J} \boldsymbol{v}_d. \tag{4}$$

The low-level controller manages the angular velocity of each omnidirectional wheel using four independent PI compensators:

$$\tau_i = k_p \triangle\omega_i + k_i \int \triangle\omega_i \quad (i = 1, 2, 3, 4). \tag{5}$$

This controller computes the motor torques $\boldsymbol{\tau} = [\tau_1, \tau_2, \tau_3, \tau_4]^T$ required to minimize velocity error $\triangle\omega_i$. By doing so, the cart maintains the desired speed and ensures consistent performance regardless of varying payloads or floor surface conditions.

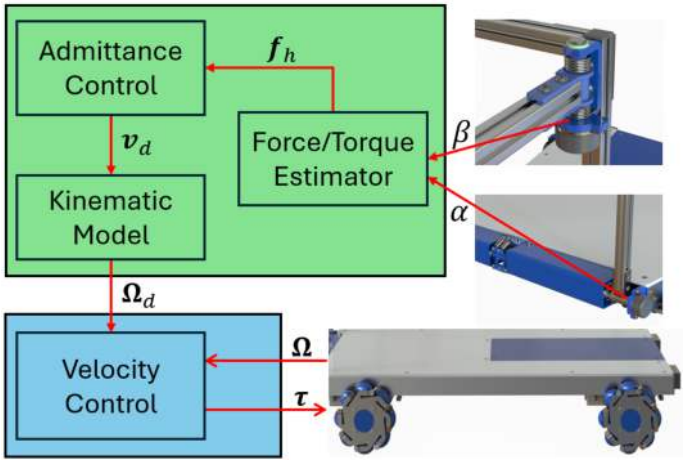

Figure 2: Block diagram of the proposed controller.

4 EXPECTED RESULTS

The mechanical design and the proposed control method are expected to provide intuitive interaction for the human operator. On one hand, it allows the operator to flexibly maneuver the cart forward, backward, and in rotation. On the other hand, the virtual mass and damping are defined as tunable system parameters. This allows for personalization, where control sets can be adjusted to match the strength or preference of each individual operator.

While this design focuses on the core interaction and transport tasks, additional safety features, such as an emergency brake, must be integrated for real-world deployment. Furthermore, omnidirectional wheels perform optimally on clean, level surfaces and may encounter traction issues on dusty floors. Alternative wheel designs or specialized tread materials may need to be considered to mitigate these environmental challenges.

REFERENCES

[1] A. Lecours, B. Mayer-St-Onge and C. Gosselin, *"Variable admittance control of a four-degree-of-freedom intelligent assist device"*, 2012 IEEE International Conference on Robotics and Automation, Saint Paul, MN, USA, 2012, pp. 3903-3908.

[2] P. Muir and C. Neuman, *"Kinematic modeling for feedback control of an omnidirectional wheeled mobile robot"*, 1987 IEEE International Conference on Robotics and Automation, Raleigh, NC, USA, 1987, pp. 1772-1778.

TOLERANCE ANALYSIS OF MECHANISMS WITH UNILATERAL CONSTRAINTS

Wanting Wang[1], Zhihua Zhao[1]

[1] School of Aerospace Engineering, Tsinghua University, Beijing, China, {zhaozh@tsinghua.edu.cn}

1 INTRODUCTION

Tolerance analysis of multibody systems evaluates how part-level design variable tolerances and joint clearances propagate to assembly-level tolerances, and is a fundamental technique in product design. However, prior research has primarily focused on systems with bilateral constraints [1, 2], while systems involving unilateral constraints remain underexplored. Here, we propose a worst-case tolerance analysis method for multibody systems with unilateral constraints. The method utilizes a linear programming algorithm derived from first-order approximate constraint equations with inequalities to solve the optimization problem. To verify the method, we conduct a tolerance analysis of a biological system: a bird forelimb with ligaments. The results highlight the critical role of ligaments in enhancing the robustness of biological tissues. Furthermore, we show that the capacity of unilateral constraints to improve system reliability depends on the design variables, such as ligament attachment location, which can be effectively modeled using our method. Ultimately, this approach provides a new pathway for improving product quality and reliability through the strategic design of unilateral constraints.

2 METHODOLOGY

2.1 The worst-case tolerance analysis method

The pipeline for the worst-case tolerance analysis is illustrated as a flowchart in Figure 1. The constraint equations $\mathbf{C}(\mathbf{l},\mathbf{q}) = \mathbf{0}$ and inequalities $\mathbf{D}(\mathbf{l},\mathbf{q}) \leq \mathbf{0}$ must be established prior to performing the tolerance analysis. These inequalities account for the effects of unilateral constraints on the system. The design variables $\mathbf{l}$ comprises linearly independent variables representing the lengths of the rods and strings, while the generalized coordinates $\mathbf{q}$ describe the global configuration. Finally, tolerance analysis aims to reveal the relation between the parameter tolerances $\delta\mathbf{l}$ and the assembly tolerances $f(\delta\mathbf{q})$.

The pipeline consists of four steps. First, list the constraint equations and inequalities considering the existence of the tolerances. In general, the constraint equations and inequalities are nonlinear. Second, find the linear approximation to the functions by the first order Taylor expansion. The linearization gives the linear approximation of the relation between the parameter tolerances $\delta\mathbf{l}$ and configuration tolerances $\delta\mathbf{q}$. The third and forth part combine linear and non-linear optimization to calculate the worst-case bounds of the assembly tolerance.

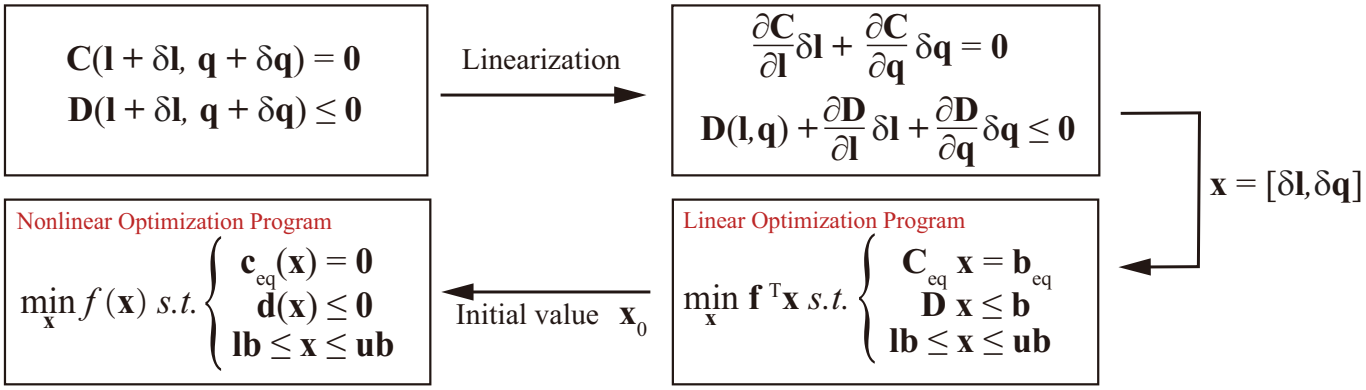

Figure 1: Flowchart of the worst-case tolerance analysis method.

2.2 Typical system with unilateral constraints: bird forelimb

Bird forelimb consists of humerus, ulna, radius metacarpal and digits. A prominent ligament begins at the craniolateral aspect of the humerus(shoulder joint) and ends at the ventral aspect of the digit(wrist joint) over elbow joint [3]. Here the bird forelimb is modeled as a planar linkage mechanism with string.

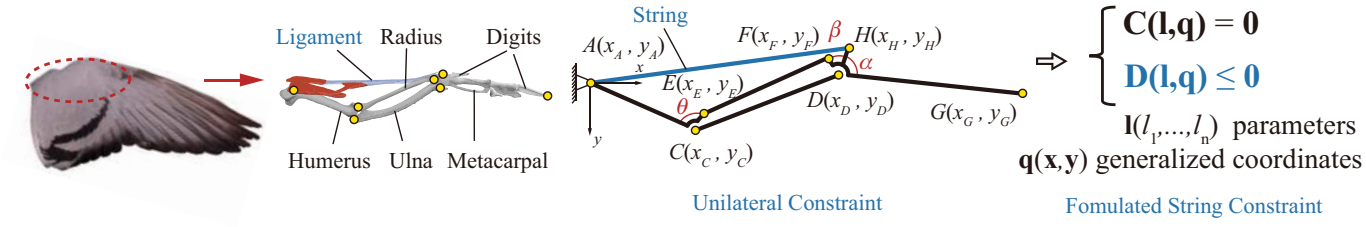

Figure 2: Overview of the forelimb, anatomy and simplified model of rock pigeon (*Columba livia*). Right limb, dorsal view.

3 RESULT

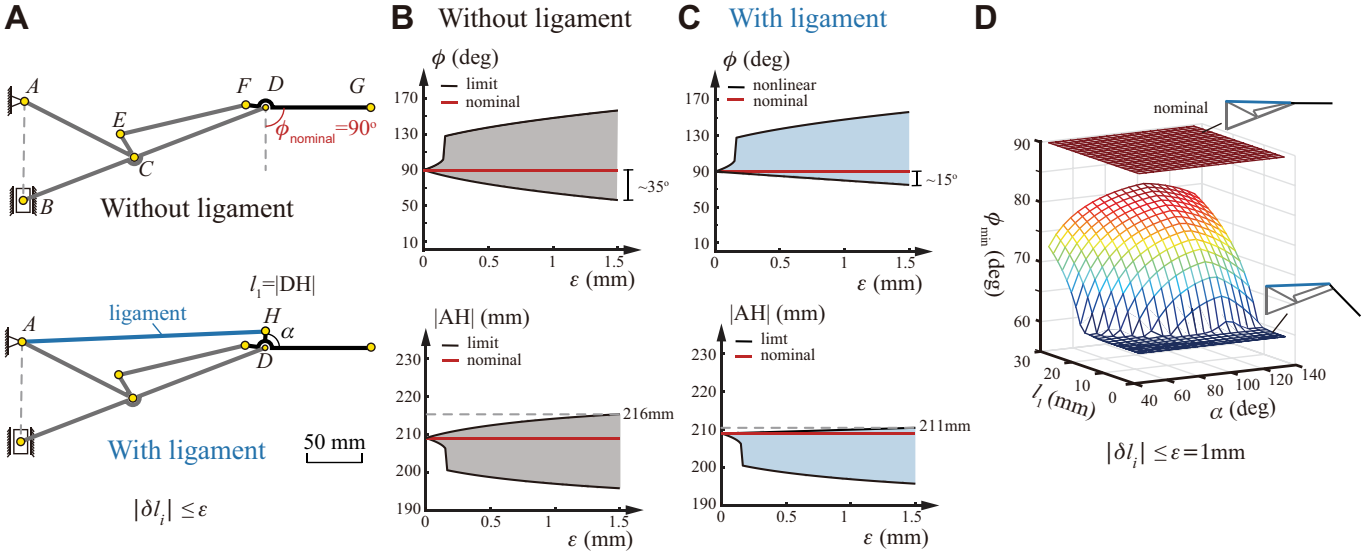

Figure 3: Mechanism of ligaments enhancing the structural reliability of biological tissue. (**A**) Models of the nominal extension configuration of bird forelimb. (**B**,**C**) Effect of ligament presence on wing extension range. (**D**) Influence of attachment location (point H) on the lower bound of the extension angle ϕ.

When the lengths of the wing skeletal segments (l_i) deviate from their nominal values due to biological variability (represented by the tolerance ε, $|\delta l_i| \leq \varepsilon$), the resulting wing extension angle ϕ also deviates from its nominal value and varies within a bounded range. We aim to investigate whether the presence of a ligament effectively narrows the variability range ($\phi - \phi_{\text{nominal}}$), thereby enhancing the structural reliability of the biological tissue. In addition, we investigate how the ligament attachment location (point H, parameterized by l_1 and α) influence the lower bound of the extension angle.

A worst-case tolerance analysis is performed on a bird forelimb model. Comparing Figure 3 (B), (C) reveals that the unilateral constraint imposed by the ligament effectively narrows the fluctuation range of ϕ by shifting its lower bound $\phi_{\min}$ upward. The mechanism is further elucidated by the fact that the ligament acts as a physical tether, effectively limiting the maximum distance between points A and H. Furthermore, the proposed method quantifies how unilateral constraint design parameters affect assembly tolerances. Taking the ligament attachment location point H (parameterized by l_1 and α) as an example, we evaluate its impact on $\phi_{\min}$. As shown in Figure 3 (D), an increase in l_1 shifting $\phi_{\min}$, while the optimal limiting effect is achieved when $\alpha \approx 90°$.

According to the result, we demonstrate the significance of ligaments for enhancing the reliability of biological tissues. The attachment of ligaments affects the result of the enhancement, which is an explanation about the ligament attachment location from a new perspective. Furthermore, we can apply the unilateral constraints in the engineering mechanisms to restrict the assembly tolerances in order to enhance the reliability.

REFERENCES

[1] B. Schleich and S. Wartzack, "A discrete geometry approach for tolerance analysis of mechanism," *Mechanism and Machine Theory*, vol. 77, pp. 148–163, 2014.

[2] N. Shao, X. Ding, and J. Liu, "Tolerance analysis of spur gears based on skin model shapes and a boundary element method," *Mechanism and Machine Theory*, vol. 144, p. 103658, 2020.

[3] D. Razmadze, A. A. Panyutina, and N. V. Zelenkov, "Anatomy of the forelimb musculature and ligaments of psittacus erithacus (aves: Psittaciformes)," *Journal of Anatomy*, vol. 233, no. 4, pp. 496–530, 2018.

A COUPLED MULTIBODY–GRANULAR DYNAMICS FRAMEWORK FOR HIGH-FIDELITY SIMULATION OF LUNAR ROBOT LOCOMOTION

Kaiming Zhang[1], Yang Yu[1], Zhijun Song[1], Jingchang Xie[1], Kunen Peng[1]

[1] Beihang University, Street 37 Xueyuan Road, Haidian District, Beijing, China
{zhkaiming@buaa.edu.cn; yu.yang@buaa.edu.cn; zhijunsong@buaa.edu.cn; sy2308208@buaa.edu.cn; pengkunen@buaa.edu.cn}

1 INTRODUCTION

Recent advances in robotics have been strongly driven by learning-based control techniques, particularly reinforcement learning, which require reliable simulation environments for training and validation. High-fidelity simulators play a critical role in sim-to-sim and sim-to-real transfer, significantly influencing the deployment performance of learned policies.

In space exploration missions, experimental testing is extremely costly and limited, making numerical simulation indispensable for system design and performance evaluation. The mechanical behavior of lunar regolith exhibits strong nonlinearity, discontinuity, and heterogeneity, posing major challenges for accurate modeling of robot–terrain interactions[1].

Although high-accuracy simulators are crucial for realistic performance assessment, their high computational cost often prevents direct integration into large-scale reinforcement learning training processes. Consequently, accurate and efficient simulation frameworks are especially valuable in the sim-to-sim validation stage, where trained control policies are evaluated under realistic physical conditions.

This work presents a coupled multibody-granular dynamics framework for high-fidelity simulation of lunar exploration robots operating on granular terrain. The proposed method integrates detailed contact modeling, efficient numerical implementation, and flexible robotic system representation, providing a reliable platform for locomotion analysis and control validation.

2 COUPLED DYNAMICS FRAMEWORK

The proposed framework integrates discrete element modeling of granular materials with multibody dynamics formulation of robotic systems.

Granular media are represented by assemblies of spherical particles, which is a widely adopted approximation in DEM due to its computational efficiency and its ability to reproduce key macroscopic behaviors of granular systems. Particle–particle and particle–surface interactions are described using a comprehensive contact model that simultaneously considers normal, tangential, torsional, and rolling effects. Linear spring–dashpot formulations with Coulomb-type friction limits are adopted to account for elastic deformation and energy dissipation during collisions[2].The contact parameters are selected based on commonly used values for granular and rock-like materials in DEM simulations, which are sufficient to capture the general mechanical response of granular media.

The target robotic platform considered in this study is a spherical rolling robot equipped with twelve telescopic legs uniformly distributed on the face centers of a regular dodecahedron[3]. By coordinating the extension and contraction of these legs, the robot achieves rolling-based locomotion. This design enables omnidirectional mobility while eliminating the risk of overturning, as the robot remains statically stable in all orientations. Such characteristics make it particularly suitable for exploration tasks in rugged and uncertain extraterrestrial environments.

Rigid bodies are discretized into triangular surface facets to facilitate contact detection and force evaluation. Particle–surface contact forces and moments are computed using the same constitutive relations as particle-particle interactions, with geometric modifications to account for surface discretization and effective contact area.

The robotic system is modeled using Lagrange's equations of first kind. Each rigid component is treated as a rigid body connected by kinematic constraints and actuated joints. The equations of motion are derived using generalized coordinates and solved in conjunction with granular dynamics.

A unified coupling strategy is developed to ensure consistent force and moment transmission between particles and rigid bodies. Contact forces generated at the interfaces are mapped to both subsystems, enabling fully bidirectional interaction.

3 NUMERICAL IMPLEMENTATION

To improve computational efficiency, a spatial grid-based neighbor searching strategy is employed for preliminary identification of potential contact candidates. Only particles and surface facets located in neighboring grid cells are subjected to further geometric evaluation.

Exact contact detection and contact area computation are performed using a robust geometric algorithm for sphere-mesh intersection[4]. This approach enables accurate determination of contact states and effective contact regions, ensuring reliable force evaluation.

Time integration is conducted using an explicit leapfrog scheme, which provides good numerical stability for large-scale particle systems. Parallel computation based on OpenMP is implemented to further enhance computational performance on multi-core processors.

4 PRELIMINARY VALIDATION

Preliminary numerical tests have been conducted to verify the correctness and stability of the proposed framework. A representative example involves a rigid cubic body undergoing free fall onto a granular bed composed of spherical particles as shown in Fig. 1. The simulation reproduces characteristic impact phenomena, including monotonic

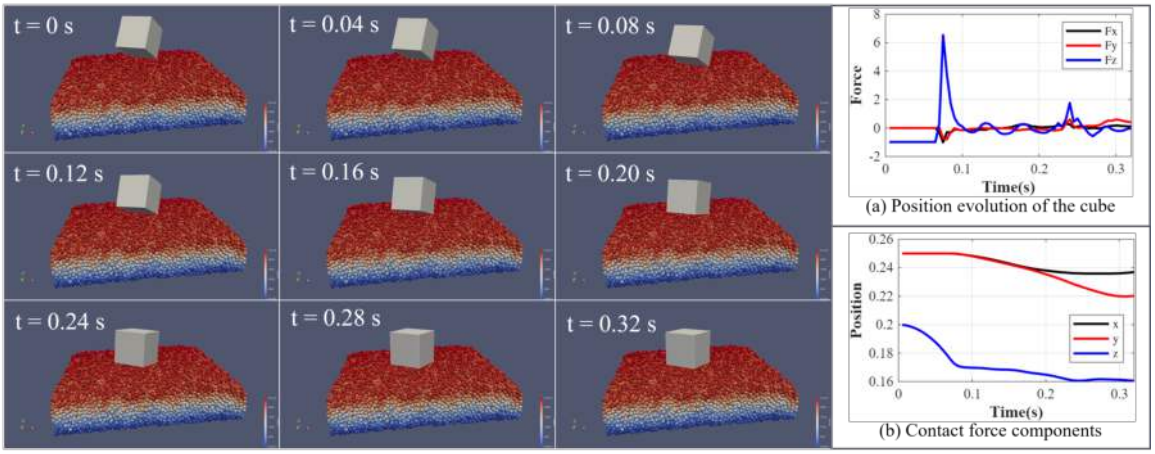

Figure 1: Cube falling process.

increase of contact force during penetration, energy dissipation during collision, and realistic particle rearrangement patterns beneath the impacting body. These observations are consistent with typical granular impact responses and the results demonstrate physically consistent contact behavior and stable numerical performance.

Further validation studies, including isolated granular tests, multibody benchmark problems, and robot–terrain interaction scenarios, are currently in progress and will be presented in the full paper.

5 CONCLUSIONS

A coupled multibody–granular dynamics framework for high-fidelity simulation of lunar robot locomotion has been presented. The proposed method integrates detailed contact modeling, efficient numerical implementation, and flexible robotic system representation.

The framework provides a reliable numerical platform for sim-to-sim validation of learning-based control strategies and performance analysis of exploration robots operating on granular terrain. Future work will focus on extensive experimental validation, large-scale parametric studies, and reinforcement learning integration.

REFERENCES

[1] M. Jiang, Z. Shen, and C. Thornton. “Microscopic contact model of lunar regolith for high efficiency discrete element analyses”.*Computers & Geotechnics*, vol. 54, pp. 104-116, 2013.

[2] C. Richter, T. Roessler, H. Otto, A. Katterfeld, 2021. “Coupled discrete element and multibody simulation, part I: implementation, verification and validation”. *Powder Technology*, vol. 379, pp. 494–504, 2021.

[3] D. Yang, Y. Liu, and Y. Yu, “A General Locomotion Approach for a Novel Multi-legged Spherical Robot”. in *2023 IEEE International Conference on Robotics and Automation (ICRA)*, London, United Kingdom, May 2023.

[4] S. Strobl, A. Formella, T. Pöschel, “Exact calculation of the overlap volume of spheres and mesh elements”. *Journal of Computational Physics*, vol. 311, pp. 158–172, 2016.

HIGHER-ORDER KINEMATIC ANALYSIS OF COMPLIANT FOUR-BAR LINKAGE: THEORY AND APPLICATION TO A FLEXIBLE ROBERTS MECHANISM

Marco Cirelli, Luca D'Angelo, Gabriele Alcamo, Pier Paolo Valentini

University of Rome Tor Vergata, via del Politecnico 1, 00133 Rome, Italy {luca.d.angelo@uniroma2.it; marco.cirelli@uniroma2.it; gabriele.alcamo@alumni.uniroma2.eu; valentini@ing.uniroma2.it}

1. INTRODUCTION

Higher-order kinematic analysis provides advanced tools for mechanism design, enabling control not only of position, velocity, and acceleration, but also of local trajectory properties such as curvature, inflection, and higher-order stationarity [1]. In rigid-body planar kinematics, these properties are associated with well-known geometric loci and special points, including higher-order Bresse circles [2], the cubic of stationary curvature, and points with vanishing higher-order kinematic invariants, such as the Ball point, which is of particular interest due to its locally straight trajectory up to higher infinitesimal orders.

While these results are well established for rigid mechanisms, their extension to mechanisms with flexible joints is not straightforward. In compliant mechanisms, the relative motion between connected bodies depends also on the applied loads, leading to an elastokinematic behaviour. Recent studies have shown that, under a pure moment applied to the moving body, the relative motion across a flexural pivot can be effectively approximated by an equivalent one-degree-of-freedom epicyclic mechanism, whose centrodes can be approximated as circular curves [3]. This equivalence has been validated for several types of flexural joints [4, 5] and has enabled the development of rigid equivalent models suitable for kinematic analysis and synthesis. However, the adoption of such equivalent epicyclic models to investigate higher-order kinematic properties of more complex compliant mechanisms has not yet been addressed in the literature. Although a four-bar linkage with flexible joints can be modeled through the equivalent epicyclic mechanism proposed in [6], this approach has so far been limited to the analysis of lower-order kinematic quantities. The aim of this work is to extend higher-order kinematic analysis to planar compliant mechanisms by exploiting the epicyclic pseudo-rigid model of flexural joints. First, a general theoretical framework is developed to identify and describe geometric loci associated with higher-order kinematic properties in compliant planar mechanisms, using the rigid equivalent epicyclic representation. In particular, a four-bar linkage with flexible joints is modeled using equivalent epicyclic gear trains, enabling the application of classical higher-order kinematic tools to the coupler link's motion. This approach enables the identification and analytical characterization of higher-order kinematic special points and loci of the coupler trajectory in the presence of joint compliance. Subsequently, the proposed formulation is specialized to compliant straight-line generating mechanisms. A flexible-joint Roberts linkage is investigated as a case study, showing how higher-order kinematic conditions can be used to interpret and enhance approximate straight-line motion in compliant mechanisms.

2. HIGHER-ORDER KINEMATICS OF THE EQUIVALENT COMPLIANT FOUR-BAR LINKAGE

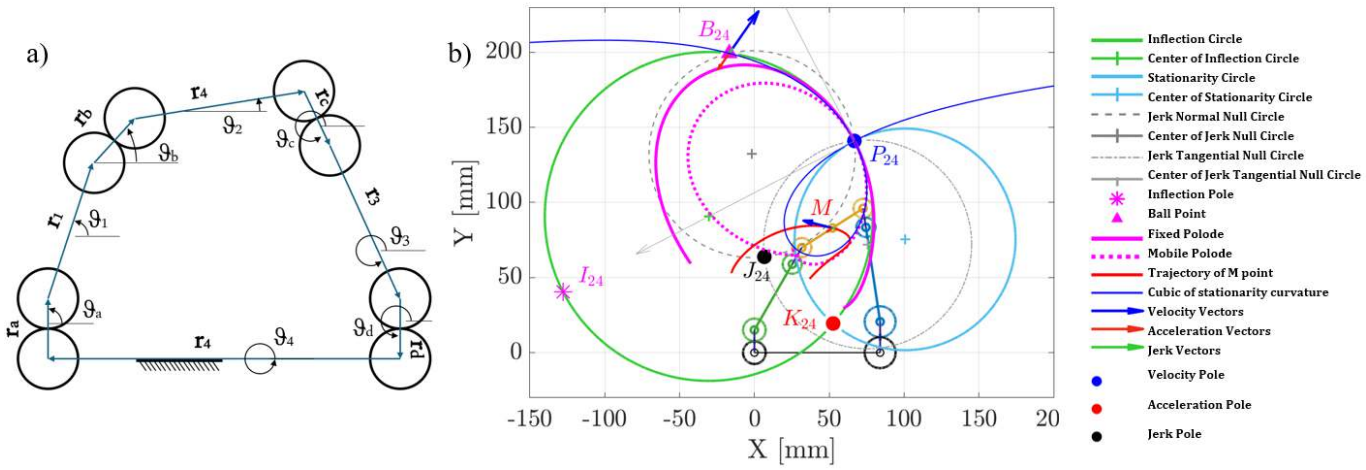

Figure 1 a) Scheme adopted for the closure loop equations; b) Kinematic loci of the coupler link

Considering the configuration shown in Fig. 1a, the closure loop equations of the four-bar linkage with flexible joints modeled through the epicyclic pseudo-rigid-body approach were derived (Eq. 1). In addition to the closure equations, the kinematic characteristics of the relative motion within the equivalent epicyclic gear trains were obtained using the integrated Willis' equations (Eq. 2). By differentiating the resulting system of equations up to the fourth order, the rigid-body motion of all links

in the mechanism was fully characterized. Focusing on the motion of the coupler link, geometric loci associated with fourth-order kinematic properties were identified and plotted, as shown in Fig. 1b.

$$\mathbf{r_a} + \mathbf{r_1} + \mathbf{r_b} + \mathbf{r_2} + \mathbf{r_c} + \mathbf{r_3} + \mathbf{r_d} + \mathbf{r_4} = 0 \tag{1}$$

$$\begin{cases} (\theta_4 - \theta_{4,0}) - (\theta_a - \theta_{a,0}) = -\tau_a \left[(\theta_1 - \theta_{1,0}) - (\theta_a - \theta_{a,0}) \right] \\ (\theta_1 - \theta_{1,0}) - (\theta_b - \theta_{b,0}) = -\tau_b \left[(\theta_2 - \theta_{2,0}) - (\theta_b - \theta_{b,0}) \right] \\ (\theta_2 - \theta_{2,0}) - (\theta_c - \theta_{c,0}) = -\tau_c \left[(\theta_3 - \theta_{3,0}) - (\theta_c - \theta_{c,0}) \right] \\ (\theta_3 - \theta_{3,0}) - (\theta_d - \theta_{d,0}) = -\tau_d \left[(\theta_4 - \theta_{4,0}) - (\theta_d - \theta_{d,0}) \right] \end{cases} \tag{2}$$

3. APPLICATION TO A COMPLIANT ROBERTS STRAIGHT-LINE MECHANISM

To validate the proposed method, a specific family of four-bar linkages, namely straight-line generating mechanisms, was considered, with particular focus on the Roberts linkage. In this study, a compliant Roberts mechanism was analyzed in a limiting configuration in which the side links (rockers) of the four-bar are fully flexible (Fig. 2b). This condition represents a more complex and limiting case compared to mechanisms with localized flexural pivots. According to [7], flexural members exhibiting an inflection point in their deformed shape can be modeled as a series of two interconnected pseudo-rigid epicyclic mechanisms. Based on this approach, the geometry of the equivalent mechanism was defined and the fundamental geometric loci were identified. Since the mechanism under investigation is intended to generate an approximate straight-line trajectory, the Ball point was identified and used as a reference. The trajectory of a coupler point initially coincident with the Ball point was then analyzed, and its motion was evaluated to verify the straight-line generating capability predicted by the higher-order kinematic formulation.

4. VALIDATION, NUMERICAL RESULTS AND CONCLUSIONS

The proposed method was validated by comparing results from the pseudo-rigid equivalent model with those from a flexible multibody model. The latter accounts for the compliance of the flexural members through a discrete flexible multibody formulation, in which equivalent inertia and stiffness properties are assigned to reproduce the system's physical behavior. As shown in Fig. 2, the trajectory of point **M** predicted by the two models exhibits very good agreement, with discrepancies increasing only when the mechanism undergoes large elastic deformations. Moreover, in both models, the trajectory can be approximated as a straight line over a segment whose length is comparable to that of the linkage members, confirming the higher-order straight-line behavior predicted by the proposed formulation. These results confirm that higher-order kinematic properties of compliant mechanisms can be effectively captured through the proposed equivalent modeling framework. The approach provides a new theoretical basis for the synthesis of compliant mechanisms with prescribed local trajectory characteristics, such as straight-line generation and higher-order curvature control. Future developments will address the integration of these higher-order conditions into synthesis procedures and optimization frameworks for precision compliant devices and micro-mechanisms.

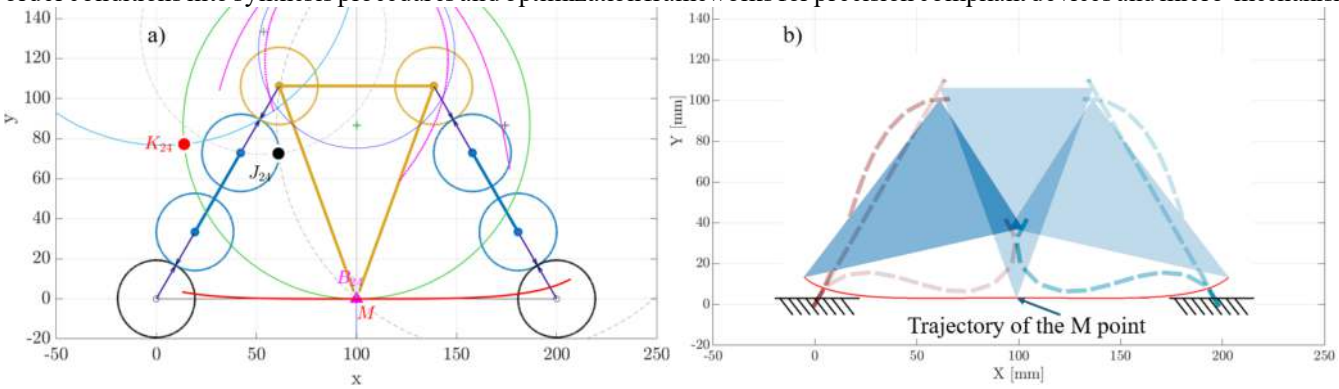

Figure 2: a) Roberts pseudo-rigid equivalent mechanism; b) Roberts mechanism with rockers fully compliant.

REFERENCES

[1] G. Figliolini, C. Lanni and L. Tomassi, «First- and Second-Order Centrodes of both Coupler Links of Stephenson III Six-Bar Mechanisms,» *Machines*, pp. 13,93, 2025.

[2] G. Figliolini, C. Lanni, M. Cirelli, and E. Pennestrì, «Kinematic properties of nth-order Bresse circles intersections for a crank-driven rigid body,» *Mechanism and Machine Theory*, p. 105445, 2023.

[3] P. P. Valentini e E. Pennestri, «Second-order approximation pseudo-rigid model of leaf flexure hinge,» *Mechanism and Machine Theory,* vol. Volume 116, pp. 352-359, 2017.

[4] M. Cera, M. Cirelli, L. Colaiacovo, and P. P. Valentini, «Second-order approximation pseudo-rigid model of circular arc flexure hinge,» *Mechanism and Machine Theory*, vol. 175, p. 104963, 2022.

[5] C. Iandiorio, M. Cirelli, P. Salvini, and P. P. Valentini, «Elasto-Kinematics and second-order pseudo-rigid model of cross-axis flexure hinges,» *Mechanism and Machine Theory*, vol. 205, p. 105894, 2025.

[6] P. P. Valentini and E. Pennestrì, «Compliant four-bar linkage synthesis with second-order flexure hinge approximation,» *Mechanism and Machine Theory*, vol. 128, pp. 225-233, 2018.

[7] Cirelli, M.; Autiero, M.; D'Angelo, L.; Valentini, P.P. Second-Order Kinematic Invariants for the Design of Compliant Auxetic Symmetrical Structures. *Symmetry* 2025, 17, 134.

APPLICATION OF DIGITAL TWIN IN THE CONTROL SYSTEM FOR THE ZIRCONIA-BASED CERAMICS ELECTROCONSOLIDATION DEVICE

Waldemar Samociuk[1], Edvin Hevorkian[1], Dmitrij Morozow[2], Leszek Chałko[2], Paweł Stączek[3], Mirosław Rucki[2,4]

[1] Faculty of Production Engineering, University of Life Sciences in Lublin, Gleboka 28, 20-612 Lublin, Poland, {waldemar.samociuk@up.lublin.pl; e.gevorkian@urad.edu.pl}

[2] Faculty of Mechanical Engineering, Casimir Pulaski Radom University, Stasieckiego 54, 26-600 Radom, Poland, {d.morozow@urad.edu.pl; leszek.chalko@urad.edu.pl}

[3] Department of Automation, Lublin University of Technology, Nadbystrzycka 36, 20-618, Lublin, Poland; {p.staczek@pollub.pl}

[4] Institute of Mechanical Science, Vilnius Gediminas Technical University, Sauletekio al. 11, LT-10223 Vilnius, Lithuania, {m.rucki@urad.edu.pl}

1. INTRODUCTION

The mechanical properties of ceramics fabricated using powder metallurgy techniques are dependent directly on the obtained microstructure, homogeneity, grain size and shape, relative density and pore dimensions [1]. The digital twin (DT) technique has been recognized as an effective tool to simulate the dynamics of thermochemical sintering processes with the real-time interaction between physical system and cyberspace [2]. This work concerns the control of a novel electroconsolidation process used for fabrication of yttria-stabilized zirconia based ceramics. The main goal of this work was to develop and implement a control algorithm with application of a digital twin. The research focuses on comparing the control effectiveness using a process model for different sample compositions. The digital twin of the sintering process was matured through a series of expensive and time-consuming experiments.

2. ELECTROCONSOLIDATION DEVICE AND PROCESS

The sintering method for fabrication of zirconia-based ceramics is a modified spark plasma sintering (SPS) technique. The main idea of electroconsolidation consists of direct application of the alternating current reaching ca. 5,000 A to the molds with the initial powders under uniaxial pressure of 30-45 MPa. The sintering process involves interfacial particles tension under the mechanical pressure, electrical current and high temperature, which requires precise parameter control to ensure repeatable and optimal properties of the sintered samples [3]. During the electroconsolidation of zirconia, several process stages can be distinguished, as follows: (1) Initial stage of activation, (2) Main stage of compaction and densification, (3) Intermediate stage of completion the sintering, (4) Final stage of stabilization of the formed structure. Figure 1 presents the example of such a process in time *t* with the stages emphasized.

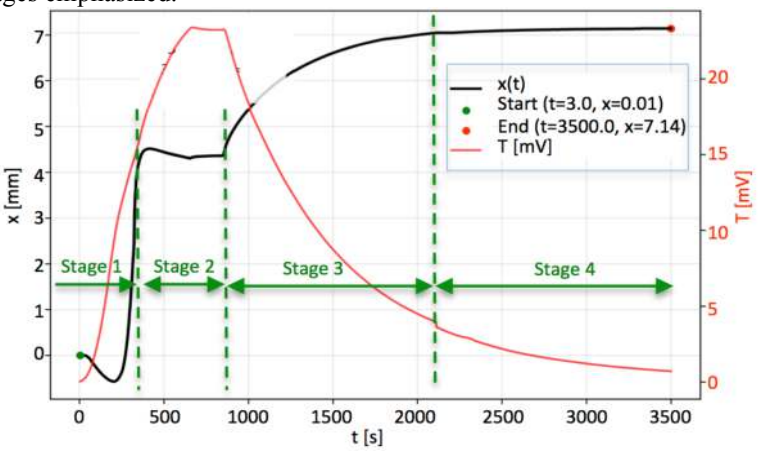

Figure 1. Diagrams of shrinkage *x* and temperature *T* during electroconsolidation process.

The quality indicators of the obtained sintered samples are their mechanical and physical properties dependent on their structural homogeneity and microstructural features. To achieve repeatability of the entire process, the control system must ensure proper heating rate and other parameters, exhibiting relevant overshoot, integral quality indicators, etc. To achieve that, it was found useful to apply the algorithm involving DT technology.

3. CONTROL ALGORITHM

A model of the heating process dynamics was developed in the form of a differential equation, as follows:

$$T_1 \frac{d^2y}{dt^2} + T_2 \frac{dy}{dt} + y(t) = ku(t-\tau), \quad (1)$$

where T_1, T_2 are the substitute time constants, $y(t)$ is the modeled output value, $u(t)$ is the control signal, t is time, τ is transport delay. On the basis of this model, analytical selection of the PID controller parameters (Kp, Ti, Td) was performed. The control algorithm was implemented in an industrial PLC environment, which was used to control and monitor the electroconsolidation process. Figure 2 presents the control loop of the developed algorithm. The process parameters T, F, and t denote temperature, mechanical pressing force, and time, respectively.

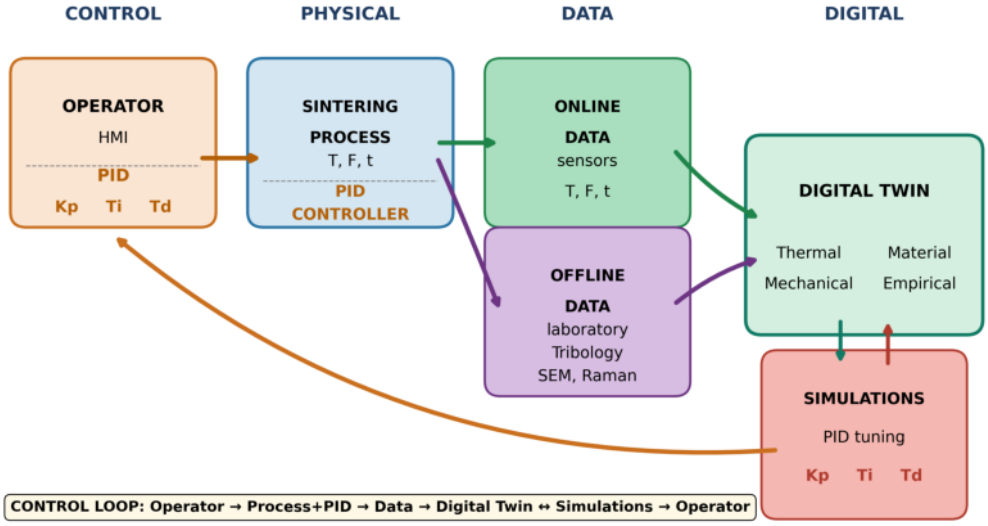

Figure 2. The developed control algorithm for the electroconsolidation process.

Based on the step characteristics, controller settings were selected and control system simulations were performed. The obtained results were used to make corrections of process parameters for subsequent select cycles and for the future research. The alterations of settings and control parameters during simulation allowed for prediction of the results.

4. DISCUSSION

The analysis of the quality of the control system is closely connected with the quality of the obtained zirconia-based materials, which is assessed using the following methods: scanning electron microscopy (SEM), field emission scanning electron microscopy (FE-SEM), X-ray diffraction analysis (XRD), energy dispersive X-ray spectroscopy (EDS) microhardness and nanoindentation mapping techniques, etc. The collected data is assessed using various statistical methods, including Weibull distribution estimation method. The proposed algorithm and simulation allowed for reducing the number of expensive experiments and measurements while keeping the required quality and repeatability.

5. CONCLUSIONS

The presented DT-based control algorithm enables robust control of the electroconsolidation process of zirconia composites. Simulation and analysis enabled to reduce the number of expensive samples and measurements. The research provided practical guidance and recommendations for engineers in designing control systems for non-standard, advanced manufacturing processes in materials science.

ACKNOWLEDGMENTS

This research was funded by National Science Centre Poland, grant number OPUS-24 NCN UMO-2022/47/B/STS/01041.

REFERENCES

[1] J. Fan, S. Yao, J. Liu, K. Zhao, L. An, D. Liu, "Effect of dynamic pressure on grain boundary energy and mechanical performance of high-strength zirconia ceramics fabricated via dynamic sinter forging". *Journal of the European Ceramic Society*, 46(3), 117898, 2026.

[2] X. Ding, W. Liu, J. Ye, C. Chen, X. Guan, "Online Dynamic Modelling for Digital Twin Enabled Sintering Systems: An Iterative Update Data-Driven Method". *IET Signal Processing*, 2023, 6665657, 2023.

[3] M. Rucki, E. Hevorkian, J.N. Latosińska, V. Kolodnitskyi, L. Chalko, D. Morozow, W. Samociuk, J. Matijosius, M. Masař, T. Ryba, "Reproducibility Assessment of Zirconia-Based Ceramics Fabricated out of Nanopowders by Electroconsolidation Method". *Applied Sciences*, 15, 4955, 2025.

CUBOID-SHAPED BRICARD-SARRUS METASTRUCTURES WITH CONSTANT-ZERO STIFFNESS

Shiwei Liu[1], Long Li[1], Shengnan Lyu[1], Xilun Ding[1]

[1] Beihang University, No.37 Xueyuan Road Haidian District Beijing, China, {swliu@buaa.edu.cn; bhlilong@buaa.edu.cn; Shengnan_Lyu@buaa.edu.cn; xlding@buaa.edu.cn}

1. INTRODUCTION

This study presents an over-constrained cuboid-shaped Bricard-Sarrus metastructure (CBSM) exhibiting constant-zero-stiffness (CZS) characteristics across its entire range of motion. The CZS metastructure comprises rectangular plane-symmetric Bricard linkage (RBL) and Sarrus-derived linkage (SDL) units, with tension springs arranged between rotation joints to provide elastic output. Using screw theory, kinematic models of the RBL and SDL units are established, along with the parameterized coordinates of each rotation joint during deployment. Subsequently, an equivalent stiffness model of the CZS metastructure is developed through the energy method, and the dynamic response is then obtained. Quasi-static experiments on a fabricated prototype validate its excellent constant-force output characteristics, while vibration tests verify its superior ultra-low-frequency isolation capability. This study broadens the application scope of spatial over-constrained mechanisms and offers a novel technical approach for designing CZS metastructures.

2. THE CUBOID-SHAPED BRICARD-SARRUS METASTRUCTURE

Figure 1 depicts the developed CBSM in its general configuration. The CBSM consists of a bottom base, a top platform, and spatial over-constrained linkages assembled on its sides. The two primary constituent units of the CBSM are the rectangular plane-symmetric Bricard linkage (RBL) and the Sarrus-derived linkage (SDL), with elastic elements strategically placed at the joints. Movement at each joint results in corresponding displacements of the elastic elements, allowing the CBSM to exhibit the desired mechanical properties. Consequently, optimal output from the CBSM requires reasonable joint movement trajectories and geometric structure parameters.

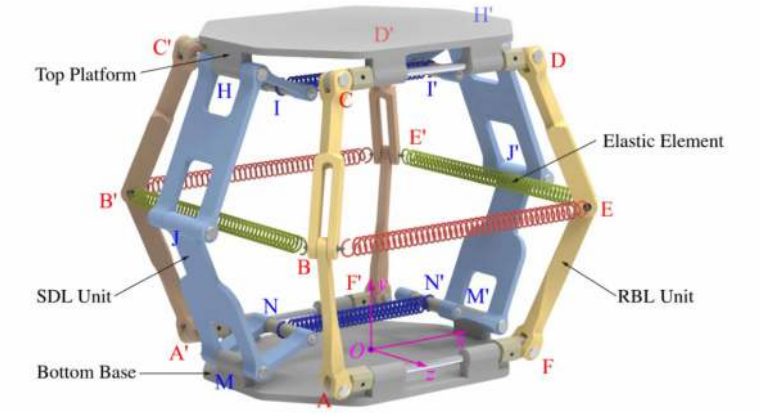

Figure 1. The cuboid-shaped Bricard-Sarrus metastructure.

3. MECHANICAL MODEL OF THE CBAM

According to the energy method, the elastic potential energy generated by the CBSM can be obtained by the sum of the potential energies of each spring, that is:

$$F = \sum_{i=1}^{3} F_i = \sum_{i=1}^{3} \frac{dE_i}{du} = \sum_{i=1}^{3} \frac{dE_i}{d\theta} \frac{d\theta}{du} \tag{1}$$

where F is the output of the CBSM. n_i is the number of the springs, b and d are the lengths of the link AB and MN, respectively, β is the twist angle of the Bricard, u is the compression displacement.

$$\begin{cases} F_1 = \dfrac{64n_1k_1b^4(2b-u)\cos^2\beta}{\left[8b^2-4bu+u^2+(4b-u)u\cos 2\beta\right]^2}, \\ F_2 = \dfrac{2n_2k_2(2b-u)\left[32b^4-64b^3u+32b^2u^2-8bu^3+u^4-u^2(u-4b)^2\cos 2\beta\right]\sin^2\beta}{\left[8b^2-4bu+u^2+(4b-u)u\cos 2\beta\right]^2}, \\ F_3 = \dfrac{n_3k_3d^2}{b^2}u. \end{cases} \tag{2}$$

The necessary condition of CZS and the output force for the CBSM is:

$$\begin{aligned} n_1k_1b^2 &= n_2k_2b^2 = n_3k_3d^2 \\ F_{\text{out}} &= 2n_1k_1b = 2n_3d^2k_3/b \end{aligned} \tag{3}$$

Figure 2 shows the output force and displacement responses of the developed CBSM according to Eq. (3). The theoretical calculations are based on the parameters: $k_1 = k_2 = k_3 = 1$ N/mm, $n_1 = n_2 = n_3 = 2$, and $d = b = 100$ mm. Meanwhile, the values of β for the three subfigures are 30°, 45°, and 60°, respectively.

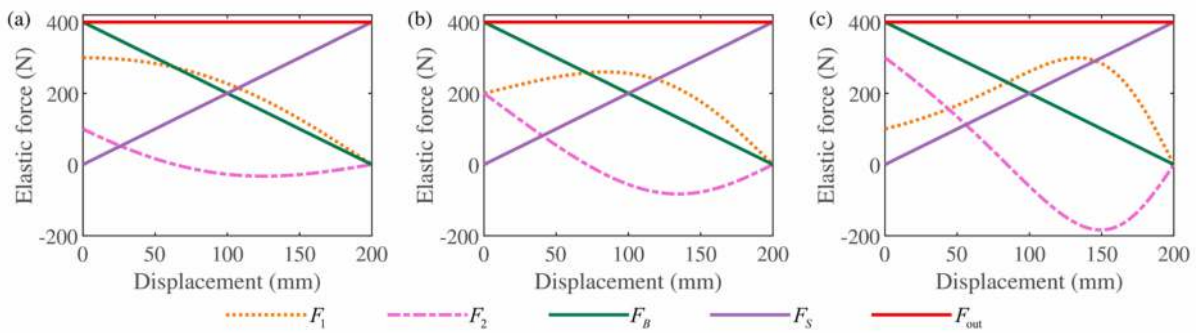

Figure 2. Elastic force component curves of the CBSM at various twist angles β: (a) β = 30°, (b) β = 45°, (c) β = 60°.

4. EXPERIMENTAL RESULTS

Figure 3 presents the experimental results of the prototype. Fig. 3(a) gives the quasi-static experimental result. As the compression distance increases (30-80 mm), the elastic force curve evolves into a relatively horizontal segment, showing close alignment with the trend predicted by theoretical models. Fig. 3(b)-(e) display single-frame time-domain signals captured at frequencies of 2 Hz, 5 Hz, 10 Hz, and 15 Hz, respectively. Fig. 3(f) compares theoretical predictions with experimental measurements. At lower excitation frequencies, such as 2 Hz, the output excitation signal experiences significant distortion, resulting in high-order harmonic components in both the excitation and response signals. Fig. 3(f) demonstrates that the experimental data align closely with the theoretical predictions.

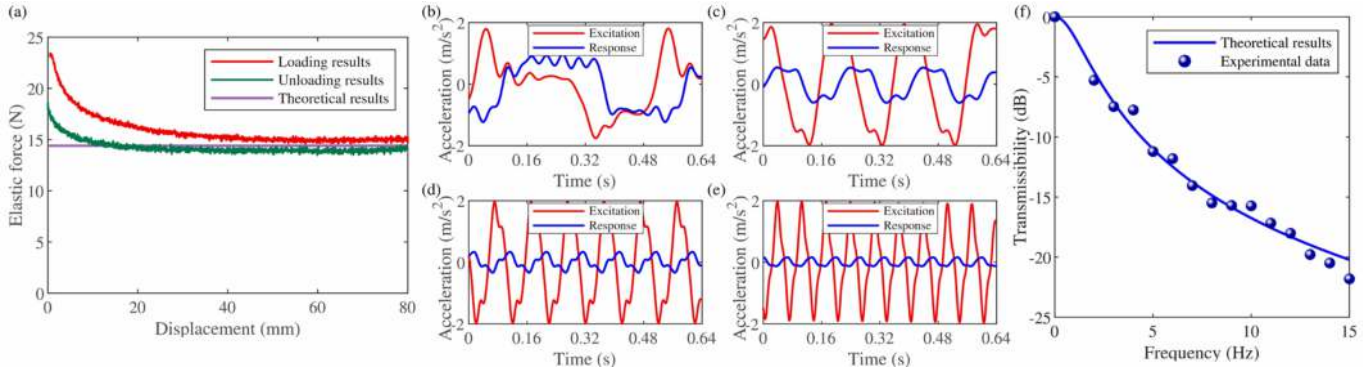

Figure 3. Quasi-static test and vibration isolation test results of the CBSM prototype.

ACKNOWLEDGMENTS

This work was supported by the National Natural Science Foundation of China (Grant No. 52405004, 52192632, T2121003).

REFERENCES

[1] S.W. Liu, S.N. Lyu, X.Y. Xing, X.L. Ding, "Ellipsograph-derived vibration isolator with stiffness mode switching", *International Journal of Mechanical Sciences*, 285, 109795, 2025.

[2] S.W. Liu, G.L. Peng, Z.X. Li, W.H. Li, K. Jin, H.Z. Lin, "Design and experimental study of an origami-inspired constant-force mechanism", *Mechanism and Machine Theory*, 179, 105117, 2023.

DATA-DRIVEN STRUCTURAL STRAIN ESTIMATION FOR A FORESTRY CRANE USING LSTM AND TRANSFORMER NETWORKS

Sohaib M. Saeed[1], Victor Zhidchenko[1], Heikki Handroos[1]

[1] Laboratory of Intelligent Machines, LUT University, Yliopistonkatu 34, 53850 Lappeenranta, Finland, {sohaib.saeed@lut.fi; victor.zhidchenko@lut.fi; heikki.handroos@lut.fi}

1 INTRODUCTION

Hydraulically actuated forestry cranes exhibit strongly coupled hydraulic and mechanical dynamics, where operational variations generate complex time-varying structural strains. Accurate strain estimation is therefore important for structural health monitoring, fatigue assessment, and digital twin applications. Physics-based multibody–hydraulic models have been widely applied to heavy machinery for state estimation [1] and faster-than-real-time digital twin simulation [2], and have recently been extended to structural performance prediction in telescopic boom cranes [3]. However, their application to real-time strain monitoring is constrained by modeling complexity, parameter uncertainty, lack of experimental dataset, and computational cost.

To address these limitations, data-driven surrogate modeling approaches have been investigated for structural response estimation in heavy hydraulic machinery [4]. Machine learning methods have demonstrated the feasibility of estimating structural strains from indirect measurements such as accelerations [5], including successful applications in bridge monitoring [6]. In the crane domain, data-driven identification of crane dynamics has further shown the potential of machine learning for capturing system behavior under operational conditions [7]. Building on these developments, recurrent deep learning models have been applied to strain estimation in hydraulic crane structures, but considering simulation data [8]. In this work, LSTM- and Transformer-based models are evaluated for fast strain estimation using the PATU655 Forestry Crane experimental dataset. The dataset contains the sensor data recorded from the real crane and covers multiple payloads, supply pressure, voltage inputs, crane postures, and operating modes. Strain data contains recordings from five strain gauges installed at the maximum stress locations.

2 METHODOLOGY

Two sequence learning architectures are investigated: a Long Short-Term Memory (LSTM) network and a Transformer-based model. The LSTM captures temporal dependencies through recurrent memory states, while the Transformer uses self-attention to model both short- and long-range temporal relationships. To ensure a fair comparison, identical preprocessing, sequence construction, data splitting, and training procedures are applied to both models. Figure 1 illustrates the adopted data-driven strain estimation pipeline.

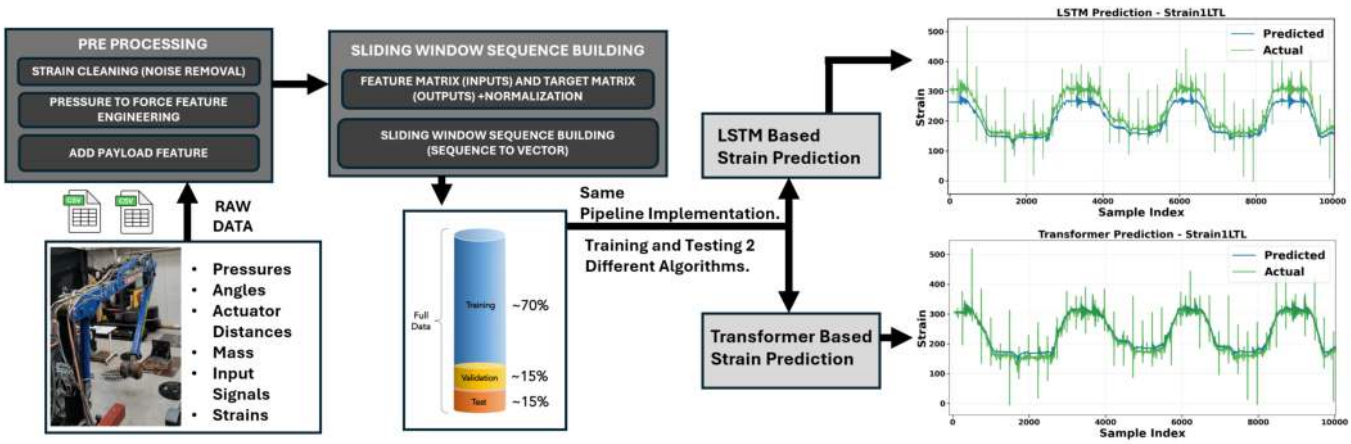

Figure 1: Overview of the data-driven strain estimation pipeline for LSTM and Transformer models.

Raw sensor signals are preprocessed by noise removal, hydraulic-pressure-to-force conversion based on cylinder geometry, and inclusion of payload mass as an input feature. The processed signals are normalized and organized into

fixed-length sliding windows to preserve temporal information. At each time step, a fixed-length sequence of operational measurements is provided to the learning model to predict the corresponding vector of structural strains. The learning task is expressed as

$$\hat{\boldsymbol{\varepsilon}}_t = g_\phi\big(f_\theta(\mathbf{X}_t)\big), \tag{1}$$

where $\mathbf{X}_t$ denotes the input sequence, $f_\theta(\cdot)$ is the sequence encoder, and $g_\phi(\cdot)$ maps the encoded representation to strain outputs. The models differ only in the sequence encoder: the LSTM uses recurrent layers to capture short- and medium-term dynamics, while the Transformer employs self-attention to model long-range dependencies. This enables a direct comparison of recurrent and attention-based approaches for data-driven strain estimation.

3 RESULTS

The LSTM and Transformer models were evaluated using experimental recordings from the PATU655 dataset with an unseen payload of 148 kg, while training was performed using payloads of 95, 180, and 278 kg to assess generalization. Prediction accuracy was evaluated using MSE, MAE, RMSE, and R^2 for the strain channel exhibiting the highest strain in the crane lift boom. Table 1 summarizes the quantitative accuracy and inference results for a representative unseen test sequence, highlighting differences in accuracy and robustness between the models.

Table 1: Comparison of LSTM and Transformer performance on unseen 148 kg payload data.

(a) Evaluation Metrics for the best predicted strain channel

Model	**RMSE** ($\mu\varepsilon$)	R^2	**MAE** ($\mu\varepsilon$)
LSTM	13.05	0.94	11.86
Transformer	10.29	0.96	8.82

(b) Average inference time per sequence

Model	**Time (ms)**
LSTM	0.33
Transformer	0.71

The Transformer achieves lower prediction errors and higher R^2 values than the LSTM under unseen payload conditions, particularly for strain channels influenced by long-range load interactions. While the LSTM shows reduced generalization, the Transformer maintains sub-millisecond inference time, demonstrating its suitability for real-time embedded strain estimation in hydraulically actuated cranes.

4 CONCLUSIONS

This study evaluates LSTM and Transformer models for data-driven strain estimation in a hydraulically actuated PATU 655 forestry crane. Both models accurately predict strain responses from operational measurements, while the Transformer shows improved generalization under unseen payload conditions. Sub-millisecond inference times demonstrate the suitability of attention-based models for real-time embedded control, structural monitoring, and digital twin applications in heavy machinery.

REFERENCES

[1] Q. Khadim *et al.*, "State estimation in a hydraulically actuated log crane using Unscented Kalman Filter," *IEEE Access*, vol. 10, pp. 63554–63566, 2022.

[2] V. Zhidchenko *et al.*, "Faster than real-time simulation of mobile crane dynamics using digital twin concept," *J. Phys.: Conf. Ser.*, vol. 1096, p. 012071, 2018.

[3] X. Cao, K. Lin, B. Yan, and C. Zhang, "Digital twin-based structural performance prediction method for telescopic boom cranes," in *Proc. 9th Int. Conf. Advances in Construction Machinery and Vehicle Engineering (ICACMVE)*, H. Saman, Y. Peng, D. Zhao, and Y. Bian, Eds., Lecture Notes in Mechanical Engineering, Springer, Singapore, 2025, Art. no. 21.

[4] Y.-X. Liu, H.-Z. Huang, Y. Lu, T. Huang, and Z. Deng, "Reliability evaluation and optimal design of hydraulic excavator working device using integrated optimal machine learning algorithm," *Journal of Mechanical Science and Technology*, vol. 39, pp. 3725–3734, 2025.

[5] R. Ishak, "Predictions of strains from accelerations using machine learning," M.Sc. dissertation, KTH Royal Institute of Technology, Stockholm, Sweden, 2023.

[6] N. S. Gülgeç *et al.*, "Structural sensing with deep learning: Strain estimation from acceleration data for fatigue assessment," *Comput.-Aided Civ. Infrastruct. Eng.*, vol. 35, no. 12, pp. 1349–1364, 2020.

[7] T. Kusznir, J. Smoczek, and B. Karwat, "Data-driven identification of crane dynamics using regularized genetic programming," *Applied Sciences*, vol. 14, no. 8, Art. no. 3492, 2024.

[8] S. Saeed, "Intelligent stress estimation in hydraulic crane structures using deep sequential models," M.Sc. thesis, University of Vaasa, Vaasa, Finland, 2025.

ANALYTICAL APPROACH FOR COMPLIANCE IDENTIFICATION IN LIGHTWEIGHT SPUR GEARS

Luca D'Angelo[1], Marco Cirelli[1], Oliviero Giannini[2], Pier Paolo Valentini[1]

[1]University of Rome Tor Vergata, via del Politecnico 1, 00133 Rome, Italy {luca.d.angelo@uniroma2.it; marco.cirelli@uniroma2.it; valentini@ing.uniroma2.it}

[2]University Niccolò Cusano, Via Don Carlo Gnocchi, 3, 00166, Rome, Italy {oliviero.giannini@unicusano.it}

1. INTRODUCTION

The evolution of high-performance power transmissions in several industrial fields, such as aerospace, automotive, and energy applications, is increasingly driven by the need for structural lightweighting to improve fuel efficiency and power density [1]. Gear mass reduction, commonly achieved through web-thickness reduction or lightweighting holes (Fig. 1), effectively limits inertial effects during transient operation [2]. However, these modifications increase gear-body compliance [3], altering the Time-Varying Mesh Stiffness (TVMS) and the resulting Static Transmission Error (STE). Non-axisymmetric features may further introduce low-frequency harmonics that excite resonances and degrade NVH performance. While Finite Element Analysis (FEA) accurately captures these effects, its computational cost is prohibitive for design and optimization studies [4]. Conversely, analytical models such as the Sainsot-Velex formulation [5] are computationally efficient but limited to solid, axisymmetric gears, thus inadequately representing lightweight configurations.

To address this limitation, the present work extends the Sainsot-Velex formulation through a lean analytical framework capable of representing lightweighting features. The model is validated against nonlinear FEA across geometrically dissimilar gears and lightweighting strategies. It enables fast, reliable gear-foundation stiffness estimation for lightweight gear design and optimization by incorporating gear-body compliance alongside tooth-bending and contact stiffness components into the analytical mesh-stiffness formulation [6] or lumped multibody models [7].

2. METHODOLOGY

The proposed methodology focuses on the contribution of the gear-body structural foundation to the total mesh compliance. To adapt the bidimensional analytical formula of Sainsot and Velex to lightweight gear configuration, two virtual parameters are introduced, dependent on dimensional and dimensionless gear-body parameters as illustrated in Figure 1: the equivalent thickness t_{eq} for webbed structures and the equivalent Young's modulus E_{eq} for holed gear bodies, as defined in Eq. (1).

$$t_{eq} = t^*(t_i, l_i) X_t \left(\frac{t_1}{t_2}, \frac{l_1}{h_t}, \frac{l_3}{h_t}, \frac{r_{ded}}{r_h} \right), \qquad E_{eq} = E^*(E, N, R_h, R_{ch}, r_{ded}, r_h) X_E \left(N, \frac{R_h}{r^*}, \frac{R_{ch}}{r^*}, \frac{r_{ded}}{r_h} \right) \tag{1}$$

For gears with reduced web thickness, the constant ring width in the traditional formulation is replaced by t_{eq}, which is derived from the section-wise thickness distribution.

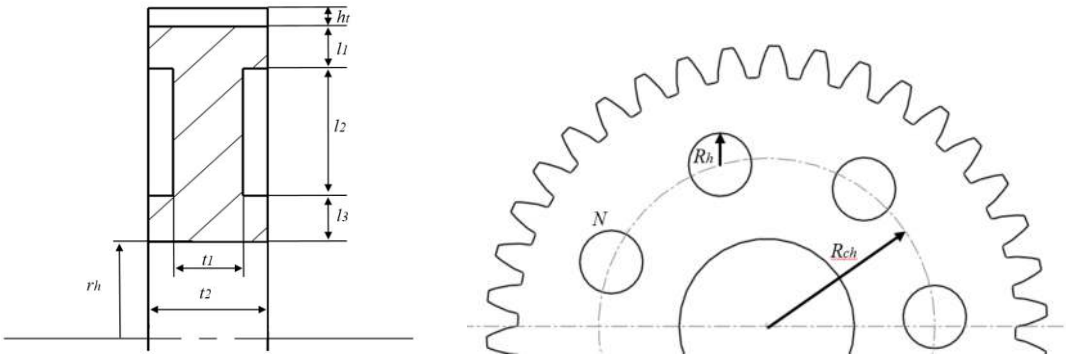

Figure 1. Geometric parameters for web-thickness reduction (left) and hole-based lightweighting (right).

On the other hand, in cases involving lightening holes, the material's Young's modulus is substituted by E_{eq}, to suppress the stiffness contribution of voided regions while retaining the influence of hole size, position, and spatial distribution. To ensure applicability across different gear sizes, dimensionless scaling coefficients are introduced (X_t, X_E). In both cases, these

coefficients are calculated as a weighted average of the individual second-order polynomial functions x_i expressed in terms of dimensionless geometric quantities, as given in Eq. (2).

$$X_i(\alpha,\beta,\chi,\delta) = \frac{x_1(\alpha)w_1 + x_2(\beta)w_2 + x_3(\chi)w_3 + x_4(\delta)w_4}{\sum_{i=1}^{4} w_i} \tag{2}$$

These functions are identified via a Design of Experiments (DOE) campaign performed on a Z50 reference gear using high-resolution 2D FEA, as shown in Figure 2.

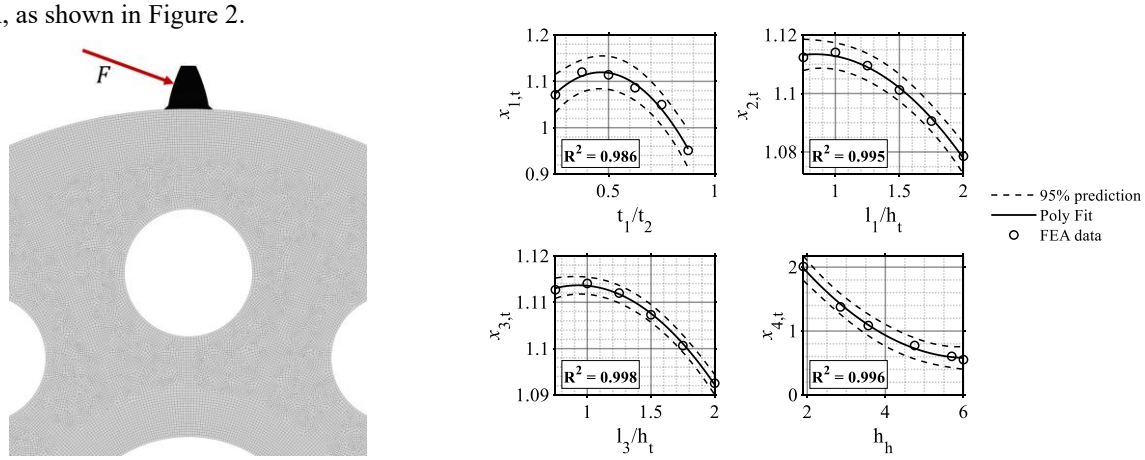

Figure 2. Z50 gear 2D FE model with lightweighting holes (left) and polynomial functions identification from DOE (right).

3. RESULTS AND CONCLUSIONS

The proposed analytical model was validated by comparing predicted foundation-induced displacements at the pitch radius with non-linear FEA results for a wide range of spur gear models (Z38–Z80), as shown in Figure 3.

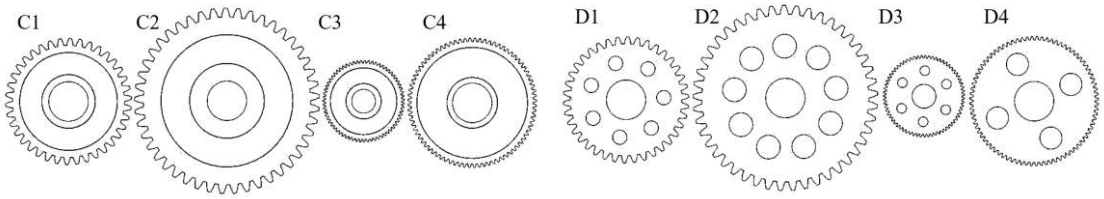

Figure 3. Validation spur gear set.

For gears lightened solely by web-thickness reduction, the average relative error of the proposed model is below 4%. In spur gears with lightweighting holes, two load conditions were considered: the tooth-on-hole and tooth-between-hole configurations. The dimensionless scaling polynomials account for both situations, and the mean relative error with respect to FEA results is lower than 3.5% and 3%, respectively.

In conclusion, this research provides a robust analytical tool for the early-stage design of lightweight transmissions. By scaling the Sainsot-Velex formulation through generalizable dimensionless corrective polynomials, the influence of complex gear lightweighting strategies on mesh stiffness can be accurately predicted without resorting to case-specific FE models, with a drastic reduction in computational cost and enabling rapid NVH-oriented and structural optimization.

REFERENCES

[1] Z. Sun, J. Tang, S. Chen, H. Li, X. Tao, and Z. Hu, «Dynamical modeling and characteristics analysis of tooth spalling in gear system with weight reduction structure,» Mechanism and Machine Theory, vol. 189, 2023.

[2] S. Shweiki, A. Rezayat, T. Tamarozzi, and D. Mundo, «Transmission Error and strain analysis of lightweight gears by using a hybrid FE-analytical gear contact model,» Mechanical Systems and Signal Processing, vol. 123, pp. 573-590, 2019.

[3] S. Li, «Experimental investigation and FEM analysis of resonance frequency behavior of three-dimensional, thin-walled spur gears with a power-circulating test rig,» Mechanism and Machine Theory, vol. 43, n. 8, pp. 934-963, 2008.

[4] X. Kong, Z. Hu, J. Tang, S. Chen and Z. Wang, «Effects of gear flexibility on the dynamic characteristics of spur and helical gear system,» Mechanical Systems and Signal Processing, vol. 184, 2022.

[5] P. Sainsot, P. Velex and O. Duverger, «Contribution of gear body to tooth deflections - A new bidimensional analytical formula,» Journal of Mechanical Design, vol. 126, n. 4, pp. 748-752, 2004.

[6] M. Autiero, G. Paoli, M. Cirelli, and P. Valentini, «The effect of different profile modifications on the static and dynamic transmission error of spur gears,» Mechanism and Machine Theory, vol. 201, 2024.

[7] L. D'Angelo, M. Cirelli, P. Valentini, and O. Giannini, «Bidimensional fuzzy-based propagation of interdependent uncertainty in pseudo-rigid multibody models of spur gears,» Mechanism and Machine Theory, vol. 216, 2025.

FRAME FRICTION MODEL IDENTIFICATION FOR A WEAVING LOOM SYSTEM

V. Smeets[1,2], K. Gryllias[1,2], F. Naets[1,2]

[1] Departement of Mechanical Engineering, KU Leuven, Leuven, Belgium, {victor.smeets@kuleuven.be}
[2] Flanders Make@KU Leuven, Leuven, Belgium

1 INTRODUCTION

This abstract presents a parameter identification framework, that identifies the frame friction at the sliding contact interface of a weaving loom system. The proposed method combines measured signals with virtual sensors, derived from a lumped parameter model, in a Linear Least Squares (LLS) formulation to identify the friction model parameters. These identified parameters can subsequently be used for condition monitoring purposes [1]. Future work will investigate the effect of different system model formulations, i.e. flexible multibody, and different nonlinear friction models.

2 EXPERIMENTAL SETUP

The experimental setup is depicted in Figure 1. The system motors are instrumented with internal sensors that measure the motor angle, speed, current and torque at a sampling rate of 1 kHz. Two machine settings are changed throughout the testing: the frame mass, $m = 7.5$ kg or $m = 8.7$ kg, and the frame boundary condition, *Free* or *Clamped*. The dataset contains RPM sweeps for each combination of settings, with the sley speed ranging from 300-1250 rpm. Resulting in a total of 120 runs of approximately 10 seconds each.

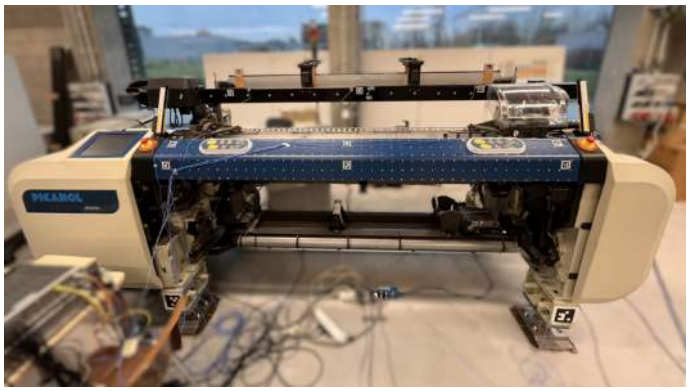

Figure 1: Experimental weaving loom setup

3 MODEL DEFINITION

Three levels of model complexities are available: a lumped parameter model, a rigid multibody model, and a flexible multibody model. This work utilizes the lumped parameter model, constructed in Simcenter Amesim [2], with a custom electromotor model by Asrih [3]. This is computationally efficient and allows for a faster quality estimation, making online applications possible. In addition to measured motor signals, z_m, virtual measurements, z_v, are obtained through the model-based simulation. More specifically, the frame speed is required to model the frictional behavior of the weaving frame.

3.1 Parameter identification

The friction torque is defined as the difference between the measured torque value and the simulated torque:

$$\Delta T = T_{meas} - T_{sim} = A \cdot \rho, \tag{1}$$

with

$$A = [\mathbf{1} \quad \mathbf{v_{frame}} \quad sign(\mathbf{v_{frame}})] \,. \tag{2}$$

This works considers a Coulomb–viscous friction model with static friction term. The formulation is linear with respect to the parameter vector $\boldsymbol{\rho}$, enabling closed-form estimation via LLS. The identified parameters are shown in Fig. 2.

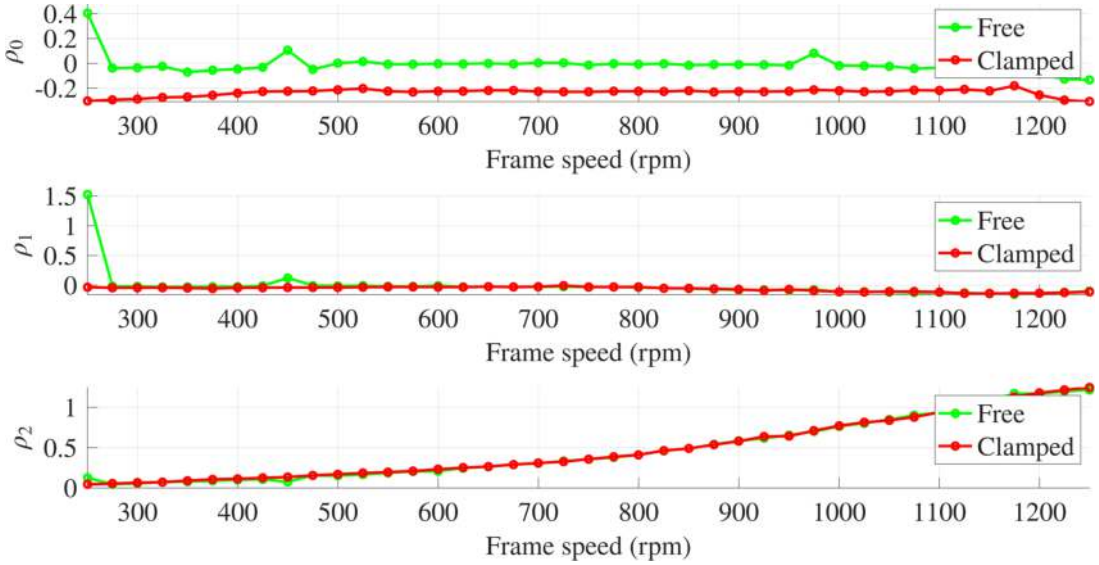

Figure 2: Results friction model parameter identification, ρ_0, ρ_1, and ρ_2 the static friction, viscous friction parameter, and Coulomb friction parameter, respectively

A clear offset is observed in the static torque parameter ρ_0 between the *Clamped* and *Free* boundary conditions. The viscous parameter ρ_1 and the Coulomb friction parameter ρ_2 remain highly consistent across both regimes. However, the estimated Coulomb friction parameter exhibits a dependency on speed, which may be attributed to several factors:

- The Coulomb parameter may be compensating for unmodeled nonlinear velocity effects. This can be investigated by applying more complex friction models, i.e. Stribeck.
- Unmodeled physical effects, such as frame deformation, may alter the normal contact force and thus be reflected in the estimated Coulomb parameter. This hypothesis can be evaluated using a flexible multibody formulation.

ACKNOWLEDGMENTS

Internal Funds KU Leuven are gratefully acknowledged for their support. This research was partially supported by Flanders Make, the strategic research centre for the manufacturing industry.

REFERENCES

[1] F. Angeloni, M. Ermidoro, F. Previdi, and S. M. Savaresi, "A friction estimation approach to fault detection in electromechanical systems," *IFAC-PapersOnLine*, vol. 48, no. 21, pp. 720–725, 2015.

[2] Siemens Digital Industries Software, "Simcenter amesim," https://plm.sw.siemens.com/en-US/simcenter/systems-simulation/amesim/, 2026, commercial system simulation platform.

[3] K. Asrih, W. Desmet, K. Roelstraete, F. Naets, K. L. F. of engineering science. Department of mechanical engineering degree granting institution, and P. G. other, "Flexible multibody dynamics for design optimisation and parameter identification: With application on reciprocating mechanisms," Leuven, 2019. [Online]. Available: https://lirias.kuleuven.be/handle/123456789/643057

ADDITIVELY MANUFACTURED CYCLOIDAL GEARS: COMPARATIVE ANALYSIS OF THREE MATERIALS

Krzysztof Olejarczyk[1], Marcin Wikło[1], Mirosław Rucki[2], Artūras Kilikevičius[2]

[1] Faculty of Mechanical Engineering, Casimir Pulaski Radom University, Stasieckiego 54, 26-600 Radom, Poland, {k.olejarczyk@urad.edu.pl; marcin.wiklo@urad.edu.pl}

[2] Institute of Mechanical Science, Vilnius Gediminas Technical University, Sauletekio al. 11, LT-10223 Vilnius, Lithuania, {m.rucki@urad.edu.pl; arturas.kilikevicius@vilniustech.lt}

1. INTRODUCTION

The cycloidal teeth are known to be stronger than the involute ones [1]. The torque transfer in cycloidal drives involves the rotation of disks with cycloidal profiles, reducing backlash [2]. However, cycloidal gears have to exhibit extremely high geometric accuracy to keep high effectiveness and durability [3]. Numerous AM techniques can be used for gear manufacturing out of various polymer materials [4]. The 3D-printed cycloidal gearbox from PA12CF15 was demonstrated to exhibit cost-effectiveness, low wear, and thus long operating time [5]. However, AM fabrication of the gears is challenging, since it is difficult to ensure the required precision. In the present study, cycloidal gears were 3D-printed using three different materials and their accuracy was compared to the conventionally fabricated structural steel disc.

2. EXAMINED GEARS

The original cycloidal gear was fabricated using electrical discharge machining (EDM) method from the structural steel 32CDV13 usually applied for the components requiring high fatigue and impact resistance. The gear was grinded and underwent thermal treatment to obtain surface hardness of 58±1 HRC. To fabricate the 3D-printed copies of the cycloidal gear, the method of Fused Filament Fabrication (FFF) was chosen. Dual-head printer Raise3D Pro 3 (Raise3, Stafford, TX, US) with electronic lifting system was used. Three copies of the cycloidal gear were printed out of the following materials: PLA, PC, and PA12CF15. Steel nozzle diameter was 0.6 mm, layer height 0.2 mm, and infill density 30%. To prepare digital models, program ideaMaker was applied. Figure 1 presents the gears used for analysis.

(a) (b) (c) (d)

Figure 1. The cycloidal gears used for the analysis made out of the different materials: a) 32CDV13, b) PLA, c) PC, d) Nylon PA12CF15.

The measurements were performed with the scanner GOM Scan 1 MV 400 which works using the blue light technology and fringe projection. In the analysis, the following features were measured and compared:

- The scanned and digitized surface was compared with the CAD model.
- The nominal element was set on the maximal distance of 10.00 mm, importing tolerances from the CAD project.
- All the intersections of the profile were projected to the plane Z, according to the respective reference coordinate systems for each object.
- A cone was built at all chamfer locations on the parts to determine the chamfer angle. It was created on the CAD model and then compared to the measured model using the Gaussian best-fit method for all measurement points.
- The relevant angles of the gear were built at the xyz direction and compared with the tolerances of the CAD model.
- Width of the gear was measured at 1% clearance and 1 mm radius of the measuring jaws in relation to the Z-axis direction.

- The openings and their positioning, as well as the epicycloid profile curves were analyzed based on the cylindrical surfaces. For the openings, the Gaussian best-fit method was applied, while the epicycloid vertex was calculated using the minimal circumscribed element method related to the Z-axis direction. In turn, the epicycloid valleys were calculated using the maximal inscribed element method related to the Z-axis.
- The diameter of the pattern of holes' axes was calculated using the Chebyshev minimum zone fitting method with the center location for the associated Z-axis line.
- Out-of-cylindricity values for the holes were based on the tolerances specified in the documentation, input manually.

3. RESULTS AND DISCUSSION

Figure 2 presents the example of the measurement results in form of deviations measured in the intersection plane for the gear PA12CF15. From the presented data it can be concluded that 3D-printed PA12CF15 exhibited comparable accuracy to the EDM-fabricated original cycloidal gear 32CDV13. However, other geometrical parameters did not fit as good, for instance, deviations of the orifice diameters presented in Table 1.

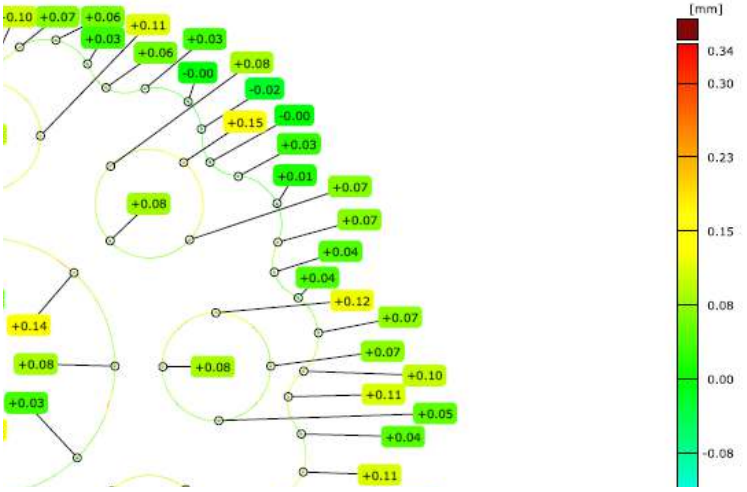

Figure 2. Example of the graphic presentation of the measurement results for PA12CF15.

Table 1. Deviations of the orifice diameters.

	Material	Average deviation [mm]	Deviations range [mm]	Remarks
1	PLA	≈ 0.15	−0.17 ÷ +0.13	Dimensionally stable, slight asymmetry to positive values
2	PC	≈ 0.18	−0.23 ÷ −0.15	Larger dispersion, narrower diameters
3	PA12CF15	≈ 0.17	−0.20 ÷ −0.14	Steady, negative values of the deviations, high repeatability between two specimens
4	32CDV13	≈ 0.01	−0.06 ÷ +0.01	Very high dimensional accuracy

4. CONCLUSIONS

It can be concluded from the obtained data, that PLA material can be used for the prototyping, but it requires dimensional compensations when higher accuracy is required. In turn, PC copy required correction of the CAD model, since the systematical errors of the diameters could be problematic for the assembling process. PA12CF15 exhibited high homogeneity and predictability, which is important for the fabrication of the cycloidal drive components. 32CDV13 original exhibited very small deviations with very small dispersion.

REFERENCES

[1] D. Petrov, P. Dobrev, S. Alexiev, "Experimental comparison of wear resistance and cyclic loading to bending between cycloid and involute gears", *Proceedings of the International Conference on Engineering, Technologies and Systems*, Technical University – Sofia, Bulgaria, May 26–28, 2016.

[2] R. Król, "Analysis of the backlash in the single stage cycloidal gearbox". *Archive of Mechanical Engineering*, 69(4), 693–711, 2022.

[3] J. Mo, X. Gong, S. Luo, S. Fu, X. Chang, L. Liao, "Geometric design and dynamic characteristics of a novel abnormal cycloidal gear reducer". *Advances in Mechanical Engineering*, 15(3), 1–14, 2023.

[4] G. Budzik and J. Pisula, "Additive manufacturing of polymer gears". In: S. Thomas, M. Huskić, H.J. Maria, J. Tavćar (Eds.), *Polymer Gears*. Amsterdam, 2025, pp. 375–397. https://doi.org/10.1016/B978-0-443-21457-8.00018-2

[5] C. Barsomian, N.B.P. Eswaran, M. Pesenti, M. Gandolla, F. Braghin, E. Carpanzano, L. Roveda, "Dynamic characterization and control of a back-support exoskeleton 3D-printed cycloidal actuator". *CIRP Annals*, 73(1), 29–32, 2024.

TOPOLOGY OPTIMIZATION AND ASSEMBLY DYNAMICS OF A LARGE SPACE STRUCTURE VIA HETEROGENEOUS MODULES

Jialiang Sun[1], Quanchen Duan[1], Dingfeng Ding[1]

[1] Nanjing University of Aeronautics and Astronautics, No. 29, Yudao Street, Nanjing 210016, China, {sunjialiang@nuaa.edu.cn; duanquanchen@nuaa.edu.cn; dfding@nuaa.edu.cn}

1. INTRODUCTION

The construction of large-scale space infrastructure, such as space telescopes, large antenna arrays and solar power stations, faces significant constraints from launch vehicle volume limits. With an increasing demand for large-scale space missions, on-orbit assembly of modular and deployable mechanisms has emerged as a promising strategy for large space structures [1-2]. However, the modules for large space structures are usually designed as homogeneous ones, which may lead to mass redundancy and weak dynamic performance. As an advanced structural design approach, topology optimization can effectively reduce redundant mass and improve material utilization while maintaining mechanical performance [3]. This makes it highly compatible with the development requirements of aerospace engineering and highlights its broad application prospects. Therefore, in this work, we try to simultaneously optimize the large space structure and corresponding assembly modules via a multiscale topology optimization and validate the dynamic performance of the modules via a flexible multibody dynamic simulation and micro-gravity experiment.

2. MULTISCALE TOPOLOGY OPTIMIZATION

Under the macroscopic and microscopic volume constraints, the multiscale topology optimization problem of macroscopic and microscopic concurrent design with minimum compliance as the objective function can be expressed as

$$\begin{aligned} &\text{find} && \mathbf{x}_M, \mathbf{x}_m \\ &\text{to minmize} && J(\mathbf{x}_M, \mathbf{x}_m) = \frac{1}{2}\mathbf{U}_M{}^{\mathrm{T}}\mathbf{K}_M(\mathbf{x}_M, \mathbf{x}_m)\mathbf{U}_M \\ &\text{subject to} && \mathbf{K}_M(\mathbf{x}_M, \mathbf{x}_m)\mathbf{U}_M = \mathbf{F}_M \\ & && \mathbf{K}_m(\mathbf{x}_m)\mathbf{U}_m = \mathbf{F}_m \\ & && V_M(\mathbf{x}_M)/V_0 - V_{\max} \le 0 \\ & && v_M(\mathbf{x}_m)/v_0 - v_{\max} \le 0 \\ & && 0 \le x_M^i \le 1; 0 \le x_m^j \le 1 (i = 1,2,\cdots,N_M; j = 1,2,\cdots,N_m) \end{aligned} \tag{1}$$

where the objective function J represents the compliance of the structure to be optimized. The macroscopic design domain and the microscopic design domain are discretized into N_M and N_m finite elements, respectively. The element densities x_M^i and x_m^j of the two scales are selected as the design variables, where x_M^i determines the macroscopic scale topology, while x_m^j determines the microscopic scale topology. x_m^j also affects the macroscopic scale material properties. $\mathbf{U}_m$ and $\mathbf{F}_m$ are respectively the global displacement vector and the external force vector under test strain. During the optimization process, volume constraints at the two scales must be satisfied, that is, the total volume consumption of the two scales is required to be less than the prescribed maximum volume fraction $V_{\max}$ and $v_{\max}$. $V_M(\mathbf{x}_M)$ and $v_M(\mathbf{x}_m)$ are the current volume of the two scales. V_0 and v_0 are the maximum admissible volume of the two scales. Finally, all the macroscopic and microscopic design variables are between 0 and 1.

3. OPTIMIZATION RESULTS

Figure 1 illustrates the multiscale topology optimization results of a parabolic antenna, which is simplified as a hexagonal design domain with various hexagonal modules. From this figure, we can observe that for such a large space structure, the topology of the modules keeps invariant with different numbers of modules. With an increasing number of modules, the stiffness of the large space structure will increase as well. More modules, however, will definitely increase the cost for manufacturing and the complexity for on-orbit assembly.

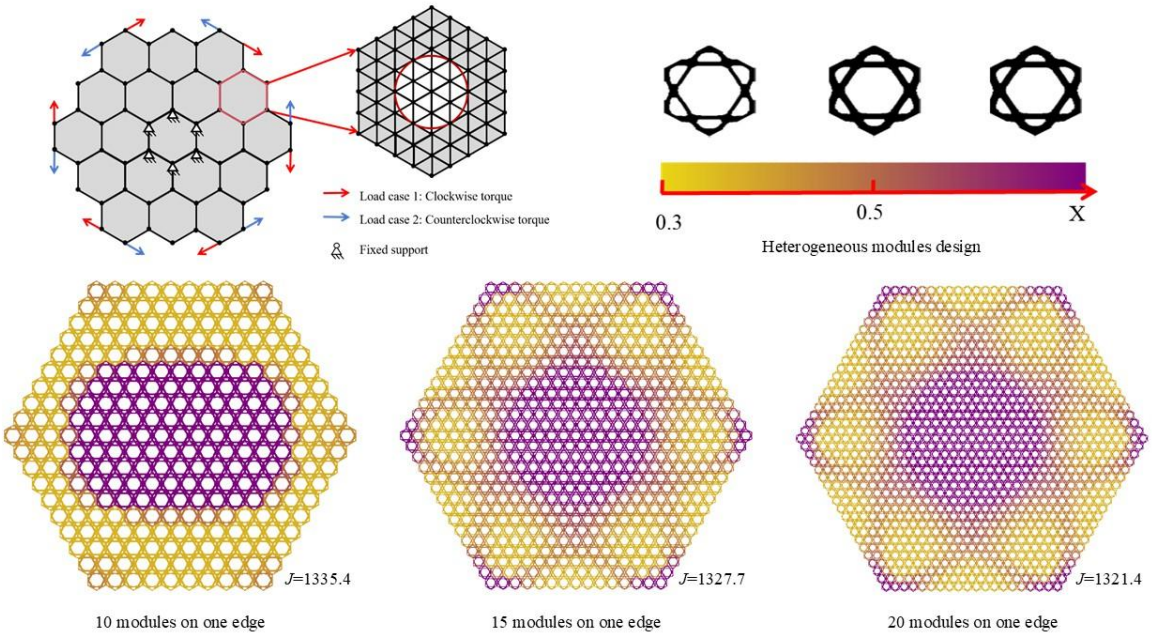

Figure 1. Topology optimization results for a parabolic antenna with different numbers of modules.

4. ASSEMBLY DYNAMICS VALIDATIONS

To validate the assembly dynamics of a module, a flexible multibody dynamic model for the morphing module is established and corresponding micro-gravity experiments are conducted to demonstrate the whole assembly process including of geometric error measurement, morphing control, motion control, docking and locking, as shown in Figure 2.

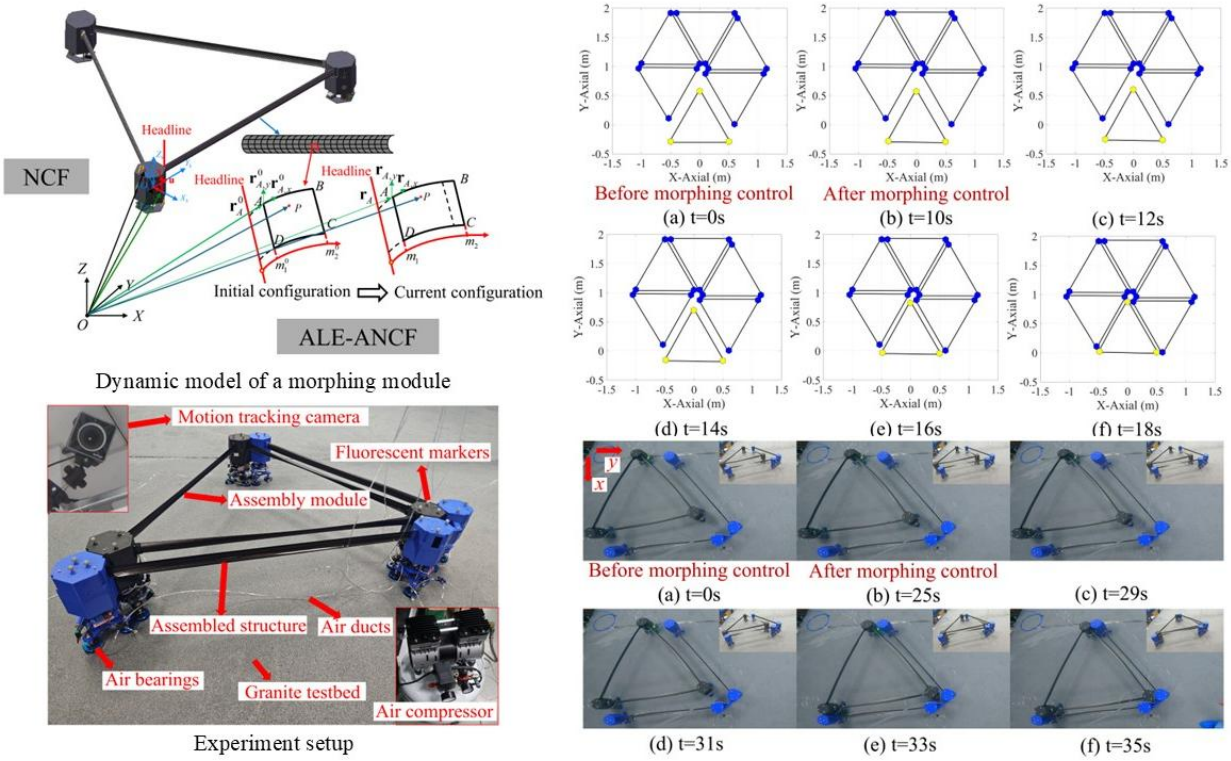

Figure 2. Dynamic simulations and micro-gravity experiments for the assembly dynamics of a morphing module.

REFERENCES

[1] X. Ma, T. Li, J. Ma, et al., “Recent advances in space-deployable structures in China”. *Engineering*. 17, 207-19, 2022.

[2] Q. Duan, C. Tang, J. Sun, et al., “Design and dynamics of a deployable assembly module via rollable booms”. *Acta Astronautica*, 225, 634-655, 2024.

[3] J. Sun, H. Hu, “Dynamic topology optimization of flexible multibody systems”. *Nonlinear Dynamics*, 112(14), 11711-11743, 2024.

DESIGN AND VALIDATION OF AN IMPEDANCE-CONTROLLED ROBOTIC SYSTEM FOR BIOMECHANICAL JOINT CHARACTERIZATION

Lorenzo Maggi[1], Matilde Tomasi[1], Nicola Secciani[2], Benedetto Allotta[2], Alessio Artoni[3]

[1] R&D Department, Orthokey Italia S.r.l., 50127, Florence, Italy, {l.maggi@orthokey.eu; m.tomasi@orthokey.eu}
[2] Department of Industrial Engineering, Università di Firenze, 50139, Florence, Italy, {nicola.secciani@unifi.it; benedetto.allotta@unifi.it}
[3] Department of Civil and Industrial Engineering, Università di Pisa, 56122, Pisa, Italy, {alessio.artoni@unipi.it}

1 INTRODUCTION

Objective biomechanical characterization of biological joints poses significant engineering challenges due to their highly coupled multi–Degree-of-Freedom (DoF) kinematics and nonlinear stiffness profiles. Conventional techniques for evaluating joint mobility suffer from poor repeatability and rely on subjective force application by the operator during the maneuver [1]. This work presents the mechanical design, control architecture, and experimental validation of a novel collaborative robotic framework engineered for automated, highly repeatable joint laxity and stiffness profiling. By integrating advanced force control with real-time optical tracking, the system applies standardized dynamic loads while actively accommodating the natural kinematic constraints of the investigated joint. In this work, the knee joint was chosen as a case study to demonstrate the system's capability for precise varus–valgus (VV) laxity and stiffness assessment. Such robotic framework has potential applications in orthopedics, biomechanics, and rehabilitation, with possible extension to other joints.

2 MATERIALS AND METHODS

The proposed robotic framework integrates three subsystems: the actuation hardware, the optical tracking system, and the impedance control architecture (Fig. 1-C). Core actuation is provided by a 7-DoF collaborative manipulator (KUKA LBR Med 14), while a custom end-effector (EE) with orthogonal translation stages and quick-acting cam levers ensures secure adaptation to patient-specific joint geometries without rigid over-constraint (Fig. 1-A/B). Real-time tracking is achieved with an optical infrared camera (NDI Polaris Vega ST), continuously updating anatomical and robotic reference frames via reflective markers, allowing the control loop to compensate for unconstrained bone motion or external disturbances. Sub-millimeter registration is achieved through a simultaneous world–hand–eye calibration [2], which, combined with the manipulator's forward kinematics, provides continuous estimation of the EE pose relative to the anatomical frames defined from bony landmarks according to the ISB recommendations [3]. Safe human–robot interaction is ensured by a Cartesian impedance control strategy (KUKA SmartServo) following Eq. (1):

$$\mathbf{F}_{\text{ext}} = \mathbf{K}_d(\mathbf{x}_d - \mathbf{x}) + \mathbf{D}_d(\dot{\mathbf{x}}_d - \dot{\mathbf{x}}) \tag{1}$$

where: $\mathbf{F}_{\text{ext}}$ is the desired robot wrench, $\mathbf{K}_d$ is the anisotropic stiffness matrix, $\mathbf{D}_d$ is the damping matrix, $\mathbf{x}_d$ is the desired pose, and $\mathbf{x}$ is the actual flange pose. High stiffness (5000 N/m translational, 300 Nm/rad rotational) applied along loading directions preserves positional accuracy, while low stiffness and near-zero impedance (400 N/m, 20 Nm/rad) applied to coupled physiological DoFs prevents joint overstress. The system operates in two modes: *Operator-Guided Trajectory Learning*, where passive physiological motion trajectories performed by the operator are tracked by the camera and then replicated by the robot; *Autonomous Impedance Profiling*, where the robot applies standardized multi-axis loads at predefined angular targets while continuously enforcing safety constraints. In this work, the knee joint was used as a case study to assess stiffness k_{VV} (Nm/deg) in the VV direction:

$$k_{\text{VV}} = \frac{\Delta\tau_{\text{VV}}}{\Delta\theta_{\text{VV}}} = \frac{\max(\tau_{\text{VV}}) - \min(\tau_{\text{VV}})}{\max(\theta_{\text{VV}}) - \min(\theta_{\text{VV}})} \tag{2}$$

where: $\Delta\tau_{\text{VV}} = F_{\text{ML}} d_z$ is the variation in torque applied by the EE (F_{ML} is the medio-lateral force recorded by the EE and d_z its lever arm), and $\Delta\theta_{\text{VV}}$ is the variation in angular displacement (tracked by the camera). System performance was assessed in three stages: (i) benchtop testing of robotic force accuracy against a calibrated universal testing machine; (ii) in-vitro evaluation of kinematic tracking on a knee surrogate using an external motion capture (MoCap) system as ground truth (Fig. 1-C); (iii) ex-vivo experiment on anatomical specimen to evaluate operational feasibility and sensitivity to stiffness variations under progressively altered joint conditions, including soft tissue resection. In the last two stages, experiments were reproduced under both the operation modes.

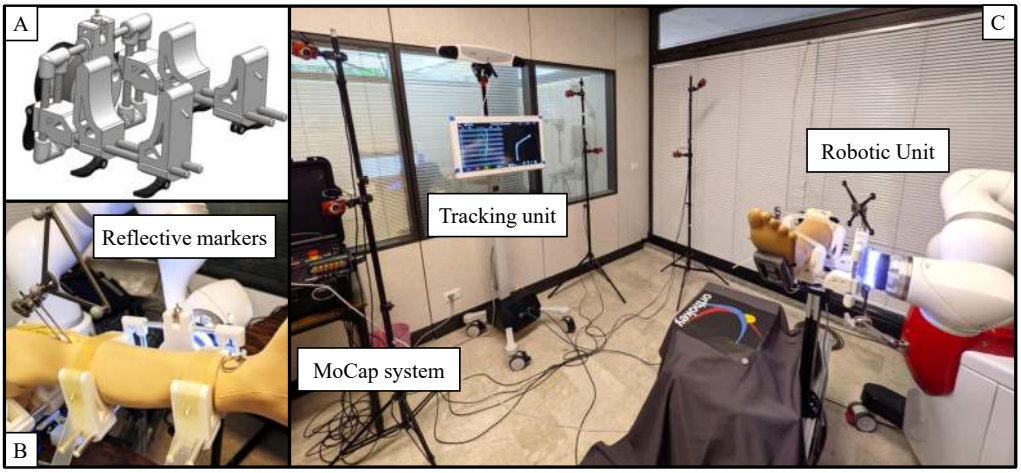

Figure 1: A-B) EE close-up. C) Experimental setup for in-vitro validation including the 7-DoF manipulator, the knee joint surrogate, the optical tracking unit, and the MoCap system.

3 RESULTS AND CONCLUDING REMARKS

Benchtop testing revealed sub-Newton repeatability in torque and force application across 100 consecutive cycles. In-vitro kinematic validation showed that the robotic spatial reconstruction closely matched the external motion capture ground truth, with angular discrepancies consistently below 1 degree over the full range of motion. Ex-vivo experiments demonstrated the robot's capability to replicate the recorded knee angle trajectories (Fig. 2-A) and to extract multi-dimensional joint laxity (Fig. 2-B) and stiffness profiles (Fig. 2-C), revealing systematic changes in response to structural modifications such as increased laxity and reduced stiffness following anterior cruciate ligament (ACL) removal. The obtained results revealed high intra-specimen repeatability and sensitivity in distinguishing structural joint states, supporting the system's role as an objective biomechanical measurement tool. The proposed mechatronic framework translates complex joint assessment into a deterministic and quantifiable robotic task through anisotropic Cartesian impedance control combined with real-time tracking, enabling controlled load application alongside coupled joint kinematics. Despite limitations related to invasiveness and laxity assessment mainly in the VV direction, the platform offers a basis for more standardized, operator-independent joint characterization in research and applied biomechanics.

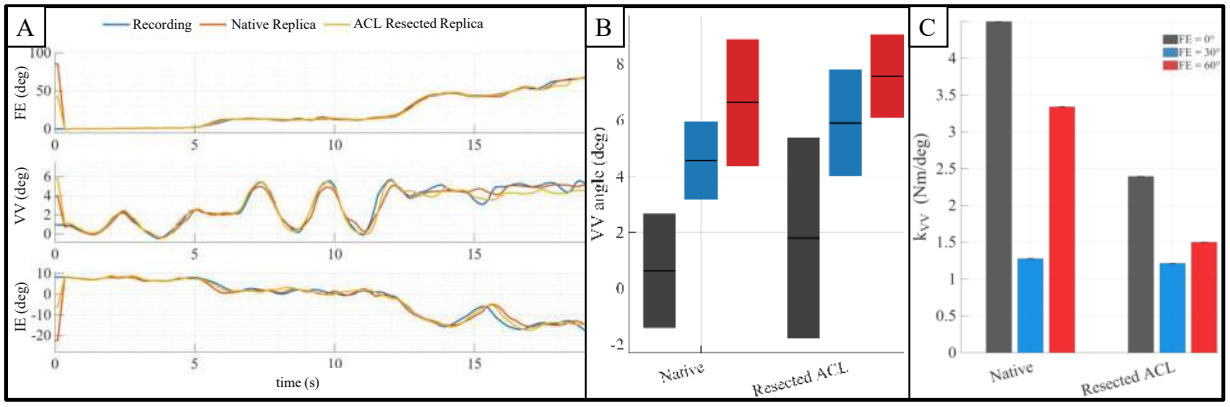

Figure 2: Experimental validation results: (A) knee joint angle trajectories (flexion-extension (FE), varus-valgus (VV), int-ext rotation (IE)); (B) knee joint laxity (VV angle), (C) knee joint stiffness (k_{VV}). (A) was obtained under *Operator-Guided Trajectory Learning*, while (B) and (C) under *Autonomous Impedance Profiling*.

REFERENCES

[1] M. Ahldén, *et al.*, "Dynamic knee laxity measurement devices", *Knee Surg. Sports Traumatol. Arthrosc.*, 20(4), 621-632, 2012.

[2] A. Li, *et al.*, "Simultaneous robot-world and hand-eye calibration using dual-quaternions and Kronecker product", *Int. J. Phys. Sci.*, 5(10), 1530–1536, 2010.

[3] G. Wu, *et al.*, "ISB recommendation on definitions of joint coordinate system of various joints for the reporting of human joint motion—Part I: ankle, hip, and spine", *J. Biomech.*, 35(4), 543–548, 2002.

THERMO-MECHANICAL MODELLING OF HYBRID POLYMER GEARS

Rui E.F. Mouzinho[1,2], Stephane Portron[1], Carlos M.C.G. Fernandes[1,2]

[1] INEGI, Rua Dr. Roberto Frias 400, Porto, 4200-465, , Portugal {rmouzinho@inegi.up.pt; sportron@inegi.up.pt; cfernandes@inegi.up.pt}
[2] FEUP, Rua Dr. Roberto Frias s/n, Porto, 4200-465, , Portugal {cfernandes@fe.up.pt}

1 INTRODUCTION

Polymer gears are gaining relevance in power transmission applications. However, high performance materials or specific gear designs are required to achieve such goal. In previous works [1, 2], a hybrid polymer gear concept was proposed to improve thermal behaviour and consequently increase the load-carrying capacity of polymer gears. The concept involves overmoulding a polymer material over a metallic insert, made of a thermally conductive material with higher stiffness than the polymer. An example of such concept is presented in Fig. 1.

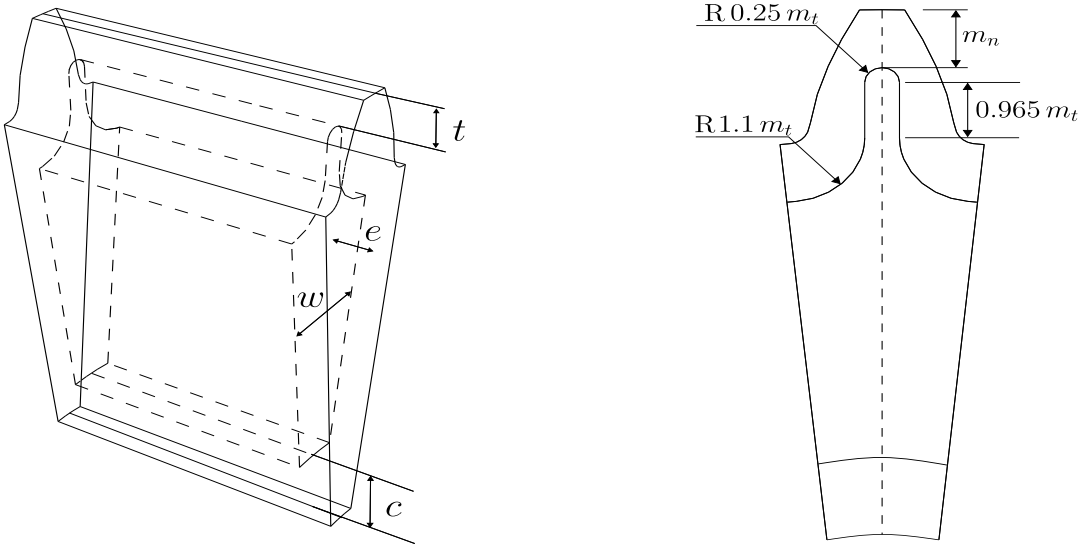

a) Hybrid polymer gear concept

b) Hybrid polymer gear tooth geometry

Figure 1: Hybrid polymer gear - concept and tooth geometry.

2 METHODOLOGY

The present work presents a methodology to characterize the thermal and mechanical behaviour of both standard and hybrid polymer gears based on different modeling strategies: analytical mechanical model coupled with a semi-analytical thermal model[3] or a fully numerical thermo-mechanical model. To achieve those models, an analytical model is proposed based on loaded tooth contact analysis (LTCA), flank and tooth root stress calculation of hybrid polymer gears (Fig. 2).

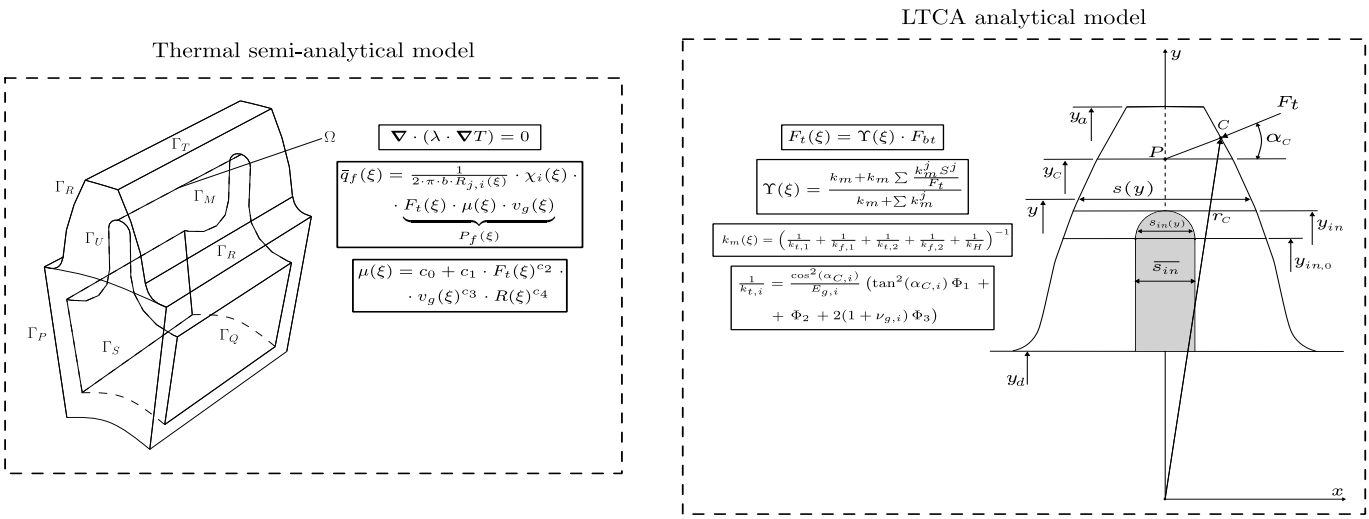

Figure 2: Thermal and mechanical analytical model formulation.

Subsequently, this model serves as input to a numerical model, completing a semi-analytical strategy, whose process can be visualized in the flowchart of Figure 3. The fully numerical thermo-mechanical model consists on a parametric numerical model allowing to verify the accuracy of the semi-analytical approach.

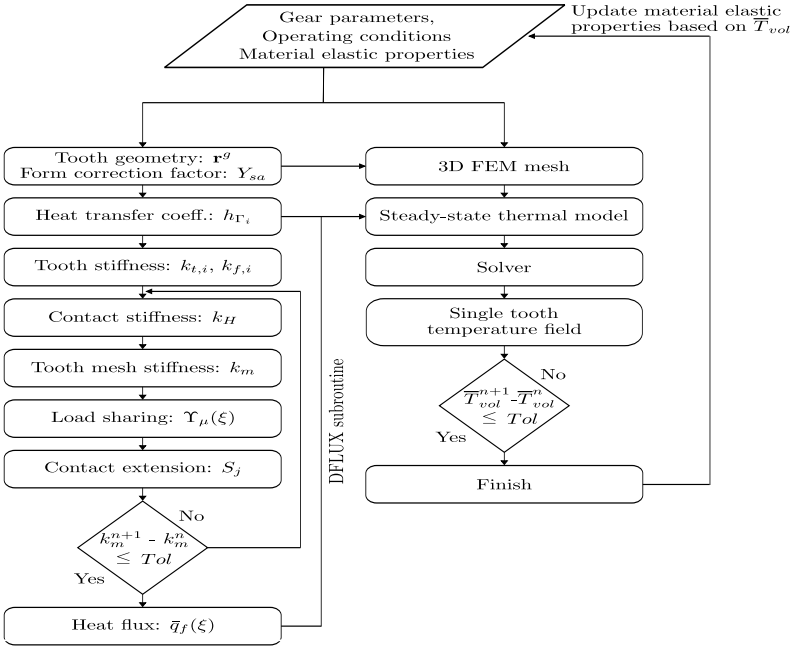

Figure 3: Flowchart of the semi-analytical thermo mechanical approach.

3 CONCLUSIONS

Preliminary results seem to evidence that the addition of the metallic insert in the polymeric matrix tend to lower average tooth temperature, improving fatigue response in the contact and tooth root regions. The average stiffness also increases, which lowers tooth deformation and tooth flank wear.

REFERENCES

[1] Carlos M. C. G. Fernandes et al., "Hybrid Polymer Gear Concepts to Improve Thermal Behavior", in *Journal of Tribology*, vol. 141, 2008.

[2] James D.S. Hooton and David E.P. Gonçalves and Carlos M.C.G. Fernandes, "Experiments and finite element analysis on a hybrid polymer gear rack", in *Mechanism and Machine Theory*, vol. 186, 2023.

[3] Carlos M. C. G. Fernandes et al., "Finite element method model to predict bulk and flash temperatures on polymer gears", in *Tribology International*, vol. 120, 2018.

AN ALE-SE(3) BEAM FORMULATION FOR THE SIMULATION OF CABLE-DRIVEN SOFT ROBOTS

Olivier Devigne, Olivier Brüls

University of Liège, Allée de la Découverte 9, 4000 Liège, Belgium, {o.devigne@uliege.be; o.bruls@uliege.be}

1 INTRODUCTION

Cable-driven actuation plays a central role in various applications such as soft robotics or deployable structures. In many practical systems, cables are routed through pulleys, sleeves, eyelets, or internal cavities, where they remain in permanent contact with the surrounding structure over small, localized and *a priori* known regions. Outside these contact zones, the cables are often free of interaction. This coexistence of localized sliding or guiding contact and free deformation poses significant challenges for numerical models.

In classical finite element formulations based on a purely Lagrangian description, resolving contact regions accurately requires a fine spatial discretization of the cable. In these formulations, the motion of the nodes through the contact interfaces can also be a source of numerical artefacts. Applying a uniformly fine mesh to the entire cable is computationally inefficient, especially when contact is confined to a few small regions on the robotic structure. These limitations motivate the development of alternative formulations better suited to sliding interactions.

In this work, we propose to combine a geometrically exact beam model formulated on the Lie group $SE(3)$ with an arbitrary Lagrangian–Eulerian (ALE) description of the cable. The key objective is to provide a consistent and efficient framework for the simulation of cable-driven soft robots undergoing large deformations, while accurately representing localized sliding contact conditions.

2 GEOMETRICALLY EXACT BEAM FORMULATION ON $SE(3)$

The proposed model relies on a geometrically exact beam formulation defined on the Lie group $SE(3)$ [1]. While the $SE(3)$ formalism is classically considered for the kinematic description of rigid body systems [2], it also provides a natural representation of the configuration space of slender deformable structures. Each cross-section of the cable is described by a frame $\mathbf{H}(s) \in SE(3)$ where s denotes the material coordinate along the reference configuration. The frame encodes both the centerline position and the orientation of the cross-section.

This Lie group representation offers several advantages. It provides a coordinate-free and geometrically exact description of large rotations. Strain measures are naturally obtained by differentiation with respect to the material coordinate s and are expressed as elements of the Lie algebra $\mathfrak{se}(3)$. The components of these strain measures coincide with the axial, shear, torsional and bending strains of the classical beam theory. Furthermore, the equilibrium equations can be written in the local frame (attached to the cross-section) rather than in a global inertial frame.

The spatial discretization also relies on geometrically-consistent operations on $SE(3)$, leading to a robust and locking-free finite element model. This geometrically exact setting forms the starting point for the proposed ALE extension.

3 ALE BEAM FORMULATION

To efficiently handle sliding contact at known locations, we introduce an arbitrary Lagrangian–Eulerian description of the cable. The motivation is to decouple the material motion from the spatial discretization in selected regions. At a given referential or mesh coordinate ξ, the beam can undergo both a spatial motion represented by the mapping $\mathbf{H} = \boldsymbol{\varphi}_{\mathbf{H}}(\xi)$ and a material motion represented by the mapping $s = \Phi_s(\xi)$.

In the present context, the ALE formulation allows to fix some nodes of the cable with respect to the robot structure in predefined contact regions. Mathematically, this condition is defined by constraining the spatial motion for these referential coordinates:

$$\mathbf{g}_{\mathbf{H}}(\boldsymbol{\varphi}_{\mathbf{H}}(\xi)) = \mathbf{0}_{6\times 1} \tag{1}$$

In these regions, the mesh is attached to the structure, while the cable material is allowed to flow through the nodes, i.e., the mapping $\Phi_s(\xi)$ is unconstrained. Out of these contact regions, the cable follows a standard Lagrangian description, where nodes move with the material.

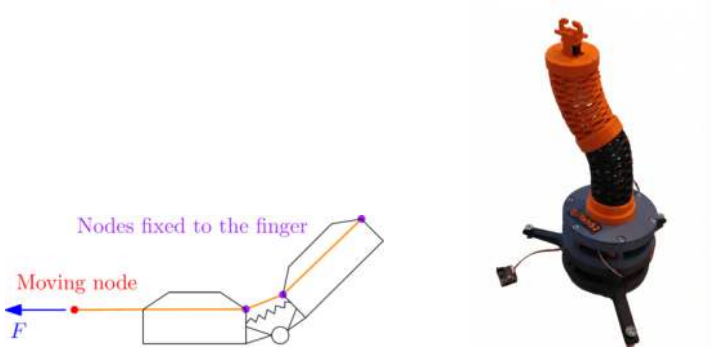

Figure 1: Left: 2D finger model for a robotic hand. Right: 3D model of a soft robot

In a quasi-static setting, the governing equations are derived from the principle of virtual work. The total variation of the potential energy includes contributions from both spatial variations (with fixed material coordinate) and material variations (with fixed spatial coordinate)

$$\delta\mathcal{W} = \delta_{\mathbf{H}}\mathcal{W} + \delta_s\mathcal{W} \tag{2}$$

This decomposition reflects the dual nature of the ALE description. The resulting equations form a coupled system involving spatial equilibrium and configurational (material) equilibrium. This structure is consistent with previously developed ALE cable models [3] and is here extended to the geometrically exact beam setting. Finally, we will show in the presentation that Coulomb friction can be introduced between the cable and the contact point or the guiding element (e.g., a pulley or a slider) using an augmented Lagrangian formulation, allowing the simulation of transitions between sticking and sliding conditions.

4 EXAMPLES

The proposed formulation will be illustrated for elementary test problems of a cable interacting with simple components, such as sliders, pulleys or eyelets. These tests permit some comparisons of the numerical results with analytical solutions and with results from the literature. Then, some results will be shown for cable-actuated robotic systems, such as a 2D finger model for a robotic hand and a 3D model of a soft robot, as shown in Fig. 1.

5 CONCLUSION

We present a geometrically exact ALE beam formulation on $SE(3)$ tailored to the simulation of cable-driven soft robots. The method efficiently captures sliding and sticking contact at predefined contact points while preserving a consistent large-deformation kinematic framework. It relies on a combination of methods from multibody dynamics, geometrically exact beam theory, and ALE methods, and offers a robust basis for the modeling of complex cable-routing mechanisms in soft robotic systems. Future work will focus on dynamic extensions and on the integration of detailed structural models of the soft robot.

REFERENCES

[1] V. Sonneville, A. Cardona and O. Brüls, "Geometrically exact beam finite element formulated on the special Euclidean group SE(3)". *Computer Methods in Applied Mechanics and Engineering*, vol. 268, pp. 451–474, 2014.

[2] K.M. Lynch and F.C. Park, *Modern Robotics: Mechanics, Planning, and Control*. Cambridge University Press, 2017.

[3] O. Devigne, A. Cosimo and O. Brüls, "A quasistatic ALE cable formulation for multibody systems applications". *Multibody System Dynamics*, vol. 65, no. 2, pp. 173–201, 2025.

ENHANCING SNAKE ROBOT STIFFNESS IN CONFINED SPACES: POSE OPTIMIZATION WITH OBSTACLE AVOIDANCE

Y. Zhao[1], P. D. Maddio[2], A. Cammarata[2], R. Sinatra[2], Y. Tian[3], F. Xi[4]

[1] School of Mechanical Engineering, University of Shanghai for Science and Technology, Shanghai 200093, China, {zhaoyinjun@usst.edu.cn}
[2] Dipartimento di Ingegneria Civile e Architettura, University of Catania, Via S.Sofia 64, 95123, Catania, Italy, {pietro.maddio@unict.it; alessandro.cammarata@unict.it; rosario.sinatra@unict.it}
[3] School of Mechatronic Engineering and Automation, Shanghai University, Shanghai 200444, China, {troytian@shu.edu.cn}
[4] Department of Aerospace Engineering, Ryerson University, Toronto, ON M5B 2K3, Canada, {fengxi@torontomu.ca}

1 INTRODUCTION

Snake robots offer exceptional shape adaptability in unstructured environments, surpassing traditional manipulators in confined-space applications [1]. However, their slender structure inherently compromises end-effector operational stiffness, limiting them to light-load tasks such as inspection, welding, or minimally invasive surgery. Recent research has explored various methods to enhance end-effector stiffness, primarily focusing on different mechanism configurations, locking components, or variable stiffness techniques from soft robotics [2]. While effective to varying degrees, these approaches predominantly address the issue through structural design. Critically, even with inherently stiff joints, the end-effector stiffness of a snake arm exhibits substantial variation across different configurations. Therefore, planning the snake-arm's pose to achieve optimal end-effector stiffness is essential for high-precision, load-bearing operations. A secondary challenge arises when seeking an optimal stiffness pose within constrained spaces: the potential conflict between stiffness-based pose planning and obstacle avoidance. This work proposes a bio-inspired three-stage motion strategy and a constrained pose optimization method to enhance operational stiffness while ensuring collision-free operation.

In this work, we decompose the task into three sequential stages: (1) obstacle-avoiding navigation using Serial Mechanism Motion Modes (SMMMs) with follow-the-leader control; (2) precise end-effector positioning through Parallel Mechanism Motion Modes (PMMMs); and (3) stiffness-optimized pose adjustment. The strategy is implemented on a modular snake arm comprising five underactuated Variable Geometry Truss Mechanism (VGTM) modules mounted on a 2-DOF mobile platform. Each module integrates two diagonal lockable prismatic joints and two axial linear actuators, enabling reconfigurable kinematics. In SMMMs, locked P joints and moving platforms serve as rigid links connected by R joints, forming equivalent serial robots whose kinematics is modeled via the Product of Exponentials (POE) formulation. In PMMMs, each VGTM functions as a parallel manipulator achieving 3-DOF control through a two-step motion topology switching process.

Once the end-effector reaches its target pose $(p^*_{\mathrm{EE}}, \theta^*_{\mathrm{EE}})$, the robot exploits its kinematic redundancy to maximize structural stiffness. The optimization variables are the link lengths $\mathbf{x} = [L_1^1 \dots L_4^5]^{\mathrm{T}}$, and the cost function minimizes weighted end-effector displacements under external loads:

$$f_{\mathrm{stiff}}(\mathbf{q}(\mathbf{x})) = w_1|d_{x_{EE}}| + w_2|d_{y_{EE}}| + w_3 L_c|\phi_{EE}| \tag{1}$$

where $d_{x_{EE}}$, $d_{y_{EE}}$, and ϕ_{EE}, respectively, are the displacements of the end-effector along the x, y directions and the rotation of the end-effector coming from the deformation obtained from the elastostatic relation $\mathbf{K}(\mathbf{x})\mathbf{q} = \mathbf{F}_{\mathrm{ext}}$, as described by the same authors in [3], and L_c is a characteristic length ensuring dimensional homogeneity. In realistic confined space applications, the workspace is significantly constrained by surrounding obstacles. These physical boundaries restrict the feasible configuration space, requiring the stiffness optimization to account for collision avoidance. To address this challenge, a penalty-based obstacle avoidance strategy is integrated directly into the objective function.

Obstacles are discretized into sequences of points and topologically classified as intrados or extrados relative to the robot's initial configuration, based on their distance to the lower and upper actuator segments of each module. This classification must be preserved throughout the reconfiguration: transitioning an obstacle from one side to the other would require the robot to pass through it, which is physically impossible. The complete optimization problem is

formulated as:

$$\begin{aligned} \min_{\mathbf{x}} \quad & f_{\text{stiff}}(\mathbf{q}(\mathbf{x})) + \sum_{n=1}^{N_{\text{mod}}} \sum_{\eta=1}^{N_{\text{obs}}} P^{n,\eta}(\mathbf{q}(\mathbf{x})) \\ \text{subject to:} \quad & \mathbf{p}_{\text{EE}}(\mathbf{x}) = \mathbf{p}^*_{\text{EE}}, \quad \theta_{\text{EE}}(\mathbf{x}) = \theta^*_{\text{EE}} \\ & L_{\min} \leq L^n_j \leq L_{\max}, \quad \forall n, j \end{aligned} \tag{2}$$

where $P^{n,\eta}$ is the penalty for module n and obstacle point η, equality constraints enforce the desired end-effector pose, and inequality constraints reflect the stroke limits of actuators and lockable joints.

A case study involving drilling operations inside an aircraft wing-box validates the approach, as shown in Fig. 1. The manipulator first navigates through the access hole using follow-the-leader control, then performs localized configuration optimization under discrete boundary constraints defined by the wing-box internal surfaces. With optimization weights $w_1 = 0.80$, $w_2 = 0.10$, $w_3 = 0.10$ prioritizing stiffness along the x-direction, end-effector displacements under load are reduced from $[1.62 \times 10^{-2}, 6.64 \times 10^{-3}, 4.84 \times 10^{-2}]$ to $[1.21 \times 10^{-2}, 5.34 \times 10^{-3}, 4.19 \times 10^{-2}]$ (m, m, rad), corresponding to approximately 25%, 20%, and 13% improvement in x, y, and θ directions, respectively. These results demonstrate significant stiffness enhancement while maintaining safe clearances from obstacles throughout the reconfiguration process.

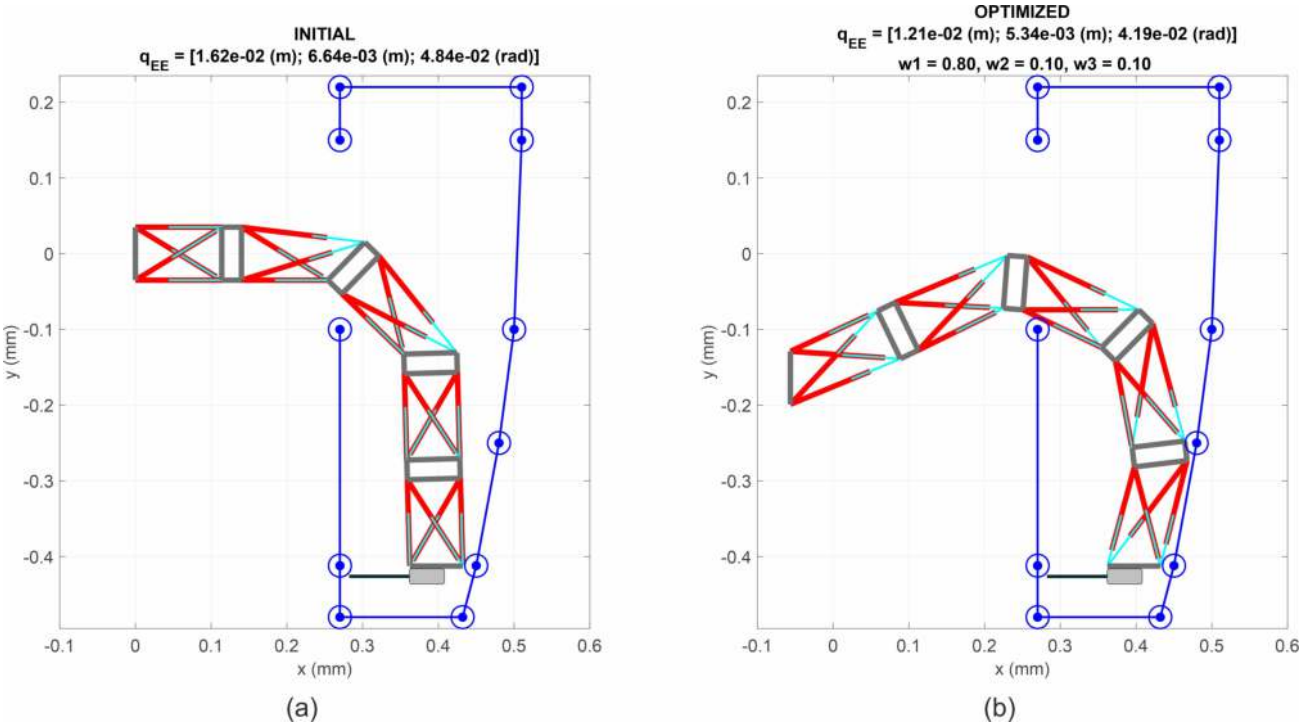

Figure 1: Wing-box case study: (a) initial configuration after obstacle-avoidance navigation; (b) optimized configuration for stiffness enhancement.

REFERENCES

[1] Z. Mu, L. Zhang, L. Yan, Z. Li, R.Dong, C. Wang, N. Ding, "Hyper-Redundant Manipulators for Operations in Confined Space: Typical Applications, Key Technologies, and Grand Challenges". *IEEE Trans. Aerosp. Electron. Syst.*, Vol. 58, No. 6, pp. 4928–4937, 2022.

[2] D.G. Chung, J. Kim, D. Baek, J. Kim, D.-S. Kwon, "Shape-Locking Mechanism of Flexible Joint Using Mechanical Latch with Electromagnetic Force", in *IEEE Robot. Autom. Lett.*, Vol. 4, No. 3, pp. 2661–2668, 2019.

[3] A. Cammarata, P.D. Maddio, R. Sinatra, Y. Tian, Y. Zhao, F. Xi, "Elastostatic Analysis of a Module-Based Shape Morphing Snake-Like Robot". *Mechanism and Machine Theory*, Vol. 194, 105580, 2024.

MORPHOLOGICAL INTELLIGENCE IN PASSIVE DYNAMICS: A DESIGN INVESTIGATION OF BIOMECHANICALLY-INSPIRED BIPEDAL ROBOTS

Aikaterini Smyrli[1,2,3], Evangelos Papadopoulos[1,2,3]

[1] HERON - Hellenic Robotics Center of Excellence, Athens, Greece
[2] Robotics Institute, ATHENA Research Center, Marousi, Greece {katerina.smyrli@athenarc.gr; egpapado@athenarc.gr}
[3] National Technical University of Athens, Greece

1 INTRODUCTION

This work investigates the dynamics of bipedal locomotion through the modeling and progressive refinement of passive bio-inspired mechanical walkers, with emphasis on applications in robotics and lower-limb prosthetic systems. The study follows a structured mechanism-design progression, beginning from a minimal passive configuration and incrementally incorporating anatomically inspired elements that shape hybrid gait dynamics. The central hypothesis is that stable and energetically efficient walking behavior emerges primarily from mechanical morphology. By systematically augmenting structural features, quantitative relationships between geometry, mechanism design, inertial distribution, and passive gait characteristics are established.

2 BASE PASSIVE MODEL

The investigation begins with a compliant bipedal base model equipped with semicircular feet and axial leg elasticity (Figure 1a). Despite its structural simplicity, this system exhibits stable passive walking cycles on a shallow negative slope, reproducing key characteristics of human gait [1].

A nondimensional formulation is introduced to eliminate scale dependence and to express gait behavior through a compact set of design parameters. This representation enables fixed-point identification of periodic gaits and systematic sensitivity analysis with respect to design parameters. The base model establishes the fundamental mapping between morphology and gait stability, step frequency, hip displacement, and energetic efficiency.

The analytical predictions are validated through multibody simulations of a digital twin and through experimental evaluation of a physical prototype, demonstrating strong agreement between theoretical and physical behavior [2].

3 FOOT MORPHOLOGY AND ROLLOVER DYNAMICS

Building upon the base configuration, the first stage of augmentation concerns foot geometry. The classical circular rocker (Figure 1b) is first replaced by a semielliptical profile (Figure 1c) that approximates the evolving curvature of the human foot during rollover [3]. This modification enables parametric investigation of curvature progression and its influence on ground reaction forces, ankle trajectory, gait stability, and walking velocity.

The formulation is subsequently generalized to accommodate any convex foot geometry (Figure 1d). This extension allows the direct integration of biomimetic rollover shapes extracted from human walking experiments [4]. The resulting passive walkers reproduce ankle trajectories of increasing biomechanical fidelity and enable prediction of ground contact behavior across arbitrary foot profiles.

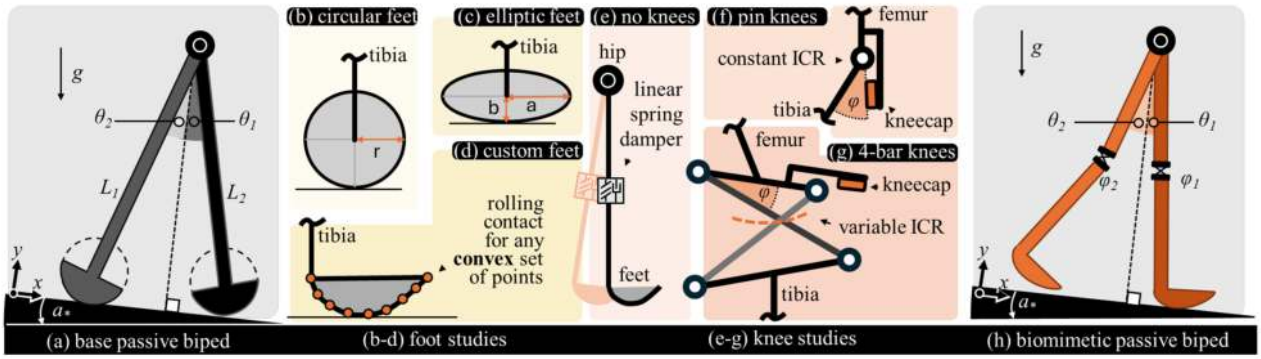

Figure 1: Design evolution of the investigated biped systems. (a) Base passive biped descending a slope a_*. (b) Circular feet. (c) Elliptic feet. (d) Detail of the custom convex foot geometries defined as arbitrary point sets. (e) No-knees biped with compliant legs. (f) Pin-joint knees. (g) Detail of the biomimetic four-bar knee mechanism. (h) Biomimetic passive biped.

4 KNEE MECHANISM DESIGN

The straight-leg model (Figure 1e) is further enriched through the introduction of knee joints. An initial passive kneed configuration employing pin joints (Figure 1f) enables swing-phase ground clearance while preserving gait stability [5]. Stable periodic gaits are identified and evaluated under parameter variations.

Subsequently, a biomimetic four-bar knee mechanism inspired by the human cruciate ligament system is introduced (Figure 1g). The four-bar architecture generates a variable instantaneous center of rotation (ICR) and configuration-dependent mechanical advantage [6]. Comparative analysis demonstrates improved compliance, reduced peak impact loads, and enhanced energetic performance relative to simple pin-joint knees. These findings highlight the decisive role of joint-level mechanism design in shaping global locomotion dynamics.

5 PASSIVITY-INSPIRED LEVEL-GROUND WALKING

Once a biped exhibits stable passive gait behavior, the same dynamically efficient motion can be sustained on level ground while preserving the low energy costs associated with the passive trajectory [7]. The analysis demonstrates that the establishment of passive stability constitutes the essential prerequisite for efficient level-ground locomotion. Thus, passive dynamic design serves as the foundation for energetically favorable walking beyond sloped environments.

6 HUMAN WALKING INTEGRATION

In parallel, a markerless stereo-camera-based gait analysis framework was developed to extract sagittal-plane kinematic and kinetic data from human walking trials [8, 9]. Using neural-network pose estimation and inverse dynamics, joint torques and ground reaction forces are estimated without markers or force plates. These human data inform and calibrate the mechanical models, ensuring convergence of the studied behaviors toward real biomechanical patterns.

7 CONCLUSION

This work presents a mechanism-driven framework for passive biped design, progressing from a minimal compliant walker without knees to configurations with biomimetic feet and knee architectures, each evaluated in terms of stability, impact mitigation, and energetic efficiency.

The results demonstrate that locomotion behavior is governed by morphological intelligence: rollover geometry, joint architecture, and inertial distribution determine the emergence and characteristics of stable hybrid gait cycles. Grounding design in biomechanically-inspired passive dynamics enables energy-efficient walking consistent with human biomechanics, providing theoretical guidance for biomimetic robots and lower-limb prosthetic systems.

ACKNOWLEDGMENTS

This project is funded by the European Union under Horizon Europe (grant No. 101136568 - HERON).

Funded by the European Union

REFERENCES

[1] Smyrli, A., Bertos, G., and Papadopoulos, E., "A generalized model for compliant passive bipedal walking: sensitivity analysis and implications on bionic leg design," *ASME J. of Biomech. Eng.*, Oct 2021, 143(10): 101008.

[2] Vasileiou, C., Smyrli, A., Drogosis, A., and Papadopoulos, E., "Development of a passive biped robot digital twin using analysis, experiments, and a multibody simulation environment," *Mechanisms and Machine Theory*, v. 163, Sep 2021.

[3] Smyrli, A., Ghiassi, M., Kecskemethy, A., and Papadopoulos, E., "On the effect of semielliptical foot shape on the energetic efficiency of passive bipedal gait," *IEEE/RSJ Int. Conf. on Int. Rob. and Sys.*, Macau, China, 2019.

[4] Smyrli, A. and Papadopoulos, E., "A methodology for the incorporation of arbitrarily-shaped feet in passive bipedal walking dynamics," *IEEE Int. Conf. on Robotics and Automation*, Paris, France, May 31-June 4, 2020.

[5] A. Smyrli and E. Papadopoulos, "Modeling, Validation, and Design Investigation of a Passive Biped Walker with Knees and Biomimetic Feet," *Int. Conf. on Robotics and Automation*, Philadelphia, PA, USA, 2022.

[6] Smyrli, K., and Papadopoulos, E., "Improved biped walking performance around the kinematic singularities of biomimetic four-bar knees," *IEEE/RSJ Int. Conf. on Intelligent Robots and Systems*, Kyoto, Japan, 2022.

[7] D. Maligianni, F. Valouxis, A. Kantounias, A. Smyrli and E. Papadopoulos, "A Virtual Gravity Controller for Efficient Underactuated Biped Robots," *IEEE Int. Conf. on Robotics and Automation*, Atlanta, GA, USA, 2025.

[8] K. Tsintzira, A. Smyrli, A. Mastrogeorgiou and E. Papadopoulos, "Low-Cost Markerless Gait Analysis Using a Minimal Human Model," *IEEE Int. Conf. on Bioinformatics and Bioengineering*, Athens, Greece, 2025.

[9] O. I. Stavrakakis, *et al.*, "Guidelines For Optimal Human Mesh Generation Using Deep Learning-Driven Avatar Reconstruction For Gait Analysis," *IEEE-RAS Int. Conference on Humanoid Robots*, Nancy, France, 2024.

NON-DIMENSIONALIZED SPECTRAL ANALYSIS OF GEAR SHAPE DEVIATION NETWORKS: IDENTIFICATION OF KINEMATIC ERRORS VIA NODE-NORMALIZED LAPLACIAN AND SCALE-INVARIANT DISCRETE FOURIER TRANSFORM

JingChong Low[1], Daisuke Iba[1], Yuichiro Seo[1], Shu Takata[1], Naoki Yamashita[1], Kunitoshi Kawano[2]

[1] Precision Manufacturing Laboratory, Kyoto Institute of Technology, Matsugasaki, Sakyo-ku, Kyoto, 606-8585, Japan, jingchong1998@gmail.com.jp; iba@kit.ac.jp; seoyuu1210@gmail.com; shukun0617@gmail.com; naoki@kit.ac.jp}

[2] KASHIFUJI WORKS, LTD., 6 Kamonden-cho, Kamitoba, Minami-ku, Kyoto 601-8131, Japan, {kawano@kashifuji.co.jp}

1. INTRODUCTION

Gear hobbing induces complex kinematic errors arising from synchronization mismatches and tool inaccuracies. While traditional quality assurance focuses on localized, individual-tooth deviations, this approach overlooks the correlated systemic errors inherent to the manufacturing process. To address this, our previous research modeled the gear as a "Gear Shape Deviation Network" to quantify manufacturing errors. In this study, we discover that the resulting spectral ratio λ_3/λ_2 exhibits an exceptional, highly predictable linearity ($R^2 \approx 0.99$) with workpiece face runout (Fig. 1). However, a fundamental limitation remains as standard Laplacian eigenvalues scale with network size (tooth count), rendering direct comparison across different gear specifications impossible. To overcome this, we introduce a Node-Normalized Laplacian(NNL) L_{nn} framework that establishes a standardized eigenvalue metric independent of gear parameters. Furthermore, we propose a diagnostic method utilizing the Scale-Invariant Discrete Fourier Transform (SI-DFT) to non-dimensionalize eigenvectors, transforming spatially dependent mode shapes into size-independent harmonic orders to separate and quantify manufacturing errors.

2. METHODOLOGY

We employ a two-stage spectral framework to quantify gear manufacturing errors independent of specifications.

2.1. Non-dimensionalization of the graph Laplacian

First, we construct a shape deviation network in which each tooth is a node, and the edges represent the phase correlation between deviations. To evaluate gears of varying specifications, we initially investigated the conventional Symmetric Normalized Laplacian(SNL) L_{sn} . However, our preliminary analysis revealed that L_{sn} fails to eliminate size-dependency as eigenvalue spectra for gears with identical error conditions but differing tooth counts did not converge to a unified characteristic curve. To address this discrepancy and ensure rigorous comparability, we propose the Node-Normalized Laplacian L_{nn}. By normalizing the combinatorial Laplacian L (defined as the Degree matrix D minus the Adjacency matrix A) by the total number of nodes N, the resulting eigenvalues are effectively non-dimensionalized. The formulation is defined as:

$$\boldsymbol{L_{nn}} = \frac{\boldsymbol{L}}{N} = \frac{\boldsymbol{D-A}}{N} \tag{1}$$

This approach ensures that the eigenvalue distribution remains bounded and consistent regardless of the gear's dimension, establishing a robust universal metric for structural error evaluation.

2.2. Eigenvector non-dimensionalization via Scale-Invariant Discrete Fourier Transform

Eigenvalues calculated with L_{nn} quantify the global error intensity, the eigenvectors $u^{(i)}$ contain the spatial distribution of these deviations. A critical reference point in this analysis is the Fiedler vector (associated with the algebraic connectivity λ_2), which physically corresponds to the fundamental kinematic error mode. However, direct comparison of raw eigenvectors across differing gear specifications Z presents significant challenges. As the nodal dimension changes, the eigenvector indices do not align, and the mode shapes exhibit amplitude scaling discrepancies. Furthermore, numerical solvers introduce sign indeterminacy (arbitrary polarity), causing eigenvectors to appear "flipped" or inverted between identical error modes of different gears. To resolve these inconsistencies, we propose a Scale-Invariant Discrete Fourier Transform (SI-DFT). This transformation maps the spatial domain to the frequency domain while explicitly compensating for the energy distribution differences inherent to varying node counts. The non-dimensionalized eigenvector spectral magnitude $\widehat{U}_{nd}^{(i)}(n)$ for the n-th harmonic order is defined as:

$$\widehat{U}_{nd}^{(i)}(n) = \sqrt{Z} \cdot \left| \sum_{k=1}^{Z} u_k^{(i)} e^{-j\frac{2\pi}{Z}n(k-1)} \right| \tag{2}$$

where Z is the total number of teeth, $u_k^{(i)}$ is the component of the i-th eigenvector at the k-th tooth, n represents the harmonic order, and j is the imaginary unit. By introducing the scaling factor $\sqrt{Z}$, the spectral amplitudes are normalized, ensuring that identical error shapes yield consistent magnitude values regardless of the gear's tooth count.

Table 1. Gear Specifications

Parameter	Gear 1	Gear 2	Gear 3
Normal Module [mm]	2	1	0.5
Number of Teeth [-]	30	60	120
Normal Pressure Angle [deg.]	20	20	20
Helix Angle [deg.]	0	0	0
Face Width [mm]	10	10	10
Profile shift coefficient [-]	0	0	0
Face Runout [μm]	0, 10~50	0, 10~50	0, 10~50

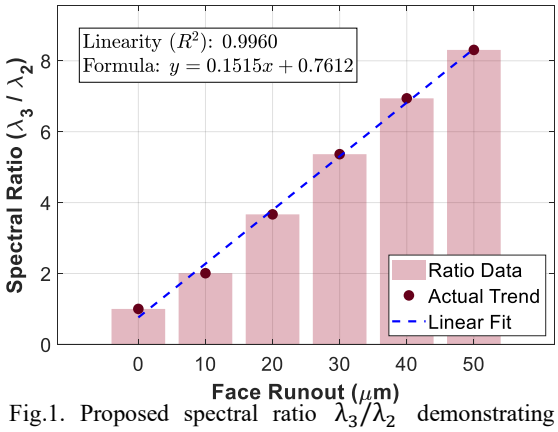

Fig.1. Proposed spectral ratio λ_3/λ_2 demonstrating linear correlation with workpiece face runout deviation.

3. RESULTS AND DISCUSSION

To validate the proposed non-dimensionalization framework, hobbing simulations were conducted to generate spur gears with varying dimensions. The simulation parameters were designed to introduce controlled kinematic errors, specifically "Workpiece Face Runout" and "Workpiece Radial Runout". To test the robustness of the method against network size variations, three distinct gear models were generated with tooth counts Z of 30, 60, and 120, as detailed in Table 1.

3.1. Evaluation of Eigenvalue Non-dimensionalization

We first evaluated the performance of the graph Laplacian normalization. Initially, the raw combinatorial Laplacian eigenvalues exhibited significant magnitude scaling proportional to the network size, rendering direct comparison impossible. Subsequently, as observed in Fig. 2a, the eigenvalue spectra derived from the conventional Symmetric Normalized Laplacian L_{sn} exhibited discrepancies between the gear models. Despite having identical unit error conditions, the characteristic curves for $Z = 30, 60, 120$ did not converge, indicating a residual dependency on network size. In contrast, the proposed Node-Normalized Laplacian L_{nn} demonstrated superior consistency. As shown in Fig. 2b, the eigenvalue distributions for all three gear specifications overlapped almost perfectly, converging to a unified characteristic curve bounded between 0 and 0.5. This confirms that the Node-Normalized Laplacian L_{nn} formulation successfully eliminates the dimension-dependency of the spectral intensity, establishing a robust metric for cross-specification comparison.

3.2. Evaluation of Eigenvector Non-dimensionalization

Next, we analyzed the spatial error distributions. Due to the differing node counts, the mode shapes of raw eigenvectors appear compressed or stretched, and their amplitudes vary, making direct quantitative comparison infeasible. However, by applying the proposed Scale-Invariant Discrete Fourier Transform (SI-DFT), these spatial discrepancies were effectively resolved. Fig. 3 presents the spectral intensity of the transformed eigenvectors. All three gears, regardless of tooth count, exhibited a distinct, singular peak at harmonic order $n = 1$ with a consistent normalized intensity (≈ 0.7). This result verifies that the SI-DFT method successfully extracts the fundamental kinematic error as a size-independent harmonic signature.

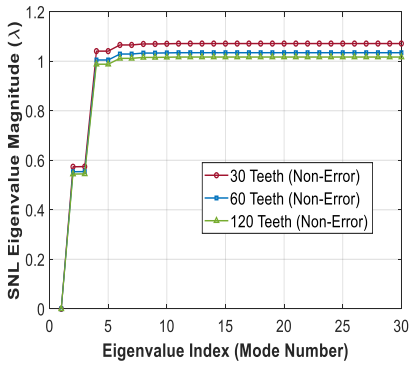

Fig.2a. Conventional SNL showing residual size-dependency.

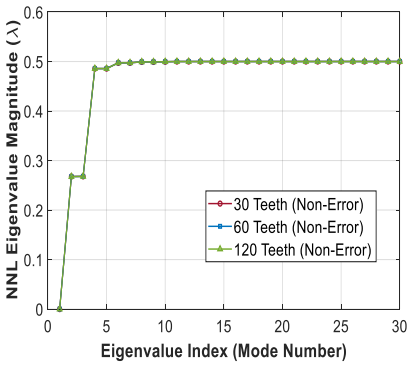

Fig.2b. Proposed NNL achieving size-independent spectral convergence.

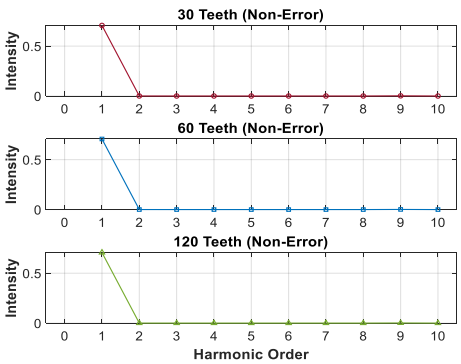

Fig.3. SI-DFT spectral magnitude(0μm face runout) isolating the fundamental kinematic error at harmonic order $n = 1$ regardless of gear tooth count.

4. CONCLUSION

This study establishes a unified spectral framework that overcomes the size-dependency inherent in the spectral analysis of gear shape deviation networks. The proposed Node-Normalized Laplacian achieves spectral convergence across varying tooth counts, where the standard Symmetric Normalized Laplacian exhibited residual size-dependency. Furthermore, the Scale-Invariant Discrete Fourier Transform successfully converts spatial error mode shape vectors into standardized, size-independent harmonic signatures. This framework establishes a rigorous, universal metric for isolating kinematic errors regardless of gear specification, paving the way for more precise identification and quantification of gear manufacturing deviations.

DEGREE OF FREEDOM ANALYSIS OF MULTI-LOOP COUPLED MECHANISMS BASED ON MECHANISM-TRUSS TRANSFORMATION METHOD

Yu Wang[1], Xiaofei Liu[1*], Yuantao Bu[1], Yuan Jiang[1], Jiantao Yao[1], Yongsheng Zhao[1]

[1] Parallel Robot and Mechatronic System Laboratory of Hebei Province, Yanshan University, Qinhuangdao 066004, China {17864277601@163.com; liuxf@ysu.edu.cn; boyuantao72@gmail.com; shadovor@foxmail.com; jtyao@ysu.edu.cn; yszhao@ysu.edu.cn;}

1. INTRODUCTION

Multi-loop coupled mechanisms exhibit desirable characteristics such as high stiffness and high positioning accuracy, and they have been widely employed in modern aerospace engineering applications [1]. However, the complex loop constraints inherent in multi-loop coupled mechanisms make their degree of freedom (DOF) analysis highly challenging [2]. To date, numerous methods have been proposed for calculating the DOF of multi-loop coupled mechanisms, but some of these methods lack unified rules [3], while others are highly complex, making them difficult to popularize [4].

This paper proposes a new method for rapidly calculating the DOF of multi-loop coupled mechanisms based on the Mechanism-Truss Transformation (MTT) method. Instead of analyzing the coupling characteristics and overconstraints of the mechanism, the method converts the mechanism into a truss following unified transformation rules and determines its DOF through truss stability analysis. The proposed method offers broader applicability and simplifies the analytical process.

2. FUNDAMENTALS OF TRUSS STABILITY THEORY

Assume that a spatial truss contains j joints and b bars, denoting the equilibrium matrix of the truss system by $\boldsymbol{H}$. Assuming that the rank of equilibrium matrix $\boldsymbol{H}$ is r, then the number of independent inextensional mechanism m and the number of independent states of self-stress s of the truss system can be obtained:

$$\begin{cases} m = 3j - 6 - r \\ s = b - r \end{cases} \tag{1}$$

When $m > 0$ and $s > 0$, the truss possesses both static indeterminacy and kinematic indeterminacy, thus manifesting as an overconstrained mechanisms, where m represents the DOF of the mechanism and s denotes its degree of overconstraint.

3. MECHANISM-TRUSS TRANSFORMATION RULES

As shown in Table 1, the corresponding truss forms of revolute-type joints (including R, U, and S joint) and link are presented.

Table 1. Transformation rules for joint and link.

Model	Joint			link
	R-joint	U-joint	S-joint	
Mechanism model				
Truss model				

Regarding the P-joint, as illustrated in Figure 1, it is replaced by the corresponding truss form of a Sarrus linkage, which consists solely of R-joints. Verification shows that the final number of DOF remains unchanged; however, it should be noted that each introduction of a Sarrus linkage introduces one additional overconstraint.

The truss-form transformation of coupling components must meet the following requirements: the final truss framework remains closed; the transformed forms of all connected joints are correct; the bar count satisfies $b = 3j - 6$.

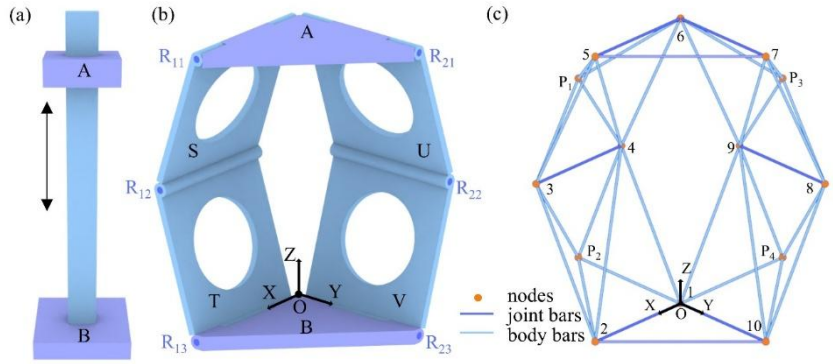

Figure 1. (a) P-joint; (b) mechanism form of Sarrus; (c) truss form of Sarrus (P-joint).

4. RESULTS

Figure 2 and Figure 3 display the truss forms of a planar multi-loop coupled deployable mechanism and 3RR-3RRR mechanism, respectively. The DOF for both, calculated using the MTT method, are consistent with the expected results.

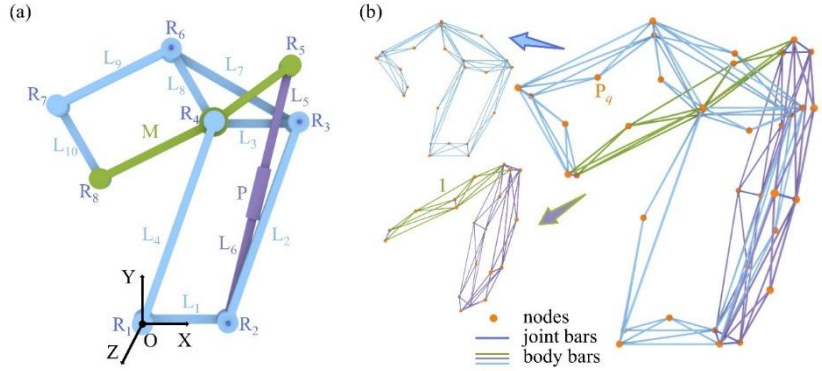

Figure 2. The planar multi-loop coupled deployable mechanism. (a) mechanism form; (b) truss form.

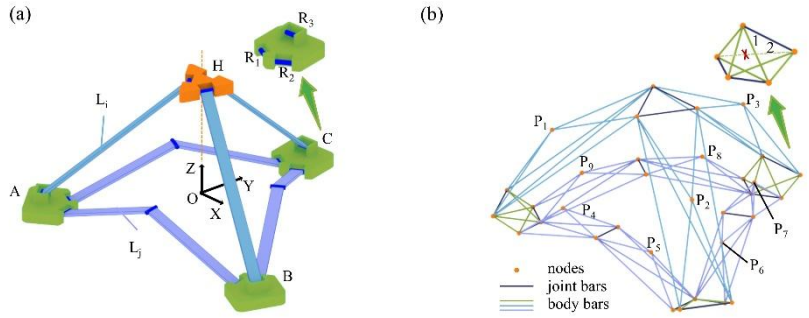

Figure 3. The 3RR-3RRR. (a) mechanism form; (b) truss form.

ACKNOWLEDGMENTS

This work was supported by the National Natural Science Foundation of China (Grant No. 52105036 & 52075467).

REFERENCES

[1] Q.Z. Meng, F.G. Xie, R.J. Tang, X.J. Liu, “Novel closed-loop deployable mechanisms and integrated support tr usses for planar antennas of synthetic aperture radar”. *Aerospace Science and Technology*, 129, 107819, 2022.

[2] Y. Zhang, W.X. Wang, X. Kang, B. Li, “Design, analysis, and experimentation of deployable multi-closed-loop truss modules for aerospace platforms”. *Mechanism and Machine Theory*, 205, 105897, 2025.

[3] X.X. Chai, G.C. Zheng, S.Y. Zheng, F. Wen, Y. Xiao, L.M. Xu, Q.C. Li, “Theoretical analysis and experiment al verification of a 3RR-3RRR multi-loop coupling mechanism based on geometric algebra”. *Robotica*, 43(7), 25 04-2526, 2025.

[4] C.Y. Li, H.W. Guo, D.W. Tang, R.Q. Liu, Z.Q. Deng, X.K. Song, S.I. Zahin, “Cell division method for mobili ty analysis of multi-loop mechanisms”. *Mechanism and Machine Theory*, 141, 67-94, 2019.

TOLERANCE DESIGN AND METROLOGY-ASSISTED FABRICATION AND ASSEMBLY OF PARALLEL ROBOTS FOR HIGH PRECISION SURGICAL OPERATIONS

Aislinn McAleenan[1], Yan Jin[1], Dan Sun[1], Johnny Moore[2]

[1] School of Mechanical and Aerospace Engineering, Queen's University Belfast, Stranmillis Road, Belfast, UK, {a.mcaleenan@qub.ac.uk; y.jin@qub.ac.uk; d.sun@qub.ac.uk}

[2] Cathedral Eye Clinic, 89-91 Academy St, Belfast, UK, {Johnny@cathedraleye.com}

1. INTRODUCTION

Robotic assisted minimally invasive surgery (MIS) has seen widespread clinical adoption, helping surgeons to perform precise surgical tool motions through small incisions. This has provided patient benefits that include lower blood loss, less scarring, reduced pain, quicker recovery and a lower risk of complications post-operation. Surgical robots achieve such merits by using a remote center of motion (RCM) point. This is a fixed virtual point made coincident with the incision on the patient, and all motions of the surgical tool are constrained to act at this point. An RCM can be realized by different kinematic designs, many of which are parallel mechanisms [1] - [3] for their accuracy, stiffness, and resistance to error accumulation [4].

However, the fabrication of a high precision medical robot is a difficult task as achieving the stringent geometric constraints of the RCM mechanism is challenging in practice. The errors accumulated across the entire manufacturing and assembly process may add up to produce constraint errors that violate the geometric constraint requirements of the mechanism [5]. The presence of constraint errors can cause the parallel mechanism to not rotate about the rotational center, leading to increased friction at the joints, bending of the mechanism and thus reduced accuracy of the end-effector [6]. Furthermore, assembly of a closed-loop parallel robot without external force or deformation is a difficult task due to potential manufacturing and assembly errors; and, if assembly has been achieved, the force required to do so could induce negative internal stress in the mechanism. This may cause joints to dislocate, negatively affecting the in-service performance in terms of accuracy and reliability [7]. This is a major problem as it could render the mechanism useless because the desired motion characteristics no longer exist in the physical assembly.

While constraint errors affect all parallel RCM mechanisms, spherical parallel mechanisms (SPMs) pose more of a problem. The geometric constraint of all revolute joint axes intersecting at one point is essential in realizing the desired end-effector motion, yet the farther away from the point of rotation, the more an angular mis-position is magnified.

Computer aided design has facilitated design and visualization, yet other key aspects of the fabrication process are still vague, such as tolerance allocation by mapping the effects of fabrication errors at the joint space into the accuracy of the RCM. Furthermore, a measurement routine for characterizing the actual rotation center has not been reported in literature. Studies have instead attempted to quantify the effect of constraint errors on the RCM [8] – [11] by measuring the pose error of the moving platform or end-effector, however, this provides the combination of these constraint errors and does not distinguish where those errors come from.

To bridge this knowledge gap, this work presents a tolerance design and metrology-assisted fabrication and assembly methodology in which the tolerance at the joint space of critical components were mapped via an error model to the virtual RCM. This was then validated through unique metrology strategies using a coordinate measurement machine (CMM) and laser displacement sensors (LDS).

2. METHODOLOGY

The proposed methodology, shown in Fig. 1. was evaluated through a case study on CASPER [12], a 3R1T spherical parallel medical robot for MIS. First, the sub-assemblies of the mechanical design that had the greatest influence on the RCM were identified. Subsequentially the kinematically critical components within these sub-assemblies were identified and datums established. An error model was developed and applied to map the errors at the joint space to the RCM to permit tolerance allocation.

A metrology gauge was designed to serve as a geometric reference for the evaluation and assembly of the spherical mechanism. The metrology gauge was characterized using a Hexagon Global S 07.10.07 CMM. A Micro Epsilon Laser-optical displacement measuring system consisting of two ILD2300-10 LDS was used to assess the radial runout of the shafts after each assembly stage.

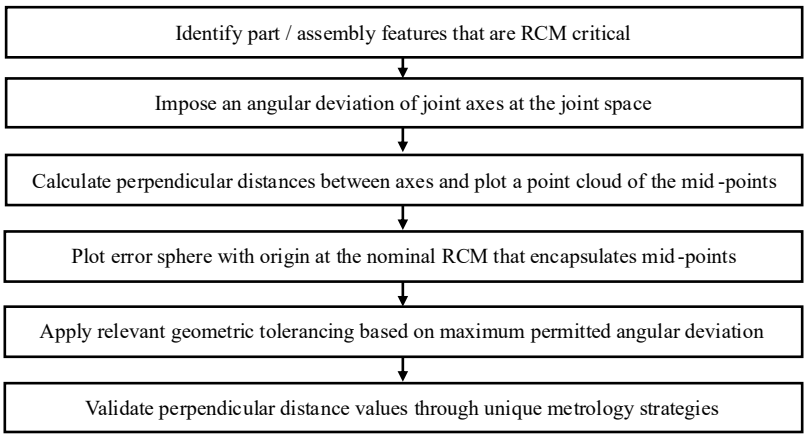

Figure 1. Tolerance design and metrology-assisted fabrication and assembly methodology.

3. RESULTS

Based on the error model, the maximum expected RCM variation between axes for the mechanism was determined to be ± 52.1 μm for perpendicular offset. From the metrology data, in each of the individual spherical links, and the assembled spherical limbs, it was confirmed that the variation from the RCM ranged from ± 3.0 μm to ± 43.4 μm, which was within the maximum tolerance of ± 52.1 μm. For all three input shafts the bearing journals were identified as critical features that needed to be evaluated to maintain the accuracy of the RCM point. The coaxiality results ranged from ± 3.2 μm to ± 40.5 μm. Furthermore, the radial runout caused by the shaft center offset after assembly of the three shafts was measured and calibrated. The shaft center offset is the amount that the center of the rotating shaft is misaligned from the intended central axis. The calibrated radial runout for the coaxial input shafts once assembled was reduced to within 0.1 μm.

4. CONCLUSIONS

The proposed methodology enables tolerance design and quantitative assessment of manufacture and assembly quality at multiple stages, from individual components to assembled sub-systems. A key achievement of this work is the introduction of a targeted measurement strategy to quantitatively assess error effects at the virtual RCM point, enabling more precise performance evaluation. The methodology was experimentally validated, and it will be instrumental to assure the quality and performance of parallel robots' implementation.

ACKNOWLEDGMENTS

Support from Cathedral Eye Clinic, Queen's University Belfast and Invest Northern Ireland is acknowledged.

REFERENCES

[1] M. Azizian, *et al.*, "The da Vinci Surgical System," *Handbook of Robotic and Image-Guided Surgery*, Sunnyvale, Elsevier Inc, 39-55, 2020.
[2] Y. Jian, *et al.*, "A Parallel Robot With Remote Centre-of-Motion for Eye Surgery: Design, Kinematics, Prototype, and Experiments," *Int. J. Med. Robot. Comput. Assist. Surg.,* 20(4), 1-26, 2024.
[3] A. McAleenan, *et al.* (2025). Design and Control System Development of a New 3R1T Parallel Robot for Minimally Invasive Surgery. In: Laribi, M.A., Carbone, G., Pisla, D., Zeghloul, S. (eds) MESROB 2025. *Mech. Mach. Sci.,* vol 186. Springer, Cham.
[4] A. Chaker, *et al.* Synthesis of Spherical Parallel Manipulator for Dexterous Medical Task. *Front. Mech. Eng.* 7(2), 1-13, 2012.
[5] Y. Jin and I-M. Chen, "Effects of constraint errors on parallel manipulators with decoupled motion," *Mech. Mach. Theory*, 41(8), 912-928, 2006.
[6] Q. Zhao, *et al.*, "Assembly Precision Prediction for Planar Closed-Loop Mechanism in View of Joint Clearance and Redundant Constraint," *J. Mech. Sci. Technol.,* 32(7), 3395-3405, 2018.
[7] M. Aurrekoetxea, *et al.,* "Towards advanced prediction and control of machining distortion: a comprehensive review," *Int. J. Adv. Manuf. Technol.,* 122, 2823–2848, 2022.
[9] G. Palmieri, "On the positioning error of a 2-DOF spherical parallel wrist with flexible links and joints – an FEM approach," *Mechanical Sciences,* 6(1), 9–14, 2015.
[9] G. Cui, *et al.*, "Kinematic Reliability Solution of 3-UPS-PU Parallel Mechanism Based on Monte Carlo Simulation," *Open Mech. Eng. J.,* 9(1), 324-332, 2015.
[10] A. Jain and H. Jawale, "Study of the effects of link tolerances to estimate mechanical errors in 3-RRS parallel manipulator," *Proc. IMechE Part C: J. Mech. Eng. Sci.*, 236(3), 1598–1615, 2022.
[11] A. Singh and J. Khatait, "Sensitivity analysis of a double-parallelogram based RCM mechanism used for MIS robots," *Proc. IMechE Part C: J. Mech. Eng. Sci.,* 237(20), 4813-4827, 2023.
[12] Jin, Y., *et al.*: Apparatus for positioning a tool. Patent No. GB2618205 (2025)

SAFE AND ROBUST AUTONOMOUS DRIFTING OF VEHICLES

Ricardo de Castro[1], Basilio Lenzo[2], Marco Adami[2], Marco Cortese[2], Marco Cazzola[2], Giovanni Righetti[2], Tommaso Belluco[2], Matteo Massaro[2], Berrydal Moshe[1], Justin Arroyo[1]

[1] University of California, Merced, 5200 N. Lake Road, Merced, CA 95343, USA {rpintodecastro@ucmerced.edu}
[2] University of Padova, Via Venezia, 1, 35131 Padova, Italy {basilio.lenzo@unipd.it}

1 INTRODUCTION

Drifting is an extreme vehicle operating regime characterized by large chassis sideslip angles and the saturation of the the rear tire forces. Unlike conventional cornering, where vehicle dynamics exhibit locally stable equilibria and approximately linear responses, drifting typically occurs at unstable steady-state equilibria. As a result, small disturbances or modeling inaccuracies can lead to rapid divergence from the desired operating point and ultimately to vehicle spin-out. Although drifting is often associated with motorsport, it plays an important role in several practical scenarios, including beyond-the-limit emergency maneuvers, obstacle avoidance, and recovery on low-friction surfaces [1]. Moreover, drifting has been shown to be a necessary condition for minimum-time maneuvers in aggressive driving and off-road applications [2].

From a control perspective, autonomous drifting poses significant challenges due to the strong nonlinearities of tire forces near the friction limits and the inherent instability of drifting equilibria [3]. Linear control techniques such as linear quadratic regulators (LQR) have been successfully applied to drifting in nominal conditions; they are attractive for practical deployment due to their simplicity and low computational burden [4]. However, even moderate mismatch in friction estimation may cause LQR-based controllers to fail, leading to a loss of drift. Nonlinear model predictive control (MPC) is another widely-used method for drifting, capable of explicitly enforcing state and input constraints [5]. Despite their advantages, MPC-based solutions can be difficult to deploy on automotive embedded systems with limited computational resources.

Control barrier functions (CBFs) offer a systematic framework for enforcing safety constraints through set invariance methods [6]. CBFs have been successfully applied to automotive control problems including adaptive cruise control, lane keeping, obstacle avoidance, and vehicle lateral stability. However, their application to autonomous drifting—where rear tire saturation must be actively induced while simultaneously preventing excessive yaw rate and sideslip—remains largely unexplored. This work addresses this gap by developing a CBF framework for safe and robust autonomous drifting under model uncertainty with experimental validation (Figure 1).

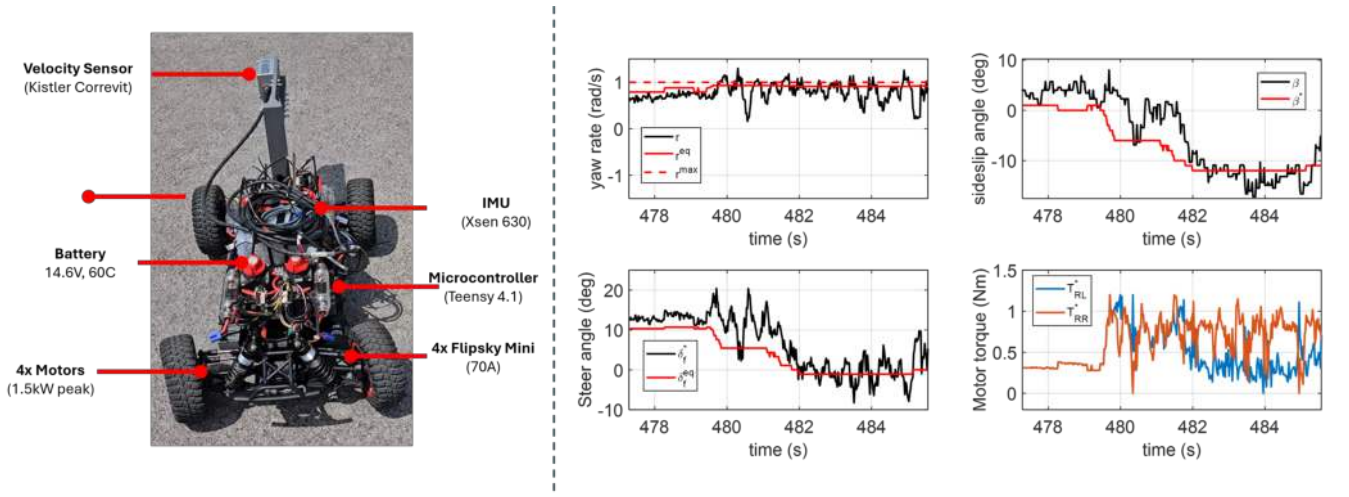

Figure 1: (Left) Overview of the small-scale vehicle prototype used to validate the autonomous drifting maneuvers; (Right) Experimental results during autonomous drifting (r^{eq}, β^* correspond to the reference yaw rate and chassis sideslip angle).

2 METHODOLOGY

The proposed drifting controller is organized into three layers: i) steady-state equilibrium computation, ii) linear stabilization, and iii) cascade CBFs for enforcement of safety constraints

- *Steady-state equilibrium computation*: For a desired cornering curvature (R^*) and reference sideslip angle(β^*), a drifting equilibrium is first computed. The resulting equilibrium provides the feedforward steering angle (δ_f^*) and rear torques (T_{rl}^*, T_{re}^*), required to sustain a drift with the desired sideslip (under the assumption of a nominal model with no uncertainty).
- *LQR*: The nonlinear vehicle model is linearized around the computed equilibrium. An LQR is then designed to stabilize deviations from this operating point, providing corrective steering and total rear torque adjustments. Although this approach is effective under nominal conditions, it is sensitive to friction mismatch and does not guarantee constraint satisfaction.
- Cascade CBFs. To improve the robustness and safety of the LQR controller, a CBF is proposed to manage the rear longitudinal slip. The objective is to guarantee that the rear wheel slip remains above a minimum threshold required to sustain tire saturation and initiate drift. When slip is insufficient, the CBF modifies the rear wheel torques to drive the system toward the desired slip (drift) region. Once drift is established, the lateral motion is regulated through yaw-rate and sideslip CBFs. These constraints bound the vehicle within a recoverable region in the sideslip–yaw-rate plane, preventing excessive rotation and spin-out. The sideslip constraint is enforced indirectly via a sideslip-dependent yaw-rate limit. The CBFs are applied in a cascade structure, where drift initiation has lower priority than lateral stabilization. This reduces the control problem to a series of low-dimensional quadratic programs (QP), which are suitable for real-time embedded implementation.

3 RESULTS

The proposed controller was evaluated in both simulation and experiments and compared against a baseline LQR controller. Under nominal tire–road friction conditions, the LQR was able to stabilize the drifting equilibrium and tracks the desired sideslip angle with small steady-state error. However, when moderate friction mismatch is introduced, the LQR fails to induce sufficient rear tire slip, leading to a failure of the drifting maneuver. In contrast, the proposed CBF-based controller maintains drift performance under the same mismatch conditions, enabling consistent drift initiation. The yaw-rate CBF successfully limits excessive rotational motion, preventing spin-out during aggressive transients. Different approximations of the yaw-rate dynamics were also evaluated. Model-free implementations based on measured yaw acceleration demonstrated improved robustness compared to model-based approximations subject to parametric uncertainty. Experimental validation on a 1:5-scale vehicle prototype confirms the simulation findings. The controller achieves stable drift transitions and sustained operation with bounded yaw rate and sideslip (see Figure 1).

4 CONCLUSION

This paper presents a control barrier function framework for robust autonomous drifting under model uncertainty. The approach integrates steady-state equilibrium computation, LQR stabilization, and prioritized CBF constraints to bound yaw-rate and sideslip behavior during drifting. Unlike LQR alone, the proposed method maintains drift performance under friction mismatch while preventing spin-out during aggressive transients. Simulation and experimental results on a small-scale vehicle prototype demonstrate the effectiveness and robustness of the proposed methodology. Future work will extend this control framework to perform drifting along prescribed paths.

REFERENCES

[1] T. Zhao, E. Yurtsever, and G. Rizzoni, "Justifying emergency drift control for automated vehicles," *IFAC-PapersOnLine*, vol. 55, no. 24, pp. 141–148, 2022.

[2] D. Tavernini, M. Massaro, E. Velenis, D. I. Katzourakis, and R. Lot, "Minimum time cornering: the effect of road surface and car transmission layout," *Vehicle system dynamics*, vol. 51, no. 10, pp. 1533–1547, Oct. 2013.

[3] G. Righetti, E. Binetti, R. Pinto de Castro, R. Lot, M. Massaro, and B. Lenzo, "On the investigation of car steady-state cornering equilibria and drifting," in *SAE Technical Paper Series*, vol. 1, no. 2024-01-2764. SAE International, Apr. 2024.

[4] B. Lenzo, T. Goel, and J. C. Gerdes, "Autonomous drifting using torque vectoring: Innovating active safety," *IEEE Transactions on Intelligent Transportation Systems*, vol. 25, no. 11, pp. 1–9, 2024.

[5] T. P. Weber and J. C. Gerdes, "Modeling and control for dynamic drifting trajectories," *IEEE transactions on intelligent vehicles*, vol. 9, no. 2, pp. 3731–3741, Feb. 2024.

[6] A. D. Ames, S. Coogan, M. Egerstedt, G. Notomista, K. Sreenath, and P. Tabuada, "Control barrier functions: Theory and applications," in *2019 18th European Control Conference (ECC)*, Jun. 2019, pp. 3420–3431.

MORPHING OF PLANAR FLEXURES

Orazio Sorgonà[1], Luca Bruzzone[2], Oliviero Giannini[1], Matteo Verotti[2]

[1] Department of Engineering, Niccoló Cusano University of Rome, Rome, Italy
{orazio.sorgona@unicusano.it; oliviero.giannini@unicusano.it}
[2] Department of Mechanical, Energy, Management and Transport Engineering, University of Genoa, Genoa, Italy
{luca.bruzzone@unige.it; matteo.verotti@unige.it}

1 INTRODUCTION

Compliant mechanisms are arrangements of rigid links connected by elastic elements, or flexures. The kinetostatic response of the system, and the possible fields of displacements of its output link, depend both on its topological structure and on the elastic properties of its flexures. As a consequence, the design procedures can focus on the output port, on the mechanism, or on the element levels [1]. The problem of synthesis at the element level consists in the definition of the geometric and material properties of the elastic element, starting from an assigned kinetostatic relation. This task is not trivial, and has been addressed in several ways [2]. In this scenario, the geometric model of the ellipse of elasticity represents the linear behavior of any planar two-port suspension, and can be implemented at any level, regardless of the topological complexity of the elastic suspension. At the element level, this model consists of the momental ellipse of the flexure compliance distribution.
In the present work, this model is exploited to define a synthesis procedure based on affine deformations. The procedure starts from any assigned elastic beam, and generates infinite solutions to the synthesis problem. More specifically, the assigned elastic element is *morphed* into other kinetostatically-equivalent flexures. A case study consisting of a flexure with initial curvature is considered, and the results are tested through finite elements analysis.

2 METHODOLOGY

The proposed morphing method can be applied to every planar flexure $\mathcal{F}_1$, considering its associated ellipse of elasticity $\mathcal{E}_1$ with elastic weight w_1 [3, 4]. The flexure is defined by the axis coordinates $\{x_1(t),\, y_1(t)\}$, and by the cross-section moment of inertia $I_1(t)$, $t \in [t_0, t_1]$. The coordinates refer to the reference frame with origin at the center of the ellipse, and $x-$ and the $y-$axis overlapping the ellipse semiaxes a_1 and $b_1 \leq a_1$, respectively.
The assigned flexure $\mathcal{F}_1$ is morphed into the flexure $\mathcal{F}_2$, with ellipse of elasticity $\mathcal{E}_2 \equiv \mathcal{E}_1$. The flexure $\mathcal{F}_2$ is defined by the coordinates

$$x_2(t) = \quad \cos(\alpha)\, x_1(t) + \frac{1}{e_1} \sin(\alpha)\, y_1(t), \tag{1}$$

$$y_2(t) = -\, e_1 \sin(\alpha)\, x_1(t) + \cos(\alpha)\, y_1(t), \tag{2}$$

where $e_1 = b_1/a_1$, and $\alpha \in [-\pi/2, \pi/2]$. The cross-section moment of inertia of $\mathcal{F}_2$ correspondingly becomes

$$I_2(t) = \frac{\left[\lambda \left(\frac{dx_1}{dt}\right)^2 + \mu \left(\frac{dy_1}{dt}\right)^2 + \nu \left(\frac{dx_1}{dt}\right)\left(\frac{dy_1}{dt}\right)\right]^{1/2}}{\left[\left(\frac{dx_1}{dt}\right)^2 + \left(\frac{dy_1}{dt}\right)^2\right]^{1/2}} I_1(t)\,, \tag{3}$$

where

$$\lambda = \cos(\alpha)^2 + e_1^2 \sin(\alpha)^2\,, \qquad \mu = \frac{1}{e_1^2} \sin(\alpha)^2 + \cos(\alpha)^2\,, \qquad \nu = 2\left(\frac{1}{e_1} - e_1\right) \sin(\alpha) \cos(\alpha)\,.$$

Given the input parameter e_1, infinite solutions can be generated by setting the parameter α.

3 CASE STUDY

As case study, a uniform constant-curvature flexure $\mathcal{F}_1$ is considered, with radius $R = 100$ mm and subtending the semiangle $\theta = \pi/3$. The corresponding ellipse of elasticity $\mathcal{E}_1$ is calculated according to the procedure described in [3], and is characterized by an eccentricity parameter $e_1 = 0.2790$. To define the flexure $\mathcal{F}_2$, kinetostatically equivalent

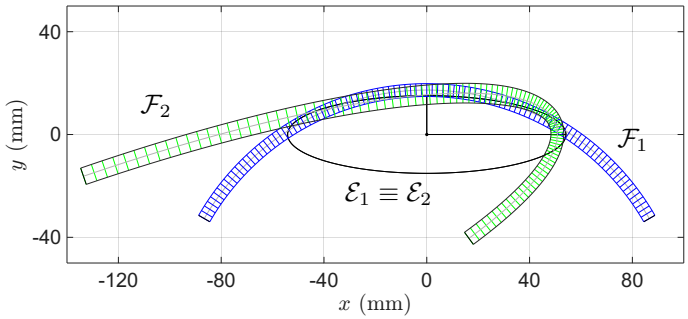

Figure 1: Flexures $\mathcal{F}_1$ and $\mathcal{F}_2$, and overlapping ellipses $\mathcal{E}_1 \equiv \mathcal{E}_2$

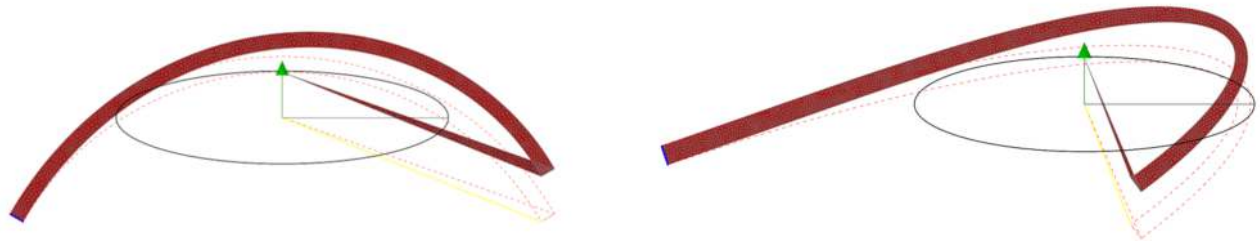

(a) (b)

Figure 2: Responses of $\mathcal{F}_1$ (a) and of $\mathcal{F}_2$ (b) to the applied load $\mathbf{f_y}$

to $\mathcal{F}_1$, the parameter α is set to $\alpha = \pi/6$. The flexures are shown in Fig.1, where the line spacing represents equal fractions of elastic weight w. As it can be noted from the figure, the spacing is uniform in $\mathcal{F}_1$, but it varies for $\mathcal{F}_2$.

Table 1: Comparison of the generalized displacements. Lengths in mm, angles in rad, forces in N, moment in Nm

Load	Theory			$\mathcal{F}_1$			$\mathcal{F}_2$		
	δ_x	δ_y	θ	δ_x	δ_y	θ	δ_x	δ_y	θ
$f_x = 2000$	9.13	0.00	0.00	9.27	0.00	0.00	9.22	0.04	0.00
$f_y = 500$	0.00	29.36	0.00	0.00	29.40	0.00	-0.01	29.40	0.00
$m = 10$	0.00	0.00	0.20	0.00	0.00	0.20	-0.00	0.02	0.20

The kinetostatic behavior of the two flexures has been tested by finite element analysis. Three load cases have been considered, consisting of a pure moment $\mathbf{m}$ and of two forces applied to the point P rigidly connected to the free-end section. In the neutral configuration, the point P is coincident to the center of the ellipse C. For the ellipse properties, a pure moment produces a rotation about C. Also, a force $\mathbf{f_x}$, with line of action overlapping the semiaxis a_1, produces translations parallel to a_1. Analogously, a force $\mathbf{f_y}$, as depicted in Fig. 2, with line of action overlapping the semiaxis b_1, produces translations parallel to b_1. The results, reported in Table 1, confirm the theoretical predictions.

4 CONCLUSION

In this work, a synthesis procedure for defining kinetostatic equivalent flexures has been proposed. The method is based on the ellipse of elasticity and affine deformations. Starting from any flexure, a variety of equivalent elastic elements can be generated. The procedure has been applied to a constant-curvature flexure and the theoretical results have been confirmed by finite element analysis.

References

[1] M. Ling, L. L. Howell, J. Cao, and G. Chen, "Kinetostatic and dynamic modeling of flexure-based compliant mechanisms: A survey," *Applied Mechanics Reviews*, vol. 72, no. 3, p. 030802, 01 2020.

[2] O. Weeger, "Isogeometric sizing and shape optimization of 3d beams and lattice structures at large deformations," *Structural and Multidisciplinary Optimization*, vol. 65, no. 2, Jan. 2022.

[3] O. Sorgonà, N. Belfiore, O. Giannini, and M. Verotti, "Application of the ellipse of elasticity theory to the functional analysis of planar compliant mechanisms," *Mechanism and Machine Theory*, vol. 184, p. 105308, 2023.

[4] O. Sorgonà, O. Giannini, and M. Verotti, "Projective synthesis of planar compliant mechanisms," *Mechanism and Machine Theory*, vol. 210, p. 106010, Aug. 2025.

DESIGN AND EXPERIMENTAL VALIDATION OF AN UNDERACTUATED FOUR-FINGER VARIABLE STIFFNESS GRIPPER WITH SENSORLESS FORCE ESTIMATION

Ozan Kaya[1,2], Ertugrul Bayraktar[3], Seniz Ertugrul[4]

[1] Norwegian University of Science and Technology, Trondheim, Norway, {ozan.kaya@ntnu.no}
[2] Istanbul Technical University, Istanbul, Turkey, {kayaozan@itu.edu.tr}
[3] Yildiz Technical University, Istanbul, Turkey, {eb@yildiz.edu.tr}
[4] Izmir University of Economics, Izmir, Turkey, {seniz.ertugrul@izmirekonomi.edu.tr}

1 INTRODUCTION

Collaborative robotic manipulation demands grippers that balance adaptability and compliance with stable grasping and interaction safety. Rigid grippers provide accurate positioning but low mechanical compliance, which can degrade performance on fragile/deformable objects and increase contact risk in physical human–robot interaction [1]. Variable-stiffness actuation offers a principled route to adjustable impedance [2], but many variable-stiffness grippers rely on multi-actuator architectures, antagonistic transmissions, or material-driven nonlinearities, which often increase mechanical complexity, calibration burden, and failure modes [3–5]. This paper addresses the resulting complexity–capability trade-off by presenting a four-finger variable stiffness gripper that achieves stiffness modulation with a compact two-motor architecture and a geometric lever-arm adjustment mechanism, along with experimental characterization and representative manipulation demonstrations. The main contributions of this work are (i) a four-finger gripper with variable stiffness using two DC motors; (ii) a lever-arm based stiffness adjustment mechanism; and (iii) experimental characterization of stiffness tuning and representative manipulation demonstrations.

2 MECHANISM DESIGN

The proposed VSG employs four parallel fingers, each modeled as a planar 2-DOF linkage. A compact transmission, which comprises gears, a double universal joint (DUJ), ball-screw stages, and linear springs, couples two DC motors to the fingers: one motor drives grasp closure/opening, while the second adjusts stiffness through a purely mechanical geometry change. Stiffness regulation is achieved by varying the spring moment arm around the finger joint via relocation of the spring attachment point, thereby tuning the equivalent torsional stiffness. This geometric approach avoids material-driven nonlinearities and enables for a repeatable, design-parameterized stiffness law.
Finger motion is produced through a linear series-elastic actuation path that introduces compliance and improves tolerance to contact disturbances during grasping. In addition, external interaction forces are inferred from joint/actuator encoder readings and the kinematic transmission model, avoiding dedicated force or tactile sensors. Underactuated four-finger variable-stiffness gripper architecture highlighting the DUJ-based transmission and lever-arm stiffness adjustment is illustrated in Fig. 1.

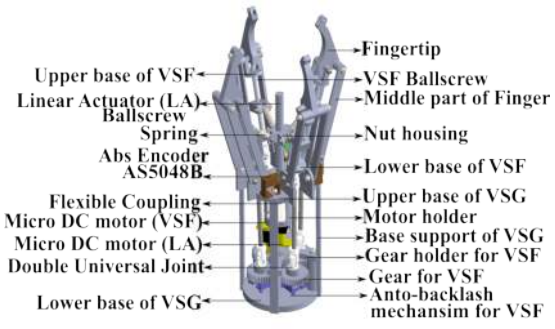

Figure 1: Proposed VSG mechanism illustrating the underactuated transmission system, and stiffness adjustment structure.

3 MODELLING AND CONTROL

A compact model was developed to support workspace analysis, stiffness characterization, and real-time control of the VSG. The kinematics of each finger are represented as a planar 2R chain, enabling computation of the fingertip workspace and admissible grasp configurations under the four-finger layout. For control-oriented dynamics, a reduced-order formulation captures the dominant effects of actuator motion, series elasticity, and spring-generated torques while avoiding unnecessary nonlinear terms that are negligible at the operating speeds considered.

The stiffness tuning behavior is identified experimentally by mapping the stiffness-adjuster position to the equivalent joint stiffness; this mapping is approximated with a low-complexity fitted function for online use. Control is implemented in a cascaded structure: an inner stiffness loop (PID) regulates the stiffness setpoint via the adjuster, and an outer position loop commands grasp motion. To maintain consistent tracking across stiffness settings, the position controller uses gain scheduling (adaptive PID) as a function of the current stiffness level. As can be seen from Fig. 2 that experimental measurements and the fitted stiffness mapping demonstrate the equivalent finger stiffness versus stiffness-adjuster position.

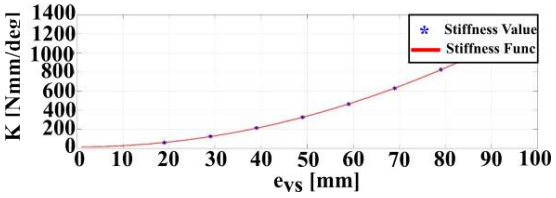

Figure 2: Equivalent finger stiffness vs. adjuster position (measured points and fitted model).

4 EXPERIMENTAL RESULTS

Experimental validation used a custom tensile-test setup instrumented with a load cell, rotary encoders, and linear displacement sensing to measure fingertip force, joint motion, and spring elongation. The prototype achieved fingertip forces of 3.68–20 N and an adjustable equivalent joint stiffness of approximately 50–800 Nmm/deg, confirming repeatable stiffness modulation via the mechanical adjuster. Closed-loop tests showed stable position tracking across multiple stiffness settings; frequency-response measurements indicated the expected trend of higher stiffness yielding increased bandwidth and lower tracking error. Finally, grasping trials on deformable objects qualitatively demonstrated stiffness-dependent regulation of object deformation while maintaining grasp closure. In Fig. 3, deformation regulation and finger position-tracking performance show the deformable object grasping under multiple stiffness settings.

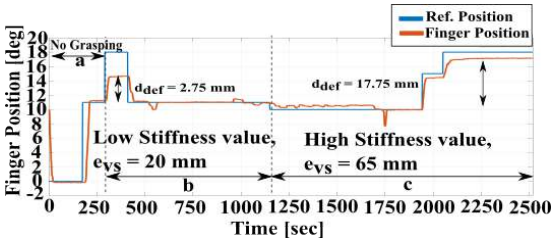

Figure 3: Deformable object grasping at different stiffness settings (deformation and tracking).

5 CONCLUSION

This paper presented a compact four-finger variable-stiffness gripper that reduces actuation complexity while enabling stiffness regulation for compliant manipulation. A DUJ-assisted transmission and a lever-arm–based spring geometry provide mechanically repeatable stiffness tuning, while series elasticity supports stable grasp motion under contact disturbances. Experiments confirmed the achievable stiffness range and force output, demonstrated stable tracking across stiffness settings, and showed representative handling of deformable objects. These results indicate the proposed architecture as a practical mechanism-level option for safe, compliant grasping in collaborative settings.

REFERENCES

[1] J. Vorndamme, A. Melone, R. Kirschner, L. Figueredo and S. Haddadin, (2025) "Safe Robot Reflexes: A Taxonomy-Based Decision and Modulation Framework," in *IEEE Transactions on Robotics*, vol. 41, pp. 982-1001.

[2] Yigit, C. B., Bayraktar, E., & Boyraz, P. (2018). "Low-cost variable stiffness joint design using translational variable radius pulleys", *Mechanism and Machine Theory*, 130, 203-219.

[3] Wu, X., Zhou, J., Ding, J., Wang, K., Tang, K., Yu, H., & Bai, S. (2025). "Stiffness modulation of an orthopedic robot based on large-range variable stiffness mechanisms", *Mechanism and Machine Theory*, 215, 106184.

[4] S. Yi, S. Liu, J. Ke, J. Liao, G. Xiaoyi and Z. Guo, (2025)"A Novel Design of Compact Serial Variable Stiffness Actuator (SVSA-III) With Predefined Stiffness Profiles," in *IEEE/ASME Transactions on Mechatronics*.

[5] Ju, W., Zhao, J., Zhang, W., Li, S., Kang, R., Dai, J. S., & Song, Z. (2024). A novel design method of a nonlinear elastic mechanism for series elastic actuators. *Mechanism and Machine Theory*, 202, 105775.

SYSTEMATIC DESIGN OF RECONFIGURABLE HYBRID ORIGAMI ROBOTS

Haoju Wen[1], Wenjun (Chris) Zhang[2]

[1] Division of Biomedical Engineering, College of Engineering, University of Saskatchewan, Saskatoon, Canada, {haw428@usask.ca}

[2] Division of Biomedical Engineering, College of Engineering, University of Saskatchewan, Saskatoon, Canada, {chris.zhang@usask.ca}

1. INTRODUCTION

Origami-inspired robotics provides a promising route toward compact, deployable, and reconfigurable robotic systems. Most existing origami robots are based on rigid origami, in which rigid facets and idealized hinges transmit motion and force through rigid-body mechanisms. Although effective for geometric transformation, this approach limits compliance, adaptability, and safe interaction with complex environments. To address these limitations, this work investigates hybrid origami robotics, in which compliance is embedded directly into the origami body.

In this study, hybrid origami is defined as an origami system that uses compliant mechanisms and compliant structures to transmit motion and force. A hybrid origami robot is correspondingly defined as a robot whose body architecture is based on hybrid origami. This definition establishes the basis for a systematic design methodology that links compliant structural design, modular embodiment, and reconfiguration-enabled functionality.

2. SYSTEM DESIGN FRAMEWORK

The proposed robot is constructed from modular origami limbs that act as the fundamental building blocks of the system. Each limb is designed as a compliant chain composed of multiple soft origami plates connected in series through crease lines. By combining flexible materials with embedded actuation, each limb can generate both deformation and output force, thereby supporting locomotion and manipulation within the same robotic architecture.

To determine limb geometry and actuation layout systematically, topology optimization is introduced. The design variables include the length and thickness of each plate, as well as the selection of active and passive plates. The optimization objective balances structural stiffness, deformation capability, and output force so that each limb can be tailored to a specific functional role while remaining compatible with the overall origami body. This modular strategy also improves scalability, since limbs can be added, removed, or rearranged without requiring a complete redesign of the robot.

At the robot level, graph theory is used to represent origami configurations, where nodes correspond to facets and edges represent crease connections. This abstraction supports systematic enumeration of feasible configurations and formal description of configuration transitions induced by folding and unfolding. Building on this representation, group theory is introduced to describe symmetry-preserving transformations during reconfiguration, such as rotations, reflections, and translations. Together, these tools provide a mathematical basis for analyzing structural reconfiguration and functional transformation.

3. RECONFIGURABLE FUNCTIONALITY

The proposed hybrid origami robot achieves multiple functional modes without disassembly. In a planar configuration, coordinated actuation of the origami limbs enables crawling locomotion. Through controlled folding, the structure transforms into an enclosed three-dimensional configuration that supports fixed grasping. Additional functions, including scraping, encapsulation, and redundant substitution after limb failure, can be realized through different limb arrangements and reconfiguration sequences.

Figure 1 illustrates the overall concept and functional reconfiguration of the proposed hybrid origami robot. The robot body is composed of a common-vertex origami structure connected to multiple modular origami limbs. Structural reconfiguration is achieved through coordinated folding and unfolding of the central origami facets, enabling the robot to transform between planar and three-dimensional configurations corresponding to different functional modes.

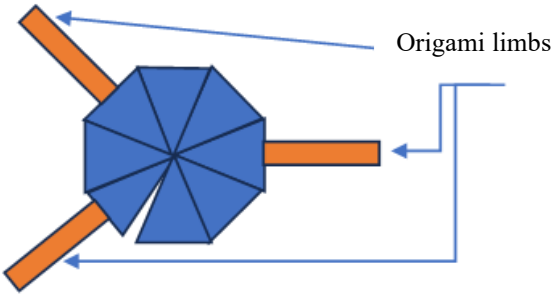

Figure 1. The concept model of hybrid origami robot.

4. EXPECTED CONTRIBUTION

By combining compliant origami structures, modular limb design, topology optimization, and formal configuration modeling, this work establishes a unified framework for the systematic design of reconfigurable hybrid origami robots. The approach enables adaptive, scalable, and multifunctional robotic behavior while preserving the compactness and transformability of origami-based systems. The framework is expected to support future developments in exploration, assistance, and adaptive manipulation in constrained environments.

By treating origami limbs as reconfigurable modules, the robot exhibits emergent multifunctionality: additional configurations arise from different limb combinations and symmetrical operations, adapting to diverse tasks. This approach ensures scalability, as modules can be added or rearranged to meet specific requirements.

The proposed framework advances hybrid origami robotics by offering a principled methodology for designing adaptive, multifunctional systems with inherent reconfigurability, holding potential for applications in exploration, assistance, and adaptive manipulation.

NON-INTRUSIVE QUASI-STATIC TORQUE MEASUREMENT IN GEARBOXES USING A HOUSING-MOUNTED FIBER BRAGG GRATING SENSOR

D. Janssens[1,2], S. Goossens[3,4], F. Naets[1,2]

[1] Department of Mechanical Engineering, KU Leuven, Belgium {Dennis.Janssens, Frank.Naets}@kuleuven.be
[2] Flanders Make@KU Leuven, Leuven, Belgium
[3] Vrije Universiteit Brussel - Brussels Photonics (B-PHOT), Pleinlaan 2, 1050 Brussel, Belgium
{Sidney.Goossens@vub.be} [4] BP&M, Flanders Make@VUB, Brussel, Belgium

1 INTRODUCTION

Torque is a fundamental quantity for the characterization, monitoring, and design of rotating transmissions. In industrial gearboxes, direct torque measurement typically requires intrusive shaft instrumentation or in-line torque flanges, increasing cost and mechanical complexity [1]. This motivates non-intrusive approaches capable of extracting torque information from stationary drivetrain components.

Transmitted torque generates gear mesh forces and bearing reactions that are transmitted into the gearbox housing, producing small but repeatable elastic deformations. Under quasi-static conditions, these deformations follow the transmitted torque through the gearbox load path. If measured with sufficient resolution, housing strain therefore provides a physically meaningful observable of quasi-static torque [2]. Even if high dynamic torque signals are present, low-pass filtering the signals can extract the quasi-static contribution of the input torque. Fiber Bragg grating (FBG) sensors are well suited for this purpose due to their high strain sensitivity, compact size, and immunity to electromagnetic interference (EMI). Their strong temperature sensitivity, however, requires additional compensation as gearboxes usually produce significant heat. Various temperature compensation strategies for FBG sensors have been reported in literature. The focus of this work is on extracting torque information from gearbox housing strain rather than developing novel temperature compensation strategies, therefore it uses a PT100 sensor to directly compensate for temperature changes in the FBG sensor.

2 MEASUREMENT CONCEPT

A minimal sensing concept is investigated using a single FBG bonded to the gearbox housing near a bearing seat, where gear and bearing loads enter the structure. The FBG wavelength shift contains contributions from both mechanical strain and temperature. A PT100 sensor mounted as close as practically possible to the FBG provides an independent temperature measurement.

The torque induced strain contribution in the FBG response is obtained by subtracting the scaled PT100 temperature from the FBG wavelength shift. This compensated wavelength shift is then mapped to the estimated input torque $\hat{M}$:

$$\hat{M}(t) = c_M(\Delta\lambda_{\mathrm{FBG}}(t) - c_T\, T_{\mathrm{PT100}}(t)), \tag{1}$$

where c_M is the torque sensitivity of the FBG on the location of FBG2 and has a value of -1.01 $[Nm/pm]$. c_T is the FBG temperature coefficient with a value of 22.9 $[pm/°C]$. This value includes both the thermo-optic effect of the fiber itself, as well as the thermal expansion effect of the gearbox housing. The coefficients are obtained through least-squares fitting of the low-pass filtered FBG wavelength signal to the reference torque. The values are consistent over multiple measurements.

3 EXPERIMENTAL SETUP

The method is evaluated on a laboratory drivetrain with two back-to-back induction machines coupled through two back-to-back gearboxes. An in-line HBM T40B torque sensor with a range of ±50 Nm provides the reference torque. As shown in Figure 1, the gearbox housing is instrumented with FBG sensors, resistive strain gauges and PT100 sensors near the bearing seat of the low speed shaft, where bearing reactions induce the largest housing deformation. Due to mechanical and practical mounting constraints, not all PT100 sensors are co-located with their corresponding FBGs, resulting in small spatial offsets between certain strain and temperature measurement points.

4 RESULTS

The results shown in Figure 2 are captured by FBG2 in Figure 1. The other FBG locations show comparable quasi-static torque correlation, with different sensitivity coefficients due to local strain distribution. Their torque estimation

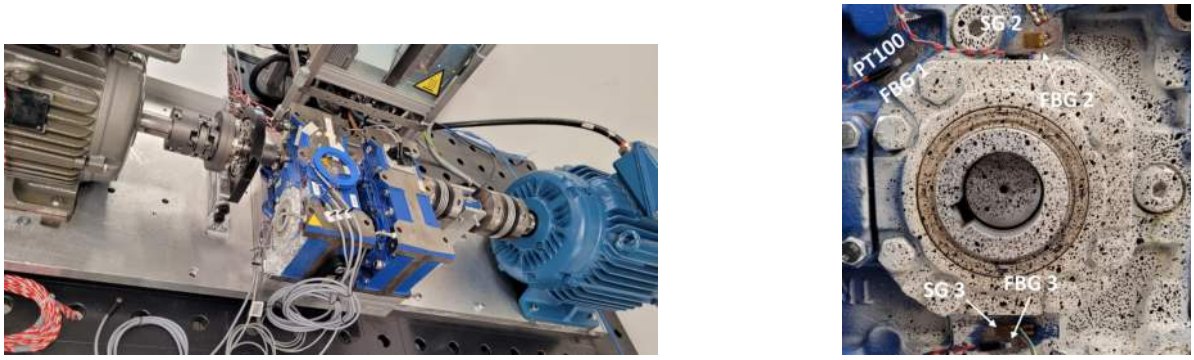

Figure 1: Laboratory drivetrain with instrumented gearbox (left) and housing-mounted FBG, strain gauges, and PT100 near the bearing seat (right).

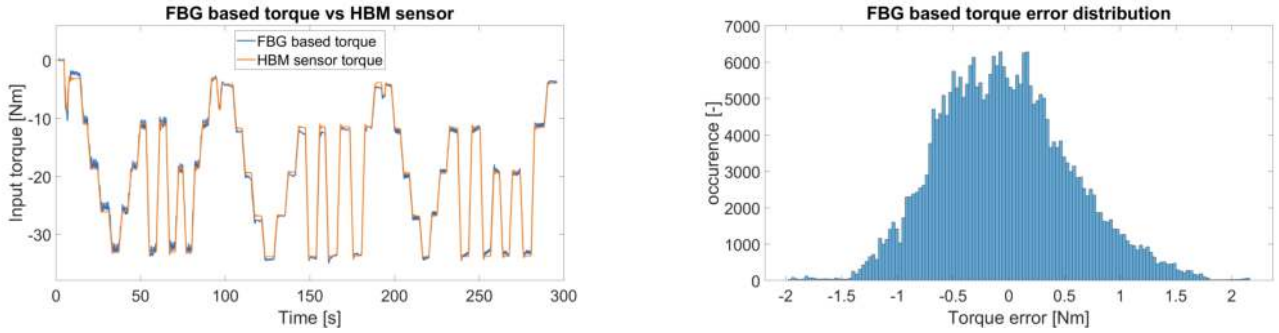

Figure 2: FBG-based torque compared to HBM T40B torque sensor reference. The signal content is limited to 0.25Hz to only capture the quasi-static torque changes. (left) Corresponding torque error distribution. (right)

accuracy is lower however, as the PT100 sensors are located further away from the actual FBG location, leading to local temperature gradients between the FBG and PT100 locations. This results in residual thermal offsets in the compensated signal.

The captured signals from both the HBM torque sensor and the FBG sensor are zero-phase low pass filtered with a cut-off frequency of 0.25Hz to only capture the quasi-static regime. The FBG-based torque estimate closely follows the applied quasi-static torque levels. Most errors remain within approximately ± 1.5 Nm as shown in Figure 2. The error approximately follows a normal distribution with mean $\mu = -0.04$ Nm and standard deviation $\sigma = 0.594$ Nm. At higher frequencies, dynamic effects such as gear mesh excitation and structural compliance between the measurement locations introduce differences between the locally measured housing strain and the corresponding torque measured at the high-speed shaft.

5 CONCLUSIONS

A minimal non-intrusive and EMI-immune torque sensing concept based on a single housing-mounted FBG sensor with external PT100 temperature compensation has been experimentally validated. The results demonstrate that quasi-static transmitted torque can be reliably obtained from gearbox housing deformation without any modification of rotating components. The consistent low torque error confirms the linear mapping of input torque to housing strain in the quasi-static regime. The results establish housing-mounted FBG sensing as a viable method for observing quasi-static transmitted torque when direct torque measurement is impractical.

ACKNOWLEDGMENTS

Internal Funds KU Leuven are gratefully acknowledged for their support. This research was partially supported by Flanders Make, the strategic research centre for the manufacturing industry.

REFERENCES

[1] D. E. Kakaley, R. E. Altieri, and G. D. Buckner, "Non-contacting measurement of torque and axial translation in high-speed rotating shafts," *Mechanical Systems and Signal Processing*, vol. 138, p. 106520, 2020, doi: 10.1016/j.ymssp.2019.106520.

[2] J. Bosmans, S. Gallas, V. Smeets, M. Kirchner, L. Geens, J. Croes, and W. Desmet, "Experimental validation of virtual torque sensing for wind turbine gearboxes based on strain measurements," *Wind Energy*, vol. 28, no. 2, 2025.

DEVELOPMENT OF A PROTOTYPE COMPRESSED-AIR GENERATOR USING WATER HAMMER ENERGY

P. Zevzikov[1], M. Bogdevicius[1]

[1] Vilnius Gediminas Technical University, Vilnius, Lithuania, { pavel.zevzikov@vilniustech.lt }

[1] Vilnius Gediminas Technical University, Vilnius, Lithuania, { marijonas.bogdevicius@vilniustech.lt }

1. INTRODUCTION

The water hammer is a transient hydraulic phenomenon that occurs in hydraulic systems owing to rapid changes in fluid velocity, leading to pressure surges [1]. These surges pose significant risks to pipeline systems [2,3]. However, under specific conditions, the effect of the water hammer can be used to convert and accumulate the energy of the fluid flow [4]. An example is the hydraulic ram, a device known since ancient times that is used to elevate water. One possible application is the compression of air by directing pressure surges to a liquid-air tank. Although the concept offers a promising approach to harvesting energy from natural sources (e.g. rivers and waterfalls) for low-cost sustainable green energy applications, it involves several technical challenges [5]. The present study was conducted through laboratory-scale investigations using a customized modular experimental rig. The prototype device represents a coupled dynamic system involving transient wave propagation, damping, valve actuation, and fluid-structure interaction.

2. OBJECTIVES OF THE RESEARCH

This study aimed to develop and experimentally investigate a hydromechanical system that converts the kinetic energy of water flow into the potential energy of compressed air by utilising transient fluid flow effects during cyclic water hammer events.

3. METHODOLOGY

Laboratory experiments were conducted using a specially designed experimental setup, as shown in Figure 1, which contains a centrifugal motor-pump unit (nominal hydraulic power 3,5 kW, nominal pressure 4.7 Bar according to a flow rate of 32.5 l /min), a water reservoir, a combined pipe system, and a compressed-air accumulation device. The main hydraulic line contains a long multilayer composite (PE-RT / Al / PE-RT) pipe section (a–b), coiled on the frame of the rig, with an inner diameter of 16 mm and length of 107 m, and a steel pipe section (b–c–e) with an inner diameter of 22 mm and length of 1.43 m, connected to the liquid-air tank (volume 26 l) through a branch pipe (c–d, inner diameter 18 mm and length 0.7 m).

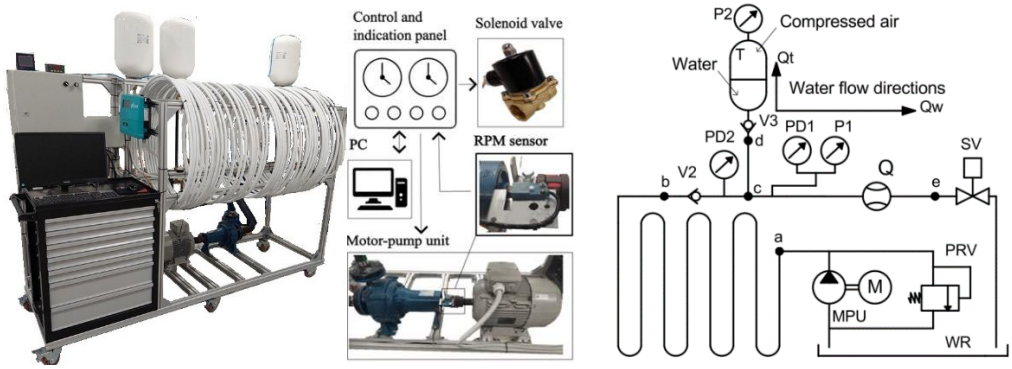

Figure 1. Constructed modular laboratory rig (left), structure of water flow control system (middle) and simplified principal scheme of prototype built for provided experiments (right, where: P1, P2 – piezoresistive pressure transducers; PD1, PD2 – piezoelectric pressure transducers; Q – ultrasonic fluid flow meter; SV – solenoid shut-off valve; WR – 200 l water reservoir; MPU – motor pump unit; PRV – pressure relief valve; V2,V3 – check valves; T – liquid-air tank; a, b ,c ,d ,e – junctions of pipe sections; Qt and Qw – flow rate to the tank and waste pipe respectively).

The water hammer excitation was generated using a normally closed solenoid valve. It was assumed that the key parameters that determine the dynamic response of the prototype are the timing of the cyclic actuation of the solenoid valve, the geometry and material properties of the pipes, valves, and junctions. The impact of these parameters on the efficiency of pressure transfer to the liquid-air tank was investigated.

The measurement equipment included a non-invasive ultrasonic flow meter for steady flow measurement before valve closure (response time 1 s), piezoresistive pressure transducers (response time 0.001 s) for quasi-static pressure observation, piezoelectric transducers (response time up to 0.000005 s) for measurements of high-frequency dynamic pressure response, and a multichannel

data acquisition system with a sampling rate of 250 kS/s [6,7]. Thus, the manometric and dynamic pressures at the selected points of the hydraulic system, air pressure in the liquid-air tank, and volumetric balance between the water delivered to the tank and the water discharged through the waste line were all monitored. The experiments were conducted under different conditions: flow velocities of 0.5–1.15 m/s, solenoid valve actuation time of 0.1 ± 0.02 s, and valve cycle period of 0.5–2 s. The initial pressure in the liquid-air tank was set depending on the pressure generated by the pump in the steady flow regime from 2.3 to 4.7 bar, with respect to the flow velocity.

4. RESULTS AND CONCLUSIONS

A modular rig and prototype of a compressed-air generator were developed, and experiments confirmed the technical feasibility of such a system.

- Single closure with a disconnected liquid-air tank. Peaks of pressure surges were observed: for flow velocity 0.5 m/s – 7.35 bar and for 1.15 m/s – 16.9 bar (total uncertainty of measurements and data sampling < 2%) [7].
- Cyclic closure with a connected liquid-air tank. The results for a flow velocity of 1.0 m/s and cycle period of 1.2 ± 0.05 s are presented in Figure 2, where the pressure in the liquid-air tank was increased from 5.2 to 5.74 bar within 20 s.

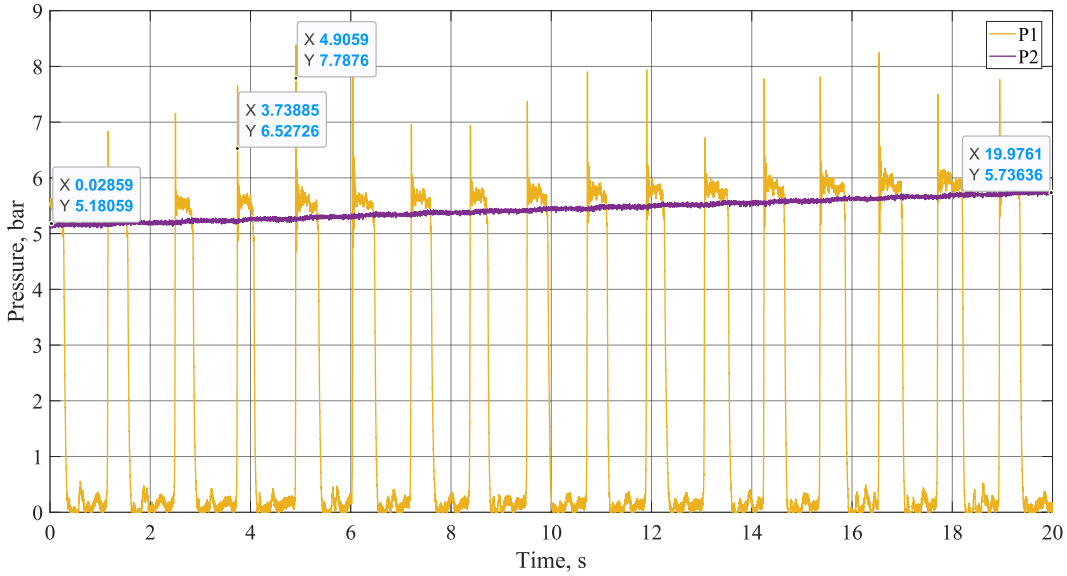

Figure 2. The results of the experiment were obtained with an initial flow velocity of 1 m/s and a valve closure cycle period of 1.2 s. P1 is the manometric water pressure (bar) and P2 is the pressure in the water-air tank (bar).

4.1. Conclusions:

1. The measured first pressure peak values were observed to be ~10% less than the result of the classical Joucowsky formulation; these discrepancies should be attributed to the viscoelastic damping of the elements of the hydraulic system and non-instantaneous valve closure. The maximum air pressure that can be generated in the liquid-air tank was observed to be 80 – 90% of the classically predicted first peak value, whereas the filling time strongly depended on the variable air compression efficiency.
2. The air compression efficiency evaluated by monitoring the volumetric balance Qt/Qw under different conditions was between 10 and 40 %, depending on the initial flow velocity and valve timing combination. Signs of convergence to the maximum efficiency for the investigated configuration of the system were observed for a valve actuation period near 0.5 s.
3. The analysis of the results led to the hypothesis that the air compression efficiency mostly depends on the time and period of valve closure actuation, the length and diameter of the device connection pipe, and the ratios of these factors. In the next stages of research, we plan to optimize the sensitive parameters of the system prototype and check the scalability of the observed ratios on large-scale equipment.

REFERENCES

[1] Di Nucci, C. Urbanowicz, K. Michele, S. Celli, D. Pasquali, D. & Di Risio,“On water hammer waves”, *Wave Motion*, 2025
[2] M. Kurbak, “Water hammer mitigation by internal rubber hose”, *Archives of Civil Engineering*, 2024
[3] I. Solomon, G. Dundulis, “Modeling of Pipe Whip Phenomenon Induced by Fast Transients Based on Fluid-Structure Interaction Method Using a Coupled 1D/3D Modeling Approach”, *Multidisciplinary Digital Publishing Institute*, 2023
[4] L. A. Cox, „Hydraulic ram type water pump”, *patent US4911613*, 1990
[5] G. O. Lungudi et al., “Numerical and experimental analyses of hydraulic rams,” *Journal of Hydraulic Research*, 2024
[6] J. Fraden, “Handbook of modern sensors: Physics, designs, and applications”. *Springer International Publishing*, 2016
[7] S. M. Alan, “Measurement and Instrumentation Principles”. *Butterworth-Heinemann Linacre House, Oxford*, 2010

COLLOCATED CONTROL OF AN UNDERACTUATED CABLE-DRIVEN PARALLEL ROBOT THROUGH DISTURBANCE OBSERVER AND INVERSE DYNAMICS

Jason Bettega[1], Salvatore Marrazzo[1], Dario Richiedei[1], Alberto Trevisani[1]

[1] Department of Management and Engineering, University of Padova, Stradella S. Nicola 3, 36100 Vicenza, Italy, {jason.bettega@unipd.it; salvatore.marrazzo@studenti.unipd.it; dario.richiedei@unipd.it; alberto.trevisani@unipd.it }

1 INTRODUCTION

1.1 State of the art

Cable-driven parallel robots (CDPRs) are manipulators in which the end-effector (EE) is actuated by cables. Their large workspaces and high payload-to-weight ratios enable lightweight designs and have attracted increasing interest in the fields of robotics and multibody system dynamics. Despite these advantages, motion planning and control are challenging due to the unilateral nature of cables, which can transmit only tensile forces. To cope with this issue, most existing solutions rely on overactuated architectures, where the number of independently actuated cables exceeds the number of degrees of freedom (DOFs) of the EE. While this simplifies control design, it increases mechanical complexity and the risk of cable interference. To simplify mechanical design, underactuated architectures have recently gained growing attention. In general, a dynamical system is said to be underactuated when the number of independent control inputs is smaller than the number of its DOFs [1]. In cable robotics, underactuated CDPRs are often referred to as *kinematically deficient*, since the EE pose cannot be uniquely determined through cable lengths alone. Due to these characteristics, several problems related to inverse dynamics and control of underactuated CDPRs are still open. Considering inverse dynamics, different approaches have been proposed in the general field of multibody systems, including both non-causal [2] and causal solutions [1]. In the specific context of CDPRs, most of the literature focuses on overactuated architectures [3], while only limited works address the inverse dynamics of underactuated CDPRs [4]. Similarly, from the feedback control standpoint, several advanced techniques have been investigated in recent years, such as model predictive control, disturbance observer-based control and sliding mode control. Nevertheless, the majority of contributions deal with overactuated CDPRs [5], whereas control strategies specifically tailored for underactuated architectures [6] remain relatively unexplored.

1.2 Motivations and goals of the paper

Considering underactuated CDPRs, the combined use of inverse dynamics techniques and disturbance observer-based (DOB) control strategies has received limited attention so far. Motivated by this gap, this paper proposes a two-stage control framework that exploits the synergy between these approaches. In the first stage, given a desired EE trajectory, an inverse dynamics procedure based on the input-output normal form is employed to handle underactuation. This stage yields the required control forces and the corresponding motor position and velocity references. In the second stage, motor trajectory tracking is achieved through a nested feedback control structure composed of two loops: an outer position control loop and an inner velocity control loop. The outer loop employs a proportional (P) controller, while the inner loop relies on a proportional controller enhanced with a disturbance observer, to improve robustness against modeling uncertainties and external disturbances. The effectiveness of the proposed control strategy is numerically validated on a planar underactuated CDPR.

2 TWO-STAGE CONTROL ARCHITECTURE

Given a desired reference trajectory for a subset of EE coordinates, the goal of the first stage is to achieve good performances in terms of trajectory tracking, compensating for possible oscillations coming from the underactuation property. This task is performed by inverting the nonlinear Ordinary Differential Equations of the dynamic model, computing the required control cable tensions and the corresponding reference trajectories for the electric motors. This goal is achieved by exploiting the input-output normal of the unconstrained EE, which allows relating the cable tensions with the acceleration of the controlled output. This relationship is defined by the equation $\ddot{\mathbf{y}} = \mathbf{P}\mathbf{u}+\mathbf{H}\mathbf{M}^{-1}\mathbf{f}_\mathbf{w}$, where $\mathbf{P}$ is the decoupling matrix [1], $\mathbf{H}$ is related to the kinematic output equations, $\mathbf{M}$ is the EE mass matrix and $\mathbf{f}_\mathbf{w}$ is the external wrench. In the second stage, a disturbance observer (DOB) is incorporated into the inner velocity

control loop to track the desired motor reference trajectories coming from the previous stage. The DOB compensates for model mismatches, such as uncertainties in the motor parameters, disturbances coming from the EE and unknown disturbances, thereby enhancing the overall robustness. To further increase system performance, the required control cable tensions, coming from the previous stage, are translated into required control motor torques that can be used as feedforward control input.

3 NUMERICAL RESULTS

The method is validated through the planar cable-driven robot sketched in Fig. 1, which consists of three-DOF EE controlled through just two cables, leading to a degree of underactuation equal to one. These features allow the imposition of two coordinates of the EE; in the proposed example, the two Cartesian coordinates of the EE center of mass are imposed, leading to the output vector $\mathbf{y} = \{x_{CoM} \quad y_{CoM}\}^{\mathrm{T}}$. The test consists of a rest-to-rest motion of the EE from an initial stable equilibrium configuration to a final one; for each Cartesian coordinate, a polynomial motion law is designed with the goal to be exactly tracked at any time step. Trajectory tracking errors are reported in Fig.2 for two different scenarios: an ideal scenario and a more realistic one, where unknown disturbances and model mismatches are introduced. It can be seen that, in both scenarios, low tracking errors are achieved.

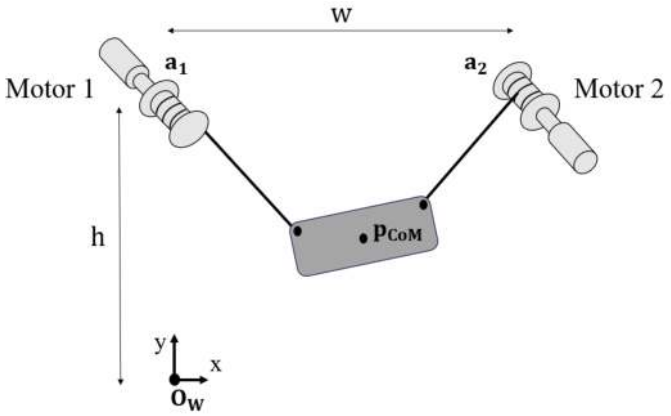

Figure 1: System under investigation.

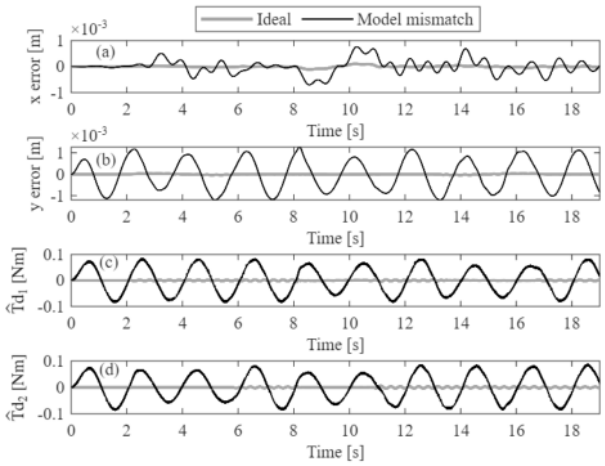

Figure 2: Numerical trajectory tracking errors (a)-(b) and estimated torque disturbances (c)-(d).

4 CONCLUSIONS

The numerical results confirm the effectiveness of the proposed technique, which allows to achieve good performances in terms of trajectory tracking while increasing the robustness of the overall system against unknown disturbances and model mismatches. More precisely, in the proposed test, which lasts 19 s, and in the presence of model mismatches and external torque disturbances, the maximum absolute tracking error is equal to 1.3 mm and the maximum Root-Mean Square value is equal to 0.7 mm, both values referred to the y axis.

References

[1] R. Seifried, "Two approaches for feedforward control and optimal design of underactuated multibody systems," *Multibody System Dynamics*, vol. 27, no. 1, pp. 75–93, 2012.

[2] S. Devasia, D. Chen, and B. Paden, "Nonlinear inversion-based output tracking," *IEEE Transactions on Automatic Control*, vol. 41, no. 7, pp. 930–942, 1996.

[3] D. Q. Nguyen, M. Gouttefarde, O. Company, and F. Pierrot, "On the analysis of large-dimension reconfigurable suspended cable-driven parallel robots," in *2014 IEEE International Conference on Robotics and Automation (ICRA)*, pp. 5728–5735, 2014.

[4] G. Piva, D. Richiedei, and A. Trevisani, "Model inversion for trajectory control of reconfigurable underactuated cable-driven parallel robots," *Nonlinear Dynamics*, vol. 113, no. 8, pp. 8697–8712, 2025.

[5] X. Gao, W. Shang, and B. Zhang, "Disturbance observer-based model predictive control for cable-driven parallel robots," *IEEE Transactions on Robotics*, vol. 41, pp. 6307–6326, 2025.

[6] J. Bettega, D. Richiedei, and A. Trevisani, "Precise path following and trajectory tracking in cable-driven parallel robots through model predictive control with embedded reference dynamics," *The International Journal of Advanced Manufacturing Technology*, vol. 136, pp. 3465–3490, Feb 2025.

KINEMATIC SYNTHESIS OF A VERTEX-COUPLED SINGLE-DOF OPEN-SHEET, FINITE-THICKNESS YOSHIMURA PATTERN USING SLIDING MULTI-HINGE FOLD MODULES

Enrique Roberto Carrillo Li[1]; Lena Zentner[2]; Enrique Pujada Gamarra[1,2]; Daniel Lavayen Farfan[1]; Jorge Antonio Rodríguez Hernández[1]

[1] Pontificia Universidad Católica del Peru (PUCP) {ecarrillol@pucp.edu.pe; dlavayen@pucp.edu.pe; crodrig@pucp.edu.pe}

[2] Technische Universität Ilmenau, Germany, {lena.zentner@tu-ilmenau.de}{enrique.pujada-gamarra@tu-ilmenau.de}

1. INTRODUCTION

Origami is an ancient Japanese craft whose techniques provide a kinematic framework for realizing deployable three-dimensional geometries in structures, mechanisms, and robots [1]. Recent large-scale, uniformly thick origami systems highlight the importance of manufacturable thick-panel tessellations for adaptable load-carrying applications [2]. Among triangular-based patterns, Yoshimura tessellations are attractive because open sheets can be folded to approximate planar or gently curved surfaces reducing enclosed volume. In practice, however, ideal folds are replaced by finite-thickness facets and mechanical joints. While multi-hinge thickness-accommodation can reduce interference, it can also introduce extra local coordinates and relative displacements that accumulate across repeated cells [3]. Moreover, most Yoshimura studies focus on tubular mechanisms and deployment modes [4], [5], whereas open-sheet designs with explicit single-degree-of-freedom (1-DOF) control remain less explored; surveys emphasize the need for joint architectures that are both manufacturable and kinematically well-constrained [6]. Related work includes Yoshimura-compatible thick vertices (including a degree-6 vertex) [2], modular Yoshimura approaches [7], and several 1-DOF thick-panel and sliding-hinge concepts [8], [9], [10]. In this work, we propose a constraint-based kinematic synthesis framework for thick open-sheet Yoshimura tessellations. The approach integrates (i) a compact fold-substitution module combining sliding and multi-hinge thickness accommodation and (ii) a vertex-level equal-angle coupling condition that enforces a single global degree of freedom (1-DOF) across the tessellation. The existence of a unique actuation mode is verified through constraint-Jacobian rank analysis and further validated via multibody simulations incorporating friction and clearance effects, as well as experimental tests on 3D-printed panel prototypes.

2. KINEMATIC MODEL

An open Yoshimura sheet is modeled as a spatial linkage: rigid facets are links and each crease is replaced by a joint module. Let $q \in \mathbb{R}^{n_q}$ includes dihedral angles and prismatic coordinates of the fold modules [1]. Compatibility between adjacent facets is enforced by holonomic constraints $g(q)=0$, assembled from (a) hinge/slider joint constraints inside each module and (b) facet adjacent constraints that preserve the shared crease line in 3D.

2.1. Constraint-based mobility assessment

Local and global mobility are evaluated from the constraint Jacobian **J**. With one facet grounded to remove rigid-body motions, the instantaneous degrees of freedom are computed

$$\mathrm{DOF} = n_q - \mathrm{rank}(\mathbf{J}), \tag{1}$$

where n_q is the number of generalized coordinates and Jacobian $\mathbf{J} = \partial g/\partial q$. This formulation supports systematic detection of over-constraint, singularities and parasitic modes in thick origami mechanisms [6], [11]. Let λ denote a scalar global deployment parameter (actuator input). To enforce a single global DOF, we augment the baseline set with explicit vertex-coupling constraints $c(q,\lambda) = 0$ and define the augmented constraint vector:

$$\mathbf{H}(q,\lambda) = \begin{bmatrix} g(q) & ; c(q,\lambda) \end{bmatrix} = \mathbf{0}. \tag{2}$$

We verify a one-parameter motion manifold by tracking the rank of the augmented Jacobian $\mathbf{J}_{aug} = \partial \mathbf{H}/\partial q$ along the deployment path and checking that:

$$\mathrm{rank}(\mathbf{J}_{aug}) = n_q - 1 \tag{3}$$

The numerical rank is evaluated via Singular Value Decomposition by counting singular values $\sigma_i / \sigma_{max} > \varepsilon$ (relative tolerance).

3. THICKNESS-ACCOMMODATED FOLD MODULE AND SINGLE DOF VERTEX COUPLING

Each ideal fold is substituted by a compact offset-linkage module that combines a multi-hinge arrangement with a prismatic (sliding) element. The multi-hinge branch provides rotational freedom while separating facets to prevent collision near intersecting folding lines; the slider absorbs the geometric mismatch introduced by finite thickness and offsets. Compared with hinge-only thickening, the additional prismatic coordinate enables controlled clearance and tunable stroke. The module is

parameterized by the facet thickness t, an offset distance δ between hinge axis and folding line, and the slider stroke s. Geometric constraints relate the effective dihedral angle ρ at the fold to the parameters, enabling design-space exploration for interference-free folding and for limiting relative facet displacements [3]. To obtain controlled global motion, all folds incident to an interior vertex v are coupled to share a common fold angle. For a vertex of degree D, with effective dihedral angles $\rho_i(q)$ the coupling constraints impose:

$$\rho_i(q) - f(\lambda) = 0, \quad i = 1, \cdots, D. \tag{4}$$

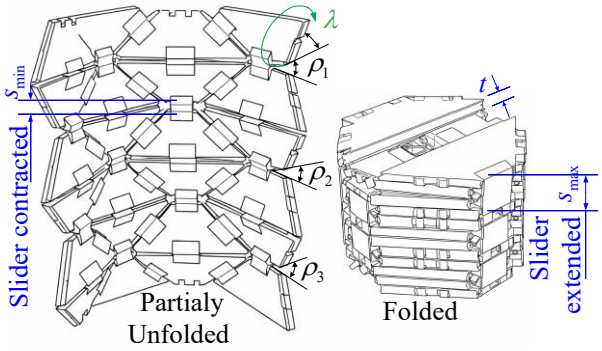

Figure 1 Folded and unfolded structure.

The function $f(\lambda)$ denotes the prescribed actuation law relating the single global input λ to the effective dihedral angles of all folds incident to a vertex. Mechanically, this is implemented by a shared slider or synchronizing linkage within the vertex hub, which drives each fold module so that its effective dihedral angle satisfies $\rho_i = f(\lambda)$. Imposing the vertex-coupling constraints reduces the local vertex mobility to 1 DOF and suppresses drift caused by uneven folding across neighboring cells. In the assembled tessellation, the combination of vertex coupling and facet-compatibility constraints yields a one-parameter motion manifold, verified by the rank condition in (3) along the folding path. This single-DOF enforcement is particularly useful for actuator-driven sheets where repeatability and predictable deployment trajectories are required.

4. NUMERICAL AND EXPERIMENTAL RESULTS: SINGLE-DOF DEPLOYMENT AND DRIFT SUPPRESSION

The proposed open-sheet mechanism is evaluated by (i) tracking the augmented constraint-Jacobian rank over the full deployment, (ii) running multibody simulations with joint clearances and Coulomb friction to probe sensitivity and detect parasitic modes, and (iii) testing 3D-printed multi-cell prototypes to measure fold trajectories and drift accumulation over repeated cycles; these analyses confirm a single actuation mode along the folding path (1-DOF rank condition with a one-dimensional null space), show that vertex coupling suppresses parasitic modes and reduces drift relative to uncoupled folding under realistic friction/clearance conditions, and demonstrate improved cyclic repeatability in experiments with trajectories consistent with simulation.

REFERENCES

[1] R. J. . Lang, *Twists, tilings, and tessellations : mathematical methods for geometric origami*. CRC Press, 2018.

[2] Y. Zhu and E. T. Filipov, "Large-scale modular and uniformly thick origami-inspired adaptable and load-carrying structures," *Nat. Commun.*, vol. 15, no. 1, Dec. 2024, doi: 10.1038/s41467-024-46667-0.

[3] E. Pujada-Gamarra, L. Zentner, D. Lavayen-Farfán, and J. A. Rodriguez-Hernandez, "Analysis of the relative displacements in a thick Origami with double-hinge technique for thickness accommodation," *Mech. Mach. Theory*, vol. 210, Aug. 2025, doi: 10.1016/j.mechmachtheory.2025.106000.

[4] C. Wang, D. Xu, S. Song, Y. Zhao, and J. Zhang, "Design and Analysis of Yoshimura Tubular Origami Mechanisms," *Applied Sciences (Switzerland)*, vol. 14, no. 24, Dec. 2024, doi: 10.3390/app142412048.

[5] Y. Yoshimura, "On The Mechanism Of Buckling Of A Circular Cylindrical Shell Under Axial Compression," Jul. 1955. Accessed: Feb. 09, 2026. [Online]. Available: https://hdl.handle.net/2060/19930093840

[6] R. J. Lang, K. A. Tolman, E. B. Crampton, S. P. Magleby, and L. L. Howell, "A Review of Thickness-Accommodation Techniques in Origami-Inspired Engineering," Jan. 01, 2018, *American Society of Mechanical Engineers (ASME)*. doi: 10.1115/1.4039314.

[7] A. Micheletti, I. Giannetti, G. Mattei, and A. Tiero, "Kinematic and Static Design of Rigid Origami Structures: Application to Modular Yoshimura Patterns," *Journal of Architectural Engineering*, vol. 28, no. 2, Jun. 2022, doi: 10.1061/(asce)ae.1943-5568.0000531.

[8] J. Yang and Z. You, "IDETC2019-97946 COMPACTLY FOLDING RIGID PANELS WITH UNIFORM THICKNESS THROUGH ORIGAMI AND KIRIGAMI," 2019.

[9] A. Micheletti, A. Tiero, and G. Tomassetti, "Simulation and design of isostatic thick origami structures," *Meccanica*, vol. 59, no. 9, pp. 1403–1423, Sep. 2024, doi: 10.1007/s11012-024-01815-0.

[10] R. J. Lang, T. Nelson, S. Magleby, and L. Howell, "Thick rigidly foldable origami mechanisms based on synchronized offset rolling contact elements," *J. Mech. Robot.*, vol. 9, no. 2, Apr. 2017, doi: 10.1115/1.4035686.

[11] T. Tachi, "Evolution and Trends in Design, Analysis and Construction of Shell and Spatial Structures Generalization of Rigid Foldable Quadrilateral Mesh Origami," 2009.

Book of Abstracts of MMT Symposium
Mechanism and Machine Theory Symposium
Flores et al. (Eds)

MMT Symposium
60th Anniversary of Mechanism and Machine Theory
June 21-23, 2026 Porto, Portugal

ANALYSIS AND IMPROVEMENTS OF THE CLASSICAL MODEL OF RAILWAY WHEELSET DYNAMICS

Mate Antali[1]

[1] Szechenyi Istvan University, Department of Applied Mechanics, Egyetem ter 1, H-9026, Gyor, Hungary, antali.mate@sze.hu

1 INTRODUCTION

Stability loss of railway wheelsets due to conical shape and creep forces has been a key problem in the literature since the first publications by Carter [1]. The equations of motion of the wheelset have been extended in several directions, including various types of nonlinearities and different vehicle structures. Still, the core dynamical model is roughly the same even in recent papers. However, in most literature sources, of the literature, the equations are not exact; they contain approximations, even in the linear terms. Although the quantitative effect of these approximations is typically low or moderate, it is worth gaining a deeper insight into the problem, not just to obtain the exact linearised equations but also to better understand several non-trivial modelling assumptions.

2 EQUATIONS OF MOTION IN THE LITERATURE

As a reference, let us briefly recall the equations of motion from the literature.

2.1 General model of a wheelset

The configuration of an unconstrained wheelset is described by the coordinates x, y, z of the geometric centre C and Euler angles ψ, ϑ, φ (see Fig. 1). For the wheelset moving on the rails, we can typically find the following form of differential equations in the literature:

$$m\ddot{y} = F_y(y, \dot{y}, \psi, \dot{\psi}), \qquad J_1\ddot{\psi} = M_\psi(y, \dot{y}, \psi, \dot{\psi}). \tag{1}$$

In this two-degree-of-freedom model, the generalised forces F_y, M_ψ originate from several sources, including contact, suspension, gravity and inertial forces. In this formulation, different linear and nonlinear effects can be included, and the wheelset can also be coupled with the dynamics of a whole vehicle.

2.2 Minimal model of an isolated, conical wheelset

For a benchmark model, consider the simplest possible model that exhibits most important dynamic phenomena. In Fig. 1, we can see an isolated wheelset affected purely by the gravity and the contact forces at the rails. For this model with a *conical* profile

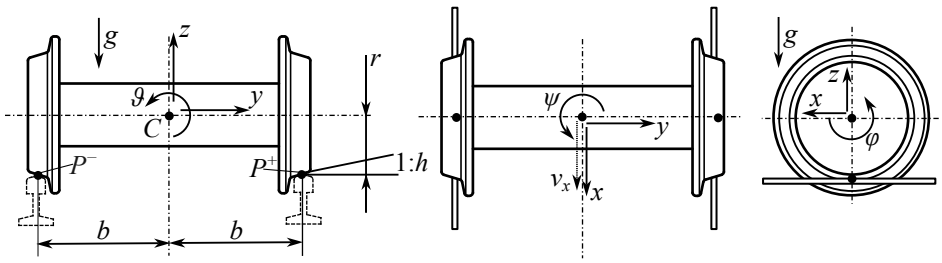

Figure 1: Variables and parameters of the dynamic model of the railway wheelset. The wheel is described by the rolling radius r, half gauge b, nominal conicity h, mass m and transversal moment of inertia J_1. The gravitational acceleration is denoted by g.

and the simplest possible creep model with longitudinal and transversal coefficients C_l, C_t, the literature typically provides the following form of equations:

$$m\ddot{y} + 2C_t\zeta_t + mghy/b = 0, \qquad J_1\ddot{\psi} - 2bC_l\zeta_l = 0, \tag{2}$$

where the creepages are defined by $\zeta_t = \dot{y}/v - \psi$, $\zeta_l = -b\dot{\psi}/v - hy/r$. We focus on the analysis of this *minimal model*, but the results can be transferred to the more general system (1). For an overview of modelling wheelsets, see [2].

3 ISSUES OF THE NONLINEAR DESCRIPTION

First, we analyse the differences between the exact derivation of the equations and the usual derivation in the literature.

3.1 Proper linearisation

The equations (1)-(2) both implicitly include geometric linearisation. (Even in the case when nonlinear forces are added to (1).) The linearised approach appears both in the variables (displacements and rotations are considered small) and in the parameters (the conicity h is considered small). It can be shown that by the exact linearisation of the full nonlinear dynamics, we get slightly different equations compared to (1)-(2). For the case of the pure rolling (kinematic) motion of the wheelset, it was derived for conical [3] and general curved [4] profiles. Now, we demonstrate the same for the dynamic problem with creepages at the contact point. We get that most terms in the equations have only a slight qualitative change in the exact equations, but there are terms and cases when the difference can be significant.

3.2 Role of the third degree of freedom

A further issue in the derivation concerns the degrees of freedom of the system. When applying the constraint of the constant vehicle speed and the two normal contact conditions on the wheelset, the remaining system should have three degrees of freedom. However, the systems such as (1)-(2) contain only two, which is not explained well in the literature. When performing the exact derivation, we get that in the *linearised* equations, the third degree of freedom is decoupled from (2), and that third component (corresponding to the average longitudinal creepage) is decaying in time. In addition, it can be shown that there is still a *nonlinear coupling* between the variables.

3.3 Sequence of the Euler angles

When the directions of the axes of the Euler angles are fixed (such as in Fig. 1), the form of the linearised equations is the same regardless of the sequence of the rotations; however, the sequence of rotations does matter in the full nonlinear equations. As an interesting fact, the exact nonlinear geometric constraints can be expressed explicitly for the pure conical wheel only for a specific sequence of rotations.

4 ISSUES OF THE CREEP FORCE MODELS

Other interesting questions arise regarding the modelling of the contact (creep) forces.

4.1 Creepages at the two sides

In the equations (2) of the literature, there is a definition for each of the *longitudinal* and *transversal* creepages ζ_l and ζ_t, respectively. In other words, it is implicitly assumed that the magnitudes of the corresponding creepages are the same at the left and right contact points. However, in the exact description, this is not true. The lateral creepages of the wheels are geometrically constrained, but only their linear part are equal, and they differ in the nonlinear terms. The issue of transversal creepages is more complicated and is related to the third degree of freedom mentioned above.

4.2 Definition of the longitudinal and transversal directions

Even the definition of the longitudinal and transversal directions is ambiguous. These directions can be fixed either to the wheel or the rail (and the actual rolling direction is between the two). This choice does not affect the linearised equations but becomes independent in the nonlinear description.

4.3 Definition of the creepages

Finally, even the definition of creepages is not clear enough. The creepages are defined as a ratio between the *creep velocities* of the contact point and some *reference velocity*. In the literature, this reference velocity is usually the velocity of the v vehicle (see (2)). However, it would be reasonable to use the velocities of the centre of the wheels. Moreover, for a local description, the normalised angular velocity $r\dot{\varphi}$ could also be used instead of v. These choices are not equivalent in the nonlinear description.

ACKNOWLEDGMENTS

The research is supported by the National Research, Development and Innovation Office under grant no. NKFI-150659 and by the Janos Bolyai Research Scholarship of the Hungarian Academy of Sciences.

REFERENCES

[1] F. W. Carter , “The electric locomotive”. *Minutes Proc. Instit. Civil Engin.*, vol. 201, pp. 221-252, 1916.

[2] S. Iwnicki, “Simulation of wheel–rail contact forces”. *Fatigue Fract. Engng. Mater. Struct.*, vol. 26, pp. 887–900, 2003.

[3] M. Antali, G. Stepan and S. J. Hogan, “Kinematic oscillations of railway wheelsets”. *Multibody Syst. Dyn.*, vol. 34, no. 3, pp. 259–274, 2015.

[4] M. Antali and G. Stepan , “On the nonlinear kinematic oscillations of railway wheelsets”. *Journal of Computat. and Nonlin. Dyn.*, vol. 11, no. 5, CND-15-1436 pp. 1–10, 2016.

GEOMETRY OF MULTIBODY MOTION: AN INTRINSIC LIE GROUPOID APPROACH

Robin Chhabra[1], Yael Karshon[2], M. Reza Emami[3]

[1] Department of Mechanical, Industrial, and Mechatronics Engineering, Toronto Metropolitan University, Toronto, Canada, {robin.chhabra@torontomu.ca}
[2] Department of Mathematics, University of Toronto, Toronto, Canada, {karshon@math.toronto.edu}
[3] University of Toronto Institute for Aerospace Studies, Toronto, Canada, {emami@utias.utoronto.ca}

1 SCOPE AND OBJECTIVES

A rigid multibody system comprises a collection of interconnected rigid bodies whose relative motions are restricted by mechanical joints, and it constitutes the dominant mathematical paradigm for describing motion and force transmission in robotics and mechanical engineering. A rigorous treatment of such systems requires both an accurate characterization of single–body rigid motion and a principled representation of joint constraints. The study of rigid motion has deep roots in geometric mechanics [1]; classical screw theory—systematized by Ball [2] and originating in the works of Euler [3], Chasles [4], Poinsot [5], and Clifford [6]—established a geometric language for displacements and forces. Contemporary formulations typically employ Lie groups and Lie algebras, most notably the Special Euclidean group $\mathbf{SE}(3)$ and its algebra $\mathbf{se}(3)$, to encode configurations via coordinate frames and homogeneous transformations [7, 8]. While analytically powerful and ubiquitous in practice, these approaches intrinsically depend on ambient embeddings and frame assignments, which can introduce singularities, ambiguities, and artifacts unrelated to the underlying relational nature of motion. This work develops an intrinsic, coordinate–free formulation of multibody kinematics that dispenses with ambient embeddings and prescribed reference frames. Rather than identifying rigid bodies with subsets of $\mathbb{R}^3$ and configurations with elements of $\mathbf{SE}(3)$, we model each body by its associated oriented Euclidean space and represent relative motion through orientation–preserving isometries organized within a Lie groupoid. This perspective captures the relational geometry of motion directly, while retaining modularity and scalability for complex articulated mechanisms. Fundamental notions of configuration, velocity, and constraint geometry are revisited through graph–theoretic and subgroupoid constructions, enabling an unambiguous symbolic and computational description of multibody kinematics suitable for generic and modular software architectures, with direct pathways toward numerical implementation. By replacing coordinate–dependent Lie group embeddings with an intrinsic Lie groupoid formalism, the proposed framework provides a geometrically faithful, globally smooth, and singularity–free foundation for mechanism analysis, robotic modeling, and geometric control.

2 METHODOLOGY

We build the kinematic framework by first revisiting *relative* rigid-body motion using intrinsic constructions inspired by screw theory [7], but without embedding bodies in a common ambient $\mathbb{R}^3$ or assigning coordinate frames. A rigid body is modeled as a 3D oriented Euclidean affine space $\mathcal{E}$ with an associated oriented vector space $V \cong \mathbb{R}^3$ acting freely and transitively (thus $T\mathcal{E} \simeq \mathcal{E} \times V$). A rigid observer is modeled similarly by an oriented Euclidean space $\mathcal{I}$ with vector space U and $T\mathcal{I} \simeq \mathcal{I} \times U$. The *relative configuration* of $\mathcal{E}$ with respect to $\mathcal{I}$ is the manifold

$$P := \{\, r : \mathcal{E} \xrightarrow{\cong} \mathcal{I} \text{ orientation-preserving isometry} \,\},$$

which is diffeomorphic (but not canonically isomorphic) to $\mathbf{SE}(3)$; crucially, P has no natural Lie group structure independent of frame choices. Instead, we assemble the four manifolds P, $\bar{P} := P^{-1}$, $\mathbf{SE}(\mathcal{E})$, and $\mathbf{SE}(\mathcal{I})$ into a *configuration Lie groupoid*. This groupoid viewpoint induces commuting left/right actions of $\mathbf{SE}(\mathcal{I})$ and $\mathbf{SE}(\mathcal{E})$ on P, yielding canonical trivializations of TP and two intrinsic "translations to identity":

$$\mathcal{L} : TP \to \mathbf{se}(\mathcal{E}), \quad (r, \nu) \mapsto r^{-1}\nu, \qquad \mathcal{R} : TP \to \mathbf{se}(\mathcal{I}), \quad (r, \nu) \mapsto \nu r^{-1}.$$

Given a relative motion $\sigma : \mathbb{T}' \to P$ (with $\mathbb{T}$ an affine time axis), the relative velocity $\nu(t) = \dot{\sigma}(t) \in T_{\sigma(t)}P$ admits two equivalent *observed* representations ${}^{\mathcal{E}}\nu = \mathcal{L} \circ \nu$ and ${}^{\mathcal{I}}\nu = \mathcal{R} \circ \nu$, related by the groupoid adjoint map ${}^{\mathcal{I}}\nu(t) = \mathbf{Ad}_{\sigma(t)}\big({}^{\mathcal{E}}\nu(t)\big)$ that reduces to the standard adjoint action when restricted to $\mathbf{SE}(\mathcal{E})$ or $\mathbf{SE}(\mathcal{I})$. This provides an intrinsic, frame-free characterization of body/spatial velocity duality.

Relative *screw motion* is then defined as the class of relative motions whose observed relative velocity is constant (equivalently, the motion evolves by a one-parameter subgroup in the appropriate isotropy group). Concretely, for a

screw motion passing through $r \in P$ at t_0, there exists a unique ${}^{\mathcal{E}}\nu \in \mathbf{se}(\mathcal{E})$ such that

$$\sigma(t) = r\, \exp\big({}^{\mathcal{E}}\nu\,(t-t_0)\big), \qquad \sigma(t) = \exp\big({}^{\mathcal{I}}\nu\,(t-t_0)\big)\, r, \quad {}^{\mathcal{I}}\nu = \mathbf{Ad}_r({}^{\mathcal{E}}\nu).$$

3 RESULTS

The single-body constructions serve as the local building blocks for the multibody setting: interconnected rigid bodies are organized as a graph, with edges carrying relative poses (groupoid arrows) and joints encoded as constraint subsets that, in the ideal case, form subgroupoids. The results highlight three core aspects: (i) global configuration modelling via configuration Lie groupoids, (ii) intrinsic forward kinematics and Jacobian maps independent of coordinate frames, and (iii) seamless incorporation of holonomic joint constraints through graph–based restrictions.

Extension to General Multibody Systems. Let $\{\mathcal{E}_i \mid i \in \mathcal{B}\}$ be a finite collection of rigid bodies with configuration Lie groupoid $\mathcal{P} \rightrightarrows \mathcal{B}$ and unconstrained configuration manifold Q, where $\mathcal{P} = \bigsqcup_{i,j\in\mathcal{B}} P_i^j$ and P_i^j are the relative configuration manifolds. Configurations are treated as compatible collections of relative poses $q = (r_i^j)_{(i,j)\in\mathcal{B}\times\mathcal{B}}$, satisfying $r_i^k = r_j^k r_i^j$. This characterization realizes Q globally as an embedded submanifold of $\prod_{(i,j)} P_i^j$.

Result 1 (Global Parametrization). For any configuration tree $\mathcal{T} \subset \mathcal{B}\times\mathcal{B}$ capturing inter–body measurements, the forward kinematics map $F_{\mathcal{T}}\colon Q_{\mathcal{T}} \to Q$ is a global diffeomorphism. Hence, every configuration admits a unique tree representation, and transitions between trees are smooth cocycle–satisfying diffeomorphisms.

Result 2 (Intrinsic Jacobian). The differential $dF_{\mathcal{T}'\leftarrow\mathcal{T}}\colon TQ_{\mathcal{T}} \to TQ_{\mathcal{T}'}$ defines a fibre–wise linear isomorphism that generalizes the classical manipulator Jacobian to arbitrary configuration trees. This Jacobian arises as the tangent lift of the reparametrization diffeomorphism and relates observed relative velocities through canonical trivializations of tangent bundles.

Constraint Incorporation. Holonomic joints are modeled by constraint graphs whose edges correspond to admissible relative configuration manifolds $Q_i^j \subseteq P_i^j$. The resulting admissible configuration space is a smooth submanifold obtained by restricting relative poses to these subsets.

Result 3 (Restricted Kinematics). Forward kinematics and Jacobian maps restrict smoothly to constrained configuration manifolds. When joint constraints are imposed, the admissible configuration space becomes a smooth submanifold of the unconstrained one. The same intrinsic forward kinematics maps remain valid by simple restriction to this space, and their differentials yield constrained Jacobians with the same fibre–wise linear structure. In essence, constraints are incorporated without redefining the kinematic operators—only their domains are reduced.

4 CONCLUSION

This work presented a coordinate–free formulation of rigid multibody kinematics based on configuration Lie groupoids. By modeling bodies as oriented Euclidean affine spaces and expressing configurations through relative isometries rather than assigned frames, the approach provides a geometrically faithful and singularity–free description of motion. The framework extends naturally from single–body motion to general multibody systems, yielding intrinsic forward kinematics and Jacobian maps defined through graph structures and configuration trees. Holonomic joint constraints are incorporated seamlessly via subgroupoid restrictions, unifying constrained and unconstrained kinematics within the same formalism. Overall, the proposed perspective offers a modular and globally smooth foundation for multibody modeling, with clear potential for scalable computation and future extensions to dynamics and geometric control, as well as applications to Cosserat continua and multi–robot systems. Ongoing work focuses on computational realization on representative multibody systems.

References

[1] A. D. Lewis, "The physical foundations of geometric mechanics," *Journal of Geometric Mechanics*, vol. 9, no. 4, p. 487, 2017.

[2] R. S. Ball, *A Treatise on the Theory of Screws.* first ed., Cambridge university press, Cambridge, 1900.

[3] L. Euler, "Nova methodus motum corporum rigidorum degerminandi," *Novi commentarii academiae scientiarum Petropolitanae*, pp. 208–238, 1776.

[4] M. Chasles, "Note sur les propriétés générales du système de deux corps semblables entr'eux," *Bulletin des Sciences Mathématiques, Férussac*, vol. 14, pp. 321–326, 1830.

[5] L. Poinsot, *Théorie nouvelle de la rotation des corps.* Bachelier, 1851, no. 143.

[6] W. K. Clifford, "Preliminary sketch of biquaternions," *Proceedings of the London Mathematical Society*, vol. 1, no. 1, pp. 381–395, 1871.

[7] R. M. Murray, Z. Li, and S. S. Sastry, *A mathematical introduction to robotic manipulation.* CRC press, 2017.

[8] K. M. Lynch and F. C. Park, *Modern robotics.* Cambridge University Press, 2017.

DESIGN AND KINEMATIC CHARACTERISTIC ANALYSIS OF A NOVEL REDUNDANTLY ACTUATED PARALLEL MECHANISM FOR HIGH-PRECISION GRINDING

Yanhua Tang[1], Yaning Li[1], Yu Wang[1], Xiaofei Liu[1*], Jinyang He[1], Yuantao Bu[1]

[1] School of Mechanical Engineering, YanShan University, Qinhuangdao, China, {yhtang@ysu.edu.cn; lyn793174@gmail.com; 17864277601@163.com; liuxf@ysu.edu.cn; hejinyang0303@163.com; boyuantao72@gmail.com }

1. INTRODUCTION

Redundantly actuated parallel robot enhances load capacity and force distribution, but existing research is primarily focused on low-order redundancy, whereas higher-order cases remain largely unexplored despite their considerable potential for performance optimization and more complex design challenges.

This study presents a novel redundantly actuated parallel grinding mechanism with three degrees of actuation redundancy. Key components of the mechanism are designed, analyzed, and optimized for performance. The mobility of the robot is analyzed based on screw theory. The topological characteristics of the robot are investigated, leading to its structural design. The motion/force transmission performance is evaluated using both local and global indices. By employing performance atlases and dimensionless structural parameters, the transmission performance is optimized, resulting in the optimal structural dimensions and the best possible distribution of transmission performance. The findings of this research provide a significant reference for the future study and application of redundantly actuated hybrid grinding robots.

2. RESEARCH PROCEDURE

Figures 1 and 2 illustrate the structural and configuration diagrams of the novel parallel grinding mechanism. The mechanism consists of a 2R1T (two rotations and one translation) parallel mechanism in series with a grinding spindle head. The parallel mechanism adopts a symmetrical, over-redundantly actuated 6-PRS architecture. It comprises six identical PRS limbs, where P, R, and S denote prismatic, revolute, and spherical joints, respectively. The circumradius of the equilateral triangle $A_1A_2A_3$ on the fixed platform is R_1, and that of triangle $A_4A_5A_6$ is R_2. The circumradius of the equilateral triangle $B_1B_2B_3$ on the moving platform is r. The prismatic joints connected to the fixed platform are the actuated joints, while all other joints are passive.

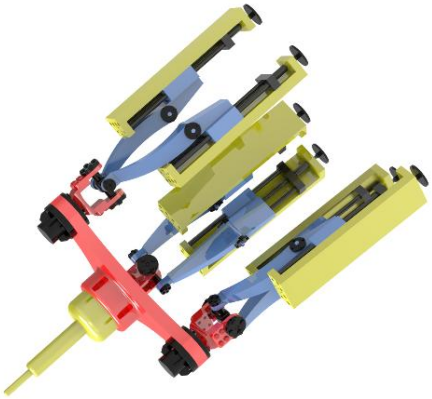

Figure 1. Structural diagram of novel grinding mechanism

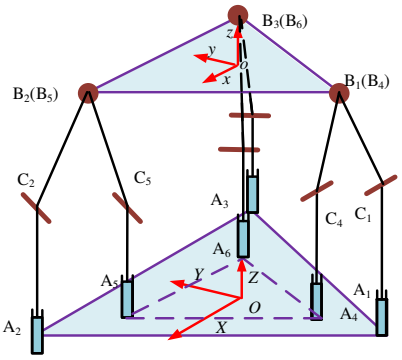

Figure 2. Configuration diagram of novel grinding mechanism

The motion screw system of the moving platform is given by equation (1), which indicates that the mechanism is a 3-DOF parallel mechanism with two rotational and one translational degree of freedom. The translational DOF is along the Z-axis, where the grey single-headed arrows denote rotations and the grey double-headed arrows denote translation. Figure 3 illustrates the constraint wrench system of the moving platform, and figure 4 illustrates the motion screw system. Since the prismatic joints in all six limbs are selected as the actuated joints, this 6-PRS architecture becomes a redundantly actuated parallel mechanism, with a redundancy of three.

$$\begin{cases} \$_{41} = \left(1 \quad 0 \quad 0; \quad 0 \quad z_{B1} \quad -y_{B1}\right) \\ \$_{42} = \left(0 \quad 1 \quad 0; \quad \dfrac{\sqrt{3}}{2} z_{B2} \quad \dfrac{z_{B2}}{2} \quad -\dfrac{y_{B2}}{2} - \dfrac{\sqrt{3}}{2} x_{B2}\right) \\ \$_{43} = \left(0 \quad 0 \quad 0; \quad 0 \quad 0 \quad 1\right) \end{cases} \tag{1}$$

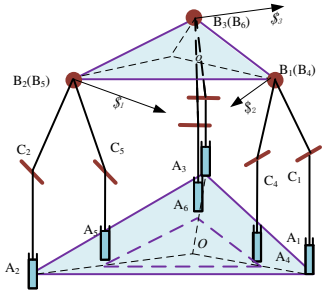

Figure 3. Constraint wrench system of the mechanism

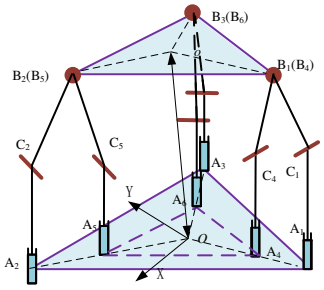

Figure 4 Motion screw system of the mechanism

The key parameters for the mechanism design are $OA_1=R_1$, $oB_1=r$, $OA_5=R_2$, $B_1C_1=B_2C_2=B_3C_3=B_4C_4=B_5C_5=B_6C_6=l$. Assuming l is constant, the parameters R_1, R_2 and r can be normalized according to equation (2) and mapped from a three-dimensional space to a two-dimensional plane.

$$\begin{cases} D=\dfrac{R_1+r+R_2}{3} \\ d_1=\dfrac{R_1}{D}, d_2=\dfrac{r}{D}, d_3=\dfrac{R_2}{D} \end{cases}, \begin{cases} d_1>d_2 \\ d_3<d_1 \\ 0<d_1,d_2,d_3<3 \\ d_1+d_2+d_3=3 \end{cases} \Rightarrow \begin{cases} s=d_3 \\ t=\dfrac{d_3-d_2}{\sqrt{3}} \end{cases} \tag{2}$$

The workspace ratio σ_T and distribution rate ζ_T of good transmission performance are selected as evaluation criteria. Under the condition of D=100mm and l=240mm, the spatial distributions of these two performance indices for the mechanism are illustrated in figure 5. Higher values of these indices indicate better transmission performance of the mechanism. Setting the optimization objectives as $\sigma_T > 0.98$ and $\zeta_T > 0.88$, the optimal parameter configuration for the mechanism is determined as R_1=130mm, R_2=62.5mm, and r=107.5mm.

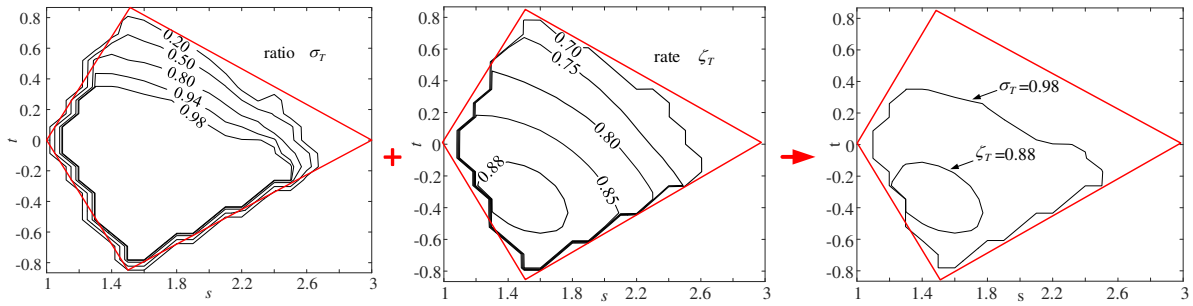

Figure 5. Distributions of workspace ratio and distribution rate of good transmission performance

The configuration R_1=120 mm, R_2=80 mm and r=100 mm is selected as a comparative design configuration for the performance analysis of the mechanism. The left portion of figure 6 illustrates the distribution of local motion/force transmission performance of the mechanism under the comparative configuration, while the right portion shows the corresponding distribution under the optimal configuration. It is observed from the figure that the performance distribution of the mechanism is significantly improved through the parameter optimization process.

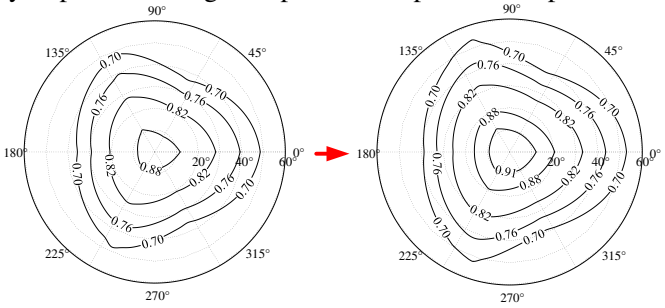

Figure 6. Distributions of transmission performance with the comparative and optimal configuration

ACKNOWLEDGMENTS

This research is funded by the National Natural Science Foundation of China (No. 52105036) and the authors declare that they have no conflict of interest.

REFERENCES

[1] L. Wang, Y.F. Fang, H.B. Qu, et al, “Design and analysis of novel 2R1T generalized parallel mechanisms with large rotational angles”. *Mechanism and Machine Theory*, 150, 103879, 2020.

[2] L.M. Xu, W. Ye, Q.C. Li, “Design, analysis, and experiment of a new parallel manipulator with two rotational and one translational motion”. *Mechanism and Machine Theory*, 177, 105064, 2022.

MMT Symposium
60th Anniversary of Mechanism and Machine Theory
June 21-23, 2026 Porto, Portugal

DEVELOPMENT OF A MICROFLUIDIC DEVICE THAT CONVERTS CHANNEL DEFORMATION INTO FLUID DISPLACEMENT: EXPERIMENTAL EVALUATION OF THE INFLUENCE OF CHANNEL CONSTRICTION WIDTH ON FLUID MOVING DISTANCE

Sogo KOMA[1], Daisuke IBA[1], Mitsuki NABETA[1], Rintaro MITA[1], Naoki YAMASHITA[1], Hitoshi SHIMASAKI[1], Junichi HONGU[2]

[1] Kyoto Institute of Technology, 1 Matsugasakihashigami-cho, Sakyo-ku, Kyoto 606-8585, Japan
{ koma.sogo.2003@gmail.com; iba@kit.ac.jp; nabeta.kit@gmail.com; m25623108@edu.kit.ac.jp; naoki@kit.ac.jp; simasaki@kit.ac.jp }

[2] Tottori University, 4-101 Koyama-cho Minami, Tottori 680-8550, Japan, { hongu@tottori-u.ac.jp }

1. INTRODUCTION

To monitor the cumulative value of strain generated on the surface of mechanical components subjected to cyclic loading, we have been developing a device utilizing microchannels. In this study, we propose a microfluidic device featuring continuously arranged check valve structures that mimic biological venous valves proposed by Nose et al. [1], and investigate its characteristics. In this paper, we experimentally clarify the effect of the constriction width of the check valve structure, which is a critical parameter on fluid transport performance and discuss design guidelines for optimizing transport capability.

2. OPERATING PRINCIPLE AND DESIGN

2.1. Operating Principle

When a microchannel is installed on the surface of a target object that deforms due to an external force, the fluid within the channel is repeatedly discharged or suctioned from a minute section of the channel, using the deformation of that minute section accompanying the deformation of the target object as the driving force. In this study, to convert this fluid movement into a unidirectional cumulative moving distance, a check valve structure mimicking the shape of a venous valve is used within the channel. Fig. 1 shows the check valve structure used in this study. Although the check valve structure shown in the figure has a fixed geometry with no moving parts, it generates a rectification effect through fluid behavior when passing through the channel constriction. During backflow, branched flows are generated, creating anisotropy in flow resistance due to the geometry, which makes it possible to convert the amount and number of deformations into the cumulative moving distance of the fluid.

2.2. Check Valve Design and Geometric Parameters

The design of the check valve used in this study is shown in Fig. 2. In this study, we focused on the constriction width, w, which is considered to have the most significant influence on fluid behavior. While narrowing w is expected to improve the backflow suppression effect, excessive constriction is simultaneously thought to hinder the fluid transport itself. To verify this trade-off, we designed devices with three levels: $w = 12.5,\ 25,$ and 50 μm.

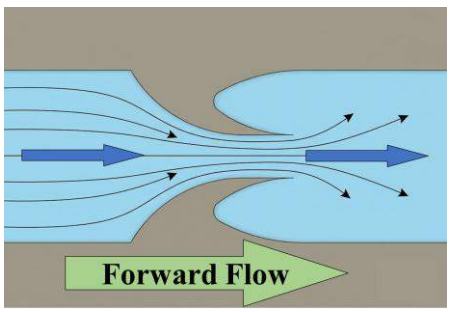

(a) Forward flow

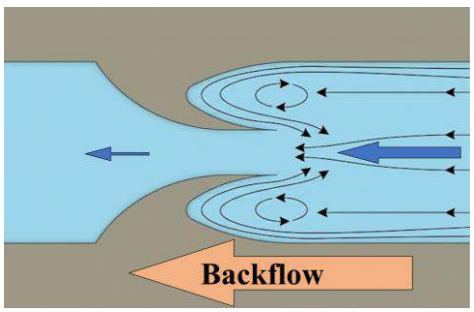

(b) Backflow

Figure 1. Conceptual diagram of the rectification mechanism

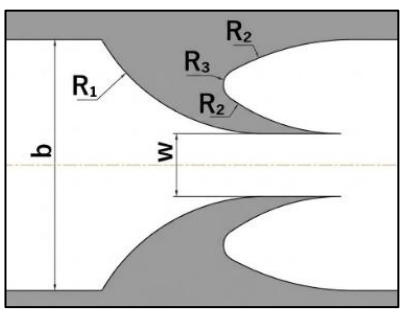

Figure 2. Geometric parameters of the check valve

3. EXPERIMENTAL APPARATUS AND EVALUATION METHODS

In this study, a vibration test using a cantilever beam was conducted to apply cyclic strain to the device. The appearance of the experimental apparatus used is shown in Fig. 3. The fabricated PDMS microfluidic device was attached near the fixed end of a stainless steel beam, which had a vise installed at its tip as a mass element, and was excited using a vibration shaker. Additionally, the displacement of the vise at the beam tip was measured using a laser displacement meter, and the beam deflection was calculated from the result. In this experiment, colored polyethylene glycol (PEG) was used as the working fluid to improve visibility. Fluid behavior was captured using a high-speed camera, and the moving distance was measured by tracking the position of the fluid interface from the obtained images, as shown in Fig. 4.

The product of the beam strain per cycle, calculated from the measurement results of the laser displacement meter, and the number of cycles was defined as "accumulated strain," and this was introduced as a unified evaluation index. Furthermore, to evaluate the intrinsic characteristics by excluding factors other than the check valve geometry — such as changes in beam stiffness, heat generation, and changes in fluid viscosity associated with cyclic deformation — we focused on the initial stage of strain accumulation (a range of 0 to 0.05×10^3, corresponding to approximately 1/5 of the total). The fluid moving distance per unit accumulated strain within this range was defined as "detection sensitivity [mm/ε]," and performance was evaluated using this as an index.

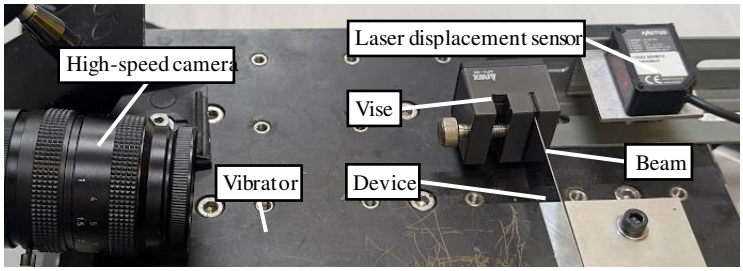

Figure 3. Experimental apparatus

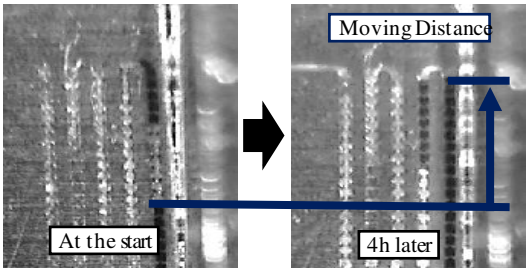

Figure 4. Observation of fluid behavior

4. RESULTS AND DISCUSSION

A comparison of the detection sensitivity for each constriction width is shown in Fig. 5(a). The error bars in the figure represent the range between the maximum and minimum sensitivity values observed for each constriction width. The device with $w = 25\ \mu m$ exhibited extremely high sensitivity (approximately $82.4\ mm/\varepsilon$) compared to the other conditions. Additionally, it can be seen that the sensitivity for $w = 50\ \mu m$ is low and shows large variation. We discuss the factors causing this performance difference using the transition of the fluid moving distance with respect to the accumulated strain, as shown in Fig. 5(b). For $w = 25\ \mu m$, although local stagnation is observed, the moving distance increases significantly with strain accumulation, indicating that the rectification mechanism is functioning. In contrast, for $w = 50\ \mu m$, the slope is small, and the increase in moving distance is limited. This is considered to be because the constriction width is too wide to obtain a sufficient rectification effect, allowing backflow. On the other hand, almost no movement was observed for $w = 12.5\ \mu m$. This is attributed to the excessive channel resistance caused by the excessive constriction, resulting in insufficient pressure to drive the fluid and leading to a state of flow stoppage.

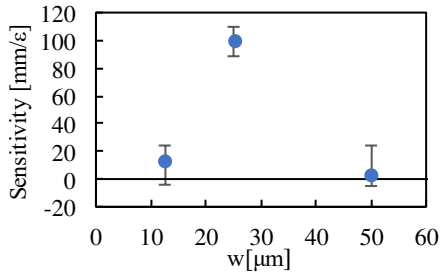

(a) Relationship between constriction width and detection sensitivity

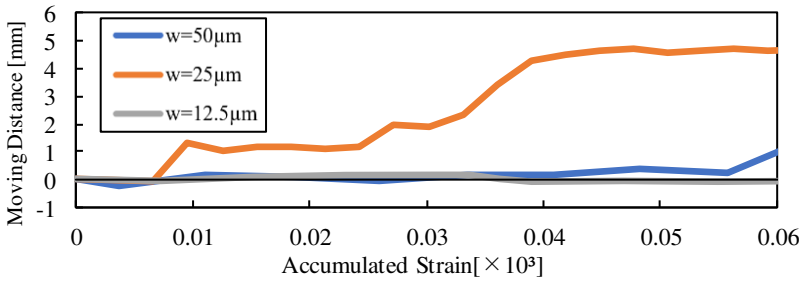

(b) Fluid displacement versus accumulated strain (representative trajectories)

Figure 5. Experimental results

5. CONCLUSION

The results of this study suggest that a trade-off relationship exists between the constriction width and the rectification performance, and it is inferred that an optimal value exists around $w = 25\ \mu m$ under the present conditions.

ACKNOWLEDGMENTS

The present study has been a project supported by JSPS KAKENHI Grant Number 24K00790.

REFERENCES

[1] T. Nose and Y. Nishijima, "Design and Evaluation of Tesla Valve for Microfluidic Applications". *BUNSEKI KAGAKU*, 71(7.8), 417-423, 2022.

A COMPUTER-AIDED OPTIMIZATION METHOD FOR COMPLEX TRANSMISSION SYSTEMS OF FACE GEARS VIA MECHANISM-DATA FUSION

Bingquan Lu[1,2], Yuansheng Zhou[1,2], Zhongwei Tang1[1,2], Jinyuan Tang[1,2]

[1] State Key Laboratory of Precision Manufacturing for Extreme Service Performance, Central South University, Changsha, China
[2] College of Mechanical and Electrical Engineering, Central South University, Changsha, China

1. INTRODUCTION

Face gear transmission systems offer significant advantages such as excellent power-split capability, compact structure, and a weight reduction of approximately 40% compared to bevel gears. It establishes them as a key technological solution for the main gearboxes and high-performance transmissions [1-3]. With increasingly stringent demands for load capacity, vibration/noise control, and operational lifespan, achieving efficient and precise, optimization of face gear transmission systems become a critical bottleneck hindering their engineering application. However, these systems consist of multiple coupled gear pairs, and their contact performance is highly sensitive to the tooth surface modification parameters. Traditional design finite element analysis requires massive computation and optimization time; the results of data-driven design cannot provide a reasonable physical mechanism explanation. mechanism-data fusion provides a promising solution.

Current research confronts three primary challenges. First, difficulty in parameter-geometry mapping: There is no direct analytical mapping between tooth surface modification parameters (e.g., modification amount, modification length, tooth profile) and the nodal coordinates of discrete mesh. Consequently, any parameter adjustment necessitates complete 3D model reconstruction and re-meshing, resulting in extremely low optimization iteration efficiency [4]. Second, difficulty in quantitative contact performance evaluation: Performance indicators such as contact pattern location, morphology, and edge contact risk have traditionally relied on visual inspection by engineers. The lack of mathematical characterization methods embeddable within optimization algorithms prevents the mathematical expression and automated processing of "no edge contact." Third, difficulty in balancing nonlinear solution stability and efficiency: Tooth Contact Analysis (TCA) requires solving a system of five independent nonlinear equations with five unknowns. Classical Newton-Raphson methods are highly sensitive to initial guesses and prone to local convergence, while the complex tooth surface geometry of face gears causes computational time to increase exponentially [5]. These combined challenges have confined face gear system optimization predominantly to "single-objective, small-parameter, offline tuning" stages, making it difficult to achieve globally optimal designs for complex multi-input, multi-output coupled systems [6].

2. METHODS

We propose a computer-aided optimization method for complex transmission systems of face gears via mechanism-data fusion, which incorporates parametric mapping, quantitative performance evaluation, and efficient optimization algorithms. First, a modification parameter-mesh coordinate mapping mechanism is established: For both upper and lower face gears and the driving pinion, a comprehensive set of modification parameters (including tip relief amount, lead crowning length, and profile crowning curve) is defined. An analytical expression for the normal deviation of the modified tooth surface relative to the theoretical surface is derived. A parameter-driven automatic mesh morphing algorithm is developed, enabling millisecond-level response between "modification parameter adjustment and FE mesh update," fundamentally eliminating repetitive modeling costs. Second, a quantitative contact performance evaluation method based on image processing is proposed: Contact stress contour plots generated from FE analysis are converted into grayscale digital matrices. Image segmentation algorithms extract contact pattern boundaries. The Euclidean distance between the pattern centroid and the tooth width midpoint serves as a quantitative location metric, while the integrated stress intensity at tooth tip/root edge pixels quantifies edge contact risk. This transforms engineering constraints—"contact pattern centered along tooth width" and "edge contact avoidance"—into computable objective functions. Third, a two-stage hybrid optimization strategy is constructed: At the contact point solution level, the traditional direct solution of five-variable nonlinear equations is abandoned. From a kinematic perspective of the face gear pair meshing process, three motion parameters within the meshing equations are analytically eliminated using geometric constraints, yielding a simplified model with only two optimization variables. Particle Swarm Optimization (PSO) performs a global search for initial values, followed by local refinement using the Quasi-Newton method, enhancing solution robustness while improving computational efficiency by an order of magnitude. At the system optimization level, a multi-objective framework minimizes loaded transmission error fluctuation amplitude and maximizes symmetry of the parabolic unloaded transmission error curve while centering the contact pattern. The modification parameters are optimized by NSGA- || . To further reduce calls to high-

fidelity FE simulations, a Kriging surrogate model replaces the original simulation, balancing optimization efficiency and accuracy.

3. RESULTS

The proposed methodology was validated in the face gear split-torque transmission system for a prototype main gearbox. Results demonstrate that the integrated framework compresses single-cycle modeling and optimization time from tens of hours (traditional methods) to under 0.5 hours. Optimized tooth surfaces exhibit contact patterns stably centered along the tooth width, ideally symmetric geometric transmission error curves, a >60% reduction in loaded transmission error fluctuation amplitude, and complete elimination of edge contact risks. This research elucidates the intrinsic mapping relationship between "modification parameters and contact performance" in face gear drives, providing both theoretical foundations and an engineering-implementable pathway for the digital and intelligent design of high-performance face gear systems.

ACKNOWLEDGMENTS

This work was supported by the National Natural Science Foundation of China (Grant No. 52505165、52575084), the Science and Technology Innovation Program of Hunan Province (Grant No. 2021RC3012), the Central South University Innovation-Driven Research Program (Project No. 2023CXQD050), the Fundamental Research Funds for the Central Universities of Central South University (Grant No. CX20230255), The Project of State Key Laboratory of Precision Manufacturing for Extreme Service Performance (Grant No. ZZYJKT2025-07), The Natural Science Foundation of Hunan Province [grant numbers: 2025JJ80227].

REFERENCES

[1] Zanzi C, Pedrero J I. Application of modified geometry of face gear drive[J]. Computer Methods in Applied Mechanics and Engineering, 2005, 194(27-29): 3047-3066.

[2] Wang S, Zhou Y, Tang J, et al. Digital tooth contact analysis of face gear drives with an accurate measurement model of face gear tooth surface inspected by CMMs[J]. Mechanism and Machine Theory, 2022, 167: 104498.

[3] Peng X, Zhou J. Optimization design for dynamic characteristics of face gear drive with surface-active modification[J]. Mechanism and Machine Theory, 2022, 176: 105007.

[4] Yu, Z.; Tang, Z.; Zhou, Y.; Tang, W.; Tang, J.; Lu, B.; Wu, Z.; Hong, X. A Fast Integration Method of Analysis and Optimization for the Contact Performance Design of a Face Gear Split-Torque Transmission. Mathematics 2025

[5] Lu X, Zhou Y, He D, et al. A novel two-variable optimization algorithm of TCA for the design of face gear drives[J]. Mechanism and Machine Theory, 2022, 175: 104960.

[6] Tang Z, Wang M, Zhao M, et al. Modification and noise reduction design of gear transmission system of emu based on generalized regression neural network[J]. Machines, 2022, 10(2): 157.

THREE-PARAMETER BIFURCATION ANALYSIS OF A MINIMAL MECHANICAL MODEL WITH LUGRE FRICTION

Balazs J. Bekesi, Gabor Csernak

Department of Applied Mechanics, Faculty of Mechanical Engineering, Budapest University of Technology and Economics, Műegyetem rkp. 3., Budapest, H-1111, Hungary, {bekesi@mm.bme.hu; csernak@mm.bme.hu}

1 INTRODUCTION

The frictional interaction between contacting bodies is based on very complex physical processes, which explains the abundance of the related literature. In order to model the frictional effects, several empirical models have been introduced in the last decades [1]. The present paper focuses on the *LuGre friction model* that is among the most frequently used models in multibody dynamical applications. To capture the essence of the nonlinear effects associated with friction, a so-called *minimal mechanical model* (see Fig. 1(a)) [2] is considered: a block sliding on a horizontal surface, which is subjected to a constant external force F and the LuGre friction force F_f which includes a viscous damping term C; as well as bristle damping c that are related to the macroscopic and microscopic motion, respectively.

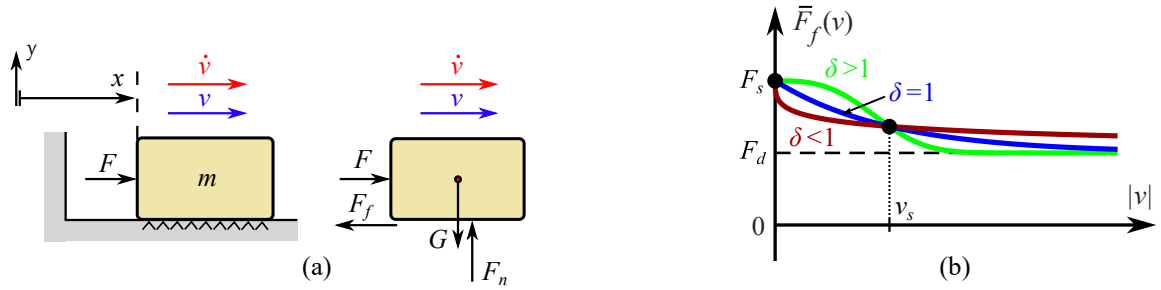

Figure 1: (a) Minimal test problem and its free body diagram; (b) typical shapes of the Stribeck characteristic depending on δ

The steady-state conditions of the LuGre model are described by the *Stribeck characteristic*

$$\bar{F}_f(v) = F_d + (F_s - F_d)\, e^{-\left(\frac{|v|}{v_s}\right)^{\delta}}, \tag{1}$$

which is influenced by the *Stribeck exponent* (or shape factor) δ, as it can be seen in Fig. 1(b). It is well-known [3] that the shape – i.e., the empirical parameter δ – of these curves depends on the lubrication and the contacting materials, and on other external conditions, as well.

2 THREE-PARAMETER BIFURCATION ANALYSIS

The bifurcations of the model solutions were analyzed with respect to three parameters: external force F, damping coefficient C, and bristle damping c, for three different ranges of the Stribeck exponent: $\delta > 1$, $\delta = 1$, and $\delta < 1$ (cf. Fig. 1(b)).

Despite the simplicity of the mechanical model, complex, three-parameter bifurcation diagrams could be constructed (see the panels in the top right corners of Fig. 2). We classified the parameter diagrams into distinct domains $\mathcal{D}^{i_1,\ldots,i_k}$ based on the number and nature of equilibrium states, with domain boundaries corresponding to *saddle-node* and possibly ($\delta > 1$) *nonsmooth transcritical* [4] bifurcations. In each of the aforementioned domains, *saddle* and *focus/node type equilibria* can be distinguished and categorized according to their velocity coordinate.

We showed that all the existing focus/node type slipping equilibria ($v \neq 0$) can lose their stability via *Hopf bifurcation* at sufficiently large bristle damping c, regardless of the Stribeck exponent δ. Therefore, the parameter diagrams

can be supplemented with *supercritical* (blue) and *subcritical* (red) Hopf bifurcation regions according to the sign of the Poincaré-Lyapunov constant Δ, alongside with the $\Delta = 0$ boundary between them, as it is depicted in the top right corners of Fig. 2. The so-called *singular points* S are appointed, where the Hopf bifurcation boundaries $\Delta = 0$ terminate at the saddle-node bifurcation boundaries.
In the neighborhood of these singularities, various topologically different phase spaces can be found by varying the bifurcation parameters F, C and c. The present paper explores the possible scenarios and categorizes them based on the number and type of stable solutions. As two remarkable examples, we highlight the phase-space structures depicted in Fig. 2, that also shows the relevant part of the three-parameter bifurcation diagram at $\delta = 2$:

- a *bistable stick-slip scenario* with a stable sticking type equilibrium $\mathbf{y}^0$ and a stable limit cycle around the unstable $\mathbf{y}_3^+$ (left panel of Fig. 2);
- a *tristable slip-slip-slip scenario* with two stable slipping solutions $\mathbf{y}_1^+$, $\mathbf{y}_3^+$, and with a stable and two unstable limit cycles (right panel of Fig. 2).

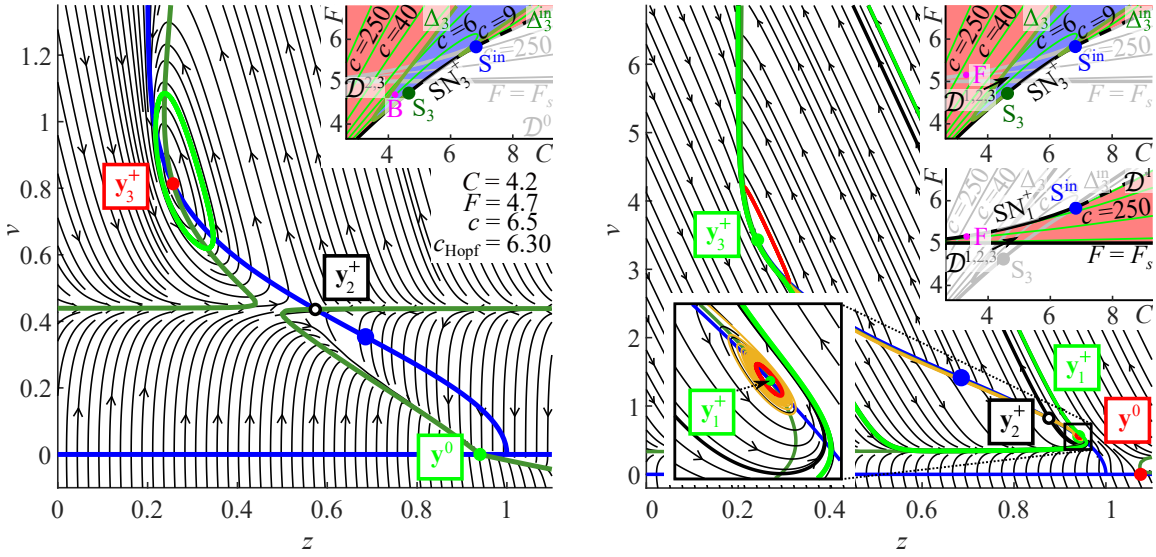

Figure 2: Left panel: *bistable stick-slip scenario* with a stable limit cycle. Right panel: *tristable slip-slip-slip scenario* with a stable limit cycle encircling the two stable slipping equilibria $\mathbf{y}_1^+$, $\mathbf{y}_3^+$ and the two unstable limit cycles

3 CONCLUSIONS

With the help of the qualitative three-parameter bifurcation analysis, several equilibria of different types and bifurcations – including saddle-node and Hopf bifurcation – were pointed out. Various bifurcation scenarios were examined revealing rich phase-space structures with several coexisting equilibria and limit cycles. We underscore the careful selection of the Stribeck exponent δ and the bristle damping parameter c. These parameters are pivotal, as the system's phase-space topology can change significantly due to bifurcations if these parameters are varied.

ACKNOWLEDGMENTS

This research was supported by the Hungarian National Research, Development and Innovation Office grant No. NKFI ADVANCED 152506; and by the Doctoral Excellence Fellowship Programme (DCEP) that is funded by the National Research Development and Innovation Fund of the Ministry of Culture and Innovation and the Budapest University of Technology and Economics.

REFERENCES

[1] F. Marques, P. Flores, J.C.P. Claro and H.M. Lankarani, "A survey and comparison of several friction force models for dynamic analysis of multibody mechanical systems". *Nonlinear Dynamics*, vol. 86, 1407–1443, 2016.

[2] B.J. Bekesi and G. Csernak, "Self-excited fluctuation of sliding velocity induced by LuGre friction in a minimal mechanical model". *International Journal of Solids and Structures*, vol. 315, 113293, 2025.

[3] B. Armstrong-Hélouvry, *Control of Machines with Friction*. Kluwer Academic Publishers, Massachusetts, 1991.

[4] B.J. Bekesi, M. Antali and G. Csernak, "Phase portraits and bifurcations induced by static and dynamic friction models". *Nonlinear Dynamics*, vol. 113, pp. 15863–15899, 2025.

A GOUGH-STEWART PLATFORM BASED EXTERNAL FIXATION SYSTEM FOR DEFORMITY CORRECTION IN ORTHOPEDICS

Yogesh Pratap Singh[1], Kiran Saldanha[2], Ashitava Ghosal[3]

[1] Department of Mechatronics, Indian Institute of Technology, Bhilai, India, {yogeshsingh@iitbhilai.ac.in}
[2] Mersey & West Lancashire Teaching Hospitals, NHS Trust, Liverpool, UK, {kiransaldanha@yahoo.com}
[3] School of Engineering and Applied Science, Ahmedabad University, Ahmedabad, India, {ashitava.ghosal@ahduni.edu.in}

1 INTRODUCTION

External fixation devices offer the advantages of being minimally invasive and are widely used in orthopaedic surgery for fracture stabilization, limb lengthening, and correction of complex multiplanar bone deformities [1]. Circular external fixators devised by Ilizarov [1] have superior biomechanical properties but require sequential hinge-based adjustments that are time-consuming and unintuitive for multi-axis corrections. Hexapod fixators based on the Gough–Stewart platform (GSP), such as Taylor Spatial Frame [2], overcome this by enabling simultaneous six degrees of freedom (DOF) correction using six variable-length struts as shown in Fig. 1(a). Most existing systems depend on proprietary software that requires two orthogonal (Anteroposterior radiograph (AP) and lateral views similar to Fig. 1(c)) X-rays to extract frame, deformity, and mounting parameters for correction planning [1, 2]. This process requires an accurate mathematical model relating 2D radiographs to the six parameters describing the position and orientation of the moving platform as well as the corresponding strut-length adjustments for multiplanar deformity correction.

Our proposed GSP system is based on extracted co-ordinates of key features from the two images and a general purpose inverse kinematics algorithm which takes into account a wide variety of geometries of the GSP and connection points of the struts. These aspects results in a user-friendly web-based interface for the surgeon while maintaining high parameter extraction accuracy and providing a detailed motion plan of the struts to correct the observed deformities. Additionally, our proposed GSP based system uses a modular, surgeon-assembled strut design which significantly reduces hardware and operational cost.

2 DESIGN AND METHODOLOGY

2.1 GSP Architecture

The GSP consists of proximal and distal rings connected by six adjustable struts forming a parallel manipulator as shown in Fig. 1(a). The distal and proximal bone fragments are rigidly fixed to their respective rings, and their relative positions can be predicted based on the movements of the rings. Each strut comprises a threaded rod, aluminum barrel, and detachable connectors (refer to Fig. 1(b)). In our hardware innovation, struts with universal/cardan joints are replaced with modular threaded-rod struts assembled and adjusted directly in the hospital, enabling customizable stroke, greater flexibility, and low-cost rod-only replacement instead of the full strut changes required in conventional systems. The GSP is modeled as an assembly of rigid bodies [3], and the jth strut length is obtained from the inverse kinematic (IK) loop-closure relation, given by:

$$l_j = \boldsymbol{x}_j \cdot \boldsymbol{s}_j + {}^{B}[\mathbf{R}]_P \left({}^{P}\boldsymbol{p}_j - {}^{P}\boldsymbol{H}_c\right) \cdot \boldsymbol{s}_j - {}^{B}\boldsymbol{b}_j \cdot \boldsymbol{s}_j \tag{1}$$

where the vectors denote the attachment-point positions and directions shown in Fig. 1(a). The orientation of one platform with respect to the other is given by rotation matrix ${}^{B}[\mathbf{R}]_P$.

2.2 Software Interface

Our web-based interface allows surgeons to upload orthogonal X-rays (refer to Fig. 1(c)), mark rings and anatomical landmarks (refer to Fig. 1(d)), automatically compute mounting and deformity parameters, and generate day-wise strut adjustment prescriptions based on the initial setting and desired final alignment. To know the initial configuration, frontend image tools (Fig. 1(d)) allow enhancement and precise marking of points/anatomical features on the rings and bone segments – the points A, B O, C_0 and P shown in Fig. 1(a) need to be obtained accurately. The system calibrates X-rays images using simple references (points, lines, or ellipses), enabling sub-micrometer computational accuracy and reliable parameter extraction required for inverse kinematics. To correct for the deformities, the difference between the initial configuration and the surgeon specified desired final configuration is computed and inverse kinematics of the GSP is used to compute the desired strut lengths (see equation (1)). The surgeon may choose complete alignment or residual angulation/translation between the two bone segments.

Our software algorithm employs inverse kinematics of the GSP to enable trajectory planning, reduce bone conflict risks, and allow controlled correction rates while achieving high accuracy through a novel coordinate-based method

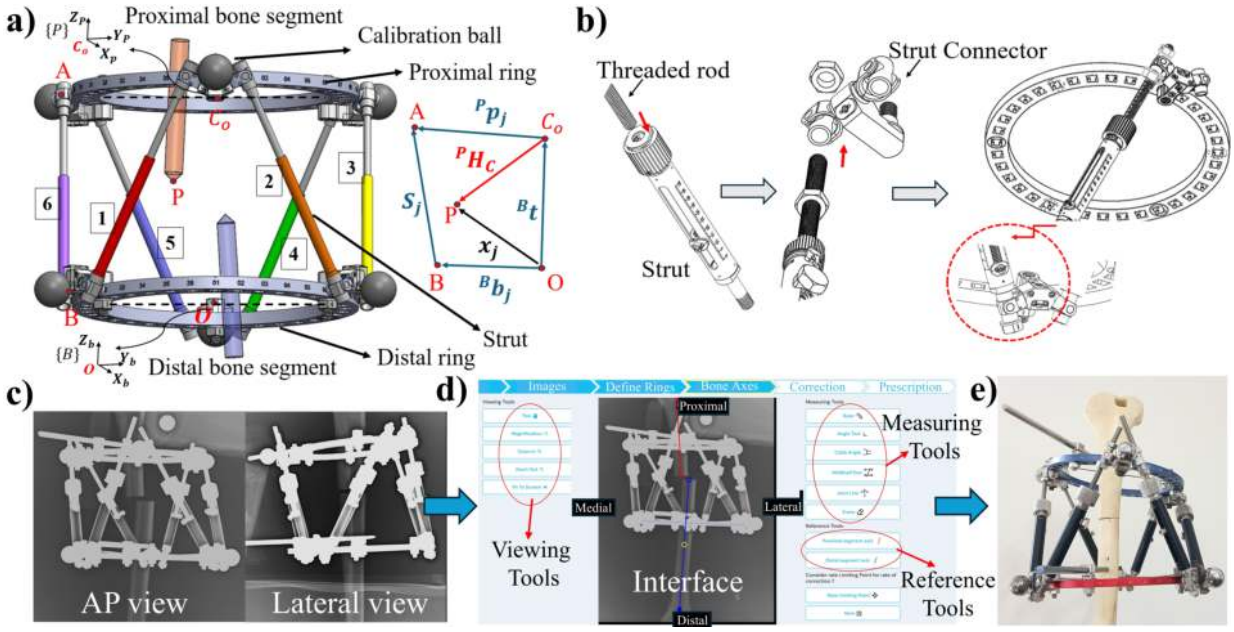

Figure 1: (a) GSP-based external fixator, (b) Custom assembled low-cost struts, (c) AP and lateral X-ray view of the initial configuration, (d) Web-based planning interface with image tools, (e) Post-correction configuration

to extract parameters from a few radiographic points, instead of CT reconstruction, graphical overlays, or complex image-recognition methods used in existing systems [2].

3 RESULTS AND DISCUSSION

Several tests were performed using CAD simulations, numerical IK evaluation and preliminary hardware experiments. Artificial deformities were introduced in SolidWorks models under different practical and clinical scenario like unequal ring sizes, non-orthogonal mounting, rotational deformities, and flexible connector placements. The required orthogonal views were obtained from the CAD models. A summary of the validation studies are as follows:

Software vs. CAD–Across all cases, the interface (software) predicted strut lengths closely matched the CAD values with mean absolute errors (MAE) within 1–2 % in both initial and final configurations. Translational correction errors were typically below 0.5 mm, well within clinical tolerance.

Software vs. Experiment– A prototype hexapod as shown in Fig. 1(c)-(e) assembled with a polyurethane bone model was evaluated using orthogonal radiographs. Experimental results are shown in Table 1 with MAE 0.9–2 % confirming systems' robustness against practical uncertainties such as imaging misalignment and marking variability. The experimental measurements were taken using a vernier caliper, whereas the software reports results in millimeters, resulting in differences in significant digits.

Table 1: Comparison of Strut lengths [in mm] for initial and final configuration.

	Strut lengths (Software)	Strut lengths (Experiment)	MAE (%)
Initial	125, 140, 143, 130, 145, 143	125.58, 138.58, 142.22, 130.54, 148.04, 141.60	0.91
Final	126, 132, 136, 123, 135, 141	131.52, 132.90, 131.21, 122.03, 135.84, 143.73	1.98

4 CONCLUSION

This work presents the development and validation of a novel Gough–Stewart platform based orthopaedic hexapod integrating modular hardware with a user-friendly software interface. The system simplifies deformity correction while maintaining high accuracy, reliability, and low cost. Key contributions include a surgeon-assembled modular strut design and a coordinate-calibrated inverse-kinematics algorithm, achieving performance comparable or superior to existing hexapods. Comparative analysis shows reduced operational costs, fewer strut replacements, and lower risk of clinical errors. Validation through CAD and preliminary experiments confirms accuracy within clinically acceptable error limits. Ongoing software improvements and ISO 13485 certification support future clinical translation and adoption.

REFERENCES

[1] M. Massobrio and R. Mora, *Hexapod External Fixator Systems: Principles and Current Practice in Orthopaedic Surgery*. Springer, Cham, Switzerland, 2021.

[2] C. Iobst, N. Ferreira and S. Kold, "A review and comparison of hexapod external fixators: Current concept review". *Journal of the Pediatric Orthopaedic Society of North America*, vol. 5, no. 1, pp. 627-644, 2023.

[3] A. Ghosal, *Robotics: Fundamental Concepts and Analysis*. Oxford University Press, 2009.

A NOVEL GRIPPER FOR SPACE DEBRIS COLLECTION

Silvia Logozzo[1], Sebastiano Angelella[2], M. Cristina Valigi[1]

[1] University of Perugia, via G. Duranti 93 06125, Perugia, Italy, silvia.logozzo@unipg.it,mariacristina.valigi@unipg.it}

[2] University of L'Aquila, Piazzale Ernesto Pontieri 1, Monteluco di Roio 67100, L'Aquila, Italy,

1. INTRODUCTION

Space activity has created a rapidly growing debris problem in Low Earth Orbit, with millions of fragments traveling at extreme speeds that can damage or destroy spacecraft. Debris comes from defunct satellites, rocket stages, and collisions [1]. Current mitigation includes regulations, deorbiting systems, tracking radar and AI, and Active Debris Removal (ADR) technologies. Existing ADR capture methods fall into four categories: robotic fingers (precise but complex and low capture rate), nets/ropes (high capture rate but hard to release and not reusable), anchors/harpoons (fast but damaging and single-use), and adhesive systems (non-damaging but weak grip).This paper proposes a new end-effector that combines key advantages: high capture rate, fast closing speed, and simple release. The design is inspired by a biomimicry-based snap mechanism, with a large catch zone and two closing clamps, which were built in both rigid and soft (net-based) versions. A full-scale prototype was developed and validated through theoretical, numerical, and experimental kinematic analyses, followed by grasping tests on debris-like objects. Additionally, a catch logic control for the gripper was developed according to its design.

2. PROPOSED GRIPPER DESIGN AND SPACE STRUCTURE

The proposed gripper, shown in Fig.1a, is a bio-inspired gripper which tries to replicate the clamping action of a *Venus flytrap* (Fig 1.b). Space debris comes into contact at the center of the gripper mouth and actuates a button which releases a spring that makes the gripper claws snap and close in a quick, non-destructive manner. A laboratory prototype was designed with two 3D printed semi-spherical structures in PETG material. This was later updated to use more adaptable versions of the end-effector, such as using ripstop nylon fabric for the claws instead of solid PETG.

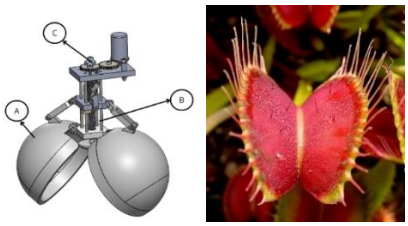

(a) (b)

Figure 1. Biomimetic mechanism: (a) space gripper with clamps; (b) Venus flytrap.

By analyzing the impact forces through FEM simulations Fig. 2, a working range for the gripper was identified, relating to the mass of the debris to the relative velocities needed on impact.

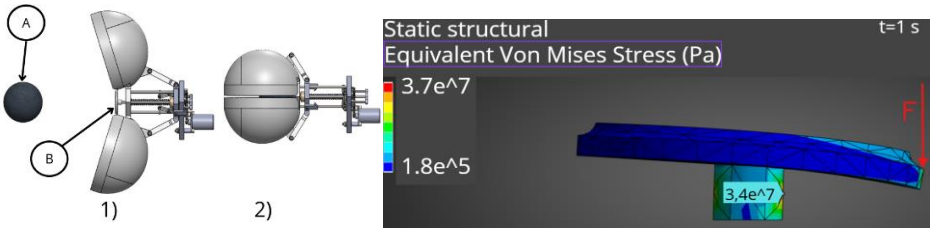

(a) (b)

Figure 2. Debris' impact: (a) Target debris moving towards the gripper (A) and release button for the spring lock mechanism (B); b) FEM Analysis on peak conditions.

3. CATCH LOGIC OF THE GRIPPER IN PROXIMITY OF THE ORBITAL TRAJECTORY

The gripper's catching strategy relies on vision systems: a stereocamera to estimate the target's position and distance, and a monocamera to align the end effector with the target's trajectory. The goal of the catching motion is to have both an optimal relative velocity at contact by approaching the debris along a path parallel to its orbit and have the optical axis (y) aligned with the relative line of sight (LOS), which is the direction (l) connecting the end effector to the debris to be caught, so that $y \cdot l = 1$

[3]. The capture process is divided into three stages: (i) positioning the robotic arm using inverse kinematics so the end effector follows the target's line of motion, (ii) rotating the end effector through closed-loop control to achieve proper alignment, and (iii) accelerating the chaser spacecraft to reach the required impact velocity for capture. To generate the required motion, a two-link robotic arm is modeled using cubic polynomial trajectory planning with specified boundary conditions on joint positions and velocities. By assuming quasi-parallel orbits of the chaser and target, the motion is simplified to near-linear relative trajectories. This planning ensures that the end effector approaches the target along its path at a controlled distance and speed before the final capture phase.

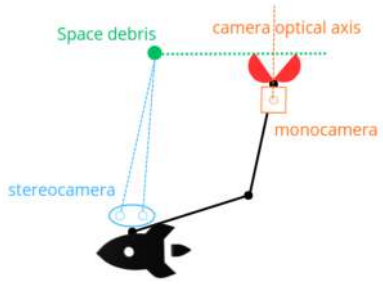

Figure 3. Gripper set up for in-orbit catch of debris

After achieving a simulation for the point-to-point trajectory planning (stage i), the paper presents a closed loop for an effective rotation of the gripper on the target, considering the gripper inertia along the three-axis direction and the actuation torque using the following Euler dynamics equation (stage ii):

$$I\dot{\omega} = -[\omega] \times I\omega + \tau \tag{1}$$

4. SIMULATIONS AND RESULTS

The simulation of the gripper is focused on the control over the end effector joint rotation for alignment of the gripper along the three axes in a closed loop control (fig.4a) and the evaluation of kinematic parameters during the trajectory interpolation of the robotic arm positioned parallel to the orbit trajectory considering three different starting positions (fig.4b). The closing and opening kinematics of the gripper was also tested to evaluate velocities and trajectories of the claws.

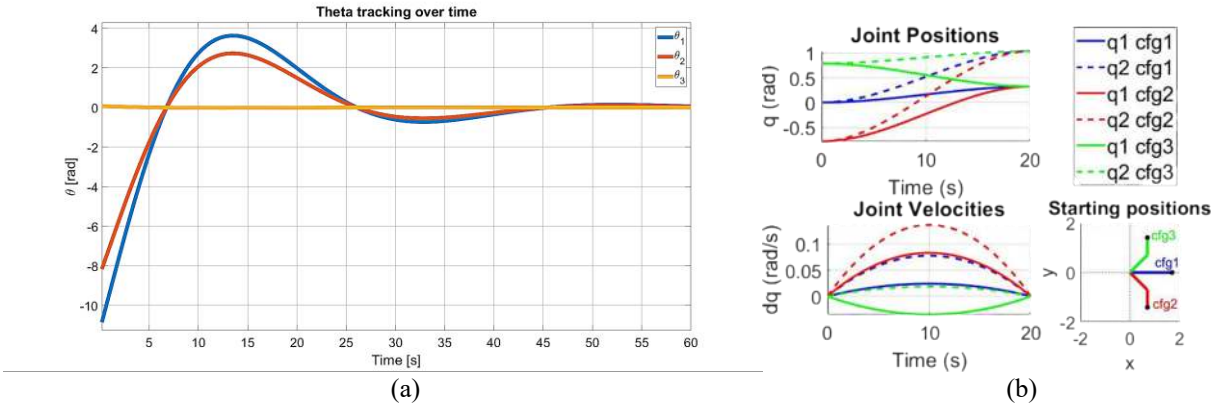

(a) (b)

Figure 4. Simulation results: (a) gripper alignment with the space debris; (b) trajectory interpolation for three different starting positions, considering joint position and velocity

ACKNOWLEDGMENTS This research was funded by the University of Perugia, WP 4.3: Progetto "Colonize".

REFERENCES

[1] M. Rathnasabapathya, D. Wood, M. Jah, D. Howard, C. Christensen, A. Schiller,F. Letizia, H. Krag, S. Lemmens, N. Khlystov, et al., "Space sustainability rating: towards an assessment tool to assuring the long-term sustainability of the space environment," in Proceedings of the 70rd international astronautical congress, 2019.

[2] G. Zhai, Y. Qiu, B. Liang, and C. Li, "Development of on-orbit capture technology," Jiqiren/Robot, vol. 30, no. 5, pp. 467–480, 2008.

[3] Segal, Shai & Gurfil, Pini & Shahid, Kamran. (2014). In-Orbit Tracking of Resident Space Objects: A Comparison of Monocular and Stereoscopic Vision.Aerospace and Electronic Systems, IEEE Transactions. 50. 676-688.

DESIGN OF A RIGID AND COMPLIANT INVERTED 4-BAR MECHANISM TO EMULATE POLYCENTRIC MISALIGNMENT FOR LOWER-LIMB EXOSKELETON MANNEQUINS

Mele C. [1], Bose J. [1], Tung J.[1], Mombaur, K.[2,1]

[1] University of Waterloo, 200 University Avenue West, Waterloo, Canada, {cmele@uwaterloo.ca; jbose@uwaterloo.ca; james.tung@uwaterloo.ca}
[2] Karlsruhe Institute of Technology, Adenauerring 12, Karlsruhe, Germany, {katja.mombaur@kit.edu}

1 INTRODUCTION

Lower limb exoskeletons (LLEs) are wearable assistive devices that provide assistance and stability for gait and postural tasks. A component of the LLE design and donning processes is the alignment of the user and exoskeleton joint centers. When the primary axes of the exoskeleton and user joints are misaligned, either rotationally or translationally, there is an increase in experienced loads and torques in the joints and at the coupling interface [1]. These loads are challenging to characterize during in vivo exoskeleton use. As LLEs gain popularity in research and clinical settings, the question of measuring, modelling, and minimizing misaligned joints is still an open question. To address this, mannequins, or anthropomorphic test devices (ATDs), have been proposed as a replacement for in vivo LLE evaluations, offering an intermediary step between modeling and user testing. Mannequin devices currently focus on kinematic misalignment during initial donning [2], but do not account for polycentric misalignment caused by the knee joint or dynamic tissue deformation. Approximating biological mechanisms as linkage mechanisms replicates their non-linear and complex motion in planar representations. Polycentric cams or 4-bar mechanisms have been applied to track and emulate knee motion in prosthetics, orthoses, and exoskeletons [3]. However, their benefits and applications for emulating real user motion to assess exoskeletons remain unexplored. The objective of this abstract is to present the design and modeling process of a knee joint mechanism based on an inverted Chebyshev 4-bar linkage to capture polycentric motion for mannequins (Figure 1). A rigid and elastic 4-bar linkage mechanism are proposed herein to mimic cadaveric polycentric knee flexion and compliance.

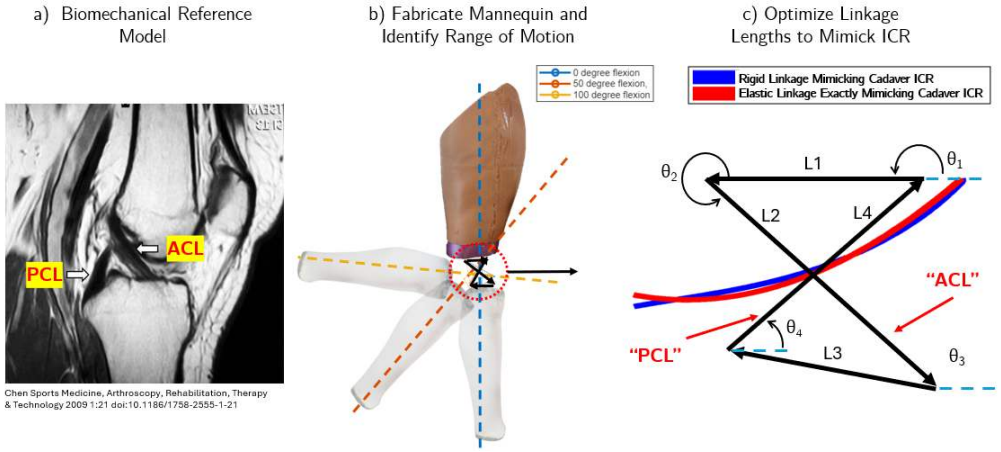

Figure 1: Illustration of lower-limb exoskeleton mannequin knee joint implementation: (a) ACL and PCL labeled (Wikimedia Commons) (b) Limb Segment manufacturing and range of motion tests (c) Optimize linkages for desired range of flexion mimicking polycentric inverted 4-bar linkages with ACL and PCL linkages highlighted.

2 KINEMATIC DESIGN OF RIGID KNEE MECHANISM

A number of approaches exist to modify and implement to model the polycentric behavior of the knee joint in literature [3, 4]. Polynomials representing the anterior-posterior and distal-proximal translation of ICR trajectory are commonly used from open datasets [4]. Using a combination of closed-loop Freudenstein equations, and 4-bar mechanisms with a supporting cam to drive the ICR as a function of flexion-extension is a common approach to track the ICR [3].

Freudenstein equations (Eq. 1 & Eq. 2) define the 4-bar linkages seen in Figure 1 (c). This is treated as a system of equations relating the input (θ_1) and output angles (θ_3). The Freudenstein equations were re-derived to relate crank to coupling rod to track the angular change of the coupler.

$$K_3 = K_2 sin(\theta_3) + K_1 cos(\theta_3) \tag{1}$$

$$K_1 = cos(\theta_2) - \frac{l_1}{l_2}, K_2 = sin(\theta_2), K_3 = \frac{l_4^2 - l_3^2 - l_2^2 - l_1^2}{2 l_2 l_3} + \frac{l_1}{l_2} cos(\theta_2) \tag{2}$$

A least-squares approach was used to track the centre of rotation and flexion angle of the coupler segment. The ICR trajectory was taken from [4]. Linkage lengths (l_1, l_2, l_3, l_4), initial angle (θ_2), and its range were control variables. The optimization goal was to minimize the error in the ICR trajectory and the delta of θ_3 to match the desired flexion range. A total flexion angle of 100 degrees was used to simulate walking gait. The rigid tracking curvature is accurate but cannot perfectly match the ideal or "elastic" curvature as seen in Figure 1 (c), bottom right.

3 ELASTIC LINKAGE MODIFICATION

Despite the knee motions reported in literature and used in this study being tracked by deterministic polynomials [4], actual knee motion exhibits some compliancy that is not captured by rigid linkages. By substituting the rigid ACL/PCL linkages with elastic elements, tracking can be shifted to the CAM, introducing tensile loads during flexion. In this configuration, Figure 2 (left),the cam shifts the system's designed ICR (blue to red curve in Figure 1 (c)). This shift introduces stress within the linkages in pseudo-static configurations during flexion (Figure 2 right). Using a material designed to buckle, these springs will only provide tensile force during flexion.

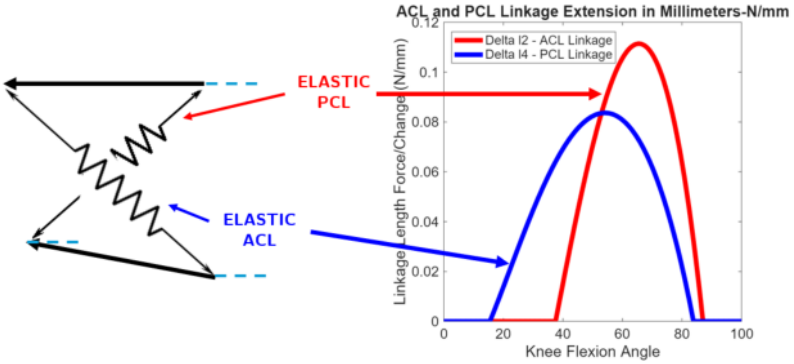

Figure 2: Pseudo-static Knee linkage with elastic elements. New Elastic elements allow for the tracking the exact desired knee trajectory, introducing stress in the linkages. Force curves (right), represent only tensile stresses introduced in flexion.

4 FUTURE WORK

Deriving the Euler-Lagrange equations of motion for the elastic linkage design to implement on the existing mannequin. Future design work will focus on the exploration of pre-tensioning and material selection on mechanism function in replicating compliancy in the human knee joint.

ACKNOWLEDGMENTS

Funding by NSERC and the TriAgency CERC program in Canada and the Hector Foundation in Germany is gratefully acknowledged.

REFERENCES

[1] S. Massardi et al., "Characterization and Evaluation of Human–Exoskeleton Interaction Dynamics: A Review," *Sensors*, vol. 22, no. 11, p. 3993, Jan. 2022.

[2] Miha Dežman et al., "A mechatronic leg replica to benchmark human–exoskeleton physical interactions," *Bioinspiration & Biomimetics*, vol. 18, no. 3, pp. 036009–036009, Apr. 2023.

[3] M. Gao et al., "Design and optimization of exoskeleton structure of lower limb knee joint based on cross four-bar linkage," *AIP Advances*, vol. 11, no. 6, Jun. 2021.

[4] P. S. WALKER, H. Kurosawa, J. S. Rovick, and R. A. Zimmerman, "External Knee Joint Design Based on Normal Motion," *The Journal of Rehabilitation Research and Development*, vol. 22, no. 1, p. 9, 1985.

THE EFFECT OF CONTACT FORCE MODELS ON THE STABILITY OF TWO-WHEELED TRAILERS WITH A SIMPLIFIED MODEL

Hanna Zsofia Horvath[1], Mate Antali[2]

[1] Department of Applied Mechanics, Faculty of Mechanical Engineering, Budapest University of Technology and Economics, Műegyetem rkp. 3., H-1111 Budapest, Hungary, hanna.horvath@mm.bme.hu
[2] Szechenyi Istvan University, Department of Applied Mechanics, Egyetem ter 1, H-9026, Gyor, Hungary, antali.mate@sze.hu

1 INTRODUCTION

Trailers are often involved in road accidents due to incorrectly chosen towing speed or payload position. In this study, the stability of towed two-wheeled trailers is investigated with a simplified 2 degree-of-freedom (DoF) model. In vehicle handling, the modeling of the tire-ground contact has a relevant effect on the resulting vibrations. Therefore, different contact force models are considered and compared.

2 MECHANICAL MODEL AND GOVERNING EQUATIONS

The 2-DoF mechanical model can be seen in Fig. 1(a), where the motion is described with the yaw angle ψ and the lateral displacement of the kingpin u. The trailer is towed with constant towing speed v, and the connection with the towing car is modeled by a lateral spring and a damper. The trailer is modeled as a rigid body with mass m and mass moment of inertia J_C^z at the center of gravity C. The geometry of the trailer is described with parameters l, a, h, w and h_0, where h_0 is the fixed height of the kingpin. The rotation of the wheels is neglected and the skate model is considered, see [1].

The equations of motion are derived based on the free-body diagram of Fig. 1(b) with the Newton-Euler equations. The gravitational force can be calculated as $G = -mg$, where g is the gravitational acceleration. The lateral component of the force at the kingpin takes into account the deformation of the lateral spring and damper as $F_A^{y_0} = -k_{lat}u - c_{lat}\dot{u}$. No braking is considered, therefore the longitudinal forces at the contact points R' and L' are equal to zero: $F_R^{long} = F_L^{long} = 0$. It is assumed that lateral tire forces depend linearly on the normal loads N_R and N_L. Thus, the lateral tire forces are calculated as follows:

$$F_R^{lat} = -N_R\,\mu(\alpha)\,, \qquad F_L^{lat} = -N_L\,\mu(\alpha)\,, \tag{1}$$

where $\mu(\alpha)$ is the normalized tire force characteristics and α is the side slip angle.

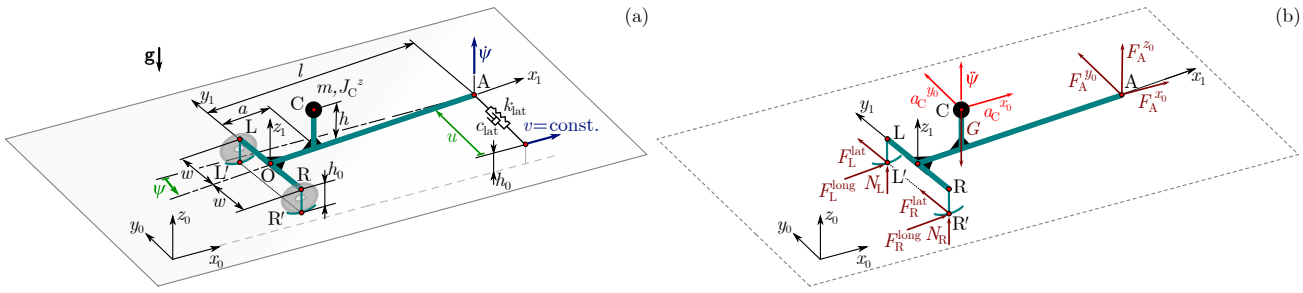

Figure 1: (a) The 2-DoF model of two-wheeled trailers, (b) the free-body diagram of the system.

The governing equations can be written as

$$\ddot{\psi} = \frac{(l(l-a)\cos\psi + hl\mu(\alpha)\sin\psi)\,F_A^{y_0} + (l-a)(l\sin^2\psi + a\cos^2\psi)\mu(\alpha)mg - (l-a)(l(l-a)\sin\psi - ah\mu(\alpha)\cos\psi)m\cos\psi\dot{\psi}^2}{J_A^z l\sin^2\psi + J_C^z l\cos^2\psi + J_1 h\mu(\alpha)\cos\psi\sin\psi}, \tag{2}$$

$$\ddot{u} = \frac{J_A^z l F_A^{y_0} - (l-a)J_1\mu(\alpha)mg\cos\psi - (l-a)\left(J_A^z l\sin\psi + J_1 h\mu(\alpha)\cos\psi\right)m\dot{\psi}^2}{m(J_A^z l\sin^2\psi + J_C^z l\cos^2\psi + J_1 h\mu(\alpha)\cos\psi\sin\psi)}, \tag{3}$$

where $J_A^z = J_C^z + m(l-a)^2$ and $J_1 = J_C^z - ma(l-a)$. Note that the external constraint force components $F_A^{x_0}$, $F_A^{z_0}$, N_R and N_L can also be expressed.

3 CONTACT FORCE MODELS

Previous studies show that the contact force used has a significant effect on the results. Therefore, different contact force models are introduced in Eq. (1). The widely used semi-empirical Magic Formula of [2] calculates the normalized tire force characteristics with constant factors B, C, D, E as

$$\mu(\alpha) = D \sin\left(C \arctan\left(B\alpha - E\left(B\alpha - \arctan(B\alpha)\right)\right)\right) . \tag{4}$$

With the brush tire model of [2], the lateral tire force can be calculated with the static μ_0 and the dynamic μ coefficient of friction, the cornering stiffness $\tilde{C}$, the critical side slip angle α_{cr} and the nominal vertical load $N_0 = mg/2$ as

$$\mu(\alpha) = \begin{cases} \frac{\tilde{C}}{N_0}\tan\alpha - \frac{\tilde{C}^2}{3N_0^2\mu_0}\left(2 - \frac{\mu}{\mu_0}\right)\tan^2\alpha\,\mathrm{sign}\alpha + \frac{\tilde{C}^3}{9N_0^3\mu_0^2}\left(1 - \frac{2\mu}{3\mu_0}\right)\tan^3\alpha\,, & \text{if} \quad 0 \le |\alpha| \le \alpha_{cr}\,, \\ \mu\,\mathrm{sign}\alpha\,, & \text{if} \quad |\alpha| > \alpha_{cr}\,. \end{cases} \tag{5}$$

A family of analytical functions that capture the essential properties of tire forces are called creep models, see e.g. [3]. For our analysis, the normalized tire force characteristics are calculated with the lateral creep coefficient $\bar{c}_{lat}$ as

$$\mu(\alpha) = \mu\,\mathrm{sigmoid}\left(\frac{\bar{c}_{lat}\tan\alpha}{\mu N_0}\right) \qquad \text{with} \qquad \mathrm{sigmoid}(x) = \tanh(x). \tag{6}$$

Instead of the $\tanh(x)$, one can choose other sigmoid functions such as $x/\sqrt{1+x^2}$ or $\mathrm{erf}\left(\sqrt{\pi}x/2\right)$. The normalized tire force characteristics calculated with the Magic Formula, the brush model and the creep models are shown in Fig. 2(a).
The present trailer model is a simplified version of the 4-DoF model of [4, 5], namely, the pitch and roll motions are neglected. The numerical bifurcation diagrams of that system [4, 5] showed that the contact force model has a significant effect, see Fig. 2(b). Namely, the structure and the nature of the emerging limit cycles, and the vibration amplitudes are strongly affected by the different contact force models.

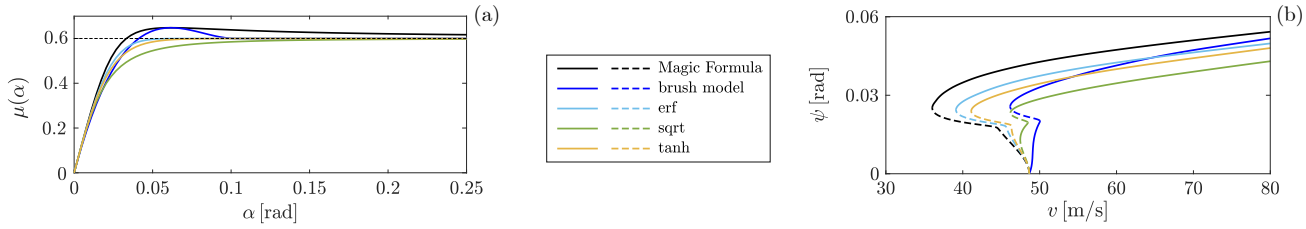

Figure 2: (a) The normalized tire force characteristics $\mu(\alpha)$, (b) bifurcation diagrams of the 4-DoF system of [4, 5].

The advantage of the present 2-DoF model is that the form of the equations is not too complex and keeps the possibility for a deeper analysis. The different contact force models are planned to be compared on the 2-DoF model to gain a deeper understanding of the underlying dynamical effects of contact forces.

ACKNOWLEDGMENTS

The research reported in this paper was supported by the National Research, Development and Innovation Office under grant no. NKFI-150659.

REFERENCES

[1] W. B. Qin, Y. Zhang, D. Takacs, G. Stapan and G. Orosz, “Nonholonomic dynamics and control of road vehicles: moving toward automation”. *Nonlinear Dynamics*, vol. 110, pp. 1959-2004, 2022.

[2] H. B. Pacejka, *Tyre and Vehicle Dynamics*. Elsevier Butterworth-Heinemann, 2002.

[3] M. Antali, “Dynamics of Railway Wheelsets with a Nonsmooth Contact Force Model”, in *Perspectives in Dynamical Systems II — Numerical and Analytical Approaches. DSTA 2021. Springer Proceedings in Mathematics & Statistics*, Dec. 2021.

[4] H. Z. Horvath and D. Takacs, “Stability and local bifurcation analyses of two-wheeled trailers considering the nonlinear coupling between lateral and vertical motions”. *Nonlinear Dynamics*, vol. 107, pp. 2115-2132, 2022.

[5] H. Z. Horvath, “Stabilization of two-wheeled vehicles: trailers and electric scooters”, PhD Thesis, Budapest University of Technology and Economics, 2025.

HIGHER-ORDER CAYLEY TRANSFORMS AND SHADOW RODRIGUES DUAL VECTORS: A UNIFIED FRAMEWORK FOR RIGID-BODY KINEMATIC

Daniel Condurache [1,2], Mihail Cojocari [1]

[1] "Gheorghe Asachi" Technical University of Iasi, D. Mangeron Street no.59, 700050, Iasi, Romania, {daniel.condurache@tuiasi.ro; mihail.cojocari@academic.tuiasi.ro}

[2] Research Center for Industrial Robots Simulation and Testing, Technical University of Cluj-Napoca, Memorandumului 14, 400114, Cluj-Napoca, Romania.

1. INTRODUCTION AND MOTIVATION

The parameterization of three-dimensional rigid-body motions is a cornerstone topic for mechanism and machine theory, with direct implications in robotics, multibody dynamics, spacecraft attitude determination, and computational kinematics [1-3]. Classical representations—rotation matrices, Euler angles, unit quaternions, and exponential coordinates—each exhibit a characteristic balance between minimality, absence of singularities, and computational convenience. Minimal vectorial parameterizations $SE(3)$ based on the Lie algebra $se(3)$ usually rely on the exponential map and involve transcendental trigonometric functions, which can complicate both symbolic manipulation and numerical implementations in large-scale multibody simulations [1-3]. Rational parametrizations, such as the Gibbs–Rodrigues vector and the Wiener–Milenković (Modified Rodrigues) parameters, are generated by Cayley-type transforms and admit purely algebraic expressions in the underlying vector parameter. They have long been appreciated in astrodynamics and robotics for their simplicity and computational efficiency, at the price of singularities on certain great circles of the rotation manifold. Building upon the classical Cayley map and on earlier contributions by Tsiotras, Junkins, and Schaub on higher-order Cayley transforms, this work develops a general, coordinate-free, closed-form framework for higher-order Cayley maps and the associated generalized Rodrigues vectors, together with the corresponding kinematic structures (tangent operators and differential kinematic equations) [4].

2. HIGHER-ORDER CAYLEY TRANSFORMS IN CLOSED FORM

We consider the usual isomorphism between the Lie algebra of skew-symmetric dual tensors and three-dimensional dual vectors with the cross-product: product [5-6]. For a dual vector parameter $\rho \in \mathbb{D}^3$, we denote by $\tilde{\rho}$ the associated skew-symmetric dual tensor, $\tilde{\rho}v = \rho \times v$ for all $v \in \mathbb{D}^3$. The classical Cayley transform is

$$\mathrm{cay}(\rho) = (I - \tilde{\rho})^{-1}(I + \tilde{\rho}), \tag{1}$$

which generates the well-known Gibbs–Rodrigues vector $\rho = \tan(\alpha/2)u$ for a dual angle α and axis u. We generalize this construction by defining, for any natural number $n \geq 1$,

$$\mathrm{cay}_n: \mathbb{D}^3 \to \underline{SO}(3),\ \mathrm{cay}_n(\rho) = (I - \tilde{\rho})^{-n}(I + \tilde{\rho})^n. \tag{2}$$

The main result can be stated as follows. The higher-order Cayley transform is well-defined and surjective, and admits the closed-form representation

$$\mathrm{cay}_n(\rho) = \frac{1}{(1+\| \rho \|^2)^n}\left(P_n(\| \rho \|^2)\,\tilde{\rho}^2 + Q_n(\| \rho \|^2)\,\tilde{\rho}\right) + I, \tag{3}$$

where $P_n, Q_n \in \mathbb{D}[X]$ are polynomials, whose coefficients are given in terms of binomial coefficients. Two auxiliary polynomials $p_n, q_n \in \mathbb{D}[X]$ and obtain an equivalent, more compact expression,

$$\mathrm{cay}_n(\rho) = \frac{2\,p_n(\|\rho\|)}{(1+\| \rho \|^2)^n}\left(p_n(\| \rho \|)\,\tilde{\rho}^2 + q_n(\| \rho \|)\,\tilde{\rho}\right) + I. \tag{4}$$

This formulation highlights the map's rationality and coordinate-frame independence.

3. GENERALIZED RODRIGUES VECTORS AND QUATERNIONIC REPRESENTATION

The inverse map cay_n^{-1} is shown to be multivalued. For a dual orthogonal tensor $R(\alpha, u)$ with dual angle α and dual unit vector u, we prove that there exist exactly n vectors $\rho_k \in \mathbb{D}^3$ such that

$$\text{cay}_n(\rho_k) = R(\alpha, u), k = 0,1, \dots, n-1, \tag{5}$$

where

$$\rho_k = \tan \frac{\alpha+2k\pi}{2n}\, u. \tag{6}$$

We call $\rho_0 = \tan(\alpha/2n)u$ the principal higher-order Rodrigues dual vectors ρ_k the shadow parameters. This generalizes, in a unified way, the standard Gibbs–Rodrigues vector (for $n = 1$) and the Modified Rodrigues / Wiener–Milenković parameters (for $n = 2$) and clarifies the structure of shadow sets for higher orders. The motion can also be described by the unit dual quaternions $\hat{q}$, which we express in closed form in terms of ρ the polynomials p_n, q_n. This highlights the coherence among higher-order Cayley parametrizations, generalized Rodrigues dual vectors, and dual-quaternionic representations, and provides ready-to-use formulas for implementations combining vector- and quaternion-based kinematics.

4. TANGENT OPERATORS AND KINEMATIC EQUATIONS

Beyond static parametrization, we study rigid-body motion $R(t) \in \underline{SO}(3)$ and its instantaneous dual angular velocity. For a rigid body motion, the angular velocity dual tensor and vector are

$$\widetilde{\omega} = \dot{R}R^T, \omega = \text{vect}(\widetilde{\omega}), \tag{7}$$

and the body-fixed dual angular velocity is $\omega_B = R^T\omega = \text{vect}(R^T\dot{R})$. For any vector parameter $v(t)$ of the motion (Euler vector, Rodrigues vector, generalized Rodrigues vector, etc.), we define the tangent operator $T(v)$ by

$$\omega = T(v)\,\dot{v}. \tag{8}$$

When $T(v)$ it is invertible, its inverse $K(v) = T^{-1}(v)$ yields the kinematic equation

$$\dot{v} = K(v)\,\omega, \tag{9}$$

which is an alternative to the Poisson–Darboux equation $\dot{R} = \widetilde{\omega}R$. For the exponential Euler dual vector parameterization $\alpha(t)$, we derive closed-form, coordinate-free expressions for the tangent operator dexp_α and its inverse K_α, valid in both space and body frames. Analogously, for each higher-order Cayley parametrization $\rho(t)$, we obtain explicit formulas for $\text{dcay}_n(\rho)$ and $K_n(\rho)$ in terms of ρ, $\rho \otimes \rho$, $\tilde{\rho}$, and the polynomials p_n, q_n. In particular, the kinematic equations

$$\omega = \text{dcay}_n(\rho)\,\dot{\rho}, \dot{\rho} = K_n(\rho)\,\omega, \tag{10}$$

are given by compact rational expressions in ρ. A notable result is that the analytical expressions for angular velocity, tangent operators, and kinematic equations are identical for the principal higher-order Rodrigues dual vector and all its shadows. This property significantly simplifies the handling of branch changes in numerical algorithms, such as attitude filters or geometric integrators that must switch between shadow sets to avoid singularities.

For the higher-order Cayley parameterization ρ, the paper provides explicit expressions for the tangent operator $\text{dcay}_n(\rho)$ and its inverse $K_n(\rho)$, using the dyadic product $\rho \otimes \rho$ and the polynomials p_n, q_n. In compact form:

$$\omega = \text{dcay}_n(\rho)\,\dot{\rho}, \dot{\rho} = K_n(\rho)\,\omega, \tag{11}$$

$$K_n(\rho) = \frac{1+\|\rho\|^2}{2n\|\rho\|^2}\,\rho \otimes \rho - \frac{q_n(\|\rho\|)}{2\|\rho\|^2 p_n(\|\rho\|)}\,\tilde{\rho}^{\,2} - \frac{1}{2}\tilde{\rho}. \tag{12}$$

A remarkable and practically important fact is that the analytical expressions for ω, ω_B, dcay_n, and K_n are identical for the parametrization by the principal vector and by its shadows, which greatly simplifies the treatment of branch changes and shadow sets in numerical applications.

The proposed framework thus offers a unified, coordinate-free, and fully rational description of higher-order Cayley transforms, generalized Rodrigues dual vectors, and their associated kinematic structures. It is directly applicable to the modeling, simulation, and control of mechanisms and multibody systems, and it integrates naturally with Lie-group-based numerical methods. In the context of the 60th anniversary of Mechanism and Machine Theory, this work can be seen as a continuation of the classical geometric and algebraic approaches to rigid-body motion, extended to a systematic family of minimal, rational motion parameterizations with clear theoretical properties and clear potential for practical impact in kinematics, dynamics, and control.

REFERENCES

[1] J. Angeles, *Fundamentals of Robotic Mechanical Systems*, 4th ed., Springer, Cham, 2014.
[2] R.M. Murray, Z. Li and S.S. Sastry, *A Mathematical Introduction to Robotic Manipulation*. CRC Press, Boca Raton, 1994.
[3] H. Schaub and J.L. Junkins, *Analytical Mechanics of Space Systems*, 4th ed., AIAA Education Series, AIAA, Reston, 2018.
[4] P. Tsiotras, J.L. Junkins and H. Schaub, "Higher-Order Cayley Transforms with Applications to Attitude Representations", *Journal of Guidance, Control, and Dynamics*, 20(3), 528–534, 1997.
[5] A. Müller, "Screw and Lie group theory in multibody dynamics – Recursive algorithms and equations of motion of tree-topology systems", *Multibody System Dynamics*, 42, 219–248, 2018.
[6] D. Condurache, M. Cojocari and I.-A. Ciureanu, "A Closed Form of Higher-Order Cayley Transforms and Generalized Rodrigues Vectors Parameterization of Rigid Motion", *Mathematics*, 13(1), 114, 2025.

CLOSED-FORM BAKER–CAMPBELL–HAUSDORFF–DYNKIN FORMULA FOR RIGID BODY DISPLACEMENTS AND ITS SIGNIFICANCE FOR MECHANISM AND MACHINE THEORY

Daniel Condurache [1,2], Mihail Cojocari [1]

[1] "Gheorghe Asachi" Technical University of Iasi, D. Mangeron Street no.59, 700050, Iasi, Romania,
{daniel.condurache@tuiasi.ro; mihail.cojocari@academic.tuiasi.ro}

[2] Research Center for Industrial Robots Simulation and Testing, Technical University of Cluj-Napoca, Memorandumului 14, 400114, Cluj-Napoca, Romania.

t

1. INTRODUCTION

Over the past sixty years, *Mechanism and Machine Theory* has played a decisive role in consolidating the mathematical foundations of kinematics and advancing the analysis and synthesis of mechanical systems. Central to this development has been the systematic use of Lie groups and Lie algebras for modeling rigid-body motion, particularly the special Euclidean group $SE(3)$ and its Lie algebra $se(3)$ [1,2]. Within this framework, the Baker–Campbell–Hausdorff–Dynkin (BCHD) formula plays a fundamental role, governing the composition of finite motions from their infinitesimal generators.

The BCH problem originated in the early twentieth century with Baker and Hausdorff [3,4], and was later expanded by Dynkin, who provided a clear form of the commutator series and examined its convergence [5]. In its general form, the BCHD formula expresses

$$\exp(A)\exp(B) = \exp(C), \tag{1}$$

where the generator C is given by an infinite series of nested commutators,

$$C = A + B + \frac{1}{2}[A,B] + \frac{1}{12}[A,[A,B]] + \frac{1}{12}[B,[B,A]] + \cdots . \tag{2}$$

Although formally exact, this series representation is difficult to exploit in applications involving non-nilpotent Lie algebras. For the Lie algebra underlying spatial mechanisms, robotic manipulators, and multibody systems, it has been commonly believed that a closed-form BCHD expression does not exist [6,7].

In this contribution, the BCHD problem is revisited from the perspective of spatial kinematics, and a closed-form, coordinate-free formulation of rigid-body displacements is derived. The approach exploits the intrinsic structures of the rotation group and the special Euclidean group, along with their associated exponential maps, which have been extensively used in robotics and mechanism theory.

2. CLOSED-FORM BCHD FORMULA FOR ROTATIONS

Let $\widehat{\omega}_1, \widehat{\omega}_2 \in so(3)$ denote the skew-symmetric tensors associated with two finite rotations. Their composition satisfies

$$\exp(\widehat{\omega}_1)\exp(\widehat{\omega}_2) = \exp(\widehat{\omega}), \tag{3}$$

where the resulting generator admits the closed-form representation

$$\widehat{\omega} = \alpha_1\widehat{\omega}_1 + \alpha_2\widehat{\omega}_2 + \alpha_{12}[\widehat{\omega}_1, \widehat{\omega}_2]. \tag{4}$$

The scalar coefficients $\alpha_1, \alpha_2, \alpha_{12}$ are explicit functions of the rotation magnitudes and depend only on trigonometric invariants of the composed motion. This result eliminates the need for series truncation and provides a singularity-free determination of the Euler rotation vector, a feature of particular importance in kinematic analysis and numerical simulation.

3. EXTENSION TO RIGID BODY DISPLACEMENTS IN $se(3)$

A general element of the Lie algebra $se(3)$ is written as

$$\hat{\xi} = \begin{bmatrix} \widehat{\omega} & v \\ 0 & 0 \end{bmatrix}, \tag{5}$$

with $\widehat{\omega} \in so(3)$ and $v \in \mathbb{R}^3$. The exponential map yields the corresponding rigid body displacement

$$\exp(\hat{\xi}) = \begin{bmatrix} \exp(\hat{\omega}) & \mathrm{dexp}_{\hat{\omega}}\, v \\ 0 & 1 \end{bmatrix}, \tag{6}$$

where $\mathrm{dexp}_{\hat{\omega}}$ denotes the differential of the exponential map [1].
Given two rigid body motions $\hat{\xi}_1 = (\hat{\omega}_1, v_1)$ and $\hat{\xi}_2 = (\hat{\omega}_2, v_2)$, the BCHD equation

$$\hat{\omega} = \alpha_1\hat{\omega}_1 + \alpha_2\hat{\omega}_2 + \alpha_{12}[\hat{\omega}_1, \hat{\omega}_2], v = T_1 v_1 + T_2 v_2, \tag{7}$$

where the tensors T_1 and T_2 depend solely on the rotational generators. This formulation yields the screw parameters of the composite displacement directly and is fully consistent with the geometric interpretation of rigid-body motion developed in classical and modern mechanism theory [6,7].

4. DUAL ALGEBRA AND SCREW INTERPRETATION

An equivalent and highly compact formulation is obtained through the isomorphism between $se(3)$ and the algebra of dual vectors. Introducing the dual Euler (screw) vectors

$$\underline{\omega}_1 = \omega_1 + \varepsilon v_1, \underline{\omega}_2 = \omega_2 + \varepsilon v_2, \tag{8}$$

the BCHD formula reduces to

$$\underline{\omega} = \underline{\alpha}_1\underline{\omega}_1 + \underline{\alpha}_2\underline{\omega}_2 + \underline{\alpha}_{12}(\underline{\omega}_2 \times \underline{\omega}_2), \tag{9}$$

where $\underline{\omega} = \omega + \varepsilon v$ fully characterizes the resulting rigid-body displacement. This expression unifies rotation and translation within a single algebraic object and highlights the deep connection between Lie algebraic structure and screw theory, a cornerstone of mechanism science [2,6].

5. RELEVANCE FOR MECHANISM AND MACHINE THEORY

Closed-form BCHD expressions have direct implications for mechanism and machine theory. They enhance numerical robustness, simplify error propagation analysis, and enable real-time computation in applications such as robot motion planning, spatial mechanism synthesis, calibration, and multibody dynamics [1,2,8-10]. Moreover, they complement recent efforts to identify closed BCH formulas in special algebraic settings [6-8].
As *Mechanism and Machine Theory* celebrates its 60th anniversary, this contribution illustrates how classical problems originating in the early theory of Lie groups [3–5] continue to generate new insights when revisited through the lens of spatial kinematics. The availability of closed-form BCHD expressions for rigid-body displacements underscores the enduring role of rigorous geometric and algebraic methods in advancing the theory and practice of mechanisms and machines [11].

REFERENCES

[1] R.M. Murray, Z. Li and S.S. Sastry, *A Mathematical Introduction to Robotic Manipulation*, CRC Press, Boca Raton, 1994.
[2] J. M. Selig, *Geometric Fundamentals of Robotics*, 2nd ed., Springer, New York, 2005.
[3] H.F. Baker, "On the Exponential Theorem for a Simply Transitive Continuous Group, and the Calculation of the Finite Equations from the Constants of Structure", *Proceedings of the London Mathematical Society*, s1 34 (1), pp. 91–129, 1901.
[4] F. Hausdorff, "Die symbolische Exponentialformel in der Gruppentheorie", *Ber. Verh. Kgl. SÃ¤chs. Ges. Wiss. Leipzig., Math.-phys.*, Kl. 58, pp. 19–48, 1906.
[5] E.B. Dynkin, "Calculation of the coefficients in the Baker–Campbell–Hausdorff formula", *Dokl. Akad. Nauk SSSR*, vol. 57, pp. 323–326, 1947.
[6] D. Condurache and I. Ciureanu, "Baker–Campbell–Hausdorff–Dynkin Formula for the Lie Algebra of Rigid Body Displacements", *Mathematics*, vol. 8, art. 1185, 2020.
[7] D. Condurache, "Closed Form of the Baker–Campbell–Hausdorff Formula for the Lie Algebra of Rigid Body Displacements", *Multibody Dynamics 2019*, A. Kecskeméthy and G. Flores (eds.), *Computational Methods in Applied Sciences*, vol. 53., Springer, Cham, 2019.
[8] S. Blanes and F. Casas, "On the convergence and optimization of the Baker–Campbell–Hausdorff formula": *Linear Algebra and its Applications*, vol. 378, pp. 135–158, 2004.
[9] A. Moakher, "Means and averaging of rotations", *SIAM Journal on Matrix Analysis and Applications*, vol. 24, no. 1, pp. 1–16, 2002.
[10] A. Iserles, H.Z. Munthe-Kaas, S.P. Nørsett and A. Zanna, "Lie group methods": *Acta Numerica*, vol. 9, pp. 215–365, 2000.
[11] R. Achilles and A. Bonfiglioli, "The early proofs of the theorem of Campbell, Baker, Hausdorff, and Dynkin", *Arch. Hist. Exact Sci.*, vol. 66, pp. 295–358, 2012.

INFLUENCE OF HUMAN BODY VARIABILITY ON SEAT-TO-HEAD TRANSMISSIBILITY

Linan Yin[1], Jianqiao Guo*[1,2], Yanfei Jin[1,2], Jingwei Meng[2], Qiang Tian[1,2], Haiyan Hu[2]

[1] Aerospace and Informatics Domain, Beijing Institute of Technology, No. 6, Jinfeng Road, Tangjiawan, 519088, Zhuhai, China,

[2] Department of Mechanics, Beijing Institute of Technology, No. 5, Zhongguancun South Street, Haidian District, 100081, Beijing, China, {guojianqiao@bit.edu.cn (J. Guo), jinyf@bit.edu.cn (Y. Jin)}

1. INTRODUCTION

Whole-body vibration transmitted from vehicle seats to the human body is a key factor affecting musculoskeletal health and driving comfort [1]. Most existing studies focus on the influence of seat structural parameters on seat-to-head vibration transmission. However, less attention is given to the effect of subject-specific biomechanical differences—such as variations in muscle stiffness and joint damping—on vibration propagation in the coupled human-seat system. Meanwhile, high-dimensional hybrid uncertain parameters introduce computational difficulties in multi-degree-of-freedom biomechanical systems. To address this, a planar human-seat coupled multibody dynamic model with 4 rigid bodies and 12 degrees of freedom was developed. A hierarchical polynomial surrogate modeling approach was further employed to establish the mapping relationship between biodynamic parameters and vibration transmissibility.

2. MEASUREMENT AND ANALYSIS METHODS

The experimental apparatus used in this study was a four-post road simulator. One of the posts was employed as the vibration excitation source. A rigid seat was fastened to the road simulator using high-strength bolts. The experiment aimed to measure the vibration acceleration at the seat transmitted from the simulator input ($\ddot{z}_{\mathrm{seat}}$), as well as the vertical acceleration ($\ddot{z}_{\mathrm{head}}$) and fore-aft acceleration ($\ddot{x}_{\mathrm{head}}$) at the head of an occupant seated in a backrest seat, induced by vibrations transmitted through the human body.

To examine the influence of inter-individual variability on the seat-to-head transmissibility, a synchronous measurement scheme for head and seat accelerations was adopted for three adult subjects (two males and one female, age: 24.0±2.7 years; BMI: 22.3±4.2 kg/m²). To reduce transmission errors between the simulator and the seat, the Z-axis acceleration at the human–seat contact surface and the vertical and pitch-direction accelerations at the subject's forehead under vibration were measured [2,3], as shown in Fig. 1.

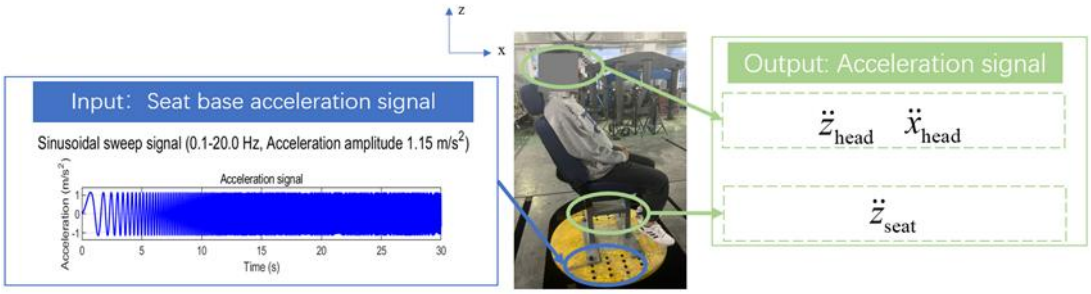

Figure 1. Schematic of the experimental setup: the seat, coordinate directions, and accelerometer arrangement used to measure seat-to-head transmissibility; as well as the seated posture and motion measurements at the head and at the human–seat contact surface.

The direct vertical seat-to-head transmissibility (DV STHT) and the cross-axis fore-aft seat-to-head transmissibility (CAFA STHT) for head motion during vertical vibration are given by Eq. (1).

$$\mathrm{DVSTHT}(f)=\frac{\left|P_{\ddot{z}_{\mathrm{seat}}\ddot{z}_{\mathrm{head}}}(f)\right|}{\left|P_{\ddot{z}_{\mathrm{seat}}\ddot{z}_{\mathrm{seat}}}(f)\right|},\quad \mathrm{CAFASTHT}(f)=\frac{\left|P_{\ddot{z}_{\mathrm{seat}}\ddot{x}_{\mathrm{head}}}(f)\right|}{\left|P_{\ddot{z}_{\mathrm{seat}}\ddot{z}_{\mathrm{seat}}}(f)\right|} \tag{1}$$

A 12-degree-of-freedom multibody biodynamics model of the seated human was utilized to identify subject characteristics and investigate the influence of human variability on seat-to-head transmissibility [4], as illustrated in Fig. 2(a). The model includes

four rigid bodies (head, upper torso, lower torso, and thigh-pelvis) connected by spring-damper elements, each possessing vertical (Z-axis) and pitch (X-axis) motions, and features an inclined backrest support.

Considering the large number of parameters, a sensitivity analysis was conducted on all 15 stiffness and 15 damping parameters. Using a genetic algorithm [4], the anthropometric data of three subjects were mapped onto the seated human biodynamics model, i.e., to identify the inter-body joint and seat contact parameters for each subject, thereby obtaining the ranges of stiffness and damping parameters, as shown in Fig. 2(b), where ε_D represents the error of DVSTHT and ε_C represents the error of CAFASTHT.

To investigate the influence of differences in biomechanical parameters on human response and quantify their impact on the seat-to-head vibration transmissibility, eight mass-related parameters in the model, including segmental mass (m) and moment of inertia (I), were categorized into two types and characterized as random variables. Forty-four parameters related to inter-body joints and seat contact were classified into four categories—muscle stiffness (k), joint damping (c), joint rotation center (J), and center of mass of rigid body (G)—and characterized as interval variables.

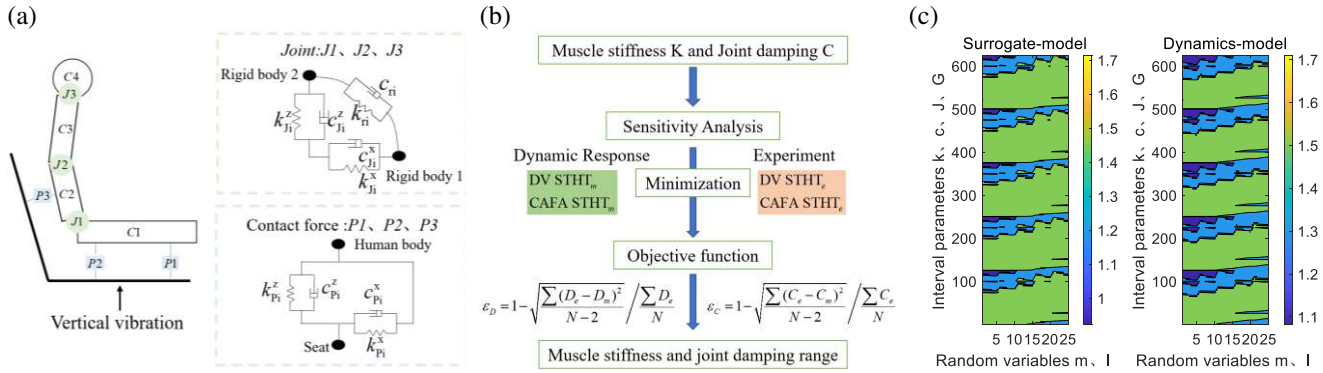

Figure 2. (a) Human sitting posture multibody dynamics model; (b) Genetic algorithm for parameter identification; (c) Validation of sitting posture surrogate model

To handle high-dimensional hybrid uncertain parameters, the high-dimensional model representation (HDMR) expansion was employed to decompose the complex response of the multi-input parameter system into a superposition of a series of low-dimensional component functions [5]. Specifically, through a hierarchical strategy, the total response is decomposed into a constant term, first-order main effect terms, and second-order interaction effect terms. The first-order main effect terms describe the contribution of individual interval or random parameters to the system response when varied independently, while the second-order interaction effect terms describe the coupling effects when any two parameters (two random parameters, two interval parameters, or one interval parameter and one random parameter) are varied simultaneously. This hierarchical strategy effectively addresses the propagation of hybrid uncertain parameters (coexisting interval and random variables) while significantly reducing the required number of sample points, thereby replacing the original multibody dynamics model and enabling efficient prediction of vibration transmissibility and uncertainty analysis.

3. RESULTS AND DISCUSSIONS

Since the peak of seat-to-head transmissibility is mainly concentrated between 4 Hz and 4.5 Hz, Fig. 2(c) shows a comparison of the direct vertical seat-to-head transmissibility calculated by the multibody dynamics model and the surrogate model at 4.1 Hz. The accuracy of the surrogate model in predicting the statistical characteristics and boundary conditions of the dynamic response was validated.

Subsequently, the influence of uncertainties in single and mixed biodynamic parameters on the vibration transmission characteristics of the human-seat coupled system was systematically discussed. Numerical results indicate that variations in the center of mass have a significant impact on seat-to-head transmissibility. The importance of considering biodynamic differences in this study provides a theoretical foundation and a quantitative simulation framework for vehicle seat design and comfort evaluation.

REFERENCES

[1] S. Rahmatalla and J. DeShaw, “Effective seat-to-head transmissibility in whole-body vibration: Effects of posture and arm position”. *Journal of Sound and Vibration*, 330(25), 6277-6286, 2011.

[2] A. Singh, S. Samuel, Y.K. Dhabi and H. Singh, “Whole-body vibration: Characterization of seat-to-head transmissibility for agricultural tractor drivers during loader operation”. *Smart Agricultural Technology*, 4, Article 100164, 2023.

[3] S. Mandapuram, S. Rakheja, P. Marcotte and P.-É. Boileau, “Analyses of biodynamic responses of seated occupants to uncorrelated fore-aft and vertical whole-body vibration”. *Journal of Sound and Vibration*, 330(16), 4064-4079, 2011.

[4] R. Desai, A. Guha and P. Seshu, “Modelling and simulation of an integrated human-vehicle system with non-linear cushion contact force”. *Simulation Modelling Practice and Theory*, 106, Article 102206, 2021.

[5] J. Meng and Y. Jin, “A dimension reduction metamodeling approach for hybrid uncertainties quantification and response prediction”. *Nonlinear Dynamics*, 113(17), 22723-22746, 2025.

METHODS OF TCA AND LTCA FOR PURE-ROLLING BEVEL LINE GEAR WITH THE ACTIVELY DESIGNED CONTACT TRACE

Xiaoping Xiao[1,2], Hualin Xie[1], Chao He[1], Kai Zhu[1], Zhen Chen[1,3*], Yangzhi Chen[1]

[1] Guangdong Ocean University, No. 1 Haida Road, Mazhang District, Zhanjiang City, Guangdong Province 524088, China, {xiaoping.xiao@foxmail.com; xiehualin@stu.gdou.edu.cn; 1257655470@qq.com; kaychu0523@foxmail.com; mezhenchen@gdou.edu.cn; meyzchen@scut.edu.cn;}

[2] Zhongshan MLTOR Numerical Control Technology Co., Ltd., No. 36 Keji West Road, Torch Development Zone, Zhongshan City, Guangdong Province 528401, China, {xiaoping.xiao@foxmail.com;}

[3] State Key Laboratory of Mechanical Transmission for Advanced Equipment, Chongqing University, No. 174 Shazheng Street, Shapingba District, Chongqing 400044, China, {mezhenchen@gdou.edu.cn;}

1. INTRODUCTION

Bevel gears are used to transfer the power and motion of intersecting axes, and have been widely used in aerospace, ships, automobiles, robots and other fields[1]. The involute tooth profile is the most common tooth profile of bevel gear. In order to improve the transmission performance of bevel gear, many scholars have studied different tooth profiles based on the meshing theory of conjugate surface, such as cosine tooth profile, cycloid tooth profile, arc tooth profile, etc. However, these profiles have a common weakness, that is, there is non-uniform relative sliding during meshing process. Some studies have shown that the non-uniform relative sliding is a noteworthy cause of transmission failures[2], such as gear wear, scuffing, and plastic deformation. Therefore, the control of sliding rate is very important in the actual transmission process of bevel gear.

Recently, Chen et al.[3] proposed a line gear based on the meshing theory of space conjugate curve. In the transmission process of line gear, there is always a pair of conjugated spatial curves to maintaining the state of contact point, so it is easy to control the sliding rate during meshing process. For example, Chen et al.[2] desigined the pure-rolling cylindrical and bevel gears, and studied the contact characteristics of pure-rolling gears with different tooth profiles. The pure-rolling design is expected to improve the transmission failure caused by relative sliding, but the existence of manufacturing and installation errors may damage the ideal conjugated contact state, resulting in edge contact, stress concentration, vibration and noise, etc., which limits the engineering application of pure-rolling gear.

To reduce the sensitivity of pure-rolling bevel gears to manufacturing and installation errors, a pure-rolling bevel line gear (PBLG) with the actively designed contact trace is proposed. The geometric transmission error curve is adjusted by directly designing the driving contact trace and transmission ratio function, so as to achieve the effect of tooth surface modification. Furthermore, to analyze the contact characteristics in the meshing transmission, the methods of TCA and LTCA for PBLG is introduced. In addition, an experiment to verify the contact pattern is also performed.

2. TOOTH CONTACT ANALYSIS OF PBLG

Before conducting TCA, a mathematical model of PBLG is established. The meshing coordinate systems can be found in Ref. [4] and it is assumed that the position vector of the driving contact trace can be represented by Eq. (1).

$$c_1^{(p)} = (mt\sin t, mt\cos t, nt)^T \tag{1}$$

where, m and n are the design parameters.

And, the transmission error curve can be adjusted by directly designing the transmission ratio function $f_i(t)$. Assuming that the designed transmission error function is shown in Eq. (2).

$$f_i(t) = i_{12} - k_i(t) \tag{2}$$

where, i_{pg} is the transmission ratio and k_i is a given coefficient.

Based on Eqs. (1) and (2), and the meshing equation, the driven contact trace can be obtained, and then the mathematical model and 3D solid model of the tooth surface can be obtained by sweeping method, as shown in Fig. 1(a). According to the positional relationship shown in Fig. 1(a), a TCA program is developed to analyze the contact areas of the discrete tooth surfaces. As shown in Fig. 1(b), the contact patterns of PBLG pair under different installation errors are obtained.

3. LOADED TOOTH CONTACT ANALYSIS OF PBLG

To analyze the contact characteristics under load, the LTCA algorithm for PBLG is developed. Contact pressure and contact deformation are solved by FFT technology combined with conjugate gradient, while the deformations of tooth and base are solved by physics-informed neural network. The physical information mainly refers to the bending, shear and other deformations obtained by slice method. The deformation of a single slice is solved by the superposition of tooth deformation obtained from the analytical method and the base deformation obtained from the finite element method. As shown in Fig. 2, the pressure nephograms and loading transmission error curves of PBLG pairs are obtained.

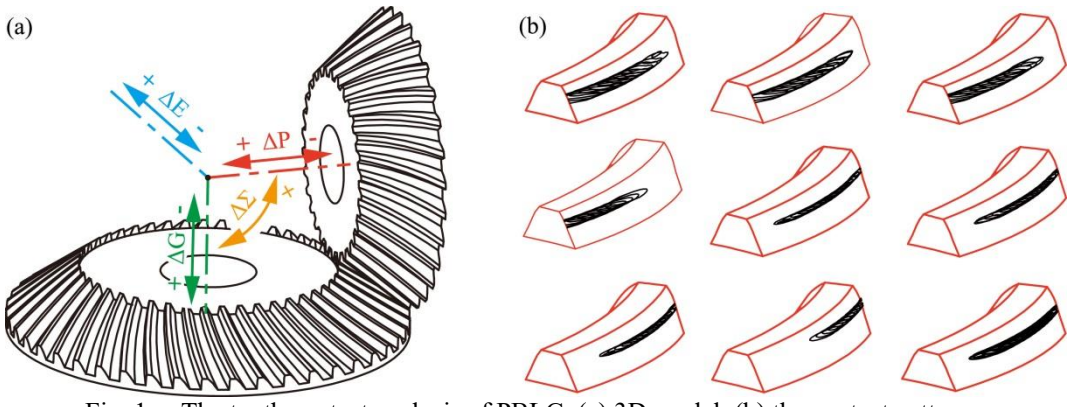

Fig. 1. The tooth contact analysis of PBLG. (a) 3D model; (b) the contact patterns.

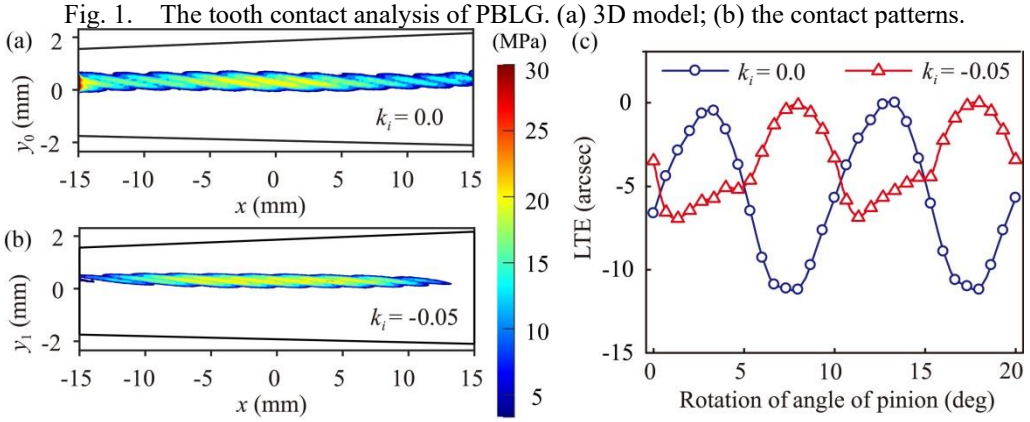

Fig. 2. The loaded tooth contact analysis of PBLG. (a) and (b) are pressure nephograms; (c) loading transmission error.

4. EXPERIMENTS FOR VERIFYING THE CONTACT PATTERN

A five axis four linkage machine tool was used to fabricated the prototypes of PBLGs. Then, kinematic experiments were conducted on the testing device, and the obtained contact patterns is shown in Fig. 3. The contact pattern of PBLG is distributed in the middle of the tooth surface in the tooth depth direction, and almost occupies the entire tooth surface in the tooth width direction. The experimental results of the contact patterns are in good agreement of the meshing analysis results, which means that the proposed active design method can effectively avoid edge contact.

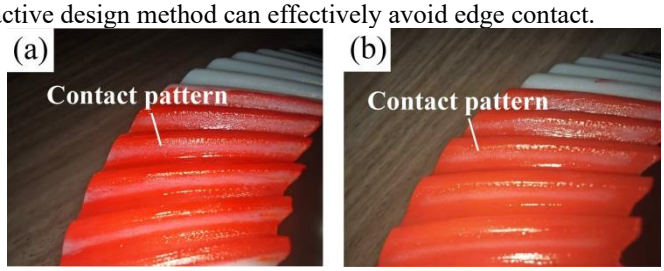

Fig. 3. The contact patterns of PBLGs. (a) $k_i = 0$; (b) $k_i = -0.05$.

5. CONCLUSIONS

A pure-rolling bevel line gear (PBLG) with a preset contact trace is proposed in this work, and the geometric transmission error is controlled by directly designing the transmission ratio function. To analyze the contact characteristics, the TCA and LTCA algorithms for PBLG are also developed. The experimental results of contact patterns demonstrate the feasibility of actively designing contact traces.

ACKNOWLEDGMENTS

The authors would like to acknowledge the support of the program for National Natural Science Foundation of China (Nos.52405056, 52275073, and 51575191), Scientific Research Start-up Funds of Guangdong Ocean University (Nos. YJR23002 and YJR22016), the Quality Engineering Project of Guangdong Province (No. PX-1372025008).

REFERENCES

[1] F. Litvin, A. Fuentes, Gear geometry and applied theory, Cambridge university press, 2004.
[2] Z. Chen, B. Lei, M. Zeng, Y. Li, A. Fuentes-Aznar, Computerized design, simulation of meshing and stress analysis of pure rolling internal helical gear drives with combined tooth profiles, Mechanism and Machine Theory, 176 (2022) 104959.
[3] Y. Chen, Y. Lv, J. Ding, Z. Chen, Fundamental design equations for space curve meshing skew gear mechanism, Mechanism and Machine Theory, 70 (2013) 175-188.
[4] X. Xiao, Y. Chen, C. Ye, D. Zhang, Study on face-milling roughing method for line gears–design, manufacture, and measurement, Mechanism and Machine Theory, 170 (2022) 104684.

UNSTEADY-STATE TIRE CORNERING UNDER DYNAMIC NORMAL LOAD VARIATIONS

Witold Luty[1], Karol Zielonka[2]

[1] Military University of Technology, ul. gen. Sylwestra Kaliskiego 2, 00-908 Warsaw, Poland, witekluty@gmail.com
[2] Łukasiewicz Research Network - Automotive Industry Institute, ul. Jagiellońska 55, 03-301 Warsaw, Poland, karol.zielonka@pimot.lukasiewicz.gov.pl

1. INTRODUCTION

The non-linear influence of the wheel normal load on the tire cornering stiffness coefficient causes a decrease in the effective lateral response transmitted by the vehicle's wheels during cornering. Under extreme conditions, the reduction of the available lateral reaction can lead to significant disturbances in vehicle motion or even loss of stability and steerability. Two primary reasons are identified for the reduction of the available lateral reaction resulting from the non-linear effect of the wheels' normal load on their cornering stiffness. [1, 2, 3]:

a) changes in the normal load distribution of the driving axles' wheels resulting from the roll moment of the vehicle,

b) dynamic changes in the normal load of each wheel caused by driving on an uneven surface.

Such causes may occur simultaneously and collectively result in a decrease of the available lateral reaction force transmitted by the wheels by even more than 30%.

There is an additional cause for the reduction in the effective lateral reaction force transmitted by the tire under cornering conditions. This cause lies in the tire properties under unsteady-state cornering conditions. Unsteady-state cornering conditions arise as a result of rapid changes in wheel motion conditions, which induce changes in the value of the transmitted lateral reaction force, but with a specific delay called relaxation. In a simplified model, under certain motion conditions, the relaxation process is described by a first-order differential equation, an essential parameter of which is the relaxation length L_n [1,2,3]:

– in the time domain (t) - $F_y(t) = F_{yu} - \frac{L_n}{v_x} \cdot \dot{F}_y(t)$ (1)

– in the longitudinal wheel displacement domain (l_x) - $F_y(l_x) = F_{yu} - L_n \cdot \dot{F}(l_x)$ (2)

It follows from the presented expressions that the relaxation length L_n determines the rate of increase/decrease of the lateral reaction force F_y(t) in the process of following the value appropriate for the current, steady-state wheel motion conditions F_{yu}. The results of the author's own research and those available in the literature show that the relaxation length depends on the wheel cornering angle and the normal load [4,5]. An example of this relationship is shown in the figure (Fig. 1).

The identified dynamic properties of the tire in unsteady-state cornering conditions lead to specific conclusions. Based on the analysis of the relaxation length L_n, it can be stated (Fig. 1):

- an increase of the tire relaxation length L_n slows down the process of the lateral reaction force F_y increasing, while the normal load F_z is rising,
- a decrease in the tire relaxation length L_n makes faster the process of the lateral reaction force F_y decreasing, while the normal load F_z is decreasing.

Thus, dynamic, oscillatory changes in the wheel normal load during cornering lead to an asymmetric distribution of the transmitted lateral reaction force F_y around the value possible to achieve under steady-state motion conditions. Consequently, as a result of wheel vibrations induced by road irregularities, a reduction in the effective available lateral reaction force transmitted by the vehicle's wheels can be expected during cornering. This phenomenon may be significantly amplified when wheel loses the contact with the ground, during vertical vibrations. To examine and verify the formulated conclusions quantitatively and qualitatively, a series of research were planned and conducted. Due to significant difficulties in ensuring the required and repeatable conditions for vertical wheel vibrations while cornering, a simulation method was chosen to achieve the intended objectives.

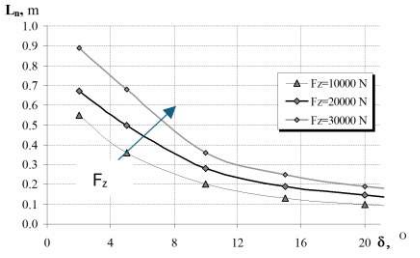

Figure. 1. Influence of cornering angle (δ) and normal load (F_z) on tire relaxation length (L_n) (author's own research)

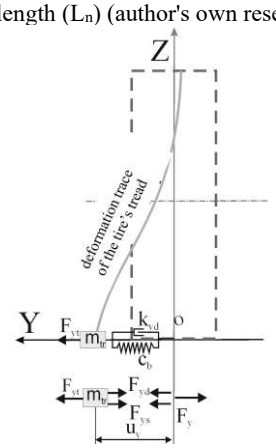

Figure. 2. Dynamics model in conditions of wheel cornering with tire relaxation

2. TIRE DYNAMICS MODEL

The adopted research method requires the use of a tire dynamics model that enables the determination of the lateral reaction force F_y transmitted under dynamic changes in the wheel normal load during cornering. For this purpose, a dedicated tire relaxation dynamics model was developed, taking into account the lateral tire deformation resulting from the lateral reaction force F_{yt} in the tire-ground contact patch (Fig. 2). The DFS model [6] was applied to calculate its

value. Lateral tire deformation is the fundamental basis of its relaxation process. The dynamics model accounts for the lateral elastic stiffness resistance (c_b), as well as the inertia of the reduced mass (m_{tr}) and the damping resistance (k_{yd}) of the tire carcass during the deformation process under variable cornering conditions.

3. RESEARCH CONDITIONS

Under road conditions, dynamic changes in the wheel normal load may occur as a result of single road irregularity, during passage over cyclically repeating road irregularities or while free vibration phase of the wheel after it loses contact with the irregularities [7,8]. In the planned simulation research, a unified vertical vibration excitation was adopted, consisting of a sinusoidal vertical force acting on the wheel over a wide range of amplitudes relative to the static load (F_{zstat}) and continuously increasing frequency (Fig. 3). The study also accounted for variations in the wheel rolling speed. The tests were conducted under comparable conditions for the following tire model variants: variant without relaxation versus a variant including tire relaxation, including versus excluding the inertial resistance m_{tr}, including versus excluding the damping resistance (k_{yd}). A comparison of the results obtained for these variants is the basis of the conducted analysis.

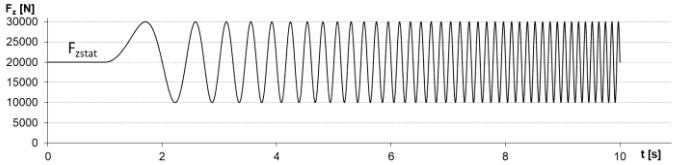

Figure 3. Example course of variations in the wheel normal load (F_z) relative to the static load (F_{zstat})

4. RESEARCH RESULTS AND CONCLUSIONS

The research results are presented as the time-domain characteristics of the lateral reaction force F_y transmitted by the tire, obtained for the wheel model in two variants (without and with relaxation). A sample compilation of the results is shown in figure (Fig. 4).

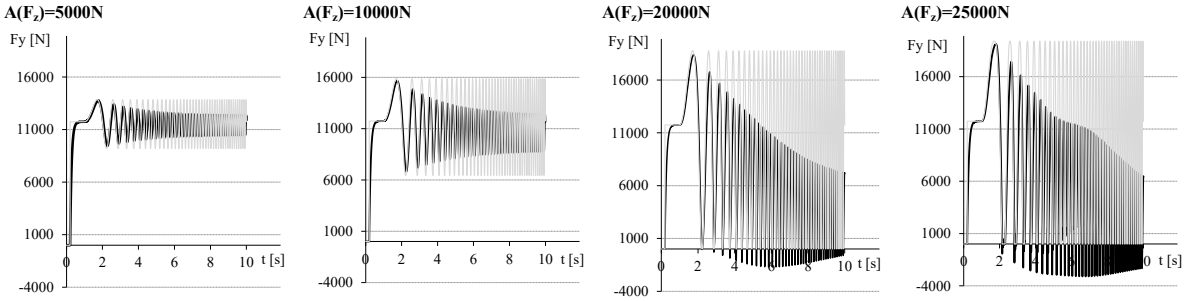

Figure. 4. Sample test results for the increasing amplitude of normal wheel load variations (F_z) (v=30 km/h)

The selected example demonstrates that tire relaxation during cornering under dynamic normal load changes affects:
– a significant reduction in the amplitude of lateral reaction force F_y variations induced by vertical wheel vibrations,
– a decrease in the effective value of the lateral reaction force F_y,
– dynamic phenomena occurring during moments of tire-ground contact loss.

The results, covering wider range of motion conditions and model options, will be presented during the conference. The obtained research results allow for the formulation of conclusions regarding:
– the influence of tire dynamic properties on the available lateral reaction force achieved under dynamic cornering conditions,
– the impact of the applied tire dynamics model on the resulting simulation study outcomes,
– specific dynamic phenomena occurring during wheel cornering, which are exceptionally difficult to identify in experimental settings.

REFERENCES

[1] Takahashi, T., Pacejka, H.B.: Cornering on Uneven Roads. Proc. of 10th IAVSD Symposium, 1987, Supplement to Vehicle System Dynamics, Vol. 17, 1988.
[2] Willumeit H.P., Böhm F.: Wheel Vibrations and Transient Tire Forces, Vehicle System Dynamics Volume 24, Issue 6-7, 1995.
[3] Schieschke R, Hiemenz R.: The relevance of tire dynamics in vehicle simulation. XXIII FISITA Congress, Torino, Italy. May 7-11, 1990.
[4] Rill G.: First order tire dynamics, III European Conference on Computational Mechanics, Solids, Structures and Coupled Problems in Engineering C.A. Mota Soares et.al. (eds., Lisbon, Portugal, 5–8 June 2006.
[5] Ma Y., Lu D., Yin H., Li L., Lv M.,Wang W.: The Unsteady-State Response of Tires to Slip Angle and Vertical Load Variations. Machines 2022, 10, 527. https://doi.org/10.3390/machines10070527.
[6] Dugoff H, Fancher P.S., Segel L.: *An analysis of tire traction properties and their influence on vehicle dynamic performance*, SAE Transactions 700377, vol. 79.
[7] Negrus E. M., Cocosila M.: Flexible Model to Simulate Wheel Pass Over Singular Road Obstacles, Proceedings of the 2nd International Colloquium on Tyre Models for Vehicle Dynamic Analysis (Supplement to Vehicle System Dynamics, Volume 27), held at the Technical University of Berlin, Germany, February 20-21, 1997.
[8] Bandel P. Monguzzi C.: Simulation model of the dynamic behavior of a tire running over an obstacle. Tire Science and Technology: April 1988, Vol. 16, No. 2.

EXPLOITING PASSIVE DYNAMICS FOR STEADY-STATE WALKING ON LEVEL AND INCLINED TERRAIN

Anargyros-Nektarios Skafidas[3], Aikaterini Smyrli [1,2,3], Evangelos Papadopoulos [1,2,3]

[1] HERON - Hellenic Robotics Center of Excellence, Athens, Greece
[2] Robotics Institute, ATHENA Research Center, Marousi, Greece {katerina.smyrli@athenarc.gr; egpapado@athenarc.gr }
[3] School of Mechanical Engineering, National Technical University of Athens, Athens, Greece {askafidas@mail.ntua.gr}

1. INTRODUCTION

In passive dynamic walking, stable and energy-efficient bipedal gait is performed through the exploitation of the inherent dynamics of appropriately designed mechanical systems. However, purely passive bipeds are necessarily restricted to downhill walks, where gravity compensates for impacts and other losses. Extending such motions to level and uphill terrain while preserving the desirable characteristics of passive gait remains a significant challenge. Here, an under-actuated biped robot, designed to rely on and exploit its passive dynamics while in active locomotion, is studied for its ability to generate stable and energy-efficient locomotion on level and positively sloped ground.

2. FROM PASSIVE TO UNDERACTUATED BIPED

The base passive biped [1] has been incrementally augmented with biomechanically-inspired design elements that improve the robustness of its passive gait: a biomimetic footshape is incorporated [2] to facilitate rollover, and a four-bar mechanism is employed at the knees to decrease impact propagation [3]. The base passive biped is shown schematically in Fig. 1(a). Repetitive gait is enabled as potential energy gains balance dissipative losses, whilst gait stability solely depends on the system's mechanical design. It is intuitive that repetitive walking on level or positively inclined terrain cannot be achieved without external energy input. Direct actuation of all joints, as needed in a feedback linearization scheme, is impractical in legged systems. To preserve passive dynamics while in underactuation, a counterweight (CW) link is introduced [4], shown in Fig. 1 (b). This additional link acts similarly to a torso and allows the generation and balancing of the motor torques required to replicate the passive gait.
The model-based Underactuated Virtual Gravity (UVG) controller [4] is utilized to control actively the gait. The UVG computes the gravitational torques experienced by the passive biped during gait on negative sloped terrain and imposes them on the underactuated active biped. The result is an active gait on level ground that emulates the passive gait on a downward slope, called the *passivity angle* of the UVG. In the present study, the walkable domain of the robot is extended to positively inclined terrain through systematic variation of the active biped's walking slope and controller passivity angles.

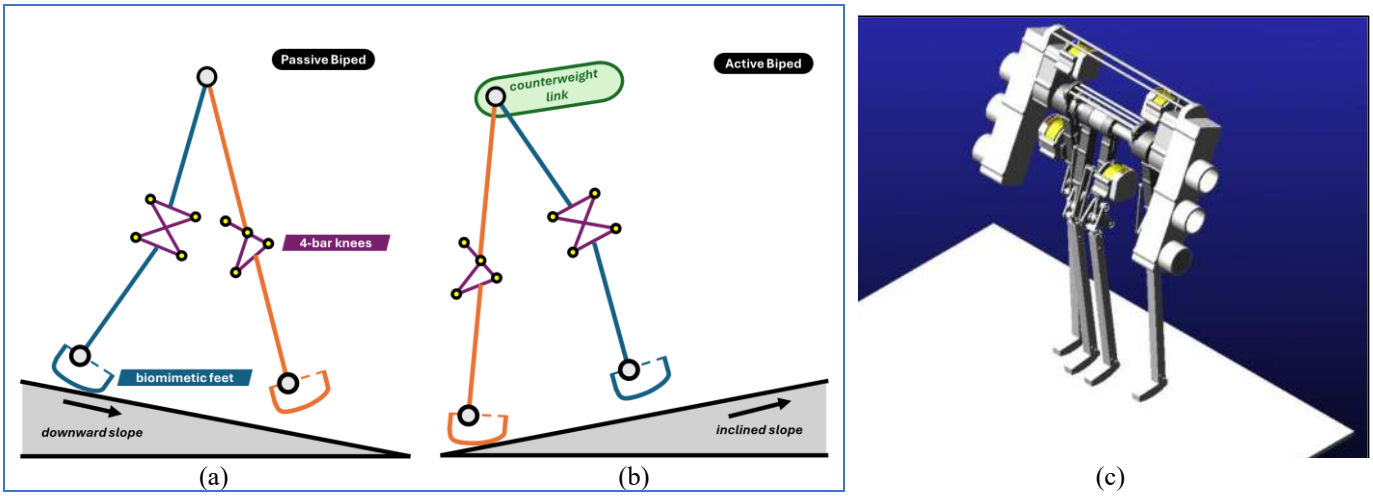

Figure 1. (a) Passive biped model. (b) The resulting active biped model with the addition of a counterweight link ascends an inclined slope. (c) The active biped model simulated in MSC Adams.

3. RESULTS & DISCUSSION

Two independent dynamic models were developed to evaluate the developed biped design: an analytical model implemented in MATLAB and a CAD-based multibody dynamics model constructed in SolidWorks and simulated in MSC Adams. The computationally efficient MATLAB formulation enabled systematic investigation of the system dynamics and controller behavior.

The computationally intensive MSC Adams environment, interfacing with Simulink to implement control feedback, provided a high-fidelity representation of the 3D dynamics and was used for validation.
Stable periodic gaits were obtained for level and uphill terrain across a range of the UVG controller's passivity angles, corresponding to downhill slopes that the UVG controller attempts to emulate. Performance was evaluated using the non-dimensional Cost of Transport (COT), providing a measure of energetic efficiency. In Fig. 2 (a-e), the resulting COT is depicted as a function of the controller's passivity angle for different ground slopes. For level ground, the COT values closely matched those of the corresponding passive downhill gait, which is theoretically equal to the sine of the passive gait's slope angle [4]. As the active ground slope increased, the COT also diverged from the passive prediction, and the range of UVG passivity angles leading to stable locomotion progressively narrowed, reflecting the higher energetic demands of uphill walking.

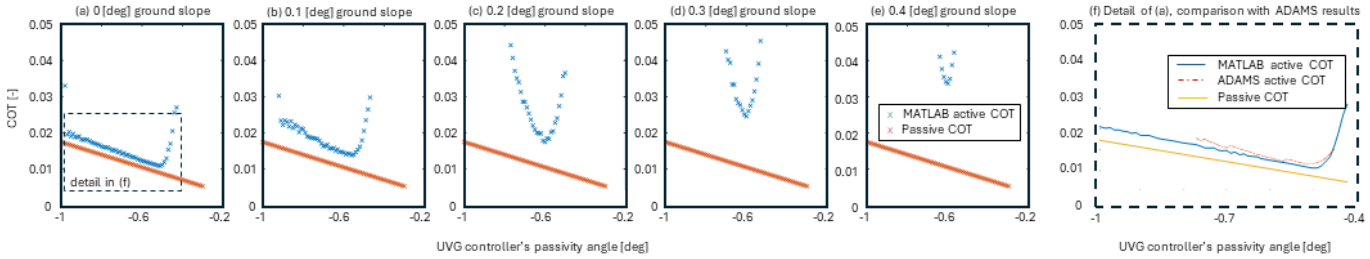

Figure 2. (a-e) COT as a function of the UVG controller's passivity angle for various ground slope configurations (f) Detail of (a), comparison of MATLAB's and MSC Adams active COT as a function of the controller's passivity angle for level ground slope.

Extremely small and large passivity angles produced sharp increases in COT. Notably, the passive biped was originally designed for a nominal slope of −0.6 [deg], and the minimum COT across all active configurations consistently occurred at this emulated passivity angle. This indicates that robustness of the underlying passive template directly translates to its active counterpart.
Finally, Fig. 1(f) presents a comparison between the MATLAB and MSC Adams models for level ground locomotion. Despite the differences in model fidelity, a close quantitative agreement between the predicted COT values is demonstrated. However, a reduction in the range of stable passive angles is observed for the ADAMS, as a result of non-modeled dynamics that are fully simulated in the ADAMS model while absent in MATLAB's analytical simulations and Simulink's UVG controller calculations.

4. CONCLUSION

This work demonstrates the generation of stable active gait for an underactuated biped on level and positively sloped terrain, through the emulation of passive downhill gait by a model-based controller. By introducing a counterweight joint on the biped and by applying the analytical Underactuated Virtual Gravity (UVG) controller, the system preserves the fundamental characteristics of passive dynamic via gravitationally inspired energy injection. The proposed control scheme is validated through comparison between an analytical dynamics model and a multibody co-simulation environment, displaying close agreement between the models as quantified by various results including the non-dimensional Cost of Transport.
Planned next steps of this work will focus in experimental validation. It is necessary that real-world applications of the developed method, and of similar model-informed approaches, must ensure backdrivability in the actuation system, in order to preserve the system dynamics that are exploited by the control and design scheme.
The results of this study highlight the potential of exploiting passive dynamic templates to achieve energy-efficient locomotion beyond descending terrain conditions. Mechanical design of the control system can be manipulated to promote specific desirable passive tendencies, which increase robustness around particular locomotion modes, enabling the efficient emulation of these motions beyond nominal conditions through morphologically-aware model-based controllers such as the UVG.

ACKNOWLEDGMENTS

This project is funded by the European Union under Horizon Europe (grant No. 101136568 - HERON).

Funded by the European Union

REFERENCES

[1] Vasileiou, C., Smyrli, A., Drogosis, A., and Papadopoulos, E., "Development of a passive biped robot digital twin using analysis, experiments, and a multibody simulation environment," *Mechanisms and Machine Theory,* v. 163, September 2021
[2] Smyrli, A. and Papadopoulos, E., "A methodology for the incorporation of arbitrarily-shaped feet in passive bipedal walking dynamics," *IEEE Int. Conf. on Robotics and Automation (ICRA '20)*, Paris, France, May 31-June 4, 2020.
[3] Smyrli, K., and Papadopoulos, E., "Improved biped walking performance around the kinematic singularities of biomimetic four-bar knees," *IEEE/RSJ Int. Conf. on Intelligent Robots and Systems (IROS '22),* Kyoto, Japan, October 23–27, 2022.
[4] Maligianni, D., Valouxis, F., Kantounias, A., Smyrli, A., and Papadopoulos, E., "A Virtual Gravity Controller for Efficient Underactuated Biped Robots," *IEEE Int. Conf. on Robotics and Automation, (ICRA '25),* Atlanta, GA, USA, May 19-23, 2025.

KINEMATIC AND STATIC ANALYSIS OF A CABLE DRIVEN CONTINUUM ROBOT

Akshay Menon[1], Ashitava Ghosal[1]

[1] School of Engineering and Applied Science, Ahmedabad University, Ahmedabad, India
{akshay.m, ashitava.ghosal}@ahduni.edu.in

1. INTRODUCTION

Continuum robots have gained significant attention recently due to their ability to negotiate narrow passages and gaps in unstructured and cluttered environments. This increased dexterity is due to their ability to deform thereby effectively possessing infinite degrees of freedom. In this work, we focus on the kinematics and statics of cable driven continuum robot (CCR) consisting of a flexible backbone to which are attached rigid disks, each of which contain holes through which a cable can pass from the fixed base to the free end. As one or more cables are pulled, thereby applying either displacements or tension, the backbone deforms and the CCR can attain a shape which depends on the amount of actuation and the routing of the cable(s) (Fig. 1(a) & 1(b)). In this work, we study the kinematics and statics of a CCR with four cable actuations which allow the CCR to achieve out of plane motion. In this work we also study the structural aspects of the CCR and obtain stress in the backbone using a finite element software tool. Finally, we present the design of a CCR with a super-elastic nitinol wire as the backbone, discs made of ABS plastics and cable made of stainless steel.

2. MODELING OF CCR

2.1 KINEMATIC MODELING

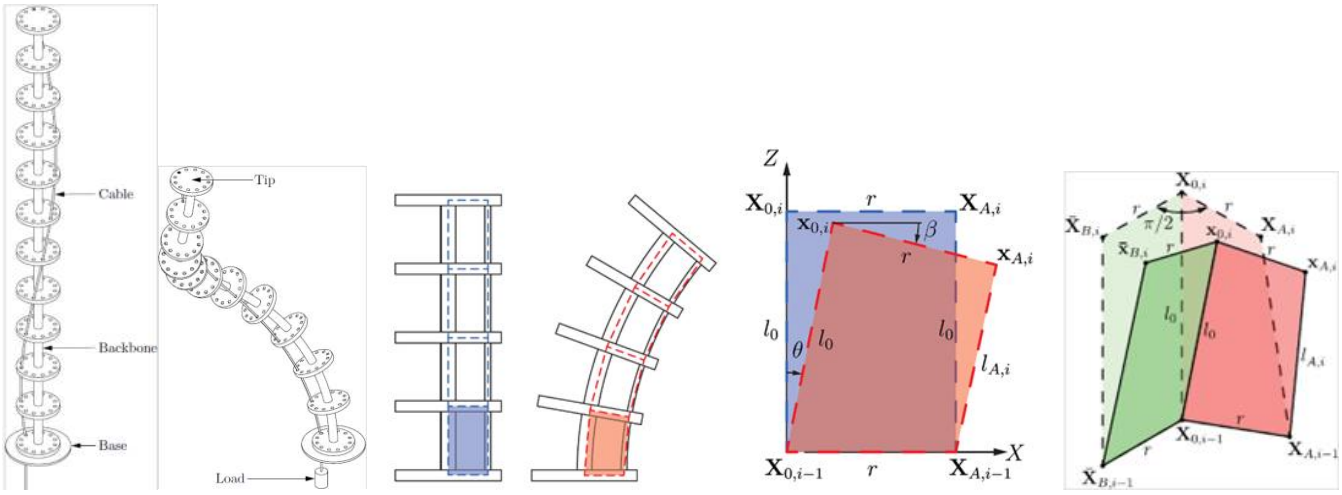

(a) (b) (c) (d) (e) (f)

Figure 1. (a) & (b) Schematics of a CCR with generally routed cable before and after actuation, (c) & (d) Straight routed CCR before and after actuation, (e) Imaginary four-bars before and after actuation superimposed, (f) two 4-bars

Figure 1 (c) & (d) shows a straight routed CCR before and after actuation. As shown in [1], the final shape of the four-bar can be found by minimizing the coupler angle – the angle made by the coupler link and the fixed base (shown as β in Fig. 1 (e)). For two cables at 90 degrees to each other, we consider two four-bars as in Fig. 1 (f), and the optimization can be written as

$$\{\mathbf{x}_i, \mathbf{x}_i^A, \mathbf{x}_i^B\} = \arg\min_{\mathbf{x}_i, \mathbf{x}_i^A, \mathbf{x}_i^B} \left[\left(1 - \frac{(\mathbf{x}_{i-1}^A - \mathbf{x}_{i-1}) \cdot (\mathbf{x}_i^A - \mathbf{x}_i)}{\| \mathbf{x}_{i-1}^A - \mathbf{x}_{i-1} \| \ \| \mathbf{x}_i^A - \mathbf{x}_i \|}\right) + \left(1 - \frac{(\mathbf{x}_{i-1}^B - \mathbf{x}_{i-1}) \cdot (\mathbf{x}_i^B - \mathbf{x}_i)}{\| \mathbf{x}_{i-1}^B - \mathbf{x}_{i-1} \| \ \| \mathbf{x}_i^B - \mathbf{x}_i \|}\right)\right] \quad (1)$$

Subject to

$$\| \mathbf{x}_i - \mathbf{x}_{i-1} \| = l_0, \ \| \mathbf{x}_i^N - \mathbf{x}_{i-1}^N \| = l_{N,i}^{\text{target}}, \| \mathbf{x}_i^N - \mathbf{x}_i \| = r_i, \ (\mathbf{x}_i^A - \mathbf{x}_i) \cdot (\mathbf{x}_i^B - \mathbf{x}_i) = \cos(\theta_{\text{ref}}) r_i^2 \text{ ; where } N \text{ is } A \text{ or } B$$

2.2 STATICS OF CCR

To study the statics of the CCR, a finite element model of the CCR was created in ANYSYS. The boundary conditions were chosen as a) fixed base, b) cable is rigidly attached to the top disk, and a c) force of xx N is applied on the steel wire. To obtain stress and deformation of the CCR, due to the large deformation, non-linear FEM was employed.

3. RESULTS AND DISCUSSION

Equation (1) is solved numerically in MATLAB with initial conditions. Fig. 2 (a) shows the shape of the ccr for a cable pull of 5% in one and 7% in the other. From the figure it can be seen that the ccr, as expected, bends in the *z-x* and *z-y* plane. Fig. 2 (b) shows that when the steel cable in the ccr is pulled by 20mm, it leads to a displacement of the tip of about 50 mm.

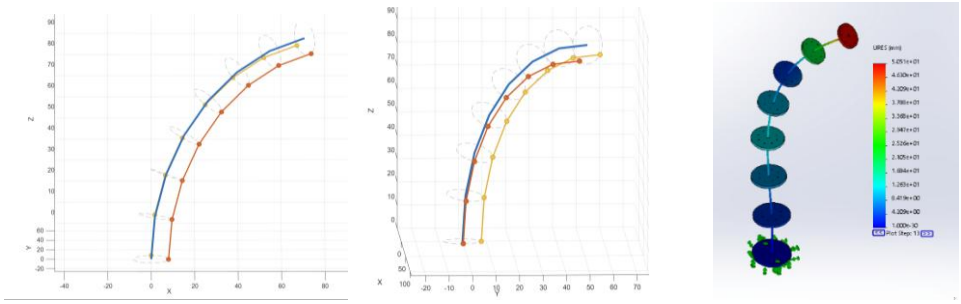

(A) (B)

Figure 2. (A) Kinematics of CCR, (B) Static analysis of CCR

4. DESIGN OF CCR

Based on the kinematic and statics analysis, a prototype has been designed taking into consideration various mechanical, material and manufacturing considerations. The backbone of the CCR was chosen as 1.5 mm diameter of super-elastic Nitinol wire in order to provide the required rigidity-flexibility ratio needed to support the structure. Thin disks of 3 cm diameter, made out of 3-D printed ABS plastic, are placed at regular intervals on the backbone. The diameters of the disks taper towards the top of the gripper finger to provide a tentacle shaped structure. The holes in the disk provide suitable cable routing as well make the CCR lightweight and the actuation is done using 0.4 mm diameter high carbon steel cables. Four cables are organized as two antagonistic pairs to enable the CCR to move in and out of a plane and left or right. Figure 3 below shows the designed CCR.

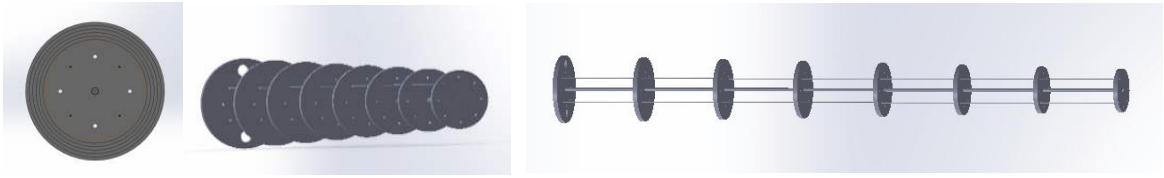

Figure 3. Design of CCR

5. CONCLUSION

In this work, we have presented the kinematic and static analysis of a cable driven continuum robot. The optimization based approach gives reasonably accurate results for the forward kinematics of the CCRs. The static analysis performed using ANSYS shows that the CCR can withstand applied loads and cable pulls. Future plans include fabrication and testing of a light-weight three-fingered gripper, with each finger being a CCR, capable of gripiing uneven objects and manipulating them.

ACKNOWLEDGMENTS

The authors would like to thank Dr. Soumya Kanti Mahapatra. The optimization-based approach is from his Ph D work done at the Robotics and Design Lab at IISc Bangalore.

REFERENCES

[1] Mahapatra, S. K., *Modeling of cable-driven robots and their applications*, Ph D Thesis, Department of Mechanical Engineering, IISc Bangalore, 2024.

DEM-MULTIBODY COUPLING SIMULATIONS OF SPRING TIRES INTERACTING WITH GRANULAR TERRAIN

Kun Wang[1], Qiang Tian[1], Haiyan Hu[1]

[1] Beijing Institute of Technology, No 5 Zhongguancun South Street, Haidian District, Beijing, China, {wangkuner@outlook.com; tianq@bit.edu.cn; haiyan_hu@bit.edu.cn}

1. INTRODUCTION

Future lunar and Martian missions require rover mobility systems that can travel longer distances, operate more continuously, and endure harsher terrain than their predecessors. Conventional metallic wheels, such as those on the Mars Curiosity rover, are lightweight but prone to puncture and fatigue when exposed to abrasive surfaces [1], leading to operational constraints and reduced efficiency. These challenges motivate the development of alternative wheel concepts that combine durability, compliance, and resilience under extreme environmental conditions. The woven spring tire represents a promising non-pneumatic wheel concept for planetary exploration rovers, offering high compliance and damage tolerance. However, the dynamic simulation of such structures poses significant computational challenges due to the geometric nonlinearity of the hundreds of interlaced springs and the topological complexity of thousands of evolving frictional contact interactions. In addition, predicting the interaction between the spring tire and granular terrain is a very costly task. This study proposes a high-fidelity co-simulation framework that couples a non-smooth multibody dynamics (MBD) formulation for the spring tire with a GPU-accelerated discrete element method (DEM) solver for the granular terrain. This approach allows for the efficient handling of the tire's complex geometric constraints and the massive particle counts required to model realistic soil interactions, providing a robust tool for optimizing rover tractive performance.

2. METHODS

The spring tire, constructed from toroidal networks of coiled wires, is modeled as a constrained multibody system [2]. As shown in Fig. 1a, the springs are woven together and clamped to the rigid rim. The constituent springs are modeled using geometrically exact Kirchhoff beam elements, while the complex frictional interactions are formulated through the cone complementarity problem (CCP). The dynamic equations of the spring tires are

$$\begin{cases} \dot{\boldsymbol{q}} = \boldsymbol{T}\boldsymbol{v} \\ \boldsymbol{M}\dot{\boldsymbol{v}} + \boldsymbol{F}_{\text{int}} + \boldsymbol{F}_{\text{cop}} + \boldsymbol{\Phi}_{\boldsymbol{q}}^{\text{T}}\boldsymbol{\lambda}_{\text{b}} - \boldsymbol{D}^{\text{T}}\boldsymbol{\lambda}_{\text{u}} = \boldsymbol{0} \\ \boldsymbol{\Phi}(\boldsymbol{q}, t) = \boldsymbol{0} \\ \boldsymbol{D}\boldsymbol{v} + \boldsymbol{b} \in \mathcal{C}^*,\ \boldsymbol{\lambda}_{\text{u}} \in \mathcal{C},\ \boldsymbol{\lambda}_{\text{u}}(\boldsymbol{D}\boldsymbol{v} + \boldsymbol{b}) = 0 \end{cases}, \tag{1}$$

where $\boldsymbol{q}$ is the vector of generalized coordinates, $\boldsymbol{v}$ is the vector of the generalized velocity, $\boldsymbol{T}$ is the transformation matrix, $\boldsymbol{M}$ is the mass matrix, $\boldsymbol{F}_{\text{int}}$ and $\boldsymbol{F}_{\text{cop}}$ are vectors of internal and coupling forces, $\boldsymbol{\Phi}$ is the vector functions of bilateral constraints, $\boldsymbol{\Phi}_{\boldsymbol{q}}$ is the Jacobi matrix of bilateral constraints with respect to generalized coordinates, $\boldsymbol{\lambda}_{\text{b}}$ is the vector of multipliers associated with bilateral constraints and $\boldsymbol{\lambda}_{\text{u}}$ is the vector representing the contact forces. $\mathcal{C}$ is a cone space and $\mathcal{C}^*$ is its dual space. The dynamic equations of the spring tire are solved using the generalized-α method embedding a CCP solver. The CCP solver is developed by using the alternating direction method of multipliers (ADMM) [3].

To simulate the granular terrain with sufficient resolution, the DEM is implemented on a graphics processing unit (GPU) using the CUDA architecture. The terrain is modeled as a collection of millions of spherical particles interacting via Hertz-Mindlin contact laws. The dynamics of particles are governed by Newton-Euler equations formulated in the body-frame:

$$\begin{cases} m_i \boldsymbol{a}_i = \boldsymbol{f}_i \\ J_i \dot{\boldsymbol{\omega}}_i = \boldsymbol{m}_i \end{cases}, \tag{2}$$

where m_i is the mass of particle i and J_i is the mass moment of inertia, $\boldsymbol{a}_i$ is the vector acceleration of the mass center, $\boldsymbol{\omega}_i$ is the vector of angular velocity, $\boldsymbol{f}_i$ and $\boldsymbol{m}_i$ are vectors of total force and torques acted on the particle i. To detect

contact between massive particles, a uniform spatial hash grid-based neighbor search algorithm is implemented for broad phase contact detection.

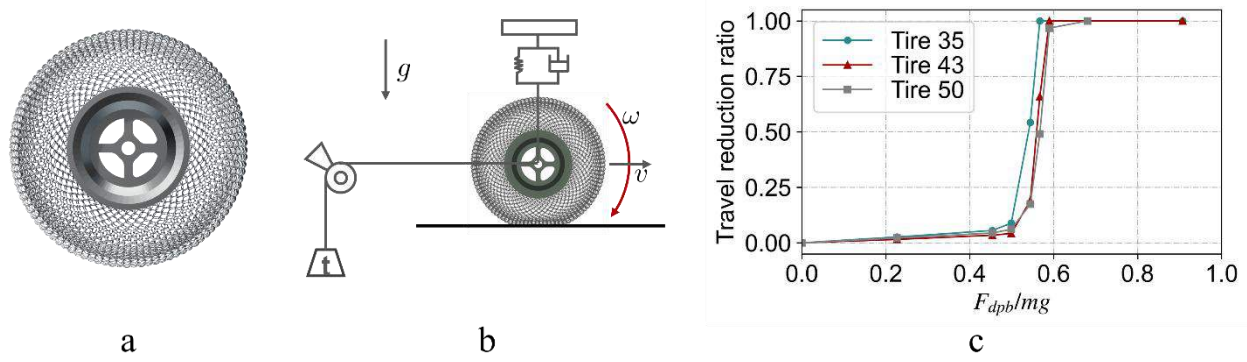

Figure 1. a The spring tire model. b Drawbar pull force test. c Travel reduction of three spring tires.

The co-simulation is established through a weak coupling strategy between the MBD solver and the DEM solver [4]. At the beginning of each step, the MBD solver exports the position, orientation, and velocity of the tire's boundary elements (rim and spring components) to the DEM solver. The DEM solver computes the contact forces exerted by the granular particles on the tire geometry. These forces are aggregated and transferred back to the MBD solver as external wrenches applied to the relevant bodies.

3. RESULTS

The co-simulation framework was validated through a series of tests focusing on key performance metrics for planetary rovers, specifically drawbar pull (Fig. 1b), sinkage, and general mobility on granular terrain. The comparative tractive ability of three distinct tire configurations is depicted in Fig. 1c, demonstrating the model's capability to predict traction under load. Additional comprehensive results detailing the impact of varying tire structural parameters and terrain properties will be presented in the final presentation.

4. CONCLUSIONS

This study presents a robust numerical framework for analyzing the performance of non-pneumatic spring tires on granular terrain. By coupling non-smooth multibody dynamics with GPU-based discrete element methods, the proposed framework provides a valuable tool for the design and optimization of future planetary rover wheels, allowing for extensive parameter sweeps of spring stiffness and tread geometry without the cost of physical prototyping. Future work will focus on extending the tire model to include shape memory effect of internal wire elements and introducing irregularly shaped particles in the DEM solver to better mimic the interlocking behavior of sharp dust.

ACKNOWLEDGMENTS

The authors greatly acknowledge the support by the National Natural Science Foundation of China under grants 12125201, 12402040 and 12494561.

REFERENCES

[1] A. Rankin, N. Patel, E. Graser, et al, "Assessing Mars Curiosity Rover Wheel Damage", *IEEE Aerospace Conference (AERO)*, Big Sky, MT, USA, March 5-12, 2022.

[2] K. Wang, Q. Tian, "Dynamic simulation of frictional contact between slender beams via cone complementarity formulations", *Computational Mechanics*, 2025.

[3] A. Tasora, D. Mangoni, S. Benatti, et al., "Solving variational inequalities and cone complementarity problems in nonsmooth dynamics using the alternating direction method of multipliers", *International Journal for Numerical Methods in Engineering*, 122, 4093–4113, 2021.

[4] G. Sanborn, J. Choi, J.H. Choi, "Strategy for co-simulation of multi-flexible-body dynamics and the discrete element method", *Journal of Mechanical Science and Technology*, 35, 4363–4380, 2021.

MMT Symposium
60th Anniversary of Mechanism and Machine Theory
June 21-23, 2026 Porto, Portugal

RECONFIGURATION-ENABLED WORKSPACE RESHAPING AND MOTION PLANNING FOR A LEGGED LANDER

Ziyue Li[1], Weizhong Guo[1,*]

[1] State Key Laboratory of Mechanical System and Vibration, School of Mechanical Engineering, Shanghai Jiao Tong University, Shanghai 200240, China, {lwhylzy@sjtu.edu.cn; wzguo@sjtu.edu.cn}

1. INTRODUCTION

Prior studies have treated configuration selection as an additional planning dimension for motion planning of reconfigurable robots [1]. In contrast, this work embeds reconfiguration into the motion-planning loop, enabling configuration regulation and motion decision-making to be co-optimized within a unified closed loop to improve feasibility and maneuverability. A legged reconfigurable lander integrates landing, adjusting, and roving, and its reconfigurability allows mode switching among landing–adjusting–roving [2]. In the roving mode, the usable workspace of an individual leg is limited due to constraints imposed by the parallel-leg configuration and load-bearing capacity, which undermines adaptability over complex terrain. To address this issue, we propose a motion planning approach for reconfigurable landers that performs workspace shaping via configuration adjustment, thereby enhancing traversability and robustness in challenging environments.

2. METHODS AND RESULTS

2.1. Reconfiguration-enabled workspace reshaping

To address the issue that, in the roving mode of a legged reconfigurable lander, the single-leg workspace is constrained and constraint violations are readily triggered by a bottleneck leg, this study treats reconfigurability as a capability-regulation mechanism embedded within the motion-planning loop. Specifically, by adjusting configuration parameters (e.g., clutch phases and/or configuration states), the shape of the single-leg workspace and the distribution of available motion margin can be altered. On this basis, we propose the concept of workspace reshaping: under given task requirements and environmental constraints, a configuration is preferentially selected to enhance reachability and margin along task-critical directions while mitigating the bottleneck-leg effect. This allows subsequent gait and body-motion planning to operate within a more favorable capability boundary, rather than being forced into shortened steps or overly conservative strategies under a fixed configuration. The reshaping process can be triggered and updated on demand during execution to accommodate feasibility variations caused by ground-contact disturbances, terrain changes, or leg capability degradation. Fig.1 presents a representative workspace-reshaping example, and Fig.2(b) reports the scores of reconfiguration parameters in workspace reshaping.

2.2. Reconfiguration-based motion planning method

This study incorporates reconfiguration capability as an internal decision variable in gait planning rather than an external preprocessing step, allowing configuration adjustment to coordinate with gait parameters and foothold selection within a unified planning loop. This co-design improves reachability margin along task-critical directions and enhances multi-step continuous feasibility. Fig.2(a) illustrates the flowchart of the proposed reconfiguration-based motion planning framework. First, environmental and state information are used to evaluate each leg's available motion margin and potential bottleneck constraints, thereby identifying the margin requirements associated with the "constrained leg" and the "critical direction." A configuration update is triggered on demand to reshape the single-leg workspace, providing a more favorable reachability boundary for subsequent step-length determination and foothold selection. On this basis, gait planning jointly determines the swing leg, step length, and foothold location within the reshaped workspace, while infeasible candidates are eliminated by enforcing stability and reachability constraints. The resulting reconfiguration–gait coupling mechanism can be updated in closed loop during execution, enabling the lander to maintain improved traversability and robustness under complex terrain, asymmetric capabilities, or weak-leg constraints.

2.3. NURBS-based smooth trajectory generation

Given that the single-leg workspace of the lander's parallel-leg mechanism is highly limited, even after reconfiguration-driven workspace reshaping, planning must still make full use of the remaining motion resources. Accordingly, this study proposes a NURBS-based foot trajectory planning method. By constructing a convex envelope of the terrain, the proposed approach

generates trajectories that remain as close as possible to obstacle surfaces while maintaining trajectory smoothness. The method reliably converts the discrete outputs of gait planning into executable motions, and improves traversability and robustness in complex environments under reachability and safety constraints.

3. CONCLUSION

Overall, the innovations of this study can be summarized in three aspects. Firstly, reconfiguration is elevated from an "external configuration selection" step to an internal capability-regulation mechanism within motion planning, such that configuration regulation and motion decision-making are co-optimized in the same closed loop to improve feasibility and maneuverability. Secondly, configuration reconfiguration is directly mapped to a controllable reshaping of the single-leg reachable set, providing the planner with increased motion margin along task-critical directions and thereby alleviating workspace tightness caused by the parallel-leg configuration and load-bearing constraints. Thirdly, we propose a NURBS-based foot trajectory generation method for complex terrain, which constructs foot-end trajectories close to obstacle boundaries via a terrain convex-envelope representation, offering effective support for robust locomotion of workspace-limited legged robots in challenging environments.

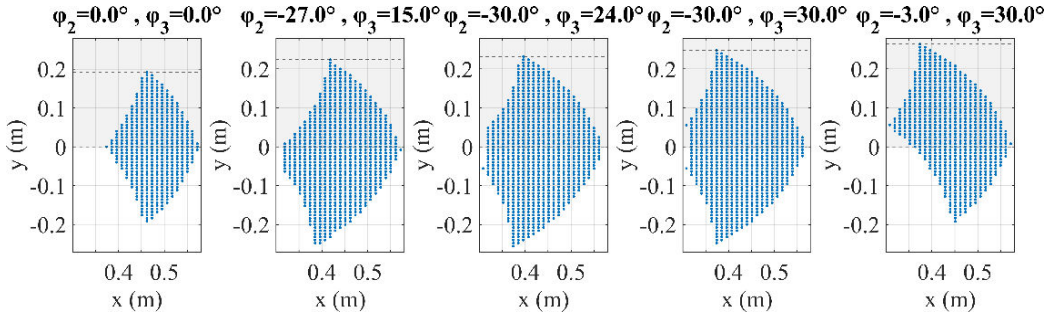

Figure 1. Workspace reshaping (critical cross-section).

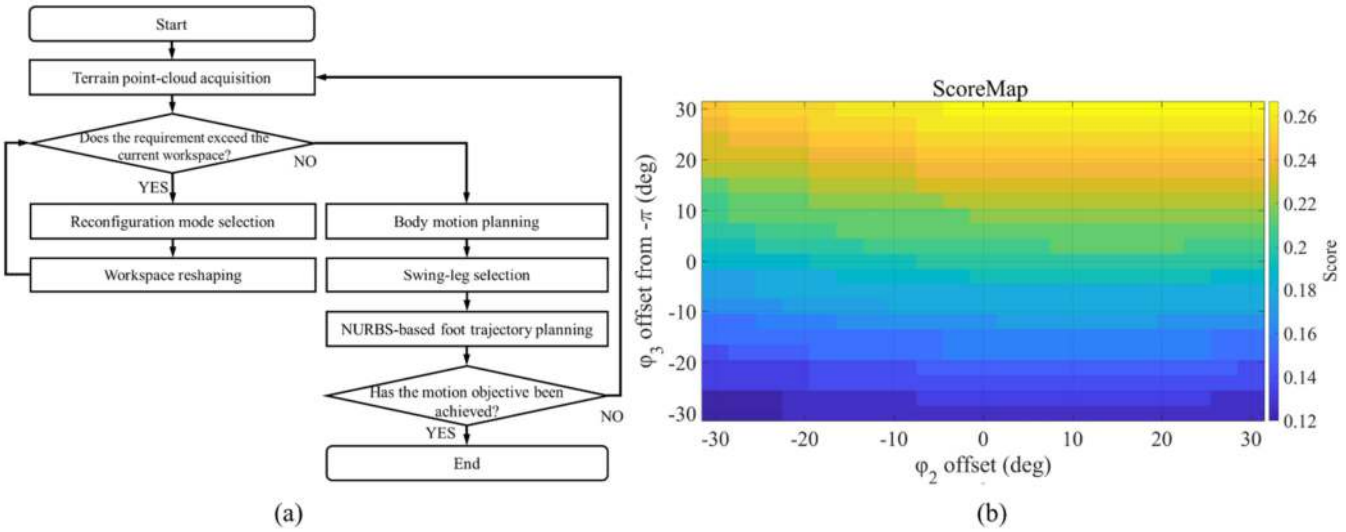

Figure 2. Reconfiguration-based motion planning method (a) Flowchart. (b) Workspace reshaping optimization.

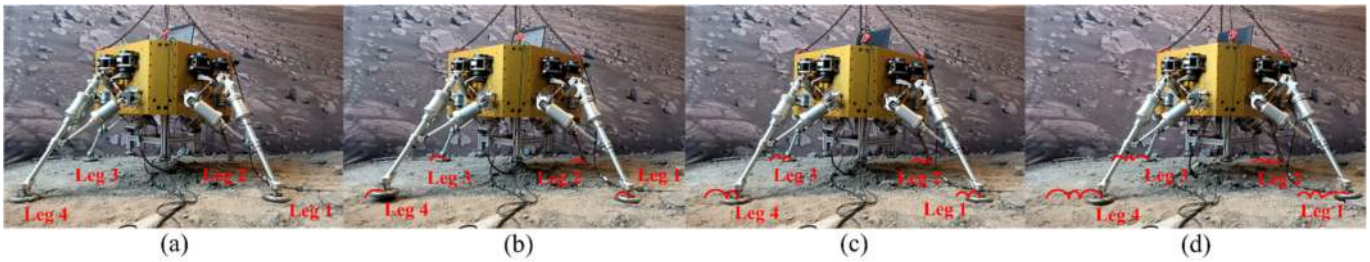

Figure 3. Motion planning experiments for a legged reconfigurable lander.

REFERENCES

[1] J. Daudelin,G. Jing, T. Tosun, et al., "An integrated system for perception-driven autonomy with modular robots". *Science Robotics*, 23(3), 2018.

[2] Y. Han, W. Guo, C. Zhao, et al., "Structural synthesis of the reconfigurable legged mobile lander for strong geometry-physical interaction with extraterrestrial environment". *Mechanism and Machine Theory*, 189, 2023,105446.

MODELING AND CONTROL-ORIENTED SIMULATION OF DBD PLASMA ACTUATORS FOR AERODYNAMIC PERFORMANCE ENHANCEMENT

Raul A. Bernal-Orozco[1], Oliver M. Huerta-Chavez[1], Genaro Carreon-Carrera[1]

[1] Instituto Politécnico Nacional, SEPI ESIME Ticoman, Mexico, {rbenalo@ipn.mx, ohuertac@ipn.mx, gcarreonc@ipn.mx}

1 INTRODUCTION

Dielectric Barrier Discharge (DBD) plasma actuators have attracted considerable attention for active flow control and flow manipulation applications due to their fast response, low power consumption, and absence of moving components [1, 3, 4]. These characteristics make them attractive for integration into closed-loop aerodynamic control systems.

DBD actuators generate an electrohydrodynamic (EHD) body force that modifies near-wall flow structures, enabling separation control, lift enhancement, and drag reduction. From a systems engineering perspective, plasma actuators can be regarded as solid-state control devices capable of interacting with fluid-dynamic systems in real time.

Despite extensive experimental research, the numerical modeling of plasma–flow interaction remains challenging due to its multiscale and multiphysics nature [3, 4]. Reliable reduced-order and phenomenological models are therefore essential for the development of control-oriented simulation frameworks.

In this work, a calibrated numerical framework recently developed by the authors [5] is employed to investigate the effectiveness of DBD plasma actuators in controlling flow separation over a NACA 0015 airfoil operating near stall conditions. The objective is to provide a predictive modeling tool suitable for aerodynamic control design and system-level optimization.

2 NUMERICAL METHODOLOGY

The flow field is simulated by solving the incompressible Reynolds-averaged Navier–Stokes equations using a finite-volume solver. Turbulence effects are modeled with the k–ω SST model due to its robustness in adverse pressure gradient flows.

The plasma actuator is represented using a modified Suzen–Huang phenomenological model [2]. The electric potential and charge density are obtained from coupled Poisson equations, and the resulting EHD body force is incorporated as a momentum source term. A semi-empirical calibration based on thrust measurements is applied to improve quantitative accuracy.

An independent-domain technique is employed to decouple the plasma and fluid solvers, allowing independent mesh refinement while preserving physical consistency. This modular structure facilitates future integration with control algorithms and reduced-order models for real-time applications.

Simulations are conducted for a NACA 0015 airfoil with a chord length of 0.2 m at a Reynolds number of 2.5×10^5 and an angle of attack of 14°. A DBD actuator is located at $x/c = 0.1$ on the suction side and operates at an applied voltage of 18 kVpp and an AC frequency of 2 kHz.

3 RESULTS AND DISCUSSION

Figure 1 presents the pressure and skin-friction coefficient distributions for baseline and actuated configurations. The baseline case exhibits an early pressure recovery and low skin-friction values, indicating extensive flow separation.

Under plasma actuation, the minimum pressure coefficient decreases from approximately -2 to -5, reflecting enhanced suction and improved aerodynamic loading. The skin-friction coefficient increases by nearly 40%, revealing a re-energized boundary layer and delayed separation.

Velocity field visualizations, shown in Fig. 2, confirm that plasma actuation substantially reduces the separated region and promotes flow reattachment near the trailing edge. The wake structure becomes more coherent and narrower compared to the baseline case.

These results demonstrate that the calibrated plasma model is capable of capturing the main features of plasma-induced flow control and its interaction with turbulent separated flows.

These improvements demonstrate the effectiveness of plasma actuation as an active control mechanism capable of modifying the dynamic behavior of separated flows.

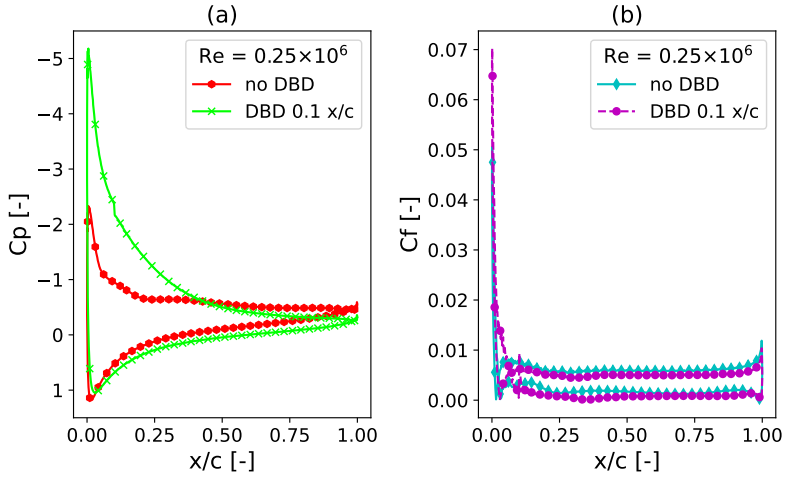

Figure 1: Pressure and skin-friction coefficients along the airfoil surface with and without DBD actuation.

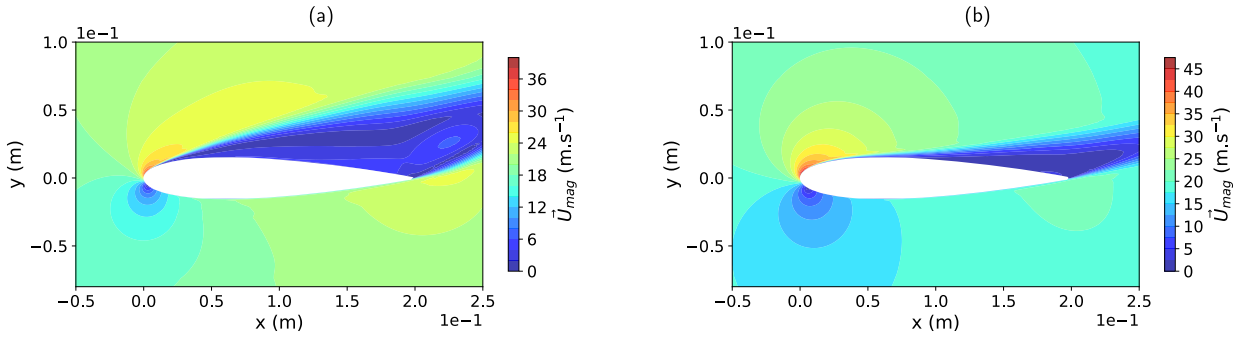

Figure 2: Velocity field around the airfoil at $\alpha = 14°$: (a) baseline case and (b) DBD actuated case.

4 CONCLUSIONS

A numerical investigation of DBD plasma actuators applied to a NACA 0015 airfoil operating near stall conditions has been presented. A modified Suzen–Huang model combined with an independent-domain technique was employed to represent plasma effects [5].

The results indicate that plasma actuation significantly enhances boundary layer momentum, delays flow separation, and improves aerodynamic loading. From a systems perspective, the actuator behaves as an effective solid-state flow control device capable of modifying the dynamic response of the airfoil.

The proposed modeling framework provides a reliable and computationally efficient tool for the analysis, design, and optimization of plasma-based aerodynamic control systems. The modular structure also enables future extensions toward closed-loop control and mechatronic integration.

REFERENCES

[1] T. C. Corke, C. L. Enloe, and S. P. Wilkinson, "Dielectric barrier discharge plasma actuators for flow control," *Annual Review of Fluid Mechanics*, vol. 42, no. 1, pp. 505–529, 2010.

[2] Y. Suzen, G. Huang, and D. Ashpis, "Numerical simulations of flow separation control in low-pressure turbines using plasma actuators," in *Proc. 45th AIAA Aerospace Sciences Meeting and Exhibit*, Reno, NV, USA, 2007, Paper AIAA-2007-937. doi: 10.2514/6.2007-937.

[3] J. Kriegseis, B. Simon, and S. Grundmann, "Towards in-flight applications? A review on dielectric barrier discharge-based boundary-layer control," *Applied Mechanics Reviews*, vol. 68, no. 2, p. 020802, 2016.

[4] K. V. Karthikeyan and R. Harish, "Advancements in flow control using plasma actuators: A comprehensive review," *Engineering Research Express*, vol. 7, no. 1, p. 012502, 2025.3.

[5] R. A. Bernal-Orozco, I. Carvajal-Mariscal, O. M. Huerta-Chavez, and G. Guevara-Morales, "Solver for phenomenological modeling of a DBD using an independent domain technique," *Journal of Aerospace Engineering*, 2025.

MODELING BALL RECIRCULATION IN MULTIBODY BALL SCREW DRIVES

Antonio Carlo Bertolino[1], Roberto Guida[1], Andrea De Martin[1], Massimo Sorli[1]

[1] Politecnico di Torino, Corso Duca degli Abruzzi 24, Turin, Italy, {antonio.bertolino@polito.it; roberto.guida@polito.it; andrea.demartin@polito.it; massimo.sorli@polito.it}

1. INTRODUCTION

Ball screw drives are widely employed in high-precision and high-dynamic machine tools due to their high efficiency, load capacity, and positioning accuracy. Their mechanical behavior is governed by the rolling contact between balls and raceways in the screw-nut pair, which determines load distribution, stiffness, friction, vibration, and positioning accuracy. As a consequence, a large part of literature has concentrated on the static, quasi-static, and dynamic modeling of ball screw feed drives and related rolling kinematic joints [1]. Most existing literature models focus on the load-bearing region of the screw-nut interface, where the balls transmit force through Hertzian contact along an helical path. In this context, several studies have addressed various nonlinear stiffness, load distribution, and time-dependent contact effects, including the influence of ball passage and transient loading at the entry and exit of the loaded zone [2]. However, comprehensive reviews highlight that the recirculation system of the ball screw is often neglected or treated in a highly simplified manner in both static and dynamic formulations, not guaranteeing continuity of motion or force evolution [1]. The recirculation of balls introduces a distinct kinematic and dynamic regime, in which the balls transition from a loaded state in the helical raceway to an unloaded state in the return channel and back into the load zone. Usually, in literature this transient phase is described primarily in terms of quasi-static geometry and local impact phenomena, emphasizing the role of impact forces, vibration excitation, and resonance conditions [3]. These approaches successfully identify critical design parameters of the transition zone and return device but remain limited to localized force models and are not suitable to be included in multibody dynamic models. More recent dynamic models include time-dependent contact forces associated with the variation in the number of load-carrying balls during the transition phase [2]. While these formulations capture important excitation mechanisms related to ball passage, they typically rely on reduced-order representations and are not able to enforce continuity of kinematic and dynamic state variables throughout the entire recirculation path. Experimental and numerical investigations further show that imperfections in the return device can significantly affect vibration and dynamic response, highlighting the importance of complete and accurate recirculation modeling in high-speed and high-precision applications of ball screw mechanisms [4]. From a multibody modeling perspective, the recirculation process poses specific challenges, especially if a full three-dimensional description of the mechanism is adopted: the balls undergo changes in their multidirectional contact conditions, constraint topology, and reference frames as they move between the helical groove and the return channel. Ensuring a physically consistent and continuous description of ball motion across these regions is essential to avoid artificial state resets and nonphysical force discontinuities. Although physically detailed multibody formulations of ball screw contact have been developed for the load-bearing region [5], the extension of such models to include ball recirculation in a unified framework remains limited. In this work, a physics-based approach for modeling ball recirculation in multibody ball screw systems is presented. The proposed formulation enables a continuous description of ball motion along the entire circulation loop, including the transition between loaded and unloaded regions, while preserving kinematic and dynamic consistency. The model is conceived to integrate naturally with multibody formulations and vectorized implementations, allowing the simultaneous treatment of multiple balls without specific assumptions.

2. MATERIALS AND METHODS

The proposed multibody formulation is structured as a modular architecture in which bodies' dynamics, contact mechanics, and geometric tracking are consistently integrated, as schematically illustrated in Fig. 1. The model is mainly composed of three primary dynamic subsystems, each describing the full three-dimensional dynamic motion of the screw, the nut, and the set of recirculating spheres through their own equations of motion. The obtained kinematic states are then fed into dedicated contact models, which govern the interactions between the different bodies. No kinematic constraint is imposed a priori on the motion of any entity: the motion of each sphere is entirely physics-based, and its motion through the closed loop path is regulated by the contacts with the raceways of the screw and nut and with the recirculation tube. Since a gothic arch profile is assumed for both the screw shaft and nut raceways, each sphere can have up to four concurrent contact points. The location of each contact point is identified by deriving the relative position of the center of the sphere with respect to the raceway profile. The latter is considered as a continuous surface based on the ball screw geometrical parameters. The location of the candidate contact point, which is the closest point to the ball surface identified by the common normal vector in each time step, is a function of the sphere's helical

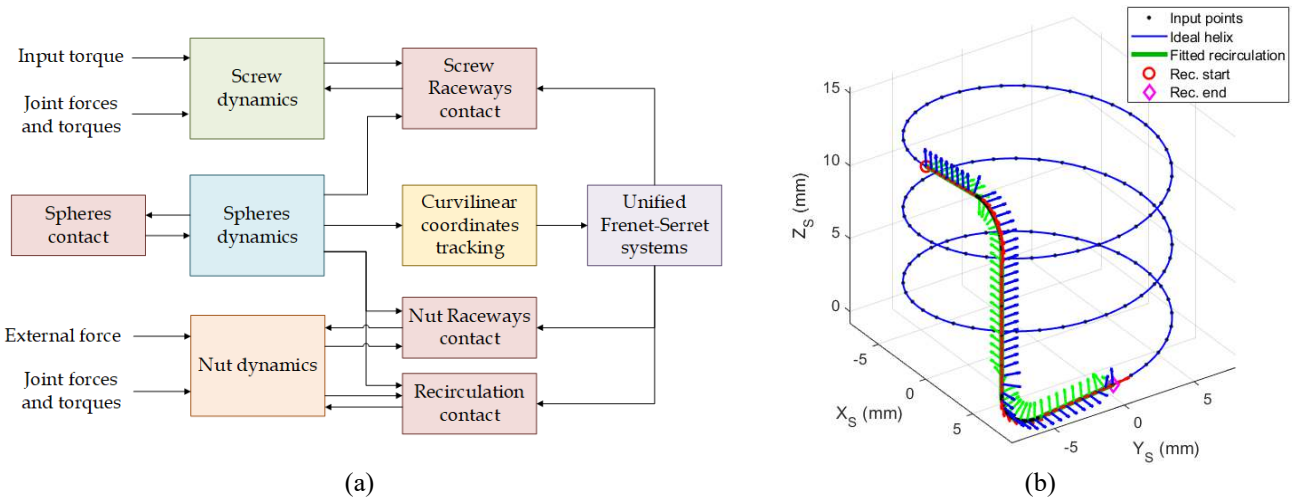

Figure 1. Mathematical dynamic model structure (a) and recirculation path representation (b).

coordinate, which uniquely identify the reference Frenet-Serret frame located on the ideal helix such that the local section plane contains the center of the sphere. In the literature approach [5], the location of the Frenet-Serret frame is identified by the azimuth angle leading to unprecise estimation of the real Frenet-Serret frame and to the unfeasibility of describing location for the Frenet-Serret frame different from the prescribed ideal helix. A key element of the proposed formulation is the adoption of a unified geometric layer based on curvilinear coordinates defined along the ball trajectory. In such a way, a consistent Frenet-Serret reference system is constructed over the entire circulation loop, including the recirculating part. In this work, a simple shape for the recirculating element is considered, shown in Fig. 1b, composed of three linear segments alternated with two circular arches. Starting from the spatial points, a constrained open-uniform polynomial B-spline curve of degree p, determined via equality-constrained and penalized least-squares fitting in $\mathbb{R}^3$ has been used to continuously represent the recirculation path, providing a continuous parametrization of position, orientation, and local contact frames without discontinuities in the transition points between the ideal helix equation and the spline in terms of position and derivatives. In the rectilinear portions of the recirculation, a Bishop frame has been exploited to avoid fast switching in the Frenet-Serret torsion due to small numerical noise. This approach enables a continuous tracking of each sphere through the helical groove and the recirculation path, avoiding artificial constraint switching or discontinuous reinitialization of states. All the bodies are considered rigid, hence the non-compenetrating condition is enforced by a Hertzian-based penalty regularizing normal force in the contact points. If a contact occurs, the relative speed of the two mating surfaces is used to calculate the friction forces according to the Stribeck curve, characteristic of lubricated contacts. To avoid numerical instability and unphysical behavior, the coefficient of friction is smoothly set to zero in a narrow region close to the null speed condition. This approach inherently takes into account the effect of the clearance between the spheres and the raceways, allowing at the same time different operative conditions to be analyzed, such as the case in which a preload is applied by means of oversized spheres. The same contact model is applied also between adjacent spheres.

3. CONCLUSIONS

The proposed formulation provides a unified and fully three-dimensional multibody representation of ball motion over the complete screw-nut-recirculation circuit, ensuring continuity of kinematics, contact states, and force evolution. By combining physics-based contact modeling with a continuous curvilinear geometric description of the closed loop path, the approach overcomes the limitations of reduced-order and event-based recirculation models. The resulting framework enables consistent and realistic investigation of ball screw dynamic behavior under different operating conditions.

ACKNOWLEDGEMENTS

This work was realized within the project PRIN2022 [1265/2023] "Multi-phase fault tolerant MW range generation systems for hybrid-electric aircrafts" funded by the Italian Ministry of University and Research (MIUR).

REFERENCES

[1] C. Li, M. Xu, W. Song, H. Zhang, A review of static and dynamic analysis of ball screw feed drives, recirculating linear guideway, and ball screw, Int. J. Mach. Tools Manuf. 188 (2023) 104021.
[2] M. Xu, H. Zhang, Z. Liu, C. Li, Y. Zhang, Y. Mu, C. Hou, A time-dependent dynamic model for ball passage vibration analysis of recirculation ball screw mechanism, Mech. Syst. Signal Process. 157 (2021) 107632.
[3] J.Z. Sobolewski, Vibration of the ball screw drive, Eng. Fail. Anal. 24 (2012) 1–8.
[4] W. Ma, C. Zhou, Y. Liang, J. Xie, J. Shen, W. Li, C. Yu, W. Shen, H. Feng, Dynamic modeling and vibration analysis of ball recirculation system considering return device assembly error, Mech. Syst. Signal Process. 242 (2026) 113649.
[5] A.C. Bertolino, G. Jacazio, S. Mauro, M. Sorli, Developing of a Simscape Multibody Contact Library for Gothic Arc Ball Screws: A Three-Dimensional Model for Internal Sphere/Grooves Interactions, in: ASME (Ed.), IMECE2019 Volume 4: Dynamics, Vibration, and Control, American Society of Mechanical Engineers, Salt Lake City, UT, USA, 2019: pp. 1–8. https://doi.org/10.1115/IMECE2019-10709.

MODAL ANALYSIS OF ENGINES AND POWERTRAINS WITH AVL EXCITE™: AN OVERVIEW

Tigran Parikyan[1,2]

[1] Center for Research and Education in Mechanisms and Machines (CREMM), Kalsdorf/Graz, Austria, t.parikyan@cremm.eu
[2] Advanced Simulation Technologies, AVL List GmbH, Graz, Austria, tigran.parikyan@avl.com

1. INTRODUCTION

Rapid development of high-quality engines and powertrains for modern vehicles, gensets and stationary electromechanical drives cannot be achieved without using efficient engineering tools.
A software suite called AVL EXCITE™ [1] is designed to simulate multibody dynamics (MBD), NVH, efficiency and durability of powertrains based either on internal combustion engines (ICE) or electric drive units (EDU), or on both of them. Besides calculating and visualizing the full dynamic forced response, it can perform several types of modal analysis (MA) that are especially useful in the early phase of powertrain simulation projects – to verify the components and predict their dynamic behavior within the multi-body system (MBS) of engine or powertrain.

2. DYNAMIC MODELS OF ENGINE PARTS AND POWERTRAIN SUB-SYSTEMS USED IN MODAL ANALYSIS

To generate dynamic models of engine parts having complex shape, like e.g. crankshafts, finite element (FE) method is used. Although one can perform modal analysis on full volumetric FE model using specialized FE analysis software, such a calculation takes relatively long because of a large number of degrees of freedom (DOF) and is therefore not used frequently.
To overcome this drawback affecting both MA and dynamic force response, order reduction of the FE model of each engine part is performed, either through *condensation* of the volumetric FE model or by generating a *structured FE model* representing a generalization of bar-mass (or beam-mass) model [2]. Despite having a smaller number of DOFs, reduced models approximate the dynamic properties of the full volumetric FE models with an accuracy sufficient to perform engineering calculations.
Additionally, to be time efficient in the early phase of engine or powertrain simulation, it is essential to use well justified simplifications when modeling MBS [3]. Following that approach, a) elastic block of the resiliently mounted engine can be considered rigid in the low-frequency range [4], or b) to focus on torsional vibrations of crankshaft or transmission, their models can be reduced to a single rotational dimension only [5, 6].

3. MODAL ANALYSIS TYPES AND PURPOSES

3.1. Types of modal analysis and areas of their application

For weakly damped metallic engine parts, performing *undamped* modal analysis gives sufficiently accurate results. Having elements with high viscous or structural damping can significantly influence both the frequency spectrum and mode shapes, therefore performing *damped* modal analysis of strongly damped engine parts (like crankshafts with torsional vibration dampers, or engines with rubber mounts) is more appropriate in those cases. For fast rotating shafts and rotors, spin effects becoming more pronounced under higher rotation speeds are captured by *gyroscopic* modal analysis. Damped MA and gyroscopic MA together are often referred to as *complex* modal analysis [7].

3.2. Verification of modal characteristics of separate engine parts

Free (or “free-free”) modal analysis of separate engine parts is used to determine their intrinsic dynamic properties, i.e. the spectra of natural frequencies and corresponding mode shapes. Thus, undamped free MA is used to verify the modal behavior of a) structured FE models of free crankshaft [2] and b) piston rings [8].

3.3. Consideration of boundary conditions

While being suitable for verification purposes (e.g., structured FE model vs full volumetric FE model), free MA cannot be used to determine the critical speeds or to predict the resonances of MBS. For these purposes, *supported* modal analysis is used taking the influence of radial stiffness in main bearings and effective masses of pistons and conrods into account [3].

3.4. Parameter study and optimization

Performing gyroscopic MA with parameter variation, one can select optimal range of values of radial stiffness of bearings of pump shaft for a resonance-free operation of stationary electromechanical drive [6].

3.5. Selection of modes used in condensation of volumetric FE models of engine parts

To generate numerically efficient dynamic FE models of transmission or whole powertrain, a set of representative dynamic modes is selected to be used in process of condensation of these FE structures [9, 10].

4. MODAL ANALYSIS VS DYNAMIC FORCED RESPONSE

As a result of modal analysis of different MBS's, critical speeds diagram indicates the engine speeds of potential resonances [3, 7]. Comparing the results of MA with those of dynamic forced response shows which of these potential resonances become the real ones. Here are some real-life industrial application examples: a) for a resiliently mounted engine with linearized model of engine mounts, the dynamic forced response performed in frequency domain showed a good agreement with resonance predicted by damped MA [4]; b) for a turbocharger rotor supported in bearings, gyroscopic MA delivered results matching with those of dynamic analysis [11]; c) results of NVH simulation of EDU performed in frequency-domain shows acoustic behavior similar to that predicted by its modal analysis (Fig. 1) [10].

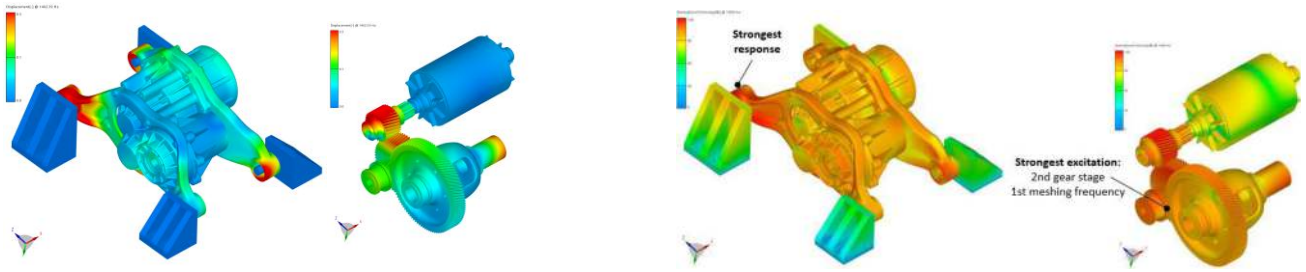

Figure 1. Results of modal analysis of EDU at e-motor speed of 6000 rpm: mode corresponding to 1462 Hz (left) compared to the normal velocity levels as a result of dynamic forced response at 1460 Hz (right) [10].

REFERENCES

[1] AVL EXCITE™ — Software Suite to Simulate Dynamics and Vibrations, NVH, Efficiency and Durability of Powertrains based on Internal Combustion Engines and Electric Drive Units, AVL List GmbH (Version 2025 R1)

[2] Parikyan, T., Resch, T., and Priebsch, H. H. "Structured Model of Crankshaft in the Simulation of Engine Dynamics With AVL/EXCITE." Proceedings of the ASME 2001 Internal Combustion Engine Division Fall Technical Conference. Volume 3: Engine Systems: Lubrication, Components, Exhaust and Boosting, System Design and Simulation. Argonne, Illinois, USA. September 23–26, 2001. p. 105-114. ASME. DOI: https://doi.org/10.1115/2001-ICE-435

[3] Parikyan, T. (2022). Efficient Modeling of Engine Parts and Design Analysis Tasks in Simulation of Powertrain Dynamics: An Overview. In: Parikyan, T. (eds) Advances in Engine and Powertrain Research and Technology. Mechanisms and Machine Science, vol 114. Springer, Cham. https://doi.org/10.1007/978-3-030-91869-9_1

[4] T. Parikyan, N. Naranca, and J. Neher, "Powertrain Resilient Mounting Design Analysis", *ASME Paper* ICEF2018-9539, San Diego, CA, USA (2018). DOI: 10.1115/ICEF2018-9539

[5] Parikyan, T.: Unified approach to generate crankshaft dynamic models for 3D and torsional vibration analyses. ASME Paper ICES2003-591 (2003). https://doi.org/10.1115/ICES2003-0591

[6] M. Janic, M. Miklautschitsch, T. Parikyan, S. Bukovnik, "Development of Industrial Continuously Variable Electromechanical Drivetrain Systems Based on Virtual Model Approach", *Proc. 1st Int. Conf. Mechanical Engineering Solutions: Design, Simulation, Testing and Manufacturing (MES-2018)*, Paper No. MES2018-05, Yerevan, Armenia (2018).

[7] T. Parikyan, "Complex modes analysis for powertrain and driveline applications", *Proceedings of International Conference on Noise and Vibration Engineering – ISMA 2016*, Leuven, Belgium, pp. 2761-2774 (2016).

[8] K. G. Mahmoud, O. Knaus, T. Parikyan, G. Offner and S. Sklepic, "An integrated model for the performance of piston ring pack in internal combustion engines", *Proc. IMechE Part K: J Multi-body Dynamics*, Vol. 232(3) 371–384 (2018). DOI: 10.1177/1464419317736676

[9] Haslinger J., Offner G., Sopouch M., and Zinkiewicz B., Modal Analysis of Vehicle Power Trains. PAMM · Proc. Appl. Math. Mech. **15**, 53 – 54 (2015) / DOI: 10.1002/pamm.201510017

[10] K.-D. Bauer, J. Haslinger, B. Zinkiewicz, J. Steiner, F. Diwoky, M. Sopouch, Ch. Schweiger, G. Offner and T. Parikyan, "Analysis of Dynamics and NVH of Electric Drive Unit using Frequency- and Time-Domain Solutions", In: Okada, M. (eds) Advances in Mechanism and Machine Science. 16th IFToMM World Congress, 2023, Tokyo, Japan. Mechanisms and Machine Science, vol 147. Springer (2023). https://doi.org/10.1007/978-3-031-45705-0_98

[11] T. Parikyan, S. Bukovnik, "Turbocharger dynamic analysis: concept-phase simulation in frequency domain", *SIRM 2019 – 13th International Conference on Dynamics of Rotating Machines*, Paper No. SIRM2019-38, Copenhagen, Denmark (2019).

INITIALLY-CURVED VARIABLE-THICKNESS FLEXURES IMPROVE PERFORMANCE IN COMPLIANT MECHANISMS, A STRAIGHT-LINE GENERATOR EXAMPLE

F.W.F. Colin[1], A. Yasir[1], E. Mulder[2], J.L. Herder[1]

[1] Delft University of Technology, Delft, The Netherlands {j.l.herder@tudelft.nl; a.yasir@tudelft.nl}
[2] ASML, Veldhoven, The Netherlands, {flip.colin@asml.com; erwin.mulder@asml.com}

1. INTRODUCTION

By far, most compliant mechanisms, even modern complex ones [1-3], consist of initially straight beams of constant cross-section. This makes good sense when small deflections are considered, but for large deflections, important properties such as support stiffness (i.e. stiffness in other directions than the degree(s) of freedom) are dramatically compromised [4]. The underlying reason is that torsion of flexures occurs at large deflections, the stiffness of which for flexures is much lower than in-plane bending. While methods have been proposed to remedy this [5], the present paper proposes an approach where this effect is reversed, in that all flexures will be initially curved so that upon deflection, some will straighten and take over the load from those that are curved. It will be shown how this idea can be exploited to maintain performance throughout the range of motion.

2. METHOD

To generate initially curved design geometries with non-prismatic flexures, Matlab optimization is used in combination with SPACAR [6], a nonlinear finite element software package in Matlab. The optimizer finds optimal locations of multiple control points that are used to generate Bezier curves that represent the leaf flexures with initial curvature. These Bezier curves are discretized in beam sections that are used by SPACAR. Besides the curvature, the variable thickness of each flexure is optimized at the same time and to parameterize this, 3 parameters per flexure are added. Since SPACAR uses beam elements and runs natively in Matlab, it is very fast in comparison with other commercial FEA software packages, making it ideal for these optimizations with large sets of parameters and highly nonlinear behaviour.

To parameterize the variable thickness, a modified Akima piecewise cubic Hermite interpolation is used. The spline is interpolated between 3 control points, at the base, somewhere between 0.1 and 0.9 of its length, and at the end of the flexure. At each point a thickness was defined (Fig. 1a).

The input topology uses 2 flexures fixed on one side and connected to an intermediate body on the other side, from this intermediate body 2 flexures are connected to the output body. This topology is chosen so that the algorithm, in theory, can make something resembling a double parallelogram and a Roberts mechanism (see the right to schemes in Fig. 1a).

Three cases are evaluated. The first case aims to generate a mechanism with a near-constant support stiffness over the full stroke. Case 2 aims to generate a mechanism with a very low parasitic error and case 3 optimizes a mechanism with a maximum stroke subject to parasitic motion, stress and minimum stiffness ratio constraints. These cases are evaluated in terms of stiffness increase in case 1 and 2, and in decreased stress peaks and thus increased range of motion for case 3. First only initial curvature was considered, subsequently variable thickness was added as design parameters. An intermediate SPACAR model is shown in Fig. 1b, where element collision is switched off.

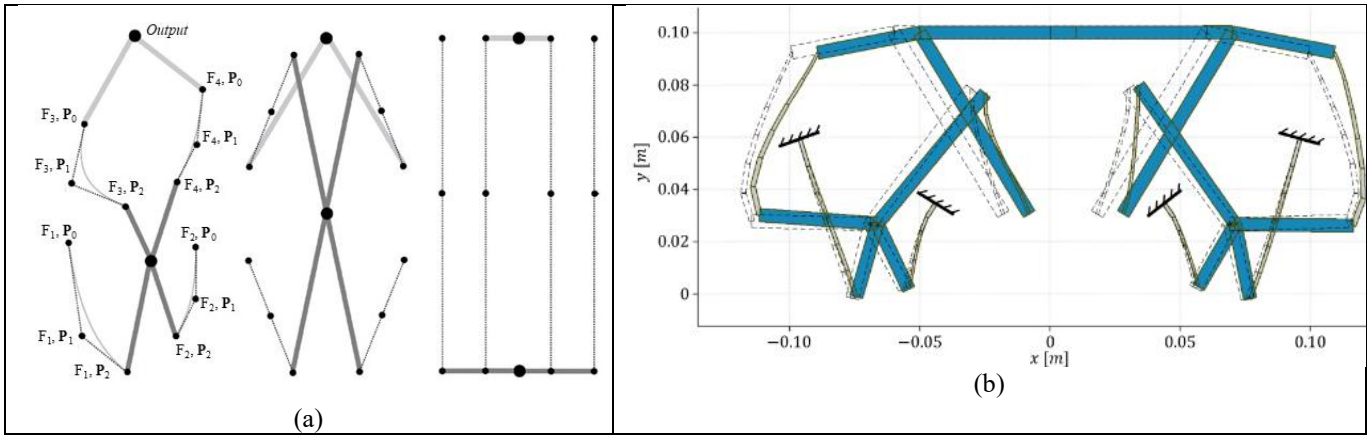

Figure 1. Mechanism topology: (a) two flexures connect the base with an intermediate body, from where two other flexures connect to the end-effector, (b) intermediate SPACAR model with compliant elements in gray and rigid bodies in blue.

3. RESULTS

The experimental test setup (Fig. 2) consists of 3 laser distance sensors and a linear motion stage. One sensor measures the x position while the other 2 simultaneously measure the parasitic translation of 2 points on the output body. The mechanism is pushed and pulled over its stroke using the linear motion stage. Using the x-translation and the 2 top distance sensors, the parasitic translation as well as rotation can be measured. This test is done multiple times without an external load applied and subsequently with an additional load of 9.81N applied above the center of the output body. A good coherence in terms of parasitic translation and rotation are observed, while a small deviation in the results for induced parasitic motion are measured. The induced parasitic motion is less constant compared to the SPACAR and Ansys models.

Case 1 resulted in a mechanism with a support stiffness variance of only 0.1% with a parasitic translation of 10 µm and a stiffness ratio (support stiffness divided by the motion stiffness) of 248. Incorporating variable thickness increases this stiffness ratio further to 503, an increase of 103%. Case 2 results in a mechanism with a parasitic motion of only 0.2 µm and a stiffness ratio of 729. When variable thickness is added, an increase of 84% in stiffness ratio and an increase of 26% in mean support stiffness can be achieved. The last case aims to maximize the stroke for a mechanism with a maximum parasitic translation of 10 µm and a minimum stiffness ratio of 100. Using constant thickness flexures, a stroke of 27.65 mm can be achieved and by using variable thickness flexures this can be increased to 30.60 mm, an increase of 10.7%.

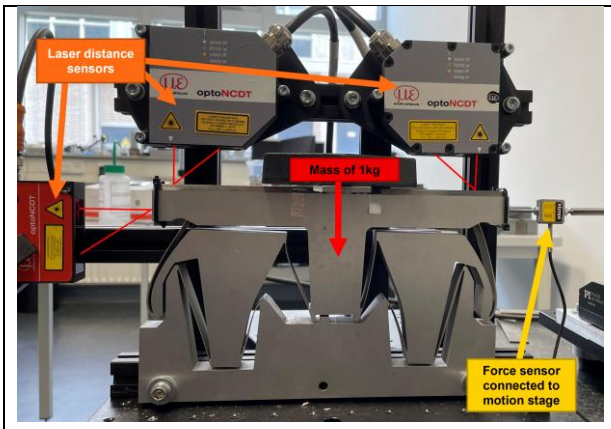

(a)

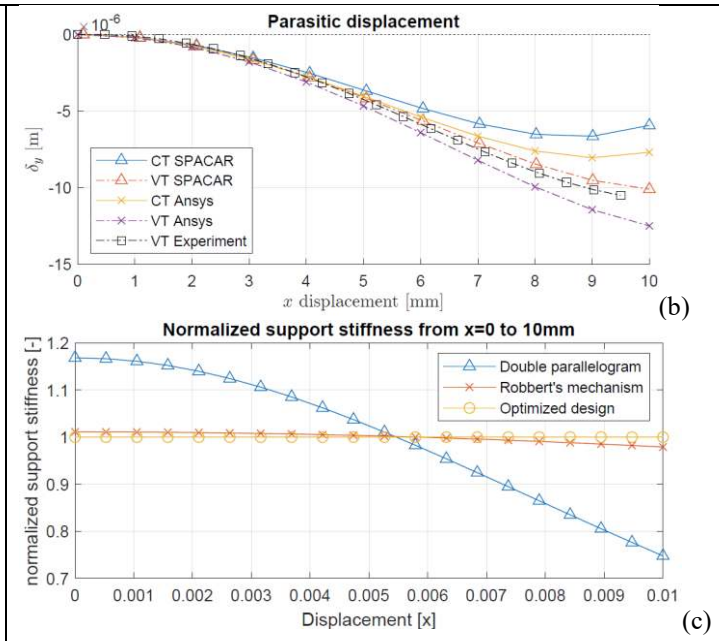

Figure 2. (a) prototype in the experimental test set-up, (b) parasitic displacement, (c) normalized support stiffness (CT is constant thickness, VT is variable thickness; blue is double parallelogram, red is Robert's mechanism variant, yellow is optimized design discussed in this paper)

4. DISCUSSION AND CONCLUSION

It can be concluded that initially curved, variable thickness flexures offer significant improvements over commonly used initially straight, constant thickness flexures in terms of increased support stiffness and decreased maximum stress levels. It is expected that generating mechanisms using initially curved and/or variable thickness flexures shows advantages in many fields, such as constant support stiffness, high precision and increased range of motion. If initial curvature and variable thickness are combined, typically ever higher increase in performance in terms of increasing support stiffness and range of motion can be achieved making it a very promising method that can influence many different designs in a variety of applications.

REFERENCES

[1] E.G. Merriam, J.E. Jones, S.P. Magleby, L.L. Howell, Monolithic 2DoF fully compliant space pointing mechanism, *Mechanical Sciences*, 2013

[2] S. Wan, Q. Xu, Design and analysis of a new compliant XY micropositioning stage based on Roberts mechanism, *Mech. Mach. Theory*, 2016

[3] G. Hao and J. Yu. "Design, modelling and analysis of a completely-decoupled XY compliant parallel manipulator". *Mechanism and Machine Theory* 102 (Aug. 2016), pp. 179–195.

[4] D. M. Brouwer, J. P. Meijaard, and J. B. Jonker. "Large deflection stiffness analysis of parallel prismatic leaf-spring flexures". *Precision Engineering* 37.3 (July 2013), pp. 505–521.

[5] J. Rommers, M. Naves, D.M. Brouwer, J.L. Herder (2021) A flexure-based linear guide with torsion reinforcement structures, J Mechanisms Robotics (DOI: 10.1115/1.4052971)

[6] J. B. Jonker and J. P. Meijaard. "SPACAR — Computer Program for Dynamic Analysis of Flexible Spatial Mechanisms and Manipulators". In: Multibody Systems Handbook (1990), pp. 123–143.

KINEMATIC PROPERTIES OF THE INSTANTANEOUS CENTERS OF ZERO VELOCITY AND ACCELERATION ACCORDING TO THEIR TRAJECTORIES AND CENTRODES

Giorgio Figliolini, Chiara Lanni, Luciano Tomassi

Department of Civil & Mechanical Engineering, University of Cassino & Southern Lazio, G. Di Biasio 43, 03043 Cassino (Fr), Italy, {giorgio.figliolini@unicas.it; chiara.lanni@unicas.it; luciano.tomassi@unicas.it}

1. INTRODUCTION

The kinematic analysis of planar mechanisms has long relied on the concept of centrodes, defined as the loci of the instantaneous centers of rotation associated with the relative motion of rigid bodies. Early geometric investigations established fundamental properties of centrodes and related point trajectories, showing that they are, in general, algebraic curves of high order and that particular motion conditions lead to notable degeneracies or special curve families [1]. Within this classical framework, centrodes were primarily studied as geometric entities, aimed at characterizing rigid-body motion at the position level and providing insight into the qualitative structure of planar motions [2]. Subsequent developments extended centrode theory through analytical formulations suitable for systematic computation in planar linkages. Vector-loop and inversion-based approaches enabled the explicit determination of instantaneous centers and fixed and moving centrodes for multi-link mechanisms, including four-bar chains, thus bridging classical geometry with modern kinematic analysis [3]. Beyond first-order kinematics, the center of zero acceleration, along with the corresponding second-order centrodes, has been introduced to account for the distribution of accelerations within planar mechanisms. The instantaneous center of zero acceleration was formally defined and analytically characterized for rigid-body planar motion, providing a natural extension of the instantaneous center of rotation [4, 5]. Graphical and semi-analytical procedures were later developed to locate secondary instantaneous centers and acceleration centers in single-degree-of-freedom linkages, with particular emphasis on synthesis-oriented applications [6, 7]. Parametric descriptions of acceleration pole loci and related constructions have been proposed for slider–crank and four-bar mechanisms, enabling the design of linkages satisfying prescribed acceleration constraints [8, 9]. Despite these advances, second-order centrodes and acceleration centers have generally been treated as configuration-dependent loci, without an explicit investigation of their kinematic evolution as moving points. A unifying theoretical framework for centrodes of arbitrary order has been provided by the theory of instantaneous geometric and kinematic invariants. Within this approach, first- and second-order centrodes can be systematically derived and traced using invariant-based formulations, with applications to slider–crank mechanisms and validation through Bresse's circles, as reported in [10]. Moreover, the authors have introduced the concepts of n^{th}-order Bresse's circles and higher-order centrodes in [11,12], while these geometric and kinematic loci have been extended to multi-loop mechanisms, such as Stephenson III six-bar chains [13,14]. In this wide context, the proposed abstract deals with the kinematic properties of the instantaneous centers of zero-velocity (ICZV) and zero-acceleration (ICZA) according to their trajectories and centrodes. In particular, a novel algorithm is proposed to determine their corresponding position, velocity and acceleration vector functions, during the simultaneously tracing of the coupler trajectory and their fixed and moving centrodes.

2. INSTANTANEOUS CENTERS OF ZERO VELOCITY AND ACCELERATION

Each materialized IC has proper displacement velocity and acceleration, while tracing both pairs of the centrode curves, which are the corresponding trajectories with respect to the fixed and moving planes. Consequently, the ICZV and the ICZA trace the first and second order centrodes, respectively. Moreover, each IC traces also a coupler curve, when considered as belonging or attached to the coupler plane, instead to be considered as independent and materialized point. In other words, the ICZV and ICZA trace three trajectories respectively and simultaneously, during the planar motion of a rigid body.

The proposed algorithm proofs that these three trajectories for each IC, both centrodes included, satisfy the relative motion kinematic properties, in the form the Galilei and Coriolis theorems. The first order centrodes are tangent each other at the ICZV and related between them by a pure-rolling contact condition, since the instantaneous center of rotation has zero velocity, when considered attached to the coupler plane. Consequently, the coupler curve shows a cup, as inversion point of motion, which acceleration vector is different by zero and orthogonal to both first order centrodes at the ICZV. Conversely, the second order centrodes are not tangent each other, since they usually intersect in more than one point, even if, the ICZA is unique. Thus, the right position and the kinematic properties of the ICZA cannot be found easily, without the aid of other geometric loci, such as, the Bresse circles. Therefore, a specific algorithm has been formulated and then implemented in Matlab and validated by considering the coupler-link of a four-bar linkage, which has been supposed to be crank-driven at constant speed. Significant results are reported in Fig. 1a, where the ICZV P_3 of the coupler link 3 (AB) is shown along with its coupler trajectory with cusp and both first order centrodes λ_3 and l_3. The corresponding velocity and acceleration vectors are also represented in congruence

with the Galilei and Coriolis theorems. Likewise, referring to Fig. 1b, the ICZA K_3 is shown in the same mechanism configuration for the assigned crank angle θ_2, along with its trajectory and both second order centrodes $\bar{\lambda}_3$ and $\bar{l}_3$. The corresponding velocity and acceleration vectors are also represented and with particular reference to the ICZA, each component is tangent to its trajectory, i.e. the fixed and moving second order centrodes, $\bar{\lambda}_3$ and $\bar{l}_3$ respectively, and the coupler trajectory of K_3.

3. CONCLUSIONS

The proposed algorithm allows the determination and the representation of all velocity and acceleration vectors of both ICZV and ICZA, according to the Galilei and Coriolis theorems, and along with their first and second order centrodes and trajectories, which are simultaneously traced by each IC, during the coupler motion of a generic planar mechanism. Additionally, the determination of the normal acceleration components of the ICs, along with the corresponding velocities, allows the centrodes curvature analysis without using differential geometry. Several Matlab results have allowed the proposed algorithm validation.

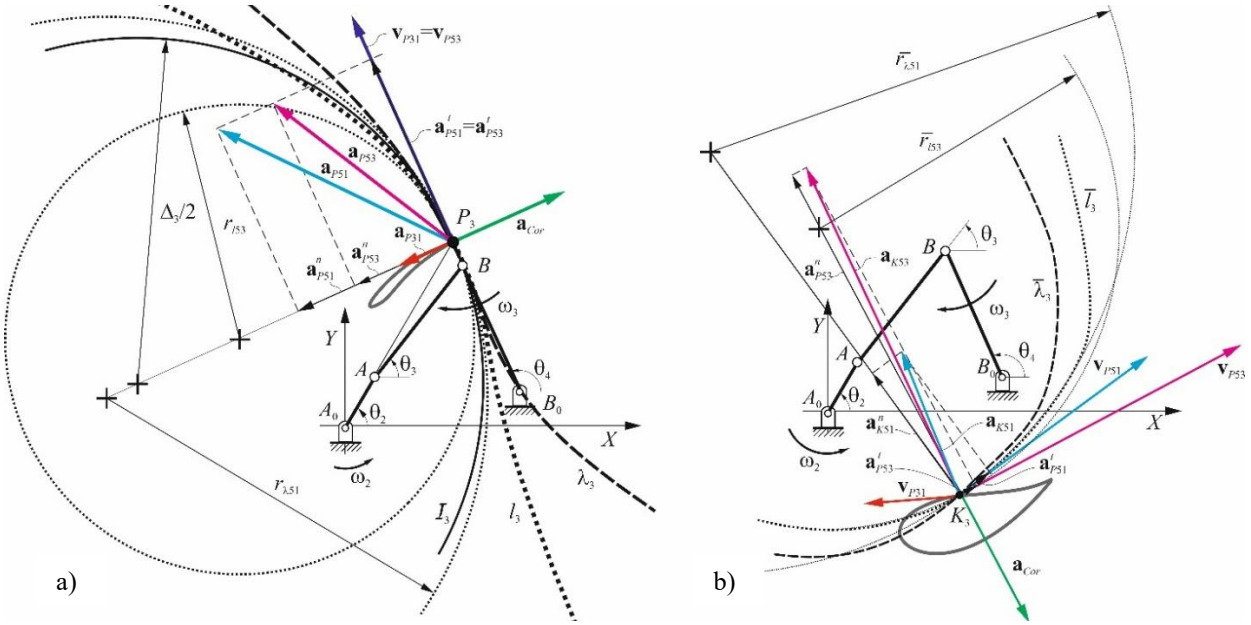

Figure 1. Kinematic properties of the ICZV and ICZA according to their trajectories and centrodes: a) ICZV (Instantaneous Center of Zero-Velocity); b) ICZV (Instantaneous Center of Zero-Acceleration).

REFERENCES

[1] E. W. McDonald, Determination of the reducible cases of the fixed centrode of three-bar motion, *The American Mathematical Monthly*, 33(2), 90–93, 1926.

[2] J. Bloom, L. Whitt, The geometry of rolling curves, *The American Mathematical Monthly*, 88(6), 420–426, 1981.

[3] B. J. Gilmore, R. J. Cipra, An analytical method for computing the instant centers, centrodes, inflection circles, and centers of curvature of the centrodes by successively grounding each link, ASME *Journal of Mechanisms, Transmissions, and Automation in Design*, 105(3), 407–414, 1983.

[4] H. Sun, T. Liu, Analysis of instantaneous center of zero acceleration of rigid body in planar motion, *Modern Applied Science*, 3(4), 191–195, 2009.

[5] W. Meyer zur Capellen, G. Dittrich, Note on the determination of accelerations in plane kinematics, *Journal of Mechanisms*, 1, 315–319, 1966.

[6] D. E. Foster, G. R. Pennock, Graphical methods to locate the secondary instant centers of single-degree-of-freedom indeterminate linkages, *ASME Journal of Mechanical Design*, 127, 249–256, 2005.

[7] J. T. Kimbrell, Graphical synthesis of a 4-bar mechanism, *Mechanism and Machine Theory*, 19(1), 45–49, 1984.

[8] W.-M. Hwang, Y.-S. Fan, Coordination of two crank angles and two acceleration poles for a slider-crank mechanism using parametric equations, *Proceedings of the Institution of Mechanical Engineers*, Part C, 222(5), 483–491, 2008.

[9] N. Diab, A new graphical technique for acceleration analysis of four bar mechanisms using the instantaneous center of zero acceleration, *SN Applied Sciences*, 3, Art. 327, 2021.

[10] G. Figliolini, C. Lanni, L. Tomassi, First and second order centrodes of slider-crank mechanisms by using instantaneous invariants, In: Altuzarra O., Kecskeméthy A. (Eds.): *18th ARK International Symposium on Advances in Robot Kinematics*, Proc. in Advanced Robotics, Vol. 24, Springer, Cham (CH), pp. 303–310, 2022.

[11] G. Figliolini, C. Lanni, M. Cirelli, E. Pennestrì, Kinematic properties of nth-order Bresse circles intersections for a crank-driven coupler link, *Mechanism and Machine Theory*, 190(11):105445, 2023.

[12] C. Lanni, G. Figliolini, L. Tomassi, Higher-order centrodes and Bresse's circles of slider-crank mechanisms, *Proc. of the ASME IDETC-CIE Conference*, August 20-23, 2023, Boston, Massachusetts, DETC2023-116627, 2023.

[13] G. Figliolini, C. Lanni, L. Tomassi, First- and second-order centrodes of both coupler links of Stephenson III six-bar mechanisms, *Machines*, 13(2), Art. 93, 2025.

[14] G. Figliolini, C. Lanni, L. Tomassi, Synthesis and analysis of Stephenson III six-bar motion generators with an instantaneous stop link. *ASME Journal of Mechanisms and Robotics*, 17(4): 044510, 2025.

SPHERICAL FOUR-BAR CONTROL MOMENT GYROSCOPE: CONCEPT AND ROTATING-TORQUE GENERATION

Sajjad Keshtkar[1], Hirohisa Kojima[1], Francisco Geu Flores[2], Wojciech Kowalczyk[2]

[1] Department of Aeronautics and Astronautics, Tokyo Metropolitan University, 6–6 Asahigaoka, Tokyo 191–0065, Japan, {s.keshtkar@tmu.ac.jp; hkojima@tmu.ac.jp}
[2] Chair of Mechanics and Robotics, University of Duisburg-Essen, Lotharstr. 1, 47057 Duisburg, Germany {francisco.geu@uni-due.de; wojciech.kowalczyk@uni-due.de}

1 INTRODUCTION

Control moment gyroscopes (CMGs) are attractive for spacecraft attitude control because they produce large torque without expending propellant. Recent work has emphasized steering and robustness in double-gimbal and variable-speed CMGs, including singularity-aware steering laws and fault-tolerant tracking [1]. This extended abstract introduces a novel spherical four-bar CMG architecture that simplifies traditional multi-wheel CMG systems by using a single actuator and one rotor to tailor torque direction in constrained volumes. Unlike conventional CMG arrays that require multiple wheels to generate three-dimensional control authority, the proposed one-DOF linkage mechanism achieves directional control through kinematic transmission. This work presents the direction-locus characterization of this new architecture and reports a focused low Earth orbit (LEO) case study based on recent Mechanism and Machine Theory developments in spherical mechanisms [2, 3].

2 KINEMATIC MODEL AND DIRECTION LOCUS

The mechanism is a spherical four-bar linkage in which all joint axes intersect at the sphere center. As shown in Fig. 1, O and C are fixed pivots, and A and B are moving pivots. The input crank OA, coupler AB, output crank BC, and ground OC are great-circle arcs with central angles $(\alpha, \eta, \beta, \gamma)$ on the unit sphere. A single input rotation θ drives OA; the closure constraint determines the output angle $\psi(\theta)$, and the coupler angle $\phi(\theta)$ measures the coupler's cumulative rotation about the OA axis. The example presented uses link lengths $(\alpha, \beta, \gamma, \eta) = (40°, 90°, 70°, 80°)$, selected to satisfy Grashof and transmission-angle criteria, with $\dot{\theta} = 1$ rad/s over $\theta \in [0, 2\pi]$.

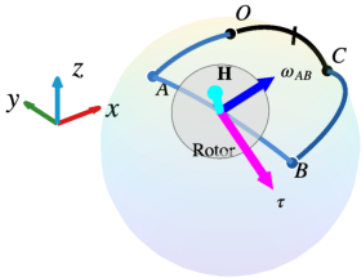

Figure 1: Spherical four-bar CMG at $\theta = \pi - \pi/12$, with pivots O, C, A, B.

Using the unit vector $\hat{\mathbf{k}} = [0, 0, 1]^T$ and standard rotations R_y, R_z, the input and output link directions are

$$\hat{\mathbf{a}} = R_z(\theta)R_y(\alpha)\hat{\mathbf{k}}, \qquad \hat{\mathbf{b}} = R_y(\gamma)R_z(\psi)R_y(\beta)\hat{\mathbf{k}}, \tag{1}$$

where $\hat{\mathbf{a}}$ and $\hat{\mathbf{b}}$ denote the link directions of OA and BC, respectively. The closure constraint $\hat{\mathbf{a}} \cdot \hat{\mathbf{b}} = \cos\eta$ gives $\psi(\theta)$. The rotor is mounted on coupler AB, with its spin axis along the bisector of the coupler plane. Thus the rotor momentum direction is $\hat{\mathbf{h}} = (\hat{\mathbf{a}} + \hat{\mathbf{b}})/\|\hat{\mathbf{a}} + \hat{\mathbf{b}}\|$, and the momentum Jacobian is $\mathbf{J}_h(\theta) = \partial\hat{\mathbf{h}}/\partial\theta$. The CMG torque is

$$\boldsymbol{\tau} = H_0\mathbf{J}_h(\theta)\dot{\theta}, \tag{2}$$

where H_0 is the rotor momentum magnitude. Following McCarthy and Soh's spherical linkage theory [4], the instantaneous rotation axis intersects the coupler plane at angle ρ (measured in the fixed xz plane from the $+z$ direction),

giving the output and coupler velocity ratios

$$\frac{\dot{\psi}}{\dot{\theta}} = \frac{\sin\rho}{\sin(\rho-\gamma)}, \qquad \frac{\dot{\phi}}{\dot{\theta}} = \frac{\sin\rho}{\sin(\alpha-\rho)}. \tag{3}$$

Equation (3) maps $\dot{\theta}$ to output and coupler rates, showing how geometry controls kinematic transmission. Importantly, the coupler velocity ratio $\dot{\phi}/\dot{\theta}$ can exceed unity, allowing the coupler to spin faster than the input crank; this kinematic amplification motivates the chosen coupler-mounted rotor configuration. Link-length selection follows spherical Grashof and transmission-angle criteria to ensure a full input sweep and reliable motion transfer.

The geometry factor $\kappa(\theta) = \|\mathbf{J}_h\|$ bounds achievable torque magnitude as $\tau_{\max} = \kappa_{\max} H_0 \dot{\theta}_{\max}$. The achievable torque directions form a locus on the unit sphere, $\mathcal{L}_\tau \subset S^2$, a direct indicator of directional capability. Because the mechanism has one DOF, directions outside $\mathcal{L}_\tau$ are not directly achievable; tracking them requires residual torque or multi-actuator composition. This locus framework complements and extends prior CMG analyses that focus primarily on steering laws and singularity avoidance [1, 2].

The torque follows $\boldsymbol{\tau} = \dot{\mathbf{H}} = \boldsymbol{\omega}_{AB} \times \mathbf{H}$, where $\boldsymbol{\omega}_{AB}$ denotes the coupler angular velocity in the inertial frame. Thus $\boldsymbol{\tau} \perp \mathbf{H}$ at every instant. As θ sweeps a cycle, the unit directions $\hat{\mathbf{h}}(\theta)$ and $\hat{\boldsymbol{\tau}}(\theta) = \boldsymbol{\tau}/\|\boldsymbol{\tau}\|$ trace closed curves on S^2. In Fig. 2, the left panel shows torque direction and tip loci together with the mission-direction path (black dashed) used in the LEO benchmark, the middle panel shows momentum direction and tip loci, and the right panel compares momentum-direction and $\boldsymbol{\omega}_{AB}$-direction loci. The "Tip" traces are endpoints of vectors drawn from a moving coupler reference point $\mathbf{P}_{mid}$, i.e., $\mathbf{r}_{tip} = \mathbf{P}_{mid} + \lambda\hat{\mathbf{v}}$, where $\lambda > 0$ is a fixed plotting length scale and $\hat{\mathbf{v}}$ is the unit direction used in that panel ($\hat{\boldsymbol{\tau}}$, $\hat{\mathbf{h}}$, or $\hat{\boldsymbol{\omega}}_{AB} = \boldsymbol{\omega}_{AB}/\|\boldsymbol{\omega}_{AB}\|$). Therefore, tip traces are not constrained to the unit sphere.

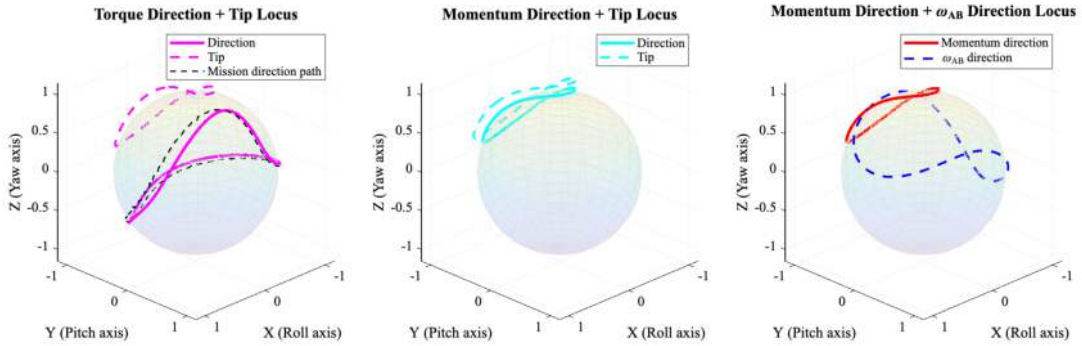

Figure 2: Combined direction and tip loci, including momentum and $\boldsymbol{\omega}_{AB}$ direction comparison.

3 DISCUSSION

The spherical four-bar CMG defines a one-DOF feasible torque-direction set $\mathcal{L}_\tau$ shown in Fig. 2. To assess feasibility, a 500 km LEO benchmark was conducted using a one-orbit scheduled torque request with rate-limited input allocation. The key metrics are: peak commanded torque $\max\|\tau_{\text{req}}\| = 0.51$ N·m, residual RMS $= 0.018$ N·m (the unachievable component), mean residual ratio $= 0.10$, 90th-percentile direction mismatch $= 9.4°$, and saturation ratio $= 0$. These results indicate that the selected geometry can track typical LEO attitude-control demands with minor residual error, supporting the viability of the four-bar CMG for low-orbit missions. The full paper presents the mathematical formulation, mechanism analysis, and extended case-study results.

REFERENCES

[1] H. Kojima, R. Nakamura, and S. Keshtkar, "Steering control law for double-gimbal scissored-pair cmg," *Advances in Space Research*, vol. 66, no. 10, pp. 2460–2472, 2020.

[2] T. Essomba and W.-H. Wang, "Design of a spherical parallel mechanism with controllable center of rotation using a spherical reconfiguration linkage," *Mechanism and Machine Theory*, vol. 191, p. 105672, 2024.

[3] R. Di Gregorio, "Dynamic model of multi-dof spherical mechanisms based on instantaneous pole axes," *Mechanism and Machine Theory*, vol. 214, 2025.

[4] J. M. McCarthy and G. S. Soh, *Geometric Design of Linkages*, 2nd ed., ser. Interdisciplinary Applied Mathematics. New York, NY: Springer, 2011, vol. 11.

THERMAL-BASED STIFFNESS MODULATION OF FLEXIBLE SURGICAL INSTRUMENTS FOR ROBOT-ASSISTED MINIMALLY INVASIVE SURGERY

D. Pisla[1,2,4], B. Gherman [1,2,*], I. Zima[1,2], A. Pusca[1,2], A. Pisla[1,2], M. Miclaus[1,2], C. Vaida[1,2], D. Chablat[1,3]

[1] CESTER – Research Centre for Robots Testing and Simulation, Technical University of Cluj-Napoca, Memorandumului 28, 400114 Cluj-Napoca, Romania, {Doina.Pisla@mep.utcluj.ro; Bogdan.Gherman@mep.utcluj.ro; Ionut.Zima@mept.utcluj.ro; Alexandru.Pusca@mep.utcluj.ro ; Adrian.Pisla@muri.utcluj.ro; Marius.Miclaus@mep.utcluj.ro; Calin.Vaida@mep.utcluj.ro; Damien.Chablat@mep.utcluj.ro}

[2] European University of Technology, European Union

[3] École Centrale Nantes, Nantes Université, CNRS, LS2N, UMR 6004, F-44000 Nantes, France, {damien.chablat@ec-nantes.fr}

[4] Technical Sciences Academy of Romania, B-dul Dacia, 26, 030167 Bucharest, Romania, {Doina.Pisla@mep.utcluj.ro}

*Corresponding author

1. INTRODUCTION

Flexible tendon-driven instruments for robot-assisted minimally invasive surgery (RAMIS) require both compliance for safe navigation and stiffness for stable grasping, two opposing mechanical properties [1]. Current variable stiffness solutions such as granular, layer, and fiber jamming, shape memory alloys, and antagonistic actuation require additional structural elements such as membranes, pressure sources, or dedicated actuators, increasing complexity and which limits miniaturization within the 10 mm laparoscopic port constraint [1, 2]. This work presents a new approach for stiffness modulation of flexible surgical instruments based on the thermo-viscoelastic behavior of the photopolymer material. The flexible section is manufactured from Elastico Clear [3], a PolyJet photopolymer whose stiffness can vary at body temperature (~37°C), the material is natively compliant. Through active cooling via an integrated fluidic circuit toward 18 – 23°C, stiffness increases by over one order of magnitude, enabling stable grasping and retraction, while increasing the temperature of the fluid the material returns to its compliant state. A Cosserat viscoelastic rod framework [4] with temperature-dependent constitutive properties is identified as the modeling approach to determine the stiffness modulation across all proposed geometries.

2. DESIGN OF DIFFERENT TYPE OF FLEXIBLE ELEMENTS

A series of flexible elements with different configurations are proposed to fit within the 10 mm trocar diameter while embedding both tendon actuation channels and the integrated fluidic cooling circuit. The proposed geometries, illustrated in Figure 1, include: two-sided notched (a), one-sided notched (b), fully flat (c), and rounded notches (d). The notch patterns are introduced to reduce the actuation force required for bending. Since the full mechanical properties of the material across the operational temperature range are not yet available, these different geometries also serve to investigate material failure limits under repeated bending. Additional geometries will be developed based on experimental findings.

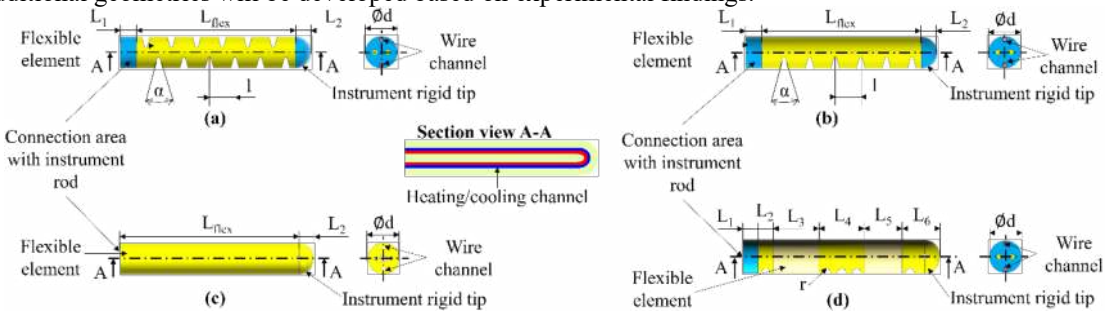

Figure 1. Different configurations of the flexible element

Each geometry integrates dedicated channels for actuation tendons and two capillary tubes creating a closed-loop fluidic circuit. Pre-cooled fluid circulated by a proximal peristaltic pump reduces the element temperature from body temperature toward 18–23°C, achieving the required stiffness. A medical-grade silicone sheath covers the flexible element, serving as a biocompatible barrier while reducing thermal exchange with surrounding tissue. Material characterization will include Dynamic Mechanical Analysis (DMA) to determine E'(T), E"(T), and tan δ across the 18 – 45°C range, complemented by bending tests at multiple temperatures to extract the equivalent elastic modulus E(T) through inverse identification. These parameters will be used in the Cosserat viscoelastic rod model [4] providing a unified framework for all geometries. The proposed instrument is designed for integration with the Athena parallel robot (Figure 2a), a 3–DOF parallel mechanism with a passive spherical joint that maintains the remote center of motion for the flexible instrument (Figure 2b) that was integrated with Athena robot [5].

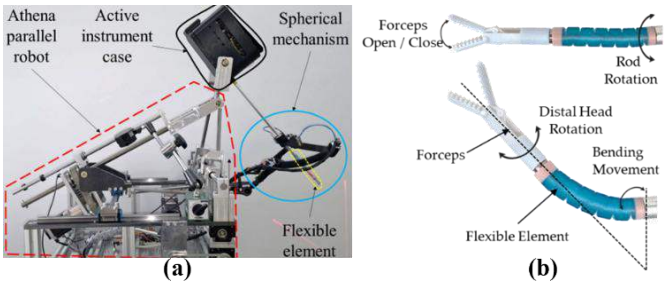

Figure 2. Flexible instrument for tissue manipulating integrated with the Athena parallel robot in pancreatic surgery

3. PRELIMINARY RESULTS

Preliminary stiffness characterization was performed on the PolyJet–printed flexible element by progressively varying the specimen temperature within 18 – 45°C and measuring the corresponding mechanical response under a constant transverse loading condition. The equivalent stiffness illustrated in Figure 3 exhibits a marked and nonlinear dependence on temperature, decreasing by more than one order of magnitude over the measured range. To highlight distinct sensitivity ranges, the data is presented in three intervals (18 – 23°C, 23 – 30°C, 30 – 45°C) as follows: the strongest stiffness drop occurs at the lowest temperatures (first interval), while the slope becomes progressively smaller above ~30 °C. The associated displacement-temperature trend illustrated in Figure 4, presents an increase in deflection as temperature rises, with a comparatively mild variation around 30 – 37°C followed by a steeper increase at higher temperatures.

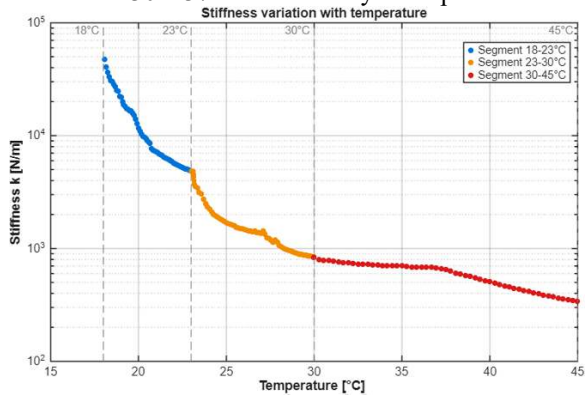

Figure 3. Stiffness variation with temperature

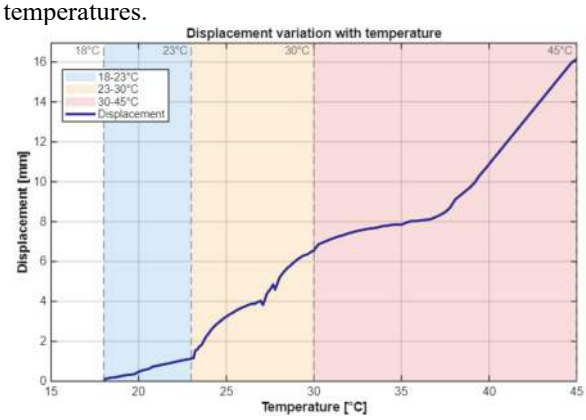

Figure 4. Displacement variation with temperature

The preliminary characterization confirms a pronounced thermo-mechanical dependency in the PolyJet-printed flexible element, with equivalent stiffness decreasing by more than one order of magnitude across the 18 – 45°C temperature range and three distinct sensitivity ranges identified. This behavior can be directly used as a compact variable-stiffness mechanism: the element remains compliant at elevated temperatures to adapt to irregular anatomical geometries and stiffer at lower temperatures for stable grasping and retraction.

4. CONCLUSION AND FUTURE WORK

This work presents a temperature-based stiffness modulation concept for flexible surgical instruments in robot-assisted minimally invasive surgery, where the photopolymer serves as the variable stiffness mechanism without additional structural components. Four geometries were manufactured within the 10 mm constraint with integrated fluidic channels. Preliminary tests confirmed stiffness variation exceeding one order of magnitude (18 – 45°C). Future work will include DMA characterization, Cosserat rod modeling, thermo–mechanical FEA, and force validation.

ACKNOWLEDGMENTS

This research was funded by the project New smart and adaptive robotics solutions for personalized minimally invasive surgery in cancer treatment – ATHENA, funded by European Union—Next Generation EU and Romanian Government, under National Recovery and Resilience Plan for Romania, contract no. 760072/23.05.2023, code CF 116/15.11.2022, through the Romanian Ministry of Research, Innovation and Digitalization, within Component 9, investment I8.

REFERENCES

[1] M. Manti, et al.” Stiffening in Soft Robotics: A Review of the State of the Art.” *IEEE Robot. Autom. Mag.*, 23, 93–106, 2016.
[2] H.M. Le, L. Cao, T.N. Do, S.J. Phee, “Design and modelling of a variable stiffness manipulator for surgical robots.” *Mechatronics*, 53, 109–123, 2018.
[3] S. Chokshi, et al. “Medical 3D Printing Using Material Jetting: Technology Overview, Medical Applications, and Challenges.” *Bioengineering*, 12(3), 249, 2025.
[4] J. Till, V. Aloi, C. Rucker, “Real-Time Dynamics of Soft and Continuum Robots Based on Cosserat Rod Models.” *Int. J. Robot. Res*., 38(6), 723–746, 2019.
[5] D. Pisla, A. Pusca, B. Gherman, A. Pisla, I. Birlescu, P. Tucan, C. Vaida, D. Chablat “Modeling and Simulation of a Novel Parallel Robotic System for Minimally Invasive Pancreatic Surgery.”, *ASME. J. Mechanisms Robotics*, 18(2): 024501, 2026.

RING-DOWN ANALYSIS USING A THREE-AXIS ACCELEROMETER FOR A TRAJECTORY WITH A TRAPEZOIDAL VELOCITY PROFILE

E. E. Franco-Ortiz[1], C. Rodriguez-Donate[1], J. Gonzalez-Villagomez[1], L. M. Ledezma-Carrillo[1]

[1] Departamento de Estudios Multidisciplinarios, División de Ingenierías, Campus Irapuato-Salamanca, Universidad de Guanajuato, Yuriria C.P. 38944, Guanajuato, México, {edgar.franco@ugto.mx; c.rodriguezdonate@ugto.mx, j.gonzalezvillagomez, lm.ledezma@ugto.mx}

1 INTRODUCTION

The motion dynamics of industrial robots are affected by residual vibrations induced during task execution. Which degrade positioning accuracy, compromise process quality, and reduce the service life of mechanical components [1]. In robotic systems, such vibrations are strongly related to the motion profile. Consequently, the design of motion profiles that achieve fast movements while maintaining low vibration levels has become a relevant research topic in control engineering, offering an effective means of vibration reduction without altering the robot's mechanical structure [2, 3]. Most existing studies focus on synthesizing motion profiles using polynomial functions or S-curves, with limited experimental evaluation of how these profiles excite vibratory modes or affect the mechanical structure. In this context, ring-down analysis, defined as the damped oscillatory response following mechanical excitation, emerges as an effective tool for characterizing the interaction between the imposed trajectory and the system's structural dynamics. This work employs ring-down analysis as a central metric to evaluate and compare the vibration response induced by different motion profiles in robotic systems. In particular, the effect of smoothing a trapezoidal velocity profile using FIR filtering is analyzed, as FIR-based trajectory generation techniques have been shown to effectively limit acceleration and attenuate frequency components that may excite structural vibration modes [4]. Experimental results show that ring-down analysis provides a sensitive and physically interpretable measure of the dynamic impact of the trajectory, allowing clear identification of the improvements achieved through low-cost smoothing techniques.

2 METHODOLOGY

The proposed methodology is based on the sequential processing of acceleration signals to locate and analyze ring-down responses induced at the jerk instants of a trapezoidal velocity profile. Figure 1 presents a general diagram of the proposed signal processing workflow. Acceleration signals were acquired at $1kHz$ using an triaxial accelerometer mounted on an AC sevomotor and the described processign was applied to each channel. As an initial step, pre-processing is applied to the acceleration signals of each axis using a band-pass filter to suppress noise and frequency components not associated with structural vibrations. Frequencies of interest are identified using Fourier analysis and correspond to vibratory modes excited during the jerk instants of the trapezoidal velocity profile. Short-time Fourier transform (STFT) is then employed to accurately localize these events in time. Once te relevant frequencies and time instants are identified, a $0.3s$ time window centered on each detected event is isolated. A narrowband filter around the dominant frequency is applied to focus the analysis on a single vibratory mode. The ring-down phenomenon describes the free vibration response of a mechanical system after an impulsive excitation ceases. In underdamped systems, the time-domain response can be modeled as a damped oscillation, expressed by Eq. (1) as described in [5]:

$$x(t) = A\mathrm{e}^{-\zeta\omega_n t}\sin(\omega_d t + \phi) \tag{1}$$

Where A_0 represents the initial amplitude, ω_d is the damped angular frequency, and ϕ is the initial phase. The exponential decay of the envelope provides direct information about energy dissipation and the dynamic behavior of the system. The filtered signal is subsequently processed using the Hilbert transform to obtain the analytic signal and estimate the ring-down envelope. From this envelope, the system's dynamic parameters are extracted, enabling quantitative comparison of the vibration response induced by the original trapezoidal velocity profile and the FIR-smoothed profile.

3 RESULTS AND CONCLUSIONS

To validate the proposed methodology and evaluate the effect of motion profile smoothing on the system's vibration response, two experimental cases are compared with the same design parameters: (I) a standard trapezoidal velocity

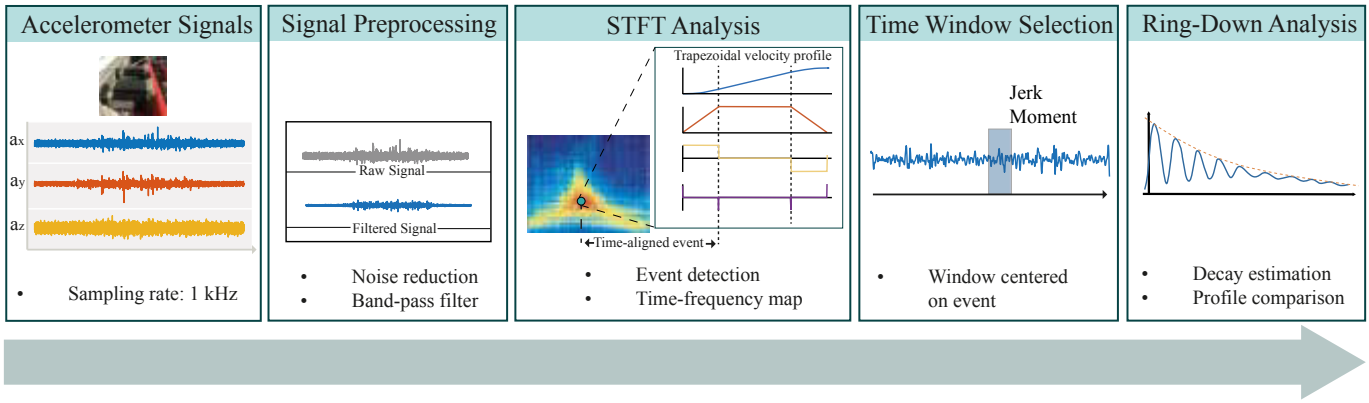

Figure 1: Proposed methodology fot time-frequency event detection and ring-down analysis

profile and (II) a trapezoidal profile smoothed using FIR filtering. Figure 2 presents the ring-down behavior obtained from the Hilbert envelope for each accelerometer axis, for both the normal and smoothed profiles. A consistent reduction in the initial vibration amplitude is observed when the smoothed profile is applied, indicating a lower level of dynamic excitation.

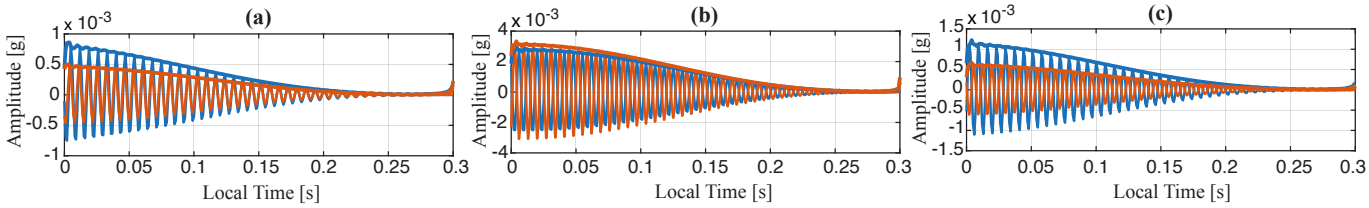

Figure 2: Ring-down responses for the normal (blue) and smoothed (orange) velocity profiles. (a) X-axis, (b) Y-axis, (c) Z-axis.

Table 1 summarizes the metrics obtained from the ring-down analysis for both profiles. The initial amplitude A_0, the decay rate σ (represents the exponential attenuation of the vibration envelope and is directly related to the system damping and natural frequency, $\sigma = \zeta\omega_n$), and the vibratory energy E were estimated from the exponential fit of the envelope over the free ring-down interval. The results show that profile smoothing leads to a significant reduction in A_0 and vibratory energy, while the decay rate remains nearly unchanged across all axes.

Table 1: Ring-down metrics per axis.

	Normal			Smoothed		
Axis	A_0	σ	E	A_0	σ	E
X	0.00091926	7.3343	2.4897×10^{-08}	0.00052692	5.9445	9.6084×10^{-09}
Y	0.0031626	4.5887	4.0199×10^{-07}	0.0035735	4.9669	4.904×10^{-07}
Z	0.0012978	6.4308	5.4338×10^{-08}	0.0007042	6.3277	1.6189×10^{-08}

REFERENCES

[1] Y. Fang, G.-N. Zhu, Y. Zhao, and C. Gu, "Design procedure for motion profiles with sinusoidal jerk for vibration reduction", *Applied Sciences*, vol. 13, no. 24, p. 13320, 2023.

[2] F. Rubio, C. Llopis-Albert, F. Valero, and J. L. Suñer, "Industrial robot efficient trajectory generation without collision through the evolution of the optimal trajectory", *Robotics and Autonomous Systems*, vol. 86, pp. 106-112, 2016.

[3] H. Gurocak, *Industrial motion control: motor selection, drives, controller tuning, applications.* John Wiley & Sons, 2015.

[4] Y. Altintas, M. A. Esfahani, B. Karimi, O. Gatenby, "Cascated FIR and half-sine filter-based smooth trajectory generation algorithm", *CIRP Annals - Manufacturing Technology*, vol. 74, pp. 559-562, 2025.

[5] D. J. Inman, *Engineering Vibrations*, 5th ed., Hoboken, NJ: Pearson, 2022

PSEUDO-RIGID-BODY MODELING CAN SIMULATE COMPLEX COMPLIANT MECHANISMS WITHOUT SOLVING KINEMATICS

Domas M. Syaifoel[1*], Michaël Wiertlewski[1], Just L. Herder[1]

[1] Delft University of Technology, The Netherlands, {* d.m.syaifoel@tudelft.nl}

1 INTRODUCTION

Pseudo-rigid-body models (PRBMs) are commonly used to model compliant mechanisms, requiring less computational resources than finite element models (FEM) while retaining accuracy. When designing a compliant mechanism, the kinematics of a rigid-link equivalent are usually analyzed first, which is computationally expensive, especially for spatial and parallel mechanisms. Then, a compliant version is devised, usually using lumped compliance. This method has been validated for complex kinematics [1, 2, 3]. However, this approach requires computationally expensive calculation of the kinematics and was validated mostly for lumped compliance in planar mechanisms. In this paper, we present an energy-based method in which the kinematics do not need to be calculated, allowing faster design iterations. We show that both lumped and distributed compliance can be considered, and extend PRBMs to spatial mechanisms. Additionally, we provide a user-friendly code and validate its performance using a representative design example.

2 METHOD

To avoid computationally expensive calculations, we allow the mechanism to assume arbitrary configurations, including those kinematically inconsistent with rigid links. This is achieved by introducing prismatic joints with linear springs into the links and minimizing the total potential energy of the system. Following standard PRBM conventions, the part of the flexure between the joints is modeled to have length $l'_0 = \gamma l$, where $\gamma \approx 0.85$ [4, 5] and l is the original length of the flexure. The energy as function of the attached body poses $\mathbf{q}_1, \mathbf{q}_2$ is then $V_\kappa = \frac{1}{2}\kappa(\theta_1^2(\mathbf{q}_1, \mathbf{q}_2) + \theta_2^2(\mathbf{q}_1, \mathbf{q}_2))$ where $\kappa = \frac{2\gamma\kappa_\theta EI}{l}$ and $\kappa_\theta \approx 2.65$ [4, 5], E is the Young's modulus of the material, I is the second moment of area of the flexure in bending direction. We propose adding the prismatic joint with a linear spring, between each revolute joint, see Figure 1: $k = \frac{EA}{l'_0}$, $V_k = \frac{1}{2}k(l'(\mathbf{q_1}, \mathbf{q}_2) - l'_0)^2$, $V_{\text{flexure}} = V_\kappa + V_k$, with A the cross sectional area of the flexure, and l' the distance between the revolute joints. We create a PRBM of rigid bodies i with poses $\mathbf{q}_i$, with flexures between bodies as desired. Then we can calculate the total energy of the PRBM as function of all poses. By minimizing this energy, we can calculate the following without considering kinematics: the equilibrium pose of the system due to imposed displacements; the reaction forces needed to hold a certain pose, i.e. the gradient of the energy using e.g. finite differences; and the equilibrium pose due to an imposed conservative force using an additional potential. We 3D-print a "twister" model in Figure 2, which is a complex parallel mechanism with distributed compliance, consisting of a base, and end-effector and an intermediate platform, and visualize its PRBM using our novel software package (Figure 3). We validate this package using an experimental setup consisting of three linear stages and one 6-axis force-torque sensor, as shown in Figure 4. We evaluate three scenarios: the steady-state force-displacement behavior of each sample, the compression-relaxation behavior of a sample over time, and the behavior over time of a sample following a more complex path of compression and shear.

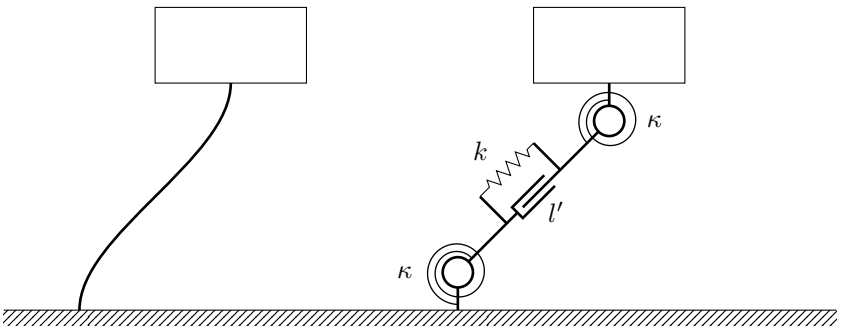

Figure 1: A novel PRBM of a flexure with an additional prismatic joint containing a linear spring with stiffness k.

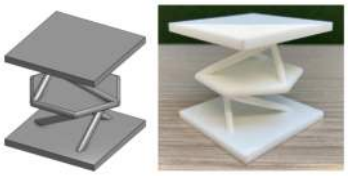

Figure 2: A 3D model and 3D print.

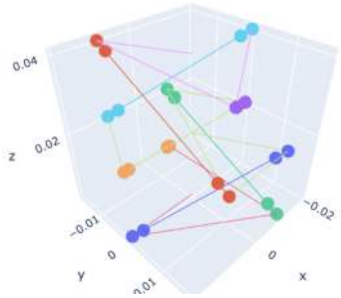

Figure 3: Visual output of the PRBM.

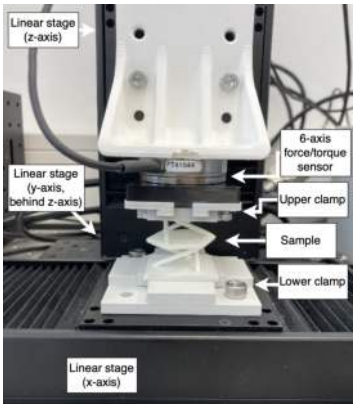

Figure 4: Experimental setup.

3 RESULTS

We compare predicted values (lines) with measured values (crosses). Figure 5: static displacement-force curves (blue, red, green denote a scaling factor of 1.0, 1.2, 1.4 respectively). Figure 6: dynamic reaction force due to imposed compression. Figure 7: dynamic reaction forces due to multi-DoF imposed displacement (blue, red, green denote x, y, z respectively).

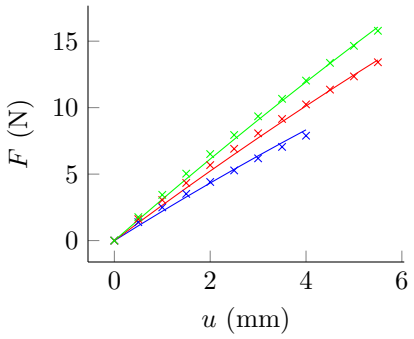

Figure 5: Static displacement-force results over different scaling factors.

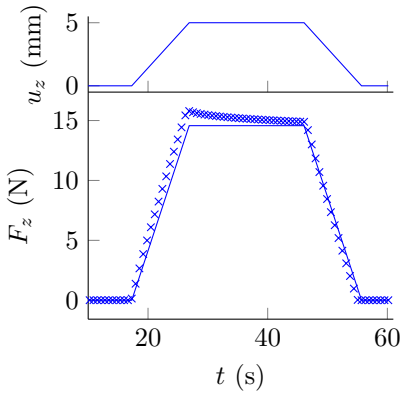

Figure 6: Dynamic compression-force results over time.

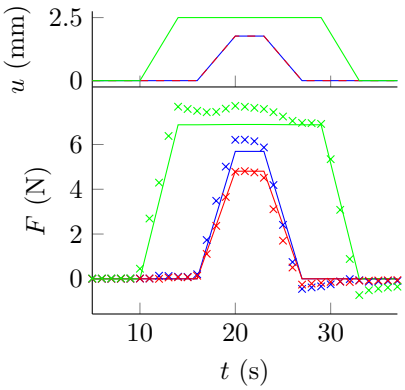

Figure 7: Dynamic displacement-force results for a complex path.

On the free Google Colab runtime, the code determines the pose due to an imposed displacement in less than 5 ms and solves all six reactions required to hold a displacement in less than 1 s.

4 DISCUSSION AND CONCLUSION

We observe that the measured force response aligns with the predicted values, except for non-static, i.e. visco-elastic, behavior, which was not included in the scope of the method. We conclude that the proposed method can be used to accurately design compliant mechanisms, including complex spatial and parallel mechanisms, allowing for an iterative design approach without expensive FEM simulations. The code is available open-source at `https://github.com/dmsyaifoel/pyRBM`.

References

[1] Ruizhou Wang and Heng Wu. "Design and Performance of a Spatial 6-RRRR Compliant Parallel Nanopositioning Stage". In: *Micromachines* 13.11 (2022). Cited by: 11; All Open Access, Gold Open Access, Green Open Access. DOI: 10.3390/mi13111889.

[2] Jihao Liu et al. "A novel miniature spatial hybrid compliant-paralleled mechanism for film micropump". In: Cited by: 2. 2015, pp. 2010–2015. DOI: 10.1109/ICIEA.2015.7334443.

[3] Defu Zhang et al. "Design and Assessment of a 6-DOF Micro/Nanopositioning System". In: *IEEE/ASME Transactions on Mechatronics* 24.5 (2019). Cited by: 36; All Open Access, Green Open Access, pp. 2097–2107. DOI: 10.1109/TMECH.2019.2931619.

[4] Craig Lusk. "Using Pseudo-Rigid Body Models". In: *Handbook of Compliant Mechanisms* (2013), pp. 55–76.

[5] Christopher A Mattson. "Synthesis through rigid-body replacement". In: *Handbook of compliant mechanisms* (2013), pp. 109–121.

ZERO STIFFNESS MECHANISM FOR CONSTANT COMPRESSION PRESSURE ON PRISMATIC AND POUCH CELLS IN BATTERY MODULES

Chinmaya Patil[1], Madhusudan Raghavan[1], Shashank Ramesh[2]

[1] General Motors Research & Development, 30470 Harley Earl Blvd, Warren, MI 48092, USA. {Chinmaya.patil@gm.com; Madhu.Raghavan@gm.com}

[2] Computational Robot Design and Control, University of Notre Dame, USA. {sramesh@nd.edu}

1. INTRODUCTION

Lithium ion cells in prismatic and pouch cell formats undergo geometric deformation along the thickness dimension, reversibly during cycling operation due to material movement between electrodes, and irreversibly over time due to unwanted side reactions between the active materials and electrolyte, as shown in Figure 1 (a). When the cells are arranged in a module or pack as shown in a schematic representation in Figure 1 (b), a compliant material is applied between the cells to provide room for the cells to grow over time. The challenge with this arrangement is that the compression force on the cells has to be kept small at the time of assembly (or beginning of life (BOL)) since the force increases over time up to end of life (EOL) with increase in cell thickness.

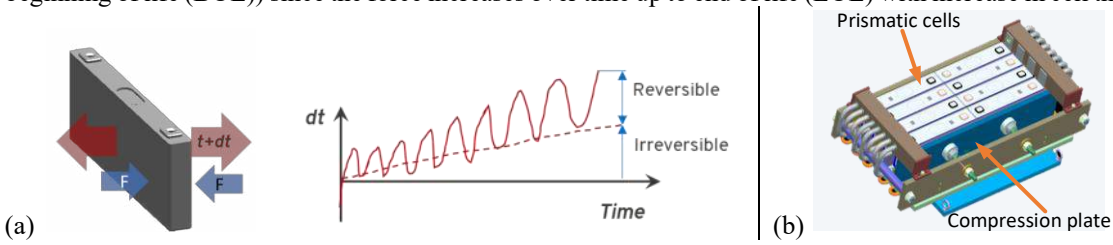

Figure 1. Lithium ion cells schematic representation; (a) thickness growth over time, (b) arrangement of prismatic cells in a test module.

Researchers have shown that applying a constant high compression force on the cells from BOL to EOL can yield significant improvement in the cycle life of the cells [1][3]. Deich et. al. [1] use a pneumatically controlled experimental setup to study the impact of varying module stiffness and compression pressures on a lithium ion pouch cell aging, concluding that the combination of high compression pressure and very low module stiffness results in up to 10% lower capacity face over 1000 charge-discharge cycles. Similar results were presented by Aufschläger el. al. [3], also using precision pneumatic controlled bellow springs to apply different constant compression forces on the cells.

In this paper, we present a passive mechanical device with near zero stiffness that can apply constant compression force to the cells over the range of the dimensional changes from cell cycling and aging. The underlying kinematics of the device are based on the classical 'double slider constant force mechanism' that is used in several industrial applications such as mechanical overload protection, biomedical application, precision watches and robot end-effectors [4]. The parameters of the mechanism geometry and spring stiffnesses are determined to apply the required cell compression force for a representative prismatic cell. A proof of concept of the mechanism is built and the force versus displacement behavior is characterized experimentally.

2. ZERO STIFFNESS MECHANISM OVERVIEW

Figure 2 shows a schematic representation of a double slider constant force mechanism and its operation. The mechanism has a single degree of freedom, namely, translation along the Y-axis. The movable plate is in contact with the cell sidewall. As the cell expands and contracts during cycling, the cell sidewall causes displacement of the movable plate which results in a reaction force on the cell due to the mechanism springs. The kinematics of the mechanism keeps the reaction force constant over the allowable displacement range of the cell/movable plate, as is determined by the following governing equations.

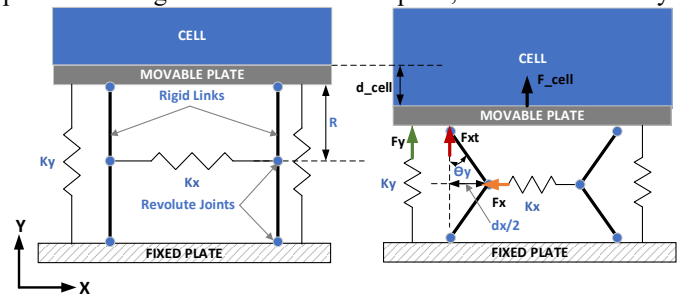

The reaction force on the cell is given by,

$$F_{cell} = F_y + 2 * F_{xt} = \overbrace{K_y * d_{cell}} + 2 * \overbrace{(2 * K_x * R - K_x * d_{cell})} \quad (1)$$

Define, $K_y = 2 * K_x = K$, (2)

Then, $F_{cell} = 2 * K * R.$ (3)

Also, $d_{cell} = 2R - \sqrt{(4R^2 - d_x^2)}.$ (4)

Figure 2. Schematic representation of the double crank constant force mechanism, and the governing equations.

Thus, by proper selection of the mechanism parameters of the rigid link length and spring stiffness, the mechanism can be designed to apply the desired constant compression force on the cells in the battery module.

3. PROOF OF CONCEPT MECHANISM, SIMULATION AND EXPERIMENTAL VALIDATION

Figure 3 (a) shows a schematic representation of a proof-of-concept double slider mechanism design. In order to achieve the desired single degree of freedom of motion for the movable plate along the Y axis, the proposed design uses symmetry about the X-Y plane and actual sliders on rails in place of double cranks. The relationship between the X and Y axes stiffnesses from Eqn. (2) is achieved by using identical springs, two of them in the X-direction and four in the Y-direction as seen in the CAD representation of the mechanism design as shown in Figure 3 (b). The rigid links are mounted to the movable plate and the sliders via ball bearings to replicate revolute joints. For the proof-of-concept mechanism, the rigid link length was chosen as 32.8 mm, and the spring stiffness was chosen as 0.245 N/mm, to yield a constant reaction force of 64.3 N. Figure 3 (c) shows the assembled mechanism installed in a force tester for experimental characterization of displacement and reaction force.

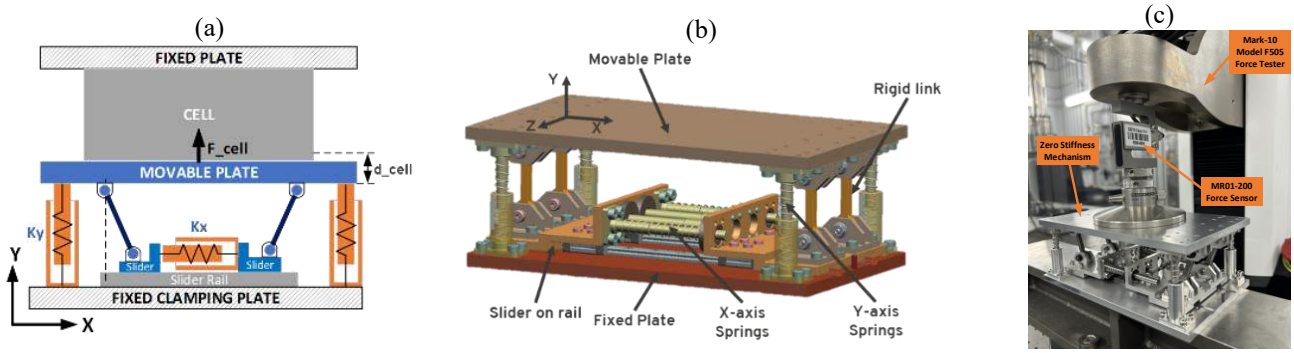

Figure 3. Proof-of-concept design of a double slider zero stiffness mechanism; (a) schematic, (b) CAD, (c) mechanism under force tester.

Figure 4 (a) shows the results of quasi-static simulation of the proof-of-concept mechanism, using the constitutive equations developed in the previous section. Within the physical limit of the mechanism displacement, the reaction force on the cell is constant (64.3 N). Figure 4 (b) shows the experimentally measured reaction force plotted versus the displacement of the movable plate. The speed of the movable plate was held constant at 0.0155 mm/s during the experiment. The predicted constant reaction force from the mechanism is overlaid on the force axis for reference.

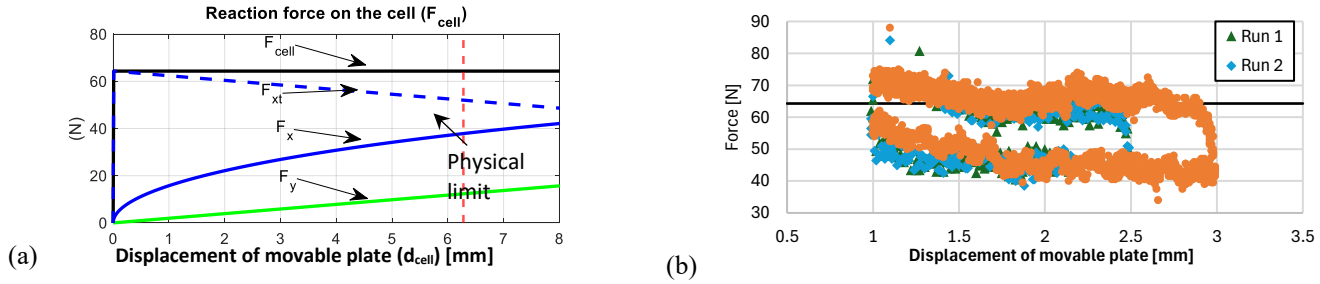

Figure 4. Force versus displacement results for the Proof-of-concept mechanism: (a) simulation results, (b) experimental results.

From the experimental data, it is observed that the mechanism exhibits hysteresis in the reaction force, with the magnitude of the force dependent upon the direction of motion of the movable plate. It is observed that the force is lower than the predicted value in compression, while in relaxation mode the reaction force is very close to the predicted value. This phenomenon is indicative of static friction within the mechanism. However, within small displacement ranges, the reaction force is nearly constant in both compression and relaxation modes. For example, in the 1.5 mm to 2.5 mm displacement region, the reaction force in the compression and relaxation modes is steady at 44 N and 65 N, respectively. Modifying the design by replacing the mechanism joints by compliant flexure joints [5] is possible approach to eliminate the static friction and hence the hysteresis in the reaction force. The zero-stiffness mechanism has potential application in battery pack designs to manage the prismatic and/or pouch cell thickness growth over time.

REFERENCES

[1] Deich et.al., (2021), "Effects of module stiffness and initial compression on lithium-ion cell aging", *Journal of Power Sources*, 506 (2021) 230163.

[2] Cui et.al., (2021), "Effect of continuous pressures on electrochemical performance of Si anodes", *Materials Today Energy*, 20, 100632.

[3] Aufschläger, A., et. al., (2024), "Optimizing mechanical compression for cycle life and irreversible swelling of high energy and high power lithium-ion pouch cells", *Journal of Energy Storage*, 76, 109883.

[4] Wang P., et.al., (2018), "Design and modeling of constant-force mechanisms: A survey", *Mechanism and Machine Theory*, Volume 119, Pages 1-21.

[5] Carson, J., et.al., (2024), "An Introduction to Flexure Design", *47th Aerospace Mechanisms Symposium*, Virginia Beach, VA, May 15 – 17, pp. 413 – 428.

SNAPPING FOUR BAR MECHANISMS: DISCRETE ASSEMBLY CONFIGURATIONS IN CLOSED-LOOP LINKAGES

Andreas Mair, Daren A. Thimm, Martin Pfurner

University of Innsbruck, Unit of Geometry and Surveying, Technikerstraße 13, 6020 Innsbruck, Austria,
{and.mair@uibk.ac.at; daren.thimm@uibk.ac.at; martin.pfurner@uibk.ac.at}

1 INTRODUCTION

The study of mobile spatial closed-loop four-bar linkages constitutes a well-established domain in kinematic analysis [1, 2, 3, 4, 5]. In contrast, the synthesis of snapping four-bar mechanisms remains comparatively under-researched [6, 7]. While the former relies on special geometric conditions to enable continuous motion – most notably in the Bennett mechanism [8] – the general spatial closed 4R linkage is a rigid structure with zero degrees of freedom, typically admitting only a single assembly configuration. This work focuses on the synthesis of bistable snapping mechanisms, a specific subclass of these rigid loops designed to possess two discrete, isolated assembly modes. Consequently, the transition between these equilibrium configurations is not a kinematic motion, but a deformation-driven snap governed by the system's compliance. This bistable behavior distinguishes them from both standard rigid structures and continuous-motion linkages, offering defined output states without the requirement for continuous actuation.

2 THEORETICAL BACKGROUND

In the context of spatial kinematics we use dual quaternions to represent rigid body displacements. By interpreting dual quaternions as elements in projective 7-space $\mathbb{P}^7$, the set of all rigid body displacements corresponds to points on the Study quadric defined by dual quaternions with real, non-zero norm, i.e.

$$\mathcal{S} \coloneqq \{q \in \mathbb{DH} \mid qq^* \in \mathbb{R} \setminus \{0\}\} = \{\mathbf{x} \in \mathbb{P}^7 \mid x_0x_4 + x_1x_5 + x_2x_6 + x_3x_7 = 0\} \tag{1}$$

For a $2R$ chain, the possible displacements of the end-effector can be parametrized using dual quaternions representing displacements about the two axes

$$(t_1 - \ell_1)(t_2 - \ell_2) = t_1t_2 - t_1\ell_2 - t_2\ell_1 + \ell_1\ell_2, \tag{2}$$

where ℓ_i is the vectorial dual quaternion representing the line of the i-th revolute joint axis, and t_i is the cotangent of half of the rotation angle of the i-th joint. This parametrization defines a motion quadric on $\mathcal{S}$ located within a 3-dimensional linear subspace of $\mathbb{P}^7$, spanned by the basis $\text{span}\{1, \ell_1, \ell_2, \ell_1\ell_2\}$.
The assembly modes of a closed-loop 4R mechanism are determined by the intersection of the linear projective subspaces associated with two such $2R$ chains [9, 10]. In $\mathbb{P}^7$, two arbitrary 3-dimensional subspaces are generically skew; thus, four randomly chosen spatial links generally cannot be assembled into a closed loop. For an assembly to exist, specific geometric constraints must be satisfied to force these subspaces to intersect.

- **Rigid Structure (Single Assembly):** The subspaces intersect in a single point. If this point lies on the Study quadric, it corresponds to the unique assembly configuration of a standard zero-DOF structure.
- **Snapping Mechanisms (Bistable):** In this case, the subspaces intersect in a line. The valid configurations correspond to the intersection points of this line with the Study quadric, typically yielding two distinct, real solutions. These solutions represent the two stable equilibrium poses of the snapping mechanism.
- **Shaky Mechanism:** This is a special case of the previous one, where the line is tangent to the Study quadric. Although it is theoretically rigid, it slightly moves in physical realizations because of joint clearances and compliance of the material.
- **Bennett Mechanism (Mobile):** The geometric constraints are more restrictive, causing the subspaces to coincide. The intersection of the coincident subspaces with the Study quadric then forms a degree 4 curve, enabling the mechanism's 1-DOF motion.

3 SYNTHESIS OF SNAPPING CLOSED-LOOP LINKAGES

The synthesis of snapping four-bar mechanisms involves determining the geometric constraints such that the two $2R$ subspaces intersect in a line that intersects the Study quadric in two distinct points. We would like to freely choose these two positions and obtain the necessary conditions on the axes of the revolute joints to achieve this. We call the axes of our first $2R$ chain ℓ_1, ℓ_2, and the axes of the second $2R$ chain ℓ_3, ℓ_4, where ℓ_1 and ℓ_4 are the axes attached to the fixed frame link. This problem can be simplified without loss of generality as follows.

1. One of the two positions can be set to be the identity. For two poses $P_1, P_2 \in \mathbb{DH}^\times := \{h \in \mathbb{DH} \mid hh^* \in \mathbb{R} \setminus \{0\}\}$ we can put
$$\tilde{P}_1 := 1, \quad \tilde{P}_2 := P_1^{-1} P_2. \tag{3}$$
2. The placements of the two base axes of the resulting $4R$ chain can be chosen to have unit distance where ℓ_1 coincides with the z-axis and the common normal of ℓ_1 and ℓ_4 coincides with the x-axis. This can be achieved by a suitable choice of the fixed frame. Therefore, $\ell_1 := \mathbf{k}$ and $\ell_4 := \mathbf{j} + \kappa\mathbf{k} + \nu\varepsilon\mathbf{i}$ for some $\kappa, \nu \in \mathbb{R}$.

From this data we can derive the necessary conditions for the closure of the loop. We want to determine ℓ_2, ℓ_3 such that
$$(t_1 - \ell_1)(t_2 - \ell_2) = (t_4 - \ell_4)(t_3 - \ell_3) = \tilde{P}_2, \tag{4}$$
where all equalities are to be understood in $\mathbb{P}^7$ and $t_i \in \mathbb{P}^1$. Furthermore, ℓ_2, ℓ_3 are constrained to be Plücker coordinates. Therefore, we have $4 + 2 + 2 \times 6 = 18$ unknowns in $2 + 2 \times 8 = 18$ equations. This system of equations is generically solvable. The solution of this system gives us a closed-loop 4R linkage that can be assembled in two poses. The joint angles are given by inverse cotangents of the parameters t_i where the identity pose is the one with $t_i = \infty$ for all i.

ACKNOWLEDGMENTS

We gratefully acknowledge the support of the bilateral Austrian–Korean project "Surface generation via integrable evolution of curves," which is funded by OeAD-GmbH (Austria's Agency for Education and Internationalization, project no. KR 02/2025), and the National Research Foundation of Korea (project no. RS-2025-1435299).

REFERENCES

[1] J. Krames, "Zur Geometrie des Bennett'schen Mechanismus". *Sitzungsberichte der Akademie der Wissenschaften in Wien, Mathem.-naturw. Klasse, Abteilung IIa*, vol. 146, 1. und 2. Heft, pp. 159–173, 1937.

[2] J.M. Hervé and M. Dahan, "The two kinds of Bennett's mechanism". In *Proceedings of the 6th World Congress on the Theory of Machines and Mechanisms*, New Delhi, India, 1983.

[3] J.E. Baker, "The Bennett linkage and its associated quadric surfaces". *Mechanism and Machine Theory*, vol. 23(2), pp. 147-156, 1988, doi:10.1016/0094-114X(88)90092-4.

[4] A. Perez and J.M. McCarthy, "Bennett's linkage and the cylindroid". *Mechanism and Machine Theory*, vol. 37, pp. 1245–1260, 2002.

[5] M. Pfurner and T. Stigger and M.L. Husty, "Algebraic analysis of overconstrained single loop four link mechanisms with revolute and prismatic joints". *Mechanism and Machine Theory*, vol. 114, pp. 11-19, 2017, doi:10.1016/j.mechmachtheory.2017.03.014.

[6] H. Stachel and D. Huczala, "From Henrici's flexible hyperboloid to snapping spatial four-bars". *Mechanism and Machine Theory*, vol. 212, pp. 106057, 2025, doi:10.1016/j.mechmachtheory.2025.106057.

[7] M. Pfurner and D. Huczala, "Change of Kinematic Structures via Snapping Mechanisms". In *Proceedings of 8th International Workshop on Computational Kinematics (CK2025)*, Springer, in production. doi: 10.5281/zenodo.15736611 (supplementary material).

[8] G.T. Bennett, "A new mechanism". *Engineering*, vol. 76, pp. 777-778, 1903.

[9] J.M. Selig, *Geometric Fundamentals of Robotics*. Springer, New York, Monographs in Computer Science, 2005.

[10] T.-D. Rad, D.F. Scharler, H.-P. Schröcker, "The kinematic image of RR, PR, and RP dyads". *Robotica* vol. 36(10), pp. 1477-1492, 2018, doi:10.1017/S0263574718000504.

COMPARISON OF PRISM-BASED TENSEGRITY JOINT ARCHITECTURES

Karol Muñoz[1], Mathieu Porez[2], Philippe Wenger[3]

Nantes Université [1,3], École Centrale Nantes[1,3], IMT Atlantique[2], CNRS[3], LS2N, UMR 6004, F-44000 Nantes, France

[1]{karol.munoz-salas@ls2n.fr}
[2]{mathieu.porez@imt-atlantique.fr}
[3]{philippe.wenger@ls2n.fr}

1 INTRODUCTION

Cable-based transmission is widely used in lightweight and redundant robotic manipulators [1]. By relocating actuators and transmitting forces through tension elements, these approaches reduce moving inertia and enable distributed force transmission. Such transmission is employed in different classes of robotic mechanisms, including continuum robots [2] and joint-based manipulators incorporating spherical or universal joints. However, since cables can only transmit tensile forces, motion and stability depend on maintaining appropriate tension distribution [1]. As a result, controlling torsional behavior can become challenging and may limit positioning accuracy and load transmission.

Tensegrity-inspired mechanisms introduce an alternative approach by combining tension elements with compression members. In such designs, geometric constraints may directly influence torsional behavior and motion definition. Several tensegrity-based joint designs have been proposed, including asymmetric architectures with variable stiffness capabilities [3]. In the present study, however, the focus is placed on symmetric architectures inspired by the classical prism described by Burkhardt [4], which provide a simple layout well suited for systematic design analysis.

The present work considers three symmetric joint architectures derived from a two-degree-of-freedom prism-based tensegrity joint previously introduced in [5, 6]. The mechanism consists of two platforms connected by three compression legs and three peripheral cables, each associated with a passive linear spring. The three variants share this peripheral arrangement and differ only in the nature of the central element: (i) a passive universal joint, (ii) a telescopic U–P–U central leg, and (iii) a passive central spring. The objective of this work is to compare closely related prism-based tensegrity joints in order to understand how design choices affect mechanical behavior and to clarify the associated trade-offs.

2 DESCRIPTION OF THE JOINT ARCHITECTURES

Building on the architectures introduced above, this section analyzes the latter two joint architectures, which share the same prism-based topology and peripheral cable–spring arrangement but differ in the nature of the central element governing the joint kinematics and torsional behavior.

The first architecture incorporates a rigid telescopic U–P–U central leg, as shown in Fig. 1. This leg geometrically constrains the relative motion between the platforms by suppressing torsional freedom about the leg axis. The joint kinematics are therefore explicitly defined by this central constraint, resulting in predictable motion behavior and inherent resistance to torsional disturbances. This design, however, reduces geometric adaptability and increases mechanical complexity.

Figure 1: Tensegrity joint with a rigid telescopic U–P–U central leg.

The second architecture replaces the rigid U–P–U central leg with a passive linear spring. In this case, the central element does not impose a geometric torsional constraint on the moving platform. Relative torsional motion emerges from force equilibrium within the cable–spring network rather than from an explicit kinematic restriction. As a consequence, the mechanism becomes more compliant. The deformation of the central spring contributes to the global

equilibrium and directly influences the relative architecture of the moving platform. The joint behavior is therefore governed by the coupling between geometry and internal force distribution, leading to increased adaptability but reduced torsional stiffness compared to the rigid-leg architecture.

3 COMPARATIVE ANALYSIS FRAMEWORK

The comparison of the considered architectures is carried out within a unified kinetostatic framework, consistent with the modeling approach adopted in our previous works [5, 6].

For each architecture, the analysis is structured into three complementary stages. First, the set of admissible geometric configurations of the moving platform is determined by enforcing the constraints imposed by the compression members and cable attachment locations. This step defines the geometric workspace. Second, the static equilibrium of the mechanism is formulated to establish the relationship between cable tensions and external wrenches applied to the moving platform, following standard approaches in parallel mechanism analysis [8, 9]. This leads to the characterization of the wrench feasible workspace. Third, the stiffness properties of the mechanism are evaluated by analyzing the linearized relationship between incremental wrenches and the resulting platform displacements about equilibrium configurations. Since stiffness depends on both the geometry and the internal tension distribution, it is inherently influenced by the actuation or pre-tension levels applied to the cables. This stage enables the assessment of how architecture and geometric parameters jointly affect rigidity and its evolution under actuation.

By applying this common analytical procedure to each complete mechanism, a consistent comparison of geometric mobility, wrench transmission capability, and stiffness behavior across architectures is achieved.

4 DISCUSSION AND PERSPECTIVES

The comparative framework adopted in this work focuses on mechanisms that share a common prism-based topology and similar peripheral components. By restricting the comparison to closely related architectures, the analysis isolates the mechanical implications of targeted design choices rather than pursuing parameter optimization.

The comparison reveals explicit trade-offs between geometric workspace, wrench-feasible workspace, and stiffness. Architectures that achieve larger geometric workspaces do so at the cost of reduced wrench transmission capability or stiffness, whereas designs favoring force transmission and rigidity inherently operate over more restricted geometric ranges. The interaction between geometric design parameters defines trade-offs between the different capabilities of the mechanism, such that improvements do not occur independently. In this sense, the purpose of the analysis is not to identify optimal parameter sets, but to clarify what must be conceded in order to gain geometric workspace, and conversely, which limitations arise when wrench transmission or stiffness is prioritized.

This work thus provides a comparison of prism-based tensegrity joints, highlighting the advantages and limitations associated with each architecture. Future numerical investigations will further quantify these trade-offs across relevant parameter ranges and support informed design decisions based on task-specific performance requirements.

REFERENCES

[1] Zhang, X., Chen, Q., Gao, F., and Hao, K., "State-of-the-art on theories and applications of cable-driven parallel robots," *Frontiers of Mechanical Engineering*, vol. 17, no. 3, pp. 1–25, 2022.

[2] Russo, M., Sadati, S. M. H., and Rucker, D. C., "Continuum robots: An overview," *Advanced Intelligent Systems*, vol. 5, no. 3, 2023.

[3] I. John, S. Mohan, and P. Wenger, "Kinetostatic Analysis of a Spatial Cable-Actuated Variable Stiffness Joint," *ASME Journal of Mechanisms and Robotics*, vol. 16, no. 9, p. 091003, 2024. doi: 10.1115/1.4064254.

[4] R. W. Burkhardt, *A Practical Guide to Tensegrity Design*, Cambridge, USA, 2008.

[5] K. Muñoz, M. Porez, and P. Wenger, "Kinematic and static analyses of a 3-DOF spatial tensegrity mechanism," in *Advances in Robot Kinematics 2024*, J. Lenarčič and M. Husty, Eds., Springer Proceedings in Advanced Robotics, vol. 31, Springer, 2024, p. 36.

[6] K. Muñoz, M. Porez, and P. Wenger, "Modeling and analysis of a four-leg tensegrity mechanism," *Mechanism and Machine Theory*, vol. 211, p. 106009, 2025.

[7] S. Venkateswaran, D. Chablat, and D. Creusot, "Design and Analysis of a Series–Parallel Hybrid 3-SPS-U Mechanism," in *Proceedings of the ASME 2023 International Design Engineering Technical Conferences and Computers and Information in Engineering Conference (IDETC/CIE)*, Vol. 8: 47th Mechanisms and Robotics Conference (MR), ASME, 2023, Paper No. V008T08A006. doi: 10.1115/DETC2023-115225.

[8] J.-P. Merlet, "Direct kinematics and static analysis of parallel manipulators using a distance matrix," *International Journal of Robotics Research*, vol. 11, no. 4, pp. 326–333, 1992.

[9] W. Khalil and E. Dombre, *Modeling, Identification and Control of Robots*, Taylor & Francis, 2002.

CABLE ANCHOR SENSITIVITY ANALYSIS FOR RECONFIGURABLE CABLE ROBOTS

Hung Hon Cheng[1], Josie Hughes[1]

[1] CREATE LAB, EPFL, Switzerland, {hung.cheng@epfl.ch; josie.hughes@epfl.ch}

1 INTRODUCTION

Traditional single-link cable-driven parallel robots have limited moment-arm capability near workspace boundaries. Even small wrenches may require large cable forces, resulting in highly unbalanced tension distributions. Reconfigurable cable robots resolve this issue by introducing actuation redundancy through mechanisms such as linear rails, mobile platforms, or spatial reconfiguration systems (e.g., aerial or mobile bases) [1]. Although this redundancy improves wrench feasibility, it increases workspace complexity and complicates control, especially when multiple reconfigurable elements are involved.

A key challenge is selecting which cable(s) to reconfigure. Existing approaches mainly consider low-dimensional mechanism-level reconfiguration and rely on manual selection or exhaustive search. A straightforward method evaluates all candidate anchor configurations [2], but the number of combinations grows rapidly with the number of reconfigurable cables (r) and the dimension of the reconfiguration mechanism ($1 \leq d \leq 3$). The complexity scales as $\mathcal{O}(dr)$, followed by solving a cable-force via quadratic program for each case, and eventually searching for optimal configuration, this makes real-time implementation impractical. To address this limitation, this work proposes a computationally efficient sensitivity analysis that identifies the most beneficial cable for reconfiguration. The sensitivity metric is obtained directly from the quadratic programming solution of cable tensions without additional computation. Combined with a closed-form reconfiguration formulation, the problem can be expressed as a linear or quadratic program, making real-time implementation or integration within a model predictive control framework possible. The following section summarizes the formulation and representative results. Complete proofs are later provided in the full-length version.

2 METHOD SUMMARY AND RESULT

This section presents a compact sensitivity analysis model of a reconfigurable cable robot. Only the kinematics is considered and inertia and dynamics of moving anchor points are not included. For an n-DoF system with m cables and $r \leq m$ reconfigurable elements, the equation of motion is

$$M(\mathbf{q})\ddot{\mathbf{q}} + \mathbf{C}(\mathbf{q}, \dot{\mathbf{q}}) + \mathbf{G}(\mathbf{q}) + \mathbf{w}_{ext} = \mathbf{J}(\mathbf{U})\mathbf{f}. \tag{1}$$

Here $M(\mathbf{q}) \in \mathbb{R}^{n\times n}$ is the mass–inertia matrix, $\mathbf{C}(\mathbf{q}, \dot{\mathbf{q}}) \in \mathbb{R}^n$ is the Coriolis/centrifugal term, and $\mathbf{G}(\mathbf{q}), \mathbf{w}_{ext} \in \mathbb{R}^n$ are gravity and external wrenches. $\mathbf{J}(\mathbf{U}) \in \mathbb{R}^{n\times m}$ is the structure matrix depending on the reconfiguration vector $\mathbf{U} \in \mathbb{R}^{dr}$, where each $\mathbf{u}_i \in \mathbf{U} = [u_{ix}, u_{iy}, u_{iz}]^\top$ are the x-y-z coordinate of each anchoring point. $\mathbf{f} \in \mathbb{R}^m$ denotes the cable forces. For simplicity, we define $\mathbf{w} = M(\mathbf{q})\ddot{\mathbf{q}} + \mathbf{C}(\mathbf{q}, \dot{\mathbf{q}}) + \mathbf{G}(\mathbf{q}) + \mathbf{w}_{ext}$. Cable forces are obtained from the quadratic program

$$\min_{\mathbf{f}} \ \frac{1}{2}\mathbf{f}^T\mathbf{f} \quad \text{s.t.} \quad \mathbf{w} = \mathbf{J}(\mathbf{U})\mathbf{f}, \quad \mathbf{f} \geq \mathbf{0}. \tag{2}$$

Let the objective function's cost in changing $\mathbf{f}$ or $\mathbf{U}$ be $V(\mathbf{f}, \mathbf{U})$. Under a small anchor displacement $\Delta\mathbf{U}$ inducing $\Delta\mathbf{J}$, the cost variation (proof omitted) is

$$\Delta V = \lambda^T \Delta\mathbf{J}\mathbf{f}, \tag{3}$$

where $\lambda \in \mathbb{R}^n$ is the sensitivity variable obtained directly from solving (2). ΔV measures how reconfiguration affects the objective function. A larger $|\Delta V|$ with respect to $\delta\mathbf{u}_i$ indicates that cable i has stronger influence on the cost, while the sign indicates increase or decrease. This allows fast ranking of cables' sensitivity for a given wrench and pose. Figure 1(i) shows a redundant spatial cable robot whose base anchors can move freely in space. The robot tracks a 6-DoF trajectory from $\mathbf{q}_0 = [0.5, 0.5, 0.61, 0, 0, 0]^\top$ with

$$\mathbf{q}(\theta) = \begin{bmatrix} q_{0,1} + 0.46\sin\theta & q_{0,2} + 0.46\sin(2\theta) & q_{0,3} & q_{0,4} + 0.092\cos(2\theta) & q_{0,5} + 0.31\sin\theta & q_{0,6} \end{bmatrix}^\top$$

During the trajectory, the most sensitive cable (among 8 cables in 3D) is obtained at each step using a single QP

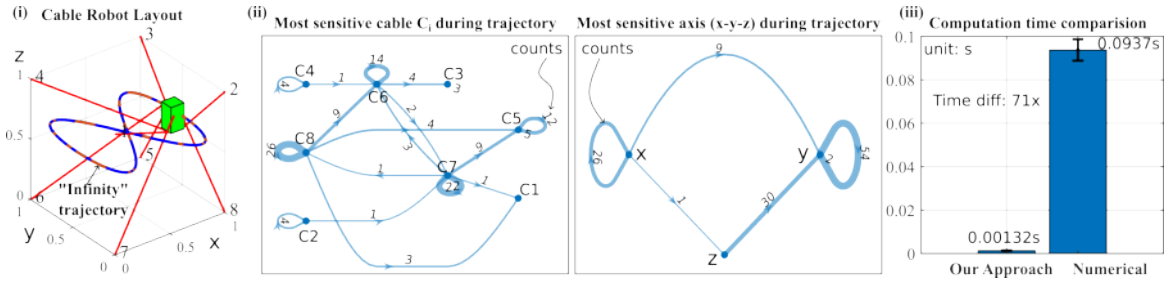

Figure 1: (i) Layout of cable robot with 8 freely movable base anchors and trajectory. (ii) Most sensitive cable and axis (x–y–z) along the trajectory(thicker edges indicate larger sensitivity magnitude) (iii) Computation time comparison between the proposed method and numerical method)

solution followed by a matrix multiplication. Figure 1(ii) shows which cables are most sensitive and their preferred x-y-z directions (Thicker edge means more sensitive). Figure 1(iii) compares computation time with finite-difference evaluation of all combinations. The proposed approach is 71× faster for all the 8×3 elements.
By leveraging this method, anchor points can be ranked for different objectives (e.g., minimizing cable-force norm in (2)). Figure 2 compares optimized reconfiguration and fixed configuration under force bounds 0–200 N. Without reconfiguration, the robot fails to generate the required wrenches in part of the trajectory (shaded region). With reconfiguration, all wrenches are achieved with smooth force transitions, whereas the fixed configuration exhibits force jumps (e.g., time step 20–40). At each step, two iterations are performed. Sensitivity is evaluated for all cables under the current configuration, and the cable that most reduces the objective while satisfying the wrench constraint is selected for reconfiguration. The optimization fomulation are extended from [3] (details omitted due to length).

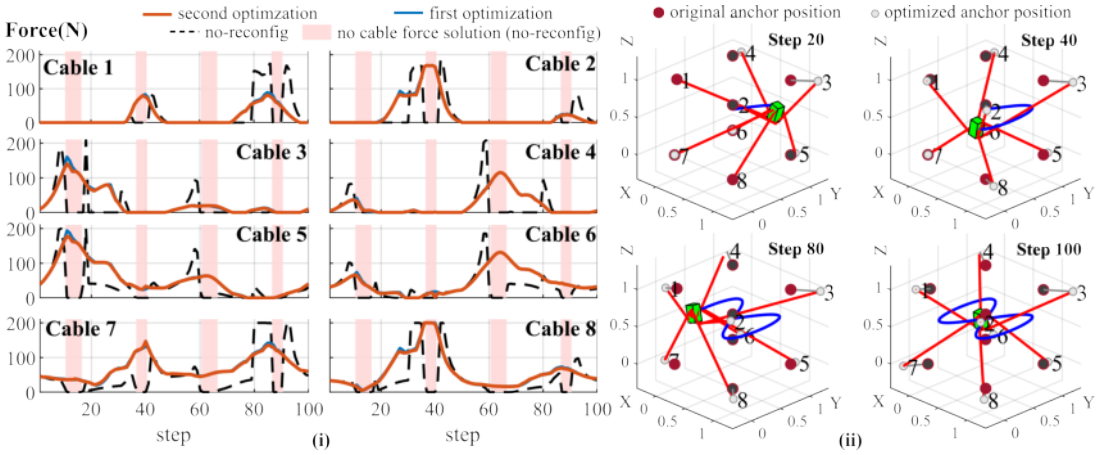

Figure 2: Reconfiguration performance comparison. (i) Cable forces under optimized reconfiguration (solid) and fixed configuration (dashed) with force bounds of 0–200 N; shaded regions indicate wrench infeasibility without reconfiguration. (ii) Representative configurations at selected time steps, showing original and optimized anchor positions.

3 CONCLUSION

The proposed method highlights a rapid evaluation strategy for each reconfigurable cable. The main contribution is the ability to rank cable significance at any given pose, enabling a single-variable and computationally efficient reconfiguration optimization. The reconfiguration step can be formulated under different LP/QP objectives, such as minimizing cable force ratio under wrench-feasibility (or closure) constraints.

REFERENCES

[1] A. Lucarini, E. Idà, and M. Carricato, "Optimal design of a deployable and reconfigurable cable-driven parallel robot," in *2024 20th IEEE/ASME International Conference on Mechatronic and Embedded Systems and Applications (MESA)*. IEEE, 2024, pp. 1–6.

[2] Z. Liang, Z. Chen, S. Tang, L. Kong, H. Wang, and G. Chen, "An offline path planning framework for reconfigurable cable-driven parallel mechanisms via lie algebra interpolation," *Mechanism and Machine Theory*, vol. 220, p. 106349, 2026.

[3] H. H. Cheng and D. Lau, "Cable attachment optimization for reconfigurable cable-driven parallel robots based on various workspace conditions," *IEEE Transactions on Robotics*, vol. 39, no. 5, pp. 3759–3775, 2023.

CREATION OF A CLASS OF SELF-REGULATING MECHANISMS

Konstantin S. Ivanov[1]

[1] Joldasbekov Institute of Mechanics and Engineering MON RK, 050010, Almaty, Shevchenko street, 28, Kazakhstan {dgpimmash@mail.ru}

1. INTRODUCTION

The object of the study is a toothed kinematic chain with two degrees of freedom and with an additional force constraint. Earlier at the MMT Symposium, it was proved that a two-mobile kinematic chain with external translationally moving links can have definability of motion [1]. For this purpose, an additional constraint was introduced into the initial kinematic chain of the mechanism, creating not a kinematic, but a force constraint. The resulting definable structural chain is a self-regulating mechanism that independently changes the gear ratio when the external load changes. Any two-movable kinematic chain is similarly transformed into a definable self-regulating mechanism. The article discusses the transformation of a two-movable kinematic chain of a toothed planetary mechanism into a self-regulating variator and sets out the theory of creating a class of self-regulating mechanisms.

2. DESCRIPTION OF TWO-MOVABLE SINGLE-INPUT SYSTEM WITH ADDITIONAL FORCE CONSTRAINT

The simplest flat two-movable toothed planetary kinematic chain with a single input, with a rotational movement of the outer links (Fig. 1) contains a rack 0, an input solar wheel 1, an intermediate link satellite 2 and an output carrier 3. Link 2 performs a plane-parallel movement, which is reduced to a rotation around the instantaneous center of velocities P. Tension screw 4 in the joint C creates a tunable reaction and frictional moment M_{f32}, which replaces the action of R_{02} the reaction in the pole P when there is no connection to the rack 0. External forces: F- driving force, R - resistance force.

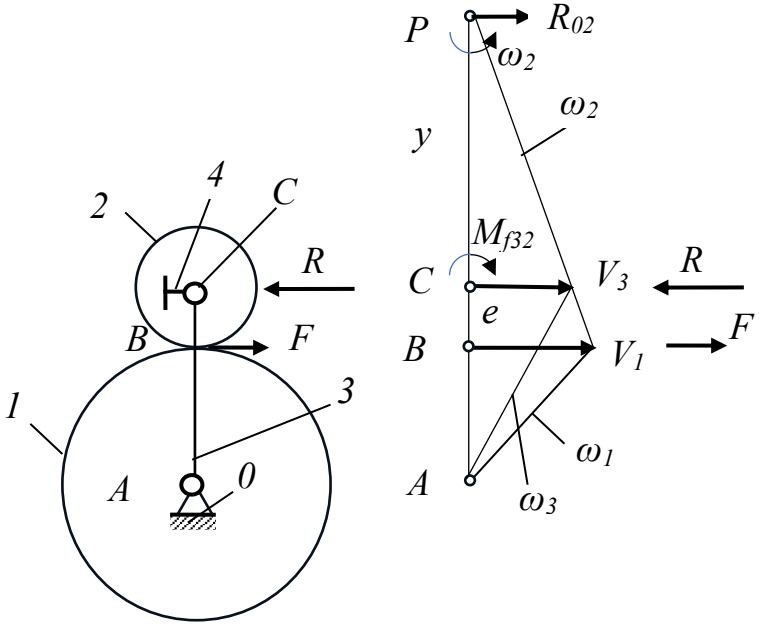

Figure 1. Two-movable toothed planetary structural chain and linear velocity plan.

Let us denote: - the distance between the lines of action of external forces. $BC = e$
$PC = y$ is a variable parameter for the location of the instantaneous center of velocities, determined from the condition or $PC/PB = V_3/V_1$
From here $y = V_3 e/(V_1 - V_3)$.

Here are V_1, V_3 −the linear velocities of points *B* and *C* of links 1 and 3.
$\omega_1 = \frac{V_1}{r_1}, \omega_3 = \frac{V_3}{r_3}$ - angular velocities of external links 1 and 3.
The angular velocity of the intermediate link 2 can be determined by the formula $\omega_2 = (V_1 - V_3)e$.
Formulation of the research task: for the considered two-mobile kinematic circuit under given external forces, to search for means that ensure the achievement of definability of motion.
The definability of the motion of a mechanical system conciseness is considered to be the one-to-one correspondence between the velocity of the output link and the velocity of the input link in the presence of equilibrium in uniform motion with the equality of the work (power) of the motive forces and the resistance forces [2]. The equilibrium of the system is determined by the equations of statics.

3. ANALYSIS OF THE INTERACTION OF PARAMETERS OF A TOOTHED PLANETARY TWO - MOVABLE KINEMATIC CHAIN WITH A FORCE CONSTRAINT

The analysis contains the equations of statics of link 2.
Equilibrium and definability of motion of a two-movable chain can be achieved by replacing the action of the moment of the required reaction R_{02}at the fixed-point *P* with the action of the momentM_{f32} of the interacting forces of the moving links 2 and 3 in the rotational pair *C* [1]. Based on the analysis, a theorem on the definability of the motion of a toothed structural chain is formulated and proved. The principle of virtual work (power) of external forces of link 2 according to equation (5) theoretically determines the necessary and sufficient equilibrium condition of the entire system.

$$FV_1 - RV_3 = 0. \tag{1}$$

The value of the substituting frictional moment acting on link 2 is determined from the condition $\sum M_C = 0$, from which follows the equality of the substituting moment to the required moment $M_{f32} = R_{02}y$.
In order to maintain equilibrium, it is necessary to add the corresponding driving moment, which is contained in the equilibrium condition $\sum M_C = 0$ simultaneously with the addition of the moment of resistance M_{f32}. We will get

$$F(V_1 - V_3) - M_{f32}\omega_2 = 0. \tag{2}$$

The equations (1) and (2) will determine the existence of a two-movable mechanism: equation (2) characterizes the method of creation, and equation (1) determines the technology of self-regulating.
A two-movable toothed planetary kinematic chain with one input acquires the definability of motion if the moment of the required force applied at the instantaneous velocity center is replaced in the equilibrium equations by an equal moment of resistance in the hinge connecting the satellite with the moving link and this moment is balanced by the corresponding motive moment.
As a result of adding equations (1) and (2), we obtain a complete total condition for the interconnection of parameters

$$FV_1 + F(V_1 - V_3) = RV_3 + M_{f32}\omega_2 \quad \text{or} \quad F(2V_1 - V_3) = RV_3 + M_{f32}\omega_2 \tag{3}$$

The expression of efficiency, we get as the ratio of useful power to all spent

$$h = [F(2V_1 - V_3) - M_{f32}\omega_2]/F(2V_1 - V_3) \tag{4}$$

It has been proved that a definable two-movable toothed planetary kinematic chain, defined by two equations of statics, is a self-regulating mechanism. A class of fundamentally new self-regulating mechanisms has been created.

ACKNOWLEDGMENTS

The author sincerely thanks the Ministry of Science and Higher Education of the Republic of Kazakhstan and Joldasbekov Institute of Mechanics and Engineering MON RK for the financial support of fundamental research (grant number: BR31715767).

REFERENCES

[1] K.S. Ivanov. Theorem on the definability of motion of a two-movable kinematic chain with a single input. Books of Abstracts of MMT Symposium – Journal of Mechanism and Machine Theory. Flores et al (Eds). Guimaraes, Portugal. 2024.
[2] N.I. Levitsky. Theory of Mechanisms and Machines. M. Nauka. 1979. 576 p. (In Russian)

COMPUTERIZED GENERATION, TOOTH CONTACT ANALYSIS AND STRESS ANALYSIS OF PERICYCLIC GEAR DRIVES

Ignacio Gonzalez-Perez[1], Ramon Ruiz-Orzaez[1], Alfonso Fuentes-Aznar[2]

[1] Universidad Politécnica de Cartagena, Dept. Mech. Eng., Spain, {ignacio.gonzalez@upct.es; ramon.ruizo@upct.es}
[2] Rochester Institute of Technology, Dept. Mech. Eng., USA, {afeme@rit.edu}

1. INTRODUCTION

A pericyclic gear drive is a compact transmission that utilizes external and internal bevel gears to achieve high gear ratios, typically around 50:1. Fig. 1 shows an example where the input shaft acts as the carrier, driving gears 2 and 3 in a combined rotational and nutational motion, while gear 4 acts as the output member.

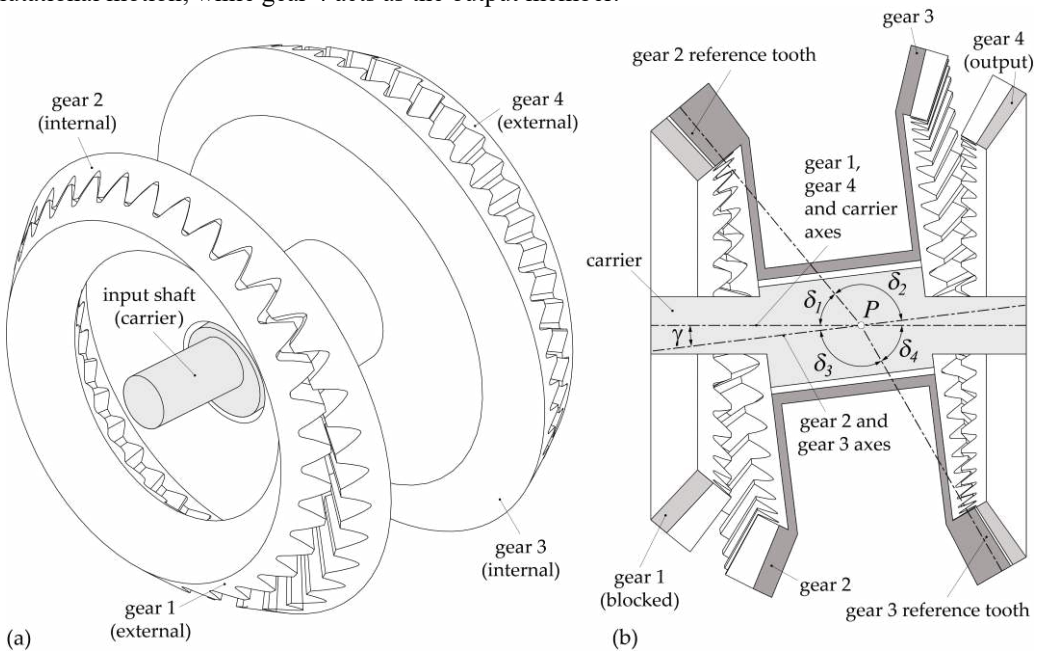

Figure 1. Pericyclic gear drive: (a) 3D view and (b) cross section indicating the pitch angles δ_i and shaft angle γ.

Pericyclic gear drives have been widely studied over the past three decades. Their potential for high-ratio transmissions was first reported in [1], which presented several layouts. A design using external and internal face gears cut by a spur shaper was proposed in [2]. Later, a design method based on straight bevel gears generated by a common straight-profile crown gear was proposed in [3]. A strategy to reduce nutation effects was given in [4]. More recently, a nutation drive with a double circular-arc profile was proposed in [5].

This work proposes the theoretical generation of the external and internal bevel gears using a conical shaper with spherical involute profile. The pericyclic gear drive is first examined using an enhanced unloaded tooth contact analysis (TCA) that is applicable to any two-stage gear drive, providing the unloaded transmission errors between the carrier and gear 4. The pericyclic drive is then studied using a finite element model including the four gears and the carrier, verifying with a low torque the transmission errors predicted by the TCA. The influence of the phase angle between the reference teeth of gears 2 and 3 (see Fig. 1) on transmission errors and the load capacity of the pericyclic gear drive are studied.

2. METHODOLOGY

The shaper tooth flanks are obtained as conjugates to those of a crown gear with a spherical involute profile [6]. The shaper tooth tips are rounded with circular arcs to form the gear fillets and prevent singularities. Finally, a freeform design of the generated flanks is applied to localize the contact.

An equivalent transmission to the one illustrated in Fig. 1 with the carrier fixed and gear 1 released is considered in the unloaded TCA. The meshing cycles between gears 1 and 2 and between gears 3 and 4 required to complete one cycle of the function of transmission errors between gear 1 and gear 4 are determined. The algorithm is applied to the first stage to determine the rotation angle of gear 2 as a function of the rotation angle of gear 1. Since gears 2 and 3 are rigidly connected, the rotation of gear 3 is known before computing that of gear 4. A kinematic approach based on [7] is used for both stages and extended to multiple tooth pairs to cover the required meshing cycles. This approach yields the unloaded transmission error function between the carrier and gear 4, as well as the contact patterns and contact paths of all four gears through the consideration of a virtual marking compound thickness Δv.

A finite element model comprising four gears and a carrier is provided with enough tooth pairs to cover the required meshing cycles. An input torque T_c is applied to a carrier reference node, while gears 1 and 4 are fixed at their reference nodes. Finite rotations of the gear 4 reference node allow several contact positions to be analyzed. In order to reproduce the complex motion of gears 2 and 3, connector elements link their reference nodes and connect gear 2 to the carrier, allowing rotation relative to and with the carrier.

3. RESULTS AND CONCLUSIONS

A numerical example with Z_1=29, Z_2=33, Z_3=33 and Z_4=30 teeth, shaft angle γ = 7° and module 2 mm, providing a gear ratio 30:1, is considered. One meshing cycle between gears 1 and 2 and between gears 3 and 4 is required for this example to observe one cycle in the function of transmission errors between the carrier and gear 4. However, two cycles were considered to ensure continuity in the functions of transmission errors. Fig. 2(a) shows the contact patterns on two of the four gears, considering 5 tooth pairs, Δv=0.0065 mm and 41 contact positions along the two cycles of meshing. Localized bearing contact was achieved by applying longitudinal and profile crowning of 5.0 µm and 6.0 µm, respectively, to gears 1 and 4.

A finite element model with 7 teeth on each gear is built with a total of 511025 nodes and 420002 brick elements of first order. Fig. 2(b) shows the functions of unloaded and loaded transmission errors, predicted by the TCA and by the finite element analysis, respectively, between the carrier and gear 4 ($\Delta\phi_{4c}$). The presented results correspond to the phase angle between gears 2 and 3 that minimizes the peak-to-peak amplitude of the output function of transmission errors. However, this reduction increases the frequency of the function, an effect that diminishes as torque increases (T_c = {0.05, 0.25, 1.0, 3.0} Nm). Finally, the evolution along the cycles of meshing of (i) the maximum contact pressure at both stages and (ii) the maximum value of the maximum principal stress on the central tooth of each gear, indicates that the load capacity of pericyclic transmissions may be governed by bending fatigue failure.

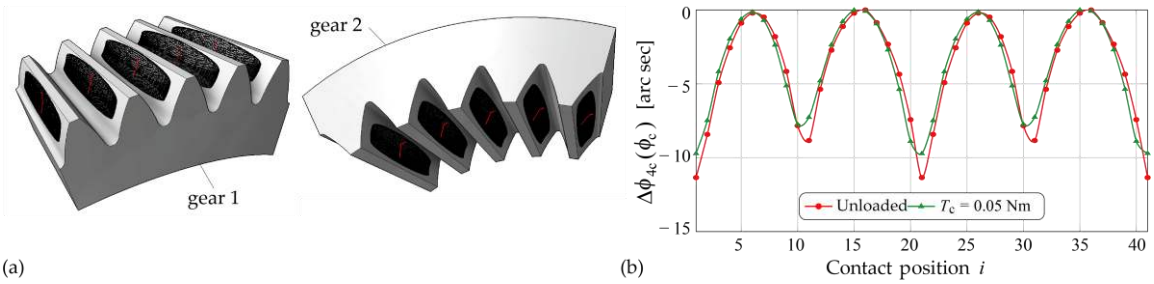

Figure 2. (a) contact patterns, and (b) unloaded and loaded transmission errors between the carrier and gear 4.

ACKNOWLEDGMENTS

Research project PID2023-152913NB-I00 funded by MICIU/AEI/10.13039/501100011033 and by FEDER, UE.

REFERENCES

[1] W. G. Molyneux, "The internal bevel gear and its applications," *Proceedings of the Institution of Mechanical Engineers, Part G: Journal of Aerospace Engineering*, 211(1), 39–61, 1997.

[2] Z. B. Saribay and R. C. Bill, "Design analysis of pericyclic mechanical transmission system," *Mechanism and Machine Theory*, 61, 102–122, 2013.

[3] T. D. Mathur, Z. B. Saribay, R. C. Bill, E. C. Smith, and H. Desmidt, "Analysis of pericyclic mechanical transmission with straight bevel gears," *56th AIAA/ASCE/AHS/ASC Structures, Structural Dynamics, and Materials Conference*. Kissimmee, Florida: American Institute of Aeronautics and Astronautics, Jan. 2015.

[4] Z. A. Cameron, E. C. Smith, H. Desmidt, and R. C. Bill, "Design space exploration of pericyclic transmission with counterbalance and bearing load analysis," *Annual Forum Proceedings - AHS International*, American Helicopter Society, May 2018.

[5] W. Tang, Y. Huang, Y. Wu, L. Yao, L. Pan, and J. Zhang, "Geometry design, meshing analysis and error influences of face-hobbed cycloidal bevel gears with double circular-arc profile for a nutation drive," *Mechanism and Machine Theory*, 176, 105001, 2022.

[6] A. Fuentes-Aznar and I. Gonzalez-Perez, "Mathematical definition and computerized modeling of spherical involute and octoidal bevel gears generated by crown gear," *Mechanism and Machine Theory*, 106, 94–114, 2016.

[7] G. I. Sheveleva, A. E. Volkov, and V. I. Medvedev, "Algorithms for analysis of meshing and contact of spiral bevel gears," *Mechanism and Machine Theory*, 42(2), 198–215, 2007.

MULTI-OBJECTIVE OPTIMIZATION OF THE FLEXIBILITY AND LIFESPAN OF GRID COUPLINGS

E. Rechreche[1*], J. Bruyère[2], Q. Le Guennec[1], P. Velex[2]

[1] CMDgears, Research and Developpment, 539 Av. du Cateau BP289, 59400 Cambrai, France,
{elias.rechreche@cmdgears.com; quentin.leguennec@cmdgears.com}
[2] INSA Lyon, CNRS, LaMCoS, UMR5259, 69621 Villeurbanne, France,
{jerome.bruyere@insa-lyon.fr; philippe.velex@insa-lyon.fr}

1. INTRODUCTION

Couplings are crucial components in mechanical transmissions and, amongst the various existing technologies, steel grid couplings (Figure 1) stand out as versatile solutions for large power units as they can compensate for parallel offsets and angular misalignments while bringing torsional compliance. They usually comprise two crowned hubs connected by a steel grid that made of one or several parts. Around the grid and hubs, a casing encapsulates the lubricant and imposes constraints on the grid axial and radial positions. Despite their recognized interest, the literature on the subject remains sparse. Notably, a model of the static and dynamic behavior of grid couplings has been proposed [1], which made it possible to understand the mechanisms controlling some of the key coupling properties. In this paper, several significant developments of the baseline model are presented and a process is described based on a multi-objective genetic algorithm aimed at optimizing design parameters according to specific objectives.

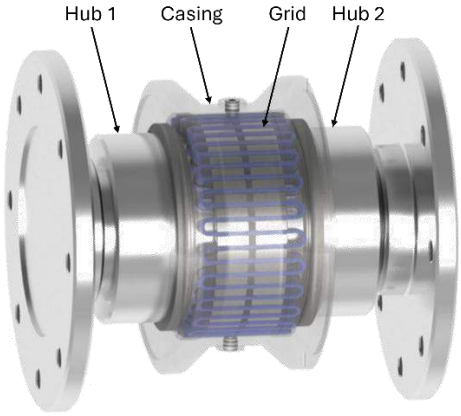

Figure 1. Grid coupling

2. MODEL DEVELOPMENT

The previously developed model [1] relies on a hybrid modeling strategy combining finite elements and lumped parameter elements to simultaneously account for the global (shafts/hubs/casing) and local (contacts) scales. However, some limitations need to be addressed in order to effectively implement it in an optimization algorithm. The tooth-grid contact simulations have been enhanced in order to account for grids of trapezoidal cross-sections and major changes have been brought to the casing model to extend the range of possible coupling geometries, reduce computational times and simulate grid radial expansions. Since coupling life-span strongly depends on the stress level in the grid, particularly in the loops, a module has been added, which gives a quick analytical estimate of these critical stresses.

A number of experimental studies focused on quasi-static torsional stiffness have been carried out on a dedicated test rig using a grid of trapezoidal cross-section. As shown in Figure 2, a good agreement has been found between the numerical and experimental results, thus validating the proposed extended grid model.

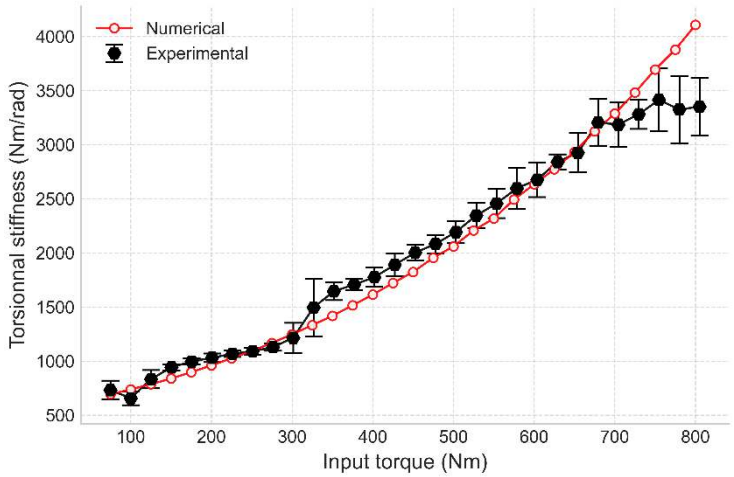

Figure 2. Numerical vs Experimental results with error bounds at $\pm 2\sigma$

3. OPTIMISATION PROCESS AND RESULTS

The extended model is still fast enough to be inserted into an optimization iterative process relying on the classic NSGA-II algorithm [2] using two objectives and multiple constraints. In practice, grid couplings are primarily used because of their low torsional stiffness, compared to other full metal couplings, in order to protect systems from shock loads. Consequently, the first objective in the optimization process is the coupling torsional stiffness, whereas the second objective retained is the contact pressure between the grid and the hub teeth since it is deemed representative of grid wear [3]. A constraint on the maximum stresses in the grid loops is added as they should remain below the ultimate fatigue limit of the grid material. The selected optimization parameters comprise the length, number of parts, and section of the grid, as well as the geometry of the crowned hubs. Figure 3 shows an example of optimization results, which illustrates the process convergence after 99 generations and its practical interest in helping designers to define relevant geometries of grid couplings.

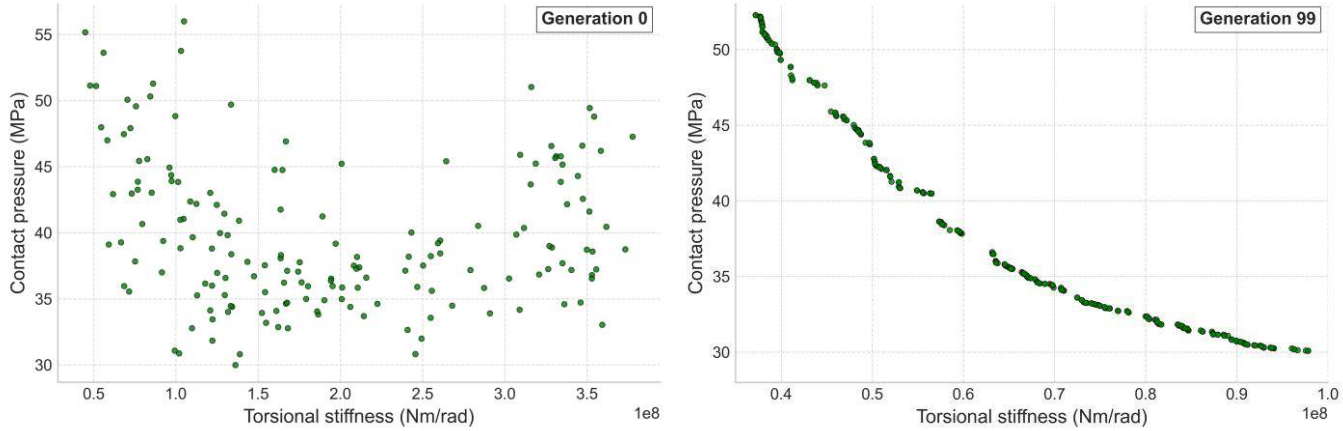

Figure 3. Convergence process

REFERENCES

[1] RECHRECHE, E., BRUYÈRE, J., LE GUENNEC, Q., et al. Experimental and numerical analyses of grid couplings in quasi-static and dynamic conditions. Mechanism and Machine Theory, 2024, vol. 203, p. 105807

[2] DEB, K., PRATAP, A., AGARWAL, S., et al. A fast and elitist multiobjective genetic algorithm: NSGA-II. IEEE transactions on evolutionary computation, 2002, vol. 6, no 2, p. 182-197.

[3] POKRANDT G. C., Falk Steelflex Couplings - Failure Analysis, 2001. www.rexnord.com.

FULL-SCALE VALIDATION OF FRETTING-MAP PREDICTIONS FOR AEROSPACE-GRADE CROWNED INVOLUTE SPLINES AISI 9310

Aurea Iñurritegui[1], Andrea Mura[2], Aitor Arana[1], Ander Elkoro[1], Francesca Cura[2]

[1] Mondragon Unibertsitatea, Loramendi 4, Arrasate-Mondragon, Spain.

[2] Politecnico di Torino, Corso Duca degli Abruzzi 24, Torino, Italy.

{ainurritegui@mondragon.edu; andrea.mura@polito.it; aarana@mondragon.edu; aelkoro@mondragon.edu; francesca.cura@polito.it}

1. INTRODUCTION

Spline couplings are widely used in aerospace transmissions (e.g., accessory gearboxes) to transfer high torque with compact geometry. Despite flank crowning and case-hardened steels, due to high normal pressure with small-amplitude oscillatory micro-motion (e.g., vibrations and misalignment), fretting wear remains as the recurrent failure mode [1]. Fretting wear produces oxidation, debris, microcracking, and material loss that can progress to fretting fatigue—an especially critical issue for aerospace splines manufactured in aerospace steels such as AISI 9310. Hertzian contact theory and 3D finite-element models are commonly used to estimate pressures, stick–slip regions, and stress concentrations in crowned spline couplings, but they require experimental validation.

Previous studies on AISI 9310 crowned spline couplings show that fretting severity is governed by load and vibration amplitude, and that crowning mitigates but does not eliminate damage. Fretting maps are an effective regime-classification tool (stick/partial slip/gross slip); however, they are rarely combined with tooth-by-tooth contact analyses and then validated with quantitative wear measurements on full-scale spline couplings at representative torque levels. While AGMA 945-A18 and ISO 4156 describe geometry, fits and failure modes, neither provides a tooth-resolved, validated workflow for fretting propensity under representative torque and micromotion in crowned splines.

This paper addresses this gap by analyzing AISI 9310 (Ni-Cr-Mo) carburized crowned spline coupling, widely used in aircraft engines tested at 100, 700, and 1000 Nm. Specifically, Hertzian contact mechanics are used to determine flank contact pressures, a 3D finite element model (FEM) is built to resolve contact pressures and relative micro-displacements, and the predictions are verified against experimental image-based damage quantifications. The resulting operating points are positioned on reference AISI 9310 fretting map to verify regime predictions, and deliver a fast and durable method for the design phase of spline solutions for aerospace gearboxes.

2. CASE STUDY AND METHODOLOGY

The component investigated is a crowned involute spline coupling representative of a turbofan engine Accessory Gearbox (AGB) connection, where compact, high-efficiency torque transmission must coexist with angular/axial misalignment tolerance under highly dynamic conditions. The specimen is a 26-tooth, side-fit crowned involute spline coupling with a module of 1.27 mm, 30º pressure angle, and 12.5 mm of face width. The external tooth flanks (hub) incorporate longitudinal crowning of 22 μm to center the contact and limit edge loading. Both hub and sleeve are carburized and quenched AISI 9310 (58–63 HRC case, tough core); for contact calculations linear-elastic properties were considered as: $E = 205$ GPa and $\nu = 0.29$.

To capture the local curvature introduced by flank crowning against the internal involute, the contact was idealized as elliptical contact along the active flank. The involute was discretized into multiple points to capture how equivalent radii change from root to tip, and classical Hertz theory provided the semi-axes (a, b) and the peak pressure p_0.

A 3D single tooth-pair model was built to resolve local contact pressures and micromotion under the applied torque. The model employed surface-to-surface contact, linear-elastic AISI 9310, and negligible friction, with a locally refined mesh in the predicted contact ellipse region. Uniform torque sharing across all teeth was assumed for the baseline calculation to isolate from uneven distributions, related to misalignment or manufacturing errors.

Full-scale couplings were tested on a servo-hydraulic frame under force-controlled cyclic axial loading at 5 Hz for 10^6 cycles, after solvent degreasing to promote dry fretting. Laboratory conditions during testing were 27.2 °C and 57.7% humidity. After testing, all teeth were imaged by optical microscopy, and the wear-affected area and oxidation were quantified in ImageJ software. Operating points for each torque level were placed on a Vingsbo–Söderberg-type fretting map using the FE model derived normal load P and contact-level slip $\delta_{contact}$. Different contact regimes (stick, partial slip, gross/near-gross slip) were identified.

3. RESULTS

Across the evaluated load cases, according to the Hertz theory, the maximum pressure along the flank of the tooth is correlated with FE model. The maximum pressure is localized near the tooth root, which is also observed in the FE model contact distribution, and it decreases as we move towards the tip of the tooth (in accordance with the increase of the curvature radius). According to the contact area, the idealized Hertz underestimates the real contact area, however flank centered elliptical contact is well captured, while it widens laterally as we move towards the top of the tooth. This confirms, that areas next to the tooth root are the most susceptible for stress concentrations, and damage. The error between analytical and numerical results is below 8%, thus it can be said that the analytical model serves as a preliminary criterion to identify the areas with the highest risk of wear occurrence.

Moreover, due to the simplifications made in the FE model, the complexity of the real contact is not captured that is why experimental tests were necessary to contrast and predict the damage. The three experimental conditions were placed on the fretting map as shown in Fig. 1 using estimated values of normal force and relative displacement derived from the FE simulations and test conditions.

At 100 Nm, post-test inspections showed no fretting oxidation on any tooth; only mild polishing with shallow longitudinal lines along several flanks. These fine, uniform marks—with no color change, debris, or cracking—are consistent with low-amplitude micro-slip / fretting-fatigue initiation, and confirm that the spline coupling is operating below the fretting threshold (Fig. 1 top ■). At 700 Nm, the coupling showed clear fretting wear with reddish oxidation concentrated near the contact region (Fig. 1 middle ★), but highly non-uniform across teeth. The most affected teeth exceeded 60% wear-affected area while others stayed at ≤ 30%. Furthermore, oxidation was above 15–20% on some teeth, while less than 5% on many others. These observations confirm that contact pressure and micromotion were sufficient to activate fretting mechanisms and indicate non-uniform tooth loading (tolerances/misalignment-induced load non-uniformity), and remarking the most susceptible regions under high load. Finally, at 1000 Nm, fretting became localized but aggressive (Fig. 1 bottom •): only around 5 from 26 teeth were affected, showing severe surface degradation with reddish oxidation covering 20–50% of the flank, while most teeth remained nearly unaffected.

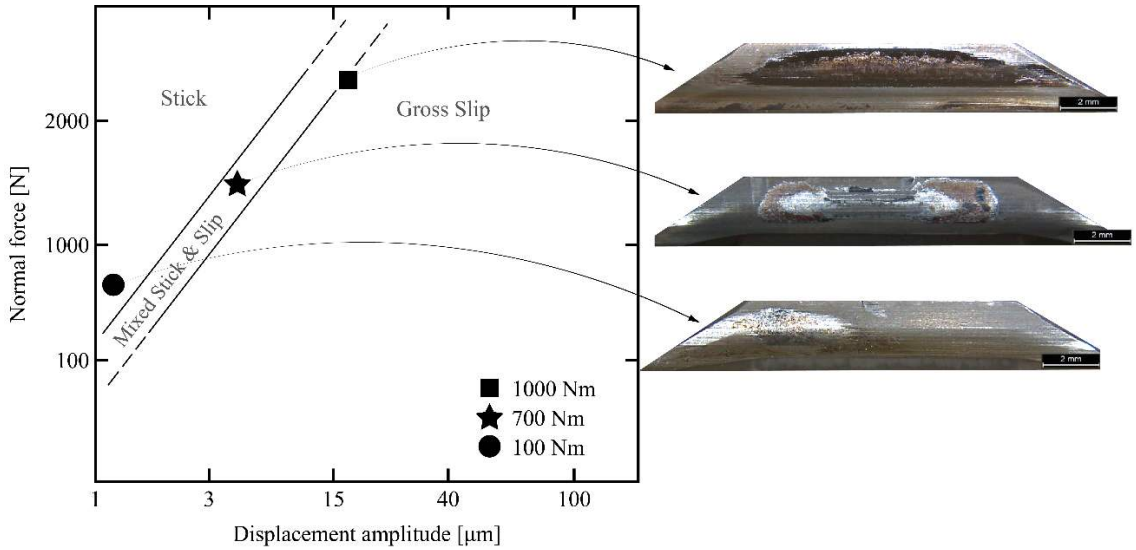

Figure 1. AISI 9310 fretting map [2] with validated experimental data and wear in tooth at different torque levels after 10^6 cycles.

4. CONCLUSIONS

A practical, validated workflow for assessing fretting in crowned involute AISI 9310 splines was demonstrated on a representative aerospace coupling. FE model and Hertzian contact pressures across different loads agree within 8%, supporting analytical calulations for rapid design checks and FE model for micromotion refinement. The experiments then reveal a practically important behavior that is not explicitly addressed by standards: at 700 Nm, fretting becomes broad but moderate (many teeth in partial slip), whereas at 1000 Nm it becomes localized but severe (few teeth carry most of the micromotion). Interpreting these outcomes through a fretting-map lens turns a qualitative tool into a quantitative, tooth-selective predictor for crowned splines. This workflow and these results enable predecition of where freeting will occur and at what torque levels, allowing early design-phase actions—adjusting crowning/fit, targeting surface treatments, and scheduling inspections—rather than performing indiscriminate inspections and costly prototypes.

REFERENCES

[1] F. Curà and A. Mura, “Evaluation of the Fretting Wear Damage on Crowned Splines”. Procedia Structural Integrity, 5, 1393-1400, 2017.

[2] O. Vingsbo and S. Söderberg, “On fretting maps”. *Wear*, 126(2), 131–147, 1988.

KINEMATICS AND WORKSPACE OF A CUSPIDAL MODULAR PARALLEL ROBOT

Adrián Peidró[1], Paula Mollá-Santamaría[1], Jorge F. Aznar-Ortega[1], Luis M. Jiménez[1], Óscar Reinoso[1]

[1]Miguel Hernández University, Avda. de la Universidad s/n 03202 Elche, Spain {apeidro@umh.es}

1. INTRODUCTION

Modular robots are robots constituted by simple units (modules) which, when combined in different ways, generate diverse morphologies. They offer advantages like robustness/self-repair (if a module fails, it can be replaced by another module) and adaptability (i.e., reconfiguration into a new morphology that better suits changing tasks). Two main classes of modular robots exist [1]: lattice type and chain type. Lattice types are simpler to control because modules only occupy discrete places in space when assembled, while chain-type modules can adopt continuous configurations relative to the neighbors they are joined to. However, most chain-type modular robots are serial, which limits their stiffness and load-bearing capacity compared to parallel robots. This abstract explores the assembly of modular chain-type parallel robots using a new module: the MASAR.

2. THE MASAR: "MODULAR AND SINGLE-ACTUATOR ROBOT"

The MASAR robotic module is illustrated in Figure 1a-b. It consists of a main body B, to which the stator of a motor M is attached. The rotor of M drives a shaft S, which rotates an angle θ. At both sides of M, there are bevel gears BG_1 and BG_2 that transmit motion to transversal feet that are orthogonal to S. Both ends of S have adhesion ports {9, 10}. The ends of all transversal feet have also adhesion ports {1…8}. By adhering one of these ports, say 7, to the floor and powering M, the module rotates about it (Fig. 1d). After adhering 8 and detaching 7, powering M now rotates the module about port 8 (Fig. 1e). Alternating this moves the module in a plane (Fig. 1f, [2]), which can also transit between orthogonal planes (e.g. floor to wall) thanks to orthogonal ports (Fig. 1g). Furthermore, by adhering ports of different modules, modular robots with higher mobility can be built. For instance, Fig. 1h shows a serial robot made of 4 modules climbing a table, an impossible task for one module.

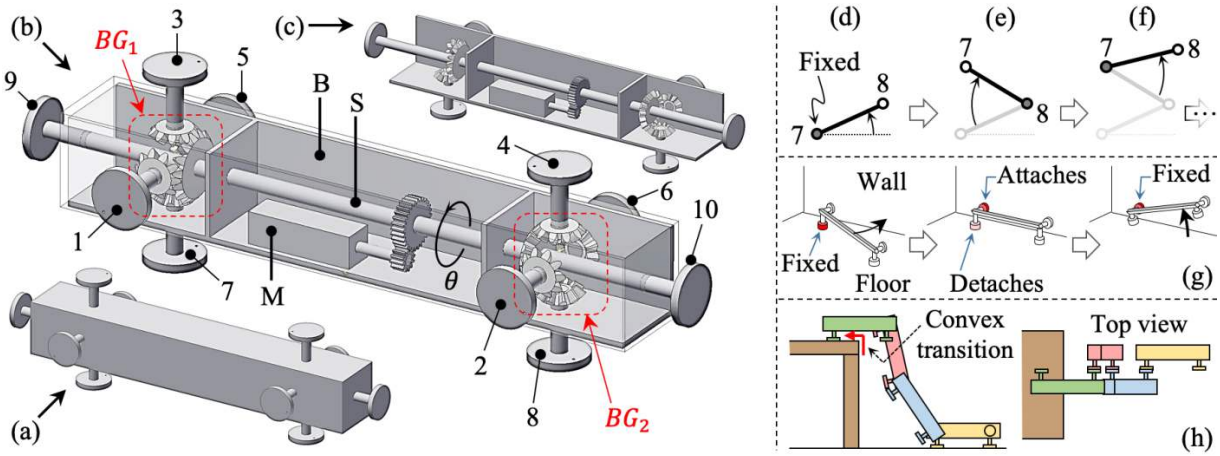

Figure 1. (a) Outer view of a MASAR module. (b) Interior view after making the case transparent, and (c) after removing some parts for clarity. (d-f) Locomotion of a single module in the plane. (g) Transition between orthogonal planes. (h) A serial modular robot.

Kinematic assembly and analysis of serial modular robots is relatively straightforward because it only requires concatenating rigid transformations one module after another. However, assembling modular parallel robots is more complex, because loop-closure kinematic equations must be satisfied. Next, the closure equations that define the assembly of several modules are formulated. To this end, with reference to Figure 2a, the following homogeneous transformation matrices (HTM) are defined:

$$\mathbf{T} = \begin{bmatrix} \mathbf{R}_X(\alpha)\mathbf{R}_Y(\beta)\mathbf{R}_Z(\gamma) & [x,y,z]^T \\ \mathbf{0}_{1\times3} & 1 \end{bmatrix},\ \mathbf{P}_1 = \begin{bmatrix} \mathbf{R}_Z(-n\theta) & [-\frac{a}{2},0,b]^T \\ \mathbf{0}_{1\times3} & 1 \end{bmatrix},\ \dots,\ \mathbf{P}_{10} = \begin{bmatrix} \mathbf{R}_Y(\pi/2)\mathbf{R}_Z(\theta) & [\frac{a}{2}+c,0,0]^T \\ \mathbf{0}_{1\times3} & 1 \end{bmatrix},\ \mathbf{A}(\psi) = \begin{bmatrix} \mathbf{R}_Z(\psi)\mathbf{R}_X(\pi) & \mathbf{0}_{3\times1} \\ \mathbf{0}_{1\times3} & 1 \end{bmatrix} \quad (1)$$

where $\mathbf{T}$ is the pose (position and orientation) matrix of frame Σ (which is attached to B) with respect to the world frame W, $\mathbf{R}_v(u)$ is a rotation matrix of angle u about axis v, $\mathbf{P}_j$ (j = 1…10) defines the pose of adhesion port $\mathcal{P}_j$ relative to Σ ($\mathbf{P}_j$ depends

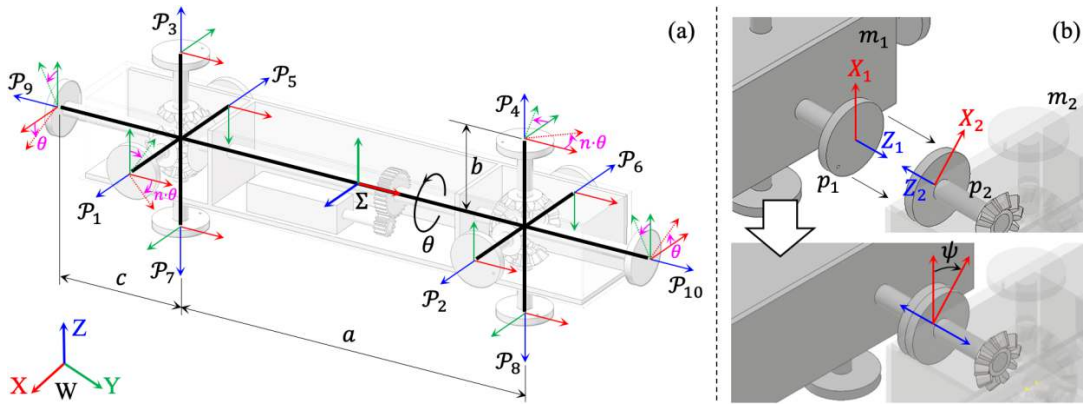

Figure 2. (a) Reference frames attached to the module and its adhesion ports. (b) Detail of the joining of ports of two modules.

on angle θ and gear ratio n), and $\mathbf{A}(\psi)$ relates the poses of two ports p_1 and p_2 of two modules m_1 and $m_2$when they are attached at angle ψ (Fig. 2b). The configuration of a module is defined by $\mathbf{X} = [x, y, z, \alpha, \beta, \gamma, \theta]$, where $\{\alpha, \beta, \gamma\}$ are Euler angles. By adding a superscript i to particularize these variables for the i-th module, the configuration of N modules is denoted by $\mathbf{Y} = [\mathbf{X}^1, \ldots, \mathbf{X}^N]^T$. Vector $\mathbf{Y}$ must satisfy inter-module kinematic constraints of the type: $\mathbf{T}^{m_i}\mathbf{P}_{p_i}^{m_i}\mathbf{A} = \mathbf{T}^{m_k}\mathbf{P}_{p_k}^{m_k}$, which means that port p_i of module m_i must be connected to port p_k of module m_k, as well as module-environment constraints of the type: $\mathbf{T}^{m_i}\mathbf{P}_{p_i}^{m_i} = \mathbf{G}^{m_i}$, which means that port p_i of module m_i must be grounded at the pose represented by the HTM $\mathbf{G}^{m_i}$.

3. MOBILITY AND WORKSPACE ANALYSIS

After formulating these connection constraints for N=9 modules forming a closed kinematic chain, they are solved iteratively via Newton-Raphson, starting from random $\mathbf{Y}$. Figure 3a shows a modular robot for which Newton-Raphson converged. Then, its mobility is analyzed by solving $\mathbf{J}\cdot\delta\mathbf{Y}=\mathbf{0}$, where $\mathbf{J}$ is the Jacobian of these constraints. The kernel of $\mathbf{J}$ reveals that this robot has 3 DOF, and module 8 (the end-effector) can translate independently along XYZ with a parasitic rotation about Z and no rotation about XY. Next, the workspace of this robot is generated by recursively propagating the configuration of Figure 3a to its neighbors via Newton-Raphson, spanning the workspace of Figure 3b. Many parts of the workspace reveal singularity cusps that can be encircled to switch between different solutions for the same end-effector position (Figure 3c).

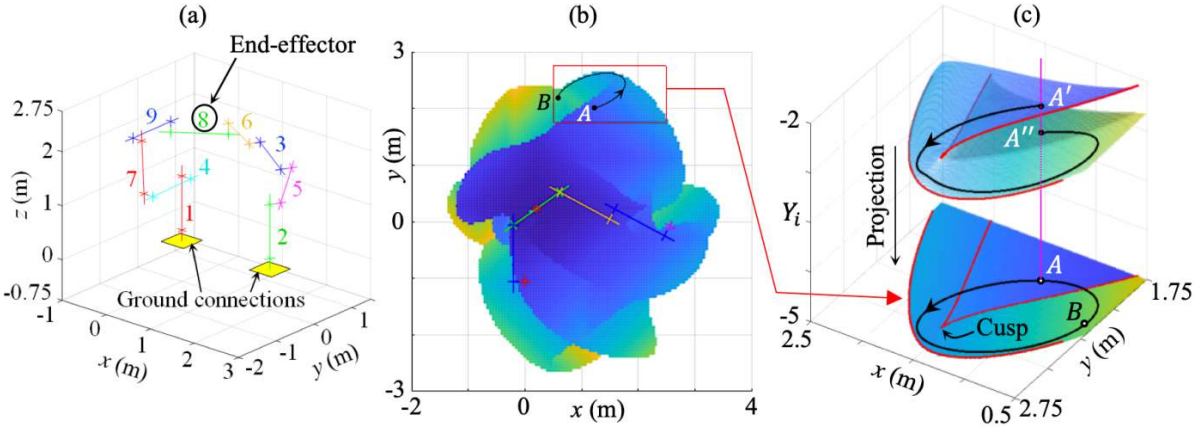

Figure 3. (a) A 3-DOF modular parallel robot. (b) Workspace consisting of (x, y) positions reachable by the end-effectorfor constant z. (c) Workspace point A can be reached by at least two configurations A' and A'' that can be connected by encircling a cusp singularity.

4. CONCLUSIONS

This abstract has presented a new module for assembling modular parallel robots. After formulating the loop-closure assembly constraints and solving them via Newton-Raphson, the mobility and workspace of a 3-DOF modular parallel robot have been analyzed, revealing that this robot is cuspidal regarding the inverse kinematics. By following the same steps summarized here, more parallel modular robots with up to 37 modules, 6 DOF, and even kinematic redundancy, have been successfully analyzed.

ACKNOWLEDGMENTS

This work is part of the project PID2024-159765OA-I00 funded by MICIU/AEI/10.13039/501100011033 and FEDER, UE.

REFERENCES

[1] M. Yim, W.M. Shen, B. Salemi, D. Rus, M. Moll, H. Lipson, E. Klavin and G.S. Chirikjian, “Modular self-configurable robot systems”. *IEEE Robotics & Automation Magazine*, 14(1), 43-52, 2007.

[2] A. Peidró, J. Gallego, L. Payá, J.M. Marín and Ó. Reinoso, “Trajectory Analysis for the MASAR: A New Modular and Single-Actuator Robot”. *Robotics*, 8(3), 78, 2019.

KINEMATIC MODELING OF A METAMATERIAL SYSTEM FOR MORPHING STRUCTURE APPLICATIONS

A. Benatar [1], F. Xi [1], A. Ghosh [1]

[1] Toronto Metropolitan University, 350 Victoria St, Toronto, ON M5B 2K3, Canada,
{abenatar@torontomu.ca; fengxi@torontomu.ca; amitabha.ghosh@torontomu.ca}

1. INTRODUCTION

Morphing structures capable of undergoing large geometric transformations while maintaining structural integrity have been increasingly studied in aerospace, robotics, and adaptive systems [1-4]. Presented in this abstract is a metamaterial system designed for aircraft morphing wing applications. This system consists of a flexible panel enclosed system integrated with an internal auxetic lattice for 2D shape morphing including expansion, contraction, or upward and downward bending, as seen in Figure 1(a). Many existing morphing concepts rely on computationally intensive finite element methods (FEM) for motion prediction. Recent work has demonstrated that flexible panel enclosed systems can be modeled as planar parallel continuum mechanisms (PCMs) [5], enabling analytical representations of morphing motion. The objective of this work is to develop a kinematic modelling and analysis method capable of replacing computationally demanding methods (FEM) for real-time morphing motion planning and control. The flexible enclosed system is composed of two flexible panels (top and bottom), with an internal auxetic structure formed by a series of bowtie-shaped unit cells. The enclosed system is modelled as a parallel continuum mechanism, while the bowtie-shaped auxetic structure is represented as a network of planar parallel mechanisms coupled to the enclosed system. For a prescribed morphing motion, a two-step solution strategy is proposed. First, inverse kinematics of the parallel continuum mechanism is applied to determine the deformed profiles of the enclosed system. Subsequently, inverse kinematics of the planar parallel mechanisms is used to solve the deformed profiles of all bowtie unit cells, resulting in a complete morphing motion solution. In what follows, a brief description of the proposed method is provided.

2. TWO-STEP SOLUTION STRATEGY

In step 1, the objective is to solve the profiles of the flexible panel enclosed system, including the top skin L_T, bottom skin L_B, and virtual middle backbone line L_M, for a given pose of the moving platform including position (X_M, Z_M) and orientation (β). It is well-known that the kinematics of continuum mechanisms is coupled with its static profile. For this reason, the classical beam theory was applied to model the deformation of both panels under their length changes [5], which were derived as two elliptic integrals in terms of L_T and L_B, and solved through either a constrained minimization method or sequential quadratic programming (SQP). However, it becomes rather challenging when attempting to perform the inverse kinematic analysis. To overcome this issue, a series of experiments were carried out, and the following empirical relations were discovered [5]:

$$L_M = (L_T + L_B)\,/\,2 \quad (1); \qquad \delta_M = (L_T - L_B) = k\beta \quad (2)$$

Equation (1) indicates that the virtual middle curve length is related to the top and bottom panel lengths by averaging the two panels, and Equation (2) indicates that their difference is proportional to the rotation of the moving platform. These two equations enabled a simplified inverse kinematic solution based on circular geometry rather than the elliptic integral evaluation mentioned before [6]. In other words, three concentric circular curves can be determined to represent the profiles of top skin, bottom skin and middle line, with the center at C and respective radius r_T, r_B, r_M, as seen in Figure 1(b).

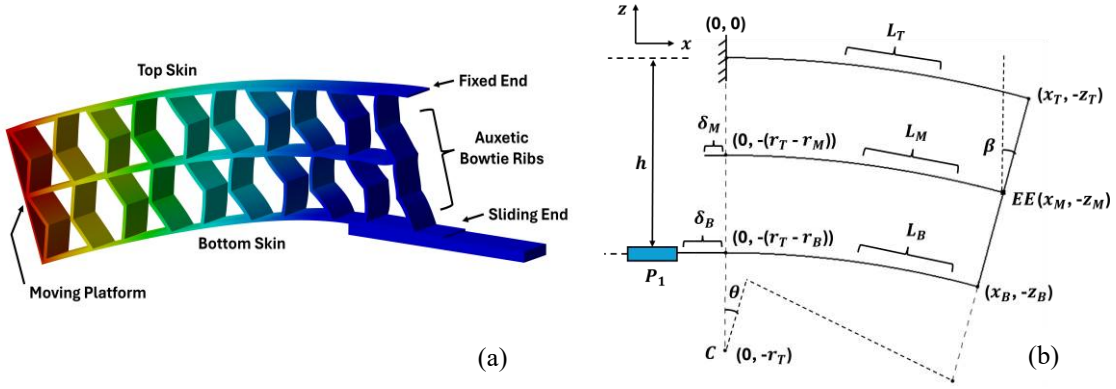

Figure 1. A metamaterial system for morphing structure applications: (a) entire system, (b) enclosed system modeling

In step 2, the goal is to solve the profile of the internal auxetic lattice using the enclosed system determined in step 1 as the basis. As shown in Figure 2, there are two stacked rows of five bowtie cells. Each bowtie cell is treated as a planar parallel mechanism of six links. The cells on the top row share their top links with the top skin and those on the bottom row share their bottom links with the bottom skin. The two rows are connected along the virtual middle line. The cell connection points form a set of nodes along the top/bottom skins and backbone, which can be defined based on the solved profiles of top/bottom skin and the virtual middle line, denoted by P_i, as shown in Figure 2. The left or right branch of each bowtie cell forms a loop equation with both ends defined, hence the intersecting point of the two links can be readily solved, denoted by T_i in Figure 2, leading to a complete solution for the entire auxetic lattice.

3. MODELING RESULTS AGAINST FEM

To validate the efficacy of the proposed modelling method, a counterpart simulation was conducted for the same metamaterial structure using both the proposed method and FEM. The proposed method followed the two-step approach outlined above based on circular curves. The FEA analysis followed the same top fixed/bottom free setup shown in Figure 1(a) and generated non-circular curves for the enclosed system's profile. The validation of the proposed framework follows two primary analyses. The first is to validate the accuracy of the parallel continuum panels representing the flexible skins and backbone structure, while the latter is to validate the bowtie cells, with both taken relative to the FEA model. The panels must be considered first in the analysis of the proposed method, since the bowtie cells are constructed from the panel's nodes. Any error in the modelling of the panels directly affects the accuracy of the bowtie geometries. To test the accuracy of the panel and bowtie nodes, three distinct bending angles of 8° (small), 14° (middle), and 20° (large), were modelled and compared with an FEA counterpart. The nodes selected for the comparison analysis include all panel nodes and bowtie intersect points, with additional midpoint nodes provided along each bowtie linkage, as well as between the panel nodes along each of the panels. Figure 2 illustrates the results of the 14° bending, while Figure 3 shows a comparison of the bowtie nodes using the proposed method panels (circular) and FEM panels (non-circular). Despite the error found with the constant curvature assumption, the overall agreement between the proposed method and FEA results remains strong across the entire auxetic structure.

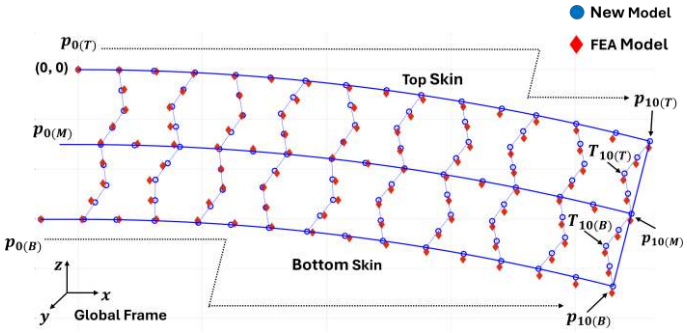

Figure 2. Comparison analysis for a 14° bending configuration

Element	Node	Circular curve Error (%)		Non-circular Error (%)	
		x	z	x	z
Top Row Cell Intersect	$T_{9(T)}$	0.24	6.91	0.66	0.63
Bottom Row Cell Intersect	$T_{9(B)}$	0.05	3.41	0.48	0.93

Figure 3. Comparison of circular & non-circular curves (14°)

4. CONCLUSIONS

The two-step method presented here provides a simplified approach for modelling and analyzing the motion behavior of a metamaterial system for morphing structure applications. The validation of circular bending curves against FEA simulations demonstrates that the nodal position errors remain below 10%, while the use of non-circular bending curves reduces this error down to 1%. However, the computational cost and time savings provided by the proposed method justifies its value for real-time morphing applications. For this reason, it is appropriate to state that the proposed method is effective for motion planning and control of the metamaterial morphing structure system under this study, which is applicable to a wide range of shape-morphing systems

REFERENCES

[1] F. Xi, D. Oguamanam, S. Kojovic, and O. Guerra, "Application of mechanisms to aircraft flexible trailing edge design," 2024 6th International Conference on Reconfigurable Mechanisms and Robots (ReMAR), pp. 258-264, Jun. 2024. doi:10.1109/remar61031.2024.10618077

[2] J. Wang, Y. Li, S. Tian, Yihan Zhao, G. Ren, F. Xi, and Yinjun Zhao, "Bio-inspired rigid-flexible coupled skin-scales system for enhanced protection in soft robotic fish," *Npj Robotics*, vol. 3, no. 35, Oct. 2025. doi:10.1038/s44182-025-00052-1

[3] G. Tian, R. Wen, J. Ma, and C. Fu, "Biomimetic shape-morphing actuators with controlled bending deformation and photo-meditated 3D shape programming for flexible smart devices," *Sensors and Actuators B: Chemical*, vol. 409, p. 135586, Jun. 2024. doi:10.1016/j.snb.2024.135586

[4] F. Hou, P. Sarkar, and A. Alipour, "A novel mechanism – smart morphing façade system – to mitigate wind-induced vibration of tall buildings," *Engineering Structures*, vol. 275, p.115152, Jan. 2023. doi:10.1016/j.engstruct.2022.115152

[5] W. Wang, F. Xi, Y. Tian, Y. Zhao, and Y. Li, "Modeling and analysis of a planar soft panel continuum mechanism," *Journal of Mechanisms and Robotics*, vol. 12, no. 4, Mar. 2020. doi:10.1115/1.4046029

[6] W. Wang, X. Yu, Y. Zhao, L. Li, Y. Li, F. Xi, " A simplified method for the inverse kinematics of a flexible panel continuum robot for real-time shape morphing," *Machines*, vol. 11, 104, pp. 1-11, (2023). doi:10.3390/machines11010104

A UNIVERSAL DESIGN AND GEAR SURFACE QUALITY CONTROL METHODOLOGY OF FACE-MILLED HYPOID GEAR WITH LARGE RANGE OF OFFSET AND SHAFT ANGLE

Liu Siyuan[1], Song Chaosheng[1], Zhu Caichao[1]
[1] Chongqing University, Shazhengjie No.174, Chongqing, China, {www.cqu.edu.cn}

1. INTRODUCTION

Hypoid gear plays an important role in spatial power transmission with unique strength of high capacity, contact behavior pre-controlling and insensitive to misalignment. Hypoid gear [1] is not limited in axle system, this type of gear transmission can be found in robot joint, machine tool transmission system, automatic production line power transmission system.

Many scholars have focused on hypoid gear geometry design [2], gear surface ease-off topography [3], tooth contact analysis [4] and machining [5] in orthogonal configuration. Only few papers [6-7] have studied the hypoid gear in extreme geometric scale. With the extension of application scenario, orthogonal hypoid gear is not satisfied for all the conditions. The new condition needs large range of offset and low to obtuse shaft angle. There remains a significant gap in the development of non-orthogonal hypoid gears. The objectives of this study can be summarized as follows: (1) Development of a novel approach for pitch cone and gear blank design based on the geometric limitation for hypoid gears in large range of offset and shaft angle configuration. (2) Enhancement of a calculated methodology of machine-tool settings determination for both pinion and wheel. (3) Development of an approach for selecting the geometric parameters to maintain the gear surface quality.

2. PITCH CONE DESIGN AND GEOMETRIC PARAMETERS CALCULATION

The mathematical model of pitch cone of pinion and wheel is shown in Figure.1 (a). The pitch cone of pinion and wheel are tangent at point M which also considered as reference point M. The detailed derivation process can be found in Ref [1]. Figure.1 (b) shows the three main geometric relationships of hypoid gear which can be found in Ref [1]. This method can transfer hyperboloid pairs contacting into cones calculation involving the gear ratio, offset and shaft angle.

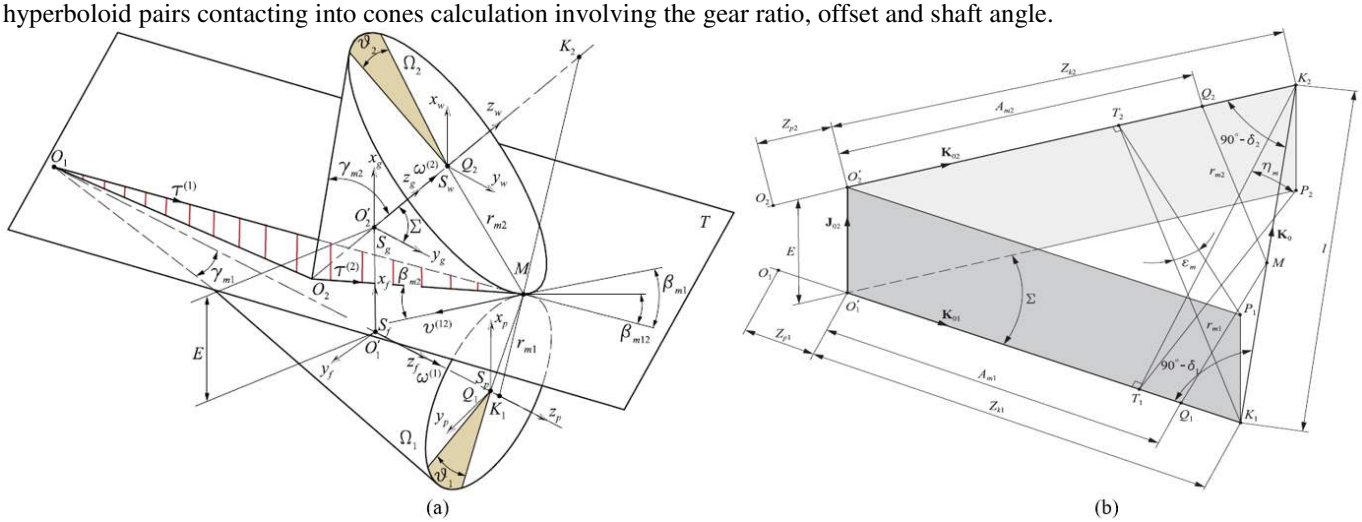

Figure.1 A novel approach of hypoid gear geometric design: (a) pitch cone design; (b) gear blank parameters calculation

3. DETERMINATION OF MACHINE-TOOL SETTINGS FOR BOTH PINION AND WHEEL

To obtain the machine-tool settings of gear surface of pinion and wheel, the enhancement local synthesis method has been proposed considering preset contact behavior which can be found in Ref [6]. The preset contact behavior parameters contain length of contact ellipse, contact path direction and transmission error value. The tooth topography of hypoid gear in non-orthogonal configuration is extremely sensitive to preset contact behavior parameters. Therefore, selecting methodology of geometric parameters need to be checked to avoid the defect of gear surface.

4. SELECTING METHODOLOGY OF GEOMETRIC PARAMETERS FOR QUALITY SURFACE

Figure.2 shows defect of gear surface of hypoid gear in low and obtuse shaft angles. For low shaft angle configuration, the singularity point locus easily moves down which contributes to undercutting of gear surface. For obtuse shaft angle configuration, the cone angles of wheel is increasing with increment of shaft angle which may beyond the 90° which contributes to interference

between cutting trace and gear blank. The convex and concave surfaces are generated by two types of machine-tool settings, therefore, the smoothness of root part needs to be guaranteed with re-modifying the machine root angle.

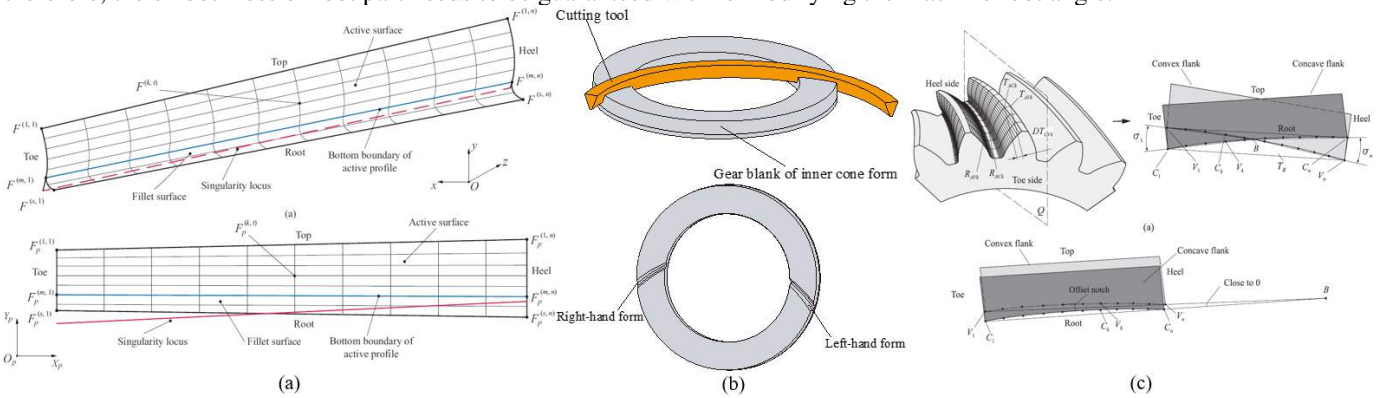

Figure.2 Defect of gear surface: (a) undercutting of gear surface considering singularity point; (b) interference between cutting trace and gear blank; (c) smoothness of gear surface between convex and concave surfaces

5. VERIFICATION OF HYPOID GEAR IN LOW AND OBTUSE SHAGT ANGLE CONFIGURATION

To verify the correctness of the above methodology, two cases of hypoid gear in low and obtuse shaft angle configurations has been selected to perform the contact behavior through the FE analysis and experiment which are shown in Figure.3.

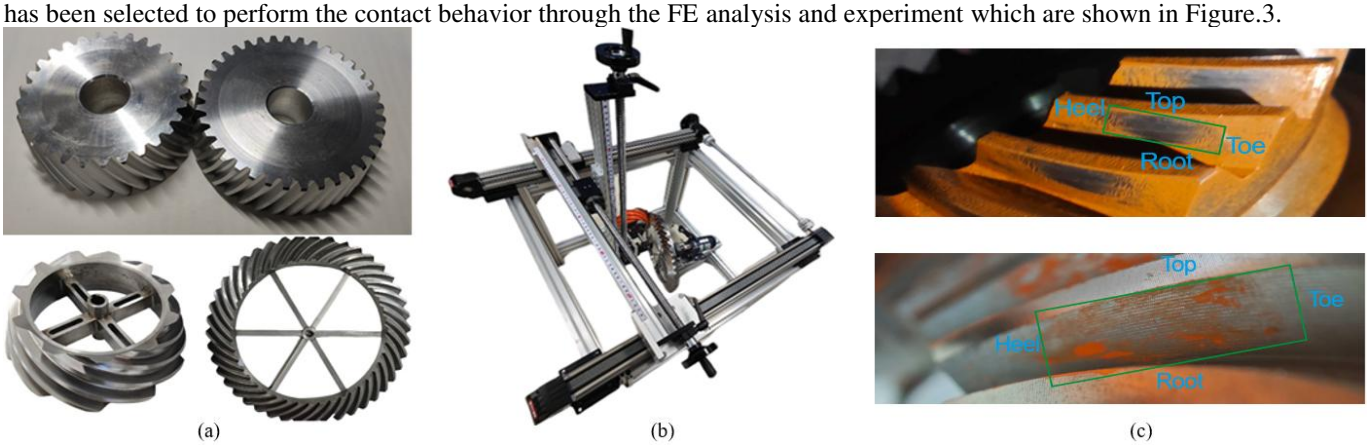

Figure.3 Verification: (a) work pieces of hypoid gear; (b) experimental equipment of different shaft angle; (c) contact pattern

6. CONCLUSION

A universal design and gear surface quality control methodology of face-milled hypoid gear with large range of offset and shaft angle has been proposed. A novel approach for pitch cone and gear blank design based on the geometric limitation for hypoid gears in large range of offset and shaft angle configuration has been performed. The surface of hypoid gear in low and obtuse shaft angles is extremely sensitivity to design parameters. To avoid the surface defection, a selecting methodology of geometric parameters has been proposed to maintain the gear surface quality.

ACKNOWLEDGMENTS

The authors would like to thank the National Natural Science Foundation of China (52575051).

REFERENCES

[1] Liu, S., Zhu, C., Fuentes-Aznar, A., Song, C.: Computerized approach for design and generation of face-milled non-generated hypoid gears with low shaft angle. Mech. Mach. Theory. 155, 104084 (2021)
[2] Fuentes-Aznar, A., Ruiz-Orzaez, R., Gonzalez-Perez, I., “Computational approach to design face-milled spiral bevel gear drives with favorable conditions of meshing and contact”, Meccanica, Vol. 53(1), pp. 2669–2686, 2018.
[3] Artoni, A., Gabiccini, M., Kolivand, M., “Ease-off based compensation of tooth surface deviations for spiral bevel and hypoid gears: Only the pinion needs corrections”, Mechanism and Machine Theory, Vol. 61, pp. 84–101, 2013.
[4] Pang J, Liu S, Song C, et al. General multi-tooth contact analysis of spiral bevel and hypoid gears with arbitrary shaft angles considering the point clouds reconstruction of gear surface based on deep neural network[J]. Mechanism and Machine Theory, 2025, 214(000).DOI:10.1016/j.mechmachtheory.2025.106139.
[5] Fan, Q., Dafoe, R.S., Swanger, J.W., “Higher-order tooth flank form error correction for face-milled spiral bevel and hypoid gears”, Journal of Mechanical Design, Vol. 130(7), 2008.
[6] Liu, S., Zhu, C., Fuentes-Aznar, A., et al.: Computerized determination of the qualified region of main design parameters of face-milled hypoid gears with low shaft angle. Mech. Mach. Theory. 159, 104259 (2021)
[7] Dooner, D.B.: On evolutoids and spatial involutoids to define hypoid flank geometry. Mech. Mach. Theory. 156, 104150 (2021)

OPTIMIZATION OF NONLINEAR ACTIVE ABSORBING FOR COMPLIANT PLANAR MECHANISMS

Zbyněk Šika[1], Jan Krivošej[1], Jakub Švadlena[1]

[1] Czech Technical University in Prague, Faculty of Mechanical Engineering, Department of Mechanics, Biomechanics and Mechatronics, Technická 4, Prague 6, 160 00, Czech Republic, {zbynek.sika@fs.cvut.cz; jan.krivosej@fs.cvut.cz; jakub.svadlena@fs.cvut.cz}

1 INTRODUCTION

The pursuit of energy efficiency in robotics inevitably leads to lightweight structures that are inherently vulnerable to unwanted vibrations. Moreover, when searching for a suitable solution for various operations in industry, a dilemma often arises whether to use a completely universal robot, often with 6 degrees of freedom, or a single-purpose machine designed more or less ad hoc for a given operation. This search creates room for less standard solutions, including supplementing basic lightweight working structures with active absorbers to improve their overall dynamic behavior. While many successful active vibration suppression strategies, such as the delayed resonator [1, 2], offer high performance, they essentially operate with small vibrations and thus consider linear dynamics of the absorbers. On the other hand, static balancing techniques [3] effectively reduce actuator load but do not address dynamic oscillations induced by high-speed tracking.

The aim of the presented work is to extend the methodology of active absorption of small oscillations of linear or linearized mechanical systems to large periodic motions of nonlinear machine mechanisms. These works, on the one hand, follow up on the research of the concept of "eigenmotion" generalizing the natural vibrations of linear systems for nonlinear multi-DOF systems [4] and also extend research supplemented by the building of demonstrators of active absorbers of non-traditional shapes, such as a planar dynamically isotropic 3 DOF multibody absorber, the properties and identification of which are given in [5] (see Figure 1).

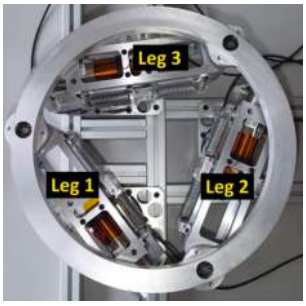

Figure 1: Demonstrator of planar dynamically isotropic 3 DOF multibody active absorber [5].

2 DYNAMICALLY NONLINEAR MECHANISMS WITH LARGE STROKE ABSORBERS

The absorber investigated in [5] is particularly suitable for absorbing "small" vibrations and the absorber can be kinematically considered as a linear system. Nonlinearity is essentially introduced only by dissipative forces in the bearings [5]. At maximum voice-coil amplitudes, the system becomes slightly nonlinear. However, current research focuses on situations where primary system, together with absorbers, operates in a fully nonlinear domain.

Several types of such mechanical systems equipped with absorbers are being considered and investigated. The system shown in Figure 2 was chosen as an illustration. This mechanism is also selected for the construction of a new demonstrator, which is currently underway. The basis of this system is a planar serial chain mechanism consisting of three rigid links. The primary objective is to control the required motion of the end point $E = [x_E(t), y_E(t)]$ using a combination of two primary drives and actuators in two absorbers. The first two joints (O, A) are driven by rotary drives through gears with stiffnesses k_{t1} and k_{t2}. The third joint (B) represents the flexible underactuated part of the system which features a nonlinear stiffness realized by two springs attached between Link 3 and Link 4. Two active vibration absorbers with large strokes driven by a linear voice-coil actuator are connected to the Link 2.

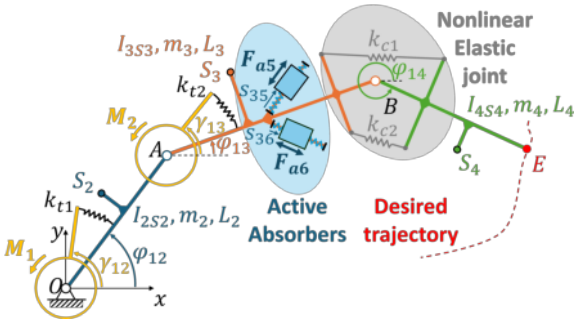

Figure 2: Scheme of the new compliant planar demonstrator for testing nonlinear active absorbing.

When synthesizing nonlinear absorbers and their effect on the primary system, multilevel optimization of the mechanical structure, actuators, and control of the entire resulting system is necessary. The problem of absorbing nonlinear vibrations of a multi-body system with absorbers typically not collocated with the end-effector becomes a dual task of coordinated motion control with classical drives and absorber actuators and optimization of the mechanical system. For the first stage of optimization of the mechanical structure and the placement of the absorbers, a method has proven successful, where the precise control of the end-effector along a given generalized trajectory is replaced by kinematic excitation. The couples and forces of future control input vector $\boldsymbol{\tau}$ in this auxiliary model serve as some constraint forces not collocated with the considered kinematic excitation constraints. As an example, for the benchmark from Figure 2, one has the following system of dynamic equations with constraint conditions $\mathbf{f}$ corresponding to requested motion of end-point E.

$$\begin{bmatrix} \mathbf{M} & -\mathbf{B} \\ \mathbf{J} & \mathbf{0} \end{bmatrix} \begin{bmatrix} \ddot{\mathbf{q}} \\ \boldsymbol{\tau} \end{bmatrix} = \begin{bmatrix} \mathbf{n} \\ -\dot{\mathbf{J}}\dot{\mathbf{q}} - \mathbf{a}_E(t) \end{bmatrix}, \mathbf{f} = \mathbf{0} = \begin{bmatrix} x_E(t) - L_2\cos\varphi_{12} - L_3\cos\varphi_{13} - L_4\cos\varphi_{14} \\ y_E(t) - L_2\sin\varphi_{12} - L_3\sin\varphi_{13} - L_4\sin\varphi_{14} \end{bmatrix}, \mathbf{J} = \begin{bmatrix} \frac{\partial f_1}{\partial q_1} & \cdots \\ \frac{\partial f_2}{\partial q_1} & \cdots \end{bmatrix}, \tag{1}$$

where the generalized coordinates of the primary structure are $\mathbf{z} = [\varphi_{12}, \gamma_{12}, \varphi_{13}, \gamma_{13}, \varphi_{14}]^T$, and the absorber masses positions are $\mathbf{s}_a = [s_{a1}, s_{a2}]^T$, $\mathbf{q} = [\mathbf{z}^T, \mathbf{s}_a^T]^T$, $\mathbf{M}(\mathbf{q})$ is mass matrix, $\mathbf{n}(\dot{\mathbf{q}}, \mathbf{q})$ captures the position and velocity dependent nonlinear and other forces, future control input vector is $\boldsymbol{\tau} = [M_1, M_2, F_{a5}, F_{a6}]^T$, $\mathbf{B}(\mathbf{q})$ is control input distribution matrix, $\mathbf{J}$ is Jacobi matrix and $\mathbf{a}_E(t)$ acceleration vector of end-point E. The goal of optimizing this auxiliary model is typically to minimize the forces in the actuators for reference trajectories with limiting the motions of the inertial masses of the absorbers. The optimization parameters are the geometric, stiffness and mass parameters of the system.

3 CONCLUSION

It should be emphasized that the feasibility of planned control along set trajectories with the help of active absorbers is not guaranteed, especially due to the often non-collocation of the acting forces with respect to end-effector. Therefore, it is often necessary to include not only parametric but also topological optimization of the entire mechanical-actuator system. Only after the above-mentioned optimization of the mechanical structure and placement of absorbers can the synthesis of the control of the entire system follow. This can be based on computed torque or similar strategies.

ACKNOWLEDGMENTS

The work has been supported by the Czech Science Foundation project 25-16357S “Absorbing mechanisms with nonlinear dynamics for active reduction of periodic motions and forces in machines”.

REFERENCES

[1] N. Olgac and R. Jenkins, “Actively Tuned Noncollocated Vibration Absorption: An Unexplored Venue in Vibration Science and a Benchmark Problem,” *IEEE Trans. Contr. Syst. Techn.*, vol. 29/1, pp. 294-304, 2021.

[2] Z. Šika, J. Krivošej and T. Vyhlídal, “Three dimensional delayed resonator of Stewart platform type for entire absorption of fully spatial vibration,” *Journal of Sound and Vibration*, 571, p.118154, 2024.

[3] V. L. Nguyen, “Gravity Compensation of Articulated Robots Using Spring Four-Bar Mechanisms,” in *Multibody Mechatronic Systems*: MuSMe 2021, Springer, 2022, pp. 201-209.

[4] J. Krivošej, P. Beneš, J. Zavřel, A. Balon, V. Halamka and Z. Šika, “Energy efficient robots based on structures with tensegrity features,” *Mechanism and Machine Theory*, no. 105364, 2023.

[5] K. Kraus, P. Kočandrle and Z.Šika, “Identification and modeling of 3-DoF mechanism with nonlinear friction effects by combination of LuGre and neural network modeling,” *Mechanical Systems and Signal Processing*, 239, p.113218, 2025.

DEVELOPABLE TRIANGLE-BASED KOKOTSAKIS POLYHEDRA

Yucai Hu[1], Guoqiang Zhu[1], Ke Chen[1]

[1] School of Mechanical Engineering, Hefei University of Technology, Hefei, Anhui 230009, China {huyc@hfut.edu.cn}

1 INTRODUCTION

A Kokotsakis polyhedron consists of an n-gon base with all vertices of degree-4. Kokotsakis formulated the problem of determining the conditions under which such polyhedral surfaces are flexible (or rigid-foldable) and investigated both their infinitesimal and finite mobility [1]. For the case of $n = 3$ (a triangular base), he established its equivalence to the three types of Bricard octahedra. The case of $n = 4$, corresponding to a quadrilateral base, is much more involved; although several special flexible types were identified early on [1, 2], a complete classification remained open. This problem was later revisited using a kinematic approach, modeling each degree-4 vertex as a spherical coupler mechanism [3, 4]. The full classification for the quadrilateral base was ultimately resolved by Izmestiev [5]. This general treatment does not assume developable vertices, and its solutions are formulated in the complexified domain, which may not always correspond to physically realizable configurations.

In origami, developability is a fundamental constraint. The crease pattern surrounding a planar polygon with developable degree-4 (DD4) vertices is commonly referred to as an origami twist [6, 7]. Consequently, the problem of rigid-foldability for such a local region is equivalent to identifying flexible *developable* Kokotsakis polyhedra, where all degree-4 vertices are developable [8]. This constraint simplifies the solution for the fold angles of the vertices. However, a dedicated analysis confined to the developable, real-domain setting of origami has been lacking in the literature. This talk addressed that gap for the case of flexible developable Kokotsakis with a triangular base (DK3). We first summarize the three known types of flexible DK3 and present their direct correspondence to the three types of Bricard octahedra. We then discuss configurations involving vertices with collinear creases. Finally, the existence of flexible DK3 with parallel pleats within these three categories is investigated.

2 THREE TYPES OF FLEXIBLE DK3

A DK3 is generally not rigid-foldable. To achieve rigid-foldability, the folding motions of its three vertices must be compatible. In this light, the types of flexible DK3 are determined according to the fold-angle solution space of the vertices. When fold angles are represented by their half cotangents, i.e., $x = \cot(\rho_x/2)$, etc, the loop condition can be expressed as $x_2 = y_1, x_3 = y_2$, and $x_1 = y_3$, as shown in Fig. 1. For a flat-foldable DD4 vertex, the relationship between x and y is linear

$$y = \mu x \quad \text{with} \quad \mu(\alpha, \beta, \sigma) = \frac{\sigma \sin\alpha - \sin\beta}{\sin(\alpha + \beta)} \tag{1}$$

where σ denotes the folding mode, and α and β are the sector angles. For a general DD4 vertex, i.e., non-flat-foldable and without collinear creases, the relationship is implicit and given by:

$$x = \varepsilon\sqrt{|a|}\frac{\mathrm{sgn}(a)\exp(\xi) + \exp(-\xi)}{2}, \tag{2}$$

$$y = \tau\sqrt{|b|}\frac{\mathrm{sgn}(b)\exp(\xi - \varphi) + \exp(-\xi + \varphi)}{2}, \tag{3}$$

where $\varepsilon = \pm$, $\tau = \varepsilon\mathrm{sgn}\left(\sin(\gamma + \delta)\right)$. All dependent on the sector angles, the parameters a and b are magnitudes, φ is a phase shift; and ξ is the free parameter characterizing the folding motion. Detailed expressions are provided in [8]. Based on the presence of flat-foldable vertices, the three types of DK3 are: 1) Equimodular type; 2) Linear coupling and one flat-foldable DD4 vertex; 3) Three flat-foldable DD4 vertices, as illustrated in Fig. 1. While the third type matches the one established by Kokotsakis, the first two types are specific subsets of his classification [1], distinguished by the constraint that every vertex is developable.

In this talk, the correspondence between the three types of DK3 and the three types of Bricard octahedra is clarified. Additionally, it remains unclear whether DD4 vertices with collinear creases can be paired to construct flexible DK3, and if so, how. The DK3 with parallel pleats (for instance, where crease z_1 and w_2 are parallel) is commonly used in origami artworks and origami-inspired applications. These additional constraints further restrict the solution space, and their existence for the three types of flexible DK3 is systematically investigated.

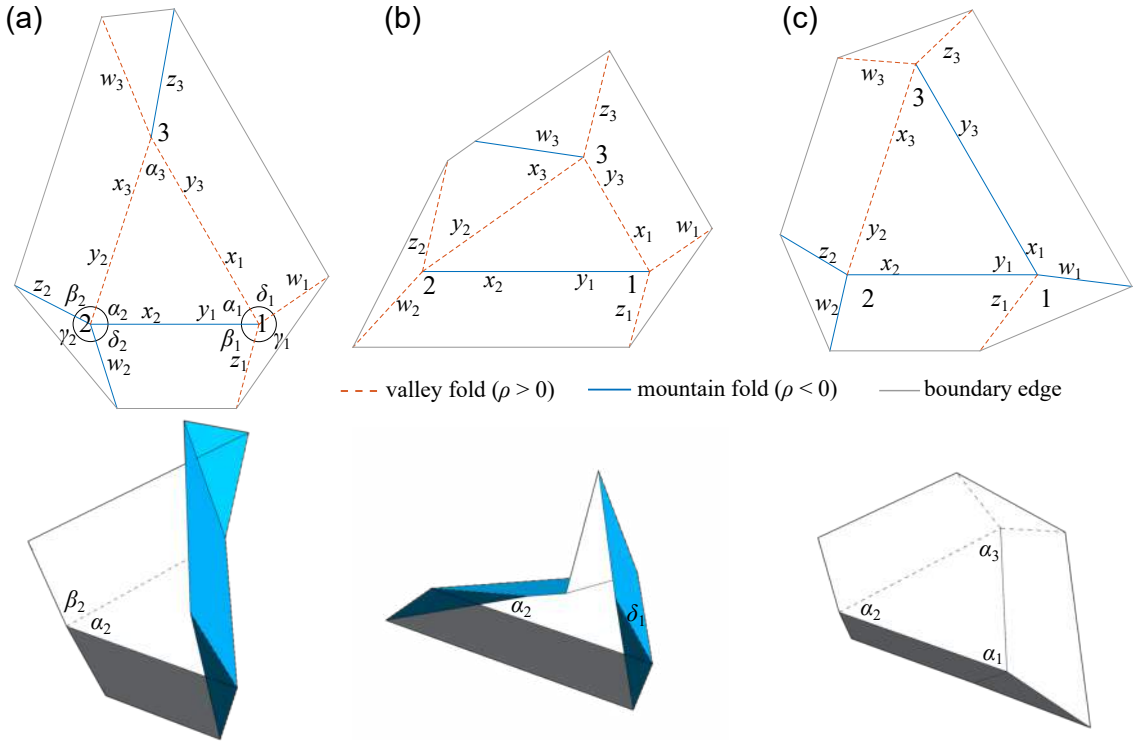

Figure 1: Three types of flexible DK3. Columns (a), (b), and (c) correspond to: 1) Equimodular type; 2) Linear coupling and one flat-foldable DD4 vertex; 3) Three flat-foldable DD4 vertices, respecitively [8].

3 CONCLUSION

This talk focuses on developable triangle-based Kokotsakis polyhedra (DK3). We explore the full configuration space of flexible DK3, with particular emphasis on analyzing cases that involve collinear developable degree-4 vertices and those incorporating parallel pleats, due to their distinct geometric characteristics and relevance in origami applications. The correspondence with the three types of Bricard octahedra is demonstrated. These findings strengthen the connection between classical mechanisms and rigid origami, providing valuable building blocks for deployable structures and origami designs.

ACKNOWLEDGMENTS

This work is supported by the National Natural Science Foundation of China (Grant No. 12102163) and the Fundamental Research Funds for the Central Universities (Grant No. JZ2024HGTB0236).

REFERENCES

[1] A. Kokotsakis, "Über bewegliche polyeder," *Mathematische Annalen*, vol. 107, no. 1, pp. 627–647, 1933.

[2] R. Sauer and H. Graf, "Über Flächenverbiegung in Analogie zur Verknickung offener Facettenflache," *Mathematische Annalen*, vol. 105, pp. 499–535, 1931.

[3] H. Stachel, "A kinematic approach to Kokotsakis meshes," *Computer Aided Geometric Design*, vol. 27, no. 6, pp. 428–437, 2010.

[4] G. Nawratil, "Reducible compositions of spherical four-bar linkages with a spherical coupler component," *Mechanism and Machine Theory*, vol. 46, no. 5, pp. 725–742, 2011.

[5] I. Izmestiev, "Classification of flexible Kokotsakis polyhedra with quadrangular base," *International Mathematics Research Notices*, vol. 2017, no. 3, pp. 715–808, 2016.

[6] T. A. Evans, R. J. Lang, S. P. Magleby, and L. L. Howell, "Rigidly foldable origami twists," in *Origami 6*, vol. 1, pp. 119–130, 2015.

[7] H. Feng, R. Peng, J. Ma, and Y. Chen, "Rigid foldability of generalized triangle twistorigami pattern and its derived 6R linkages," *Journal of Mechanisms and Robotics*, vol. 10, no. 5, p. 051003, 2018.

[8] Y. Hu and K. Chen, "Explicit kinematics of developable equimodular degree-4 vertex couplings and triangle-based Kokotsakis polyhedra," *Thin-Walled Structures*, vol. 207, p. 114369, 2025.

OPTIMAL DESIGN OF A SUSPENDED PARALLEL ROBOT FOR WALL PLASTERING

Jorge F. Aznar-Ortega[1], Adrián Peidró[1], Paula Mollá-Santamaría[1], Óscar Reinoso[1]

[1] Universidad Miguel Hernández, Avda. Universidad s/n, 03202 Elche, Spain, {jorge.aznar@goumh.umh.es}

1. INTRODUCTION

The construction industry still shows low levels of automation and remains a hazardous environment for workers [1]. Many tasks are manual, repetitive, and demand both precision and skills. Coupled with harsh and dirty working conditions, this has contributed to a decline in skilled labor, highlighting the need for robotic solutions to address workforce shortages [2]. Plastering vertical walls is one such task that is largely performed manually. While it poses minimal risk in small buildings, plastering tall structures often requires workers to operate from scaffolds, cranes, or suspended positions, increasing the risk of falls and accidents. Although plastering robots already exist, most rely on a trolley system with a vertically extendable mast [3,4]. This design limits their applicability, particularly when wall heights exceed the mast's range or when there is no stable horizontal surface to support the trolley, such as in cases involving sloped roofs or irregular bases. To overcome these limitations, a new suspended parallel robot was proposed in [5] for wall plastering. The objective of the present abstract is to optimize the design of this robot.

2. ROBOT DESCRIPTION

The analyzed wall plastering robot, shown in Fig. 1, consists of a gondola suspended by cables that moves up and down along building façades. Attached to the gondola, there is a three-degree-of-freedom 3RPR parallel robot, which controls the position and orientation of the scraper during plaster application. Furthermore, the gondola carries a retractile wall adhesion mechanism that keeps the robot firmly attached to the wall while plastering, compensating reaction forces produced while spreading mortar, which could push the robot away from the wall. This is required because cables alone cannot balance this pushing.

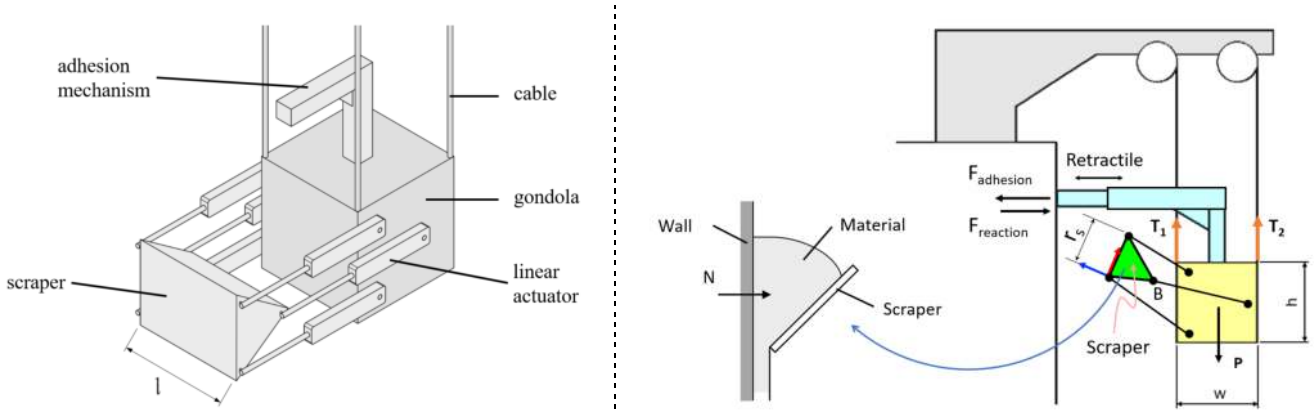

Figure 1. (a) Simplified CAD model of the analyzed robot. (b) Planar side view, with required notation. The legs L_i of the parallel robot can vary between L_{min} and L_{max}. The local coordinates of point B in the scraper reference frame are x^B_{local} and y^B_{local}.

3. OPTIMAL DESIGN

In [5], an initial design of this robot was proposed, and its feasible workspace was studied, which consists of all positions that can be reached by the scraper for a given orientation while providing enough pressure to the mortar and keeping the adhesive force to the wall positive, as well as all cable tensions. This feasible workspace depends on geometric design parameters (shown in Fig. 1b) as well as other physical parameters [5] such as friction coefficients, density of mortar, etc. While these physical parameters cannot be modified, the geometric design of the robot can be tuned in order to maximize the workspace. To achieve this, in this abstract we depart from the initial design proposed in [5] and optimize, via the Gradient Ascent algorithm, a merit function F defined as the number of discrete points of the feasible workspace $WS_{feasible} = \{(x, y) : F_{reaction}(x, y) > 0,$

$T_1(x,y) > 0,\ T_2(x,y) > 0,\ L_{min} < L_i < L_{max}\ (i = 1,2,3),\ N(x,y) > 100\}$, where this workspace is discretized with a step size of 0.01 mm. Then, we update all geometric design parameters in the direction of this gradient, repeating the whole process for a prescribed number of iterations.

4. RESULTS

Fig. 2 shows the design of the robot at different stages of the optimization, as well as the corresponding workspaces. It can be observed that the feasible workspace effectively increases in extension until reaching the wall, but after several iterations, the width of the scraper (r_s), which affects the amount of mortar and pressure exerted to the plastered wall, reduces too much and applies insufficient pressure for the plastering task. For this reason, r_s is saturated at 0.28 m if the optimization tries to reduce it below this threshold, while the rest of the parameters continue to vary. Once the workspace optimization simulations are completed, the variation of the workspace in the first, last, and two intermediate iterations can be seen in Fig 2.

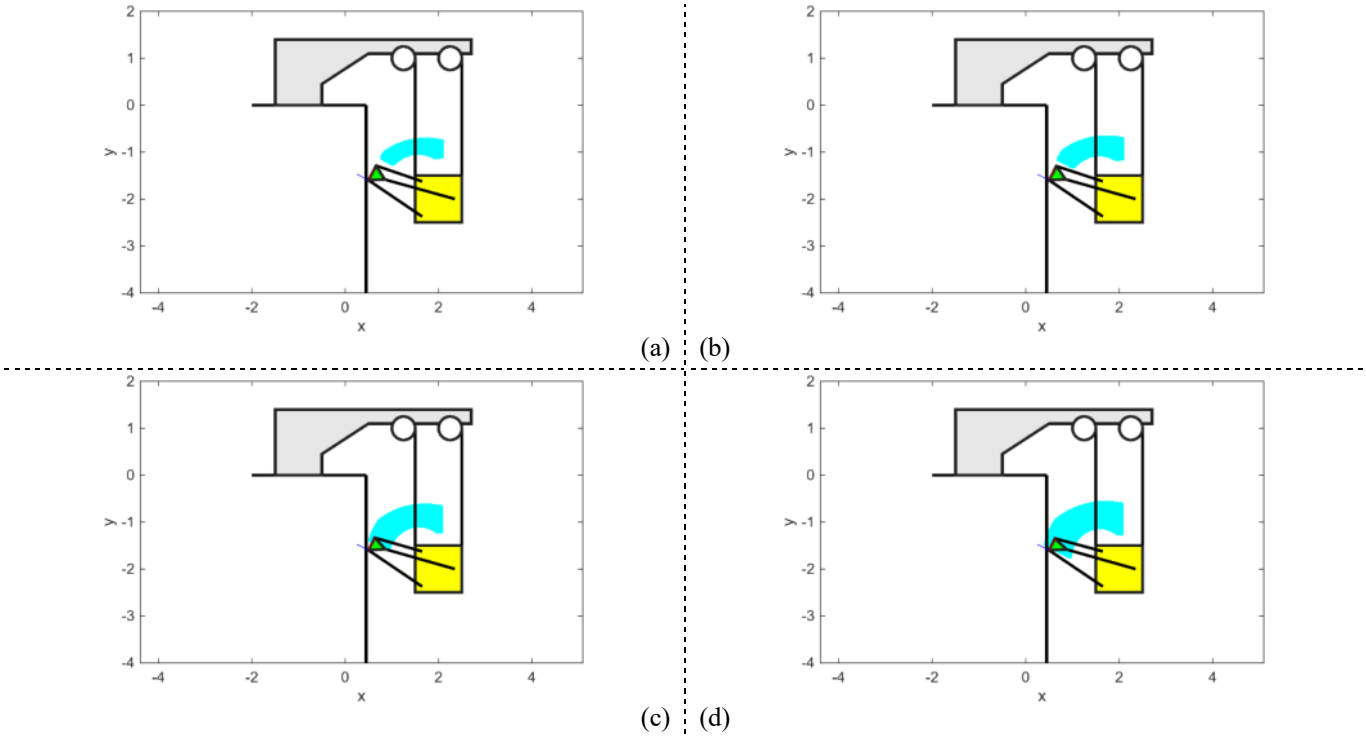

Figure 2. Design of the robot at different stages of optimization with its corresponding workspace. (a) Initial design. (b) After 35 iterations. (c) After 70 iterations. (d) After 100 iterations.

5. CONCLUSIONS AND FUTURE WORK

Optimization of the design of the proposed plastering robot shows that an increase of the feasible workspace (i.e., the workspace where adhesion and cable tension forces are positive) is favored by a reduction in key parameters such as r_s, but this reduction may prejudice the pressure that the parallel robot must exert to the mortar while spreading it on the wall, which should not fall below a minimum threshold [5]. Thus, a trade-off is required, which we will address via multi-objective optimization in the future.

ACKNOWLEDGMENTS

This work is part of the project PID2024-159765OA-I00 funded by MICIU/AEI/10.13039/501100011033 and FEDER, UE.

REFERENCES

[1] Aghimien, D. O., Aigbavboa, C. O., Oke, A. E., & Thwala, W. D. (2020). Mapping out research focus for robotics and automation research in construction-related studies: A bibliometric approach. *Journal of Engineering, Design and Technology, 18(5)*, 1063–1079.

[2] Liu, Y., AH, A., Haron, N. A., NA, B., & Wang, H. (2024). Robotics in the construction sector: Trends, advances, and challenges. *Journal of intelligent & Robotic systems, 110(2)*, 72.

[3] Liu, G., Li, Z., Zhang, J., & Bao, H. (2024, August). A mortar scraping robot for a whole wall in construction. In 2024 *IEEE International Conference on Mechatronics and Automation (ICMA)* (pp. 1688-1693). IEEE.

[4] Wang, Y., Xie, L., Chen, J., Chen, M., Hu, T., Liao, H., Sun, S., & Chen, J. (2024). Mortar spraying and plastering integrated robot for wall construction. *Automation in Construction, 165*, 105533.

[5] Aznar-Ortega, J. F., Peidró, A., Payá, L., & Reinoso, Ó. (2025). Design of a hanging parallel robot for plastering brick walls in construction. *Annals of DAAAM & Proceedings, 36*.

A BIPEDAL ROBOT BASED ON MULTI-LOOP COUPLED PARALLEL LEG MECHANISM

Donglai Xu[1, 2], Sheng Guo[1], Fuqun Zhao[1], Xiaodong Jin[1], Marco Carricato[2]

[1] Robotics Institute, School of Mechanical, Electronic and Control Engineering, Beijing Jiaotong University, Beijing 100044, PR China, {23115166@bjtu.edu.cn; shguo@bjtu.edu.cn, fqzhao@bjtu.edu.cn ; xdjin@bjtu.edu.cn }

[2] IRMA L@B, Department of Industrial Engineering, University of Bologna, Bologna 40137, Italy, { marco.carricato@unibo.it }

1. INTRODUCTION

Bipedal robots (BRs) possess human-like leg structures and modes of locomotion, enabling them to replace humans in hazardous tasks such as reconnaissance, material transportation, and firefighting rescue. The leg mechanism (LM) plays a crucial role in control performance and locomotion capability, and can generally be categorized into three types: serial[1], parallel[2], and serial–parallel hybrid[3] configurations. As a generalized parallel mechanism, the multi-loop Coupled parallel mechanism not only inherits the advantages of high speed, low inertia, and high stiffness, but also enhances the load-carrying capacity through the coupling relationships among its limbs. Therefore, it demonstrates broad application prospects in the design of LM.

2. STRUCTURAL DESIGN

The overall structure of the proposed BR is shown in Fig. 1(a), consisting of two LMs and one waist mechanism (WM). The LM adopts a multi-loop coupled parallel mechanism configuration, and its schematic diagram is illustrated in Fig. 1(b). All joints in LM are revolute pairs. The closed loop ABIDC forms a planar five-link mechanism[4], whose output motion at point I is 2T, while the output motion at link BJ is 1T1R. Let $\{L_i\}$ and $\{L_{ij}\}$ denote the output displacement subgroups or submanifolds of the mechanism at joint i and link ij, respectively. Based on Lie group theory[5], the output motion of the foot can be derived as:

$$\begin{aligned}\{L_{KJ}\} &= \{L_K\} \bigcap \{L_J\} \\ &= (\{L_{GI}\} \bigcup \{R(H,u)\}\{R(K,u)\}) \bigcap (\{L_{BI}\} \bigcup \{R(J,u)\}) \\ &= ((\{R(E,u)\}\{R(F,u)\}\{R(G,u)\} \bigcap \{R(I,u)\}) \bigcup \{R(H,u)\}\{R(K,u)\}) \bigcap (\{R(B,u)\}\{T(v)\} \bigcup \{R(J,u)\}) \\ &= \{R(I,u)\}\{R(H,u)\}\{R(K,u)\} \bigcap \{R(B,u)\}\{T(v)\}\{R(J,u)\} \\ &= \{G(u)\}\end{aligned} \tag{1}$$

According to Eq. (1), the foot is capable of planar translational motion and flexion–extension, enabling it to adapt to walking even on slope terrain. The actuators are installed at joints A, C, and E, which are connected to the WM, thereby significantly reducing the weight of the LM.

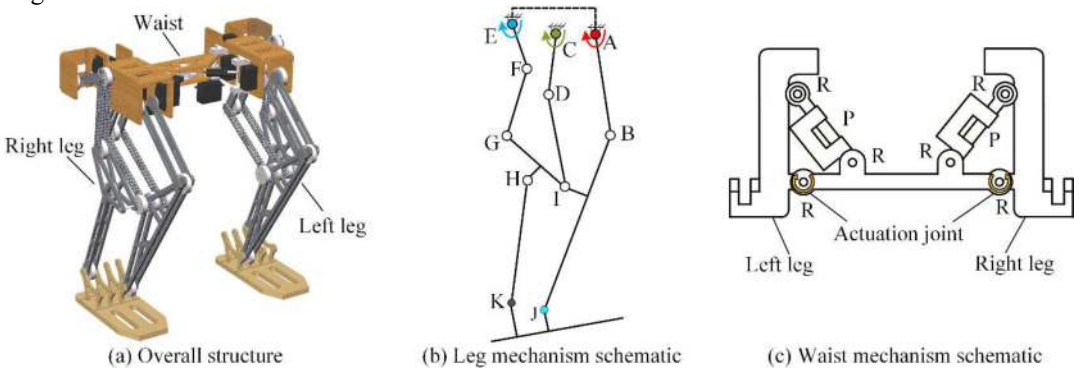

(a) Overall structure (b) Leg mechanism schematic (c) Waist mechanism schematic

Figure 1. Structure of the BR

3. PERFORMANCE ANALYSIS OF THE LM

Based on the established kinematic model, the workspace, dexterity, and stiffness performance of the LM are analyzed. Among these, the workspace is a key index in gait planning for BRs. Given the motion ranges of the actuated joints as $\alpha_1 \in [0, 90°]$, $\alpha_2 \in [90°, 180°]$, $\alpha_3 \in [-90°, 90°]$, the reachable workspace of joint J is obtained, as shown in Fig. 2(a). The results indicate that the

walking step length of the BR is at least 250 mm, and the maximum step height is approximately 160 mm. When the foot reaches its highest position, the overall height of the robot is 340 mm.

The dexterity illustrates the capability of the LM to achieve desired target poses. As shown in Fig. 2(b), the BR attains its highest dexterity when y = -50mm, z = -350 mm and θ = 0. Stiffness is another key index reflecting the LM's ability to resist deformation. When $\theta \in [0, 45°]$, $y \in$[-50, 100]mm, $z \in$ [-400,-300]mm, the stiffness of the LM remains at a relatively high level, as illustrated in Fig. 2(c). The stiffness variation along the y-axis is relatively moderate.

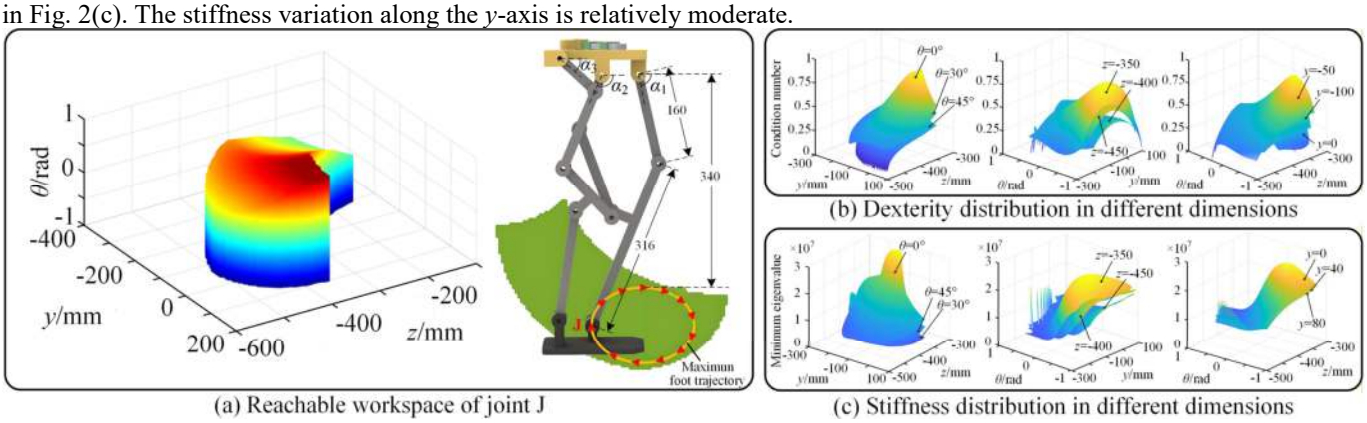

(a) Reachable workspace of joint J

(b) Dexterity distribution in different dimensions

(c) Stiffness distribution in different dimensions

Figure 2. Performance indicators of the LM

4. WALKING SIMULATION

Based on the gait and trajectory planning of the BR, its capabilities for slope walking and turning walking are verified through simulations. As shown in Fig. 3(a), the BR achieves a smooth transition from flat terrain to slope terrain and then back to flat terrain. Fig. 3(b) illustrates the process by which the BR completes a right-angle turn after two adjustment steps.

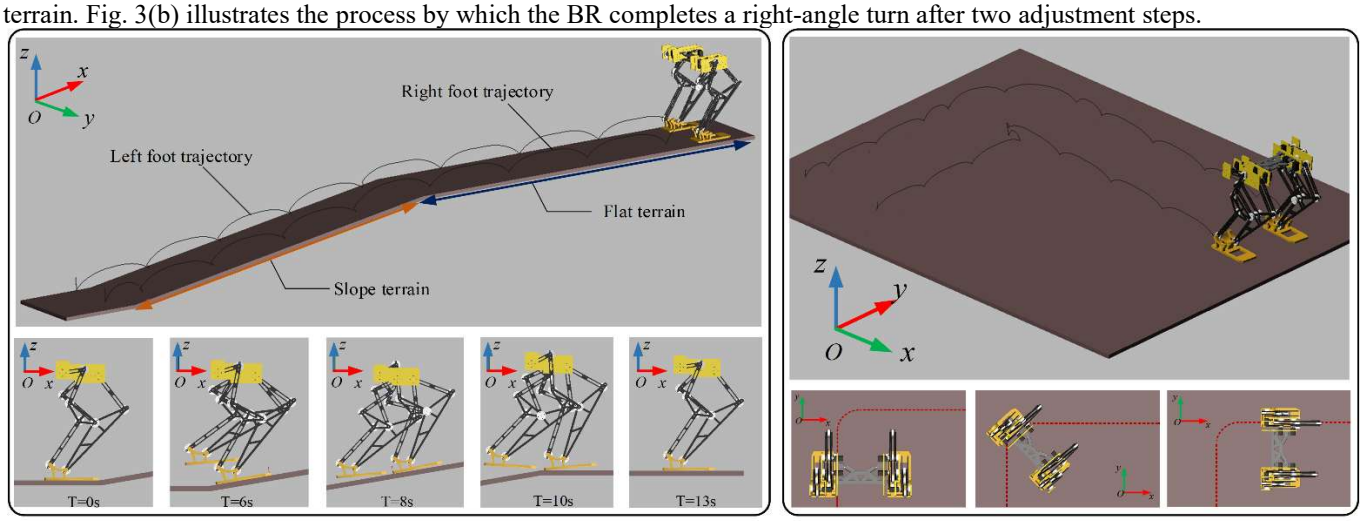

(a) Slope walking process

(b) Turning walking process

Figure 3. Functional verification of the BR

ACKNOWLEDGMENTS

D. Xu is grateful for the financial support of the Fundamental Research Funds for the Central Universities (Grant No. 2025YJS151) and the China Scholarship Council (Grant No. 202507090218).

REFERENCES

[1] W. Zhu, L. Qiao, Y. Lu, X Rong, Y Fan, Y Li, R Song, G Zhang, "Design and control of halfMan: a human-sized bipedal robot with high payload". *IEEE/ASME Transactions on Mechatronics*, 31(1), 278-289, 2025.

[2] Z. Xia, D. Zhang, Y. Chen, C Tian, J Liu, C Wu, "A novel 6 DOFs generalized parallel manipulator design and analysis based on humanoid leg". *Mechanism and Machine Theory*, 176, 105029, 2022.

[3] K. Hirashima, N Myers, DC Zamora, KG Gim, J Kim, "Implementation of untethered biped robots utilizing serial-parallel hybrid leg mechanisms", *2024 IEEE-RAS 23rd International Conference on Humanoid Robots (Humanoids)*, Nancy, France, November 22-24, 2024.

[4] D. Xu, S. Guo, X. Jin, F Zhao, Y Fang, "Design and analysis of a novel class of hybrid parallel manipulators with 3+3 degrees of freedom and remotely operated grippers". *Mechanism and Machine Theory*, 212, 106073, 2025.

[5] J. M. Hervé, "The Lie group of rigid body displacements, a fundamental tool for mechanism design". *Mechanism and Machine theory*, 34(5), 719-730, 1999.

APPROACHES TO MODELING LEAF SPRINGS IN RAILWAY VEHICLES AND THEIR VALIDATION

Pavel Polach, Michal Hajžman, Ondřej Skála, Kamil Šimeček

Research and Testing Institute Plzen, Research Centre Řež, Tylova 1581/46, 301 00 Plzen, Czech Republic, {pavel.polach@vzuplzen.cz; michal.hajzman@vzuplzen.cz; ondrej.skala@vzuplzen.cz; kamil.simecek@vzuplzen.cz}

1. INTRODUCTION

Leaf springs are an important structural component of (not only) railway vehicles. The leaf springs are complex spatial suspension elements. They can transmit forces and torques in all three directions. Their properties are influenced by the leaves flexibility, by contact and friction forces between the leaves and between chain links (shackles) and by other operational conditions. When creating multibody models of such vehicles, they must be included in the overall vehicle model. Approaches to modeling these springs are relatively well known (e.g. [1-3]). However, when developing a computational model of a specific vehicle, it is necessary to consider the suitability of the chosen spring model, which depends on the planned type of vehicle operation simulations as well as on the availability and quality of input data for spring modeling. The spring model should account for both their elastic and damping properties, as well as changes in these properties when individual leaves come into contact with adjacent leaves. Various types of leaf spring models in the framework of multibody models are described in [4].
This paper presents approaches to modeling the spring–damping properties of two types of freight railway wagons, each designed for a different purpose, with the performed simulations focused on different aspects of investigating their dynamic behavior.

2. APPROACHES TO THE LEAF SPRINGS MODELING AND THEIR VALIDATION

The first wagon (see Fig. 1), a British Rail MGR Coal Hopper HAA two-axle open coal wagon, was tested on a test rig (its running on a railway track was not modeled) [5]. The purpose of the laboratory tests and their simulations was to assess the suitability of replacing the existing steel leaf springs with composite springs.

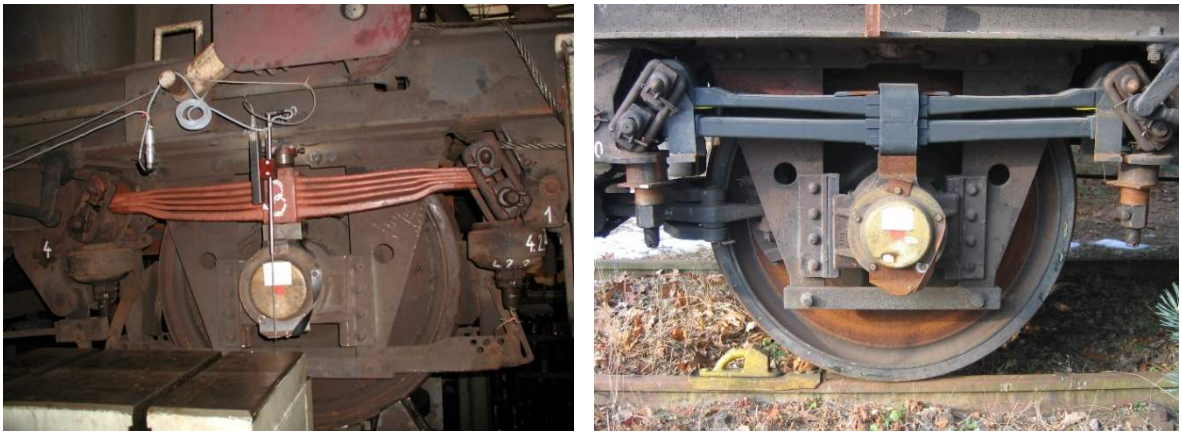

Figure 1. The parabolic steel spring and the composite spring of the MGR Coal Hopper HAA wagon.

The second non-standard special 32-axle wagon (see Fig. 2), intended for transporting exceptionally large and heavy loads, is currently in the conceptual design stage [6]. For the imagination: the net weight of the wagon is 295 tons, the maximum weight of the load is 170 tons. The aim of the simulations was to evaluate the running behavior of the wagon with respect to meeting the operating conditions for railway track operation in accordance with the EN 14363 standard “Railway applications – Testing and Simulation for the acceptance of running characteristics of railway vehicles – Running Behaviour and stationary tests”, which, among other aspects, includes requirements for railway vehicles related to derailment safety.
Multibody models of the MGR Coal Hopper HAA wagon were created using the SIMPACK and the Alaska simulation tools. A special approach was applied for the modelling of leaf springs on the basis of the measured static vertical force-deformation characteristics. These characteristics were nonlinear and exhibited clear hysteresis effects. The finite segment method in

combination with nonlinear torque and friction elements was employed to represent the spring behavior [7]. The chosen approach was a compromise between a complex massless force model [8] and a full flexible body model [9]. One common challenge in modelling real railway vehicles is ensuring consistency between measured physical parameters and idealized parameters derived from drawings or CAD models. For this reason, a sensitivity analysis was conducted to evaluate how variations in selected multibody model parameters affect the dynamic response of the vehicle. The transverse and longitudinal flexibility of the leaf springs was subsequently estimated based on the previously determined vertical stiffness characteristics. The simulation results were validated with the results of laboratory dynamic tests on a test rig.

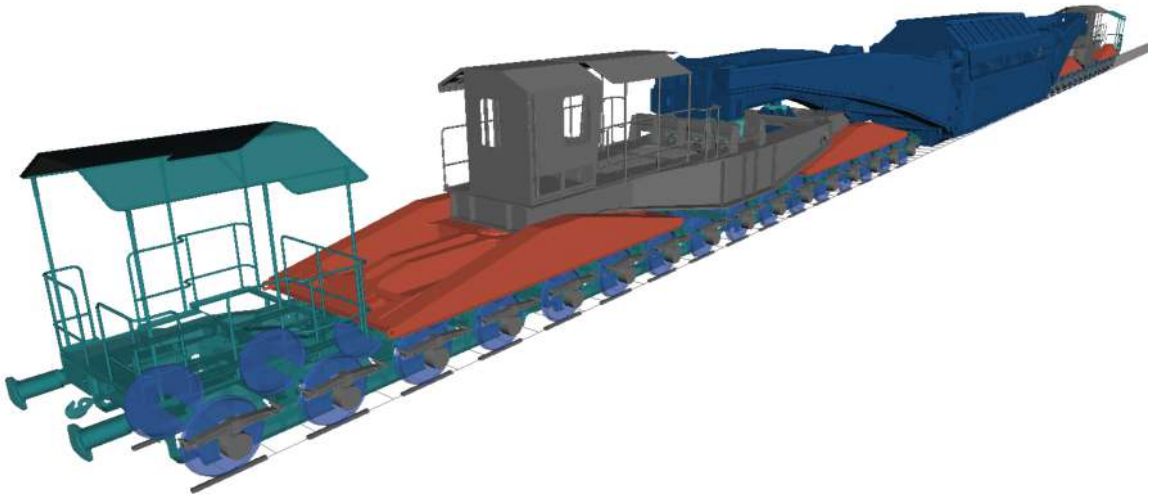

Figure 2. Visualisation of the non-standard 32-axle wagon in the SIMPACK software.

Multibody models of the special 32-axle wagon were also created using the SIMPACK software. The linear stiffness and damping coefficients representing the leaf springs were derived partly from technical documentation provided by the manufacturer and partly from expert estimates supported by published literature in this field [4]. In the multibody models, the leaf springs were represented using bushing elements.

3. CONCLUSION

The paper presents approaches to modeling leaf springs within multibody simulations of freight railway wagons with different operational purposes. For the MGR Coal Hopper HAA wagon, a nonlinear model based on measured force-deformation characteristics was implemented and validated through sensitivity analysis, while the conceptual 32-axle wagon was represented using linearized stiffness and damping parameters derived from available documentation and literature. The results highlight that the level of model complexity should reflect both the intended simulation objectives and the availability of reliable input data.

ACKNOWLEDGMENTS

This research was supported by the project CZ.02.01.01/00/23_021/0009165 “Development of digital twins of structural components with support of on-line monitoring of their operational loading and simulations in laboratory conditions” funded by the Johannes Amos Comenius Programme. The project is co-funded by the European Union.

REFERENCES

[1] S. Iwnicki, M. Spiryagin, C. Cole and T. McSweeney, *Handbook of Railway Vehicle Dynamics. Second Edition.* Boca Raton, CRC Press, 2019.

[2] B. Kadziela, M. Manka, T. Uhl and A. Toso, “Validation and optimization of the leaf spring multibody numerical model”. *Archive of Applied Mechanics*, 85(12), 1899-1914, 2015.

[3] K. Addepalli, N. Remisoski, A. Sleath and S. Liu, “A Multibody Dynamics Approach to Leaf Spring Simulation for Upfront Analyses”. *SAE Technical Paper*, 2015-01-2228, 2015.

[4] M. Hajžman and P. Polach, “Modelling of leaf springs in the framework of multibody models”, *Proceedings of 9th International Scientific Conference Applied Mechanics 2007*, Ostrava, Czech Republic, April 16–19, 2007.

[5] P. Polach and M. Hajžman, “Computer simulations of the freight wagon laboratory excitation”. *Mechanics Based Design of Structures and Machines: An International Journal*, 39(2), 194-209, 2011.

[6] P. Polach and M. Hajžman, “Computational Support for the Structural Design of a Non-standard Railway Wagon”, *Proceedings of The 11th Asian Conference on Multibody Dynamics 2024 ACMD2024*, Suwon, Korea, August 26–28, 2024.

[7] A.A. Shabana, “Flexible Multibody Dynamics: Review of Past and Recent Developments”. *Multibody System Dynamics*, 1(2), 189-222, 1997.

[8] M. Hoffmann, *Dynamics of European two–axle freight wagons*. Lyngby, PhD Thesis, Technical University of Denmark, 2003.

[9] H. Sugiyama, A.A. Shabana, M.A. Omar and W.-Y. Loh, “Development of nonlinear elastic leaf spring model for multibody vehicle systems”. *Computer Methods in Applied Mechanics and Engineering*, 195(50-51), 6925-6941, 2006.

A PLANAR PARALLEL ROBOT WITH A REMOTE-CONTROLLED ORIENTABLE TWO-FINGER GRIPPER

Tan Sy Nguyen[1], Simon Foucault[2]

[1] Université du Québec à Rimouski, Rimouski, QC, Canada{tansy_nguyen@uqar.ca}
[2] Université Laval, Québec, QC, Canada {Simon.Foucault@gmc.ulaval.ca}

In industry, robots are typically used in two main object manipulation tasks: assembly and inspection/sorting. Serial robots are typically preferred for the former, while parallel robots are widely used for the latter. The main advantage of parallel robots is that all actuators can be fixed at the base. Therefore, the moving mass and inertia are significantly reduced, and operational speed can accordingly be increased to boost productivity. Also, from a control perspective, the inverse kinematics are simpler compared to those of serial robots [1]. Furthermore, it is unique to parallel architectures to design configurable platforms and remotely operated grippers based on kinematic redundancy, which can also be applied to avoid singularities and to enlarge the robot's workspace [2]. As many industrial tasks are simple and only require movements in a single plane, especially pick-and-place, this work targets simple point-to-point tasks and proposes a planar parallel architecture featuring a remotely operated gripper.

1 PROPOSED ARCHITECTURE

In this work, the authors present a conceptual design of a four-degree-of-freedom planar parallel mechanism. The proposed architecture consists of two identical legs, as shown in Figure 1a. In each leg, two actuators are fixed at the base. The first actuator controls a serial arm. The first parts of both legs (the black parts) are connected together to position point S in the plane. This base structure forms a standard 5-bar mechanism. Meanwhile, the second actuator drives two parallel mechanisms that are connected to one of the fingers at the end-effector. The second part of the leg (the red part) is coupled to the first part and allows each finger to be manipulated independently. Therefore, the gripper can actively change its opening width and orientation during motion.

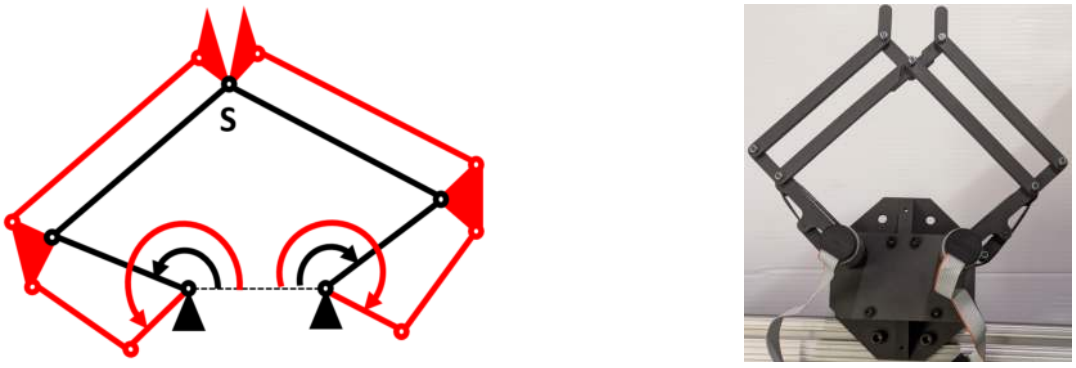

(a) Proposed architecture. (b) Robot prototype.

Figure 1: The proposed (2+2)-DOF planar parallel robot.

2 KINEMATIC ANALYSIS

Robot parameters and position vectors are defined in the fixed frame Oxy and illustrated in Figure 2a. Two angles on each leg (corresponding to $i = 1, 2$) are combined and defined as the joint coordinate vector of this robot, $\boldsymbol{\theta} = [\theta_{11}, \theta_{12}, \theta_{21}, \theta_{22}]^T$. The Cartesian coordinates of the robot are defined as $\boldsymbol{x} = [\boldsymbol{p}^T, \boldsymbol{\delta}^T]^T$, in which vector $\boldsymbol{p} = [x, y]^T$ and $\boldsymbol{\delta} = [\delta_1, \delta_2]^T$ are respectively the Cartesian position of the robot and the angles of the robot gripper with respect to x-axis

The authors analyze the kinematics of the position part and the gripping part separately, the corresponding velocity equation of each part can be obtained in the matrix form as $\boldsymbol{J}_p[\dot{x}, \dot{y}]^T = \boldsymbol{K}_p[\dot{\theta}_{11}, \dot{\theta}_{12}, \dot{\theta}_{21}, \dot{\theta}_{22}]^T$ and $\boldsymbol{J}_g[\dot{\delta}_1, \dot{\delta}_2]^T = \boldsymbol{K}_g[\dot{\theta}_{11}, \dot{\theta}_{12}, \dot{\theta}_{21}, \dot{\theta}_{22}]^T$, in which $\boldsymbol{J}_p \in \mathbb{R}^{2\times2}, \boldsymbol{K}_p \in \mathbb{R}^{2\times4}$ and $\boldsymbol{J}_g \in \mathbb{R}^{2\times2}, \boldsymbol{K}_g \in \mathbb{R}^{2\times4}$ are respectively Jacobian matrices of the position part and the gripping part. The general velocity equation of the robot can be derived from these two

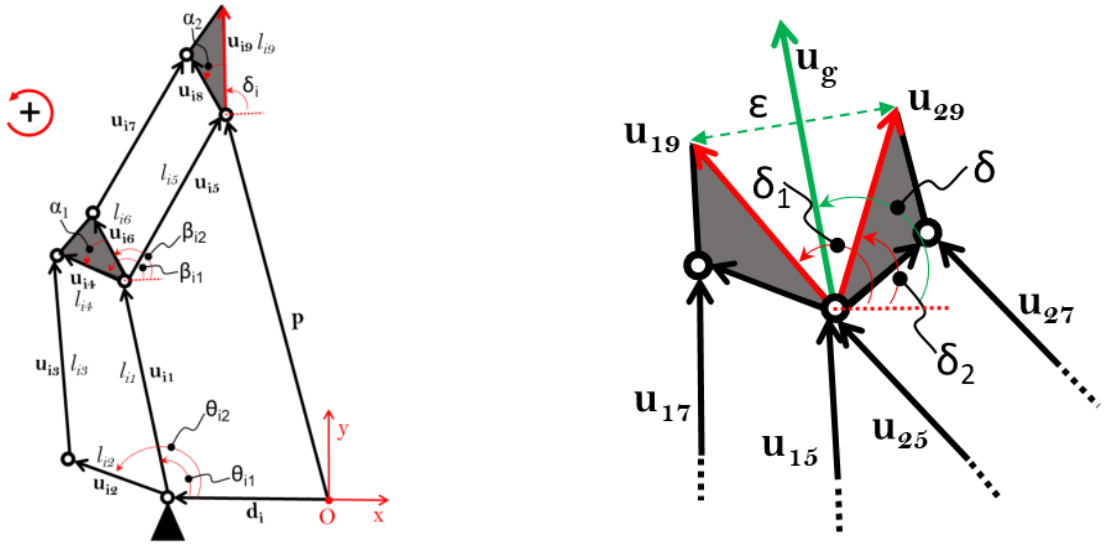

(a) (b)

Figure 2: Robot parameters and position vectors.

equations with the definition of Jacobian matrices $\boldsymbol{J}, \boldsymbol{K}$ as follows

$$\boldsymbol{J}\begin{bmatrix}\dot{x} & \dot{y} & \dot{\delta}_1 & \dot{\delta}_2\end{bmatrix}^T = \boldsymbol{K}\begin{bmatrix}\dot{\theta}_{11} & \dot{\theta}_{12} & \dot{\theta}_{21} & \dot{\theta}_{22}\end{bmatrix}^T, \boldsymbol{J} = \begin{bmatrix}\boldsymbol{J}_p & \boldsymbol{0}_{2\times2} \\ \boldsymbol{0}_{2\times2} & \boldsymbol{J}_g\end{bmatrix}, \boldsymbol{K} = \begin{bmatrix}\boldsymbol{K}_p \\ \boldsymbol{K}_g\end{bmatrix} \tag{1}$$

The singularity of this robot can be categorized into two types: Type I and Type II as introduced in [3]. A Type I singularity occurs when either Jacobian matrix $\boldsymbol{K}_p$ or $\boldsymbol{K}_g$ becomes singular, which happens at the boundary of the workspace. A Type II singularity occurs when either Jacobian matrix $\boldsymbol{J}_p$ or $\boldsymbol{J}_g$ is singular, which is often more challenging to avoid as it occurs inside the workspace. The singularity analysis can be performed separately on the position part and the gripping part. Then, the forward kinematics and inverse kinematics of this robot can be analytically computed to control the robot movements. However, due to kinematic coupling, the kinematics of the positioning part must be solved first, followed by those of the gripping part. In order to facilitate the grasping action, the orientation and the opening are typically preferred control parameters and they are respectively represented in Figure 2b as ε, the distance between two fingertips, and δ, the angle between the bisector vector $\boldsymbol{u}_g$ and x-axis. The relationship between these two parameters and the two Cartesian coordinates δ_1, δ_2 is given as $\delta = \frac{\delta_1+\delta_2}{2}$ and $\varepsilon = 2l_{i9}\sin(\delta - \delta_2)$

3 PROTOTYPING AND OPERATION

The coupled motion between the positioning and gripping parts introduces complexities in trajectory planning, for example, when the gripper holds an object while the robot is in motion. Several alternative mechanisms can be used to replace the parallel mechanisms of the gripping part to not only decouple this motion but also to avoid singularities. In the first prototype of the robot, shown in Figure 1b, the authors implemented a timing belt on the proximal link of the gripping part of each leg. The robot was programmed to perform a simple pick-and-place task, with a trajectory specifically planned to demonstrate its simultaneous translation and gripping capabilities. This demonstration can be viewed in the video accompanying this abstract at the following link: `https://youtu.be/z0qaUjCNwZc`.

ACKNOWLEDGMENTS

The authors would like to thank Prof. Clément Gosselin (Université Laval) for the practical advice to improve the architecture of the robot.

REFERENCES

[1] J. -P. Merlet, *Parallel Robots*. Springer-Verlag, 2006.

[2] K. Wen et al. , "A Backdrivable Kinematically Redundant (6+3)-Degree-of-Freedom Hybrid Parallel Robot for Intuitive Sensorless Physical Human–Robot Interaction". *IEEE Transactions on Robotics*, vol. 37, no. 4, pp. 1222-1238, 2021.

[3] C. Gosselin and J. Angeles, "Singularity analysis of closed-loop kinematic chains". *IEEE Transactions on Robotics and Automation*, vol. 6, no. 3, pp. 281-290, 1990.

GRAVITY COMPENSATION MECHANISMS FOR PASSIVE AND QUASI-PASSIVE EXOSKELETONS

Marla Weltken[1], Sérgio B. Gonçalves[1], Miguel Tavares da Silva[1]

[1]IDMEC, Instituto Superior Técnico, Universidade de Lisboa, Av. Rovisco Pais 1, 1049-001 Lisboa, Portugal
{marla.weltken, sergio.goncalves, miguelsilva}@tecnico.ulisboa.pt

1. INTRODUCTION

Passive and quasi-passive exoskeletons are assistive technologies designed to support the human body during functional tasks by providing mechanical assistance that may enhance task performance or reduce the muscular effort required to execute movements. Unlike active exoskeletons, which rely on powered actuators and external energy sources, passive systems employ mechanical elements such as springs, counterweights, elastic bands, or compliant mechanisms to generate assistive forces without the use of external power sources [1].

Within the broader category of passive and quasi-passive exoskeletons, gravity compensation-based mechanisms stand out. These systems are specifically designed to counteract gravitational loads acting on body segments, thereby reducing the net joint torque that must be generated by the user. Gravity compensation is especially beneficial for individuals with neurological impairments or musculoskeletal disorders, for whom muscle weakness or impaired motor control limits functional performance. By partially offsetting segmental weight and other external loads, these devices can facilitate movement execution, promote rehabilitation, and improve functional independence.

The widespread adoption of passive and quasi-passive exoskeletons in rehabilitation and assistive technologies has led to the development of various gravity compensation mechanisms tailored to different joints and body segments. However, the existing literature remains fragmented, with heterogeneous design methodologies, evaluation metrics, and reporting standards, limiting objective comparison across devices and hindering systematic design optimization. Therefore, this systematic review aims to synthesize the current state of the art in human exoskeletons that integrate gravity compensation mechanisms, categorizing the underlying mechanical strategies and mapping their application to different joints and body segments.

2. METHODS

A systematic literature search was conducted following the PRISMA 2020 guidelines to identify passive and quasi-passive exoskeletons that include gravity compensation-based mechanisms. The search was conducted on the Web of Science, Scopus, IEEE Xplore, and PubMed databases, covering studies published up to September 2025.

The inclusion criteria comprised peer-reviewed articles describing mechanical gravity compensation mechanisms integrated into wearable assistive devices for the human body. Studies involving fully active exoskeletons, powered robotic systems without passive gravity compensation components, or robotic devices not intended for human assistance were excluded from this analysis. The selected articles were examined with respect to their underlying mechanical principles, targeted joints, and gravity compensation strategies. The extracted data included anatomical joint or body part addressed, mechanism type, target population, validation methodology, reported effectiveness in reducing muscle activity and/or joint loading, and device dimensions and mass.

3. RESULTS

After duplicate removal and multi-stage screening (titles, abstracts, and full texts), 80 studies met the inclusion criteria and were retained for analysis. As illustrated in Figure 1a, the temporal distribution of the identified studies indicates an increase in the development and application of gravity compensation mechanisms over the past 25 years, showing a clear trend for the integration of these mechanisms in rehabilitation exoskeletons.

The majority of studies targeted the upper limbs, particularly multi-joint shoulder–elbow systems (38), followed by lower-limb exoskeletons (20). A smaller number of works addressed single-joint devices, including shoulder-only (9) and elbow-only (5) exoskeletons, with fewer studies addressing the wrist (1) and lower back/trunk (2). Spring-based mechanisms were the most common, appearing in 59 studies. Hybrid systems, combining springs with other elements, were found in 10 studies, while compliant mechanisms were used in 9. Counterweight mechanisms were the least common, appearing in only 2 studies. In terms of transmission architecture, direct actuation mechanisms were the most prevalent (40), followed by linkage-based structures (28 studies). Pulley/cable-driven systems were used in 12 studies. Most studies, 25 in total, used proof-of-concept (non-human) testing, while 23 studies employed computational modeling. Validation on healthy subjects was conducted in 14 studies, and only 10 studies tested the exoskeletons in target user groups, as shown in Figure 1b.

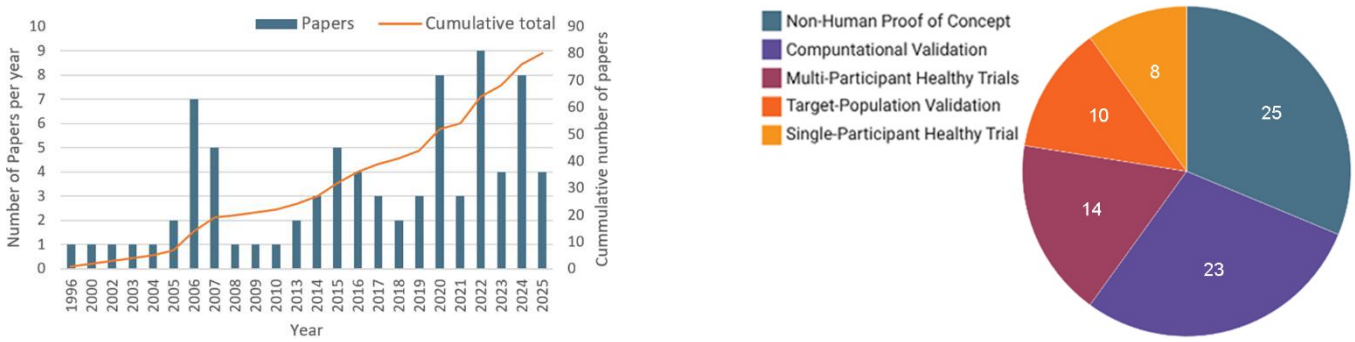

Figure 1. a) Temporal distribution of the included studies, showing the number of publications per year and the cumulative total (left); b) Distribution of validation approaches across the included studies (right).

4. DISCUSSION

The findings of this review reveal that passive and quasi-passive exoskeletons primarily rely on spring-based mechanisms for gravity compensation, which are favored for their mechanical simplicity, energy efficiency, low weight, and ease of integration. However, while simple spring-based solutions are highly effective for 1 DoF joints, they may be insufficient for anatomically complex joints, such as the shoulder, where the gravitational load is nonlinear and varies across the range of motion [2]. Consequently, constant-stiffness torsional or linear springs cannot perfectly match the joint torque profile throughout the full workspace. To address this limitation, hybrid systems, combining springs with linkages or pulleys, are typically more effective, as these architectures enable modulation of the effective moment arm or transmission ratio, allowing a closer approximation of the gravitational torque curve, particularly in multi-DOF configurations. In contrast, the elbow, primarily a single-DOF revolute joint, allows for simpler compensation strategies. The results show that spring-only systems are often sufficient to achieve near-complete gravity compensation in elbow exoskeletons across the entire range of motion, provided that appropriate stiffness and attachment geometry are selected [3]. The relatively predictable gravitational torque profile facilitates effective assistance with limited mechanical complexity, making such solutions particularly attractive for lightweight and cost-effective designs.

While compliant mechanisms were less common in the studies reviewed, they offer a lightweight alternative to traditional spring-based systems, with the potential for compact designs in elbow and wrist exoskeletons. However, the performance of these mechanisms can be limited by material fatigue and nonlinear deformation, which may hinder their long-term effectiveness [4].

Another trend identified in this review is the growing interest in hybrid mechanisms that combine multiple passive components to better approximate complex torque profiles across broad ranges of motion. While these systems provide improved flexibility and compensation accuracy, their increased mechanical complexity may negatively impact device weight, bulk, and user comfort. Careful mechanical optimization is therefore essential to balance compensation performance with wearability and usability [5].

Finally, the importance of user comfort and usability cannot be overstated. The majority of studies emphasize the need for lightweight designs and adjustable support levels, especially for rehabilitation exoskeletons. Exoskeletons must be not only mechanically effective but also comfortable to wear for extended periods, particularly in daily functional tasks.

5. CONCLUSION

This systematic review provides a comprehensive overview of passive and quasi-passive gravity compensation-based mechanisms integrated in exoskeletons. The findings indicate that while spring-based mechanisms are the most prevalent due to their simplicity and effectiveness, hybrid and compliant systems are increasingly used for more complex joints like the shoulder. The review also highlights the importance of considering user comfort and wearability, particularly in rehabilitation settings, where long-term use is essential. Future research should focus on optimizing hybrid systems and ensuring their practical applicability through user-centered studies and long-term evaluations.

ACKNOWLEDGMENTS

The authors acknowledge Fundação para a Ciência e a Tecnologia (FCT) for its financial support via LAETA (project https://doi.org/10.54499/UID/50022/2025).

REFERENCES

[1] L.P. Quinto, P. Pinheiro, S.B. Gonçalves, I. Roupa, P.P. Simões, M.T. d. Silva, Analysis of a passive ankle exoskeleton for reduction of metabolic costs during walking, Defence Technology 37 (2024). https://doi.org/10.1016/j.dt.2023.11.015.

[2] S.D. Ghazaryan, M.G. Harutyunyan, Y.L. Sargsyan, V. Arakelian, Design of Statically Balanced Assistive Devices, Mechanisms and Machine Science 115 (2022) 165–192. https://doi.org/10.1007/978-3-030-95750-6_7.

[3] M. Tschiersky, E.E.G. Hekman, D.M. Brouwer, J.L. Herder, Gravity Balancing Flexure Springs for an Assistive Elbow Orthosis, IEEE Trans. Med. Robot. Bionics 1 (2019) 177–188. https://doi.org/10.1109/TMRB.2019.2930341.

[4] R. Altenburger, D. Scherly, K.S. Stadler, Design of a passive, iso-elastic upper limb exoskeleton for gravity compensation, ROBOMECH Journal 3 (2016). https://doi.org/10.1186/S40648-016-0051-5.

[5] G. Vazzoler, P. Bilancia, G. Berselli, M. Fontana, A. Frisoli, Preliminary Analysis and Design of a Passive Upper Limb Exoskeleton, 2021 20th International Conference on Advanced Robotics, ICAR 2021 (2021) 569–574. https://doi.org/10.1109/ICAR53236.2021.9659373.

EXPERIMENTAL VALIDATION OF A MECHANICALLY SYNCHRONIZED MODULAR LEGGED ROBOT FOR IN-PIPE LOCOMOTION

Esdras S. da Silva[1], Rafael W. Duarte[1], Gustavo Q. Fernandes [1], Duber F. Garzon[1], Gustavo V. Souza[1], Henrique Simas[1], Tiago C. Pinto[1], Daniel Martins[1]

[1] Federal University of Santa Catarina (UFSC), Florianópolis - SC, Brazil, {https://ufsc.br; esdras.silva@ufsc.br}

1 INTRODUCTION

Flexible risers used in offshore oil and gas production require periodic internal inspection to ensure structural integrity under severe operational conditions [1]. Due to geometric confinement, limited accessibility, and hazardous environments, robotic systems have become a suitable alternative to human inspection [2, 3]. Among locomotion strategies, legged mechanisms present advantages in constrained cylindrical environments due to improved traction, adaptability, and tolerance to local geometric variations [4]. However, ensuring continuous radial contact, mechanical synchronization, and stable propulsion inside pipes remains a challenging mechanism design problem.

This work presents the experimental validation of a complete modular robotic platform for internal pipe locomotion. The robot is based on a patented planar six-bar leg mechanism with a single degree of freedom. Previous studies addressed the design and kinematic feasibility of a single walking leg [5] and the development and evaluation of a three-legged motor unit [6]. The present contribution advances this research by integrating multiple motor units into a fully assembled robotic structure and experimentally validating its performance inside cylindrical tubes.

2 ROBOT ARCHITECTURE

The locomotion system is based on a planar six-bar linkage with one global degree of freedom. The mechanism was designed to generate a walking trajectory compatible with radial contact inside cylindrical surfaces, promoting extended contact intervals and smooth transitions between support and swing phases.

Three legs are radially arranged at 120° within each motor unit. The complete robot consists of four motor units aligned along a central shaft. A NEMA 17 stepper motor with a through-shaft configuration is positioned centrally, and all motor units are mechanically coupled through this shaft. Consequently, all twelve legs share the same actuation input, resulting in a globally synchronized single-DOF system. Fig. 1 summarizes the robot architecture, six-bar leg trajectory, modular integration, and experimental validation inside a transparent tube.

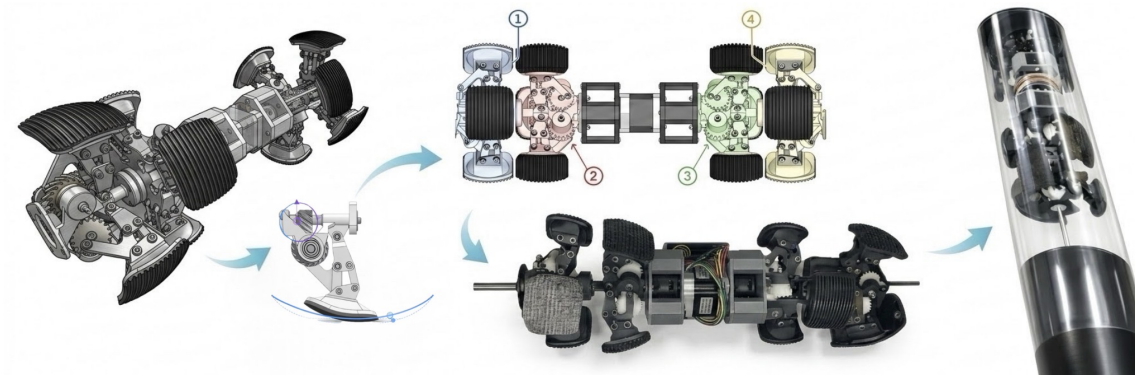

Figure 1: Robot architecture and validation sequence: (i) CAD model; (ii) single-leg trajectory; (iii) four synchronized motor units; (iv) manufactured prototype; (v) operation inside a transparent tube.

Synchronization is achieved purely through mechanical assembly and phase offset between units, eliminating the need for electronic phase control. The alternation strategy ensures that while one group of legs performs swing motion, another group maintains radial contact with the internal pipe wall, preserving stability and continuous propulsion.

3 EXPERIMENTAL SETUP

To validate the complete robotic structure, experimental tests were conducted inside a cylindrical tube compatible with the robot dimensions. The tube was manufactured in transparent material, allowing direct visual inspection of internal contact behavior and gait dynamics during operation.

The transparent configuration enabled qualitative assessment of radial contact, alternation between support and swing phases, stability during locomotion, and potential slip events. This visual feedback was essential to confirm whether the intended contact pattern and mechanical synchronization were effectively achieved.

The evaluation focused on continuous locomotion over successive gait cycles, maintenance of support during phase alternation, repeatability of synchronized motion, and structural integrity under confined operation.

4 RESULTS AND DISCUSSION

The complete robotic platform successfully achieved continuous locomotion inside the transparent cylindrical tube. The mechanically imposed phase difference between motor units produced a stable alternation pattern, ensuring that a subset of legs remained in radial contact at all times. Visual inspection confirmed the intended gait behavior. During operation, one group of legs maintained contact and provided propulsion while the complementary group transitioned to the next support configuration. No significant phase drift or synchronization loss was observed, validating the purely mechanical coordination strategy.

The radial contact behavior appeared continuous and stable, with no evident macroscopic sliding under steady motion conditions. The structural arrangement of four motor units provided sufficient mechanical balance for confined cylindrical locomotion. These results consolidate the progression from single-leg validation [5] and three-leg motor units [6] to a fully integrated multi-unit robotic platform. The experimental validation confirms the feasibility of a mechanically synchronized multi-legged architecture for in-pipe inspection applications.

5 CONCLUSIONS

This work presented the experimental validation of a modular legged robot designed for internal pipe locomotion.

The main contributions are: Integration of multiple six-bar leg mechanisms into a complete robotic system; Purely mechanical synchronization of twelve legs with a single global DOF; Alternating radial support strategy enabling continuous propulsion; Experimental validation inside a transparent cylindrical tube.

The results demonstrate that mechanically synchronized multi-leg architectures constitute a viable solution for confined in-pipe robotic locomotion. Future developments include structural optimization, adaptation to different pipe diameters, integration of inspection sensors, and quantitative performance metrics such as velocity, energy consumption, and torque distribution.

ACKNOWLEDGMENTS

This work was financially supported by CNPq (grants 312980/2025-6 and 305344/2024-2), CAPES, and FAPESC (grant 2024TR000091). Additional support was provided by FINEP (R&D project 0378/2023), Embraer (project GDT0045-2024), ANEEL and Celesc (R&D projects 5697-0923/2023, 5697-1123/2023, and 05697-0423/2023), and FEESC.

REFERENCES

[1] M. Xie and Z. Tian, "A review on pipeline integrity management utilizing in-line inspection data," *Engineering Failure Analysis*, vol. 92, pp. 222–239, 2018.

[2] S. S. H. Hajjaj and I. B. Khalid, "Design and development of an inspection robot for oil and gas applications," *International Journal of Engineering & Technology*, vol. 7, no. 435, p. 5, 2018.

[3] A. Nayak and S. Pradhan, "Design of a new in-pipe inspection robot," *Procedia engineering*, vol. 97, pp. 2081–2091, 2014.

[4] T. Hoeltgebaum, E. Salgado da Silva, R. L. Pereira Barreto, E. R. Maletz, F. V. Morlin, A. P. Carboni, and D. Martins, "Walking mechanisms-a state of the art survey and new developments opportunities," in *Multibody Mechatronic Systems: Papers from the MuSMe Conference in 2020 7*. Springer, 2021, pp. 35–43.

[5] E. S. da Silva, F. V. Morlin, L. G. Adami, L. J. Imanisi, L. M. Rincon, and D. Martins, "Walking robot applied to the tube inspection activity," in *Synergetic Cooperation Between Robots and Humans*, E. S. E. Youssef, M. O. Tokhi, M. F. Silva, and L. M. Rincon, Eds. Cham: Springer Nature Switzerland, 2024, pp. 69–81.

[6] E. S. da Silva, J. C. Frantz, J. P. V. Goulart, G. V. Souza, H. Simas, T. L. F. da C. Pinto, and D. Martins, "Prototyping of a tripedal walking unit for in-pipe inspection robots," in *AI Enabled Robotic Loco-Manipulation*, Q. Li, M. Xie, M. O. Tokhi, and M. F. Silva, Eds. Cham: Springer Nature Switzerland, 2026, pp. 150–161.

CONFIGURATION DESIGN AND CONTINUOUS WORKSPACE FEASIBILITY ANALYSIS OF AN OVER-REDUNDANT CABLE-DRIVEN REFUELING MECHANISM BASED ON A SHIPBORNE GANTRY CRANE

Zhiwei Jia[1, 2], Erwei Li[1, 2, 3 *], Hansen Ma[1, 2]

[1] Hebei Provincial Key Laboratory of Parallel Robot and Mechatronic System, Yanshan University, Qinhuangdao, China, {m18230484153@163.com; lierwei@ysu.edu.cn; 1972525450@qq.com}

[2] Key Laboratory of Advanced Forging & Stamping Technology and Science (Yanshan University), Qinhuangdao, China, {m18230484153@163.com; lierwei@ysu.edu.cn; 1972525450@qq.com}

[3] School of Computing, Engineering and the Built Environment, Edinburgh Napier University, Edinburgh, UK, {E.Li@napier.ac.uk}

1. MOTIVATION

For floating nuclear power plants, the fuel replacement process—particularly the lifting, guiding, and docking stages—is highly susceptible to coupled wind–wave–swell disturbances and the six-degree-of-freedom motions of the floating platform. Meanwhile, fuel replacement operations must be conducted underwater, where pool excitation induced by platform motion, hydrodynamic added mass, fluid damping, and other hydrodynamic disturbances cannot be neglected. As nuclear fuel assemblies are typically slender and heavy rod-like structures, they are prone to vibration amplification, oscillation, and relative pose drift in an excited water pool environment, resulting in reduced replacement efficiency and increased risks of amplified collision, scraping, or jamming impacts. Therefore, developing a fuel replacement system capable of large workspace operation, heavy-load lifting, and high-precision docking under complex sea conditions is of great significance for ensuring the long-term stable energy supply of floating nuclear power plants.

For fuel replacement devices in floating offshore nuclear power plants, drawing upon terrestrial refueling systems and shipborne crane anti-sway technologies, the replacement mechanisms can generally be classified into rigid and flexible types. Rigid refueling devices typically adopt multi-segment coaxial telescopic sleeve structures, in which the inner sleeve is rigidly connected to the fuel assembly and performs lifting, guiding, and docking operations along a common axial direction. This configuration ensures high docking accuracy and good motion synchronization. However, due to the complexity of the offshore environment, underwater operations involving slender and heavy fuel assemblies can significantly amplify structural self-weight and inertial effects, increasing bending risks and impact loads. Moreover, since the stiffness and natural frequency of rigid structures are primarily determined by their configuration and material properties and are essentially not actively adjustable, it is difficult to avoid the dominant frequency range of pool excitation, resulting in insufficient adaptability under complex sea conditions.

In contrast, cable-driven flexible refueling systems offer a large workspace, high load-to-weight ratio, low inertia, and active compensation capability. Their stiffness and natural frequency are tension-dependent and can be actively regulated to avoid dominant excitation frequency ranges. However, high-precision, heavy-load underwater operations typically require over-redundant cable-driven mechanisms, which lead to extremely high structural and control complexity. Tension distribution becomes highly sensitive to parameter perturbations, and lateral hydrodynamic disturbances may induce local tension degradation, causing the positive-tension feasible region to exhibit non-convex or piecewise characteristics. As a result, discrete sampling methods struggle to guarantee feasibility coverage over a continuous workspace. Therefore, under the coupled constraints of high-precision heavy-load docking and complex sea conditions, neither a purely rigid nor a purely flexible configuration can simultaneously satisfy the requirements of positive-tension existence and structural stability throughout a continuous operational workspace.

2. CONTENT

To address the aforementioned refueling requirements of floating nuclear power plants, this paper proposes a rigid–flexible hybrid over-redundant cable-driven mechanism based on the existing shipborne gantry crane main hoisting system, as shown in Fig. 1. Through rigid–flexible coupling, the mechanical constraint configuration of the refueling process is reconstructed, enabling the system to shift from a structure-stiffness-dominated scheme to a tension–stiffness-coupled scheme. The proposed design adopts a 13-cable, 6-degree-of-freedom over-redundant cable-driven mechanism. Its end-effector platform consists of a hollow sleeve rigidly connected to the nuclear fuel assembly. The hollow sleeve is guided and docked to the upper core guiding structure via the over-redundant cable-driven mechanism and rigidly connected, after which fuel insertion is achieved through

coordinated retraction and release of the central main hoisting cable together with directional guidance provided by the hollow sleeve.

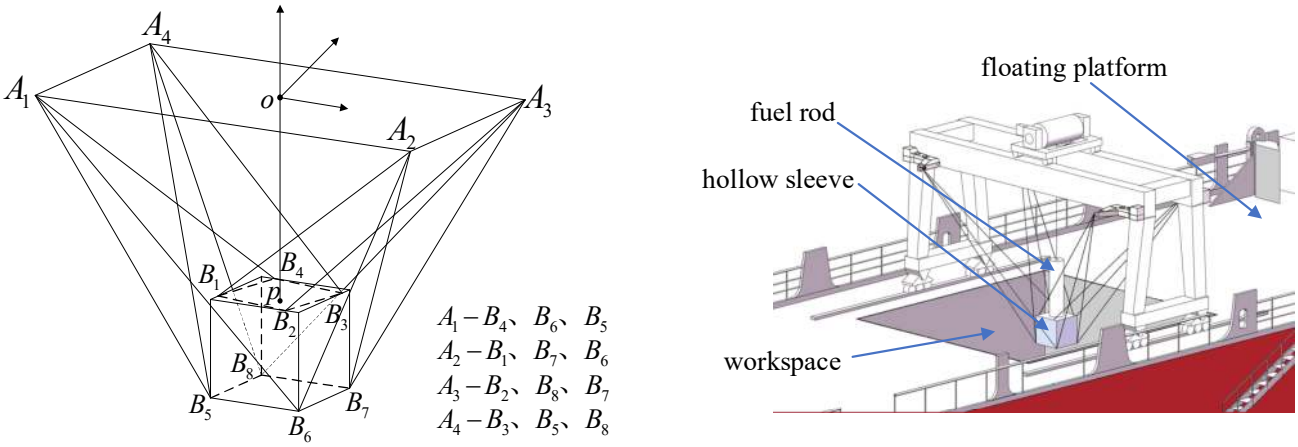

Figure 1. rigid–flexible hybrid over-redundant cable-driven mechanism

Meanwhile, to address the consistency evaluation of positive tension continuity and structural stability over the continuous workspace during the docking process, a progressive analysis framework combining hierarchical contraction–conservative expansion with vertex-based conservative extremum estimation is established, as shown in Fig. 2.

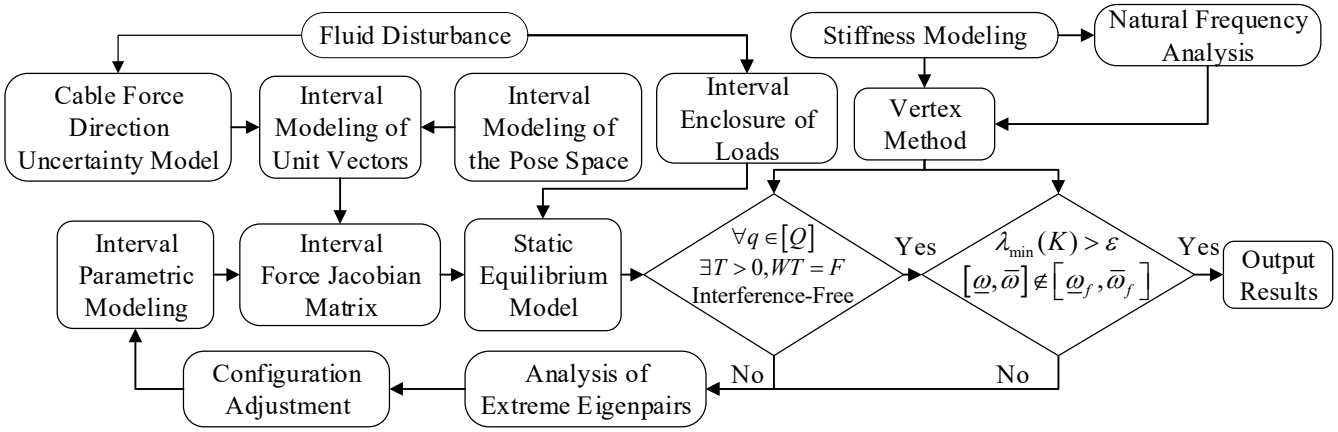

Figure 2. progressive analysis framework

The end-effector pose continuous interval of the over-redundant rope-pulling mechanism is defined by Eq. (1).

$$q \in [Q] = [\underline{x} \quad \overline{x}] \times [\underline{y} \quad \overline{y}] \times [\underline{z} \quad \overline{z}] \times [\underline{\alpha} \quad \overline{\alpha}] \times [\underline{\beta} \quad \overline{\beta}] \times [\underline{\gamma} \quad \overline{\gamma}] \tag{1}$$

Based on the SO(3) exponential map, the attitude interval perturbation model is constructed. Under the influence of fluid disturbances, the interval Jacobian matrix $[W]$ and the external load generalized force interval envelope $[F]$ are established [1]. The system's static equilibrium relationship is shown in Eq. (2).

$$[W] \cdot T = [F] \tag{2}$$

The continuous positive tension and rope non-crossover problem are determined based on the vertex method [2]. Under the premise that a feasible tension solution exists, the rope elasticity is ignored, and the inherent frequency and stiffness model of the over-redundant rope-driven mechanism is established as shown in Eq. (3).

$$K\phi = \omega^2 M\phi \quad \text{and} \quad K = W diag(T) W^{\mathrm{T}} \tag{3}$$

If the continuous interval fails to satisfy the requirements of positive tension, interference-free operation, or stiffness constraints, the configuration parameters can be adjusted according to the procedure illustrated in Fig. 2.

REFERENCES

[1] X. Jin, X. Jiang and Q. Li, “Interval-analysis-based determination of the trajectory-reachable workspace of planar cable-suspended parallel robots”. *Mechanism and Machine Theory*, 177, 105060, 2022.

[2] M. Arslan, C. Chevallereau, P. Wenger and S. Caro, “Compound Cable-Driven Parallel Robots for improved wrench-feasible workspace and stiffness modulation”. *Mechanism and Machine Theory*, 217, 106262, 2025.

MESHING THEORY OF POINT-CONTACT ARCHIMEDEAN FACE WORM GEAR DRIVE

Shibo Mu[1], Xingwei Sun[1], Zhixu Dong[1], Jianlong Zhao[1], Liya Jin[1], Weifeng Zhang[1], Yin Liu[1], Heran Yang[1], Haosheng Dong[1], Yaping Zhao[2]

[1] School of Mechanical Engineering, Shenyang University of Technology, Shenyang 110870, P. R. China
{mushibo_neu@163.com; sunxingw@126.com; dong_zhixu@126.con}
[2] School of Mechanical Engineering and Automation, Northeastern University, Shenyang 110819, P. R. China
{zhyp_neu@163.com}

1. ABSTRACT

The mixed mismatch modification technique is a key approach to enhancing the meshing performance and optimizing the load carrying capacity of worm gear drives. Based on this technique, this paper proposes a novel conical-surface enveloping cylindrical worm–Archimedes worm gear drive, and develops a meshing theory framework that incorporates essential components such as point-contact condition equations and an instantaneous transmission ratio model. To address the core challenge of solving high-dimensional nonlinear equation systems in point-contact meshing theory, a mixed mismatch parameter design method is introduced, which is based on the zero point of angular error . By employing the vector rotation property, a simplified model of the instantaneous transmission ratio function is established, and its mapping relationship with tooth surface geometry is constructed. The reference point is positioned at the midpoint of the instantaneous contact trace, ensuring that the angular error curve exhibits an ideal parabolic distribution. Further studies are conducted on tooth surface contact characteristics and error sensitivity verification. Numerical results demonstrate that the reference point of the proposed transmission is precisely located in the central region of the tooth surface, while both sides of the surface exhibit excellent geometric compatibility and kinematic meshing performance, with remarkable insensitivity to installation errors.

2. INTRODUCTION

Studies have shown that the meshing process of line-conjugate worm gear drives strictly depends on the satisfaction of the meshing equations. However, in practical operating conditions, the presence of manufacturing errors or elastic deformations may lead to the absence of solutions to these equations, resulting in discontinuities in transmission [1]. To reduce sensitivity to manufacturing and deformation errors and to enhance the load carrying capacity of the system, mismatch modification techniques are commonly employed. The essence of this approach is to relax the original line-conjugate meshing condition into a point-contact condition, thereby transforming the transmission form from line conjugation to point conjugation.

Mismatch-based point-contact worm gear drives effectively address the challenge of conventional line-contact transmissions, where errors or deformations may render the meshing equations unsolvable and disrupt continuous operation [2]. In the manufacturing of worm gear pairs, the worm wheel accounts for the majority of production cost. To further reduce this cost, research efforts have focused on modifying the geometry of the worm wheel or adopting alternative materials — such as replacing the worm wheel with a helical gear, or employing hybrid mismatch schemes using steel, plastics, or other materials. Following this approach, Wang et al. [3] utilized high-precision diamond-dressed gears to envelope and modify TI worms, thereby forming a hybrid mismatch transmission with involute helical gears. Building on this concept, Liu et al. [4] proposed a novel plastic–steel worm gear pair, in which a plastic involute helical gear meshes with a steel involute worm. Zhan et al. [5] analyzed the shear strength of plastic gears meshing with steel worms, while Dong et al. [6] investigated the transmission performance of point-contact ZI worm – helical gear drives under large transmission ratios. Hao et al. [7] conducted finite element analyses of contact stress in aluminum-matrix composite helical gears paired with steel worms. Ye et al. [8] developed a novel adjustable-backlash worm drive composed of a double-lead involute cylindrical worm and an involute helical gear. Liu et al. [9] studied the dynamic characteristics of TI worms meshing with helical gears made of different materials. More recently, Meng et al. [10] established a kinematic theory for evaluating the motion stability of point-conjugate gear drives and introduced a hybrid mismatch conical worm transmission.

At present, most hybrid mismatch methods rely on replacing traditional worm wheels with helical gears, primarily to avoid the high manufacturing cost of enveloping-type worm gear cutters. However, although the aforementioned hybrid mismatch schemes reduce manufacturing costs, they also compromise the inherent advantages of conventional worm gear drives. Compared with helical gears, worm gears can achieve larger transmission ratios with more compact structures, provide smoother meshing with lower noise and vibration, and even exhibit self-locking capability under certain conditions to prevent

back-driving. In this study, an alternative approach is adopted from the perspective of cutter design, whereby costly enveloping cutters are replaced with lower-cost trajectory-surface cutters for worm wheel machining. This strategy aims to eliminate dependence on costly enveloping tools while preserving the performance advantages of worm gear drives, thereby offering a novel technical pathway for cost reduction and efficiency improvement. Based on this mismatch modification concept, a trajectory-surface Archimedean cylindrical cutter is proposed as a substitute for the conventional enveloping cutter in worm wheel machining. Furthermore, a novel transmission system is developed, consisting of a conical-envelope cylindrical worm and an Archimedean-surface worm wheel.

To explore whether such a hybrid mismatch face worm gear drive can achieve continuous and stable transmission as well as to investigate its meshing characteristics, the meshing theory is first established and followed by a tooth-surface contact analysis. The method of tooth contact analysis was initially proposed by Baxter for studying the contact and kinematic characteristics of point-contact transmissions [11, 12].

The above studies indicate that for the newly proposed hybrid mismatch face worm gear drive, the core challenge in conducting tooth-surface contact analysis and subsequent dynamic investigations lies in the precise determination of the instantaneous contact point. This requires solving a nonlinear system of equations with 7–9 unknowns, established from the point-contact conditions. Existing literature typically employs multigrid methods or pre-solution approaches, followed by numerical computation after appropriate elimination and simplification. However, point-contact transmission must not only satisfy the contact conditions but also ensure meshing quality, in particular achieving a parabolic distribution of angular transmission error. Current research remains insufficient in simultaneously fulfilling both the point-contact condition and the meshing quality requirements.

The angular transmission error curve is defined with the instantaneous contact point of zero error as its vertex, and the instantaneous contact points at the engaging-in and engaging-out ends as its endpoints. Therefore, to obtain a parabolic ATE distribution, the zero-error contact point must be located at the midpoint of the contact trace. According to kinematic principles , the instantaneous transmission ratio at this zero-error contact point is also zero. On this basis, the present study proposes a hybrid mismatch parameter design method centered on the zero angular error contact point. First, a simplified transmission ratio function model is constructed based on vector rotation characteristics, establishing a mapping relationship between the function and the tooth-surface geometric parameters, thereby reducing the dimensionality of the nonlinear system at the reference point. Second, the initial values of the reference point and boundary points are employed as pre-solution conditions for determining the intermediate instantaneous contact points. Finally, by optimizing the mismatch parameters, the reference point is stably located at the midpoint of the instantaneous contact trace, ensuring that the angular error curve exhibits the desired parabolic profile.

In this study, a tooth-cutting meshing model of the conical-envelope cylindrical worm is first established, followed by a geometrical model of the Archimedean cylindrical cutter. Subsequently, the hobbing meshing equations of the Archimedean-surface worm wheel are formulated. Based on these geometrical models, a meshing model of the hybrid mismatch conical-envelope cylindrical worm–Archimedean-surface worm wheel drive is developed, from which both the meshing model and the kinematic error function are derived. By combining an elimination method based on vector rotation properties with a geometric construction approach, the high-order nonlinear equations encountered are effectively solved. Finally, numerical examples are provided to carry out tooth-surface contact analysis and error-sensitivity evaluation of the proposed worm gear drive.

REFERENCE

[1] F.L. Litvin, A. Fuentes, *Gear Geometry and Applied Theory*, 2nd ed, Cambridge University Press, Cambridge, 2004.

[2] I. Dudas, *The Theory & Practice of Worm Gear Drives*. Penton Press, London, 2000.

[3] S. Wang, D. Zhan, H. Liu and S. Wang, “Tooth contact analysis of toroidal involute worm mating with involute helical gear”. *Mechanism and Machine Theory*, 37(7), 685-691, 2002.

[4] Z.Y. Liu , C.C. Huang , Y.H.Hao and C.C. Lin. “The Mesh Property of the Steel Involute Cylindrical Worm with a Plastic Involute Helical Gear”. *Journal of Mechanics*, 30(2):185-192, 2013.

[5] J. Zhan and K. Ilie, “Static shear strength calculation of plastic helical gears mating with steel worm”. *International Journal of Precision Engineering and Manufacturing*, 15(2), 235-239, 2014.

[6] L. Dong, P. Liu, W. Wei, X. Dong and H. Li, “Study on ZI worm and helical gear drive with large transmission ratio”. *Mechanism and Machine Theory*, 74, 299-309, 2014.

[7] Y. Hao and Y. Shi, “Contact stress analysis for a pair of aluminum matrix composite helical gear and steel worm”. Journal of Reinforced Plastics and Composites, 34(3), 213-221, 2014.

[8] X. Ye, Y. Chen, B. Lu, W. Luo and B. Chen, “Study on a novel backlash-adjustable worm drive via the involute helical beveloid gear meshing with dual-lead involute cylindrical worm”. *Mechanism and Machine Theory*, 167, 104466, 2022.

[9] F. Liu, Y. Chen, D. Chen, W. Luo and B. Chen, “Study on the vibration characteristics of toroidal involute worm meshing with different plastic gears”. *Mechanical Systems and Signal Processing*, 209, 111096, 2024.

[10] Q. Meng, Y. Zhao, J. Cui, S. Mu, G. Li and X. Chen, “Kinematics of point-conjugate tooth surface couple and its application in mixed mismatched conical worm drive”. *Mechanism and Machine Theory*, 167, 104528, 2022.

[11] F.L. Litvin, *Development of Gear Technology and Theory of Gearing*, NASA Reference Publication, Cleveland, 1997.

[12] F.L. Litvin, I. Gonzalez-Perez, A. Fuentes, D. Vecchiato, B.D. Hansen and D. Binney, “Design, generation and stress analysis of face-gear drive with helical pinion”. *Computer Methods in Applied Mechanics and Engineering*, 194(36-38), 3870-3901, 2005.

INVERSE ACOUSTIC FINGERPRINTING FOR NON-INVASIVE IDENTIFICATION OF PRECESSING VORTEX CORE IN COMBUSTION CHAMBERS

Leonel Maximiliano Gómez Villarejo[1], Oliver Marcel Huerta Chavez[1], Raul Alberto Bernal Orozco[1], Luis Alfonso Rodríguez Salinas[1], Gibran Jalil Garnica Castro [2]

[1] Instituto Politécnico Nacional, Escuela Superior de Ingeniería Mecánica y Eléctrica Unidad Ticomán, Calz. Ticomán 600, La Purisima Ticomán, 07340, Mexico City, {lgomezv1902@alumno.ipn.mx, ohuertac@ipn.mx, rbernalo@ipn.mx, lrodriguezs1601@alumno.ipn.mx}

[2] Universidad Nacional Autónoma de México, Unidad de Alta Tecnología, Fray Antonio de Monroy e Hijar 260, Juriquilla, Santiago de Querétaro, 76230, Mexico City, {ggarnicac1500@alumno.ipn.mx}

1. INTRODUCTION

Thermoacoustic instabilities represent one of the most significant challenges regarding structural and operational efficiency of next-generation aerospace propulsion systems [1]. These instabilities arise from the non-linear coupling between acoustic pressure oscillations and flame heat-release fluctuations. This feedback loop, governed by Rayleigh criterion, can lead to severe mechanical vibrations, compromised combustion performance, and potentially catastrophic engine failures [2].

Therefore, the identification and characterization of Coherent Dynamic Structures (CDS), are fundamental to predicting combustion behavior within the engine during instability phenomena. Among these CDS, the Precessing Vortex Core (PVC) represents a prominent instability pattern in swirl-stabilized combustor [3]. Traditional monitoring methods often require invasive and expensive instrumentation that can perturb the flow dynamics or fail in high-temperature environments. Consequently, there is a critical requirement for non-invasive diagnostic techniques capable of identifying internal chamber dynamics through external acoustic signatures.

2. METHODOLOGY

This project describes the development of a specialized computational framework aimed at the non-invasive identification of combustion regimes. The methodology consists of a data generation phase utilizing Computational Fluid Dynamics (CFD) employing Reynolds-Averaged Navier-Stokes equations (RANS), Scale-Adaptive Simulation (SAS) and Large-Eddy Simulation (LES) modeling the transient behavior of the PVC as a representative CDS [4, 5].

To support the systematic extraction of acoustic data within the numerical domain, two custom interfaces were implemented: Hurakan, facilitates the automated deployment of virtual pressure transducers, ensuring spatial coverage for capturing pressure fluctuations; Axon, serves as a data-packing module to synchronize multi-channel time-series signals into a consolidated architecture for analysis.

The proposed identification core is based on a Constellation Mapping Approach derived from the combinational hashing algorithm developed by Wang [6]. Acoustic signals are processed via Short-Time Fourier Transform (STFT) to isolate spectral landmarks (energy peaks). These points are paired into specific target zones to generate discrete hash codes, intended to facilitate high-speed retrieval and characterization of acoustic signatures. This architecture is designed to provide low-latency path for identifying instability precursors through external signatures without perturbing the internal flow physics.

3. RESULTS AND DISCUSSION

The integrated monitoring workflow was evaluated by processing acoustic pressure data obtained from high-fidelity SAS and LES CFD environments. Preliminary analysis indicates that a capacity for the inverse acoustic fingerprinting algorithm to generate distinct spectral interest maps and corresponding hash codes for different combustion regimes. This approach suggests that the transformation of complex pressure signals into discrete fingerprints allows for identification of characteristic patterns without the requirement for invasive instrumentation.

As illustrated in Figure 1, the transition from a stable flame configuration (a) to a regime dominated by the PVC (b) produces unique acoustic signatures that are captured by the constellation mapping process. While these initial results demonstrate a consistent distinction between stable and unstable modes, the robustness of the hashing under varying signal-to-noise ratios and diverse operation envelopes remains under investigation. This methodology represents a development toward low-latency diagnostic tools, although further validation is necessary to quantify its reliability in real-world propulsion environments.

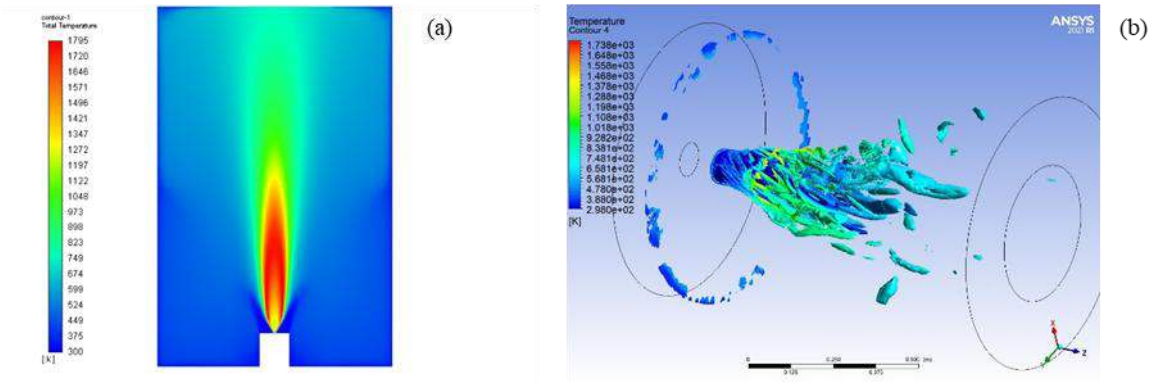

Figure 1. Representative results of internal chamber dynamics: (a) Stable flame configuration and (b) Precessing Vortex Core (PVC) instability pattern.

4. CONCLUSIONS AND FUTURE WORK

The present research demonstrates the implementation of a non-invasive monitoring framework capable of identifying thermoacoustic instability patterns through an inverse acoustic approach. The development of the Hurakan and Axon interfaces facilitates the systematic management of high-fidelity CFD data, enabling the generation of a robust spectral database. Preliminary results suggest that the application of the combinational hashing algorithm developed by Wang [6] allows for distinction of the PVC signatures from stable combustion states with low latency.

Building upon this infrastructure, future work will focus on the integration of deep learning architectures, such as Koopman Networks and denoising convolutional neural networks, to enhance the system's reliability in high-noise environments [7, 8]. This phase aims to provide a hybrid diagnostic tool capable of characterizing non-linear flame-flow interactions and predicting instability precursors across diverse operational envelopes. The fusion of acoustic fingerprinting with neural-based classification represents a promising path toward autonomous and non-intrusive engine health monitoring.

ACKNOWLEDGMENTS

The authors would like to thank the Instituto Politécnico Nacional (IPN) and the Sección de Estuidos de Posgrado e Investigación (SEPI) for the institutional support, technical facilities, and resources that made this research possible.

REFERENCES

[1] T. Lieuwen, *Unsteady Combustor Physics*. Cambridge University Press, Cambridge, UK, 2012.

[2] T. Poinsot, "Prediction and control of combustion instabilities in real engines", *Proceedings of the Combustion Institute*, 36(1), 1-54, 2017.

[3] K. Schadow, E. Gutmark, T.P. Parr, D.M. Parr, K.C. Wilson and J.H. Crump, "Large-scale coherent structures as drivers of combustion instability", *Combustion Science and Technology*, 64(4-6), 167-186, 1989.

[4] M.A. Abad Romero, "Comparación de las capacidades SAS/DES para la reproducción de una combustión turbulenta y la captación de estructuras coherentes", Tesis de Maestría, Instituto Politécnico Nacional, México, 2022.

[5] P.L. Viruegas Álvarez, "Detección de inestabilidades termoacústicas mediante redes neuronales artificiales utilizando señales acústicas", Tesis de Maestría, Instituto Politécnico Nacional, México, 2021.

[6] A.L.-C. Wang, "An Industrial-Strength Audio Search Algorithm", *Proceedings of the 4th International Conference on Music Information Retrieval*, Baltimore, USA, 2003.

[7] K. Omi, "Detection of thermoacoustic combustion instabilities using neural networks for non-invasive identification", *International Symposium on Space Technology and Science (ISTS)*, 2025.

[8] C.K.W. Tam, "A phenomenological approach to jet noise: the two-source model", *International Journal of Aeroacoustics*, 18(2-3), 114-124, 2019.

SYNTHESIS AND STRUCTURAL CHARACTERIZATION OF NANOSTRUCTURED TIN DIOXIDE VIA SOL-GEL FOR ACETONE SENSING APPLICATION

Luis Alfonso Rodríguez Salinas[1], Georgina García Pacheco[1], Jacobo Esteban Munguia Cervantes[2], Alfredo López Monroy[1], Leonel Maximiliano Gómez Villarejo[1]

[1] Instituto Politécnico Nacional, Escuela Superior de Ingeniería Mecánica y Eléctrica Unidad Ticomán, Calz. Ticomán 600, La Purísima Ticomán, 07340, Mexico City, Mexico, {lrodriguezs1601@alumno.ipn.mx; ggarciap@ipn.mx; alopezmo@ipn.mx; lgomezv1902@alumno.ipn.mx}

[2] Instituto Politécnico Nacional, Centro de Nanociencias y Micro y Nanotecnologias (CNMN), Luis Enrique Erro s/n, Unidad Profesional Adolfo López Mateos, Zacatenco, 07700, Mexico City, Mexico, {jmunguia@ipn.mx}

1. INTRODUCTION

Diabetes mellitus represents a major global public health challenge, affecting approximately 537 million people, a figure projected to rise to 783 million by 2045 [1]. Specifically, Type 1 Diabetes Mellitus (T1DM) requires rigorous and constant glycemic control to prevent severe complications such as ketoacidosis, vision loss, and cognitive impairment. Currently, the monitoring standard relies on frequent capillary punctures to measure blood glucose concentrations. In response to the burden of invasive monitoring, this work proposes the development of a gas sensor as a non-invasive alternative. This approach is based on the biological processes of the disease: diabetes originates from the deficiency or absence of pancreatic beta cells responsible for insulin release. This deficiency prevents glucose from being utilized as an energy source, leading to hyperglycemia. Consequently, the body triggers lipolysis and hepatic beta-oxidation, producing ketone bodies, including acetone. Acetone acts as a reliable breath biomarker; individuals diagnosed with T1DM exhale concentrations exceeding 2.19 ppm, whereas healthy individuals present levels below 0.9 ppm [2].

To detect these trace concentrations, metal-oxide semiconductor (MOS) sensors, specifically tin dioxide (SnO_2), offer a viable technological platform due to their exceptional sensitivity and compatibility with microfabrication. This study focuses on optimizing the sol-gel synthesis of SnO_2 nanoparticles to maximize surface area and ensure crystalline phase purity. This optimization is fundamental for the subsequent functionalization with Multi-Walled Carbon Nanotubes (MWCNTs), a strategy designed to establish p-n heterojunctions that facilitate charge transport and reduce the operating temperature [3]. The prototype integrates a micro-heater designed via Micro-Electromechanical Systems (MEMS) technology.

2. METHODOLOGY

Tin dioxide was synthesized via the sol-gel method, using 8.6429 g of tin (IV) chloride pentahydrate ($SnCl_4 \cdot 5H_2O$) as the precursor and 33.7 mL of double-distilled water as the solvent. To control the reaction kinetics and the final particle size, the solvent was added in two stages under constant stirring at room temperature: an initial volume of 3.7 mL, followed by 10 mL additions every 2 minutes until the total volume was reached. Since precursor hydrolysis inevitably acidifies the medium due to residual hydrochloric acid and intermediate tin chloride species, a purification protocol consisting of two successive washing cycles with double-distilled water was implemented. In the first cycle, 3.5392 g of the dry powder was stirred in 35 mL of solvent for 30 minutes; after drying at 100 °C for 24 hours, the mass decreased to 2.3174 g, evidencing the removal of soluble subproducts. A second washing cycle under the same conditions resulted in a final mass of 1.9093 g. This progressive weight loss confirms the leaching of H^+ and Cl^- ions, shifting the chemical equilibrium toward a high-purity precursor and eliminating transition phases that could act as charge-scattering centers in the sensor.

The purified material underwent a final drying process at 100 °C for 24 hours. This stage is critical, as controlled evaporation promotes the condensation of hydroxyl groups and the formation of oxygen bridges, consolidating the porous network. Finally, the powders were calcined at 350 °C for 2 hours to induce the crystallization of the tetragonal rutile phase. This optimization of the base material is fundamental for its future integration with multi-walled carbon nanotubes (MWCNTs) into a MEMS platform, aiming to achieve the sensitivity required for acetone detection. The MEMS platform serves as the thermo-mechanical transducer for the sensing layer, which is critical to achieving the precise operating temperature required for surface redox reactions. The device architecture incorporates a network of micro-electrodes embedded beneath the SnO_2/MWCNTs matrix. These nodes are designed to monitor the modulation of electrical resistance resulting from the adsorption of oxygen species and their subsequent interaction with acetone molecules. By measuring the transducer's resistance across these integrated nodes, it is possible to correlate the change in charge carrier density within the nanomaterial with the concentration of the biomarker in the breath.

3. RESULTS AND DISCUSSION

The structural characterization by XRD confirmed the formation of SnO_2 with a tetragonal rutile phase. The diffraction pattern shown in Fig. 1a exhibited characteristic peaks at 26.6° (110), 33.9° (101), and 37.9° (200), which match the reference diffraction pattern JCPDS 21-1250, with no evidence of secondary phases. Notably, a broadening at the base of the peaks was observed, which is attributable to a nanometric particle size according to the Scherrer equation. The presence of a moderate amorphous background along with defined peaks indicates a partially crystalline structure. Moreover, slight deviations in peak positions (2θ) and relative intensities are attributable to anisotropy in the crystal orientation, which may be induced during the drying and calcination processes. Scanning electron microscopy shown in Fig. 1b revealed nodular nanoparticles with sizes ranging from 28 to 34 nm, consistent with the high surface area requirements for gas adsorption.

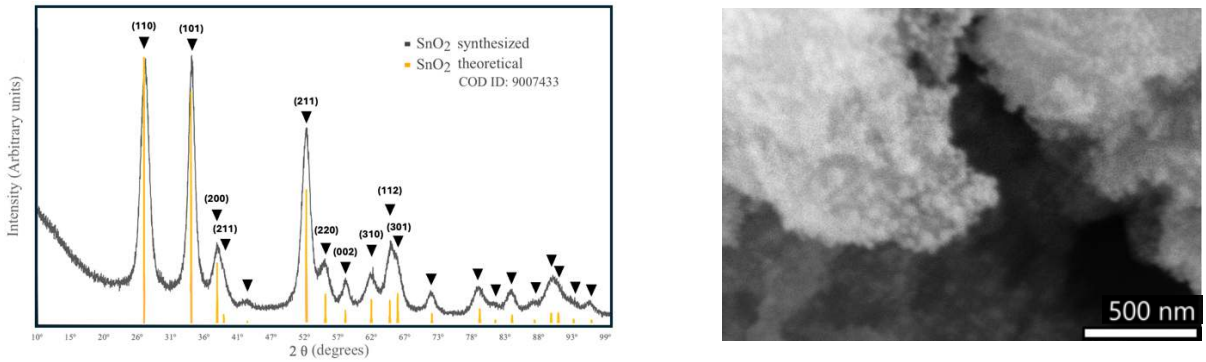

Figure 1. a) XRD pattern powder of SnO_2 and b) SEM micrograph of SnO_2 powders.

4. CONCLUSION

The controlled synthesis of nanostructured SnO_2 via the sol-gel method was achieved. X-ray diffraction analysis revealed well-defined peaks consistent with tetragonal SnO_2. The calculated average particle size was found to be within the nanometric range. This nanoscale structure is essential for enhancing gas sensing performance. These structural features indicate a favorable surface-to-volume ratio that supports improved sensitivity and reactivity for acetone detection. The next phase of this research involves the functionalization of this purified matrix with multi-walled carbon nanotubes (MWCNTs) to establish p-n heterojunctions, aimed at enhancing charge carrier mobility and sensitivity. Furthermore, the resulting nanocomposite will be integrated onto a MEMS platform featuring an embedded micro-heater and sensing nodes. This integration will allow for precise thermal activation and real-time resistance monitoring, providing a robust, non-invasive mechanism for detecting acetone concentrations.

ACKNOWLEDGMENTS

The authors gratefully acknowledge the Instituto Politécnico Nacional (IPN) and the Sección de Estudios de Posgrado e Investigación (SEPI) for their invaluable institutional support, administrative cooperation, technical facilities, and resources provided throughout this research.

REFERENCES

[1] OPS/OMS, “Diabetes”. *Organización Panamericana de la salud*, 2024.
[2] Y. Li, M. Zhang and H. Zhang, “Acetone sensors for non-invasive diagnosis of diabetes based on metal-oxide-semiconductor materials”. *Chinese Physics B*, 29(9), 090702, 2020.
[3] M. Narjinary, P. Rana, A. Sen and M. Pal, “Enhanced and selective acetone sensing properties of SnO2-MWCNT nanocomposites: Promising materials for diabetes sensor”. *Materials & Design,* 115, 158-164, 2017.
[4] A. Rydosz, “Sensors for enhanced detection of acetone as a potential tool for noninvasive diabetes monitoring”. *Sensors,* 18(7), 2298, 2018.
[5] H. Ji, W. Zeng and Y. Li, “Gas sensing mechanisms of metal oxide semiconductors: a focus review”. *Nanoscale*, 11(47), 22664-22684, 2019.

Book of Abstracts of MMT Symposium
Mechanism and Machine Theory Symposium
Flores et al. (Eds)

MMT Symposium
60th Anniversary of Mechanism and Machine Theory
June 21-23, 2026 Porto, Portugal

ON THE FEASIBILITY OF PREDICTING ROLLING CONTACT FATIGUE FROM UNIAXIAL S-N CURVES

I. Ulacia [1], I. Llavori[1], M. Maiztegui[1], A. Arana[1], J. Larrañaga[1]

[1] Mondragon Unibertsitatea, Loramendi 4, Mondragon, Spain, {iulacia@mondragon.edu}

1 INTRODUCTION

Rolling contact fatigue (RCF) is a frequent failure mode in gears operating under rolling and sliding conditions. Repeated contact loading can initiate small pits or spalls that progressively degrade tooth flanks and reduce transmission performance. Although standards such as AGMA 2101 and ISO 6336 provide conservative sizing rules, their wide safety margins may lead to oversized components in applications where weight, efficiency, or cost must be optimised. This motivates the development of predictive methods capable of estimating RCF life with greater accuracy.

RCF is intrinsically multiaxial, with subsurface stress gradients and rotating principal directions as the contact passes a material point. In contrast, fatigue data commonly available for engineering materials are uniaxial S–N curves obtained from tensile tests. Whether such data are suitable for predicting RCF life remains unclear. Multiaxial approaches such as the Fatemi–Socie or Smith–Watson–Topper criteria have been applied to contact problems, but their applicability to RCF initiation still requires systematic assessment.

This study evaluates the feasibility of predicting RCF life from uniaxial S–N data by combining numerical modelling with dedicated experiments. Model predictions are compared with controlled three-roller tests to assess their accuracy and identify the conditions under which uniaxial fatigue data may be appropriate for RCF-related analyses.

2 NUMERICAL RCF MODEL AND FATIGUE LIFE PREDICTION

A numerical framework was developed to analyse rolling contact fatigue (RCF) under line-contact loading. The contacting bodies are modelled as a 2D cylinder-on-cylinder system with diameters $d_1 = 54.15$ mm and $d_2 = 12$ mm. A prescribed normal load, friction coefficient and rolling velocity reproduce the subsurface stress history during rolling and sliding. RCF involves non-proportional multiaxial loading due to the continuous rotation of principal stress directions as the contact passes a material point. Equivalent stress approaches are therefore inadequate, and a critical-plane formulation is adopted. Two multiaxial fatigue parameters are considered: the Fatemi–Socie (FS) shear-strain-based criterion and the Smith–Watson–Topper (SWT) energy-type parameter.

2.1 Critical-plane identification

At each integration point, the critical plane is determined by sweeping through possible orientations and projecting the stress/strain history onto each plane. For every angle, shear and normal components are extracted over all increments, their envelopes are constructed, and the fatigue indicator parameter (FIP) is evaluated. The plane giving the maximum FIP is selected as the critical plane. The FS parameter falls within the range of experimentally observed failure lives, whereas SWT remains well below the fatigue limit (Figure 1(a)). This reflects the shear-dominated nature of RCF under the present loading conditions.

2.2 FS life prediction using uniaxial S–N data

Shear fatigue properties are often unavailable for practical materials such as 42CrMo4. To allow life prediction using only tensile S–N curves, the FS relation is rewritten in terms of uniaxial fatigue parameters [1]:

$$\underbrace{FS = \frac{\Delta\gamma_{\max}}{2}\left(1 + k\,\frac{\sigma_{n,\max}}{\sigma_y}\right) = \frac{\tau'_f}{G}(2N_f)^{b_0} + \gamma'_f(2N_f)^{c_0}}_{\text{original FS equation (shear fatigue properties)}} \quad = \quad \underbrace{\left[(1+\nu_e)\,\frac{\sigma'_f}{E}(2N_f)^{b}\right]\left[1 + k\,\frac{\sigma'_f}{2\sigma_y}(2N_f)^{b}\right]}_{\text{modified FS equation (from uniaxial S–N data)}} \quad . \quad (1)$$

where $\Delta\gamma_{\max}$ is the shear strain range on the critical plane, $\sigma_{n,\max}$ the corresponding normal stress, k the normal-stress sensitivity, σ_y the yield stress, ν_e the effective Poisson ratio, and σ'_f and b the uniaxial fatigue strength coefficient and exponent (taken from published data for 42CrMo4 [2]).

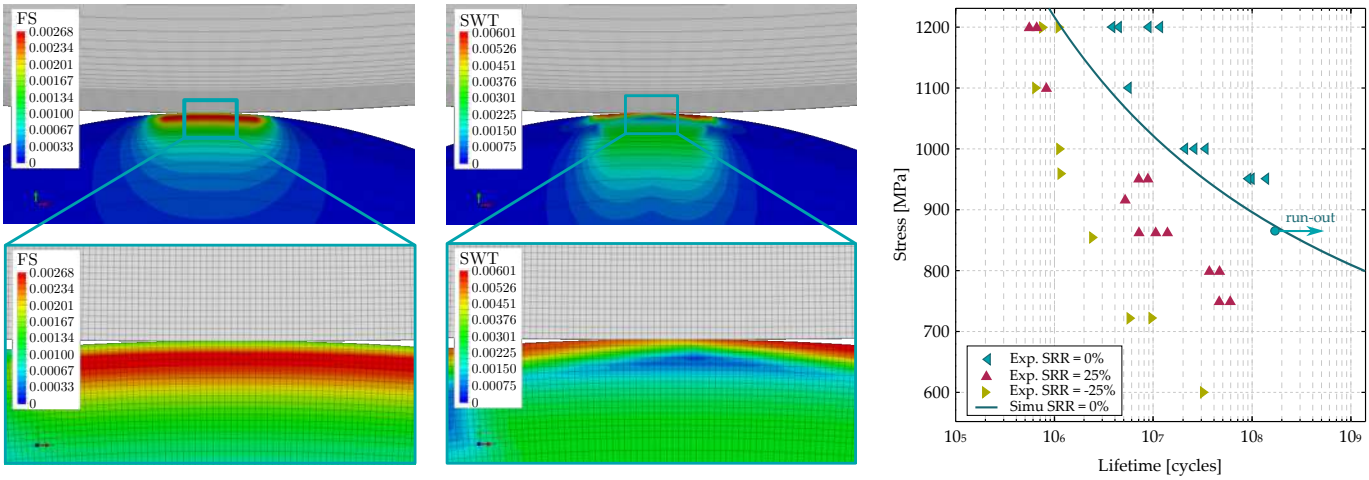

(a) (b)

Figure 1: (a) Fatigue indicators computed using the FS and SWT criteria, and (b) comparison between predicted fatigue life (continuous line) and experimental measurements (markers).

3 EXPERIMENTAL VALIDATION

Experimental tests were carried out using a PCS®-MPR three-roller rig. The specimens were made from 42CrMo4 steel (hardness ≈ 304 HV) and lubricated with ISO VG 320 oil at 60°C. Rolling speed was 4 m/s, and tests were conducted for three Slide-to-Roll Ratios (SRR): 0%, +25%, and −25%. Interrupted tests were performed to observe early crack initiation and pitting development.

Figure 1(b) compares predicted and experimental fatigue lives. All predictions are lower than measured values but remain within the same order of magnitude, indicating that the model captures the correct life scale under pure rolling. At SRR = 0%, the FS parameter accurately reflects the onset of RCF damage.

For SRR = ±25%, experimental lives decrease markedly due to increased shear and surface traction. Under these conditions, numerical predictions deviate from experimental results, suggesting that additional slide-related mechanisms—such as frictional heating, micro-slip damage or altered subsurface stress gradients—play a dominant role and are not captured by the simplified FE model.

Overall, the experiments show that the FS-based critical-plane method provides reasonable life estimates in pure rolling, while larger SRR values require extended modelling approaches that incorporate slide-induced effects.

4 CONCLUSIONS

This work examined the feasibility of predicting rolling contact fatigue life in 42CrMo4 steel using a multiaxial critical-plane framework calibrated solely with uniaxial S–N data. A finite element model of a line-contact configuration was developed to capture the subsurface stress and strain fields, and the Fatemi–Socie parameter was used to estimate fatigue life. Experimental tests performed on a three-roller rig were then used to evaluate the predictions.

The results show that the numerical model provides conservative but reasonable life estimates under pure rolling conditions (SRR = 0%), where shear-dominated subsurface stresses govern fatigue initiation. At higher sliding levels (SRR = ±25%), experimental lives decrease significantly and the numerical predictions no longer match the observed behaviour, indicating that additional mechanisms linked to sliding—such as frictional heating, micro-slip or modified stress gradients—need to be incorporated for accurate predictions.

Overall, the study demonstrates that uniaxial S–N data can support RCF life predictions under limited conditions, but extended models and additional material data are required when sliding becomes significant.

ACKNOWLEDGMENTS

This research was partially supported by the Basque Government through the Department of Education (PIBA-2023-1-0052) and the Department of Industry (KK-2024/00048). The authors gratefully acknowledge this financial support.

REFERENCES

[1] N.R. Gates and A. Fatemi, “On the consideration of normal and shear stress interaction in multiaxial fatigue damage analysis”, *Int. J. of Fatigue*, 2017.

[2] J. Papuga, et al., “Investigation of the size effect on 42CrMo4 + QT steel in the high-cycle fatigue domain part I: Experimental campaign”, *Int. J. of Fatigue*, 2023.

Book of Abstracts of MMT Symposium
Mechanism and Machine Theory Symposium
Flores et al. (Eds)

MMT Symposium
60th Anniversary of Mechanism and Machine Theory
June 21-23, 2026 Porto, Portugal

OPTIMIZING BALL BEARING CONTACT ANGLE FOR MINIMUM POWER LOSS UNDER COMBINED LOADS

P. Alberdi [1], A. Arana [1], A. Oyanguren [1], J. Larrañaga [1], I. Ulacia [1]

[1] Mondragon Unibertsitatea, Loramendi 4, Mondragon, Spain, {palberdi@mondragon.edu}

1 INTRODUCTION

Ball bearings are widely employed in rotating machinery due to their ability to operate under combined axial and radial loads at high rotational speeds [1]. In most applications, lubrication is used to enhance performance, reduce friction, and improve reliability.

One of the most critical geometric parameters of a ball bearing is the nominal contact angle. It is defined as the angle between the line connecting the inner and outer raceway contact points and the radial plane of the bearing. Depending on the contact angle, ball bearings are classified into different types. Deep groove ball bearings feature small contact angles, typically between 0° and 10°, and are primarily designed to support radial loads, allowing high-speed operation. Thrust ball bearings exhibit contact angles close to 90° and are intended to support predominantly axial loads. Angular contact ball bearings typically present contact angles between 15° and 60° and are designed to support combined axial and radial loads. Consequently, bearing designers select a specific bearing type and contact angle based on the load combination and operating conditions dictated by the target application.

The objective of this work is to analyse the influence of combined axial and radial loading in order to determine the optimal nominal contact angle that minimises sliding power losses for different load combinations. To this end, the non-uniform distribution of contact load and ball kinematics are systematically analysed. The results provide practical guidelines for selecting ball bearings with an optimal contact angle tailored to specific applications.

2 METHODOLOGY

2.1 Theoretical model

The theoretical prediction of load distribution, contact kinematics, and the resulting sliding power losses is carried out using a quasi-static ball bearing model based on the minimum energy dissipation principle, as proposed in [2]. The model computes the sliding power losses for lubricated contacts by explicitly accounting for the coupled effects of load, contact kinematics, and friction. The frictional behaviour is characterised using a elastohydrodynamic lubrication model, which accounts for the non-uniform sliding speed distribution within the contact.

2.2 Case study definition

A parametric study is conducted using a reference angular contact ball bearing 6205, for which the nominal contact angle is systematically varied from 15° to 60°. All simulations are performed under equivalent operating conditions by maintaining a constant rotational speed of 5000 rpm and a constant magnitude of the applied external force, $F = 1581$ N, while varying only its direction. The direction of the external force is defined by the angle ϕ, where $\phi = 0°$ corresponds to a purely axial load and $\phi = 90°$ to a purely radial load. Intermediate values of ϕ represent combined axial and radial loading conditions (see Figure 1).

In angular contact ball bearings, for each nominal contact angle there exists a maximum allowable radial load associated with the induced axial force. This phenomenon corresponds to an internal axial force component generated by an external radial load due to the inclination of the contact angle. To avoid non-admissible operating conditions, the simulated domain is restricted to the admissible radial load range corresponding to each nominal contact angle.

3 RESULTS

Figure 1 illustrates the resulting sliding power loss map as a function of the nominal contact angle and load combination. Three distinct contact-angle regimes can be identified in terms of minimising sliding power losses under different combined axial and radial loading conditions. For contact angles in the range $15° < \alpha^0 < 34°$, the minimum sliding power losses are obtained under predominantly radial loading. When the contact angle increases to $34° < \alpha^0 < 40°$, an optimal compromise is achieved for combined axial and radial loads. Finally, for higher contact angles in the range $40° < \alpha^0 < 60°$, predominantly axial loading conditions yield the lowest sliding power losses, making this range preferable for applications dominated by axial forces.

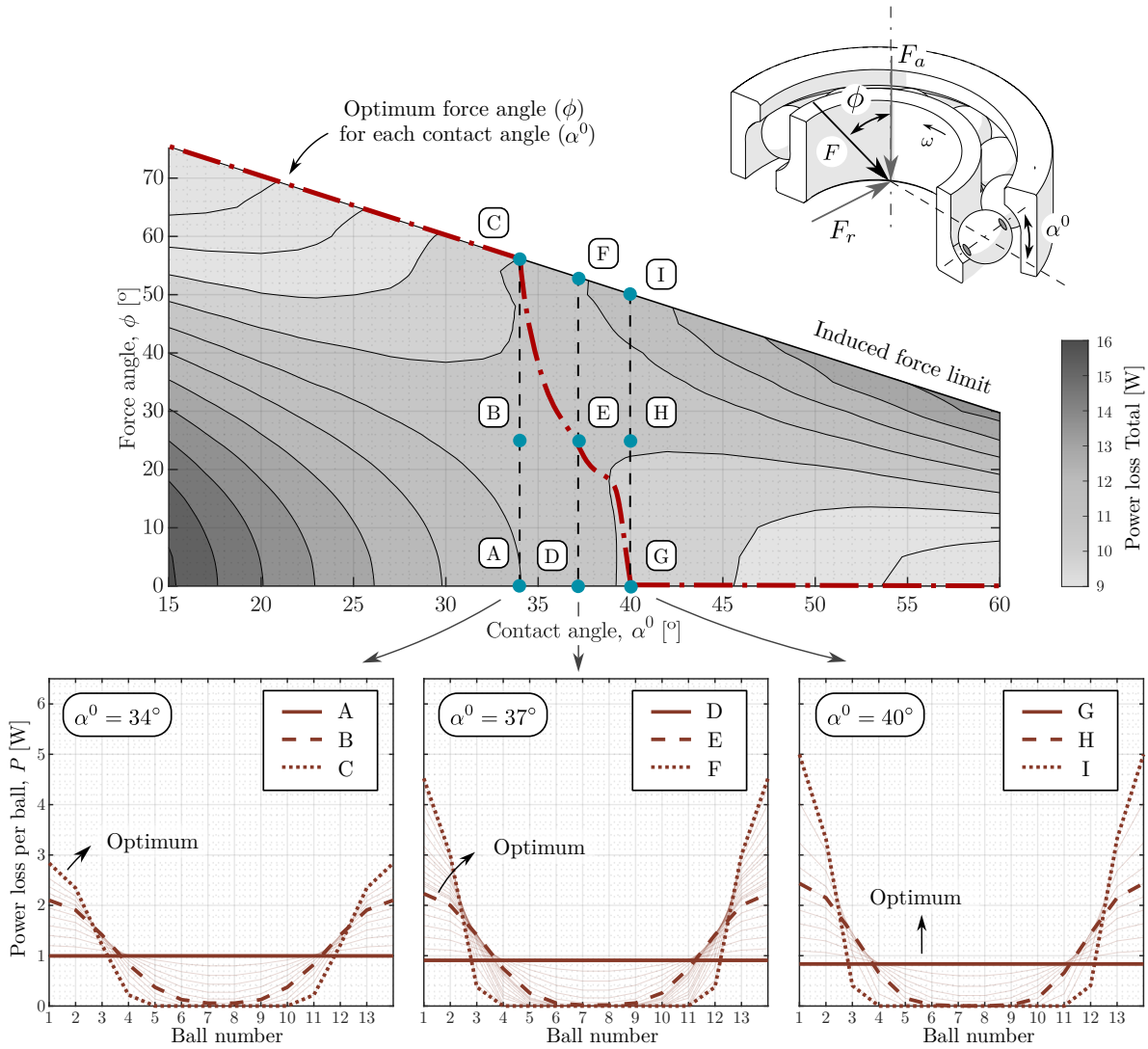

Figure 1: Optimisation map of sliding power losses with respect to nominal contact angle and load direction.

As observed, within the narrow range $34° < \alpha^0 < 40°$, the optimal load combination transitions from radially governed to axially governed conditions. The origin of this transition is analysed by examining the distribution of sliding power losses at the level of each individual ball. This behaviour is illustrated in Figure 1, where the sliding power loss distribution among the balls is shown for specific three different nominal contact angles $\alpha^0 = 34°$, 37° and 40°. For comparison, three representative axial–radial load combinations are highlighted for each contact angle.
The variation in power loss distribution arises because changes in the axial–radial load combination modify the number of balls effectively carrying load, thereby altering the contact load per ball, the associated contact kinematics, and the resulting sliding power losses [3]. The same external axial and radial load combination generates a totally different load distribution, depending on the contact angle. In this way, the optimal power loss distribution differs from each contact angle, leading on each contact angle to an improved performance under either predominantly axial or predominantly radial loading conditions.

4 CONCLUSIONS

This study provides a detailed investigation of sliding power losses through the analysis of load distribution and contact kinematics, enabling a clearer understanding of the governing mechanisms behind the optimal load combination for each nominal contact angle. The analysis is further extended to different operating conditions, including variations in applied external load and rotational speed, in order to assess their influence on the sliding power loss map. These findings offers quantitative design guidelines for improving bearing performance under combined loading conditions.

REFERENCES

[1] T. Harris and M. Kotzalas, *Rolling Bearing Analysis*. CRC Press, 2006.

[2] P. Alberdi *et al.*, "A general kinematic model for lubricated ball bearings based on the minimum energy hypothesis". *Trib. Int.*, 2024.

[3] P. Alberdi *et al.*, "Influence of Ball Bearing Contact Angle on Interface kinematics, Load, and Sliding Power Losses". *Mech. Mech. Theo*, 2026.

OPTIMAL MEASUREMENT AREA IDENTIFICATION AND ACCURACY ENHANCEMENT OF A CMM BASED ON IPSO-SAA

Zishuai Wang [1], Zeru Lyu [1], Zhaoyao Shi [1], Hongfang Chen [1]

[1] Faculty of Mechanical and Energy Engineering, Beijing University of Technology, Beijing 100124, China, {Zishuaiwang@emails.bjut.edu.cn; krislyu@emails.bjut.edu.cn; shizhaoyao@bjut.edu.cn; hfchen@bjut.edu.cn}

1. INTRODUCTION

The Coordinate Measuring Machine (CMM) is a large-scale precision motion system that is widely applied in aerospace, shipbuilding, automotive, and large-scale equipment manufacturing, where high precision is required. The error distribution within the CMM measurement area exhibits significant spatial non-uniformity because it is influenced by structural geometric errors, guideway motion errors, and kinematic coupling effects. Intelligent optimization algorithms have been extensively employed in machine tools, industrial robots, and precision measurement systems for error evaluation and optimal workspace identification, owing to their adaptive search capability for complex nonlinear objectives. To address the problem that spatially non-uniform error distribution in the CMM measurement area significantly affects measurement accuracy improvement, this study proposes an optimal measurement area identification method for CMMs based on an improved intelligent optimization algorithm.

2. METHOD FOR IDENTIFYING THE OPTIMAL MEASUREMENT AREA OF A CMM

A laser tracer multi-station measurement technique was employed to obtain the volumetric errors at the planned points within the CMM measurement area, and a single geometric error model was established based on the least-squares method[1]. Considering that the number of planned measurement points in the CMM measurement area was limited, the Inverse Distance Weighting (IDW) method was adopted to densify the measurement area, thereby obtaining the volumetric error distribution over the entire measurement area, as shown in Figure 1.

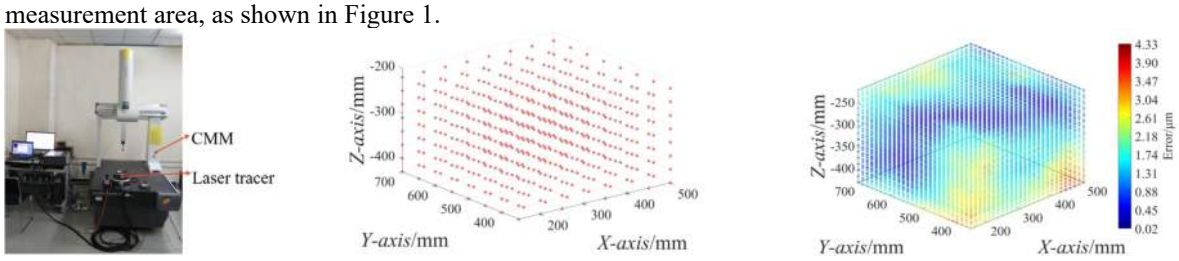

(a) Multi-station measuring system. (b) Distribution of measurement points. (c) Volumetric error distribution.

Figure 1. Acquisition of Volumetric Errors in the Measurement Area.

For two representative measurands, straight lines and circular arcs, objective function models were constructed by comprehensively considering CMM geometric errors and the non-uniform distribution of measurement area errors. Considering that standard Particle Swarm Optimization (PSO) was prone to entrapment in local optima, an Improved Particle Swarm Optimization–Simulated Annealing Algorithm (IPSO-SAA) was further proposed[2]. The algorithm enhances global exploration capability through adaptive inertia weight and adaptive disturbance force mechanisms, introduces a constriction factor to dynamically regulate particle velocity, and integrates a simulated annealing strategy that probabilistically accepts inferior solutions to enable escape from local optima, thereby suppressing premature convergence and improving global optimization robustness. The specific expression is as follows:

$$\begin{aligned} \boldsymbol{V}_{\mathrm{id}}^{\mathrm{k}} &= \chi\left\{\boldsymbol{V}_{\mathrm{id}}^{\mathrm{k-1}} + c_1 r_1\left(\ \mathrm{Pbest}_{\mathrm{id}} - \boldsymbol{A}_{\mathrm{id}}^{\mathrm{k-1}}\right) + c_2 r_2\left(\ \mathrm{Gbest}_{\mathrm{id}} - \boldsymbol{A}_{\mathrm{id}}^{\mathrm{k-1}}\right)\right\} + F_{\mathrm{i}}\left(k\right) \\ \boldsymbol{A}_{\mathrm{id}}^{\mathrm{k}} &= \boldsymbol{A}_{\mathrm{id}}^{\mathrm{k-1}} + \boldsymbol{A}_{\mathrm{id}}^{\mathrm{i-1}} \end{aligned} \tag{1}$$

Where d denotes the spatial dimension; $\boldsymbol{V}_{\mathrm{id}}^{\mathrm{k}}$ denotes the velocity of particle i in dimension d at iteration k; $r_1$and r_2 are uniformly distributed random numbers in [0, 1]; $\mathrm{Pbest}_{\mathrm{id}}$ and $\mathrm{Gbest}_{\mathrm{id}}$ denote the individual and global best positions, respectively; $F_i(k)$ is

the disturbance force; χ is the constriction factor; A_{id}^{k} represents the d-th component of the position vector of particle i at iteration k.

3. EXPERIMENTS

To further assess the comprehensive performance of IPSO-SAA, it was compared with PSO and Adaptive Particle Swarm Optimization (APSO). Fifty independent runs were conducted for a randomly selected area to obtain the average time, the average fitness value, and the standard deviation of the fitness values, as shown in Table 1. The results demonstrated that IPSO-SAA achieved improved stability and enhanced optimization capability.

Table 1 Comparison of test results of PSO, APSO and IPSO-SAA algorithms.

Measurand	Algorithm	Average time(s)	Average fitness value(μm)	Standard deviation of fitness(μm)
Lines	PSO	0.798009	2.289077	6.90×10^{-2}
	APSO	0.823510	2.286177	5.20×10^{-2}
	IPSO-SAA	0.707694	2.267197	4.35×10^{-2}
Circular arcs	PSO	4.577170	4.616136	1.62×10^{-4}
	APSO	4.225911	4.616192	1.29×10^{-4}
	IPSO-SAA	3.613146	4.615903	7.60×10^{-5}

A platform was established for validation of the optimal measurement area. The optimal measurement area identified by IPSO-SAA, the area with the maximum error, and eight randomly selected areas were chosen for comparative experiments. Figures 2 and 3 present the comparison between simulation and experimental results as well as the identification outcomes. The optimal measurement area is represented by a red cube.

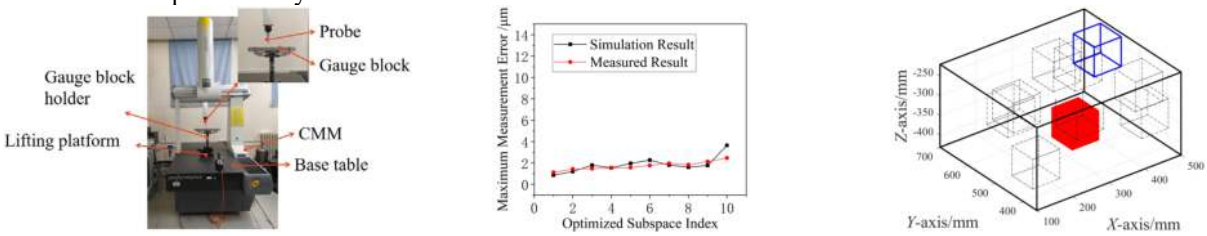

(a) Experimental platform. (b) Comparison between simulated and measured. (c) Partial subspace area distribution.

Figure 2. Identification results for the 50 mm straight line.

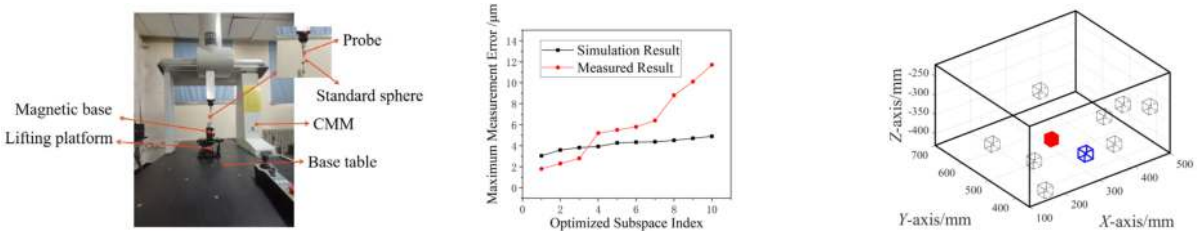

(a) Experimental platform. (b) Comparison between simulated and measured. (c) Partial subspace area distribution.

Figure 3. Identification results for the circular arc with ϕ = 15.8747 mm.

4. CONCLUSION

By integrating adaptive inertia weight, adaptive disturbance force, and simulated annealing mechanisms, the proposed IPSO-SAA enhances global search capability and reduces the risk of entrapment in local optima. Comparative results against PSO and APSO further confirmed the superior performance of IPSO-SAA. The proposed method provides a practical basis for measurement area selection and demonstrates potential for extension to workspace performance optimization of other precision motion systems.

ACKNOWLEDGMENTS

This research was supported by National Natural Science Foundation of China (NSFC) under Grant No. 52575606 and National Major Scientific Research Instrument Development Project under Grant No. 52175491.

REFERENCES

[1] Chen H, Zhang S, Wang G, et al, “LASSO based compensation method for geometric errors of large coordinate measuring machine”. *Measuremen*t, 2022,196:111157.

[2] Chen H, Wu H, Gao Y, et al, “Particle swarm algorithm-based identification method of optimal measurement area of coordinate measuring machine”. *Review of Scientific Instruments*, 2024,95(8):85105.

VIRTUAL MODEL OF A BUS USING THE FMI STANDARD FOR CO-SIMULATION WITH MATLAB/SIMULINK

Jozef Bucha[1], Ján Danko[1], Tomáš Milesich[1], Ján Čulík[1]

[1] Slovak University of Technology in Bratislava, Faculty of Mechanical Engineering, Námestie slobody 17, Bratislava, Slovakia, {jozef.bucha@stuba.sk; tomas.milesich@stuba.sk; jan.culik@stuba.sk}

1. INTRODUCTION

Modern vehicle development increasingly relies on virtual prototyping and simulation-based testing. Digital twins — highfidelity virtual replicas of physical systems — have emerged as powerful tools enabling engineers to predict vehicle behaviour, validate control algorithms, and reduce costly physical testing. Multi-Body Dynamics (MBD) tools such as MSC Adams/Car provide accurate mechanical representations of vehicles, while control-oriented environments like MATLAB/Simulink offer rich libraries for implementing advanced driver-assistance and autonomous driving algorithms.

The Functional Mock-up Interface (FMI) standard provides an open, tool-independent format for exchanging dynamic simulation models between different software environments [1]. By exporting an Adams/Car vehicle model as a Functional Mock-up Unit (FMU), it becomes possible to perform co-simulation with MATLAB/Simulink acting as the master solver. This paper presents

2. METHODOLOGY

The vehicle model was constructed in Adams/Car following its three-level hierarchy [2]: Templates define the parametric topology of each functional component (suspension, steering, powertrain, braking, tires, chassis); Subsystems instantiate templates with specific geometric and inertial parameters; and the Full Vehicle Assembly combines all subsystems into an analyzable system. The bus model includes a electric powertrain with differential, a double-wishbone suspension architecture, pitman steering, and brake system.

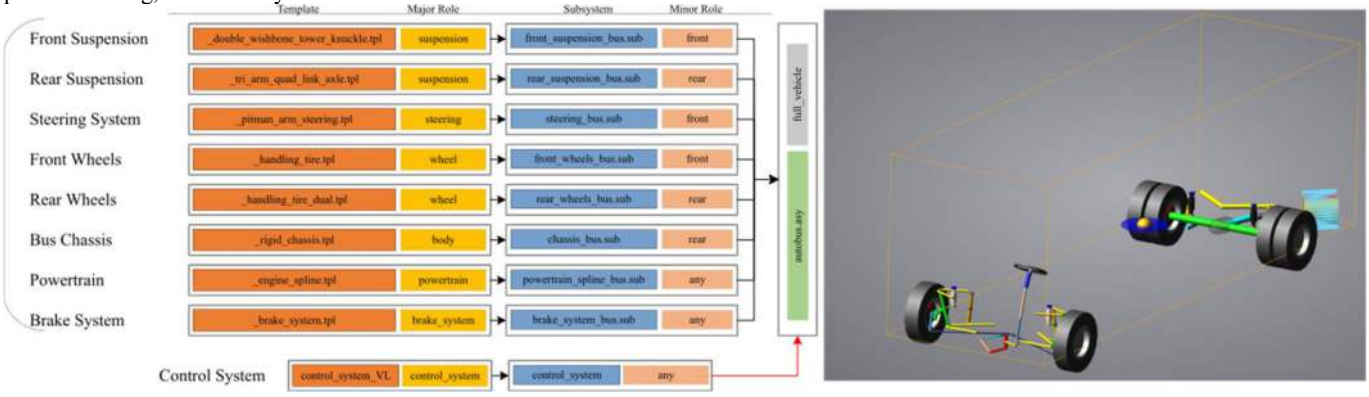

Figure 1. Block diagram and assembly of MBD bus model.

A dedicated control subsystem (Fig. 1) was added to the vehicle assembly to serve as the FMI interface layer. It defines one input plant (*Vehicle_controls_input*) receiving steering, throttle, brake, gear, and clutch signals, and two output plants (*InertFrm_CG* and *BodyFrm_CG*) transmitting position, orientation, velocity, angular velocity, and acceleration data referenced to both the inertial and body frames (Markers used in calculation are showed in Fig.2 - right) [3]. The Driving Machine was configured in Pure Open Loop mode (Fig. 2 - left).|so that all five control channels are driven by VARVAL function calls referencing Adams state- variable IDs, allowing the master solver in Simulink to assume full control. Block schemes of other events are in [3],[4].

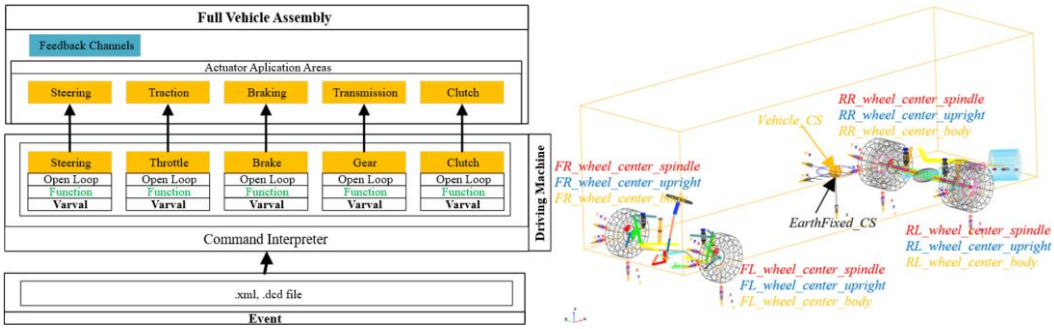

Figure 2. Open Loop Event using Varval function, markers used in Control System [5]

The FMU was exported from Adams/Car via the Adams/Controls plugin in Co-Simulation mode (FMI v2.0). The exported package includes the full vehicle assembly files (adm, .acf), the event XML file, the road model, and tire data. Within Simulink, the FMU block is imported, and its input/output ports are handled as buses with unitless signals. A virtual driver block in Simulink generates the five control signals and reads back the vehicle state outputs, closing the co-simulation loop (Fig.3).

3. VALIDATION

Model validation was conducted through experimental measurements performed on a real hydrogen-powered city bus. A highprecision GNSS measurement system was used to record vehicle trajectory, longitudinal and lateral velocities, and accelerations during standardized test scenarios including straight-line acceleration, braking, and combined driving maneuvers. Simulated outputs from the co-simulation framework were compared against the measured data. Compared results can be found in [6].

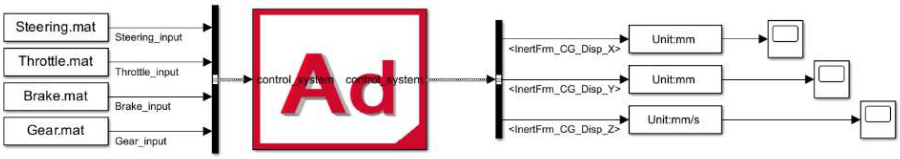

Figure 3. Data Driven Simulation in Simulink

4. RESULTS AND CONCLUSION

The presented work successfully demonstrates an end-to-end methodology for creating a digital twin of a city bus through FMI based co-simulation between Adams/Car and MATLAB/Simulink. The key contributions are: (1) a reusable control system template enabling any Adams/Car vehicle assembly to be exported as an FMU with a standardized input/output interface; (2) a co-simulation framework in Simulink incorporating a virtual driver capable of executing arbitrary driving maneuvers; and (3) an experimental validation protocol using GNSS measurements on a real vehicle.

The tool-independent nature of the FMI standard ensures that the vehicle model can be shared and integrated with different simulation platforms without exposing source code, facilitating collaboration across development teams. The resulting digital twin serves as a versatile platform for vehicle control system development, ride comfort and dynamics evaluation, virtual ADAS testing, and design decision support — all within a realistic and validated vehicle dynamics environment [6].

ACKNOWLEDGMENTS

This research was supported by the Slovak Research and Development Agency under Contracts No. APVV-23-0650, APVV-24-0526

REFERENCES

[1] “Functional Mock-up Interface”, [online] Available at: https://fmi-standard.org/ [Accessed: date (20.3.2026)].

[2] “Adams/Car user's guide”, Version 2025.2, MSC Software Corporation, Santa Ana, USA 2025

[3] F.R.E. Crossley, “Dynamic mechanisms and nonlinear control systems”, *Proceedings of the International Conference for Teachers of Mechanisms*, Yale University, USA, March 27–30, 1961.

[4] J. Bucha, Z. Miskovic, T. Milesich, “Integration of MBD Vehicle Models with Matlab/Simulink via FMI”. *International Journal of Modern Research in Engineering and Technology (IJMRET)* , 10(11), Muzffarnagar, India, ISSN 2456-5628, 2025.

[5] J. Bucha, R. Jančo, Ľ. Magdolen, J. Čulík, “Application of FMI Standard in Bus MBD model Development”, 27th International Conference Applied Mechanics 2026, České Budejovice, Czechia, 2026

[6] J. Bucha, “Digital twin of the Bus”. *Habilitation Thesis*, Slovak University of Technology in Bratislava Bratislava, Slovakia, 2026

Book of Abstracts of MMT Symposium
Mechanism and Machine Theory Symposium
Flores et al. (Eds)

MMT Symposium
60th Anniversary of Mechanism and Machine Theory
June 21-23, 2026 Porto, Portugal

ENHANCING DISTAL MOTION-FORCE INTERACTION PERFORMANCE OF ARTICULATED-PLATFORM PARALLEL MECHANISMS VIA INTERNAL PARAMETER DESIGN OF CLOSED-LOOP PASSIVE LIMBS

Qizhi Meng[1], Burkhard Corves[2], Andrés Kecskeméthy[1]

[1] Chair for Mechanics and Robotics, Faculty of Engineering, University of Duisburg-Essen, Duisburg 47057, Germany, {mqz15@tsinghua.org.cn; andres.kecskemethy@uni-due.de}
[2] Institute of Mechanism Theory, Machine Dynamics and Robotics, RWTH Aachen University, Kackertstraße 16-18, Aachen 52072, Germany, {corves@igmr.rwth-aachen.de}

1 INTRODUCTION

Although remarkable work has advanced the understanding of performance for articulated-platform high-speed parallel mechanisms [1], the internal closed-loop limbs contain both length and width information, of which the effect of width on robot performance remains unknown. The core reason lies in the fact that these analyses and performance metrics primarily followed the paths below when modeling the robot: (1) During kinematic analysis, such as when establishing the Jacobian matrix, closed-loop limbs like RPa (R: revolute joint; Pa: parallelogram linkage) were often simplified and modeled as RUU limbs [2], as illustrated in Fig. 1(a). In this process, the length information L_b of the closed-loop limb was retained, but its width information K was lost and neglected due to the equivalence treatment. (2) When analyzing motion/force transmission and constraint performance, the transmission and constraint effects were evaluated separately. This required identifying transmission and constraint wrenches independently. However, the constraint wrenches were also equivalently treated and considered as constraint couples acting on the mobile platform, as shown in Fig. 1(b). Since the width parameter K of the closed-loop limb does not affect the result of the identifications of these constraint couples, this width information K was again overlooked.

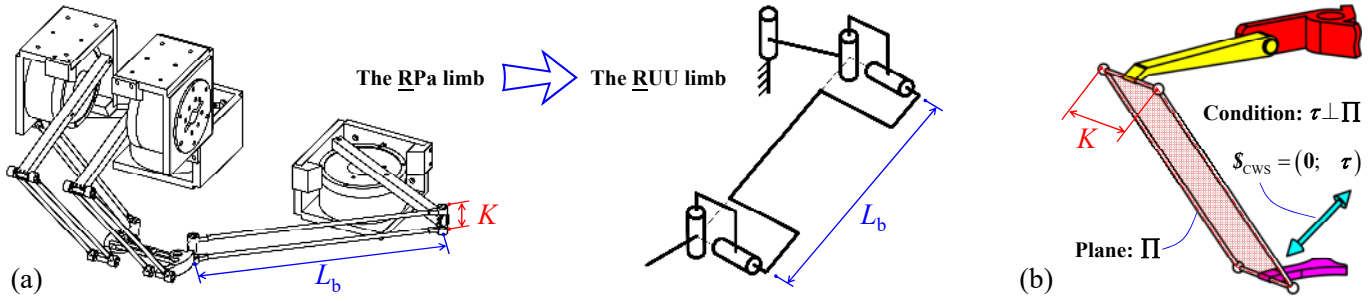

Figure 1: Modeling of parallel mechanisms with closed-loop passive limbs: (a) the H4 parallel mechanism and its equivalent RUU limb; (c) the identification of the constraint wrench in the RPa limb.

This paper proposes an evaluation approach for the distal motion-force interaction of articulated-platform high-speed parallel mechanisms by adopting physically available wrenches within the closed-loop passive limbs. The investigated mechanisms feature an 8-degree-of-freedom (DOF) articulated mobile platform constrained by 8 wrenches from passive limbs, which is also referred to as an 8-wrench-8-DOF system. The power coefficient is adopted to quantify the relationship between each distal wrench and its corresponding virtual distal twist. Then the minimum power coefficient serves as an evaluation index of overall distal motion-force interaction. A representative mechanisms Heli4 is analyzed. The results show that the proposed approach effectively reveals how the structural parameters of closed-loop limbs influence the distal motion-force interaction performance of the parallel mechanism. Specifically, within the considered range, increasing the internal parameter K leads to enhanced distal motion-force interaction performance, providing guidance for robot performance enhancement design. The methodology in this paper offers a new perspective for evaluating articulated-platform parallel mechanisms and provides a theoretical foundation for future work, including dimension optimization and type selection.

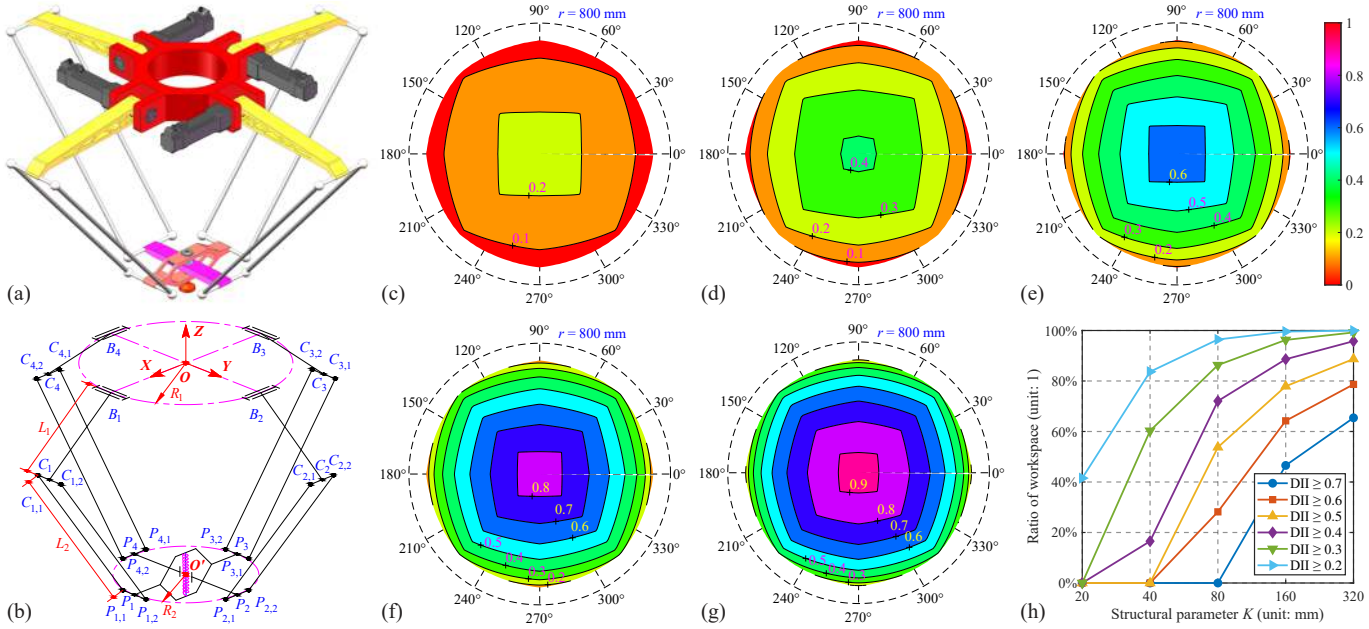

Figure 2: Performance distribution of the Heli4 parallel mechanism with $\theta = 0°$ on $Z = -800$ mm: (a) CAD model; (b) kinematic diagram with geometric parameters; (c) DII with $K = 20$ mm; (d) DII with $K = 40$ mm; (e) DII with $K = 80$ mm; (f) DII with $K = 160$ mm; (g) DII with $K = 320$ mm; (h) ratio evolution of workspace regions with different DII thresholds relative to the reachable workspace.

2 PERFORMANCE INDEX

To evaluate the overall effect of the set of distal wrenches from the limbs acting on the mobile platform, and based on the worst-case criterion, the minimum value of the power coefficients between each pair of distal wrench $\$^j_{\mathrm{DW}}$ and its corresponding virtual distal twist $\$^j_{\mathrm{VDT}}$ is defined as follows [3]:

$$\xi = \min_j \{\lambda_j\} = \min_j \left\{ \frac{\left| \$^j_{\mathrm{DW}} \circ \$^j_{\mathrm{VDT}} \right|}{\left| \$^j_{\mathrm{DW}} \circ \$^j_{\mathrm{VDT}} \right|_{\max}} \right\}, \qquad j = 1, 2, \ldots, M. \tag{1}$$

where $M = 8$ for a 8-wrench-8-DOF system. The index ξ characterizes the power interaction efficiency between the distal wrench $\$^j_{\mathrm{DW}}$ and the corresponding virtual distal twist $\$^j_{\mathrm{VDT}}$. It reflects the distal interaction characteristics between wrenches and twists, and is therefore referred to as the distal interaction index (DII).

3 RESULTS AND CONCLUSIONS

The Heli4 parallel robot is analyzed as a example, as shown in Fig. 2(a). Its geometric parameters are defined in Fig. 2(b). $L_1 = B_iC_i = 375$ mm, $L_2 = C_{i,1}P_{i,1} = C_{i,2}P_{i,2} = 825$ mm, $OB_i = R_1 = 275$ mm, $OP_i = R_2 = 105$ mm, and $P = 100$ mm, where $i = 1, \ldots, 4$ and P is the pitch of the helix joint inside the articulated mobile platform. Keeping these parameters constant, the influence of the key structural parameter $K = C_{i,1}C_{i,2}$, i.e., the short-link length of the passive limbs forming the parallelogram linkages, on the distal motion-force interaction performance of the articulated-platform parallel mechanism with closed-loop passive limbs is investigated. Fig. 2(c)–Fig. 2(g) present the DII distribution of the Heli4 parallel mechanism at $\theta = 0°$ on the plane $Z = -800$ mm, which correspond to $K = 20$ mm, 40 mm, 80 mm, 160 mm, and 320 mm, respectively. Comparative analysis indicates that as the key internal parameter K of the closed-loop limbs increases, the distal interaction performance improves consistently. Fig. 2(h) illustrates the ratio of workspace regions exceeding different DII thresholds relative to the total reachable workspace. The ratio increases monotonically with K for all thresholds examined (0.2, 0.3, 0.4, 0.5, 0.6, and 0.7).

REFERENCES

[1] Y. H. Li, Y. Ma, S. T. Liu, Z. J. Luo, J. P. Mei, T. Huang, and D. G. Chetwynd, "Integrated design of a 4-DOF high-speed pick-and-place parallel robot," *CIRP Annals*, vol. 63, no. 1, pp. 185–188, 2014.

[2] H.-B. Choi and J. Ryu, "Singularity analysis of a four degree-of-freedom parallel manipulator based on an expanded 6×6 Jacobian matrix," *Mechanism and Machine Theory*, vol. 57, pp. 51–61, 2012.

[3] Q. Meng, X.-J. Liu, and A. Kecskeméthy, "Motion-force interaction performance of parallel robotic mechanisms," *SmartBot*, p. e12006, 2025.

ON THE NUMERICAL ERRORS OF MULTIBODY DYNAMICS JACOBIANS INDUCED BY THE RODRIGUES FORMULA

Jiayi Zhou[1], Zhiwen Xiao[1], Gexue Ren[1*]

[1] School of Aerospace Engineering, Tsinghua University, Beijing, China, {zhou-jy24@mails.tsinghua.edu.cn}

1 INTRODUCTION

The Rodrigues formula, which expresses the rotation matrix as $\mathbf{R}(\boldsymbol{\phi}) = \mathbf{I} + h_1(\phi)\tilde{\boldsymbol{\phi}} + h_2(\phi)\tilde{\boldsymbol{\phi}}^2$ with $h_1(\phi) = \sin\phi/\phi$ and $h_2(\phi) = (1-\cos\phi)/\phi^2$, is fundamental to the rotation vector parametrization in multibody dynamics [1, 2]. The associated scalar auxiliary function $h_3(\phi) = (\phi - \sin\phi)/\phi^3$ appears in the angular velocity mapping $\boldsymbol{\omega} = \mathbf{H}^T(\boldsymbol{\phi})\dot{\boldsymbol{\phi}}$. These functions and their radial derivatives ($\frac{D}{D\phi} = \frac{1}{\phi}\frac{d}{d\phi}$) are essential for computing Jacobian matrices in rigid body dynamics [4, 5]. While recent studies have thoroughly analyzed the numerical accuracy of these functions themselves [6, 7], the propagation of their errors to system-level quantities like the Jacobian matrix has not been systematically quantified. This paper addresses this gap by demonstrating how errors induced by the Rodrigues formula—particularly in the second radial derivatives—are amplified in the Jacobian, potentially compromising the convergence and stability of implicit integrators in real-time applications.

2 PROBLEM STATEMENT AND METHODOLOGY

The closed-form expressions derived from the Rodrigues formula suffer from numerical singularities as $\phi \to 0$ due to catastrophic cancellation [8]. For the first radial derivatives Dh_i, these errors remain moderate, but for the second radial derivatives DDh_i, they become severe—reaching relative errors of 10^{-3}, 10^4, and 10^6 for DDh_1, DDh_2, and DDh_3 respectively in the critical region $\phi \approx 10^{-3}$. To isolate and quantify the impact of these Rodrigues-induced errors on the Jacobian, we consider the term $K_1 = (\boldsymbol{\phi}\cdot\dot{\boldsymbol{\phi}})C\dot{\boldsymbol{\phi}}$, a key component of the rotational Jacobian derived in our companion work. We compute $\partial K_1/\partial\boldsymbol{\phi}$ using three methods: (i) analytic formulas employing the closed-form second derivatives (directly from the Rodrigues formula), (ii) the same analytic formulas after replacing the second derivatives with a high-order Taylor series (20th order, evaluated via Horner's scheme), and (iii) a high-order central finite difference reference (step size 10^{-8}). The optimized series serves as a tool to eliminate the base-function errors, allowing us to observe their propagation.

3 RESULTS AND DISCUSSION

Fig. 1 presents the relative error of $\partial K_1/\partial\boldsymbol{\phi}$ computed with and without optimization, compared to the finite difference reference. Before optimization, the analytic Jacobian exhibits large errors, exceeding 10^{-4} in the region $\phi \approx 10^{-3}$. This directly mirrors the behavior of the second radial derivatives, confirming that errors induced by the Rodrigues formula propagate into the Jacobian. After replacing the second derivatives with the optimized series, the analytic Jacobian aligns nearly perfectly with the reference, achieving relative errors below 10^{-7} across the entire range $\phi \in [10^{-6}\pi, 0.95\pi]$.

This result has important implications: even if the base functions from the Rodrigues formula are considered "acceptably accurate" in isolation, their errors can be amplified in derived quantities like the Jacobian, potentially degrading the performance of implicit integrators that rely on exact linearization. The optimized series effectively removes this source of numerical instability, restoring the analytic Jacobian's accuracy to machine precision. Performance measurements confirm that the multi-segment Taylor approach is also efficient, achieving 6–11× speedups for the base functions while maintaining 10^{-15} accuracy.

4 CONCLUSION

This work provides the first systematic quantification of how numerical errors induced by the Rodrigues formula propagate to the Jacobian matrix in multibody dynamics. Using the term K_1 as a representative example, we show that errors in the second radial derivatives are directly amplified in the Jacobian, leading to relative errors exceeding 10^{-4} in the critical small-angle region. By replacing these derivatives with an optimized high-order Taylor series, we eliminate the error propagation and restore analytic accuracy to below 10^{-7}. Our findings serve as a cautionary note for practitioners: local function accuracy derived from the Rodrigues formula does not guarantee system-level accuracy. The optimized routines have been integrated into a production simulation kernel, providing a reliable foundation for

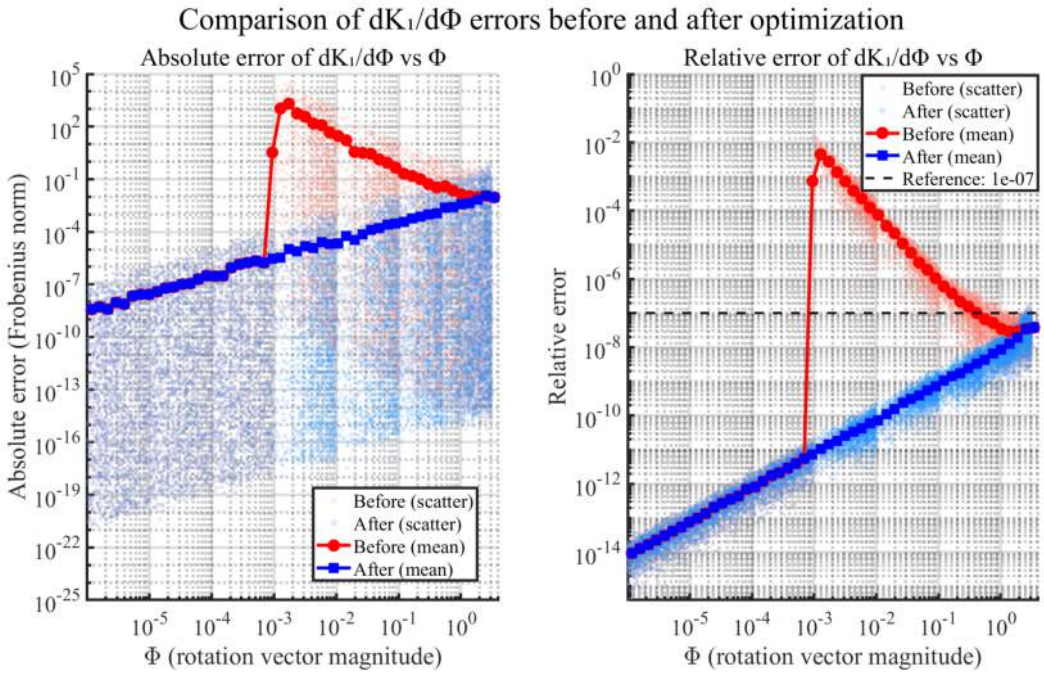

Figure 1: Relative error of $\partial K_1/\partial \phi$ computed analytically before and after optimization of the second radial derivatives, compared to a high-order finite difference reference. The large errors in the unoptimized case stem from catastrophic cancellation in the closed-form second derivatives derived from the Rodrigues formula.

real-time multibody applications. Future work will extend this analysis to flexible bodies [10] and explore implications for controller design and parameter identification.

REFERENCES

[1] J. Stuelpnagel, "On the parametrization of the three-dimensional rotation group," *SIAM Rev.*, vol. 6, no. 4, pp. 422–430, 1964.

[2] O. A. Bauchau and L. Trainelli, "The vectorial parameterization of rotation," *Nonlinear Dyn.*, vol. 32, no. 1, pp. 71–92, 2003.

[3] A. Müller, "Coordinate mappings for rigid body motions," *J. Comput. Nonlinear Dyn.*, vol. 12, no. 2, p. 021010, 2016.

[4] E. Celledoni and B. Owren, "Lie group methods for rigid body dynamics and time integration on manifolds," *Comput. Methods Appl. Mech. Eng.*, vol. 192, no. 3–4, pp. 421–438, 2003.

[5] M. Arnold, A. Cardona, and O. Brüls, "A Lie algebra approach to Lie group time integration of constrained systems," in *Structure-preserving Integrators in Nonlinear Structural Dynamics and Flexible Multibody Dynamics*, P. Betsch, Ed. Springer, 2016, pp. 91–158.

[6] J. Todesco and O. Brüls, "Highly accurate differentiation of the exponential map and its tangent operator," *Mech. Mach. Theory*, vol. 190, p. 105451, 2023.

[7] A. Müller, "Review of the exponential and Cayley map on SE(3) as relevant for Lie group integration," *Proc. R. Soc. A*, vol. 477, no. 2253, p. 20210303, 2021.

[8] M. Ritto-Corrêa and D. Camotim, "On the differentiation of the Rodrigues formula," *Int. J. Numer. Methods Eng.*, vol. 55, no. 9, pp. 1005–1032, 2002.

[9] E. A. de Souza Neto, "The exact derivative of the exponential of an unsymmetric tensor," *Comput. Methods Appl. Mech. Eng.*, vol. 190, no. 18–19, pp. 2377–2383, 2001.

[10] V. Sonneville, A. Cardona, and O. Brüls, "Geometrically exact beam finite element formulated on the special Euclidean group SE(3)," *Comput. Methods Appl. Mech. Eng.*, vol. 268, pp. 451–474, 2014.

MULTIBODY DYNAMICS-BASED FEEDFORWARD CONTROL STRATEGIES FOR WELLBORE TRAJECTORY TRACKING IN DIRECTIONAL DRILLING SYSTEMS

Xinrong Li[1], Kejie Wang[1], Jiaqi Chen[1], Ningyu Wang[2], Gexue Ren[1]

[1] School of Aerospace Engineering, Tsinghua University, Beijing, China
{xrli0932@gmail.com; 1043641442@qq.com; chenjiaqi0512@163.com; rengx@mail.tsinghua.edu.cn}

[2] State Key Laboratory of Hydroscience and Engineering, Tsinghua University, Beijing, China
{wang-ningyu@mail.tsinghua.edu.cn}

1 INTRODUCTION

Directional drilling involves guiding a drill bit along a predetermined spatial trajectory to reach subsurface targets. The drill string is a slender, flexible multibody system extending several kilometers, characterized by strong geometric nonlinearity and complex contact-friction interactions[1]. Traditional slide drilling strategies rely heavily on manual interpretation of rig data and engineer experience. Due to the inherent minute-level delay in Measurement While Drilling (MWD) systems and the spatio-temporal lag in torque transmission, manual operations often result in overshoot, oscillatory corrections, and significant non-productive time. To bridge the gap between geometric targets and mechanical control inputs, this study establishes an intelligent closed-loop feedforward control framework driven by high-fidelity multibody dynamics (MBD) simulations. The overall schematic workflow and the control block diagram of this proposed framework are illustrated in Fig. 1(a) and (b), respectively.

2 MULTIBODY DYNAMICS MODELING AND CONTROL STRATEGIES

To capture full drill string dynamics efficiently, an Arbitrary Lagrangian-Eulerian (ALE) beam formulation is employed, elegantly handling continuous mass flow without the computational overhead of element birth/death techniques[2, 3]. To ensure continuous accuracy, bit-rock interaction parameters are calibrated in real-time using actual logging data, enabling the model to seamlessly adapt to varying geological conditions. Furthermore, to achieve the super-real-time computational efficiency required for field operations, a segmented decoupling model separates the upper drill pipe—approximately 90% of the total length—from the Bottom Hole Assembly (BHA). By iteratively solving their separate equilibrium equations through boundary condition coupling, computational complexity is drastically reduced, ensuring the uninterrupted generation of precise feedforward control commands on-site[4].

Building upon this highly accurate and adaptive MBD model, an adaptive trajectory planning method is introduced. The spacing of trajectory control points is dynamically adjusted using a sensitivity factor based on the formation drillability index. To accommodate complex field scenarios, multiple decoupled shooting strategies were developed, including flexure-parameter dominant, distance dominant, hybrid, and Weight-on-Bit (WOB) dominant methods. Notably, the WOB-dominant strategy releases the axial force constraint at segment nodes, enabling simultaneous optimization of trajectory tracking and drilling efficiency.

3 LONG-TERM SEQUENCE FEEDFORWARD CONTROL

Conventional step-wise feedforward methods impose constant control inputs (e.g., top drive angle and hook load) within a single drill pipe length. This rigid approach fails to adapt to continuous high-dogleg-severity steering or unexpected formation perturbations, inevitably leading to cumulative tracking errors over multiple pipes.

To resolve this, a Long-Term Sequence Feedforward Control method is proposed. Rather than treating inputs as discrete steps, this method establishes a continuous functional mapping for control variables over the well depth domain $S \subset \mathbb{R}^+$. Specifically, hook velocity inputs are parameterized using B-spline interpolation within a piecewise cubic spline space, denoted as $\{v_k\}_{k=1}^n \in \mathcal{P}_3(S)$[5]. The algorithm employs a dual-stage iteration structure. The first stage solves for the pre-equilibrium states of the segment nodes (e.g., axial force and rotation angle) to ensure initial stability. The second stage iterates toward the target trajectory parameters (curvature and principal normal angle). Convergence is achieved when the relative error norm $||\epsilon_{rel}^i||$ falls below 1%. This mathematical formulation achieves dynamic, intra-pipe continuous control adjustments, significantly reducing trajectory tortuosity.

4 FIELD VALIDATION AND RESULTS

The proposed framework has been integrated into an intelligent drilling software platform and successfully deployed in actual field engineering operations. In the Fukang well (measured depth 1682 m, tracking a drop-angle section), a trajectory correction that previously required approximately 7 hours of manual adjustment and 40 m of drilling was resolved computationally in minutes. The algorithm generated an optimal tool face angle of 183.7° and a 3.35 m slide distance, demonstrating rapid response capability and eliminating trial-and-error oscillations. Furthermore, in the Junggar horizontal well (depth 4880 m), the system utilized live rig data to dynamically update formation parameters. The feedforward algorithm computed precise control inputs, suggesting a 6.64 m slide distance and an optimal tool face angle of 71.2°. This highly efficient alternative effectively replaced the 2.5 hours and 15 m of manual adjustments recorded in the field.

Finally, a long-section simulation (800 to 890 m, spanning 9 drill pipes) was conducted to evaluate multi-pipe continuous steering. As illustrated in Fig. 1(c), the Long-Term Sequence method successfully suppressed the cumulative Root Mean Square (RMS) error to 0.64 m. In contrast, the baseline step-wise method yielded a divergent cumulative error of 1.18 m. This confirms that the proposed continuous functional mapping maintains stable computational efficiency while drastically improving tracking accuracy over extended intervals.

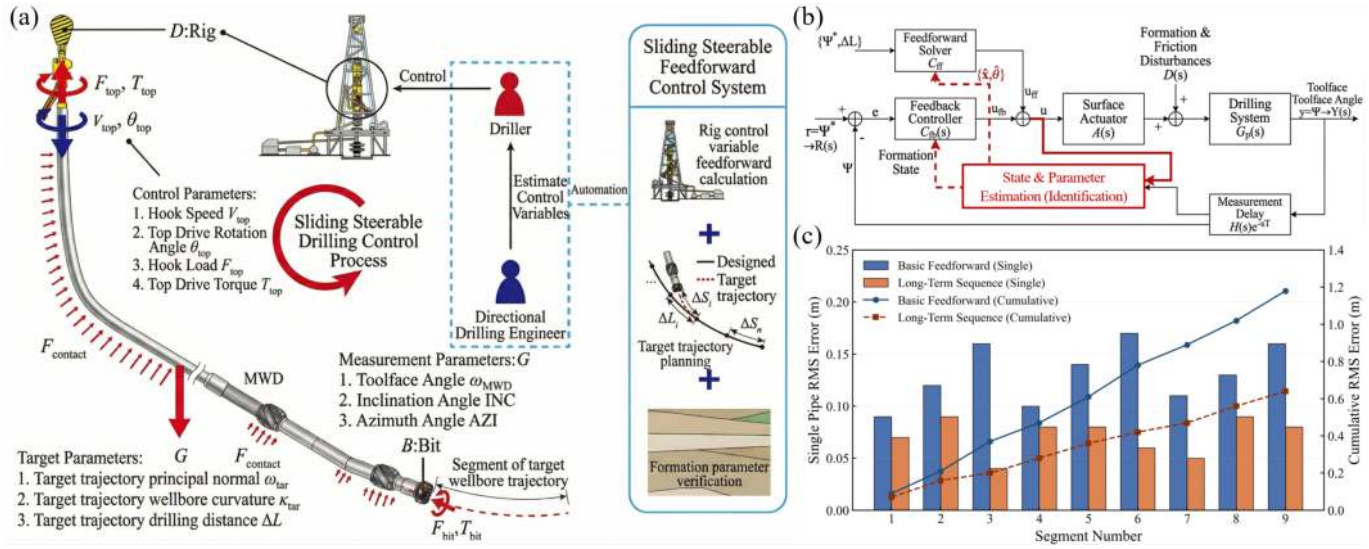

Figure 1: (a) Schematic diagram of the feedforward control process; (b) Block diagram of the feedforward control system; (c) Comparison of single and cumulative RMS tracking errors over multiple drill pipes.

5 CONCLUSION

Integrating ALE-based MBD simulation with the Long-Term Sequence Feedforward Control strategy significantly enhances directional drilling autonomy. The proposed framework directly translates geometric targets into continuous mechanical inputs. This effectively minimizes operator intervention and reduces error accumulation. Ultimately, this work provides a solid theoretical foundation for fully automated drilling systems.

REFERENCES

[1] W. R. Tucker and C. Wang, "An integrated model for drill-string dynamics". *Journal of Sound and Vibration*, vol. 224, no. 1, pp. 123-165, 1999.

[2] J.-P. Liu, Z.-B. Cheng, and G.-X. Ren, "An Arbitrary Lagrangian–Eulerian formulation of a geometrically exact Timoshenko beam running through a tube". *Acta Mechanica*, vol. 229, no. 8, pp. 3161-3188, 2018.

[3] H. Zhang, J.-Q. Guo, J.-P. Liu, and G.-X. Ren, "An efficient multibody dynamic model of arresting cable systems based on ALE formulation". *Mechanism and Machine Theory*, vol. 151, p. 103892, 2020.

[4] J.-Q. Chen, K.-J. Wang, X.-Y. Tang, and G.-X. Ren, "Steering ability rapid evaluation of the slide drilling system based on multi-body dynamics model". *Geoenergy Science and Engineering*, vol. 237, p. 212813, 2024.

[5] S. Macfarlane and E. A. Croft, "Jerk-bounded manipulator trajectory planning: design for real-time applications". *IEEE Transactions on Robotics and Automation*, vol. 19, no. 1, pp. 42-52, 2003.

NVH-AWARE CO-OPTIMIZATION OF TOPOLOGY, PARAMETER AND CONTROL FOR DISTRIBUTED RANGE-EXTENDED ELECTRIC POWERTRAINS

Yuxin Zhang[2], Yunge Zou[1], Xin Ye[2]

[1]Chongqing Changan Automobile Co Ltd, Apartment 2nd Room 208, Yonghe Road 39, Yubei District, Chongqing 401133, China, {yunge_zou@cqu.edu.cn}

[2]Chongqing University of Technology, No. 69, Hongguang Avenue, Banan District, Chongqing 40054, China, {yuxin_zhang@cqut.edu.cn;yexin.cqu@gmail.com }

1. INTRODUCTION

Distributed range-extended electric vehicle (D-REEVs) powertrains have emerged as a key development direction for new energy vehicle configurations globally, offering enhanced fuel economy, stability, and power performance[1]. However, integrating an auxiliary power unit (APU) and multiple distributed motors creates a multi-source, high-degree-of-freedom architecture[2]. While this configuration delivers significant energy-saving and acceleration potential, it also introduces highly complex power flow distribution and “ mechanical-electrical-NVH ” coupling challenges[3-4]. Therefore, this study innovatively approaches the problem from a powertrain architecture perspective. By analyzing and comparing the optimization potential of different distributed transmission schemes in terms of fuel economy, acceleration, and NVH performance, it proposes a novel multi-mode, multi-gear distributed transmission system. To fully exploit the NVH optimization potential of the APU, this paper introduces a Topology-Parameter-Control Multi-Layer Collaborative Optimization (TPCMC) method. At the topology layer, this study reveals the energy flow characteristics, power characteristics, and energy-saving noise-reduction mechanisms of range-extended distributed vehicles. At the parameter and control level, a novel near-optimal energy management strategy — Super Rapid Dynamic Programming (Super Rapid-DP) — is introduced by integrating Pareto optimization, slope filtering, and NVH optimization techniques. This strategy achieves 8.4%-11.1% NVH improvement while enhancing computational efficiency by 3500-fold. Results demonstrate that compared to range-extended electric vehicles, the optimized powertrain achieves a 28.9% improvement in acceleration performance, a 5.02% – 7.1% increase in fuel economy, and an 8.9% – 11.5% reduction in NVH performance across various driving conditions. This study contributes to reducing NVH performance in electrified transportation through the advanced TPCMC methodology.

2. METHODOLOGY

This study focuses on a specific distributed range-extended electric vehicle, whose powertrain configuration is shown in Figure 1. To address the optimization of the range extender’s NVH performance, this paper proposes an integrated topology-parameter-control optimization method at the powertrain system level. This method embeds the parameter layer within the configuration layer and provides inputs to the control layer; for the design parameters, a grid-based exhaustive search method is employed to solve the problem. The study selects two continuous variables—the motor-end gear ratio (M/R) and the final reduction ratio (FR)—and discretizes the design space using fixed step sizes to generate multiple sets of feasible design solutions. To comprehensively compare the performance potential of different solutions, the value range for the motor-end gear ratio M/R is set to[1.5, 4], with a calculation step size of 0.25; and the range for the final reduction ratio FR was set to [2, 4.5] with a calculation step size of 0.25. The overall optimization process is shown in Figure 2.

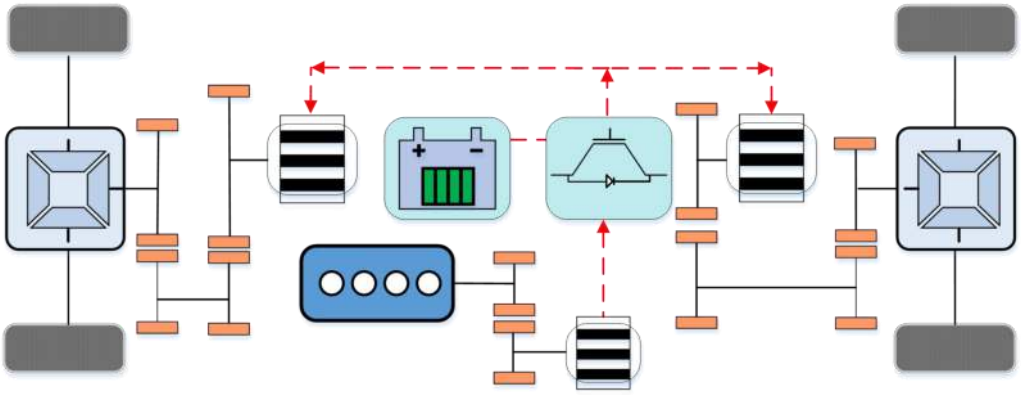

The vehicle parameters are shown in Table 1

（1）Optimize the configuration layer, then generate candidate solutions for nested configuration parameters.

（2）Since the simulation time for the accelerated model is less than 1 second, this study first screens candidate configuration parameters based on acceleration metrics.

（3）The candidate parameters that satisfy the acceleration criteria are used as inputs to the control layer, and NVH-aware Super Rapid-DP is employed to jointly optimize NVH performance and fuel economy.

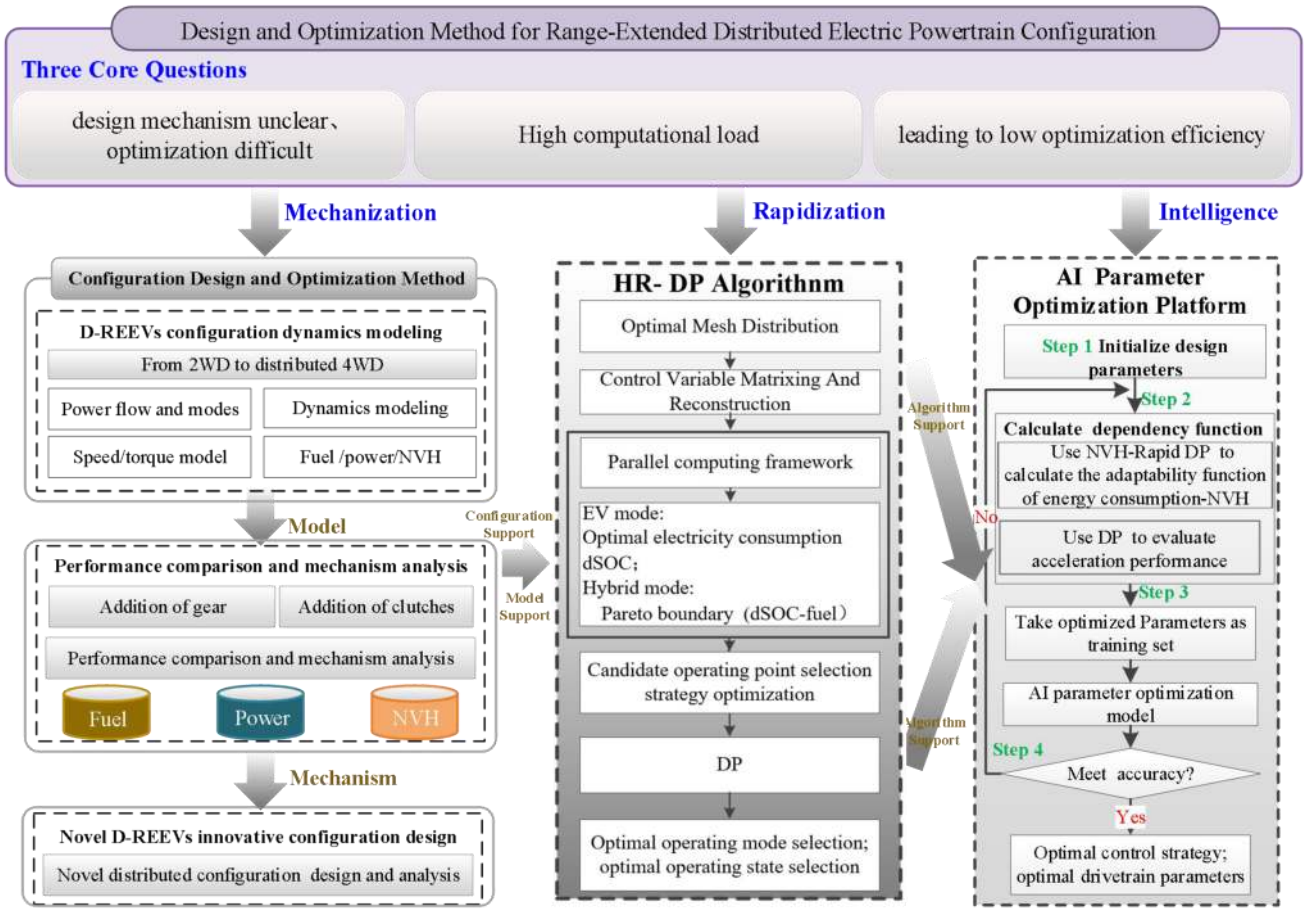

Figure 2: Research for design optimization and rapid performance optimization of distributed range-extender transmission configurations.

3. RESULTS

To systematically investigate the influence of the powertrain's physical and control layers on NVH performance, this paper proposes an advanced NVH-aware Topology Parameter Control Multi-layer Cooperative Offline Optimization (TPCMC) method. The main research conclusions are summarized as follows. (1) The effectiveness and efficiency of the proposed NVH-aware Rapid-DP+ method were analyzed. Compared to the DP method, it achieved a 3,500-fold reduction in CPU time, a 8.4% – 11.1% reduction in NVH performance degradation, and an average fuel accuracy error of only 3.88%. (2) Through the collaborative configuration-parameter-control layers, a 28.9% improvement in acceleration performance and a 5.02% – 7.1% increase in fuel economy are achieved. The significant value of the multi-layer collaborative optimization method in improving the whole vehicle performance was confirmed compared to optimizing the EMS control layer alone.

4. CONCLUSION

This study analyzed and compared the optimization potential of different distributed transmission schemes in terms of fuel economy, acceleration, and NVH performance. At the topology layer, this study reveals the energy flow characteristics, power characteristics, and energy-saving noise-reduction mechanisms. At the parameter and control level, a novel near-optimal strategy is introduced by integrating Pareto optimization, slope filtering, and NVH optimization techniques.

REFERENCES

[1] Cao K, Hu M, Wang D, et al. All-Wheel-Drive Torque Distribution Strategy for Electric Vehicle Optimal Efficiency Considering Tire Slip[J]. IEEE Access, 2021, 9: 25245-25257.

[2] Chen J, Kong X, Li P. Analysis of the control strategy of range extender system on the vehicle NVH performance[J]. Vibroengineering Procedia, 2020, 33: 90-95.

[3] Xu X, Zhao J, Zhao J, et al. Comparative study on fuel saving potential of series-parallel hybrid transmission and series hybrid transmission[J]. Energy Conversion and Management, 2022, 252: 114970.

[4] Anselma P G, Biswas A, Belingardi G, et al. Rapid assessment of the fuel economy capability of parallel and series-parallel hybrid electric vehicles[J]. Applied Energy, 2022, 275: 115319.

Book of Abstracts of MMT Symposium
Mechanism and Machine Theory Symposium
Flores et al. (Eds)

MMT Symposium
60th Anniversary of Mechanism and Machine Theory
June 21-23, 2026 Porto, Portugal

REDUCED-ORDER MODELING OF BEARINGS AND GEARS FOR ACCURATE STRESS COMPUTATION

Zhiwen Xiao[1], Zhilu Qi[1], Xinrong Li[1], Gexue Ren[1]

[1] School of Aerospace Engineering, Tsinghua University, Beijing, China, {xiaozw21@mails.tsinghua.edu.cn}

1 INTRODUCTION

Accurate simulation of systems involving both motion and elasticity is critical in engineering applications such as mechanical design, robotics, and aerospace engineering. Traditional finite element methods offer high precision but incur substantial computational costs when modeling large-scale complex systems. Ziegler et al.[1] employed truncated characteristic modes to represent linear elastic deformations in gear contact dynamics. However, such global mode sets cannot effectively capture high stress gradients in local regions[2]. To address this, a dynamically complete mode set including static correction modes is needed to compensate for the quasi-static response of omitted modes[3]. In structural dynamics, component mode synthesis methods are generally categorized into fixed-interface[4] and free-interface[5] approaches. Fixed-interface methods, such as the Craig–Bampton method, are commonly used in commercial multibody software and have been applied to gear contact simulations. However, they require mode switching to represent dynamically changing contact interfaces[6, 7], which increases problem size and computational complexity. An alternative free-interface method proposed by Yao et al.[8] retains a few key modes for global response while compensating for local quasi-static contributions through statically equivalent residual modes. Nevertheless, this method cannot handle exact displacement interfaces. In this paper we propose an efficient reduced-order modeling strategy for bearings and gears by combining the Craig–Bampton method with a quasi-static force compensation at contact interfaces.

2 METHODOLOGY AND APPLICATION

The proposed reduced-order modeling strategy distinguishes displacement boundaries and load boundaries. Displacement boundaries, e.g. shaft–inner ring connection boundaries in bearings, are modeled using the modified Craig–Bampton method with multipoint constraints linking the interface nodes to a six-degree-of-freedom reference node. This ensures exact kinematic compatibility with the multibody system. Load boundaries, i.e. gear tooth flanks and roller–raceway contacts, are augmented by a precomputed quasi-static force compensation term that captures local contact deformation without adding online degrees of freedom. Cutoff frequencies are chosen based on operating conditions: 10 kHz for bearings and 5 kHz for gears, retaining only a few elastic normal modes per component.

2.1 Rolling bearing

The bearing (eight rollers, inner and outer rings) originally modelled with over 16,000 FE nodes is reduced to only 95 generalized coordinates: each roller contributes six rigid-body DOFs, the inner ring retains 16 elastic modes, and the outer ring 19 elastic modes. The stress contours in Fig.1(b) shows the method correctly capture the local contact stress concentration.

2.2 Planetary reducer

The planetary reducer (planet carrier, sun gear, five planet gears, ring gear) with original FE nodes totalling over 250,000 is reduced to 133 DOFs, including 25 Lagrange multipliers for rotation constraints between the carrier and planet gears. Fig.1(d) displays the resulting stress field, accurately reflecting tooth root and contact stresses.

3 CONCLUSION

A reduced-order modeling strategy for bearings and gears has been presented, combining the displacement-boundary accuracy of the Craig–Bampton method with quasi-static force compensation at load boundaries. The method compresses components originally modelled with tens of thousands of finite element nodes into reduced models with only tens of generalized coordinates, while accurately capturing local contact stresses. This drastic reduction in system-level degrees of freedom enables efficient multibody simulations of complex transmission systems that would otherwise be computationally prohibitive. The approach is compatible with existing Craig–Bampton workflows and can be readily extended to other components with mixed boundary conditions.

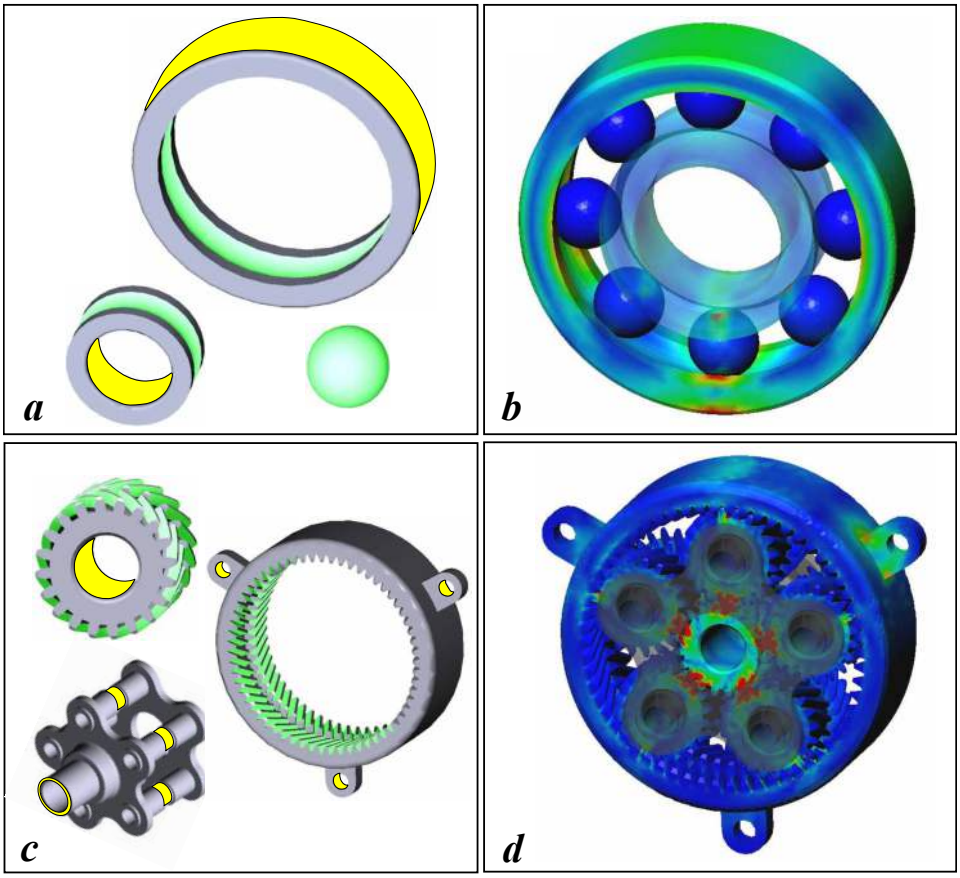

Figure 1: Boundary configuration and dynamic simulation results for the ball bearing and planetary reducer: (a,c) displacement boundaries connected to MPC reference nodes (yellow) and load boundaries (green); (b,d) corresponding von Mises stress distributions during dynamic simulation.

REFERENCES

[1] P. Ziegler, P. Eberhard, and B. Schweizer, "Simulation of impacts in geartrains using different approaches," *Archive of Applied Mechanics*, vol. 76, no. 9, pp. 537–548, 2006.

[2] D. Schurr, P. Holzwarth, and P. Eberhard, "Investigation of dynamic stress recovery in elastic gear simulations using different reduction techniques," *Computational mechanics*, vol. 62, no. 3, pp. 439–456, 2018.

[3] K. Sherif, W. Witteveen, and K. Mayrhofer, "Quasi-static consideration of high-frequency modes for more efficient flexible multibody simulations," *Acta Mechanica*, vol. 223, no. 6, pp. 1285–1305, 2012.

[4] W. C. HURTY, "Dynamic analysis of structural systems using component modes," *AIAA Journal*, vol. 3, no. 4, pp. 678–685, apr 1965. [Online]. Available: https://doi.org/10.2514/3.2947

[5] R. H. MacNeal, "A hybrid method of component mode synthesis," *Computers &amp Structures*, vol. 1, no. 4, pp. 581–601, dec 1971. [Online]. Available: https://doi.org/10.1016/0045-7949(71)90031-9

[6] J.-P. Liu, X.-B. Shu, H. Kanazawa, K. Imaoka, A. Mikkola, and G.-X. Ren, "A model order reduction method for the simulation of gear contacts based on Arbitrary Lagrangian Eulerian formulation," *Computer Methods in Applied Mechanics and Engineering*, vol. 338, pp. 68–96, Aug. 2018.

[7] J.-W. Liu, J.-P. Liu, X.-B. Shu, A. Mikkola, and G.-X. Ren, "An efficient multibody dynamic model of three-dimensional meshing contacts in helical gear-shaft system and its solution," *Mechanism and Machine Theory*, vol. 142, p. 103607, Dec. 2019.

[8] J.-L. Yao, X.-B. Shu, and G.-X. Ren, "A free-interface component mode synthesis of moving contact multibodies and its application to gear contacts," *International Journal for Numerical Methods in Engineering*, vol. 123, no. 14, pp. 3317–3343, 2022.

RESEARCH ON THE DESIGN AND OPTIMIZATION METHODOLOGY OF MULTI-MODE MULTI-GEAR TRANSMISSION ARCHITECTURE FOR ELECTRIC VEHICLES BASED ON GRAPH THEORY

Yunge Zou [1,3], Yuxin Zhang [2,3], Yantao Si [1]

[1] Chongqing Changan Automobile Co Ltd, Apartment 2nd Room 208, Yonghe Road 39, Yubei District, Chongqing 401133, China, { yunge_zou@cqu.edu.cn, siyt@changan.com.cn }

[2] Chongqing University of Technology, No. 69, Hongguang Avenue, Banan District, Chongqing 40054, China, { yuxin_zhang@stu.cqu.edu.cn }

[3] Chongqing University, No. 174, Shazhengjie, Shapingba District, Chongqing 400044, China. { yunge_zou@cqu.edu.cn, }

1. INTRODUCTION

Compared to conventional single-speed transmissions, multi-gear and multi-mode (MMMG) transmissions improve the efficiency and acceleration performance of electric vehicles (EVs) more effectively. Currently, efforts for EV configurations are mainly focused on optimizing the parameters and energy management control of single motor single gear (SMSG), dual gear (SMDG), and dual motor speed-coupling (DMSC) and torque-coupling (DMTC) transmissions, mainly for electric power consumption. However, from the perspective of powertrain configuration design, there is still a gap in the intrinsic mechanism and configuration design methodology for this type of MMMG-EVs. To address these issues, this study proposes three methods: First, a topology configuration graph theory design method is proposed to design and optimize MMMG-EVs. Second, a novel MMMG-EV powertrain that combines speed and torque coupling is proposed, and the economy, acceleration, and battery life degradation of the above designs are compared. Third, this study proposes a joint MOEA/D and fast dynamic programming (FDP) algorithm to speed up parameter optimization by more than 10,000 times. This study provides a new theoretical approach to accelerating EV powertrain system configuration and parameter calibration.

2. TOPOLOGICAL TREE GRAPH MODELING OF ELECTRIC VEHICLES

The graph theory elements are defined in Table 1. Since trees in nature have obvious logical, hierarchical information, this paper defines each configuration as a tree, and defines the input and output power components as branches, with yellow circles as branch nodes, and the planetary coupling components as leaves, with green circles as leaf nodes. Based on this, this section proposes a novel topological tree graph theory to analyze EV transmissions, primarily encompassing the following aspects: 1) The adjacency matrix exhaustively enumerates configuration patterns such as speed coupling and torque coupling; 2) Dynamical matrix equations for EV transmissions with different coupling types are automatically generated based on the configuration topological tree matrix; 3) Generating comprehensive MMMG-EV designs through the combination of configuration modes.

Table 1. Definition of symbols in graph theory model.

Symbol	Representation of components	Symbol	Representation of components
	Power Components		Internal engagement between the gears
	Planetary gears and vehicle frame		Connection between planetary gears and input/output components
	External engagement between the gears		Components sharing a rotational center (R, H and S)
	Single joint rotary		Components connected by a clutch
	Components connected by a Synchronizer		

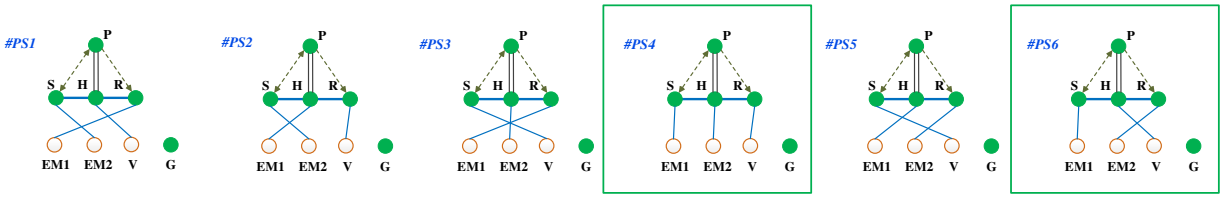

Figure 1. Graph-theoretic model of six power-split EV configurations.

Based on the modeling rules in Table 1, six basic power-split electric vehicle (EV) transmission configurations were modeled as a topological tree diagram using a graph theory model. This model is shown in Figure 1. These configurations are designated as Power Split (#PS1–#PS6). Multiple operating modes that combine the advantages of power split and torque coupling are achieved by adding synchronizers and brakes. Figure 2 shows the three major steps to generate the MMMT-EVs configuration. Step 1: Add a brake to the PG node to reduce one degree of freedom (DOF) and form a torque-coupled mode. There are three possible configurations. Step 2: Add synchronizers to the motor EM ends to enable switching between speed-coupled and torque-coupled modes. Step 3: Apply the above architecture to the basic planetary gear architecture described in Figure 1 (#PS1–#PS6).

In summary, 54 potential MMMT-EV configurations are generated: 3×3×6. Design #29 exhibits superior performance among them.

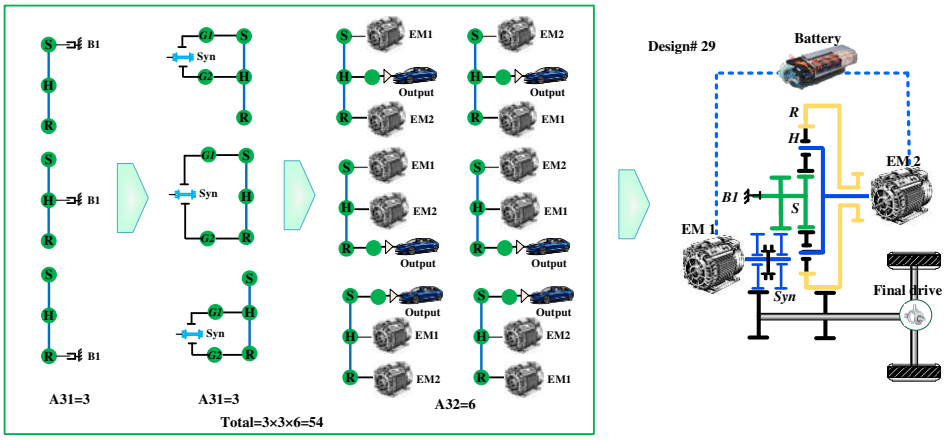

Figure 2. The improved proposed design #29 physical schematic.

3. RESULTS AND DISCUSSION

In order to quantitatively analyze the performance of the above powertrain, in this section, the dynamic programming (DP) algorithm is employed to ascertain the requisite time for acceleration from 0 to 100 km/h. Also, a new fast DP method is proposed to evaluate fuel economy and battery aging simultaneously. They are nested together by a parameter optimization algorithm of MOEA/D. Based on them, the 0-100 km/h acceleration test and the energy efficiency and battery aging performance tests (UDDS, HWFET, and WLTC driving cycles) were conducted. Meanwhile, the computational efficiency and optimality of MOEA/D and FDP are analyzed, and hardware-in-the-loop (HIL) tests are conducted under real operating conditions.

Based on the above tests, Design #29 was determined to offer the best overall performance. Its operating modes, as shown in Figure 3, include the following four modes: EV1 drive, EV2 drive, speed coupling, and torque coupling. Due to the combination of multiple operating modes, it is able to combine the acceleration performance and high-speed efficiency of dual-motor torque coupling (DMTC) with the fuel economy of speed coupling (DMSC), as well as the flexible control of the two single-motor modes. Compared to traditional SMSG systems, it achieves energy savings of 5.6%–8.7%, acceleration that is 42.6% faster, and a reduction in battery degradation of 5.1%–12.3%.

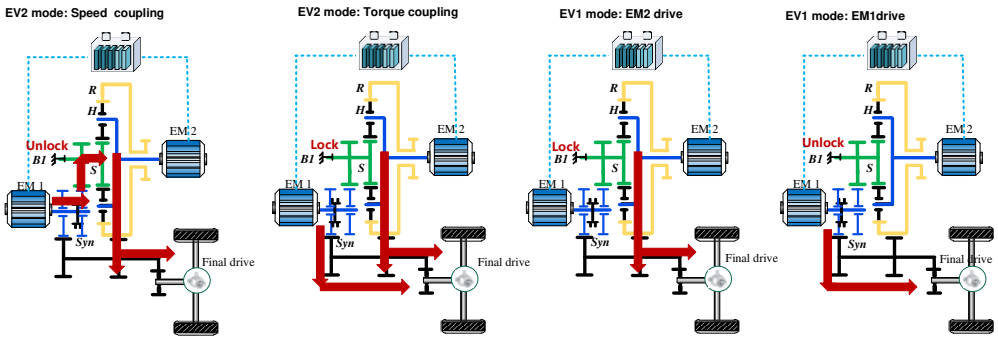

Figure 3. Operating mode power flow for proposed design #29.

4. CONCLUSION

In this study, to systematically explore the performance potential of multi-mode multi-gear (MMMG) electric vehicle powertrains and address the lack of intrinsic mechanism and configuration design methodology, a topology configuration graph theory-based design and multi-objective parameter co-optimization framework is presented. The main conclusions are summarized as follows.

(1) A novel MMMG-EV powertrain (Design # 29) that combines speed and torque coupling is proposed, with 5.6%-8.7% energy savings and 42.6% faster acceleration better than SMSG.

(2) The joint MOEA/D and fast dynamic programming (FDP) algorithm is used to complete the parameter optimization, which speeds up the optimization speed by more than 10,000 times.

REFERENCES

[1] Gao Y, Feng L, Liu D, et al, “Multi-objective co-optimization of powertrain sizing, energy management, and eco-driving for the architectural design of electric vehicles”. Applied Energy, 2025, 398: 126402.

[2] Zou Y, Zhang Y, and Yang Y. "Multi-perspective evaluation of a novel powertrain integrating series-parallel and power-split modes: An ultra-rapid hierarchical control approach." Mechanism and Machine Theory 210, 2025: 106034.

[3] Tian, Yang, et al. "A search method integrating configuration synthesis, screening, and optimization for a dual-planetary gear set four-mode configuration in battery electric vehicles." Mechanism and Machine Theory 211, 2025: 106021.

BIOMECHANICAL ASSESSMENT OF RECLINED OCCUPANT POSTURES IN AUTOMATED VEHICLES USING LS-DYNA SIMULATIONS

Nuno Carmo[1], Ana Martins[1], Marta Carvalho[1,2]

[1] UNIDEMI, Department of Mechanical and Industrial Engineering, NOVA School of Science and Technology Universidade NOVA de Lisboa, 2829-516 Caparica, Portugal, {nm.carmo@campus.fct.unl.pt; apc.martins@campus.fct.unl.pt}
[2] LASI, Laboratório Associado de Sistemas Inteligentes, 4800-058 Guimarães, Portugal {mip.carvalho@fct.unl.pt}

1 INTRODUCTION

Automated mobility allows occupants to adopt reclined seating, yet current crashworthiness regulations still rely on traditional upright positions. This discrepancy raises serious safety concerns, as reclining alters pelvic orientation, seatbelt routing, and load transfer during impacts. Such changes can compromise restraint effectiveness and lead to more severe injury patterns in frontal collisions. To address this, this work provides a numerical investigation into occupant kinematics and the sensitivity of injury criteria relative to seatback angles, aiming to improve passive safety standards for future autonomous vehicles.

2 METHODOLOGY

Crash simulations were performed using the explicit finite element solver LS-DYNA. A vehicle interior and restraint configuration was developed, comprising a seat structure with variable seatback inclination and a three-point seatbelt system with defined anchorage geometry and contact interactions.

The occupant was modeled using a Hybrid III 50th percentile anthropomorphic test device (ATD) [1]. The airbag system was intentionally excluded to isolate belt–occupant interaction mechanisms and to enable a clearer assessment of load transfer characteristics.

Six seatback inclination angles were evaluated: $0°, -10°, -20°, -30°, -40°, -50°$. For each configuration, a prescribed frontal crash pulse was applied. The analysis included standard injury criteria, namely the Head Injury Criterion (HIC), Neck Injury Criterion (Nij), Chest Severity Index (CSI), thoracic deflection, Viscous Criterion (VC), and Tibia Index (TI). Additionally, segmental accelerations, forces, bending moments, pelvis displacement, torso rotation, and head excursion were examined to characterize both global and local kinematic responses.

3 RESULTS AND DISCUSSION

The simulations demonstrate that seatback reclination significantly influences occupant kinematics and restraint system interaction. For upright and moderately reclined configurations (up to $-20°$), the lap belt remained effectively engaged with the pelvic structure, ensuring appropriate load transfer through the iliac crests. Although minor variations in torso pitch and head excursion were observed, the global kinematic response and restraint performance remained consistent with conventional seating conditions.

A distinct transition in kinematic behavior was identified from $-30°$ onward. Increased seatback reclination promoted forward and downward rotation of the pelvis relative to the seat cushion, resulting in partial or complete submarining beneath the lap belt. This altered the intended load path by reducing effective pelvic engagement and promoting belt migration toward the abdominal region. Consequently, torso rotation patterns, belt loading distribution, and thoraco-abdominal interaction were substantially modified.

As illustrated in Fig. 1, submarining was consistently identified for inclinations equal to or greater than $-30°$, whereas no such behavior was observed up to $-20°$. This establishes a clear correlation between seatback reclination and the propensity for submarining under frontal impact conditions.

The identification of submarining was based on detailed kinematic analysis, including forward and downward pelvic rotation, upward migration of the lap belt above the anterior superior iliac spine region, and anterior translation of the hip sliding beneath the belt webbing, in agreement with the mechanisms described in [2].

Despite the pronounced kinematic alterations associated with submarining, the evaluated biomechanical injury criteria did not exhibit systematic exceedance of regulatory thresholds in the affected configurations. Most global metrics, including HIC, Nij, and thoracic indices, remained within prescribed limits. Nevertheless, posture-dependent trends were observed, including increased variability in neck loading and modified thoracic response with increasing reclination.

The absence of threshold exceedance does not imply equivalent safety performance. Submarining compromises the

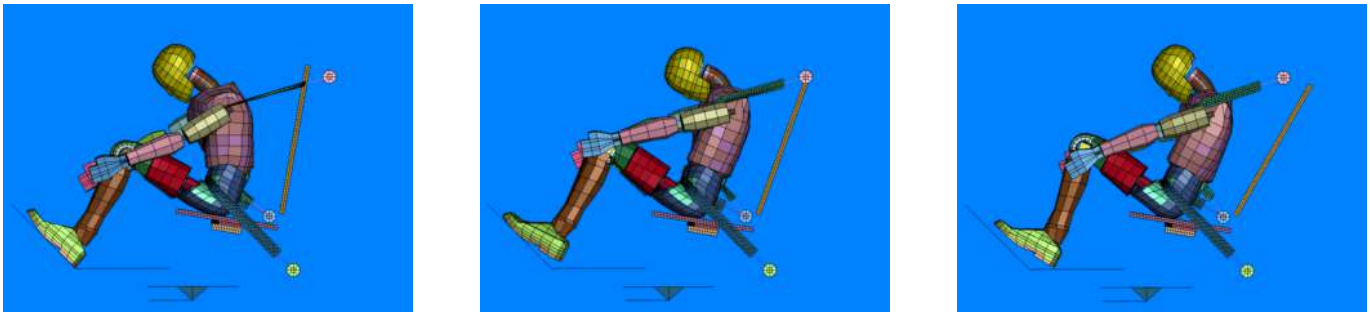

0° – No | -10° – No | -20° – No

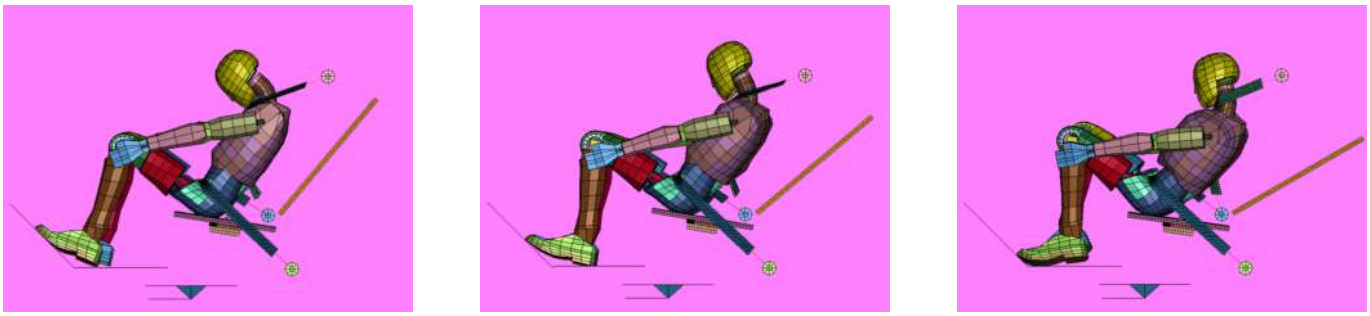

-30° – Yes | -40° – Yes | -50° – Yes

Figure 1: Simulation results for different backrest inclinations (Yes – occurrence of submarining; No – absence). Observations were recorded at approximately 80 ms into the simulation, the point at which submarining becomes most evident.

biomechanical function of the lap belt by reducing load transfer to the pelvic structure and increasing abdominal belt interaction, thereby elevating the risk of soft tissue and internal injuries that may not be fully captured by conventional injury criteria. Similar conclusions with the THUMS human body model are reported in [3].
Overall, the results demonstrate that initial occupant posture is a decisive parameter in crash biomechanics. Seatback reclination alters the geometric and mechanical relationship between the pelvis, torso, and restraint system, directly influencing load paths and energy absorption mechanisms. These findings suggest that compliance with existing regulatory criteria under nominal seating assumptions may not guarantee equivalent protection in automated vehicle interiors with reclined configurations.

4 CONCLUSIONS

This study provides a quantitative assessment of the biomechanical response of reclined occupants during frontal impacts using numerical simulations. Seatback reclination significantly alters occupant kinematics, with submarining emerging from $-30°$ onward as a dominant failure mechanism compromising lap belt effectiveness.
Although traditional injury criteria may remain within regulatory limits, posture-induced modifications in load transfer mechanisms highlight the need for posture-sensitive safety assessment approaches. These results support the reassessment of passive safety methodologies in the context of automated vehicles, where non-conventional seating configurations are expected to become increasingly prevalent.

ACKNOWLEDGMENTS

The authors acknowledge Fundação para a Ciência e a Tecnologia I.P. for its financial support via the project UID/00667: Unidade de Investigação e Desenvolvimento em Engenharia Mecânica e Industrial.

REFERENCES

[1] S. Guha, D. Bhalsod and J. Krebs. LSTC Hybrid III 50th Fast Dummy: Positioning & Post Processing. Dummy Version: LSTC.H3_50TH_FAST.111130_V2.0, Documentation Date: November 30, 2011. LSTC Michigan. 2011

[2] K. Rawska, B. Gepner, D. Moreau, and J. R. Kerrigan, J. R. "Submarining sensitivity across varied seat configurations in autonomous driving system environment". *Traffic injury prevention*, vol. 21, sup1, S1-S6, 2020.

[3] X. Yang, Q. Wang, Y. Liu, J. Fei, P. Wang, Z. Li, Z. Bai. Comprehensive injury assessment of reclined occupant across varied seat configurations with the THUMS human body model. Technical report, SAE Technical Paper, 2025.

Book of Abstracts of MMT Symposium
Mechanism and Machine Theory Symposium
Flores et al. (Eds)

MMT Symposium
60th Anniversary of Mechanism and Machine Theory
June 21-23, 2026 Porto, Portugal

ACCURATE REAL CONTACT AREA COMPUTATION OF ANISOTROPIC ROUGH SURFACES

Mattin Maiztegui[1], Jon Larrañaga[1], Ibai Ulacia[1]

[1] Mondragon Unibertsitatea, Loramendi 4, Arrasate-Mondragon, Spain,
{mmaiztegui@mondragon.edu; jlarranaga@mondragon.edu; iulacia@mondragon.edu}

1 INTRODUCTION

The accurate computation of the real contact area A_R is essential for tribological applications, governing friction, wear, and thermal phenomena. While numerical simulations are effective, high-resolution grids are computationally expensive. Most numerical studies in the literature focus on Gaussian surfaces, for which effective real contact area correction methods have been developed [1] to use on low-resolution grids. However, real machinery component surfaces rarely present purely Gaussian characteristics, as machined profiles tend to exhibit highly directional features with high anisotropy. This work addresses the gap in the current literature by proposing a correction methodology tailored for anisotropic, machined-like rough surfaces, developed based on Boundary Element Method (BEM) simulations.

2 ANISOTROPIC SURFACE ROUGHNESS

Machined surfaces usually present linear grooves along the machining direction with smaller-scale undulations along their length. While regular numerical roughness generation focuses on Gaussian profiles, techniques for generating machined-like surface roughness exist [2]. In this work, anisotropic profiles are generated via the geometric modification and combination of two isotropic surfaces constructed using distinct spectral parameters for the longitudinal (x) and transversal (y) directions. The generation parameters include low and high cutoff frequencies of $q_{l,x} = 2$, $q_{h,x} = 32$, $q_{l,y} = 8$, and $q_{h,y} = 32$. Hurst exponents (H) and RMS amplitudes (h_{rms}) are varied to create a broad dataset: H_x and H_y range from 0.3 to 0.7, while $h_{rms,x}$ ranges from 0.5 to 2.5×10^{-4} and $h_{rms,y}$ from 3.0 to 5.0×10^{-4}. The resulting surface profiles are highly anisotropic, with their PSD spectrum analysis showing a low Texture Aspect Ratio $S_{tr} < 0.1$ and high Anisotropy Index $AI > 0.9$. All surface profiles are generated with a discretization of $n = 12$ (2^{12}) points per side, significantly higher than any contact model considered, ensuring accurate down-sampling.

3 REAL CONTACT AREA CORRECTION METHOD

The proposed correction method relies on the observation that, unlike Gaussian surface contact areas, which tend toward circular profiles [1], linear roughness profile contact areas tend toward lines as shown in Fig. 1 for various mesh discretization configurations.

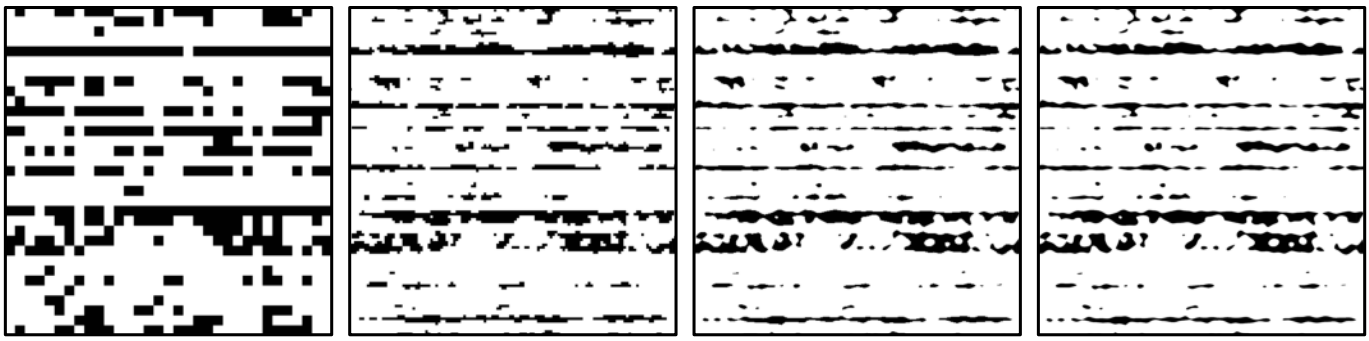

(a) (b) (c) (d)

Figure 1: Contact area evolution with refined discretization: (a) $n = 5$; (b) $n = 7$; (c) $n = 9$; (d) $n = 11$.

As discretization is refined, the contact lines maintain their length but drastically reduce in transversal thickness. Based on this observation, an assumption is made: interior elements, those fully surrounded by others, constitute the "bulk" area and remain fully engaged. Conversely, exterior boundary elements are only partially engaged, exhibiting distinct area reduction behaviors along their horizontal and vertical edges.

To implement this correction, the perimeter edges in the horizontal ($N_{side,H}$) and vertical ($N_{side,V}$) directions are counted separately. The corrected real contact area, $A_{R,corr}$, is then calculated by subtracting a weighted fraction of these boundary elements from the initial detected area, as formulated in Eq. (1):

$$A_{R,corr} = A_E \cdot (N_T - N_{side,H} \cdot C_H - N_{side,V} \cdot C_V) \tag{1}$$

where A_E is the area of a single element, N_T is the total count of contact elements, with C_H and C_V being the reduction coefficients for horizontal and vertical edges, respectively. The selected discretization range for coefficient computation and validation is $n = \{5, 6, 7, 8, 9, 10, 11\}$, constituting square grids of 2^n points per side. Computation of C_H and C_V is performed using a genetic algorithm to minimize the total global error relative to the $n = 11$ reference, based on 625 surface parameter combinations and 10 applied normal loads per case, obtaining 5,846 data points per discretization group after discarding non-converging cases.

4 RESULTS

Initial attempts using all discretizations show that lower-fidelity models ($n = 5, 6$) limit the improvement of higher discretization models due to their inability to replicate high-frequency contact features originating in the profile generation and combination process, predicting a different contact area morphology (see Fig. 1). Applying the Nyquist-Shannon sampling theorem, mesh discretizations are restricted to $n \geq 7$ based on the highest frequency present in the surface generation ($q_h = 32$).

Real contact area fraction results obtained for the raw data, Gaussian correction [1], and the proposed correction are shown in Fig. 2. The root mean square area error on coarse meshes ($n = 7$) over the $n = 11$ reference is 19.04% for raw data. Applying the Gaussian correction formulation reduces this to 5.89%, while the proposed correction method lowers the error further to 2.05%. Similarly, the error for fine discretization meshes ($n = 10$) is reduced from a raw 1.18% to 0.21% with the proposed correction, while the Gaussian formulation achieves a higher 0.70% error. The results indicate that the real linear contact area marginally grows horizontally but decreases significantly vertically as discretization refines, consistent with the observed thinning of contact lines.

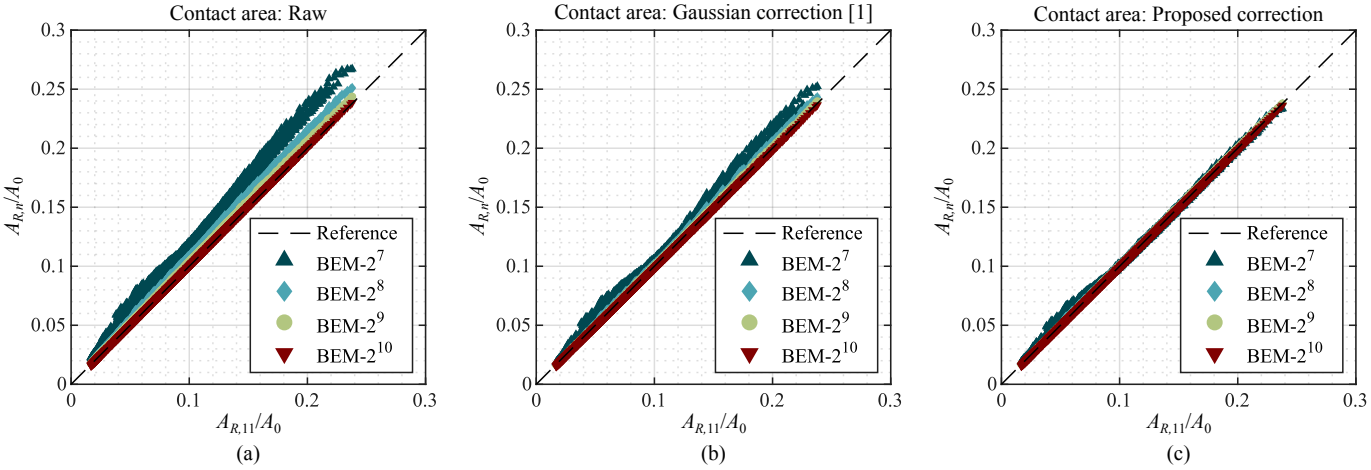

Figure 2: Contact Area Fraction vs. $n = 11$ reference: (a) Raw data; (b) Gaussian correction from [1]; (c) Proposed correction.

5 CONCLUSIONS

The proposed method effectively corrects real contact area calculations for anisotropic, machined-like surfaces. While the employed profile generation method forces the discretization to be at least double the original surface frequencies to correctly represent contact topology, the formulation allows for accurate A_R computation without requiring extremely fine meshes. This offers significant computational benefits for tribological simulations of machined components.

ACKNOWLEDGMENTS

The authors acknowledge financial support from the Basque Government under grant PREDOC 2025-2026.

REFERENCES

[1] V. A. Yastrebov, G. Anciaux, and J. F. Molinari, "On the accurate computation of the true contact-area in mechanical contact of random rough surfaces". *Tribology International*, vol. 114, pp. 161–171, 2017.

[2] M. Maiztegui, J. Larrañaga, I. Ulacia, J.F. Molinari, "An efficient 3D finite element implementation for frictionless elliptical contact analysis in layered rough surfaces". *Tribology International*, vol. 217, pp. 111602, 2026.

STUDY OF PLANET PHASING INFLUENCE ON THE EFFICIENCY OF A PLANETARY GEAR

J. Moncalian-Cruz[1], M. Iglesias[1], J. Sanchez-Espiga[1], A. Diez- Ibarbia[1], A. Fernandez-del-Rincon[1], F. Viadero[1]

[1] Structural and Mechanical Engineering Department, University of Cantabria. Avda, Los Castros s/n, 39005, Santander, Spain, moncalianja@unican.es

1. INTRODUCTION

Wind energy has become one of the pillars to achieve a global transition towards sustainable power generation [1]. Modern wind turbines operate under high-demanding mechanical conditions, where large amounts of instantaneous power must be efficiently converted into electrical energy. To achieve the required speed increase between the slow-rotating rotor and the high-speed generator, multi-stage gearboxes are commonly employed, with planetary gear trains forming the core of the transmission system [2]. The first stage of the epicyclic train is crucial due to the fact that is subjected to extremely high torques and must withstand enormous loads while ensuring reliable operation over long service life [3]. Given the significant levels of power transmitted in multi-megawatt turbines, even small efficiency losses at this stage can result into substantial energy losses over time.

For this reason, the efficiency of epicyclic gear systems is not merely a secondary design parameter, but a critical factor in the overall performance, durability, and economic/sustainable viability of wind turbines. In the first planetary stage —where the highest torques are transmitted— the dominant source of power loss is typically sliding friction between gear tooth flanks [4]. Under such heavy loading conditions, the combination of high contact forces and relative sliding velocities intensifies frictional energy dissipation, making them significantly more relevant than other dissipative phenomena. These sliding power losses not only reduce the mechanical efficiency of the drivetrain, but also increase heat generation, influencing lubrication regimes, surface integrity, and long-term reliability.

2. METHODOLOGY

The procedure to study power losses and efficiency (η) is based on a numeric model developed by the A. Fernández del Rincon, M. Iglesias, A. Diez Ibarbia and J. Sanchez Espiga [5]. This planetary-gear transmission numeric model simulates the global deflections in each tooth, which stands a linear relation between deformation and load, as well as the local effect, which affects the contact surface, introduced with the non-linear formulation developed by Weber and Banaschek [6]. This approach requires of an iterative procedure to determine the load sharing, while also granting it a bigger accuracy [7].

Here lies one of the strong points of the model, as the load calculation is necessary in order to obtain satisfactory results regarding the power losses due to sliding friction. Another parameter which is directly proportional to these losses is the sliding relative speed between the point of each tooth which is contacting in every moment. This is a purely geometrical value and consequently, will not be further addressed. The third factor on which this study relies is the friction coefficient, which in this case is formulated as a constant value that depends on the geometry of the gears, as well as torque and sliding velocity.

3. CASE OF STUDY

The study will be done for 3-planet 10 MW gear trains with an input speed in the carrier of 15 rpm. After this, equivalent configurations will be studied, in terms of planet dimensioning. This means that for configurations with more than 3 planets the tangential force on each of them will be the same, meaning an escalation in the power and consequently, on the input torque. As it stands, the input power will be 10-13.33-16.67-20 MW for 3-4-5-6 planets, respectively. The configurations studied are shown in Table 1, and are designed to withstand these tangential loads in the planet.

The sequence of mesh phasing is the parameter that must be used as a comparation. Every considered configuration is Equally Spaced (ES) and when there are simultaneous contacts (In Phase - IP) in every planet produce a constant load sharing, while a consecutive mesh phasing produces a retard between the N plane, which translates to a gap in the load sharing with T/N period [8]. It can be noted that all Sequentially Phased (SP) configurations are consecutive for the sake of comparation.

Table 1. Sets of gears studied and configuration for each number of planets.

Set of gears			Number of planets			
Z_R	Z_S	Z_P	3	4	5	6
84	36	23	ESIP	ESIP	ESSP (Cons.)	ESIP
85	35	24	ESSP (Cons.)	ESSP (Cons.)	ESIP	ESSP (Cons.)

4. RESULTS

The efficiency results presented below correspond to the study of the Equally Spaced-In Phase (ESIP) configuration and the ESSP configuration from 3 to 6 planets. Specifically, the mean (η_{mean}), minimum (η_{min}) and maximum (η_{max}) efficiency for both kinds of configurations are presented in Table *2* and, as example, the instantaneous efficiency along one sun meshing cycle is shown in Figure 1.

Table 2. Mean, minimum and maximum efficiency in the ESIP configuration from 3 to 6 planets (left) and difference for the efficiency values of ESSP with respect to ESIP configurations (right).

	ESIP				ESSP			
Nº of planets	**3**	**4**	**5**	**6**	**3**	**4**	**5**	**6**
η_{mean}	99.35555	99.35555	99.37594	99.3555	0.00763	0.00826	-0.02008	0.00775
η_{min}	98.99539	98.99539	99.04305	98.99539	0.35632	0.32679	0.29509	0.36322
η_{max}	99.73915	99.73915	99.71052	99.73915	-0.35881	0.33337	-0.33642	-0.36630

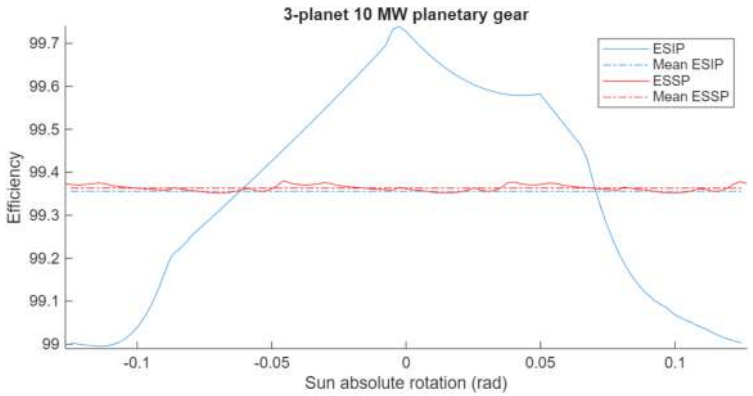

Figure 1. Instantaneous and mean efficiency for ESIP and ESSP configurations.

5. CONCLUSIONS

While an ESIP and ESSP configuration have an almost equal mean efficiency, the range of values differs. An ESSP configuration presents a more stable value por instantaneous power losses due to the cyclical effect, while the ESIP shows a 0.7% difference between the maximum and the minimum. Another insight for the analyzed transmissions is that the influence of the number of planets on the mean efficiency is almost negligible in the ESIP configuration as well as in the consecutive-ESSP configurations.

ACKNOWLEDGMENTS

This work is part of the project PID2023-147249OB-I00 funded by MICIU/AEI /10.13039/501100011033 and by FEDER, EU.

REFERENCES

[1] X. Liang, "Emerging Power Quality Challenges Due to Integration of Renewable Energy Sources," *IEEE Trans. Ind. Appl.*, vol. 53, no. 2, pp. 855–866, Mar. 2017, doi: 10.1109/TIA.2016.2626253.

[2] T. Wang, Q. Han, F. Chu, and Z. Feng, "Vibration based condition monitoring and fault diagnosis of wind turbine planetary gearbox: A review," Jul. 01, 2019, *Academic Press*. doi: 10.1016/j.ymssp.2019.02.051.

[3] W. Dong, Y. Xing, T. Moan, and Z. Gao, "Time domain-based gear contact fatigue analysis of a wind turbine drivetrain under dynamic conditions," *Int. J. Fatigue*, vol. 48, pp. 133–146, 2013, doi: 10.1016/j.ijfatigue.2012.10.011.

[4] Hu Y., Talbot D., and Kahraman A., "A load distribution model for planetary gear sets," *Journal of Mechanical Design*, 2018.

[5] J. Sanchez-Espiga, A. Fernandez-del-Rincon, M. Iglesias, and F. Viadero, "Influence of errors in planetary transmissions load sharing under different mesh phasing," *Mech. Mach. Theory*, vol. 153, Nov. 2020, doi: 10.1016/j.mechmachtheory.2020.104012.

[6] K. Weber and C. Banashek, "The deformation of loaded gears and the effect on their load carrying capacity," London, 1951.

[7] A. Diez-Ibarbia, A. Fernandez-Del-Rincon, P. Garcia, A. De-Juan, M. Iglesias, and F. Viadero, "Assessment of load dependent friction coefficients and their influence on spur gears efficiency," *Meccanica*, vol. 53, no. 1–2, pp. 425–445, Jan. 2018, doi: 10.1007/s11012-017-0736-8.

[8] M. Iglesias, A. Fernandez del Rincon, A. de-Juan, P. Garcia, A. Diez-Ibarbia, and F. Viadero, "Planetary transmission load sharing: Manufacturing errors and system configuration study," *Mech. Mach. Theory*, vol. 111, pp. 21–38, May 2017, doi: 10.1016/j.mechmachtheory.2016.12.010.

SYNTHESIS AND STRUCTURAL CHARACTERIZATION OF NANOSTRUCTURED TITANIUM DIOXIDE VIA SOL-GEL FOR MEMRISTIVE CO SENSING IN AEROSPACE APPLICATIONS

Jorge Luis Cervantes Fraustro[1], Georgina García Pacheco[1], Jacobo Esteban Munguía Cervantes[2], Gerardo Villa Martínez[1]

[1] Instituto Politécnico Nacional, Escuela Superior de Ingeniería Mecánica y Eléctrica Unidad Ticomán, Calz. Ticomán 600, La Purísima Ticomán, 07340, Mexico City, Mexico, {jcervantesf1800@alumno.ipn.mx; ggarciap@ipn.mx; gvillam@ipn.mx}

[2] Instituto Politécnico Nacional, Centro de Nanociencias y Micro y Nanotecnologias (CNMN), Luis Enrique Erro s/n, Unidad Profesional Adolfo López Mateos, Zacatenco, 07738, Mexico City, Mexico, {jmungia@ipn.mx}

1. INTRODUCTION

Aircraft operations contribute significantly to air pollution near airports due to the emission of pollutants such as carbon monoxide (CO), a product of incomplete fuel combustion [1, 3]. CO is a potentially lethal gas that requires continuous monito ring to prevent harm to human health and the environment [2]. Metal-oxide semiconductors (MOS), particularly titanium dioxide (TiO_2), offer a promising future for gas sensing due to their chemical stability, non-toxicity, and low cost [5]. Among its crystalline phases, anatase is the most suitable for gas detection due to its open tetragonal structure, which provides high surface area and enhanced reactivity with gas molecules [6].

The memristor, a resistive switching device, offers non-volatile memory and sensitivity to chemical species, making it an ideal transducer for gas sensing applications [7]. A memristor based on a TiO_2/TiO_{2-x} heterostructure changes its resistance accord ing to the direction and magnitude of the applied voltage, due to the motion of oxygen vacancies. This principle can be exploited to detect reducing gases such as CO, which interact with the oxide surface and modulate the charge carrier concentration [4].

This work focuses on the synthesis and structural characterization of anatase-phase TiO_2 nanoparticles via the sol-gel method, aiming to develop a memristive device for CO detection in aerospace environments. The sol-gel technique is chosen for its simplicity, low cost, and ability to control particle size and phase purity through parameters such as pH, solvent type, and thermal treatment [5].

2. METHODOLOGY

Titanium dioxide nanoparticles were synthesized via the sol-gel method using titanium (IV) isopropoxide (TTIP, 97% purity) as the precursor and deionized water as the solvent. The hydrolysis reaction proceeds via nucleophilic substitution, forming tit anium tetrahydroxide ($Ti(OH)_4$) and isopropanol as a byproduct. The solution was maintained under constant stirring at 90°C for 12 hours to promote gel formation and solvent evaporation. The resulting dry powder was mechanically ground and subsequently subjected to thermal treatment at 500°C for 3 hours to induce crystallization and remove organic residues. This temperature was selected to favor the anatase phase while avoiding transformation to the rutile phase.

Structural characterization was performed by X-ray diffraction (XRD) using a Bruker D8 Advance Eco diffractometer operated at 40 kV and 25 mA with Cu Kα radiation (λ = 1.5406 Å). Diffractograms were recorded over a 2θ range of 10° to 100° with a step size of 0.02° and a counting time of 1 s per step. Phase identification was carried out using QualX software and reference crystallographic cards.

Morphological analysis was conducted by scanning electron microscopy (SEM) using a Jeol JSM-IT200 microscope at an accelerating voltage of 20 kV. Samples were prepared by dispersing the powder on carbon tape and coated with a thin gold layer to avoid charging. Particle size distribution was analyzed using Fiji software.

3. RESULTS AND DISCUSSION

X-ray diffraction analysis confirmed the formation of TiO_2 with a predominant anatase phase. The diffraction pattern (Figure 1) exhibited characteristic peaks at 25.68° (101), 37.52° (103), 38.39° (004), 48.22° (200), and 54.34° (105), which match the reference crystallographic cards [00-101-0942] and [00-152-6931] for tetragonal anatase. However, additional peaks corresponding to the brookite phase were identified, particularly around 30.7° and 43.5°, attributed to the rapid, uncontrolled hydrolysis rate when using only deionized water as solvent. This fast kinetics favors the formation of brookite during calcination. Peak broadening indicated a nanometric crystallite size. The presence of both phases suggests that synthesis conditions need optimization to obtain pure anatase.

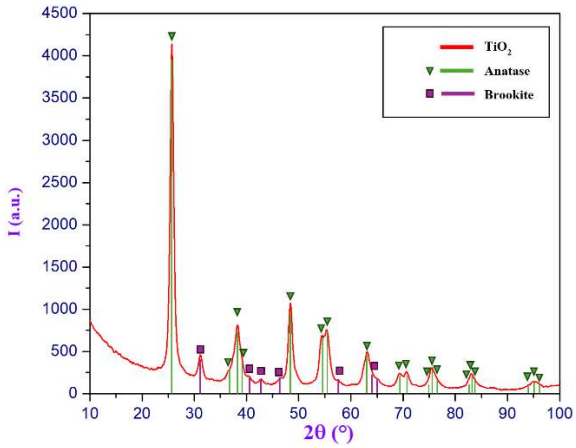

Figure 1. XRD pattern of TiO_2 nanoparticles synthesized by sol-gel method, showing characteristic and brookite secondary phases.

Scanning electron microscopy (Figure 2) revealed nodular nanoparticles with sizes ranging from 45 to 180 nm. The particles exhibit a relatively broad size distribution, typical of sol-gel synthesis without strict pH control. The nanometric scale is suitable for high-surface-area gas adsorption, as the sensing mechanism in metal-oxide sensors relies on surface interactions between the oxide layer and reducing gases such as CO [4]. The presence of agglomerates is also observed, which can be reduced by optimizing the dispersion and washing steps.

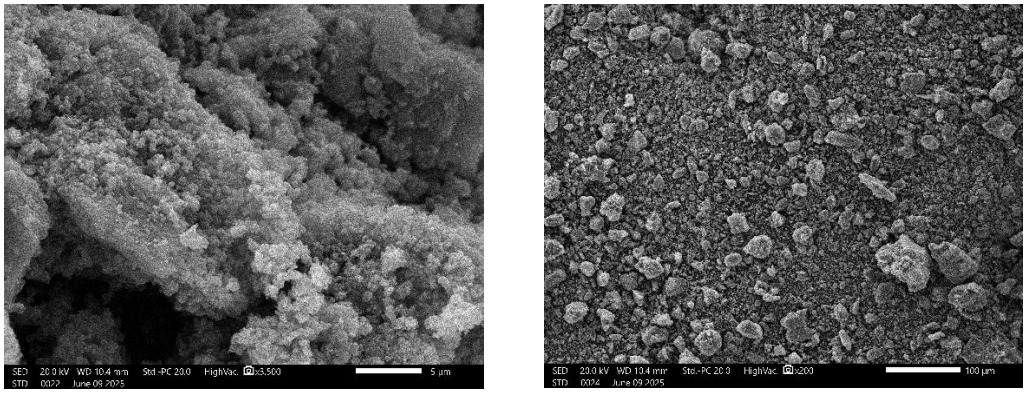

Figure 2. SEM micrographs of TiO_2 nanoparticles synthesized by sol-gel method, revealing nodular morphology with particle sizes ranging from 45 to 180 nm.

4. CONCLUSION

The controlled synthesis of nanostructured anatase TiO_2 via the sol-gel method was successfully achieved. XRD analysis confirmed the formation of the anatase phase, although the presence of brookite indicates the need for stricter control of the hydrolysis kinetics. Future syntheses will employ an isopropanol-deionized water medium to moderate the reaction rate and suppress secondary phases. SEM micrographs confirmed particle sizes within the nanometric range (45–180 nm), providing the high surface area essential for gas sensing performance. These nanoparticles will serve as the foundation for fabricating memristive devices with a TiO_{2-x}/TiO_2 heterostructure, targeting carbon monoxide detection in aerospace cabin air quality monitoring systems [3].

ACKNOWLEDGMENTS

The authors acknowledge the financial and technical support from the Instituto Politécnico Nacional (IPN) through the Secretaría de Investigación y Posgrado (SEPI), as well as the use of laboratory facilities at the Centro de Nanociencias y Micro y Nanotecnologías (CNMN) of the IPN.

REFERENCES

[1] R. Miake-Lye, et al., "White paper on air quality: aviation impacts on air quality", *International Civil Aviation Organization*, 2016.
[2] J. H., "Carbon monoxide: the invisible killer", *The Journal of the Royal Society for the Promotion of Health*, 118(3), 1998.
[3] S. Ramanavicius, A. Jagminas, and A. Ramanavicius, "Gas sensors based on titanium oxides", *Coatings*, 12(5), 699, 2022.
[4] H. Ji, W. Zeng, and Y. Li, "Gas sensing mechanisms of metal oxide semiconductors: a focus review", *Nanoscale*, 11(47), 22664-22684, 2019.
[5] W. Selmi, N. Hosni, J.B. Naceur, H. Maghraoui-Meherzi, and R. Chtourou, "Titanium dioxide thin films for environmental applications", *Titanium Dioxide-Advances and Applications*, 2022.

EQUIVALENT TRANSFORMATIONS OF MSA- AND VJM-BASED STIFFNESS MODELS

Alexandr Klimchik[1], Anatol Pashkevich[2]

[1] University of Lincoln, Brayford Pool, Lincoln, LN6 7TS, UK, aklimchik@lincoln.ac.uk

[2] IMT Atlantique, 4 Rue Alfred-Kastler, Nantes, 44307, France, anatol.pashkecich@imt-atlantique.fr

1. INTRODUCTION

In robotics, Virtual Joint Modelling (VJM) and Matrix Structural Analysis (MSA) are two main methods for stiffness modelling [1, 2]. Both methods can integrate sophisticated 6-DOF virtual springs that describe the mechanical properties of the corresponding components [3, 4]. However, they use different model components, making it difficult to integrate components from one method into another. In particular, in the VJM method, the basic component is represented by a 6x6 stiffness matrix, whereas in the MSA, the same components are represented by a rank-deficient 12x12 matrix. Another fundamental difference between the two methods is the coordinate frame in which the model components are represented. The VJM approach uses stiffness matrices in the local coordinate frames, and all rotations are handled by the corresponding Jacobian matrices. In contrast, in the MSA method, stiffness properties are described in the global coordinate frame, and all model components must be rotated before being used in the global model. In this work, we are going to reveal the relation between the key model components of VJM and MSA methods, which will make it possible to combine the advantages of both techniques in the stiffness modelling for complex robotic structures.

2. STIFFNESS MODEL OF AN ELASTIC LINK IN VJM AND MSA

In the frame of the VJM, the stiffness model for a link (see Fig. 1) is represented by the following force-deflection relation $\mathbf{W} = \mathbf{J}_\theta^{-\mathrm{T}} \mathbf{K}^{(link)} \mathbf{J}_\theta^{-1} \Delta\mathbf{t}$, where $\mathbf{K}^{(link)}$ is 6×6 stiffness matrix describes link stiffness properties in the local coordinate frame, $\mathbf{J}_\theta$ is the corresponding Javobian matrix. In the frame of the MSA, the same link stiffness is described by 12×12 stiffness matrix and the force deflection relation relating the 6-dimensional wrenches $(\mathbf{W}_u, \mathbf{W}_v)$ applied to the nodes *u*, *v* and the corresponding displacements $(\Delta\mathbf{t}_u, \Delta\mathbf{t}_v)$. has the form

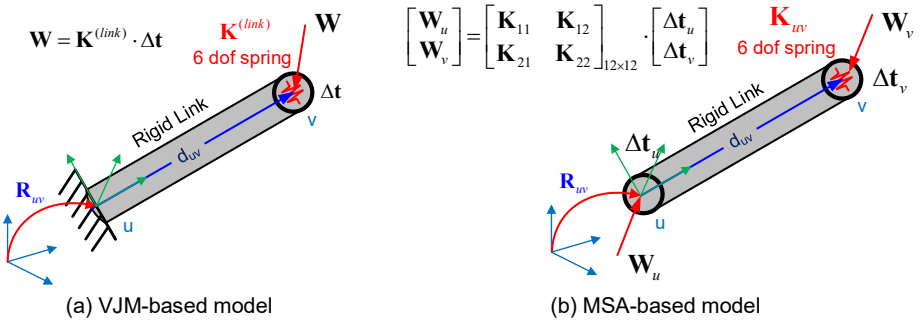

Figure 2. Stiffness models of VJM and MSA flexible links

$$\begin{bmatrix}\mathbf{W}_u\\ \mathbf{W}_v\end{bmatrix} = \begin{bmatrix}\mathbf{K}_{11} & \mathbf{K}_{12}\\ \mathbf{K}_{21} & \mathbf{K}_{22}\end{bmatrix}_{12\times12} \cdot \begin{bmatrix}\Delta\mathbf{t}_u\\ \Delta\mathbf{t}_v\end{bmatrix} \tag{1}$$

It is clear that the matrices $\mathbf{K}_{11}, \mathbf{K}_{12}, \mathbf{K}_{21}, \mathbf{K}_{22}$ describe the same physical properties and can be expressed via the stiffness matrix $\mathbf{K}^{(link)}$ and link geometry vector $\mathbf{d}_{uv}$ [3, 5] yielding the following expression

$$\begin{bmatrix}\mathbf{W}_u\\ \mathbf{W}_v\end{bmatrix} = \begin{bmatrix}\mathbf{D}_{uv}^T\mathbf{K}_{uv}\mathbf{D}_{uv} & -\mathbf{D}_{uv}^T\mathbf{K}_{uv}\\ -\mathbf{K}_{uv}\mathbf{D}_{uv} & \mathbf{K}_{uv}\end{bmatrix}_{12\times12} \cdot \begin{bmatrix}\Delta\mathbf{t}_u\\ \Delta\mathbf{t}_v\end{bmatrix}, \qquad \text{with} \quad \mathbf{D}_{uv} = \begin{bmatrix}\mathbf{I}_{3\times3} & -(\mathbf{d}_{uv}\times)\\ \mathbf{0}_{3\times3} & \mathbf{I}_{3\times3}\end{bmatrix}_{6\times6} \tag{2}$$

which includes 6×6 geometric transformation matrix $\mathbf{D}_{uv}$ with a 3×3 skew-symmetric matrix $(\mathbf{d}_{uv}\times)$ derived from the vector $\mathbf{d}_{uv}$ and the stiffness matrix $\mathbf{K}_{uv}$ expressed in the global coordinate frame, which can be computed from $\mathbf{K}^{(link)}$ as $\mathbf{K}_{uv} = \mathbf{Q}_{uv}\mathbf{K}^{(link)}\mathbf{Q}_{uv}^T$ with $\mathbf{Q}_{uv} = diag(\mathbf{R}_{uv}, \mathbf{R}_{uv})$, where the matrix $\mathbf{R}_{uv}$ describes the link orientation.

$$\begin{bmatrix}\mathbf{W}_u\\ \mathbf{W}_v\end{bmatrix} = \begin{bmatrix}\mathbf{D}_{uv}^T\mathbf{Q}_{uv}\mathbf{K}^{(link)}\mathbf{Q}_{uv}^T\mathbf{D}_{uv} & -\mathbf{D}_{uv}^T\mathbf{Q}_{uv}\mathbf{K}^{(link)}\mathbf{Q}_{uv}^T\\ -\mathbf{Q}_{uv}\mathbf{K}^{(link)}\mathbf{Q}_{uv}^T\mathbf{D}_{uv} & \mathbf{Q}_{uv}\mathbf{K}^{(link)}\mathbf{Q}_{uv}^T\end{bmatrix}_{12\times12} \cdot \begin{bmatrix}\Delta\mathbf{t}_u\\ \Delta\mathbf{t}_v\end{bmatrix} \tag{3}$$

Hence, for a single link with the spring located at the end of the link, after equating corresponding components in the VJM and MSA stiffness models, one can get $\mathbf{J}_\theta^{-1} = \mathbf{Q}_{uv}^T$, leading to. $\mathbf{J}_\theta = \mathbf{Q}_{uv}$.

3. STIFFNESS MODEL OF MECHANICAL STRUCTURE

To demonstrate the transformation between the VJM and MSA models, let us consider a star-type structure that is centrally symmetric and composed of identical beams (see Fig. 2) and derive force-deflection relations between the nodes of the structure. Here, we will assume that the stiffness of each link is described by 6×6 stiffness matrix $\mathbf{K}^{(link)}$.

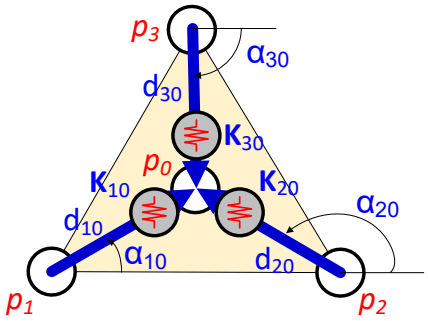

Figure 1. Stiffness model for the Y-type structure.

According to the VJM technique, the stiffness matrices between the nodes p_1 p_2 and p_3 $\mathbf{K}_{\mathrm{Y}}^{(12)}$, $\mathbf{K}_{\mathrm{Y}}^{(23)}$ and $\mathbf{K}_{\mathrm{Y}}^{(31)}$ are computed through the serial connection of two virtual springs, which yields

$$\begin{aligned}
\mathbf{K}_{\mathrm{Y}}^{(12)} &= \mathbf{J}_{10}^{(2)}\cdot\mathbf{K}^{(link)}\cdot\mathbf{J}_{10}^{(2)T} + \mathbf{J}_{20}^{(2)}\cdot\mathbf{K}^{(link)}\cdot\mathbf{J}_{20}^{(2)T}\\
\mathbf{K}_{\mathrm{Y}}^{(23)} &= \mathbf{J}_{20}^{(3)}\cdot\mathbf{K}^{(link)}\cdot\mathbf{J}_{20}^{(3)T} + \mathbf{J}_{30}^{(3)}\cdot\mathbf{K}^{(link)}\cdot\mathbf{J}_{30}^{(3)T}\\
\mathbf{K}_{\mathrm{Y}}^{(31)} &= \mathbf{J}_{30}^{(1)}\cdot\mathbf{K}^{(link)}\cdot\mathbf{J}_{30}^{(1)T} + \mathbf{J}_{10}^{(1)}\cdot\mathbf{K}^{(link)}\cdot\mathbf{J}_{10}^{(1)T}
\end{aligned} \tag{4}$$

Where the Jacobian matrix $\mathbf{J}_{ij}^{(k)}$ describe the transformation from the virtual spring ij origin (in the local coordinate frame) to the reference node (k). To obtain corresponding properties from the MSA stiffness modelling, we need to consider a full stiffness model for the star-type structure [5]

$$\begin{bmatrix}\mathbf{W}_1\\ \mathbf{W}_2\\ \mathbf{W}_3\\ \mathbf{W}_0\end{bmatrix} = \begin{bmatrix}\mathbf{D}_{10}^T\mathbf{K}_{10}\mathbf{D}_{10} & \mathbf{0}_{6\times6} & \mathbf{0}_{6\times6} & -\mathbf{D}_{10}^T\mathbf{K}_{10}\\ \mathbf{0}_{6\times6} & \mathbf{D}_{20}^T\mathbf{K}_{20}\mathbf{D}_{20} & \mathbf{0}_{6\times6} & -\mathbf{D}_{20}^T\mathbf{K}_{20}\\ \mathbf{0}_{6\times6} & \mathbf{0}_{6\times6} & \mathbf{D}_{30}^T\mathbf{K}_{30}\mathbf{D}_{30} & -\mathbf{D}_{30}^T\mathbf{K}_{30}\\ -\mathbf{K}_{10}\mathbf{D}_{10} & -\mathbf{K}_{20}\mathbf{D}_{20} & -\mathbf{K}_{30}\mathbf{D}_{30} & \mathbf{K}_{10}+\mathbf{K}_{20}+\mathbf{K}_{30}\end{bmatrix}_{24\times24}\cdot\begin{bmatrix}\Delta\mathbf{t}_1\\ \Delta\mathbf{t}_2\\ \Delta\mathbf{t}_3\\ \Delta\mathbf{t}_0\end{bmatrix} \tag{5}$$

And then reduce it down to the reaction between corresponding nodes by means of fixing one point and putting all forces except for the opposite one equal to zero. After relevant transformations, one can get the following relation

$$\mathbf{K}_{\mathrm{Y}}^{(12)} = \mathbf{D}_{20}^T\left(\mathbf{K}_{10}^{-1}+\mathbf{K}_{20}^{-1}\right)^{-1}\mathbf{D}_{20};\quad \mathbf{K}_{\mathrm{Y}}^{(23)} = \mathbf{D}_{30}^T\left(\mathbf{K}_{20}^{-1}+\mathbf{K}_{30}^{-1}\right)^{-1}\mathbf{D}_{30};\quad \mathbf{K}_{\mathrm{Y}}^{(31)} = \mathbf{D}_{10}^T\left(\mathbf{K}_{30}^{-1}+\mathbf{K}_{10}^{-1}\right)^{-1}\mathbf{D}_{10} \tag{6}$$

where the compliance matrices $\mathbf{K}_{10}^{-1}$, $\mathbf{K}_{20}^{-1}$ and $\mathbf{K}_{30}^{-1}$ are related to the Y-structure springs parameters $\mathbf{K}^{(link)}$ in the following way $\mathbf{K}_{i0}=\mathbf{Q}_{i0}\mathbf{K}^{(link)}\mathbf{Q}_{i0}^T$, $i=1,2,3$ and matrices $\mathbf{D}_{ij}$.describe corresponding geometric transformations. After equating corresponding components in the VJM and MSA stiffness models, one can get the following relations for the Jacobian matrices

$$\begin{aligned}
&\mathbf{J}_{10}^{(1)} = \mathbf{D}_{10}^{-1}\mathbf{Q}_{10} \quad \mathbf{J}_{10}^{(2)} = \mathbf{D}_{20}^{-1}\mathbf{Q}_{10} \quad \mathbf{J}_{20}^{(3)} = \mathbf{D}_{30}^{-1}\mathbf{Q}_{20}\\
&\mathbf{J}_{30}^{(1)} = \mathbf{D}_{10}^{-1}\mathbf{Q}_{30} \quad \mathbf{J}_{20}^{(2)} = \mathbf{D}_{20}^{-1}\mathbf{Q}_{20} \quad \mathbf{J}_{30}^{(3)} = \mathbf{D}_{30}^{-1}\mathbf{Q}_{30}
\end{aligned} \tag{7}$$

It should be known that here $\mathbf{D}_{ij}^{-1}=\mathbf{D}_{ji}$.
Hence, the Jacobian matrix $\mathbf{J}_{ij}$ used in the VJM modelling can be presented as a product of the shift of the origin of the reference frame by means of the geometric transformation $\mathbf{D}_{ji}$ and rotation of the end-effector reference frame with respect to the local reference frame of the link $\mathbf{Q}_{ij}$, i.e. $\mathbf{J}_{ij}=\mathbf{D}_{ji}\mathbf{Q}_{ij}$.

ACKNOWLEDGMENTS

The work was supported by French Agence Nationale de la Recherche (ANR), reference ANR-23-CE10-0004-02', RAPHy.

REFERENCES

[1] A. Klimchik, A. Pashkevich, D. Chablat, Fundamentals of manipulator stiffness modeling using matrix structural analysis, Mechanism and Machine Theory, 133 (2019) 365-394.
[2] A. Klimchik, D. Chablat, A. Pashkevich, Stiffness modeling for perfect and non-perfect parallel manipulators under internal and external loadings, Mechanism and Machine Theory, 79 (2014) 1-28.
[3] A. Klimchik, E. Paul, H. Krishnaswamy, A. Pashkevich, Enhanced computational technique for stiffness matrix identification of robotic manipulator components, 2024 10th International Conference on Control, Decision and Information Technologies (CoDIT), 2024, pp. 1897-1902.
[4] A. Klimchik, A. Pashkevich, D. Chablat, CAD-based approach for identification of elasto-static parameters of robotic manipulators, Finite Elements in Analysis and Design, 75 (2013) 19-30.
[5] A. Klimchik, A. Pashkevich, Δ-Y transformations in manipulator's stiffness analysis, 22nd International Conference on Informatics in Control, Automation and Robotics (ICINCO 2025), SciTePress, Marbella, Spain, 2025, pp. 72-81.

STABILITY INVESTIGATION OF THE MODEL PREDICTIVE CONTROLLER: A SEMI-ANALYTICAL APPROACH

Bálint Bodor[1], Szabolcs Berezvai[1]

[1] Budapest University of Technology and Economics, Budapest, Műegyetem rkp. 5., Hungary, {bodor@mm.bme.hu; berezvai@mm.bme.hu}

1 INTRODUCTION

The control of soft and flexible robotic manipulators is a hot topic in today's scientific discussion [1]. These systems require sophisticated algorithms with stability guarantees to achieve proper performance. It is important to take into account that the parameter values of the system might be varying in a wider interval due to the uncertainties of the material properties and manufacturing process of these soft robotic structures, or the change of the payload too. The aim of this work is to develop a stability analysis technique of the *model predictive controller* (MPC) [2] possessing an efficient computation. This creates the opportunity of evaluating the stability properties for large parameter sets, supporting the investigation of the stability's sensitivity to the varying parameters. The approach is demonstrated on an underactuated robotic manipulator shown in Figs. 1 and 2 .

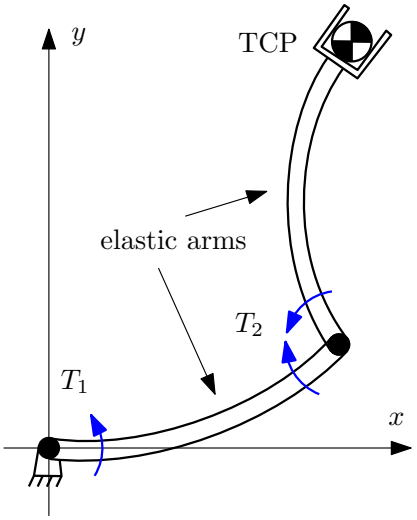

Figure 1: Underactuated RR manipulator consisting of elastic robotic arms. The position of the TCP is controlled by the input torques T_1 and T_2.

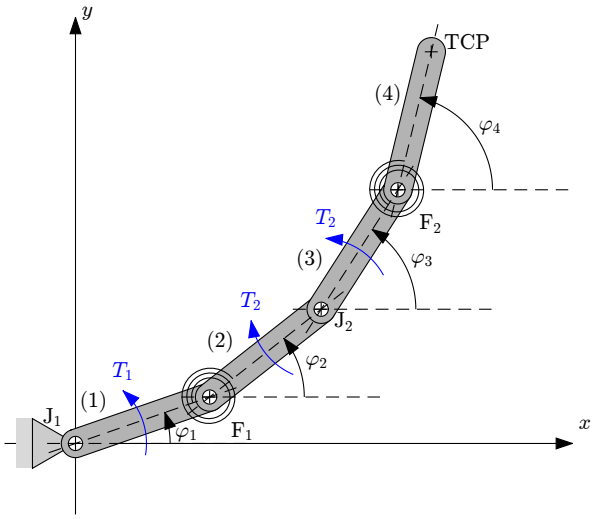

Figure 2: The simplified 4 DoF multibody model of the flexible manipulator. Each elastic arm is modeled by two beams connected by a passive joint and a torsional spring.

2 THE MODEL PREDICTIVE CONTROLLER AND ITS STABILITY ANALYSIS

The investigated optimal control problem is defined by the state-space model $\mathbf{H}(\mathbf{x})\dot{\mathbf{x}} + \mathbf{h}(\mathbf{x}, \mathbf{u}) = \mathbf{0}$ and the objective functional

$$I\langle \mathbf{x}, \mathbf{u} \rangle = \int_{t_\mathrm{s}}^{t_\mathrm{f}} f(\mathbf{x}, \mathbf{u})\, \mathrm{d}t, \tag{1}$$

Here, the system's state is denoted by $\mathbf{x}$ and the input is $\mathbf{u}$. The objective functional (1) is defined over the time horizon $[t_\mathrm{s},\ t_\mathrm{f}]$ delimited by the starting and final time instants. Since this nonlinear optimal control problem is complicated to tackle, the model predictive control approach is applied:
1) The problem is linearized around an equilibrium configuration of the system.
2) The linearized optimal control problem is solved using the solution to the corresponding Riccati equation. This solution is derived on a Δt_p long prediction time horizon.

3) A sequence of solutions to the linearized problem is concatenated in time by truncating the Δt_p long solutions, and applying the inputs $\mathbf{u}$ to the system on the control time horizon length Δt_c. This approach is called the receding horizon approach [2].

The two time horizon parameters Δt_p and Δt_c are the most important control parameters to be chosen during the controller design. ODEs are solved during the solution to the linear optimal control problem on a Δt_p long prediction horizon, resulting the computational demand roughly linearly dependending on the prediction time horizon length Δt_p. On the other hand, the available computational time is limited by the control time horizon length Δt_c. To balance between the required performance and the computational resources, these parameters must be selected carefully. Ideally, this is done based on the stability analysis of the controller.
This stability analysis is possible to carry out when the controller is defined to stabilize an equilibrium configuration of the system. A recursion representing the state transition corresponding to the initial time instants of the optimization problems are derived as

$$\mathbf{x}_{\mathrm{s},k+1} = \mathbf{A}_\mathrm{stab}\mathbf{x}_{\mathrm{s},k} + \mathbf{b}_\mathrm{stab}. \tag{2}$$

Here, $\mathbf{x}_{\mathrm{s},k}$ is the value of the state in the initial time instant of the k^th control horizon. $\mathbf{A}_\mathrm{stab}$ is the constant state transition matrix and $\mathbf{b}_\mathrm{stab}$ is a constant vector term. These coefficients are computed numerically using the solution to the Riccati differential equation corresponding to the linearized optimal control problem. This approach enables a rapid computation of $\mathbf{A}_\mathrm{stab}$ and $\mathbf{b}_\mathrm{stab}$ for any controller and system parameter set.
The stability of this difference equation (2) is characterized by the eigenvalues μ_i of the state transition matrix $\mathbf{A}_\mathrm{stab}$, which must lay inside the unit circle in the imaginary plane. Although it decides between stability and instability, the exact values of these eigenvalues are dependent on the selected control time horizon length Δt_c, too. Therefore, the equations are transformed to the time-domain by calculating the characteristic exponents a_i from the eigenvalues μ_i. The characteristic exponents show the decay rate of the system's motion in time. The control system is stable upon $a_\mathrm{max} = \max(a_i) < 0$.
An example is shown in Fig. 3, where the stability map of the elastic manipulator was determined for varying flexibilities, i.e. torsional spring stiffness values. These stability maps show that the right selection of the controller time horizons, especially the lower limit for the prediction time horizon length, is sensitive to the system parameters, which must be taken into account during the design of the controller.

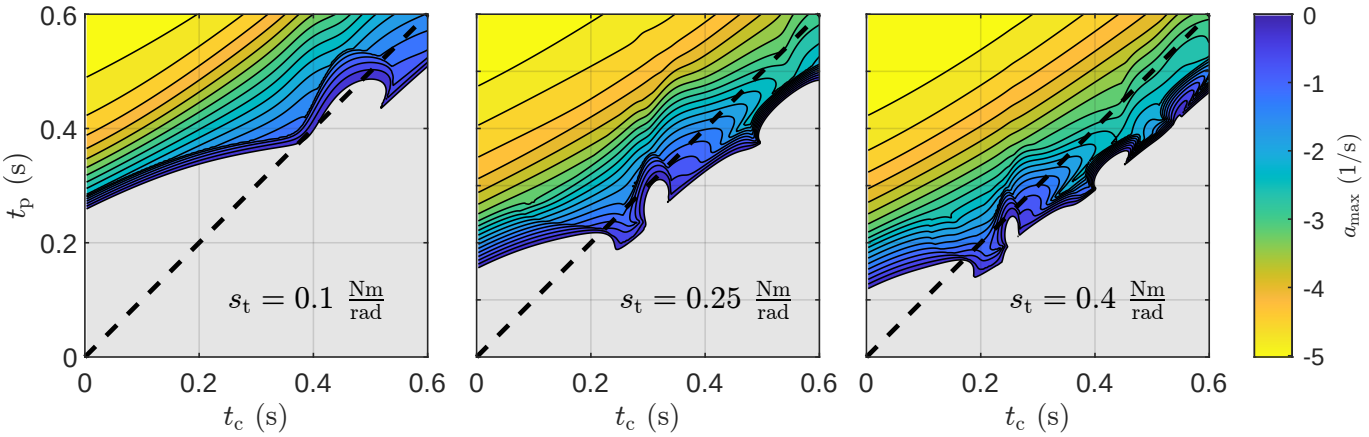

Figure 3: Stability maps of the flexible robotic manipulator for three values of the torsional spring stiffness s_t. The color scale shows the maximal characteristic exponent a_max. The dashed lines show the points, where the prediction and control horizon lengths equal. The stable regions on the plane of the time horizons Δt_c and Δt_p shrink as the spring stiffness is lowered and the manipulator becomes more elastic.

ACKNOWLEDGMENTS

The research has been supported by the Hungarian National Research, Development and Innovation Office, Hungary (NKFIH NKKP STARTING 149473).

REFERENCES

[1] Bodor, B., and Bencsik, L. Variational Principles for the Trajectory Tracking Control of Underactuated Mechanical Systems. ASME. J. Comput. Nonlinear Dynam. June 2023; 18(6): 061002. https://doi.org/10.1115/1.4056593

[2] F. Borrelli, A. Bemporad, and M. Morari, Predictive Control for Linear and Hybrid Systems. Cambridge: Cambridge University Press, 2017.

DMLAB®: DESIGN AND MODELLING OF MACHINE ELEMENTS

I. Ulacia [1], A. Iñurritegui[1], A. Arana[1], J. Larrañaga[1]

[1] Mondragon Unibertsitatea, Loramendi 4, Mondragon, Spain, {iulacia@mondragon.edu}

1 INTRODUCTION

Machine elements such as gears, bearings, cam–follower systems, and ball screws are fundamental components in many mechanical systems. Teaching their behaviour and design requires combining theoretical concepts with practical tools that help students understand how these elements function individually and within larger assemblies. As design and simulation software become more complex, there is a growing need for educational platforms that make these concepts easier to explore and apply.

Digital tools and simulation environments are increasingly used in engineering education to support the study of machine elements. Commercial software provides reliable models, but these solutions are often fragmented, requiring several separate programs to analyse different components. This complicates learning, increases costs, and limits the ability to compare results across tools. Many programs also lack automated finite element model generation, reducing their usefulness for validating analytical calculations in academic settings.

To address these limitations, DMLab® integrates multiple machine-element modules within a single environment. It offers an accessible platform for the calculation and analysis of cams, gears, ball screws, and bearings, enabling users to adjust design parameters and immediately observe their effects. The software also provides automated finite element model generation, supporting both teaching and research by facilitating detailed validation of analytical models.

2 SOFTWARE DEVELOPMENT

The tool was designed with three goals: separating the numerical engine from the user interface, enabling multiplatform deployment, and controlling user access to specific modules. For this purpose, the front–end (Flutter) communicates with a back–end service through an authentication layer, while a microservice architecture keeps components independent. Data exchange uses JSON, ensuring portability, and containerisation (Docker) is employed to deploy the API, databases and MATLAB-based functions in isolated and scalable environments.

All DMLab® modules share a common workflow: input parameters, analytical calculations and graphical results. Analytical equations follow classical machine-element design steps, and each module can automatically generate finite element models and export solver-ready input files. The platform currently includes modules for cams, gears, spline couplings, ball screws and bearings, with additional modules under development (Figure 1).

DMLab® is already used in teaching and research within the mechanical engineering group. Its distribution is regulated through an End-User License Agreement (EULA) to support future adoption by external users.

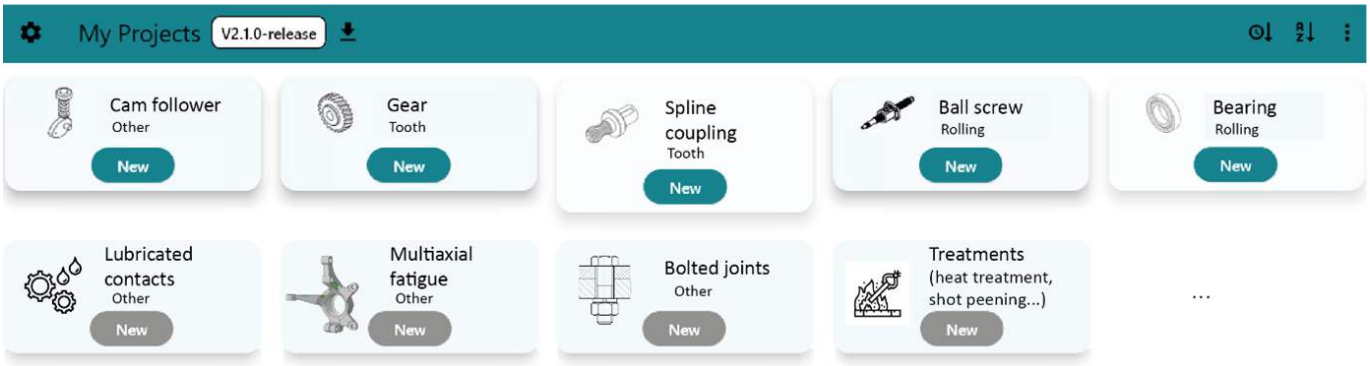

Figure 1: DMLab® interface with released modules (top) and modules under development (bottom)[1]

[1]Access to DMLab® for teaching and research purposes can be requested at `https://dmlab.mondragon.edu`.

3 TEACHING APPLICATION EXAMPLE

DMLab® is used in a laboratory assignment of the "Machine Design, Calculation and Verification" course in the Industrial Engineering Master's programme. Students work in groups to design, manufacture and test the cams and gears of a small automatic mechanism. Figure 2(a) shows the didactic rig, driven by an electric motor through a gear train and two cams that coordinate the vertical positioning of a housing and the horizontal insertion of pins. Using DMLab®, students analyse the motion laws, synchronisation and force transmission, checking pressure angles, curvature radii and contact forces. For the gears, they compute the speed ratio, apply profile shifting, and evaluate sliding, bending stresses and contact pressures. After manufacturing the components—typically by water-jet cutting—they verify synchronisation, assemble the mechanism and test it at increasing speeds to observe follower lift-off and compare experimental behaviour with their predictions (Fig. 2(b)).

4 RESEARCH APPLICATION EXAMPLE

DMLab® is also used in research activities to generate finite element models of gears, spline couplings, rack–pinion drives, bearings and ball screws. The tool provides rapid geometry definition, meshing and model export, enabling a unified workflow for different machine elements.

Figures 2(c)–(d) illustrate two examples. For toothed elements, the software has been applied to analyse meshing strategies for involute gears, compare different FE solvers, study thermal deformation and stress distributions, model pitting damage, and generate complex geometries such as crowned spline couplings. For rolling elements, DMLab® allows ball–raceway contact modelling through structured meshes or connector-based simplifications, supporting studies on angular-contact bearings and ball screws where full solid-ball modelling is computationally demanding.

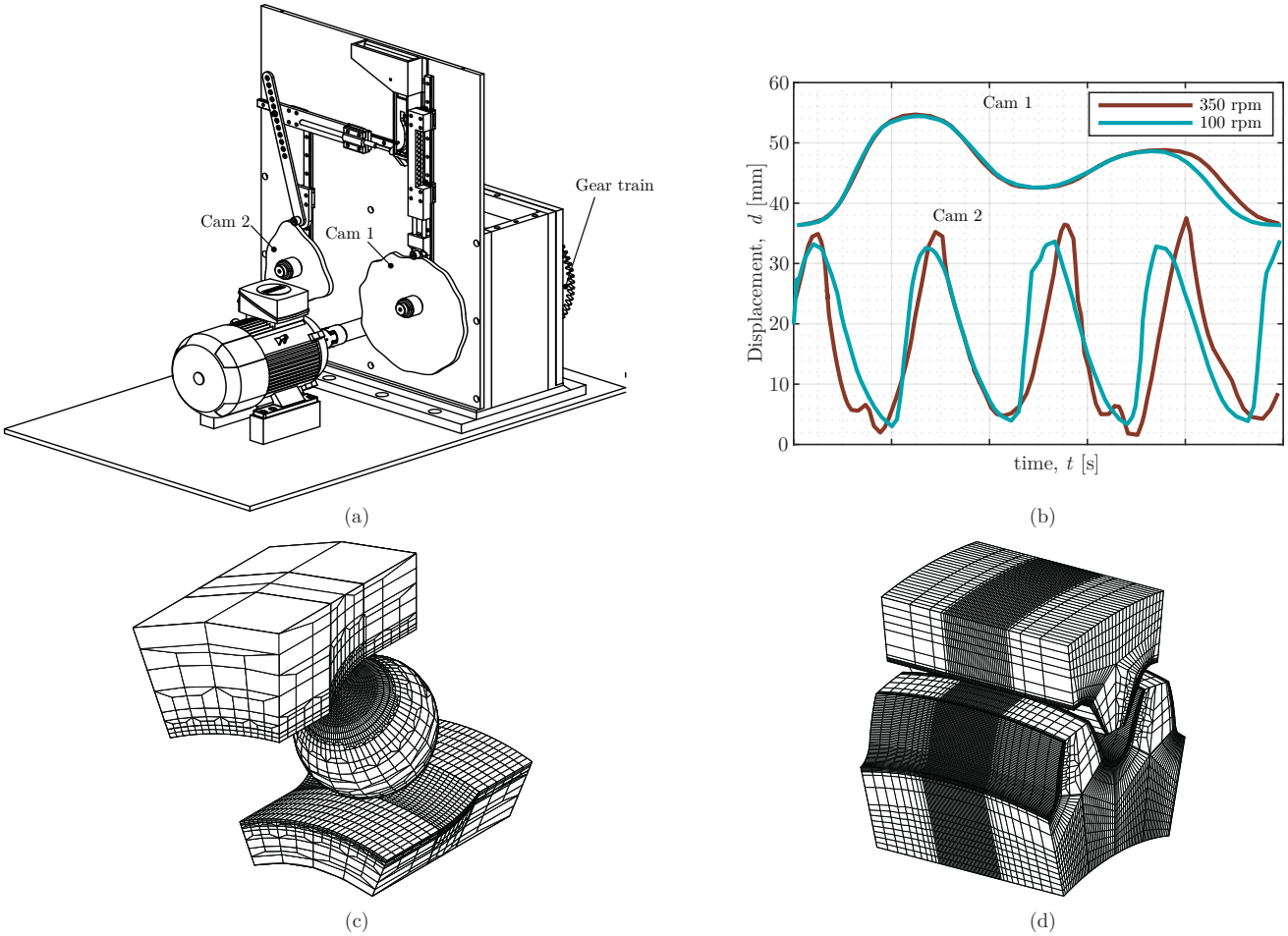

Figure 2: (a) Didactic rig used in the teaching assignment. (b) Experimental verification of follower motion and lift-off. (c)-(d) Examples of FE models for ball-bearings and spline couplings generated with DMLab® [1].

REFERENCES

[1] J. Larrañaga, et al., "Efficient multiblock approach for automated and refined 3D hexahedral mesh generation: applied to machine elements", in *Mechanism and Machine Theory Symposium*, Guimaraes, June 2024.

COMPARISON OF DIFFERENT WHEEL-RAIL CONSTRAINT-BASED CONTACT APPROACHES

Erik Snellman[1], Xinxin Yu[1]

[1] Tampere University, Korkeakoulunkatu 6, 33720 Tampere, Finland, {erik.snellman@tuni.fi; xinxin.yu@tuni.fi}

1 INTRODUCTION

Wheel-rail interaction has a major influence in the dynamics of railway vehicles. Accurate modelling of wheel-rail contact is essential for prediction of contact forces, which are further needed for assessment of railway vehicle stability, safety and prediction of wheel-rail wear.

Wheel–rail contact modelling approaches for normal contact forces range from elastic-based methods, such as Hertzian and non-Hertzian theories [1], to constraint-based methods, including lookup-table (LUT) and knife-edge contact approaches [2]. A key difference between elastic and constraint-based approaches is the determination of the contact point locations. Contact point searches can be performed using online approaches, in which the contact points are solved at each time step of the dynamic simulation, or offline approaches, in which the contact points are computed during a preprocessing stage for a range of wheelset lateral positions relative to the track and stored in a lookup table. During the dynamic simulation, the contact information is then obtained through interpolation of the stored data. In this context, constraint-based approaches are generally more computationally efficient. Nevertheless, interpolating the lookup table at every time step still incurs a non-negligible computational cost. This motivates an investigation into whether LUT of wheel–rail contact geometry can be represented using analytical expressions or a small number of parameters, such as equivalent conicity, and how such representations affect computational efficiency and accuracy. In this work, three constraint-based contact methods are compared for modelling wheel–rail of interaction within the framework of railway multibody dynamics. The first method employs a LUT approach. The second method uses analytical exponential functions to represent the saved LUT. The third method simplifies the LUT by using constant parameters, such as constant equivalent conicity. These approaches are implemented on a dynamic model of a wheelset on a tangent track with irregularities, and the results are compared against commercial software Simpack.

2 CONTACT GEOMETRY MODELLING APPROACHES

Wheelset with new and worn S1002 wheel profiles are paired with a new UIC60 rail profile are used throughout the work. Figure 1 compared the new and worn S1002 wheel profiles.

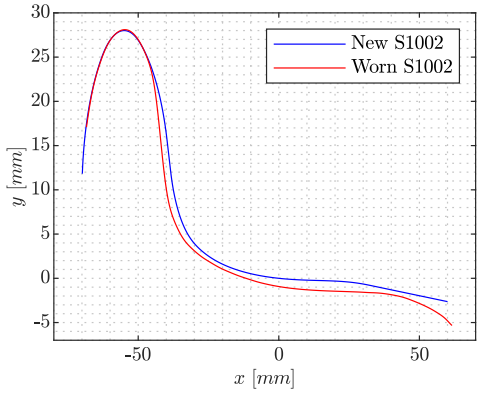

Figure 1: Comparison between new and worn S1002 wheel profiles

For the first approach, the contact point search to form LUT is carried out using algorithm presented in [3]. Figure 2(a) compared the LUT of rolling radius with respect to Simpack. The nominal gauge of 1.435 m and rail inclination of 1/40 is used for the calculation. It can be seen that the rolling radius obtained for LUT method match well with Simpack equivalents for both nominal and worn profiles.

In the second approach, the rolling-radius LUT is replaced by fitted exponential functions. The curve fitting is

performed using the MATLAB lsqcurvefit function. Figure 2(b) shows the fitted rolling-radius functions for the new and worn wheel profiles. The fitting process prioritizes accuracy in the tread region. However, beyond the onset of flange contact, the fitted functions notably underestimate the rolling radius.

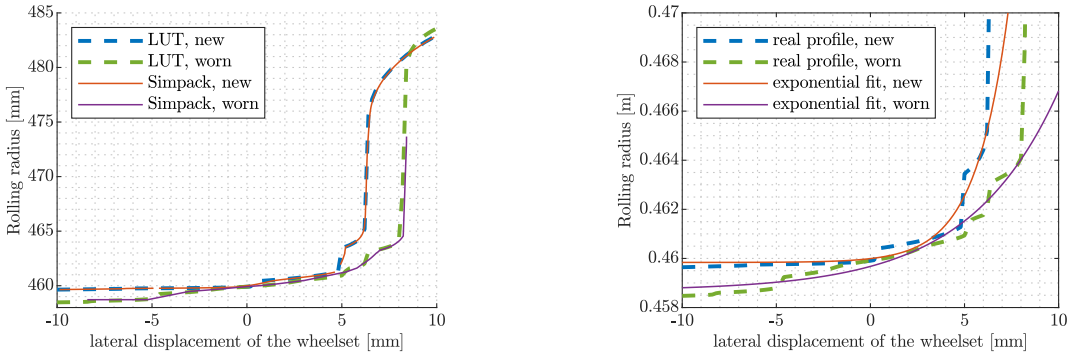

(a) (b)

Figure 2: (a) Comparison of rolling radius new and worn S1002 wheel profiles when using Simpack and LUT approach used in this work (b) Rolling radius functions fitted to data for both new and worn profiles

In the third approach, the contact angles at a wheelset lateral displacement of 3 mm are used. These angles are 0.0920 rad for the new wheels and 0.1282 rad for the worn wheels.

3 RESULTS AND CONCLUSION

The three contact modelling approaches are compared on a straight track with track irregularities. The LUT, exponential fitting, and constant conicity approaches are evaluated against the commercial software Simpack. All simulations are performed at a constant velocity of 5 m/s with a wheel–rail coefficient of friction of 0.4. The simulated lateral displacements for the new and worn wheel profiles are shown in Figure 3. The results indicate that the LUT and exponential fitting approaches show better agreement with Simpack than the constant conicity approach for both new and worn wheel profiles.

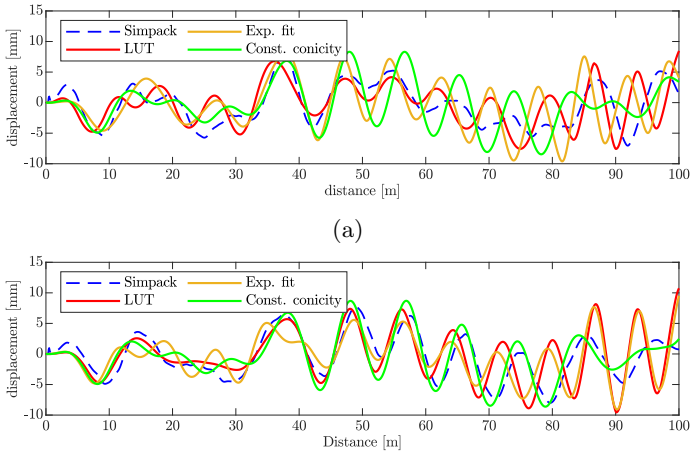

(a)

(b)

Figure 3: Wheelset lateral displacement using (a) new wheel profile and (b) worn wheel profile

REFERENCES

[1] S.Z. Meymand, A. Keylin, M. Ahmadian, "A survey of wheel–rail contact models for rail vehicles", Vehicle System Dynamics, 54(3), 386-428, 2016.

[2] J. L. Escalona, X. Yu, J. F Aceituno, "Wheel–rail contact simulation with lookup tables and KEC profiles: a comparative study", Multibody System Dynamics, 52(4), 339-375, 2021.

[3] Z. Li, "Wheel-rail rolling contact and its application to wear simulation", PhD thesis, Delft University of Technology, Delft, The Netherlands, 2002.

[4] A. Keck, C. Schwarz, T. Meurer, A. Heckmann, G. Grether,"Estimating the wheel lateral position of a mechatronic railway running gear with nonlinear wheel–rail geometry", Mechatronics, 73, 102457, 2021.

KINEMATIC GEOMETRY AND ENVELOPE CURVES OF VEHICLES WHILE MOVING ALONG LINEAR TRACTRICES

Giorgio Figliolini[1], Chiara Lanni[1], Jorge Angeles[2]

[1] Department of Civil & Mechanical Engineering, University of Cassino & Southern Lazio, G. Di Biasio 43, 03043 Cassino (Fr), Italy, {giorgio.figliolini@unicas.it; chiara.lanni@unicas.it}

[2] Department of Mechanical Engineering & CIM, McGill University, 817 Sherbrooke Street West, Quebec H3A 0C3817, Montreal, Canada, {jorge.angeles@mcgill.ca}

1. INTRODUCTION

The movement of wheeled vehicles like cars, buses, and trucks while parking, lane changing upon overtaking other vehicles and obstacles, as well as navigating roundabouts and exits, is significant not only for the safety of pedestrians, bicycles, and motorcycles, but also for developing secure roads and highways [1-4]. In particular, assuming a bicycle model, the path of the rear wheel is a tractrix or equi-tangential curve, which is different from that traced by the front wheel, that plays the role of directrix. The study of surfaces of constant curvature and related geometric concepts, including applications of tractrices in planar and curved motion analysis modelled using a bicycle model, was addressed Apostol and Mnatsakanian [5], while a method to test trailer trajectories along a tractrix path modified by slip steering and centrifugal effects is reported Brell and Thambiratnam [6]. For low-speed maneuvers, tractrix curves are a widely accepted method for estimating trailing axle paths for a given steering axle path and vehicle geometry; in particular, Neighborgall [7] introduced new numerical tractrix algorithms and implemented models to compare different trailer configurations through a variety of maneuvers. A deep study evaluated the accuracy of simulated tractrix curves for modern agricultural machines [8], while also investigating their use in estimating bend dimensions, comparing experimental measurements with simulation results. Instead, the real and simulated tractrices of modern agricultural machines were analyzed by Hürter et al. [9]. According to the fundamentals mechanical-system kinematics [10], the authors developed the curvature analysis of linear and circular tractrices [11] and [12] for the planar motion of four-wheeled vehicles. The authors also introduced the concepts of n^{th}-order Bresse's circles and higher-order centrodes [13], which were later extended [14] to multi-loop mechanisms, such as Stephenson III six-bar chains.

In this abstract, referring to the sketch of Fig. 1a, a specific algorithm for analyzing the kinematic geometry and to determine the envelope curves of vehicles, with a suitable chassis shape (trapezoidal, but also rectangular), when moving along linear tractrices, is formulated and validated by means of several examples, as those shown in Figs. 1b and c.

2. KINEMATIC GEOMETRY AND ENVELOPE CURVES

Figure 1 shows a kinematic sketch in 1a) and significant Matlab algorithm results in 1b) and 1c), which first two contain the main geometric and kinematic loci for analyzing the planar motion of a vehicle, when the front wheel center A of the bicycle model follows a straight line and the corresponding rear wheel center B of the drawbar AB, traces the tractrix curve $\mathcal{T}$. The starting position of AB is A_0B_0, where A_0 coincides with the origin O of the fixed frame OXY, which X-axis passes through B_0 and the Y-axis is coinciding with the asymptote line of $\mathcal{T}$. Moreover, the fixed and moving centrodes λ and l, in the form of catenary and straight line, respectively, are represented in tangency at the instantaneous center of rotation I, which is coincident, in this case, with the center of curvature Ω_B of the B point of $\mathcal{T}$. The inflection $\mathcal{I}$ and return $\mathcal{R}$ circles, along with the evolute curve e of λ, are also shown.

In addition, as main novel contribution of this abstract, and also referring to Fig. 1c, the vehicle bicycle model, in the form of the drawbar AB, has been provided of a suitable chassis shape (trapezoidal) with an inclined straight side η, in order to determine its envelope $\mathcal{E}$ and base $\mathcal{B}$ curves. At this aim, the envelope theory has been applied by determining first, the families of the straight lines η and their corresponding normal lines across I, which are generated during the vehicle chassis motion, when the front and rear wheel centers A and B, move along the Y-axis and the tractrix curve, respectively. Secondly, the equations of both envelope $\mathcal{E}$ and base $\mathcal{B}$ curves are obtained by adding the equation of meshing to the respective families of straight lines. In particular, the family of η is shown in Fig. 1c along with its envelope curve $\mathcal{E}$. Moreover, it is interesting to note that the base curve $\mathcal{B}$ is also the locus of the centers of curvature of the envelope curve $\mathcal{E}$, which assumes the role of the involute of $\mathcal{B}$, and consequently, $\mathcal{E}$ can be indifferently traced as envelope of η during the pure-rolling motion of l on λ, but even, as the trajectory of M (Fig. 1a) during the pure-rolling motion of the normal line to η, and passing through I, on the base curve $\mathcal{B}$.

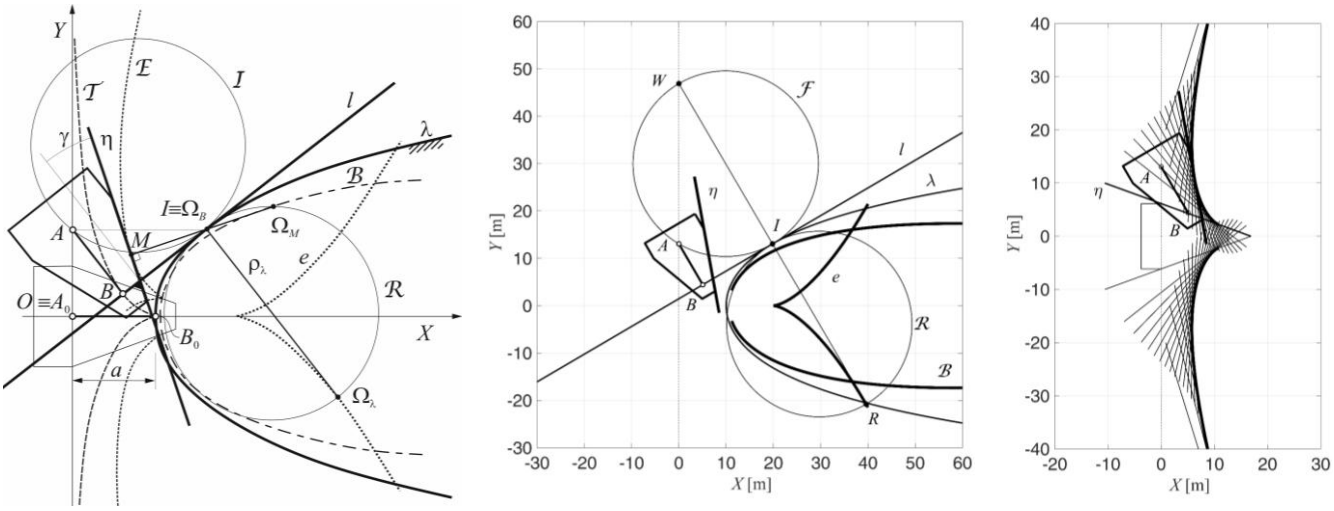

a) b) c)

Figure 1. Kinematic geometry and envelope curves of a vehicle when moving along a linear tractrix $\mathcal{T}$ curve (centrodes λ and l, evolute e of λ, inflection $\mathcal{I}$ and return $\mathcal{R}$ circles, involute $\mathcal{E}$ and base $\mathcal{B}$ curves): a) Kinematic sketch; b) and c) Matlab algorithm results.

3. CONCLUSIONS

The proposed algorithm is general and allows the kinematic and curvature analysis of a vehicle planar motion with a suitable chassis shape (trapezoidal, but also rectangular), when the front wheel center A of the bicycle model follows a straight line and the corresponding rear wheel center B of the drawbar AB, traces a linear tractrix curve $\mathcal{T}$. This algorithm has been implemented in Matlab and validated by means of several examples and results, as those of Figs. 1b and c, which show the fixed and moving centrodes λ and l, the evolute curve e of λ, the inflection and return circles, $\mathcal{I}$ and $\mathcal{R}$, respectively, the involute $\mathcal{E}$ and base $\mathcal{B}$ curves; also the family of the η straight lines and its respective envelope curve $\mathcal{E}$ are shown.

The proposed algorithm can be useful for practical applications, since the size and the shape of the vehicle chassis give several envelope curves, which can be significantly different by the rear wheel center trajectory, in the form of tractrix curves, and this could generate dangerous operating conditions during the vehicles maneuvering.

REFERENCES

[1] J.C. Alexander, J. H. Maddocks, “On the Maneuvering of Vehicles”. *SIAM Journal on Applied Mathematics*, 48(1), 38–51, 1988.

[2] G.E. Prince, S.P. Dubois, “Mathematical Models for Motion of the Rear Ends Vehicles”. *Math. and Computer Modelling*, 49, 2049–2060, 2009.

[3] H.I. Freedman, S.D. Riemenschneider, “Determining the Path of the Rear Wheels of a Bus”. *Society for Industrial and Applied Mathematical*, 25(4), 561–567, 1983.

[4] R. L. Foote, M. Levi, S. Tabachnikov, “Tractrices, Bicycle Tire Tracks, Hatchet Planimeters, and a 100-year-old Conjecture”, *The American Mathematical Monthly*, 120(3), 1–20, 2012.

[5] T. M. Apostol, M. A. Mnatsakanian, “A New Look at Surfaces of Constant Curvature”. *American Mathematical Monthly*, 123(5), 439–447, 2016.

[6] E. Brell, D. Thambiratnam, “Tractrix Trajectory with Slip Steering”. *Journal of Road Safety*, 30(2), 66–72, 2019.

[7] C. R. Neighborgall, “Low-Speed Maneuverability, High-Speed Roll-Stability, and Brake Type Performance of Heavy Truck 33-ft Double Trailers”, *PhD Dissertation*, Virginia Polytechnic Institute and State University, Blacksburg, VA (2022).

[8] G. Qin, C. Li, H. Wu, A. Ji, “Wall-Climbing Mobile Robot for Inspecting DEMO Vacuum Vessel”. *Appl. Sci.*, 12, 9260, 2022.

[9] S. Hürter, S. Götz, H. Bernhardt, “Analyse of real and simulated tractrix of modern agricultural machines”, *Int. Conf. of Agricultural Engineering*, Ref. C0074, 2014.

[10] J. Angeles, S. Bai, Kinematics of Mechanical Systems: Fundamentals, Analysis and Synthesis, Springer, Cham, 2022.

[11] G. Figliolini, C. Lanni, J. Angeles, “Kinematic analysis of the planar motion of vehicles when traveling along tractrix curves”. *ASME Journal of Mechanisms and Robotics*, 12(5): 054502, 2020.

[12] C. Lanni, G. Figliolini, J. Angeles, “Curvature analysis of linear and circular tractrices for the planar motion of vehicles”, *Proc. of the ASME IDETC-CIE Conference*, August 20-23, 2023, Boston, Massachusetts, DETC2023-116658, 2023.

[13] G. Figliolini, C. Lanni, L. Tomassi, “First- and second-order centrodes of both coupler links of Stephenson III six-bar mechanisms”. *Machines*, 13(2), Art. 93, 2025.

[14] G. Figliolini, C. Lanni, L. Tomassi, “Synthesis and analysis of Stephenson III six-bar motion generators with an instantaneous stop link”. *ASME Journal of Mechanisms and Robotics*, 17(4): 044510, 2025.

A COMPACT SPS-BASED PARALLEL MECHANISM FOR WORM-LIKE ROBOT LOCOMOTION IN CONFINED ENVIRONMENTS

Angelos Iliakis[1], George Nikolakopoulos[1], Panagiotis Koustoumpardis[1]

[1] University of Patras, Department of Mechanical Engineering and Aeronautics, Greece, {a.iliakis,gnikolak,koust}@upatras.gr

1 ABSTRACT

Locomotion and steering of worm- and snake-like robots in confined environments are particularly challenging when high axial forces must be transmitted through compact mechanical structures. Most existing approaches rely on serial bending joints or wave-based gaits, which typically exhibit limited stiffness and reduced force transmission under constrained conditions. This work presents a compact parallel mechanism based on a combination of Spherical–Prismatic–Spherical (SPS) joints, designed as the core kinematic unit of a modular worm-like robot for confined and tubular environments. The mechanism enables controlled axial motion and local orientation adjustment using three coordinated linear actuators, while inherently distributing external loads across multiple parallel load paths. A concise forward and inverse kinematic formulation is derived, and the attainable workspace is analyzed under geometric constraints imposed by a cylindrical robotic module.

2 INTRODUCTION

Robotic locomotion in confined and tubular environments is critical for subsurface exploration and drilling. Most worm- and snake-like robots rely on serial bending joints or wave-based strategies, which suffer from limited stiffness and reduced force transmission under high axial loads. In thrust-driven confined systems, steering must coexist with significant load transfer within compact cylindrical envelopes. Also steering and load transmission must be structurally coupled. Parallel kinematic mechanisms inherently distribute loads across multiple chains, yet their integration into worm-like architectures remains a challenging research problem [1], [2], [3].

3 MECHANISM ARCHITECTURE

The proposed mechanism follows a Spherical–Prismatic–Spherical (SPS) parallel configuration composed of three identical linear actuators symmetrically arranged around the central axis.

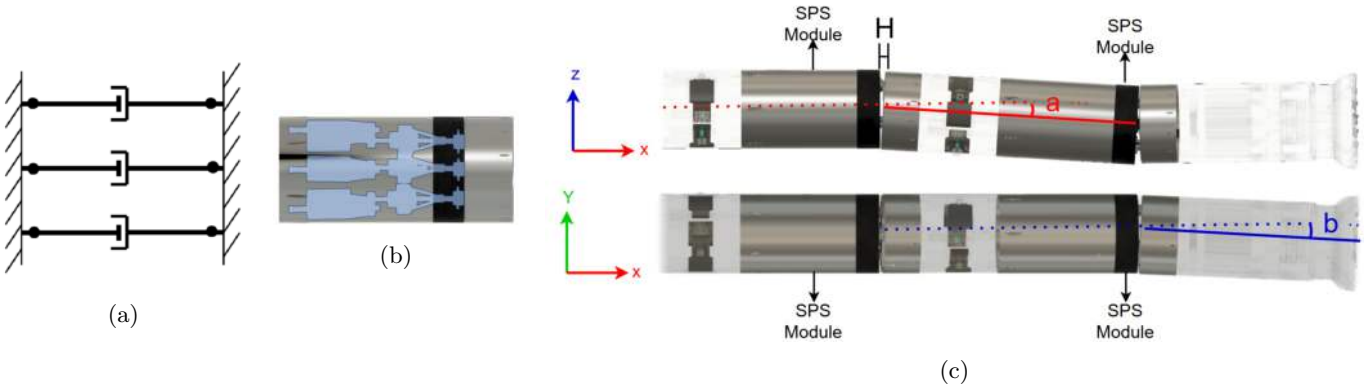

(a) (b) (c)

Figure 1: Assembly of the robotic system with the SPS module integrated: (a) SPS joint configuration, (b) CAD model, and (c) SPS actuation angles within the robot.

Each leg connects the base and the moving platform through a spherical joint at the base, an actuated prismatic joint, and a spherical joint at the platform. The mechanism is integrated within a cylindrical robotic module, imposing strict geometric constraints. Coordinated actuation enables axial translation and controlled tilting about two orthogonal axes while distributing external loads across parallel chains.

4 KINEMATICS

The SPS mechanism is modeled as a three-degree-of-freedom parallel system. The generalized coordinate vector is defined as

$$\mathbf{q} = \begin{bmatrix} \alpha & \beta & h \end{bmatrix}^T, \tag{1}$$

where α and β denote the platform tilting angles about the base x- and y-axes, respectively, and h represents the translation along the local platform axis.

The platform orientation is expressed by the rotation matrix $\mathbf{R}(\alpha, \beta)$. Let the head (tool tip) be located at a fixed offset L_h along the local platform axis. Its position in the global frame is given by

$$\mathbf{p}_h = \mathbf{p}_0 + (h + L_h)\,\mathbf{R}(\alpha, \beta)\,\hat{\mathbf{z}}, \qquad \hat{\mathbf{z}} = \begin{bmatrix} 0 & 0 & 1 \end{bmatrix}^T, \tag{2}$$

where $\mathbf{p}_0$ is a fixed reference point on the base.

The attainable head workspace is then defined as

$$\mathcal{W}_h = \left\{ \mathbf{p}_h \in \mathbb{R}^3 \;\middle|\; h_{\min} \le h \le h_{\max},\ |\alpha| \le \alpha_{\max},\ |\beta| \le \beta_{\max} \right\}. \tag{3}$$

(a) (b)

Figure 2: Workspace of the SPS mechanism: (a) head workspace visualization and (b) full reachable workspace of the mechanism.

The inverse kinematic problem consists of determining the required actuator elongations for a desired platform pose. The desired position of the platform reference point is computed through Eqs.(1-2) and substituting the desired pose into the forward kinematic relations yields the actuator commands

$$l_{i,d} = \left\| \mathbf{p}_d + \mathbf{R}(\alpha_d, \beta_d)\mathbf{r}_i - \mathbf{b}_i \right\|, \qquad i = 1, 2, 3. \tag{4}$$

5 CONCLUSIONS

This work presented a compact SPS-based parallel mechanism and its concise kinematic formulation for worm-like robot locomotion in confined environments. By distributing axial loads across parallel kinematic chains, the proposed joint mechanism architecture enhances force transmission compared to conventional serial designs. The derived forward and inverse kinematics establish a well-conditioned and compact workspace suitable for sensor-driven steering and thrust generation.

6 ACKNOWLEDGMENTS

This work was supported by the European Union's Horizon Europe Research and Innovation Programme under Grant Agreement No. 101178775 (MINOTAUR).

REFERENCES

[1] A. Cammarata, P. D. Maddio, R. Sinatra, Y. Tian, Y. Zhao, and F. Xi, "Elastostatic analysis of a module-based shape morphing snake-like robot," *Mechanism and Machine Theory*, vol. 194, p. 105580, 2024.

[2] L. Douadi, D. Spinello, W. Gueaieb, and H. Sarfraz, "Planar kinematics analysis of a snake-like robot," *Robotica*, vol. 32, no. 5, pp. 659–675, 2013.

[3] I. Virgala, M. Kelemen, P. Bozek, Z. Bobovsky, and M. Hagara, "Investigation of snake robot locomotion possibilities in a pipe," *Symmetry*, vol. 12, no. 6, p. 939, 2020.

Book of Abstracts of MMT Symposium
Mechanism and Machine Theory Symposium
Flores et al. (Eds)

MMT Symposium
60th Anniversary of Mechanism and Machine Theory
June 21-23, 2026 Porto, Portugal

MODELING OF SCREW MECHANISMS FOR CONTROL – A MULTIBODY APPROACH

Márton Kuslits[1]

[1] Unaffiliated, United Kingdom, {kuslitsm@gmail.com}

1 INTRODUCTION

Screw mechanisms (incl. ballscrew drives) are studied from various aspects but one of their peculiarity – their asymmetric efficiency – is rarely taken into account although that property might have an important role when back-driveability is an inherent feature of the application, e.g., in steering actuators. A typical modeling approach is shown in [1] where the asymmetry is not accounted. An improved solution is presented in [2], however, the efficiency is considered as a constant parameter instead of resulting from a friction model. Possibly, the most comprehensive study in this topic is [4] where a framework is developed to derive the equations of motion (EoM) of any rigid gear transmissions exhibiting asymmetric efficiency and stiction is captured, too. A key characteristic of [4] is that the resulting EoM is practically reduced to a single coordinate besides featuring the contact force as an algebraic variable.
In this paper, an alternative modeling approach is proposed for screw mechanisms, aiming at control-related applications in the first place. The method follows the well-known index-1 differential-algebraic (DAE) multibody formalism with contact friction (see also in [3]) and able to capture friction- and asymmetry-related intricacies while remaining computationally inexpensive.

2 MULTIBODY MODEL OF THE SCREW MECHANISM

The main model of the screw mechanism is shown in Fig. 1a. In this model, the nut rotates while the screw translates w.r.t. an arbitrarily chosen inertial frame $\{O_I, x_I, y_I, z_I\}$ and these motions are characterized by the coordinates φ and y, respectively. It is assumed that the components of the screw mechanism are perfectly rigid and the contact along the thread surface is ideal hence the load and the induction of friction forces are distributed uniformly. Further, the thread geometry is simplified to an ideal helical curve characterized by the mean radius r and the lead l. As a consequence of the former assumptions, the thread contact can be reduced to an arbitrarily selected contact point along the thread curve. By defining the unit vectors $\boldsymbol{e}_j,\ j \in \{x, y, t, n\}$, we may specify the forces acting on the nut and screw as shown in Fig. 1b where T is the torque driving the nut, F_y is the force loading the screw, F_n is the normal force, F_f is the friction force, F_{s_x} and F_{s_y} are support forces not contributing to the dynamics.

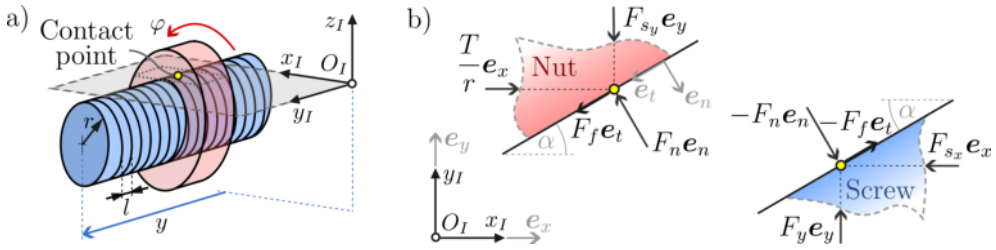

Figure 1: a) Inertial frame, coordinates and main parameters of the model b) Free body diagram of the reduced model

To derive the friction model, let us specify the velocities of the nut and the screw as $\boldsymbol{v}_\varphi = [r\dot{\varphi} \quad 0]^{\mathrm{T}}$ and $\boldsymbol{v}_y = [0 \quad \dot{y}]^{\mathrm{T}}$, respectively, from which the relative speed in the contact point may be calculated as $\Delta v = \boldsymbol{e}_t^{\mathrm{T}}(\boldsymbol{v}_y - \boldsymbol{v}_\varphi)$. As stiction is not covered by this model, regularization is applied to avoid numerical difficulties, resulting in the friction force

$$F_f = \left(\sqrt{F_n^2 + \epsilon^2} + F_p\right)\left(\mu \tanh\left(\Delta v/\epsilon\right) + b\,\Delta v\right) \approx (|F_n| + F_p)\,(\mu \operatorname{sgn}\Delta v + b\,\Delta v), \tag{1}$$

where ϵ is the regularization parameter, F_p is the preload, μ and b are the static and viscous friction coefficients, respectively. The ideal friction law (combined Coulomb-viscous model with additional preload) is shown on the right hand side of Eq. 1 for reference. An advantage of this approach is that any kind of a friction model might be easily introduced without sacrificing the model's simplicity.

To derive the multibody formalism, let us specify the constraint equation $c = i\varphi + y = 0$ by introducing the transmission ratio $i = {}^{l}/_{2\pi}$. Calculating the elements of the constraint Jacobian $\partial c/\partial\varphi = i$ and $\partial c/\partial y = 1$, we may write the index-1 DAE form of the EoM as

$$\underbrace{\begin{bmatrix} J & 0 & i \\ 0 & m & 1 \\ i & 1 & 0 \end{bmatrix}}_{\widehat{\boldsymbol{M}}} \underbrace{\begin{bmatrix} \ddot{\varphi} \\ \ddot{y} \\ -\lambda \end{bmatrix}}_{\boldsymbol{x}} = \underbrace{\begin{bmatrix} T_\Sigma \\ F_\Sigma \\ 0 \end{bmatrix}}_{\hat{\boldsymbol{f}}}, \quad \text{where} \quad \begin{aligned} r\boldsymbol{e}_x^{\mathrm{T}} \left(\frac{T}{r}\boldsymbol{e}_x + F_n\boldsymbol{e}_n + F_f\boldsymbol{e}_t + F_{s_y}\boldsymbol{e}_y \right) &= \underbrace{T - rF_f\cos\alpha}_{T_\Sigma} + \underbrace{rF_n\sin\alpha}_{i\lambda}, \\ \boldsymbol{e}_y^{\mathrm{T}} \left(F_y\boldsymbol{e}_y - F_n\boldsymbol{e}_n - F_f\boldsymbol{e}_t + F_{s_x}\boldsymbol{e}_x \right) &= \underbrace{F_y + F_f\sin\alpha}_{F_\Sigma} + \underbrace{F_n\cos\alpha}_{\lambda}, \end{aligned} \tag{2}$$

J is the moment of inertia of the nut, m is the mass of the screw, $\alpha = \mathrm{atan}({}^{l}/_{2\pi r})$ is the lead angle and λ is the Lagrange multiplier. Given that Eq. 2 is implicit in λ, i.e., $T_\Sigma(\dot{\varphi}, \dot{y}, \lambda)$ and $F_\Sigma(\dot{\varphi}, \dot{y}, \lambda)$, any further utilization of Eq. 2 requires the algebraic solution of

$$\boldsymbol{g}(T, F_y, \dot{\varphi}, \dot{y}, \ddot{\varphi}, \ddot{y}, \lambda) := \boldsymbol{B}\left(\widehat{\boldsymbol{M}}^{-1}\hat{\boldsymbol{f}} - \boldsymbol{x} \right) = \boldsymbol{0}, \quad \text{where} \quad \boldsymbol{B} = \begin{bmatrix} 1 & 0 & 0 \\ 0 & 0 & 1 \end{bmatrix} \tag{3}$$

is a Boolean matrix removing the redundant equation to make the solution procedure easier. Equation 3 may be utilized in two ways: if T, $\dot{\varphi}$, $\dot{y}$, $\ddot{\varphi} = 0$ and $\ddot{y} = 0$ are substituted then F_y and λ are obtained forming a steady-state solution; if T, F_y, $\dot{\varphi}$, $\dot{y}$ are substituted then $\ddot{\varphi}$ and λ are obtained from which the former can be integrated resulting in a dynamic solution.

3 SIMULATION RESULTS

After defining the parameter set ($m = 2$, $J = 1.5 \cdot 10^{-4}$, $l = 0.005$, $r = 0.0125$, $\mu = 0.008$, $b = 0.004$, $F_p = 300$, $\epsilon = 0.01$, SI-units), simulations can be carried out. Figure 2a shows an efficiency map resulted from steady-sate simulations. It is clearly observable that the model successfully captures the asymmetric efficiencies depending on the direction of power transmission. Moreover, the resulting efficiency map shows some variations as a consequence of the friction model and the preload. Figure 2b shows a dynamic simulation case where F_y is increased step-like, resulting in the reversal of power transmission. One may observe that model is able to capture the efficiency changes in the dynamic case as well.

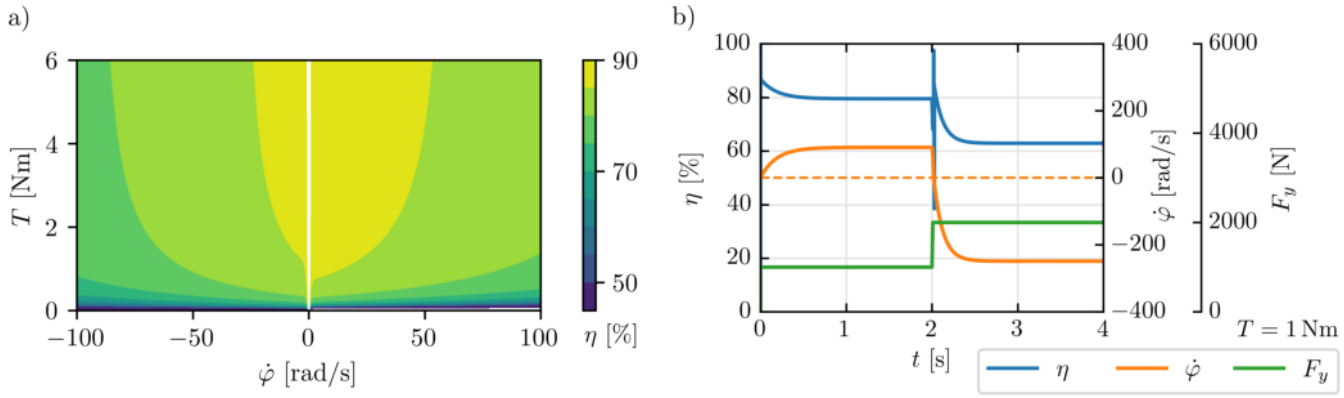

Figure 2: a) Efficiency map resulted from steady-sate simulations b) Results of a dynamic simulation case

REFERENCES

[1] C. Guo, L. Chen and J. Ding, "A novel dynamics model of ball-screw feed drives based on theoretical derivations and deep learning". *Mechanism and Machine Theory*, vol. 141, pp. 196-212, 2019.

[2] D. Dona', B. Lenzo and P. Boscariol, "Energy-optimal motion laws for servo-actuated systems considering asymmetric transmission efficiency". *International Journal of Dynamics and Control*, vol. 13, article ID 382, 2025.

[3] A. Verulkar, C. Sandu and A. Sandu, "Simultaneous optimal system and controller design for multibody systems with joint friction using direct sensitivities". *Multibody System Dynamics*, vol. 64, pp. 1-31, 2025.

[4] R. Kikuuwe, "Dynamics modeling of gear transmissions with asymmetric load-dependent friction". *Mechanism and Machine Theory*, vol. 179, article ID 105116, 2023.

METHOD FOR OPTIMIZATION OF PLANAR PARALLEL ROBOTS TAKING INTO ACCOUNT SINGULARITIES BASED ON AUTOMATIC DERIVATION OF KINEMATIC DEPENDENCIES

Rybak L.[1], Malyshev D.[1], Dyakonov D.[1]

[1] Federal Research Center "Computer Science and Control" of the Russian Academy of Sciences, Moscow, Russia, {rlbgtu@gmail.com; malyshev.d.i@ya.ru; furno.xl@yandex.ru}

1 INTRODUCTION

This work addresses automated generation of kinematic equations for 3-DoF planar parallel robots and their multi-criteria optimization. The previously proposed symbolic framework [1, 2] is extended to account for singularities and link intersections. Workspace estimation is performed using Monte Carlo and interval analysis, and the effect of constraints on Pareto fronts is investigated.

2 MODIFICATION OF THE ALGORITHM FOR AUTOMATICALLY OBTAINING A SYSTEM OF EQUATIONS FOR AUTOMATED ANALYSIS OF SINGULARITIES

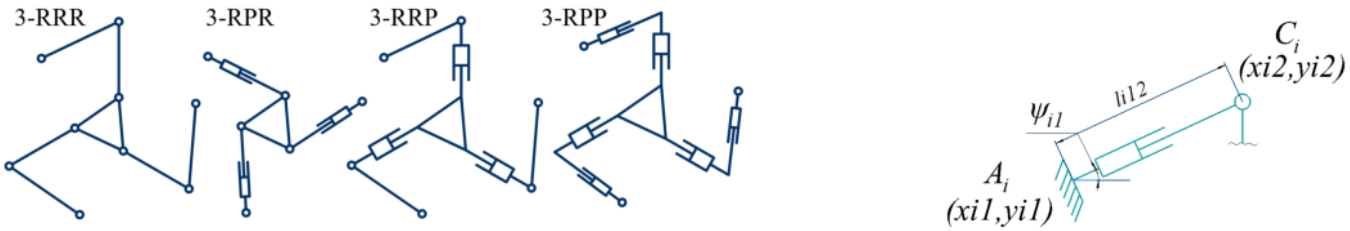

Figure 1: a) Diagrams of 3-DOF parallel robots; b)The first joints of the kinematic chain for which the modification is performed.

Let us consider a class of 3-DoF planar parallel robots (Fig. 1a). To account for singular configurations, the Jacobian matrix $J(x)$ is constructed from matrices $J_A(x)$ and $J_B(x)$, obtained by symbolic differentiation of the constraint (coupling) equations with respect to generalized and output coordinates. The proximity to singularity is evaluated using the conditioning number $k_2(J) = \frac{\sigma_{\max}(J)}{\sigma_{\min}(J)}$, where $\sigma_{max}(J)$ and $\sigma_{min}(J)$ are the maximum and minimum singular values of $J(x)$. The algorithm in [1, 2]was modified to reduce the Jacobian dimension and introduce missing generalized coordinates. This was achieved by redefining the reference point enumeration (Fig. 1b) and expressing coordinates through link parameters, eliminating redundant constraints. Symbolic differentiation was performed in SymPy. The resulting equations and Jacobians are given in Appendix A.

3 NUMERICAL SIMULATION

Multi-criteria optimization was implemented in Python using a genetic algorithm with weighted aggregation of criteria. The objectives were minimization of total geometric dimensions and maximization of workspace area estimated via Monte Carlo sampling.Four scenarios were analyzed: (1) without constraints; (2) with link intersection constraints; (3) with singularity constraints based on a conditioning number threshold k_{lim}; (4) with both constraints. Pareto fronts for the 3-RRR robot are shown in Fig. 2. Link intersection constraints reduce the hypervolume by 22% ($\Delta HV = -0.199$), while singularity constraints produce a stronger effect ($\Delta HV = -0.454$). The combined constraints lead to the greatest degradation of the Pareto front.

4 CONCLUSION

The automated generation of kinematic equations significantly simplifies modeling and enables scalable analysis of planar parallel robot structures. The proposed integration of symbolic equation generation, singularity analysis, and multi-criteria optimization allows direct comparison of configurations without manual model adaptation. The approach can be extended to other robot architectures

(a) (b)

Figure 2: Pareto front of optimal 3-RRR robot configurations for: a) scenario 1 (excluding singularities and intersections of links), b) scenario 4 (including singularities and intersections of links intersections of links).

ACKNOWLEDGMENTS

This work was supported by the Ministry of Science and Higher Education of the Russian Federation, project no. 075-15-2024-544.

REFERENCES

[1] L. Rybak, D. Malyshev, and D. Dyakonov, "Algorithm for automatic generation of systems of equations for determining the workspace of a class of 3-DOF planar parallel robots," in *Proc. I4SDG Workshop 2025 – IFToMM for Sustainable Development Goals*, G. Carbone and G. Quaglia, Eds., ser. Mechanisms and Machine Science, vol. 179. Cham: Springer, 2025. DOI: 10.1007/978-3-031-91151-4_9.

[2] L. Rybak, M. Ceccarelli, D. Malyshev, and D. Dyakonov, "Automated determination of the 3-DOF planar parallel robots workspace based on symbolic notations," in *New Advances in Mechanisms, Transmissions and Applications. MeTrApp 2025*, Y. R. Wu, T. Essomba, K. L. Hsu, and M. A. Laribi, Eds., ser. Mechanisms and Machine Science, vol. 192. Cham: Springer, 2026. DOI: 10.1007/978-3-032-05466-1_26.

A AUTOMATICALLY GENERATED EQUATIONS

Automatically obtained system of equations after modification:

$$[-L123 * *2 + (-L112 * sin(psi11) + x13l * sin(phi) - y11 + y13l * cos(phi) + yP) * *2 + (-L112 * cos(psi11) - x11 + x13l * cos(phi) + xP - y13l * sin(phi)) * *2, -L223 * *2 + (-L212 * sin(psi21) + x23l * sin(phi) - y21 + y23l * cos(phi) + yP) * *2 + (-L212 * cos(psi21) - x21 + x23l * cos(phi) + xP - y23l * sin(phi)) * *2, -L323 * *2 + (-L312 * sin(psi31) + x33l * sin(phi) - y31 + y33l * cos(phi) + yP) * *2 + (-L312 * cos(psi31) - x31 + x33l * cos(phi) + xP - y33l * sin(phi)) * *2]$$

The automatically obtained Jacobi matrices:

$$Ja = Matrix([[-2 * L112 * cos(psi11) - 2 * x11 + 2 * x13l * cos(phi) + 2 * xP - 2 * y13l * sin(phi), -2 * L212 cos(psi21) - 2 * x21 + 2 * x23l * cos(phi) + 2 * xP - 2 * y23l * sin(phi), -2 * L312 * cos(psi31) - 2 * x31 + 2* x33l * cos(phi) + 2 * xP - 2 * y33l * sin(phi)], [-2 * L112 * sin(psi11) + 2 * x13l * sin(phi) - 2 * y11 + 2 * y13l cos(phi) + 2 * yP, -2 * L212 * sin(psi21) + 2 * x23l * sin(phi) - 2 * y21 + 2 * y23l * cos(phi) + 2 * yP, -2* L312 * sin(psi31) + 2 * x33l * sin(phi) - 2 * y31 + 2 * y33l * cos(phi) + 2 * yP], [(-2 * x13l * sin(phi) - 2 * y13l cos(phi)) * (-L112 * cos(psi11) - x11 + x13l * cos(phi) + xP - y13l * sin(phi)) + (2 * x13l * cos(phi) - 2 * y13l sin(phi)) * (-L112 * sin(psi11) + x13l * sin(phi) - y11 + y13l * cos(phi) + yP), (-2 * x23l * sin(phi) - 2 * y23l cos(phi)) * (-L212 * cos(psi21) - x21 + x23l * cos(phi) + xP - y23l * sin(phi)) + (2 * x23l * cos(phi) - 2 * y23l sin(phi)) * (-L212 * sin(psi21) + x23l * sin(phi) - y21 + y23l * cos(phi) + yP), (-2 * x33l * sin(phi) - 2 * y33l cos(phi)) * (-L312 * cos(psi31) - x31 + x33l * cos(phi) + xP - y33l * sin(phi)) + (2 * x33l * cos(phi) - 2 * y33l sin(phi)) * (-L312 * sin(psi31) + x33l * sin(phi) - y31 + y33l * cos(phi) + yP)]])$$

$$Jb = Matrix([[-2 * L112 * (-L112 * sin(psi11) + x13l * sin(phi) - y11 + y13l * cos(phi) + yP) * cos(psi11) +2 * L112 * (-L112 * cos(psi11) - x11 + x13l * cos(phi) + xP - y13l * sin(phi)) * sin(psi11), 0, 0], [0, -2 L212 * (-L212 * sin(psi21) + x23l * sin(phi) - y21 + y23l * cos(phi) + yP) * cos(psi21) + 2 * L212 * (-L212 cos(psi21) - x21 + x23l * cos(phi) + xP - y23l * sin(phi)) * sin(psi21), 0], [0, 0, -2 * L312 * (-L312 sin(psi31) + x33l * sin(phi) - y31 + y33l * cos(phi) + yP) * cos(psi31) + 2 * L312 * (-L312 * cos(psi31) -x31 + x33l * cos(phi) + xP - y33l * sin(phi)) * sin(psi31)]])$$

TOWARDS A METHODOLOGY FOR INTERPRETABLE EMBODIED KINEMATIC INTELLIGENCE VIA NULL-SPACE ANALYSIS OF G-POSE MATRIX

Qiaode Jeffrey Ge[1], Huan Liu[1]

[1] Department of Mechanical Engineering, Stony Brook University, Stony Brook, NY 11794, USA,
{Qiaode.Ge@stonybrook.edu; Huan.Liu.1@stonybrook.edu}

1 INTRODUCTION

This paper proposes a new methodology for uncovering geometric constraints from planar pose data of a rigid body. The methodology fits the general framework of Information Lattice Learning (ILL) in the field of Artificial Intelligence (AI) research [1] to learn interpretable rules and insights arranged in a hierarchy from the original data. It builds on the work on "kinematic acquisition of geometric constraints" in [2] as well as algebraic fitting of planar four-bar linkages [3, 4].

2 THE POSE POLYNOMIAL

Consider a set of n planar poses of a rigid body, $(d_{ix}, d_{iy}, \theta_i)$ $(i = 1, 2, ..., n)$, where (d_{ix}, d_{iy}) and θ_i represent the location and orientation of a moving frame M attached to the moving body with respect to a fixed frame F. As points and lines are basic elements of plane geometry, the hidden rules for interpreting the pose data may be described in terms of geometric shapes generated by a moving point or line under the given pose data. To this end, let $\mathbf{x} = (x_1, x_2, x_3)$, $\mathbf{l} = (l_1, l_2, l_3)$, and $\mathbf{X} = (X_1, X_2, X_3)$, $\mathbf{L} = (L_1, L_2, L_3)$, denote the homogeneous coordinates of such point and line measured in M and F, respectively. They are related by

$$\mathbf{X} = [H_i]\mathbf{x} = \begin{bmatrix} \cos\theta_i & -\sin\theta_i & d_{ix} \\ \sin\theta_i & \cos\theta_i & d_{iy} \\ 0 & 0 & 1 \end{bmatrix} \mathbf{x}, \quad \mathbf{L} = [\hat{H}_i]\mathbf{l} = \begin{bmatrix} \cos\theta_i & -\sin\theta_i & 0 \\ \sin\theta_i & \cos\theta_i & 0 \\ \bar{d}_{ix} & \bar{d}_{iy} & 1 \end{bmatrix} \mathbf{l}, \quad \begin{matrix} \bar{d}_{ix} = -d_{ix}\cos\theta_i - d_{iy}\sin\theta_i \\ \bar{d}_{iy} = d_{ix}\sin\theta_i - d_{iy}\cos\theta_i \end{matrix} \tag{1}$$

where $\bar{d}_{ix}$ and $\bar{d}_{iy}$ have the property that $\bar{d}_x^2 + \bar{d}_{iy}^2 = d_{ix}^2 + d_{iy}^2$. In this paper, we consider only geometric shapes defined by the zero set or near zero set of a polynomial in point or line coordinates in F:

$$f(\mathbf{X}) = \epsilon \quad \text{or} \quad f(\mathbf{L}) = \epsilon, \tag{2}$$

where ϵ denotes a small scalar, and in particular, when $\epsilon = 0$, Eq.(2) results in a projective algebraic plane curve. When $\epsilon \neq 0$, Eq.(2) results in a banded region centered around the polynomial curve.
For a given set of planar poses, the goal is to identify a special point $\mathbf{x}$ or a line $\mathbf{l}$ in the moving frame M such that the resulting point or line cloud exhibits the shape characterized by (2), i.e.,

$$f_i([H_i]\mathbf{x}) = \epsilon_i \quad \text{or} \quad f_i([\hat{H}_i]\mathbf{l}) = \epsilon_i. \tag{3}$$

The above equations can be written into a new polynomial g_i, called the *pose polynomial*, with coefficient p_j and pose elements

$$1, \quad \cos\theta_i, \quad \sin\theta_i, \quad d_{ix}, \quad d_{iy} \tag{4}$$

as its bases.

3 THE G-POSE MATRIX AND ITS APPROXIMATE NULL SPACE

For n planar poses, Eq.(3) leads to a linear system $[A]\mathbf{p} = \mathbf{0}$, where $[A]$ is an $n \times m$ matrix whose elements are the terms in the pose polynomial g_i arranged with increasing degrees. The unknown vector $\mathbf{p} = (p_1, p_2, \cdots, p_m)$ are related to unknown parameters in the algebraic function f in (2). The components of $\mathbf{p}$ are in general not independent but are constrained by another set of polynomial equations Q_i, called *shape constraints*, that are derived from (2). As the term *pose matrix* has been used to refer to the displacement matrix $[H_i]$, this paper calls the matrix $[A]$ the *generalized pose matrix* or G-pose matrix for short.
The minimal norm solution to $[A]\mathbf{p} = \mathbf{0}$ can be found using the Singular Value Decomposition (SVD) method. The

right singular vectors $\mathbf{v}_j$ associated with singular values λ_j in increasing order define an approximate null space of $[A]$. In this way, the problem of extracting hidden rules from the pose data is transformed into that of exploring the approximate null space of $[A]$ such that the shape constraints Q_i are satisfied.

4 EXAMPLES

The simplest pose polynomial is a linear combination of the pose elements in $[H_i]$ (see Eq.(1)):

$$p_1 + \cos\theta_i p_2 + \sin\theta_i p_3 + d_{ix} p_4 + d_{iy} p_5 = 0. \tag{5}$$

It has been shown in [4] that Eq.(5) defines a planar motion for which one of its points stays on a fixed line. It can be realized by a planar PR dyad, where P stands for a prismatic joint and R for a revolute joint.
Likewise, a linear combination of the pose elements in $[\hat{H}_i]$ (see Eq.(1)):

$$p_1 + \cos\theta_i p_2 + \sin\theta_i p_3 + \bar{d}_{ix} p_6 + \bar{d}_{iy} p_7 = 0, \tag{6}$$

corresponds to the motion for which one of its moving lines is constrained such that it intersects with a fixed point. The motion can be realized by a planar RP dyad.
The following pose polynomial contains a linear combination of all elements in $[H_i]$, $[\hat{H}_i]$ and $d_{ix}^2 + d_{iy}^2$:

$$p_1 + \cos\theta_i p_2 + \sin\theta_i p_3 + d_{ix} p_4 + d_{iy} p_5 + \bar{d}_{ix} p_6 + \bar{d}_{iy} p_7 + (d_{ix}^2 + d_{iy}^2) p_8 = 0, \tag{7}$$

If, in addition, the following two quadratic shape constraints are satisfied:

$$Q_1(\mathbf{p}) = 2p_3p_8 - p_4p_7 + p_5p_6 = 0, \quad Q_2(\mathbf{p}) = 2p_2p_8 + p_4p_6 + p_5p_7 = 0, \tag{8}$$

then the pose polynomial given by Eq.(7) corresponds to a planar motion for which one point stays on a fixed circle, which can be realized by a planar RR dyad. It is noted that pose polynomials (5) and (6) are special cases of (7). Figure 1 shows an example of using Eqs.(7) and (8) to identify a line constraint and circular ring constraint from a set of 45 poses. Future research is to explore higher order pose polynomials in relation to mechanism motion generation.

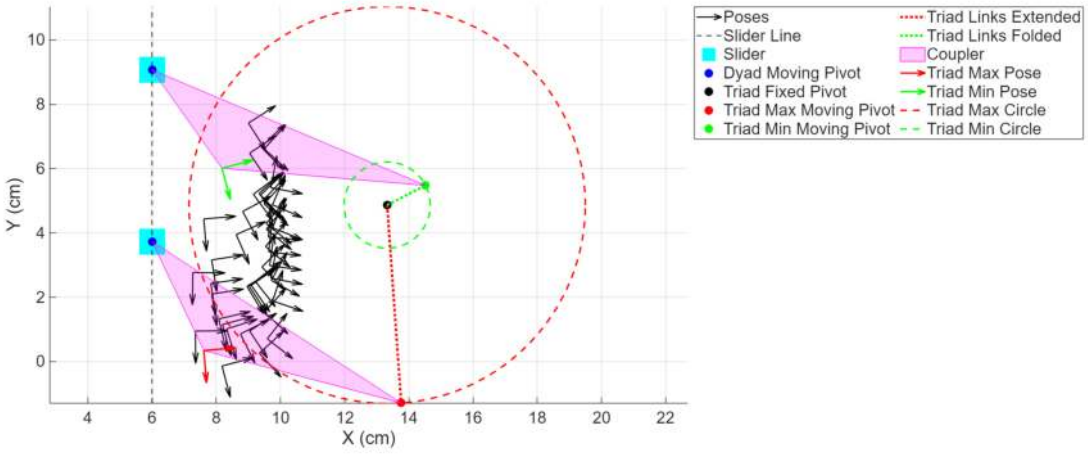

Figure 1: A set of 45 poses constrained by a line and a circular ring with the coupler link at the outer and inner circles of the ring respectively.

References

[1] H. Yu, J. A. Evans, and L. R. Varshney, "Information lattice learning," *Journal of Artificial Intelligence Research*, vol. 77, pp. 971–1019, 2023.

[2] J. Wu, Q. J. Ge, H.-J. Su, and F. Gao, "Kinematic acquisition of geometric constraints for task-oriented design of planar mechanisms," *Journal of Mechanisms and Robotics*, vol. 5, no. 1, p. 011003, 10 2012.

[3] Q. J. Ge, P. Zhao, A. Purwar, and X. Li, "A novel approach to algebraic fitting of a pencil of quadrics for planar 4r motion synthesis," *Journal of Computing and Information Science in Engineering*, vol. 12, no. 4, p. 041003, 09 2012.

[4] Q. J. Ge, A. Purwar, P. Zhao, and S. Deshpande, "A task-driven approach to unified synthesis of planar four-bar linkages using algebraic fitting of a pencil of g-manifolds," *Journal of Computing and Information Science in Engineering*, vol. 17, no. 3, p. 031011, 05 2017.

AUTOMATED EXTRACTION AND GRAPH-BASED REPRESENTATION OF MECHANISM DIAGRAMS: BRIDGING COMPUTER VISION, STRUCTURAL SYNTHESIS, AND ENGINEERING EDUCATION

Gustavo V. Souza[1], Angel E. G. Caceres[1], Daniel Martins[1], Andrea P. Carboni[1]

[1] Laboratory of Applied Robotics, Federal University of Santa Catarina, Rua Engenheiro Agronômico Andrei Cristian Ferreira, s/nº, Trindade, Florianópolis - SC, Brazil, {gustavo.valdatti@ufsc.br}

1 INTRODUCTION

The synthesis of mechanisms is a fundamental stage in engineering design, traditionally relying heavily on the experience, creativity, and intuition of designers [2]. A significant problem in modern mechanical design and academic research is the manual interpretation of structural diagrams. Analyzing functional representations of mechanisms found in literature, historical archives, or patent databases is a subjective and error-prone task, especially when dealing with complex kinematic chains [1]. To overcome this bottleneck, this work proposes an interactive software framework that uses computer vision to automate the identification and evaluation of mechanism features directly from structural diagrams, translating visual data into actionable mathematical structures.

2 TRAINING AND SYSTEM DEVELOPMENT

To transform visual mechanism features into computer-readable data, the framework models mechanisms as graphs. The automated translation of these visual features was achieved using the YOLOv11 object detection and segmentation architecture [5].

Instead of collecting images from public repositories, the dataset was built synthetically. A Python script employing the Nauty Generator was used to create mechanism graphs, which were subsequently transformed into functional diagrams by a second script. The initial dataset consisted of 200 images, partitioned into 170 for training and 30 for validation. To ensure robustness and improve the model's generalization capabilities, data augmentation techniques—specifically horizontal and vertical flips, as well as 90° rotations—were applied to the training set, expanding it to an effective total of 501 images.

The YOLO algorithm was specifically trained for instance segmentation, instructed to learn the exact contours (segmentation masks) of the components rather than just bounding boxes. To capture the topological essence of the mechanisms, seven distinct classes were annotated: kinematic joints (Junta), binary links (Binario), ternary links (Ternario), quaternary links (Quaternario), pentanary links (Pentanario), hexanary links (Hexanario), and independent loops (Circuito).

Once these elements are segmented, a hybrid computational geometry algorithm utilizes the Shapely library [6] to evaluate spatial connectivity. The system calculates the distances between the polygons of the joints and all links, connecting each joint to the two closest links, which corrects potential segmentation flaws and automatically builds the adjacency matrix.

The complete analysis process is integrated into an interactive graphical interface using OpenCV (Fig. 1), which is divided into three horizontal panels. The left panel displays the segmentation, allowing the user to alternate between a clean mode (masks only) and a complete mode (masks, bounding boxes, and labels) via mouse clicks. The central panel offers three visualization modes: connectivity analysis over the original image, visual graph overlay on the original image, and visual graph on a white background. Finally, the right panel presents the theoretical mechanism graph generated with NetworkX and Matplotlib, showing the topological representation of the connections.

3 RESULTS

The trained YOLO model was subjected to a validation set to evaluate its extraction capabilities. The algorithm demonstrated a high capacity to accurately segment objects even in complex diagrams.

The algorithm successfully evaluated mechanisms containing up to hexanary links (links with six joints), mapping them correctly to the adjacency matrix without losing topological fidelity. This proves that the combination of YOLO segmentation masks and the proximity heuristic can reliably parse complex kinematic chains that would otherwise be difficult to interpret manually.

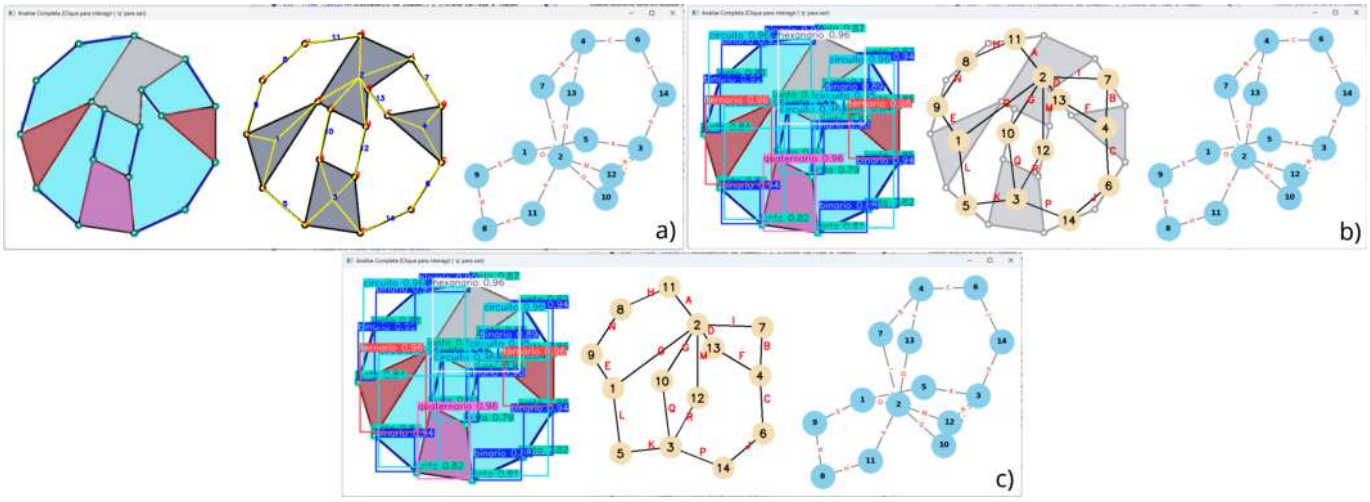

Figure 1: The interactive application interface divided into three panels: (a) YOLOv11 segmentation view, (b) connectivity analysis and visual graph overlay, and (c) the theoretical topological graph.

4 CONCLUSIONS

Although this is an incipient work, the proposed application demonstrates significant potential for automating the extraction of mechanism features. It can serve as a powerful educational and practical tool to automatically digitize and analyze mechanisms from scientific papers and literature, accelerating structural synthesis research.

The application seamlessly bridges visual detection and structural calculations, automatically extracting the number of links (n) and joints (j) to apply the Grübler equation (Eq. 1):

$$M = \lambda(n - 1 - j) + j \tag{1}$$

where λ is the workspace parameter defined by the user. This approach transforms abstract diagrammatic analysis into an interactive and highly structured process.

For future work, beyond expanding the dataset for higher-degree chains, there is a disruptive potential in integrating Large Language Models (LLMs) to automatically extract mechanism requirements from technical documents. Furthermore, ongoing research is currently being developed to expand the framework's capabilities to specifically identify and analyze gear trains, thereby broadening the application's scope to encompass a wider variety of complex mechanical transmission systems.

ACKNOWLEDGMENTS

The authors acknowledge the support of the Universidade Federal de Santa Catarina (UFSC) and the researchers involved in the development of mechanism synthesis methodologies.

REFERENCES

[1] H. Ding, W. Yang, and A. Kecskeméthy, *Automatic Structural Synthesis and Creative Design of Mechanisms*. Singapore: Springer, 2022.

[2] R. Simoni, "Síntese Estrutural de Cadeias Cinemáticas e Mecanismos", Master's thesis, Universidade Federal de Santa Catarina, Brazil, 2008.

[3] R. Diestel, *Graph Theory*. Springer, 2017.

[4] D. Martins and E. H. Murai, *Mecanismos: síntese e análise com aplicações em robótica*. Editora UFSC, 2019.

[5] I. Goodfellow, Y. Bengio, and A. Courville, *Deep Learning*. MIT Press, 2016.

[6] S. Gillies, "Shapely: Geometric objects, predicates, and operations", toblerity.org, 2019.

[7] M. Grübler, *Getriebelehre: eine Theorie des Zwanglaufes und der ebenen Mechanismen*. Springer, 1917.

DEVELOPMENT AND RESEARCH OF A MULTIMODAL ROBOT WITH GROUND AND AERIAL MODES

Larisa A. Rybak, Dmitry I. Malyshev, Vladislav V. Cherkasov

Federal Research Center "Computer Science and Control" of the Russian Academy of Sciences (FRC CSC RAS), 44/2, Vavilova Street, 119333, Moscow, Russia, {rlbgtu@gmail.com}

1. INTRODUCTION

The development of multimodal robotic systems capable of moving both on the ground and through the air is relevant for tasks that require a combination of terrain mobility and the ability to quickly overcome local obstacles (steps, debris, terrain gaps). The versatility of such platforms is largely determined by their mechanical architecture: layout configuration, load-bearing structure, type of propulsion system, and the strength margin of components under dynamic loads.

The key engineering challenge lies in combining high structural stiffness (to withstand ground impact loads, contact forces, and vibrations) with strict mass constraints that are critical for aerial operation. Therefore, the literature emphasizes the selection of frame design, the placement of the aerial thrust unit and energy sources, as well as the analysis of load paths and peak stresses in transition modes "ground–air–ground." Stability and controllability in ground mode depend on the geometry of the support polygon, the position of the center of mass, and the mass distribution among modules; for dynamically complex platforms, online trajectory and foothold planning algorithms are considered with stability requirements taken into account [1]. Control stability issues are also addressed through hierarchical controllers and neural network–based methods for compensating external disturbances [2]. When integrating aerial and ground modes, it is necessary to account not only for the dynamics of each mode but also for contact interactions during transitions between modes of motion [3]. Additional research directions include propulsion systems and precision landing technologies [4], as well as increasing autonomy, including battery servicing and replacement using auxiliary robotic systems.

2. MECHANICAL LAYOUT AND LOAD-BEARING STRUCTURE

Based on the analysis of existing multimodal platforms, a mechanical layout has been proposed that integrates two fundamentally different modes of locomotion—ground mobility and aerial thrust—within a unified load-bearing structure. The concept of the multimodal robot is founded on combining ground and aerial movement within a single mechanical configuration and structural scheme. The aerial thrust unit is treated not as an external add-on, but as a structurally integrated element of the load-bearing frame. This approach preserves the geometric stability and stiffness of the body during ground operation while increasing structural resistance to dynamic loads in transition modes (takeoff, landing, descending a step, obstacle impact).

The layout follows a modular principle and includes a central load-bearing frame, a ground propulsion system, and an aerial thrust unit. A key feature is that reactive forces and vibrations from the thrust module are transmitted through predefined load paths within the frame rather than being absorbed by local attachments of thin-walled elements. This reduces stress concentrations at module interfaces, increases joint durability, and ensures repeatable mechanical behavior of the platform under cyclic loading.

In ground mode, the dominant loads include vertical support reactions during impacts, torsional moments during diagonal wheel lift, and shock loads when descending steps or contacting obstacles. In aerial and transition modes, additional impulsive forces occur during touchdown and landing, overloads associated with roll and pitch compensation, and vibrations from the propulsion system. Therefore, the structural scheme is designed to form a closed stiffness loop resistant to torsion, while module interfaces are reinforced locally by increasing support areas and incorporating structural stiffeners.

Ground stability is ensured by selecting an appropriate support polygon geometry and arranging components so that the center of mass remains within an admissible region relative to the support polygon during motion, turning, and step climbing. The influence of the aerial module on mass distribution is considered separately: it must not shift the center of mass into a region that degrades stability during braking or on inclined surfaces. Consequently, the layout and attachment points are selected based on a balance between stiffness, mass, and stability.

Transition modes "ground–air–ground" are regarded as the primary source of peak loads defining strength and durability requirements. Structurally, specific zones are identified that must withstand landing impulses without geometric distortion due to sufficient frame stiffness and local reinforcement, provide controlled impact energy absorption through damping elements or deformable inserts, and maintain alignment and relative positioning of modules to ensure repeatable subsequent takeoff and stable ground motion after contact. The modular principle enhances manufacturability and scalability: the type and size of the

ground propulsion system, thrust unit parameters, and energy module can be modified without redesigning the entire structural scheme, preserving the base frame and primary load paths. This enables adaptation of the platform to different operating conditions and simplifies maintenance after testing, as access to key joints and highly loaded areas is incorporated at the design stage. The prototype layout is shown in Figure 1.

Figure 1. Scheme of the proposed multimodal robot.

Ground locomotion is implemented using geared motor-wheels that provide increased torque at low speeds. The gearbox housings and mounting seats are designed to prevent shaft misalignment and ensure coaxial alignment. Quick replacement of the motor and wheel is without disassembling the entire frame.

For aerial operation, a propulsion system with propellers and a mounting frame rigidly connected to the central structure is used (Figure 2 a,b,c). The mounting unit is designed to withstand reactive torques and impact loads during landing. The position of the propulsion system relative to the center of mass is selected to minimize parasitic moments and simplify stabilization. For protection, power cables are routed inside the frame and secured to prevent abrasion.

a) b) c)) d) e) f)

Figure 2. Robot movement in flight mode. a – initial point of the заданная trajectory. b – flight phase. c – intermediate point of the trajectory. Experimental study of the ground mobility mode. d – movement trajectory. e – measurement of trajectory length at the end point. f – measurement of total trajectory length.

Ground mobility tests were conducted on a flat surface, along with transition tests to aerial mode for overcoming a route gap and a series of landings with integrity monitoring of structural units (Figure 3 d,e,f). Stable motion was recorded without failure of fasteners and without displacement of the battery or electronic components. The observed vibration during ground operation did not lead to trajectory deviation or structural deformation.

CONCLUSION

The study proposes and implements a multimodal robot concept that combines ground locomotion with short-term aerial flight through a unified mechanical layout and powertrain scheme. A key feature of the design is the structural integration of the aerial thrust unit into the main frame, allowing reactive forces and vibrations to be transmitted along predefined load paths within the frame, preventing overload of local connections. This approach enables the platform to meet the stiffness and strength requirements necessary for ground operation while adhering to strict mass constraints critical for flight, enhancing the repeatability of the robot's mechanical behavior under cyclic loads.

ACKNOWLEDGMENTS

The investigation funded by grant of the Russian Science Foundation № 25-29-01619, https://rscf.ru/project/25-29-01619.

REFERENCES

[1] R. Buchanan, L. Wellhausen, M. Bjelonic, T. Bandyopadhyay, N. Kottege, M. Hutter, "Perceptive whole-body planning for multilegged robots in confined spaces," *J. Field Robotics*, no. 38, pp. 68–84, 2021. DOI: 10.1002/rob.21974.

[2] W. Junming, D. Huang, G. Xiuxian, S. Zekai, S. Tianxiang, L. Fangming, C. Heming, "OMEGA: Efficient Occlusion-Aware Navigation for Air-Ground Robot in Dynamic Environments via State Space Model," 2024. DOI: 10.48550/arXiv.2408.10618.

[3] S. Manuel, T. Manuel, B. Juan, S. Javier, V. Pablo, V. Ricardo, F. Juan, M. Anthony, G. Alfonso, "Remote Planning and Operation of a UGV Through ROS and Commercial Mobile Networks," in *ROBOT2022: Fifth Iberian Robotics Conference*, 2022.

[4] X. Liu, S. Zhang, J. Tian, L. Liu, "An Onboard Vision-Based System for Autonomous Landing of a Low-Cost Quadrotor on a Novel Landing Pad," *Sensors*, vol. 19, no. 21, article 4703, 2019. DOI: 10.3390/s19214703.

A GEOMETRIC CHARACTERIZATION FOR PERFORMANCE EVALUATION OF LUBRICATED CLEARANCE JOINTS IN MULTIBODY SYSTEMS

Bassam J. Alshaer[1], Paulo Flores[2], Hamid M. Lankaranir[3]

[1] Department of Mechanical Engineering, Jordan University of Science and Technology, Jordan, {bjalshaer@just.edu.jo}
[2] Department of Mechanical Engineering, University of Minho, Guimaraes, Portugal, {pflores@dem.uminho.pt}
[3] Department of Mechanical Engineering, Wichita State University, Wichita, Kansas, USA, {hamid.lankarani@wichita.edu}

1. INTRODUCTION

Lubricated clearance joints exert a pivotal influence on the dynamic response of multibody mechanical systems, wherein geometric determinants critically govern hydrodynamic pressure evolution, load transference, and vibratory characteristics. Although classical lubrication theory offers well-established steady-state descriptors, such as the Sommerfeld number, such metrics prove to be inadequate for mechanisms subjected to transient loading regimes. Consequently, a critical lacuna persists regarding the availability of a purely geometry-based parameter capable of characterizing lubricated joint behavior within dynamically loaded multibody dynamics. This investigation proposes a Generalized Geometrical Factor (G), formulated from exact analytical solutions to the Reynolds' equation applicable to finite journal bearings. This construct delineates the contributions of bearing length, journal radius, and radial clearance independently of operational parameters and is subsequently embedded within an inverse-dynamics multibody computational framework. A slider-crank mechanism operating at a constant speed serves as a benchmark to assess the influence of varying the matric G under invariant operational scenarios.

2. METHODOLOGY

An exact closed-form solution of the Reynolds' equation is derived for infinite and finite journal bearings by introducing a side-leakage parameter p_o and employing Sommerfeld's transformation $\{1 + \cos\phi = (1 - \xi^2)/(1 - \cos\delta)\}$, to simplify geometric dependence. This enables analytical integration over the active fluid-film region $[\phi_1, \phi_2]$, yielding explicit expressions for radial and tangential hydrodynamic reaction forces [1] as

$$F_r = 12\mu\frac{R_b^3}{c^2}\left(\frac{L(p_o+2)}{3}\right)\left(\frac{d\xi}{dt}\frac{(\delta_2-\delta_1)+0.5(\sin(2\delta_2)-\sin(2\delta_1))}{(1-\xi^2)^{1.5}} + \xi\varpi\frac{(\cos(\delta_2)-\xi)^2-(\cos(\delta_1)-\xi)^2}{4\,(1-\xi^2)^2} - \frac{3\xi^2\varpi}{4(2+\xi^2)}\frac{(1-\xi(\cos(\delta_2))^2)-(1-\xi(\cos(\delta_1))^2)}{(1-\xi^2)^2}\right) \quad (1)$$

$$F_t = 12\mu\frac{R_b^3}{c^2}\left(\frac{L(p_o+2)}{3}\right)\left(\frac{d\xi}{dt}\frac{(\cos(\delta_1)-\cos(\delta_2))(\cos(\delta_1)+\cos(\delta_2)-2\xi)}{(1-\xi^2)^2} - 3\xi^2\varpi\frac{\xi(\sin(2\delta_2)-\sin(2\delta_1))-4(\xi^2+1)(\sin(\delta_2)-\sin(\delta_1))+6\xi(\delta_2-\delta_1)}{8(2+\xi^2)(1-\xi^2)^{2.5}} - \xi\varpi\frac{(\sin(2\delta_2)-\sin(2\delta_1))-4\xi(\sin(\delta_2)-\sin(\delta_1))+4(\delta_2-\delta_1)(\xi^2+0.5)}{8(1-\xi^2)^{2.5}}\right) \quad (2)$$

where R_b is the bearing radius, L is the bearing length, c is radial clearance, ϕ is the circumferential coordinate, ϕ_1 and ϕ_2 are zero pressure angles, μ is the dynamic viscosity, ξ is the eccentricity ratio , ϖ is the angular velocity difference between the bearing and the journal, and δ is the Sommerfeld's variable. The Sommerfeld number (S) is a fundamental parameter for steady bearing performance but is unsuitable for multibody dynamics? Its definition

$$S = \frac{r^2}{c^2}\frac{\mu\,\omega}{P} \quad (3)$$

relies on static loads (P) and cannot account for time-varying forces from coupled system motion. In order to address this limitation of the lubricant force not being constant and not being known at any instant and to be calculated based on the system's state (positions and velocities), the present work introduces a purely geometric descriptor, named the Generalized Geometrical Factor (G), is defined as

$$G = \frac{L\,R_b^3}{c^2} \quad (4)$$

Thus, this study employs a typical multibody dynamics formulation and numerical algorithm to define state variables and directly compute hydrodynamic reaction forces. Lubricated joints are modeled as active force generators in constrained multibody systems, with motion governed by dynamic relations. The motion of constrained multibody systems that include such lubricated connections is governed by the following dynamic relation [2] as

$$\begin{bmatrix}\mathbf{M} & \mathbf{\Phi}_q^T\\ \mathbf{\Phi}_q & \mathbf{0}\end{bmatrix}\begin{Bmatrix}\ddot{\mathbf{q}}\\ \boldsymbol{\lambda}\end{Bmatrix} = \begin{Bmatrix}\mathbf{g}\\ \boldsymbol{\gamma}\end{Bmatrix} \quad (5)$$

Here, **M** represents the system's mass matrix, **q** the generalized coordinates, and $\boldsymbol{\Phi}=\mathbf{0}$ the holonomic constraint equations. $\boldsymbol{\Phi}_{\mathbf{q}}$ is the constraint Jacobian, $\boldsymbol{\lambda}$ are the Lagrange multipliers, and **g** includes all external and hydrodynamic forces derived from Equations (1) and (2).

3. DEMONSTRATIVE EXAMPLE OF APPLICATION

The study considers a multibody system of a slider-crank mechanism with a constant crank angular velocity of 5000 rpm, as it is illustrated in Figure 1. The driving torque and journal center trajectory over crank revolutions are shown in Figures 2. Three simulations were conducted with varying Generalized Geometrical Factor (G) values. This comparison evaluates how design changes in G affect fluid-film pressure and journal eccentricity.

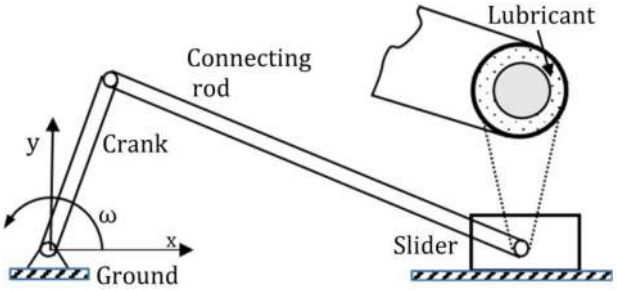

Figure 1. Slider-crank mechanism with a lubricated imperfect joint.

The Generalized Geometrical Factor (G) governs joint behavior: smaller G increases torque fluctuations and orbit size due to reduced load capacity, especially during slider reversal. Higher G values promote smoother torque transmission and better film stability, while lower G indicates vulnerability to transient disturbances and film collapse.

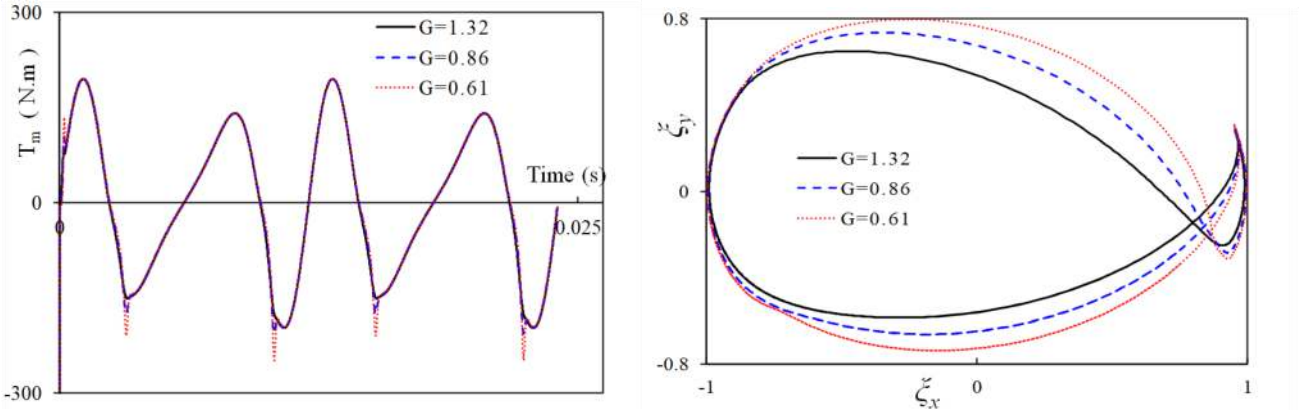

(a) Motor sizing (b) Path of the center of the journal

Figure 2. Slider-crank mechanism response with a lubricated imperfect joint for different values of G

4. CONCLUSION

The Geometric Characterization Metric G was proposed in this study for quantifying performance of lubricated clearance joints in multibody systems. Computational outcomes elucidate that diminishing G amplifies transient torque overshoot proximate to crank reversal and displaces the journal-center trajectory toward elevated eccentricity ratios, thereby compromising the minimum film thickness margin. Conversely, augmented G values enhance effective hydrodynamic stiffness and damping characteristics, facilitating smoother torque propagation and augmented systemic stability. The presented metric constitutes a parsimonious, yet physically cogent instrument for geometric design refinement, tolerance specification, and performance prognostication within lubricated multibody mechanical systems.

REFERENCES

[1] B.J. Alshaer and H.M. Lankarani, An exact analytical solution for dynamic loads generated by imperfect lubricated joints in multibody systems. *Multibody System Dynamics*, 65, 35-50, 2025.

[2] P. Flores and H.M. Lankarani, State-of-the-Art and Challenges of Contact-Impact Problems Using Multibody Dynamics Methodologies. Mechanisms and Machine Science, 165, 233-241, 2024.

MMT Symposium
60th Anniversary of Mechanism and Machine Theory
June 21-23, 2026 Porto, Portugal

MODELING, SIMULATION AND SENSITIVITY TESTING OF AUTOMOTIVE AUTOMATIC CONTROL SYSTEMS DUE TO BACKLASH AND FRICTION

Dariusz Żardecki[1], Mirosław Gidlewski[1,2], Marek Jaśkiewicz[3], Leszek Jemioł[4], Karol Zielonka[2]

[1] Military University of Technology, Department of Mechanical Engineering, Institute of Vehicles and Transportation, Gen. Sylwestr Kaliski 2 Street, 00-908 Warsaw, Poland, {dariusz.zardecki@wat.edu.pl; miroslaw.gidlewski@wat.edu.pl}

[2] Łukasiewicz Research Network – Automotive Industry Institute (Łukasiewicz-PIMOT), Jagiellońska 55 Street, 03-301 Warsaw, Poland, {karol.zielonka@pimot.lukasiewicz.gov.pl}

[3] University of Technology, Department of Automotive Engineering and Transport, Faculty of Mechatronics and Mechanical Engineering, Ave. Tysiąclecia Państwa Polskiego 7 Street, 25-314 Kielce, Poland, {m.jaskiewicz@tu.kielce.pl}

[4] University of Radom, Department of Mechanical Engineering, Malczewski 29 Street, 26-600 Radom, Poland, {leszek.jemiol@urad.edu.pl}

1. INTRODUCTION

Autonomous vehicles are one of the main development trends in the modern automotive industry [1, 2]. An increasing number of vehicles equipped with numerous mechatronic control systems are appearing on the market. These systems consist of both electronic and mechanical components. Electronic components based on digital technology can be considered invariant during operation. Such components either function properly or fail completely. On the other hand, mechanical components can slowly change their properties due to wear and tear during long-term operation. This applies primarily to tribological properties related to backlash and friction. A perfectly functioning motion control system in a "new" vehicle can deteriorate over time due to changes in backlash and friction values in the steering mechanisms. This is an interesting area of analysis that is not reported in publications.

Understanding the sensitivity of vehicle motion control systems to backlash and friction in the steering system seems important from an operational perspective. It is worth emphasizing that such analyses can only be conducted using simulation methods based on mathematical modeling. It's difficult to imagine a situation in which, during subsequent experiments conducted on a real object, its control device would gradually become increasingly mechanically damaged (and less precise). Modeling and simulation of systems operating with backlash and friction are quite difficult due to the nonlinearity and variable structure of multi-body systems. However, analyzing the dynamics of so-called non-smooth systems is very attractive from a scientific perspective.

2. RESEARCH METHODOLOGY

Previous publications, including [3], presented design and research work on a steering controller with an autonomous lane-changing process for a vehicle. The controller algorithms were successfully synthesized. The developed controller algorithm was successfully subjected to simulation tests on a virtual truck treated as a three-dimensional (3D) and discrete (MBS) model of a vehicle equipped with an active steering system, but without consideration of backlash and friction. These studies covered a wide range of road and operating conditions, even the occurrence of delays and signal interference.

It is time to expand the scope of research to include the controller's sensitivity to backlash and friction in the vehicle's steering system. Such studies should help answer the important question of whether autonomous vehicles after long-term use, i.e., mechanically worn but equipped with efficient electronics, will be sufficiently safe for users. Therefore, the previously used dynamics model of the virtual truck was supplemented with elements that describe backlash and friction in the steering system in the simplest possible way. To model the nonlinearity of backlash and friction, piecewise-linear projections of backlash(...) and tar(...) and their surprisingly simple mathematical apparatus were used.

Simulation studies were conducted for multiple data sets (including for various driving speeds and truck loads, as well as for various road surface types and conditions). In these tests, the values of the play were changed: in the steering mechanism $ff=0\div10^{o}$ and in the steering knuckle mechanism $\Delta\delta_1=0\div0.15^{o}$, as well as the friction moment values in the kingpin-knuckle connection $M_T=0\div200$Nm.

Lane changes were performed by the same controller designed based on the reference model under the same operating conditions, regardless of whether or not steering play and friction were considered. No interference with the measurement signals was considered in the tests. The vehicle was tasked with changing lanes in the shortest possible distance under traffic conditions close to the limit.

In tests to assess the controller's sensitivity to steering play and friction, two simulations were conducted for each case: one based on the nominal model (Model 1 – without steering play and friction) and the other based on a model that considered various values of steering play and friction (Model 2). Based on the results of these simulations, numerical indices W_X (1) were introduced as measures of the controller's relative sensitivity:

$$W_x = 100 \frac{\int_0^\tau (x_1(t) - x_2(t))^2 dt}{\int_0^\tau (x_1(t))^2 dt} \quad (1)$$

where:
$x_1(t)$, $x_2(t)$ – output signals from Model 1 and Model 2.
The following output signals were recorded and analyzed: steering wheel rotation angle δ_H, lateral displacement of the vehicle's center of mass Y, and vehicle yaw angle Ψ.

3. RESULTS OF SIMULATION STUDIES

Example simulation results are shown in the figures below. The simulation models show a lane change by a fully loaded truck traveling at 70 km/h on a wet asphalt road. Figure 1 shows the time histories of the steering wheel angle δ_H, lateral displacement Y, and yaw angle Ψ (black line - ff = 0°, $\Delta\delta_I$=0°, blue line - ff = 5°, $\Delta\delta_I$=0°, red line - ff = 5°, $\Delta\delta_I$=0.075°, green line - ff = 5°, $\Delta\delta_I$=0.15°). The time histories of the analyzed quantities show that the controller successfully completed the lane change task in all considered cases. Of course, as the backlash/friction parameters increased, so did the differences between the calculated time histories. It was noted that the effect of backlash in the steering system is more important than the effect of friction. Steering play noticeably worsens the lane change curves, while the friction effect is minor. However, vibrations of the steered wheels were observed at high M_T friction torque values.
The graphs of the controller sensitivity indicators (Fig. 2) show that the influence of changes in the steering system play values is quite regular. Of course, the sensitivity indicators increase faster when the friction values are higher.

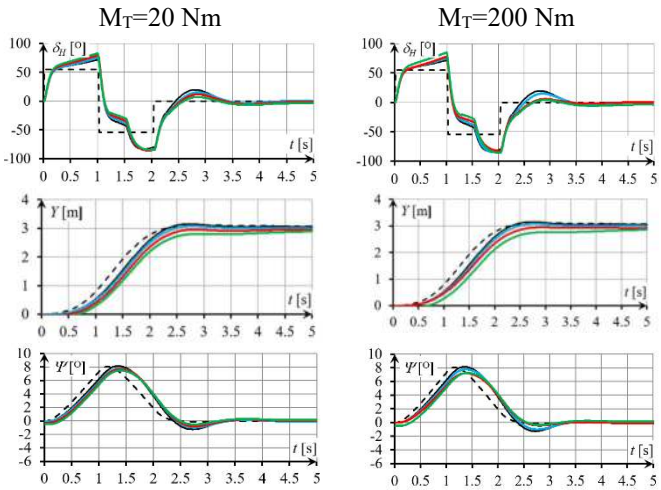

Figure 1. Comparison of the curves for different clearances and different dry friction parameters (dashed line – reference curves. Continuous lines – curves with regulator operation).

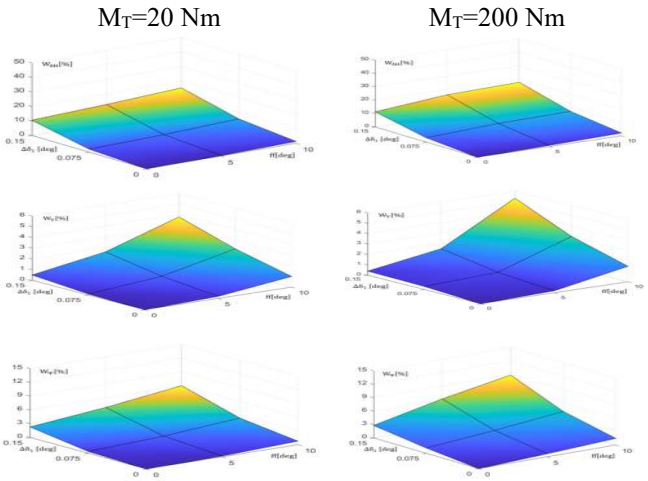

Figure 2. Sensitivity indices as a function of ff and $\Delta\delta_I$.

4. CONCLUSIONS AND SUMMARY

This article presents research analyzing the sensitivity of a lane change controller to backlash and dry friction (kinetic and static) in the steering system, which were omitted in the controller's design.
The influence of backlash in the steering system is quite pronounced. As backlash increases, a greater difference in the curves of the variables under consideration was observed.
The effect of friction on lane change behavior is relatively small, but at high friction values it can cause torsional vibrations.
Overall, however, simulation tests have shown that the lane change control system performs well even with some mechanical wear of the steering system.
The work was supported by the University Research Grant UGBWIM 531-000102-W100-22.

REFERENCES

[1] Wu, X.; Qiao, B.; and Su, Ch., *Trajectory Planning with Time-Variant Safety Margin for Autonomous Vehicle Lane Change*. Applied Sciences, 10 (5), 2020.
[2] Parekh, D. i inni, *Review on Autonomous Vehicles: Progress, Methods and Challenges*. Electronics, 11(14), 2022.
[3] Gidlewski, M.; Jackowski, J.; Jemioł, L.; Żardecki, D., *Sensitivity of a vehicle lane change control system to disturbances and measurement signal errors – Modeling and numerical investigations*. Mechanical Systems and Signal Processing, 147, 2021.

ACTUATION REDUNDANCY MANAGEMENT OF THE 3-DOF PERCUCOB-RCM PARALLEL MANIPULATOR

Kevin Gaitan[1], Juan Sandoval[1], Stéphane Caro[1]

[1] Nantes Université, École Centrale de Nantes, CNRS, LS2N, UMR 6004, 44321 Nantes, France, {kevin.gaitan@ls2n.fr; juan.sandoval@ls2n.fr; stephane.caro@ls2n.fr}

1 INTRODUCTION

The PercuCob project[1] aims to develop a robotic architecture for operating room integration to assist clinicians during ultrasound-guided ablation procedures (Fig. 1(a)). The system comprises a macro-robot carrying a mini-robot mounted on its end-effector and directly manipulated by the practitioner. The mini-robot is based on the URRR–URR parallel manipulator (PM) described in [1, 2], hereafter referred to as the PercuCob-RCM. This 3-*dof* PM consists of two limbs, each connected to the base by a universal joint. A second robotic arm holds the ultrasound probe to provide continuous imaging of the instrument and surrounding anatomy.

The development of the PercuCob-RCM robot involves a sophisticated integration of advanced mechanical design and control theory. Central to its architecture is the implementation of spherical parallel mechanisms used to actuate universal joints, which requires precise geometric and kinematic modeling to ensure accuracy during medical procedures. Control strategies that manage actuation redundancy are synthesized and implemented to improve robot performance and reliability. Finally, the paper bridges the gap between theory and application through rigorous prototyping and experimental validation, confirming that the theoretical models remain valid under real-world testing conditions.

(a) (b)

Figure 1: (a) PercuCob project's experimental platform with the overactuated PercuCob-RCM circled in red and (b) CAD model of the PercuCob-RCM with the actuated angles highlighted in red.

2 DESIGN OF THE PERCUCOB-RCM

Based on the task requirements, a design solution is identified that covers every pose within a regular cone-shaped workspace (Fig. 2(a)). The objective is to minimize both the mechanism size and the average motor torques required to balance an external wrench applied to the moving platform (MP) (Fig. 2(b)).

2.1 Actuation redundancy

To reduce overall dimensions and actuator size, both universal joints are fully actuated resulting in four motors. Each universal joint is driven by a 2-*dof* spherical parallel mechanism based on [3]. Since the PercuCob-RCM provides 3-*dof*, this configuration introduces an overactuation problem requiring an appropriate redundancy resolution strategy.

Redundancy management is addressed by introducing the reduced twist with the formulated kinematic model obtained through the wrench analysis. Applying the principle of virtual work yields the static equilibrium equation:

[1]This project is supported by the French government under the France 2030 Investment Plan, by the Pays de la Loire Region and by NExT.

$$\mathbf{W}\boldsymbol{\tau} + \mathbf{w}_e = 0 \tag{1}$$

where, $\mathbf{W}$ is the wrench matrix derived from the reduced Jacobians, $\boldsymbol{\tau}$ is the vector of motor torques, and $\mathbf{w}_e$ is the external wrench applied to the MP.

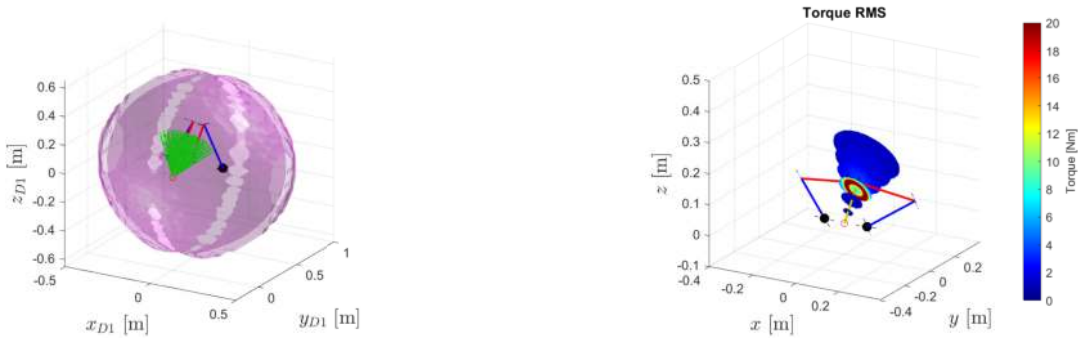

(a) (b)

Figure 2: (a) Prescribed cone-shaped workspace represented in green and maximum Cartesian workspace in purple and (b) distribution of the motor torques over the desired cone-shaped workspace for the design of the PercuCob-RCM.

3 SOLUTION ANALYSIS

The first prototype, shown in Fig. 3, integrates Maxon DC motors with incremental encoders, complemented by magnetic rotary encoders for absolute joint position measurements. The system's motion capabilities were assessed through trajectory testing, alongside an evaluation of its positioning accuracy.

(a) (b)

Figure 3: (a) Front view and (b) back view of the constructed PercuCob-RCM.

REFERENCES

[1] K. Gaitan, J. Sandoval, and S. Caro, "Geometrical design analysis of a URRR-URR parallel mechanism for percutaneous interventions," in *New Trends in Medical and Service Robotics*, M. A. Laribi, G. Carbone, D. Pisla, and S. Zeghloul, Eds. Cham, Switzerland: Springer Nature Switzerland, 2025, pp. 119–129, doi: 10.1007/978-3-031-96081-9_13.

[2] K. Gaitan, J. Sandoval, and S. Caro, "Kinematic modeling and task-based design of a URRR-URR parallel mechanism for percutaneous interventions," *ASME Letters in Translational Robotics*, vol. 2, no. 1, p. 011001, 2026, doi: 10.1115/1.4070147.

[3] R. Ur-Rehman, S. Caro, D. Chablat, and P. Wenger, "Kinematic and dynamic analysis of the 2-DOF spherical wrist of Orthoglide 5-axis," arXiv preprint arXiv:0904.0145, Apr. 2009, doi: 10.48550/arXiv.0904.0145.

DESIGN AND OPTIMISATION OF A TILT-IN-SPACE WHEELCHAIR MECHANISM

Leonor Guimarães[1], Mariana Rodrigues da Silva[1,2], Filipe Marques[1,2]

[1] CMEMS-UMinho, Universidade do Minho, Campus de Azurém, 4804-533, Guimarães, Portugal, {pg55711@alunos.uminho.pt; m.silva@dem.uminho.pt; fmarques@dem.uminho.pt}

[2] LABBELS - Associate Laboratory, Braga/Guimarães, Portugal

1. INTRODUCTION

A considerable number of wheelchair users remains seated for extended periods of time, which results in sustained pressure on bony prominences. This situation, combined with other factors, increases the risk of developing pressure ulcers [1], which can lead to severe health complications and reduced quality of life. In order to mitigate these risks, assistive technologies that promote pressure redistribution and postural adjustments play a key role in improving user health and comfort. Among these technologies, tilt-in-space wheelchairs represent an effective solution. These systems allow the seat and backrest assembly to tilt as a rigid unit, while maintaining constant joint angles between body segments. This motion allows to increase the area responsible to support the body weight and, hence, helps redistribute contact pressure and improves user's comfort and postural stability [2,3]. Despite their clinical benefits, the performance and usability of such devices strongly depend on the mechanical design of the tilt mechanism, which directly influences the required actuation effort, system stability, and overall user safety.

The continuous improvement of medical devices is essential to enhance user comfort, reliability, and accessibility [4]. In this context, computational modelling and simulation are important tools in the design process, allowing to analyse system behaviour, evaluate different configurations, and predict mechanical performance before physical prototypes are built. This approach reduces dependence on trial-and-error development, lowering design time and costs leading to more efficient and accessible assistive technologies.

Motivated by these challenges, this study investigates the tilt-in-space mechanism of a wheelchair currently under development. A multibody modelling approach is used to analyse and optimise the dynamic behaviour of the mechanism, with particular focus on the motion of the seat-backrest assembly, the required actuation force, and the trajectory of the centre of gravity of the user-wheelchair system. By evaluating the influence of geometric parameters, namely the relative positions of the joints and actuator attachment points, the study aims to establish design guidelines that reduce actuation effort, while maintaining system stability.

2. MECHANISM DESCRIPTION

The developed tilt-in-space mechanism is based on a reverted slider–crank configuration, allowing the seat and backrest to rotate simultaneously as a rigid unit. This motion produces an overall angular variation of the assembly relative to the fixed base of the wheelchair. Figure 1 illustrates two representative configurations of the mechanism, corresponding to the upright reference position (a) and the fully tilted configuration (b).

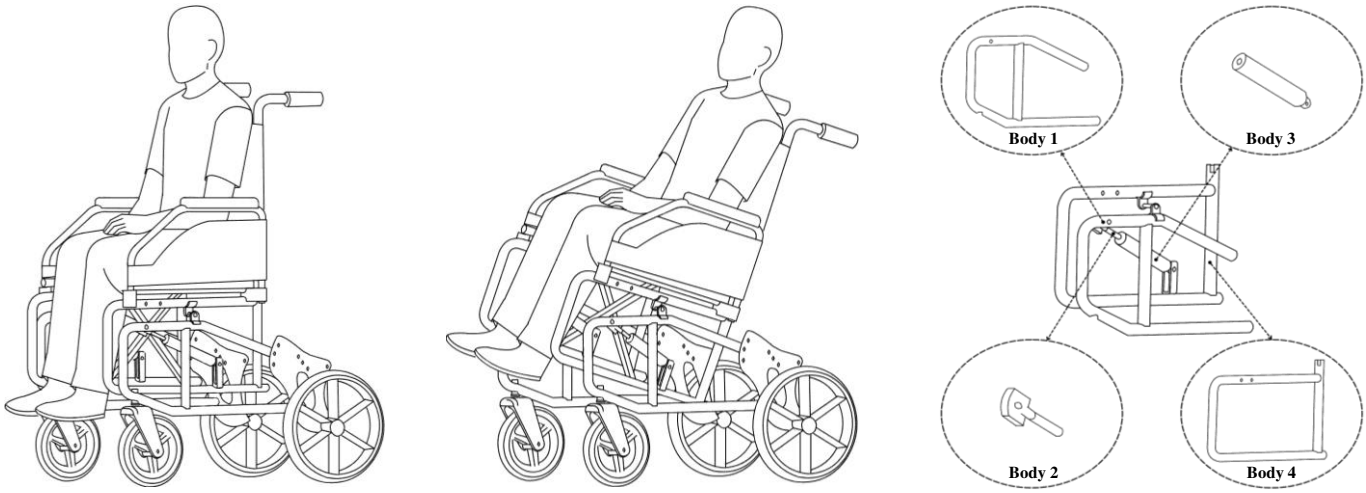

(a) (b) (c)

Figure 1. Tilt-in-space mechanism: (a) Upright reference posture; (b) Activated configuration; (c) Bodies considered in the model.

The mechanism consists of four rigid bodies (see Figure 1c), which are connected by three revolute joints and one translational joint. Body 1 corresponds to the external frame of the wheelchair, which is attached to the wheels' assembly. Bodies 2 and 3 constitute the two moving parts of the pneumatic linear drive, responsible for controlling the angle of inclination of the system. Finally, Body 4 integrates the internal frame of the wheelchair, associated with the seat, backrest and other elements attached to the user, which are all taken into account when determining the inertial properties of this body. Thus, the tilt motion of the seat-backrest assembly (Body 4) is driven by the extension or retraction of the actuator (Bodies 2 and 3). Figure 2 shows the position of the centers of mass of each body in the upright configuration, as well as the corresponding coordinate systems.

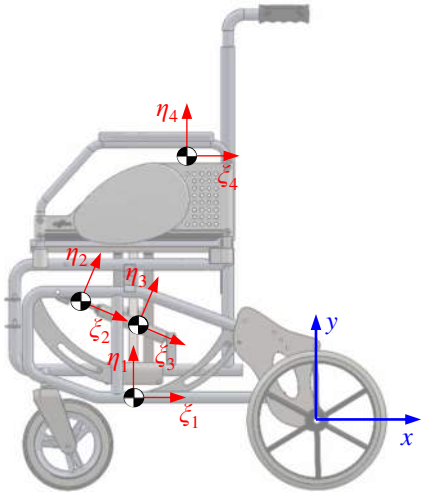

Figure 2. Schematic representation of the centre of mass of the bodies composing the wheelchair.

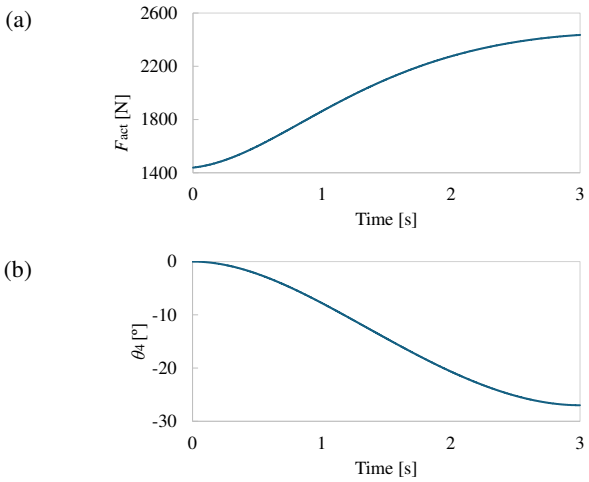

Figure 3. Simulation results: (a) Force exerted by the actuator; (b) Angle of rotation of Body 4.

For the dynamic analysis, a user with a height of 185.0 cm and a mass of 125.0 kg was considered, representing the most critical expected usage condition for the developed wheelchair. The mechanism was modelled as a two-dimensional multibody system, formulated using the Newton-Euler method with cartesian coordinates. The model includes gravitational forces acting on each body and the force applied by the linear actuator is accounted through a kinematic driving constraint. The inertial properties of the bodies considered are provided in Table 1. The numerical simulations were performed using an in-house multibody dynamics code implemented in MATLAB, employing a variable time-step integration algorithm to solve the equations of motion. The simulations consider a 3 s actuation period, representing realistic operating conditions for the wheelchair tilting movement.

Table 1. Inertial properties of the bodies.

Body	**1**	**2**	**3**	**4**
Mass [kg]	6.88	0.26	1.40	137.07
Mass Moment of Inertia [kg·m²]	4.20×10^{-1}	1.54×10^{-5}	1.56×10^{-4}	2.75×10^{1}

3. RESULTS AND DISCUSSION

The tilting motion of the wheelchair was first simulated using the initial design configuration of the mechanism. The analysis showed that a maximum actuator force exceeding 2400 N is required to achieve a tilt angle of 27°, as shown in Figure 3. In order to improve the mechanism performance, an optimisation procedure was applied with the objective of reducing the required actuation force, while maintaining the stability of the system's centre of mass and ensuring an adequate tilt range. The optimisation focused on the geometric configuration of the mechanism, particularly the relative positions of the joints, i.e., the actuator attachment points. The results of this procedure allowed the reconfiguration of the mechanism geometry, leading to an improved design with reduced actuation effort while preserving the desired kinematic behaviour of the tilt-in-space system.

ACKNOWLEDGMENTS

This work is funded by national funds through the FCT – Fundação para a Ciência e a Tecnologia, I.P., within the scope of the project doi.org/10.54499/UID/04436/2025.

REFERENCES

[1] D. Beeckman, A. Van Lancker, A. Van Hecke, and S. Verhaeghe, "A Systematic Review and Meta-Analysis of Incontinence-Associated Dermatitis, Incontinence, and Moisture as Risk Factors for Pressure Ulcer Development," *Res. Nurs. Health,* 37(3), 204-218, 2014.

[2] M. Hischke, and R.F. Reiser, "Effect of Rear Wheel Suspension on Tilt-in-Space Wheelchair Shock and Vibration Attenuation," *PM&T*, 10(10), 1040-1050, 2018.

[3] Y.K. Jan, M. A. Jones, M. H. Rabadi, R. D. Foreman, and A. Thiessen, "Effect of Wheelchair Tilt-in-Space and Recline Angles on Skin Perfusion Over the Ischial Tuberosity in People with Spinal Cord Injury," *Arch. Phys. Med. Rehabil.*, 91(11), 1758–1764, 2010.1

[4] Rodrigues da Silva, M., Marques, F., Silva, M. T. and Flores, P., "A comprehensive review on biomechanical modeling applied to device-assisted locomotion," Archives of Computational Methods in Engineering, vol. 30(3), pp. 1897–1960, 2023.

IMPACT OF NEW JOINING PROCESSES OF NEW MATERIALS OF THE STRUCTURE OF AN AUTOMOBILE ON ITS VEHICLE HANDLING DYNAMICS

Jorge Ambrósio[1], Pedro Millan[1], Lucas da Silva[2]

[1] IDMEC, IST, Av. Rovisco Pais 1, 1049-001 Lisboa, Portugal, {jorge.ambrosio, pedro.millan}@tecnico.ulisboa.pt
[2] INEGI, FEUP, Rua Dr. Roberto Frias, 4200-465 Porto, Portugal, lucas@fe.up.pt

1. INTRODUCTION

The Body-in-White (BiW) is the backbone for the structural integrity of road vehicles, as it connects to the wheels via the suspension to carry the passengers, the goods, and the engine. The use of new materials and structural joints in the BiW requires to understand how the BiW construction affects the vehicle dynamic behavior. To that purpose, suitable computational tools are required. The finite element (FE) method allows to develop models to study the static structural deformation and vibration characteristics of components, and to simulate vehicle crash scenarios. However, these models tend to oversimplify the tire-road interaction and the suspension elements, being often used to study the BiW alone, for noise-vibration-harshness (NVH) analysis, instead of vehicle handling and ride. Flexible multibody (FMB) simulations, on the other hand, allow considering the tire-road contact, the suspension systems, and to include the structural flexibility of components, being suitable to study how BiW construction affects the vehicle dynamics [1].

Some authors have studied the effect of the structural flexibility of the BiW in vehicle dynamics, of which the most relevant works include the works by Gonçalves et al. [1] and Coox et al. [2], respectively. However, most of the works on the matter, including the ones cited, consider simple tubular chassis structures, or, when they consider more complex BiW constructions, the FMB models resort to some kind of simplification of the structure. Additionally, the works are not unanimous when it comes to the relevance of including the BiW flexibility into the multibody simulations of road vehicles as well as the effect of the BiW stiffness in the ride and handling behavior of the vehicles. Therefore, this work extends the understanding on the topic by: (1) incorporating a detailed BiW model in the FMB model of a luxury sports car; (2) discussing the FMB formulation used in the in-house code MUBODyn [3], and; (3) exploring the impact of BiW design in vehicle dynamics. To this end, several simulations are performed using the FMB model of luxury sports car with different BiW structures. The dynamic maneuvers considered include the step steer input, the sine-with-dwell, the sweep steering, bump crossing, among others.

2. METHODS

The methodology used here to study a top end automobile vehicle performance in selected driving scenarios is outlined in Fig. 1. It involves the finite element method (FE) to model the vehicle chassis, in this case the BiW. The original FE model, developed for crash studies is first defeatured, to coarsen the structural parts for which a linear elastic behavior is expected and to eliminate structural details irrelevant to its normal operation behavior, with the purpose of building the flexible multibody model of the car used in this work. With high relevance to this application are the structural adhesives used in the vehicle construction, which are preserved in full detail in the flexible multibody model.

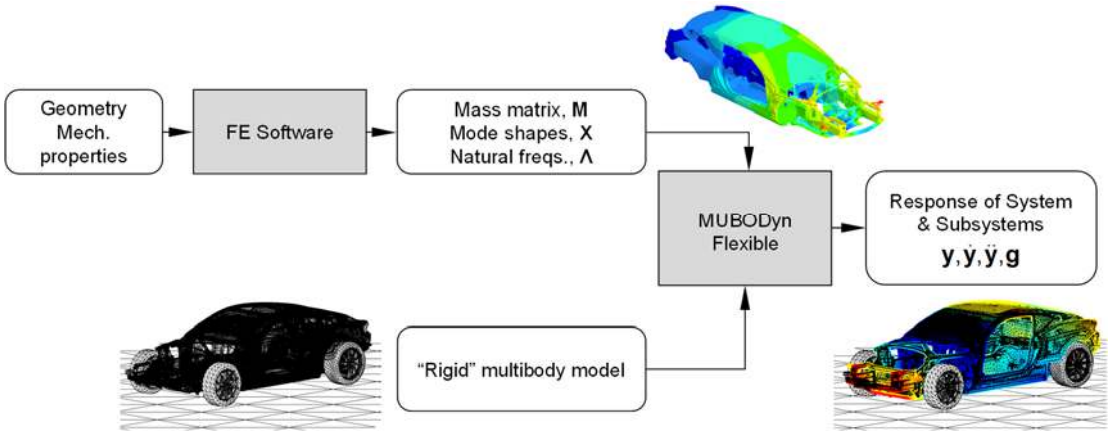

Figure 1. Overview of the data flow of the flexible multibody methodology applied.

The suspension elements of the vehicle are modeled with a rigid multibody description, in which the joints that connect the different rigid bodies are either kinematic constraints or, in some particular cases, joints with clearances with the presence of bushings. The tire-road contact is modelled via the enhanced UA tire model [4] and by a 3D geometric road description [5]. Notice that the tire model used is suitable for steady-state manoeuvers in asphalted road, being unsuited for off-road driving simulations or for extreme transient manoeuvers. Thus, the driving scenarios that can be simulated with the models developed here have to respect these limitations.

3. SIMULATION SCENARIO AND PRELIMINARY RESULTS

The flexible multibody vehicle model is studied in various driving scenarios, selected among those used in applicable norms and automotive manufacturers to evaluate the handling and stability of road vehicles. The results from the combined steer-bump manoeuver are shown in Fig. 2, for several variations of the construction of the vehicle in which the thickness of the structural and windshield adhesives are varied or the different material, with different elasticity modulus, are tested for the sills.

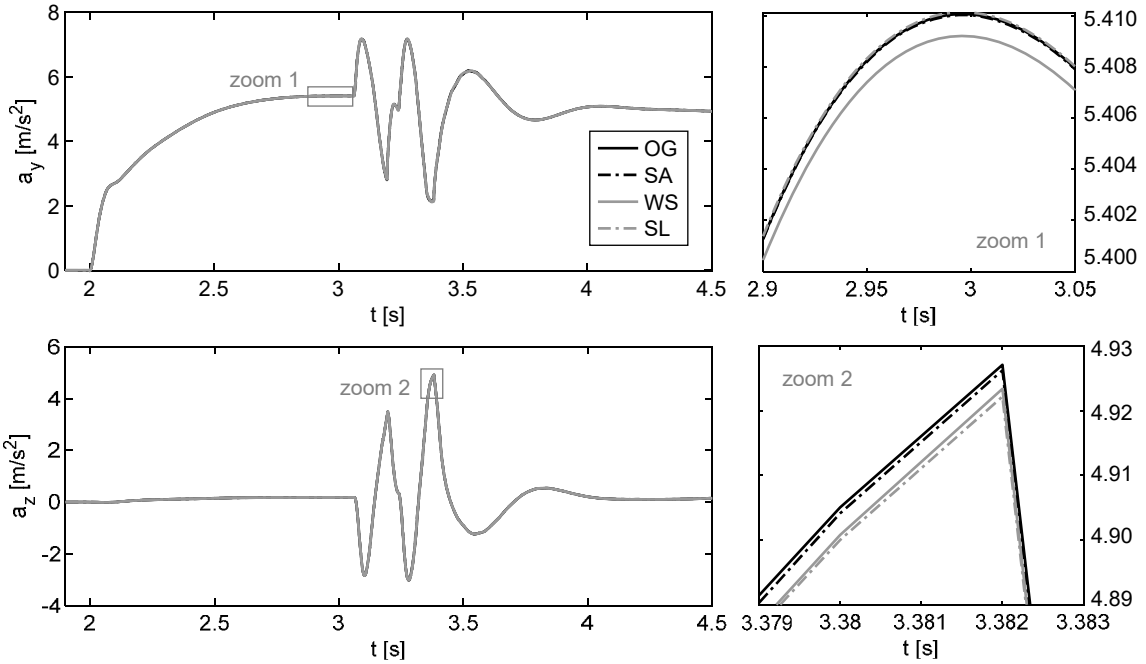

Figure 2. Lateral acceleration (a_y) and vertical acceleration (a_z), during combined step steer input with single sided bump crossing, for the four different extended BiW models (OG-Original; SA-Structural adhesive thickness increase; WS-Windshield adhesive thickness increase; SL-Sills material elasticity modulus increase).

The preliminary results of the vehicle simulations for handling and stability of the diverse driving scenarios allow to conclude that only in extreme construction cases is the vehicle performance sensitive to the adhesive materials and geometries used in its construction. Because the car studied here is a top end sportive model of a well-known car manufacturer, its performance in more demanding transient manoeuvers is of great importance. In these limit conditions, the results allow to understand the trends in the vehicle performance in face of the structural changes in its Body-in-White, thus demonstrating the importance of using the full capabilities of the flexible multibody dynamics methods and the ability to include the bushing elements and clearances in the suspension systems.

ACKNOWLEDGMENTS

The authors acknowledge Fundação para a Ciência e a Tecnologia (FCT) for its financial support via LAETA (project https://doi.org/10.54499/UID/50022/2025).

REFERENCES

[1] J. Ambrósio and J. Gonçalves, “Optimization of vehicle suspension systems for improved comfort of road vehicles using flexible multibody dynamics”. *Nonlinear Dynamics*, 40, 50-62, 2003.

[2] L. Coox, M. Vivet, T. Tamarozzi, T. Geluk, L. Cremers and W. Desmet, “Numerical assessment of the impact of vehicle body stiffness on handling performance”. *Structural Dynamics*, 5, 3711-3723, 2012.

[3] J. Ambrosio, and J. Pombo, *MUltiBOdy DYnamics Analysis Program - MUBODyn: User's Manual*. IDMEC, Lisbon, Portugal, 2006.

[4] P.Millan and J. Ambrósio, “Enhanced UA Tire Model for Computationally Efficient and Stable Multibody Simulations”. *Vehicle System Dynamics*, 63(6), 1157-1184, 2025

[5] P. Millan and J. Ambrósio. “Tire–road contact modelling for multibody simulations with regularised road and enhanced UA tire models”. *Multibody System Dynamics*, 63(1/2), 273–302, 2025

MECHANISM AND MACHINE THEORY SYMPOSIUM 2026

ISBN 978-989-49155-0-8

U.PORTO
FEUP FACULDADE DE ENGENHARIA
UNIVERSIDADE DO PORTO

inegi

University of Minho
School of Engineering

ELSEVIER

IFToMM